2010

A&A 515, A19 (2010)
DOI: 10.1051/0004-6361/200912000

Astronomy & Astrophysics

A lower-limit flux for the extragalactic background light

T. M. Kneiske[1] and H. Dole[2]

[1] Institut für Experimentalphysik, University of Hamburg, Luruper Chaussee 149, 22761 Hamburg, Germany
e-mail: tanja.kneiske@desy.de
[2] Institut d'Astrophysique Spatiale, Université Paris Sud 11 & CNRS (UMR 8617), Bât 121, 91405 Orsay, France

Received 6 March 2009 / Accepted 14 January 2010

ABSTRACT

Context. The extragalactic background light (EBL) contains information about the evolution of galaxies from very early times up to the present. The spectral energy distribution is not known accurately, especially in the near- and mid-infrared range. Upper limits and absolute measurements come from direct observations which might be be polluted by foreground emission, while indirect upper limits can also be set by observations of high energy gamma-ray sources. Galaxy number counts integrations of observable galaxies, missing possible faint sources, give strict lower limits.
Aims. A model is constructed, which reproduces the EBL lower limit flux. This model can be used for a guaranteed minimum correction of observed spectra of extragalactic gamma-ray sources for extragalactic absorption.
Methods. A forward evolution model for the metagalactic radiation field is used to fit recent observations of satelites like Spitzer, ISO, Hubble and GALEX. The model is applied to calculate the Fazio-Stecker relation, and to compute the absorption factor at different redshifts and corrected blazar spectra.
Results. A strict lower-limit flux for the evolving extragalactic background light (and in particular the cosmic infrared background) has been calculated up to a redshift of five. The computed flux is below the existing upper limits from direct observations, and agrees with all existing limits derived from very-high energy gamma-ray observations. The corrected spectra still agree with simple theoretical predictions. The derived strict lower-limit EBL flux is very close to the upper limits from gamma-ray observations. This is true for the present day EBL, but also for the diffuse flux at higher redshift.
Conclusions. If future detections of high redshift gamma-ray sources require a lower EBL flux than derived here, the physics assumptions used to derive the upper limits have to be revised. The lower-limit EBL model is not only needed for absorption features in active galactic nuclei and other gamma-ray sources, but is also essential when alternative particle processes are tested, which could prevent the high energy gamma-rays from being absorbed. It can also be used for a guaranteed interaction of cosmic-ray particles. The model is available online.

Key words. diffuse radiation – Galaxy: formation – infrared: galaxies

1. Introduction

Diffuse extragalactic background radiation has been observed over a broad range of the energy spectrum from radio to high energy gamma-rays. A main contribution at almost all wavelengths (except for the cosmic microwave background, CMB) are faint point sources (sometimes unresolved), emitting in the energy band of interest. Therefore the extragalactic background radiation turns out to be a good tool to study global parameters of source populations and universal physics. The optical to infrared extragalactic diffuse radiation, also called extragalactic background light (EBL), is the relic emission of galaxy formation and evolution and is produced by direct star light (UV and visible ranges) and light reprocessed by the interstellar dust (infrared to sub-millimeter ranges). Minor contribution may include genuine diffuse emission (e.g. galaxy clusters described in Chelouche et al. 2007) or other faint sources (e.g. population III stars as shown in Raue et al. 2009).

While it is possible to measure extragalactic diffuse emission in the sub-mm range (Puget et al. 1996; Hauser et al. 1998; Hauser & Dwek 2001), the EBL is difficult to measure directly in the infrared because of strong foreground contamination. Thus upper limits have been derived by observing the isotropic emission component (see Hauser & Dwek 2001; Kashlinsky 2005 for reviews, as well as Lagache et al. 2005; Dole et al. 2006). Lower limits can be derived by integrated galaxy number counts. The method has been improved during the last years by sensitive telescopes like Spitzer (Werner et al. 2004). This technique gives good constraints at wavelengths shorter than 24 microns. At larger wavelengths, higher confusion and lower sensitivities lead to very small lower limits. To overcome the poor constraints at far-infrared wavelengths, a stacking analysis of near- and mid-infrared sources is used (e.g. Dole et al. 2006) to significantly resolve the cosmic infrared background (CIB), leading to constraining lower limits.

Other constraints on the EBL are coming from the study of distant sources of very high energy gamma-ray emission. High-energy gamma rays traveling through intergalactic space can produce electron-positron pairs in collisions with low energy photons from the extragalactic background light (Nikishov 1962; Goldreich & Morrison 1964; Gould & Schreder 1996; Jelley 1966). Despite this effect, Cherenkov telescopes have discovered a great number of extragalactic high energy gamma-ray sources at unexpected high redshifts. The discovery of 3C279 by the MAGIC telescope collaboration (Albert et al. 2008) shows that 80−500 GeV gamma-rays photons can travel distances from redshift $z = 0.536$ without being too heavily absorbed. From the observation of H2356-309 and 1ES 1101-232, the HESS collaboration derived an upper limit for the EBL between 1 and 4 micron (Aharonian et al. 2006), which is very close to the optical number counts by the *Hubble Space Telescope* (Madau & Pozzetti 2000). They verified their result in

Aharonian et al. (2007a) with the BL Lac 1ES 0347-121 and extended their limit to the mid-infrared using 1ES 0229+200 Aharonian et al. (2007b). The caveat is that the upper limit strongly depends on the assumption of the intrinsic blazar spectrum.

Different types of models for the EBL flux have been developed. The simplest method (backwards evolution) extrapolates present day data or template spectra to high redshift in a certain wavelength range (for the most recent ones see Chary & Elbaz 2001; Malkan & Stecker 2001; Totani & Takeuchi 2002; Lagache et al. 2003, 2004; Xu et al. 2003; King et al. 2003; Stecker et al. 2006; Franceschini et al. 2008). Cosmic chemical evolution models self-consistently describe the temporal history of globally averaged properties of the Universe (Pei et al. 1999), but fall short when it comes to comparisons with data of individual galaxies. Semi-analytical models are invoking specific hierarchical structure formation scenarios to predict the metagalactic radiation field (MRF, i.e. the EBL at various redshifts) (e.g. Balland et al. 2003; Primack 2005). The model used in this paper is an updated version of the Kneiske et al. (2002, 2004) forward evolution model. Simple stellar population models are used to describe the evolution of stars in the universe from their very first formation up to the present. Not only the physics of stars but also the composition and spatial distribution of the interstellar medium are taken into account.

In this work lower-limit EBL data are used to derive a lower-limit EBL flux model. In the next section, the data and their uncertainties are discussed. The minimum EBL flux model is derived in the third section by choosing parameters for the global star formation and the interstellar medium. The results are presented in the fourth section, together with the resulting optical depth for gamma-rays in the universe. Throughout this paper, a cosmology with $h = 0.72$, $\Omega_M = 0.3$ and $\Omega_\Lambda = 0.7$ is adopted.

2. Current lower limits on the cosmic optical and infrared backgrounds

Lower limits on the extragalactic background light measurements are reviewed briefly. Most are derived from the integration of number counts, not from direct measurements of surface brightness, which is subject to strong foreground emission contamination. This method is based on the simple counting of detected galaxies on a given sky area of a deep survey, a completeness correction, and the flux integration of the number counts. Variance due to large-scale structure may affect the results and is usually taken into account in the error bars. However, another source of uncertainty at near-infrared wavelengths is the usually poor detected galaxy statistics at high flux densities and the subtraction of stars; these uncertainties affect the number counts at high flux densities and can give different results when integrating them to get the background lower limit. Any model of the EBL should thus lie above these observed limits. In the past not all EBL models met this criterion and are therefore not realistic and in contradiction with the data. The lower limit data are shown in Fig. 3 as data points with the errors discussed below.

2.1. Ultraviolet and visible EBL

Counts and integration were done by Xu et al. (2005) (*GALEX*); Brown et al. (2000) and Gardner et al. (2000) (*HST/STIS*); Madau & Pozzetti (2000) and Totani et al. (2001) (*HST/WFPC2*).

2.2. Near- and mid-infrared EBL

The integration of number counts on deep surveys done with the HST was done by Madau & Pozzetti (2000) and Thompson 2003 Thompson et al. (2007) (*NICMOS*), and Totani et al. (2001) (*SUBARU*).

Fazio et al. (2004a) obtained number counts with *Spitzer/IRAC* at 3.6, 4.5, 5.8 and 8.0 μm, and derived lower limits. These counts have been confirmed by Magdis et al. (2008) at these four wavelengths and by Franceschini et al. (2006) at 3.6 μm. At 8.0 μm, however, Franceschini et al. (2008) recomputed the counts at larger flux densities with better statistics and re-integrated the whole number counts; they claim that their integration gives a 50% smaller value that Fazio et al. (2004a). The value published by Franceschini et al. (2008) will be used as a lower value at 8.0 μm. Similarly the 5.8 μm estimate would need to be recomputed. At 3.6 μm, Levenson & Wright (2008) integrated the extrapolated number counts (with constraints from the image noise) and came close to the DIRBE minus 2MASS value, giving an estimate of the CIB at this wavelength. As a strict 3.6 μm lower limit, the Fazio et al. (2004a) value is used. It should be noticed though that IRAC counts at this wavelength may not be that reliable when integrated to give CIB lower limits, although number counts are very accurately measured in deep surveys at faint flux densities (e.g. agreement between Fazio et al. (2004a), Franceschini et al. (2006) and Magdis et al. (2008) at 3.6 μm). Counts are contaminated by the presence of bright and faint stars and extended local galaxies, biasing the measure at high and intermediate flux densities, where deep surveys have very poor statistics. Deep and shallow surveys have better statistics, but the star contribution subtraction could be inaccurate and could dominate the systematics uncertainty. Nevertheless the data point will be included in our analysis, where the error bars represent the large uncertainties.

In the mid-infrared, the counts by Elbaz et al. (2002) at 15 μm with *ISOCAM* are used. At 24 μm with *Spitzer/MIPS*, the counts by Papovich et al. (2004), Marleau et al. (2004) and Chary et al. (2004), Rodighiero et al. (2006) are used. At these wavelengths, contributions of stars and extended galaxies are negligible. The stellar spectra can be described Rayleigh-Jeans approximation and the point spread functions are larger than 6 arcsec. The lower limits are therefore reliable.

2.3. Far-infrared and sub-millimeter EBL

Above 30 μm wavelength, another method than integrating the number counts is used, because individual detected far-infrared sources do not contribute more than 25% to the background (e.g. Dole et al. (2004), Frayer et al. (2006) except in the GOODS 70 μm survey (about 60% Frayer et al. (2006b). This method consists of stacking a longer-wavelength signal at the position of known short wavelength sources and then measuring the resulting total flux, which is also a lower limit. At 70 μm and 160 μm, the lower limits of Dole et al. (2006) obtained with a stacking analysis of *Spitzer/MIPS* 24 μm sources is used. The submillimeter *COBE/FIRAS* spectrum of direct detection comes from Lagache et al. (2000).

3. Lower-limit EBL model

In this section an EBL model is constructed which reproduces the EBL flux lower limits from source counts. The EBL model is described in detail in Kneiske et al. (2002) and the main features are summarized below. The idea is to describe cosmological

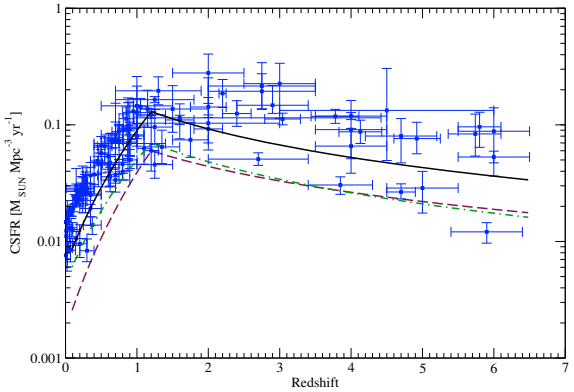

Fig. 1. Comoving cosmic star formation rate. The data are taken from 2006. The solid line shows the model total star formation rate, while the dashed and dashed-dotted line accounts the contribution from dust-poor and dust-rich regions respectively.

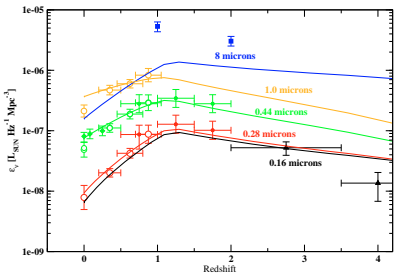

Fig. 2. Comoving emissivity as a function of redshift. The lines are calculated for the wavelength indicated in the figure and have to be compared with the data points of the same color. Data come from: Ellis et al. (1996), Lilly et al. (1996), Connolly et al. (1997), Pozzetti et al. (1998), Caputi et al. (2007).

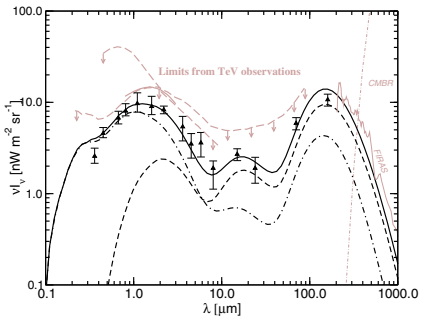

Fig. 3. Extragalactic Background Light Spectral Energy Distribution. Data are lower limits (filled triangles), discussed in Sect. 2. The total model flux is shown as black solid line, together with the contribution from dust rich (dashed line) and dust poor star forming regions (dot-dashed line). The red dashed line are model-dependant upper limits on the EBL as derived from high energy blazar observations (Aharonian et al. 2006; Aharonian et al. 2007a,b; Albert et al. 2008; Mazin & Raue 2007). Other long-wavelength detections are plotted: the submillimeter EBL and the CMB.

stellar evolution with a simple stellar population model depending on different stellar masses. The cosmological evolution is set by an input comoving star formation rate density (SFR). The model computes emissivities and the EBL flux, which can be directly compared with observations at individual wavelengths. Two different star forming regions are distinguished phenomenologically: "optical" star forming regions with low extinction due to the presence of dust ($E(B-V) = 0.06$), and "infrared" star forming regions with higher extinction aiming at reproducing the emission properties of luminous and ultra-luminous infrared galaxies (LIRG and ULIRG; $E(B-V) = 0.8$). For these two populations, spectral energy distributions (SED) are generated with a spectral synthesis model, adding a consistent model accounting for dust absorption and reemission. Three components of dust are taken into account by modified black body spectra with different temperatures. The goal is thus to fit the EBL observed lower limit by adjusting the input SFR and dust parameters.

The EBL model flux was fitted to the observed lower limits summarized in the last section by integrating the emissivities on the redshift range zero to two. This takes into account the fact that data are only able to resolve galaxies up to a certain redshift, which depends on the flux limit of the instrument and the survey. It is not possible to give the exact maximum redshift for each survey, since the redshift is not known automatically for each detected source. The chosen maximum redshift of two seems a good average for most surveys taken into account. Our result is only weakly dependent on this parameter. The model parameters were chosen to minimize the χ^2 between EBL observed limits and the model.

4. Results and discussion

4.1. Cosmic star formation rate and emissivity

The model output cosmic star formation rate is shown in Fig. 1. It is lower by a factor of two to three than the data compiled by Hopkins & Beacom (2006). This is not surprising, as a lower limit EBL is used, which by definition is missing some amount of emission yet the shape is consistent with the data.

Since the star formation rate is a model-dependent value which shows a wide range of scatter, it is useful to compare the model emissivities at different redshifts with integrated luminosity functions at various wavelengths. As shown in Fig. 2, the agreement between optical ($\lambda \leq 1\ \mu$m) data and the model emissivity is good for redshifts below three. The model, however, is underestimating the emissivity at 8 μm by a factor three to five. The origin of this discrepancy might be twofold: 1) the simplistic galaxies' spectral energy distribution used, which lack detailed aromatic bands and have a very small grains continuum description; and 2) a slight overestimation of the observed 8 μm emissivity, obtained trough the rest-frame 8 μm luminosity function integration (Caputi et al. 2007) and an extrapolation to the infrared bolometric luminosity density. Despite the care taken, this last operation might slightly overestimate the emissivity. This might be the reason why the model does not strongly disagree with the EBL shape at 8 μm (Fig. 3), despite a disagreement with the 8 μm emissivity.

4.2. Extragalactic background light (EBL)

The observed EBL lower limits (Sect. 2) are plotted in Fig. 3 together with the model. The model reproduces the data well, keeping in mind that a physical model was used instead of a functional fit, and that the minimum χ^2 used. Almost all EBL flux (wavelengths $0.3 \leq \lambda \leq 160\ \mu$m) comes from galaxies up to a redshift of two, as expected (e.g. Lagache et al. 2005). There is no significant change in the computed EBL spectrum when including emission from redshifts above two, since the cosmic star formation rate drops by half an order of magnitude. The robustness of our EBL derivation is checked by integrating the emissivities up to a redshift of $z = 5$: this does not change the final result by more than 4%. The optical and infrared EBL are dominated by their respective components (optical and infrared galaxies), and the transition region between both contributions, located around 5 microns, can be probed by *Spitzer*. The 5.8 micron data point lies above our model flux by more than 1σ. As discussed in Sect. 2, this point might suffer from a poor statistics. At 8 micron, the new estimate of Franceschini et al. (2008) lies on our model, but the Fazio et al. (2004a,b) estimate is higher. While a consistent new estimate of all IRAC points would be needed, it is possible yet to conclude if this discrepancy is a common feature of EBL models (see also Franceschini 2008; Primack et al. 2008), and/or if the data points around 5 microns are overestimated (this last possibility cannot be ruled out, as discussed in Sect. 2). Finally, our EBL model lies below the observed upper limits derived from gamma-ray observations, as expected.

4.3. EBL and γ-ray absorption at high redshift

The lower limit EBL model can be used to calculate the optical depth for photon-photon pair production. The effect is mainly important for extragalactic sources like blazars (Salamon & Stecker 1998; Primack et al. 1999; Kneiske et al. 2004) or gamma-ray bursts. The absorption can result in a drastic change of the high energy spectrum or even make it impossible to observe the source at all at gamma-ray energies. The effect of absorption for extragalactic gamma-ray sources at different redshift is shown in Fig. 4. The EBL flux is plotted next to the absorption factor $\exp(-\tau)$ at the same redshift. The spectral region of the EBL flux responsible for the so cut-off region is indicated by vertical red lines and arrows. The cosmic microwave background is also plotted as a dot-dashed line on the right of the EBL flux diagram. The results of our new lower-limit EBL model are compared with the so called "best-fit" EBL model from Kneiske et al. (2004). It is clearly visible that a lower EBL flux leads to an absorption closer to one, which means less absorption of gamma-ray photons in the cut-off region.

Table 1. Model input parameters (definitions see Kneiske et al. 2004).

	α	β	z_p	$\dot{\rho}_*(z_p)$ $[M_\odot\ \mathrm{Mpc}^{-3}\ \mathrm{yr}^{-1}]$
Strict lower-limit model				
SFR_{OPT}	3.5	−1.2	1.2	0.07
SFR_{LIG}	4.5	−1.0	1.2	0.06
$f_{esc} = 0$				
$c_2 = 10^{-24}$				

4.4. Fazio-Stecker relation

The attenuation of gamma-rays can also be expressed by the Fazio-Stecker relation, also known as the gamma-ray horizon. It is shown in Fig. 5 for a source-independent description. The redshift of a high energy gamma-ray source is plotted against gamma-ray energy for an optical depth $\tau_{\gamma\gamma}(E_c, z) = 1$ (black line), $\tau_{\gamma\gamma}(E_c, z) = 2$ (green line), $\tau_{\gamma\gamma}(E_c, z) = 3$ (red line). These lines are calculated by the lower-limit model derived in this work. Limits from blazar observations are plotted as well taken from Albert et al. (2008). The blazars all lie in the transparent region ($\tau < 1$) according to our model. For a given energy, blazars at a slightly higher redshift than already measured might be detected. All data agree with the lower limit model. Although a lower-limit EBL has been used, there is a little room left for a higher EBL flux resulting in a higher optical depth for high energy gamma-rays.

Finally the result is compared with the models by Primack (2005), Albert et al. (2008) and Stecker et al. (2006) (dashed, dot-dot-dashed, and dot-dash lines). Note that the EBL "upper-limit" model derived in Albert et al. (2008) is based on the same code as presented here, but with a completely different set of parameters, like star-formation rate, dust and gas opacity etc. (see Table 1). Our lower-limit model predicts the smallest correction for extragalactic absorption, as expected, except at very low redshifts ($z < 0.2$), where the Primack (2005) model is slightly above ours. This can be explained by the underestimation in the far-infrared of this model, below the lower limits.

5. Conclusions

A lower-limit EBL model was derived utilising the lower limit data from the integration of galaxy number counts from the optical to the far infrared region. The model takes into account time-evolution of galaxies and includes the effect of absorption and re-emission of the interstellar medium. To get such a low EBL, the assumption of a quite low cosmic SFR has to be made, which has a maximum at a redshift of 1.2 of about 0.1 $M_\odot\ \mathrm{yr}^{-1}\ \mathrm{Mpc}^{-3}$ and falls to a value of about 0.03 at a redshift of 5. As expected the present-day lower-limit EBL is still below the upper limits derived so far from the process of pair production with very high energy gamma-ray emission by BL Lacs (see red-dashed line in Fig. 3).

This model can be used to calculate the interaction of cosmic-ray particles with ambient photon fields. Cosmic-ray protons loose energy due to pion production with stellar photons if their energy lies in the range between 10^{16} and 10^{19} eV. Using the EBL model a minimum, guaranteed energy loss of protons can be derived.

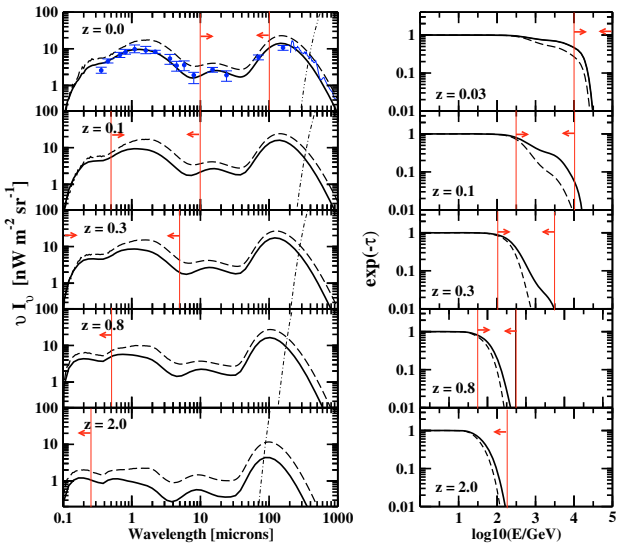

Fig. 4. *left*: comoving flux of the extragalactic background light at five different redshifts. The solid line represents the lower-limit EBL introduced here, while the dashed line is the old "best-fit" model described in Kneiske et al. (2004). The spectral EBL region responsible for the cut-off at high energy is represented by thin vertical lines and arrows. *right*: extinction factor of gamma-rays as a function of gamma-ray photon energy at five different redshifts.

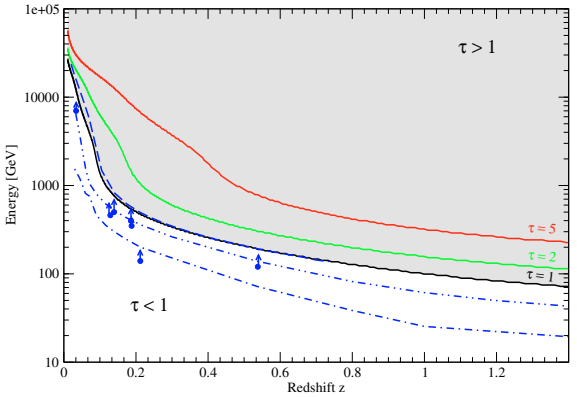

Fig. 5. Gamma-ray horizon $\tau_{\gamma\gamma}(E_c, z) = 1$ (black line), $\tau_{\gamma\gamma}(E_c, z) = 2$ (green line), $\tau_{\gamma\gamma}(E_c, z) = 3$ (red line) for the lower limit EBL model derived in this work. Observed limits (dots) are taken from Fig. 3 of Albert et al. (2008). For comparison, horizons based on three other EBL models are shown in blue, *from the bottom*: Stecker et al. 2006 (dot-dashed), Albert et al. (2008) (dot-dot-dashed) and Primack (2005)(dashed).

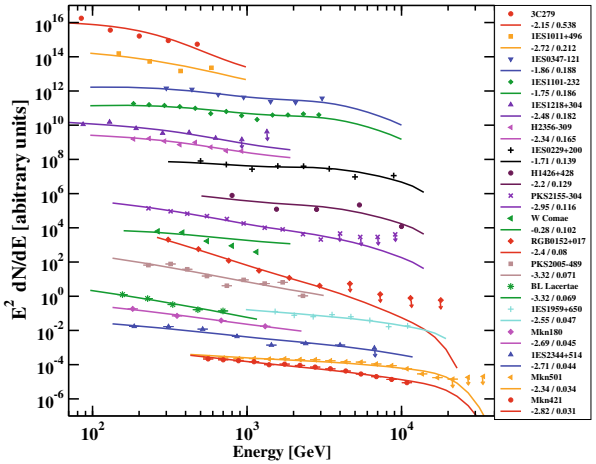

Fig. A.1. Observed spectral energy distributions for blazars (indicated at the right of the figure): dots (data), lines (model). The sources are ordered by their redshift, from high (*top*) to low redshift (*bottom*). The total flux is normalized for a better visualization. The lines are model spectra corrected for minimum EBL absorption, described in the text. Numbers on the right indicate the spectral index α and the redshift of the source.

A lower-limit EBL model is also essential to test exotic particle physics scenarios in the universe. Particles like axions (Sanchez-Conde et al. 2009) or hidden photons (Zechlin et al. 2008) can prevent high energy gamma-ray photons from being absorbed. Other mechanisms like Lorentz invariance violations (Protheroe & Meyer 2000) can only be studied if the uncertainty of the EBL is as small as possible. A minimum absorption due to a guaranteed low energy photon field from galaxies is essential to look for such particles and effects.

This was used to compute the absorption factor for gamma-rays and observed blazar spectra at some selected redshifts. The Fazio-Stecker relation, which describes the absorption of high energy gamma-rays from extragalactic sources as a function of redshift was also calculated. From this it can be concluded that the lower-limit EBL flux can be used to correct high energy gamma-ray spectra at all redshifts. The minimum correction done with this model seems to lead to realistic intrinsic gamma-ray spectra of AGN even at high redshift, which can be modeled with standard acceleration scenarios in relativistic jets. Up to now it was only possible to show the agreement between lower-limit data and indirect upper limits for the present day EBL flux. In this paper we show that also at higher redshift only an EBL close to a lower-limit extragalactic diffuse photon flux, taking into account the complete cosmic evolution of galaxies, agrees with upper limits from high redshift blazar observations.

The recent detection of 3C279 blazar at $z = 0.536$ by the MAGIC collaboration Albert et al. (2008), Errando et al. 2009) has brought up the question of the transparency of the Universe to the γ-rays and of the level of the cosmic infrared background (e.g. Aharonian et al. 2006; Aharonian et al. 2007a,b; Stecker & Scully 2009). We confirm that the current lower limits of the EBL flux also at a redshift as high as $z = 0.536$ are fully compatible with γ-ray observations, both on the blazar SED and on the γ-ray horizon.

If in the future EBL limits from TeV observations become lower, maybe even dropping below the strict lower-limit EBL, the assumptions leading to EBL limits from gamma-ray observations may have to be revised. On the other hand, the discovery of AGN showing a spectral behavior which disagrees with our derived gamma-ray horizon would challenge AGN physics.

The lower limit EBL data, the EBL flux and optical depth as a function of wavelength/energy and redshift are electronically available[1].

Acknowledgements. We thank Andrew Hopkins for providing us with an electronic form of the CSFR compilation. We thank Wolfgang Rhode and Martin Raue for useful discussions. T.K. acknowledges the support of DFG grant Kn 765/1-2. H.D. acknowledges the support of ANR-06-BLAN-0170.

Appendix A: Application to the SED of blazars

The lower-limit EBL model is used to calculate spectral energy distribution for observed TeV-blazars. To compare the spectra with the observations, a single power-law is employed with a spectral index indicated below the source name in the table right to Fig. A.1. Figure A.1 shows the spectra of blazars sorted by increasing redshift (from bottom to top) and multiplied by an arbitrary constant to ease visibility. The spectral index and normalization has been taken from a fit of the corrected data points of each source. Then the power law was multiplied by the extinction factor shown in Fig. 4 depending on the redshift of the gamma-ray source. With this method we get a continuous spectrum for each source.

The intrinsic spectra can all be described by power laws with spectral indices still in agreement with very simple jet models in AGN, like the synchrotron-self Compton model (SSC). This was not surprising, given the lower limit EBL which has been used. But this might be another indication that the opacity to γ-rays is still low ($\tau < 1$), even at higher redshift $z \sim 0.5$.

[1] In Orsay: http://www.ias.u-psud.fr/irgalaxies/ and in Hamburg: http://www.astroparticle.de.

References

Aharonian, F., Akhperjanian, A. G., Bazer-Bachi, A. R., et al. 2006, Nature, 440, 1018
Aharonian, F., Akhperjanian, A. G., Barres de Almeida, U., et al. 2007a, A&A, 473, L25
Aharonian, F., Akhperjanian, A. G., Barres de Almeida, U., et al. 2007b, A&A, 475, L9
Albert, J., Aliu, E., Anderhub, H., et al. 2008, Science, 320, 1752
Balland, C., Devriendt, J., & Silk, J. 2003, MNRAS, 343, 107
Brown, T. M., Kimble, R. A., Ferguson, et al. 2000, AJ, 120, 1153
Caputi, K. I., Lagache, G., Yan, L., et al. 2007, ApJ, 660, 97
Chary, R., & Elbaz, D. 2001, ApJ, 556, 562
Chary, R., Casertano, S., Dickinson, M. E., et al. 2004, ApJS, 154, 80
Chelouche, D., Koester, B. P., & Bowen, D. V. 2007, ApJ, 671, 97
Connolly, A. J., Szalay, A. S., Dickinson, M., et al. 1997, ApJ, 486, L11
Dole, H., Le Floc'h, E., Pérez-Gonzalez, P., et al. 2004, ApJS, 154, 87
Dole, H., Lagache, G., Puget, J.-L., et al. 2006, A&A, 451, 417
Elbaz, D., Flores, H., Chanial, P., et al. 2002, A&A, 381, L1
Ellis, R. S., Colless, M., Broadhurst, T., et al. 1996, MNRAS, 280, 235
Errando, M., Bock, R., Kranich, D., et al. 2009, AIPC, 1085, 423
Fazio, G. G., Ashby, M. L. N., Barmby, P., et al. 2004a, ApJS, 154, 39
Fazio, G. G., Hora, J. L., Allen, L. E., et al. 2004b, ApJS, 154, 10
Franceschini, A., Rodighiero, G., Cassata, P., et al. 2006, A&A, 453, 397
Franceschini, A., Rodighiero, G., & Vaccari, M. 2008, A&A, 487, 837
Frayer, D., Fadda, D., Yan, L., et al. 2006, AJ, 131, 250
Frayer, D., Huynh, M. T., Chary, R., et al. 2006, ApJ, 647, L9
Gardner, J. P., Brown, T. M., & Ferguson, H. C. 2000, ApJ, 542, L79
Goldreich, P., & Morison, P., JETP, 18, 239
Gould, R. S., & Schreder, G. 1966, Phys. Ref. Lett., 16, 252
Hauser, M. G., Arendt, R. G., Kelsall, T., et al. 1998, ApJ, 508, 25
Hauser, M. G., & Dwek, E. 2001, ARA&A, 39, 249
Hopkins, A. M., & Beacom J. F. 2006, ApJ, 651, 142
Jelley, J. V. 1966, Phys. Ref. Lett., 16, 479
Kashlinsky, A. 2005, ApJ, 633, 5
King, A. J., & Rowan-Robinson, M. 2003, MNRAS, 339, 260
Kneiske, T. M., Mannheim, K., & Hartmann, D. 2002, ApJ, 386, 1
Kneiske, T. M., Bretz, T., Mannheim, K., et al. 2004, ApJ, 413, 807
Lagache, G., Haffner, L. M., Reynolds, R. J., et al. 2000, A&A, 354, 247
Lagache, G., Dole, H., & Puget, J.-L. 2003, MNRAS, 338, 555
Lagache, G., Dole, H., Puget, J.-L., et al. 2004, ApJS, 154, 112
Lagache, G., Puget, J.-L., & Dole, H. 2005, ARA&A, 43, 727
Levenson, L. R., & Wright, E. L. 2008, ApJ, 683, 585
Lilly, S. J., Le Fevre, O., Hammer, F., et al. 1996, ApJ, 460, L1
Madau, P., & Pozzetti, L. 2000, MNRAS, 312, L9
Magdis, G. E., Rigopoulou, D., Huang, J. S., et al. 2008, MNRAS, 386, 11
Malkan, M. A., & Stecker, F. W. 2001, ApJ, 555, 641
Marleau, F. R., Fadda, D., Storrie-Lombardi, L. J., et al. 2004, ApJS, 154, 66
Mazin, D., & Raue, M. 2007, A&A, 471, 439
Nikishov, A. I. 1962, Sov. Phys. JETP, 14, 393
Papovich, C., Dole, H., Egami, E., et al. 2004, ApJS, 154, 70
Pei, Y. C., & Fall, S. M., & Hauser, M. G. 1999, ApJ, 522, 604
Pozzetti, L., Madau, P., & Zamorani, G., et al. 1998, MNRAS, 298, 1133
Primack, J. R., Bullock, J. S., Somerville, R. S., et al. 1999, APh, 11, 93
Primack, J. 2005, AIPC, 745, 23
Primack, J., Gilmore, R. C., & Somerville, R. S. 2008, AIPC, 1085, 71
Protheroe, R. J., & Meyer, H. 2000, PhLB, 493, 1
Puget, J.-L., Abergel, A., Bernard, J.-P., et al. 1996, A&A, 308, L5
Raue, M., Kneiske, T. M., & Mazin, D. 2009, A&A, 498, 25
Rodighiero, G., Lari, C., Pozzi, F., et al. 2006, MNRAS, 371, 1891
Salamon, M. H., & Stecker, F. W. 1998, ApJ, 439, 547
Sánchez-Conde, M. A., Paneque, D., Bloom, E., Prada, F., & Domínguez, A. 2009, Phys. Rev. D, 79, 123511
Stecker, F. W., Malkan, M. A., & Scully, S. T., 2006 ApJ, 648, 774
Stecker, F. W., & Scully, S. T. 2009, ApJ, 691, L91
Thompson, R. I. 2003, ApJ, 596, 748
Thompson, R. I., Eisenstein, D., Fan, X., et al., 2007, ApJ, 657, 669
Totani, T., & Takeuchi, T. T. 2001, ApJ, 570, 470
Totani, T., Yoshii, Y., Iwamuro, F., et al. 2001, ApJ, 550, L137
Werner, M., Roellig, T. L., Low, F. J., et al. 2004, ApJS, 154, 1
Xu, C. K, Donas, J., Arnouts, S., et al. 2005, ApJ, 619, L11
Zechlin, H.-S., Horns, D., & Redondo, J. 2008, AIPC, 1085, 727

A&A 512, A78 (2010)
DOI: 10.1051/0004-6361/200913279

Astronomy & Astrophysics

Spitzer deep and wide legacy mid- and far-infrared number counts and lower limits of cosmic infrared background⋆

M. Béthermin[1], H. Dole[1], A. Beelen[1], and H. Aussel[2]

[1] Institut d'Astrophysique Spatiale (IAS), Bt. 121, 91405 Orsay, France; Université Paris-Sud 11 and CNRS (UMR8617)
e-mail: mattieu.bethermin@ias.u-psud.fr
[2] Laboratoire AIM, CEA/DSM-CNRS-Université Paris Diderot, IRFU/Service d'Astrophysique, Bt. 709, CEA-Saclay, 91191 Gif-sur-Yvette Cedex, France

Received 11 September 2009 / Accepted 5 January 2010

ABSTRACT

Aims. We aim to place stronger lower limits on the cosmic infrared background (CIB) brightness at 24 μm, 70 μm and 160 μm and measure the extragalactic number counts at these wavelengths in a homogeneous way from various surveys.
Methods. Using *Spitzer* legacy data over 53.6 deg^2 of various depths, we build catalogs with the same extraction method at each wavelength. Completeness and photometric accuracy are estimated with Monte-Carlo simulations. Number count uncertainties are estimated with a counts-in-cells moment method to take galaxy clustering into account. Furthermore, we use a stacking analysis to estimate number counts of sources not detected at 70 μm and 160 μm. This method is validated by simulations. The integration of the number counts gives new CIB lower limits.
Results. Number counts reach 35 μJy, 3.5 mJy and 40 mJy at 24 μm, 70 μm, and 160 μm, respectively. We reach deeper flux densities of 0.38 mJy at 70, and 3.1 at 160 μm with a stacking analysis. We confirm the number count turnover at 24 μm and 70 μm, and observe it for the first time at 160 μm at about 20 mJy, together with a power-law behavior below 10 mJy. These mid- and far-infrared counts: 1) are homogeneously built by combining fields of different depths and sizes, providing a legacy over about three orders of magnitude in flux density; 2) are the deepest to date at 70 μm and 160 μm; 3) agree with previously published results in the common measured flux density range; 4) globally agree with the Lagache et al. (2004) model, except at 160 μm, where the model slightly overestimates the counts around 20 and 200 mJy.
Conclusions. These counts are integrated to estimate new CIB firm lower limits of $2.29^{+0.09}_{-0.09}$ nW m^{-2} sr^{-1}, $5.4^{+0.4}_{-0.4}$ nW m^{-2} sr^{-1}, and $8.9^{+1.1}_{-1.1}$ nW m^{-2} sr^{-1} at 24 μm, 70 μm, and 160 μm, respectively, and extrapolated to give new estimates of the CIB due to galaxies of $2.86^{+0.19}_{-0.16}$ nW m^{-2} sr^{-1}, $6.6^{+0.7}_{-0.6}$ nW m^{-2} sr^{-1}, and $14.6^{+7.1}_{-2.9}$ nW m^{-2} sr^{-1}, respectively. Products (point spread function, counts, CIB contributions, software) are publicly available for download at http://www.ias.u-psud.fr/irgalaxies/

Key words. cosmology: observations – diffuse radiation – galaxies: statistics – galaxies: evolution – galaxies: photometry – infrared: galaxies

1. Introduction

The extragalactic background light (EBL) is the relic emission of all processes of structure formation in the Universe. About half of this emission, called the Cosmic Infrared Background (CIB) is emitted in the 8–1000 μm range, and peaks around 150 μm. It is essentially due to the star formation (Puget et al. 1996; Fixsen et al. 1998; Hauser et al. 1998; Lagache et al. 1999; Gispert et al. 2000; Hauser & Dwek 2001; Kashlinsky 2005; Lagache et al. 2005).

The CIB spectral energy distribution (SED) is an important constraint for the infrared galaxies evolution models (e.g. Lagache et al. 2004; Franceschini et al. 2010; Le Borgne et al. 2009; Pearson & Khan 2009; Rowan-Robinson 2009; Valiante et al. 2009). It gives the budget of infrared emission since the first star. The distribution of the flux of sources responsible for this background is also a critical constraint. We propose to measure the level of the CIB and the flux distribution of the sources at 3 wavelengths (24 μm, 70 μm and 160 μm).

In the 1980's, the infrared astronomical satellite (IRAS) and COBE/DIRBE performed the first mid-infrared (MIR) and far-infrared (FIR) full-sky surveys. Nevertheless, the detected sources were responsible for a very small part of the CIB. Between 1995 and 1998, the ISO (infrared space observatory) performed deeper observations of infrared galaxies. Elbaz et al. (2002) resolved into the source more than half of the CIB at 15 μm. At larger wavelengths, the sensitivity and angular resolution was not sufficient to resolve the CIB (Dole et al. 2001).

The *Spitzer* space telescope (Werner et al. 2004), launched in 2003, has performed deep infrared observations on wide fields. The multiband imaging photometers for *Spitzer* (MIPS) (Rieke et al. 2004) mapped the sky at 24 μm, 70 μm and 160 μm. About 60% of the CIB was resolved at 24 μm (Papovich et al. 2004) and at 70 μm (Frayer et al. 2006). Because of confusion (Dole et al. 2003), only about 7% were resolved at 160 μm (Dole et al. 2004). Dole et al. (2006) managed to resolve most of the 70 μm and 160 μm by stacking 24 μm sources.

The cold mission of Spitzer is over, and lots of data are now public. We present extragalactic number counts built homogeneously by combining deep and wide fields. The large sky surface used significantly reduces uncertainties on number counts. In order to obtain very deep FIR number counts, we used a stacking analysis and estimate the level of the CIB in the three MIPS bands with them.

⋆ Counts and CIB contributions are only available in electronic form at the CDS via anonymous ftp to cdsarc.u-strasbg.fr (130.79.128.5) or via http://cdsweb.u-strasbg.fr/cgi-bin/qcat?J/A+A/512/A78

Table 1. Size, 80% completeness flux density, and calibration scaling factor (see Sect. 2.1) of the used fields.

Field name	Surface area			80% completeness flux			Scaling factor		
	24 μm	70 μm	160 μm	24 μm	70 μm	160 μm	24 μm	70 μm	160 μm
	deg^2			μJy	mJy				
FIDEL eCDFS	0.23	0.19	–	60.	4.6	–	1.0157	1	–
FIDEL EGS	0.41	–	0.38	76.	–	45.	1.0157	–	0.93
COSMOS	2.73	2.41	2.58	96.	7.9	46.	1	0.92	0.96
SWIRE LH	10.04	11.88	11.10	282.	25.4	92.	1.0509	1.10	0.93
SWIRE EN1	9.98	9.98	9.30	261.	24.7	94.	1.0509	1.10	0.93
SWIRE EN2	5.36	5.34	4.98	267.	26.0	90.	1.0509	1.10	0.98
SWIRE ES1	7.45	7.43	6.71	411.	36.4	130.	1.0509	1.10	0.98
SWIRE CDFS	8.42	8.28	7.87	281.	24.7	88.	1.0509	1.10	0.98
SWIRE XMM	8.93	–	–	351.	–	–	1.0509	–	–
Total	53.55	45.51	42.91						

Notes. Some fields are not used at all wavelengths.

2. Data, source extraction and photometry

2.1. Data

We took the public *Spitzer* mosaics[1] from different observation programs: the GOODS/FIDEL (PI: M. Dickinson), COSMOS (PI: D. Sanders) and SWIRE (PI: C. Lonsdale). We used only the central part of each field, which was defined by a cut of 50% of the median coverage for SWIRE fields and 80% for the other. The total area covers 53.6 deg^2, 45.5 deg^2, 42.9 deg^2 at 24 μm, 70 μm and 160 μm respectively. The surface of the deep fields (FIDEL, COSMOS) is about 3.5 deg^2. Some fields were not used at all wavelengths for different reasons: There is no public release of FIDEL CDFS data at 160 μm; the pixels of the EGS 70 μm are not square; XMM is not observed at 70 and 160 μm. Table 1 summarises the field names, sizes and completenesses.

In 2006, new calibration factors were adopted for MIPS (Engelbracht et al. 2007; Gordon et al. 2007; Stansberry et al. 2007). The conversion factor from instrumental unit to MJy/sr is 0.0454 (resp. 702 and 41.7) at 24 μm (resp. 70 μm and 160 μm). The COSMOS GO3 and SWIRE (released 22 Dec. 2006) mosaics were generated with the new calibration. The FIDEL mosaics were obtained with other factors at 24 μm and 160 μm (resp. 0.0447 and 44.7). The 70 μm and 160 μm COSMOS mosaics were color corrected (see Sect. 2.3). Consequently we applied a scaling factor (see Table 1) before the source extraction to each mosaic to work on a homogeneous sample of maps (new calibration and no color correction).

2.2. Source extraction and photometry

The goal is to build homogeneous number counts with well-controlled systematics and high statistics. However, the fields present various sizes and depths. We thus employed a single extraction method at a given wavelength, allowing the heterogeneous datasets to combine in a coherent way.

2.2.1. Mid-IR/far-IR differences

The MIR (24 μm) and FIR (70 μm and 160 μm) maps have different properties: in the MIR, we observe lots of faint blended sources; in the FIR, due to confusion (Dole et al. 2004), all these faint blended sources are only seen as background fluctuations. Consequently, we used different extraction and photometry methods for each wavelength. In the MIR, the priority is the deblending: accordingly we took the SExtractor (Bertin & Arnouts 1996) and PSF fitting. In the FIR, we used efficient methods with strong background fluctuations: wavelet filtering, threshold detection and aperture photometry.

2.2.2. Point spread function (PSF)

The 24 μm empirical PSF of each field is generated with the IRAF (image reduction and analysis facility[2]) DAOPHOT package (Stetson 1987) on the 30 brightest sources of each map. It is normalized in a 12 arcsec radius aperture. Aperture correction (1.19) is computed with the S Tiny Tim[3] (Krist 2006) theoretical PSF for a constant νS_ν spectrum. The difference of correction between a $S_\nu = \nu^{-2}$ and a ν^2 spectrum is less than 2%. So, the hypothesis on the input spectrum is not critical for the PSF normalization.

At 70 μm and 160 μm, we built a single empirical PSF from the SWIRE fields. We used the Starfinder PSF extraction routine (Diolaiti et al. 2000), which median-stacks the brightest non-saturated sources (100 mJy $< S_{70} <$ 10 Jy and 300 mJy $< S_{160} <$ 1 Jy). Previously, fainter neighboring sources were subtracted with a first estimation of the PSF. At 70 μm (resp. 160 μm), the normalization is done in a 35 arcsec (resp. 80 arcsec) aperture, with a sky annulus between 75 arcsec and 125 arcsec (resp. 150 arcsec and 250 arcsec); the aperture correction was 1.21 (resp. 1.20). The theoretical signal in the sky annulus and the aperture correction were computed with the S Tiny Tim Spitzer PSF for a constant νS_ν spectrum. These parameters do not vary more than 5% with the spectrum of sources. Pixels that were affected by the temporal median filtering artifact, which was sometimes present around bright sources, were masked prior to these operations.

2.2.3. Source extraction and photometry

At 24 μm, we detected sources with SExtractor. We chose a Gaussian filter (gauss_5.0_9x9.conv) and a background filter of the size of 64 × 64 pixels. The detection and analysis thresholds were tuned for each field. We performed PSF fitting photometry

[1] from the Spitzer Science Center website: http://data.spitzer.caltech.edu/popular/

[2] http://iraf.noao.edu/

[3] http://ssc.spitzer.caltech.edu/archanaly/contributed/stinytim/

with the DAOPHOT allstar routine. This routine is very efficient for blended sources flux measurement.

At 70 μm and 160 μm, we applied the a-trou wavelet filtering (Starck et al. 1999) on the maps to remove the large scale fluctuations (10 pixels) on which we performed the source detection with a threshold algorithm (Dole et al. 2001, 2004). The threshold was tuned for each field. Photometry was done by aperture photometry on a non filtered map at the positions found on the wavelet filtered map. At 70 μm, we used 10 arcsec aperture radius and a 18 arcsec to 39 arcsec sky annulus. At 160 μm, we used an aperture of 20 arcsec and a 40 arcsec to 75 arcsec annulus. Aperture corrections were computed with the normalized empirical PSF: 3.22 at 70 μm and 3.60 at 160 μm. In order to estimate the uncertainty on this correction, aperture corrections were computed using five PSF built on five different SWIRE fields. The uncertainty is 1.5% at 70 μm and 4.5% at 160 μm.

2.3. Color correction

The MIPS calibration factors were calculated for a 10 000 K blackbody (MIPS Data Handbook 2007[4]). However, the galaxies SED are different and the MIPS photometric bands are large ($\lambda/\Delta\lambda \approx 3$). Thus, color corrections were needed. We used (like Shupe et al. (2008) and Frayer et al. (2009)) a constant νS_ν spectrum at 24 μm, 70 μm and 160 μm. Consequently, all fluxes were divided by 0.961, 0.918 and 0.959 at 24 μm, 70 μm and 160 μm due to this color correction. Another possible convention is $\nu S_\nu \propto \nu^{-1}$. This convention is more relevant for the local sources at 160 μm, whose spectrum decreases quickly with wavelength. Nevertheless, the redshifted sources studied by stacking are seen at their peak of the cold dust emission, and their SED agrees better with the constant νS_ν convention. The difference of color correction between these two conventions is less than 2%, and this choice is thus not critical. We consequently chose the constant νS_ν convention to more easily compare our results with Shupe et al. (2008) and Frayer et al. (2009).

3. Catalog properties

3.1. Spurious sources

Our statistical analysis may suffer from spurious sources. We have to estimate how many false detections are present in a map and what their flux distribution is. To do so, we built a catalog with the flipped map. To build this flipped map, we multiplied the values of the pixels of the original map by a factor of −1. Detection and photometry parameters were exactly the same as for normal catalogs. At 24 μm, there are few spurious sources (<10%) in bins brighter than the 80% completeness limit flux density. At 70 μm and 160 μm, fluctuations of the background due to unresolved faint sources are responsible for spurious detections. Nevertheless, the ratio between detected source numbers and fake source numbers stayed reasonable (below 0.2) down to the 80% completeness limit (see the example of FIDEL CDFS at 70 μm in Fig. 1).

3.2. Completeness

The completeness is the probability to extract a source of a given flux. To estimate it, we added artificial sources (based on empirical PSF) on the initial map and looked for a detection in a 2 arcsec radius at 24 μm around the initial position (8 arcsec at 70 μm and 16 arcsec at 160 μm). This operation was done for different fluxes with a Monte-Carlo simulation. We chose the number of artificial sources in each realization in a way that they have less than 1% probability to fall at a distance shorter than 2 PSF FWHM (full width at half maximum). The completeness is plotted in Fig. 2, and the 80% completeness level is reported in Table 1.

[4] http://ssc.spitzer.caltech.edu/mips/dh/

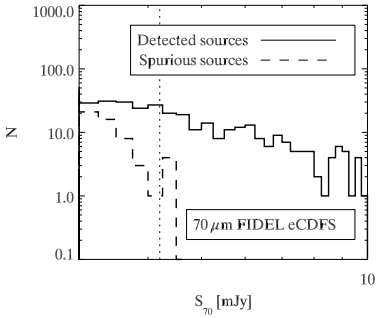

Fig. 1. Flux distribution of sources extracted from normal *(solid line)* and flipped *(dash line)* maps, at 70 μm in FIDEL eCDFS. The vertical dashed line represents the 80% completeness flux density.

3.3. Photometric accuracy

The photometric accuracy was checked with the same Monte-Carlo simulation. For different input fluxes, we built histograms of measured fluxes and computed the median and scatter of these distributions. At lower fluxes, fluxes are overestimated and errors are larger. These informations were used to estimate the Eddington bias (see next section). The photometric accuracy at 70 μm in FIDEL CDFS is plotted as an example in Fig. 3.

We also compared our catalogs with published catalogs. At 24 μm, we compared it with the GOODS CDFS catalog of Chary et al. (2004), and the COSMOS catalog of LeFloc'h et al. (2009). Their fluxes were multiplied by a corrective factor to be compatible with the νS_ν = constant convention. Sources were considered to be the same if they are separated by less than 2 arcsec. We computed the standard deviation of the distribution of the ratio between our and their catalogs. In a 80–120 μJy bin in the CDFS, we found a dispersion of 19%. In a 150–250 μJy bin in COSMOS, we found a scatter of 13%. The offset is +3% with COSMOS catalog and −1% with GOODS catalog. At 70 and 160 μm, we compared our catalogs with the COSMOS and SWIRE team ones. In all cases, the scatter is less than 15%, and the offset is less than 3%. At all wavelengths and for all fields, the offset is less than the calibration uncertainty.

3.4. Eddington bias

When sources become fainter, photometric errors increase. In addition, fainter sources are more numerous than brighter ones (in general $dN/dS \sim S^{-r}$). Consequently, the number of sources in faint bins are overestimated. This is the classical Eddington bias (Eddington 1913, 1940). The example of FIDEL CDFS at 70 μm is plotted in Fig. 4.

To correct for this effect at 70 μm and 160 μm, we estimated a correction factor for each flux bin. We generated an input flux catalog with a power-law distribution (r = 1.6 at 70 μm, r = 3 at 160 μm). We took into account completeness and photometric errors (coming from Monte-Carlo simulations) to generate a mock catalog. We then computed the ratio between the number of mock sources found in a bin and the number of input sources. This task was done for all fields. This correction is more important for large r (at 160 μm). At 24 μm, thanks to the PSF fitting, the photometric error is more reduced and symmetrical. Less faint sources are thus placed in brighter flux bins. Because of this property and the low r (about 1.45), this correction can be ignored for 24 μm counts.

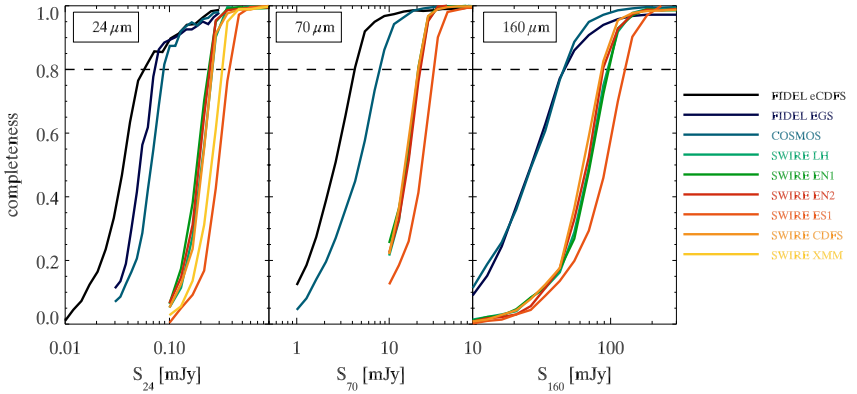

Fig. 2. Completeness at 24 μm *(left)*, 70 μm *(center)*, and 160 μm *(right)* as a function of the source flux for all fields. The dashed line represents 80% completeness.

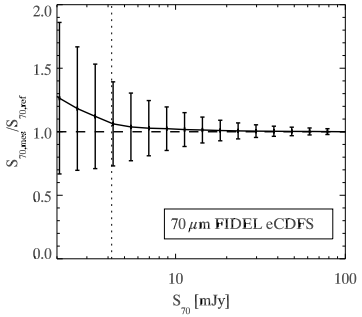

Fig. 3. Ratio between measured flux and input flux computed from Monte Carlo simulations at 70 μm in FIDEL eCDFS. Error bars represent 1σ dispersion. The vertical dashed line represents the 80% completeness flux density.

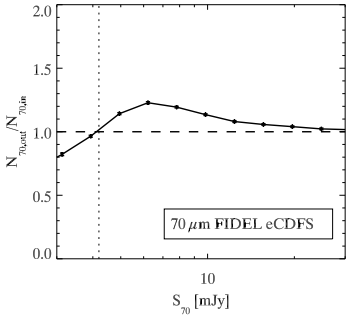

Fig. 4. Eddington bias: ratio between the number of detected sources and the number of input sources at 70 μm in FIDEL eCDFS. The vertical dashed line represents the 80% completeness flux density.

4. Number counts

4.1. Removing stars from the catalogs

To compute extragalactic number counts at 24 μm, we removed the stars with the $K - [24] < 2$ color criterion and identification procedure following Shupe et al. (2008). The K band magnitudes were taken from the 2MASS catalog (Skrutskie et al. 2006). We ignored the star contribution at 70 μm and 160 μm, which is negligible (<1% in all used flux density bins) according to the DIRBE Faint Count model (Arendt et al. 1998).

4.2. 24 μm number counts

We counted the number of extragalactic sources for each field and in each flux bin. We subtracted the number of spurious detections (performed on the flipped map). We divided by the

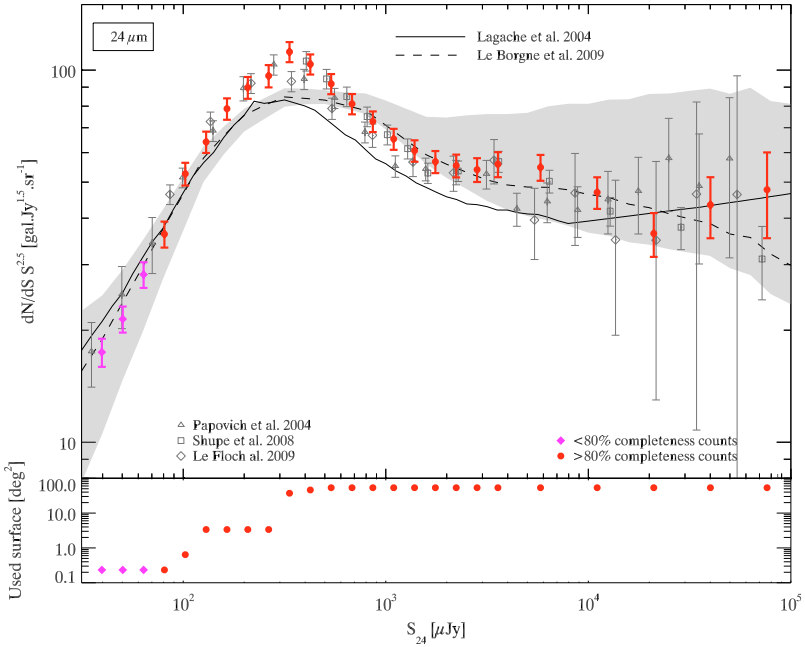

Fig. 5. Differential number counts at 24 μm. *Filled circle*: points obtained with ≥80% completeness; *filled diamond*: points obtained with a 50% to 80% completeness; *open triangle*: Papovich et al. (2004) GTO number counts obtained with PSF fitting photometry; *open square*: Shupe et al. (2008) SWIRE number counts obtained with aperture photometry; *open diamond*: LeFloc'h et al. (2009) COSMOS number counts obtained with PSF fitting photometry; *continuous line*: Lagache et al. (2004) model; *dashed line and grey region*: Le Borgne et al. (2009) model and 90% confidence region. Error bars take into accounts clustering (see Sect. 4.5) and calibration uncertainties (Engelbracht et al. 2007).

completeness. As a next step, the counts of all fields were combined together with a mean weighted by field size. Actually, a weighting by the number of sources in each field overweighs the denser fields and biases the counts. Counts from a field were combined only if the lower end of the flux bin was larger then or equal to the 80% completeness. We thus reached 71 μJy (71 μJy to 90 μJy bin) in the counts. However, to probe fainter flux densities, we used the data from the deepest field (FIDEL eCDFS) between a 50 and 80% completeness, allowing us to reach 35 μJy.

Our number counts are plotted in Fig. 5 and are written in Table 2. We also plot data from Papovich et al. (2004), Shupe et al. (2008) and LeFloc'h et al. (2009), and model predictions from Lagache et al. (2004) and Le Borgne et al. (2009). The Papovich et al. (2004) fluxes are multiplied by a factor 1.052 to take into account the update in the calibration, the color correction and the PSF. This correction of flux also implies a correction on number counts, according to:

$$\left(\frac{\mathrm{d}N}{\mathrm{d}S_f}S_f^{2.5}\right)_{S_f} = \left(c^{1.5}\frac{\mathrm{d}N}{\mathrm{d}S_i}S_i^{2.5}\right)_{cS_i}, \quad (1)$$

where S_i is the initial flux, S_f is the corrected flux and c the corrective factor ($S_f = cS_i$). A correction of the flux thus corresponds to a shift in the abscissa (factor c) and in the ordinate (factor $c^{1.5}$). Papovich et al. (2004) do not subtract stars and thus overestimate counts above 10 mJy. We have a very good agreement with their work below 10 mJy. We also have a very good agreement with Shupe et al. (2008). The LeFloc'h et al. (2009) fluxes are multiplied by 1.05 to take into account a difference of the reference SED: 10 000 K versus constant νS_ν, and by another correction of 3% corresponding to the offset observed in Sect. 3.3. There is an excellent agreement with their work.

The Lagache et al. (2004)[5] and Le Borgne et al. (2009)[6] generally agree well with the data, in particular on the faint end below 100 μJy, and on the position of the peak around 300 μJy. However, the Lagache et al. (2004) model slightly underestimates (about 10%) the counts above 200 μJy. The Le Borgne et al. (2009) model is flatter than the data, and agrees reasonably well above 600 μJy.

[5] Lagache et al. (2004) model used a ΛCDM cosmology with Ω_Λ = 0.73, Ω_M = 0.27 and h = 0.71.

[6] Le Borgne et al. (2009) model used a ΛCDM cosmology with Ω_Λ = 0.7, Ω_M = 0.3 and h = 0.7.

Table 2. Differential number counts at 24 μm.

⟨S⟩	S_{min}	S_{max}	$dN/dS.S^{2.5}$	$\sigma_{poisson}$	$\sigma_{clustering}$	$\sigma_{clus.+calib.}$	Ω_{used}
	(in mJy)			(in gal Jy$^{1.5}$ sr^{-1})			deg^2
0.040	0.035	0.044	17.5	1.0	1.1	1.3	0.2
0.050	0.044	0.056	21.4	1.0	1.1	1.4	0.2
0.064	0.056	0.071	28.2	1.2	1.5	1.8	0.2
0.081	0.071	0.090	36.2	1.5	1.9	2.4	0.2
0.102	0.090	0.114	52.6	1.3	1.9	2.9	0.6
0.130	0.114	0.145	64.1	1.0	1.7	3.1	3.4
0.164	0.145	0.184	78.7	1.1	2.2	3.8	3.4
0.208	0.184	0.233	89.8	1.3	2.8	4.5	3.4
0.264	0.233	0.295	96.5	1.5	3.3	5.1	3.4
0.335	0.295	0.374	112.0	0.8	1.8	4.8	37.2
0.424	0.374	0.474	103.7	0.6	1.7	4.5	46.1
0.538	0.474	0.601	91.9	0.6	1.5	4.0	53.6
0.681	0.601	0.762	81.2	0.6	1.5	3.6	53.6
0.863	0.762	0.965	72.8	0.7	1.6	3.3	53.6
1.094	0.965	1.223	65.3	0.8	1.6	3.1	53.6
1.387	1.223	1.550	60.8	0.9	1.7	3.0	53.6
1.758	1.550	1.965	56.7	1.0	1.8	2.9	53.6
2.228	1.965	2.490	55.4	1.2	2.1	3.0	53.6
2.823	2.490	3.156	54.0	1.5	2.3	3.2	53.6
3.578	3.156	4.000	55.9	1.8	2.7	3.5	53.6
5.807	4.000	7.615	54.8	1.5	2.9	3.6	53.6
11.055	7.615	14.496	46.9	2.3	3.6	4.1	53.6
21.045	14.496	27.595	36.4	3.3	4.4	4.6	53.6
40.063	27.595	52.531	43.4	5.9	7.7	7.9	53.6
76.265	52.531	100.000	47.7	9.9	12.0	12.2	53.6

Notes. $\sigma_{clustering}$ is the uncertainty taking into account clustering (see Sect. 4.5). $\sigma_{clus.+calib.}$ takes into account both clustering and calibration (Engelbracht et al. 2007).

Table 3. Differential number counts at 70 μm.

⟨S⟩	S_{min}	S_{max}	$dN/dS.S^{2.5}$	$\sigma_{poisson}$	$\sigma_{clustering}$	$\sigma_{clus.+calib.}$	Ω_{used}
	(in mJy)			(in gal Jy$^{1.5}$ sr^{-1})			deg^2
4.197	3.500	4.894	2073.	264.	309.	342.	0.2
5.868	4.894	6.843	2015.	249.	298.	330.	0.2
8.206	6.843	9.569	1690.	289.	332.	353.	0.2
11.474	9.569	13.380	2105.	123.	202.	250.	2.6
16.044	13.380	18.708	2351.	148.	228.	281.	2.6
22.434	18.708	26.159	1706.	153.	208.	240.	2.6
31.369	26.159	36.578	2557.	69.	124.	218.	38.1
43.862	36.578	51.146	2446.	73.	123.	211.	45.5
61.331	51.146	71.517	2359.	90.	141.	217.	45.5
85.758	71.517	100.000	2257.	112.	164.	228.	45.5
157.720	100.000	215.440	2354.	121.	198.	257.	45.5
339.800	215.440	464.160	2048.	200.	276.	311.	45.5
732.080	464.160	1000.000	2349.	381.	500.	526.	45.5

Notes. $\sigma_{clustering}$ is the uncertainty taking into account clustering (see Sect. 4.5). $\sigma_{clus.+calib.}$ takes into account both clustering and calibration (Gordon et al. 2007).

4.3. 70 μm number counts

Counts in the flux density bins brighter than the 80% completeness limit were obtained in the same way as at 24 μm (Fig. 6 and Table 3). In addition, they were corrected from the Eddington bias (cf. Sect. 3.4). We reached about 4.9 mJy at 80% completeness (4.9 to 6.8 bin). We used CDFS below 80% completeness limit to probe fainter flux density level. We cut these counts at 3.5 mJy. At this flux density, the spurious rate reached 50%. We used a stacking analysis to probe fainter flux density levels (cf. Sect. 5).

We can see breaks in the counts around 10 mJy and 20 mJy. These breaks appear between points built with a different set of fields. Our counts agree with earlier works of Dole et al. (2004), Frayer et al. (2006) and Frayer et al. (2009). However, these works suppose only a Poissonian uncertainty, which underestimates the error bars (see Sect. 4.5). Our data also agree well with these works. The Lagache et al. (2004) model agrees well with our data. The Le Borgne et al. (2009) model gives a reasonable fit, despite an excess of about 30% between 3 mJy and 10 mJy.

Table 4. Differential number counts at 160 μm. $\sigma_{clustering}$ is the uncertainty taking into account clustering (see Sect. 4.5).

$\langle S \rangle$	S_{min}	S_{max}	$dN/dS.S^{2.5}$	$\sigma_{poisson}$	$\sigma_{clustering}$	$\sigma_{clus.+calib.}$	Ω_{used}
	(in mJy)			(in gal $Jy^{1.5}$ sr^{-1})			deg^2
45.747	40.000	51.493	16855.	1312.	2879.	3519.	3.0
58.891	51.493	66.289	14926.	1243.	2704.	3243.	3.0
75.813	66.289	85.336	13498.	1319.	2648.	3104.	3.0
97.596	85.336	109.860	12000.	1407.	2442.	2835.	3.0
125.640	109.860	141.420	10687.	457.	991.	1621.	36.2
161.740	141.420	182.060	7769.	425.	773.	1211.	42.9
208.210	182.060	234.370	7197.	472.	810.	1184.	42.9
268.040	234.370	301.710	5406.	487.	734.	979.	42.9
345.050	301.710	388.400	5397.	585.	843.	1063.	42.9
444.200	388.400	500.000	4759.	662.	891.	1059.	42.9
750.000	500.000	1000.000	6258.	685.	1158.	1380.	42.9
1500.000	1000.000	2000.000	4632.	989.	1379.	1487.	42.9

Notes. $\sigma_{clus.+calib.}$ takes into account both clustering and calibration (Stansberry et al. 2007).

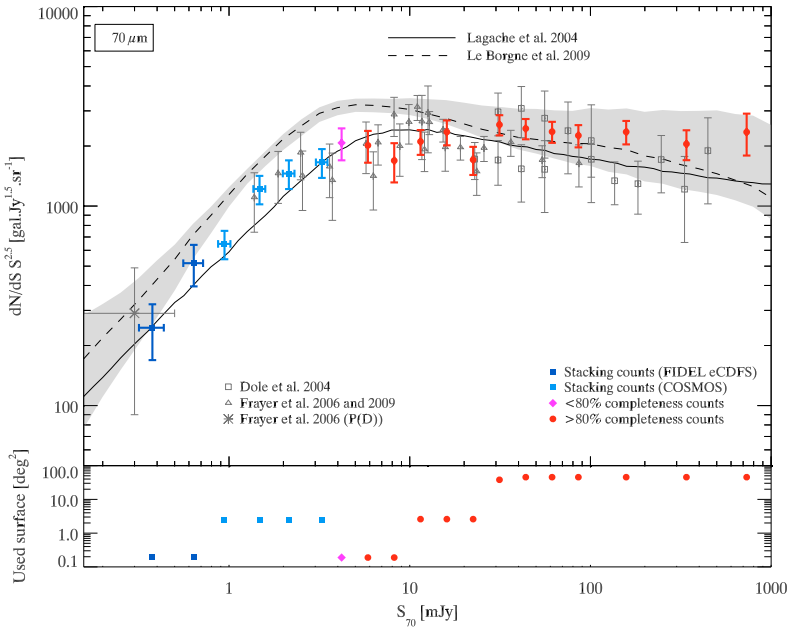

Fig. 6. Differential number counts at 70 μm. *Filled circle*: points obtained with ≥80% completeness; *filled diamond*: points obtained with less than 50% spurious sources and less than 80% completeness; *filled square*: stacking number counts (clear: FIDEL eCDFS, dark: COSMOS); *open square*: Dole et al. (2004) number counts in CDFS, Bootes and Marano; *open triangle*: Frayer et al. (2006) in GOODS and Frayer et al. (2009) in COSMOS; *cross*: Frayer et al. (2006) deduced from background fluctuations; *continuous line*: Lagache et al. (2004) model; *dashed line and grey region*: Le Borgne et al. (2009) model and 90% confidence region. Error bars take into account clustering (see Sect. 4.5) and calibration uncertainties (Gordon et al. 2007).

4.4. 160 μm number counts

The 160 μm number counts were obtained exactly in the same way as at 70 μm. We used COSMOS and EGS to probe counts below the 80% completeness limit. We reached 51 mJy at 80% completeness (51 mJy to 66 mJy bin) and 40 mJy for the 50% spurious rate cut (Fig. 7 and Table 4). We used a stacking analysis to probe fainter flux density levels (cf. Sect. 5).

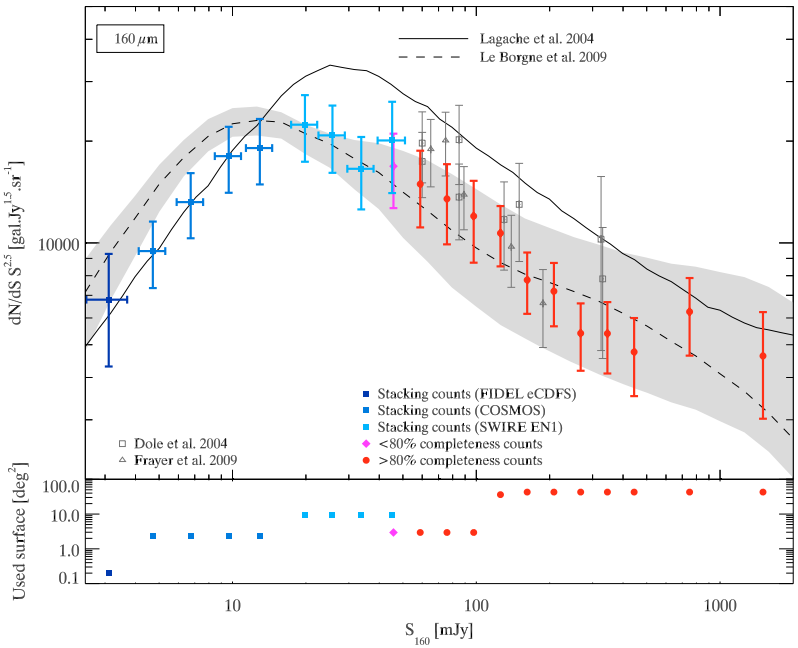

Fig. 7. Differential number counts at 160 μm. *Filled circle*: points obtained with ≥80% completeness; *filled diamond*: points obtained with less than 50% spurious sources and less than 80% completeness; *filled square*: stacking number counts (clear: FIDEL/GTO CDFS, *middle*: COSMOS, dark: SWIRE EN1); *open square*: Dole et al. (2004) number counts in CDFS and Marano; *open triangle*: Frayer et al. (2009) in COSMOS; *continuous line*: Lagache et al. (2004) model; *dashed line and grey region*: Le Borgne et al. (2009) model and 90% confidence region. Error bars take into account clustering (see Sect. 4.5) and calibration uncertainties (Stansberry et al. 2007).

Our counts agree with the earlier works of Dole et al. (2004) and Frayer et al. (2009). We find like Frayer et al. (2009) that the Lagache et al. (2004) model overestimates the counts by about 30% above 50 mJy (see the discussion in Sect. 7.2). On the contrary, the Le Borgne et al. (2009) model underpredicts the counts by about 20% between 50 mJy and 150 mJy.

4.5. Uncertainties on number counts including clustering

Shupe et al. (2008) showed that the SWIRE field-to-field variance is significantly higher than the Poisson noise (by a factor of three in some flux bins). They estimated their uncertainties on number counts with a field bootstrap method. We used a more formal method to deal with this problem.

The uncertainties on the number counts are Poissonian only if sources are distributed uniformly. But, actually, the infrared galaxies are clustered. The uncertainties must thus be computed taking into account clustering. We first measured the source clustering as a function of the flux density with the counts-in-cells moments (c-in-c) method (Peebles 1980; Szapudi 1998; Blake & Wall 2002). We then computed the uncertainties knowing these clustering properties of the sources, the source density in the flux density bins and the field shapes. The details are explained in the Appendix A.

This statistical uncertainty can be combined with the *Spitzer* calibration uncertainty (Engelbracht et al. 2007; Gordon et al. 2007; Stansberry et al. 2007) to compute the total uncertainty on differential number counts.

5. Deeper FIR number counts using a stacking analysis

5.1. Method

The number counts derived in Sect. 4 show that down to the 80% completeness limit, the source surface density is 24100 deg^{-2}, 1200 deg^{-2}, and 220 deg^{-2} at 24, 70, and 160 μm, respectively, i.e. 20 times (resp. 110 times) higher at 24 μm than at 70 μm (resp. 160 μm). These differences can be explained by the angular resolution decreasing with increasing wavelength, thus increasing confusion, and the noise properties of the detectors. There are thus many 24 μm sources without detected FIR

counterparts. If we want to probe deeper into the FIR number counts, we can take advantage of the information provided by the 24 μm data, namely the existence of infrared galaxies not necessarily detected in the FIR, and their positions.

We used a stacking analysis (Dole et al. 2006) to determine the FIR/MIR color as a function of the MIR flux. With this information, we can convert MIR counts into FIR counts. The stacking technique consists in piling up very faint far-infrared galaxies which are not detected individually, but are detected at 24 μm. For this purpose, it makes use of the 24 μm data prior to tracking their undetected counterpart at 70 μm and 160 μm, where most of the bolometric luminosity arises. This method was used by Dole et al. (2006), who managed to resolve the FIR CIB using 24 μm sources positions, as well many other authors (e.g Serjeant et al. (2004); Dye et al. (2006); Wang et al. (2006); Devlin et al. (2009); Dye et al. (2009); Marsden et al. (2009); Pascale et al. (2009)).

To derive the 70 μm or 160 μm versus 24 μm color, we stacked the FIR maps (cleaned of bright sources) at the positions of the 24 μm sources sorted by flux, and performed aperture photometry (same parameters as in Sect. 2). We thus get

$$\overline{S_{\rm FIR}} = f(\overline{S_{24}}), \tag{2}$$

where $\overline{S_{\rm FIR}}$ is the average flux density in the FIR of the population selected at 24 μm, $\overline{S_{24}}$ the average flux density at 24 microns, and f is the function linking both quantities. We derive f empirically using the $S_{\rm FIR}$ versus S_{24} relation obtained from stacking.

We checked that f is a smooth monotonic function, in agreement with the expectation that the color varies smoothly with the redshift and the galaxy emission properties. Assuming that the individual sources follow this relation exactly, the FIR number counts could be deduced from

$$\left.\frac{{\rm d}N}{{\rm d}S_{\rm FIR}}\right|_{S_{\rm FIR}=f(S_{24})} = \left.\frac{{\rm d}N}{{\rm d}S_{24}}\right|_{S_{24}} \Big/ \left.\frac{{\rm d}S_{\rm FIR}}{{\rm d}S_{24}}\right|_{S_{24}}. \tag{3}$$

In practice, the two first terms are discrete. In addition, the last term is computed numerically in the same S_{24} bin, using the two neighboring flux density bins ($k-1$ and $k+1$). We finally get

$$\frac{{\rm d}N}{{\rm d}S_{\rm FIR}}(\overline{S_{{\rm FIR},k}}) = \left(\frac{{\rm d}N}{{\rm d}S_{24}}\right)_k \Big/ \frac{\overline{S_{{\rm FIR},k+1}} - \overline{S_{{\rm FIR},k-1}}}{\overline{S_{24,k+1}} - \overline{S_{24,k-1}}}, \tag{4}$$

where $\langle S_{\rm FIR}\rangle$ is measured by stacking. In reality, sources do not follow Eq. (2) exactly, but exhibit a scatter around this mean relation

$$S_{\rm FIR} = f(S_{24}) + \sigma. \tag{5}$$

Our method is still valid under the condition $\frac{\sigma}{f} \ll 1$, and we verify its validity with simulations (see next section).

To obtain a better signal to noise ratio, we cleaned the resolved bright sources from the FIR maps prior to stacking. We used 8 S_{24} bins per decade. We stacked a source only if the coverage was more than half of the median coverage of the map. Uncertainties on the FIR mean flux were estimated with a bootstrap method. Furthermore, knowing the uncertainties on the 24 μm number counts and the mean S_{24} fluxes, we deduced the uncertainties on the FIR number counts according to Eq. (4).

At 70 μm, we used the FIDEL eCDFS (cleaned at $S_{70} > 10$ mJy) and the COSMOS (cleaned at $S_{70} > 50$ mJy) fields. At 160 μm, we used 160 μm the GTO CDFS (cleaned at $S_{160} > 60$ mJy), the COSMOS (cleaned at $S_{160} > 100$ mJy) and the SWIRE EN1 (no clean to probe the $S_{160} > 20$ mJy sources) fields.

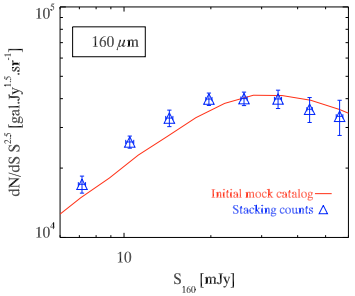

Fig. 8. Simulated number counts at 160 μm, computed from stacking counts *(triangle)* and from the input mock catalog *(solid line)*. The good agreement (better than 15%) validates the stacking counts method (see Sect. 5.2). Twenty realizations of the 2.9 deg^2 field maps with about 870 000 mock sources each were used.

5.2. Validation on simulations

We used the Fernandez-Conde et al. (2008) simulations[7] to validate our method. These simulations are based on the Lagache et al. (2004) model, and include galaxy clustering. We employed 20 simulated mock catalogs of a 2.9 deg^2 field each, containing about 870 000 mock sources each. The simulated maps have the same pixel size as the actual Spitzer mosaics (1.2″, 4″, and 8″ at 24 μm, 70 μm, and 160 μm, resp.) and are convolved with our empirical PSF. A constant standard deviation Gaussian noise was added. We applied the same method as for the real data to produce stacking number counts. At 160 μm, for bins below 15 mJy, we cleaned the sources brighter than 50 mJy. Figure 8 shows 160 μm number counts from the mock catalogs down to $S_{160} = 1$ mJy (diamond) and the number counts deduced from the stacking analysis described in the previous section (triangle). The error bars on the figure are the standard deviations of the 20 realization. There is a good agreement between the stacking counts and the classical counts (better than 15%). Nevertheless, we observed a systematic bias, intrinsic to the method, of about 10% in some flux density bins. We thus combined this 10% error with the statistical uncertainties to compute our error bars. We also validated the estimation of the statistical uncertainty in the stacking counts: we check that the dispersion of the counts obtained by stacking, coming from different realizations, was compatible with our estimation of statistical uncertainties. The results are the same at 70 μm.

5.3. Results

At 70 μm, the stacking number counts reach 0.38 mJy (see Fig. 6 and Table 5). The last stacking point is compatible with the Frayer et al. (2006) P(D) constraint. The stacking points also agree very well with the Lagache et al. (2004) model. The Le Borgne et al. (2009) model predicts slightly too many sources in 0.3 to 3 mJy range. The turnover around 3 mJy and the power law behavior of the faint counts ($S_{70} < 2$ mJy), observed by Frayer et al. (2006) are confirmed with a better accuracy.

At 160 μm, the stacking counts reach 3.1 mJy (see Fig. 7 and Table 6). We observed for the first time a turnover at about 20 mJy, and a power-law decrease at smaller flux densities. The stacking counts are lower than the Lagache et al. (2004) model around 20 mJy (about 30%). Below 15 mJy, the stacking counts agree with this model. The Le Borgne et al. (2009) model agree quite well with our points below 20 mJy. The results at 160 μm will be discussed in Sect. 7.2.

[7] Publicly available at http://www.ias.u-psud.fr/irgalaxies/

Table 5. Stacking extragalactic number counts at 70 μm.

$\langle S\rangle$	dN/dS.$S^{2.5}$	$\sigma_{\rm clus.}$	$\sigma_{\rm clus.+calib.}$	Field
(in mJy)	(in gal Jy$^{1.5}$ sr^{-1})			
0.38 ± 0.05	246.	72.	76.	FIDEL CDFS
0.64 ± 0.07	517.	109.	122.	FIDEL CDFS
0.94 ± 0.03	646.	80.	105.	COSMOS
1.48 ± 0.04	1218.	151.	198.	COSMOS
2.14 ± 0.05	1456.	183.	239.	COSMOS
3.27 ± 0.07	1657.	211.	273.	COSMOS

Notes. $\sigma_{\rm clus.}$ is the uncertainty taking into account clustering (see Sect. 4.5). $\sigma_{\rm clus.+calib.}$ takes into account both clustering and calibration (Gordon et al. 2007).

Table 6. Stacking extragalactic number counts at 160 μm.

$\langle S\rangle$	dN/dS.$S^{2.5}$	$\sigma_{\rm clus.}$	$\sigma_{\rm clus.+calib.}$	Field
(in mJy)	(in gal Jy$^{1.5}$ sr^{-1})			
3.11 ± 0.46	6795.	2163.	2485.	GTO CDFS
4.71 ± 0.16	9458.	1236.	2104.	COSMOS
6.74 ± 0.22	13203.	1627.	2880.	COSMOS
9.65 ± 0.26	18057.	2307.	3986.	COSMOS
12.95 ± 0.37	19075.	2388.	4182.	COSMOS
19.82 ± 0.48	22366.	2944.	4987.	SWIRE EN1
25.71 ± 0.81	20798.	2811.	4682.	SWIRE EN1
33.74 ± 0.98	16567.	2671.	4004.	SWIRE EN1
45.18 ± 2.08	20089.	4849.	6049.	SWIRE EN1

Notes. $\sigma_{\rm clus.}$ is the uncertainty taking into account clustering (see Sect. 4.5). $\sigma_{\rm clus.+calib.}$ takes into account both clustering and calibration (Stansberry et al. 2007).

6. New lower limits and estimates of the CIB at 24 μm, 70 μm and 160 μm

6.1. 24 μm CIB: lower limit and estimate

By integrating the measured 24 μm number counts between 35 μJy and 0.1 Jy, we can estimate a lower value of the CIB at this wavelength. The counts were integrated with a trapeze method. We estimated the uncertainty on the integral by adding (on 10000 realisations) a random Gaussian error to each data point with the σ given by the count uncertainties taking into account clustering. We then added the 4% calibration error of the instrument (Engelbracht et al. 2007). We found $2.26^{+0.09}_{-0.09}$ nW m^{-2} sr^{-1}. The very bright source counts ($S_{24} > 0.1$ Jy) are supposed to be euclidian (dN/d$S = C_{\rm eucl}S^{2.5}$). We used the three brightest points to estimate $C_{\rm eucl}$. We found a contribution to the CIB of $0.032^{+0.003}_{-0.003}$ nW m^{-2} sr^{-1}. Consequently, very bright sources extrapolation is not critical for the CIB estimation (1% of CIB). The contribution of $S_{24} > 35$ μJy is thus $2.29^{+0.09}_{-0.09}$ nW m^{-2} sr^{-1} (cf. Table 7).

We might have wanted to estimate the CIB value at 24 μm. To do so, we needed to extrapolate the number counts on the faint end. Below 100 μJy, the number counts exhibit a power-law behavior (Fig. 5). We assumed that this behavior (of the form dN/d$S = C_{\rm faint}S^r$) still holds below 35 μJy. r and $C_{\rm faint}$ are determined using the four faintest bins. We found $r = 1.45 \pm 0.10$ (compatible with 1.5 ± 0.1 of Papovich et al. 2004). Our new estimate of the CIB at 24 μm due to infrared galaxies is thus $2.86^{+0.19}_{-0.16}$ nW m^{-2} sr^{-1}. The results are plotted in Fig. 9. We conclude that resolved sources down to $S_{24} = 35$ μJy account for 80% of the CIB at this wavelength.

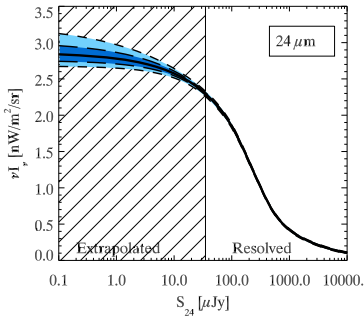

Fig. 9. Cumulative contribution to the surface brightness of the 24 μm CIB as a function of $S_{24\,\mu{\rm m}}$. The colored area represents the 68% and 95% confidence level. The shaded area represents the $S_{24} < 35\mu$Jy power-law extrapolation zone (see Sect. 6.1). The 4% calibration uncertainty is not represented. The table corresponding to this figure is available online at http://www.ias.u-psud.fr/irgalaxies/

Table 7. Summary of CIB results found in this article.

		24 μm	70 μm	160 μm
$S_{\rm cut,resolved}$	mJy	0.035	3.50	40.0
$S_{\rm cut,stacking}$		–	0.38	3.1
$\nu B_{\nu,\rm resolved}$	nW m^{-2} sr^{-1}	$2.29^{+0.09}_{-0.09}$	$3.1^{+0.2}_{-0.2}$	$1.0^{+0.1}_{-0.1}$
$\nu B_{\nu,\rm resolved+stacking}$		–	$5.4^{+0.4}_{-0.4}$	$8.9^{+1.1}_{-1.1}$
$\nu B_{\nu,\rm tot}$		$2.86^{+0.19}_{-0.16}$	$6.6^{+0.7}_{-0.6}$	$14.6^{+7.1}_{-2.9}$

6.2. 70 μm and 160 μm CIB: lower limit and estimate

At 70 μm and 160 μm, the integration of the number counts was done in the same way as at 24 μm, except for the stacking counts, which are correlated. To compute the uncertainties on the integral, we added (on 10 000 realizations) a Gaussian error simultaneously to the three quantities and completely recomputed the associated stacking counts: 1- the mean density flux given by the stacking; 2- the 24 μm number counts; 3- the mean 24 μm flux density. At 70 μm, and 160 μm, the calibration uncertainty is 7% (Gordon et al. 2007) and 12% (Stansberry et al. 2007), respectively. We estimated the CIB surface brightness contribution of resolved sources ($S_{70} > 3.5$ mJy and $S_{160} > 40$ mJy) of $3.1^{+0.2}_{-0.2}$ nW m^{-2} sr^{-1} and $1.0^{+0.1}_{-0.1}$ nW m^{-2} sr^{-1}. The contribution of $S_{70} > 0.38$ mJy and $S_{160} > 3.1$ mJy is $5.4^{+0.4}_{-0.4}$ nW m^{-2} sr^{-1} and $8.9^{+1.1}_{-1.1}$ nW m^{-2} sr^{-1}, respectively.

Below 2 mJy at 70 μm, and 10 mJy at 160 μm, the stacking counts are compatible with a power-law. Like at 24 μm, we assumed that this behavior can be extrapolated and determined the law with the five faintest bins at 70 μm, and the four faintest at 160 μm. We found a slope $r = 1.50 \pm 0.14$ at 70 μm, and

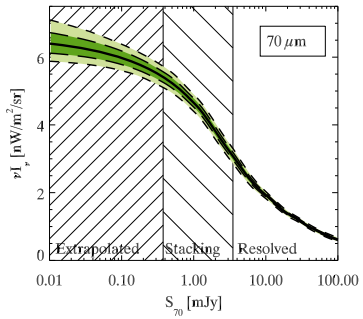

Fig. 10. Cumulative contribution to the surface brightness of the 70 μm CIB as a function of $S_{70\,\mu m}$. The colored area represents the 68% and 95% confidence level. The shaded areas represent the $0.38 < S_{70} < 3.3$ mJy stacking counts zone and the $S_{70} < 0.38$ mJy power-law extrapolation zone (see Sect. 6.2). The 7% calibration uncertainty is not represented. The table corresponding to this figure is available online at http://www.ias.u-psud.fr/irgalaxies/

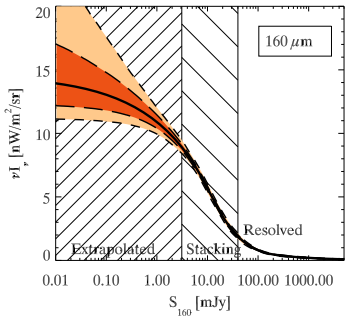

Fig. 11. Cumulative contribution to the surface brightness of the 160 μm CIB as a function of $S_{160\,\mu m}$. The colored area represents the 68% and 95% confidence level. The shaded areas represent the $3.1 < S_{160} < 45$ mJy stacking counts zone and the $S_{160} < 3.1$ mJy power-law extrapolation zone (see Sect. 6.2). The 12% calibration uncertainty is not represented. The table corresponding to this figure is available online at http://www.ias.u-psud.fr/irgalaxies/

1.61 ± 0.21 at 160 μm. The slope of the number counts at 70 μm is compatible with the Frayer et al. (2006) value (1.63 ± 0.34). The slope at 160 μm is measured for the first time. Our new estimate of the CIB at 70 μm and 160 μm due to infrared galaxies is thus $6.6^{+0.7}_{-0.6}$ nW m^{-2} sr^{-1}, and $14.6^{+7.1}_{-2.9}$ nW m^{-2} sr^{-1}, respectively. We conclude that resolved and stacking-studied populations account for 82% and 62% of the CIB at 70 μm and 160 μm, respectively. These results are summarized in Table 7, and Figs. 10 and 11.

7. Discussion

7.1. New lower limits of the CIB

The estimations of CIB based on number counts ignore a potential diffuse infrared emission like dust in galaxy clusters (Montier & Giard 2005). The extrapolation of the faint source counts supposes no low luminosity population, like population III stars or faint unseen galaxies. Accordingly, this type of measurement can provide in principle only a lower limit.

At 24 μm, Papovich et al. (2004) found $2.7^{-0.7}_{1.1}$ nW m^{-2} sr^{-1} using the counts and the extrapolation of the faint source counts. We agree with this work and significantly reduced the uncertainties on this estimation. Dole et al. (2006) found a contribution of 1.93 ± 0.23 nW m^{-2} sr^{-1} for $S_{24} > 60$ μJy sources (after dividing their results by 1.12 to correct an aperture error in their photometry at 24 μm). Our analysis gives 2.10 ± 0.08 nW m^{-2} sr^{-1} for a cut at 60 μJy, which agrees very well. Rodighiero et al. (2006) gave a total value of 2.6 nW m^{-2} sr^{-1}, without any error bar. Chary et al. (2004) found 2.0 ± 0.2 nW m^{-2} sr^{-1}, by integrating sources between 20 and 1000 μJy (we find 2.02 ± 0.10 for the same interval).

At 70 μm, using the number counts in the ultra deep GOODS-N and a P(D) analysis, Frayer et al. (2006) found a $S_{70} > 0.3$ mJy source contribution to the 70 μm CIB of 5.5 ± 1.1 nW m^{-2} sr^{-1}. Using the stacking counts, we found 5.5 ± 0.4 nW m^{-2} sr^{-1} for the same cut, in excellent agreement and with improved uncertainties. In Dole et al. (2006), the contribution at 70 μm of the $S_{24} < 60$ μJy sources was computed with an extrapolation of the 24 μm number counts and the 70/24 color. They found 7.1 ± 1.0 nW m^{-2} sr^{-1}, but the uncertainty on the extrapolation took only into account the uncertainty on the 70/24 color and not the uncertainty on the extrapolated 24 μm contribution, and was thus slightly underestimated. This is in agrees with our estimation.

At 160 μm they found with the same method, 17.4 ± 2.1 nW m^{-2} sr^{-1} (a corrective factor of 1.3 was applied due to an error on the map pixel size). This estimation is a little bit higher than our estimation, and can be explained by a small contribution (of the order of 15%) of the source clustering (Bavouzet 2008).

Our results can also be compared with direct measurements made by absolute photometers. These methods are biased by the foreground modeling, but do not ignore the extended emission. Fixsen et al. (1998) found a CIB brightness of 13.7 ± 3.0 at 160 μm, in excellent agreement with our estimation ($14.6^{+7.1}_{-2.9}$ nW m^{-2}). From the discussion in Dole et al. (2006) (Sect. 4.1), the Lagache et al. (2000) DIRBE WHAM (FIRAS calibration) estimation at 140 μm and 240 μm of 12 nW m^{-2} sr^{-1} and 12.2 nW m^{-2} sr^{-1} can be also compared with our value at 160 μm. A more recent work of Odegard et al. (2007) found 25.0 ± 6.9 and 13.6 ± 2.5 nW m^{-2} sr^{-1} at 140 μm and 240 μm respectively (resp. 15 ± 5.9 nW m^{-2} sr^{-1} and 12.7 ± 1.6 nW m^{-2} sr^{-1} with the FIRAS scale). Using ISOPHOT data, Juvela et al. (2009) give an estimation of the CIB surface brightness between 150 μm and 180 μm of $20.25 \pm 6.0 \pm 5.6$ nW m^{-2} sr^{-1}.

The total brightness due to infrared galaxies at 160 μm corresponds to the total CIB level at this wavelength. We thus have probably resolved the CIB at this wavelength. Nevertheless, the uncertainties are relatively large, and other minor CIB contributors cannot be excluded.

In addition, upper limits can be deduced indirectly from blazar high energy spectrum. Stecker & de Jager (1997) gave an upper limit of 4 nW m^{-2} sr^{-1} at 20 μm using Mkn 421. Renault et al. (2001) found an upper limit of 4.7 nW m^{-2} sr^{-1} between 5 and 15 μm with Mkn 501. This is consistent with our lower limit at 24 μm.

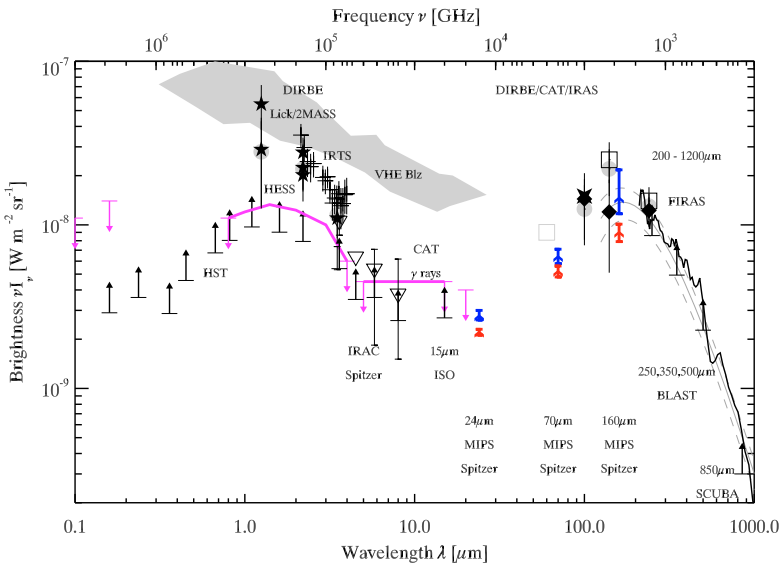

Fig. 12. Current measurement of the extragalactic background light spectral energy distribution from 100 nm to 1mm, with the cosmic optical background (COB, $\lambda < 8\,\mu$m) and cosmic infrared background (CIB, $\lambda > 8\,\mu$m). Our new points at 24 μm, 70 μm and 160 μm are plotted (*triangle*). Lower (red) triangles correspond to the CIB resolved with the number counts and stacking counts. Upper (blue) triangles correspond to the total extrapolated CIB due to infrared galaxies. BLAST lower limits at 250 μm, 350 μm and 500 μm (Devlin et al. 2009; Marsden et al. 2009) are represented in *black arrows*. The FIRAS measurements of Fixsen et al. (1998) between 125 μm and 2000 μm are plotted with a *grey solid line*, and the 1-σ confidence region with a *grey dashed line*. Other points come from different authors (see Dole et al. (2006) for complete details). Old MIPS points are not plotted for clarity.

An update of the synthetic EBL SED of Dole et al. (2006) with the new BLAST (balloon-borne large-aperture submillimeter telescope) lower limits from Devlin et al. (2009) and our values is plotted in Fig. 12. The BLAST lower limits are obtained by stacking of the Spitzer 24 μm sources at 250 μm, 350 μm and 500 μm (Devlin et al. 2009; Marsden et al. 2009).

7.2. 160 μm number counts

At most, we observed a 30% overestimation of the Lagache et al. (2004) model compared to the 160 μm number counts (Sect. 4.4 and 5.3 and Fig. 7), despite good fits at other wavelengths. This model uses mean SEDs of galaxies sorted into two populations (starburst and cold), whose luminosity functions evolve separately with the redshift. A possible explanation of the model excess is a slightly too high density of local cold galaxies. By decreasing the density of this local population a little, the model might be able to better fit the 160 μm number counts without significantly affecting other wavelengths, especially at 70 μm (more sensitive to warm dust rather than cold dust), and in the submillimetre range (more sensitive to redshifted cold dust at faint flux densities for wavelengths larger than 500 μm).

The Le Borgne et al. (2009) model slightly overpredicts faint 160 μm sources, probably because of the presence of too many galaxies at high redshift; this trend is also seen at 70 μm. With our number counts as new constraints, their inversion should give more accurate parameters.

Herschel was successfully launched on May 14th, 2009 (together with *Planck*). It will observe infrared galaxies between 70 μm and 500 μm with an improved sensitivity. It will be possible to directly observe the cold dust spectrum of high-z ULIRG (ultra luminous infrared galaxy) and medium-z LIRG (luminous infrared galaxy). PACS (Photodetectors Array Camera and Spectrometer) will make photometric surveys in three bands centred on 70 μm, 100 μm and 160 μm. *Herschel* will allow us to resolve a significant fraction of the background at these wavelengths (Lagache et al. 2003; Le Borgne et al. 2009). SPIRE (spectral and photometric imaging receiver) will observe around 250 μm, 350 μm and 500 μm, and will be quickly confusion limited. In both cases, the stacking analysis will allow us to probe fainter flux density levels, as it is complementary to *Spitzer* and BLAST.

8. Conclusion

With a large sample of public *Spitzer* extragalactic maps, we built new deep, homogeneous, high-statistics number counts in three MIPS bands at 24 μm, 70 μm and 160 μm.

At 24 μm, the results agree with previous works. These counts are derived from the widest surface ever used at this wavelength (53.6 deg^2). Using these counts, we give an accurate estimation of the galaxy contribution to the CIB at this wavelength ($2.86^{+0.19}_{-0.16}$ nW m^{-2} sr^{-1}).

At 70 μm, we used the stacking method to determine the counts below the detection limit of individual sources, by reaching 0.38 mJy, allowing us to probe the faint flux density slope of differential number counts. With this information, we deduced the total contribution of galaxies to the CIB at this wavelength ($6.6^{+0.7}_{-0.6}$ nW m^{-2} sr^{-1}).

At 160 μm, our counts reached 3 mJy with a stacking analysis. We exhibited for the first time the maximum in differential number counts around 20 mJy and the power-law behavior below 10 mJy. We deduced the total contribution of galaxies to the CIB at this wavelength ($14.6^{+7.1}_{-2.9}$ nW m^{-2} sr^{-1}). *Herschel* will likely probe flux densities down to about 10 mJy at this wavelength (confusion limit, Le Borgne et al. (2009)).

The uncertainties on the number counts used in this work take carefully into account the galaxy clustering, which is measured with the "counts-in-cells" method.

We presented a method to build very deep number counts with the information provided by shorter wavelength data (MIPS 24 μm) and a stacking analysis. This tool could be used on *Herschel* SPIRE data with a PACS prior to probe fainter flux densities in the submillimetre range.

We publicly release on the website `http://www.ias.u-psud.fr/irgal/`, the following products: PSF, number counts and CIB contributions. We also release a stacking library software written in IDL.

Acknowledgements. We wish to acknowledge G. Lagache, who has generated simulations used in this work. We acknowledge J.L. Puget, G. Lagache, D. Marcillac, B. Bertincourt, A. Penin and all members of the cosmology group of IAS for their comments and suggestions. We wish to thank the members of ANR D-SIGALE for their valuable comments, in particular D. Le Borgne for providing us an electronic version of his model. We also thank E. Le Floc'h for quickly providing us the table of his counts. This work is based in part on archival data obtained with the Spitzer Space Telescope, which is operated by the Jet Propulsion Laboratory, California Institute of Technology under a contract with NASA. Support for this work was provided by an award issued by JPL/Caltech. This publication makes use of data products from the Two Micron All Sky Survey, which is a joint project of the University of Massachusetts and the Infrared Processing and Analysis Center/California Institute of Technology, funded by the National Aeronautics and Space Administration and the National Science Foundation.

Appendix A: Uncertainties on number counts including clustering

A.1. Counts-in-cells moments

We consider a clustered population with a surface density ρ. The expected number of objects in a field of the size Ω is $\overline{N} = \rho\Omega$. In the Poissonian case, the standard deviation around this value is $\sqrt{N}$. For a clustered distribution, the standard deviation σ_N is given by (Wall & Jenkins 2003)

$$\sigma_N = \sqrt{y.\bar{N}^2 + \bar{N}}. \quad (A.1)$$

The expected value of y is given by (Peebles 1980)

$$y = \frac{\int_{\text{field}}\int_{\text{field}} w(\theta)\mathrm{d}\Omega_1\mathrm{d}\Omega_2}{\Omega^2}, \quad (A.2)$$

where $w(\theta)$ is the angular two points auto correlation function of the sources.

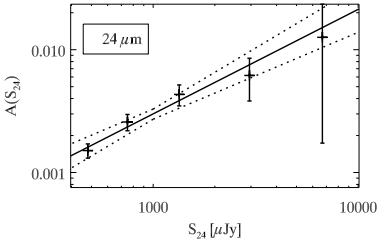

Fig. A.1. Amplitude of the auto correlation as a function of the flux density of the sources at 24 μm, and best power-law fit.

A.2. Measuring source clustering as a function of flux density

We assume the classical power law description $w(\theta) = A(S,\lambda)\theta^{1-\gamma}$ with an index $\gamma = 1.8$. So, y depends only on A and on the shape of the field:

$$y = A(S,\lambda)\frac{\int_{\text{field}}\int_{\text{field}}\theta^{1-\gamma}\mathrm{d}\Omega_1\mathrm{d}\Omega_2}{\Omega^2}. \quad (A.3)$$

The uncertainty on y is given by (Szapudi 1998):

$$\sigma_y = \sqrt{\frac{2}{N_{\text{cell}}\bar{N}^2}}. \quad (A.4)$$

To measure $A(S,\lambda)$, we cut our fields in 30′×30′ square boxes, in which we count the number of sources and compute the variance in five, three and three flux density bins at 24 μm, 70 μm and 160 μm. We calculate the associate $A(S,\lambda)$ combining Eqs. (A.1) and (A.3)

$$A(S,\lambda) = \frac{\sigma_N^2 - \bar{N}}{\bar{N}^2} \times \frac{\Omega^2}{\int_{\text{field}}\int_{\text{field}}\theta^{1-\gamma}\mathrm{d}\Omega_1\mathrm{d}\Omega_2}. \quad (A.5)$$

The fit of $A(S_{24}, 24\,\mu\text{m})$ versus S_{24} (see Fig. A.1) gives (χ^2 = 2.67 for five points and two fitted parameters)

$$A(S, 24\,\mu\text{m}) = (2.86 \pm 0.29) \times 10^{-3}\left(\frac{S}{1\text{ mJy}}\right)^{0.90\pm0.15}. \quad (A.6)$$

The measured exponent in A.6 of 0.90 ± 0.15 corresponds to $\gamma/2$, which is the expected value in the case of a flux-limited survey in an Euclidean universe filled with single luminosity sources. We fix this exponent to fit $A(S_{70}, 70\,\mu\text{m})$ and $A(S_{160}, 160\,\mu\text{m})$. We find $A(1\text{ mJy}, 70\,\mu\text{m}) = (0.25 \pm 0.08).10^{-3}$ and $A(1\text{ mJy}, 160\,\mu\text{m}) = (0.3 \pm 0.03).10^{-3}$.

A.3. Compute uncertainties due to clustering

With this model of $A(S,\lambda)$ and the field shape, we compute y (Eq. (A.3)). Assuming $\bar{N} = N$ (N to be the number of detected sources in a given field and flux density bin), we deduce $\sigma(N)$ from Eq. (A.1), and consequently the error bar on the number counts for a single field.

To compute the final uncertainty on the combined counts, we use the following relation

$$\sigma_{\text{comb},\frac{\mathrm{d}N}{\mathrm{d}S}} = \frac{\sqrt{\sum_i \Omega_i^2 \sigma^2_{i,\frac{\mathrm{d}N}{\mathrm{d}S}}}}{\sum_i \Omega_i}, \quad (A.7)$$

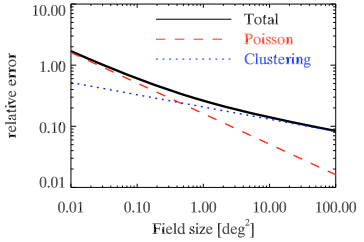

Fig. A.2. Relative error on the number count as a function of the field size. We have chosen $A = 0.019$ and $\rho = 38.5$ deg^{-2} (values for a 80–120 mJy flux density bin at 160 μm). The field is a square.

where $\sigma_{\text{comb},\frac{\mathrm{d}N}{\mathrm{d}S}}$ is the uncertainty on the combined number counts, Ω_i the solid angle of the ith field, and $\sigma_{i,\frac{\mathrm{d}N}{\mathrm{d}S}}$ the uncertainty on the number counts in the ith field (given by Var(N), Eq. (A.1)).

A.4. Discussion about clustering and number count uncertainties

For a clustered distribution of sources, the uncertainties on the number counts are driven by two quadratically combined terms (Eq. (A.1)): a Poissonian term $\sqrt{N}$ and a clustering term $\sqrt{y}.N$ (see Fig. A.2). We have $N \propto \Omega$ and $y \propto \Omega^{(\gamma-1)/2}$ (Blake & Wall 2002). When the uncertainty is dominated by the Poissonian term (small field), the relative uncertainty is thus proportional to $\sqrt{\Omega}^{-1/2}$. When the uncertainty is dominated by the clustering term (large field), the relative error is proportional to $\Omega^{(1-\gamma)/4}$ ($\Omega^{-0.2}$ for $\gamma = 1.8$).

Consequently uncertainties decrease very slowly in the the clustering regime. Averaging many small independent fields gives more accurate counts than a big field covering the same surface. For example, in the clustering regime, if a field of 10 deg^2 has a relative uncertainty of 0.2, the relative uncertainty is $0.2/\sqrt{10} = 0.063$ for the mean of ten fields of this size, and $0.2\times10^{-0.2} = 0.126$ for a single field of 100 deg^2. Consequently, if one studies the counts only, many small fields give better results than one very large field. But, this is not optimal if one studies the spatial properties of the galaxies, which requires large fields.

References

Arendt, R. G., Odegard, N., Weiland, J. L., et al. 1998, ApJ, 508, 74
Bavouzet, N. 2008, Ph.D. Thesis, Université Paris-Sud 11 `http://tel.archives-ouvertes.fr/tel-00363975/`
Bertin, E., & Arnouts, S. 1996, A&AS, 117, 393
Blake, C., & Wall, J. 2002, MNRAS, 337, 993
Chary, R., Casertano, S., Dickinson, M. E., et al. 2004, ApJS, 154, 80
Devlin, M. J., Ade, P. A. R., Aretxaga, I., et al. 2009, Nature, 458, 737
Diolaiti, E., Bendinelli, O., Bonaccini, D., et al. 2000, A&AS, 147, 335
Dole, H., Gispert, R., Lagache, G., et al. 2001, A&A, 372, 364
Dole, H., Lagache, G., & Puget, J.-L. 2003, ApJ, 585, 617
Dole, H., Le Floc'h, E., Pérez-González, P. G., et al. 2004, ApJS, 154, 87
Dole, H., Lagache, G., Puget, J.-L., et al. 2006, A&A, 451, 417
Dye, S., Eales, S. A., Ashby, M. L. N., et al. 2006, ApJ, 644, 769
Dye, S., Ade, P. A. R., Bock, J. J., et al. 2009, ApJ, 703, 285
Eddington, A. S. 1913, MNRAS, 73, 359
Eddington, Sir, A. S. 1940, MNRAS, 100, 354
Elbaz, D., Cesarsky, C. J., Chanial, P., et al. 2002, A&A, 384, 848
Engelbracht, C. W., Blaylock, M., Su, K. Y. L., et al. 2007, PASP, 119, 994
Fernandez-Conde, N., Lagache, G., Puget, J.-L., & Dole, H. 2008, A&A, 481, 885
Fixsen, D. J., Dwek, E., Mather, J. C., Bennett, C. L., & Shafer, R. A. 1998, ApJ, 508, 123
Franceschini, A., Rodighiero, G., Vaccari, M., Marchetti, L., & Mainetti, G. 2010, A&A, accepted [arXiv:0906.4264]
Frayer, D. T., Huynh, M. T., Chary, R., et al. 2006, ApJ, 647, L9
Frayer, D. T., Sanders, D. B., Surace, J. A., et al. 2009, AJ, 138, 1261
Gispert, R., Lagache, G., & Puget, J. L. 2000, A&A, 360, 1
Gordon, K. D., Engelbracht, C. W., Fadda, D., et al. 2007, PASP, 119, 1019
Hauser, M. G., & Dwek, E. 2001, ARA&A, 39, 249
Hauser, M. G., Arendt, R. G., Kelsall, T., et al. 1998, ApJ, 508, 25
Juvela, M., Mattila, K., Lemke, D., et al. 2009, A&A, 500, 763
Kashlinsky, A. 2005, Phys. Rep., 409, 361
Krist, J. 2006, Tiny Tim/Spitzer User's Guide
Lagache, G., Abergel, A., Boulanger, F., Désert, F. X., & Puget, J.-L. 1999, A&A, 344, 322
Lagache, G., Haffner, L. M., Reynolds, R. J., & Tufte, S. L. 2000, A&A, 354, 247
Lagache, G., Dole, H., & Puget, J.-L. 2003, MNRAS, 338, 555
Lagache, G., Dole, H., Puget, J.-L., et al. 2004, ApJS, 154, 112
Lagache, G., Puget, J.-L., & Dole, H. 2005, ARA&A, 43, 727
Le Borgne, D., Elbaz, D., Ocvirk, P., & Pichon, C. 2009, A&A, 504, 727
LeFloc'h, E., Aussel, H., Ilbert, O., et al. 2009, ApJ, 703, 222
Marsden, G., Ade, P. A. R., Bock, J. J., et al. 2009, ApJ, 707, 1729
Montier, L. A., & Giard, M. 2005, A&A, 439, 35
Odegard, N., Arendt, R. G., Dwek, E., et al. 2007, ApJ, 667, 11
Papovich, C., Dole, H., Egami, E., et al. 2004, ApJS, 154, 70
Pascale, E., Ade, P. A. R., Bock, J. J., et al. 2009, ApJ, 707, 1740
Pearson, C., & Khan, S. A. 2009, MNRAS, 399, L11
Peebles, P. J. E. 1980, The large-scale structure of the universe
Puget, J.-L., Abergel, A., Bernard, J.-P., et al. 1996, A&A, 308, L5
Renault, C., Barrau, A., Lagache, G., & Puget, J.-L. 2001, A&A, 371, 771
Rieke, G. H., Young, E. T., Engelbracht, C. W., et al. 2004, ApJS, 154, 25
Rodighiero, G., Lari, C., Pozzi, F., et al. 2006, MNRAS, 371, 1891
Rowan-Robinson, M. 2009, MNRAS, 394, 117
Serjeant, S., Mortier, A. M. J., Ivison, R. J., et al. 2004, ApJS, 154, 118
Shupe, D. L., Rowan-Robinson, M., Lonsdale, C. J., et al. 2008, AJ, 135, 1050
Skrutskie, M. F., Cutri, R. M., Stiening, R., et al. 2006, AJ, 131, 1163
Stansberry, J. A., Gordon, K. D., Bhattacharya, B., et al. 2007, PASP, 119, 1038
Starck, J. L., Aussel, H., Elbaz, D., Fadda, D., & Cesarsky, C. 1999, A&AS, 138, 365
Stecker, F. W., & de Jager, O. C. 1997, ApJ, 476, 712
Stetson, P. B. 1987, PASP, 99, 191
Szapudi, I. 1998, ApJ, 497, 16
Valiante, E., Lutz, D., Sturm, E., Genzel, R., & Chapin, E. 2009, ApJ, 701, 1814
Wall, J. V., & Jenkins, C. R. 2003, Practical Statistics for Astronomers
Wang, W.-H., Cowie, L. L., & Barger, A. J. 2006, ApJ, 647, 74
Werner, M. W., Gallagher, D. B., & Irace, W. R. 2004, Adv. Space Res., 34, 600

A&A 516, A43 (2010)
DOI: 10.1051/0004-6361/200913910

Astronomy & Astrophysics

Submillimeter number counts at 250 μm, 350 μm and 500 μm in BLAST data

M. Béthermin, H. Dole, M. Cousin, and N. Bavouzet

Institut d'Astrophysique Spatiale (IAS), Université Paris-Sud 11 and CNRS (UMR8617), Bât. 121, 91405 Orsay, France
e-mail: matthieu.bethermin@ias.u-psud.fr

Received 18 December 2009 / Accepted 6 March 2010

ABSTRACT

Context. The instrument BLAST (Balloon-borne Large-Aperture Submillimeter Telescope) performed the first deep and wide extragalactic survey at 250, 350 and 500 μm. The extragalactic number counts at these wavelengths are important constraints for modeling the evolution of infrared galaxies.

Aims. We estimate the extragalactic number counts in the BLAST data, which allow a comparison with the results of the P(D) analysis of Patanchon et al. (2009).

Methods. We use three methods to identify the submillimeter sources. 1) Blind extraction using an algorithm when the observed field is confusion-limited and another one when the observed field is instrumental-noise-limited. The photometry is computed with a new simple and quick point spread function (PSF) fitting routine (FASTPHOT). We use Monte-Carlo simulations (addition of artificial sources) to characterize the efficiency of this extraction, and correct the flux boosting and the Eddington bias. 2) Extraction using a prior. We use the *Spitzer* 24 μm galaxies as a prior to probe slightly fainter submillimeter flux densities. 3) A stacking analysis of the *Spitzer* 24 μm galaxies in the BLAST data to probe the peak of the differential submillimeter counts.

Results. With the blind extraction, we reach 97 mJy, 83 mJy and 76 mJy at 250 μm, 350 μm and 500 μm respectively with a 95% completeness. With the prior extraction, we reach 76 mJy, 63 mJy, 49 mJy at 250 μm, 350 μm and 500 μm respectively. With the stacking analysis, we reach 6.2 mJy, 5.2 mJy and 3.5 mJy at 250 μm, 350 μm and 500 μm respectively. The differential submillimeter number counts are derived, and start showing a turnover at flux densities decreasing with increasing wavelength.

Conclusions. There is a very good agreement with the P(D) analysis of Patanchon et al. (2009). At bright fluxes (>100 mJy), the Lagache et al. (2004) and Le Borgne et al. (2009) models slightly overestimate the observed counts, but the data agree very well near the peak of the differential number counts. Models predict that the galaxy populations probed at the peak are likely $z \sim 1.8$ ultra-luminous infrared galaxies.

Key words. cosmology: observations – galaxies: statistics – galaxies: evolution – galaxies: photometry – infrared: galaxies

1. Introduction

Galaxy number counts, a measurement of the source surface density as a function of flux density, are used to evaluate the global evolutionary photometric properties of a population observed at a given wavelength. These photometric properties mainly depend on the source redshift distribution, spectral energy distribution (SED), and luminosity distribution in a degenerate way for a given wavelength. Even though this is a rather simple tool, measurements of number counts at different observed wavelengths greatly help in constraining those degeneracies. Backward evolution models, among these Chary & Elbaz (2001); Lagache et al. (2004); Gruppioni et al. (2005); Franceschini et al. (2009); Le Borgne et al. (2009); Pearson & Khan (2009); Rowan-Robinson (2009); Valiante et al. (2009) are able to broadly reproduce (with different degrees of accuracy) the observed number counts from the near-infrared to the millimeter spectral ranges, in addition to other current constraints, like such as measured luminosity functions and the spectral energy distribution of the Cosmic Infrared Background (CIB) (Puget et al. 1996; Fixsen et al. 1998; Hauser et al. 1998; Lagache et al. 1999; Gispert et al. 2000; Hauser & Dwek 2001; Kashlinsky 2005; Lagache et al. 2005; Dole et al. 2006). In the details, however, the models disagree in some aspects like the relative evolution of luminous and ultra-luminous infrared galaxies (LIRG and ULIRG) and their redshift distributions, or the mean temperature or colors of galaxies, as is shown for instance in LeFloc'h et al. (2009) from Spitzer 24 μm deep observations.

One key spectral range lacks valuable data to get accurate constraints as yet: the sub-millimeter range, between 160 μm and 850 μm, where some surveys were conducted on small areas. Fortunately this spectral domain is intensively studied with the BLAST balloon experiment (Devlin et al. 2009) and the *Herschel* and *Planck* space telescopes. This range, although it is beyond the maximum of the CIB's SED in wavelength, allows us to constrain the poorly-known cold component of galaxy SED at a redshift greater than a few tenths. Pioneering works have measured the local luminosity function (Dunne et al. 2000) and shown that most milli-Jansky sources lie at redshifts $z > 2$ (Ivison et al. 2002; Chapman et al. 2003a, 2005; Ivison et al. 2005; Pope et al. 2005, 2006). Other works showed that the galaxies SED selected in the submillimeter range (Benford et al. 1999; Chapman et al. 2003b; Sajina et al. 2003; Lewis et al. 2005; Beelen et al. 2006; Kovács et al. 2006; Sajina et al. 2006; Michałowski et al. 2010) can have typically warmer temperatures and higher luminosities than galaxies selected at other infrared wavelengths.

Data in the submillimeter wavelength with increased sensitivity are thus needed to match the depth of infrared surveys, conducted by Spitzer in the mid- and far-infrared with the MIPS instrument (Rieke et al. 2004) at 24 μm, 70 μm and 160 μm (Chary et al. 2004; Marleau et al. 2004; Papovich et al. 2004; Dole et al. 2004; Frayer et al. 2006a,b; Rodighiero et al. 2006; Shupe et al. 2008; Frayer et al. 2009; LeFloc'h et al. 2009; Béthermin et al. 2010) as well as the near-infrared range with the IRAC instrument (Fazio et al. 2004b) between 3.6 μm and 8.0 μm (Fazio et al. 2004a; Franceschini et al. 2006; Sullivan et al. 2007; Barmby et al. 2008; Magdis et al. 2008; Ashby et al. 2009). Infrared surveys have allowed the resolution of the CIB by identifying the contributing sources – directly at 24 μm and 70 μm, or indirectly trough stacking at 160 μm (Dole et al. 2006; Béthermin et al. 2010).

Although large surveys cannot solve by themselves all the unknowns about the submillimeter SED of galaxies, the constraints given by the number counts can greatly help in unveiling the statistical SED shape of submillimeter galaxies as well as the origin of the submillimeter background.

The instrument BLAST (Balloon-borne Large-Aperture Submillimeter Telescope, Pascale et al. 2008) performed the first wide and deep survey in the 250–500 μm range (Devlin et al. 2009) before the forthcoming *Herschel* results. Marsden et al. (2009) show that sources detected by *Spitzer* at 24 μm emit the main part of the submillimeter background. Khan et al. (2009) claimed that only 20% of the CIB is resolved by the sources brighter than 17 mJy at 350 μm. Patanchon et al. (2009) has performed a $P(D)$ fluctuation analysis to determine the counts at BLAST wavelength (250 μm, 350 μm and 500 μm). In this paper we propose another method to estimate the number counts at these wavelengths and compare the results with those of Patanchon et al. (2009).

2. Data

2.1. BLAST sub-millimeter public data in the Chandra Deep Field South (CDFS)

The BLAST holds a bolometer array, which is the precursor of the spectral and photometric imaging receiver (SPIRE) instrument on *Herschel*, at the focus of a 1.8 m diameter telescope. It observes at 250 μm, 350 μm and 500 μm, with a 36″, 42″ and 60″ beam, respectively (Truch et al. 2009).

An observation of the Chandra Deep Field South (CDFS) was performed during a long duration flight in Antarctica in 2006, and the data of the two surveys are now public: a 8.7 deg^2 shallow field and a 0.7 deg^2 confusion-limited (Dole et al. 2004) field in the center part of the first one. We use the non-beam-smoothed maps and associated point spread function (PSF) distributed on the BLAST website[1]. The signal and noise maps were generated by the SANEPIC algorithm (Patanchon et al. 2008).

2.2. Spitzer 24 μm data in the CDFS

Several infrared observations were performed in the CDFS. The *Spitzer* Wide-Field InfraRed Extragalactic (SWIRE) survey overlaps the CDFS BLAST field at wavelengths between 3.6 μm and 160 μm. We used only the 24 μm band, which is 80% complete at 250 μJy. The completeness is defined as the probability to find a source of a given flux in a catalog. The Far-Infrared Deep Extragalactic Legacy (FIDEL) survey is deeper but narrower (about 0.25 deg^2) than SWIRE and 80% complete at 57 μJy at 24 μm. We used the Béthermin et al. (2010) catalogs constructed from these two surveys. These catalogs were extracted with SExtractor (Bertin & Arnouts 1996) and the photometry was performed with the allstar routine of the DAOPHOT package (Stetson 1987). The completeness of this catalog was characterized with Monte-Carlo simulations (artificial sources added on the initial map and extracted).

[1] http://www.blastexperiment.info

3. Blind source extraction and number counts

We started with a blind source extraction in the BLAST bands. Each wavelength was treated separately. For each wavelength we defined two masks: a shallow zone (about 8.2 deg^2) covering the whole field except the noisier edge; and a deep zone (about 0.45 deg^2) in the center of the confusion-limited area. We used different extraction methods in the shallow zone and the deep one, but the photometry and the corrections of the extraction bias were the same.

3.1. Detector noise-limited extraction (shallow zone)

In the shallow zone we used the non-smoothed map and the corresponding map of the standard deviation of the noise. The map was then cross-correlated by the PSF. The result of this cross-correlation is

$$m_{\rm conv}(i_0, j_0) = \sum_{i=-N}^{+N} \sum_{j=-N}^{+N} m(i_0 + i, j_0 + j) \times PSF(i, j), \quad (1)$$

where $m_{\rm conv}(i_0, j_0)$ is the flux density in the pixel (i_0, j_0) of the cross-correlated map, $m(i, j)$ the flux density in the pixel (i, j) of the map, and PSF(i, j) the value of the normalized PSF in the pixel (i, j) (the center of the PSF is in the center of the pixel $(0, 0)$). The PSF size is $(2N + 1)\times(2N + 1)$ pixels. The standard deviation of the noise in the cross-correlated map is thus

$$n_{\rm conv}(i_0, j_0) = \sqrt{\sum_{i=-N}^{+N} \sum_{j=-N}^{+N} n^2(i_0 + i, j_0 + j) \times PSF^2(i, j)}, \quad (2)$$

where n ($n_{\rm conv}$) is the initial (cross-correlated) map of the standard deviation of the noise.

We found the pixels where $m_{\rm conv}/n_{\rm conv} > 3$ and kept the local maxima. The precise center of the detected sources was computed by a centroid algorithm. This low threshold caused lots of spurious detections, but helped to deblend the fluxes of 3 to 4-sigma sources and avoided to overestimate their fluxes. We could thus limit the flux boosting effect. A final cut in flux after the PSF fitting photometry eliminated the main part of these sources. We performed the extraction algorithm on the flipped map (initial map multiplied by a factor of –1) to check it. We found few spurious sources brighter than the final cut in flux determined in the Sect. 3.4. We found a spurious rate of 12%, 11% and 25% at 250 μm, 350 μm and 500 μm, respectively.

3.2. Confusion-limited extraction (deep zone)

In the confusion-limited zone we also used a non-smoothed map. In this region the noise is dominated by the confusion and not by the instrumental noise. Consequently, the method based on instrumental noise presented in the Sect. 3.1 is not relevant. We used an atrou wavelet filtering (Starck et al. 1999; Dole et al. 2001) to remove fluctuations at scales larger than 150″. Then we divided the resulting map by $\sigma_{\rm filtered\ map}$, which is the standard

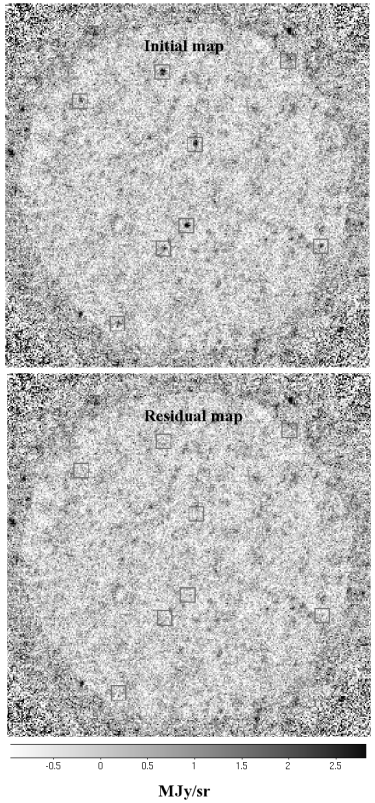

Fig. 1. Position of sources brighter than the 95% completeness flux at 250 μm in deep zone. *Top*: initial map. *Bottom*: residual map. The area out of the mask are represented darker. These 1°×1° map are centered on the coordinates (RA, Dec) = (3h32min30s, –27°50′). The horizontal axis is aligned with the right ascension.

deviation of the pixel values on the filtered map in the working area. We finally kept local maxima with a signal greater than 3. The center of the sources was also determined by a centroid algorithm. The initial map and the cleaned map are shown in Fig. 1. When we flip the map, we find no spurious source brighter than the final cut in flux determined in Sect. 3.4.

3.3. A simple and quick PSF fitting routine: FASTPHOT

For both noise- and confusion-limited extraction, we apply the same quick and simple PSF fitting routine on the non-beam-smoothed map. This routine fits all the detected sources at the same time and is consequently efficient for deblending (although no source was blended in this case; but source-blending will be an issue for an extraction using a prior, detailed in Sect. 4. We suppose that the noise is Gaussian and the position of sources is known. We then maximize the likelihood

$$L(m|S) = \prod_{\text{pixels}} C(n) \times \exp\left[-\frac{\left(m - \sum_{i=1}^{\text{Nsources}} PSF_{x_i,y_i} \times S_i\right)^2}{2n^2}\right], \quad (3)$$

where m and n are the map and the noise map. PSF_{x_i,y_i} is a unit-flux PSF centered at the position (x_i, y_i), which are the coordinates of the ith source. These coordinates are not necessarily integers. $C(n)$ is a normalization constant and depends only of the value of the noise map. $\boldsymbol{S}$ is a vector containing the flux of the sources.

The value of S, which maximizes the likelihood, satisfies the following linear equation stating that the derivative of the likelihood logarithm equals zero

$$\forall i, 0 = \frac{\partial \log\left(L(m|S)\right)}{\partial S_i} = A.S + B, \quad (4)$$

where A is a matrix and B a vector defined by

$$A = (a_{ij}) = -\sum_{\text{pixels}} \frac{PSF_{x_i,y_i} \times PSF_{x_j,y_j}}{n^2} \quad (5)$$

$$B = (b_i) = \sum_{\text{pixels}} \frac{PSF_{x_i,y_i} \times map}{n^2}. \quad (6)$$

To perform this operation fast, we used a 70″ × 70″ (respectively 90″ × 90″ and 110″ × 110″) PSF at 250 μm (respectively 350 μm and 500 μm). This PSF, provided by the BLAST team, is the response for a unit-flux source and takes into account all the filtering effects. We used the conjugate gradient method to solve the Eq. (4) quickly.

This routine was tested with 200 × 200 pixels simulated maps containing 400 sources at a known positions with a beam of 10 pixels $FWHM$. The flux of all sources was perfectly recovered in the case where no noise was added. This routine (FASTPHOT) performs simultaneous PSF fitting photometry of 1000 sources in less than 1 s. It is publicly available[2].

3.4. Completeness and photometric accuracy

The completeness is the probability to detect a source of a given flux density. We measured it with a Monte-Carlo simulation. We added artificial point sources (based on PSF) on the initial map at random positions and performed the same source extraction and photometry algorithm as for the real data. A source was considered to be detected if there was a detection in a 20″ radius around the center of the source. Table 1 gives the 95% completeness flux density (for which 95% of sources at this flux are detected) for different wavelengths and depths.

The photometric noise was estimated with the scatter of the recovered fluxes of artificial sources. We computed the standard deviation of the difference between input and output flux. This measurement includes instrumental and confusion noise ($\sigma_{\text{tot}} = \sqrt{\sigma^2_{\text{instr}} + \sigma^2_{\text{conf}}}$). The results are given in Table 1. In the deep

[2] On the IAS website http://www.ias.u-psud.fr/irgalaxies/

Table 1. 95% completeness flux density and photometric noise for different depths at different wavelengths.

	95% completeness		Instrumental noise		Total photometric noise		Deduced confusion noise	
	mJy		mJy		mJy		mJy	
	Shallow	Deep	Shallow	Deep	Shallow	Deep	Shallow	Deep
250 μm	203	97	37.7	11.1	47.3	24.9	28.6	22.3
350 μm	161	83	31.6	9.3	35.8	20.3	16.8	18.0
500 μm	131	76	20.4	6.0	26.4	17.6	16.7	16.5

Notes. The instrumental noise is given by the noise map. The total photometric noise includes the instrumental and confusion noise and is determined by Monte-Carlo simulations. The confusion noise is computed with the formula $\sigma_{\text{conf}} = \sqrt{\sigma^2_{\text{tot}} - \sigma^2_{\text{instr}}}$.

area, the photometric uncertainties are thus dominated by the confusion noise. The estimations of the confusion noise between the deep and shallow areas are consistent. It shows the accuracy and the consistency of our method.

Note that the uncertainties on flux densities in the Dye et al. (2009) catalog (based only on instrumental noise) are consequently largely underestimated in the confusion-limited area. Indeed, their 5σ detection threshold (based only on instrumental noise) at 500 μm in the deep zone corresponds to 1.76σ if we also include the confusion noise.

The faint flux densities are overestimated due to the classical flux boosting effect. This bias was measured for all bands for 60 flux densities between 10 mJy and 3 Jy with the results of the Monte-Carlo simulations. The measured fluxes were deboosted with this relation. We cut the catalogs at the 95% completeness flux, where the boosting factor is at the order of 10%. Below this cut, the boosting effect increases too quickly to be safely corrected. We also observed a little underestimation at high flux of 1%, 0.5% and 0.5% at 250 μm, 350 μm and 500 μm. It is due to FASTPHOT, which assumes that the position is perfectly known, which is not true, especially for a blind extraction.

3.5. Number counts

We computed number counts with catalogs corrected for boosting. For each flux density bin we subtracted the number of spurious detections estimated in the Sects. 3.1 and 3.2 to the number of detected sources and divided the number of sources by the size of the bin, the size of the field and the completeness.

We also applied a corrective factor for the Eddington bias. We assumed a distribution of flux densities in $\mathrm{d}N/\mathrm{d}S \propto S^{-r}$ with $r = 3 \pm 0.5$. This range of possible values for r was estimated considering the Patanchon et al. (2009) counts and the Lagache et al. (2004) and Le Borgne et al. (2009) model predictions. We then randomly kept sources with a probability given by the completeness and added a random Gaussian noise to simulate photometric noise. Finally we computed the ratio between the input and output number of sources in each bin. We applied a correction computed for $r = 3$ to each point. We estimated the uncertainty on this correction with the difference between corrections computed for $r = 2.5$ and $r = 3.5$. This uncertainty was quadratically combined with a Poissonian uncertainty (clustering effects are negligible due to the little number of sources in the map, see Appendix A).

The calibration uncertainty of BLAST is 10%, 12% and 13% at 250 μm, 350 μm and 500 μm respectively (Truch et al. 2009). This uncertainty is combined with other uncertainties on the counts. The results are plotted in Fig. 2 and given in Table 2 and interpreted in Sect. 6.

3.6. Validation

We used simulations to validate our method. We generated 50 mock catalogs based on the Patanchon et al. (2009) counts, and which covered 1 deg^2 each. These sources are spatially homogeneously distributed. We then generated the associated maps at 250 μm. We used the instrumental PSF, and added a Gaussian noise with the same standard deviation as in the deepest part of real map.

We performed an extraction of sources and computed the number counts with the method used in the confusion limited part of the field (Sect. 3.2). We then compared the output counts with the initial counts (Fig. 3). We used two flux density bins: 100–141 mJy and 141–200 mJy. We found no significant bias. The correlation between the two bins is 0.46. The neighbor points are thus not anti-correlated as in the Patanchon et al. (2009) P(D) analysis.

The same verification was done on 20 Fernandez-Conde et al. (2008) simulations (based on the Lagache et al. 2004 model). These simulations include clustering. This model overestimates the number of the bright sources, and the confusion noise is thus stronger. The 95% completeness is then reach at 200 mJy. But there is also a very good agreement between input and output counts in bins brighter than 200 mJy. We found a correlation between two first bins of 0.27.

4. Source extraction using *Spitzer* 24 μm catalog as a prior

In addition to blind source extraction in the BLAST data (Sect. 3) we also performed a source extraction using a prior.

4.1. PSF fitting photometry at the position of the Spitzer 24 μm

The catalogs of infrared galaxies detected by *Spitzer* contain more sources than the BLAST catalog. The 24 μm Spitzer PSF has a Full Width at Half Maximum ($FWHM$) of 6.6″. It is smaller than the BLAST PSF (36″ at 250 μm). Consequently, the position of the Spitzer sources is known with sufficient accuracy when correlating with the BLAST data.

We applied the FASTPHOT routine (Sect. 3.3) at the positions of 24 μm sources. We used the Béthermin et al. (2010) SWIRE catalog cut at $S_{24} = 250$ μJy (80% completeness). In order to avoid software instabilities, we kept in our analysis only the brightest *Spitzer* source in a 20″ radius area (corresponding to 2 BLAST pixels). The corresponding surface density is 0.38,

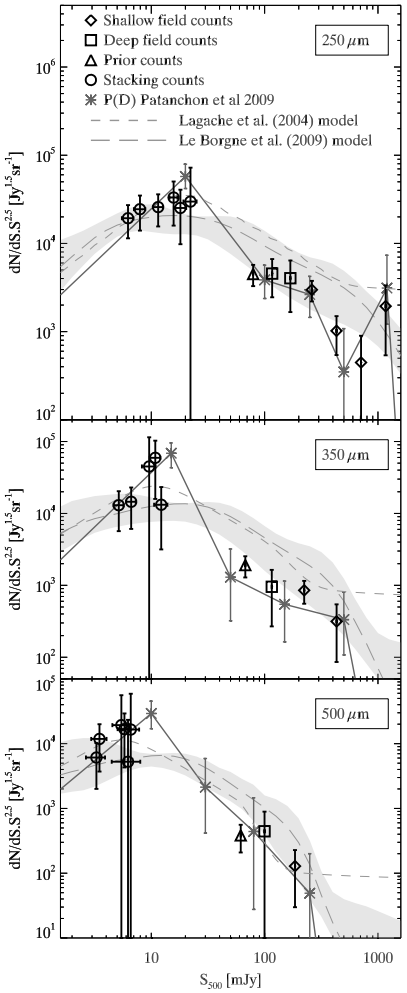

Fig. 2. Extragalactic number counts at 250 μm in the BLAST data. *Diamond*: counts deduced from the source catalog on the whole shallow field; *square*: counts deduced from the catalog of the deep part of the field; *triangle*: counts deduced from catalog of the deep part of the field with a 24 μm prior (this measurement gives only a lower limits to the counts); *cross*: counts computed with a stacking analysis; *grey asterisk*: counts computed with a P(D) analysis by Patanchon et al. (2009); *grey short dashed line*: Lagache et al. (2004) model prediction; *grey long dashed line and grey area*: Le Borgne et al. (2009) model prediction and 1-σ confidence area.

0.49 and 0.89 Spitzer source per beam[3] at 250 μm, 350 μm and 500 μm, respectively.

This method works only if there is no astrometrical offset between the input 24 μm catalog and the BLAST map. We stacked the BLAST sub-map centered on the brightest sources of the SWIRE catalog and measured the centroid of the resulting artificial source. We found an offset of less than 1″. It is negligible compared to the PSF $FWHM$ (36″ at 250 μm).

We worked only in the central region of the deep confusion-limited field (same mask as for blind extraction), where the photometric noise is low.

4.2. Relevance of using Spitzer 24 μm catalog as a prior

The S_{250}/S_{24} (S_{350}/S_{24} or S_{500}/S_{24}) color is not constant, and some sources with a high color ratio could have been missed in the prior catalog (especially high-redshift starbursts). We used the Lagache et al. (2004) and Le Borgne et al. (2009) models to estimate the fraction of sources missed. We selected the sources in the sub-mm flux density bin and computed the 24 μm flux density distribution (see Fig. 4). According to the Lagache et al. (2004) model, 99.6%, 96.4% and 96.9% of the sub-mm selected sources[4] are brighter than S_{24} = 250 μJy for a selection at 250 μm, 350 μm and 500 μm, respectively The Le Borgne et al. (2009) model gives 99.8%, 98.3% and 95.0%, respectively.

4.3. Photometric accuracy

The photometric accuracy was estimated with Monte-Carlo artificial sources. We added five sources of a given flux at random positions on the original map and add them to the 24 μm catalog. We then performed a PSF fitting and compared the input and output flux. We did this 100 times per tested flux for 10 flux densities (between 10 and 100 mJy). In this simulation we assumed that the position of the sources is exactly known. It is a reasonable hypothesis due to the 24 μm PSF $FWHM$ (6.6″) compared to the BLAST one (36″ at 250 μm).

We did not detect any boosting effect for faint flux densities as expected in this case of detection using a prior. For a blind extraction there is a bias of selection toward sources located on peaks of (instrumental or confusion) noise. This is not the case for an extraction using a prior, for which the selection is performed at another wavelength.

The scatter of output flux densities is the same for all the input flux densities. We found a photometric noise σ_S of 21.5 mJy, 18.3 mJy and 16.6 mJy at 250 μm, 350 μm and 500 μm, respectively. It is slightly lower than for the blind extraction, for which the position of source is not initially known.

4.4. Estimation of the number counts

From the catalog described in Sect. 4.1 we give an estimation of the submillimeter number counts at flux densities fainter than reached by the blind-extracted catalog. We cut the prior catalog at 3 σ_S, corresponding to 64 mJy, 54 mJy and 49 mJy at 250 μm, 350 μm and 500 μm, respectively. We worked in a single flux density bin, which is defined to be between this value and the cut of the blind-extracted catalog[4]. There is no flux boosting effect, but we needed to correct the Eddington bias. The completeness could not be defined in the same way as for the blind extraction, because the selection was performed at another wavelength. We thus cannot suppose power-law counts, because the selection function is unknown and the distribution of the extracted sources cannot be computed.

The Eddington bias was estimated with another method. We took the sub-mm flux of each of the sources selected at 24 μm and computed how many sources lie in our count bin. We added a Gaussian noise σ_S to the flux of each source to simulate the photometric errors. We computed the number of sources in the counts bin for the new fluxes. We then compute the mean of the ratio between the input and output number of sources in the selected bin for 1000 realizations. The estimated ratios are 0.42, 0.35 and 0.21 at 250 μm, 350 μm and 500 μm, respectively. These low values indicate that on average the photometric noise introduces an excess of faint sources in our flux bin. This effect is strong because of the steep slope of the number counts, implying more fainter sources than brighter sources. The results are interpreted in the Sect. 6.

[3] The beam solid angles are taken as 0.39 arcmin^2, 0.50 arcmin^2 and 0.92 arcmin^2 at 250 μm, 350 μm and 500 μm respectively.

[4] The bins are defined as 64 to 97 at 250 μm, 54 to 83 at 350 μm and 49 to 76 at 500 μm.

Table 2. Number counts deduced from source extraction. The not normalized counts can be obtained dividing the $S^{2.5}.dN/dS$ column by the S_{mean} column.

Wavelength	S_{mean}	S_{min}	S_{max}	$N_{sources}$	$S^{2.5}.dN/dS$	$\sigma_{S^{2.5}.dN/dS}$	Method
μm		mJy		galaxies	gal Jy$^{1.5}$ sr^{-1}		
250	79	64	97	26	4451	1203	Prior
250	116	97	140	5	4529	2090	Deep
250	168	140	203	3	4040	2377	Deep
250	261	203	336	34	2987	784	Shallow
250	430	336	552	5	1023	479	Shallow
250	708	552	910	1	445	449	Shallow
250	1168	910	1500	2	1939	1401	Shallow
350	67	54	83	17	1913	630	Prior
350	115	83	161	2	955	687	Deep
350	223	161	310	16	854	299	Shallow
350	431	310	600	2	314	228	Shallow
500	61	49	76	7	388	178	Prior
500	99	76	131	1	443	448	Deep
500	185	131	262	4	129	99	Shallow

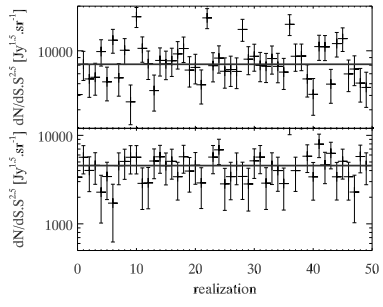

Fig. 3. Number counts at 250 μm deduced from a blind extraction for 50 realizations of a simulation based on the Patanchon et al. (2009) counts. The horizontal *solid line* represents the input count value. The lower panel is the result of the 100–141 mJy bin, the upper panel is the 141–200 mJy bin.

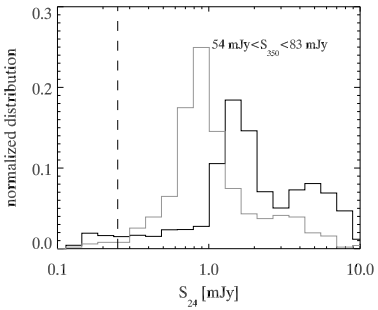

Fig. 4. Flux density distribution at 24 μm of the 54 mJy < S_{350} < 83 mJy sources. The Lagache et al. (2004) model is plotted in *black* and the Le Borgne et al. (2009) model is plotted in *grey*. The *dashed line* represents the cut of our catalog at 24 μm.

4.5. Sub-mm/24 color

In this part we work only on $S > 5\sigma_S$ sources of the catalog described in Sect. 4.1 to avoid bias due to the Eddington bias in our selection. At 250 μm, we have two sources verifying this criterion with a S_{250}/S_{24} color of 16 and 60. No sources are brighter than 5 σ_S at larger wavelengths. For this cut in flux ($S_{250} > 5\sigma_S$), the Lagache et al. (2004) and Le Borgne et al. (2009) models predict a mean S_{250}/S_{24} color of 39 and 41, respectively. The two models predict a mean redshift of 0.8 for this selection, and the K-correction effect explains these high colors.

5. Non-resolved source counts by stacking analysis

5.1. Method

In order to probe the non-resolved source counts, we used same method as Béthermin et al. (2010), i.e. the stacking analysis applied to number counts (hereafter "stacking counts"). We first measured the mean flux at 250 μm, 350 μm or 500 μm as a function of the 24 μm flux ($\overline{S_{250,\ 350\ or\ 500}} = f(S_{24})$). This measurement was performed by stacking in several S_{24} bins. We used the

Table 3. Number counts deduced from stacking.

Wavelength	S	σ_S	$S^{2.5}.dN/dS$	$\sigma_{S^{2.5}.dN/dS}$
μm	mJy		gal Jy$^{1.5}$ sr^{-1}	
250	6.2	0.7	19 313	7892
250	7.9	0.9	24 440	10 466
250	11.5	1.2	25 816	10 236
250	15.7	1.3	33 131	17 213
250	18.1	2.3	25 232	15 428
250	22.2	2.9	29 831	42 448
350	5.2	0.5	13007.	7343.
350	6.6	0.6	14519.	8434.
350	10.8	1.2	59314.	43418.
350	9.6	1.3	44944.	69505.
350	12.2	1.6	13200.	10044.
500	3.5	0.5	11842.	8134.
500	3.3	0.6	6115.	4112.
500	5.8	0.8	16789.	12498.
500	5.4	0.9	19338.	36659.
500	6.6	1.2	16526.	42476.
500	6.2	1.8	5263.	18087.

Notes. The not normalized counts can be obtained dividing the $S^{2.5}.dN/dS$ column by the S column.

Béthermin et al. (2010) catalog at 24 μm of the FIDEL survey. It is deeper than the SWIRE one used in Sect. 4, but covers a smaller area (0.25 deg^2). The photometry of stacked images was performed with the PSF fitting method (Sect. 3.3), and the uncertainties on the mean flux are computed with a bootstrap method (Bavouzet 2008). We then computed the counts in the sub-mm domain with the following formula:

$$\left.\frac{\mathrm{d}N}{\mathrm{d}S_{\mathrm{submm}}}\right|_{S_{\mathrm{submm}}=f(S_{24})} = \left.\frac{\mathrm{d}N}{\mathrm{d}S_{24}}\right|_{S_{24}} \Big/ \left.\frac{\mathrm{d}S_{\mathrm{submm}}}{\mathrm{d}S_{24}}\right|_{S_{24}} . \quad (7)$$

We show in Appendix B that the clustering effect can be neglected. The results are given in Table 3 and are plotted in Fig. 2.

5.2. Validity of the stacking analysis in the sub-mm range

There are 1.8, 2.4 and 4.5 S_{24} >70 μJy sources per BLAST beam at 250 μm, 350 μm and 500 μm, respectively. We thus stacked several sources per beam. Béthermin et al. (2010) showed that the stacking analysis is valid at 160 μm in the *Spitzer* data, where the size of the beam is similar to the BLAST one.

To test the validity of the stacking analysis in the BLAST data from a *Spitzer* 24 μm catalog, we generated a simulation of a 0.25 deg^2 with a Gaussian noise at the same level as for the real map and with source clustering, following Fernandez-Conde et al. (2008). We stacked the 24 μm simulated sources per flux bin in the BLAST simulated maps. We measured the mean BLAST flux for each 24 μm bin with the same method as applied on the real data. At the same time we computed the mean sub-mm flux for the same selection from the mock catalog associated to the simulation. We finally compared the mean BLAST fluxes measured by stacking with those directly derived from the mock catalog to estimate the possible biases (see Fig. 5). The stacking measurements and expected values agree within the error bars. We notice a weak trend of overestimation of the stacked fluxes at low flux density ($S_{24} < 200$ μJy) however, but it is still within the error bars. We can thus stack 24 μm *Spitzer* sources in the BLAST map.

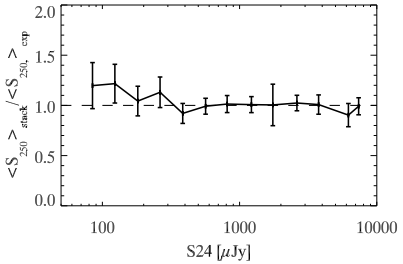

Fig. 5. Ratio between the mean flux density at 250 μm found by the stacking analysis and the expected flux for different S_{24} bins. It is based on a Fernandez-Conde et al. (2008) simulation of a 0.25 deg^2 field with a noise and PSF similar to the BLAST deep region.

5.3. Mean 24 μm to sub-mm color deduced by stacking analysis

The stacking analysis allowed to measure the mean 24 μm to sub-mm colors of undetected sub-mm galaxies. These colors depends on the SED of galaxies (or K-correction) and the redshift distribution in a degenerate way. The $S_{\mathrm{submm}}/S_{24}$ color and $\mathrm{d}S_{\mathrm{submm}}/\mathrm{d}S_{24}$ as a function of S_{24} are plotted in Fig. 6.

The colors are higher for the fainter 24 μm flux ($S_{24} <$ 100 μJy). This behavior agrees with the model expectations: the faint sources at 24 μm lie at a higher mean redshift than the brighter ones. Due to the K-correction, the high-redshift sources have a brighter sub-mm/24 color than local ones.

The colors found by the stacking analysis are lower than those obtained by an extraction at 250 μm (Sect. 4.5). It is an effect of selection. The mid-infrared is less affected by the K-correction than the sub-mm, and a selection at this wavelength selects lower redshift objects. We thus see lower colors because of the position of the SED peak (around 100 μm rest-frame).

We also investigated the evolution of the derivative $\mathrm{d}S_{\mathrm{submm}}/\mathrm{d}S_{24}$ as a function of S_{24}, which explicits how the observed sub-mm flux increases with the 24 μm flux densities. At high 24 μm flux densities ($S_{24} >$ 400 μJy) the derivative is almost constant and small (<20 and compatible with zero), meaning that the observed sub-mm flux density does not vary much with S_{24}. For these flux bins we select only local sources and do not expect a strong evolution of the color. At fainter 24 μm flux densities the observed decrease can be explained by redshift and K-correction effects, as above.

The color in the faintest 24 μm flux density bin (70 to 102 μJy) is slightly fainter than in the neighboring points. It can be due to the slight incompleteness of the 24 μm catalog (about 15%), which varies spatially across the field: the sources close to the brightest sources at 24 μm are hardly extracted. The consequence is a bias to the lower surface density regions, leading to a slight underestimation of the stacked flux measurement.

5.4. Accuracy of the stacking counts method on BLAST with a Spitzer 24 μm prior

Béthermin et al. (2010) showed that the stacking counts could be biased: the color of sources can vary a lot as a function of the redshift. The assumption of a single color for a given S_{24}

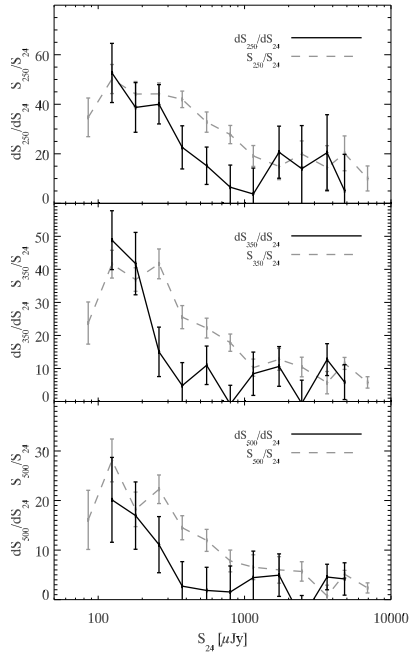

Fig. 6. *Black solid line*: $\mathrm{d}S_{\mathrm{submm}}/\mathrm{d}S_{24}$ as a function of S_{24}. *Grey dashed line*: $S_{\mathrm{submm}}/S_{24}$ color as a function of S_{24}.

is not totally realistic and explains some biases. We used two simulated catalogs (containing for each source S_{24}, S_{250}, S_{350} and S_{500}) to estimate this effect: a first one based on the Lagache et al. (2004) model that covered 20 × 2.9 deg^2 and a second one based on the Le Borgne et al. (2009) model and that covered 10 deg^2. The large size of these simulations allows us to neglect cosmic variance.

In order to compute the stacking counts, we first computed the counts at 24 μm from the mock catalog. Then we computed the mean $S_{250,\ 350\ or\ 500}$ flux density (directly in the catalog) in several S_{24} bins to simulate a stacking. We finally applied the Eq. (7) to compute stacking counts at the BLAST wavelengths.

The ratio between the stacking counts and the initial counts is plotted in Fig. 8 for the two mock catalogs. Between 1 mJy and 10 mJy we observe an oscillating bias. This bias is less than 30% at 250 μm and 50% at other wavelengths. When the flux becomes brighter than 25 mJy at 250 μm (18 mJy at 350 μm and 7.5 mJy at 350 μm), we begin to strongly underestimate the counts. The analysis of real data also shows a very strong decrease in the counts around the same fluxes (see Fig. 7). Consequently, we cut our stacking analysis at these fluxes and we applied an additional uncertainty to the stacking counts of 30% at 250 μm (50% at 350 μm and 500 μm).

Using the 24 μm observations as a prior to stack in the BLAST bands seems to give less accurate results than in the *Spitzer* MIPS bands. For a given S_{24} flux, the sub-mm emission can vary a lot as a function of the redshift. But the simulations shows that this method works for faint flux densities. It is due to the redshift selection which is similar for faint flux densities (see Fig. 9) and very different at higher flux densities (see Fig. 10). For example, $S_{24} \sim 100$ μJy sources are distributed around $z = 1.5$ with a broad dispersion in redshift. $S_{350} \sim 4$ mJy (based on averaged colors, 4 mJy at 350 μm corresponds to $S_{24} \sim 100$ μJy) sources have quite a similar redshift distribution except an excess for $z > 2.6$. At higher flux densities (around 2 mJy at 24 μm) the distribution is very different. The majority of the 24 μm-selected sources lies at $z < 1$ and the distribution of 350 μm-selected sources peaks at $z \sim 1.5$. Another possible explanation is that fainter sources lies near $z = 1$ and are thus selected at the 12 μm rest-frame, which is a very good estimator of the infrared bolometric luminosity according to Spinoglio et al. (1995).

In order to limit the scatter of the sub-mm/24 color, we tried to cut our sample into two redshift boxes following the Devlin et al. (2009) IRAC color criterion ([3.6]–[4.5] = 0.068([5.8]–[8.0])–0.075). But we had not enough signal in the stacked images to perform the analysis.

6. Interpretation

6.1. Contribution to the CIB

We integrated our counts assuming power-law behavior between our points. Our points are not independent (especially the stacking counts), and we thus combined errors linearly. The contribution of the individually detected sources ($S_{250} >$ 64 mJy, $S_{350} >$ 54 mJy, $S_{500} >$ 49 mJy) is then $0.24^{+0.18}_{-0.13}$ nW.m^2.sr^{-1}, $0.06^{+0.05}_{-0.04}$ nW.m^2.sr^{-1} and $0.01^{+0.01}_{-0.01}$ nW.m^2.sr^{-1} at 250 μm, 350 μm and 500 μm, respectively. Considering the total CIB level of Fixsen et al. (1998) (FIRAS absolute measurement), we resolved directly only 2.3%, 1.1% and 0.4% at 250 μm, 350 μm and 500 μm, respectively.

The populations probed by the stacking counts ($S_{250} >$ 6.2 mJy, $S_{350} >$ 5.2 mJy, $S_{500} >$ 3.5 mJy) emit $5.0^{+2.5}_{-2.6}$ nW m^2 sr^{-1}, $2.8^{+1.8}_{-2.0}$ nW m^2 sr^{-1} and $1.4^{+2.1}_{-1.3}$ nW m^2 sr^{-1} at 250 μm, 350 μm and 500 μm, respectively. This corresponds to about 50% of the CIB at these three wavelengths.

6.2. Comparison with Patanchon et al. (2009)

The agreement between our resolved counts built from the catalogs and the P(D) analysis of Patanchon et al. (2009) is excellent (Fig. 2). We confirm the efficiency of the P(D) analysis to recover number counts without extracting sources. The stacking counts probe the flux densities between 6 mJy and 25 mJy at 250 μm (between 5 mJy and 13 mJy at 350 μm and 3 mJy and 7 mJy at 500 μm). In this range there is only one P(D) point. At the three BLAST wavelengths the P(D) points agree with our stacking counts (Fig. 2). Our results thus confirm the measurement of Patanchon et al. (2009) and give a better sampling in flux.

6.3. Comparison with ground-based observations

We compared our results with sub-mm ground-based observations of SHARC. Khan et al. (2007) estimated a density of $S_{350} > 13$ mJy sources of $0.84^{+1.39}_{-0.61}$ arcmin^{-2}. For the same cut,

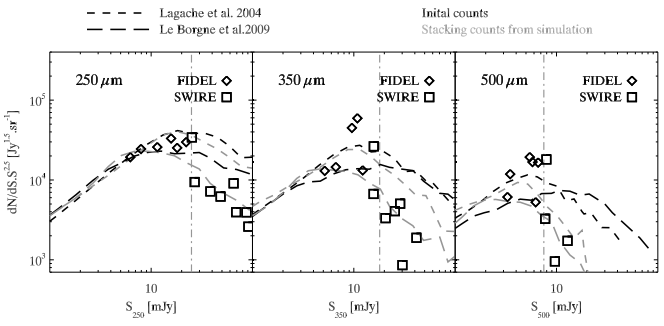

Fig. 7. Number counts at BLAST wavelengths coming from the data (*points*) and the models (*lines*). *Short dashed line*: initial *(black)* and stacking *(grey)* counts from the Lagache et al. (2004) mock catalog; *long dashed line*: initial *(black)* and stacking *(grey)* counts from Le Borgne et al. (2009); *diamond*: stacking counts built with the FIDEL catalog; *square*: stacking counts built with the SWIRE catalog; *grey vertical dot-dash line*: flux cut for stacking counts.

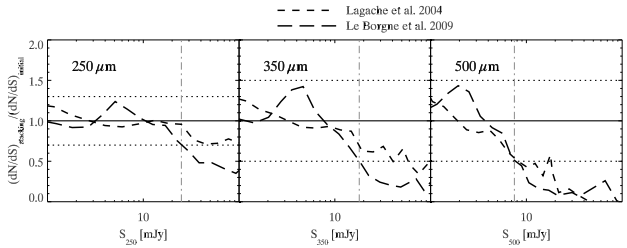

Fig. 8. Ratio between stacking counts and initial counts for two mock catalogs; *short dashed line*: Lagache et al. (2004) catalog; *long dashed line*: Le Borgne et al. (2009); *grey vertical dot-dash line*: flux cut for stacking counts; *horizontal dot line*: estimation of the uncertainty intrinsic to the stacking method.

we found 0.26 ± 0.13 arcmin^{-1}, which agrees with their work. Our measurement (175 ± 75 sources deg^{-2} brighter than 25 mJy) agrees also with that of Coppin et al. (2008) ones at the same wavelength (200–500 sources deg^{-2} brighter than 25 mJy).

We also compared our results at 500 μm with the SCUBA ones at 450 μm. Borys et al. (2003) find 140^{+140}_{-90} gal deg^{-2} for $S_{450} > 100$ mJy. We found 1.2 ± 1.0 gal.deg^{-2}. We significantly disagree with them. Borys et al. (2003) claim 5 4-σ detections in a 0.046 deg^2 field in the *Hubble* deep field north (HDFN). These five sources are brighter than 100 mJy. We find no source brighter than 100 mJy in a 0.45 deg^2 field at 350 μm nor at 500 μm. The cosmic variance alone thus cannot explain this difference. A possible explanation is that they underestimated the noise level and their detections are dominated by spurious sources. It could also be due to a calibration shift (by more than a factor 2). The observation of the HDFN by *Herschel* will allow us to determine whether that these bright sources might be spurious detections.

We also compared our results with the estimations based on lensed sources at 450 μm with SCUBA (Smail et al. 2002; Knudsen et al. 2006). For example, Knudsen et al. (2006) find 2000–50 000 sources deg^2 brighter than 6 mJy. It agrees with our 3500^{+7700}_{-3400} sources deg^2.

6.4. Comparison with the Lagache et al. (2004) and Le Borgne et al. (2009) models

At 250 μm and 350 μm the measured resolved source counts are significantly lower (by about a factor of 2) than the Lagache et al. (2004) and Le Borgne et al. (2009) models. Nevertheless, our counts are within the confidence area of Le Borgne et al. (2009). The same effect (models overestimating the counts) was observed at 160 μm (Frayer et al. 2009; Béthermin et al. 2010). It indicates that the galaxies' SED or the luminosity functions used in both models might have to be revisited. At 500 μm our counts and both models agree very well, but our uncertainties are large, which renders any discrimination difficult.

Concerning the stacking counts, they agree very well with the two models. Nevertheless, our uncertainties are larger than 30%. We thus cannot check if the disagreement observed between the Lagache et al. (2004) model and the stacking counts at 160 μm (Béthermin et al. 2010) of 30% at $S_{160} = 20$ mJy still holds at 250 μm.

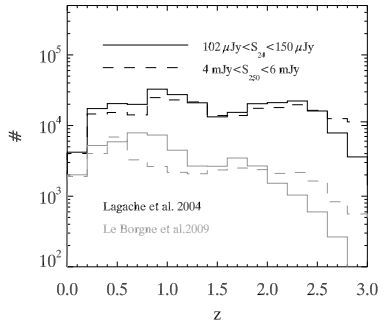

Fig. 9. *Solid line*: distribution in redshift of the sources with 102 μJy < S_{24} < 150 μJy for the mock catalogs generated with the Lagache et al. (2004) *(black)* and the Le Borgne et al. (2009) *(grey)* models; *dashed line*: distribution in redshift of the sources with 4 mJy < S_{250} < 6 mJy (determined using the mean 250/24 color).

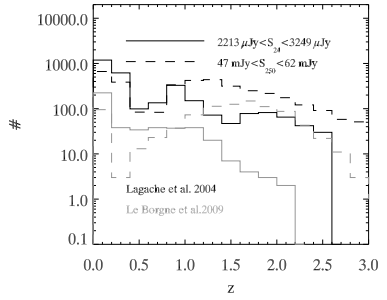

Fig. 10. *Solid line*: distribution in redshift of the sources with 2213 μJy < S_{24} < 3249 μJy for the mock catalogs generated with the Lagache et al. (2004) *(black)* and Le Borgne et al. (2009) *(grey)* models; *dashed line*: distribution in redshift of sources with 47 mJy < S_{250} < 62 mJy (determined using the mean 250/24 color).

6.5. Implications for the probed populations and the models

We showed that the two models nicely reproduce the sub-mm counts, especially below 100 mJy. We can thus use them to estimate which populations are constrained by our counts. For each flux density bin we computed the mean redshift of the selected galaxies in both models. We then used the SEDs given by the models at that mean redshift and at that flux bin and derived the infrared bolometric luminosity. The luminosities are shown in dashed lines in Fig. 11 for 350 μm as an example, and the redshift is given in solid lines.

The stacking counts reach 6.2 mJy, 5.3 mJy and 3.5 mJy at 250 μm, 350 μm and 500 μm, respectively. This corresponds to faint ULIRGs ($L_{IR} \approx 1.5 \times 10^{12}\ L_\odot$) around $z = 1.5$, 1.8 and 2.1 at 250 μm, 350 μm and 500 μm, respectively. Our measurements show that the predicted cold-dust emissions (between 100 μm and 200 μm rest frame) of this population in the models are believable.

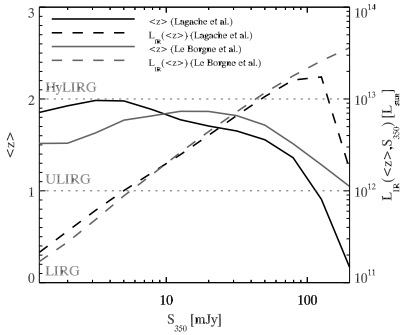

Fig. 11. Mean redshift (*solid line*) of sources for different fluxes at 350 μm for the Lagache et al. (2004) *(black)* and Le Borgne et al. (2009) *(grey)* models and corresponding infrared luminosity defined in Sect. 6.5 *(dashed line)*.

At 250 μm and 350 μm the resolved sources ($S_{350} > 85$ mJy) are essentially $z \sim 1$ ULIRGs ($L_{IR} > 10^{12} L_\odot$) and HyLIRGs ($L_{IR} > 10^{13}\ L_\odot$) according to the models. In Lagache et al. (2004) the local cold-dust sources contribute at very bright flux (>200 mJy). This population is not present in the Le Borgne et al. (2009) model. It explains the difference between the two models for fluxes brighter than 100 mJy at 350 μm (see Fig. 11). At 500 μm, Lagache et al. (2004) predict that bright counts are dominated by local cold-dust populations and Le Borgne et al. (2009) that they are dominated by medium redshift HyLIRGs. Nevertheless, there is a disagreement with the observations for this flux density range, suggesting that there could be less HyLIRGs than predicted. But these models do not currently include any AGN contribution, which is small except at luminosities higher than $10^{12}\ L_\odot$ (Lacy et al. 2004; Daddi et al. 2007; Valiante et al. 2009).

7. Conclusion

Our analysis provides new stacking counts, which can be compared with the Patanchon et al. (2009) P(D) analysis. We have a good agreement between the different methods. Nevertheless, some methods are more efficient in a given flux range.

The blind extraction and the extraction using a prior give a better sampling in flux and slightly smaller error bars. The P(D) analysis uses only the pixel histogram and thus looses the information on the shape of the sources. The blind extraction is a very efficient method for extracting the sources, but lots of corrections must be applied carefully. When the confusion noise totally dominates the instrumental noise, the former must be determined accurately, and the catalog flux limit must take this noise (Dole et al. 2003) into account.

Estimating the counts from a catalog built using a prior is a good way to deal with the flux boosting effect. This method is based on assumptions however. We assume that all sources brighter than the flux cut at the studied wavelength are present in the catalog extracted using a prior. We also assume a flux

distribution at the studied wavelength for a selection at the prior wavelength to correct for the Eddington bias. Consequently an extraction using a prior must be used in a flux range where the blind extraction is too affected by the flux boosting to be accurately corrected.

P(D) analysis and stacking counts estimate the counts at flux densities below the detection limit. These methods have different advantages. The P(D) analysis fits all the fluxes at the same time, where the stacking analysis flux depth depends on the prior catalog's depth (24 μm *Spitzer* for example). But the P(D) analysis with a broken power-law model is dependent on the number and the positions of the flux nodes. The uncertainty due to the parameterization was not evaluated by Patanchon et al. (2009). The stacking counts on the other hand are affected by biases due to the color dispersion of the sources. The more the prior and stacked wavelength are correlated, the less biased are the counts. A way to overcome this bias would be to use a selection of sources (in redshift slices for example), which would reduce the color dispersion, and the induced bias; we did not use this approach here because of a low signal-to-noise ratio.

The stacking and P(D) analysis are both affected by the clustering in different ways. For the stacking analysis this effect depends on the size of the PSF. This effect is small for BLAST and will be smaller for SPIRE. The clustering broadens the pixel histogram. Patanchon et al. (2009) show that it is negligible for BLAST. Clustering will probably be an issue for SPIRE. The cirrus can also affect the P(D) analysis and broaden the peak. Patanchon et al. (2009) use a high-pass filtering that reduces the influence of these large scale structures.

The methods used in this paper will probably be useful to perform the analysis of the *Herschel* SPIRE data. The very high sensitivity and the large area covered will reduce the uncertainties and increase the depth of the resolved source counts. Nevertheless, according to the models (e.g. Le Borgne et al. (2009)), the data will also be quickly confusion-limited and it will be very hard to directly probe the break of the counts. The P(D) analysis of the deepest SPIRE fields will allow us to constrain a model with more flux nodes and to better sample the peak of the normalized differential number counts. The instrumental and confusion noise will be lower, and a stacking analysis per redshift slice will probably be possible. These analyses will give stringent constraints on the model of galaxies and finally on the evolution of the infrared galaxies.

Acknowledgements. We warmly acknowledge Guillaume Patanchon for his precious comments and discussions. We thank Damien Le Borgne and Guilaine Lagache for distributing their model and their comments. We also acknowledge Alexandre Beelen and Emeric Le Floc'h for their useful comments. We thank Maxime Follin, for his help during his Licence 3 training at the Université Paris Sud 11. We thank the BLAST team for the well-documented public release of their data. We warmly thank the referee Steve Willner, who helped a lot to improve the quality of this paper. This work is based in part on archival data obtained with the Spitzer Space Telescope, which is operated by the Jet Propulsion Laboratory, California Institute of Technology under a contract with NASA. Support for this work was provided by an award issued by JPL/Caltech.

Appendix A: Effect of clustering on the uncertainties of number counts

Béthermin et al. (2010) showed how the clustering is linked with the uncertainties of the counts. We used the formalism of Béthermin et al. (2010) to estimate the effect of the clustering on our BLAST counts. There are few sources detected at 250 μm and the BLAST coverage is inhomogeneous. It is consequently very hard to estimate the clustering of the resolved population. We thus used the clustering measured at 160 μm by Béthermin et al. (2010) and assumed a 250/160 color equal to unity. We then used the same method to compute the uncertainties. We then compare the uncertainties with and without clustering. Neglecting the clustering implies an underestimation of the uncertainties on the counts of 35% in the 203–336 mJy bin at 250 μm, and less than 20% in the other bins. We can thus suppose a Poissonian behavior, knowing that the Poisson approximation underestimates the error bars for the 203–336 mJy bin at 250 μm. Nevertheless, our model of clustering at 250 μm has strong assumptions (single 250/160 color, same clustering at 250 μm as measured at 160 μm), and it would be more conservative to update it with *Herschel* clustering measurements.

Appendix B: Effect of clustering on stacking

B.1. A formalism to link clustering and stacking

The clustering can bias the results of a stacking. We present a formalism based on Bavouzet (2008) work.

The expected results for mean stacking of an N non-clustered populations is

$$M(\theta) = \overline{S_\mathrm{s}} \times PSF(\theta) + \int_0^\infty S \frac{\mathrm{d}N}{\mathrm{d}S} \mathrm{d}S, \tag{B.1}$$

where M is the map resulting from stacking, θ the distance to the center of the cutout image, $\overline{S_\mathrm{s}}$ the mean flux of the stacked population. The integral is an approximation because the central source is treated in the first term. This approximation is totally justified in a strongly confused field where the number of sources is enormous. PSF is the instrumental response and is supposed to be invariant per rotation ($\theta = 0$ corresponds to the center of this PSF). $\frac{\mathrm{d}N}{\mathrm{d}S}$ is the number of the source per flux unit and per pixel. We assume an absolute calibration. The integral in the Eq. (B.1) is equal to the CIB brightness

$$I_\mathrm{CIB} = \int_0^\infty S \frac{\mathrm{d}N}{\mathrm{d}S} \mathrm{d}S. \tag{B.2}$$

This term is constant for all pixels of the image and corresponds to a homogeneous background.

The stacked sources can actually be autocorrelated. The probability density to find a stacked source in a given pixel and another in a second pixel separated by an angle θ ($p(\theta)$) is linked with the angular autocorrelation function ($\omega(\theta)$) by

$$p(\theta) = \rho_\mathrm{s}^2(1 + \omega(\theta)), \tag{B.3}$$

where ρ_s is the number density of the stacked source.

If we assume that there is no correlation with other populations, the results of the stacking of N autocorrelated sources is

$$M(\theta) = \overline{S_\mathrm{s}} \times PSF(\theta) + I_\mathrm{CIB,s}(1 + \omega(\theta)) * PSF(\theta) + I_\mathrm{CIB,ns}, \tag{B.4}$$

where $I_\mathrm{CIB,s}$ and $I_\mathrm{CIB,ns}$ is the CIB contribution of stacked and non-stacked sources. If we subtract the constant background of the image, we find

$$M(\theta) = \overline{S_\mathrm{s}} \times PSF(\theta) + I_\mathrm{CIB,s} \times \omega(\theta) * PSF(\theta). \tag{B.5}$$

The second term of this equation corresponds to an excess of flux due to clustering. This signal is stronger in the center of the stacked image. The central source appears thus brighter than expected, because of the contribution due to clustering.

The flux of the central stacked source computed by PSF-fitting photometry is

$$S_\mathrm{mes} = \frac{\int\int M \times PSF \mathrm{d}\Omega}{\int\int PSF^2 \mathrm{d}\Omega} = \overline{S_\mathrm{s}} + S_\mathrm{clus}, \tag{B.6}$$

where S_clus, the overestimation of flux due to clustering is given by

$$S_\mathrm{clus} = I_\mathrm{CIB,s} \times \frac{\int\int \left((\omega * PSF) \times PSF\right) \mathrm{d}\Omega}{\int\int PSF^2 \mathrm{d}\Omega}. \tag{B.7}$$

Basically, the stronger the clustering, the larger the bias. In addition, the wider the PSF, the larger the overestimation. The stacked signal can be dominated by the clustering, if the angular resolution of the instrument is low compared to the surface density of the sources (like *Planck*, cf. Fernandez-Conde et al. (2010)) or if strongly clustered populations are stacked.

B.2. Estimation of the bias due to clustering

The estimation of S_clus with Eq. (B.7) requires particular hypotheses. The stacked population is $S_{24} > 70$ μJy sources detected by *Spitzer*. Their contribution to the CIB is 5.8 nW m^{-2} sr^{-1}, 3.4 nW m^{-2} sr^{-1} and 1.4 nW m^{-2} sr^{-1} at 250 μm, 350 μm and 500 μm, respectively (estimated by direct stacking of all the sources). Following the clustering of 24 μm sources estimated by Béthermin et al. (2010), we suppose the following autocorrelation function:

$$\omega(\theta) = 2.3 \times 10^{-4} \times \left(\frac{\theta}{\mathrm{deg}}\right)^{-0.8}. \tag{B.8}$$

The excess of flux due to clustering (S_clus) is then 0.44 mJy, 0.35 mJy and 0.16 mJy at 250 μm, 350 μm and 500 μm, respectively. This is significantly lower than the bootstrap uncertainties on these fluxes. We can thus neglect the clustering.

B.3. Measurement of the angular correlation function by stacking

This new formalism provides a simple tool to measure the angular autocorrelation function (ACF) from a source catalog. This method uses a map called "density map". One pixel of this map contains the number of sources centered on it. It is equivalent of a map of unit flux sources with the $PSF = \delta$ (Dirac distribution). The result of the stacking is thus

$$M(\theta) = \rho_\mathrm{s} \times \delta(\theta) + \rho_\mathrm{s}(1 + \omega(\theta)). \tag{B.9}$$

The ACF can then be easily computed with

$$\forall \theta \neq 0, \omega(\theta) = \frac{M(\theta)}{\rho_\mathrm{s}} - 1. \tag{B.10}$$

References

Ashby, M. L. N., Stern, D., Brodwin, M., et al. 2009, ApJ, 701, 428
Barmby, P., Huang, J., Ashby, M. L. N., et al. 2008, ApJS, 177, 431
Bavouzet, N. 2008, Ph.D. Thesis, Université Paris-Sud 11 http://tel.archives-ouvertes.fr/tel-00363975/
Beelen, A., Cox, P., Benford, D. J., et al. 2006, ApJ, 642, 694
Benford, D. J., Cox, P., Omont, A., Phillips, T. G., & McMahon, R. G. 1999, ApJ, 518, L65
Bertin, E., & Arnouts, S. 1996, A&AS, 117, 393
Béthermin, M., Dole, H., Beelen, A., et al. 2010, A&A, 512, A78
Borys, C., Chapman, S., Halpern, M., et al. 2003, MNRAS, 344, 385
Chapman, S. C., Blain, A. W., Ivison, R. J., et al. 2003a, Nature, 422, 695
Chapman, S. C., Helou, G., Lewis, G. F., et al. 2003b, ApJ, 588, 186
Chapman, S. C., Blain, A. W., Smail, I., et al. 2005, ApJ, 622, 772
Chary, R., & Elbaz, D. 2001, ApJ, 556, 562
Chary, R., Casertano, S., Dickinson, M. E., et al. 2004, ApJS, 154, 80
Coppin, K., Halpern, M., Scott, D., et al. 2008, MNRAS, 384, 1597
Daddi, E., Alexander, D. M., Dickinson, M., et al. 2007, ApJ, 670, 173
Devlin, M. J., Ade, P. A. R., Aretxaga, I., et al. 2009, Nature, 458, 737
Dole, H., Gispert, R., Lagache, G., et al. 2001, A&A, 372, 364
Dole, H., Lagache, G., & Puget, J.-L. 2003, ApJ, 585, 617
Dole, H., Le Floc'h, E., Pérez-González, P. G., et al. 2004, ApJS, 154, 87
Dole, H., Lagache, G., Puget, J.-L., et al. 2006, A&A, 451, 417
Dunne, L., Eales, S., Edmunds, M., et al. 2000, MNRAS, 315, 115
Dye, S., Ade, P. A. R., Bock, J. J., et al. 2009, ApJ, 703, 285
Fazio, G. G., Ashby, M. L. N., Barmby, P., et al. 2004a, ApJS, 154, 39
Fazio, G. G., Hora, J. L., Allen, L. E., et al. 2004b, ApJS, 154, 10
Fernandez-Conde, N., Lagache, G., Puget, J.-L., et al. 2008, A&A, 481, 885
Fernandez-Conde, N., Lagache, G., Puget, J.-L., et al. 2010, A&A, 515, A48
Fixsen, D. J., Dwek, E., Mather, J. C., Bennett, C. L., & Shafer, R. A. 1998, ApJ, 508, 123
Franceschini, A., Rodighiero, G., Cassata, P., et al. 2006, A&A, 453, 397
Franceschini, A., Rodighiero, G., Vaccari, M., Marchetti, L., & Mainetti, G. 2009, A&A, accepted [arXiv:0906.4264]
Frayer, D. T., Fadda, D., Yan, L., et al. 2006a, AJ, 131, 250
Frayer, D. T., Huynh, M. T., Chary, R., et al. 2006b, ApJ, 647, L9
Frayer, D. T., Sanders, D. B., Surace, J. A., et al. 2009, AJ, 138, 1261
Gispert, R., Lagache, G., & Puget, J. L. 2000, A&A, 360, 1
Gruppioni, C., Pozzi, F., Lari, C., Oliver, S., & Rodighiero, G. 2005, ApJ, 618, L9
Hauser, M. G., & Dwek, E. 2001, ARA&A, 39, 249
Hauser, M. G., Arendt, R. G., Kelsall, T., et al. 1998, ApJ, 508, 25
Ivison, R. J., Greve, T. R., Smail, I., et al. 2002, MNRAS, 337, 1
Ivison, R. J., Smail, I., Dunlop, J. S., et al. 2005, MNRAS, 364, 1025
Kashlinsky, A. 2005, Phys. Rep., 409, 361
Khan, S. A., Chanial, P. F., Willner, S. P., et al. 2009, ApJ, 706, 319
Khan, S. A., Shafer, R. A., Serjeant, S., et al. 2007, ApJ, 665, 973
Knudsen, K. K., Barnard, V. E., van der Werf, P. P., et al. 2006, MNRAS, 368, 487
Kovács, A., Chapman, S. C., Dowell, C. D., et al. 2006, ApJ, 650, 592
Lacy, M., Storrie-Lombardi, L. J., Sajina, A., et al. 2004, ApJS, 154, 166
Lagache, G., Abergel, A., Boulanger, F., Désert, F. X., & Puget, J.-L. 1999, A&A, 344, 322
Lagache, G., Dole, H., Puget, J.-L., et al. 2004, ApJS, 154, 112
Lagache, G., Puget, J.-L., & Dole, H. 2005, ARA&A, 43, 727
Le Borgne, D., Elbaz, D., Ocvirk, P., et al. 2009, A&A, 504, 727
LeFloc'h, E., Aussel, H., Ilbert, O., et al. 2009, ApJ, 703, 222
Lewis, G. F., Chapman, S. C., & Helou, G. 2005, ApJ, 621, 32
Magdis, G. E., Rigopoulou, D., Huang, J., et al. 2008, MNRAS, 386, 11
Marleau, F. R., Fadda, D., Storrie-Lombardi, L. J., et al. 2004, ApJS, 154, 66
Marsden, G., Ade, P. A. R., Bock, J. J., et al. 2009, ApJ, 707, 1729
Michałowski, M. J., Hjorth, J., & Watson, D. 2010, A&A, 514, A67
Papovich, C., Dole, H., Egami, E., et al. 2004, ApJS, 154, 70
Pascale, E., Ade, P. A. R., Bock, J. J., et al. 2008, ApJ, 681, 400
Patanchon, G., Ade, P. A. R., Bock, J. J., et al. 2008, ApJ, 681, 708
Patanchon, G., Ade, P. A. R., Bock, J. J., et al. 2009, ApJ, 707, 1750
Pearson, C., & Khan, S. A. 2009, MNRAS, 399, L11
Pope, A., Borys, C., Scott, D., et al. 2005, MNRAS, 358, 149
Pope, A., Scott, D., Dickinson, M., et al. 2006, MNRAS, 370, 1185
Puget, J.-L., Abergel, A., Bernard, J.-P., et al. 1996, A&A, 308, L5
Rieke, G. H., Young, E. T., Engelbracht, C. W., et al. 2004, ApJS, 154, 25
Rodighiero, G., Lari, C., Pozzi, F., et al. 2006, MNRAS, 371, 1891
Rowan-Robinson, M. 2009, MNRAS, 394, 117
Sajina, A., Borys, C., Chapman, S., et al. 2003, MNRAS, 343, 1365
Sajina, A., Scott, D., Dennefeld, M., et al. 2006, MNRAS, 369, 939
Shupe, D. L., Rowan-Robinson, M., Lonsdale, C. J., et al. 2008, AJ, 135, 1050
Smail, I., Ivison, R. J., Blain, A. W., et al. 2002, MNRAS, 331, 495
Spinoglio, L., Malkan, M. A., Rush, B., Carrasco, L., & Recillas-Cruz, E. 1995, ApJ, 453, 616
Starck, J. L., Aussel, H., Elbaz, D., Fadda, D., & Cesarsky, C. 1999, A&AS, 138, 365
Stetson, P. B. 1987, PASP, 99, 191
Sullivan, I., Cooray, A., Chary, R., et al. 2007, ApJ, 657, 37
Truch, M. D. P., Ade, P. A. R., Bock, J. J., et al. 2009, ApJ, 707, 1723
Valiante, E., Lutz, D., Sturm, E., Genzel, R., & Chapin, E. 2009, ApJ, 701, 1814

A&A 515, A48 (2010)
DOI: 10.1051/0004-6361/200912924

Astronomy & Astrophysics

Simulations of the cosmic infrared and submillimeter background for future large surveys

II. Removing the low-redshift contribution to the anisotropies using stacking

N. Fernandez-Conde, G. Lagache, J.-L. Puget, and H. Dole

Institut d'Astrophysique Spatiale (IAS), Bât. 121, Université Paris-Sud 11 and CNRS (UMR 8617), 91405 Orsay, France
e-mail: nestorconde@gmail.com, [guilaine.lagache;jean-loup.puget;herve.dole]@ias.u-psud.fr

Received 17 July 2009 / Accepted 17 January 2010

ABSTRACT

Context. Herschel and Planck are surveying the sky at unprecedented angular scales and sensitivities over large areas. But both experiments are limited by source confusion in the submillimeter. The high confusion noise in particular restricts the study of the clustering properties of the sources that dominate the cosmic infrared background. At these wavelengths, it is more appropriate to consider the statistics of the unresolved component. In particular, high clustering will contribute in excess of Poisson noise in the power spectra of CIB anisotropies.

Aims. These power spectra contain contributions from sources at all redshift. We show how the stacking technique can be used to separate the different redshift contributions to the power spectra.

Methods. We use simulations of CIB representative of realistic Spitzer, Herschel, Planck, and SCUBA-2 observations. We stack the 24 μm sources in longer wavelengths maps to measure mean colors per redshift and flux bins. The information retrieved on the mean spectral energy distribution obtained with the stacking technique is then used to clean the maps, in particular to remove the contribution of low-redshift undetected sources to the anisotropies.

Results. Using the stacking, we measure the mean flux of populations 4 to 6 times fainter than the total noise at 350 μm at redshifts $z = 1$ and $z = 2$, respectively, and as faint as 6 to 10 times fainter than the total noise at 850 μm at the same redshifts. In the deep Spitzer fields, the detected 24 μm sources up to $z \sim 2$ contribute significantly to the submillimeter anisotropies. We show that the method provides excellent (using COSMOS 24 μm data) to good (using SWIRE 24 μm data) removal of the $z < 2$ (COSMOS) and $z < 1$ (SWIRE) anisotropies.

Conclusions. Using this cleaning method, we then hope to have a set of large maps dominated by high redshift galaxies for galaxy evolution study (e.g., clustering, luminosity density).

Key words. methods: statistical – infrared: galaxies – galaxies: evolution

1. Introduction

The first observational evidence of the cosmic infrared background (CIB) was reported by Puget et al. (1996) and confirmed by Fixsen et al. (1998) and Hauser et al. (1998). The CIB is composed of the relic emission at infrared wavelengths of the formation and evolution of galaxies and consists of contributions from infrared starburst galaxies and to a lesser degree from active galactic nuclei. Deep cosmological surveys of this background have been carried out with ISO (see Genzel & Cesarsky 2000; Elbaz 2005, for reviews) mainly at 15 μm with ISOCAM (e.g., Elbaz et al. 2002); at 90 and 170 μm with ISOPHOT (e.g., Dole et al. 2001); with Spitzer at 24, 70, and 160 μm (e.g., Papovich et al. 2004; Dole et al. 2004) and with ground-based instruments SCUBA (e.g., Blain et al. 2002), LABOCA (e.g., Beelen et al. 2008), and MAMBO (e.g., Bertoldi et al. 2000) at 850, 870, and 1300 μm respectively. The balloon-borne experiment BLAST performed the first deep extragalactic surveys at wavelengths 250–500 μm capable of measuring large numbers of star-forming galaxies, and their contributions to the CIB (Devlin et al. 2009). These surveys allowed us to obtain a far clearer understanding of the CIB and its sources (see Lagache et al. 2005, for a general review) but many questions remain unanswered such as the evolution of their spatial distribution with redshift.

The spatial distribution of infrared galaxies as a function of redshift is a key component of the scenario of galaxy formation and evolution. However, its study has been hampered by high confusion and instrumental noise and/or by the small size of the fields of observation. Tentative studies, with a small number of sources at 850 μm (Blain et al. 2004), found evidence of a relationship between submillimeter galaxies and the formation of massive galaxies in dense environments. Works by Farrah et al. (2006) and Magliocchetti et al. (2008) measured a strong clustering of ultra luminous infrared galaxies (ULIRG) detected with Spitzer at high redshifts. Alternatively, the infrared background anisotropies could also provide information about the correlation between the sources of the CIB and dark matter (Haiman & Knox 2000; Knox et al. 2001; Amblard & Cooray 2007), and its redshift evolution. Lagache et al. (2007) and Viero et al. (2009) reported the detection of a correlated component in the background anisotropies using Spitzer/MIPS (160 μm) and BLAST (250, 350, and 500 μm) data. These authors found that star formation is highly biased at $z > 0.8$. The strong evolution of the bias parameter with redshift, caused by the shifting of star formation to more massive halos with increasing redshift, infers that environmental effects influence the vigorous star formation.

To improve our understanding of the formation and evolution of galaxies using CIB anisotropies, we need more information about the redshift of the sources contributing to the CIB. We also need a method that allows to go deeper than the confusion noise level. In this context, an invaluable tool is the stacking technique, which allows a statistical study of groups of sources that cannot be detected individually at a given wavelength. Its requires the knowledge of the positions of the sources being "stacked" as inferred from their individual detection at another wavelength. This knowledge is then used to stack the signal of the sources at the wavelength at which they cannot be detected individually. Since the signal of the sources increases with the number of sources N and the noise (if Gaussian) increases with $\sqrt{N}$, the signal-to-noise ratio will increase with $\sqrt{N}$. For an additional description of the basics of stacking techniques we refer to for example Dole et al. (2006) and Marsden et al. (2009).

Stacking was used to measure the contribution of 24 μm galaxies to the background at 70 and 160 μm using MIPS data (Dole et al. 2006). Contribution from galaxies down to 60 μJy at 24 μm is at least 79% of the 24 μm, and 80% of the 70 and 160 μm backgrounds, respectively. At longer wavelengths studies used this technique to determine the contribution of populations selected in the near- and mid-infrared to the FIRB (far-infrared background) background: 3.6 μm selected sources to the 850 μm background (Wang et al. 2006) and 8 μm and 24 μm selected sources to the 850 μm and 450 μm backgrounds (Dye et al. 2006; Serjeant et al. 2008). Finally, Marsden et al. (2009) measured total submillimeter intensities associated with all 24 μm sources that are consistent with 24 micron-selected galaxies generating the full intensity of the FIRB. Similar studies with Planck and Herschel will provide even more evidence about the nature of the FIRB sources.

Theoretically, a stacking technique also could be used to study the mean SED (spectral energy distribution) of the stacked sources (e.g., Zheng et al. 2007). The main potential limitations would be caused by the errors in the redshifts of the sources and an insufficiently large number of sources to stack per redshift bin. The observation of sufficiently large fields to which the technique can be applied is now assured by the to Spitzer legacy surveys FIDEL, COSMOS, and SWIRE[1] and Planck and Herschel surveys. Advances in the measurement of the redshift have also been accomplished, although for very small fields for sources up to $z \sim 2$ (e.g. Caputi et al. 2006), and for the larger COSMOS fields up to $z \sim 1.3$ with very high accuracy (Ilbert et al. 2009). Future surveys are planned to measure the redshifts in larger fields such as the dark energy survey (DES[2]) or the GAMA spectroscopic survey (e.g. Baldry et al. 2008).

The difficulties in separating the contribution to the signal coming from different redshifts have handicapped the study of CIB anisotropies. However, once the mean SEDs of infrared galaxies per redshift bin are obtained we can use this information to analyze CIB anisotropies. The SEDs obtained with the stacking technique can be used to "clean" the low-redshift anisotropies (or at least a significant part of them) from the CIB maps. This can be performed by subtracting the undetected low-redshift ($z < 1-2$) populations from the maps using their mean colors and thus build maps dominated by sources at higher redshifts. This also facilitates the study of the evolution of large-scale structures at high redshift by removing the noise coming from low redshifts.

In this paper, we use the simulations and catalogs presented in Fernandez-Conde et al. (2008)[3] to study the limitations of stacking techniques in CIB anisotropy analysis. We stack 24 μm sources detected with MIPS in Planck, Herschel, and SCUBA-2 simulated observations. The catalogs and maps were created for different levels of bias between the fluctuations of infrared galaxy emissivities and the dark matter density field. We use a bias $b = 1.5$, which is very close to that measured by Lagache et al. (2007).

The paper is organized as follows. In Sect. 2, we explain the method used to study the capabilities of the stacking once the redshift of the sources is known. Section 3 details the elements that limit the accuracy of the stacking technique. In Sect. 4, we test the technique for studying the mean SEDs of galaxies. In Sect. 5, the feasibility of using information about the SEDs to clean the observations of low-redshift anisotropies is studied. The results are summarized in Sect. 6. Throughout this paper, the cosmological parameters are assumed to be $h = 0.71, \Omega_\Lambda = 0.73, \Omega_m = 0.27$. For the dark-matter linear clustering, we set the normalization to be $\sigma_8 = 0.8$.

2. Description of the method

Dole et al. (2006) considered every MIPS 24 μm source in selected fields with fluxes >60 μJy and then sorted the 24 μm sources by decreasing flux at 24 μm (hereafter S_{24}). The sources were placed in 20 bins of increasing flux density. These bins were of equal logarithmic width $\Delta S_{24}/S_{24} \sim 0.15$, except for the bin corresponding to the brightest flux, to take all the bright sources. They then corrected the average flux obtained by stacking each S_{24} bin for incompleteness using the correction of Papovich et al. (2004). This allowed them to determine lower limits to the CIB at 70 μm and 160 μm, and to find the contribution from galaxies down to 60 μJy at 24 μm to be at least 79% of the 24 μm, and 80% of the 70 and 160 μm backgrounds.

While these measurements of the total flux are useful for estimating the overall energy emitted by these populations (see also Marsden et al. 2009), it does little to improve our knowledge of individual sources. To use the average flux efficiently we have to decrease the dispersion in the individual fluxes (at the long wavelength) around the average flux of the population. We can do this by separating large populations of sources into smaller and more homogeneous SED populations.

One of the main sources of flux dispersion is the measurement of the mean flux using galaxies with very different redshifts. The lack of accurate redshifts (up to $z \sim 2$) across large fields has so far limited the use of detailed redshift information in stacking analysis. Because of this, the fluxes of sources with different SEDs are averaged together and the mean flux is a poor estimator of the fluxes of individual sources. However advances in the measurement of the redshifts are expected in the coming years with the new generation of spectroscopic and photometric redshift surveys such as GAMA (e.g. Baldry et al. 2008), (Big-)BOSS[4], DES[5]. We developed a method that assumes that redshifts are known and investigated the limitations of stacking

[1] http://ssc.spitzer.caltech.edu/legacy/
[2] http://www.darkenergysurvey.org/
[3] The simulations are publicly available at http://www.ias.u-psud.fr/irgalaxies
[4] http://www.sdss3.org/cosmology.php
[5] http://www.darkenergysurvey.org/

techniques caused by the uncertainties in the redshifts. We assessed the dispersion in the fluxes of individual sources with different redshift errors and the influence of this dispersion on the quality of the results using our simulations since this information will not be available in the real observations.

2.1. Stacking technique

We used our simulations to study the limitations of the stacking technique using 24 μm MIPS sources in Planck, Herschel, and SCUBA-2 observations. The choice of this wavelength (24 μm) is motivated by several reasons. Firstly, 24 μm is a good tracer of infrared galaxies (unlike e.g., near-infrared detections). Secondly, 24 μm-selected galaxies emit the bulk of the CIB up to at least 500 μm (Dole et al. 2006; Marsden et al. 2009). Thirdly, 24 μm Spitzer observations provide large and deep surveys, with redshift distribution of its sources extending up to redshift $z \sim 2.5$. The schematic description of our stacking process follows. The only requirements are knowledge of both the redshifts of the sources and their fluxes at 24 μm.

The detected sources at 24 μm will be characterized by two parameters S_{24} and z. We first remove from the long wavelength map (hereafter λ map) the sources detected individually, using the criteria described in Fernandez-Conde et al. (2008). These sources are no longer considered in the discussion, so whenever we refer to sources we refer to those detected at 24 μm with S_{24} greater than the detection threshold and not those detected individually in the λ map. The sources are then distributed into redshift bins. The width of the redshift bins have to be optimized for each observation. These bins cover the redshift interval between $z = 0$ and $z = z_{\rm max}$, where $z_{\rm max}$ is chosen depending on the goals of the work[6]. We stack independently the sources in each redshift slice. For the sources in a given redshift slice i ($z^i_{\rm Slice}$), the process of detection is as follows:

1. Firstly, we order the sources by decreasing S_{24}. We start by stacking in the λ map the sub-images of the two sources with higher S_{24} (that have not been detected individually). Then we measure the signal-to-noise ratio of the resulting image. A detection is achieved when the signal-to-noise ratio is higher than a certain detection threshold. This detection threshold is optimized for different observations. For the cases discussed in this paper, we use a detection threshold of three. If we do not achieve a detection we stack more sources (always selecting the next brighter sources at 24 μm)[7]. This is done until we attain the required signal-to-noise ratio.
2. Once a detection is achieved, we assign to all sources stacked together a flux equal to the total flux measured in the stacked image divided by the number of sources.
3. After detection, we restart the process starting from the brightest sources that we have not yet stacked.
4. Sometimes the last (and therefore faintest) group of sources in the redshift slice is not successfully stacked by this algorithm because an insufficient number of faint sources remains to be stacked in this last iteration. To correct for this, we simply carry out the algorithm starting this time from the faintest sources and stacking progressively brighter sources until we achieve a detection. Although in this procedure the last two mean flux bins are not independent, the consequences in terms of systematic errors are negligible (since the sources affected are few, faint, and the relative error in the stacking is small).

Once this process is complete we assign a mean "stacked" flux to every source of the redshift slice. The errors in the fluxes of the sources measured by stacking are computed to be the total noise measured in the map (following the method described in Fernandez-Conde et al. 2008) multiplied by $\sqrt{N}/N$, where N is the number of stacked sources. We repeat this process for all the redshift slices until we have a measurement of the flux at λ for all the sources in the catalog. In the 3 dimensional space of $S_{24} - z - S_\lambda$, we then have a set of points $S^{St}_{24} - z^{St} - S^{St}_\lambda$ corresponding to different successful stackings. For each successful stacking, the coordinates in each of the three axes are the following:

- $S^{St'}_\alpha$: The mean S_α of the sources of the ith stacked population, where α is the reference wavelength (here 24 μm).
- $z^{St'}$: The mean redshift of the sources of the ith stacked population.
- $S^{St'}_\lambda$: The mean S_λ found for the sources using the stacking technique for the ith stacked population.

Redshift slice optimization: Our algorithm assumes that sources at similar z and of similar S_{24} have similar characteristics at other wavelengths. Our best option to avoid substantial variance in S_λ between the stacked sources is to try to avoid stacking together sources of very different S_{24} or z. In this context, the size of the redshift bins were empirically optimized to ensure that (1) our detections are of high signal-to-noise ratio; (2) we achieve successful detections in each redshift slices without having to stack together sources of very different S_α (by more than a factor of three); and (3) the redshift slices are as thin as possible while complying with the first conditions. The redshift slices are chosen differently for each observation to comply with these criteria.

2.2. Color smoothing

The algorithm discussed above is quite simplified because it assumes that all sources detected in the same redshift bin have the same color S_λ/S_α. In contrast we would expect there to be a continuous variation of S_λ/S_α with both S_α and z. Following this assumption allows us to interpolate values between detections at different S_α for each redshift slice. A more complicated means of correction is to smooth our predictions by interpolating S_λ through the grid formed by the set of points $S^{St}_\alpha - z^{St} - S^{St}_\lambda$ found with the stacking algorithm described above for the whole $S_\alpha - z$ plane. We do this with the IDL function TRIGRID, which given data points defined by the parameters $S^{St}_\alpha - z^{St} - S^{St}_\lambda$ and a triangulation of the planar set of points determined by S^{St}_{24} and z^{St} returns a regular grid of interpolated S_λ values. We tried both approaches and found that the differences between the results for the two different smoothings is very small so from now on we use only the "S_λ smoothing". Figure 1a shows the fluxes at 350 μm (with $1.5 < z < 1.6$) before and after the two dimensional smoothing. It shows the real fluxes of the sources (known from the simulations), the recovered fluxes using the smoothing technique, and the recovered fluxes without smoothing. We can see that the smoothing greatly improves the accuracy of the fluxes. After this correction, the results are in very good agreement with the input fluxes.

[6] We analyze the stacking up to $z_{\rm max} = 2$ since reliable estimates of the redshift up to that redshift are available (although over quite small areas).

[7] To decrease the computation time, we increase the number of sources to be stacked using a logarithmic step of $dN/N = 1.5$.

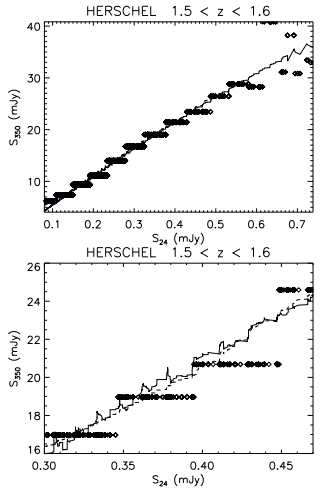

Fig. 1. *Top*: input fluxes of the sources in the redshift slice $1.5 < z < 1.6$ (solid line) together with estimates of the fluxes of the sources using the smoothing technique (dashed line) and estimates of the fluxes of the sources without smoothing (diamond). *Bottom*: the same but zoomed for 0.3 mJy $< S_{24} <$ 0.47 mJy.

3. Limitations of the method

We now test the limitations of the method related to the difficulties we expect to face when real data are analyzed (e.g., intrinsic dispersion in the colors of the sources, errors in the measurement of the fluxes and in redshifts, clustering)[8]. To illustrate the limitations, in this section we use the simulations at 350 μm. We reached the same conclusions using other far-infrared and submillimeter wavelengths. The size of the redshift slices that divide the $S_{24} - z$ space was chosen to be $dz = 0.1$; wider redshift slices would stack together sources with very different fluxes; smaller redshift slices led to too low signal-to-noise ratios.

Two different Spitzer surveys are used, COSMOS and SWIRE. COSMOS is a deep observation with a completeness of ~100% up to $S_{24} = 80$ μJy (Sanders et al. 2007). It allows us to test the stacking of faint sources. COSMOS covers a smaller field than SWIRE (2 sq. deg. versus 50 sq. deg.) hence its stacking measurements are less accurate for bright sources. Thus we also use the much larger SWIRE survey (Lonsdale et al. 2004), which is less deep ($S_{24} > 270$ μJy) but covers ~25 times more area[9]. We analyze the stacking of 24 μm sources for two study cases: observations in the far-infrared with Herschel at 350 μm and (in the next section) observations in the submillimeter with Planck and SCUBA-2 at 850 μm. The characteristics of the Herschel/SPIRE, Planck/HFI, and SCUBA-2 observations are the following:

Stacking in the COSMOS field:

- Detection limit: $S^D_{24} > 80$ μJy at 24 μm.
- Size of the field: 2 sq. deg.
- Linear bias: $b = 1.5$.
- Type of observation with Herschel: 350 μm "Deep" (with $1\sigma = 12.3$ mJy).
- Type of observation with SCUBA-2: 850 μm (with $1\sigma =$ 1 mJy).

Stacking in the SWIRE fields:

- Detection limit: $S^D_{24} > 270$ μJy at 24 μm.
- Size of the field: 50 sq. deg.
- Linear bias: $b = 1.5$.
- Type of observation with Herschel: 350 μm "deep" (with $1\sigma = 12.3$ mJy).
- Type of observation with SCUBA-2 and Planck: 850 μm (with $1\sigma = 1$ mJy and $1\sigma = 46.7$ mJy – see Table 4 from Fernandez-Conde et al. 2008– respectively).

3.1. Cold and starburst populations

Figure 2 shows the histograms of the fluxes at 350 μm for a stacking box with $0.5 < z < 0.6$ and $0.5 < S_{24} < 1$ mJy. The main source of error in the estimate of the fluxes for this case would not be the dispersion in either S_{24} or z but the presence of two different populations, which are indistinguishable using observations at shorter wavelengths. These two populations are the starburst and the normal (cold) populations described in Lagache et al. (2003). Figure 3 shows the number of starburst and normal sources as a function of z for sources with $80 < S_{24} < 270$ μJy, $0.27 < S_{24} < 1$ mJy, and $S_{24} > 1$ mJy. For the three afore mentioned cases, the cold sources are the dominant population for $z < 0.8$, $z < 0.6$, and $z < 0.5$ respectively. There are no effective ways of separating these two populations, and this will cause poor estimates of the mean colors of each population. This is particularly important when the number of sources of each type is approximately equal. This is because we add together two populations of very different S_{350} (cold sources are in general brighter in the submillimeter than starburst sources at the same redshifts and with similar S_{24}). When one of the populations dominates, this problem becomes negligible.

3.2. Errors caused by intrinsic dispersion in colors

Because of the lack of constraints on SEDs at long wavelengths and their evolution with redshift, the Lagache et al. (2004) model does not take into account that galaxies of the same luminosity and redshift could have different values of S_λ (apart from the distinction between normal and starburst sources). To assess the effect of this dispersion, we introduce a random Gaussian error into the flux estimated with the stacking for each of the stacked sources. The errors that we make using this procedure are equivalent to those that we would make if we were to use a model with an intrinsic Gaussian dispersion in the S_λ of the sources. This type of error does not affect the results for the mean of the sources but the average difference between this mean and the fluxes of the individual sources. We test the effect on our results for different levels of dispersion (measured in terms of

[8] The problems associated with errors in the measurement of S_{24} are considered negligible (see Sanders et al. 2007).

[9] And therefore should have $\sqrt{N} = 5$ times more signal-to-noise ratio for similar populations of sources.

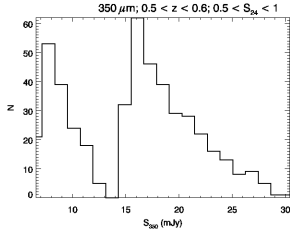

Fig. 2. Histogram of the fluxes at 350 μm for a stacking box with $0.5 < z < 0.6$ and $0.5 < S_{24} < 1$ mJy. The mean value of the sources is $S_{350} \sim 17$ mJy. The two different populations are the normal cold sources (*left* population) and the starburst sources (*right* population). It is clear that the main cause of error in our flux measurement comes from us stacking together two different populations. As expected, we checked that reducing the redshift slice does not reduce the dispersion.

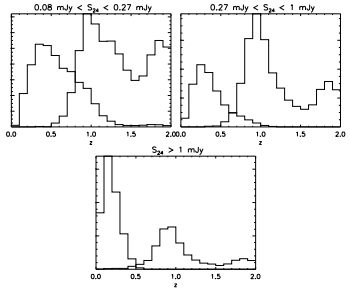

Fig. 3. Histograms of the number of cold (thin line) and starburst (thick line) sources per 24 μm flux bin (histograms are normalized to the higher number of sources per histogram). The problematic regions are those where both populations have similar number of galaxies. This is especially important for $0.6 < z < 0.7$ and faint sources.

the standard deviation in the dispersion compared to the mean flux of the sources). In Fig. 4, we can see the histograms of the errors for a dispersion of 0%, 10%, 25% for all sources with $S_{24} > 270$ μJy. As expected, the figure illustrates how the histograms broaden with dispersion. For a standard deviation in the errors of the fluxes associated with the stacking $\sigma_{\rm St}$ and a standard deviation associated with the fluxes $\sigma_{\rm Disp}$, the final standard deviation in our errors $\sigma_{\rm Tot}$ would be $\sigma_{\rm Tot} = \sqrt{\sigma^2_{\rm St} + \sigma^2_{\rm Disp}}$. We do not analyze other statistical representations of this effect (i.e., non-Gaussian intrinsic dispersion) since we do not have any strong observational constraints.

3.3. Redshift uncertainty

The effect of redshift errors are difficult to evaluate. This is because they combine with the non-linear k-correction, making the variation in S_λ with z complex. In Sect. 4, we study the effect of redshift errors for two different relative errors $\frac{\Delta z}{z} = 3\%$ and $\frac{\Delta z}{z} = 10\%$.

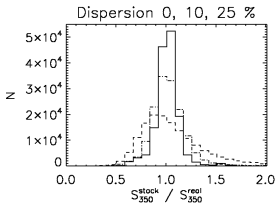

Fig. 4. Ratio of recovered fluxes from stacking ($S^{\rm stack}_{350}$) to input fluxes in the simulation ($S^{\rm real}_{350}$) for sources with $S_{24} > 270$ μJy, with no additional dispersion in the fluxes at 350 μm (thick solid line), and with 10% (dotted-dashed line) and 25% (dashed line) additional dispersion.

3.4. Problematic areas of the S24-z space

Figure 5 shows the errors in the estimate of the mean fluxes in the $S_{24}-z$ space for a 350 μm Herschel observation of the COSMOS field with redshift errors $\frac{\Delta z}{z} = 3\%$ and $\frac{\Delta z}{z} = 10\%$. For the estimates of the fluxes, we can easily identify several problematic areas in the $S_{24}-z$ space. These are: data points at very low redshifts ($z < 0.1$), the brightest sources because of small number statistics and the faintest sources because of flux errors[10].

Low z: There are very few sources at $z < 0.1$. This prevents the stacking from achieving high signal-to-noise ratio levels. This translates into large errors in the measurement of the mean fluxes for sources with $z < 0.1$.

Bright sources: These sources are rare and we are therefore unable to reach signal-to-noise ratios as good as for fainter sources. We expect the results for bright sources to be better when the stacking technique is applied to larger fields (for example using the WISE survey Mainzer et al. 2005). We should keep this in mind when analyzing the results in our study cases.

Faint sources: Another shortcoming of the method is that the smoothing techniques cannot be applied to sources fainter than the stacked flux of the faintest bin. The best solution is to assume for the last point given by the stacking that all the sources have the same color, which is equivalent to assuming that their color is the same as that of the sources that are slightly brighter than them.

4. Application of the method

We now verify the accuracy of the method with realistic simulations of observations including redshift errors and by using existing observations at 24 μm with Spitzer.

[10] Note that the top right area with no data plotted corresponds to a region where they are no sources at 24 microns; note also that in color representations as in Fig. 5, small differences in estimated value can have a great visual impact due to the variation in colors. A mere 20% change in the estimate can change the color from green to red. The general variation is consistent with our detection threshold of 3σ.

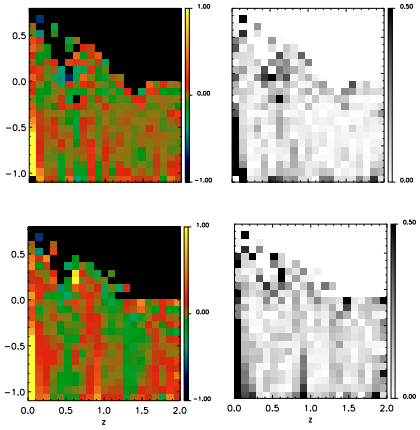

Fig. 5. Accuracy in the mean recovered fluxes at 350 μm in a COSMOS-like observation when considering redshift errors of $\frac{\Delta z}{z} = 3\%$ (*top*) and $\frac{\Delta z}{z} = 10\%$ (*bottom*). The colors (shading) correspond to different values of the accuracy, while the vertical axis is S_{24} and the horizontal axis is the redshift bin. *Left*: relative errors in the mean recovered fluxes ($\nabla\bar{S}^{\rm Stack}_{350} = (\bar{S}^{\rm Stack}_{350} - \bar{S}^{\rm Real}_{350})/\bar{S}^{\rm Real}_{350}$) for all the $S_{24} - z$ space. *Right*: the same but in absolute values $\left|\nabla\bar{S}^{\rm Stack}_{350}\right| = \left|(\bar{S}^{\rm Stack}_{350} - \bar{S}^{\rm Real}_{350})/\bar{S}^{\rm Real}_{350}\right|$ and decreasing the dynamic range of the plot (0–0.5) to illustrate the errors more clearly. The $S_{24} - z$ space is divided linearly in z and logarithmically in S_{24}. Redshifts are given on the bottom-right figure, Log(S_{24}) (in mJy) on the left figures.

4.1. Stacking Herschel data in the far-infrared: 350 μm

We comment on the main issues and sources of error encountered when stacking 24 μm sources in Herschel/Spire observations at 350 μm and considering a detection threshold of 3σ. We note that the difficulties faced by the stacking technique at 250 and 500 μm are similar. We use a division in the z axis with redshift slices of $dz = 0.1$. We analyze the results for two redshift errors, an optimistic one of $\frac{\Delta z}{z} = 3\%$ and a pessimistic one of $\frac{\Delta z}{z} = 10\%$. This illustrates the degradation in the quality of the results with redshift error.

Errors in individual recovered fluxes: Figure 6 shows the errors in the estimate of the fluxes of the sources with the stacking technique for redshifts $0 < z < 1$ and $1 < z < 2$ for an observation of the COSMOS field at 350 μm. Three different estimates are shown: one compiled using stacking without "smoothing" and two others created using two different smoothing techniques (in either z or both z and S_{24}, cf. Sect. 2.2). The differences between the estimates obtained using the two smoothing techniques are quite small for most sources. The figures show rather good agreement between the input values of the fluxes and those found by the stacking technique. The results improve for $z > 1$ compared to those at $z < 1$. This is because of the low signal-to-noise ratio at low z and the two-population problem. As expected, the results degrade with the redshift error. The results also improve when either of the two smoothing algorithms are used. Figure 7 shows the results for a SWIRE observation. The recovered fluxes are more accurate because the larger number of sources allows us to obtain higher signal-to-noise ratios for the stacking (but it is limited to $S_{24} > 270$ μJy).

Limit for faint sources: Stacking in the COSMOS field allows the detection of sources as faint as $S_{350} = 2.1 \pm 0.7$ mJy at $z \sim 1$, which is 6 times lower than the noise (1σ). At $z \sim 2$, we achieve detections for sources with $S_{350} = 3 \pm 1$ mJy or 4 times lower than the noise. This is equivalent to a gain in the signal-to-noise ratio of a factor of 18 and 12, respectively, with respect to the 3σ detection. If the Spitzer data were complete down to lower fluxes, we should be able to successfully detect those sources too. The stacking method at 350 μm is limited by the Spitzer detection limits.

Mean errors: The final results for the fluxes and colors of the sources obtained using the stacking technique are compared with the *real* (input) values in Figs. 8 and 9. They are in very good agreement with the input fluxes (called *real* fluxes in the figures) but to obtain a clearer idea of the errors we show in Fig. 10 two plots of the mean flux relative error[11] per box of $S_{24} - z$. The left figure shows the relative differences between our mean estimated flux (using the stacking technique) and the flux of the sources introduced in the model. Yellowish colors represent overestimates of the source fluxes compared to their input fluxes. Darker colors represent underestimates. The right figure shows the same relative error but this time in absolute value. We can see that the larger errors, which can be as high as 50%, are made for sources at $z < 0.1$. This is because the small number of sources at these redshifts prevents the stacking from achieving sufficiently high signal-to-noise ratios. For the bulk of sources however, the errors in the mean flux are smaller than 10%. The errors associated with the problem of 2 populations cannot be illustrated by these figures because this problem does not affect the accuracy of the mean value found for a set of sources but the dispersion in the fluxes of individual sources around this mean value.

4.2. Stacking Planck and SCUBA-2 data at 850 μm

When applying the same technique to Planck observations at 850 μm, we encounter a fundamental limitation of the stacking technique. In the stacked image, we can discern two contributions to the peak, one associated with the stacked sources, which has the shape of the PSF, and another broader peak around it which is associated with the sources correlated with the stacked sources. The method works easily when the PSF width is much smaller than the width of the correlation peak. However, this condition is not fulfilled for Planck observations where the width of the correlation signal around sources is not very different from the width of the PSF. Furthermore, when stacking faint sources, $S_{24} \sim 100$ μJy, the signal associated with the correlations is much stronger than that of the sources: it becomes impossible to distinguish between the signal from the sources being stacked and the signal from the clustering. Figure 11 shows a cut of a stacked image for very faint sources ($S_{24} \sim 100$ μJy). The figure shows the total signal, the signal coming from both the clustering and the sources. For these faint sources, we can see that the signal from the clustering of the sources is more important than that of the stacked sources and their FWHMs are very similar.

[11] Note that the mean flux relative error is equivalent to the mean color relative error since there is no error in our S_{24} measurements.

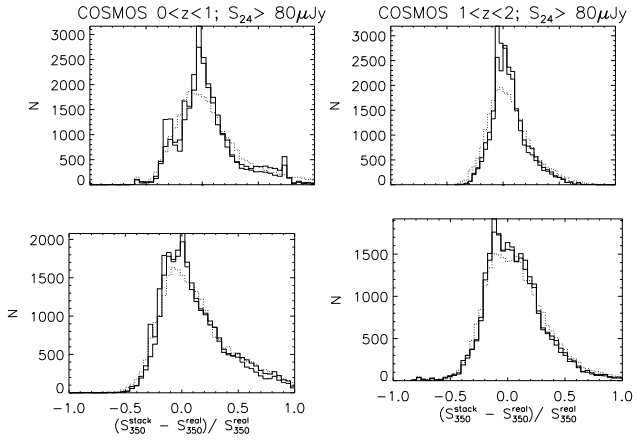

Fig. 6. Relative errors in recovered fluxes for individual sources at 350 μm in a COSMOS-like observation for redshift errors $\frac{\Delta z}{z} = 3\%$ (*top figures*) and $\frac{\Delta z}{z} = 10\%$ (*bottom figures*). *Left*: for $S_{24} > 80\,\mu$Jy and redshifts $0 < z < 1$. *Right*: for $S_{24} > 80\,\mu$Jy and $1 < z < 2$. The zeros represents a perfect estimate. Three estimates are shown: direct values obtained with the stacking (dotted line); values obtained with the stacking and smoothed in z (thin solid line), and smoothed both in z and in S_{24} (thick solid line).

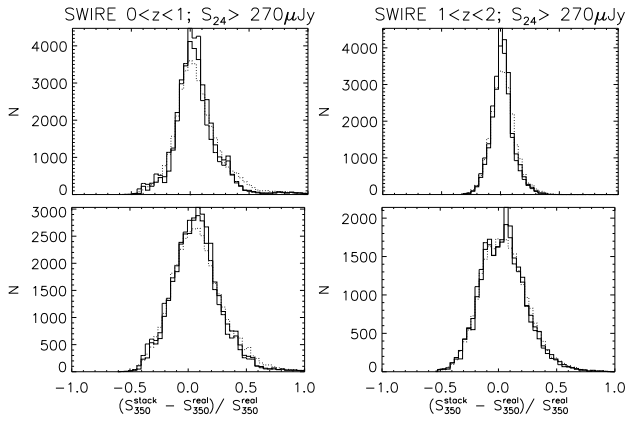

Fig. 7. Same as Fig. 6 but for an observation at 350 μm if the SWIRE fields.

Several attempts were made to correct this problem. By far the most effective solution is to use additional observations with a narrower PSF at similar wavelengths to estimate the fraction of the flux that is associated with the clustering. This method is described hereafter. Another possible solution that does not rely on complementary observations is presented in Appendix A.

The problem caused by the clustering contribution to the flux measured with Planck/HFI makes it difficult to use this instrument alone to estimate the fluxes accurately . It is therefore necessary to use observations with other instruments with smaller *FWHM*. In the far-infrared, we could use Herschel (for the same channel as Planck at 350 μm). For the submillimeter observations, we will have to use ground-based submillimeter instruments (e.g., future camera SCUBA-2 at 850 μm or LABOCA at 870 μm).

SCUBA-2 observation of the COSMOS field at 850 μm

We analyze here the stacking of sources in the COSMOS field observed with SCUBA-2. SCUBA-2 will have a very good

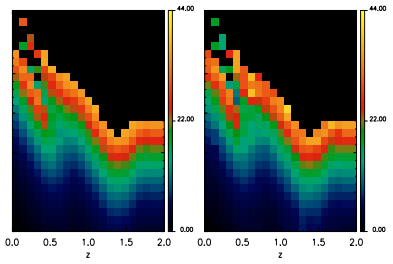

Fig. 8. *Left*: real fluxes of the sources at 350 μm (in mJy) in the space $S_{24} - z$. *Right*: fluxes found by the smoothed stacking technique. The colors correspond to different values of the flux, while the vertical axis is S_{24} and the horizontal axis is the redshift bin.The $S_{24} - z$ space is divided linearly in z and logarithmically in S_{24}.

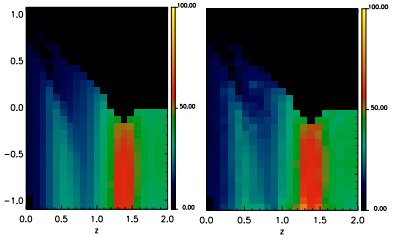

Fig. 9. *Left*: real S_{350}/S_{24} flux ratio of the sources in the space $S_{24} - z$. *Right*: S_{350}/S_{24} flux ratio found by the smoothed stacking technique (*right*). The colors correspond to different values of the ratio, while the vertical axis is S_{24} and the horizontal axis is the redshift bin. The $S_{24} - z$ space is divided linearly in z and logarithmically in S_{24}.

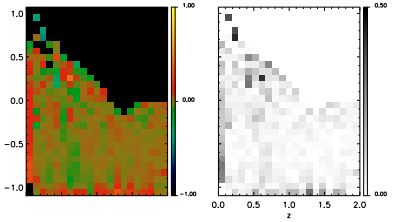

Fig. 10. Same as Fig. 5 but with no redshift errors.

sensitivity; we use an estimate of the noise for these observations of $\sigma = 1$ mJy, close to that specified in the SCUBA-2 webpage[12]. Because the signal of the sources at 850 μm is much fainter relative to the noise than with Herschel at 350 μm, we have to increase the size of the redshift bins to achieve

[12] http://www.jach.hawaii.edu/JCMT/surveys/Cosmology.html

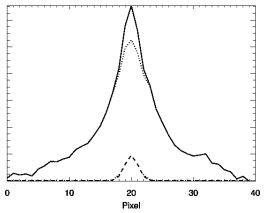

Fig. 11. Lateral cut of a stacking image (Planck/HFI at 850 μm) for very faint sources ($S_{24} \sim 100\,\mu$Jy). The total signal (normalized to 1 at the peak), the signal from both the clustering and the sources are the solid, dotted, and dashed lines, respectively. One pixel equals 25 arcsec.

detections. We take the following boundaries for the redshift slices 0, 0.1, 0.4, 0.8, 1., 1.2, 1.5, 1.8, and 2.2. We use the same detection threshold as that used for Herschel at 350 μm ($D_{\rm thres} = 3$).

Figure 12 shows the errors in the estimate of individual fluxes of 850 μm sources for $S_{24} > 80\,\mu$Jy and redshifts $1 < z < 2$ with redshift errors of $\frac{\Delta z}{z} = 0\%$ (top), 3% (middle), and 10% (bottom). The results are poorer than those at 350 μm (Fig. 6). This is because the signal of the individual sources is weaker relative to the noise at 850 μm than at 350 μm. The results are clearly dependent on the redshift errors.

The sources detected with the stacking technique at $z \sim 1$ are as faint as $S_{850} = 0.10 \pm 0.03$ mJy, which is 10 times smaller than the noise. At $z \sim 2$ we can achieve detections of sources with $S_{850} = 0.17 \pm 0.05$ mJy, which is 6 times smaller than the noise. This is equivalent to a gain in the signal-to-noise ratio of a factor of 30 and 18, respectively, with respect to the 3σ detection. As for 350 μm the stacking method is limited by the Spitzer detection limit.

Figure 13 shows the errors in the estimated mean fluxes at 850 μm in the $S_{24} - z$ space for a COSMOS observation stacked with SCUBA-2 at 850 μm with redshift error $\frac{\Delta z}{z} = 3\%$ before and after the "smoothing" correction. It shows the improvement of the accuracy with the "smoothing" correction. Figure 13 also shows the errors in the estimate of the mean fluxes for $\frac{\Delta z}{z} = 10\%$ (smoothing applied). As at 350 μm, we lose accuracy in our predictions when the redshift errors are higher. When comparing with observations at 350 μm, we see that our estimates are not as accurate, the mean errors at 850 μm being around 15% compared to 5–10% at 350 μm. The problems we discussed for 350 μm observations are yet greater at 850 μm. The problem at low redshift is far more important here because the sources at $z \leq 0.9$ are in general fainter than at higher z.

Planck 850 μm

The Planck observation is hindered by the clustering problem caused by its large PSF (5'), rendering its flux estimates completely useless unless a correction is applied. The problem is clearly illustrated in Fig. 14, where we show the histograms of the ratio of the flux estimates to the input fluxes for a Planck observation of the SWIRE fields for two selected redshift bins. We developed a simple method to correct this problem.

When stacking sources in a given redshift bin with Planck, we measure the added contribution of the sources and the clustering. To correct the stacked fluxes with Planck for the effects of clustering, we use source fluxes at 850 μm obtained by

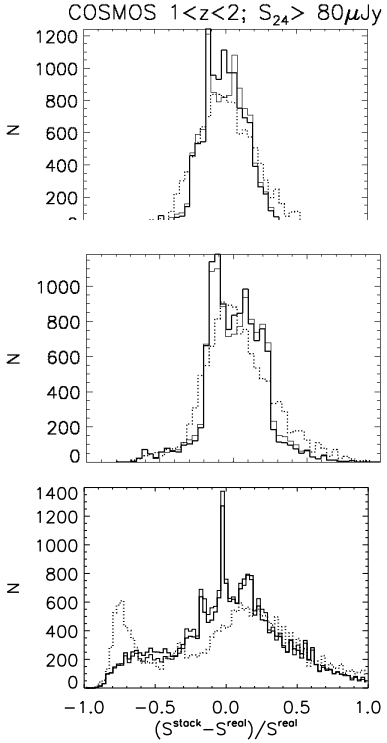

Fig. 12. Relative errors in recovered fluxes for individual sources at 850 μm in a COSMOS-like observation for redshift errors $\frac{\Delta z}{z}$ equal to 0 (*top*), 3% (*middle*), and 10% (*bottom*), for $S_{24} > 80$ μJy and $1 < z < 2$. Three estimates are shown: direct values obtained with the stacking (dotted line); values obtained with the stacking and smoothed in z (thin solid line); and values smoothed both in z and in S_{24} (thick solid line).

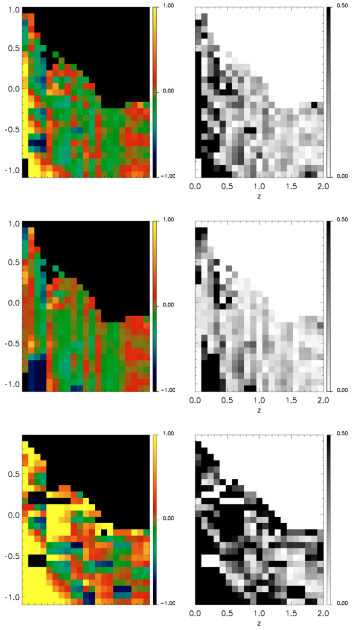

Fig. 13. Accuracy of the mean recovered fluxes at 850 μm in a COSMOS-like observation when considering a redshift error of $\frac{\Delta z}{z}$ = 3% and no smoothing (*top*), a redshift error of $\frac{\Delta z}{z}$ = 3% and the smoothing (*middle*) and a redshift error of $\frac{\Delta z}{z}$ = 10% and the smoothing (*bottom figures*). The colors (shading) correspond to different values of the accuracy, while the vertical axis is S_{24} and the horizontal axis is the redshift bin. The $S_{24} - z$ space is divided linearly in z and logarithmically in S_{24}. Redshifts are given on the right figures, log(S_{24}) (in mJy) on the left figures. *Left figures* show the relative errors on the mean recovered fluxes ($\nabla\bar{S}_{850}^{\rm Stack} = (\bar{S}_{850}^{\rm Stack} - \bar{S}_{850}^{\rm Real})/\bar{S}_{850}^{\rm Real}$) for all the $S_{24} - z$ space. Right figures show the absolute values $\left|\nabla\bar{S}_{850}^{\rm Stack}\right| = \left|(\bar{S}_{850}^{\rm Stack} - \bar{S}_{850}^{\rm Real})/\bar{S}_{850}^{\rm Real}\right|$.

stacking SCUBA-2 data. If we stack sources detected by Planck for which we have an estimate of their fluxes inferred from SCUBA-2 data, we can obtain the contribution of the clustering in the Planck stacking by calculating the difference between the total measured flux and that measured in the SCUBA-2 stacking. For each redshift bin, we therefore stack Planck data for all the sources in a SWIRE observation with fluxes $0.27 < S_{24} < 1$ mJy. We do not use the brighter sources because their flux estimates are poorer. Once we have estimated the effect of the clustering for different redshift bins, we can correct the fluxes found with Planck. Figure 15 shows the effect of applying this correction. We can see that the results are greatly improved. After the correction, the results for the bright sources $S_{24} > 1$ mJy are indeed superior for Planck than with SCUBA-2, because of its larger sky coverage. We note that the correction is assumed to be the same inside a redshift bin for all S_{24}.

4.3. Combination of different observations

4.3.1. Observations in the far-infrared (350 μm)

We analyzed the Herschel observation of the COSMOS and SWIRE fields. We have seen that the SWIRE stacking is more accurate when estimating the flux of the brightest sources. Figure 16 shows the flux estimates at 350 μm when we combine the strengths of both observations. For sources with $S_{24} <$ 0.27 mJy, we have only COSMOS estimates, which are therefore compelled to use. Since we know that the SWIRE observations have higher signal-to-noise ratios than COSMOS observations at high fluxes, we chose to use these estimates for

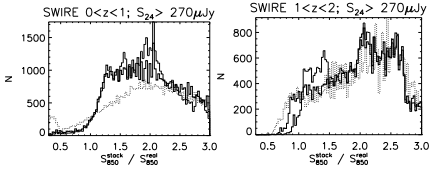

Fig. 14. Ratio of recovered to input fluxes of individual sources at 850 μm for an observation of the SWIRE fields, redshift errors $\frac{\Delta z}{z}$=10%, and two redshift bins, $0 < z < 1$ (*left*) and $1 < z < 2$ (*right*). Three estimates are shown: direct values obtained with the stacking (dotted line); values obtained with the stacking and smoothed in z (thin solid line); and values smoothed both in z and in S_{24} (thick solid line). The value 1 represents a perfect measurement. The recovered fluxes have not been corrected from the clustering and are thus highly overestimated.

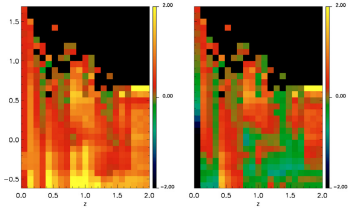

Fig. 15. Relative error in the mean recovered fluxes at 850 μm ($\nabla\bar{S}_{850}^{\rm Stack} = (\bar{S}_{850}^{\rm Stack} - \bar{S}_{850}^{\rm Real})/\bar{S}_{850}^{\rm Real}$) for a Planck observations of the SWIRE fields with $\frac{\Delta z}{z}$ = 10% before (*left*) and after (*right*) correcting from the clustering. The colors (shading) correspond to different values of the relative error, while the vertical axis is S_{24} and the horizontal axis is the redshift bin.

sources with $S_{24} > 0.34$ mJy. For the fainter sources stacked in SWIRE $0.27 < S_{24} < 0.34$ mJy data, we obtained errors larger than those of COSMOS since we assume that the colors of the faintest sources are as described in Sect. 3.4. For these sources, the COSMOS estimates have therefore to be used.

4.3.2. Observations in the submillimeter (850 μm)

As performed at 350 μm, we analyzed the COSMOS/SCUBA-2 and SWIRE/Planck observations separately and we now combine their respective strengths. Figure 17 shows the error estimates for these combined observations. For faint sources with $S_{24} < 0.27$ mJy, we use COSMOS/SCUBA-2. For the faintest sources stacked in SWIRE ($0.27 < S_{24} < 1$ mJy), it is more accurate to use COSMOS/SCUBA-2 than Planck measurements due to the errors induced by the uncertainty in the clustering contribution. For brighter sources ($S_{24} > 1$ mJy), the corrected Planck estimations are more accurate than those of SCUBA-2 and we prefer to use them. Figure 17 shows the relative errors in the mean recovered fluxes with respect to the input fluxes at 850 μm, when combining both observations. They are typically of the order of 15% for $\frac{\Delta z}{z}$ = 3%.

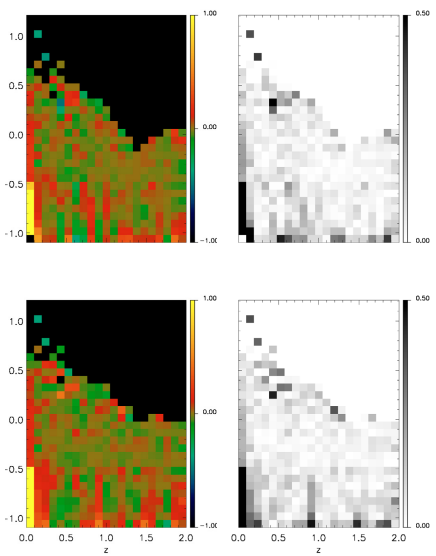

Fig. 16. Combined observations at 350 μm with redshift errors $\frac{\Delta z}{z}$ = 3% (*top figures*) and $\frac{\Delta z}{z}$ = 10% (*bottom figures*). *Left*: relative errors of the estimate of the mean fluxes ($\nabla\bar{S}_{350}^{\rm Stack} = (\bar{S}_{350}^{\rm Stack} - \bar{S}_{350}^{\rm Real})/\bar{S}_{350}^{\rm Real}$) for the $S_{24} - z$ space. *Right*: absolute values $\left|\nabla\bar{S}_{350}^{\rm Stack}\right| = \left|(\bar{S}_{350}^{\rm Stack} - \bar{S}_{350}^{\rm Real})/\bar{S}_{350}^{\rm Real}\right|$. The colors (shading) correspond to different values of the error, while the vertical axis is S_{24} and the horizontal axis is the redshift bin.

4.3.3. Observations at other wavelengths

For observations in the far-infrared and because of the issues discussed in Sect. 4.2 and lower typical noise level, the stacking technique produces more accurate estimates of the fluxes with Herschel than with Planck, although the latter has the advantage of covering the entire sky. We did not present separately the Herschel observations at 250 μm or 500 μm since the analysis of the results at these two wavelengths are similar to those for 350 μm observations. At 550 μm, a wavelength where there is a Planck but not a Herschel channel, it is more advisable to use the values found by Herschel at 500 μm after applying a small correction than to use the Planck values. At 850 μm, we combined the Planck observations with those of SCUBA-2 although other submillimeter data (e.g., LABOCA) could have been used. At 1380 μm (Planck/HFI 217 GHz), we tested the same approach using MAMBO/IRAM simulated observations to complement the Planck observations, obtaining similar results as for 850 μm.

The complete mean SEDs for the different populations can provide information about the mean galaxy properties, such as star-formation rate and dust content. Figure 18 shows our measurements at 70, 160, 250, 350, 500, and 850 μm of the flux of the 800 faintest sources detected in our simulated COSMOS survey at $1 < z < 1.1$ and at $2 < z < 2.1$ relative to both their true fluxes and the SED of a typical source at these fluxes

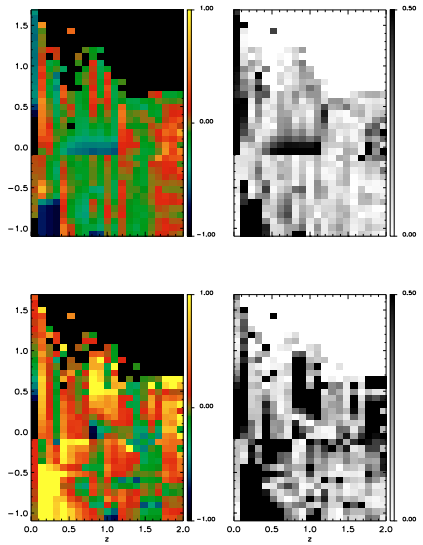

Fig. 17. Same as Fig. 16 for combined observations at 850 μm.

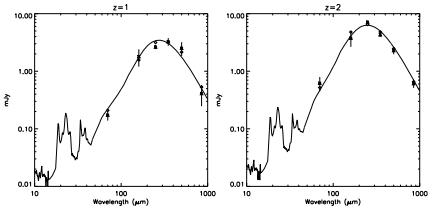

Fig. 18. True mean fluxes (diamonds) compared to the mean fluxes found by stacking (triangles) with the estimated errors at 70, 160, 250, 350, 500, and 850 μm of the 800 faintest sources above 80 μJy (mean fluxes $S_{24} = 110$ μJy and $S_{24} = 135$ μJy at redshifts $1 < z < 1.1$ and $2 < z < 2.1$, respectively) in our simulated COSMOS observation. The points at 70 and 160 μm are from a Spitzer simulation with instrumental noise taken from Sanders et al. (2007). The solid lines show the Starburst SEDs from the library of Lagache et al. (2004) that has the same mean S_{24} at those two redshifts.

and redshifts. The largest errors are found at 70 μm, 160 μm, and 850 μm. For both redshifts, the errors in our estimates are smaller than 10%. The same method could be applied to fainter populations, if they were detected individually with Spitzer. As mentioned before, the limitation of the method is the detection limit of the Spitzer observations at 24 μm.

5. Cleaning maps of undetected source populations

5.1. Contribution to the CIB

An obvious application of the results provided by the stacking technique is the measurement of the total energy emitted by different galaxy populations at wavelengths where they can not be seen directly. This would give us the CIB fraction at those wavelengths coming from the chosen population. We compare the total contribution from sources brighter than $S_{24} = 80\,\mu$Jy at redshifts $z < 2$ in our simulations with that determined using the stacking technique, and obtain very similar results. At 350 μm, we find (using our stacking estimates) that these sources account for 35.4% and 35.8% of the CIB when the redshift errors are 3% and 10%, respectively. This is a 0.4% and 0.8% overestimate of their contribution (35%) to the CIB of the underlying model. At 850 μm, we estimate that these sources account for 19% and 20% of the CIB when the redshift errors are 3% and 10%, respectively, which is a slight 2–3% overestimate of their contribution (17%) to the CIB in the model.

5.2. Removing anisotropies due to low-z infrared galaxies

A more sophisticated use of the present results is the statistical removal of the contribution of these populations at long wavelengths. If we accurately extract a sufficiently large fraction of the background anisotropies at low z, this will allow us to study the CIB anisotropies at high z. For the first time, we could then separate the contributions to the CIB anisotropies at different redshifts. This would allow us to study large-scale structures at high redshift. To remove from the observed maps the contribution of sources up to a certain redshift, we create a map of sources for whose fluxes were estimated using the stacking technique. We subtract this map from the observed maps, which is equivalent to individually subtracting all the stacked sources. We estimate the source fluxes from the colors obtained by combining the different observations, as described in Sect. 4.3. However, we know that the flux estimates have significant errors for very bright sources and sources at redshifts $z < 0.1$ at 350 μm and $z < 0.8$ at 850 μm. These errors will affect the accuracy of our removal of the low-z background anisotropies. We also studied the effect of a Gaussian dispersion in the fluxes of the sources (as described in Sect. 2.2) on the power spectra. For dispersions as high as 25%, the results are equivalent with and without dispersion. This is because of the large number of sources contributing to each bin.

To assess the importance of these errors, we compare the map compiled using the flux estimates by stacking with a second map where these sources have their true input fluxes. Comparing the power spectrum of both maps gives the accuracy of the anisotropy estimates for the first map. Figure 19 shows the two power spectra at 350 μm for sources at $z < 2$ for both a SWIRE observation (with $S_{24} > 270$ μJy) and a COSMOS observation (with $S_{24} > 80$ μJy) and for two redshift errors $\frac{\Delta z}{z} = 3\%$ and $\frac{\Delta z}{z} = 10\%$. At 350 μm, the accuracy of our estimation is superior to 0.5% for both the correlated and Poissonian part of the spectrum in both the SWIRE and COSMOS observations in the case of a small redshift error ($\frac{\Delta z}{z} = 3\%$). When the redshift error is greater, our estimate of the Poissonian noise increases moderately with mean errors of 3%. Figure 20 shows the same result at 850 μm. Because of the small redshift error in the COSMOS survey, we overestimate the correlated part by 40% and the Poissonian part by 24%. For larger redshift errors, our overestimates increase to 60% and 50% of the correlated and

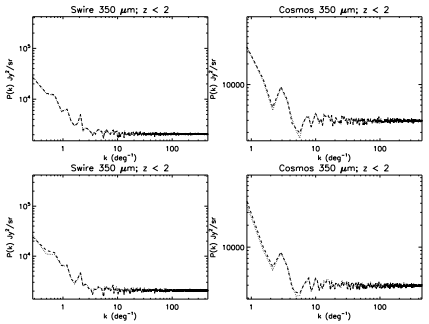

Fig. 19. Power spectra of two maps in which we placed the sources with either their input fluxes from the simulations (dotted line) or their stacked fluxes (dashed line). The results are shown for a SWIRE observation (*left figures*) and COSMOS observation (*right figures*) at 350 μm for stacked sources up to $z = 2$ with redshift errors $\frac{\Delta z}{z} = 3\%$ (*top*) and $\frac{\Delta z}{z} = 10\%$ (*bottom*).

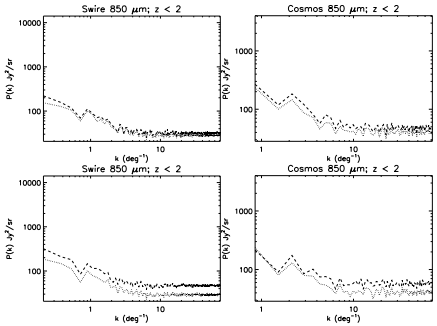

Fig. 20. Same as Fig. 19 at 850 μm.

Poissonian part, respectively. In this case, this shows the importance of accurate redshifts. The differences in the overestimates of the Poissonian and correlated part are caused by the populations contributing to these two regimes not being exactly the same, bright sources contributing more in relative terms to the Poissonian fluctuations than to the correlated part.

5.3. High-redshift power spectra of CIB anisotropies

5.3.1. Observations at 350 μm

After analyzing the accuracy of the map that we intend to subtract, we investigate our capabilities to subtract a significant part of the background anisotropies for different redshift limits. Figure 21 compares the power spectra of the total background anisotropies to those at $z > 1$, $z > 1.5$, and $z > 2$ in a SWIRE observation. It also shows the power spectra of the map of CIB anisotropies from which we have subtracted the $z < 1$, $z < 1.5$, and $z < 2$ contribution, which were estimated by stacking. Since our subtraction is rather accurate, the very small difference between these last two sets of power spectra is caused by us not subtracting all the sources but only those above $S_{24} > 270$ μJy. We subtract approximately half the correlated part ($k < 8$ deg^{-1}) and two thirds of the Poissonian part ($k > 8$ deg^{-1}) independently of redshift errors.

Figure 22 shows the same results for a COSMOS observation. We have the positions of sources with $S_{24} > 80$ μJy which allows us to subtract a larger fraction of the background than in the SWIRE survey. Unfortunately because of the smaller size of the field, we do not have access to the largest scales that we were able to analyze with SWIRE. We subtract approximately ~99% of the correlated part and ~90% of the Poissonian for the small redshift error. For the large redshift error, these fractions become ~85% and ~90% of the correlated and Poissonian parts, respectively. For each of the considered redshift limits, the power spectrum of the residual left after our subtraction of the $z < z_{\rm lim}$ stacked source is in close agreement with the power spectrum at high redshifts ($z > z_{\rm lim}$). This remains true when we consider a large redshift error.

5.3.2. Observations at 850 μm

Figures 23 and 24 show the similar results but at 850 μm. For these observations, we needed to use COSMOS data because for SWIRE data we do not subtract a significant fraction of the CIB anisotropies. In terms of power spectra, we are able with SWIRE to subtract only ~30% of the correlated part and ~50% of the Poissonian part. In the case of COSMOS, we subtract approximately ~75% of both the correlated and Poissonian part of the power spectra. Figure 24 (top-right) shows that, for errors of $\frac{\Delta z}{z} = 3\%$, our method is very efficient in subtracting $z < 2$ anisotropies.

6. Summary

We have described a stacking algorithm and illustrated its capabilities using Spitzer observations. We have studied the accuracy of the stacking method as a means of determining the average fluxes of classes of undetectable sources at long wavelengths. The results show that the technique will be capable of measuring accurate fluxes at both far-infrared and submillimeter wavelengths for sources as faint as 80 μJy at 24 μm using average colors.

With the successful commissioning of the Planck and Herschel missions, large maps (even all-sky for Planck) from 250 μm to the millimeter wavelength range are now available. SCUBA-2 and other submillimeter cameras (e.g., LABOCA) will provide data of higher angular resolution in the submillimeter. We have applied the stacking method to the Herschel, Planck, and SCUBA-2 simulated data and measured the full average SED of populations of sources detected at 24 μm. The strong variation in the S_{24}/S_λ color with redshift requires us to define the populations to which the method will be applied not only in ranges of S_{24} but also in terms of (photometric) redshift. We show we are able to measure the mean flux of populations 4 to 6 times fainter than the total noise at 350 μm at redshifts $z = 1$ and $z = 2$, respectively, and 6 to 10 times fainter than the total noise at 850 μm, at the same redshifts. We have been able to reproduce the SED at wavelengths 70, 160, 250, 350, 500, and 850 μm of a population of sources with mean flux $S_{24} = 0.11$ mJy and $S_{24} = 0.135$ mJy at redshifts $z = 1$ and $z = 2$, respectively.

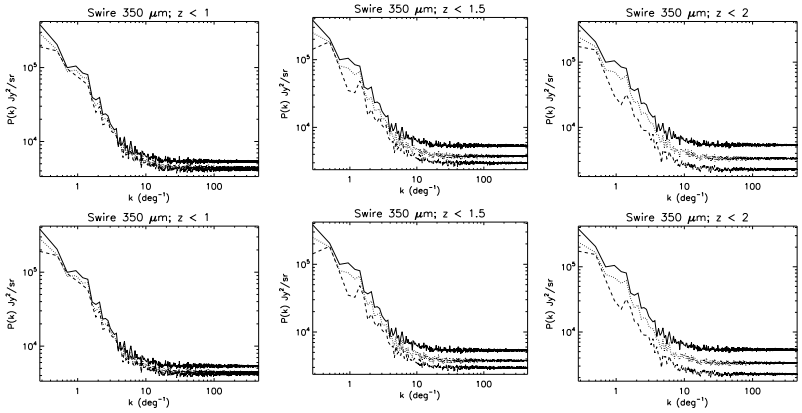

Fig. 21. Power spectra of the map for a SWIRE observation at 350 μm. The solid line is the total power spectrum of the background, the dashed line is the power spectrum of the background for $z > z_{\rm lim}$ (where $z_{\rm lim}$ is a redshift limit), and the dotted line is the power spectrum of the total background from which we have subtracted the stacked sources at $z < z_{\rm lim}$. The redshift limit $z_{\rm lim}$ is $z_{\rm lim} = 1$ (*left figures*), $z_{\rm lim} = 1.5$ (*middle figures*), and $z_{\rm lim} = 2$ (*right figures*). The redshift errors are $\frac{\Delta z}{z} = 3\%$ (*top*) and $\frac{\Delta z}{z} = 10\%$ (*bottom*).

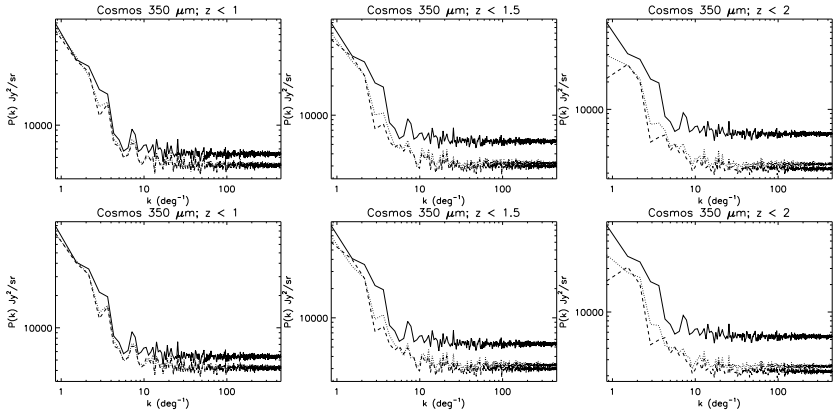

Fig. 22. Same as Fig. 21 but for the COSMOS field.

In the deep Spitzer fields, the detected 24 μm sources constitute a large fraction of the anisotropies. We have shown that the method presented in this paper enables an excellent (350–850 COSMOS) to good (350–850 SWIRE) removal of both the Poissonian and correlated low-z anisotropies. The relative contribution of sources to the background anisotropies up to $z = 2$ decreases with wavelength in the model. This property is expected to remain valid independently of the details of the model from 250 μm to the millimeter range. Although the accuracy of the subtracted map is lower at 850 μm, the cleaning of the power spectrum is quite effective (because the contribution of the low-redshift sources is small at these submillimeter wavelengths).

The same technique could also be used to remove from the observations all the contributions from sources for which we have estimated a flux, to decrease the confusion noise caused by infrared galaxies. This would be interesting for the detection of other types of sources (for example, SZ sources in Planck data).

The method allows us to build $z \gtrsim 1{-}2$ CIB maps from the submillimeter to the millimeter. We have found that the method can also be successfully applied at the other Herschel and Planck

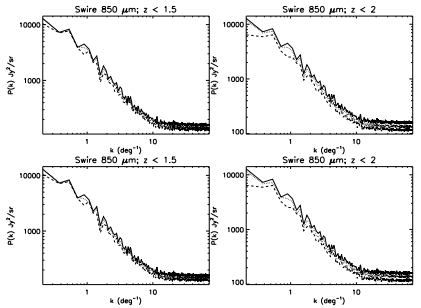

Fig. 23. Power spectra of the 850 μm map of the SWIRE fields. The solid line is the total CIB power spectrum, the dashed line is the CIB power spectrum for $z > z_{\rm lim}$ (where $z_{\rm lim}$ is a redshift limit), and the dotted line is the power spectrum of the total CIB from which we have subtracted the stacked sources at $z < z_{\rm lim}$. The redshift limit $z_{\rm lim}$ is $z_{\rm lim} = 1.5$ (*left*) and $z_{\rm lim} = 2$ (*right*). The redshift errors are $\frac{\Delta z}{z} = 3\%$ (*top*) and $\frac{\Delta z}{z} = 10\%$ (*bottom*).

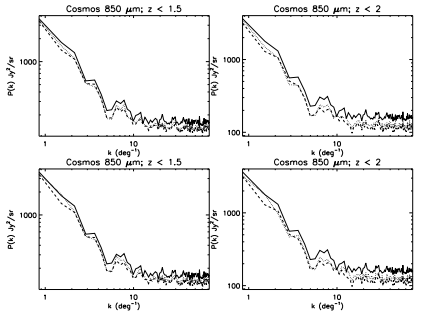

Fig. 24. Same as Fig. 23 but for the COSMOS field.

wavelengths than those tested in this paper. The longer wavelengths at which this can be achieve will depend on the success of the component separation and not on the removal of the $z < 2$ sources. We can then hope to have a set of large CIB maps dominated by high-redshift galaxies. This set of CIB maps at different wavelengths dominated by $z > 2$ sources will be a powerful tool for studying the evolution of the large-scale structure of infrared galaxies. The effect of the K-correction ensures that each of these maps (at different wavelengths) are dominated by particular high-redshift ranges. Methods of independent component separation based on the correlation matrix between these maps (e.g., Delabrouille et al. 2003) should allow us to extract maps and power spectra for a number of redshift ranges equal to the number of maps. This last step will fulfill the main objective of this work. It will allow the study of the evolution of the IR galaxy clustering at high redshifts by means of the power spectrum analysis of CIB anisotropies. These maps may also be used to help us understand the contribution of high-z IR galaxies both to the CIB and the star-formation history.

Appendix A: Alternative correction for the clustering contribution to the stacked fluxes in Planck maps

We developed an alternative method for correcting the photometry of a group of stacked sources for the effects of the clustering. If we consider that the signal measured for a population of stacked sources at a given wavelength is the combination of the signal originating from the sources and from the clustering, we can write the measured flux as:

$$S_\lambda^{\rm measured} = S_\lambda^{\rm sources} + S_\lambda^{\rm clustering} + \sigma \quad \text{(A.1)}$$

where $S_\lambda^{\rm measured}$ is the total measured signal, $S_\lambda^{\rm sources}$ is the part of the signal coming from the sources, and $S_\lambda^{\rm clustering}$ is the part of the signal coming from the sources correlated with the detected sources that we are stacking, and σ is the noise.

If two populations of sources have very similar fluxes at the wavelength of detection (24 μm) and are situated at similar redshifts, we can assume that their sources have very similar physical characteristics and hence their colors S_λ/S_{24} are very similar. In this case, we can write:

$$\left(\frac{S_{24}^{\rm sources}}{S_\lambda^{\rm sources}}\right)_A \simeq \left(\frac{S_{24}^{\rm sources}}{S_\lambda^{\rm sources}}\right)_B \quad \text{(A.2)}$$

where the A and B subscripts represent the first and second population of sources. We can measure the total flux (from the sources and the clustering) for the stacking of both source populations and express them as:

$$\left(S_\lambda^{\rm total} = S_\lambda^{\rm sources} + S_\lambda^{\rm clustering} + \sigma\right)_A \quad \text{(A.3)}$$

$$(S_\lambda^{\rm total} = S_\lambda^{\rm sources} + S_\lambda^{\rm clustering} + \sigma)_B. \quad \text{(A.4)}$$

If we were to assume that the contribution of the correlated sources to the flux is the same for both populations $(S_\lambda^{\rm clustering})_A = (S_\lambda^{\rm clustering})_B$, as expected for sources with similar spatial distributions, and that the noise is negligible, we would have a system of three equations with three unknowns that we can solve.

The main problem for the applicability of this method is that we need to stack many sources to ensure that the noise becomes negligible compared to the signal. Because of this, it is preferable to combine an observation whose photometry is affected by the clustering with another observation for which this problem does not exist, as illustrated by our present analysis. If the photometry of this second observation is affected by smaller errors (as it is the case of SCUBA-2 data relative to Planck data at 850 μm), the results will be improved by combining the two observations. However, the method discussed in this appendix is applicable to cases where we do not have an alternative observation with which we can correct from the clustering problem.

References

Amblard, A., & Cooray, A. 2007, ApJ, 670, 903
Baldry, I., Liske, J., & Driver, S. P. 2008, GAMA: a new galaxy survey, in IAU Symp. 245, ed. M. Bureau, E. Athanassoula, & B. Barbuy, 83
Beelen, A., Omont, A., Bavouzet, N., et al. 2008, A&A, 485, 645
Bertoldi, F., Menten, K. M., Kreysa, E., Carilli, C. L., & Owen, F. 2000 [arXiv:astro-ph/0010553]
Blain, A. W., Smail, I., Ivison, R. J., Kneib, J.-P., & Frayer, D. T. 2002, Phys. Rep., 369, 111
Blain, A. W., Chapman, S. C., Smail, I., et al. 2004, ApJ, 611, 725
Caputi, K. I., Dole, H., Lagache, G., et al. 2006, ApJ, 637, 727

Delabrouille, J., Cardoso, J.-F., & Patanchon, G. 2003, MNRAS, 346, 1089
Devlin, M. J., Ade, P. A. R., Aretxaga, I. 2009, Nature, 458, 737
Dole, H., Gispert, R., & Lagache, G. 2001, A&A, 372, 364
Dole, H., Le Floc'h, E., Pérez-González, P. G., et al. 2004, ApJS, 154, 87
Dole, H., Lagache, G., Puget, J.-L., et al. 2006, A&A, 451, 417
Dye, S., Eales, S. A., Ashby, M. L. N., et al. 2006, ApJ, 644, 769
Elbaz, D. 2005, Space Sci. Rev., 119, 93
Elbaz, D., Cesarsky, C. J., Chanial, P., et al. 2002, A&A, 384, 848
Farrah, D., Lonsdale, C. J., Borys, C., et al. 2006, ApJ, 641, L17
Fernandez-Conde, N., Lagache, G., Puget, J.-L., et al. 2008, A&A, 481, 885
Fixsen, D. J., Dwek, E., Mather, J. C., Bennett, C. L., & Shafer, R. A. 1998, ApJ, 508, 123
Genzel, R., & Cesarsky, C. J. 2000, ARA&A, 38, 761
Haiman, Z., & Knox, L. 2000, ApJ, 530, 124
Hauser, M. G., Arendt, R. G., Kelsall, T., et al. 1998, ApJ, 508, 25
Ilbert, O., Capak, P., Salvato, M., et al. 2009, ApJ, 690, 1236
Knox, L., Cooray, A., Eisenstein, D., et al. 2001, ApJ, 550, 7
Lagache, G., Dole, H., & Puget, J.-L. 2003, MNRAS, 338, 555
Lagache, G., Dole, H., Puget, J.-L., et al. 2004, ApJS, 154, 112
Lagache, G., Puget, J.-L., & Dole, H. 2005, ARA&A, 43, 727
Lagache, G., Bavouzet, N., & Fernandez-Conde, N. 2007, ApJ, 665, L89
Lonsdale, C., Polletta, M. D. C., Surace, J., et al. 2004, ApJS, 154, 54
Magliocchetti, M., Cirasuolo, M., McLure, R. J. 2008, MNRAS, 383, 1131
Mainzer, A. K., Eisenhardt, P., Wright, E. L., Preliminary design of the Wide-Field Infrared Survey Explorer (WISE), in MacEwen, H. A, editor, UV/Optical/IR Space Telescopes: Innovative Technologies and Concepts II, ed. MacEwen, Howard A. Proc. SPIE of Presented at the Society of Photo-Optical Instrumentation Engineers, SPIE Conf., 5899, 262,
Marsden, G., Ade, P. A. R., Bock, J. J., et al. 2009, ApJ, 707, 1729
Papovich, C., Dole, H., Egami, E., et al. 2004, ApJS, 154, 70
Puget, J.-L., Abergel, A., Bernard, J.-P., et al. 1996, A&A, 308, L5
Sanders, D. B., Salvato, M., Aussel, H., et al. 2007, ApJS, 172, 86
Serjeant, S., Dye, S., Mortier, A., et al. 2008, MNRAS, 386, 1907
Viero, M. P., Ade, P. A. R., & Bock, J. J. 2009, ApJ, 707, 1766
Wang, W.-H., Cowie, L. L., & Barger, A. J. 2006, ApJ, 647, 74
Zheng, X. Z., Dole, H., & Bell, E. F. 2007, ApJ, 670, 301

2009

Le fond infrarouge de galaxies livre ses secrets

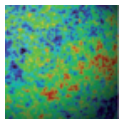

La formation et l'évolution des galaxies ne sont pas encore comprises en détail. Les nombreux relevés cosmologiques menés pour mieux en comprendre les processus physiques ont permis la découverte du rayonnement fossile des galaxies : le fond extragalactique infrarouge. Comment ce rayonnement infrarouge s'est-il formé ? Pourquoi les galaxies émettent-elles en moyenne plus d'énergie dans l'infrarouge que dans le visible ? Qu'est-ce qu'une galaxie infrarouge : est-ce un type particulier de galaxie ou une phase de l'évolution des structures ? De nouvelles observations depuis l'espace permettent de répondre en partie à ces questions, en attendant les données des satellites européens Herschel et Planck.

L'Univers extérieur à notre Galaxie est baigné de nombreux rayonnements, dont le principal est observable dans le domaine des ondes radio centimétriques et millimétriques : le fond cosmologique (ou CMB pour *Cosmic Microwave Background*), produit par un corps noir de température actuelle 2,7 Kelvin, soit environ – 270 degrés Celsius. Découvert dans les années soixante, et largement étudié depuis pour ses infimes fluctuations de température et de polarisation, il se propage librement depuis une époque située environ 400 000 ans après le big-bang. Il nous renseigne sur l'état de l'Univers primordial, sur son contenu, ainsi que sur certains processus physiques ultérieurs, comme la réionisation ou la formation des amas de galaxies.

Un autre rayonnement d'importance cosmologique a été découvert il y a seulement treize ans, dans les données du satellite COBE, mais dans le domaine de l'infrarouge lointain, vers 200 microns de longueur d'onde : *le rayonnement de fond des galaxies*, ou fond diffus extragalactique infrarouge. Il est environ 200 fois moins intense que le fond cosmologique. Cette détection a constitué une grande surprise à cause de la grande intensité relative de l'infrarouge lointain par rapport à la partie visible émise directement par les étoiles. Ce fond diffus a pour origine l'émission de toutes les galaxies depuis leur formation, et intègre ainsi toute leur histoire. Mesurer précisément ce rayonnement de fond et comprendre la nature et l'évolution des galaxies émettrices constituent l'un des objectifs importants de la cosmologie observationnelle. Ainsi, de grands relevés de galaxies sont menés, tant au sol que depuis l'espace, pour que ce rayonnement des galaxies nous livre ses secrets.

La différence entre le fond cosmologique et le fond extragalactique infrarouge lointain (nous abandonnerons dans la suite le qualificatif « lointain » pour plus de lisibilité) vient de l'époque concernée de l'Univers : l'Univers jeune (environ 400 000 ans), diffus et très homogène dans le premier cas, l'Univers plus vieux (d'environ 0,4 à 13 milliards d'années) et déjà composé de structures, comme des amas et galaxies non résolus par nos moyens d'observation, dans le second cas (*figure 1*). L'ensemble de ces fonds constitue l'essentiel du contenu électromagnétique de l'Univers actuel, largement dominé par le CMB (environ 95% de l'énergie). Nous discutons, dans cet article l'apport de l'observation du fond de rayonnement infrarouge à notre compréhension de la formation des structures[1] en cosmologie (*figure 4*).

La formation des galaxies

Avant l'époque de la formation des atomes, responsable du découplage matière-rayonnement vers 400 000 ans[2] après le big-bang, l'Univers était un plasma de matière et photons. Ce plasma oscillait selon des modes qui dépendent de son contenu et ces oscillations de matière ionisée et de photons, dites acoustiques, ont été le vecteur de transport de l'information depuis les phases primordiales.

1. On entend par « structure » ou « grande structure » les galaxies, amas de galaxies, super-amas de galaxies, filaments, et plus généralement les surdensités de matière structurées à grande échelle.
2. Correspondant à un redshift (ou décalage spectral vers le rouge cosmologique) d'environ 1100.

Article proposé par :

Hervé Dole, herve.dole@ias.u-psud.fr
Guilaine Lagache, guilaine.lagache@ias.u-psud.fr
Jean-Loup Puget, jean-loup.puget@ias.u-psud.fr

Institut d'Astrophysique Spatiale d'Orsay, UMR 8617, CNRS/Université Paris-Sud 11, Orsay

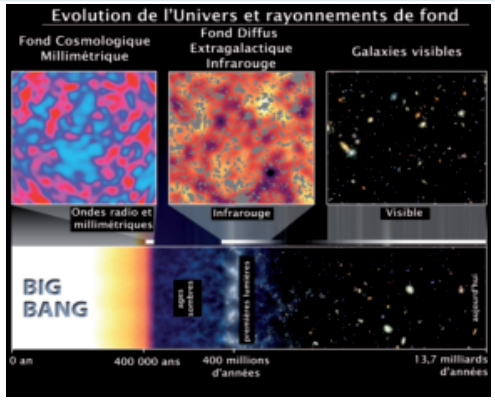

Figure 1 – Illustration de l'époque cosmique sondée avec les rayonnements de fond : le fond cosmologique dans le domaine des ondes radio et millimétriques (époque : environ 400 000 ans) ; le fond infrarouge de galaxies (dont l'émission a débuté environ 400 millions d'années après le Big-bang mais se poursuit jusqu'à aujourd'hui); les galaxies individuelles dans le domaine visible (époque : environ 1 milliard d'années à aujourd'hui). Image : H. Dole, d'après Spitzer/NASA/JPL-Caltech/Kashlinsky (GSFC).

Des oscillations acoustiques du même type se produisent d'ailleurs actuellement au cœur des étoiles et du Soleil, lesquelles transportent l'information sur la physique du cœur jusqu'à la surface où les variations correspondantes de densité du rayonnement électromagnétique les rend détectables. Après le découplage, les oscillations acoustiques se sont arrêtées ; leurs effets sont observés aujourd'hui dans les fluctuations de température du fond cosmologique. Les surdensités de matière, initiées par ces oscillations interrompues, ont ensuite pu croître par effondrement gravitationnel malgré l'expansion de l'Univers, pour former de grandes concentrations de matière (appelées halos) qui, plus tard, deviendront les structures de l'Univers – amas de galaxies et galaxies. Les halos sont dominés par la matière noire, dont le potentiel provoque l'effondrement de la matière ordinaire (un gaz de baryons), qui se condense et se refroidit pour former des étoiles. Les halos et galaxies, relativement petits au début, fusionnent puis forment des systèmes de plus en plus massifs avec le temps. C'est, en substance, ce que prévoient la plupart des modèles de formation des structures en cosmologie, dits de formation hiérarchique[3].

Ces modèles réussissent non seulement à reproduire de nombreuses observables (comme les fluctuations de température du CMB et les fluctuations de densité de matière), mais aussi à prédire des phénomènes observés ultérieurement (comme les oscillations dans la distribution spatiale des galaxies). Malgré leurs succès, ces modèles butent sur une limitation fondamentale : la physique fine des baryons, en particulier leur lien avec la matière noire, et les processus physiques de formation stellaire et d'accrétion. En effet, les modèles ne prédisent avec précision que le comportement de la matière noire. Or, l'information obtenue par l'observation des galaxies provient essentiellement du rayonnement issu du refroidissement des baryons conduisant à la formation des nuages interstellaires et des étoiles, mais pas de la matière noire. Comparer modèles et observations requiert donc l'utilisation de modèles physiques complexes pour décrire l'effondrement de gaz en galaxies et étoiles ; là réside la grande difficulté.

Afin de motiver physiquement l'utilisation de ces modèles, les astrophysiciens et cosmologistes s'intéressant à la formation des galaxies doivent rechercher des signatures observationnelles, indépendantes entre elles, afin de mieux cerner le lien entre physique des baryons et matière noire. De nombreuses approches existent et, concernant les baryons, elles utilisent les galaxies comme « particules tests », traceurs naturels des baryons à l'origine des étoiles – traceurs très certainement non linéaires. Des échantillons de galaxies massives sont par exemple utilisés pour mesurer leurs corrélations spatiales et leur évolution, en vue de comprendre la fusion des halos. D'autres traceurs sont utilisés, comme la formation stellaire *via* les galaxies infrarouges (voir *encadré 1*). Une autre méthode pour étudier la physique de la structuration du gaz de baryons consiste à mesurer *l'émission des galaxies*, ce qui permet d'une part de quantifier l'énergie rayonnée pour la confronter aux prédictions des modèles, d'autre part d'identifier les familles de processus d'émission dominants par l'étude spectrale.

3. Ceci dans le cadre cosmologique (dit de concordance) qui inclut la présence de matière noire et une constante cosmologique non nulle.

Encadré 1 — *Les galaxies infrarouges*

Notre Galaxie, la Voie Lactée, émet à peu près autant d'énergie dans le domaine visible que dans le domaine infrarouge (longueurs d'ondes supérieures à environ 5 microns). Ce n'est pas le cas de toutes les galaxies. Les galaxies dites infrarouges émettent l'essentiel de leur énergie dans ce domaine spectral. Certaines y émettent plus de 90 % : ce sont les galaxies lumineuses dans l'infrarouge (LIRG) ou ultra-lumineuses (ULIRG). La *figure E1* montre la forme des spectres de galaxies de type ULIRG, de type infrarouge à flambée de formation d'étoile (dit starburst), et de galaxies plus classiques spirales et elliptiques.

Ces distributions spectrales d'énergie des galaxies, ajustées par des modèles, permettent d'en identifier les principaux composants : populations stellaires avec leur âge, présence et nature de la poussière. Par exemple, la série de pics entre 5 et 15 microns est caractéristique de molécules planes aromatiques (ou hydrocarbones polycycliques aromatiques, ou PAH) présentes dans les zones proches des lieux de formation d'étoile. Le pic au-delà de 60 microns est dû aux gros grains de poussière (taille de l'ordre de la centaine de nanomètres), qui absorbent les photons ultraviolets (issus de la formation stellaire ou de l'accrétion), s'échauffent et émettent dans l'infrarouge lointain.

Les galaxies infrarouges peuvent être de différents types morphologiques ; un petit échantillon est présenté en *figure E2*. On remarque que les LIRG à redshift $z = 1$ sont souvent des spirales, mais pas uniquement : beaucoup présentent des morphologies perturbées, signes de fusion de galaxies.

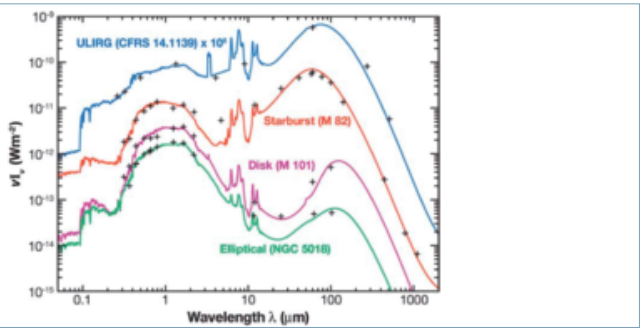

Figure E1 – Distributions spectrales d'énergie de quatre types de galaxies. De haut en bas : galaxie ultra-lumineuse dans l'infrarouge (ULIRG) ; galaxie infrarouge à flambée de formation stellaire (starburst); galaxie spirale proche ; galaxie elliptique. Les galaxies proches de type spiral et elliptique émettent l'essentiel de leur énergie dans le domaine visible (longueurs d'ondes inférieures à 5 microns), contrairement aux ULIRG et starburst qui émettent surtout dans l'infrarouge. D'après F. Galliano (thèse, 2004) cité dans Lagache *et al.* (2005). Reproduit, avec permission, de *Annual Review of Astronomy and Astrophysics*, Volume 43 ©2005 by Annual Reviews, www.annualreviews.org.

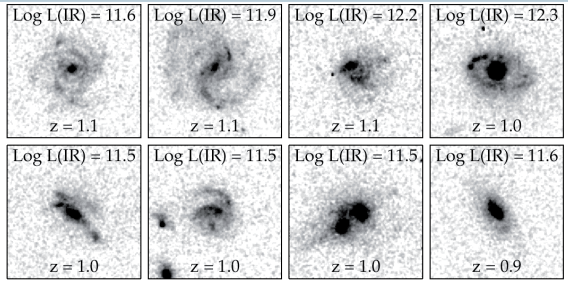

Figure E2 – Exemple de 8 galaxies lumineuses dans l'infrarouge (LIRG) à un redshift de l'ordre de 1, détectées par le satellite Spitzer, et imagées par le télescope spatial Hubble en bande I à 850 nm. Chaque image a une taille de 5 secondes d'arc de côté. La luminosité infrarouge, exprimée en logarithme d'unité de luminosité solaire, est indiquée en haut et le redshift en bas. On remarque des morphologies de galaxies perturbées et/ou en interaction, mais aussi de type spirale (en haut à gauche) ou de type elliptique (en bas à droite). Tiré de Papovich *et al.* (2004).

Ainsi, l'étude du spectre de rayonnement des galaxies sur un large domaine de longueur d'onde permet de déterminer quel processus domine entre la formation stellaire (nucléosynthèse, formation des éléments chimiques au cœur des étoiles) et/ou l'accrétion (gravitation), et permet de mesurer la masse stellaire et la quantité de poussières, le taux de formation d'étoiles et la masse d'un éventuel trou noir central. Il est cependant souvent très coûteux en temps et en technologie d'accéder à toute l'étendue du spectre des galaxies (du domaine radio aux rayons gamma), et, quand c'est possible, cela ne concerne qu'un nombre restreint de galaxies, souvent proches ou très lumineuses. Il est alors difficile dans ces conditions de sonder la formation des structures de manière fiable. S'il est compliqué d'étudier les galaxies individuelles en détail, il est néanmoins possible de les étudier en grand nombre dans un domaine spectral restreint, soit en menant une étude statistique sur les galaxies détectées, soit *via* le rayonnement de fond extragalactique diffus.

Le rayonnement de fond des galaxies

Prédit en 1967, ce rayonnement est la somme de toutes les émissions des galaxies de toutes les générations, une émission fossile de leur formation. Il a dès lors été activement recherché, mais n'a été découvert qu'en 1996 par une équipe d'Orsay dans les données du satellite COBE obtenues en 1992, à des longueurs d'ondes comprises entre 200 microns et 1 millimètre (correspondant au domaine de l'infrarouge lointain et du submillimétrique, voir *figure 2*).

Étonnamment, le maximum d'énergie a été mesuré vers 200 microns, alors que les galaxies locales rayonnent l'essentiel de leur énergie dans le domaine visible (voir *encadré 1*). La présence de ce rayonnement intense dans l'infrarouge, appelé fond extragalactique infrarouge, démontre l'accroissement d'émission infrarouge avec la distance[4] et témoigne donc de l'évolution des galaxies. Il importe de bien distinguer ici deux effets : le rougissement des rayonnements émis par les objets lointains à cause de l'expansion de l'Univers, et la part plus élevée de l'infrarouge dans l'émission intrinsèque des galaxies par le passé. C'est ce dernier effet qui domine largement et qui est discuté dans cet article. Dans la suite, nous considérerons les rayonnements corrigés des effets de l'expansion, c'est-à-dire considérés dans le référentiel propre de la source.

4. Les cosmologistes utilisent plutôt la notion de décalage Doppler spectral vers le rouge, ou **redshift**, dû à l'expansion de l'Univers. Pour fixer les idées : redshift = 0 correspond à aujourd'hui ; redshift = 1 correspond environ à la moitié de l'âge de l'Univers, soit environ 8 milliards d'années, ce qui correspond à une distance d'environ 21 milliards d'années-lumière ; redshift = 2 correspond à un quart de l'âge de l'Univers (soit il y a environ 10,3 milliards d'années), et une distance de 51 milliards d'années-lumière.

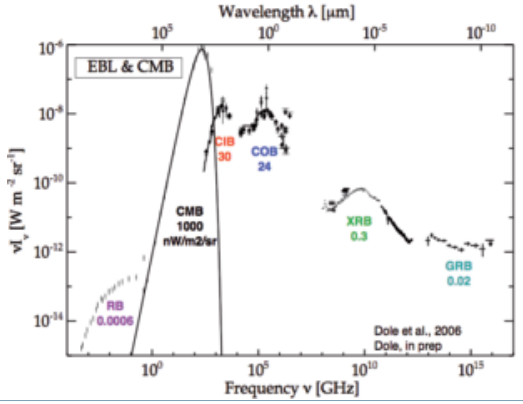

Figure 2 – Distribution spectrale d'énergie des rayonnements diffus dans l'Univers (hors de notre Galaxie), exprimée en puissance par unité de surface et d'angle solide, en fonction de la fréquence (en bas, en GHz) ou de la longueur d'onde (en haut, en microns) sur plus de 20 ordres de grandeur. Les chiffres indiquent la brillance intégrée de chaque rayonnement, en nW/m²/sr. Le rayonnement dominant est le fond cosmologique à 2,7K (noté CMB). Le reste du rayonnement est dû au fond extragalactique s'étendant du domaine radio aux rayons gammas ; son émission est maximale dans l'infrarouge lointain (noté CIB), puis dans le domaine visible (noté COB). Autres fonds : radio (RB), rayons X (XRB), rayons gammas (GRB). Figure : d'après Dole *et al.* (2006).

Il restait à comprendre l'origine de cet excès d'émission, et à identifier les populations de galaxies responsables. Ce n'était pas possible avec COBE dont la résolution angulaire trop faible ne permettait pas de détecter les galaxies individuelles. La tâche est d'autant plus complexe que de nombreux avant-plans contaminent le signal (émissions de notre système solaire et de notre Galaxie) et que ce domaine spectral n'est quasiment pas accessible depuis le sol à cause de l'absorption atmosphérique : seuls des ballons, fusées-sondes ou satellites y accèdent avec une sensibilité suffisante. Il fallait donc de nouvelles générations de satellites observant dans l'infrarouge et disposant d'une meilleure résolution angulaire capable de détecter les galaxies. Les satellites européen ISO (lancé en 1995) et américain Spitzer (lancé en 2003) ont ainsi mené des relevés profonds entre 3 et 200 microns de longueur d'onde (voir *encadré 3*) qui ont révolutionné notre vision de l'évolution des galaxies, surtout grâce aux observations effectuées dans l'infrarouge moyen, entre 5 et 30 microns de longueur d'onde (avec ISOCAM à bord d'ISO d'abord, puis IRAC et MIPS à bord de Spitzer). La technologie disponible en infrarouge lointain, entre 60 et 200 microns, n'offre cependant pas les mêmes performances, et la taille limitée du télescope (de 60 à 80 cm) conduit à une résolution dégradée des images à grande longueur d'onde (voir *encadré 2*), rendant encore plus difficile la détection de galaxies. Le fond infrarouge vers 200 microns n'est donc résolu en galaxies individuelles qu'à environ 20%, alors qu'il est résolu à environ 80% en infrarouge moyen. Ces chiffres constituent des ordres de grandeurs, car la valeur absolue de l'intensité du fond n'est pas connue avec une grande précision à ces longueurs d'ondes.

Tirant parti des derniers relevés profonds du satellite Spitzer, qui ont la particularité d'avoir été menés à 7 longueurs d'ondes (entre 3 et 160 microns), notre équipe a employé une technique originale pour sonder le faible signal du fond extragalactique infrarouge à 70 et 160 microns (voir *encadré 2*) qui permet de gagner environ un ordre de grandeur en sensibilité. En empilant le signal de près de 20 000 galaxies préalablement détectées à 24 microns, nous arrivons à mesurer la contribution au fond infrarouge de ces galaxies : nous trouvons désormais que 80 % du fond infrarouge à 70 et 160 microns est identifié en galaxies ! (*figure 3*)

Cette technique remarquable[5] nous permet de donner une valeur inférieure au fond extragalactique extrêmement contraignante pour les modèles, et de confirmer que le maximum d'énergie de ce rayonnement se situe vers 160 microns (*figure 2*). En outre, nous mesurons que ce rayonnement est plus important dans l'infrarouge que dans le visible (environ 30 et 24 nW/m^2/sr respectivement). Ainsi, les processus de formation et d'évolution des galaxies ont en moyenne émis 120 photons infrarouges lointains pour 1 photon visible. Comme l'énergie lumineuse émise par les galaxies provient pour environ 3/4 de la formation stellaire (rayonnement UV et visible) et pour environ 1/4 de l'environnement des trous noirs (rayonnement UV, X), le rayonnement extragalactique aurait dû naïvement présenter un maximum dans le visible ou à plus grande énergie. Nous avons confirmé que ce n'est pas le cas. Cela implique un rôle important de la poussière interstellaire dans les galaxies, qui absorbe le rayonnement des étoiles et le rayonnement produit dans l'environnement des trous noirs, pour le réémettre dans l'infrarouge. L'étape suivante consiste à mieux comprendre l'origine des galaxies contribuant au fond infrarouge, tout en essayant de retracer leur histoire.

5. Aussi utilisée dans le domaine radio et des hautes énergies

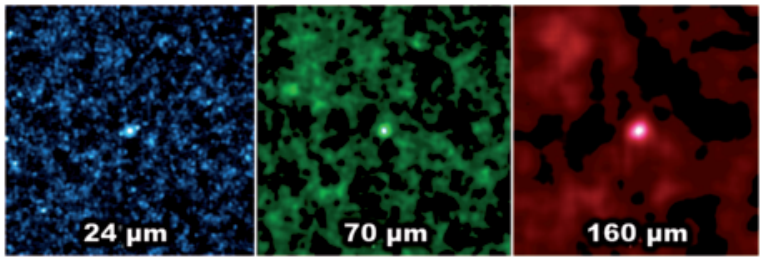

Figure 3 – L'empilement d'environ 20 000 galaxies à 24 (gauche), 70 (milieu) et 160 microns (droite) des données du satellite Spitzer, qui a permis la résolution du fond infrarouge lointain. Le signal attendu est la zone brillante au centre de chaque image. La dimension de cette zone brillante augmente avec la longueur d'onde, puisqu'elle est liée à la diffraction du télescope. Extrait de Dole *et al.* (2006) ; voir aussi Bavouzet et al. (2009, in prep).

Encadré 2 — *Confusion des galaxies et technique d'empilement*

La résolution des images provenant des télescopes en orbite dépend de la longueur d'onde, puisque la taille de l'image d'une source ponctuelle, limitée par la diffraction, est proportionnelle à la longueur d'onde d'observation divisée par le diamètre du télescope. Une image prise à 160 microns aura ainsi une résolution environ 50 fois moindre qu'une image à 3 microns prise avec le même télescope. Les images acquises vers 100 ou 200 microns de longueur d'onde subissent donc l'effet de *confusion*, effet qui noie les détails (*figure E3*). Les galaxies sont ainsi plus difficilement détectables qu'à courte longueur d'onde.

Pour mesurer le flux des galaxies à grande longueur d'onde alors que les données sont limitées par la confusion et qu'en apparence il n'y a pas de signal, nous avons utilisé la technique de l'empilement (*figure E4*). Il suffit d'additionner le signal d'une distribution de milliers de galaxies non détectées à 160 microns (mais préalablement détectées et localisées sur des images à 24 microns) pour extraire la somme de leurs flux. Cette méthode permet d'augmenter le rapport signal (flux total des galaxies individuelles) sur bruit (somme des autres fonds) d'un facteur racine de n, n étant le nombre de sources utilisées. Cette méthode ne permet que la mesure de la somme d'un grand échantillon de galaxies (à partir d'une centaine). Il n'est pas possible d'extraire le flux d'une galaxie individuelle.

Illustrons cette technique sur des cas réels : la *figure 3* montre le résultat de l'empilement d'environ 20 000 galaxies qui a permis de faire ressortir l'essentiel du fond infrarouge lointain (à 70 et 160 microns). La *figure E5* montre l'empilement d'environ 7000 galaxies à 870 microns dans les nouvelles données de la camera LABOCA du télescope APEX au Chili.

Plus d'informations, images et vidéo sont disponibles sur http://www.ias.u-psud.fr/irgalaxies/

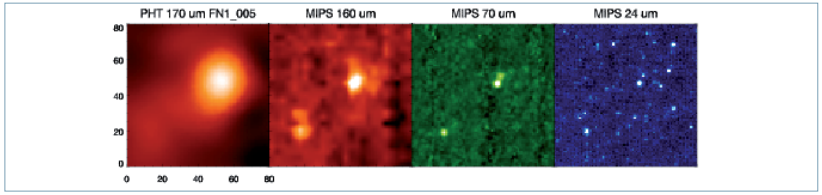

Figure E3 – De gauche à droite : une même région du ciel (environ 40 minutes d'arc carrées) observée en infrarouge par ISO à 170 microns et Spitzer à 160, 70 et 24 microns. Noter l'augmentation du nombre de sources détectées à courte longueur d'onde (vers la droite), en raison de la meilleure résolution angulaire et des propriétés des détecteurs. Image : H. Dole et Lagache *et al* (2005). Reproduit, avec permission, de Annual Review of Astronomy and Astrophysics, Volume 43 ©2005 by Annual Reviews www.annualreviews.org.

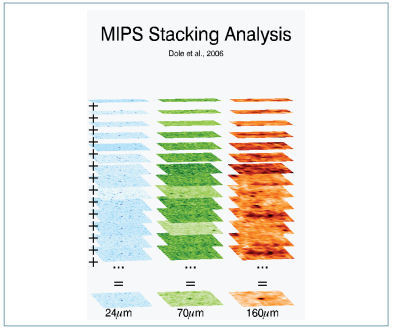

Figure E4 – Illustration de la technique d'empilement (stacking). Les galaxies sont identifiées individuellement à 24 microns (colonne de gauche), alors qu'aucune contrepartie n'est détectée à 70 (milieu) et 160 microns (à droite). Une image est extraite autour de chaque galaxie détectée aux trois longueurs d'ondes. Il suffit d'empiler les milliers d'images pour obtenir le signal total (ligne du bas).

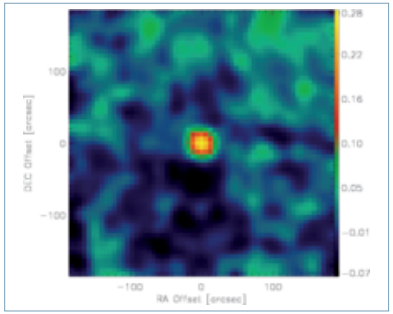

Figure E5 – L'empilement d'environ 7000 galaxies à 870 microns, des données de la caméra bolométrique submillimétrique LABOCA installée au télescope APEX au Chili. Extrait de Beelen *et al.* (2009, en préparation).

Encadré 3 *L'apport des satellites : Spitzer, Planck et Herschel*

Le domaine infrarouge (1 à 250 microns) et submillimétrique (250 microns à 1 mm) ne dispose que d'un nombre limité de fenêtres atmosphériques permettant des observations depuis le sol. Les télescopes refroidis à température cryogénique mis sur orbite constituent la seule solution pour étudier les galaxies faibles. Cependant, les fortes contraintes sur la température du télescope (quelques Kelvins à quelques dizaines de K) et de l'instrumentation (de 0,1K à 4 K) ont limité la dimension et la duré de vie des télescopes qui ont volé jusqu'à présent. IRAS (1983) a fonctionné pendant 10 mois et avait un diamètre de 60 cm. Le télescope infrarouge DIRBE sur le satellite COBE (1989) a fonctionné 10 mois et avait un diamètre de 30 cm. Tous deux ont mené des relevés complets du ciel. ISO (1995), le premier observatoire infrarouge, européen, avait un diamètre de 60 cm et a fonctionné 27 mois. Spitzer (2003) est doté d'un télescope de 85 cm et a une durée de vie d'environ 5,5 ans.

Malgré ces contraintes, l'évolution des détecteurs permet de gagner en sensibilité et en pouvoir de résolution, avec un meilleur échantillonnage de la figure de diffraction du télescope. La *figure E6* présente une même région du ciel observée par 3 télescopes différents, et montre que la détection de galaxies est beaucoup plus aisée avec les télescopes récents. Sur ces images, on remarque que les galaxies ne sont pas résolues individuellement avec IRAS, et qu'elles forment un fond diffus fluctuant spatialement (le fond infrarouge). À mesure que la résolution angulaire augmente, les instruments résolvent ce fond diffus en sources discrètes.

La prochaine génération de satellites sera européenne. L'observatoire Herschel, d'un diamètre de 3,50 m, sera le plus grand télescope astronomique jamais lancé (le Hubble ne mesurant « que » 2,40 m), et il observera entre 60 et 600 microns de longueur d'onde avec une résolution angulaire inégalée dans l'espace. Le satellite Planck, d'un diamètre de 1,50 m, observera entre 350 microns et 1 cm de longueur d'onde, avec une sensibilité et une résolution angulaire bien meilleures que ses prédécesseurs COBE et WMAP. La combinaison des données des deux missions permettra d'étudier avec une grande précision la formation et l'évolution des galaxies, au travers de l'étude des galaxies infrarouges et des fluctuations du fond infrarouge.

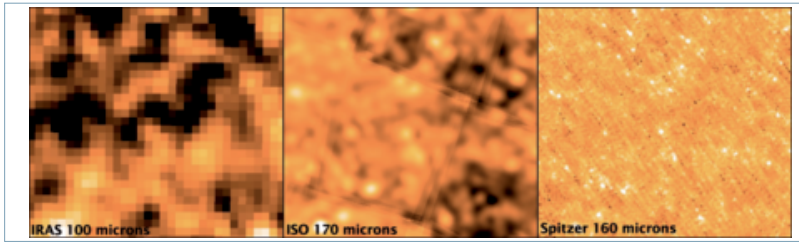

Figure E6 – La même portion du ciel (environ 1 degré carré) observée en infrarouge lointain par trois satellites de générations différentes. De gauche à droite : IRAS à 100 microns (en 1983) ; ISO à 170 microns (en 2000) ; Spitzer à 160 microns (en 2004). La résolution angulaire augmente avec les nouvelles technologies des détecteurs. Image: H. Dole et IRAS, ISO/FIRBACK, Spitzer/SWIRE.

La surprenante histoire des galaxies

L'étude fine du rayonnement de fond extragalactique infrarouge, qui exploite des campagnes de relevés cosmologiques à plusieurs longueurs d'onde – visible et infrarouge proche, mais aussi parfois ultraviolet, rayons X, submillimétrique et radio – et la spectroscopie (*figure 4*), permet d'obtenir l'époque des émissions et les luminosités des galaxies, ainsi que la contribution massique des étoiles et des poussières, celle de l'éventuel trou noir central, le taux de formation stellaire, la température des poussières et une estimation de leurs tailles.

Dans l'Univers local, rares sont les galaxies qui émettent l'essentiel de leur énergie dans l'infrarouge. En effet, l'émission stellaire, prépondérante, présente son maximum dans le domaine visible-UV. Le niveau élevé du fond extragalactique dans l'infrarouge lointain suggère que les galaxies émettaient nettement plus dans l'infrarouge par le passé. La mesure de la densité de luminosité (luminosité par élément de volume d'Univers, corrigée des effets de l'expansion) émise en fonction de la distance, ou redshift (*figure 5*) permet de connaître l'évolution de la formation stellaire avec le redshift. Ainsi, la densité de formation stellaire était-elle maximale à l'époque qui correspond au redshift de 1, et c'est une fonction lentement décroissante avec le redshift aux époques plus lointaines. Le plus intéressant réside dans la cause de cette évolution.

On constate que les galaxies visibles dans l'ultraviolet – parce que leurs étoiles se forment dans des milieux relativement libres de poussières – ont une contribution au taux de formation d'étoiles qui croît lentement lorsque le redshift augmente (*figure 5*). La population galactique qui contribue le plus au taux de formation stellaire est celle des galaxies lumineuses dans l'infrarouge (Luminous InfraRed Galaxies, ou « LIRG »), avec des luminosités intégrées comprises entre 10^{11} et 10^{12} luminosités solaires[6] (voir *encadré 1*), dont la contribution augmente d'un facteur 10 entre les redshifts 0 et 1 (courbe en tiret vert), c'est-à-dire entre le temps présent et il y a 8 milliards d'années. C'est cette population qui est responsable de l'essentiel du fond infrarouge.

Ainsi s'esquisse la surprenante évolution des galaxies et de leurs contributions au fond extragalactique infrarouge. A un redshift supérieur à 0,7, l'Univers était dans une phase active infrarouge. Des galaxies lumineuses en infrarouge (LIRG) dominaient le taux de formation stellaire dans l'Univers (vers un redshift de 1). À redshift nettement plus élevé, les ULIRG ultra-lumineuses dans l'infrarouge (plus de 10^{12} luminosités solaires) semblent avoir dominé.

Ainsi, alors que dans l'Univers local l'essentiel des galaxies rayonne dans le domaine visible, le fond infrarouge domine à cause des nombreuses LIRG et ULIRG lointaines qui émettent fortement dans l'infrarouge.

Quelle est la nature physique de ces galaxies LIRG ? Elle est en fait très variée, puisqu'une LIRG a pour seule propriété d'être très lumineuse en infrarouge et d'y émettre quasiment toute son énergie, par l'intermédiaire des pous-

6. Par comparaison, notre Voie Lactée a une luminosité d'environ 3×10^{10} luminosités solaires.

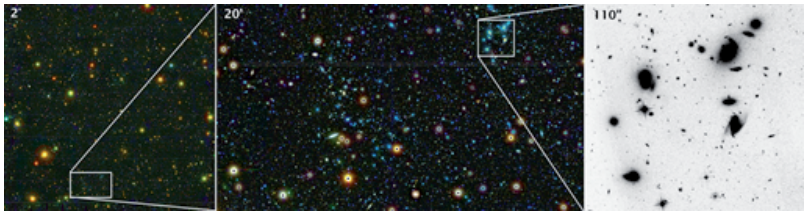

Figure 4 – Exemple de relevé profond dans le domaine visible, avec le champ COSMOS. À gauche : image du télescope au sol SUBARU (prises en bleu, vert et rouge) sur 4 degrés carrés ; au centre : zoom sur 20 minutes d'arc ; à droite : image du télescope spatial Hubble en bande I (dans le rouge), zoom sur environ 2 minutes d'arc. En identifiant les galaxies de ces images avec les données dans l'infrarouge (et parfois avec l'aide d'observations spectroscopiques supplémentaires) il est possible d'estimer le redshift, la luminosité totale et le taux de formation stellaire des galaxies. Image : H. Dole à partir des données publiques COSMOS.

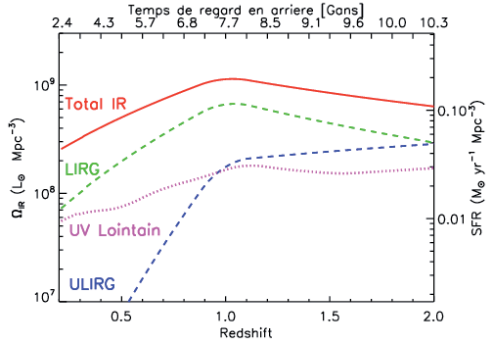

Figure 5 – Densité d'énergie intégrée sur le spectre électromagnétique (en luminosité solaire par mégaparsec cube) en unités comobiles (qui corrigent des effets de l'expansion) émise par les galaxies en fonction de l'époque cosmique (redshift en bas, ou temps de regard en arrière en haut) et par type : en vert les galaxies très lumineuses en infrarouge (LIRG), en bleu les galaxies ultra-lumineuses en infrarouge (ULIRG), en violet les galaxies observées en UV, et en rouge le total. On remarque que les LIRG dominent jusqu'au redshift 2, et qu'un très fort accroissement est observé pour les LIRG et les ULIRG jusqu'à un redshift d'environ 1. Synthèse des travaux de Le Floc'h *et al* (2005), Caputi *et al.* (2007), Tresse *et al.* (2007).

sières interstellaires chauffées par l'absorption du rayonnement électromagnétique. Par exemple, une LIRG locale n'a rien de commun avec une LIRG à un redshift de 1 : dans le premier cas, il s'agit souvent de galaxies en interaction forte ou en fusion, avec contribution importante de noyau actif ; dans le second cas (grand redshift), il s'agit souvent d'une galaxie sous forme de disque ou faiblement perturbée (voir *encadré 1*). Dans tous les cas, les LIRG sont des galaxies beaucoup plus massives que la moyenne, avec de forts taux de formation stellaire. Les ULIRG (essentiellement formées à un redshift supérieur à 2) sont encore plus massives (10^{11} masses solaires ou plus) et situées au cœur de halos de matière noire massifs (10^{12} masses solaires ou plus). La formation aussi précoce d'objets aussi lourds est actuellement difficilement explicable dans le cadre du modèle de formation hiérarchique des structures décrit précédemment (formation des galaxies). Pour affiner ces modèles, l'étude des galaxies moins lumineuses à grand redshift semble une approche prometteuse. Un moyen original pour obtenir des informations statistiques sur ces objets peu lumineux consiste à étudier les anisotropies dans les fluctuations du fond extragalactique infrarouge.

Les fluctuations du fond infrarouge : un nouvel outil pour dévoiler la structuration des galaxies

Malgré les succès de la technique d'empilement, la confusion constitue une limitation à l'analyse des données cosmologiques dans l'infrarouge (voir *encadré 2*). Cependant, comme cette confusion est due aux nombreuses galaxies plus faibles et lointaines, il est pertinent d'analyser les fluctuations de brillance de l'image infrarouge pour en extraire une information statistique sur la distribution des galaxies. Ainsi les fluctuations du fond infrarouge peuvent nous révéler des informations cruciales sur la manière dont les galaxies s'agrègent entre elles par l'analyse du spectre de puissance angulaire des images.

Nous avons ainsi combiné les données du satellite Spitzer à 160 microns (*figure 6 à gauche*) avec celles du satellite IRAS à 100 microns pour détecter des regroupements de galaxies infrarouges à un redshift de l'ordre de 1. Nous avons mesuré un spectre de puissance angulaire (*figure 6 à droite*) qui résulte de l'addition de plusieurs composantes : la poussière froide d'avant-plan de notre Galaxie (appelée cirrus, par analogie avec les nuages terrestres, en vert) domine pour $k < 0,03$, une contribution constante des galaxies non résolues individuellement mais relativement brillantes (distribution de Poisson, en bleu clair) domine pour $k > 0,2$. Enfin, entre ces deux régimes d'échelles angulaires ($0,03 < k < 0,2$ arcmin^{-1}, soit entre 5 et 30 minutes d'arc environ) se trouve le signal recherché : un excès dû aux fluctuations des galaxies lointaines qui se regroupent selon des échelles privilégiées (bleu foncé). Cet effet se remarque sur l'image à 160 microns (*figure 6 à gauche*), où les fluctuations visibles ne sont pas distribuées uniformément dans l'image, mais bien par « paquets » (même si une partie d'entre eux ont pour origine l'émission d'avant-plan due aux cirrus de notre Galaxie).

En utilisant un modèle d'évolution des galaxies, nous pouvons ensuite mesurer la corrélation spatiale des galaxies

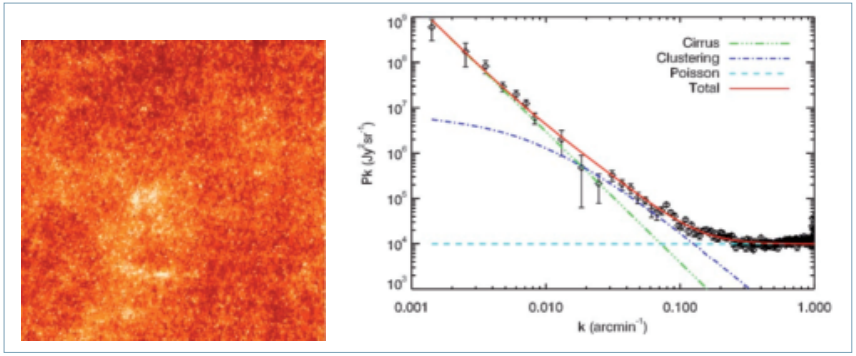

Figure 6 – À gauche : image du ciel à 160 microns vue par le satellite Spitzer, sur environ 4 degrés carrés ; les sources brillantes ont été soustraites, et les fluctuations du fond infrarouge sont bien visibles, et distribuées non uniformément. À droite : Spectre de puissance angulaire (ou analyse en fréquence spatiale du signal) de l'image de gauche. Les grandes échelles angulaires se trouvent à gauche (petit k), et les petites à droite (grand k). La courbe rouge est le spectre de puissance total. En vert : le spectre de puissance angulaire des cirrus d'avant-plan de notre Galaxie ; en tiret bleu clair : composante poissonnienne des fluctuations (absence de corrélation). En trait-point bleu foncé : anisotropies corrélées du fond infrarouge. Figures extraites de Lagache *et al.* (2007).

avec les halos de matière noire. Nous en déduisons que les galaxies lumineuses dans l'infrarouge à un redshift autour de 1 résident dans des halos de matière noire d'environ 10^{12} masses solaires. Cette corrélation s'avère trois fois plus élevée que pour les galaxies infrarouges dans l'Univers proche.

La découverte de cette corrélation des galaxies infrarouges entre elles (et avec la distribution de matière noire) à partir des fluctuations du rayonnement de fond extragalactique nous permet d'espérer pouvoir tracer l'évolution du regroupement des galaxies infrarouges jusqu'à grand redshift, grâce aux données des satellites Planck et Herschel (voir *encadré 3*). Pour cela, de nouvelles techniques d'analyse du signal sont en cours de développement : l'empilement et la séparation des composantes.

En conclusion, les avancées sur le rayonnement fossile des galaxies proviennent et proviendront surtout des progrès technologiques des télescopes spatiaux, mais aussi des techniques d'analyse du signal astrophysique et de la manière de penser et de manipuler les grandes quantités de données multi-longueur d'onde.

POUR EN SAVOIR PLUS

Puget *et al.*, *Astronomy & Astrophysics*, 308, L5, (1996).
Elbaz & Cesarsky, *Science*, 300, 270, (2003).
Lagache, Puget, Dole, 2005, *Annual Reviews of Astronomy and Astrophysics*, 43, 727.
Dole *et al.*, 2006, *Astronomy & Astrophysics*, 451, 417.
Lagache *et al.*, 2007, *Astrophysical Journal*, 665, 89.
Hauser & Dwek, *Annual Reviews of Astronomy and Astrophysics*, 37, 249 (2001).
Caputi *et al.*, *Astrophysical Journal*, 660, 97, (2007).
Fernandez-Conde *et al.*, *Astronomy & Astrophysics*, 481, 885, (2008).

Livres :

- Cosmologie, de F. Bernardeau, 2007, *CNRS Éditions / EDP Sciences.*
- « L'observation en astronomie », de Léna, Dole, Lagrange, Rouan, Binétruy, Génova, *Ellipses*, février 2009.
- « Galaxies et cosmologie », de Combes, Haywood, Collin, Mellier, Durret, Guiderdoni, *Ellipses*, février 2009.
- « Extragalactic Astronomy and Cosmology », de P. Schneider, *Springer*, (2006).
- « L'observation en Astrophysique », de P. Léna, D. Rouan *et al.*, *CNRS Editions / EDP Sciences*, (2008).

Manuscript for astroph **000**, 1–14 (2008) Printed 13 July 2010 (MN LATEX style file v2.2)

325-MHz observations of the ELAIS-N1 field using the Giant Metrewave Radio Telescope

S. K. Sirothia,[1⋆] M .Dennefeld,[2] D. J. Saikia,[1] H. Dole,[3]
F. Ricquebourg,[2] and J. Roland[2]
[1] *National Centre for Radio Astrophysics, Tata Institute of Fundamental Research, Post Bag 3, Ganeshkhind, Pune 411007, India*
[2] *Institut d'Astrophysique de Paris, 98bis Boulevard Arago, F-75014, Paris, France*
[3] *Institut d'Astrophysique Spatiale, Bât. 121, Université Paris-Sud 11 and CNRS (UMR 8617), F-91405 Orsay Cedex, France*

Accepeted for publication in MNRAS

ABSTRACT
We present observations of the European Large-Area *ISO* Survey-North 1 (ELAIS-N1) at 325 MHz using the Giant Metrewave Radio Telescope (GMRT), with the ultimate objective of identifying active galactic nuclei and starburst galaxies and examining their evolution with cosmic epoch. After combining the data from two different days we have achieved a median rms noise of $\approx 40\mu$Jy beam^{-1}, which is the lowest that has been achieved at this frequency. We detect 1286 sources with a total flux density above $\approx 270\mu$Jy. In this paper, we use our deep radio image to examine the spectral indices of these sources by comparing our flux density estimates with those of Garn et al. at 610 MHz with the GMRT, and surveys with the Very Large Array at 1400 MHz. We attempt to identify very steep spectrum sources which are likely to be either relic sources or high-redshift objects as well as inverted-spectra objects which could be Giga-Hertz Peaked Spectrum objects. We present the source counts, and report the possibility of a flattening in the normalized differential counts at low flux densities which has so far been reported at higher radio frequencies.

Key words: catalogues – surveys – radio continuum: galaxies – galaxies: active

1 INTRODUCTION

One of the key questions in extragalactic studies is to understand the evolution of galaxies, namely their star formation history, formation of active galactic nuclei (AGN), building-up of large disks and bulges and the formation and evolution of supermassive black holes over the redshift range from $z \approx 5$ to the present epoch. This is the range where the global star-formation rate has passed through a maximum between a redshift of 1 and 2 (Madau et al. 1996; Madau, Pozzetti & Dickinson 1998; see the recent compilation by Hopkins & Beacom 2006). It is conjectured that merging of galaxies has occurred significantly at these epochs, triggering collapse of molecular clouds and star formation, often in dusty environments. Many of these galaxies may also harbour an AGN and are copious emitters in the infrared region of the spectrum. It has become clear over the last decade that a population of galaxies which radiate most of their power in the infrared constitutes an important and significant component of the Universe (Lagache, Puget & Dole 2005 for a review).

⋆ Email: sirothia@ncra.tifr.res.in

Multiwavelength observations of high-redshift infrared galaxies could provide valuable insights into issues of galaxy formation and evolution. The spectral energy distribution (SED) of the cosmic infrared (IR) background (CIB, which is the emission at wavelengths larger than a few microns) is due to the formation and evolution of both AGN and starburst galaxies (e.g. Puget et al. 1996; Hauser et al. 1998; Lagache et al. 1999; Gispert et al. 2000; Kashlinsky 2005; Dole et al. 2006). The SED of the CIB peaks around 150 μm, accounting for about half the total energy in the optical/infrared extragalactic background light (cf. Hauser & Dwek 2001; Wright 2004; Aharonian et al. 2006). It has been shown recently that the mid-infrared (MIR) 24 μm selected sources contribute more than 70 per cent of the CIB at 70 and 160 μm. Galaxies contributing the most to the total CIB are z∼1 luminous infrared galaxies, which have intermediate stellar masses (Dole et al. 2006).

To explore these issues related to galaxy formation and evolution and possible relationships between AGN and starburst activity require large samples over wide enough areas, to avoid biases due to large-scale structure variations, as well as multi-wavelength coverages to have a global appraisal of the energy output and of its origin. This means, in particular, a far-IR coverage to access the "dusty" objects to get the bolometric energy output; an optical coverage as this is the range where the usual spectroscopic diagnostics are available; the ultraviolet (UV) range as this is where the massive stars have their impact and where the energy is seen in the absence of dust; the radio range to distinguish thermal from non-thermal sources and obtain the best spatial resolution; and possibly a high-energy coverage in X-rays to detect the most powerful AGNs. Amongst the different fields which are being studied extensively, a well-known one selected at infrared wavelengths is the European Large Area ISO (Infrared Space Observatory) Survey (ELAIS), from which we have selected one of the northern fields, the ELAIS-N1, observable with GMRT.

The ELAIS-N1 field has been chosen in a region of the sky with low-IR foreground emission, to allow detection of fainter (and presumably more distant) galaxies; also, because of this advantage, it has already been covered at far-IR wavelengths by the ISO-FIRBACK (Far-Infrared Background) survey at 170 μm, to find dusty, high-z galaxies expected to significantly contribute to the far-IR cosmic background and is covered by Spitzer as well, as part of the SWIRE (Spitzer Wide-area Infrared Extragalactic) legacy survey (Lonsdale et al. 2004). The details on the first far-IR data can be found in Dole et al. (2001). Our team has been studying this field in detail, and has particularly made some of the optical spectroscopic observations. Most of the sources identified up to now, essentially the IR-brighter ones, are local, cold, moderately star-forming galaxies rather than the violent starbursters expected at larger distances (Dennefeld et al. 2005). It is now understood that this is partly due to the sensitivity limit of ISO, so that the higher z sources, needed to reproduce the number counts, have to be found among the fainter IR sources detected by Spitzer. Due to its interest in studies of galaxy evolution, it has also been included in the Galex UV survey. It has already optical imaging coverage from LaPalma as part of the INT (Isaac Newton Telescope) Wide Field Survey (McMahon et al. 2001) and a band-merged catalogue is available (Rowan-Robinson et al. 2004). Redshift surveys of the region are underway (e.g. Rowan-Robinson et al. 2008) and it is also partly covered by the Sloan Digital Sky Survey (SDSS, Adelman-McCarthy et al. 2008).

Radio surveys provide important constraints in our understanding of the evolution of the Universe. Traditionally counts of the number of sources as a function of the radio flux density have provided information on the evolution of radio source populations with cosmic epoch (e.g. Longair 1966; Rowan-Robinson et al. 1993). More recently, deep radio surveys have shown a flattening of the source counts at about a mJy at both 610 and 1400 MHz (e.g. Windhorst, Mathis & Neuschaefer 1990; Prandoni et al. 2006 and references therein; Moss et al. 2007 and references therein). The change of slope is believed to be due to a new population of radio sources, the so-called sub-mJy population, consisting largely of low-luminosity AGN and starburst galaxies (e.g. Padovani et al. 2007; Smolčić et al. 2008). The source counts at higher flux densities are dominated by the classical double radio galaxies and quasars (e.g. Condon 1989).

Concerning the ELAIS-N1 field, a Very Large Array (VLA) radio survey has been made at λ20 cm by Ciliegi et al. (1999), reaching a brightness limit of ≈1 mJy beam^{-1} (5 sigma) over the 1.54 square degrees of coverage, and deeper in smaller areas. This field has been studied at λ50 cm using the Giant Metrewave Radio Telescope (GMRT) by Garn et al. (2008), hereafter referred to as G2008. They have covered a total area of ≈ 9 deg^2 with a resolution of 6×5 arcsec^2 with a total of 19 pointings. In 4 of their pointings they reach an rms of ≈ 40 μJy beam^{-1} and an rms of ≈ 70 μJy beam^{-1} in the rest of the pointings. They have catalogued 2500 sources and present a mosaic of maps from their survey. Preliminary results from a study of polarised compact sources (Taylor et al. 2007) at 1420 MHz using the Dominion Radio Astrophysical Observatory Synthesis Telescope (DRAO ST) are also available. They currently present 30% of observations from a survey of 7.4 deg^2 centered on 16^h11^m, $+55°00'$. They present maps in Stokes I, Q and U with a maximum sensitivity of 78 μJy beam^{-1}, with a resolution of ≈ 1 arcmin^2.

A GMRT coverage of this field, at $\lambda = 90$ and 200 cm, provides an ideal complement to get accurate spectral shapes and indexes over a large frequency range and help establish the nature of the objects. In particular it will help to separate the respective contribution of AGNs and starbursts, a long standing problem for the interpretation of the far-IR emission. It is also relevant to note here that there is a tight correlation between the far-IR and radio luminosities of galaxies (e.g. Helou, Soifer & Rowan-Robinson 1985; Condon 1992) which applies to both local and global properties of galaxies in the nearby and distant Universe (Garrett 2002; Luo & Wu 2005; Hughes et al. 2006; Murphy et al. 2006; Chapman et al. 2005).

As part of our program to explore the issues outlined earlier, we are making deep observations of the ELAIS-N1 field with the GMRT at low frequencies. In this paper we present the results of our GMRT observations at 325 MHz pointed towards the centre of the field ($16^h10^m, +54°36'$). We have made the observations on two different days and have made images of the first day separately to check for consistency. The final image made by combining the data of both the days has a median rms noise figure of ≈40 μJy beam^{-1} towards the centre of the field, and is amongst the deepest images made at this frequency. It is more sensitive than the low-frequency survey of the XMM-LSS (Large Scale Structure) field at 325 MHz with the VLA which has a 5σ brightness limit of ∼4 mJy beam^{-1} (Tasse et al. 2006). For comparison, the 5σ limiting brightness of the Westerbork Northern Sky Survey (WENSS; Rengelink et al. 1997) is ∼18 mJy beam^{-1}, while for the deeper surveys of selected fields with the Westerbork telescope the corresponding values range from 2.4 to 3.5 mJy beam^{-1} (Wieringa et al. 1992). The details of our observations and analysis are described in Section 2, while the results are presented in Section 3. The discussion and conclusions are summarised in Section 4.

2 OBSERVATIONS AND DATA REDUCTION

The observation summary along with the calibrators used is presented in Table 1, while some of the imaging details are listed in Table 2, both of which are self explanatory. The data were acquired with a small visibility integration time

Table 1. Observation summary

Date	2005 June 26, 2005 June 27
Working antennas	25
Centre Frequency	325 MHz
Bandwidth	32 MHz
Visibility integration time	4.19 s
Total observation time	10.3 hrs × 2
Flux Calibrator	
Source	3C286
Time	0.3 hrs × 2
Flux density	25.97 Jy
Scale	Perley-Taylor 99
Phase Calibrator	
Source	J1459+7140
Time	1.8 hrs × 2
Flux density	20.17 Jy
Target Field	
Phase centre	J1610+5440
Time	8.2 hrs × 2
Fraction (f_d) of data used	≈ 40%

Table 2. Imaging summary

Package	AIPS++ (version: 1.9, build #1556)
Image size	5000 × 5000
Pixel size	$2'' \times 2''$
Clean Algorithm	Wide-field Clark clean
Imaging Weight	Briggs (rmode='norm', robust=0)
Widefield Imaging Parameters	
Number of facets	9 with 1.5 overlap
Wproject planes	256
Primary Beam correction	Gaussian, FWHM=84.4′
Rms noise	≈ 40μJy beam^{-1}
Synthesised beam	$9.35'' \times 7.38''$, PA=73.25°

from the correlator to help in the identification of radio frequency interference (RFI) and minimize smearing effects. The data reduction was mainly done using AIPS++, and with 3C286 as the primary flux density and bandpass calibrator. After applying bandpass corrections on the phase calibrator (J1459+7140), gain and phase variations were estimated, and then flux density, bandpass, gain and phase calibration from 3C286 and J1459+7140 were applied on the target field (J1610+5440).

While calibrating the data, bad data were flagged at various stages. The data for antennas with high errors in antenna-based solutions were examined and flagged over certain time ranges. Some baselines were flagged based on closure errors on the bandpass calibrator. Channel and time-based flagging of data points corrupted by RFI were done using a median filter with a 6σ threshold. Residual errors above 5σ were also flagged after a few rounds of imaging and self calibration. The system temperature (T_{sys}) was found to vary with antenna, the ambient temperature which has a diurnal variation, and elevation (Sirothia 2008). In the

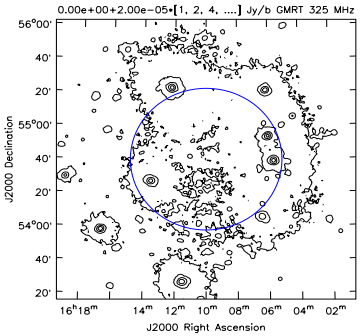

Figure 1. The variation of rms noise across the image before primary beam correction. In this figure and in all the images presented here the contour levels in units of Jy beam^{-1} are represented by mean+rms×(n) where n is the multiplication factor. These levels are shown above each image. All negative contours appear as dashed lines.

absence of regular T_{sys} measurements for GMRT antennas, this correction was estimated from the residuals of corrected data with respect to the model data. The corrections were then applied to the data. The final image was made after several rounds of phase self calibration, and one round of amplitude self calibration, where the data were normalized by the median gain for all the data. This image was made by combining the data from both the sidebands, giving a total bandwidth of 32 MHz. The final image was also primary beam corrected using the Gaussian parameter as mentioned in Table 2.

The final image has a median rms noise of ≈40 μJy beam^{-1} near the phase centre and 30 μJy beam^{-1} near the half power of the beam before primary beam correction. The noise variation across the beam is shown in Fig. 1. Issues related to dynamic range affect the quality of the image near the bright sources where the noise is greater, as can be seen in Fig. 1. An image of a strong source in the field, and the corresponding image at 610 MHz from G2008 is discussed later in the paper. The theoretically expected noise near the phase centre, is given by the following equation,

$$\sigma = \frac{\sqrt{2}T_{sys}}{G\sqrt{n(n-1)f_d\Delta\nu\tau}} \quad (1)$$

where, $T_{sys} \approx 108$K, the antenna gain $G \approx .32$K Jy^{-1}, n is the number of working antennas, $\Delta\nu$ is the bandwidth and τ is the total duration of the observations, f_d is the total fraction of data which has been used for making the final image; the last four parameters being listed in Table 1. For our data set the theoretically calculated value is ∼22 μJy beam^{-1}.

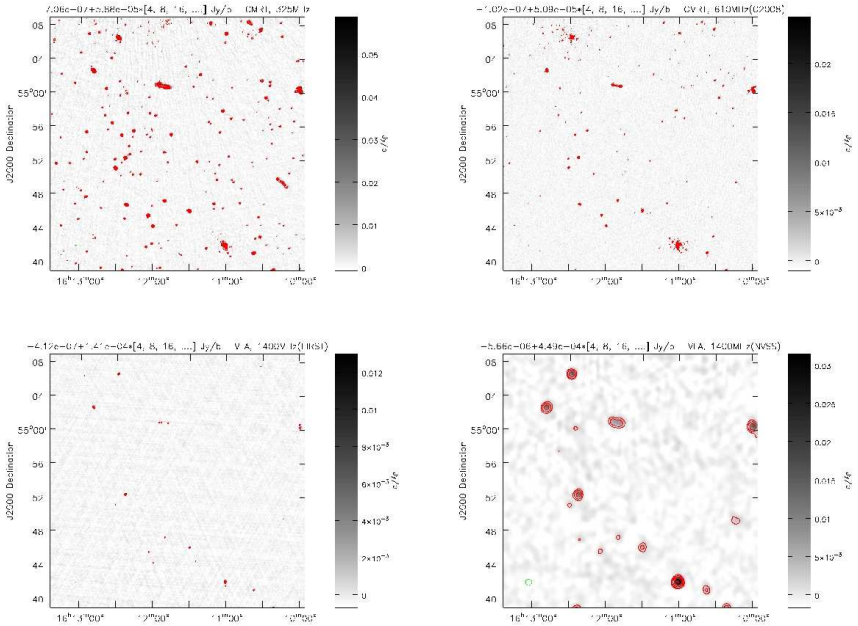

Figure 2. GMRT image of an area of 30×30 arcmin^2 from our observations at 325MHz (top left), and the corresponding images of the same area at 610 MHz with the GMRT from G2008 (top right), and from FIRST (bottom left) and NVSS (bottom right) at 1400 MHz.

3 SOURCE CATALOGUE AT 325 MHZ

As an illustration, the GMRT 325-MHz image of a region of about 30×30 arcmin^2 along with the Faint Images of the Radio Sky at Twenty-centimeters (FIRST, Becker, White & Helfand 1995), and NRAO VLA Sly Survey (NVSS, Condon et al. 1998) images at 1400 MHz and the GMRT image at 610 MHz (G2008) are shown in Fig. 2. The brighter sources are seen clearly in all the images. One of the first tasks for the entire field is to extract and list all the sources along with their positions and flux densities.

3.1 Source extraction criterion

A catalogue of sources within 1.1° radius of the phase centre, which is 18.3 per cent of the primary beam peak value, was created with the peak source brightness greater than 6 times the local rms noise value. A comparison of our sources with those detected in WENSS (Rengelink et al. 1997) for different distances from our phase centre showed no systematic effects and suggests this to be a reasonable value for this catalogue. The rms noise has been evaluated over an area of approximately 63×63 pixels excluding the source pixels. Since the local noise varies with distance from the phase centre and also in the vicinity of bright sources, this approach has helped minimize the detection of spurious sources.

An extract of sources from the full Table are listed in Table 3, along with some of their observed properties. The full Table consisting of 1286 sources, is available in the online version of the paper. Column 1: source name in J2000 co-ordinates where hhmmss represents the hours, minutes and seconds of right ascension and ddmmss represents the degrees, arcmin and arcsec of declination; columns 2 and 3: the right ascension and declination of the source which is the flux-density weighted centroid of all the emission enclosed by the 3σ contour. We have estimated the errors in the positions using the formalism outlined by Condon et al. (1998). The typical error in the positions of the sources is about 1.4 arcsec, consistent with the comparisons of our positions with those of G2008 and FIRST, as discussed in Section 4.1. Column 4: distance of the centroid from the phase centre in

degrees; column 5: the local rms noise value in units of μJy beam^{-1}. The peak and total flux densities within the 3-σ contour are listed in columns 6 and 7 respectively. The flux densities of the different sources were estimated as follows. For unresolved sources, the total flux density $S_{\rm total}$ in units of mJy has been taken equal to the peak value $S_{\rm peak}$ in our analysis, although the flux density within the 3-σ contour is also listed. For the extended sources the total flux density is the value within the 3-σ contour. Fig. 3 shows the 3-σ contours for one resolved source and two unresolved sources. For ease of readers the values of total flux densities ($S_{\rm total}$) thus estimated are mentioned in column 8. For resolved sources we list the largest angular size in column 9, while the unresolved sources have been marked as U in this column. The largest angular size has been estimated by fitting Gaussians to the resolved sources. For single sources it is the deconvolved size of a single Gaussian, while for extended sources it is the sum of the distance between the furthest Gaussian components and their semi-major axes. The categorization of unresolved sources and a discussion of the flux densities are presented in Section 3.1.1.

3.1.1 Source size and flux densities

For low signal-to-noise ratio detections, Gaussian fitting routines may be significantly affected by noise spikes leading to errors in estimating both the width and flux density of the source. The ratio

$S_{\rm total}/S_{\rm peak} = \theta_{\rm min}\ \theta_{\rm maj}\ /(b_{\rm min}\ b_{\rm maj})$

where $\theta_{\rm min}$ and $\theta_{\rm maj}$ are the major and minor axes of the detected source and $b_{\rm min}$ and $b_{\rm maj}$ are the major and minor axes of the restoring beam. The flux density ratio may be used to discriminate between unresolved sources and those which are much larger than the beam (see Prandoni et al. 2006). In Fig. 4, we plot the above ratio of the flux densities to the signal-to-noise ratio ($S_{\rm peak}/\sigma_{\rm local}$) for all sources above the $6\sigma_{\rm local}$ threshold. Clearly sources for which $S_{\rm total}/S_{\rm peak}$ <1 have been affected by noise. We first fit a functional form of the curve $f(x) = 1.0 \pm \frac{3.22}{x}$ such that almost all of the points with $S_{\rm total}/S_{\rm peak}$ <1 lie above the curve. Reflecting this curve about $S_{\rm total}/S_{\rm peak}$ =1 gives a list of all the sources which lie between the two curves and can be considered to be unresolved. This analysis shows that about 73 per cent of the sources (943/1286) are considered to be unresolved and these have been listed as 'unresolved' sources (U) in the Table.

3.2 Comparison with WENSS

To compare our estimates of the flux densities with those of the WENSS catalogue we have identified all WENSS sources which lie within 10 arcsec of our 3-σ centroid position from the catalog available via Vizier (Ochsenbein et al. 2000). We have compared the positions of the centroids of emission for the unresolved WENSS sources with our sources (as shown in Fig. 5) and find the mean and rms displacement to be 2.45 and 6.61 arcsec in right ascension and −3.45 and 5.78 arcsec in declination. The value of 10 arcsec is the half power synthesized beamwidth of our GMRT observations, while the quoted error in the WENSS positions is ∼1.5 arcsec (de Bruyn et al. 2000). Within the uncertainties, the GMRT positions are consistent with the WENSS ones.

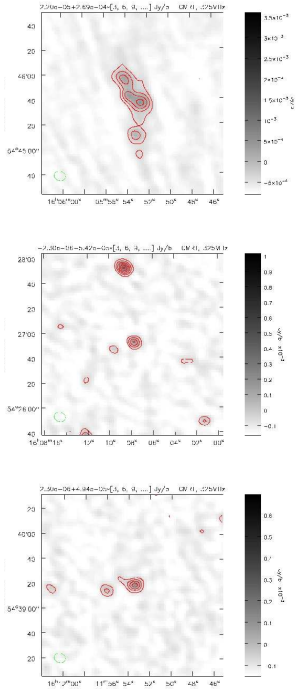

Figure 3. The figure illustrates the 3-σ contours used for estimating the corresponding flux densities of a few selected sources from our GMRT observations at 325 MHz. The upper panel shows a resolved source where the total flux density is the value within the 3-σ contour, while the middle and lower panels show two unresolved sources where $S_{\rm total}$ has been taken equal to Speak.

Figure 6 shows a comparison of the peak and integrated flux densities estimated from our GMRT observations at 325 MHz with those of the WENSS survey at 330 MHz. There are a total of 72 sources. It is clear that the peak flux densities obtained from the WENSS survey tend to be systematically larger than the GMRT ones by approximately 34 per cent on average. This would be expected in the presence of extended emission because of the larger beamwidth in the WENSS survey of 54×54 cosecδ arcsec^2 compared with ∼10 arcsec for the GMRT image. However, while comparing the integrated flux densities, the WENSS flux densities are ≈76% of the GMRT values on average. This is perhaps a reflection of the fact that the GMRT image being significantly deeper than the WENSS ones, and thereby more extended

Table 3. The source catalogue. This is a sample source catalogue; the complete catalogue appears in the on-line version.

Source name	RA	DEC	Dist	σ_{rms}	S_{peak}	$S_{total\ 3\sigma}$	S_{total}	Size	Notes
	hh:mm:ss.s	dd:mm:ss.s	deg	μJy b^{-1}	mJy b^{-1}	mJy	mJy	$''$	
(1)	(2)	(3)	(4)	(5)	(6)	(7)	(8)	(9)	(10)
GMRT160515+0544536	16:05:15.2	+54:45:38.0	0.69	231	6.56	13.22	13.22	10.7	
GMRT160522+0542924	16:05:22.4	+54:29:26.7	0.69	197	13.56	28.63	28.63	33.4	
GMRT160524+0544710	16:05:24.3	+54:47:13.7	0.67	149	1.30	1.49	1.30	U	
GMRT160538+0543919	16:05:38.5	+54:39:26.4	0.63	1692	435.71	1022.63	1022.63	77.1	
GMRT160538+0544130	16:05:38.3	+54:41:32.3	0.63	416	2.58	5.48	2.58	U	
GMRT160539+0544544	16:05:39.8	+54:45:45.5	0.63	236	3.72	3.21	3.72	U	
GMRT160542+0544640	16:05:42.6	+54:46:45.6	0.63	245	25.15	30.74	30.74	13.0	
GMRT160551+0543842	16:05:52.0	+54:38:49.1	0.60	478	4.96	11.57	11.57	12.4	
GMRT160553+0542223	16:05:53.6	+54:22:26.6	0.66	96	1.30	1.45	1.30	U	
GMRT160553+0544537	16:05:53.3	+54:45:42.0	0.60	268	3.62	26.68	26.68	57.5	
GMRT160556+0543043	16:05:56.8	+54:30:52.1	0.61	106	0.95	0.92	0.95	U	
GMRT160600+0545402	16:06:00.1	+54:54:08.8	0.62	918	327.65	1076.82	1076.82	109.7	
GMRT160602+0543937	16:06:02.2	+54:39:37.3	0.57	254	2.33	3.54	2.33	U	
GMRT160603+0545930	16:06:03.6	+54:59:37.9	0.65	140	1.40	1.42	1.40	U	
GMRT160605+0542812	16:06:05.8	+54:28:13.9	0.60	187	36.93	63.43	63.43	44.0	
GMRT160606+0542857	16:06:06.4	+54:28:62.9	0.59	160	1.24	1.25	1.24	U	
GMRT160609+0542708	16:06:09.1	+54:27:11.9	0.60	120	1.45	2.71	2.71	6.4	
GMRT160613+0543501	16:06:13.6	+54:35:07.1	0.55	131	0.92	1.58	0.92	U	
GMRT160613+0545322	16:06:13.4	+54:53:28.8	0.59	398	4.45	14.50	14.50	14.8	
GMRT160613+0550149	16:06:13.6	+55:01:50.4	0.65	200	2.70	7.90	7.90	22.4	
GMRT160621+0545636	16:06:21.3	+54:56:37.9	0.59	202	4.10	22.44	22.44	48.5	
GMRT160622+0541332	16:06:22.4	+54:13:41.4	0.69	225	64.81	83.41	83.41	45.4	
GMRT160623+0544129	16:06:23.3	+54:41:36.5	0.52	119	0.83	0.89	0.83	U	
GMRT160624+0545437	16:06:24.5	+54:54:38.4	0.57	199	1.23	0.86	1.23	U	
GMRT160626+0542113	16:06:26.9	+54:21:19.0	0.60	76	0.81	0.63	0.81	U	
GMRT160626+0544906	16:06:26.3	+54:49:07.6	0.54	178	2.27	6.09	6.09	15.0	
GMRT160632+0542453	16:06:32.3	+54:24:56.8	0.56	77	0.61	0.48	0.61	U	
GMRT160633+0544322	16:06:33.6	+54:43:23.6	0.50	98	0.66	0.48	0.66	U	
GMRT160633+0545525	16:06:33.1	+54:55:31.1	0.56	146	0.92	1.28	0.92	U	
GMRT160634+0543451	16:06:34.8	+54:34:57.9	0.50	160	10.58	70.94	70.94	108.5	
GMRT160634+0544542	16:06:34.4	+54:45:49.4	0.50	108	2.77	3.82	3.82	7.8	
GMRT160636+0543247	16:06:36.4	+54:32:53.5	0.51	137	17.34	45.50	45.50	18.0	
GMRT160638+0545918	16:06:38.5	+54:59:25.1	0.58	119	1.53	2.47	1.53	U	
GMRT160639+0542313	16:06:39.1	+54:23:13.2	0.56	77	1.14	1.40	1.14	U	
GMRT160642+0542636	16:06:42.3	+54:26:45.9	0.53	79	3.16	3.50	3.50	9.4	
GMRT160642+0542711	16:06:42.8	+54:27:17.4	0.52	81	0.79	0.68	0.79	U	
GMRT160644+0545341	16:06:44.0	+54:53:49.9	0.52	126	1.21	2.74	1.21	U	
GMRT160647+0541508	16:06:47.2	+54:15:16.6	0.62	102	5.50	10.74	10.74	34.2	
GMRT160650+0542511	16:06:50.7	+54:25:16.1	0.52	75	0.68	1.32	0.68	U	
GMRT160651+0541449	16:06:51.3	+54:14:49.1	0.62	103	1.50	4.90	4.90	24.4	
GMRT160655+0542753	16:06:55.2	+54:27:60.0	0.49	74	0.55	0.52	0.55	U	
GMRT160656+0541457	16:06:56.1	+54:14:63.0	0.61	91	1.14	1.11	1.14	U	
GMRT160657+0550156	16:06:57.5	+55:01:57.0	0.57	102	1.35	4.32	4.32	21.7	
GMRT160657+0550350	16:06:57.8	+55:03:54.9	0.59	92	1.47	1.74	1.47	U	
GMRT160658+0544328	16:06:58.0	+54:43:30.0	0.44	91	13.00	22.90	22.90	35.7	
GMRT160659+0541135	16:06:59.6	+54:11:44.0	0.64	94	0.63	0.48	0.63	U	
GMRT160700+0541343	16:07:00.1	+54:13:48.0	0.62	84	0.65	0.42	0.65	U	
GMRT160702+0542348	16:07:02.6	+54:23:54.6	0.51	61	0.58	0.53	0.58	U	
GMRT160703+0541626	16:07:03.9	+54:16:27.1	0.58	82	0.53	0.60	0.53	U	
GMRT160703+0543414	16:07:03.2	+54:34:20.6	0.44	71	1.35	1.94	1.35	U	

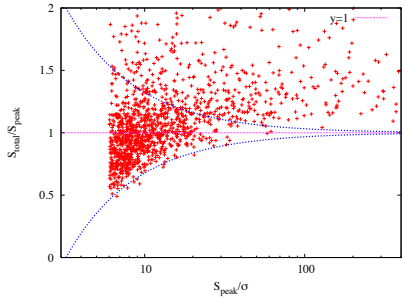

Figure 4. The ratio of the total flux density, S_{total}, to the peak value S_{peak} as a function of the source S_{peak}-to-rms noise (σ) ratio. The 6σ cut-off is adopted for the catalogue definition and the horizontal line gives $S_{total} = S_{peak}$ locus. Also shown are the lower and upper envelopes (dashed lines) of the flux density ratio distribution containing almost all the unresolved sources.

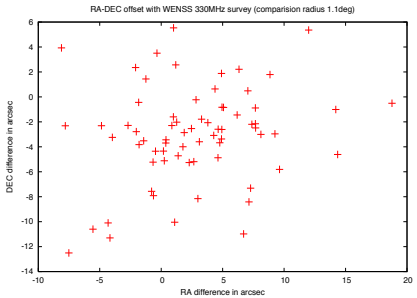

Figure 5. Position difference of the corresponding sources observed by GMRT and WENSS for the unresolved WENSS sources.

emission contributes to the flux density within the 3-σ contour level.

3.2.1 Selected extended sources

Figures 7, 8, 9 and 10 show selected images at 325 MHz of extended sources, alongwith their GMRT 610 MHz, FIRST and NVSS images. Figure 7 shows the image of the source with a high peak brightness of 1.12 Jy beam^{-1} at 325 MHz. Although artefacts from the sidelobes are still visible in the 325-MHz image, these are less than in the 610-MHz one, which has been made from a number of 'snap-shots' with the GMRT (G2008). Figures 8, 9 and 10 show that diffuse extended emission from the lobes as well as bridges of emission are better represented in the 325-MHz images compared with those at the higher frequencies.

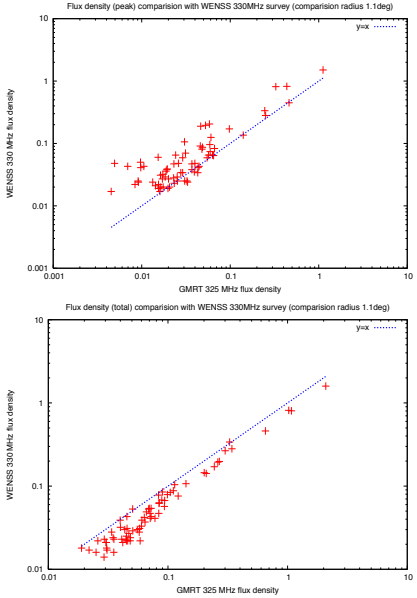

Figure 6. The peak (upper panel) and total (lower panel) flux densities from our observations plotted against the corresponding values from WENSS.

4 DISCUSSIONS

4.1 Spectral Index

4.1.1 Source matching methodology

The spectral indices for the sources which are listed in our catalogue and which also appear either in the catalogues of G2008 or FIRST have been estimated. Ideally the resolutions of the observations at the different frequencies should be identical. We have chosen the two catalogues whose resolutions are within a factor of 2 of our observations. For spectral index comparisons, we presently restrict our sample to those sources within 0.7 deg of the phase centre, the half power point of the primary beam. For a distance of 0.7 deg from the phase centre the number of sources in our sample is 844 which is approximately 65 per cent of the total number of sources we list. The corresponding numbers in the G2008 and FIRST catalogues within this distance are 553 and 134 respectively.

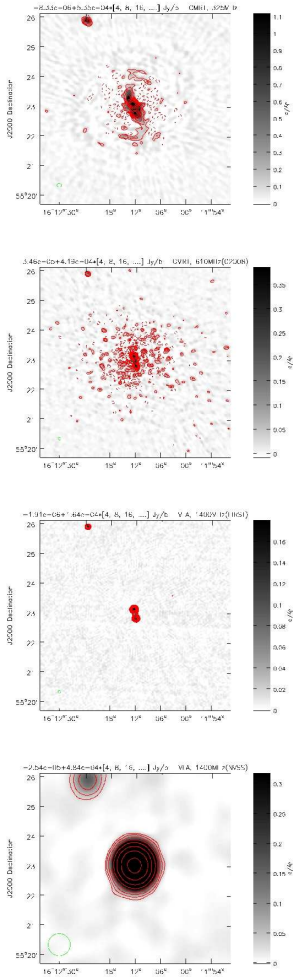

Figure 7. GMRT image at 325 MHz of a strong source in the field to illustrate the effects of dynamic range (top), and the corresponding images of the same region at 610 MHz with the GMRT from G2008, and from FIRST and NVSS at 1400 MHz in descending order.

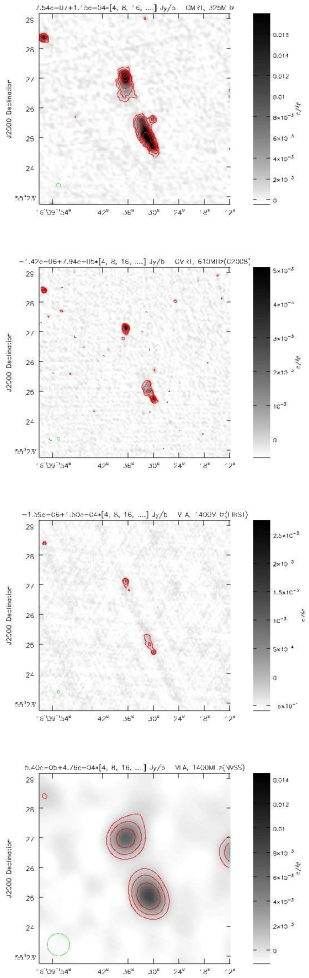

Figure 8. GMRT image at 325 MHz of a source with extended lobes of emission (top), and the corresponding images of the same region at 610 MHz with the GMRT from G2008, and from FIRST and NVSS at 1400 MHz in descending order.

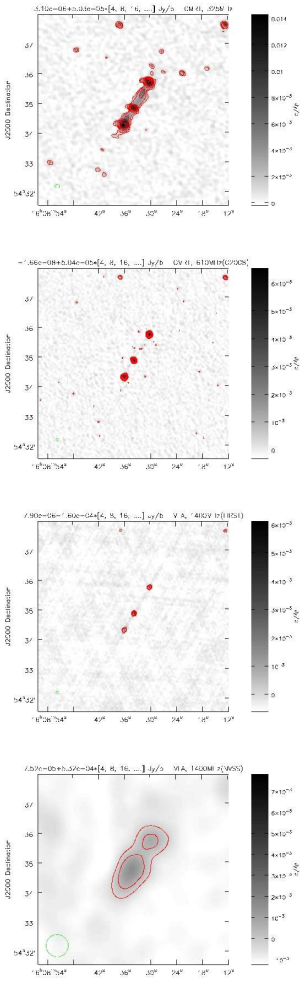

Figure 9. GMRT image at 325 MHz of a source with a bridge of emission (top), and the corresponding images of the same region at 610 MHz with the GMRT from G2008, and from FIRST and NVSS at 1400 MHz in descending order.

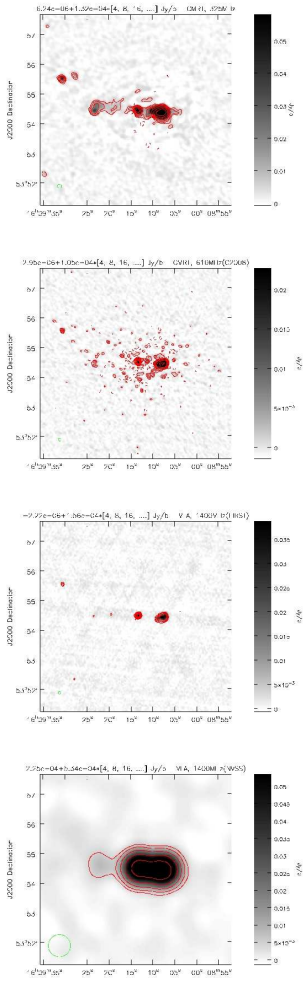

Figure 10. GMRT image at 325 MHz of a highly asymmetric double-lobed source with a possible core (top), and the corresponding images of the same region at 610 MHz with the GMRT from G2008, and from FIRST and NVSS at 1400 MHz in descending order.

To identify the sources in G2008 and FIRST which correspond to the sources in our sample, we compared the positions of the unresolved sources in the different catalogues and determined the mean shifts in both right ascension and declination relative to one another. The mean shift between 325−610 MHz is RA: 3.27±3.60 arcsec and DEC: −2.79±1.74 arcsec and between 325 MHz-FIRST is RA: 3.11±1.65 arcsec and DEC: −3.00±1.03 arcsec. After removing the mean shift, a source is considered to be a match if it lies within 7.5 arcsec of the centroid of emission for point sources and within the sum of half the largest angular size and 7.5 arcsec for an extended source. The value of 7.5 arcsec is approximately the sum of half the half power synthesized beamwidths of the observations at the two frequencies. Since the components of a double or triple source are often listed as two or more different components when no bridge emission is detected at 610 and 1400 MHz, the total flux densities at these frequencies have been estimated by summing the flux densities within the emission areas at 325 MHz for estimating the spectral indices. With these criteria 334 sources seen at 325 MHz have matches in the 610-MHz catalogue, while 102 have matches in the 1400-MHz FIRST catalogue. We have checked the number of matches by increasing 7.5 arcsec to 15 arcsec and find that the number of matches remains the same. Since the observations at 610 and 1400 MHz sometimes do not detect the bridge emission and list the components as different sources, the number of matches for these catalogues naturally increases. For instance, 360 of the 553 sources at 610 MHz (G2008) have a match at 325 MHz, while 126 of the 134 sources at 1400 MHz have a match at 325 MHz. Sources may not have a match in the catalogues due to a combination of both sensitivity and spectral indices of the sources, as seen in our recent work on a deep survey of the sky towards a couple of clusters of galaxies at 153, 244, 610 and 1260 MHz (Sirothia et al. 2008).

4.1.2 Very steep-spectrum and GPS sources

We have attempted to identify very steep spectrum radio sources with spectral index $\alpha \geqslant 1.3$ (α defined as $S \propto \nu^{-\alpha}$), as well as GPS (Giga-Hertz Peaked Spectrum) candidates which are either weak or not detected at 325 MHz and have $\alpha \leqslant -0.5$. The distributions of the spectral indices between the different frequencies are presented in Fig. 11. The distribution of spectral indices between 610 and 1400 MHz has been published by G2008 and is not reproduced here. The median values of α_{325}^{610} and α_{325}^{1400} are 1.28 and 0.83 respectively. The distribution of α_{610}^{1400} has a broad peak, with the median value of 0.51 being smaller due to a significant population of flat-spectrum objects (G2008). The median value of α_{325}^{610} appears to be on the higher side, and this could be due to more diffuse emission being detected at the lower frequency image.

There are four candidate GPS sources which satsify the above criteria. These are J1606+5427, J1613+5433, J1613+5422 and J1614+5437. J1606+5427 has a flux density of 2.96 mJy at 1400 MHz in the FIRST catalogue, while its total flux densities at 325 and 610 MHz are 0.68 and 1.3 mJy respectively. The spectral index between 325 and 1400 MHz is −1.01. J1613+5433, J1613+5422 and J1614+5437 have flux densities of 1.83, 3.49 and 4.54 mJy respectively

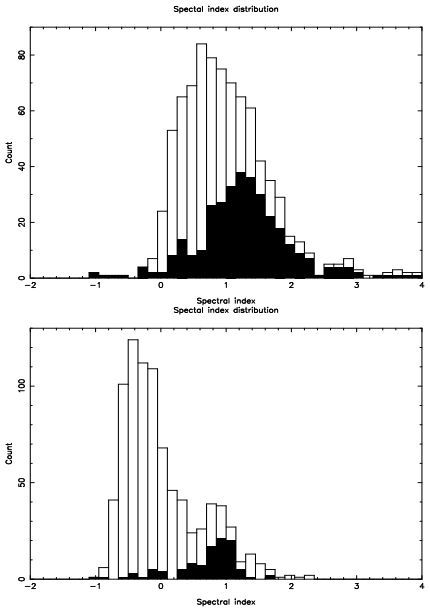

Figure 11. The spectral index distributions between 325 and 610 MHz (top panel) and between 325 and 1400 MHz (lower panel). The sources with estimated values are shown shaded while those with lower limits to the spectral indices are shown unshaded.

in the FIRST catalog but have not been detected at either 325 MHz or at 610 MHz by G2008. These sources are also not visible in NVSS and require further confirmation.

The candidate very steep spectrum sources are listed in Table 4. Images of two of the sources from our observations and the corresponding regions from G2008 and FIRST are shown in Fig. 12. Although the sources are visible in G2008, not all the extended emission seen at 325 MHz is visible in the 610-MHz image. Also, there is no significant emission seen in the FIRST images. Since these candidates have been identified from observations which differ in resolution by a factor of two, it is important to confirm their steep spectral indices from observations with the same resolution at the different frequencies.

4.1.3 Spectral index−flux density relationships

In Fig. 13 we present the plots of α_{325}^{610}, and α_{325}^{1400} against the flux density at 325 MHz. Any dependence of spectral index on flux density can be used to study the different populations of sources which may be present at different flux density levels. It is well known that the normalized

Table 4. Candidate very steep spectrum sources

Source name	RA	DEC	Dist	σ_{rms}	S_{peak}	$S_{total\ 3\sigma}$	Size	Notes
	hh:mm:ss.s	dd:mm:ss.s	deg	μJy b^{-1}	mJy b^{-1}	mJy	$''$	
(1)	(2)	(3)	(4)	(5)	(6)	(7)	(8)	(9)
GMRT160551+543842	16:05:51.9	54:38:42.7	0.60	478	4.96	11.57	12.4	*a*
GMRT160613+545322	16:06:13.3	54:53:22.6	0.59	398	4.45	14.50	14.8	*a*
GMRT160613+550149	16:06:13.6	55:01:49.1	0.65	200	2.70	7.90	22.4	
GMRT160621+545636	16:06:21.2	54:56:36.1	0.59	202	4.10	22.44	48.5	
GMRT160626+544906	16:06:26.3	54:49:06.1	0.54	178	2.27	6.09	15.0	*b*
GMRT160636+543247	16:06:36.3	54:32:47.6	0.51	137	17.34	45.50	18.0	
GMRT160725+544720	16:07:25.7	54:47:20.6	0.39	91	1.83	5.90	41.1	
GMRT160732+545106	16:07:32.0	54:51:06.3	0.40	76	2.87	6.85	29.9	
GMRT160733+545639	16:07:33.4	54:56:39.3	0.45	94	1.24	13.70	58.9	
GMRT160746+541159	16:07:46.1	54:11:59.9	0.57	71	4.93	7.38	11.5	
GMRT160757+551013	16:07:57.6	55:10:13.0	0.58	82	2.85	8.33	15.2	
GMRT160800+542144	16:08:00.9	54:21:44.8	0.42	63	3.54	9.02	34.9	*c*
GMRT160801+542025	16:08:01.8	54:20:25.2	0.43	76	8.51	25.69	23.4	
GMRT160825+551755	16:08:25.5	55:17:55.4	0.67	83	2.74	7.54	26.8	
GMRT160850+545348	16:08:50.4	54:53:48.1	0.28	58	2.04	6.21	15.9	
GMRT160931+541915	16:09:31.5	54:19:15.4	0.35	58	3.07	5.93	9.3	
GMRT160932+542028	16:09:32.7	54:20:28.5	0.33	63	1.27	6.65	33.3	*d*
GMRT160948+551646	16:09:48.9	55:16:46.9	0.61	109	2.67	17.40	57.4	
GMRT160949+540826	16:09:49.6	54:08:26.2	0.53	70	4.87	8.23	21.3	
GMRT161008+540753	16:10:08.7	54:07:53.4	0.54	66	4.14	16.77	38.7	
GMRT161013+544924	16:10:13.4	54:49:24.9	0.16	55	1.65	10.09	93.5	
GMRT161016+540143	16:10:16.8	54:01:43.1	0.64	70	4.11	5.50	11.7	
GMRT161030+540249	16:10:30.7	54:02:49.4	0.62	78	1.80	7.17	39.4	
GMRT161040+540626	16:10:40.6	54:06:26.6	0.57	65	4.74	12.69	28.7	
GMRT161040+550824	16:10:40.7	55:08:24.8	0.48	76	2.18	6.10	35.1	
GMRT161230+545105	16:12:30.5	54:51:05.3	0.41	62	3.98	7.99	10.2	
GMRT161319+541033	16:13:19.7	54:10:33.1	0.69	91	2.85	6.99	29.1	
GMRT161349+550140	16:13:49.5	55:01:40.2	0.66	86	2.04	6.41	15.1	
GMRT161358+550219	16:13:58.2	55:02:19.9	0.68	94	2.53	8.06	15.0	*e*
GMRT161424+544314	16:14:24.4	54:43:14.4	0.64	101	3.23	6.06	9.1	

Notes: *a* strong source nearby; *b* diffuse extended emission visible in the NVSS image; *c* double-lobed source; *d* northern component of an asymmetric double; *e* north-western component of a triple lobed source.

source counts tend to flatten at low flux densities corresponding to $\leqslant$0.5 mJy at 1400 MHz and 1 mJy at 610 MHz (Padovani et al. 2007; G2008 and references therein). At high flux densities the radio source counts are due to double-lobed radio galaxies and quasars with spectral indices ranging from $\sim$0.6 to 1.5 (cf. Laing & Peacock 1980). The spectral indices of these sources are known to be correlated with radio luminosity and/or redshift, leading to several searches for high-redshift galaxies amongst the very steep spectrum radio sources (e.g. McCarthy et al. 1990; De Breuck et al. 2000). The flattening of the source counts at low flux densities is generally ascribed to a population of starburst galaxies, low luminosity AGN and radio quiet QSOs (e.g. Seymour et al. 2004; Simpson et al. 2006; Padovani et al. 2007; Smolčić et al. 2008). While starburst galaxies are expected to have a radio spectral index in the range of $\sim$0.5 to 0.8 at low radio frequencies which are dominated by non-thermal emission, the nuclear components of low luminosity AGN could have spectral indices $\leqslant$0.5. In a study of the VLA Deep Field, Bondi et al. (2007) find the median spectral index to be 0.46$\pm$0.03 for sources with a flux density 0.15$\leqslant$S$<$0.50 mJy at 1400 MHz while those above this flux density have a median spectral index of 0.67$\pm$0.05. They attribute the flatter spectral index at the lower flux density level to a population of low luminosity AGN. Although we need to determine the spectral indices from similar-resolution data, Fig. 13 shows α_{325}^{610}, and α_{325}^{1400} against the flux density at 325 MHz. For α_{325}^{610}, 510 sources have limits while for α_{325}^{1400} 742 sources have limits to their spectral indices. Given the large fraction of sources with limits to their spectral indices, it is difficult to determine reliably any dependence of spectral index on flux density. It is required to observe this field with deeper sensitivity at higher frequencies to determine their spectral indices and investigate any such dependence.

4.2 Source counts

We constructed the source counts at 325 MHz for our sample of sources by binning them in different ranges of flux density starting from 315 μJy, so that even the sources in the lowest-flux density bin have a typical peak flux density to rms ratio of about 8. The corrections due to source incompleteness is negligible as can also be seen in the results from Fig. 5 of Tasse et al. (2006). The source counts were corrected for the fraction of the area (Fig. 14) over which the source could be detected because of the increase in noise near the bright sources. The flux density bins, the average flux density for each bin, the number of sources in each bin, the noise corrected number of sources, the differential source counts and the normalized source counts are listed in Table 5. The differential source counts, which have been estimated by dividing the noise corrected number of sources by the area of the image in steradians and the width of the flux density range, is shown in Fig. 15. We have also plotted the differential source counts for the WENSS sources for the same area. The WENSS sources plotted here are stronger than about 18 mJy, while the sources from our survey are much weaker, extending to about 270 μJy, although in present study for source counts we consider only those above 315 μJy. There is evidence of the source counts flattening at about a mJy, consistent with higher frequency studies, although more data at low flux density levels are required at this frequency. Since the earlier surveys in the literature at 325 MHz are limited to higher flux density levels, the flattening in the source counts at this frequency has not been reported earlier (Wieringa 1991; Tasse et al. 2006). The functional form fitted by Wieringa (1991) to the differential source counts ranging from about 4 mJy to 1 Jy from his deep 325-MHz Westerbork survey, shown in Fig. 15, also illustrates clearly the flattening of the source counts at low flux densities. This functional form is also consistent with the measurements of Tasse et al. (2006) (see their Fig. 7) whose sources range from about 3 to 500 mJy. A more detailed modeling of the source counts will be presented in a subsequent paper, after combining with data from other fields observed with the GMRT at the same frequency.

We have integrated the number counts from our survey, yielding a surface brightness of 4.04×10^{-5} nW m^{-2} sr^{-1}, which gives a lower limit to the contribution of extragalactic sources to the cosmic radio background at 325 MHz (Dwek & Barker 2002).

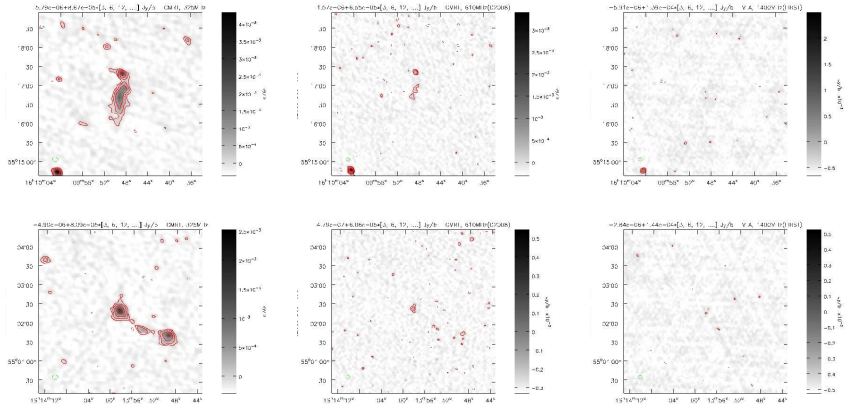

Figure 12. Images of two of the candidate very steep spectrum sources, GMRT160948+551649 (upper row) and GMRT161357+550213 (lower row) at 325 (left), 610 (middle, G2008) and 1400 MHz (right, FIRST).

Table 5. Differential source counts at 325 MHz

Flux bin	$\langle S \rangle$	N	N_c	$\frac{dN}{dS}\langle S \rangle^{2.5}$
mJy	mJy			sr^{-1}Jy$^{1.5}$
0.315-0.413	0.367	120	800.4	18.25$\pm$0.65
0.413-0.566	0.485	174	601.4	17.55$\pm$0.72
0.566-0.813	0.684	209	438.8	18.80$\pm$0.90
0.813-1.221	0.998	194	267.0	17.78$\pm$1.09
1.221-1.917	1.495	165	170.1	18.22$\pm$1.40
1.917-3.151	2.453	103	103.8	21.65$\pm$2.13
3.151-5.416	4.139	71	71.2	29.93$\pm$3.55
5.416-9.742	6.851	67	67.1	52.03$\pm$6.35
9.742-18.33	13.64	53	53.0	115.9$\pm$15.92
18.33-36.08	24.83	41	41.0	193.8$\pm$30.27
36.08-74.32	54.31	33	33.0	512.3$\pm$89.19
74.32-160.1	98.06	15	15.0	454.5$\pm$117.4
160.1-360.9	269.3	8	8.0	1294$\pm$457.6
360.9-851.2	652.4	1	1.0	605.5$\pm$605.5
851.2- 2100	1395	3	3.0	4764$\pm$2751

5 CONCLUDING REMARKS

We have presented deep observations of the ELAIS-N1 field at 325 MHz using the GMRT. This is part of an ongoing program to examine the source counts and the nature of radio sources identified from sensitive observations at low radio frequencies with the objective of identifying AGN and starburst galaxies and examining their evolution with cosmic epoch. For this data set we have achieved a median rms noise of $\approx$ 40 μJy beam^{-1} towards the phase centre by combining data from two different days, which is about the lowest that has been achieved at this frequency. We detect 1286 sources with a total flux density above $\approx$ 270μJy

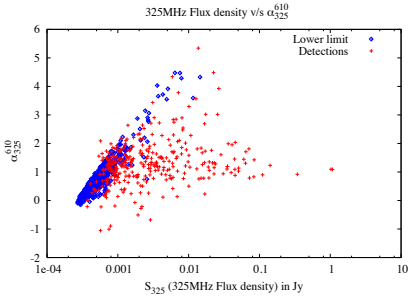

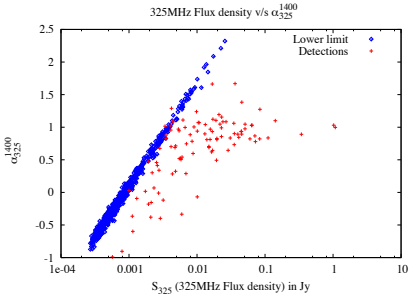

Figure 13. The spectral indices as a function of flux density. The sources with lower limits are shown by open diamonds, while those with measured values are shown by the + sign.

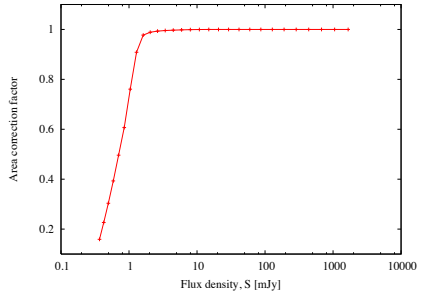

Figure 14. Visibility area as a function of radio flux density

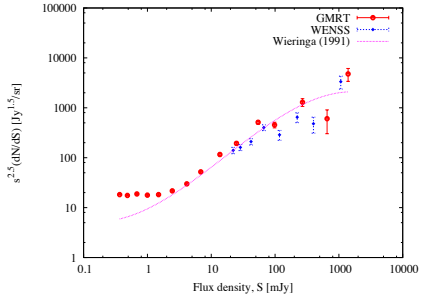

Figure 15. The normalized differential source counts at 325 MHz for sources from our present observations (circles) and WENSS at 330 MHz (diamonds) for all sources located within 1.1° of the phase centre of our observations. This is ∼18.3 per cent of the beamwidth of the GMRT primary beam at 325 MHz. The continuous curve represents the functional form of the fit to the source counts by Wierenga (1991) for sources in the flux density range of ∼4 mJy to 1 Jy.

within a radius of 1.1° of the phase centre. By comparing our results with those of G2008 and the FIRST survey, whose resolutions are within a factor of two we have identified candidate very steep spectrum sources with a $\alpha \geqslant 1.3$ and candidate GPS objects for further investigations. Considering only those sources with a flux density >315 μJy, so that any effects of incompleteness are negligible, our data show evidence of a flattening of the source counts at low flux densities at 325 MHz, which has been reported earlier at higher frequencies and attributed to both starburst galaxies and low luminosity AGN. This needs to be investigated further by combining it with sensitive observations from other fields as well at this frequency.

ACKNOWLEDGMENTS

We thank an anonymous referee and the staff of the GMRT who have made these observations possible. GMRT is run by the National Centre for Radio Astrophysics of the Tata Institute of Fundamental Research. This research has made use of the NASA/IPAC Extragalactic Database (NED) which is operated by the Jet Propulsion Laboratory, California Institute of Technology, under contract with the National Aeronautics and Space Administration.

REFERENCES

Adelman-McCarthy J. K., et al., 2008, ApJS, 175, 297
Aharonian F., Akhperjanian A. G., Bazer-Bachi A. R., HESS Collaboration 2006, Nature, 440, 1018
Becker R. H., White R. L., Helfand D. J., 1995, ApJ, 450, 559
Bondi M., et al., 2007, A&A, 463, 519

Chapman S. C., Blain A. W., Smail I., Ivison R. J., 2005, ApJ, 622, 772
Ciliegi P., et al., 1999, MNRAS, 302, 222
Condon J. J., 1989, ApJ, 338, 13
Condon J. J., 1992, ARA&A, 30, 575
Condon J. J., Cotton W. D., Greisen E. W., Yin Q. F., Perley R. A., Taylor G. B., Broderick J. J., 1998, AJ, 115, 1693
De Breuck C., van Breugel W., Röttgering H. J. A., Miley G., 2000, A&AS, 143, 303
de Bruyn G., et al., 2000, VizieR Online Data Catalog, 8062, 0
Dennefeld M., Lagache G., Mei S., Ciliegi P., Dole H., Mann R. G., Taylor E. L., Vaccari M., 2005, A&A, 440, 5
Dole H., et al., 2001, A&A, 372, 364
Dole H., et al., 2006, A&A, 451, 417
Dwek E., Barker M. K., 2002, ApJ, 575, 7
Garn T., Green D. A., Riley J. M., Alexander P., 2008, MNRAS, 383, 75 (G2008)
Garrett M. A., 2002, A&A, 384, L19
Gispert R., Lagache G., Puget J. L., 2000, A&A, 360, 1
Hauser M. G., Dwek E., 2001, ARA&A, 39, 249
Hauser M. G., et al., 1998, ApJ, 508, 25
Helou G., Soifer B. T., Rowan-Robinson M., 1985, ApJ, 298, L7
Hopkins A. M., Beacom J. F., 2006, ApJ, 651, 142
Hughes A., Wong T., Ekers R., Staveley-Smith L., Filipovic M., Maddison S., Fukui Y., Mizuno N., 2006, MNRAS, 370, 363
Kashlinsky A., 2005, Phys. Rep., 409, 361
Lagache G., Abergel A., Boulanger F., Désert F. X., Puget J. L., 1999, A&A, 344, 322
Lagache G., Puget J. L., Dole H., 2005, ARA&A, 43, 727
Laing R. A., Peacock J. A., 1980, MNRAS, 190, 903
Longair M. S., 1966, MNRAS, 133, 421
Lonsdale C., et al., 2004, ApJS, 154, 54
Luo S. G., Wu X. B., 2005, Chinese Journal of Astronomy and Astrophysics, 5, 448
Madau P., Ferguson H. C., Dickinson M. E., Giavalisco M., Steidel C. C., Fruchter A., 1996, MNRAS, 283, 1388
Madau P., Pozzetti L., Dickinson M., 1998, ApJ, 498, 106
McCarthy P. J., Kapahi V. K., van Breugel W., Subrahmanya C. R., 1990, AJ, 100, 1014
McMahon R. G., Walton N. A., Irwin M. J., Lewis J. R., Bunclark P. S., Jones D. H., 2001, New Astronomy Review, 45, 97
Moss D., Seymour N., McHardy I. M., Dwelly T., Page M. J., Loaring N. S., 2007, MNRAS, 378, 995
Murphy E. J., et al., 2006, ApJ, 638, 157
Ochsenbein F., Bauer P., Marcout J., 2000, A&AS, 143, 23
Padovani P., Mainieri V., Tozzi P., Kellermann K. I., Fomalont E. B., Miller N., Rosati P., Shaver P., 2007, in Afonso J., Ferguson H. C., Mobasher B., Norris R., eds, Deepest Astronomical Surveys. ASP Conf. series, 380, 205
Prandoni I., Parma P., Wieringa M. H., de Ruiter H. R., Gregorini L., Mignano A., Vettolani G., Ekers R. D., 2006, A&A, 457, 517
Puget J. L., Abergel A., Bernard J. P., Boulanger F., Burton W. B., Desert F. X., Hartmann D., 1996, A&A, 308, L5
Rengelink R. B., Tang Y., de Bruyn A. G., Miley G. K., Bremer M. N., Roettgering H. J. A., Bremer M. A. R., 1997, A&AS, 124, 259
Rowan-Robinson M., Benn C. R., Lawrence A., McMahon R. G., Broadhurst T. J., 1993, MNRAS, 263, 123
Rowan-Robinson M., et al., 2008, MNRAS, 386, 697
Rowan-Robinson M., et al., 2004, VizieR Online Data Catalog, 735, 11290
Seymour N., McHardy I. M., Gunn K. F., 2004, MNRAS, 352, 131
Simpson C., Martínez-Sansigre A., Rawlings S., Ivison R., Akiyama M., Sekiguchi K., Takata T., Ueda Y., Watson M., 2006, MNRAS, 372, 741
Sirothia S. K., 2008, MNRAS, submitted
Sirothia S. K., Saikia D. J., Ishwara-Chandra C. H., Kantharia N. G., 2008, MNRAS, in press, arXiv:0809.4565
Smolčić V., et. al. 2008, ApJS, 177, 14
Tasse C., et al., 2006, A&A, 456, 791
Taylor A. R., et al., 2007, ApJ, 666, 201
Wieringa M. H., 1991, PhD thesis, Rijksuniversiteit Leiden, (1991)
Wieringa M. H., de Bruyn A. G., Katgert P., 1992, A&A, 256, 331
Windhorst R., Mathis D., Neuschaefer L., 1990, in Kron R. G., ed., Evolution of the Universe of Galaxies. ASP Conf. series, 10, 389
Wright E. L., 2004, New Astronomy Review, 48, 465

Table 3. The source catalogue (available in online version only).

Source name	RA	DEC	Dist	σ_{rms}	S_{peak}	$S_{total\ 3\sigma}$	S_{total}	Size	Notes
	hh:mm:ss.s	dd:mm:ss.s	deg	μJy b^{-1}	mJy b^{-1}	mJy	mJy	$''$	
(1)	(2)	(3)	(4)	(5)	(6)	(7)	(8)	(9)	(10)
GMRT160232+0545404	16:02:32.8	+54:54:06.9	1.10	267	22.92	48.57	48.57	16.6	
GMRT160234+0544706	16:02:34.7	+54:47:10.0	1.08	212	1.56	1.59	1.56	U	
GMRT160248+0544735	16:02:48.5	+54:47:39.3	1.05	223	8.46	12.47	12.47	9.9	
GMRT160253+0545951	16:02:53.0	+54:59:51.6	1.08	205	2.23	6.17	6.17	19.1	
GMRT160255+0550533	16:02:55.1	+55:05:34.7	1.10	244	2.20	3.62	3.62	10.8	
GMRT160309+0542114	16:03:09.6	+54:21:20.9	1.04	192	1.22	0.87	1.22	U	
GMRT160309+0550028	16:03:09.3	+55:00:31.9	1.04	196	1.59	1.49	1.59	U	
GMRT160316+0543157	16:03:16.2	+54:31:60.9	0.98	209	20.06	44.96	44.96	17.5	
GMRT160317+0541310	16:03:17.9	+54:13:11.5	1.07	227	3.46	4.18	3.46	U	
GMRT160319+0542541	16:03:19.6	+54:25:41.1	1.00	191	1.63	2.32	1.63	U	
GMRT160321+0550642	16:03:21.1	+55:06:49.5	1.05	206	6.24	9.36	9.36	9.3	
GMRT160323+0543734	16:03:23.3	+54:37:34.8	0.96	162	3.10	3.70	3.10	U	
GMRT160333+0540535	16:03:33.9	+54:05:44.5	1.10	420	10.05	15.50	15.50	8.3	
GMRT160333+0542906	16:03:33.7	+54:29:08.7	0.95	210	9.76	60.57	60.57	35.1	
GMRT160335+0540510	16:03:35.5	+54:05:19.9	1.10	424	66.35	98.97	98.97	27.8	
GMRT160336+0544115	16:03:37.0	+54:41:21.0	0.92	153	1.54	1.73	1.54	U	
GMRT160340+0545124	16:03:40.2	+54:51:24.4	0.93	160	2.87	3.08	2.87	U	
GMRT160344+0540315	16:03:45.0	+54:03:22.1	1.10	239	1.45	0.92	1.45	U	
GMRT160348+0542621	16:03:48.6	+54:26:28.8	0.93	198	4.99	6.22	6.22	9.4	
GMRT160357+0542839	16:03:57.6	+54:28:48.7	0.90	162	1.61	2.03	1.61	U	
GMRT160359+0550352	16:03:59.4	+55:03:54.5	0.95	190	1.45	1.86	1.45	U	
GMRT160401+0541749	16:04:01.2	+54:17:54.4	0.94	179	1.60	1.38	1.60	U	
GMRT160401+0551459	16:04:01.4	+55:14:60.0	1.04	198	4.65	6.15	6.15	5.3	
GMRT160406+0542043	16:04:06.2	+54:20:50.9	0.91	151	3.23	4.07	4.07	5.6	
GMRT160407+0535953	16:04:07.2	+53:59:56.4	1.09	240	2.12	2.26	2.12	U	
GMRT160408+0542529	16:04:08.3	+54:25:29.6	0.88	156	1.28	1.19	1.28	U	
GMRT160408+0545810	16:04:08.6	+54:58:16.6	0.90	158	3.94	4.85	3.94	U	
GMRT160409+0540500	16:04:09.4	+54:05:00.7	1.03	194	1.37	0.96	1.37	U	
GMRT160409+0551454	16:04:10.0	+55:14:56.1	1.02	193	8.82	16.27	16.27	13.2	
GMRT160409+0551810	16:04:09.1	+55:18:11.7	1.05	203	2.04	2.60	2.04	U	
GMRT160411+0551254	16:04:11.8	+55:12:60.4	1.00	208	9.91	14.57	14.57	23.7	
GMRT160413+0543931	16:04:13.9	+54:39:33.5	0.83	160	2.60	3.27	2.60	U	
GMRT160413+0551050	16:04:13.6	+55:10:52.6	0.98	192	3.78	5.20	3.78	U	
GMRT160418+0544956	16:04:18.5	+54:49:58.2	0.84	152	9.17	25.96	25.96	28.0	
GMRT160419+0541520	16:04:19.1	+54:15:28.8	0.92	157	1.68	1.78	1.68	U	
GMRT160419+0551114	16:04:19.4	+55:11:22.8	0.97	191	4.79	6.93	4.79	U	
GMRT160420+0542317	16:04:20.2	+54:23:18.7	0.87	142	6.55	7.82	7.82	4.6	
GMRT160421+0550543	16:04:21.9	+55:05:45.6	0.92	362	140.12	208.86	208.86	99.7	
GMRT160427+0552245	16:04:27.4	+55:22:48.8	1.07	216	1.65	1.53	1.65	U	
GMRT160428+0541456	16:04:28.5	+54:14:58.1	0.91	134	2.36	2.38	2.36	U	
GMRT160429+0540916	16:04:29.2	+54:09:26.0	0.95	153	1.06	1.12	1.06	U	
GMRT160429+0544334	16:04:29.9	+54:43:42.4	0.80	160	2.47	4.19	4.19	21.3	
GMRT160430+0540057	16:04:30.0	+54:00:62.9	1.03	284	7.11	8.59	8.59	4.7	
GMRT160433+0535358	16:04:33.7	+53:53:64.7	1.10	233	11.46	16.09	16.09	6.2	
GMRT160434+0544428	16:04:34.1	+54:44:28.3	0.79	159	1.76	1.89	1.76	U	
GMRT160435+0535934	16:04:35.5	+53:59:41.1	1.04	495	97.77	200.93	200.93	48.8	
GMRT160435+0543413	16:04:35.0	+54:34:16.4	0.79	198	9.76	23.67	23.67	24.5	
GMRT160437+0552056	16:04:37.8	+55:20:64.5	1.03	219	1.57	1.33	1.57	U	
GMRT160439+0542123	16:04:39.4	+54:21:25.4	0.84	148	1.14	0.84	1.14	U	
GMRT160440+0543138	16:04:40.2	+54:31:40.1	0.78	303	47.89	89.85	89.85	23.1	

2008

A&A 479, 83–96 (2008)
DOI: 10.1051/0004-6361:20077896

Astronomy & Astrophysics

Estimating the total infrared luminosity of galaxies up to $z \sim 2$ from mid- and far-infrared observations

N. Bavouzet[1], H. Dole[1], E. Le Floc'h[2], K. I. Caputi[3], G. Lagache[1], and C. S. Kochanek[4]

[1] Institut d'Astrophysique Spatiale (IAS), Bât. 121, Université Paris-Sud 11 and CNRS (UMR 8617), 91405 Orsay Cedex, France
e-mail: nicolas.bavouzet@ias.u-psud.fr
[2] Institute for Astronomy, University of Hawaii, 2680 Woodlawn Drive, Honolulu, HI 96822, USA
[3] Institute of Astronomy, Swiss Federal Institute of Technology (ETH Zürich), 8093 Zürich, Switzerland
[4] Department of Astronomy, Ohio State University, 140 West 18th Avenue, Columbus, OH 43210, USA

Received 16 May 2007 / Accepted 9 November 2007

ABSTRACT

Aims. We present the observed correlations between rest-frame 8, 24, 70 and 160 μm monochromatic luminosities and measured total infrared luminosities $L_{\rm IR}$ of galaxies detected by Spitzer.
Methods. Our sample consists of 372 star-forming galaxies with individual detections and flux measurements at 8, 24, 70 and 160 μm. We have spectroscopic redshifts for 93% of these sources, and accurate photometric redshifts for the remainder. We also used a stacking analysis to measure the IR fluxes of fainter sources at higher redshifts.
Results. We show that the monochromatic mid and far-infrared luminosities are strongly correlated with the total infrared luminosity and our stacking analysis confirms that these correlations also hold at higher redshifts. We provide relations between monochromatic luminosities and total infrared luminosities $L_{\rm IR}$ that should be reliable up to $z \sim 2$ ($z \sim 1.1$) for ULIRGs (LIRGs). In particular, we can predict $L_{\rm IR}$ with accuracies of 37% and 54% from the 8 and 24 μm fluxes, while the best tracer is the 70 μm flux. Combining bands leads to slightly more accurate estimates. For example, combining the 8 and 24 μm luminosities predicts $L_{\rm IR}$ with an accuracy of 34%. Our results are generally compatible with previous studies, and the small changes are probably due to differences in the sample selection criteria. We can rule out strong evolution in dust properties with redshift up to $z \sim 1$. Finally, we show that infrared and sub-millimeter observations are complementary means of building complete samples of star-forming galaxies, with the former being more sensitive for $z \lesssim 2$ and the latter at higher $z \gtrsim 2$.

Key words. infrared: galaxies – galaxies: starburst – galaxies: fundamental parameters – galaxies: evolution

1. Introduction

Bright infrared galaxies play an important role in understanding the evolution of galaxies because a large fraction of the energy from star formation is reprocessed by dust and only visible in the infrared. This emission is dominated by the luminous infrared galaxies (LIRGs, defined by $10^{11}\ L_\odot < L_{\rm IR} < 10^{12}\ L_\odot$) at $z > 0.7$ (e.g. Le Floc'h et al. 2005) and by ultra-luminous infrared galaxies (ULIRGs, defined by $L_{\rm IR} > 10^{12}\ L_\odot$) at $z > 2$ (e.g. Caputi et al. 2007). The LIRGs and ULIRGs are massive star-forming galaxies (Swinbank et al. 2004; Caputi et al. 2006) but some of the emission may also come from embedded AGN (e.g. Alonso-Herrero et al. 2006). For systems dominated by star formation, the total infrared luminosity $L_{\rm IR}$ emitted between a few μm and 1 mm is a good tracer of the star formation rate (Kennicutt 1998). Thus estimating the infrared luminosity of galaxies is important for quantifying star formation activity.

Measuring the spectral energy distribution (SED) of infrared galaxies also probes physical properties such as their dust temperature, or grain size and composition. Models of nearby objects using IRAS, ISO and Spitzer have shown that the typical infrared galaxy SED peaks between 60 and 150 μm, depending on the dust temperature (e.g. the Spitzer Nearby Galaxy Survey, Kennicutt et al. 2003).

The far-infrared bands on Spitzer (the MIPS 70 and 160 μm bands) and Akari (FIS[1]) are well-suited to study this peak. Unfortunately, far-infrared detectors generally have less sensitivity and poorer resolution (given the fixed telescope aperture) than mid-infrared detectors, frequently leading to surveys that are either limited by confusion (Dole et al. 2004a,b; Frayer et al. 2006) or noisier than their mid-IR counterparts.

Ground based sub-millimeter facilities, such as e.g. the SHARC-2 instrument at the CSO[2], SCUBA[3] mounted on the JCMT[4] or APEX−2a and LABOCA[5] recently installed on the Atacama Pathfinder EXperiment, have made a number of important first steps (e.g. Chapman et al. 2005), exploiting the fact that the peak of the infrared emission is shifted into the sub-millimeter bands at high redshifts. However, sub-millimeter surveys have had difficulties in building large galaxy samples because of their limited sensitivity, and they are biased towards detecting objects with colder dust temperatures than the typical infrared selected ULIRG (e.g. Chapman et al. 2004; Pope et al. 2006).

[1] Far-Infrared Surveyor.
[2] Caltech Submillimeter Observatory.
[3] Submillimeter Common-User Bolometer Array.
[4] James Clerk Maxwell Telescope.
[5] Large Apex BOlometer CAmera.

Article published by EDP Sciences and available at http://www.aanda.org or http://dx.doi.org/10.1051/0004-6361:20077896

Chary & Elbaz (2001) and Takeuchi et al. (2005) have shown that mid-infrared monochromatic luminosities, by which we mean measurements through filters of modest widths, are sufficiently well-correlated with the total infrared luminosity to provide an estimate of $L_{\rm IR}$. In both cases, the relations were calibrated on local samples and then extrapolated to higher redshifts. This extrapolation is potentially dangerous, because the dominant source populations are considerably different at higher redshifts (ULIRGs) and locally (non-LIRGs). Marcillac et al. (2006) studied these correlations at higher redshifts ($0.4 < z < 1.2$) with a small sample of 49 15 μm-selected galaxies, but their estimates of $L_{\rm IR}$ were strongly model-dependent. Symeonidis et al. (2006) studied a similar sample of galaxies selected at 70 μm, but did not examine how the far-infrared emission was correlated with the mid-infrared emission.

In this paper we determine the correlations between $(\nu L_\nu)_{8\ \mu{\rm m,rest}}$, $(\nu L_\nu)_{24\ \mu{\rm m,rest}}$, $(\nu L_\nu)_{70\ \mu{\rm m,rest}}$, $(\nu L_\nu)_{160\ \mu{\rm m,rest}}$ and $L_{\rm IR}$. We will calibrate the relations using a large sample of galaxies at moderate redshifts ($z < 0.5$) and then test their validity at higher redshifts ($z < 2$) using a stacking analysis. We define our samples in Sect. 2 and we explain our approach to estimating $L_{\rm IR}$ in Sect. 3. The correlations and their implications are discussed in Sects. 4 and 5. We adopted an $H_0 = 71\ {\rm km\,s^{-1}\ Mpc^{-1}}$, $\Omega_{\rm M} = 0.27$, $\Omega_\Lambda = 0.73$ cosmology throughout this paper.

2. Data sample and processing

Our main imaging datasets come from the IRAC (Fazio et al. 2004) and MIPS (Rieke et al. 2004) instruments on board the *Spitzer Space Telescope* (Werner et al. 2004). We worked on three different fields: the Boötes field of the NOAO Deep Wide Field Survey (NDWFS; Jannuzi & Dey 1999), the extragalactic First Look Survey (FLS), and the *Chandra* Deep Field–South (CDFS). Characteristics of the IRAC and MIPS observations in these fields are given by Eisenhardt et al. (2004); Lacy et al. (2004); Fazio et al. (2004) and Papovich et al. (2004, 2006); Dole et al. (2004a); Frayer et al. (2006), respectively. We also used, for the stacking analysis, the ultra-deep data from the GOODS survey in the GOODS/CDFS and GOODS/HDFN fields and the galaxy sample of Caputi et al. (2007).

2.1. Optical spectra and photometry

2.1.1. Boötes and FLS

In the 8 deg^2 Boötes field, we use redshifts from the first season of the AGN and Galaxy Evolution Survey (AGES, Kochanek et al. in preparation). Samples of galaxies were restricted to $R \lesssim 20$ with well-defined sub-samples over a broad range of wavelengths. In particular, all galaxies with $S_{24\ \mu{\rm m}} \geq 1$ mJy and $R \leq 20$ were targeted. The R-band magnitude limit restricts this sample to $z < 0.5$. Papovich et al. (2006) conducted quite similar observations in the FLS field (4 deg^2), but the infrared selection is deeper ($S_{24} > 0.3$ mJy). The redshift completenesses are ~90% for sources with $i \leq 21$ and $S_{24} \geq 1$ mJy, and 35% for $i \leq 20.5$ and 0.3 mJy $\leq S_{24} < 1$ mJy sources. Both of these redshift surveys used the 300 fiber Hectospec instrument on the MMT (Fabricant et al. 2005).

After excluding stars and quasars, we have 846 (504) galaxies from the AGES (FLS) samples with spectroscopic redshifts and 24 μm detections. All of them are in the common field of view at every infrared wavelength (from 3.6 through 160 μm).

2.1.2. CDFS

The CDFS has been observed by many instruments covering a wide wavelength range (from X-rays to radio). Wolf et al. (2004) published a photometric redshifts catalog of 63 501 sources brighter than $R \sim 25$ over an area of 0.5 deg^2 of the CDFS (COMBO-17). However, as pointed by Le Floc'h et al. (2005), only the subsample of sources with $R < 24$ and $z < 1.2$ can be securely used. From this catalog, we selected objects unambiguously identified as galaxies with $R \leq 22$. The redshifts of these sources go up to $z = 0.8$ and are accurate to ≤2%. Following Wolf et al. (2004) suggestion, we excluded from our sample 7 surprisingly bright objects with $R \leq 19$ and $0.4 \leq z \leq 1.1$. The final CDFS sample is composed of 1747 optical galaxies with accurate photometric redshift determinations. Note that this sample is a complete optical flux-limited sample without the joint optical/24 μm criteria used for the Boötes and FLS samples.

2.2. Spitzer photometry

We measured infrared fluxes from 3.6 through 160 μm for all the galaxies in the Boötes, FLS and CDFS samples using the following procedures.

For each IRAC channel, we constructed a mosaic and its error maps from the post-BCD images using the MOPEX package[6]. After a fine re-centering on the IR sources, we measure the flux in an aperture 1.″5 in radius. We measured the background in a 2″ wide annulus. We optimized the radius of the annulus over the range from 7″ to 27″ in steps of 1″ by finding the annulus with the minimum $|\gamma|\sigma$ where γ and σ are the skewness and dispersion of its pixels. After subtracting the background, we corrected the source flux for the finite aperture size relative to the PSF by factors of 1.74, 1.83, 2.18 and 2.44 at 3.6, 4.5, 5.8 and 8.0 μm, respectively. Both extraction errors and photon noise were taken into account in the estimation of uncertainties. Sources are considered as securely detected if their signal to noise ratio is greater that 3. The fluxes were calibrated using calibration factors of 36.04, 34.80, 36.52 and 37.20 μJy/(MJy/sr) at 3.6, 4.5, 5.8 and 8.0 μm, and the uncertainties in these factors are less than 3% (IRAC Handbook[7]).

The MIPS observations were done using the scan map mode and were then reduced with the DAT (Gordon et al. 2005). We measured the 24 μm fluxes by fitting a PSF to the sources. A PSF model was build for each map using 10 bright, isolated sources. Our PSF fitting method is not designed to measure the flux of extended sources, so we excluded 35 nearby extended sources from the Boötes/FLS samples. At 70 and 160 μm, we used aperture photometry. After a re-centering on the sources, we determined the flux within apertures of 18″ and 25″, backgrounds in annuli of [50″−70″] and [80″−110″], and applied aperture corrections of 1.68 and 2.29 for 70 and 160 μm, respectively. We used flux calibration factors of 0.0447 MJy/sr/U_{24}, 702 MJy/sr/U_{70}, and 44.6 MJy/sr/U_{160} for the three bands (Gordon 2006) where the U_x are the standard units of the MIPS maps and the calibrations are uncertain by 4, 7 and 13%. We estimated our 3-σ detection limits of 23, 14 and 11 mJy at 70 μm and 92, 79 and 59 mJy at 160 μm in the Boötes, FLS and CDFS fields respectively by measuring the scatter σ_r in the fluxes measured at random positions on each map after rejecting outliers to the distributions. This procedure should account for both instrumental and confusion noise. A source is considered

[6] http://ssc.spitzer.caltech.edu/postbcd/index.html
[7] http://ssc.spitzer.caltech.edu/IRAC/dh/

Table 1. Galaxy sample completeness by wavelength.

Field	Initial selection	Initial sample size	3.6 μm	4.5 μm	5.8 μm	8.0 μm	24 μm	70 μm	160 μm	Final sample size
Boötes	Opt. + 24 μm	846	846	846	834	841	821[1]	428	236	185
FLS	Opt. + 24 μm	504	504	504	495	503	494[1]	378	187	162
CDFS	Opt.	1767	1731	1688	1055	707	438[2]	54[3]	38[3]	25
Total										372

[1] Extended sources are not detected with the PSF fitting photometry method and are thus excluded from our sample.
[2] Only sources first detected at 8 μm are analyzed because of the high number of sources in the initial sample. This avoids false cross-identifications of sources.
[3] Only sources first detected at 24 μm are analyzed because of the high number of sources in the initial sample. This avoids false cross-identifications of sources.

as detected if its flux exceeds $3\sigma_r$, and Table 1 summarizes the detection rates for each MIPS band.

It may appear strange that several sources detected at 160 μm are not detected at 70 μm (Table 1). Two reasons can be invoked to explain this situation. First, sources can be intrinsically brighter at 160 μm, and this can compensate for the sensitivity difference. If $S_{70,\rm lim}$ and $S_{160,\rm lim}$ are the detection limits, then a $z = 0$ source detected at 160 μm but missed at 70 μm must satisfy

$$\frac{(\nu L_\nu)_{160\ \mu\rm m,\ rest}}{(\nu L_\nu)_{70\ \mu\rm m,\ rest}} > \frac{70}{160} \times \frac{S_{160,\rm lim}}{S_{70,\rm lim}}, \quad (1)$$

corresponding to minimum ratios of 1.7, 2.4, 2.4 in the Boötes, FLS and CDFS respectively. Such rest-frame 160/70 colors are not extreme and are observed in our sample (see Fig. 9). It becomes easier to satisfy such a criterion at higher redshifts because the observed-frame 70 μm flux will tend to be smaller than the rest-frame frame flux, while the observed-frame 160 μm flux will tend to be larger than the rest-frame flux. Second, at both 70 and 160 μm, we are detecting sources below the completeness level (Dole et al. 2004a; Frayer et al. 2006), so not all the 160 μm sources are detected at 70 μm because they are below the completeness limit at this wavelength.

Our final sample consists of 372 galaxies that are detected at 8, 24, 70 and 160 μm. In the CDFS, the final sample is very small compared to its initial size (see Table 1) because we started with an optically-selected sample rather than a joint optical/24 μm-selected sample as we used for the Boötes and FLS fields.

2.3. Stacking analysis

Table 1 shows that only a fraction of the initial sample is detected in the far-IR. To overcome this low detection rate, we can use a stacking method (e.g. Dole et al. 2006) to improve our detection threshold. We start from a catalog of 24 μm sources divided into bins of redshift and flux and then stack the corresponding 70 and 160 μm images for the sources without direct detections at these wavelengths. While this yields only the average flux of the sources, it is very powerful approach if the underlying source selection at the shorter wavelength is well controlled (e.g. when sources belong to small ranges of flux and redshift).

For the Boötes field we selected galaxies detected at 24 μm but not detected at 160 μm. We used redshift bins of $0 < z < 0.25$, $0.25 < z < 0.5$, $0.5 < z < 1$ and 24 μm flux bins of and $0.8 < S_{24} < 1.5$, $1.5 < S_{24} < 3$, $3 < S_{24} < 10$ mJy. We also used the 291 arcmin^2 GOODS/CDFS and GOODS/HDFN fields to extend the analysis to higher redshifts based on the 24 μm sample described by Caputi et al. (2007). This sample consists of 24 μm selected star-forming galaxies where AGN have been excluded using both X-ray and near-infrared (power-law) criteria (see discussion in Caputi et al. 2007). For the GOODS sample we used redshift bins of $0 < z < 0.3$, $0.3 < z < 0.6$, $0.6 < z < 0.9$, $0.9 < z < 1.3$ and $1.3 < z < 2.3$ and produced stacked images at 8 μm, 70 μm and 160 μm for all sources with $S_{24} > 80$ μJy. We used the photometry methods and calibrations from Sect. 2.2 to measure the fluxes of stacked sources. By design, we can measure the fluxes in all redshift, flux and wavelength bins as summarized in Table 2 for the Boötes field and Table 3 for the GOODS fields.

As well as estimating the flux errors as in Sect. 2.2, we also estimated the uncertainties using a jackknife analysis. Given a sample of N sources, we measure the standard deviation of the fluxes found by stacking many combinations of $N - 1$ sources. The standard deviation of this distribution divided by the square root of the number of stacked sources gives the jackknife error bar. In general, the jackknife uncertainties will be larger than the photometric uncertainties because they also include the intrinsic scatter in the fluxes of the stacked population. Thus, the low "signal-to-noise" ratios implied by the jackknife uncertainties reported in Tables 2 and 3 are indicative of significant scatter in the population rather than low significance in detecting the stacked sources.

Finally, we also compare to the composite SEDs from Zheng et al. (2007), who analyzed a sample of 579 optical galaxies ($R < 24$) in the CDFS with $0.6 < z < 0.8$ and a stellar mass $M_\star > 10^{10}\ M_\odot$ based on a combination of spectroscopic (VVDS (Le Fèvre et al. 2005) and GOODS (Vanzella et al. 2005, 2006) surveys) and photometric (COMBO-17 Wolf et al. 2004) redshifts. Zheng et al. (2007) divided the galaxies with 24 μm detections into two bins with equal total 24 μm luminosities (the 58 brightest sources in one bin, and the remaining 160 detections in the second), and then put the remaining 361 galaxies without 24 μm detections into a third bin. They then measured the mean SEDs for the three samples, measuring the 24, 70 and 160 μm fluxes by stacking where there were no direct detections.

We will use these stacked "composite" sources to confirm that our low redshift results apply to sources with higher redshifts and lower infrared luminosities.

2.4. Summary

To summarize, our full set of samples consists of:

- First, we have 372 galaxies individually detected at 8 μm, 24 μm, 70 μm and 160 μm. These sources all have accurate redshifts, based on spectroscopy for AGES and FLS (93% of the sources) and COMBO-17 photometric redshifts for the CDFS (7% of the sources). While there are some variations in the selection criteria for each field, we can view these as *far-infrared* 160 μm flux-limited samples. Figure 1 compares the differential number counts at 160 μm for our sample to those from Dole et al. (2004a) and Frayer et al. (2006) to show that the completeness of this subsample is ∼50% and that the sampling is fairly uniform over a broad range of 160 μm fluxes.
- Second, we have 13 stacked points constructed from a sample of ∼1700 star-forming galaxies and extending to redshift $z \sim 2$ and 24 μm fluxes of $S_{24} = 80$ μJy that will allow us to probe higher redshifts and lower infrared luminosities. These galaxies are typical of *mid-infrared* selected galaxies because they were drawn from a complete sample selected at 24 μm.
- Third, we have 3 stacked points from Zheng et al. (2007) at redshift ∼0.7 that were built from a sample of optically-selected galaxies.

Thus our combined sample covers a wide range of 24 μm fluxes and redshifts, and is homogeneous over a wide range of 160 μm fluxes. As it is representative of both mid- and far-infrared selected sources, it is well-suited for a general statistical study of infrared galaxies, with no obvious biases towards either cool or warm infrared galaxies.

QSOs have been removed from our sample based on an optical spectroscopic diagnostic (emission lines). Obviously, not all AGNs have such signatures, so it is likely that our sample contains some un-identified AGN (e.g. Le Floc'h et al. 2007). Several criteria based on IRAC colors are proposed in the literature to select AGNs (e.g. Lacy et al. 2004; Stern et al. 2005; Richards et al. 2006), and we note that only ∼3% (10/372) of our sources lie in the Stern et al. (2005) AGN-selection region. Moreover, Caputi et al. (2007) and Fiore et al. (2007) have shown that AGN are a minority of sources (less than 10% or 5%, respectively) at $z \lesssim 1$. Thus, the presence of a few unidentified AGNs will not affect our lower redshift results ($z \lesssim 1.3$). However, contamination from AGN may not be negligible at higher redshifts (e.g. Daddi et al. 2007; Fiore et al. 2007; Papovich et al. 2007) and the mid-infrared spectra of $z \sim 2$ galaxies may be significantly contaminated by an embedded AGN. We believe our $z \sim 2$ stacking results are little affected by AGNs, since the sample was restricted to star-forming galaxies based on many well-defined criteria (Caputi et al. 2007).

Table 2. Results for the stacking analysis in the Boötes field. The mean fluxes are given in mJy where "···" means that no source were detected. The uncertainties are the jackknife uncertainties.

$S_{24\ \mu\rm m}$ bin (mJy)	Redshift bin	N_s	$\langle S_8 \rangle$ (mJy)	$\langle S_{24} \rangle$ (mJy)	$\langle S_{70} \rangle$ (mJy)	$\langle S_{160} \rangle$ (mJy)
$0.8 < S_{24} < 1.5$	$0 < z < 0.25$	191	0.48 ± 0.02	1.16 ± 0.16	16.6 ± 0.9	38.0 ± 2.4
	$0.25 < z < 0.5$	113	0.25 ± 0.01	1.18 ± 0.16	14.9 ± 1.0	38.6 ± 2.8
	$0.5 < z < 1$	17	0.13 ± 0.01	1.18 ± 0.16	12.1 ± 3.7	34.3 ± 9.4
$1.5 < S_{24} < 3$	$0 < z < 0.25$	148	0.67 ± 0.03	2.07 ± 0.42	23.2 ± 1.2	42.4 ± 2.7
	$0.25 < z < 0.5$	65	0.35 ± 0.02	2.00 ± 0.39	22.9 ± 1.7	73.7 ± 28.2
	$0.5 < z < 1$	10	0.29 ± 0.08	2.01 ± 0.43	14.7 ± 4.7	32.0 ± 9.3
$3 < S_{24} < 10$	$0 < z < 0.25$	39	0.96 ± 0.06	4.59 ± 1.66	41.9 ± 3.7	53.7 ± 5.2
	$0.25 < z < 0.5$	11	0.61 ± 0.09	3.90 ± 1.15	25.7 ± 6.0	43.1 ± 12.9
	$0.5 < z < 1$	3	0.61 ± 0.24	4.91 ± 2.51	14.5 ± 5.2	···

Table 3. Results of the stacking analysis of the Caputi et al. (2007) sample in the CDFS and HDFN fields. The mean fluxes are in mJy and the uncertainties are the jackknife uncertainties. All stacked sources are securely detected with a (photometric) signal-to-noise ratio greater than 3.

Redshift bin	$z_{\rm med}$	N_s	S_8 (mJy)	S_{24} (mJy)	S_{70} (mJy)	S_{160} (mJy)
$0 < z < 0.3$	0.20	78	0.297 ± 0.069	0.517 ± 0.116	9.32 ± 2.56	8.74 ± 1.99
$0.3 < z < 0.6$	0.46	193	0.058 ± 0.006	0.205 ± 0.013	2.41 ± 0.48	9.14 ± 1.89
$0.6 < z < 0.9$	0.73	283	0.028 ± 0.004	0.171 ± 0.012	1.82 ± 0.36	7.09 ± 3.51
$0.9 < z < 1.3$	1.02	306	0.018 ± 0.001	0.140 ± 0.006	1.06 ± 0.44	4.56 ± 1.23
$1.3 < z < 2.3$	1.68	274	0.014 ± 0.001	0.128 ± 0.005	0.12 ± 0.35	3.50 ± 1.33

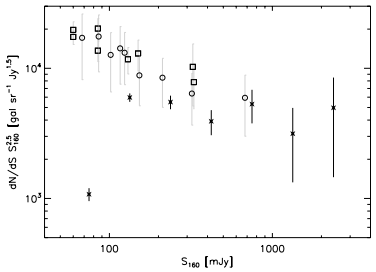

Fig. 1. 160 μm differential number counts for our sample of 372 galaxies individually detected at 8, 24, 70 and 160 μm (black stars) as compared to the counts obtained in the Marano and CDFS fields by Dole et al. (2004a) (open squares) and in the FLS by Frayer et al. (2006) (open circles). This shows that we are uniformly sampling the far-infrared population over a large range of 160 μm fluxes.

3. Getting the infrared and monochromatic luminosities

3.1. A model-independent estimate of the infrared luminosity

We define the infrared luminosity as

$$L_{\rm IR} = L_{5-1000\ \mu\rm m} = \int_{5\ \mu\rm m}^{1000\ \mu\rm m} L_\nu \mathrm{d}\nu, \quad (2)$$

where L_ν and $L_{\rm IR}$ are given in W/Hz and W, respectively. This differs from the definition of $L_{8-1000\ \mu\rm m}$ as the infrared luminosity between 8 and 1000 μm introduced by Sanders & Mirabel (1996) in order to include the PAH emission in the 5 to 8 μm

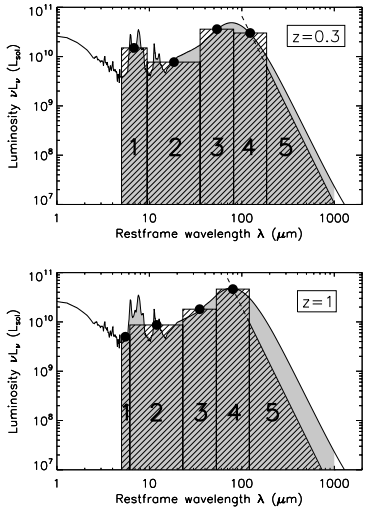

Fig. 2. Illustration, for an arbitrarily chosen template, of the method used to derive the infrared luminosity from the four observed luminosities at 8, 24, 70 and 160 μm and the redshift (*top*: $z = 0.3$; *bottom*: $z = 1$). The area of the gray regions is equal to the true infrared luminosity, while the area of the hatched regions corresponds to our estimate of $L_{\rm IR}$. The sizes and positions of the five regions are described in the text.

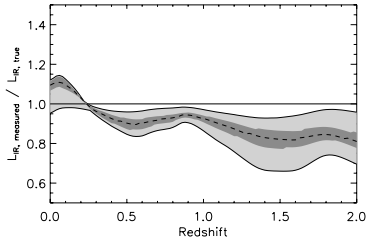

Fig. 3. Validation of the infrared luminosity estimate using the Lagache et al. (2004) template spectra. The shaded bands show the ratio between the estimated and true values for $L_{\rm IR}$ as a function of redshift. The light gray area shows the range encompassing all templates, the dark gray area shows the range encompassing all templates with "typical" luminosities $-0.5 < \log(\frac{L_{\rm IR}}{L^\star}) < 0.5$, and the dashed line is the result for the template with $L_{\rm IR} = L^\star$.

range and to put the wavelength boundary at a more physical frontier between stellar and dust emission. For the Lagache et al. (2004) templates for infrared galaxies, we find that the differences between the two definitions are $(L_{5-1000\,\mu{\rm m}}/L_{8-1000\,\mu{\rm m}}) = 1.07 \pm 0.04$.

We estimated the infrared luminosity from the redshift and the four observed luminosities at 8, 24, 70 and 160 μm without fitting model templates to the data in order to avoid any biases in the models such as contamination from AGN or limited ranges of grain temperatures. Our method simply consists of estimating the total infrared flux by adding the luminosities within the 5 regions shown in Fig. 2. Regions 2, 3 and 4 are rectangles centered at observed-frame 24, 70 and 160 μm (i.e. 24/(1+z), 70/(1+z) and 160/(1+z) μm rest-frame). Their widths are determined by forcing them to be contiguous. Region 1 is a rectangle extending from 5 μm to the beginning of Region 2. The luminosity at the center of Region 1 is calculated by linearly interpolating the νL_ν values for the observed 8 μm and 24 μm points. For $z > 1.5$, the width of this first region is equal to zero and the observed 8 μm flux is no longer used in the estimate of the infrared luminosity. Lastly, Region 5 is a triangle (on a logarithmic scale) with a slope of -4 defined so that the extrapolation of the edge passes through the observed 160 μm point. This slope models the modified black-body emission of big grains with a spectral index $\beta = 2$ and a dust temperature $T_{\rm d} = 25$ K (Sajina et al. 2006) or $\beta = 1.7$ and $T_{\rm d} = 35$ K (Taylor et al. 2005) well because the slope between 200 μm and 1 mm of these two modified black-body spectra is close to -4. The slope between 200 μm and 1 mm measured on different templates (Lagache et al. 2004; Dale & Helou 2002; Chary & Elbaz 2001) varies between -3.5 and -4, but varying the slope from -3.5 or -4.5 has little (∼1%) effect on the estimate of $L_{\rm IR}$. The rest-frame luminosity $(\nu L_\nu)_{\rm rest}$ and the observed luminosity $(\nu L_\nu)_{\rm obs}$ are then related by

$$(\nu L_\nu)_{\lambda,\,\rm rest} = (\nu L_\nu)_{\lambda(1+z),\rm obs}, \quad (3)$$

where z is the redshift of the source. The statistical uncertainties in $L_{\rm IR}$ are easily computed from the uncertainties in the 8, 24, 70 and 160 μm fluxes since $L_{\rm IR}$ is simply a linear combination of the four bands.

We tested the method using templates from the Lagache et al. (2004) library. We simulated observations at 8, 24, 70 and 160 μm as a function of redshift and compared the infrared luminosity obtained with our method to the one obtained by a proper integration of the template between 5 μm and 1 mm with the results shown in Fig. 3. For $0 < z < 1$, the errors are less than 15%. For redshifts higher than 1, we systematically underestimate the infrared luminosity and the errors are larger (between 5 and 30%) because the peak of the rest-frame FIR emission is leaving the 160 μm bandpass as the galaxy redshift increases (Fig. 2). Submillimeter data are needed to better constrain the FIR SED of $z \gtrsim 1.3$ sources. If we restrict the comparison to templates that are more representative of the typical luminosities and redshifts of our sources, the errors are smaller. For example, if we restrict ourselves to models with $-0.5 < \log(\frac{L_{\rm IR}}{L^\star}) < 0.5$, where $L^\star$ is the characteristic luminosity of the infrared luminosity function from Le Floc'h et al. (2005) (for $0 < z < 1$) or Caputi et al. (2007) (for $1 < z < 2$), then the errors are less than 15% (see the dark area in Fig. 3). Although we could try to correct the infrared luminosities for these systematic errors, we decided not do so in order to avoid introducing model-dependent correction factors. In any case, the consequences of this bias are minor and we do not include them in our error estimates for $L_{\rm IR}$. We discuss systematic uncertainties further in Sect. 4.3.

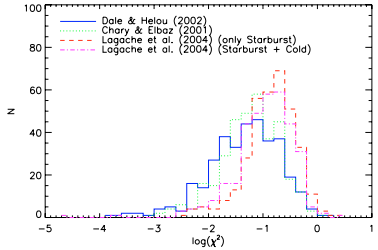

Fig. 4. χ^2 histograms obtained with the different template libraries, where $\chi^2 = \sum_\lambda (\log S_{\lambda,\rm best-fit} - \log S_\lambda)^2$. The solid blue and dotted green lines correspond to the Dale & Helou (2002) and Chary & Elbaz (2001) libraries, respectively. The dashed red and dotted-dashed purple lines are the distributions for the starburst-only and two-template (starburst + cold) templates from the Lagache et al. (2004) library.

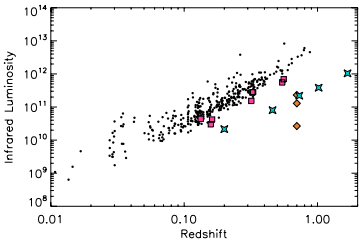

Fig. 5. Infrared luminosities as a function of redshift for all galaxies in our sample. Small black circles correspond to data from the Boötes, FLS and CDFS fields. The pink squares are the stacking results in Boötes, the orange diamonds are the data points from Zheng et al. (2007), and the blue stars are the stacking results for the Caputi et al. (2007).

3.2. K-correction

We have to apply K-corrections to compute rest-frame luminosities $(\nu L_\nu)_{\rm rest}$. We chose to use the Dale & Helou (2002) model, which is a physical model based on an incident heating intensity and a particle size distribution. Unlike other popular, but more empirical, models (e.g. Chary & Elbaz 2001; Lagache et al. 2004) developed for fitting galaxy properties and statistics (like correlations in monochromatic luminosities, luminosity functions, deep number counts), the Dale & Helou (2002) physical model covers a wide range of dust properties. For each galaxy, we search for the template that best fits the four data points ($\log(S_8)$, $\log(S_{24})$, $\log(S_{70})$ and $\log(S_{160})$) and then use it to compute the K-corrections. At higher redshifts, where observed-frame bands overlap with different rest-frame band, we use the overlapping bands to compute the K-correction in order to minimize the dependence on the templates. For example, at $z = 1.7$ we used the observed 24 μm luminosity to compute the rest-frame 8 μm luminosity. We use the average redshift and fluxes of the stacked sources to compute their K-corrections. In Appendix A we show that this approximation is reasonable and that we do not need to apply K-corrections weighted by the redshift distribution. The sources that are most affected by the model for the K-corrections are those at intermediate redshifts ($z \simeq 0.5$–0.7).

As a consistency check, we also fit the data with the template models from (Chary & Elbaz 2001; Lagache et al. 2004). For the Lagache et al. (2004) library, we fit two models, one with only the starburst component and one which was a linear combination a cold and a starburst component. In most cases, we find that the Dale & Helou (2002) library produces better fits, as illustrated in Fig. 4. The medians of the χ^2 distributions are 0.052, 0.063, 0.155, 0.128, when using the DH, CE, LDP and 2-component LDP models, respectively. Using a Kolmogorov-Smirnov test, we checked whether the χ^2 distributions are drawn from the same parent distribution. At more than 99% confidence, the CE, the single LDP and the 2-component LDP χ^2 distributions are identical, at 94% confidence the CE distribution is compatible with DH, and the DH distribution differs from the single and 2-component LDP models at 54% and 76% confidence, respectively. Since the Lagache et al. (2004) templates were constructed to model galaxy evolution rather than to fit individual spectra, finding larger χ^2 values when using this library is not very surprising. We find small variations in the monochromatic rest-frame luminosities when using different model families to compute the K-correction. These variations are smaller than 15%, 25%, 20% and 20% at 8 μm, 24 μm, 70 μm and 160 μm for the full range of templates and luminosities, and they are smaller than 10% for galaxies with $L_{\rm IR} < 10^{11}\,L_\odot$. While we discuss these questions further in Sect. 4.3, such variations have little effect on the correlations we will be exploring.

3.3. Characteristics of our sample

Figure 5 shows the infrared luminosity as a function of redshift for the 372 individual galaxies in our sample as well as for the 16 points from the stacking analysis. Our sample mostly contains galaxies with infrared luminosities between $10^{10}\,L_\odot$ and $10^{12}\,L_\odot$, which corresponds to normal star-forming galaxies and LIRGs. With the stacking results, LIRGs are well sampled up to $z = 1.1$. We directly detect a few ULIRGs up to $z = 0.9$, and then the stacking analysis adds two points at $z = 0.9$ and $z = 1.7$. Thus, the redshift-infrared luminosity plane is reasonably well covered by our data.

4. Correlations between $L_{\rm IR}$ and $(\nu L_\nu)_{\rm rest}$ at low and high redshift

We first present the correlations we obtained for the individually detected galaxies, and then compare them to the correlations obtained after adding the stacking points. These correlations then provide useful conversions between band and total luminosities.

4.1. Correlations at low redshift

We focus on the correlations between the rest-frame monochromatic luminosities and the total infrared luminosities, as shown in Fig. 6. To first order, the correlations are simply a scaling effect – stronger infrared emission implies stronger emission at all wavelengths. When we fit the relationships between νL_ν and $L_{\rm IR}$ at the different wavelengths using linear least-squares fits to the

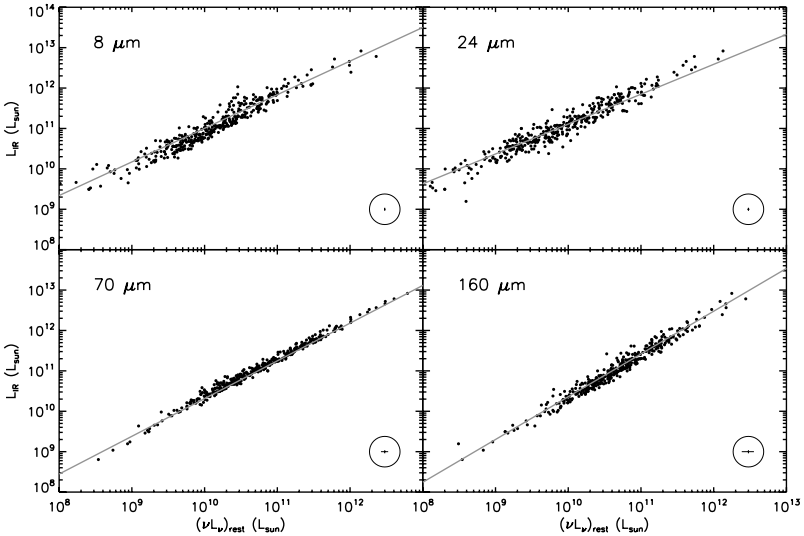

Fig. 6. Correlations between rest-frame monochromatic luminosities and total infrared luminosities at 8, 24, 70 and 160 μm. Black filled circles are the data from Boötes, FLS and CDFS fields. The gray lines are the best fit lines and correspond to Eq. (4). Typical error bars are shown in a circle in the *bottom-right corner*.

logarithms of the luminosities and including the uncertainties in both quantities, we find that

$$\begin{cases} L_{\rm IR} = 482.5 \times (\nu L_\nu)^{0.83}_{8\ \mu{\rm m,\,rest}} & (\pm 37\%) \\ L_{\rm IR} = 5113 \times (\nu L_\nu)^{0.74}_{24\ \mu{\rm m,\,rest}} & (\pm 37\%) \\ L_{\rm IR} = 9.48 \times (\nu L_\nu)^{0.93}_{70\ \mu{\rm m,\,rest}} & (\pm 16\%) \\ L_{\rm IR} = 0.596 \times (\nu L_\nu)^{1.06}_{160\ \mu{\rm m,\,rest}} & (\pm 26\%). \end{cases} \quad (4)$$

We now see that the logarithmic slopes can differ from unity, which means that the shapes of the galaxy SEDs depend on luminosity. For example, the 24 μm rest-frame luminosity makes a smaller contribution to the total infrared luminosity in faint galaxies than in brighter ones. These relations are illustrated in Fig. 6.

We also computed the 1-σ scatter of the measurements around the best fitting relations (Eq. (4)). These are defined to be the relative uncertainties in $L_{\rm IR}$ estimated from

$$\frac{\sigma_{L_{\rm IR}}}{L_{\rm IR}} = \ln 10 \times \sigma_{\log L_{\rm IR}}. \quad (5)$$

We see that the rest-frame 70 μm luminosity is the best tracer of the total infrared luminosity. This means that, for a given infrared luminosity, the scatter of $(\nu L_\nu)_{70\ \mu{\rm m,\,rest}}$ is the smallest. This can easily be understood by considering the two extreme templates shown in Fig. B.1. The two templates are normalized to have the same total infrared luminosity, and we see that the rest-frame 70 μm luminosity minimizes the scatter because it is close to the intersection of the two templates (between 80 and 90 μm). The same argument also explains why the 8 and the 24 μm luminosities are the worst tracers of $L_{\rm IR}$.

These correlations were derived based on a far-infrared (160 μm) selected sample of galaxies, which will introduce some biases. For general use, we recommend the more general relations developed in the next section, even if the differences are small.

4.2. Validation with higher redshift sources

The sample from which we derived the correlations Eq. (4) is dominated by moderate redshift galaxies (93% lie at $z < 0.4$) with direct far-infrared detections. In order to probe higher redshifts for a given infrared luminosity, we make use of the measurements from our stacking analysis (Fig. 5). For example, galaxies with $L_{\rm IR} = 3 \times 10^{11}\ L_\odot$ are directly detected up to $z = 0.2$, but the stacking points probe $0.3 < z < 0.7$. Figure 7 shows the luminosity correlations including both the individually detected galaxies and the stacking analysis data. While the general agreement is good, there are small systematic shifts between the two samples. This is probably explained by selection effects. For example, at a given 24 μm rest-frame luminosity, the stacking method allows us to detect galaxies with lower 160 μm luminosities than the direct detections, and thus includes sources with lower infrared luminosities. Equivalently, galaxies selected at 24 μm are warmer than galaxies selected at 160 μm. This hypothesis is confirmed by the simulations presented in Appendix B.

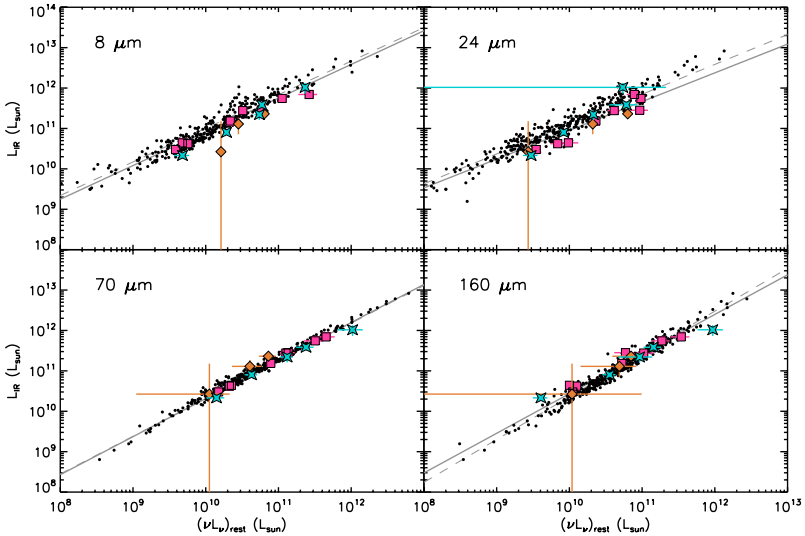

Fig. 7. The correlations as in Fig. 6, but with the addition of stacked galaxies. The symbols have the same definitions as in Fig. 5. The gray continuous lines indicate the best fits obtained with all the data points (Eq. (6)) and the gray dashed lines correspond to the best fits obtained without the stacking points (i.e., the same as in Fig. 6 and Eq. (4)).

If we recompute the correlations including the stacking data, giving each stacking point an additional weight equal to the square root of the number of stacked sources, we find that

$$\begin{cases} L_{\rm IR} = 377.9 \times (\nu L_\nu)^{0.83}_{8\ \mu{\rm m,\,rest}} & (\pm 37\%) \\ L_{\rm IR} = 6856 \times (\nu L_\nu)^{0.71}_{24\ \mu{\rm m,\,rest}} & (\pm 54\%) \\ L_{\rm IR} = 7.90 \times (\nu L_\nu)^{0.94}_{70\ \mu{\rm m,\,rest}} & (\pm 19\%) \\ L_{\rm IR} = 4.24 \times (\nu L_\nu)^{0.98}_{160\ \mu{\rm m,\,rest}} & (\pm 31\%). \end{cases} \quad (6)$$

These correlations, plotted using solid lines in Fig. 7, show small changes from the results for 160 μm-selected galaxies in Eq. (4). These new relations are representative of the total infrared galaxy population, as the full sample includes all types of galaxies (i.e. warm and cold, corresponding to mid- and far-infrared selection, respectively) over a broad range of redshifts. In particular, they are reliable up to $z = 1.1$ for LIRGs and $z \sim 2$ for ULIRGs.

Note that the scatter in the relations at 24 μm increased by far more than the scatter at the other wavelengths. We are uncertain as to the cause. While we think AGN contamination in the sample is small, it could cause part of the increase. It may also be due to extra systematic scatter in the K-corrections for sources at $z \gtrsim 0.8$ when the PAH features start to enter the 24 μm band.

4.3. Uncertainties from the integration of the SED and the K-correction

The systematic uncertainties in these relations arise from uncertainties in our estimate of $L_{\rm IR}$ and any errors in the K-corrections.

Table 4. Changes in the correlations obtained for typical starburst, LIRGs and ULIRGs when using the Chary & Elbaz (2001) model instead of the Dale & Helou (2002) templates for the K-corrections.

$L_{\rm IR}$	8 μm	24 μm	70 μm	160 μm
3×10^{10}	+3%	−6%	+5%	−11%
3×10^{11}	+8%	−6%	+3%	−4%
3×10^{12}	+13%	−6%	<1%	+3%

We showed in Fig. 3 that the errors in the estimate of $L_{\rm IR}$ can be quite large at high redshift (for example 30% at redshift $z = 1.5$). But these large errors are only found for the coldest (i.e. less luminous) templates of the Lagache et al. (2004) library and these quiescent galaxies do not seem to be representative of the distant universe. More realistic templates, with a typical luminosity of $L^\star$ from observed luminosity functions (Le Floc'h et al. 2005; Caputi et al. 2007) at these redshifts show much smaller errors (about 15%, see the dark area in Fig. 3). Thus, we estimate that the systematic uncertainties in $L_{\rm IR}$ are less than 15% for redshifts <1 and less than 20% for redshifts up to $z = 2$. As most of the galaxies in our sample lie at $z < 1$, such small uncertainties will have little effect on the estimated correlations.

To obtain the rest-frame luminosities for each band, we have to compute and apply a K-correction, which is derived from template fits to the data. The choice of the model was already seen in Sect. 3.2 to have little effect (less than 25% for $L_{\rm IR} > 10^{11}\ L_\odot$ and less than 10% for $L_{\rm IR} < 10^{11}\ L_\odot$). Table 4 shows the luminosity-dependent changes in the correlations if we use the Chary & Elbaz (2001) models instead of the Dale & Helou (2002)

Table 5. Results of the different fits (see text and Eq. (7)) on the whole sample (the directly detected galaxies plus the stacking points). An empty case means that the given a_λ was fixed to zero. For comparison, we report the previous relations given in Eq. (6).

Number of bands	a_8	β_8	a_{24}	β_{24}	a_{70}	β_{70}	a_{160}	β_{160}	1-σ
1 band	377.9	0.83							37%
			6856	0.71					54%
					7.90	0.94			19%
							4.24	0.98	31%
2 bands	5607	0.71	1.00×10^{-5}	1.50					34%
			8.9×10^{-4}	1.27	12.62	0.92			20%
					3.87	0.96	1.58	0.95	11%
3 bands	0.0071	1.11	7.4×10^{-4}	1.28	12.8	0.92			19%
			1.62	0.99	1.59	0.98	3.78	0.94	7%
4 bands	8.86	0.81	1.28	1.00	1.45	0.98	3.92	0.94	6%

models to compute the K-correction. Systematic uncertainties found for typical starbursts, LIRGs and ULIRGs are generally less than 10% at 24, 70 and 160 μm and modestly larger (15%) at 8 μm.

4.4. Useful relations to estimate L_{IR}

In the last few sections we have shown that the knowledge of one infrared flux between 8 and 160 μm can provide a very reasonable estimate of the total infrared luminosity and hence of the star formation rate. In this section we explore whether combining several monochromatic luminosities can significantly improve the estimates. We fit the infrared luminosity as a sum of power-law relations for each wavelength,

$$L_{\rm IR} = \sum_{\lambda=8,24,70,160\ \mu{\rm m}} a_\lambda (\nu L_\nu)_{\lambda,{\rm rest}}^{\beta_\lambda}, \quad (7)$$

where the coefficients a_λ and slopes β_λ are free parameters. We fit the data, including the stacking results, using combinations of two wavelengths, three wavelengths or all four wavelengths, as summarized in Table 5.

Obviously, when we use more than one monochromatic luminosity, we get a more accurate estimate of $L_{\rm IR}$. For example, estimating the infrared luminosity from the 8 and 24 μm luminosities leads to a scatter about the resulting correlation of only 34% instead of the 37% and 54% found for the individual luminosities. Using the three far-infrared bands or all four bands give very accurate results, scatters of 7% and 6% respectively, both because the infrared emission is dominated by emission from large grains that peaks between 80 and 150 μm and becuase these linear combinations can closely approximate our method for constructing $L_{\rm IR}$ from the data. Once the scatter is significantly smaller than ~25%, the uncertainties are dominated by systematic errors.

Such empirical relations may be very useful in practice for measuring the total infrared luminosity of infrared star-forming galaxies from limited data. In particular, mid-infrared fluxes (8 and 24 μm) are particularly easy to obtain for large numbers of sources and are well-suited for estimating $L_{\rm IR}$ and conducting statistical studies of star formation in LIRGs and ULIRGs. Moreover, the estimates are nearly independent of the choice of a model, so it is easy to obtain relatively precise estimates for the infrared luminosity of starburst galaxies (30% 1-σ) without any strong assumptions.

4.5. Comparison with previous studies

Figure 8 compares our correlation (Eq. (6)) between the 24 μm luminosity and $L_{\rm IR}$ to earlier results from Sajina et al. (2006) and

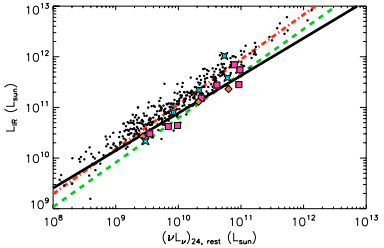

Fig. 8. Correlation between $(\nu L_\nu)_{24\ \mu{\rm m,rest}}$ and $L_{\rm IR}$ for our whole sample (same symbols as in Fig. 7). The best fit (Eq. (6)) is shown with a black solid line. The green short-dashed line is the relation from Takeuchi et al. (2005) and the red dotted-dashed line is the relation from Sajina et al. (2006).

Takeuchi et al. (2005). The Sajina et al. (2006) sample consists of ISO FIRBACK sources selected at 170 μm and the Takeuchi et al. (2005) sample was mainly selected at 100 μm because they required sources to be detected in all four IRAS bands (12, 25, 60 and 100 μm). As suggested by Sajina et al. (2006), the difference between these two results can be attributed to selection effect, with IRAS-selected sources being warmer than ISO sources. This effect is similar to the one we discussed in Sect. 4.2 and provide details for in Appendix B. Our correlation is roughly bounded by the relations from Takeuchi et al. (2005) and Sajina et al. (2006) – the warmest galaxies in our sample (the stacking points) agree well with the relation of Takeuchi et al. (2005), while the coldest points are in better agreement with the prediction of Sajina et al. (2006). We are sampling a wider range of temperature than these previous studies because of our broader selection criteria. Finally, Dale & Helou (2002) also tried to estimate the total infrared luminosity based on a linear combination of the three MIPS monochromatic luminosities. If we estimate $L_{\rm IR}$ using their relations we find good agreement, with a systematic shift of only 6% and an rms scatter of 6%.

5. Evolution of galaxies and application to the high-redshift universe

5.1. Application to the high-redshift universe

Perfect measurements of the infrared luminosity of high redshift galaxies requires well-sampled, rest-frame infrared SEDs.

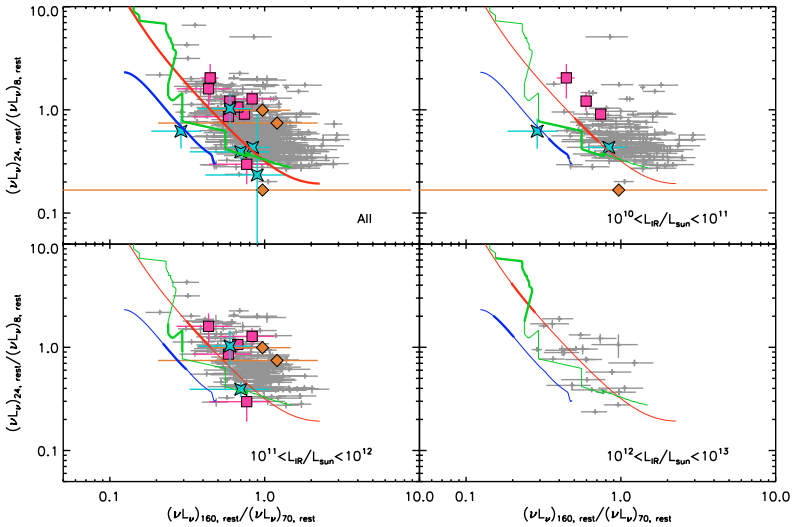

Fig. 9. Infrared colors of the galaxies in our sample using the same symbols as in Fig. 7. The *upper left panel* shows all luminosities and the other panels show different ranges of infrared luminosity $L_{\rm IR}$. The predictions of the Lagache et al. (2004), Chary & Elbaz (2001) and Dale & Helou (2002) models are shown by the blue, green and red lines, respectively. In each case, the thick part of each line corresponds to the luminosity range considered in the panel.

Unfortunately, obtaining such data is very observing-time consuming because of the relatively low sensitivity of far-infrared data. Moreover, at high redshift, the maximum of the infrared emission which is due to emission by big grains is redshifted to submillimeter wavelengths. In order to study star formation at high redshift, we need to estimate the total infrared luminosity with as few parameters as possible. Our study shows that the total infrared luminosity can be well constrained from the 8 or 24 μm rest-frame luminosities (with uncertainties of 37 and 54% respectively) and that combining these two luminosities gives a modestly better estimate (uncertainties of 34%). Caputi et al. (2007) used our conversion between the rest-frame 8 μm luminosity and the $L_{\rm IR}$ to determine the bolometric infrared luminosity function at $z \sim 2$. They show that 90% of the infrared energy density due to $z \sim 2$ star-forming systems is produced equally by LIRGs and ULIRGs, while LIRGS dominate the emission at $z \sim 1$. A more accurate estimate of $L_{\rm IR}$ can be obtained given the 70 μm luminosity, with a scatter of only 19% (1-σ). It will be very interesting to test whether these relations hold for the individually detected, faint far-IR sources that will be found in ongoing ultra-deep 70 μm surveys (e.g. Frayer et al. 2006).

5.2. Evolution of SEDs?

As our galaxies span a wide range of infrared luminosities and redshifts, it is interesting to investigate whether we observe any evolution within our sample.

Figure 9 compares the rest-frame 24/8 and 160/70 infrared colors of our low redshift, directly detected galaxies to those of the stacked galaxies at higher redshifts. The $(\nu L_\nu)_{24\ \mu{\rm m,rest}}/(\nu L_\nu)_{8\ \mu{\rm m,rest}}$ color traces the balance between PAHs and Very Small Grains (VSGs), while the $(\nu L_\nu)_{160\ \mu{\rm m,rest}}/(\nu L_\nu)_{70\ \mu{\rm m,rest}}$ color is set by the temperature of the big grains. In this rest-frame color-color diagram, all the high redshift points are compatible with the lowest redshift sources, which suggests that there is little evolution in the dust content of infrared galaxies between $z \sim 0.16$ (which is the median redshift of our sample of directly detected galaxies) and $z \sim 1.5$. If we compare the data to the predictions of several SED models (Lagache et al. 2004; Dale & Helou 2002; Chary & Elbaz 2001), we find the templates of Dale & Helou (2002) show the best agreement with the data. The Lagache et al. (2004) starburst model underestimates both colors, probably because it over estimates the dust temperature, and the Chary & Elbaz (2001) model gives intermediate results. These differences are related to the discussions of these templates in Sect. 3.2 and Fig. 4. The differences are not a consequence of our template choice – computing the K-corrections using the other templates produces similar rest frame colors for the data and similar levels of agreement between the models and the data (see Appendix C).

5.3. Far-infrared vs. submillimeter galaxies

Figure 9 also shows that the 160/70 color decreases with increasing galaxy luminosity, which means that the brightest galaxies are the warmest. This well known property of infrared galaxies (e.g. Soifer et al. 1987) is also reproduced by the models.

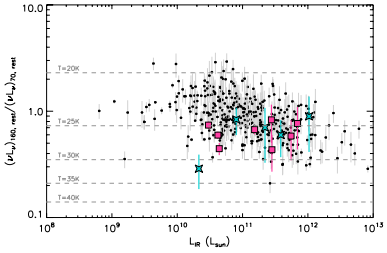

Fig. 10. Evolution of the relationship between $(\nu L_\nu)_{160\ \mu m,\,rest}/(\nu L_\nu)_{70\ \mu m,\,rest}$ and L_{IR} with redshift where the black circles correspond to the low redshift sample, the pink squares to intermediate redshifts and the blue stars to high redshifts using the same symbols as in Fig. 5. The correspondence between the rest-frame 160/70 color and the big grain temperature is shown by the gray dashed lines assuming a modified black-body spectrum with a spectral index $\beta = 2$.

In Fig. 10 we examine the evolution of the relationship between dust temperature and L_{IR} with redshift. We have, effectively, three redshift bins: a low redshift sample made up of the 372 directly detected galaxies, an intermediate redshift sample corresponding to the 8 stacking points from the Boötes field (red squares) and the high redshift sample consisting of the 5 stacking points from the CDFS and HDFN (purple stars). Figure 10 shows that there is no significant evolution in the relationship between L_{IR} and the dust temperature with redshift. All the data lie in the same region, even if we observe some small differences between the stacking points and the directly detected galaxies. At low luminosity ($L_{IR} < 10^{11}\ L_\odot$), the stacking points are warmer than the sources directly detected in all bands, while the reverse is seen at higher luminosities. This should be interpreted as a selection effect, as we confirm with the simulations presented in Appendix B.

We can also compare the relation between dust temperature and total infrared luminosity with other published samples of SMGs and AGNs (Fig. 11). Radio and submillimeter data probe the coldest dust component. In order to compare our results with longer wavelength surveys, we have to estimate the temperature $T_{d,\,cold}$ of the cold dust component. We used the Dale & Helou (2002) library to convert the far-infrared colors (100/60 and 160/70) into estimates of $T_{d,\,cold}$ by fitting a modified blackbody to the templates between 100 and 500 μm. We find typical temperatures in the range of 18−30 K. Yang et al. (2007) and Yang & Phillips (2007) found higher dust temperatures for the same range of infrared luminosities for sources with $0 < z < 1$. Their dust temperatures were determined by fitting modified black-body spectra to at least three photometric points between 60 and 850 μm. We suspect they find higher temperatures because for $z > 0.2$ their 60 μm fluxes will be contaminated by VSG emission that biases the temperature upwards. As shown in Yang et al. (2007), the difference can also be attributed to different spatial scales of the star formation process, where higher temperatures could indicate that the star formation occurs in more concentrated regions. Figure 11 shows the relation between our estimates for $T_{d,\,cold}$ and L_{IR}. We also include the data from Chapman et al. (2003) for local IRAS sources, where we used the same method to convert the 100/60 colors into cold dust temperatures. Their results are in good agreement with our own. We also included data from Sajina et al. (2006)

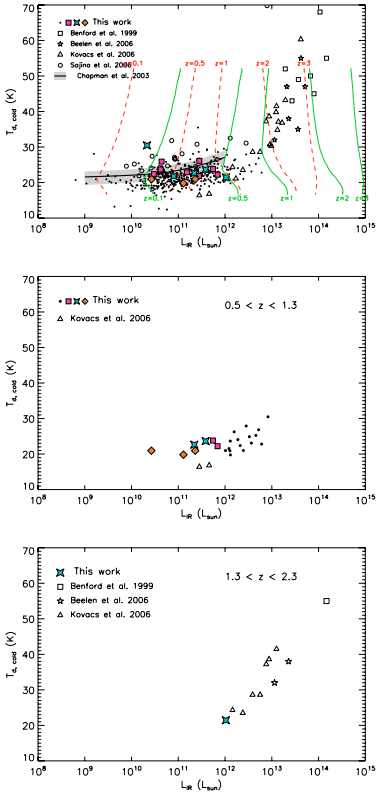

Fig. 11. *Top*: comparison of our sample with previous studies using the same symbols as in Fig. 5. The thick line is the relation found by Chapman et al. (2003) for local IRAS sources with the 1σ scatter around their best fit indicated by the light gray band. The open circles are from the sample of FIRBACK sources (Sajina et al. 2006), the open triangles are the $1.5 < z < 3.5$ SMGs from Kovács et al. (2006), and the dusty quasars from Benford et al. (1999) and Beelen et al. (2006) are marked by the open squares and open stars, respectively. The solid cyan and dashed orange lines show the detection limits for the individually detected and stacked sources in the Boötes field as a function of redshift. Only sources on the *right side of the lines* are detectable. The lower panels are the same, but we restrict the comparisons to sources with $0.5 < z < 1.3$ (*middle*) and $1.3 < z < 2.3$ (*bottom*).

(FIRBACK 170 μm sources), Kovács et al. (2006) (SMGs), and Benford et al. (1999); Beelen et al. (2006) (dusty quasars).

Sub-millimeter surveys do not detect warm or low luminosity sources (Chapman et al. 2005), so the infrared and submillimeter analyses seem to be complementary, and by comparing the two approaches we can study whether the SMGs are a

dominant or marginal population for galaxy evolution. From the previous samples we selected sub-samples consisting of the infrared galaxies in SMGs with $0.6 < z < 1.3$ and $1.3 < z < 2.3$. These sub-samples are shown in separate panels of Fig. 11. At $z \sim 1$, we see that the two SMGs are colder than our infrared sources and that we do not detect a large population of such cold galaxies in the infrared. A small fraction of cold sources could exist and would be folded into our stacking points. At $z \sim 2$, our stacking point is in good agreement with the lowest luminosity SMGs. Unfortunately, the GOODS fields we used to build our $z \sim 2$ sample are too small to include any of the higher luminosity galaxies. However, the good agreement with SMGs where they do overlap suggests that high-redshift SMGs are similar to infrared star-forming galaxies. This suggests that infrared and submillimeter/radio surveys are exploring the same source population but the methods compliment each other because the infrared is well suited for $z \lesssim 2$ sources, while the submillimeter is better for high-redshift sources because of the advantageous K-corrections in this wavelength range.

6. Conclusions

In this paper, we have presented correlations between rest-frame 8 μm, 24 μm, 70 μm and 160 μm luminosities and an estimate for the total infrared luminosity derived without making any assumption on the shape of the SED that might bias the results. For a sample of 372 far-infrared (160 μm)-selected galaxies with $z < 0.8$ we found that the infrared monochromatic luminosities are strongly correlated with the total infrared luminosity L_{IR} and we derived relations to estimate L_{IR} from the monochromatic luminosities. In order to validate this result at higher redshifts, we used a stacking analysis to extend the data to fainter and higher redshift galaxies. For $z < 2$ galaxies selected at 24 μm the new data agrees well with the local sample up to a small systematic shift that we attribute to the differences in the selection criteria – on average, galaxies selected in the mid-infrared are warmer than those selected in the far-infrared. The revised correlations including both samples are probably better for general use. As expected we find that combining several monochromatic infrared luminosities yields a more precise estimate of the total infrared luminosity than using a single luminosity. Since the correlations were derived from a large number of galaxies with a wide range of luminosities and temperatures and extending to $z \sim 2$, they should hold for most star-forming galaxies. In particular, they are applicable for LIRGs up to $z \sim 1.1$ and for ULIRGs up to $z \sim 2$. Extrapolations to higher redshifts, although not tested here, should give reasonable results. It is important to remember that all known QSOs were removed from our sample. While a similar study of AGN sample would be very interesting, we have only 7 QSOs detected in all four bads (8, 24, 70, 160 μm) and cannot carry out the analysis. Our correlations should not be used for AGNs unless further tests demonstrate their validity.

Dale et al. (2005) claim that it is dangerous to use the 8 μm luminosity as a tracer of the total infrared luminosity because they observed strong variations (about a factor 10) of this ratio for their sample of nearby galaxies (SINGS). However, their sample contains many different objects with very different dust properties and they examined different regions inside galaxies in detail. Our study shows that at higher redshift and on larger scales, the integrated galaxy and dust properties of star-forming galaxies are more homogeneous, and that using the 8 or 24 μm luminosities to estimate the total infrared luminosity has uncertainties of between 40−50% that are much smaller than those given by Dale et al. (2005). We also compared our results at 24 μm to previous studies and found good agreement. The differences we observed can be explained by differences in the sample selection criteria.

For the sample as a whole, we find no evidence for significant evolution in the far-infrared SED properties of infrared galaxies with redshift. Both the infrared colors and the relationship between dust temperature and L_{IR} of high redshift galaxies from the stacking analysis are compatible with the galaxies in the low redshift sample. A small evolution amount is not detectable because we used different selection criteria at low (far-infrared) and high (mid-infrared) redshifts. Finally, we compared our sample to submillimeter data and found that the cold SMGs observed at $z \sim 1$ are a marginal population that is not representative of infrared star-forming galaxies. The infrared is the most powerful wavelength range to study the evolution of star-forming galaxies at $z \lesssim 2$ because submillimeter surveys only select the coldest galaxies. However, submillimeter and radio wavelengths are more powerful for higher redshift, $z \gtrsim 2$ dusty galaxies, because they better probe the dust emission peak. Thus the two approaches complement each other for studies of galaxy dust properties over cosmic time.

Acknowledgements. We are grateful to the anonymous referee for a careful reading of the manuscript. We also thank David Elbaz, Alexandre Beelen and Delphine Marcillac for fruitful discussions. This work is based on observations made with the *Spitzer* Space Telescope, which is operated by the Jet Propulsion Laboratory, California Institute of Technology under a contract with NASA.

Table A.1. Maximal errors obtained with the Dale & Helou (2002) templates when doing a K-correction for redshift averaged bins instead of a K-correction weighted by the redshift distribution.

$S_{24\ \mu m}$ bin (mJy)	Redshift bin	8 μm	24 μm	70 μm	160 μm
$0.8 < S_{24} < 1.5$	$0 < z < 0.25$	5.4%	1.2%	0.7%	1.3%
	$0.25 < z < 0.5$	3.5%	1.5%	1.1%	1.3%
	$0.5 < z < 1$	8.0%	1.5%	0.8%	0.6%
$1.5 < S_{24} < 3$	$0 < z < 0.25$	4.8%	0.8%	0.6%	1.0%
	$0.25 < z < 0.5$	4.0%	1.0%	0.9%	1.0%
	$0.5 < z < 1$	10.6%	3.1%	2.3%	1.5%
$3 < S_{24} < 10$	$0 < z < 0.25$	5.1%	1.0%	0.9%	1.2%
	$0.25 < z < 0.5$	2.8%	0.8%	0.7%	0.5%
	$0.5 < z < 1$	...	...	...	...

Appendix A: The K-corrections for the stacking points

In Sect. 3.2 we K-corrected the stacking points using the mean redshift of the sources rather than averaging over the redshift distribution of the bin. We used simulations to test whether this simplification significantly affects our results.

For each template in the Dale & Helou (2002) library we built a mock sample with the redshift and S_{24} flux distributions of our Boötes sub-samples (see Table 2), computing both the rest-frame and observed-frame 8, 24, 70 and 160 μm fluxes for each source. We then compared the true, averaged rest-frame fluxes to the values found by averaging the observed-frame fluxes and K-correcting to the rest frame using the average redshift as we do in the stacking analysis. The results are given in Table A.1. The differences are negligible at 24, 70 and 160 μm. At 8 μm, the K-corrections vary strongly with redshift because of the PAH features. As a result, the errors are larger and reach ∼10% for the two $0.5 < z < 1$ bins. However, these two points have such large uncertainties in our data (see Table 2), that even 10% correction would not significantly change our results. We

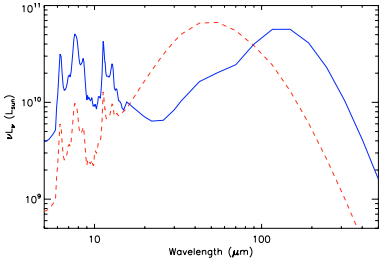

Fig. B.1. Spectral energy distribution of the two templates from the Dale & Helou (2002) library used in the simulation. The solid blue line corresponds to $\alpha = 3.5$ (the cold template) and the dashed red line corresponds to $\alpha = 1.3$ (the warm template). Both templates are normalized to the same total infrared luminosity ($L_{IR} = 10^{11}\ L_\odot$).

conclude that using the K-correction corresponding to the mean bin redshift is sufficiently accurate for our purposes.

Appendix B: Effect of the selection on the $\nu L_\nu - L_{IR}$ correlations

We used a simulation to understand and quantify the effects of selection criteria on the correlations presented in this paper.

We used two templates characterized by their α parameter from the Dale & Helou (2002) library to model the galaxies. Dale et al. (2005) found that most galaxies have SEDs in the range $1.3 < \alpha < 3.5$ so we use the two extremes of a *warm* template with $\alpha = 1.3$ and a *cold* template with $\alpha = 3.5$. These two templates are shown in Fig. B.1.

We randomly and uniformly distributed 20 000 galaxies in the $z - \log(L_{IR})$ plane over the range $0 < z < 1$, $10 < \log(\frac{L_{IR}}{L_\odot}) < 13$, and $L_{IR} < 10^{13} \times z^{1.42}$. The upper limit on the luminosity was determined empirically from our sample of 372 directly detected galaxies. We randomly assigned half of the galaxies to be warm and the other half to be cold and then computed the 8, 24, 70 and 160 μm fluxes of each galaxy. Given a set of detection limits, we can now explore which kind of galaxies will be detectable.

In the Boötes field, the difference is between the directly detected sources and the stacked sources. The directly detected sources had to exceed flux limits of [0.006, 1, 23, 92] (mJy) at 8, 24, 70 and 160 μm, respectively. The stacked sources had to be detected at 24 μm (and effectively at 8 μm) but for a stack of 100 sources they could be 10 times fainter in the longer wavelength bands. Thus, the stacked sources had to exceed flux limits of [0.006, 1, 2.3, 9.2] (mJy). Figure B.2 illustrates the consequences of these two selection criteria on the balance between the warm and cold sources as a function of luminosity. For normal galaxies with $L_{IR} < 10^{11}\ L_\odot$, directly detected galaxies tend to be cold while stacked galaxies tend to be warm. For high luminosities ($L_{IR} > 10^{12}\ L_\odot$), we see the reverse. We probe colder sources with the stacking analysis than with direct detection. Both effects are a consequence of the warm galaxies having a higher $(\nu L_\nu)_{24\ \mu m,\,rest}$ and lower $(\nu L_\nu)_{160\ \mu m,\,rest}$ than the cold galaxies (see Fig. B.1). Thus, by stacking the undetected far-infrared galaxies, we are preferentially adding warm galaxies at low luminosities and cold galaxies at high luminosities, and this explains the differences observed in Fig. 7.

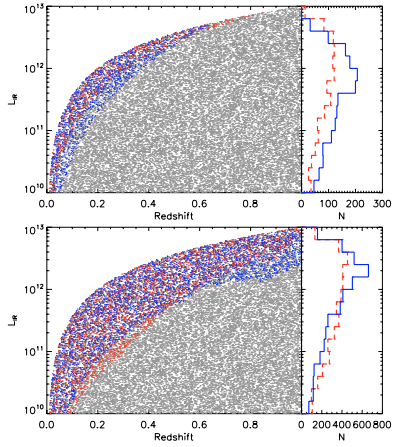

Fig. B.2. Results of the simulation with two different sets of detection limits. The black dots correspond to the 20 000 galaxies in our simulation (both warm and cold). The red and blue circles indicate warm and cold detected galaxies, respectively. *Upper panel*: direct detections using limits of [0.006, 1, 23, 92] (mJy) at 8, 24, 70 and 160 μm, respectively. *Lower panel*: stacking detections using the limits of [0.006, 1, 2.3, 9.2] (mJy). In both panels, the histograms show the distributions of detected warm (red) and cold (blue) galaxies as a function of infrared luminosity.

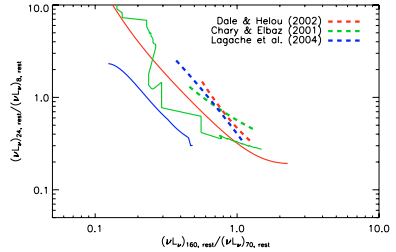

Fig. C.1. As in Fig. 9, but showing the median restframe colors (thick dashed lines) of the directly detected galaxies after computing the K-corrections with three different templates (Dale & Helou 2002; Chary & Elbaz 2001; Lagache et al. 2004).

Appendix C: Influence of the library choice on the K-corrections

While the infrared colors of our sample are in better agreement with the predictions of the Dale & Helou (2002) model (Fig. 9), one might argue that this is a consequence of using these templates to compute the K-corrections. However, we have verified that using the Lagache et al. (2004); Chary & Elbaz (2001) libraries for the K-corrections has no effect on our conclusion. Figure C.1 shows the median rest-frame colors computed with

three different SED models (Dale & Helou 2002; Chary & Elbaz 2001; Lagache et al. 2004) for the 372 galaxies directly detected at all wavelengths. We clearly see that for all three K-correction models the resulting rest-frame colors of the sample are in better agreement with the Dale & Helou (2002) model predictions.

References

Alonso-Herrero, A., Perez-Gonzalez, P. G., Alexander, D. M., et al. 2006, ApJ, 640, 167
Beelen, A., Cox, P., Benford, D. J., et al. 2006, ApJ, 642, 694
Benford, D. J., Cox, P., Omont, A., Phillips, T. G., & McMahon, R. G. 1999, ApJ, 518, L65
Caputi, K. I., Dole, H., Lagache, G., et al. 2006, A&A, 454, 143
Caputi, K. I., Lagache, G., Yan, L., et al. 2007, ApJ, 660, 97
Chapman, S. C., Helou, G., Lewis, G. F., & Dale, D. A. 2003, ApJ, 588, 186
Chapman, S. C., Smail, I., Blain, A. W., & Ivison, R. J. 2004, ApJ, 614, 671
Chapman, S. C., Blain, A. W., Smail, I., & Ivison, R. J. 2005, ApJ, 622, 772
Chary, R., & Elbaz, D. 2001, ApJ, 556, 562
Daddi, E., Alexander, D. M., Dickinson, M., et al. 2007, [arXiv:0705.2832]
Dale, D. A., & Helou, G. 2002, ApJ, 576, 159
Dale, D. A., Bendo, G. J., Engelbracht, C. W., et al. 2005, ApJ, 633, 857
Dole, H., Le Floc'h, E., Pérez-González, P. G., et al. 2004a, ApJS, 154, 87
Dole, H., Rieke, G. H., Lagache, G., et al. 2004b, ApJS, 154, 93
Dole, H., Lagache, G., Puget, J. L., et al. 2006, A&A, 451, 417
Eisenhardt, P. R., Stern, D., Brodwin, M., et al. 2004, ApJS, 154, 48
Fabricant, D., Fata, R., Roll, J., et al. 2005, PASP, 117, 1411
Fazio, G. G., Ashby, M. L. N., Barmby, P., et al. 2004, ApJS, 154, 39
Fiore, F., Grazian, A., Santini, P., et al. 2007, [arXiv:0705.2864]
Frayer, D. T., Fadda, D., Yan, L., et al. 2006, AJ, 131, 250
Gordon, K. D. 2006, in prep.
Gordon, K. D., Rieke, G. H., Engelbracht, C. W., et al. 2005, PASP, 117, 503
Jannuzi, B. T., & Dey, A. 1999, in Photometric Redshifts and High-Redshift Galaxies, ed. R. Weymann, L. Storrie-Lombardi, M. Sawicki, & R. Brunner (San Francisco: ASP), ASP Conf. Ser., 191, 111
Kennicutt, R. C. 1998, ApJ, 498, 541
Kennicutt, R. C., Armus, L., Bendo, G., et al. 2003, PASP, 115, 928
Kovács, A., Chapman, S. C., Dowell, C. D., et al. 2006, ApJ, 650, 592
Lacy, M., Storrie-Lombardi, L. J., Sajina, A., et al. 2004, ApJS, 154, 166
Lagache, G., Dole, H., Puget, J. L., et al. 2004, ApJS, 154, 112
Le Fèvre, O., Vettolani, G., Garilli, B., et al. 2005, A&A, 439, 845
Le Floc'h, E., Papovich, C., Dole, H., et al. 2005, ApJ, 632, 169
Le Floc'h, E., Willmer, C. N. A., Noeske, K., et al. 2007, ApJ, 660, L65
Marcillac, D., Elbaz, D., Chary, R. R., et al. 2006, A&A, 451, 57
Papovich, C., Dole, H., Egami, E., et al. 2004, ApJS, 154, 70
Papovich, C., Cool, R., Eisenstein, D., et al. 2006, AJ, 132, 231
Papovich, C., Rudnick, G., Le Floc'H, E., et al. 2007, ApJ, 668, 45
Pope, A., Scott, D., Dickinson, M., et al. 2006, MNRAS, 370, 1185
Richards, G. T., Lacy, M., Storrie-Lombardi, L. J., et al. 2006, ApJS, 166, 470
Rieke, G. H., Young, E. T., Engelbracht, C. W., et al. 2004, ApJS, 154, 25
Sajina, A., Scott, D., Dennefeld, M., et al. 2006, MNRAS, 369, 939
Sanders, D. B., & Mirabel, I. F. 1996, ARA&A, 34, 749
Soifer, B. T., Sanders, D. B., Madore, B. F., et al. 1987, ApJ, 320, 238
Stern, D., Eisenhardt, P., Gorjian, V., et al. 2005, ApJ, 631, 163
Swinbank, A. M., Smail, I., Chapman, S. C., et al. 2004, ApJ, 617, 64
Symeonidis, M., Rigopoulou, D., Huang, J.-S., & Davis, M. 2006, ApJ
Takeuchi, T. T., Buat, V., Iglesias-Páramo, J., Boselli, A., & Burgarella, D. 2005, A&A, 432, 423
Taylor, E. L., Mann, R. G., Efstathiou, A. N., et al. 2005, MNRAS, 361, 1352
Vanzella, E., Cristiani, S., Dickinson, M., et al. 2005, A&A, 434, 53
Vanzella, E., Cristiani, S., Dickinson, M., et al. 2006, A&A, 454, 423
Werner, M. W., Roellig, T. L., Low, F. J., et al. 2004, ApJS, 154, 1
Wolf, C., Meisenheimer, K., Kleinheinrich, M., et al. 2004, A&A, 421, 913
Yang, M., & Phillips, T. 2007, ApJ, 662, 284
Yang, M., Greve, T. R., Dowell, C. D., & Borys, C. 2007, ApJ, 660, 1198
Zheng, X. Z., Dole, H., Bell, E. F., et al. 2007, [arXiv:0706.0003]

A&A 481, 885–895 (2008)
DOI: 10.1051/0004-6361:20078188

Astronomy & Astrophysics

Simulations of the cosmic infrared and submillimeter background for future large surveys

I. Presentation and first application to Herschel/SPIRE and Planck/HFI

N. Fernandez-Conde, G. Lagache, J.-L. Puget, and H. Dole

Institut d'Astrophysique Spatiale (IAS), bâtiment 121, Université Paris-Sud 11 and CNRS (UMR 8617), 91405 Orsay, France
e-mail: [nestor.fernandez;guilaine.lagache;jean-loup.puget;herve.dole]@ias.u-psud.fr

Received 29 June 2007 / Accepted 2 October 2007

ABSTRACT

Context. The coming Planck and Herschel missions will survey the sky at unprecedented angular scales and sensitivities. Simulations are needed for better interpretating the results of the surveys and for testing new methods of, e.g., source extraction and component separation.
Aims. We present new simulations of the infrared and submillimeter cosmic background, including the correlation between infrared galaxies. The simulations were used to quantify the source-detection thresholds for Herschel/SPIRE and Planck/HFI, as well as to study the detectability of the cosmic infrared background correlated fluctuations.
Methods. The simulations are based on an empirical model of IR galaxy evolution. For these correlations, we only included the linear clustering, assuming that infrared galaxies are biased tracers of the dark-matter fluctuation density field.
Results. We used the simulations with different bias parameters to predict the confusion noise for Herschel/SPIRE and Planck/HFI and the completeness levels. We also discuss the detectability of the linear clustering in Planck/HFI power spectra, including the foreground and backgrounds components.
Conclusions. Simulated maps and catalogs are publicly available online at http://www.ias.u-psud.fr/irgalaxies/simulations.php

Key words. infrared: galaxies – galaxies: evolution – cosmology: large-scale structure of Universe – methods: numerical

1. Introduction

The cosmic infrared background (CIB) ($\lambda \geq 8\ \mu$m) is the relic emission of the formation and evolution of galaxies. The first observational evidence of this background was reported by Puget et al. (1996) and then confirmed by Hauser et al. (1998) and Fixsen et al. (1998). The discovery of a surprisingly high amount of energy in the CIB has shown the importance of studying its sources to understand how the bulk of stars was formed in the Universe. Deep cosmological surveys have been carried out thanks to ISO (see Genzel & Cesarsky 2000; Elbaz 2005, for reviews) mainly at 15 μm with ISOCAM (e.g. Elbaz et al. 2002); at 90 and 170 μm with ISOPHOT (e.g. Dole et al. 2001); to SPITZER at 24, 70, and 160 μm (e.g. Papovich et al. 2004; Dole et al. 2004) and to ground-based instruments such as SCUBA (e.g. Holland et al. 1998) and MAMBO (e.g. Bertoldi et al. 2000) at 850 and 1300 μm, respectively. These surveys have allowed for a better understanding of the CIB and its sources (see Lagache et al. 2005, for a general review). Some of the results include: the energy of the CIB is dominated by starbursts although AGN (active galactic nucleus) contribute too, and the dominant contributors to the energy output are the LIRGs (luminous IR galaxies) at $z \sim 1$ and ULIRGs (ultra luminous IR galaxies) at $z \sim 2$–3.

Determination of the CIB by the COBE satellite has been hindered by the accuracy of subtracting the foreground by only providing just upper limits at 12, 25, and 60 μm (Hauser et al. 1998), lower limit has been derived at 24 μm by Papovich et al. (2004) as well as the contribution of 24 μm galaxies to the background at 70 and 160 μm (Dole et al. 2006). The contribution of the galaxies down to 60 μJy at 24 μm is at least 79% of the 24 μm background, and 80% of the 70 and 160 μm background. For longer wavelengths, recent studies have investigated the contribution of populations selected in the near-IR to the far-infrared background (FIRB, $\lambda > 200\ \mu$m): 3.6 μm selected sources to the 850 μm background (Wang et al. 2006) and 8 μm and 24 μm selected sources to the 850 μm and 450 μm backgrounds (Dye et al. 2006). Similar studies with Planck and Herschel will provide even more evidence of the nature of the FIRB sources.

Studying correlations in the spatial distribution of IR galaxies as a function of redshift is an essential observation (parallel to the studies of individual high-redshift, infrared, luminous galaxies), to understand the underlying scenario and physics of galaxy formation and evolution. A first study has been done using the 850 μm galaxies (Blain et al. 2004). Although the number of sources is quite small, they find evidence that submillimiter galaxies are linked to the formation of massive galaxies in dense environments destined to become rich clusters. This has now been directly supported by the detection of the clustering of high-redshift 24 μm selected ULIRGs and HyperLIRGs (Farrah et al. 2006; Magliocchetti et al. 2007). Studying correlations with individual IR galaxies is very hard due to either high

Article published by EDP Sciences

confusion noises, instrumental noises, or small fields of observation. It has been shown that the IR-background anisotropies could provide information on the correlation between the sources of the CIB and dark matter for large-scale structures (Knox et al. 2001; Haiman & Knox 2000, hereafter HK) and on the large-scale structure evolution. First studies at long wavelengths have only detected the shot-noise component of the fluctuations: Lagache & Puget (2000) at 170 μm, Matsuhara et al. (2000) at 90 and 170 μm, Miville-Deschênes et al. (2001) at 60 and 100 μm. Lagache et al. (2007) and Grossan & Smoot (2007) report first detections of the correlated component using Spitzer/MIPS data at 160 μm. Lagache et al. (2007) measured a linear bias $b \sim 1.7$.

Future observations by Herschel and Planck will allow us to probe the clustering of IR and submm galaxies. Nevertheless these experiments will be limited, the confusion and instrumental noises will hinder detections of faint individual galaxies. Clustering thus has to be analysed in the background fluctuations (e.g. Negrello et al. 2007). The need for a prior understanding of what could be done by these experiments has motivated us to develop a set of realistic simulations of the IR and sub-mm sky.

In Sect. 2 we present the model on which are based our simulations. In Sect. 3 we discuss how the simulations are done and present a set of simulated sky maps and their corresponding catalogs. Different catalogs are created for 3 different levels of correlation between the IR galaxy emissivity and the dark-matter fluctuation density field (strong, medium, and no correlation). For each of these catalogs, we can create maps of the sky at any given IR wavelength and simulate how different instruments will see them. We focus in this paper on Planck/HFI and Herschel/SPIRE. In Sect. 4 we use the simulated maps to give predictions for the confusion noise, the completeness, and the detection limits for each of the study cases, including the instrumental noise. In Sect. 5 we present the power spectra of the CIB anisotropies for Planck/HFI and discuss their detectability against the significant sources of contamination (shot noise, cirrus, and cosmic microwave background (CMB)).

Throughout the paper the cosmological parameters were set to $h = 0.71, \Omega_\Lambda = 0.7, \Omega_m = 0.27$. For the dark-matter linear clustering we set the normalization to $\sigma_8 = 0.8$.

2. The model

2.1. Galaxies' empirical evolution model

The model of IR galaxies used for the simulations is from Lagache et al. (2003), revisited in Lagache et al. (2004) – hereafter the LDP model, see http://www.ias.u-psud.fr/irgalaxies/model.php. This model is a flexible tool for planning surveys and developing analysis methods. The requirement was to build the simplest model of the luminosity function (LF) evolution with redshift, with the lowest number of parameters, but accounting for all statistical observational data between 5 μm and 1 mm. These are the spectral energy distribution of the CIB and its fluctuations, galaxy luminosity functions and their redshift evolution, as well as the existing source counts and redshift distributions.

The luminosity function of IR galaxies was modelled by a bimodal star-formation process: one associated with the passive phase of galaxy evolution (normal galaxies) and one associated with the starburst phase, mostly triggered by merging and interactions (starburst galaxies). Unlike for the starburst galaxies, the normal galaxy contribution to the luminosity function was considered mostly unchanged with redshift. The spectral energy distribution (SED) changes with the luminosity of the source but is assumed constant with redshift for both populations in this simple model.

This model fits all the experimental data and has predicted that LIRGs ($10^{11} < L_{IR} < 10^{12}$) dominate at $z \simeq 0.5$–1.5 and that ULIRGs/HLIRGs ($L_{IR} > 10^{12}$) dominate at $z \simeq 2$–3 the energy distribution of the CIB. One example of the agreement between the model and the observations is shown in Fig. 2.

2.1.1. Number counts and CIB fluctuations

To illustrate the interest of studying the cosmic background fluctuations in the far-IR and submm domains, we use a simplistic approach for the number counts, following Lagache & Puget (2000). The source number counts can be schematically represented by a power law:

$$N(S > S_0) = N_0 \left(\frac{S}{S_0}\right)^{-\alpha} \quad (1)$$

where we set S_0 to be the detection limit for the sources and N_0 the number of sources with flux larger than S_0.

In a Euclidean Universe with uniform density of the sources $\alpha = 1.5$. In the far-IR and submm, a steeper slope is observed with $\alpha = 2$–3 in the regime where negative K-correction dominates. As an example, ISO observations found a slope of $\alpha = 2.2$ at 170 μm (Dole et al. 2001). Obviously, the number counts need to flatten for low fluxes to ensure that the CIB remains finite. For the rest of the discussion we will assume that $\alpha = 0$ for $S < S^*$. The total intensity of the CIB composed by all the sources up to S_{max} is given by:

$$I_{CIB} = \int_0^{S_{max}} S \frac{dN}{dS} dS.$$

For the Euclidean case the CIB intensity is dominated by sources near S^*.

Fluctuations from sources below the detection limit S_0 are given by

$$\sigma^2 = \int_0^{S_0} S^2 \frac{dN}{dS} dS.$$

Using $\frac{dN}{dS}$ given by Eq. (1) we get

$$\sigma^2 = \frac{\alpha}{2-\alpha} N_0 S_0^2 \left[1 - \left(\frac{S^*}{S_0}\right)^{2-\alpha}\right].$$

For $\alpha > 2$ CIB fluctuations are dominated by sources close to S^* so that the same sources dominate both the FIRB and its fluctuations. Therefore by studying the fluctuations of the FIRB, we are also studying the sources that form the bulk of the contribution to the FIRB. We can check this conclusion with the number counts from the LDP model. Figure 3 shows that the same sources dominate the background and the fluctuations, but only for faint sources (for example $S_{850} \lesssim 50$ mJy). Therefore, it is necessary to subtract bright sources prior to any fluctuation analysis since they would otherwise dominate the fluctuations.

2.1.2. IR galaxy emissivity

For the purpose of the model we need to compute the mean IR galaxy emissivity per unit of comoving volume [W/Mpc^3/Hz/sr]. It is defined as

$$j_d(\nu, z) = (1+z) \int_{L_{bol}} L_{\nu'=\nu(1+z)} \frac{dN}{d\ln(L_{bol})} d\ln(L_{bol})$$

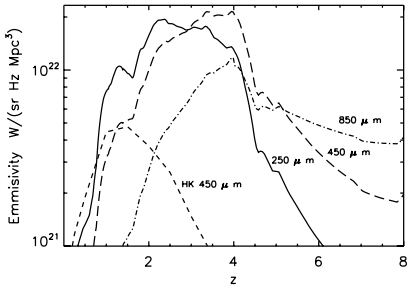

Fig. 1. Emissivities computed using the LDP model at (observed) 250 μm (continuous line), 450 μm (long-dashed line), and 850 μm (dotted-dashed line). The emissivity from HK at 450 μm (short-dashed line) is shown for comparison.

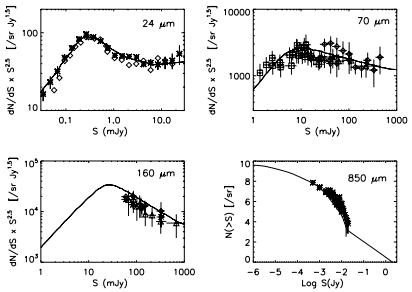

Fig. 2. Comparison of the observed source counts (data points) and model predictions (continuous lines). *Upper left*: 24 μm, *Upper right*: 70 μm, *Lower left*: 160 μm, *Lower right*: 850 μm.

where L is the luminosity (in W/Hz/sr), $\frac{dN}{d\ln(L_{bol})}$is the comoving luminosity function (in Mpc^{-3}), and ν the observed frequency. We compute j_d using the SEDs and luminosity function from the LDP model which assumes that the SED depends only on L_{bol}. The resulting j_d is different from what is used by former approaches (HK, Knox et al. 2001). We can see the difference between the emissivity from our model and that of HK in Fig. 1. The crude model used for the emissivities by HK gives much lower emissivities than ours.

2.2. IR galaxy spatial distribution

Any model trying to account for CIB fluctuations must describe the statistical properties of the spatial distribution of the sources. The absence of a completely developed theoretical model for the distribution of the whole IR galaxy populations makes the empirical modelling of different distributions for the sources of the CIB necessary in order to prepare future observations. We used an empirical description for the spatial distribution of these sources, which has been used to create the simulated sky maps.

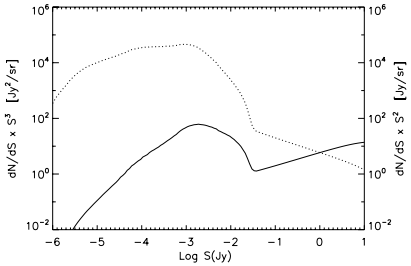

Fig. 3. Contributions of the sources of flux S (in Jy) per Log interval of S to the background (dotted line, right y axis) and fluctuations (continuous line, left y axis) at 850 μm.

The LDP model did not address the spatial distribution problem due to the lack of constraints at the time it was built. This is still mostly the case at the time of writing this work. The simulations by Dole et al. (2003) did not implement any correlation between IR galaxies and used an uncorrelated random distribution. However, since future experiments such as Herschel and Planck will be able to detect large-scale IR galaxy correlations ($\ell \lesssim 1000$), a model addressing this problem has become necessary. Herschel, with its high angular resolution, is expected to also probe correlations between galaxies in the same dark-matter haloes but in this study this correlation has not been considered for simplicity. We only consider the linear clustering i.e. IR galaxies as biased tracers of the dark matter haloes, with a linear relation between the dark-matter density-field fluctuations and IR emissivity.

We follow the prescription from Knox et al. (2001). The angular power spectrum that characterises the spatial distribution of the fluctuations of the CIB can be written as

$$C_l^\nu = \int \frac{\mathrm{d}z}{r^2}\frac{\mathrm{d}r}{\mathrm{d}z}a^2(z)\bar{j}_\mathrm{d}^2(\nu,z)b^2(k,\nu,z)P_M(k)|_{k=l/r}G^2(z). \quad (2)$$

In the equation several components can be identified, starting with a geometrical one $\frac{\mathrm{d}z}{r^2}\frac{\mathrm{d}r}{\mathrm{d}z}a^2(z)$ (these terms take all the geometrical effects into account), followed by the galaxies emissivity $\bar{j}_\mathrm{d}(\nu,z)$ already described in Sect. 2.1.2, then the bias $b(k,\nu,z)$, and finally the power spectrum of dark-matter density fluctuations today $P_M(k)|_{k=l/r}$ and the linear theory growth function $G^2(z)$. Finally ℓ is the angular multipole, in the Limber approximation $k = l/r$, and r the proper motion distance. The way the power spectrum has been obtained is developed in the following subsections.

2.2.1. Dark-matter power spectrum

The power spectrum of the dark-matter distribution at $z = 0$ can be written as

$$P_M(k) \propto kT^2(k) \quad (3)$$

where $T(k,t)$ is the transfer function for a cold dark-matter universe (Bardeen et al. 1986). The linear theory growth function $G(z)$ writes as

$$G^2(z) = \frac{g^2(\Omega(z),\Omega_\Lambda(z))}{g^2(\Omega_0,\Omega_{\Lambda 0})(1+z)^2} \quad (4)$$

with

$$g[\Omega(z),\Omega_\Lambda(z)] = \frac{5}{2}\Omega(z)\times\left[\Omega(z)^{4/7}-\Omega_\Lambda(z) + \left(1+\frac{1}{2}\Omega(z)\right)\left(1+\frac{1}{70}\Omega_\Lambda(z)\right)\right]^{-1}.$$

And $\Omega_\Lambda(z) = \frac{1-\Omega_0}{\Omega_0(1+z)^3+1-\Omega_0}$, $\Omega(z) = \frac{\Omega_0(1+z)^3}{\Omega_0(1+z)^3+1-\Omega_0}$.

2.2.2. Bias model

The bias of IR galaxies represents their level of correlation with the dark-matter density field. It can be expressed as a function of the spatial scale, the redshift, and the wavelength of observation. In this paper and due to lack of measurements for the bias, we consider a simplified constant bias b.

$$\frac{\delta j_\mathrm{d}(k,\nu,z)}{\bar{j}_\mathrm{d}(k,\nu,z)} = b\frac{\delta\rho(k,\nu,z)}{\bar{\rho}(k,\nu,z)}$$

where j_d is the emissivity of the IR galaxies per comoving unit volume, $\bar{j}_\mathrm{d}$ its mean level, and δj_d its fluctuations. Similarly, ρ is the dark matter density, $\bar{\rho}$ its mean value, and $\delta\rho$ is the linear-theory dark-matter density-field fluctuation.

We have better knowledge of the bias for optical and radio galaxies than for IR galaxies. Several studies have been able to measure the bias for the optical sources. As an example, a high bias ($b \sim 3$) has been found at $z \sim 3$ for the Lyman-Break Galaxies (Steidel et al. 1998; Giavalisco et al. 1998; Adelberger et al. 1998). It has been found as well that the bias increases with redshift both for the optical (Marinoni et al. 2006) and the radio (Brand et al. 2003) populations. The optical or radio bias could be misleading as a first guess for the bias of IR galaxies. IRAS has measured a low bias of IR galaxies at $z \sim 0$ (e.g. Saunders et al. 1992). Such a low bias is expected since the starburst activity in the massive dark-matter haloes in the local universe is very small. But we expect a higher IR bias at higher z, during the epoch of formation of galaxy clusters. Indeed, Lagache et al. (2007) report the first measurements of the bias, $b \sim 1.7$ in the CIB fluctuations at 160 μm using Spitzer data. The LDP model indicates that galaxies dominating the 160 μm anisotropies are at $z \sim 1$. This implies that infrared galaxies at high redshifts are biased tracers of mass, unlike in the local Universe. For an extensive review of the bias problem see Lahav & Suto (2004).

The IR bias could have very complex functional dependences, namely with the spatial frequency k, the redshift z, and the radiation frequency ν (for example if different populations of galaxies with different SEDs have different spatial distributions). However, for the simulations, simplified guesses for the bias were used, namely a constant bias of 1.5, 0.75, and 0.

Figures 4 show the angular power spectrum C_l for some Herschel and Planck wavelengths. The power spectra are shown for a constant bias $b = 1$. Since $C_\ell \propto b^2$, the predicted power spectrum scales as b^2.

2.3. Discussion and implications of the model

The IR galaxy SED peaks near 80 μm. This combines with the Doppler shift and causes observations at different wavelengths to probe different redshifts. Figure 5 shows the contributions to the power spectrum at $l = 1000$ for different redshifts, normalized to unity. The contributions to the same ℓ come from higher redshift as wavelengths increase. The shorter wavelengths probe

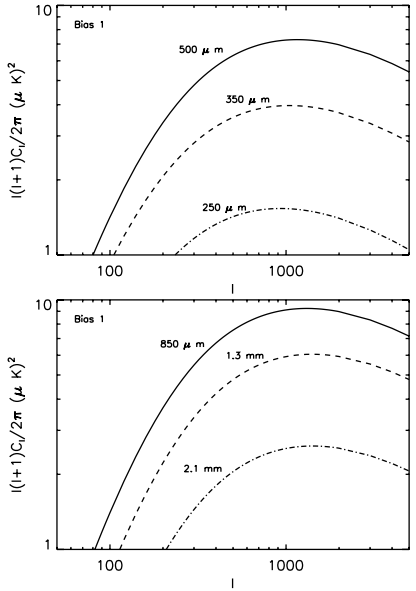

Fig. 4. *Top*: CIB Power spectrum with a bias $b = 1$ at Herschel/SPIRE wavelengths 500 μm (continuous line), 350 μm (dashed line), and 250 μm (dotted-dashed line). *Bottom*: CIB Power spectrum with a bias $b = 1$ at Planck/HFI CIB wavelengths 850 μm (continuous line), 1380 μm (dashed line), and 2097 μm (dotted-dashed line).

the lower redshifts because they are close to the maximum of the SED, while the longer wavelengths probe the higher redshifts due to the strong negative K-correction.

Figures 7 and 6 show the redshift contributions to the intensity of the CIB and to its integrated rms fluctuations for Planck/HFI and Herschel/SPIRE, assuming sources with $S > S_\mathrm{det}$ have been removed – S_det corresponds to the source detection thresholds computed in Sect. 4.3. We see that the fluctuations and the FIRB are dominated by sources at the same redshift. Therefore, studying the fluctuations at different wavelengths will allow us to study the spatial distribution of the sources forming the FIRB at different redshifts.

The amount of fluctuations that come from sources at redshifts lower than 0.25 for the Planck/HFI case at 350 μm is noticeable from Fig. 7. This contrasts with the Herschel/SPIRE predictions where the bulk of the low-z sources contributing to the fluctuations in the Planck case are resolved. These individual detections with Herschel/SPIRE could allow their subtraction in the Planck maps. A similar approach could be used between the Herschel 500 μm and the Planck 550 μm channels, although it is more marginal. Using information on the fluctuations at shorter wavelengths to remove the low-z fluctuations from longer wavelength maps could be another approach to studying the fluctuations at high redshifts directly.

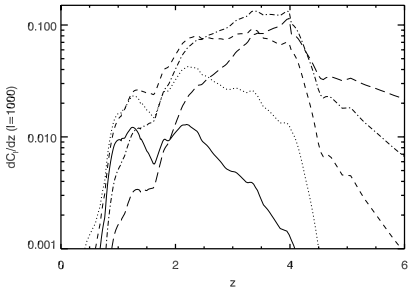

Fig. 5. Redshift contributions to the angular power spectrum $\frac{dC_l}{dz}$ at $\ell = 1000$ in μK^2 for different wavelengths: 250 μm (continuous line), 350 μm (dotted line), 550 μm (dashed line), 850 μm (dotted-dashed line), and 1380 μm (long dashed line).

A similar model has been developed by HK and revisited by Knox et al. (2001). We compare the HK and our C_l prediction at 850 μm in Fig. 8 (for the comparison, the same bias and σ_8 is used). Our model is 2 times higher mainly due to our higher prediction for the IR galaxy emissivity. Similar results are found for other wavelengths.

3. The simulations

The simulations were computed by an IDL program that calculates the dark-matter power spectrum and spreads the galaxies in the map according to their correlation with the dark-matter density field. The CIB power spectrum is calculated as explained in Sect. 2.

To create the maps, two assumptions were made: first that all the galaxies share the same spatial distribution independently of their luminosities; second that both IR and normal galaxies share the same spatial distribution. This second assumption was made to avoid too many free parameters in the simulations, the contributions of both populations being well separated in redshift this assumption is a weak one.

The process for the creation of a virtual catalog can be summarised as follows. For a given wavelength, we create the map as a superposition of maps at different redshifts from $z = 0$ to $z = 6$. The separation in redshift slices decorrelates the emission from very distant regions of the modelled volume of the universe. In order to do so, we divided the maps in slices covering $dz = 0.1$. We can see the size of these slices for different redshifts in Table 1. For all redshift ranges the size of the slices is bigger than the measured comoving correlation lengths (for all populations of galaxies). We then construct a brightness map for each redshift slice by adding: 1) a constant map with the mean surface brightness predicted by the LDP model for that z slice, 2) a map of the fluctuations for the given bias predicted by our spatial distribution model for that z slice. The fluctuations are not correlated between z slices. The brightness map is then converted into flux map. At each luminosity, this can be converted into maps of numbers of sources. These numbers of sources are then redistributed into smaller z slices (inside the 0.1 slice) to refine the luminosity/flux relation. Note that all sources have the same underlying low frequency spatial distribution (but not the same positions) per $dz = 0.1$ slice. The position, luminosity, type (normal or starburst) and redshift of all sources are stored in a catalog. Since we know these four parameters for all the sources, we can now create maps of the sky at any given wavelength. To simulate the observations, the map is convolved with the point spread function (PSF) of the chosen instrument.

For the purpose of this paper we have created Planck/HFI maps at 350, 550, 850, 1380 and 2097 microns and Herschel/SPIRE maps at 250, 350 and 500 microns. A description of the wavelengths and spatial resolution of the maps

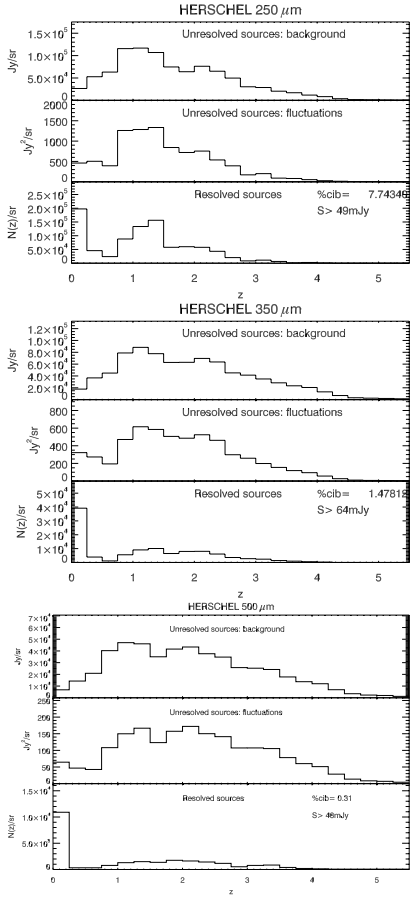

Fig. 6. Redshift contribution to the FIRB (*top panels*) and its fluctuations (*middle panels*). Also shown are the redshift distributions of the detected sources (*bottom panels*) for a typical large Herschel/SPIRE deep survey (see Sect. 4.3). *From top to bottom*: 250 μm, 350 μm and 500 μm.

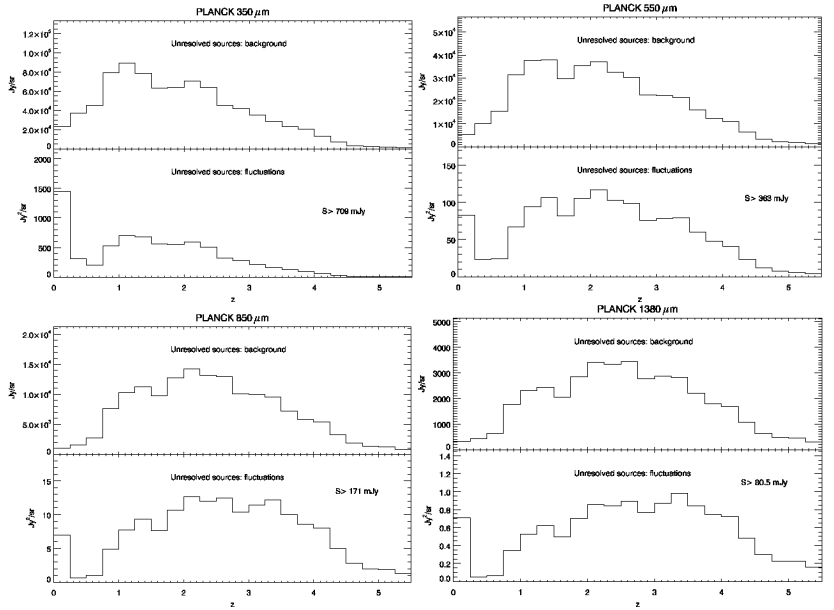

Fig. 7. Redshift contribution to the FIRB (*top panels*) and its fluctuations (*bottom panels*) for a Planck simulation ($dz = 0.25$) at 350 μm (*top-left figure*), 550 μm (*top-right figure*), 850 μm (*bottom-left figure*), 1380 μm (*bottom-right figure*). The plots are for simulations with $b = 1.5$, which sets the detection limit (see Sect. 4.3).

are given in Table 2. Three different biases were used for the simulations ($b = 0, 0.75, 1.5$). Examples of maps at 500 μm (Herschel) and 550 μm (Planck) made with $b = 1.5$ and $b = 0$ are shown in Figs. 9 and 10. The difference in the spatial correlations is easily noticed in the Planck simulations. On the other hand, the smaller size of the Herschel simulations makes it more difficult to see the correlation.

The simulated maps and their associated catalogs are publicly available at `http://www.ias.u-psud.fr/irgalaxies/simulations.php`

4. Noise and source detection

The simulations can be used to test the detection capabilities of Planck/HFI and Herschel/SPIRE. For the first time these simulations use an empirical model that reproduces all the observational constraints from 5 μm to 1.3 mm and include the spatial correlation between the IR galaxies and the dark matter density field for galaxies up to very low luminosities ($L > 10^9\ L_\odot$). They provide a useful tool for preparing future observations with Planck/HFI and Herschel/SPIRE.

4.1. Detection of bright sources

As stated previously bright sources dominate the power spectrum of the FIRB (see Fig. 3). We therefore need to subtract them before studying the fluctuations in the background. In this section we concentrate on detecting them in three steps: 1) wavelet filtering, 2) detection, 3) measurement of the flux.

– Wavelet filtering: before trying to detect the sources we perform a wavelet transform of our simulated maps with the "atrou" algorithm. We remove spatial frequencies that are both higher and lower than the *FWHM* of the PSF.
The small-scale filtering improves the estimation of the position of the sources when the instrumental noise is included in the simulations. In contrast to the confusion noise, the instrumental noise is not correlated for neighbouring pixels. This dominates errors in estimating the position of the sources.
The large-scale filtering corrects for a bias in the detection algorithm. The algorithm searches for sources using the absolute value of the pixel and not its value relative to its environment. This biases the detections towards sources in bright regions. The removal of the large spatial fluctuations corrects this effect.
The selection of spatial frequencies to be used for the detection has been manually optimised for each map to achieve a maximum number of reliable detections. This treatment is similar to what was done in the MIPS Spitzer maps (Dole et al. 2004). A comprehensive study of the application of the wavelet filtering technique for the source detections at long wavelengths for Planck and Herschel/SPIRE is beyond

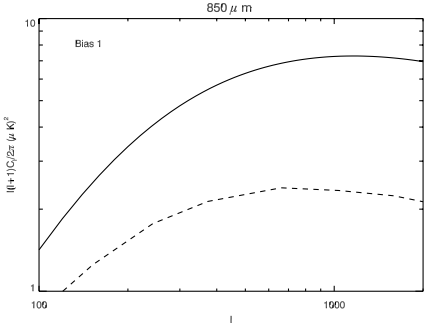

Fig. 8. Our power spectrum at 850 μm (continuous line) and that of Haiman & Knox (2000) (dashed line). The differences between both models arise from the differences in the emissivities (see Fig. 1). The lower level of the HK power spectrum comes from their lower emissivities. The emissivities of HK are at lower z and therefore favour larger angular scales for the power spectrum relative to our model.

Table 1. Physical size of the redshift slice $dz = 0.1$ (in Mpc) for different z.

z	1.0–1.1	2.0–2.1	3.0–3.1	4.0–4.1
$R_{dz=0.1}$ (Mpc)	233	139	93	67

Table 2. *FWHM* of the PSF for different wavelengths of observation (in arc seconds) for all the simulated maps.

Wavelengths (μm)	350	550	850	1380	2097
Planck HFI *FWHM* ($''$)	300	300	300	330	480
Wavelengths (μm)	250	350	550		
Herschel SPIRE *FWHM* ($''$)	17	24	35		

the scope of this paper and has been fully discussed in e.g. López-Caniego et al. (2006).

- Detection algorithm: the algorithm is based on the "find" routine of the DAOPHOT library. In the filtered image the algorithm searches for peaks higher than a certain threshold $\sigma_{\rm thres}$. It uses the PSF shape and the neighbouring pixels to analyse whether the peak is the centre of a source.
- Flux measurement: we developed a PSF fitting algorithm that we used in the original map (without filtering) to measure the flux of the sources. We decided whether the detections are real or false by two criteria: 1) proximity and 2) accuracy (see Sect. 4.1.1).

4.1.1. Bad detections

A detection is considered good or bad based on two criteria: 1) proximity with the position of an input source and 2) accuracy of flux for this source. The former requires that our detection is closer than *FWHM*/5 to at least one "neighbour" source in our catalog. The latter requires that the difference between the flux of one of the "neighbour" sources in the catalog and that of the detected source has to be smaller than the confusion and/or instrumental noise (see Tables 4 and 5). We consider the detection to be good only if both criteria are satisfied.

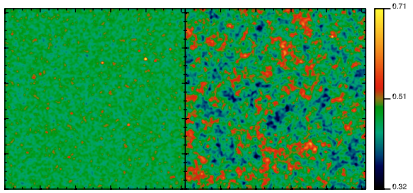

Fig. 9. Planck maps at 550 μm in MJy/sr with $b = 0$ (*left*) and $b = 1.5$ (*right*). The maps simulate a region of the sky of 49 square degrees with 1024 pixels of 25 arcsec.

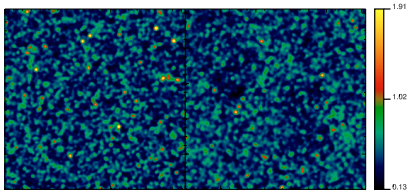

Fig. 10. Herschel maps at 500 μm in MJy/sr with $b = 0$ (*left*) and $b = 1.5$ (*right*). The maps simulate a region of the sky of 0.3 square degrees with 1024 pixels of 2 arcsec. The small size of the maps makes it difficult to appreciate the effect of the large-scale clustering.

The detection process also produces detections that do not comply with these criteria. We can see in Fig. 12 how the different $\sigma_{\rm thres}$ modify the rate of good-to-bad detections. For a low detection threshold ($\sigma_{\rm thres} = 2\sigma_{\rm map}$, i.e. for example 290 mJy/pix at Planck 350 μm for a map with $b = 0$ and no instrumental noise), the number of bad detections can become bigger than that of real detections. For a higher detection threshold ($\sigma_{\rm thres} = 3\sigma_{\rm map}$ i.e. 440 mJy/pix at 350 μm), we find that the good detections dominate the bad ones, but we do not detect as many faint sources. Thus the number of false detections depends strongly on $\sigma_{\rm thres}$. For different scientific goals, it can be interesting to use different $\sigma_{\rm thres}$. For example, if we are interested in searching for objects at high redshifts, we could allow our detections to have 25% bad sources to be able to detect some interesting sources at high z. For studies of statistical properties of the sources, it would be necessary to use a stronger threshold. For our purpose, we used $\sigma_{\rm thres} = 3\sigma_{\rm map}$ (∼10% of false detections).

4.2. Instrumental and confusion noises

Instrumental and confusion noises have been studied both separately and in combination in order to quantify their relative contribution to the total noise. The estimated instrumental noises per beam for Planck and Herschel are given in Table 3. The instrumental noise per beam for Planck is the average one over the sky for a 1-year mission. The instrumental noise per beam for Herschel is typical of large surveys. We take the sensitivity of the so-called level 5 and level 6 of the Science Activity Group 1 (SAG 1) of the SPIRE guaranteed time team.

We studied the standard deviation of the measured fluxes in random positions for different maps. These maps were one of instrumental noise, three with different bias ($b = 0$, 0.75, 1.5)

Table 3. Simulation input instrumental noise per pixel of size equal to beam for Planck and for Herschel for a deep and a shallow survey.

Wavelengths HFI (μm)	350	550	850	1380	2097
$\sigma_{\rm Inst}$(mJy)	31.30	20.06	14.07	8.43	6.38
Wavelengths SPIRE (μm)	250	350	500		
$\sigma_{\rm Inst}$ Deep (mJy)	4.5	6.1	5.3		
$\sigma_{\rm Inst}$ Shallow (mJy)	7.8	10.5	9.2		

Table 4. Noise on the retrieved sources with only instrumental noise ($\sigma_{\rm I}$), confusion noise ($\sigma_{\rm C}$), and total noise ($\sigma_{\rm C+I}$) in mJy for Planck/HFI.

Wavelengths HFI (μm)	350	550	850	1380	2097
$\sigma_{\rm I}$	61.3	39.2	27.8	16.7	12.5
$\sigma_{\rm C}$ $b = 0$	111.5	41.5	14.7	4.6	2.1
$\sigma_{\rm C}$ $b = 0.75$	124	54.3	21.3	7.7	3.5
$\sigma_{\rm C}$ $b = 1.5$	158	79.8	30.4	10.9	5.4
$\sigma_{\rm C+I}$ $b = 0$	126.7	62.3	33	17.4	13.2
$\sigma_{\rm C+I}$ $b = 0.75$	153.6	75.3	38.4	19	13.8
$\sigma_{\rm C+I}$ $b = 1.5$	188.2	95.3	46.7	21.1	14.4

Table 5. Instrumental noise ($\sigma_{\rm I}$), confusion noise ($\sigma_{\rm C}$) and total noise ($\sigma_{\rm C+I}$) in mJy for Herschel/SPIRE.

Wavelengths SPIRE (μm)	250	350	500
Deep $\sigma_{\rm I}$	8.7	11.3	10.1
Shallow $\sigma_{\rm I}$	15	20.1	18.2
$\sigma_{\rm C}$ $b = 0$, 0.75, 1.5	4.6	6.5	5.5
Deep $\sigma_{\rm C+I}$	9.8	12.3	11
Shallow $\sigma_{\rm C+I}$	16	20.8	19

but without instrumental noise, and complete maps created by adding the map of instrumental noise to the three source maps. We call these maps hereafter instrumental-only, confusion-only, and complete-maps. We fit a Gaussian to the histogram of the fluxes measured in these random positions and considered the standard deviation of this Gaussian as the best estimate of the standard deviation of the photometry of a source and therefore of the 1σ instrumental, confusion, and total noise. Results are shown in Tables 4 and 5.

The confusion noise increases with the bias. This effect is noticeable for the Planck observations, but not for the Herschel ones because of the higher Herschel/SPIRE angular resolution. Also, for the considered Herschel/SPIRE surveys, the instrumental noise is always greater than the confusion noise. For Planck the correlation effect is more noticeable for longer wavelengths since they probe progressively higher redshifts and therefore higher dark-matter power spectra, as discussed in Sect. 2.3 (see Fig. 5).

The total noise $\sigma_{\rm C+I}$ is close to the value $\sigma^2_{\rm C+I} = \sigma^2_{\rm C} + \sigma^2_{\rm I}$ (see Tables 4 and 5). For Planck at short wavelengths (350 μm and 550 μm), the confusion noise is the dominant source of noise. The instrumental noise becomes dominant at 850 μm for $b = 0$ and $b = 0.75$. For longer wavelengths, it dominates for any bias. For Herschel the instrumental noise dominates the total noise for both the shallow and deep surveys. The confusion noise is not strongly affected by the bias because of the small *FWHM* of the PSF.

4.3. Completeness

The first study of the point-sources detection limit for Planck was carried out based on a generalisation of the Wiener filtering method (Bouchet & Gispert 1999). Recently López-Caniego et al. (2006) used the most recent available templates of the microwave sky and extragalactic point source simulations, including both the radio and IR galaxies, to estimate the Planck detection limits. Here we revisit those results with new models for IR galaxies and the last noise estimates for Planck/HFI and Herschel/SPIRE.

For the study of the completeness, a number $N_{\rm A}$ of sources of equal flux are randomly distributed in the maps. Each source is placed far enough from the other to avoid these additional sources contributing to the confusion noise. The detection and photometry of these sources is carried out as described at the beginning of the section. We call $N_{\rm G}$ the number of good detections that comply with the "proximity" and "accuracy" criteria. The completeness for this flux $C_{\rm F}$ is then calculated as $C_{\rm F} = \frac{N_{\rm G}}{N_{\rm A}} \times 100$. The completeness of the detections of sources for a given flux depends on both the instrumental noise and the confusion noises. The results for the completeness are averaged over ∼3000 individual fake sources per flux. An example of the completness at 350 μm is shown in Fig. 11. Results for all wavelengths are given in Tables 6 and 7. They are consistent with the instrumental, confusion, and total noises given in Sect. 4.2 and the conclusions from that section remain valid for the completeness. For simulated maps including both extragalactic sources and instrumental noise, we find that the 80% completeness level coincide with flux limits around $4-5\sigma$.

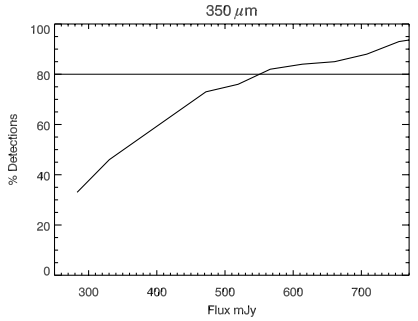

Fig. 11. Study of completeness for Planck/HFI with $b = 0$ at 350 μm. The horizontal straight line marks 80% of completeness.

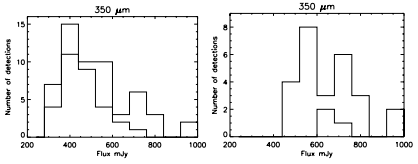

Fig. 12. Good detections (thick line) vs. bad detections (thin line) *Left*: histogram of good and bad detections using small $\sigma_{\rm thres}$ (290 mJy). *Right*: histogram of good and bad detections using higher $\sigma_{\rm thres}$ (440 mJy) in the same map. Both plots have been done using a Planck simulated map with $b = 0$.

Table 6. Completeness limits (in mJy) for the Planck/HFI maps with instrumental noise ($C_{\rm I}$), confusion noise ($C_{\rm C}$) and both ($C_{\rm C+I}$). We consider b = 0, 0.75, and 1.5.

Wavelengths HFI (μm)	350	550	850	1380	2097
$C_{\rm I}$ = 80%	236	157	108	67	50
$C_{\rm C}$ = 80% b = 0	516	174	60.5	20	8.6
$C_{\rm C}$ = 80% b = 0.75	550	239.5	88.5	30.5	15.5
$C_{\rm C}$ = 80% b = 1.5	684	300	121	40	24
$C_{\rm C+I}$ = 80% b = 0	560	234	126	71	52
$C_{\rm C+I}$ = 80% b = 0.75	607	290	141	74	55
$C_{\rm C+I}$ = 80% b = 1.5	709	360	171	80	58.5

Table 7. Completeness limits (in mJy) for the Herschel/SPIRE maps with instrumental noise ($C_{\rm I}$), confusion noise ($C_{\rm C}$), and both ($C_{\rm C+I}$).

Wavelengths SPIRE (μm)	250	350	500
Deep $C_{\rm I}$ = 80%	33	45.9	37.9
Shallow $C_{\rm I}$ = 80%	57.3	84.2	67.3
$C_{\rm C}$ = 80%	35	32	27.4
Deep $C_{\rm C+I}$ = 80%	49.8	64.4	48.4
Shallow $C_{\rm C+I}$ = 80%	70	96.5	75.5

Taking these 80% completness limits as a detection threshold, the prediciton for the number of sources detected directly by Herschel/SPIRE for the deeper survey considered here is 8.3×10^5/sr at 250 μm, 1.1×10^5/sr at 350 μm, and 1.8×10^4/sr at 500 μm. The fraction of resolved CFIRB varies between 8 and 0.3% from 250 to 500 μm.

5. CIB fluctuations

The Planck and Herschel/SPIRE surveys allow an unprecedented search for CFIRB fluctuations associated with large-scale structure and galaxy clustering. Background fluctuations probe the physics of galaxy clustering over an ensemble of sources, with the bulk of the signal contribution originating from sources well below the detection threshold. Thus a comprehensive fluctuation analysis is an essential complement to the study of individually detected galaxies. In this section, we restrict ourselves to predictions for Planck/HFI, excluding the 143 and 100 GHz channels. At these low frequencies, we are dominating by the non-thermal emission of the radiosources – that are not including in our model – and the Poisson term dominates the clustering term (e.g. González-Nuevo et al. 2005). Also, we exclude the Herschel/SPIRE case since our simulations include the clustering of CIB sources in two different halos (2h), but not the clustering within the same halo (1h). The 1h term dominates for $\ell \gtrsim 3000$ and will be accurately measured by Herschel/SPIRE. Only large-scale surveys can put strong constraints on the 2h term. Measuring the 2h clustering with CFIRB anisotropies is one of the goals of Planck/HFI.

5.1. Contributors to the angular power spectrum

From the far-IR to the millimeter, the sky is made up of the CFIRB and two other sources of signal, the galactic cirrus and the CMB (we neglect the SZ signal). Understanding our observations of the CFIRB requires understanding the contributions from these two components which act for us as foreground and background contamination.

The galactic cirrus acts as foreground noise for the CFIRB. The non-white and non-Gaussian statistical properties of its emission make it a very complex foreground component. The power spectrum of the IRAS 100 μm emission is characterised by a power law Gautier et al. (e.g. 1992). Here we compute the angular power spectrum of the dust emission following Miville-Deschenes et al. (2007). These authors analysed the statistical properties of the cirrus emission at 100 μm using the IRAS/IRIS data. We used their power spectrum normalization and slope (varying with the mean dust intensity at 100 μm). Using the average $|b| > 30°$ spectrum of the HI-correlated dust emission measured using FIRAS data, we converted the 100 μm power spectra to the Planck wavelengths. For the discussion, we considered both the total cirrus fluctuations and 10% residual fluctuations. These 10% could be achievable with Planck in low dust-column-density regions containing ancillary HI data.

The CMB acts as background noise for the CFIRB. However, the CMB angular power spectrum is known to an accuracy of 1% or better (Planck-HFI web site: http://www.planck.fr/). This combines with its well-known spectral dependence to allow for a clean subtraction of its contribution that in turn allows for detections of the CFIRB $C_{\rm l}$ even for wavelengths where the CMB dominates. We consider for the rest of the discussion a conservative assumption, that is that the residual CMB fluctuations are approximately 2%.

The angular power spectrum of IR galaxies is composed of a correlated and a Poissonian part. As discussed in Sect. 2.1, the contribution to the Poissonian part is dominated by relatively faint sources after subtracting the brightest galaxies (see Fig. 3). We consider that we can remove sources brighter than our 80% completeness detection limit (see Tables 6 and 7). For doing so, we use the technique described in Sect. 4.1 for measuring the position and fluxes of the sources and once these are known we subtract a PSF with the measured flux from the map.

The correlated $C_{\rm l}$ is obtained as described in Sect. 2.1. For the relative error on the power spectrum, we follow Knox (1995):

$$\frac{\delta C_{\rm l}}{C_{\rm l}} = \left(\frac{4\pi}{A}\right)^{0.5} \left(\frac{2}{2l+1}\right)^{0.5} \left(1 + \frac{A\sigma_{\rm pix}^2}{NC_{\rm l}W_{\rm l}}\right)$$

where A is the observed area, $\sigma_{\rm pix}$ the rms noise per pixel (instrumental plus confusion), N the number of pixels, and $W_{\rm l}$ the window function for a map made with a Gaussian beam $W_{\rm l} = {\rm e}^{-l^2\sigma_{\rm b}^2}$.

5.2. Detectability of CFIRB correlated anisotropies

The study of the $C_{\rm l}$ on different scales allows us to study different aspects of the physics of the environment of IR galaxies (see Cooray & Sheth 2002). Large scales ($l < 100$) give information on the cosmological evolution of primordial density fluctuations in the linear phase and therefore on the cosmological parameters. Intermediate scales are mostly influenced by the mass of dark halos hosting sources, which determines the bias parameter. Small scales ($l > 3000$) probe the distribution of sources in the dark-matter halos and therefore the non-linear evolution of the structures. This non linear evolution was not accounted for in our model.

We can see in Fig. 13 the different contributions to the $C_{\rm l}$ for Planck/HFI: the correlated CFIRB $C_{\rm l}$ with b = 1 and b = 3 with their respective error bars ($\Delta\ell/\ell$ = 0.5), Poissonian fluctuations, dust, and CMB contributions. The dust and CMB $C_{\rm l}$ are plotted both before and after implementing the corrections discussed above (10% and 2% residuals, respectively). For the dust we selected for the estimation of the column density a field centred on the SWIRE/ELAIS S1 field. This field has a very low level of dust contamination. For a 400 sq. deg. area centred at $(l, b) = (311°, -73°)$, we have an average HI column density of only 1.5×10^{20} at/cm^2. We also take the whole sky above $|b| > 40°$ (~150 000). The average HI column density is 2.7×10^{20} at/cm^2.

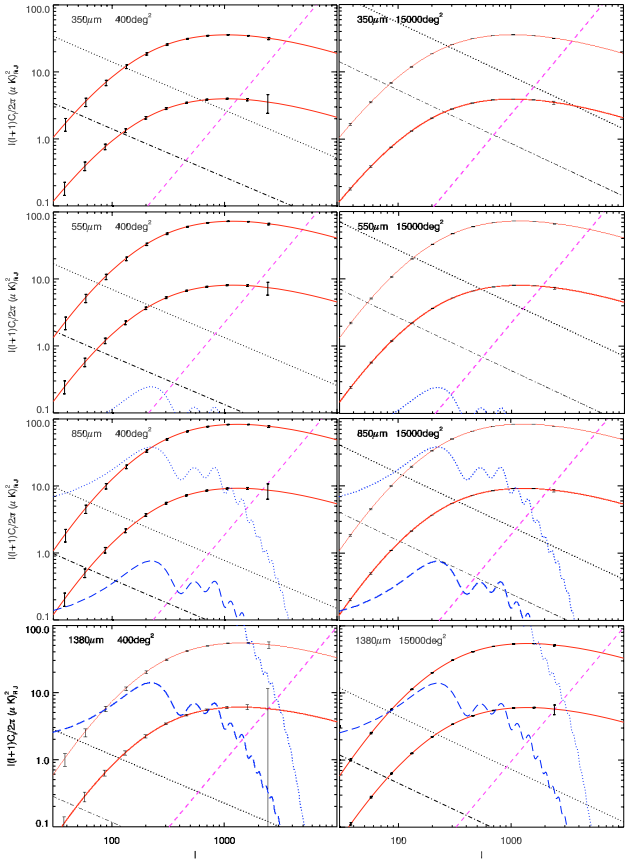

Fig. 13. Power spectra for Planck of the correlated IR galaxies with b = 1 (thick continuous line) and b = 3 (thin continuous line), Poisson fluctuations for sources fainter than 709, 363, 171, 80 mJy at 350, 550, 850 and 1380 μm respectively (short dashed line), dust with an HI column density of 1.5×10^{20} at/cm^2 and 2.7×10^{20} at/cm^2 for the 400 Sq. Deg. and ~15 000 Sq. Deg. considered regions respectively (dotted line), dust/10 (dotted-dashed line), CMB (dotted line) and CMB/50 (dashed line). Error bars are computed using $\Delta\ell/\ell = 0.5$.

At all wavelengths, the correlated CFIRB $C_{\rm l}$ is dominated by the other components on both very large and very small scales. The angular frequencies where the $C_{\rm l}$ is dominated by the galaxy correlation depends mainly on the wavelength, if the bias and cirrus level are fixed. On large scales the $C_{\rm l}^{\rm CFIRB}$ is dominated by the dust for wavelengths up to 550 μm, and for longer wavelengths it is dominated by the CMB. On small scales the Poissonian fluctuations dominate the power spectra.

We can see in Tables 8 and 9 the ranges for which CFIRB-correlated anisotropies are dominating depending on whether we consider a partial subtraction of the cirrus and CMB or not. On small angular scales (large ℓ), the range of ℓ where the correlated $C_{\rm l}$ dominates increases with the wavelength. On large angular scales (small ℓ), the results depend on whether we consider partial subtraction of the cirrus and CMB or not.

Table 8 shows the ℓ ranges for where CFIRB correlated anisotropies are dominating when no subtraction of the dust or CMB has been performed. At large angular scales and wavelengths up to 850 μm the detectability is better for the small map

Table 8. Multipole ℓ ranges where the CFIRB correlated anisotropies are higher than the cirrus and CMB components.

Wavelengths (μm)	350	550	850	1380
400 Sq. Deg. $b = 1$	$600 < \ell < 1200$	$200 < \ell < 1800$	$1000 < \ell < 2200$	Indetectable
400 Sq. Deg. $b = 3$	$120 < \ell < 3500$	$75 < \ell < 5000$	$240 < \ell < 6000$	$1800 < \ell < 6500$
15 000 Sq. Deg. $b = 1$	Indetectable	$550 < \ell < 1800$	$1200 < \ell < 2200$	Indetectable
15 000 Sq. Deg. $b = 3$	$280 < \ell < 3500$	$130 < \ell < 5000$	$230 < \ell < 6000$	$1800 < \ell < 6500$

Table 9. Multipole ℓ ranges where the CFIRB correlated anisotropies are higher than the residual cirrus and CMB components (10%, and 2% respectively).

Wavelengths (μm)	350	550	850	1380
400 Sq. Deg. $b = 1$	$200 < l < 1200$	$80 < l < 2100$	$60 < l < 2200$	Indetectable
400 Sq. Deg. $b = 3$	$40 < l < 3500$	$30 < l < 5000$	$25 < l < 6000$	$80 < l < 6500$
15 000 Sq. Deg. $b = 1$	$250 < l < 1200$	$130 < l < 1800$	$100 < l < 2200$	Indetectable
15 000 Sq. Deg. $b = 3$	$80 < l < 3500$	$55 < l < 5000$	$45 < l < 6000$	$80 < l < 6500$

because of its lower N(HI) column density. Without any dust contamination correction, this prevents us from taking advantage from the smaller errror on the estimation of the C_l in the very large area surveys and makes both kind of observation complementary. In clean regions of the sky, the best wavelengths for the observation of the large scales CFIRB anisotropies are 350 μm and 550 μm.

The large-scale detectability drastically improves in the case of partial subtraction of the CMB and dust cirrus as seen in Table 9. As discussed above we expect to be able to subtract the dust fluctuations and the CMB to a 10% and 2% of their original level. This does not change our ability to measure the correlated CFIRB C_l on small scales (due to the high confusion noise), but will allow us to probe larger scales.

6. Summary

This paper presented new simulations of the cosmic infrared and submillimeter background. The simulations are based on an empirical model of IR galaxy evolution (the LDP model) combined with a simple description of the correlation. The IR galaxy spatial distribution follows that of the dark-matter halo density field, with a bias parameter accounting for the possibility of the luminous matter being more or less correlated with the dark matter. The simulated maps and their catalogs are publicly available at http://www.ias.u-psud.fr/irgalaxies/simulations.php. Other maps are available upon request. These maps are intended to be a useful tool for planning future large IR and submillimeter surveys. In this paper, we used the maps to predict the confusion noise and completeness levels for Planck/HFI and Herschel/SPIRE. We also predicted the power spectra of correlated CFIRB anisotropies for Planck/HFI which will be a major advance in the study of the CFIRB anisotropies at large scales (i.e. $\ell <$ 2000−5000 depending on the wavelengths). Further analysis of the CFIRB anisotropies, including the use of stacking analysis to isolate the anisotropies in different redshift ranges, will be presented in a second paper, now in preparation.

References

Adelberger, K. L., Steidel, C. C., Giavalisco, M., et al. 1998, ApJ, 505, 18
Bardeen, J. M., Bond, J. R., Kaiser, N., & Szalay, A. S. 1986, ApJ, 304, 15
Bertoldi, F., Menten, K. M., Kreysa, E., Carilli, C. L., & Owen, F. 2000, ArXiv Astrophysics e-prints
Blain, A. W., Chapman, S. C., Smail, I., & Ivison, R. 2004, ApJ, 611, 725
Bouchet, F. R., & Gispert, R. 1999, New Astron., 4, 443
Brand, K., Rawlings, S., Hill, G. J., & Lacy, M. 2003, New Astron. Rev., 47, 325
Cooray, A., & Sheth, R. 2002, Phys. Rep., 372, 1
Dole, H., Gispert, R., Lagache, G., et al. 2001, A&A, 372, 364
Dole, H., Lagache, G., & Puget, J.-L. 2003, ApJ, 585, 617
Dole, H., Le Floc'h, E., Pérez-González, P. G., et al. 2004, ApJS, 154, 87
Dole, H., Lagache, G., Puget, J.-L., et al. 2006, A&A, 451, 417
Dye, S., Eales, S. A., Ashby, M. L. N., et al. 2006, ApJ, 644, 769
Elbaz, D., Cesarsky, C. J., Chanial, P., et al. 2002, A&A, 384, 848
Elbaz, D. 2005, Space Sci. Rev., 119, 93
Farrah, D., Lonsdale, C. J., Borys, C., et al. 2006, ApJ, 641, L17
Fixsen, D. J., Dwek, E., Mather, J. C., Bennett, C. L., & Shafer, R. A. 1998, ApJ, 508, 123
Gautier, III, T. N., Boulanger, F., Perault, M., & Puget, J. L. 1992, AJ, 103, 1313
Genzel, R., & Cesarsky, C. J. 2000, ARA&A, 38, 761
Giavalisco, M., Steidel, C. C., Adelberger, K. L., et al. 1998, ApJ, 503, 543
González-Nuevo, J., Toffolatti, L., & Argüeso, F. 2005, ApJ, 621, 1
Grossan, B., & Smoot, G. F. 2007, A&A, 474, 731
Haiman, Z., & Knox, L. 2000, ApJ, 530, 124
Hauser, M. G., Arendt, R. G., Kelsall, T., et al. 1998, ApJ, 508, 25
Holland, W. S., Cunningham, C. R., Gear, W. K., et al. 1998, ArXiv Astrophysics e-prints
Knox, L., Cooray, A., Eisenstein, D., & Haiman, Z. 2001, ApJ, 550, 7
Knox, L. 1995, Phys. Rev. D, 52, 4307
Lagache, G., & Puget, J. L. 2000, A&A, 355, 17
Lagache, G., Dole, H., & Puget, J.-L. 2003, MNRAS, 338, 555
Lagache, G., Dole, H., Puget, J.-L., et al. 2004, ApJS, 154, 112
Lagache, G., Puget, J.-L., & Dole, H. 2005, ARA&A, 43, 727
Lagache, G., Bavouzet, N., Fernandez-Conde, N., et al. 2007, ApJ, 665, L89
Lahav, O., & Suto, Y. 2004, Liv. Rev. Relativ., 7, 8
López-Caniego, M., Herranz, D., González-Nuevo, J., et al. 2006, MNRAS, 370, 2047
Magliocchetti, M., Silva, L., Lapi, A., et al. 2007, MNRAS, 375, 1121
Marinoni, C., Le Fevre, O., Meneux, B., & the VVDS team 2006, ArXiv Astrophysics e-prints
Matsuhara, H., Kawara, K., Sato, Y., et al. 2000, A&A, 361, 407
Miville-Deschênes, M.-A., Abergel, A., & Boulanger, F. 2001, Dust Evolution in the Cold and Diffuse Interstellar Medium: The Herschel Perspective, The Promise of the Herschel Space Observatory, ed. G. L. Pilbratt, J. Cernicharo, A. M. Heras, T. Prusti, & R. Harris, ESA SP-460, 471
Miville-Deschenes, M., Lagache, G., Boulanger, F., & Puget, J. 2007, ArXiv e-prints, 704
Negrello, M., Perrotta, F., Gonzalez-Nuevo Gonzalez, J., et al. 2007, ArXiv Astrophysics e-prints
Papovich, C., Dole, H., Egami, E., et al. 2004, ApJS, 154, 70
Puget, J.-L., Abergel, A., Bernard, J.-P., et al. 1996, A&A, 308, L5
Saunders, W., Rowan-Robinson, M., & Lawrence, A. 1992, MNRAS, 258, 134
Steidel, C. C., Adelberger, K. L., Dickinson, M., Giavalisco, M., & Pettini, M. 1998, ArXiv Astrophysics e-prints
Wang, W.-H., Cowie, L. L., & Barger, A. J. 2006, ApJ, 647, 74

Astronomy & Astrophysics manuscript no. 9500
July 14, 2010

Submillimeter observations of the J2142-4423 Lyα protocluster at $z = 2.38^{\star}$

A. Beelen[1], A. Omont[2], N. Bavouzet[1], A. Kovács[3], G. Lagache[1], C. De Breuck[4], A. Weiss[3], K. M. Menten[3], J. W. Colbert[5], H. Dole[1], G. Siringo[3], and E. Kreysa[3]

[1] Institut d'Astrophysique Spatiale, bât 121 - Université Paris-Sud, 91405 Orsay Cedex / France
e-mail: alexandre.beelen@ias.u-psud.fr
[2] Institut d'Astrophysique de Paris, CNRS and Université Pierre et Marie Curie, 98bis, bd Arago, 75014 Paris / France
[3] Max-Planck-Institut für Radioastronomie, Auf dem Hügel 69, 53121 Bonn / Germany
[4] European Southen Observatory, Karl Schwarzschild Straße 2, D-85748 Garching / Germany
[5] *Spitzer* Science Center, California Institute of Technology, Mail Code 220-6, Pasadena, CA 91125-0600 / USA

Received / Accepted

ABSTRACT

Aims. We present observations aimed at exploring both the nature of Lyα emitting nebulae ("Lyα blobs") at $z = 2.38$ and the way they trace large scale structure (LSS), by exploring their proximity to "maximum starbursts" through submillimeter emission. Our most important objectives are to make a census of associated submillimeter galaxies (SMGs), check their properties, and look for a possible overdensity in the protocluster J2142-4426 at $z = 2.38$.

Methods. We used the newly commissioned Large APEX Bolometer Camera (LABoCa) on the Atacama Pathfinder EXperiment (APEX) telescope, in its Science Verification phase, to carry out a deep $10' \times 10'$ map at 870 μm, and we performed multiple checks of the quality of data processing and source extraction.

Results. Our map, the first published deep image, confirms the capabilities of APEX/LABoCa as the most efficient current equipment for wide and deep submm mapping. Twenty-two sources were securely extracted with 870 μm flux densities in the range 3 – 21 mJy, rms noise $\sim$ 0.8 – 2.4 mJy, and far-IR luminosities probably in the range $\sim 5 - 20 \times 10^{12}$ L$_{\odot}$. Only one of the four 50 kpc-extended Lyα blobs has a secure 870 μm counterpart. The 870 μm source counts in the whole area are marginally higher than in the SHADES SCUBA survey, with a possible over-density around this blob. The majority of the 3.6 – 24 μm SEDs of the submillimeter sources indicate they are starburst dominated, with redshifts mostly $\gtrsim 2$. However, there is evidence of a high-z AGN in $\sim$ 30% of the sources.

Key words. galaxies: starburst – galaxies: high-redshift – submillimeter – infrared: galaxies – ultraviolet: galaxies – large-scale structure of universe

1. Introduction

Narrow-band surveys are a very powerful technique for detecting Lyman α emission from various structures at high redshift. In addition to numerous Lyα galaxies, they have revealed the existence of very extended (30 – 200 kpc) Lyα nebulae, generally called Lyα blobs (see e.g. Francis et al. 1996; Steidel et al. 2000; Palunas et al. 2004; Matsuda et al. 2007, and references therein). Currently, only about 10 blobs with diameter, $\Phi, \gtrsim 60$ kpc, are known, and twice more with $\Phi \gtrsim 50$ kpc (see e.g. Matsuda et al. 2004, 2007; Smith & Jarvis 2007, and references therein). They are generally part of larger structures of Lyα emitters of various sizes.

The origin of the Lyα emission in such blobs is still a matter of discussion. Widespread Lyα emission is known to be associated with starbursts and shocks. Multiple supernovae explosions, including galactic outflows, associated with giant starbursts, could be excellent candidates for powering Lyα emission. But accretion cooling flows (e.g. Nilsson et al. 2006; Smith & Jarvis 2007) and an obscured AGN have also been suggested as other possible power sources. Lyα blobs present many similarities with high redshift radio galaxies, which often have giant Lyα haloes up to 150 kpc (see Miley & De Breuck 2008, for a review). However, all Lyα blobs observed to date remain undetected in deep radio observations, excluding the possibility that their Lyα emission is powered by a radio-loud AGN like in the radio galaxies.Whatever is their power source, there is evidence that Lyα blobs are strong infrared emitters. For instance, most of the 35 Lyα blobs with $\Phi \gtrsim 30$ kpc identified by Matsuda et al. (2004) in the SA 22 region have been detected in deep Spitzer IRAC/MIPS observations (Yamada 2007, Huang et al. in preparation).

The 110 Mpc filament with 37 Lyα-emitting objects around the galaxy protocluster J2143-4423 at $z = 2.38$ is one of the largest known structures at high z (Palunas et al. 2004; Francis et al. 2004). In addition to its compact Lyα galaxies, it also includes four extended Lyα blobs ($\Phi \gtrsim 50$ kpc). From Spitzer/MIPS observations, Colbert et al. (2006) have reported the detection of a number of 24 μm sources associated with Lyα emitters. In a central $8' \times 10.5'$ area of the J2143-4423 region, they have detected five 24 μm sources with a 24 μm flux density, $F_{24} \gtrsim 150$ μJy, closely associated with Lyα emitters, three of them being extended Lyα blobs. The far-infrared luminosities, L_{FIR}, that they inferred, range from 0.5 to 5 10^{13} L$_{\odot}$. There

Send offprint requests to: A. Beelen

* This work is based on observations made with the APEX Telescope. APEX is a collaboration between the Max-Planck-Institut für Radioastronomie, the European Southern Observatory, and the Onsala Space Observatory.

are also three other similar 24 μm sources with a looser (within $\sim 10''$) association to the 50 kpc-Lyα blobs. [1]

Such a concentration of Lyα blobs suggests an exceptionally large structure (110 Mpc) above $z = 2$. However, neither Lyα, nor 24 μm emissions can give an unambiguous answer to the exact nature of the galaxies and their star formation properties. Submillimeter observations are fundamental to determine the far-IR luminosity of the various 24 μm sources associated with Lyα emitters, and thus their star formation rate. The SCUBA 870 μm study by Geach et al. (2005) of the similar structure SA 22 discovered by Steidel et al. (2000), with similar Lyα luminosity and a larger number of Lyα blobs (Matsuda et al. 2004), detected about 20% of the blobs (with possible statistical detection of the full sample). This could indicate that their FIR luminosity FIR luminosity is starburst powered, with FIR luminosities in the ultra-luminous regime ($> 5\,10^{12}$ L$_\odot$), equivalent to a star formation rate approaching 10^3 M$_\odot$/yr. However, the relation between the Lyα and even 24 μm emission of the blobs to their star formation rate is probably not straightforward, as shown by the surprising non-detection of the strongest (17 mJy) SA 22 SCUBA source in the high-resolution submillimeter imaging of Matsuda et al. (2007), indicating extended submm emission.

In this context, we used the newly commissioned Large Apex Bolometer Camera (LABoCa) (Siringo et al. 2007, 2008 in prep.) to check the properties of ultra-luminous starbursts in the J2143-4423 Lyα blobs and their surrounding field. The paper is organized as follows : Section 2 describes the observation with LABoCa of the central part of the z=2.38 Lyα-emitter overdensity at $\alpha = 21^h42^m43\overset{s}{.}7, \delta = -44°25'30\overset{''}{.}0$ (J2000), which was observed at 24 μm by Colbert et al. (2006), Section 3 presents our analysis and in Section 4 we discuss the results and report our conclusions. Throughout the paper, we assume a concordance Λ-cosmology with $H_0 = 71$ km s^{-1} Mpc^{-1}, $\Omega_\Lambda = 0.73$ and $\Omega_m = 0.27$.

2. Observation

2.1. LABoCa Observations

Observations were conducted using LABoCa (Siringo et al. 2007, 2008 in prep.) installed on the Atacama Pathfinder EXperiment (APEX, Güsten et al. 2006). LABoCa is an array consisting of 295 bolometers arranged in 9 concentric hexagons, operating in total power at 280 mK, with a half-power spectral bandwidth from 313 to 372 GHz, and an effective frequency of 345 GHz (870 μm). The number of bolometers with sky response is 266, of which 15 show signature of cross talk and 18 have very low sensitivity; in total 33 bolometers have been discarded from the data analysis. Two additional bolometers have been blinded in order to record the temperature variation of the detector wafer. The complete array field of view covers 11.4′. Using fully sampled observations of Mars, we derived, for each detector, the relative gains and relative positions of the bolometers; the latter were found to be stable within 1″. The gains have been normalized using the median value of all valid bolometers. The effective radial beam profile deduced from Mars observations is shown in Fig. 1. Once deconvolved from the size of Mars, varying from 6.5″ to 6.9″during the observations, the beam profile can be approximated, within a few percent, by a single Gaussian beam of half power beam width (HPBW) of $20.4 \pm 0.5''$ for point source studies.

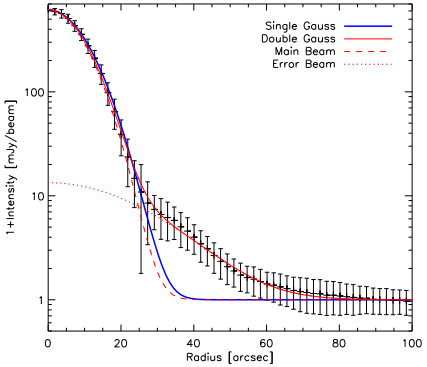

Fig. 1. Effective radial beam profile of LABoCa, combining all the bolometers that were usable during the observing run. The error bars are derived from the standard deviation of the pixels in the map. The profile is well described either by a single Gaussian of HPBW=$20.4 \pm 0.5''$ (thick line), or by a Gaussian main beam of HPBW=$19.1 \pm 0.6''$ (dashed line) and a Gaussian error beam of HPBW=$54 \pm 5''$ (dotted line), once deconvolved from the median Mars diameter at the time of observation. The peak ratio between the error and the main beam is 2.1%.

During the two disjoint observing periods, 2007 July 07-15 and August 15-28 (ESO program ID : 078.F-9030(A) and MPIfR 080.F-9502(A), respectively), the atmospheric conditions were excellent, with typical zenith opacities between 0.07 and 0.17 and a median value of 0.12 at 870 μm. The telescope pointing was checked once an hour using the nearby radio source PMN J1957-3845 and was found to be stable within a few arc seconds in azimuth and elevation. The focus setting in the Z direction was checked regularly every 2 to 3 hours on Mars, and at least every day in the X and Y direction and was found to be stable in each direction. The target area was mapped with a raster of scans in horizontal coordinates tracing spirals displaced from each other in a way to obtain optimum spatial sampling. Simulations were made using BoA (see subsection below) in order to derive the best spiral parameters to obtain a fully sampled map of the sky with the actual foot pattern of LABoCa and with little overhead compared to classical On-The-Fly observing mode. The total on sky integration time was 14+7=21 hours.

The absolute flux calibration is based on observations of Mars during the first observing run and a model[2] developed by E. Lellouch, H. Amri and R. Moreno, using general climate model predictions of martian surface and sub-surface temperatures [3], and radiative transfer within the surface. The predicted total flux of Mars varied from 660 to 711 Jy, over the first observing period. After correction for the angular extent of Mars, the derived calibration factor for LABoCa is 6.8 ± 0.5 Jy/μV. The absolute flux calibration uncertainty is thus about 7%. Flux densities quoted in the following do not include this uncertainty since it is only useful when compared to other instruments.

2.2. Data Reduction

The data were reduced with an updated version of the BOlometer Array Analysis Software (BoA), a newly designed free software package to handle bolometer array data. BoA is a collaborative effort of scientists at the Max-Planck-Institut für Radioastronomie (MPIfR), Argelander-Institut für Astronomy (AIfA), Astronomisches Institut Ruhr Universität Bochum (AIRUB) and Institut d'Astrophysique Spatiale (IAS), with the primary goal of handling data from LABoCa at APEX, but it can also be used to process data acquired with other instruments such as ASZCa (Dobbs et al. 2006) and (p)ArTéMiS at APEX or MAMBO Kreysa et al. (1998) at the IRAM 30-m telescope.

The data are corrected for atmospheric opacity at the time of the observation by a linear interpolation from a combination of skydips and APEX radiometer measurements. Using the two blind bolometers, it is possible to correct for the temperature variation of the helium-3 stage over the complete observation. Flat-fielding was then applied based on bolometer relative gains on known primary calibrators. Before any further processing, the data stream was flagged according to the telescope pattern to avoid high accelerations, responsible for microphonics, as well as low and high speed, in order to properly disentangle the sky signal spatial frequencies from the atmospheric emission. The sky emission was iteratively estimated and removed using the median value of all valid bolometers, over the whole array first, then by grouping the bolometers by electronics boxes or cables to remove any remaining correlated signal due to the electronics or micro-phonics pick-up. This removed the atmospheric emission satisfactorily across the array and no or little correlated signal is seen after applying this procedure. An iterative despiking is applied to the data, before removing a linear baseline. A last flagging was set up on the bolometers according to the Median Absolute Deviation of their variance in order to filter very noisy or dead bolometers. Finally the data are weighted by the inverse of their variance, and gridded on the sky with a pixel size of one third of the beam, about 6″, the flux in each pixel being the weighted-average of all bolometers observing that position, producing a signal (S) and a weight (W) map. Each scan was visually inspected in order to remove obvious problems like wrong sky noise removal, data corruption, canceled scans or bolometers warming up during the observations.

Other methods were tried to remove atmospheric noise, in particular one based on principal component analysis (PCA), where the signal is transformed to a coordinate system where the first axis correspond to the greatest variance of the data. By removing the first few coordinates and projecting the data back to its original basis, the atmospheric emission, responsible for most of the signal is then removed. Both methods, removing median signal and the PCA, show very similar results. Moreover the data was independently reduced following a totally different approach (see Kovács 2006, for an introduction) by using the *mini-crush* program. The final map and source list are compatible with the result presented here.

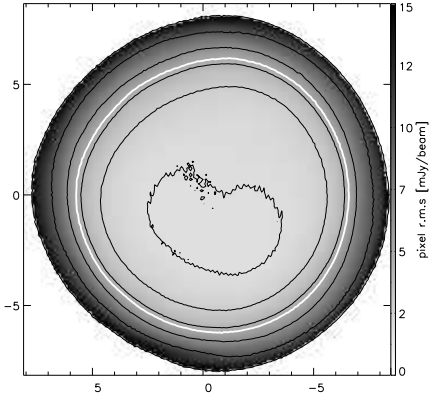

Fig. 2. Noise map around the $z = 2.38$ galaxy protocluster J2143-4423. Contours are at pixel rms 1.9, 2.9, 4.4, 6.6, 9.9, 15.0 mJy/beam in exponential progression, the thick white contour corresponds to the region of interest with pixel rms below 5 mJy/beam (see text). The axes denote the offsets in arc minutes from the map center ($\alpha = 21^h42^m43\overset{s}{.}7, \delta = -44°25'30\overset{''}{.}0$ (J2000)).

On the best 10% observed region, corresponding to a homogeneously observed surface of 45 arcmin^2, the pixel rms is 1.93 mJy/beam, which correspond roughly to a point source sensitivity rms of 1.4 mJy, as the pixel size is a fraction of the beam. By rescaling the weight map with this value, we produced a noise map shown in Fig. 2. The noise is fairly flat in the center of the map with a pixel rms between 1.95 and 5 mJy/beam and increases rapidly toward the edge of it. In the following we will limit our study to the area with better than 5 mJy/beam pixel rms, corresponding roughly to a surface of 120 arcmin^2, or 60% of our map; this corresponds to the white thick line in Fig. 2.

2.3. Source Extraction

As seen in Fig. 2, the noise is not uniform over the observed field, and the signal (S) and weight (W) map were gaussian-matched-filtered to take this into account. The FWHM of the gaussian (P) filter was set to $\sqrt{20.4^2 + 3^2} = 20.7''$, in order to take into account the HPBW of LABoCa and a typical pointing error of 3″. Following Serjeant et al. (2003), the detection threshold map after this noise-weighted convolution can be expressed as

$$\frac{F}{\Delta F} = \frac{(S\ W) \otimes P}{\sqrt{W \otimes P^2}},$$

and is presented in Fig. 3.

In order to test the robustness of the galaxy candidate identification, two tests were performed. The first test is derived from the jackknife test where the observations are divided into two randomly chosen samples of equal size. The difference of the two maps should remove both resolved and confused sources signal and its histogram should be described by a pure Gaussian. Figure 4 presents the average result of 100 jackknifed maps. A Gaussian distribution fits very well the negative part of the jackknife histogram, and shows no positive-side excess indicating

[1] The nomenclature about Lyα blobs is still a bit confused. A Lyα blob (or LAB) refers clearly to an extended or resolved region of Lyα emission. However, the evidence for extension depends on the quality of the optical image. In the prototype region SA 22, there is a list of several tens of LABs down to an extension of $\sim 5''$ (see e.g. Table 1 of Geach et al. 2005). In the J2143-4423 region, extensions are published only to $\sim 7''$ (~ 50 kpc), for four blobs, B1, B5, B6, B7 (see Table 4 of Palunas et al. 2004). However, other unresolved Lyα emitters are also labeled B2, B4, B8 and B9 (Francis et al. 1996, 1997; Palunas et al. 2004; Colbert et al. 2006). To avoid confusion, we will call extended objects of the first group 50 kpc-Lyα blobs

[2] see `http://www.lesia.obspm.fr/~lellouch/mars/`

[3] see `http://www-mars.lmd.jussieu.fr/`

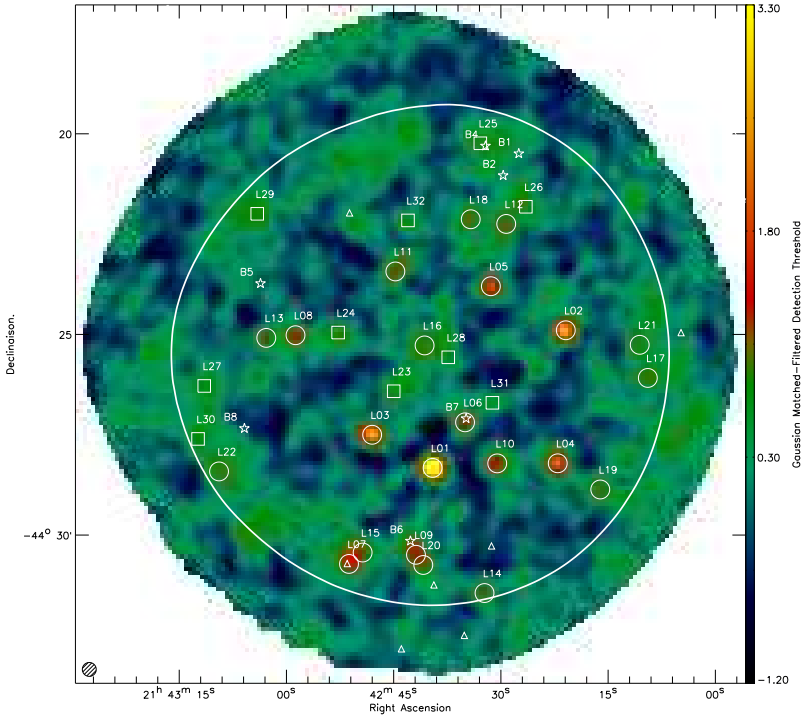

Fig. 3. The 870 μm LABoCa Gaussian-matched-filtered detection threshold map around the $z = 2.38$ galaxy protocluster J2143-4423. The map pixels are about $6'' \times 6''$. Detected sources with detection threshold greater than 1.2 (1.0) are circled (boxed). This detection threshold corresponds roughly to a signal-to-noise ratio of 4.3 (3.4). The thick white contour corresponds to the region of interest (see text). The LABoCa HPBW beam shape is represented in the lower left corner. Lyα Blobs present in the field are represented by open stars (Palunas et al. 2004). Triangles are QSOs detected by Francis et al. (2004).

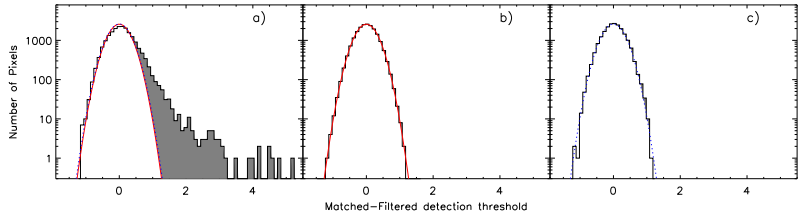

Fig. 4. Histograms in Log-Normal coordinates of the pixel signal-to-noise values of the gaussian-machted maps. a) in the signal map, where a clear excess (shaded area) on the positive-side is present compared to the jackknife histogram fit (solid line) or the astrometry-corrupted fit (dashed-line). b) in the mean jackknife and c) astrometry-corrupted map (see text) which can both be very well fitted by a Gaussian distribution (solid line in b and dashed line in c).

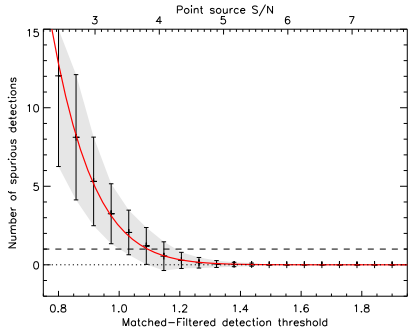

Fig. 5. Expected average spurious detection rate in our map as a function of the Gaussian matched-filtered signal-to-noise ratio. The solid line is an exponential fit to the data. Error bars are 1 σ standard deviations of the jackknifed maps. The upper axis presents roughly the corresponding signal-to-noise ratio for point sources.

that the jackknife procedure did remove all source signal. For the second test, the relative positions of the bolometers were shuffled inside the field of view, corrupting their astrometry. In the resulting co-added map, any coherent source on the sky should be smeared out in the noise, and any positive excess on the map pixel distribution will be suppressed, while the noise properties of the resulting map remain similar to the real map. Figure 4 shows the histogram of one astrometry-corrupted map, whose negative part is very well fitted by a Gaussian distribution and which presents no or very little excess on the positive side, due to the smearing over the map of the sources signal.

The histogram of the detection threshold map is also shown in Fig 4. The negative part of the histogram is highly Gaussian and is well described by the over-plotted Gaussian fits of the jackknifed and astrometry-corrupted distribution, showing a clear excess on the positive side. The galaxy candidates clearly account for this excess, as the residual map, after source extraction, does not show such a significant excess.

In order to determine the false detection rate, we produced 100 jackknifed maps and performed source extraction, using a CLEAN algorithm (Högbom 1974), with different detection thresholds. This gives a realistic picture of the number of spurious sources expected in our map at a given threshold. However, the jackknifed maps are free of confusion noise, therefore the number of spurious sources might be a slightly underestimated. The result is shown in Fig. 5, where the solid line is an exponential fit to the data as $F(r) = a\ \exp(-r^2/b)$. We find that a Gaussian matched-filtered detection threshold of 1.2 results in at most one spurious source expected at random, whereas with a threshold of 1.0 we expect about four spurious sources. Translated into the non-filtered map, these thresholds correspond roughly to a signal-to-noise ratio for point source of 4.3 and 3.4, respectively.

The measured fluxes in a map are biased toward high values due to instrumental, atmospheric and confusion noise, this is known as the "flux boosting" effect. We performed Monte-Carlo simulations to test the completeness, flux boosting and positional uncertainties of the source extraction algorithm. Using one jackknifed map we added, at a random position in the map, one source with flux between 1 and 20 mJy in steps of 0.5 mJy. Repeating this process 500 times for each flux bin, source extraction was made by selecting all regions with a detection threshold, $F/\Delta F > 1.2$, and we computed the flux densities within an aperture of 20.4″ directly in the non-filtered map. The photometry correction is derived from the high signal to noise map of Mars and is about 7%. The results of these simulations are presented in Fig. 6 for a Gaussian matched-filtered signal-to-noise threshold ratio of 1.00. As expected, the source extraction performs well in extracting all the brighter sources but degrades when dealing with fainter sources. At a flux density of 4 mJy, the completeness is about ≈ 50 per cent. The effect of flux boosting is clearly seen for faint flux densities, where the instrumental noise tends to favor detection of sources coinciding with positive noise peaks. At a flux density level of 4 mJy, this effect is on the order of 35 per cent, decreasing exponentially for higher fluxes. Last, the positional offset due to the source extraction algorithm is found to be approximately 4″ for a flux density of 4 mJy and decreasing for higher fluxes. For a flux density of 10 mJy, this positional error is about 1″, corresponding to one sixth of a pixel, negligible with respect to the pointing error.

Within the region of interest of the Gaussian matched-filtered map, we performed source extraction with a threshold of $F/\Delta F > 1.0$, leading to the detection of 22 sources with $F/\Delta F > 1.2$ and 10 additional sources below this threshold where we expect, in total on the full sample, between 1 and at most 5 spurious sources. The source candidates are listed in Tab. 1, in decreasing Gaussian matched-filtered detection threshold ($F/\Delta F$) order and are also seen in Fig. 3. The listed flux densities are corrected for the boosting flux effect and are in the range of 2.9 to 21.1 mJy. The flux uncertainties are computed from dispersion in the sky annulus and the uncertainty in the mean sky brightness. The quoted uncertainties are also corrected for the boosting flux effect but do not propagate its uncertainties.

3. Analysis

3.1. Number counts

We performed a cumulative number count analysis on the detected sources using the fluxes corrected for the flux boosting effect and for the completeness of the survey as discussed previously. Based on 22 sources, the 870 μm integrated number counts are presented in Fig. 7 and are well described by a power law of the form $N(>S) = N_0(S/S_0)^{-\alpha}$: with the parameter $S_0 = 10$ mJy, we derived $N_0 = 70 \pm 12\,\mathrm{deg}^{-2}$ and $\alpha = 1.9 \pm 0.2$. On the same figure, we also show the cumulative combined SHADES number counts obtained by Coppin et al. (2006) on a 720 arcmin^2 field down to an rms of 2 mJy where > 100 galaxies were uncovered. Our sample of 22 sources is too small to allow any meaningful detailed analysis of the number count distribution, and, for example, we do not see any trend for a break in the power law as in the SHADES data. However, we tentatively observe an over density of sources at $S_{870\mu\mathrm{m}} > 10$ mJy. This is confirmed when we look at the number counts of 4 sources in a 5′ diameter circle around the source L06, identified as a Lyα blob (see below), with a power law parametrized by $N_0 = 498 \pm 152\,\mathrm{deg}^{-2}$ and $\alpha = 1.3 \pm 0.5$. The density of submillimeter galaxies is then one order of magnitude, at a 3 σ level, higher than for unbiased submillimeter field galaxies.

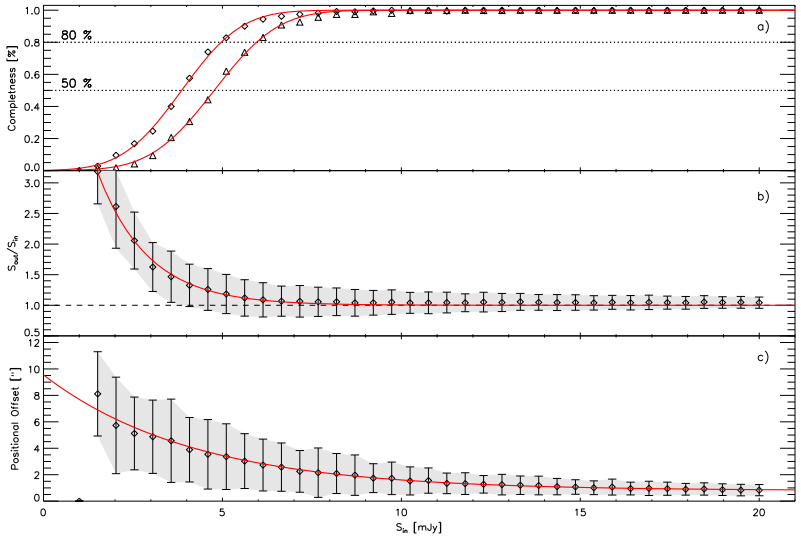

Fig. 6. Results of Monte-Carlo simulations with a Gaussian-matched-filtered detection threshold ratio of 1.0 (diamond) and 1.2 (triangle), to test for completeness, flux boosting and position uncertainties as a function of the input flux. Error bars are the 1 σ standard deviation of the jackknifed maps. a) Completeness function, i.e. the fraction of recovered sources. b) Flux boosting, i.e. the ratio between the extracted and input flux. c) Positional uncertainties, i.e. difference between the input and recovered source positions. The solid line represent fits to the data, using an error function for a), as $f(S_{in}) = (1 + \mathrm{Erf}((S_{in} - a)/b))/2$ with $a = 3.8\,(4.7)$ and $b = 1.8\,(2.0)$ for a detection threshold of 1.0 (1.2) and an exponential function of the form $f(S_{in}) = a\exp(-bS_{in}) + 1$ with $a = 6.3$ $b = 0.7$ for b) and $f(S_{in}) = a\exp(-bS_{in}) + c$ with $a = 8.7$ $b = 0.2$ and $c = 0.8$ for c). Results for b) and c) are similar for the two detection thresholds and only one is presented for clarity.

3.2. Mid-IR Source Identifications

Identification of millimeter and submillimeter galaxies has mainly used the strong correlation between the far-IR and radio luminosities, tracing respectively, warm dust heated by hot, young O-type stars and non-thermal emission resulting from supernova explosions, both phenomena of ongoing star formation. With the low density of faint radio sources, it is unlikely to have a chance association within a few arc second (see e.g. Ivison et al. 2007, and references therein). Unfortunately, no sensitive radio observation is available to date on the observed field. Nevertheless, Mid-IR imaging with e.g. Spitzer has also been used to identify SMGs (Pope et al. 2006; Ivison et al. 2007), although the position uncertainties are larger than for the radio observation and the link between Mid-IR and Far-IR emission is not as well defined as the one between Far-IR and radio (see e.g. Bavouzet et al. 2007) . We used data taken with IRAC (at 3.6, 4.5, 5.8 and 8.0 μm) (Colbert et al. in prep.) and MIPS (at 24 μm) (Colbert et al. 2006) to identify the sources detected at 870 μm. From the 3.6 μm catalog we derived the photometry in all IRAC bands and matched it to the 24 μm catalog within a search radius of 2″ to produce a global search catalog. Stars were removed using a simple color criterion of $S_{24\mu\mathrm{m}}/S_{3.6\mu\mathrm{m}} < 0.1$ (Rodighiero et al. 2006).

Following Condon (1997) and Ivison et al. (2007), the positional uncertainties of a three free parameter Gaussian fit is $\Delta\alpha = \Delta\delta = \theta\,(S/N)^{-1}/2\sqrt{\ln 2}$, where θ is the beam HPBW and (S/N) is the flux signal to noise ratio. Adopting a conservative lower value of $(S/N) = 3$, the rms position uncertainties are on the order of 4″ in both axes. Taking into account a possible shift between Spitzer and LABoCa absolute astrometric frames on the order of 5″, we have adopted a final search radius of $r = 8''$.

For each 870 μm source, we searched for all counterparts in the full Mid-IR catalog and we computed the corrected Poisson probability of a chance association P using the method described in Downes et al. (1986) with the number counts at 24 μm and 3.6 μm of Papovich et al. (2004); Lagache et al. (2004) and Fazio et al. (2004), the latter with IRAC on Spitzer. The position and flux densities of all 24 and 3.6 μm counterparts within 8″of the 870 μm LABoCa sources are presented in Table 2, where the most reliable counterparts, with $P < 0.05$, are listed in bold face. From the 22+12 detected SMGs, ten show a robust counterpart at 24 μm, 15 others have a 24 μm counterpart with a probability $P \lesssim 0.2$ of spurious association, and finally ten sources do not show a counterpart within 8″. Practically all these 24 μm sources but one, have a secure IRAC associate (within $\lesssim 1''$) detected at least at 3.6 μm (Table 2). Figure 8 presents 45″ × 45″ postage stamp images of the 3.6 and 24 μm emission centered on the 22 securely detected SMGs with $F/\Delta F > 1.2$. The lack of radio data over that field leads to only half of the sources having a secure counterpart, whereas it is of order of two-thirds in other submillimeter studies (Pope et al. 2006; Ivison et al. 2007) in which source positions are validated by radio identifications. If one takes into account less secure associations (Tab. 2), the total proportion of 24 μm associations become comparable.

From the four 50 kpc-Lyα blobs present in the observed field (Palunas et al. 2004), of which three are detected at 24 μm (Colbert et al. 2006), only one, B7, is detected at 870 μm. None of the other Lyα emitters present in the 870 μm image is securely detected, placing an upper limit on their flux densities of $S_{870\mu\mathrm{m}} \lesssim 5 - 7$ mJy (3σ). However, there are hints of emission near the Lyα blobs B4 and B6.

Mid-IR colors can be used to distinguish between starburst and AGN emission (Ivison et al. 2004; Pope et al. 2006; Ivison et al. 2007). We compared the 24 μm/8.0 μm and 8.0 μm/4.5 μm color of the 9 sources with robust and complete Mid-IR counterpart, with the SWIRE template SED library of typical galaxies described in Polletta et al. (2007). We used 14 template SEDs consisting of 6 starbursts corresponding to the SED of Arp 220, M 82, NGC 6090, NGC 6240, IRAS 22491-1808, and IRAS 20551-4250, and 6 QSO-like SED, 3 type-1 and 2 type-2 and Mrk 231. We also included 2 moderately luminous AGN representing Seyfert 1.8 and Seyfert 2 galaxies (see Polletta et al. 2007, for a detailed description). These templates were redshifted from $z = 0.5$ to 4 and flux densities where computed using the IRAC and MIPS filters. The results are presented in Fig. 9, for all the sources in Tab. 2, together with sources with secure counterparts of Pope et al. (2006) and Seymour et al. (2007). From this diagram, it appears that 6/9 sources (L02, L04, L11, L13, L15 and L33) have colors similar to starburst galaxies at redshift between 1 and 3, whereas 2/9 (L07 and L11) are more likely to be quasars. Finally, one, L06 lies close to the starburst region (see Fig.9).

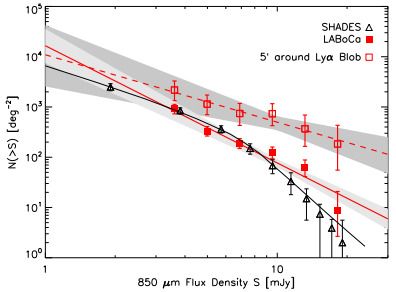

Fig. 7. Cumulative number counts at 870 μm (full square) based on the sources detected in this paper. The errors bars are the 1σ two-sided Poissonian confidence level. The thick plain line is a power law fit to the data (see text). Also shown are the 850 μm cumulative number counts and fit of the SHADES survey with triangles and thin line, respectively (Coppin et al. 2006). The 850 μm number counts have been rescaled to 870 μm with a spectral index of ν^2. Furthermore, the number counts in a 5′ diameter circle around the source L06 are presented in open squares and a dashed line that has been fitted to them is also shown. Shaded area represent the 1 σ uncertainties of the fit.

3.3. Notes on Individual Objects

L01 – This source is among the strongest submillimeter sources and is not securely associated with any Mid-IR source. No radio emission at 843 MHz is detected at the source position in the Sydney University Molonglo Sky Survey (SUMSS) (Mauch et al. 2003) placing an upper limit on the radio flux density of 10 mJy. The submm-to-radio spectral index is then $\alpha^{345\mathrm{GHz}}_{843\mathrm{MHz}} > 0.13$ which places this source at $z > 0.7$ following the submm-to-radio spectral index relation of Carilli & Yun (2000) with the spectrum of M82 as template. The possible Spitzer counterpart reported in Tab. 2 has a IR SED typical of an AGN. However, the very large $S_{870\mu\mathrm{m}}/S_{24\mu\mathrm{m}}$ ratio is incompatible with an AGN, but rather needs a strong starburst SED such as that of Arp 220. It is therefore possible that the main Spitzer counterpart is undetected. With a secure completeness limit of $S_{24\mu\mathrm{m}} < 80\,\mu$Jy, using the limit for the $S_{870\mu\mathrm{m}}/S_{24\mu\mathrm{m}}$ ratio (> 270), we can estimate a lower limit on the source's redshift at $z \gtrsim 2.8$ (although $z = 2.38$ remains possible with a highly obscured SED). It is even possible that this source is extended or associated with multiple objects within the large LABoCa beam, like other very strong submillimeter sources such as SMM J123711.7+622212 (GN20) (Pope et al. 2006; Iono et al. 2006) or LAB1-SA 22 (Matsuda et al. 2007). Using a modified blackbody with a dust temperature of 40 K and a spectral index of 1.5, this corresponds to an infrared luminosity of $L_{IR} = L_{5-1000\mu\mathrm{m}} \approx 2\,10^{13}\,L_\odot$.

L02 – This source has a very strong 24 μm flux and Mid-IR colors well within the starburst region in Fig. 9. There is a $S_{843\mathrm{MHz}} = 18.6 \pm 1.3$ mJy radio source at 9.6″ displaced from our nominal position in the SUMSS Catalog. Due to the large beam of the radio observation, it is possible that these two sources are associated, making L02 a radio loud source. Its SED would then be similar to e.g. 4C 41.17 (Seymour et al. 2007; Archibald et al. 2001) but at much lower redshift $z \sim 1.0 - 1.3$, compatible with the $S_{870\mu\mathrm{m}}/S_{24\mu\mathrm{m}}$ ratio of 9. However given this low ratio, this source could also be at higher redshift, up to 2.5.

L04 – From the IRAC color of this source, we infer a starburst template (Fig. 9) with a redshifted stellar maximum emission in the 5.8 μm band and an infrared redshift of $z_{IR} = 2.5 \pm 0.3$ inferred from a combination of the four IRAC fluxes (Pope et al. 2006) . Using Arp 220 or IRAS 20551-4250 as best matched templates, we derive an infrared luminosity of $L_{IR} \approx 1.4\,10^{13}\,L_\odot$.

L06 – This source is associated with the Lyα Blob B7 at $z = 2.38$ of Palunas et al. (2004). This is one of the sources with the largest excess flux in the narrow band Lyα filter compared to the B filter. It has a very good 24 μm association (Colbert et al. 2006). There appear to be additional MIPS sources at short distance of 15 ″. The SED of L06 is similar to IRAS 19254-7245 South, a Seyfert 2 and Starbust/ULIRG composite leading to $L_{IR} \approx 5\,10^{12}\,L_\odot$ placing this source in the ULIRG regime. With a Lyα-IR relation of $L_{Ly\alpha}/L_{bol} = 0.16\%$, this source lies on the trend found by Geach et al. (2005).

L07 – This source is associated with the QSO [FPT2004] J214251.50-443043.2 detected by Francis et al. (2004) at $z = 1.795$ with a B magnitude of $M_B = 20.26$. The SED of L07 is well described by a typical type 1 QSO SED with high IR counterpart, with an inferred luminosity of $L_{IR} = 8\,10^{12}\,L_\odot$.

L11 – As for L04, the SED rather indicates a starburst (Fig. 9) with a stellar bump in the 5.8μm band. The infrared redshift of this source is $z_{IR} = 2.9 \pm 0.3$. Using this redshift and the SED of IRAS 20551-4250, we derive an infrared luminosity of $L_{IR} \approx 2\,10^{13}\,L_\odot$.

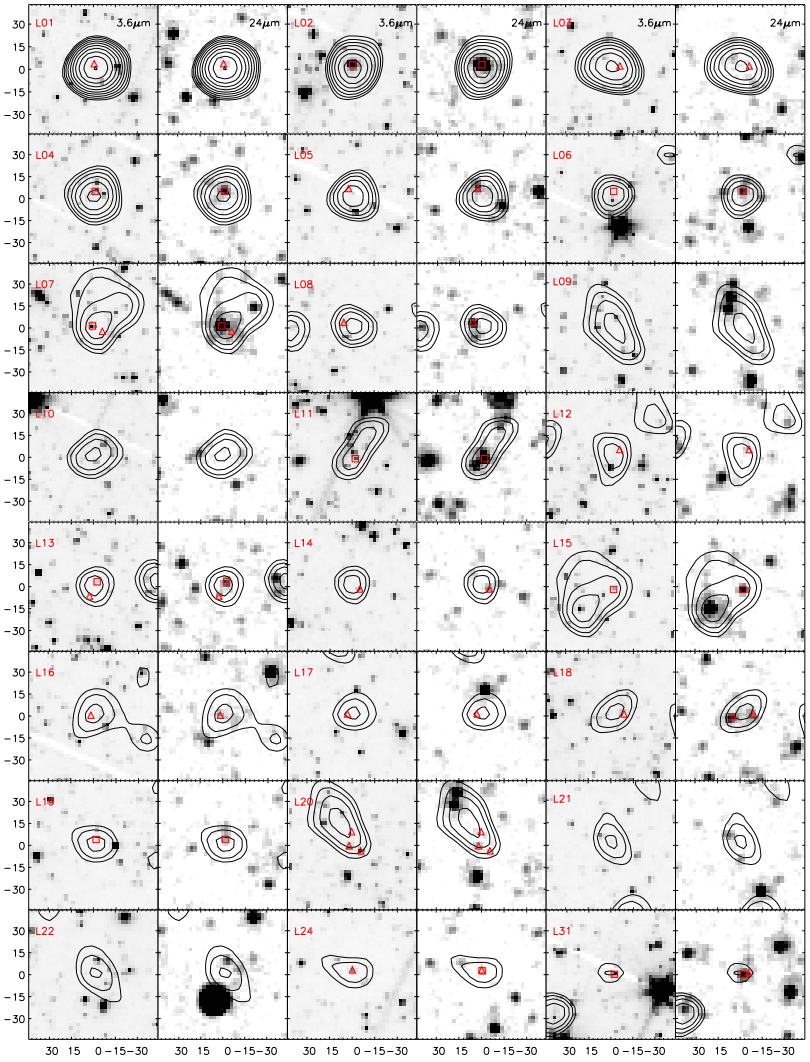

Fig. 8. Spitzer images of the sources detected at 870 μmwith $\Delta F/F > 1.2$ plus L24 and L31. From left to right, IRAC 3.6 μm and MIPS 24 μm. Contours show the 870 μm detection threshold $F/\Delta F$ at 0.8, 1.0, 1.2, ..., 5.0 in exponential progression. The axes denote the offsets in arc seconds from the 870 μm source position. Sources are labeled in the top left corner (see text and Tables 1 and 2). Squares show sources identified in Tab. 2 with $P < 0.05$ whereas triangles show identifications with $P > 0.05$.

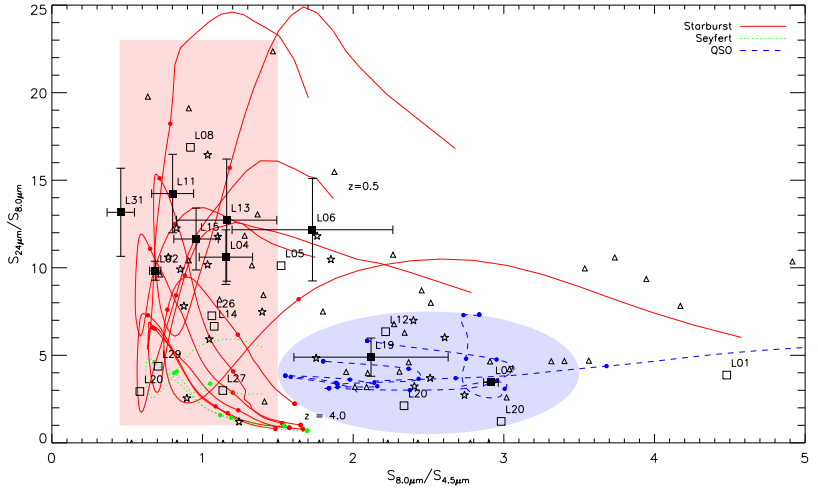

Fig. 9. $S_{24\mu m}/S_{8\mu m}$ versus $S_{8\mu m}/S_{4.5\mu m}$ color-color diagram for the SMGs of Tab. 2 with $P < 0.05$ as full square, and open square for those with $P > 0.05$. The lines are color-color tracks with redshift starting from 0.5 to 4, dots denote redshift 1 to 4, from top to bottom for the starburst-like SEDs (plain lines), Seyfert Galaxies (dotted lines) and QSOs (dashed lines). The rectangle defines the region where we expect most of the starbursts, whereas the ellipse shows the region of QSOs. Stars are the submillimeter galaxies of Pope et al. (2006) with secure Mid-IR counterparts, triangles are the radio galaxies of Seymour et al. (2007).

L13 – Having a similar SED to L04, this source has a infrared redshift of $z_{IR} = 2.7 \pm 0.3$, and an inferred infrared luminosity of $L_{IR} \approx 8\,10^{12}\,L_\odot$.

L15 – This source has a typical starburst SED like IRAS 20551-4250 with an infrared redshift of $z_{IR} = 2.8 \pm 0.3$ and luminosity of $L_{IR} \approx 1\,10^{13}\,L_\odot$. If this redshift estimate is right, the proximity on the sky of L07 and L15 (Figs. 3 and 8) is fortuitous.

L19 – If the association of Tab. 2 is correct, the mid-IR SED and colors are typical of an AGN, with an uncertain redshift, probably $z \sim 2$–3.

Nine sources have at least one counterpart within the search radius of 8″ and within the completeness limit of $S_{24\mu m} \sim 80\,\mu$Jy, but the associations are less secure with probabilities of spurious association in the range 0.05–0.20. For three of them, L03, L05 L14, the $S_{870\mu m}/S_{24\mu m}$ ratio, greater than 135, indicates most likely starburst galaxies and places them at $z \gtrsim 2.5$, but they could be at a lower redshift if their SEDs where strongly obscured. For the six other galaxy candidates, L08, L12, L16, L17, L18, L20, the $S_{870\mu m}/S_{24\mu m}$ ratio, ranging from > 35 to > 95, places them at $z > 2.2$, or around $z \sim 1.4$ if they have obscured SEDs similar to Arp 220. In the case of L12, the tentative counterpart presents typical colors of an AGN, which would place it at very high redshift ($z > 5$).

Two sources, L09 and L10, have no counterpart candidates within the completeness limit of the 24 μm observations. With respective lower limits for the $S_{870\mu m}/S_{24\mu m}$ ratio of 140 and 120, these sources are likely to be starbursts at $z > 2.5$ or at lower redshift in case of a strongly obscured starburst SED. L09 is close to the position of the Lyα Blob B6, but the blending with L20 makes the association unlikely. Last, L21 has also no counterpart candidates but with a lower $S_{870\mu m}$ flux density, this source's redshift is more likely to be around 1.5.

The quality of the submillimeter fluxes of the ten other sources, L22-32 of Tab. 1 & 2, is lower, as well as most of their possible Spitzer associations. Exceptions of L24 which has a high probability 24 μm counterpart (see Fig. 8), with $S_{870\mu m}/S_{24\mu m} \sim 55$, indicating a starburst at $z \sim 1.5$, L25 which lies close to the Lyα Blob B4, but the higher noise on the edge of the map prevents any firm conclusion and L31 which seems to lie on the edge of the starburst region on the color-color diagram presented Fig. 9 and has $z_{IR} = 2.7 \pm 0.3$.

4. Discussion & Conclusions

By detecting high-z powerful ULIRGs ($L_{FIR} \sim 5 - 20\,10^{12}\,L_\odot$), our results may cast some light on the association of such SMGs not only with the Lyα blobs themselves, but also with the $z = 2.38$ large scale structure that they trace. The meager submillimeter detection rate of only one Lyα blob confirms the findings of Geach et al. (2005) that maximum starbursts with $L_{FIR} \gtrsim 10^{13}\,L_\odot$ are present in only a minority of even 50 kpc-Lyα blobs. The detection rate of one out of four 50 kpc-Lyα blobs and none in the three other blobs may appear significantly lower than in those of SA 22 by Geach et al. (2005) who detected three out of ten 50 kpc-Lyα blobs, and two more among 15 additional moderately extended (~ 35 kpc) blobs. But one should also take into account that, except the detected blob L06/B7, all other blobs are located in regions of the map with relatively high noise, ~ 2.0−2.7 mJy, i.e. larger than the rms of the detections of

B7 or of Geach et al. (2005) by factors $\gtrsim 1.5$. Moreover there is a 2σ 870 μm detection (4.9 ± 2.0 mJy) at the 24 μm position of the B6 blob of Colbert et al. (2006). There are two 870 μm sources, L09 and L20, within $\sim 30''$ of B6. The average values of the 870 μm flux densities for undetected blobs – 2.3 ± 0.8 mJy for the 50 kpc-blobs B1, B5 & B6, and 1.2 ± 0.6 mJy for all, B1, B2, B4, B5, B6 & B8 – are also compatible with the value of Geach et al. (2005), 1.2 ± 0.4 mJy for all their blobs. Nevertheless, the non detection at 870 μm of the blobs B4 and B6 excludes the very large far-IR luminosities, $4 - 5\ 10^{13}\,L_{\odot}$, inferred by Colbert et al. (2006), placing upper limits rather $\lesssim 10^{13}\,L_{\odot}$.

More important, we have detected at least twenty additional sources at 870 μm, with indications that several of them could be associated with the $z = 2.38$ LSS traced by the Lyα blobs. As discussed in Sect. 3.3, out of 21 most secure detections outside of L06/B7, 7 sources, L03, L04 L05, L09, L10, L13 & L15, with starburst-like SED have probable redshifts in the range 2.0–2.8 compatible with the redshift of the galaxies protocluster J2143-4423 at $z = 2.38$; moreover seven additional sources, L01, L08, L12, L16, L17, L18 & L20 have more uncertain redshifts, but still not incompatible with $z = 2.38$. Only L02 and L07 have clear indication of lower redshifts. As quoted in Sect. 3.1, five detected sources, are within a circle of diameter $5'$ centred on B7, yielding an apparent strong over-density (Fig. 7), which is another argument for their possible membership of a protocluster at $z = 2.38$. However, spectroscopic determination of the redshifts will be mandatory to confirm the existence of such a compact protocluster and the membership of these SMGs.

The possible redshifts of our submillimeter detections, with most of the sources probably at $z \gtrsim 2$ are in agreement with the general distribution of the redshifts of SMGs (Chapman et al. 2005). However, regarding the nature of the sources, we note a trend for a larger proportion ($\sim 30\%$) of AGN-starburst composite mid-IR SEDs than is usually found (e.g. Valiante et al. 2007; Pope et al. 2007): L06/B7 itself has clearly such a profile, as well as L07 and L19 and possibly L12 and L20; there is a possible match of L02 with a radio galaxy although its $3.6 - 8.0\,\mu$m SED looks starburst dominated at $z \sim 1.0-1.3$. As discussed, the case of one of the strongest submillimeter sources known to date, L01 (21 mJy) is not completely clear since the mid-IR SED of a possible Spitzer counterpart looks AGN dominated, while the 870 μm/24 μm flux ratio suggests a starburst-dominated profile.

This first published deep map illustrates and confirms the capabilities of the LABoCa camera on APEX. As expected, it is currently the most efficient equipment for wide and deep submillimeter mapping. The multiple checks that we have performed about the overall quality of the map, of the achieved signal-to-noise ratio and of the source extraction demonstrate the efficiency of the observing mode and of the data processing which were used and optimized for this work.

The first priority for further work aimed at confirming the nature of these SMGs and their possible relationship with the Lyα blobs and their underlying structure, is the determination of their redshifts. Both optical and near-IR determinations should be possible if the redshifts are in the range of $z = 2.38$, and they should be especially easy for AGN. More complete optical and near-IR data could be useful for this purpose and for considering the possibility of adaptive optics studies to trace the source's inner structures. Deep radio data (with ATCA, VLA and/or GMRT) would be important to trace the star formation rates and if possible the extension of starbursts, as well as the radio spectral index for trying to disentangle AGN and starburst contributions. Stacking 870 μm intensities of radio and Spitzer 24 μm and IRAC sources will extend the information about source counts and the average star formation rate to weaker submillimeter sources. In parallel, a deeper or wider LABoCa map would be useful to increase the number of individual detections, especially of Lyα blobs, and the stacking accuracy. High resolution (sub)millimeter imaging would be essential to check the spatial structure, especially of the strongest source L01, similarly to the observation of LAB01-SA22 by Matsuda et al. (2007). Waiting for ALMA, the J2143-4423 region is just at the limit of observability with SMA.

Acknowledgements. We thank the referee for comments, which improved the manuscript. We thank F. Schuller for help during the development of the BoA software. AB thanks M. Douspis and M. Langer for their useful interactions during the writing of this paper. This work is based on observations made with the APEX Telescope and the *Spitzer Space Telescope*. APEX is a collaboration between the Max-Planck-Institut für Radioastronomie, the European Southern Observatory, and the Onsala Space Observatory. The *Spitzer Space Telescope* is operated by the Jet Propulsion Laboratory, California Institute of Technology under NASA contract 1407. We thank the APEX staff and astronomers for their support during the observations and the Bolometer Development Group at the MPIfR for providing the LABoCa bolometer array. Last, but not least, AB thanks the staff of Adobe and Cafe Export in San Pedro de Atacama.

References

Archibald, E. N., Dunlop, J. S., Hughes, D. H., et al. 2001, MNRAS, 323, 417
Bavouzet, N., Dole, H., Le Floc'h, E., et al. 2007, ArXiv e-prints, 712
Carilli, C. L. & Yun, M. S. 2000, ApJ, 539, 1024
Chapman, S. C., Blain, A. W., Smail, I., & Ivison, R. J. 2005, ApJ, 622, 772
Colbert, J. W., Teplitz, H., Francis, P., et al. 2006, ApJ, 637, L89
Condon, J. J. 1997, PASP, 109, 166
Coppin, K., Chapin, E. L., Mortier, A. M. J., et al. 2006, MNRAS, 372, 1621
Dobbs, M., Halverson, N. W., Ade, P. A. R., et al. 2006, New Astronomy Review, 50, 960
Downes, A. J. B., Peacock, J. A., Savage, A., & Carrie, D. R. 1986, MNRAS, 218, 31
Fazio, G. G., Ashby, M. L. N., Barmby, P., et al. 2004, ApJS, 154, 39
Francis, P. J., Palunas, P., Teplitz, H. I., Williger, G. M., & Woodgate, B. E. 2004, ApJ, 614, 75
Francis, P. J., Woodgate, B. E., & Danks, A. C. 1997, ApJ, 482, L25+
Francis, P. J., Woodgate, B. E., Warren, S. J., et al. 1996, ApJ, 457, 490
Geach, J. E., Matsuda, Y., Smail, I., et al. 2005, MNRAS, 363, 1398
Güsten, R., Nyman, L. Å., Schilke, P., et al. 2006, A&A, 454, L13
Högbom, J. A. 1974, A&AS, 15, 417
Iono, D., Peck, A. B., Pope, A., et al. 2006, ApJ, 640, L1
Ivison, R. J., Greve, T. R., Dunlop, J. S., et al. 2007, MNRAS, 380, 199
Ivison, R. J., Greve, T. R., Serjeant, S., et al. 2004, ApJS, 154, 124
Kovács, A. 2006, PhD thesis, Caltech
Kreysa, E., Gemuend, H.-P., Gromke, J., et al. 1998, in Presented at the Society of Photo-Optical Instrumentation Engineers (SPIE) Conference, Vol. 3357, Proc. SPIE Vol. 3357, p. 319-325, Advanced Technology MMW, Radio, and Terahertz Telescopes, Thomas G. Phillips; Ed., ed. T. G. Phillips, 319–325
Lagache, G., Dole, H., Puget, J.-L., et al. 2004, ApJS, 154, 112
Matsuda, Y., Iono, D., Ohta, K., et al. 2007, ApJ, 667, 667
Matsuda, Y., Yamada, T., Hayashino, T., et al. 2004, AJ, 128, 569
Mauch, T., Murphy, T., Buttery, H. J., et al. 2003, MNRAS, 342, 1117
Miley, G. & De Breuck, C. 2008, A&A Rev., 15, 67
Nilsson, K. K., Fynbo, J. P. U., Møller, P., Sommer-Larsen, J., & Ledoux, C. 2006, A&A, 452, L23
Palunas, P., Teplitz, H. I., Francis, P. J., Williger, G. M., & Woodgate, B. E. 2004, ApJ, 602, 545
Papovich, C., Dole, H., Egami, E., et al. 2004, ApJS, 154, 70
Polletta, M., Tajer, M., Maraschi, L., et al. 2007, ArXiv Astrophysics e-prints
Pope, A., Chary, R.-R., Alexander, D. M., et al. 2007, ArXiv e-prints, 711
Pope, A., Scott, D., Dickinson, M., et al. 2006, MNRAS, 370, 1185
Rodighiero, G., Lari, C., Pozzi, F., et al. 2006, MNRAS, 371, 1891
Serjeant, S., Dunlop, J. S., Mann, R. G., et al. 2003, MNRAS, 344, 887
Seymour, N., Stern, D., De Breuck, C., et al. 2007, ApJS, 171, 353
Siringo, G., Weiss, A., Kreysa, E., et al. 2007, The Messenger, 129, 2
Smith, D. J. B. & Jarvis, M. J. 2007, MNRAS, 378, L49
Steidel, C. C., Adelberger, K. L., Shapley, A. E., et al. 2000, ApJ, 532, 170
Valiante, E., Lutz, D., Sturm, E., et al. 2007, ApJ, 660, 1060
Yamada, T. 2007, http://sfig.pmo.ac.cn/xining/

Table 1. The 870 μm LABoCa source catalogue around the $z = 2.38$ galaxy protocluster J2143-4423.

Name (IAU)	Nickname	α (J2000)	δ (J2000)	S_ν [mJy][c,d]	$F/\Delta F$[a]	Notes[b]
LABoCa J214239-442820	L01	21 42 39.56	-44 28 20.12	21.1 ± 1.0	5.22	
LABoCa J214220-442454	L02	21 42 20.98	-44 24 54.22	13.7 ± 1.2	3.07	SB
LABoCa J214248-442730	L03	21 42 48.00	-44 27 30.62	14.1 ± 1.1	2.90	
LABoCa J214222-442813	L04	21 42 22.08	-44 28 13.16	12.0 ± 1.1	2.35	SB
LABoCa J214231-442348	L05	21 42 31.44	-44 23 48.46	10.8 ± 1.1	2.16	
LABoCa J214235-442711	L06	21 42 35.03	-44 27 11.99	8.4 ± 1.0	1.81	B7
LABoCa J214251-443043	L07	21 42 51.24	-44 30 43.73	10.6 ± 1.8	1.75	QSO
LABoCa J214258-442501	L08	21 42 58.69	-44 25 01.70	7.6 ± 1.1	1.64	
LABoCa J214241-443030	L09	21 42 41.88	-44 30 30.08	11.3 ± 1.9	1.60	
LABoCa J214230-442813	L10	21 42 30.54	-44 28 13.34	8.9 ± 1.0	1.58	
LABoCa J214244-442326	L11	21 42 44.76	-44 23 26.40	6.9 ± 1.1	1.41	SB
LABoCa J214229-442215	L12	21 42 29.30	-44 22 15.30	6.3 ± 1.2	1.41	
LABoCa J214302-442505	L13	21 43 02.77	-44 25 05.64	7.0 ± 1.2	1.40	SB
LABoCa J214232-443127	L14	21 42 32.30	-44 31 27.24	14.0 ± 2.5	1.38	
LABoCa J214249-443026	L15	21 42 49.34	-44 30 26.70	8.9 ± 1.5	1.37	SB
LABoCa J214240-442517	L16	21 42 40.68	-44 25 17.04	4.3 ± 0.8	1.32	
LABoCa J214209-442605	L17	21 42 09.52	-44 26 05.32	6.7 ± 2.3	1.31	
LABoCa J214234-442208	L18	21 42 34.25	-44 22 08.35	3.0 ± 1.0	1.30	
LABoCa J214216-442852	L19	21 42 16.14	-44 28 52.23	9.0 ± 2.4	1.29	AGN
LABoCa J214240-443045	L20	21 42 40.86	-44 30 45.31	8.1 ± 1.6	1.29	
LABoCa J214210-442515	L21	21 42 10.66	-44 25 15.82	6.7 ± 1.9	1.26	
LABoCa J214309-442825	L22	21 43 09.39	-44 28 25.24	11.1 ± 2.9	1.25	
LABoCa J214244-442625	L23	21 42 44.99	-44 26 25.55	4.3 ± 0.9	1.19	
LABoCa J214252-442457	L24	21 42 52.75	-44 24 57.77	5.2 ± 0.9	1.17	
LABoCa J214232-442014	L25	21 42 32.92	-44 20 14.71	6.6 ± 1.7	1.15	
LABoCa J214226-442149	L26	21 42 26.56	-44 21 49.64	5.0 ± 1.3	1.11	
LABoCa J214311-442617	L27	21 43 11.44	-44 26 17.39	4.9 ± 1.7	1.08	
LABoCa J214237-442534	L28	21 42 37.38	-44 25 34.77	2.9 ± 0.8	1.05	
LABoCa J214304-442200	L29	21 43 04.02	-44 22 00.10	7.1 ± 2.1	1.04	
LABoCa J214312-442736	L30	21 43 12.32	-44 27 36.62	4.8 ± 2.4	1.02	
LABoCa J214231-442642	L31	21 42 31.22	-44 26 42.79	3.2 ± 0.8	1.02	SB
LABoCa J214242-442210	L32	21 42 43.00	-44 22 10.13	4.1 ± 1.0	1.01	

[a] Gaussian matched-filtered detection threshold
[b] Identification of the source (see text)
[c] Corrected from the flux boosting effect
[d] The absolute flux uncertainty is not included

List of Objects

Table 2. The Mid-IR properties of SMG around the $z = 2.38$ galaxy protocluster J2143-4423.

Nickname	MIPS 24 μm					IRAC			
	R.A. (J2000)	DEC	$S_\nu \pm \sigma_\nu$ [μJy]	Offset $''$	P[a]	$S_{3.6\mu m}$ [μJy]	$S_{4.5\mu m}$ [μJy]	$S_{5.8\mu m}$ [μJy]	$S_{8.0\mu m}$ [μJy]
L01	21 42 39.64	-44 28 17.26	81.4 ± 5.3	2.9	0.09	4.1 ± 0.3	4.7 ± 0.6		21.0 ± 4.4
L02	21 42 21.01	-44 24 51.89	911.0 ± 5.4	2.3	**0.00**	190.8 ± 0.7	135.1 ± 0.7	139.1 ± 3.1	92.7 ± 4.6
L03	21 42 47.54	-44 27 29.19	51.1 ± 5.1	5.3	0.19	4.4 ± 0.4	4.9 ± 0.5	10.4 ± 2.7	
L04	21 42 22.07	-44 28 09.02	362.0 ± 5.5	3.3	**0.02**	27.8 ± 0.6	29.5 ± 0.6	45.3 ± 2.9	34.1 ± 4.5
L05	21 42 31.74	-44 23 42.51	230.0 ± 5.6	6.2	0.10	15.3 ± 1.2	14.9 ± 1.9	22.7 ± 3.5	22.7 ± 4.4
L06	21 42 34.97	-44 27 08.70	292.0 ± 5.7	3.4	**0.03**	10.8 ± 1.1	13.9 ± 1.2	19.9 ± 4.5	24.0 ± 5.3
L07	21 42 50.74	-44 30 46.07	175.0 ± 6.6	5.5	0.11	2.4 ± 0.6	3.3 ± 0.7	10.2 ± 3.1	
	21 42 51.49	-44 30 43.18	1640.0 ± 5.9	2.6	**0.00**	105.0 ± 0.6	163.0 ± 0.9	293.2 ± 2.8	475.2 ± 5.5
L08	21 42 59.27	-44 25 00.16	355.0 ± 5.2	6.5	0.07	17.3 ± 0.4	22.9 ± 0.6	32.0 ± 2.6	21.0 ± 4.5
L09									
L10									
L11	21 42 44.73	-44 23 28.13	659.0 ± 5.5	2.9	**0.01**	44.5 ± 2.2	57.7 ± 1.4	70.3 ± 5.8	46.3 ± 6.9
L12	21 42 28.95	-44 22 11.12	99.4 ± 5.7	6.0	0.17	5.0 ± 0.5	7.1 ± 0.6	11.2 ± 3.0	15.7 ± 4.7
L13	21 43 03.06	-44 25 12.13	109.0 ± 5.2	8.0	0.19	6.3 ± 0.3	7.8 ± 0.6		
	21 43 02.64	-44 25 03.15	238.0 ± 5.2	3.4	**0.04**	13.9 ± 0.3	16.1 ± 0.6	22.2 ± 3.0	18.7 ± 4.7
L14	21 42 31.91	-44 31 30.09	155.0 ± 5.1	5.5	0.12	32.5 ± 0.4	21.6 ± 0.5	22.9 ± 2.6	23.3 ± 4.2
L15	21 42 49.30	-44 30 29.73	372.0 ± 5.8	2.8	**0.02**	24.5 ± 0.4	33.4 ± 0.6	53.3 ± 3.0	32.0 ± 4.4
L16	21 42 40.91	-44 25 17.56	143.0 ± 5.6	2.7	0.05	9.9 ± 0.4	11.6 ± 0.7	14.1 ± 3.0	
L17	21 42 09.94	-44 26 06.06	59.3 ± 5.7	4.4	0.16	4.4 ± 0.3	6.0 ± 0.6		
L18	21 42 33.58	-44 22 09.80	229.0 ± 5.1	7.9	0.13	8.7 ± 0.7	11.3 ± 0.9	16.1 ± 2.8	
	21 42 34.81	-44 22 10.35	180.0 ± 5.4	6.4	0.13				
L19	21 42 16.07	-44 28 49.50	139.0 ± 5.8	2.3	**0.04**	9.9 ± 0.5	13.4 ± 0.8	20.2 ± 3.0	28.4 ± 5.1
L20	21 42 41.21	-44 30 47.57	113.0 ± 5.4	4.0	0.11	33.5 ± 0.4	31.0 ± 0.5	21.0 ± 2.7	92.4 ± 4.3
	21 42 41.12	-44 30 37.23	62.8 ± 5.4	7.9	0.20	8.1 ± 0.5	12.7 ± 0.6	23.6 ± 3.1	29.6 ± 4.8
	21 42 40.47	-44 30 51.02	78.1 ± 5.4	7.2	0.19	71.0 ± 0.7	45.6 ± 0.8	40.9 ± 2.7	26.6 ± 4.7
L21									
L22									
L23									
L24	21 42 52.84	-44 24 55.95	94.6 ± 5.9	2.6	0.07	31.5 ± 0.4	21.4 ± 0.5	29.6 ± 3.3	
	21 42 52.85	-44 24 56.16	97.7 ± 7.3	2.0	**0.05**				
L25									
L26	21 42 26.22	-44 21 52.39	172.0 ± 5.9	4.8	0.09	17.1 ± 0.4	22.3 ± 0.6	41.9 ± 3.0	23.7 ± 5.0
L27	21 43 11.73	-44 26 16.94	56.5 ± 5.6	2.0	0.07	16.3 ± 0.9	16.7 ± 0.7	18.1 ± 3.2	18.9 ± 4.7
L28	21 42 37.36	-44 25 29.41	79.4 ± 5.6	6.7	0.19	19.7 ± 0.4	17.9 ± 0.5	21.0 ± 2.9	
	21 42 37.98	-44 25 35.86	71.8 ± 5.7	6.5	0.19				
L29	21 43 04.22	-44 22 06.52	206.0 ± 5.4	7.0	0.12	56.2 ± 0.6	66.8 ± 0.6	65.6 ± 3.0	47.1 ± 4.3
L30									
L31	21 42 31.05	-44 26 44.61	359.0 ± 5.8	2.4	**0.01**	82.4 ± 2.0	59.6 ± 1.4	63.9 ± 3.7	27.3 ± 4.8
	21 42 30.73	-44 26 43.02	105.0 ± 6.1	5.3	0.15				
L32									

[a] P was computed with search radius of 8$''$. Reliable identifications ($P < 0.05$) are listed in bold.

‘LABoCa J214210-442515’ on page 11
‘LABoCa J214309-442825’ on page 11
‘LABoCa J214244-442625’ on page 11
‘LABoCa J214252-442457’ on page 11
‘LABoCa J214232-442014’ on page 11
‘LABoCa J214226-442149’ on page 11
‘LABoCa J214311-442617’ on page 11
‘LABoCa J214237-442534’ on page 11
‘LABoCa J214304-442200’ on page 11
‘LABoCa J214312-442736’ on page 11
‘LABoCa J214231-442642’ on page 11
‘LABoCa J214242-442210’ on page 11

2007

The Astrophysical Journal, 660:97–116, 2007 May 1

THE INFRARED LUMINOSITY FUNCTION OF GALAXIES AT REDSHIFTS $z = 1$ AND $z \sim 2$ IN THE GOODS FIELDS

K. I. Caputi,[1,2] G. Lagache,[1] Lin Yan,[3] H. Dole,[1] N. Bavouzet,[1] E. Le Floc'h,[4] P. I. Choi,[3] G. Helou,[3] and N. Reddy[5]

Received 2006 October 11; accepted 2007 January 8

ABSTRACT

We present the rest-frame 8 μm LF at redshifts $z = 1$ and $\sim$2, computed from *Spitzer* 24 μm–selected galaxies in the GOODS fields over an area of 291 arcmin^2. Using classification criteria based on X-ray data and IRAC colors, we identify the AGNs in our sample. The rest-frame 8 μm LFs for star-forming galaxies at redshifts $z = 1$ and $\sim$2 have the same shape as at $z \sim 0$, but with a strong positive luminosity evolution. The number density of star-forming galaxies with $\log_{10}(\nu L_\nu^{8\ \mu m}) > 11$ increases by a factor >250 from redshift $z \sim 0$ to 1 and is basically the same at $z = 1$ and $\sim$2. The resulting rest-frame 8 μm luminosity densities associated with star formation at $z = 1$ and $\sim$2 are more than 4 and 2 times larger than at $z \sim 0$, respectively. We also compute the total rest-frame 8 μm LF for star-forming galaxies and AGNs at $z \sim 2$ and show that AGNs dominate its bright end, which is well described by a power law. Using a new calibration based on *Spitzer* star-forming galaxies at $0 < z < 0.6$ and validated at higher redshifts through stacking analysis, we compute the bolometric IR LF for star-forming galaxies at $z = 1$ and $\sim$2. We find that the respective bolometric IR luminosity densities are $(1.2 \pm 0.2) \times 10^9$ and $(6.6^{+1.2}_{-1.0}) \times 10^8\ L_\odot\ \mathrm{Mpc}^{-3}$, in agreement with previous studies within the error bars. At $z \sim 2$, around 90% of the IR luminosity density associated with star formation is produced by luminous and ultraluminous IR galaxies, with the two populations contributing in roughly similar amounts. Finally, we discuss the consistency of our findings with other existing observational results on galaxy evolution.

Subject headings: galaxies: evolution — galaxies: high-redshift — galaxies: luminosity function, mass function — infrared: galaxies

Online material: color figure

1. INTRODUCTION

Since the *Spitzer Space Telescope* (Werner et al. 2004) became operational in 2003 December, very important progress has been made in understanding the nature and properties of infrared (IR) galaxies. This progress has been revolutionary, in particular, for the study of galaxies at high redshifts ($z > 1$), to which all of the previous IR facilities operating in the wavelength range $\lambda \sim 5$–200 μm had basically no access. Previous missions such as the *Infrared Astronomical Satellite* (*IRAS*) and the *Infrared Space Observatory* (*ISO*) allowed for multiple studies of mid- and far-IR galaxies, but they were restricted to lower redshifts ($z \lesssim 1$) due to their sensitivity limits. Until the launch of *Spitzer*, our vision of the high-redshift IR universe was biased to the relatively small number of galaxies detected in submillimeter and millimeter surveys (e.g., Scott et al. 2002; Webb et al. 2003; Greve et al. 2004).

The sensitivity achieved by the Multiband Imaging Photometer for *Spitzer* (MIPS; Rieke et al. 2004) at 24 μm is enabling us for the first time to conduct systematic studies of IR galaxies at high redshifts. Several recent works have shown that, in contrast to what happens in the local universe, the IR extragalactic light is increasingly dominated by luminous and ultraluminous IR galaxies (LIRGs and ULIRGs, respectively) with increasing redshift (e.g., Le Floc'h et al. 2004, 2005; Lonsdale et al. 2004; Yan et al. 2004; Caputi et al. 2006a, 2006c). These LIRGs and ULIRGs constitute an important fraction of the most massive galaxies present at $z \gtrsim 1$ (Caputi et al. 2006a).

In a minor but nonnegligible fraction of high-redshift IR galaxies, the IR emission is produced by the presence of an active galactic nucleus (AGN). The exact proportion of AGN-dominated IR galaxies is actually not known, and the determination of such a ratio is one of the main problems of IR astronomy. A definitive AGN/star-forming galaxy separation requires the knowledge of the far-IR spectral energy distribution (SED) of these galaxies. Unfortunately, this is not possible for most high-z galaxies, as their far-IR emission is usually below the confusion limits at far-IR wavelengths (Dole et al. 2004). This separation is also complicated by the existence of mixed systems, where both star formation and AGN activity significantly contribute to the IR emission (e.g., Lutz et al. 2005; Yan et al. 2005; Le Floc'h et al. 2007). However, the AGN discrimination is essential to disentangle how much of the IR energy density is associated with star formation.

The study of a galaxy luminosity function (LF) at different redshifts allows us to understand the composition of the extragalactic background as a function of look-back time. The analysis of the changes of the LF with redshift is one of the most direct methods to explore the evolution of a galaxy population. The first studies of the IR galaxy LF in the local universe and at low ($z \lesssim 1$) redshifts have been based on *IRAS* and *ISO* data (e.g., Saunders et al. 1990; Xu 2000; Takeuchi et al. 2003, 2006; Pozzi et al. 2004; Serjeant et al. 2004). Using the most recent *Spitzer* MIPS data, Le Floc'h et al. (2005) analyzed in detail the evolution of the IR LF from $z = 0$ to $\sim$1. They found a positive evolution in both luminosity and density between these two redshifts, implying that IR galaxies were more numerous and the IR output was dominated by brighter galaxies at $z \sim 1$ than at $z \sim 0$. The IR galaxy LFs at higher redshifts have been explored by other authors (Pérez-González et al. 2005; Babbedge et al. 2006).

Rest-frame 8 μm luminosities, in particular, are of main relevance for star-forming galaxies as they contain information on polycyclic aromatic hydrocarbon (PAH) emission. PAH molecules characterize star-forming regions (Désert et al. 1990), and the associated emission lines dominate the SED of star-forming galaxies between wavelengths $\lambda = 3.3$ and 17 μm, with a main bump located around 8 μm. Rest-frame 8 μm luminosities have been confirmed to be good indicators of knots of star formation (Roussel et al. 2001; Förster-Schreiber et al. 2004; Calzetti et al. 2005) and of the overall star formation activity of star-forming galaxies (e.g., Wu et al. 2005), except in low-luminosity galaxies with intense ultraviolet (UV) radiation fields (Galliano et al. 2005).

In this work we compute the rest-frame 8 μm LF at redshifts $z = 1$ and $\sim$2, using 24 μm–selected galaxies in the two fields of the Great Observatories Origins Deep Survey (GOODS; Giavalisco et al. 2004). At $z \sim 2$, where the fraction of AGNs appears to be significant, we analyze separately the LFs for star-forming galaxies and for the total IR galaxy population. The two GOODS fields cover a smaller area than those analyzed by some other previous studies of the IR LF. However, they benefit from uniquely deep homogeneous photometric data sets, ranging from the X-rays to radio wavelengths, as well as an important spectroscopic coverage. As we explain in § 2, this makes possible an almost complete identification of 24 μm galaxies down to faint fluxes and the derivation of accurate redshift determinations (see also Caputi et al. 2006b, 2006c). These two characteristics are essential for a proper computation of the LF at high redshifts, without any conclusion relying on either completeness or selection function corrections.

The layout of this paper is as follows: In § 2 we describe in detail the selection of our 24 μm galaxy samples at redshifts $0.9 < z < 1.1$ and $1.7 < z < 2.3$. In § 3 we explain how we perform the separation between star-forming galaxies and AGNs within our sample. We compute the rest-frame 8 μm LF at $z = 1$ in § 4 and analyze its evolution from $z \sim 0$. In § 5 we present the rest-frame 8 μm LF at $z \sim 2$ and extend the analysis of the evolution up to this high redshift. Later, in § 6 we use a new empirical calibration based on *Spitzer* galaxies to obtain the bolometric IR LF at different redshifts. Finally, in §§ 7 and 8, respectively, we discuss our results and present some concluding remarks. We adopt throughout a cosmology with $H_0 = 70\ \mathrm{km\ s^{-1}\ Mpc^{-1}}$, $\Omega_M = 0.3$, and $\Omega_\Lambda = 0.7$.

2. THE IR GALAXY SAMPLE IN THE GOODS FIELDS

The GOODS fields, namely, the GOODS/Chandra Deep Field–South (GOODS/CDF-S) and GOODS/Hubble Deep Field–North (GOODS/HDF-N), have been observed by *Spitzer* as one of the Cycle 1 Legacy Science Programs (PI: Mark Dickinson). Extended areas of the CDF-S and HDF-N have also been observed as part of the *Spitzer* IRAC and MIPS Guaranteed Time Observers (GTO) programs (PI: Giovanni Fazio and George Rieke, respectively).

GOODS/IRAC maps at 3.6–8 μm and MIPS maps at 24 μm are now publicly available. The corresponding GOODS public 24 μm catalogs have been constructed using prior positional information from the IRAC 3.6 and 4.5 μm images and by an additional blind extraction of 24 μm sources. The resulting 24 μm catalogs are basically reliable and complete for galaxies with fluxes down to $S(24\ \mu\mathrm{m}) = 80\ \mu$Jy (Chary et al. 2007, and see the *Spitzer* GOODS Web site[6]). For a comparison, we note that the 24 μm catalog constructed from the shallower MIPS/GTO observations of the CDF-S achieves $\sim$80% completeness and only has $\sim$2% of spurious sources at a similar flux level (Papovich et al. 2004). Although, in principle, fainter sources can be detected in the deeper GOODS images, we decide to only use the conservative GOODS $S(24\ \mu\mathrm{m}) > 80\ \mu$Jy galaxy catalogs for the selection of our 24 μm galaxy samples at $z \sim 1$ and $\sim$2. In this way, our computed LFs are virtually not affected by incompleteness corrections (see §§ 4 and 5).

2.1. *Multiwavelength Analysis and Redshift Determinations for* 24 μm *Sources in the GOODS/CDF-S*

In the GOODS/CDF-S, we restrict our analysis to the 131 arcmin^2, which have deep J- and K_s-band coverage by the Infrared Spectrometer and Array Camera (ISAAC) on the "Antu" Very Large Telescope (Antu-VLT) (GOODS/EIS ver. 1.0 release; B. Vandame et al. 2007, in preparation). We used the $K_s < 21.5$ (Vega mag) galaxy catalog constructed by Caputi et al. (2006b) to identify the 24 μm galaxies in the GOODS/CDF-S catalog, using a matching radius of 2″. The percentage of 24 μm galaxies with double K_s-band identifications within this radius is only $\lesssim$8%, and 95% of the associations can be done restricting the matching radius to 1.5″ (Caputi et al. 2006a). In all cases of multiple identifications, we considered that the counterpart to the 24 μm source was the K_s galaxy closest to the 24 μm source centroid. The $K_s < 21.5$ mag catalog allows us to identify 515 24 μm galaxies within the 131 arcmin^2 area, i.e., $\sim$94% of the 24 μm galaxies with $S(24\ \mu\mathrm{m}) > 80\ \mu$Jy in this field.

Caputi et al. (2006b) measured multiwavelength photometry for all their $K_s < 21.5$ mag galaxies. They ran SExtractor (Bertin & Arnouts 1996) in "double-image mode" to perform aperture photometry on the GOODS/EIS version 1.0 J-band images, centered at the position of the K_s-band extracted sources. They also looked for counterparts of the $K_s < 21.5$ mag sources in the public GOODS Advanced Camera for Surveys (ACS) catalogs, which provided photometry in the B, V, I_{775}, and z bands. The stellarity parameter measured on the z-band images allowed them to separate out galactic stars. Finally, they ran SExtractor on the *Spitzer* IRAC 3.6 and 4.5 μm images to identify the $K_s < 21.5$ mag galaxies and measured aperture photometry at these longer wavelengths. We refer the reader to Caputi et al. (2006b) for additional details about the photometric measurements and applied aperture corrections.

Caputi et al. (2006b) obtained an estimated redshift for each one of their galaxies modeling their stellar SED from the B through the 4.5 μm bands. They used the public code HYPERZ (Bolzonella et al. 2000) with the GISSEL98 template library (Bruzual & Charlot 1993) and the Calzetti et al. (2000) reddening law to account for internal dust extinction.

The HYPERZ redshift estimates have been replaced by COMBO17 photometric redshifts (Wolf et al. 2004) for those galaxies with magnitudes $R < 23.5$ mag at redshift $z < 1$, which is the regime of higher accuracy for COMBO17. In these cases, the SED fitting has been constrained to the COMBO17 redshifts. The cross-correlation of the GOODS/CDF-S 24 μm catalog with the Caputi et al. (2006b) $K_s < 21.5$ mag catalog directly gives us estimated redshifts and best-fitting SED models for all the identified 24 μm galaxies.

2.2. *Multiwavelength Analysis and Redshift Determinations for* 24 μm *Sources in the GOODS/HDF-N*

In the GOODS/HDF-N, we followed a similar strategy for the analysis of sources as in the GOODS/CDF-S. However, unfortunately, we only have access to deep K_s-band data for a part of this field (Reddy et al. 2006a). Thus, we used the *Spitzer* IRAC 3.6 μm maps to identify the 24 μm galaxies. We analyzed

[1] Institut d'Astrophysique Spatiale, F-91405 Orsay; Université Paris-Sud 11 and CNRS (UMR 8617), France.
[2] Current address: Institute of Astronomy, Swiss Federal Institute of Technology (ETH Hönggerberg), CH-8093 Zürich, Switzerland; caputi@phys.ethz.ch.
[3] *Spitzer* Science Center, California Institute of Technology, Pasadena, CA 91125.
[4] Institute for Astronomy, University of Hawaii, Honolulu, HI 96822.
[5] Astronomy Option, California Institute of Technology, Pasadena, CA 91125.

[6] Available at http://data.spitzer.caltech.edu/popular/goods.

in this case the entire GOODS/HDF-N region, i.e., the 160 arcmin^2 with deep GOODS/*Hubble Space Telescope* ACS coverage. We ran SExtractor on the IRAC 3.6 and 4.5 μm images. We constructed a catalog of 3.6 μm sources, accepting only those objects also identified in the 4.5 μm band. To encompass the technique applied by Caputi et al. (2006b) on the IRAC maps of the GOODS/CDF-S, we measured photometry in circular apertures of 2.83″ diameter[7] and applied aperture corrections of 0.50 and 0.55 mag to the 3.6 and 4.5 μm magnitudes, respectively. We then used this 3.6 μm catalog to identify the 24 μm sources in the GOODS/HDF-N, using a matching radius of 2″. This allows us to identify 856 24 μm galaxies in the 160 arcmin^2 of the GOODS/HDF-N, i.e., ~95% of the 24 μm galaxies with $S(24\ \mu\text{m}) > 80\ \mu$Jy in this field. The identification completeness achieved for 24 μm galaxies in this field using 3.6 μm sources is similar to the identification completeness obtained for 24 μm galaxies in the GOODS/CDF-S using K_s-band sources. This indicates that the two identification methods are basically equivalent. In any case, the IRAC 3.6 and 4.5 μm data are incorporated in the SED modeling of all the sources in the two fields.

We followed up in the optical bands those IRAC 3.6 μm objects that were counterparts to $S(24\ \mu\text{m}) > 80\ \mu$Jy sources. Once more, we used the public GOODS ACS catalogs to obtain aperture photometry in the B, V, I_{775}, and z bands. In addition, we looked for counterparts of the 3.6 μm sources in the U- and HK'-band images of the GOODS/HDF-N (Capak et al. 2004). Although these images are relatively shallower than the other optical/near-IR data available for this field, we decided to include these data to improve the SED coverage. Finally, we incorporated the deep J- and K_s-band data from Reddy et al. (2006a) for those galaxies lying in the region where these data were available (<40% of the analyzed area).

We used the multiwavelength data from the U to the 4.5 μm bands to model the SED and obtain photometric redshifts for all of our 24 μm galaxies in the GOODS/HDF-N using HYPERZ, in an analogous way to that in Caputi et al. (2006b). As in the latter, we applied a set of criteria to control the HYPERZ output: (1) the photometric redshifts for galaxies detected in the shallow U-band catalogs were constrained to a maximum value $z_{\rm phot} = 2$, as bright U-band sources are unlikely to be beyond these redshifts; (2) analogously, the estimated redshifts of galaxies not detected in the U band but detected in the B band were constrained to a maximum value $z_{\rm phot} = 4$; (3) for the GOODS/HDF-N catalog, we found that HYPERZ produced an overdensity of galaxies in the redshift range $1.5 < z_{\rm phot} < 1.7$. Comparison with spectroscopic redshifts (see below) suggested that this overdensity was an artifact of HYPERZ applied to our sample. Thus, to test these possible spurious redshifts, we double-checked the fitting of all the galaxies with HYPERZ redshift $1.5 < z_{\rm phot} < 1.7$ using the PÉGASE library (Le Borgne & Rocca-Volmerange 2002). We kept the HYPERZ solution for those sources confirmed by PÉGASE as belonging to the 1.5–1.7 redshift range. For all the remaining $1.5 < z_{\rm phot} < 1.7$ galaxies, we replaced the photometric redshift by the PÉGASE estimate. This strategy improved the agreement with spectroscopic redshifts. The percentage of galaxies with PÉGASE redshifts in our final 24 μm catalog for the GOODS/HDF-N is 5%.

2.3. *The Final IR Galaxy Samples in the Combined GOODS Fields*

Our final 24 μm catalog contains 1371 24 μm sources with $S(24\ \mu\text{m}) > 80\ \mu$Jy over a total area of 291 arcmin^2. We identified only 22 out of 1371 sources as galactic stars. All the remaining sources are galaxies. Our aim is to separate two subsamples of galaxies from this final catalog: (1) the 24 μm galaxies with redshifts $0.9 < z < 1.1$ for the computation of the IR LF at $z = 1$, and (2) the 24 μm galaxies with redshifts $1.7 < z < 2.3$ for the computation of the IR LF at $z \sim 2$.

[7] The aperture size has been chosen in correspondence to the aperture sizes used in the GOODS ACS catalogs.

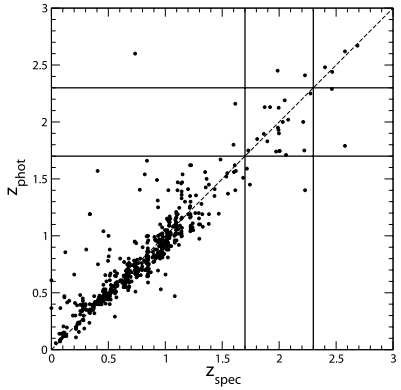

FIG. 1.—Comparison between photometric and spectroscopic redshifts for galaxies in our 24 μm–selected sample in the GOODS fields. The distribution of relative errors $dz = (z_{\rm phot} - z_{\rm spec})/(1 + z_{\rm spec})$ has a median −0.007 and a dispersion $\sigma_z = 0.05$. The horizontal lines separate the galaxies with $1.7 < z_{\rm phot} < 2.3$, and the vertical lines those with $1.7 < z_{\rm spec} < 2.3$. The distribution of relative errors for the $1.7 < z_{\rm spec} < 2.3$ subsample of galaxies has a median −0.01 and a dispersion $\sigma_z = 0.06$.

We performed a final step before separating the two definitive subsamples of 24 μm galaxies used in this work. In addition to the wealth of photometric data, both GOODS fields benefit from an important amount of spectroscopic data, most of which are publicly available (Cohen et al. 1996; Le Fèvre et al. 2004; Wirth et al. 2004; Vanzella et al. 2005, 2006; P. I. Choi et al. 2007, in preparation; among others). Some additional redshifts in the GOODS/CDF-S have been kindly made available to us by François Hammer and Héctor Flores. We compiled these data and found that more than 45% of our 24 μm galaxies in the combined fields had spectroscopic redshifts. We incorporated these spectroscopic redshifts into our catalog, which superseded the corresponding photometric values. The finally discarded photometric redshifts have been used to assess the quality of our redshift estimates. Figure 1 shows the comparison between photometric and spectroscopic redshifts for the galaxies in our sample for which both redshifts are available. We observe a good agreement between photometric estimates and real redshifts. The distribution of relative errors $dz = (z_{\rm phot} - z_{\rm spec})/(1 + z_{\rm spec})$ has a median value −0.007 and the dispersion is $\sigma_z = 0.05$.

From the definitive redshift catalog that incorporates spectroscopic redshifts, we select those 24 μm galaxies lying at $0.9 < z < 1.1$ and $1.7 < z < 2.3$.

The $0.9 < z < 1.1$ sample is composed of 227 galaxies with $S(24\ \mu\text{m}) > 80\ \mu$Jy and a median redshift $z = 1.00$. We use this sample to compute the IR LF at $z = 1$. More than 60% of these galaxies have spectroscopic redshifts $z_{\rm spec}$. The quality of photometric redshifts is similar to that for the total sample: the median of relative errors $dz = (z_{\rm phot} - z_{\rm spec})/(1 + z_{\rm spec})$ is −0.01 and the dispersion is $\sigma_z = 0.05$. In the computation of the IR LF at $z = 1$, we consider that these errors only affect those galaxies with photometric redshifts (<40%).

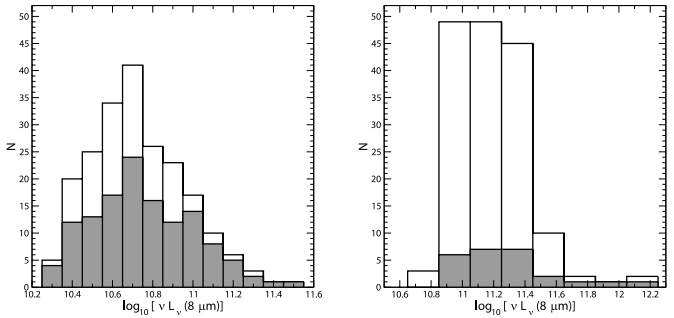

FIG. 2.—Distribution of rest-frame 8 μm luminosities for galaxies at redshifts $0.9 < z < 1.1$ (*left*) and $1.7 < z < 2.3$ (*right*). In each panel, the open and shaded histograms include all the galaxies and only those with spectroscopic redshifts, respectively.

Our $1.7 < z < 2.3$ sample contains 161 24 μm galaxies with $S(24\ \mu\text{m}) > 80\ \mu$Jy. This is the sample we use to compute the IR LF at redshift $z \sim 2$. The median redshift of these 161 galaxies is $z = 1.93$. Although for practicality we refer to these galaxies as the $z \sim 2$ sample, all the calculations made in §§ 5 and 6 take into account the actual median redshift value. More than 15% of the galaxies selected with $1.7 < z < 2.3$ have spectroscopic redshifts. The quality of photometric redshifts for the $z \sim 2$ sample can also be assessed from Figure 1. We see that the agreement between photometric and spectroscopic redshifts is still very reasonable for this high-redshift sample. The distribution of relative errors $dz = (z_{\rm phot} - z_{\rm spec})/(1 + z_{\rm spec})$ has a median −0.01 and a dispersion $\sigma_z = 0.06$. This statistics has been computed based on all sources (i.e., AGNs included; see below). This suggests that the SED templates we use to derive photometric redshifts are suitable for all our sample. The photometric redshift error bars affect the majority of galaxies in our $z \sim 2$ sample and are taken into account in the computation of the corresponding LF, as we explain in § 5.

We note that the galaxies with spectroscopic redshifts are representative of our entire 24 μm sample in each of the considered redshift bins ($0.9 < z < 1.1$ and $1.7 < z < 2.3$). The two panels in Figure 2 show the rest-frame 8 μm luminosities of all of our galaxies (*open histograms*) and those of galaxies with spectroscopic redshifts (*shaded histograms*), at these different redshifts. Details on the calculation of 8 μm luminosities are given in § 4. From Figure 2, we can see that galaxies with spectroscopic redshifts basically span the whole range of IR luminosities considered in this work. Thus, the errors derived from the comparison of photometric and spectroscopic redshifts are applicable to the entire IR LF.

3. THE NORMAL/ACTIVE GALAXY SEPARATION

In this work we would like to compare the IR LF for star-forming galaxies only with the total IR LF. To do this, we need to identify the active galaxies present in our sample.

One of the most efficient ways of identifying AGNs is through their X-ray emission. The GOODS fields have deep X-ray coverage obtained with the *Chandra X-Ray Observatory*: the 1 Ms maps for the CDF-S (Giacconi et al. 2002) and the 2 Ms maps for the HDF-N (Alexander et al. 2003). We used the corresponding public X-ray catalogs to identify the AGNs within our sample. However, given the depth of these catalogs (especially that of the HDF-N), X-ray sources include not only quasars and AGNs but also powerful starbursts that also emit in X-rays. To separate the two classes of X-ray sources, an optical versus X-ray flux diagram can be used. Figure 3 shows the R-band magnitude versus the soft X-ray flux of the X-ray–detected galaxies in our 24 μm sample in

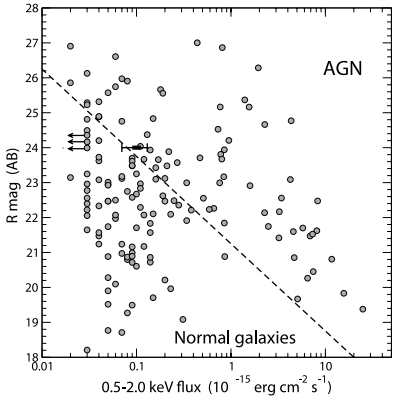

FIG. 3.—R-band magnitudes vs. soft X-ray fluxes for the X-ray-detected galaxies in our 24 μm galaxy sample in the GOODS/HDF-N. The error bar for a generic source with soft X-ray flux 10^{-16} ergs cm^{-2} s^{-1} and $R = 24$ mag is shown. The left-pointing arrows indicate that the soft X-ray flux 3×10^{-17} ergs cm^{-2} s^{-1} is an upper limit.

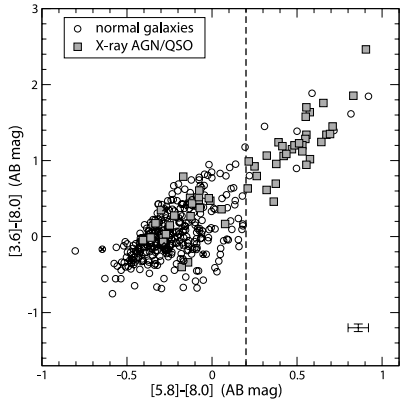

FIG. 4.—IRAC-based color-color diagram for the 24 μm sources with redshifts $z > 1.5$ in the GOODS fields. Filled squares and open circles refer to X-ray–classified AGNs and to all the other $z > 1.5$ 24 μm galaxies, respectively. The crosses indicate the few star-forming galaxies at $z > 1.5$ that are X-ray detected. The typical error bars for the colors of these sources are indicated in the lower right corner of the plot.

the HDF-N. The *R*-band magnitudes of our galaxies have been interpolated using the *V* and I_{775} magnitudes. This plot is similar to that presented in Alexander et al. (2003). The dashed line shows the empirical separation between normal galaxies and AGNs, as calibrated by Hornschemeier et al. (2001). Using this diagram, we identify the X-ray–detected AGNs within our 24 μm sample and, in particular, those at $0.9 < z < 1.1$ and $1.7 < z < 2.3$.

Some AGNs with weak soft X-ray fluxes but significant emission in the hard bands can contaminate the normal galaxy region in the *R*-band magnitude versus soft X-ray flux diagram. These AGNs are characterized by a flat photon index $\Gamma < 1.0$ (e.g., Hornschemeier et al. 2003). We also looked for these kinds of objects to identify the AGNs present in our sample.

It is known, however, that the X-ray selection can be incomplete for the selection of AGNs. Other active galaxies exist, which are not detected even in deep X-ray surveys. A complementary method to select active galaxies can be developed based on the analysis of the IR color excess in the *Spitzer* IRAC bands. Figure 4 shows the [3.6 μm] − [8 μm] versus [5.8 μm] − [8 μm] colors for all the galaxies with redshift $z > 1.5$ in our 24 μm sample. Open circles correspond to all those galaxies not classified as AGNs using X-ray data (either not detected in X-rays or X-ray sources classified as starbursts). Filled squares indicate the X-ray–classified AGNs. We restrict this diagram to high-redshift sources for the following reason. The stellar bump centered at rest-frame wavelength $\lambda \sim 1.6$ μm is shifted into the IRAC bands at $z \gtrsim 1.5$. For active galaxies, the galaxy SED at the same rest-frame wavelengths is dominated by a power-law continuum. Thus, it is expected that an IRAC-based color-color diagram is able to separate the AGNs through their IR excess. At low redshifts, this separation is much less clear, especially because star-forming galaxies with PAH emission can mimic the IR excess. Similar color-color plots have been used with the purpose of separating normal and active galaxies elsewhere (e.g., Lacy et al. 2004; Stern et al. 2005; Caputi et al. 2006a).

Inspection of Figure 4 shows that X-ray–selected AGNs display a wide range of [3.6 μm] − [8 μm] and [5.8 μm] − [8 μm] colors, while the vast majority of "normal galaxies" (i.e., non–X-ray–classified AGNs) appear on the left-hand side of this diagram, with a color [5.8 μm] − [8 μm] $\lesssim 0.2$ (AB). As we mentioned above, the relatively blue colors are produced by the stellar SED bump mapped at the IRAC wavelengths. The galaxies lying on the right-hand side, on the contrary, present an excess in the SED continuum that is characteristic of AGNs. Thus, based on this diagram, we adopt an empirical color cut to produce an additional AGN selection criterion: all the $z > 1.5$ galaxies with [5.8 μm] − [8 μm] > 0.2 (AB) within our sample are classified as AGNs. This same additional AGN selection criterion has been used by Caputi et al. (2006a).

We would like to note that while this color cut produces a safe criterion to select additional active galaxies, it is possibly not complete. The dispersion of colors displayed by X-ray–selected AGNs suggests that other active sources, not detected in X-rays and with no IRAC color excess, could also exist among the 24 μm galaxies. On the other hand, some of the X-ray–classified AGNs could be composite systems, where a fraction of the bolometric IR luminosity is actually due to star formation. Unfortunately, no AGN selection criterion appears to be both complete and reliable at the same time (e.g., Barmby et al. 2006). As we do not have information on the far-IR emission of our galaxies, our separation criteria are possibly the most adequate to discriminate AGNs.

For our sample of 227 24 μm galaxies with redshift $0.9 < z < 1.1$, only the X-ray criteria have been applied. We identify 23 out of 227 galaxies as AGNs, i.e., ~10% of the sample. We exclude the AGNs from our sample in order to determine the IR LF for star-forming galaxies at $z = 1$, but we note that the inclusion of AGNs only has a minor impact on the LF at this redshift.

For the sample at redshifts $1.7 < z < 2.3$, we applied both selection criteria to separate AGNs (X-ray and IRAC color classifications). The fraction of active galaxies at these redshifts appears to be more important than at $z \sim 1$. We identify 29 AGNs among our 161 24 μm galaxies at $1.7 < z < 2.3$, i.e., ~18% of the sample. A total of 23 out of these 29 AGNs have been identified using X-rays, and the remaining 6 AGNs have been classified through their IRAC colors. As seen below, the LFs computed including and excluding AGNs have nonnegligible differences because these objects dominate the bright end of the IR LF at these high redshifts. Throughout this paper, when we refer to the star-forming galaxies at redshift $z \sim 2$, we mean our sample of $161 - 29 = 132$ objects that we have not classified as AGNs at these redshifts.

4. THE REST-FRAME 8 μm LF AT REDSHIFT $z = 1$

4.1. *The k-Corrections from* 11.4–12.7 *to* 8 μm

Before computing the rest-frame 8 μm LF at $z \sim 2$, we aim to understand its evolution from $z \sim 0$ to redshift $z = 1$. For this, we compute the rest-frame 8 μm LF for our 204 24 μm–selected star-forming galaxies in the redshift range $0.9 < z < 1.1$. AGNs have been excluded from this analysis. AGNs constitute ~10% of our sample with $0.9 < z < 1.1$, and their exclusion does not significantly change the shape of the 8 μm LF at $z = 1$. This is in contrast to what we find at $z \sim 2$, where AGNs constitute a somewhat higher fraction of sources that dominate the bright end of the rest-frame 8 μm LF (see § 5).

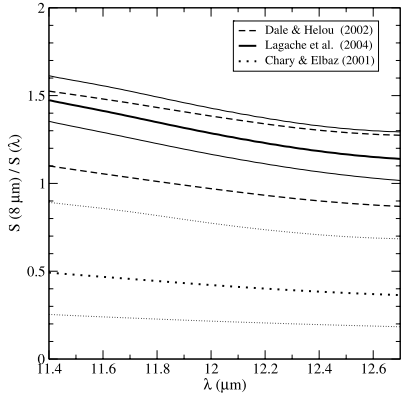

FIG. 5.—The *k*-corrections between 11.4–12.7 and 8 μm fluxes obtained using different IR galaxy model templates: Lagache et al. (2004; *solid lines*), Chary & Elbaz (2001; *dotted lines*), and Dale & Helou (2002; *dashed lines*). The thin solid and dotted lines indicate the interval of corrections obtained using the different models of Lagache et al. (2004) and Chary & Elbaz (2001), respectively, with bolometric IR luminosity $L_{\rm IR} > 10^{11}$ $L_\odot$. The corresponding thick lines indicate median *k*-corrections. The dashed line corresponds to the Dale & Helou (2002) model with parameter $\alpha = 1.1$ and 1.4.

We compute the rest-frame 8 μm luminosity ($\nu L_\nu^{8\,\mu{\rm m}}$) of each galaxy as $\nu L_\nu^{8\,\mu{\rm m}} = \nu 4\pi k(\lambda_{\rm rf}) S(24\ \mu{\rm m}) d_L^2(z)$, where $S(24\ \mu{\rm m})$ is the 24 μm flux, $d_L(z)$ is the luminosity distance, and $k(\lambda_{\rm rf})$ is the corresponding *k*-correction at the rest-frame wavelength $\lambda_{\rm rf}$. The width of the redshift bin we consider, $0.9 < z < 1.1$, implies that the observed 24 μm maps rest-frame wavelengths 11.4 $\mu{\rm m} < \lambda_{\rm rf} < 12.7$ μm. We need then to apply *k*-corrections to convert the rest-frame 11.4–12.7 μm into 8 μm fluxes.

To compute these *k*-corrections, we analyze different sets of IR galaxy templates available in the literature, namely, the models by Chary & Elbaz (2001) and Elbaz et al. (2002), Dale et al. (2001) and Dale & Helou (2002), and Lagache et al. (2004). We convolve the SED templates in all these models with the transmission function of the 24 μm filter and obtain the relation between the fluxes at 11.4–12.7 and 8 μm. Figure 5 shows the λ–to–8 μm *k*-corrections in the wavelength range $\lambda_{\rm rf} = 11.4$–12.7 μm. Different line styles indicate the *k*-corrections obtained with different SED templates. The solid and dotted lines correspond to the range of *k*-corrections derived for galaxies with bolometric IR luminosities $L_{\rm IR} > 10^{11}$ $L_\odot$, from the Lagache et al. (2004) and Chary & Elbaz (2001) models, respectively (with thick lines indicating the median values). The dashed lines show the *k*-corrections obtained with the Dale et al. (2001) SED model with parameters $\alpha = 1.1$ and 1.4 (see Dale et al. 2001). It is clear from inspection of Figure 5 that the *k*-corrections between 11.4–12.7 and 8 μm obtained with these different models have some significant dispersion. These differences are produced by the limited knowledge on PAH emission when modeling the PAH-dominated region of a star-forming galaxy SED.

In this work we adopt the median *k*-corrections obtained with the Lagache et al. (2004) models of star-forming galaxies with bolometric IR luminosities $L_{\rm IR} > 10^{11}$ $L_\odot$ (*thick solid line in* Fig. 5). As we show in § 6.1.2, the Lagache et al. (2004) templates produce an 8 μm–to–bolometric IR luminosity conversion quite close to that measured on the observed SED of *Spitzer* galaxies (Bavouzet et al. 2006). This suggests that these templates incorporate an adequate modeling of the PAH emission region in the star-forming galaxy SED.

4.2. *The* $1/V_{\rm max}$ *Method*

We compute the rest-frame 8 μm LF for star-forming galaxies at redshift $z = 1$ using the $1/V_{\rm max}$ method (Schmidt 1968). For this calculation, we consider the 204 star-forming galaxies with redshift $0.9 < z < 1.1$ within our sample. The advantage of the $1/V_{\rm max}$ technique is that it allows us to compute the LF directly from the data, with no parameter dependence or model assumption. Besides, the normalization of the LF is directly obtained from the same calculation. The comoving volume $V_{\rm max} = V_{z_{\rm max}} - V(z = 0.9)$ for each source corresponds to the maximum redshift $z_{\rm max}$ at which it would be included in the catalog, given the limiting flux $S(24\ \mu{\rm m}) = 80$ μJy, and provided that this redshift is smaller than the maximum of the considered redshift bin (in this case $z = 1.1$). Otherwise, $V_{\rm max}$ is equal to the volume corresponding to the $0.9 < z < 1.1$ bin $V_{\rm max} = V_{\rm bin}$.

As we explained in § 2, the GOODS 24 μm catalogs are basically complete down to the limiting flux and, thus, no sample completeness corrections are needed for our catalogs. However, we do apply completeness corrections to account for the percentage (5%–6%) of unidentified 24 μm sources (see § 2). These identification completeness corrections are very small, and none of the conclusions presented here depend on the application of such corrections.

We present the results of our rest-frame 8 μm LF at redshift $z = 1$ computed with the $1/V_{\rm max}$ method in Figure 6 (*triangles*) and Table 1. This LF, as well as all the others presented in this work, has been computed jointly on the GOODS/CDF-S and GOODS/HDF-N. Although we have checked the consistency within the error bars of the LF obtained in the two fields separately, the sample variance effects are more important than when considering both fields combined (see Fig. 9). We show the 8 μm LF function computed with the $1/V_{\rm max}$ method only in the completeness region of 8 μm luminosities ($\nu L_\nu^{8\,\mu{\rm m}} \gtrsim 3 \times 10^{10}$ $L_\odot$), imposed by the flux limits of the 24 μm survey and the considered redshifts. The total comoving volume probed by our survey is 1.3×10^5 Mpc^3.

The error bars for these LF values depend not only on the number of sources (Poisson statistics) but also on the errors in the photometric redshifts and in the *k*-corrections applied. The errors in the photometric redshifts affect only <40% of our galaxies at $0.9 < z < 1.1$, given the high percentage of available spectroscopic redshifts. To account for the errors in the photometric redshifts, we made Monte Carlo simulations of our $\nu L_\nu^{8\,\mu{\rm m}}$ catalogs. We produced 1000 simulated catalogs, each one with the same number of sources as our original $0.9 < z < 1.1$ catalog of star-forming galaxies (i.e., 204 sources each). The redshift of each source has been allowed to randomly vary following a Gaussian distribution centered at $z_{\rm center} = z - 0.01$ and with a dispersion $\sigma_z = 0.05(1 + z)$ (see § 2.3), where z is the redshift of the source in the original catalog. The redshift of those sources with spectroscopic determinations has been left unchanged. For the *k*-corrections, we fixed the error bars to $\epsilon = 0.50$, which is roughly the dispersion between the different Lagache et al. (2004) and Dale & Helou (2002) model predictions (see Fig. 5). To include these errors in the simulations, we computed the rest-frame 8 μm luminosity $\nu L_\nu^{8\,\mu{\rm m}}$ of each galaxy in the mock catalog allowing

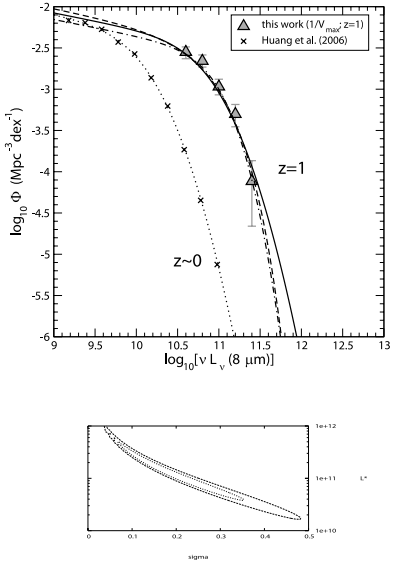

FIG. 6.—*Top*: Rest-frame 8 μm LF for star-forming galaxies at $z = 1$ in the GOODS fields, compared to the 8 μm LF at $z \sim 0$. The crosses show the 8 μm LF for star-forming galaxies at $z \sim 0$, as computed by Huang et al. (2006) with the $1/V_{\max}$ method. The dotted line represents the best χ^2 fit obtained using a double exponential function as that in eq. (1). The triangles show the $1/V_{\max}$ LF at $z = 1$ obtained in this work, only strictly in the region of completeness of 8 μm luminosities. Lines of different styles show the 8 μm LF at $z = 1$ computed with the ML STY analysis, assuming different laws: a double exponential form with bright-end slope fixed to the local value ($\sigma = 0.36$; *solid line*), the same double exponential form with a free σ parameter (*dot-dashed line*), and a Schechter function (*dashed line*). *Bottom*: The 68.3% and 95.4% confidence levels in $(\sigma, \nu L_\nu^{*8\ \mu m})$-space in the case of a double exponential law with σ as a free parameter. The parameter values yielding the ML are $\sigma = 0.20^{+0.11}_{-0.07}$ and $L^* \equiv \nu L_\nu^{*8\ \mu m} = (1.32^{+1.31}_{-0.74}) \times 10^{11}\ L_\odot$.

the corresponding *k*-correction to have a random value within the range of its error bar. Finally, the LF has been recomputed with the $1/V_{\max}$ method for each of the mock catalogs, with exactly the same procedure as for the original catalog. From the distribution of the LF values in each $\nu L_\nu^{8\ \mu m}$ bin, we determined the error bars on our original $1/V_{\max}$ results.

For a comparison, we also show the 8 μm LF of star-forming galaxies at redshift $z \sim 0$ (strictly $0 < z < 0.3$, with median $z \approx 0.2$), computed by Huang et al. (2006), using the $1/V_{\max}$ method applied to IRAC 8 μm GTO data (*crosses in* Fig. 6). No error bars have been plotted for this LF, as they are significantly smaller than the error bars of the LF we determine here. The comparison of this $1/V_{\max}$ LF with our own determination at $z = 1$ shows a substantial increment of the density of star-forming galaxies with rest-frame 8 μm luminosities $\log_{10}(\nu L_\nu^{8\ \mu m}) \gtrsim 10.5$, with increasing redshift. We note that this behavior is evident from the $1/V_{\max}$ calculation, independently of the parametric analysis we discuss below.

TABLE 1
THE REST-FRAME 8 μm LF FOR STAR-FORMING GALAXIES AT $z = 1$ OBTAINED WITH THE $1/V_{\max}$ METHOD

$\log_{10}(\nu L_\nu^{8\ \mu m})$	$\log_{10}\Phi(\mathrm{Mpc}^{-3}\ \mathrm{dex}^{-1})$
10.60	$-2.55^{+0.06}_{-0.08}$
10.80	$-2.66^{+0.07}_{-0.07}$
11.00	$-2.97^{+0.09}_{-0.10}$
11.20	$-3.30^{+0.12}_{-0.15}$
11.40	$-4.12^{+0.25}_{-0.54}$

4.3. *The Maximum Likelihood Analysis*

The shape of the $z \sim 0$ LF can be fitted with a double exponential function (Saunders et al. 1990; Pozzi et al. 2004; Le Floc'h et al. 2005):

$$\Phi(L)d\log_{10}(L) = \Phi^*\left(\frac{L}{L^*}\right)^{1-\alpha} \times \exp\left[-\frac{1}{2\sigma^2}\log_{10}^2\left(1+\frac{L}{L^*}\right)\right] d\log_{10}(L), \quad (1)$$

where, in this case, $L \equiv \nu L_\nu^{8\ \mu m}$. The parameters α and $1/\sigma^2$ correspond to the slopes at the faint and the bright ends, respectively. L^* is the characteristic $\nu L_\nu^{*8\ \mu m}$ luminosity where the transition between the faint and bright regimes occurs, and Φ^* is the normalization factor. Usually, the parameter α is fixed a priori, as the faint end of the LF is poorly constrained. Fixing $\alpha = 1.2$ (e.g., Zheng et al. 2006) and using a χ^2 minimization technique, we obtain that the best-fitting parameters for the LF at $z \sim 0$ are $\sigma = 0.36 \pm 0.01$, $L^* = (5.8 \pm 0.2) \times 10^9\ L_\odot$, and $\Phi^* = (5.7 \pm 0.1) \times 10^{-3}$ Mpc^{-3} dex^{-1}. The resulting curve (*dotted line in* Fig. 6) produces an excellent fitting of the $1/V_{\max}$ LF at $z \sim 0$.

Assuming that the form given in equation (1) is also suitable to describe the IR LF for star-forming galaxies at higher redshifts, we obtain a second independent calculation of the rest-frame 8 μm LF at redshift $z = 1$ using the STY (Sandage et al. 1979) maximum likelihood (ML) analysis. This is a parametric technique that assumes a given shape for the LF. No data binning is involved in the calculation. The advantage of the ML analysis over the $1/V_{\max}$ technique is that the former does not contain any assumption on a uniform spatial distribution of galaxies. The corresponding likelihood estimator reads

$$\mathcal{L}\left[s_k|(z_i, L_i)_{i=1,\ldots,N}\right] = \prod_{i=1}^{N}\left[\frac{\Phi(s_k, L)}{\int_{\log_{10}(Li0)}^{+\infty}\Phi(s_k, L)d\log_{10}(L)}\right]^{w_i}, \quad (2)$$

where the product is made over the $i = 1, \ldots, N$ galaxies of the sample. Here $\Phi(s_k, L)$ is the adopted form for the LF as a function of the luminosity L, and which depends on the parameters s_k, and L_0^i is the minimum luminosity at which the ith galaxy would be observable, given its redshift z_i and the flux limit of the survey. The weighting factors w_i allow us to take into account completeness corrections (Zucca et al. 1994; Ilbert et al. 2005). By maximizing $\mathcal{L}$ (or, for simplicity, its logarithm), one can obtain the values of the parameters s_k yielding the ML. The normalization factor Φ^* is recovered after the maximization, by integrating the obtained ML LF without normalization in the range of luminosities of the survey, and making it equal to the number density of observed galaxies. We note that the ML analysis provides a direct calculation of the LF (i.e., it does not constitute a fitting

TABLE 2
PARAMETER VALUES CHARACTERIZING THE REST-FRAME 8 μm LF FOR STAR-FORMING GALAXIES AT $z = 1$

Functional Form	α	σ	$\nu L_\nu^{*8\ \mu m}$ ($L_\odot$)	Φ^* ($\mathrm{Mpc}^{-3}\ \mathrm{dex}^{-1}$)
Double exponential (eq. [1])	1.2 (fixed)	0.36 (fixed)	$(3.55^{+0.52}_{-0.40}) \times 10^{10}$	$(3.95^{+0.50}_{-0.49}) \times 10^{-3}$
	1.2 (fixed)	$0.20^{+0.11}_{-0.07}$ (free)	$(1.10^{+0.99}_{-0.64}) \times 10^{11}$	$(2.54^{+0.60}_{-0.35}) \times 10^{-3}$
Schechter (eq. [3])	1.2 (fixed)	...	$(7.2^{+0.9}_{-0.7}) \times 10^{10}$	$(3.88^{+0.46}_{-0.41}) \times 10^{-3}$

procedure as the χ^2 minimization) and is completely independent of the LF obtained with the $1/V_{\max}$ technique.

For the case of our rest-frame 8 μm LF at $z = 1$, we apply the STY method using equation (1) and fixing the slopes at the faint and bright ends to the same values as at $z \sim 0$, i.e., $\alpha = 1.2$ and $\sigma = 0.36$, respectively. In this case, we obtain that the value of the characteristic luminosity that maximizes the likelihood estimator is $L^* \equiv \nu L_\nu^{*8\ \mu m} = (3.55^{+0.52}_{-0.40}) \times 10^{10}\ L_\odot$, and the derived normalization factor is $\Phi^* = (3.95^{+0.50}_{-0.49}) \times 10^{-3}$ Mpc^{-3} dex^{-1}. The error bars on L^* have been computed considering $\Delta(\ln \mathcal{L}) = -0.5$ and the uncertainties derived from the Monte Carlo simulations. The degeneracies in parameter space given by $\Delta(\ln \mathcal{L}) = -0.5$ dominate the L^* error budget. The error bars on Φ^* have been derived using the extreme values of L^* (i.e., L^* plus or minus its error). The resulting curve for the ML LF at $z = 1$, obtained with a double exponential law with $\sigma = 0.36$, is indicated with a solid line in the top panel of Figure 6 (see also Table 2).

Another possibility is to allow the slope at the bright end ($1/\sigma^2$) to be a free parameter in the ML analysis. Doing so, we obtain that the ML is produced for $\sigma = 0.20^{+0.11}_{-0.07}$, $L^* \equiv \nu L_\nu^{*8\ \mu m} = (1.10^{+0.99}_{-0.64}) \times 10^{11}\ L_\odot$, and the derived normalization is $\Phi^* = (2.54^{+0.60}_{-0.35}) \times 10^{-3}$ Mpc^{-3} dex^{-1} (*dot-dashed line in* Fig. 6, *top panel*). The degeneracy in (σ, L^*)-space is shown in the bottom panel of this figure.

The LF obtained with the ML analysis, in the case of both a free σ-value and fixed $\sigma = 0.36$, is in good agreement with the LF computed with the $1/V_{\max}$ method. This confirms that the double exponential law in equation (1) also provides a good description of the 8 μm LF at high redshifts. The degeneracy existing in the σ-value is due to the limited constraint that our data can put on the bright end of the LF at $z = 1$. In Figure 6 we see that the double exponential forms with $\sigma = 0.20$ and 0.36 only differ significantly at the very bright end of the LF ($\nu L_\nu^{*8\ \mu m} \gtrsim 10^{11.5}\ L_\odot$ at $z = 1$). Large-area surveys with a significant number of very bright IR galaxies, as, for example, the $\sim$2 deg^2 *Spitzer* COSMOS survey (Sanders et al. 2007), are necessary to set tighter constraints in (σ, L^*)-space.

Finally, we explore whether other functional forms could also be suitable to describe the rest-frame 8 μm LF at $z = 1$. We repeat the calculation of the LF with the STY method, but this time using a Schechter (1976) function:

$$\Phi(L)d\log_{10}(L) = \Phi^*\left(\frac{L}{L^*}\right)^{1-\alpha}\exp\left(-\frac{L}{L^*}\right)d\log_{10}(L). \quad (3)$$

By fixing $\alpha = 1.2$, we find that the ML is obtained for a characteristic luminosity $L^* \equiv \nu L_\nu^{*8\ \mu m} = (7.2^{+0.9}_{-0.7}) \times 10^{10}\ L_\odot$ and the derived normalization is $\Phi^* = (3.88^{+0.46}_{-0.41}) \times 10^{-3}$ Mpc^{-3} dex^{-1}. The resulting ML curve is shown with a dashed line in Figure 6. The Schechter form actually produces an LF quite close to that obtained with the $\sigma = 0.20$ double exponential form, within the observed luminosity range of our survey.

The degeneracy existing in the shape of the IR LF, as constrained from our data, produces some uncertainty in the determination of the number density of the most luminous IR galaxies (see Table 5). However, as we discuss below, this degeneracy has little impact on the derived luminosity density. This value is mainly governed by the turnover of the LF, which we can properly determine here, given the depth of our survey.

4.4. *The Evolution of the Rest-Frame* 8 μm *LF from* $z \sim 0$ *to* $z = 1$

When using the same law to describe the rest-frame 8 μm LF at both redshifts $z \sim 0$ and $z = 1$, the differences found in the characteristic luminosity L^* and the normalization parameter Φ^* can be understood as a luminosity and density evolution:

$$L^*(z_2 = 1) = L^*(z_1 \sim 0)\left(\frac{1+z_2}{1+z_1}\right)^{\gamma_L},$$
$$\Phi^*(z_2 = 1) = \Phi^*(z_1 \sim 0)\left(\frac{1+z_2}{1+z_1}\right)^{\gamma_\delta}, \quad (4)$$

where we strictly use $z_1 = 0.2$ (the median redshift of the Huang et al. [2006] sample). Parameters γ_L and γ_δ describe the evolution of the L^* and Φ^* parameters with redshift. The values of these parameters at $z \sim 0$ and $z = 1$, corresponding in both cases to a double exponential with $\sigma = 0.36$, produce (see § 4.3)

$$\gamma_L = 3.5 \pm 0.4,$$
$$\gamma_\delta = -0.7 \pm 0.1. \quad (5)$$

This implies a strong positive-luminosity evolution and a mild negative-density evolution between $z \sim 0$ and $z = 1$. The mild negative-density evolution to $z = 1$ refers to the overall normalization Φ^*. However, it is clear from Figure 6 that, within the 8 μm luminosity range spanned by our sample, the density of galaxies at $z = 1$ is larger than that at $z \sim 0$. This is consistent with what has been found by Le Floc'h et al. (2005) from the analysis of the rest-frame 15 μm LF and confirms, once more, the increasing importance of IR galaxies up to redshift $z \sim 1$. For clarity, the densities of galaxies we obtain by integrating the rest-frame 8 μm LF above different luminosity cuts at different redshifts are shown in Table 5.

By integrating the LF weighted by the luminosity values, over all luminosities, we can obtain the total rest-frame 8 μm luminosity density. In fact, for the obtention of the total luminosity density, the precise limits of integration are irrelevant, provided that the turnover of the LF is completely contained within these limits. Moreover, the use of any of the different laws that are suitable to describe the LF (see § 4.3) produces basically the same value for the luminosity density, as all of them are in close agreement around the turnover.

At $z = 1$, we find that the total rest-frame 8 μm luminosity density is $(1.4 \pm 0.1) \times 10^8$, $(1.3 \pm 0.1) \times 10^8$, and $(1.4 \pm 0.1) \times 10^8\ L_\odot$ Mpc^{-3} for the cases of a double exponential law with

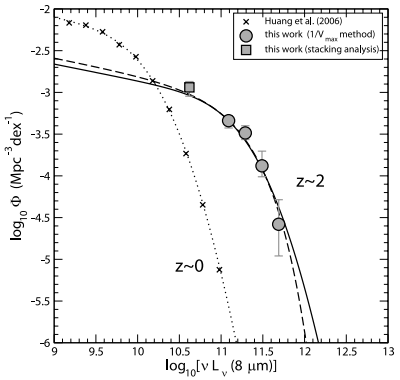

FIG. 7.—Rest-frame 8 μm LF for star-forming galaxies at $z \sim 2$ in the GOODS fields. The filled circles show the LF in the region of completeness of 8 μm luminosities, as computed with the $1/V_{\rm max}$ method. The solid and dashed lines show the 8 μm LF at $z \sim 2$ computed with the ML STY method, assuming a double exponential form as in eq. (1) and a Schechter function, respectively. The filled square is an extension of the LF at the faint end, obtained using stacking analysis (see text for details). The addition of this point a posteriori allows us to validate the extrapolated shape of the LF at the faint end. The 8 μm LF at $z \sim 0$ computed by Huang et al. (2006) has also been added for a comparison.

$\sigma = 0.36$, $\sigma = 0.20$, and a Schechter function, respectively. This is $\sim$4.0–4.3 times the corresponding luminosity density at $z \sim 0$.

5. THE REST-FRAME 8 μm LF AT REDSHIFT $z \sim 2$

5.1. *The Rest-Frame* 8 μm *LF for Star-forming Galaxies at Redshift* $z \sim 2$

The selection of 24 μm galaxies at redshift $z \sim 2$ is particularly suitable to compute the rest-frame 8 μm LF. The IR SED of star-forming galaxies is characterized by the presence of PAH emission lines from rest-frame wavelengths $\lambda = 3.3$ through 17 μm (Désert et al. 1990). In particular, one of the main features in the SED is the PAH bump around 7.7 and 8.6 μm, responsible for a positive selection effect on galaxies at $z \sim 1.9$ at 24 μm (Caputi et al. 2006c). The light associated with this bump produces a substantial fraction of the observed 24 μm output at $z \sim 2$ (the remaining part mainly being produced by AGNs). The study of the rest-frame 8 μm LF for star-forming galaxies gives direct information on the luminosity distribution of PAH emission in IR galaxies. In particular at $z \sim 2$, it should allow us to understand this PAH emission distribution when the universe was only one-fourth of its present age.

We compute the rest-frame 8 μm luminosity ($\nu L_\nu^{8\,\mu{\rm m}}$) of each galaxy in a similar way as for those galaxies at $0.9 < z < 1.1$. In this case, the width of the redshift bin we consider, $1.7 < z < 2.3$, implies that the observed 24 μm maps rest-frame wavelengths 7.2 $\mu{\rm m} < \lambda_{\rm rf} < 8.9$ μm. As we have seen in § 4.1, the k-corrections are usually computed based on SED models, which have been calibrated using local IR galaxy templates and other observables. However, we showed that this can be somewhat controversial, especially in the PAH-dominated region, where different models show important discrepancies. To compute the k-corrections from 7.2–8.9 to 8 μm, we can avoid relying on any IR SED model by directly using measured rest-frame IR spectra of star-forming galaxies at redshifts $z \gtrsim 1.5$, convolved with the 24 μm filter transmission function. These spectra have been obtained with the Infrared Spectrograph (IRS) for *Spitzer* (Lutz et al. 2005; Yan et al. 2005). These spectra correspond to star-forming ULIRGs that are on average brighter than those studied here. In spite of that, the k-corrections derived within the PAH region from these galaxies are expected to be applicable to our galaxies. For example, the equivalent widths of PAH lines in the Yan et al. (2005) star-forming galaxies are comparable to those of other lower luminosity ULIRGs. In general, PAH line equivalent widths appear to be quite independent of the bolometric IR luminosities of star-forming galaxies (Peeters et al. 2004; Brandl et al. 2006).

TABLE 3
THE REST-FRAME 8 μm LF FOR STAR-FORMING GALAXIES AT $z \sim 2$ OBTAINED WITH THE $1/V_{\rm max}$ METHOD

$\log_{10}(\nu L_\nu^{8\,\mu{\rm m}})$	$\log_{10}\Phi$(Mpc^{-3} dex^{-1})
11.09	$-3.34^{+0.06}_{-0.09}$
11.29	$-3.49^{+0.09}_{-0.08}$
11.49	$-3.88^{+0.18}_{-0.13}$
11.69	$-4.58^{+0.29}_{-0.38}$

For the wavelength range considered, the k-correction factors derived from empirical spectra vary between $k = 1$ (at $\lambda_{\rm rf} = 8$ μm) and $k = 1.44 \pm 0.36$ (at $\lambda_{\rm rf} = 8.9$ μm). These k-corrections are in good agreement with those predicted by the Lagache et al. (2004) models. The median of the differences is $\sim$5% in the considered wavelength range (7.2–8.9 μm). Thus, the use of empirical k-corrections for our rest-frame 8 μm LF at $z \sim 2$ is consistent with the use of model-dependent k-corrections at $z = 1$.

As at redshift $z = 1$, we compute the rest-frame 8 μm LF at redshift $z \sim 2$ alternatively using the $1/V_{\rm max}$ method and the ML analysis. For the star-forming galaxy LF at this redshift, we consider the 132 star-forming galaxies with $1.7 < z < 2.3$ within our sample. The rest-frame 8 μm LF for star-forming galaxies at $z \sim 2$ computed with the two methods is shown in Figure 7 (filled circles for the $1/V_{\rm max}$ method and solid and dashed lines for the ML analysis) and Tables 3 and 4. The total comoving volume probed at these redshifts is 5.7×10^5 Mpc^{-3}.

For the $1/V_{\rm max}$ calculation, we computed the error bars taking into account Poisson statistics and the errors on photometric redshifts and k-corrections through Monte Carlo simulations. We constructed 1000 mock catalogs, each one containing 132 galaxies, as the original catalog. The redshift of each source has been allowed to randomly vary following a Gaussian distribution centered at $z_{\rm center} = z - 0.01$ and with a dispersion $\sigma_z = 0.06(1+z)$ (see § 2.3), where z is the redshift of the source in the original catalog. The redshifts of those sources with spectroscopic determinations have been left unchanged. To include the uncertainties in the k-corrections, we computed the rest-frame 8 μm luminosity $\nu L_\nu^{8\,\mu{\rm m}}$ of each galaxy in the mock catalog allowing the corresponding k-correction to have a random value within the range of its error bar. Once more, we recompute the LF with the $1/V_{\rm max}$ method for each of the mock catalogs, with exactly the same procedure as for the original catalog. The distribution of the LF values in each $\nu L_\nu^{8\,\mu{\rm m}}$ bin determines the error bars on our original $1/V_{\rm max}$ LF.

The LF computed with the $1/V_{\rm max}$ method that is shown in Figure 7 exclusively corresponds to the region of $\nu L_\nu^{8\,\mu{\rm m}}$ completeness ($\nu L_\nu^{8\,\mu{\rm m}} \gtrsim 10^{11}$ $L_\odot$). This is essential to assure that our results are not affected by incompleteness effects.

TABLE 4
PARAMETER VALUES CHARACTERIZING THE REST-FRAME 8 μm LF FOR STAR-FORMING GALAXIES AT $z \sim 2$

Functional Form	α	σ	$\nu L_\nu^{*\,8\,\mu{\rm m}}$ ($L_\odot$)	Φ^* (Mpc^{-3} dex^{-1})
Double exponential (eq. [1])	1.2 (fixed)	0.36 (fixed)	$(8.3^{+1.5}_{-1.1}) \times 10^{10}$	$(9.0^{+2.1}_{-1.7}) \times 10^{-4}$
Schechter (eq. [3])	1.2 (fixed)	...	$(1.62^{+0.20}_{-0.21}) \times 10^{11}$	$(9.3^{+2.1}_{-1.3}) \times 10^{-4}$

Also at these redshifts, we analyze the field-to-field variations computing the rest-frame 8 μm LF in the GOODS/CDF-S and GOODS/HDF-N separately. The results are shown in the right panel of Figure 9. We see that, in spite of the sample variance, the two LFs are still consistent within the error bars.

We perform the ML analysis for the combined fields in the same way as for galaxies at $0.9 < z < 1.1$. Once more, we assume that the double exponential form given by equation (1) with fixed slopes $\alpha = 1.2$ and $1/\sigma^2 = 1/(0.36)^2$ can be used to describe the rest-frame 8 μm LF for star-forming galaxies at $z \sim 2$. In this case, the number of galaxies is not sufficient to allow us to leave the bright-end slope as a free parameter (i.e., the ML algorithm does not converge to reasonable values). Also, the adoption of the same σ-value as at $z \sim 0$ is useful to directly compare the resulting values of L^* and Φ^* at different redshifts. Applying the STY method with a double exponential with $\sigma = 0.36$ to our star-forming galaxies at $z \sim 2$, we obtain that the value of the characteristic luminosity that maximizes the ML estimator is $L^* \equiv \nu L_\nu^{*\,8\,\mu{\rm m}} = (8.3^{+1.5}_{-1.1}) \times 10^{10}$ $L_\odot$ and the derived normalization factor is $\Phi^* = (9.0^{+2.1}_{-1.7}) \times 10^{-4}$ Mpc^{-3} dex^{-1}. The resulting curve for the ML LF at $z \sim 2$ is indicated with a solid line in Figure 7. Once more, the LF obtained with the ML analysis is in good agreement with that computed with the $1/V_{\rm max}$ method, confirming that the double exponential form in equation (1) also provides a good description of the 8 μm LF at redshift $z \sim 2$.

As for the LF at $z = 1$, a Schechter function also appears to be an alternative suitable law to describe the rest-frame 8 μm LF for star-forming galaxies at $z \sim 2$ with the ML STY method (*dashed line in* Fig. 7).

5.2. *Testing the Faint End of the LF through Stacking Analysis*

As we mentioned in § 4.3, the faint-end slope of the IR LF is not well constrained even at $z \sim 0$, and the common procedure is to fix this slope to a given value. One could, however, put into question whether the fixed slope value we use here ($\alpha = 1.2$) is realistic to describe the faint end of the IR LF at different redshifts. In the analysis of the IR LF at redshifts $0 \lesssim z \lesssim 1.2$, Le Floc'h et al. (2005) concluded that the slope at the faint end could not be much steeper than 1.2, as otherwise the faint 24 μm number counts would be overproduced. This result has been confirmed by Zheng et al. (2006), using the stacking analysis at 24 μm of a large sample of $0.1 \lesssim z \lesssim 1$ galaxies. The stacking analysis technique allows us to gain about an order of magnitude in the IR flux detection limit (Dole et al. 2006; Zheng et al. 2006).

We do a similar stacking analysis using the $K_s < 21.5$ (Vega mag) galaxy sample presented in Caputi et al. (2006b) for the GOODS/CDF-S. We stack at 24 μm all those galaxies (except AGNs) with redshifts $1.7 < z < 2.3$ that are below the completeness limit of the $\nu L_\nu^{8\,\mu{\rm m}}$ luminosities (i.e., $\nu L_\nu^{8\,\mu{\rm m}} \lesssim 10^{11}$ $L_\odot$ at $z \sim 2$). This includes, of course, all those $K_s < 21.5$ mag galaxies at $1.7 < z < 2.3$ in the GOODS/CDF-S that are not identified in the $S(24\ \mu{\rm m}) > 80$ μJy catalog for the same field. We find that the average 24 μm flux of these stacked sources is $S(24\ \mu{\rm m}) = (49.3 \pm 1.7)$ μJy, which implies an average rest-frame 8 μm luminosity $\log_{10}(\nu L_\nu^{8\,\mu{\rm m}}) \approx 10.6$. To incorporate this stacking point in our differential LF expressed per dex unit, we need to estimate the flux (and thus the luminosity) range covered by the stacking sample. Also, we need to apply a correction factor that accounts for the fact that the $K_s < 21.5$ sample loses completeness in identifying 24 μm galaxies below the $S(24\ \mu{\rm m}) = 80$ μJy limit. We perform both steps using the 24 μm number counts obtained by Papovich et al. (2004). These number counts are already corrected for incompleteness in the 24 μm detections below the flux completeness limits of the Papovich et al. (2004) samples. From the distribution of these number counts with 24 μm flux, we obtain that the average 24 μm flux of our $S(24\ \mu{\rm m}) < 80$ μJy sample will be well reproduced if the stacked galaxies span the flux range 30 $\mu{\rm Jy} \lesssim S(24\ \mu{\rm m}) < 80$ μJy. On the other hand, from the total number counts within this flux range and ignoring the effects of sample variance, we can obtain the average identification completeness produced by the $K_s < 21.5$ sample. We estimate that the $K_s < 21.5$ sample allows us to identify $\sim$79% of the 24 μm galaxies with 30 $\mu{\rm Jy} \lesssim S(24\ \mu{\rm m}) < 80$ μJy. The inverse of the completeness fraction gives us the correction factor for the LF in the stacking luminosity bin. An intrinsic assumption here is that the identification completeness derived for this flux range is the same at all redshifts, so it can be applied to our $1.7 < z < 2.3$ sample. This assumption seems to be very plausible (compare the redshift distributions of the 83 μJy–limited and total 24 μm samples in Fig. 3 of Caputi et al. 2006c).

The resulting stacking point is indicated with a filled square in Figure 7. We note that we only add this point to our rest-frame 8 μm LF at $z \sim 2$ a posteriori, and it does not play any role in the ML analysis. The good agreement between the stacking analysis point and the ML curve confirms that the value fixed for the faint-end slope of the 8 μm LF is adequate, and significantly larger slopes would not reproduce the average density of faint IR galaxies.

We attempted to do a similar stacking analysis for sources at redshifts $0.9 < z < 1.1$, in order to test the faint end of the rest-frame 8 μm LF at redshift $z = 1$. However, the stacking at 24 μm of $K_s < 21.5$ ($K_s < 20.5$ mag) galaxies that are below the 8 μm luminosity completeness limit at those redshifts produces an average source with flux $S(24\ \mu{\rm m}) = 16.6$ (25.4 μJy). Unfortunately, no information on 24 μm number counts is available for or below such faint fluxes. This fact prevented us from obtaining an extension of the rest-frame 8 μm LF at $z = 1$ for faint luminosities.

5.3. *The Evolution of the Rest-Frame* 8 μm *LF for Star-forming Galaxies from* $z \sim 0$ *to* $z \sim 2$

We can now study the evolution of the rest-frame 8 μm LF from redshifts $z \sim 0$ and $z = 1$ to $z \sim 2$. Figure 8 shows the three LFs in the same plot. Different line styles in this plot correspond

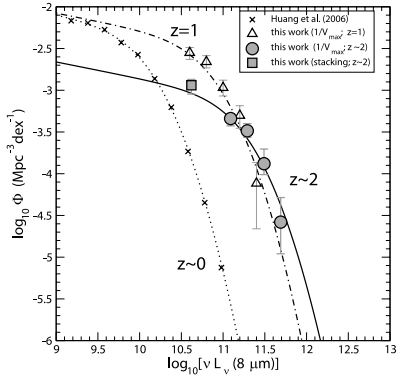

FIG. 8.—Compared rest-frame 8 μm LFs for star-forming galaxies at $z = 1$ and $\sim$2, both obtained in the GOODS fields. Symbols and lines are the same as in Fig. 7. The triangles correspond to the LF at $z = 1$, as computed with the $1/V_{\rm max}$ method. The dot-dashed line is the result of the ML analysis at the same redshift, adopting a double exponential law with $\sigma = 0.36$.

to a double exponential form with $\sigma = 0.36$. As in § 4.4, we can characterize the evolution of L^* and Φ^* with redshift. If we consider

$$L^*(z_2 \sim 2) = L^*(z_1 \sim 0)\left(\frac{1+z_2}{1+z_1}\right)^{\gamma_L},$$
$$\Phi^*(z_2 \sim 2) = \Phi^*(z_1 \sim 0)\left(\frac{1+z_2}{1+z_1}\right)^{\gamma_\delta}, \quad (6)$$

the derived γ_L and γ_δ at strictly $z_1 = 0.2$ and $z_2 = 1.93$ are

$$\gamma_L = 3.0 \pm 0.4,$$
$$\gamma_\delta = -2.1 \pm 0.4. \quad (7)$$

The obtained γ_L value indicates that the strong positive luminosity evolution of the rest-frame 8 μm LF continues up to redshift $z \sim 2$. In contrast, the density evolution has quite a different trend between $z \sim 0$ and $z = 1$ and between $z = 1$ and $z \sim 2$. We showed in § 4.4 that the density of galaxies with $\nu L_\nu^{8\,\mu{\rm m}} \gtrsim 10^{10.5}\,L_\odot$ dramatically increases from $z \sim 0$ and $z = 1$. Between $z = 1$ and $z \sim 2$, however, there appears to be a significant negative-density evolution. If we write

$$L^*(z_2 \sim 2) = L^*(z_1 = 1)\left(\frac{1+z_2}{1+z_1}\right)^{\gamma_L},$$
$$\Phi^*(z_2 \sim 2) = \Phi^*(z_1 = 1)\left(\frac{1+z_2}{1+z_1}\right)^{\gamma_\delta}, \quad (8)$$

with strictly $z_1 = 1$ and $z_2 = 1.93$, we obtain

$$\gamma_L = 2.2 \pm 0.5,$$
$$\gamma_\delta = -3.9 \pm 1.0. \quad (9)$$

A negative-density evolution at high ($z \gtrsim 1$) redshifts has also been found with some of the fittings made for the 12 μm LF by Pérez-González et al. (2005). However, these authors conclude that the result of a negative-density evolution should be taken with caution, as it could be produced by incompleteness in the faintest luminosity bins. To test this, we repeat the ML analysis of our rest-frame 8 μm LF by considering only those galaxies with $S_\nu(24\ \mu{\rm m}) > 120\ \mu$Jy (which is roughly equivalent to excluding the faintest luminosity bin in the $1/V_{\rm max}$ method). In this case, the resulting normalization parameter value Φ^* implies $\gamma_\delta = -1.6 \pm 0.6$ and $\gamma_\delta = -2.7 \pm 1.3$ for the evolution between $z \sim 0$ and $z \sim 2$ and between $z = 1$ and $z \sim 2$, respectively. We conclude, then, that the negative-density evolution result is not an effect of a plausible incompleteness at the faintest luminosities.

It should be noted that all this analysis is based on the validity of the same law to describe the LF at different redshifts and the values obtained for γ_L and γ_δ depend on the adopted functional form. A more direct understanding of the evolution of the rest-frame 8 μm LF can be achieved by comparing the integrated comoving number densities of galaxies above a given luminosity

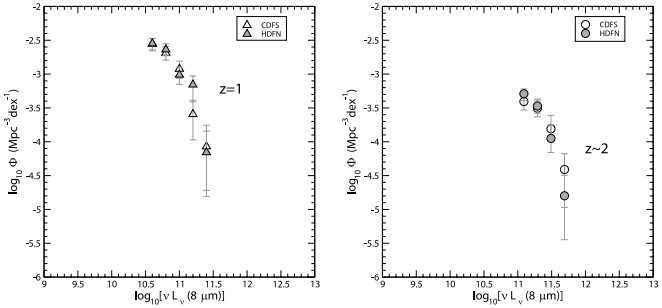

FIG. 9.—Rest-frame 8 μm LF for star-forming galaxies in the GOODS/CDF-S and HDF-N separated, as computed with the $1/V_{\rm max}$ method. *Left*: $z = 1$; *right*: $z \sim 2$.

TABLE 5
NUMBER DENSITIES OF GALAXIES WITH REST-FRAME $\nu L_\nu^{8\,\mu{\rm m}}$ ABOVE DIFFERENT LUMINOSITY CUTS AT DIFFERENT REDSHIFTS

Redshift	Functional Form	$\log_{10}(\nu L_\nu^{8\,\mu{\rm m}}) > 10.5$	$\log_{10}(\nu L_\nu^{8\,\mu{\rm m}}) > 11.0$	$\log_{10}(\nu L_\nu^{8\,\mu{\rm m}}) > 11.5$
$z \sim 0$	DE ($\sigma = 0.36$)	$(4.8 \pm 0.4) \times 10^{-5}$	$(6.7 \pm 0.9) \times 10^{-7}$	$(1.4 \pm 0.3) \times 10^{-9}$
$z = 1$	DE ($\sigma = 0.36$)	$(1.1 \pm 0.1) \times 10^{-3}$	$(1.8 \pm 0.3) \times 10^{-4}$	$(6.7 \pm 2.0) \times 10^{-6}$
	DE ($\sigma = 0.20$)	$(1.1 \pm 0.1) \times 10^{-3}$	$(1.7 \pm 0.3) \times 10^{-4}$	$(2.1 \pm 1.0) \times 10^{-6}$
	Schechter	$(1.1 \pm 0.1) \times 10^{-3}$	$(1.7 \pm 0.3) \times 10^{-4}$	$(2.9 \pm 1.5) \times 10^{-6}$
$z \sim 2$	DE ($\sigma = 0.36$)	$(5.7 \pm 0.5) \times 10^{-4}$	$(1.7 \pm 0.2) \times 10^{-4}$	$(2.0 \pm 0.4) \times 10^{-5}$
	Schechter	$(5.8 \pm 0.4) \times 10^{-4}$	$(1.7 \pm 0.2) \times 10^{-4}$	$(1.7 \pm 0.4) \times 10^{-5}$

NOTES.—These number densities have been obtained by integrating the functional form appearing in the second column and are expressed in units of Mpc^{-3}. DE stands for double exponential.

cut at different redshifts, as those we present in Table 5. If we restrict to the most luminous galaxies [$\log_{10}(\nu L_\nu^{8\,\mu{\rm m}}) > 11.5$], we find that the number density increases with redshift up to $z \sim 2$. For galaxies with $\log_{10}(\nu L_\nu^{8\,\mu{\rm m}}) > 11$, remarkably, the number density appears to be basically the same at redshifts $z = 1$ and $z \sim 2$. Finally, if we consider those galaxies with $\log_{10}(\nu L_\nu^{8\,\mu{\rm m}}) > 10.5$, we observe a clear change of trend between $z \sim 0$ and $z = 1$ and between $z = 1$ and $z \sim 2$. While the number density of these galaxies increases by a factor >20 between $z \sim 0$ and $z = 1$, the number density at $z = 1$ decays to half its value by redshift $z \sim 2$. We note that this decrement in intermediate-luminosity galaxies is not an effect of the faint-end slope $\alpha = 1.2$ we assume for our LF. Inspection of Figure 8 shows that only a much higher α-value (which would be inconsistent with the results of stacking analysis) could make equal the number densities of $\log_{10}(\nu L_\nu^{8\,\mu{\rm m}}) > 10.5$ galaxies at $z = 1$ and $z \sim 2$.

The rest-frame 8 μm luminosity density we derive at redshift $z \sim 2$ is $(7.5 \pm 0.5) \times 10^7\ [(7.6 \pm 0.5) \times 10^7]\ L_\odot\ {\rm Mpc}^{-3}$, obtained by integrating the double exponential (Schechter) function from the ML analysis. This represents more than twice the 8 μm luminosity density at $z \sim 0$, but only half the corresponding luminosity density at $z = 1$.

5.4. *The Total Rest-Frame* 8 μm *LF at Redshift* $z \sim 2$

The rest-frame 8 μm LF at $z \sim 2$ we presented in § 5.1 has been calculated only taking into account the star-forming galaxies in our 24 μm–selected sample at $1.7 < z < 2.3$. In this section we recompute the rest-frame 8 μm LF at $z \sim 2$ for the GOODS fields considering all the 161 24 μm–selected star-forming galaxies and AGNs with $1.7 < z < 2.3$.

We compute the rest-frame 8 μm luminosities as explained in § 4.2. To determine the k-corrections for the AGNs in our sample, we assume that their SED follows a power law $f_\nu \propto \nu^{\alpha_{\rm SED}}$ (with $\alpha_{\rm SED} < 0$). For each AGN, we determine the value of $\alpha_{\rm SED}$ using its IRAC 8 μm and MIPS 24 μm fluxes.

The results of the total 8 μm LF calculated with the $1/V_{\rm max}$ method are indicated with filled diamonds in Figure 10 (see also Table 6). The error bars take into account Poisson errors and Monte Carlo simulations on the redshift and luminosity catalogs, as explained in § 5.1. Comparing this total 8 μm LF with that obtained only for star-forming galaxies (Fig. 7), we can see that AGNs mainly dominate the very bright end. This excess of very bright sources suggests that neither the double exponential form given in equation (1) nor a Schechter function is optimal to describe the bright end of the total 8 μm LF. At fainter magnitudes, however, the star-forming galaxy and total LF show no significant difference, so we can safely assume the same behavior at the faint end.

Thus, to compute the total rest-frame 8 μm LF with the STY method, we consider a combination of an exponential and a power law, as follows:

$$\Phi(L) = \begin{cases} \Phi^* \dfrac{1}{\rm const}\left(\dfrac{L}{L^*}\right)^{1-\alpha} \\ \quad \times \exp\left[-\dfrac{1}{2\sigma^2}\log_{10}^2\left(1+\dfrac{L}{L^*}\right)\right], & L \le L^*, \\ \Phi^*\left(\dfrac{L}{L^*}\right)^{1-\beta}, & L > L^*, \end{cases} \quad (10)$$

where β is the slope at the bright end and the constant const = $\exp\{[-1/(2\sigma^2)]\log_{10}^2(2)\}$ guarantees continuity at $L = L^*$. The stacking analysis point (*square in* Fig. 10) is only added a posteriori to check the consistency of the results. In contrast to the 8 μm LF for star-forming galaxies, the bright end of the total 8 μm LF is sufficiently well constrained as to allow us to leave β as a free parameter. At the faint end, we fix $\alpha = 1.2$ and

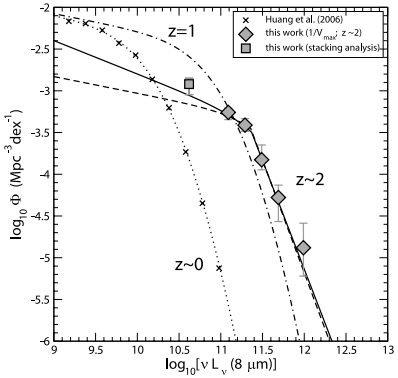

FIG. 10.—Rest-frame 8 μm LF for all the 24 μm–selected galaxies (i.e., star-forming galaxies and AGNs) at $z \sim 2$. The diamond-like symbols indicate the LF computed with the $1/V_{\rm max}$ method. The dashed and solid lines show the LF computed with the ML analysis, assuming the functional form given in eq. (10) with $\alpha = 1.2$ and 1.4, respectively. The remaining symbols and line styles are the same as in Fig. 8.

TABLE 6
THE REST-FRAME 8 μm LF FOR ALL GALAXIES AT $z \sim 2$ OBTAINED WITH THE $1/V_{\rm max}$ METHOD

$\log_{10}(\nu L_\nu^{8\,\mu{\rm m}})$	$\log_{10}\Phi({\rm Mpc}^{-3}\ {\rm dex}^{-1})$
11.09	$-3.26^{+0.05}_{-0.09}$
11.29	$-3.41^{+0.08}_{-0.07}$
11.49	$-3.83^{+0.18}_{-0.12}$
11.69	$-4.28^{+0.15}_{-0.29}$
11.99	$-4.88^{+0.29}_{-0.34}$

$\sigma = 0.36$, as in § 5.1. The free-parameter values that yield the maximum likelihood are $\beta = 3.7^{+0.4}_{-0.3}$, $L^* \equiv \nu L_\nu^{*\,8\,\mu{\rm m}} = (2.29^{+0.16}_{-0.15}) \times 10^{11}\ L_\odot$, and the derived normalization is $\Phi^* = (3.52^{+0.16}_{-0.13}) \times 10^{-4}$ Mpc^{-3} dex^{-1}. The resulting ML function is plotted with a dashed line in Figure 10. We observe that while this ML LF is in very good agreement with that obtained from the $1/V_{\rm max}$ method, the stacking analysis point indicates that the faint end is being underproduced.

At luminosities $11.0 \lesssim \log_{10}(\nu L_\nu^{8\,\mu{\rm m}}) \lesssim 11.4$, the $1/V_{\rm max}$ 8 μm LFs for star-forming and all galaxies are basically coincident. However, the slope value α that was suitable to describe the former does not seem sufficient to explain the faint end of the total LF. The explanation for this apparent contradiction is that the values of the different free parameters are coupled, and actually the definition of faint/bright ends depends on the value of L^*. In the case of the total rest-frame 8 μm LF at $z \sim 2$, the value of the characteristic luminosity L^* is significantly higher than the ML value of L^* for the star-forming galaxy LF. We recompute then the STY ML estimator for the total LF fixing the slope to a higher value $\alpha = 1.4$. The free-parameter values that yield the maximum likelihoood in this case are $\beta = 3.6^{+0.5}_{-0.3}$, $L^* \equiv \nu L_\nu^{*\,8\,\mu{\rm m}} = (2.34^{+0.29}_{-0.15}) \times 10^{11}\ L_\odot$, and the derived normalization is $\Phi^* = (3.17^{+0.15}_{-0.28}) \times 10^{-4}$ Mpc^{-3} dex^{-1}. The ML values of β and L^* are in agreement with those corresponding to $\alpha = 1.2$, within the error bars. This indicates the robustness of the determination of the bright end and the turnover of the total 8 μm LF with our survey. The resulting ML curve for the case with $\alpha = 1.4$ is plotted with a solid line in Figure 10. This new curve appears to be consistent with the stacking analysis point.

By integrating the obtained STY LF, we can compute the 8 μm luminosity density associated with the total IR galaxy population at $1.7 < z < 2.3$. This luminosity density is $\sim(9.0 \pm 0.6) \times 10^7\ L_\odot$ Mpc^{-3}, i.e., $\sim$2.7 times the total 8 μm luminosity density at $z \sim 0$. Comparing the total 8 μm luminosity density at $z \sim 2$ to that for only star-forming galaxies at the same redshift, $(7.5 \pm 0.5) \times 10^7\ L_\odot$ Mpc^{-3}, we conclude that AGNs have a minor contribution to this luminosity density even at high z ($\sim$17% at $z \sim 2$).

6. THE BOLOMETRIC IR LF AT REDSHIFTS $z = 1$ AND $z \sim 2$

6.1. *The Conversion from $\nu L_\nu^{8\,\mu{\rm m}}$ to Bolometric $L_{\rm bol}^{\rm IR}$*

6.1.1. *A New Empirical Calibration Based on Spitzer Galaxies*

In § 5 we studied the rest-frame 8 μm LF at redshift $z \sim 2$ and its evolution from $z \sim 0$. The aim of this section is to extend this study to the bolometric IR (i.e., $5\ \mu{\rm m} \lesssim \lambda < 1000\ \mu$m) LF. The bolometric IR luminosity of a galaxy is produced by the thermal emission of its gas content. In star-forming galaxies, the UV/optical radiation produced by young stars heats the interstellar dust and the reprocessed light is emitted in the IR. For this reason, in star-forming galaxies, the bolometric IR luminosity allows us to obtain a direct and quite unbiased estimate of the current star formation activity.

Different methods to convert νL_ν luminosities into bolometric IR luminosities $L_{\rm bol}^{\rm IR}$ are common in the literature. Most of them rely on calibrations made using nearby galaxies in *IRAS* or *ISO* catalogs (e.g., Chary & Elbaz 2001; Elbaz et al. 2002; Takeuchi et al. 2005) or on the use of semiempirical SEDs (e.g., Dale & Helou 2002; Lagache et al. 2003, 2004; Dale et al. 2005). The extrapolation of these νL_ν-$L_{\rm bol}^{\rm IR}$ relations to high-redshift galaxies can be justified with different recent results. For example, Egami et al. (2004) showed that composite SEDs of high-z IR galaxies are well described by local templates. Also, IR galaxy models that assume such similarity in the SEDs can fit the 24, 70, and 160 μm number counts simultaneously (Lagache et al. 2004). Nevertheless, there is always some controversy on the large error bars that can be involved in the νL_ν-$L_{\rm bol}^{\rm IR}$ conversions applied to high redshifts. For example, Dale et al. (2005) claim that the use of 24 μm data (rest-frame 8 μm at $z \sim 2$) can produce an uncertainty of up to a factor of 5 in the derived bolometric IR luminosity of $z \sim 2$ galaxies.

To explore this issue, Bavouzet et al. (2006) studied different νL_ν-$L_{\rm bol}^{\rm IR}$ relations using *Spitzer* low- to intermediate-redshift galaxies. Their sample consists of 24 μm–selected galaxies with $R < 20$ (Vega mag) in three different fields, namely, the Böotes and the *Spitzer* First Look Survey fields and the extended CDF-S. The selection criterion of this sample is the detection of each galaxy in the IRAC 8 μm channel and in all three MIPS bands (i.e., at 24, 70, and 160 μm). All these galaxies have either spectroscopic or COMBO17 photometric redshifts and span the redshift range $0.0 \lesssim z \lesssim 0.6$. AGNs have been removed from their sample.

To measure the bolometric IR luminosity $L_{\rm bol}^{\rm IR}$ of each galaxy at redshift z, Bavouzet et al. (2006) used the 8–160 μm fluxes. To integrate the corresponding empirical SED in each case, they summed up the areas below contiguous rectangles centered at rest-frame wavelengths 8 $\mu{\rm m}/(1+z)$, 24 $\mu{\rm m}/(1+z)$, 70 $\mu{\rm m}/(1+z)$, and 160 $\mu{\rm m}/(1+z)$. At longer wavelengths, they approximated the SED beyond $\lambda > [160 + (160 - 70)/2]/(1+z) = 205\ \mu{\rm m}/(1+z)$ with a triangle of slope -4. This slope is consistent with the modified blackbody emission in the far-IR produced by big grains of dust thermalized at a temperature $T \sim 15$–20 K (Draine & Lee 1984; Contursi et al. 2001). In fact, Bavouzet et al. (2006) found that the use of any slope between -3.5 and -4.5 produced variations $<1\%$ on the computed bolometric luminosities. It is important to emphasize that the measurements of bolometric IR luminosities made by Bavouzet et al. (2006) are purely based on *Spitzer* data and are completely independent of any model template.

The resulting $L_{\rm bol}^{\rm IR}$ versus rest-frame $\nu L_\nu^{8\,\mu{\rm m}}$ relation for the Bavouzet et al. (2006) sample is shown in Figure 11 (*plus signs*). In this work, however, we restrict the analysis only to those 93 galaxies in the Bavouzet et al. (2006) sample that have $\nu L_\nu^{8\,\mu{\rm m}} > 10^{10}\ L_\odot$ and signal-to-noise ratio S/N > 3 in all the MIPS bands. The rest-frame 8 μm luminosities have been obtained applying k-corrections that do depend on different SED models (Chary & Elbaz 2001; Elbaz et al. 2002; Lagache et al. 2004). The $\nu L_\nu^{8\,\mu{\rm m}}$-$L_{\rm bol}^{\rm IR}$ relation for these galaxies can be fitted with the following law (*dashed line in* Fig. 11):

$$L_{\rm bol}^{\rm IR} = 1.91[\nu L_\nu(8\ \mu{\rm m})]^{1.06}, \qquad (11)$$

with $\nu L_\nu(8\ \mu{\rm m})$ and $L_{\rm bol}^{\rm IR}$ expressed in units of $L_\odot$. The 1 σ dispersion for this relation is $\sim$55%. This formula is directly applicable in the redshift range $0.0 \lesssim z \lesssim 0.6$. We refer the reader to the Bavouzet et al. (2006) paper for a generalized version of this formula including $\nu L_\nu^{8\,\mu{\rm m}} < 10^{10}\ L_\odot$ galaxies.

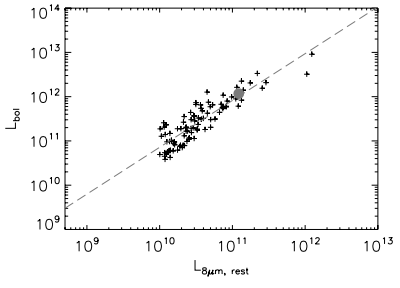

FIG. 11.—Bolometric IR vs. rest-frame 8 μm luminosity relation for galaxies with $\nu L_\nu^{8\,\mu{\rm m}} > 10^{10}\ L_\odot$ in the Bavouzet et al. (2006) sample. The plus signs indicate individual galaxies at redshifts $0.0 < z < 0.6$. The dashed line shows the best-fit relation. The filled circle shows the resulting average value of $(\nu L_\nu^{8\,\mu{\rm m}}; L_{\rm bol}^{\rm IR})$ for a sample of galaxies at $1.3 < z < 2.3$, as obtained through stacking analysis in the GOODS/CDF-S. This point shows that the average relation between $\nu L_\nu^{8\,\mu{\rm m}}$ and $L_{\rm bol}^{\rm IR}$ for $1.3 < z < 2.3$ galaxies is basically the same as for galaxies at $0.0 < z < 0.6$.

To assess whether the formula displayed in equation (11) could also be suitable to perform the $\nu L_\nu^{8\,\mu{\rm m}}$-$L_{\rm bol}^{\rm IR}$ conversion for higher redshift galaxies, Bavouzet et al. (2006) used the 24 μm–selected galaxy samples in the GOODS/CDF-S and HDF-N (the same samples we use in this work). Of course, the bolometric luminosity of the vast majority of $z \gtrsim 1$ galaxies cannot be empirically measured, as they are below the confusion limits of the *Spitzer* MIPS images at 70 and 160 μm. However, the average far-IR flux produced by these high-redshift sources can be recovered through stacking analysis (Dole et al. 2006).

Bavouzet et al. (2006) stacked all those 24 μm sources in the GOODS fields that lie at redshifts $1.3 < z < 2.3$, with a median redshift $z \approx 1.68$. The resulting $(\nu L_\nu^{8\,\mu{\rm m}}; L_{\rm bol}^{\rm IR})$ value obtained with the stacking analysis is indicated with a filled circle in Figure 11. The $L_{\rm bol}^{\rm IR}$ value for this point is corrected for the subestimation of the far-IR flux that is produced on high-redshift sources by using the triangle approximation method explained above. This correction is about 10%–15%. The locus occupied by the high-redshift stacked sources in the $\nu L_\nu^{8\,\mu{\rm m}}$-$L_{\rm bol}^{\rm IR}$ diagram strongly suggests that the relation described by equation (11) is also valid to link the 8 μm and bolometric IR luminosities of IR galaxies at $1.3 < z < 2.3$.

Thus, in this work we make use of the Bavouzet et al. (2006) relation described by equation (11) to convert the rest-frame 8 μm of our star-forming galaxies into bolometric IR luminosities. We use these resulting bolometric IR luminosities to compute the corresponding LF for star-forming galaxies at $z = 1$ and $z \sim 2$ that we present in § 6.2. As we explain in that section, the 55% dispersion found for the $\nu L_\nu^{8\,\mu{\rm m}}$-$L_{\rm bol}^{\rm IR}$ relation largely dominates the error budget of the bolometric IR LF.

As a final comment, we would like to discuss why the relation obtained by Bavouzet et al. (2006) predicts a significantly smaller dispersion on the values of bolometric IR luminosities $L_{\rm bol}^{\rm IR}$ obtained from rest-frame 8 μm fluxes than that predicted by Dale et al. (2005). First, the Dale et al. (2005) sample includes nearby galaxies of a very different nature, and they even make separate studies of different IR regions within the same IR galaxy. Thus, because of its selection, it is expected that the Dale et al. (2005) sample displays a larger variety of IR properties than the Bavouzet et al. (2006) sample. Furthermore, to extrapolate their conclusions to high redshifts, Dale et al. (2005) make use of the complete set of Dale & Helou (2002) models. However, the majority ($\gtrsim$75%) of their wide range of observed SEDs only correspond to roughly half of these models (see figures in Dale et al. 2005). The Bavouzet et al. (2006) sample has been selected with a more homogeneous criterion and includes galaxies up to intermediate ($z \approx 0.6$) redshifts. Thus, these galaxies are more likely representative of the typical galaxies selected in IR surveys. A thorough discussion of this issue is presented in the Bavouzet et al. (2006) paper.

6.1.2. *Comparison between Different $\nu L_\nu^{8\,\mu{\rm m}}$-$L_{\rm bol}^{\rm IR}$ Calibrations*

Several different laws to convert $\nu L_\nu^{8\,\mu{\rm m}}$ into bolometric IR luminosities $L_{\rm bol}^{\rm IR}$ are of common use in the literature. We analyze here how these different calibrations compare to the relation empirically derived from *Spitzer* galaxies by Bavouzet et al. (2006).

Figure 12 shows the bolometric IR $L_{\rm bol}^{\rm IR}$ versus $\nu L_\nu^{8\,\mu{\rm m}}$ luminosity relations (*left panel*) and the derived conversion factors $L_{\rm bol}^{\rm IR}/\nu L_\nu^{8\,\mu{\rm m}}$ (*right panel*), both versus $\nu L_\nu^{8\,\mu{\rm m}}$, as obtained using different calibrations or derived from different IR SED models. The thick solid line shows the empirical relation obtained by Bavouzet et al. (2006). The thick dashed and dotted lines correspond to the relations derived using the Lagache et al. (2004) and the Chary & Elbaz (2001) and Elbaz et al. (2002) templates, respectively. To obtain these relations, we convolve all these templates with the transmission function of the MIPS 24 μm filter. We find that the Lagache et al. (2004) model predicts a $\nu L_\nu^{8\,\mu{\rm m}}$-$L_{\rm bol}^{\rm IR}$ relation that is in close agreement with the Bavouzet et al. (2006) empirical calibration over all 8 μm luminosities. The Chary & Elbaz (2001) templates, on the contrary, appear to overproduce the $\nu L_\nu^{8\,\mu{\rm m}}$-$L_{\rm bol}^{\rm IR}$ conversion. The differences with the Bavouzet et al. (2006) calibration are only within a factor of $\sim$2 for galaxies with $\nu L_\nu^{8\,\mu{\rm m}} < 10^{11}\ L_\odot$ but become dramatically larger at higher luminosities.

Previous comparisons of the νL_ν-$L_{\rm bol}^{\rm IR}$ relations predicted by different models have not detected such dramatic differences (see, e.g., Le Floc'h et al. 2005). These previous comparisons analyzed longer rest-frame wavelengths, beyond the PAH-dominated region in the SEDs. The comparison we present here is made in the most critical SED region, where different models show the largest discrepancies (see also Fig. 5). From this comparison, we find that the use of the Chary & Elbaz (2001) templates to convert $\nu L_\nu^{8\,\mu{\rm m}}$ into $L_{\rm bol}^{\rm IR}$ luminosities leads to significantly overproduced bolometric IR luminosity values for galaxies with $\nu L_\nu^{8\,\mu{\rm m}} > 10^{11}\ L_\odot$.

In Figure 12 we also show the $\nu L_\nu^{8\,\mu{\rm m}}$ to $L_{\rm bol}^{\rm IR}$ derived from the Wu et al. (2005) formulae (*thin dashed lines*), which link 8 μm luminosities and star formation rates. The bolometric IR luminosities have been recovered using ${\rm SFR} = 1.72 \times 10^{-10} L_{\rm IR}$ (Kennicutt 1998). Finally, the thin dot-dashed line shows the relation used in Reddy et al. (2006b). In the latter relation, the 8 μm luminosities refer to the convolution in the wavelength range $\sim$5–8.5 μm, which is somewhat different from the transmission windows of the MIPS 24 μm filter ($\sim$6.6–9.4 μm at $z \sim 2$) or the IRAC 8 μm filter ($\sim$6.5–9.5 μm; Fazio et al. 2004). Once corrected for this difference, the Reddy et al. (2006b) relation becomes closer to the Bavouzet et al. (2006) *Spitzer* calibration.

In this work we use the new *Spitzer*-based calibration given by equation (11) to convert $\nu L_\nu^{8\,\mu{\rm m}}$ luminosities into bolometric IR luminosities $L_{\rm bol}^{\rm IR}$. After computing the bolometric IR LF, we analyze the contribution of LIRGs and ULIRGs to the total number

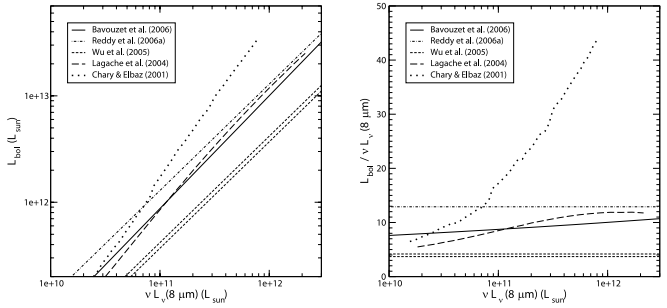

FIG. 12.—Comparison between different $L_{\rm bol}^{\rm IR}$ vs. $\nu L_{\nu}^{8\ \mu{\rm m}}$ relations (*left*) and derived conversion factors vs. $\nu L_{\nu}^{8\ \mu{\rm m}}$ (*right*), as obtained from different calibrations available in the literature.

and luminosity densities of IR galaxies at different redshifts. We warn the reader, however, of the implications of the differences between the $\nu L_{\nu}^{8\ \mu{\rm m}}$-$L_{\rm bol}^{\rm IR}$ conversions shown in Figure 12. For example, the Chary & Elbaz (2001) conversion classifies as ULIRGs those sources with $\nu L_{\nu}^{8\ \mu{\rm m}} \gtrsim 8 \times 10^{10}\ L_{\odot}$, while the Bavouzet et al. (2006) relation implies that only galaxies with $\nu L_{\nu}^{8\ \mu{\rm m}} \gtrsim (1.1\text{–}1.2) \times 10^{11}\ L_{\odot}$ are ULIRGs. These differences should be kept in mind when comparing different results from the literature, where different conversion laws are used.

6.2. *The Bolometric IR LF for Star-forming Galaxies and Its Evolution to Redshift $z \sim 2$*

As we have seen in § 6.1.2, some calibrations used in the literature to convert 8 μm into bolometric IR luminosities are quite discrepant with the empirical calibration obtained from *Spitzer* galaxies. Thus, to properly compare the bolometric IR LF at different redshifts, we convert the different 8 μm LFs using the Bavouzet et al. (2006) relation shown in equation (11). The results are shown in Figure 13.

First, we transform the Huang et al. (2006) 8 μm LF at $z \sim 0$ and compute the corresponding minimum χ^2 fitting, using the functional form given in equation (1). For the bolometric IR LF at $z \sim 0$, we obtain the following best-fit parameter values: $\sigma = 0.39 \pm 0.01$, $L_{\rm IR}^{*} = (4.0 \pm 0.2) \times 10^{10}\ L_{\odot}$, and $\Phi^{*} = (5.4 \pm 0.1) \times 10^{-3}$ Mpc^{-3} dex^{-1}. The resulting best-fit curve to the bolometric IR LF at $z \sim 0$ is shown with a dotted line in Figure 13.

The best-fit value we find for the slope at the bright end at $z \sim 0$, i.e., $\sigma = 0.39$, is very similar to the value obtained for the bright-end slope of the rest-frame 8 μm LF ($\sigma = 0.36$) at the same redshift. This similarity is due to the fact that the $\nu L_{\nu}^{8\ \mu{\rm m}}$-$L_{\rm bol}^{\rm IR}$ conversion is quasi-linear.

At redshifts $z = 1$ and $z \sim 2$, we compute the bolometric IR luminosities $L_{\rm bol}^{\rm IR}$ of all our star-forming galaxies in the relevant redshift ranges by transforming their rest-frame 8 μm luminosities $\nu L_{\nu}^{8\ \mu{\rm m}}$ using equation (1). We then obtain the bolometric IR LF using, alternatively, the $1/V_{\rm max}$ method and the ML STY analysis.

The upward-pointing triangles and circles in Figure 13 show the bolometric IR LF at $z = 1$ and $z \sim 2$, respectively, both computed with the $1/V_{\rm max}$ method. These LFs are only shown in the bins of completeness in $L_{\rm bol}^{\rm IR}$ luminosities, given the flux limits of our sample and the redshifts corresponding to each case. As for the rest-frame 8 μm LF, we applied small correction factors to account for the 5%–6% identification incompleteness of the $S(24\ \mu{\rm m}) > 80\ \mu$Jy galaxy sample. For both LFs, the error bars have been determined through Monte Carlo simulations, in a similar way as described in § 5.1. The mock catalogs generated in the simulations take into account the error bars in the redshift determinations, in the case of photometric redshifts. However, in the case of the bolometric luminosities, the error budget is mainly dominated by the uncertainty associated with the $\nu L_{\nu}^{8\ \mu{\rm m}}$-$L_{\rm bol}^{\rm IR}$ conversion. To take into account this error, we assign to each galaxy in the mock catalogs a random bolometric IR luminosity. This random luminosity $L_{\rm bol}^{\rm IR}$ is taken from a Gaussian distribution centered at the value given by equation (11) for the corresponding galaxy and with a 55% dispersion. The recomputation of the LF with the $1/V_{\rm max}$ method on all the mock catalogs allows us to determine the error bars on the original LF calculation.

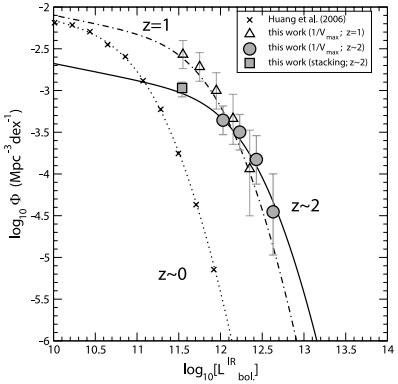

FIG. 13.—Evolution of the bolometric IR LF for star-forming galaxies from redshift $z = 0$ to ~2. Symbols and line styles are the same as in Fig. 8.

TABLE 7
PARAMETER VALUES CHARACTERIZING THE BOLOMETRIC IR LF FOR STAR-FORMING GALAXIES AT $z = 1$ AND $z \sim 2$

Redshift	Functional Form	α	σ	$L_{\rm IR}^{*}$ ($L_{\odot}$)	Φ^{*} (Mpc^{-3} dex^{-1})
$z = 1$.....	Double exponential (eq. [1])	1.2	0.39 (fixed)	$(2.5^{+0.4}_{-0.3}) \times 10^{11}$	$(4.0^{+0.6}_{-0.5}) \times 10^{-3}$
$z \sim 2$.....	Double exponential (eq. [1])	1.2	0.39 (fixed)	$(6.3^{+1.1}_{-0.9}) \times 10^{11}$	$(9.2^{+2.2}_{-1.7}) \times 10^{-4}$

The dot-dashed and solid lines in Figure 13 indicate the bolometric IR LF at $z = 1$ and $z \sim 2$, respectively, obtained with the ML analysis. We computed the bolometric IR LF using the STY method, assuming the functional form described in equation (1). The faint- and bright-end slope values have been fixed to the $z \sim 0$ values, i.e., $\alpha = 1.2$ and $\sigma = 0.39$, respectively. At $z = 1$, we obtain that the value of the characteristic luminosity that yields the ML is $L_{\rm IR}^{*} = (2.5^{+0.4}_{-0.3}) \times 10^{11}\ L_{\odot}$. The corresponding normalization factor is $\Phi^{*} = (4.0^{+0.6}_{-0.5}) \times 10^{-3}$ Mpc^{-3} dex^{-1}. At $z \sim 2$, the ML characteristic luminosity is $L_{\rm IR}^{*} = (6.3^{+1.1}_{-0.9}) \times 10^{11}\ L_{\odot}$ and the corresponding normalization factor is $\Phi^{*} = (9.2^{+2.2}_{-1.7}) \times 10^{-4}$ Mpc^{-3} dex^{-1} (see Table 7). The error bars on $L_{\rm IR}^{*}$ include the uncertainty produced by the 55% dispersion in the $\nu L_{\nu}^{8\ \mu{\rm m}}$-$L_{\rm bol}^{\rm IR}$ relation, incorporated through the mock catalogs described above. Consistently with the results obtained in §§ 4.3 and 5.1, the LFs independently calculated with the $1/V_{\rm max}$ method and the ML STY technique are in very good agreement.

Using also the $\nu L_{\nu}^{8\ \mu{\rm m}}$-$L_{\rm bol}^{\rm IR}$ relation given in equation (11), we compute the corresponding contribution of the stacked galaxies at $z \sim 2$, which are below the $L_{\rm bol}^{\rm IR}$ completeness limit of the sample, to the bolometric IR LF. Once more, the stacking analysis point appears in very good agreement with the extrapolation given by the ML analysis at the faint end of the LF.

Given the quasi-linearity of the $\nu L_{\nu}^{8\ \mu{\rm m}}$-$L_{\rm bol}^{\rm IR}$ conversion, the evolution we find for the bolometric IR LF from $z \sim 0$ to $z \sim 2$ is very similar to the evolution observed for the rest-frame 8 μm LF. For the bolometric IR LF, this implies the following:

1. The number density of galaxies with $L_{\rm bol}^{\rm IR} \gtrsim 10^{11}\ L_{\odot}$ substantially increases from the local universe to $z = 1$ (see Table 8). This confirms the increasing importance of the LIRG and ULIRG populations between these redshifts (see, e.g., Le Floc'h et al. 2005).

2. Surprisingly, at $z \sim 2$, the number density of star-forming ULIRGs (i.e., sources with $L_{\rm bol}^{\rm IR} > 10^{12}\ L_{\odot}$) is only slightly larger than at $z = 1$. This result is the combination of several factors: first, the exclusion of AGNs in this analysis produces a relatively low density of ULIRGs at $z \sim 2$, as we have seen in § 5.4 that AGNs dominate the bright end of the IR LF; second, the use of the $\nu L_{\nu}^{8\ \mu{\rm m}}$-to-$L_{\rm bol}^{\rm IR}$ conversion given in equation (11), which, in comparison to the Chary & Elbaz (2001) templates that are of common use in the literature, produces ULIRGs only from larger $\nu L_{\nu}^{8\ \mu{\rm m}}$ luminosities (see Fig. 12).

3. The number density of LIRGs (i.e., sources with $10^{11}\ L_{\odot} < L_{\rm bol}^{\rm IR} < 10^{12}\ L_{\odot}$) appears to be smaller at $z \sim 2$ than at $z = 1$. Although the limits of our survey do not allow us to directly observe LIRGs at $z \sim 2$, the ML analysis suggests this result, which is in turn validated through the stacking analysis of $z \sim 2$ K_s-band galaxies.

Thus, the ratio between the number densities of star-forming ULIRGs and LIRGs increases from $z = 1$ to $z \sim 2$. However, within our sample and given our star-forming galaxy/AGN separation, this effect appears to be mainly produced by a decrement in the density of LIRGs by $z \sim 2$, rather than a significant increment in the density of star-forming ULIRGs. If our AGN separation criterion were excluding galaxies whose bolometric IR emission is actually dominated by star formation, then the relative importance in the number density of star-forming ULIRGs would be, of course, even larger at $z \sim 2$.

We note that the decrement we find in the number density of LIRGs between $z = 1$ and $z \sim 2$ is not influenced at all by the AGN separation criterion.

6.3. *Comparison with Other Works*

As we have seen in § 6.1.2, many different recipes are used in the literature to convert νL_{ν} into $L_{\rm bol}^{\rm IR}$ luminosities. And even different conversions made from the same wavelength (in particular, rest-frame 8 μm) may lead to nonnegligible discrepancies in the derived $L_{\rm bol}^{\rm IR}$ luminosities. In spite of these differences, it is still instructive to compare the results of different bolometric IR LF calculations.

Figure 14 compares the bolometric IR LF obtained in this work with those derived by other authors, at different redshifts. In the left panel we show the local bolometric IR LF computed from the *IRAS* revised galaxy sample (Sanders et al. 2003; *diamonds*) and the bolometric IR LF derived in this work from the Huang et al. (2006) rest-frame 8 μm LF at $z \sim 0.2$. The difference between the two is mainly due to a real evolution between $z = 0$ and $z \sim 0.2$. In the same panel, we also compare our bolometric IR LF at $z = 1$ with that obtained by Le Floc'h et al. (2005) at $z = 0.9$. We observe that both LFs are in good agreement, taking into account the error bars and the evolution expected between these redshifts (cf. Le Floc'h et al. 2005).

In the right panel of Figure 14 we show our bolometric IR LF at redshift $z \sim 2$, compared to that derived from Pérez-González

TABLE 8
NUMBER DENSITIES OF STAR-FORMING LIRGS AND ULIRGS AT DIFFERENT REDSHIFTS

Redshift	Functional Form	$\log_{10} L_{\rm bol}^{\rm IR} > 11$	LIRG	ULIRG
$z \sim 0$.....	DE ($\sigma = 0.39$)	$(4.1 \pm 0.3) \times 10^{-4}$	$(4.1 \pm 0.3) \times 10^{-4}$	$(3.9 \pm 0.7) \times 10^{-7}$
$z = 1$.....	DE ($\sigma = 0.39$)	$(2.6 \pm 0.1) \times 10^{-3}$	$(2.5 \pm 0.2) \times 10^{-3}$	$(1.2 \pm 0.2) \times 10^{-4}$
$z \sim 2$.....	DE ($\sigma = 0.39$)	$(1.1 \pm 0.1) \times 10^{-3}$	$(9.5 \pm 1.5) \times 10^{-4}$	$(1.5 \pm 0.2) \times 10^{-4}$

NOTES.—These number densities have been obtained by integrating the functional form appearing in the second column and are expressed in units of Mpc^{-3}. DE stands for double exponential.

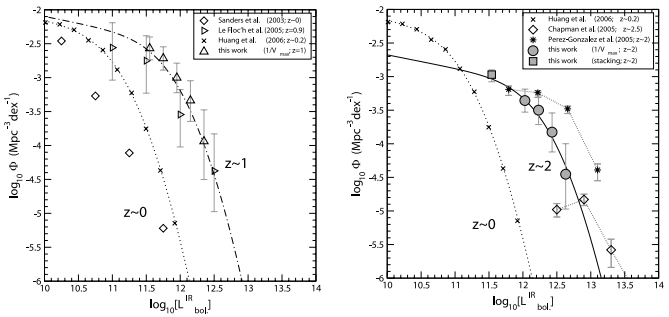

FIG. 14.—Bolometric IR LF obtained in this work compared to the determinations of other authors at similar redshifts: $z \sim 1$ (*left*) and $z \sim 2$ (*right*).

et al. (2005) at a similar redshift and that computed from radio-detected submillimeter galaxies at $z \sim 2.5$ (Chapman et al. 2005).

The bolometric IR LF derived from Pérez-González et al. (2005; *asterisks in* Fig. 14) has been obtained by converting their rest-frame 12 μm LF at $z \sim 2$, using the same recipe adopted by these authors to obtain bolometric IR luminosity densities (see eq. [1] in their paper). This conversion corresponds to the Chary & Elbaz (2001) $\nu L_{\nu}^{12\ \mu\mathrm{m}}$-$L_{\mathrm{bol}}^{\mathrm{IR}}$ formula. Our bolometric IR LF at $z \sim 2$ is in agreement, within the error bars, with that derived from Pérez-González et al. (2005) at luminosities $L_{\mathrm{bol}}^{\mathrm{IR}} \lesssim 10^{12.5}\ L_{\odot}$. At brighter luminosities, however, the two LFs present significant discrepancies. The differences between the two are produced by two factors: (1) the AGN exclusion: Pérez-González et al. (2005) only exclude the most extreme cases of AGNs, while here we adopt a more extensive separation criterion; (2) the different νL_{ν}-$L_{\mathrm{bol}}^{\mathrm{IR}}$ conversions: as we have seen in § 6.1.2, the most drastic differences between the empirical *Spitzer*-based conversion we use in this work and that derived from the Chary & Elbaz (2001) and Elbaz et al. (2002) templates occur at luminosities $L_{\mathrm{bol}}^{\mathrm{IR}} \gtrsim 10^{12}\ L_{\odot}$. This comparison illustrates the impact of using different νL_{ν}-$L_{\mathrm{bol}}^{\mathrm{IR}}$ relations, especially at high redshifts, where the most luminous IR galaxies are dominant.

The bolometric IR luminosities derived from radio-detected submillimeter galaxies only can trace the very bright end of the bolometric IR LF. The diamonds in the right panel of Figure 14 correspond to the submillimeter-derived bolometric IR LF at $z \sim 2.5$, as obtained by Chapman et al. (2005). This LF does not exclude AGNs and quickly loses completeness at $L_{\mathrm{bol}}^{\mathrm{IR}} \lesssim 10^{13}\ L_{\odot}$. Taking into account these facts and the differences in redshift, we find that the Chapman et al. (2005) bolometric IR LF at $z \sim 2.5$ is consistent with our LF based on 24 μm–selected galaxies at $z \sim 2$.

6.4. *The Evolution of the Bolometric IR Luminosity Density*

One of the final aims of computing the bolometric IR LF is to obtain an estimate of the IR luminosity density (in our case associated with star-forming galaxies) at a given look-back time. Previous works agree in a strong evolution of the IR luminosity density from the local universe up to redshift $z \sim 1$ (e.g., Flores et al. 1999; Gispert et al. 2000; Pozzi et al. 2004; Le Floc'h et al. 2005). At higher redshifts, the situation is less clear, as only recently are IR facilities allowing us to put constraints on the IR universe at $z \gtrsim 1$.

Given the discrepancies existing between different recipes to obtain bolometric IR luminosities (see § 6.1.2), we need to use the bolometric IR LF obtained with the same conversion at different redshifts, in order to properly compute the evolution of the IR luminosity density.

Figure 15 shows the evolution of the comoving IR luminosity density as a function of redshift. Our determinations of the IR luminosity density at $z = 1$ and $z \sim 2$ (strictly $z = 1.93$) are indicated with a filled upward-pointing triangle and circle, respectively: $\Omega_{\mathrm{IR}}(z = 1) = (1.2 \pm 0.2) \times 10^{9}\ L_{\odot}\ \mathrm{Mpc}^{-3}$ and

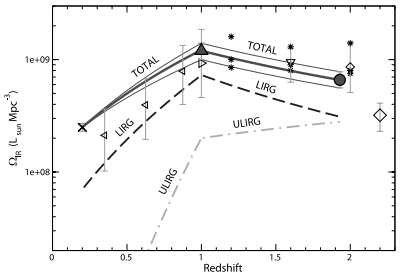

FIG. 15.—Evolution of the comoving bolometric IR luminosity density with redshift. The filled upward-pointing triangle and circle at redshifts $z = 1$ and 1.93 indicate the estimations of the respective bolometric IR luminosity density obtained in this work: $\Omega_{\mathrm{IR}} = (1.2 \pm 0.2) \times 10^{9}$ and $(6.6^{+1.2}_{-1.0}) \times 10^{8}\ L_{\odot}\ \mathrm{Mpc}^{-3}$. The density at $z = 0.2$ has been obtained from the bolometric IR LF derived from the 8 μm LF by Huang et al. (2006). The thick solid line corresponds to an interpolation between these redshifts, assuming a $[(1 + z_2)/(1 + z_1)]^{s}$ evolution. The thin solid lines indicate error bars on this evolution. Dashed and dot-dashed lines show the contributions of LIRGs and ULIRGs, respectively, at different redshifts. Other symbols refer to IR luminosity densities taken from the literature and based on different data sets: *ISO* mid-IR (Flores et al. 1999; *left-pointing triangles*), *Spitzer* mid-IR (Le Floc'h et al. 2005; Pérez-González et al. 2005; *right-pointing triangle and asterisks, respectively*), submillimeter (Barger et al. 2000; Chapman et al. 2005; *small and large diamonds, respectively*), and radio (Haarsma et al. 2000; *downward-pointing triangle*). Some of these IR luminosity densities have been obtained from the star formation rate densities compiled by Hopkins (2004) and converted with the Kennicutt (1998) formula $\mathrm{SFR} = 1.72 \times 10^{-10} L_{\mathrm{IR}}$. [*See the electronic edition of the Journal for a color version of this figure.*]

$\Omega_{\mathrm{IR}}(z \sim 2) = (6.6^{+1.2}_{-1.1}) \times 10^{8}\ L_{\odot}\ \mathrm{Mpc}^{-3}$. We obtain the values of these luminosity densities by integrating our respective bolometric IR LFs obtained with the ML likelihood analysis, weighted with the luminosity values. The error bars are determined by the extreme cases of LFs produced by the error bars on L_{IR}^{*}.

The cross in Figure 15 represents the bolometric IR luminosity density at $z \sim 0$ (strictly $z = 0.2$), as obtained from the bolometric IR LF derived from the Huang et al. (2006) 8 μm LF: $\Omega_{\mathrm{IR}}(z \sim 0) = (2.5 \pm 0.2) \times 10^{8}\ L_{\odot}\ \mathrm{Mpc}^{-3}$.

The thick solid line in Figure 15 interpolates the evolution of the total bolometric IR luminosity density between redshifts $z_1 \sim 0$ to $z_2 = 1$ and $z_1 = 1$ to $z_2 \sim 2$, assuming that this evolution follows a $[(1 + z_2)/(1 + z_1)]^{s}$ law. Between redshifts $z \sim 0$ and $z = 1$, we find that the total bolometric IR luminosity density increases as $[(1 + z_2)/(1 + z_1)]^{3.1 \pm 0.3}$ (where $z_1 = 0.2$ and $z_2 = 1.0$). This evolution is somewhat slower than that obtained by Le Floc'h et al. (2005), who found $[(1 + z_2)/(1 + z_1)]^{3.9}$ between $z_1 = 0$ and $z_2 = 1$. The bolometric IR luminosity density at $z = 1$ determined by Le Floc'h et al. (2005; *right-pointing triangle in* Fig. 15) is actually very close to the value we determine here. The difference appears to be mainly produced in the IR luminosity density at low redshifts: there has been a significant evolution of the IR LF between redshifts $z = 0$ and $z \sim 0.2$.

Other symbols in Figure 15 refer to different bolometric IR luminosity density estimations derived from different data sets: radio (Haarsma et al. 2000; *downward-pointing triangle*), submillimeter (Barger et al. 2000; *diamond*), and the different fits made on mid-IR data by Pérez-González et al. (2005; *asterisks*). Our determinations of the IR luminosity densities are in good agreement with most of these previous works within the error bars. Our results exclude, however, the highest of the three estimations made by Pérez-González et al. (2005) at $z \gtrsim 1$.

Finally, in Figure 15 we show the relative contributions of the LIRG and ULIRG populations to the total IR luminosity density, as a function of redshift. At $z \sim 0$, 28^{+11}_{-20} % of the bolometric IR luminosity density is contained in LIRGs and <1% in ULIRGs. At $z = 1$, we find that LIRGs and ULIRGs contribute 61^{+4}_{-7} % and 16^{+11}_{-12} %, respectively, to the total IR luminosity density, in agreement with Le Floc'h et al. (2005) within the error bars. By $z \sim 2$, the contribution of LIRGs and ULIRGs becomes 47^{+13}_{-11} % and 42^{+15}_{-22} % of the total budget, respectively.

Using the Kennicutt formula $\mathrm{SFR} = 1.72 \times 10^{-10} L_{\mathrm{IR}}$, we can convert the bolometric IR luminosity densities into star formation rate densities at different redshifts. At $z = 1$ and $z \sim 2$, respectively, $\Omega_{\mathrm{IR}} = (1.2 \pm 0.2) \times 10^{9}$ and $(6.6^{+1.2}_{-1.0}) \times 10^{8}\ L_{\odot}\ \mathrm{Mpc}^{-3}$ translate into star formation rate densities $\delta_{\mathrm{SFR}} \approx 0.20 \pm 0.03$ and $0.11 \pm 0.02\ M_{\odot}\ \mathrm{yr}^{-1}\ \mathrm{Mpc}^{-3}$ (assuming a Salpeter initial mass function over stellar masses $M = 0.1$–$100\ M_{\odot}$). In § 7 we make use of our current knowledge on stellar mass density evolution to discuss why these derived star formation rate densities could not be much higher than this value at redshifts $1 \lesssim z \lesssim 3$.

7. DISCUSSION

If the IR LF for star-forming galaxies follows a unique law from the local universe to high redshifts, then the results of our LF determination will imply that there is a negative evolution in the overall number density of IR star-forming galaxies between $z \sim 0$ and ~ 2. We showed here the validity of a universal law to describe the IR LF at intermediate and bright luminosities, at different redshifts. Of course, one could argue that the faint end of this LF is not sufficiently well constrained as to determine the number density of low-luminosity objects. Although a direct probe of the faint end of the IR LF will require the capabilities of next-generation telescopes such as the *James Webb Space Telescope* (*JWST*), the stacking analysis of galaxies below the limits of our 24 μm survey appears to support our conclusion. The result of stacking analysis suggests that the faint-end slope of the IR LF at $z \sim 2$ cannot be much higher than the value we considered here (and those usually considered in the literature at different redshifts).

In fact, an analogous situation is observed at other wavelengths. For example, Caputi et al. (2006b) determined the evolution of the rest-frame K_s-band LF from $z = 0$ to $z \sim 2.5$. The depth of their survey ($K_s < 21.5$ Vega mag) allowed them to properly constrain this LF down to more than a magnitude below the turnover M^{*} at $z = 2$. These authors found that a Schechter function with the same fixed slope is suitable to describe the K_s-band LF from the local universe to high redshifts, within the limits of their survey. In this case, the ML analysis (which is in good agreement with the LF computed with the $1/V_{\mathrm{max}}$ method) also indicates that there is a negative-density evolution of this LF with increasing redshift.

The similarities between the evolutions of the K_s-band and 8 μm LFs should not come as a surprise. The bright end of the mid-IR LF at $z \sim 2$ is mostly populated by massive $M \gtrsim 10^{11}\ M_{\odot}$ galaxies (Caputi et al. 2006c). At redshift $z \sim 1$, the mid-IR LF is dominated by LIRGs, the majority of which are characterized by intermediate ($\sim 10^{10}$–$10^{11}\ M_{\odot}$) stellar masses (Hammer et al. 2005; Caputi et al. 2006c). Thus, the evolution in the number density of mid-IR galaxies above a given luminosity cut is related to the global evolution of galaxies above a given mass cut.

It should be clear that the aim of this discussion is to show how the results we find in this work are perfectly consistent with other observational evidence of galaxy evolution. This does not exclude, however, that the ultimate conclusion on the faint ends of the K_s and IR LF will only be achieved in the light of future extremely deep surveys.

As we mentioned in § 6.4, the IR luminosity density associated with star-forming galaxies at $z \sim 2$ implies a star formation rate density $0.11 \pm 0.02\ M_{\odot}\ \mathrm{yr}^{-1}\ \mathrm{Mpc}^{-3}$ (Kennicutt 1998). Let us assume that this has been the average star formation rate density between redshifts $z = 1$ and 3. In our assumed cosmology, the elapsed time between these redshifts is ~3.6 Gyr. The stellar mass density formed during this period of time would be nearly $(4.0 \pm 0.7) \times 10^{8}\ M_{\odot}\ \mathrm{Mpc}^{-3}$. If we consider that the fraction of material recycled through stellar winds and supernovae could be roughly 50%, then the resulting mass density locked in stars would grow by $\sim (2.0 \pm 0.4) \times 10^{8}\ M_{\odot}\ \mathrm{Mpc}^{-3}$ between $z = 3$ and 1. This is actually the growth of the stellar mass density that has been measured from different near-IR surveys at these redshifts (see Caputi et al. 2006b and references therein). This result also shows that, unless the recycled fraction of material into the interstellar medium is much larger than 50% between redshifts $z = 1$ and 3, then the average star formation rate density along this period cannot very much exceed the value we find in this work, $\delta_{\mathrm{SFR}} \approx 0.11 \pm 0.02\ M_{\odot}\ \mathrm{yr}^{-1}\ \mathrm{Mpc}^{-3}$ at $z \sim 2$. Much higher star formation rate densities only could be explained if a high fraction of the new formed stars were very massive, in which case they would basically not contribute to the final stellar mass of the host galaxies.

Considering a star formation rate density $\delta_{\mathrm{SFR}} = 0.11 \pm 0.02\ M_{\odot}\ \mathrm{yr}^{-1}\ \mathrm{Mpc}^{-3}$ strictly in the redshift range $1.7 < z < 2.3$ and assuming again a recycled fraction of 50%, we derive that the total stellar mass density produced in this redshift interval is $(1.8 \pm 0.3) \times 10^{7}\ M_{\odot}\ \mathrm{Mpc}^{-3}$. This is nearly 4% of the total stellar mass density assembled at $z = 0$ [i.e., $(4.9 \pm 0.1) \times 10^{8}\ M_{\odot}\ \mathrm{Mpc}^{-3}$, as obtained by integrating the local stellar mass

function of, e.g., Cole et al. 2001]. In the redshift interval $0.9 < z < 1.1$, our measured star formation rate density is $\delta_{\rm SFR} = 0.20 \pm 0.03\ M_\odot\ {\rm yr}^{-1}\ {\rm Mpc}^{-3}$. With a recycled fraction of 50%, this implies a growth in stellar mass density of $(8.0 \pm 1.2) \times 10^7\ M_\odot\ {\rm Mpc}^{-3}$. Thus, more than 15% of the present-day stellar mass density is being created in IR galaxies during the time elapsed between redshifts $z = 0.9$ and 1.1 (i.e., $\sim$0.8 Gyr).

We found in this work that the number densities of ULIRGs associated with star formation are very similar at redshifts $z = 1$ and $\sim$2. This suggests that the physical mechanism responsible for galaxies to enter a star-forming ULIRG phase is similarly efficient at these two redshifts. This result imposes strong constraints on IR galaxy synthesis models. The origin of the ULIRG phase is usually associated with advanced gas-rich mergers (Sanders & Mirabel 1996). Thus, this phenomenon had to be comparably common for the production of powerful star-forming systems at redshifts $z = 1$ and 2.

8. SUMMARY AND CONCLUSIONS

In this work we have presented the IR LF of 24 μm–selected *Spitzer* galaxies at redshifts $z = 1$ and $\sim$2 in the GOODS fields. At $z \sim 2$, we separately studied the LF for star-forming galaxies only and the total 8 μm LF for star-forming galaxies and AGNs. We then used a new calibration based on *Spitzer* star-forming galaxies to convert the rest-frame 8 μm into bolometric IR luminosities of the star-forming galaxies in our sample. This allowed us to compute the bolometric IR LF and obtain an estimate of the IR luminosity densities at $z = 1$ and $\sim$2.

We found that the rest-frame 8 μm LF for star-forming galaxies at $z = 1$ and $\sim$2 is well described by a double exponential law that has evolved from $z \sim 0$. Between $z \sim 0$ and $z = 1$, there is a strong luminosity evolution and the number density of $\log_{10}(\nu L_\nu^{8\ \mu{\rm m}}) > 10.5$ increases by a factor >20. The characteristic luminosity L^* of the rest-frame 8 μm LF continues increasing up to redshift $z \sim 2$, but, at this redshift, the number density of $\log_{10}(\nu L_\nu^{8\ \mu{\rm m}}) > 10.5$ galaxies is smaller than the density at $z = 1$. This certainly does not mean that the contribution of IR galaxies has been less important at high redshifts. The rest-frame 8 μm luminosity density at $z \sim 2$ is still $\sim$2.3 times larger than the corresponding luminosity density at $z \sim 0$, but only half the value at $z = 1$.

At $z \sim 2$, the inclusion of AGNs mainly affects the bright end of the IR LF. The bright end of the total rest-frame 8 μm LF for star-forming galaxies and AGNs is correctly reproduced by a power law that accounts for the excess of bright sources. AGNs only produce $\sim$17% of the total rest-frame 8 μm luminosity density at $z \sim 2$.

The quasi-linear relation between rest-frame 8 μm and bolometric IR luminosities for star-forming galaxies produces that the bolometric IR LF is well described by a similar law as the rest-frame 8 μm LF at the same redshift. The characteristic luminosity $L^*_{\rm IR}$ of the bolometric IR LF for star-forming galaxies at $z \sim 2$ is close to $\sim 10^{12}\ L_\odot$, i.e., the limiting luminosity between the LIRGs and ULIRGs. As the luminosity density is mainly governed by the turnover of the LF, the value of $L^*_{\rm IR}$ results in roughly similar contributions of LIRGs and ULIRGs to the IR luminosity density. These two populations altogether account for $\sim$90% of the total IR luminosity density associated with star formation at $z \sim 2$.

Finally, we discussed the possibility that the total IR luminosity and corresponding star formation rate density estimated in this work could have been significantly different at any redshift between $z = 1$ and 3. Constraints from near-IR surveys suggest that the stellar mass density built up by galaxies at this epoch would be in contradiction with average star formation rate densities much larger than our estimated value (unless a much higher proportion of very massive stars were created in the past). Our results appear, then, to be consistent with this other observational evidence of galaxy evolution.

This paper is based on observations made with the *Spitzer* Observatory, which is operated by the Jet Propulsion Laboratory, California Institute of Technology, under NASA contract 1407. Also based on observations made with the Advanced Camera for Surveys on board the *Hubble Space Telescope* operated by NASA/ESA and with the Infrared Spectrometer and Array Camera on the "Antu" Very Large Telescope operated by the European Southern Observatory in Cerro Paranal, Chile, and which form part of the publicly available GOODS data sets. We thank the GOODS teams for providing reduced data products.

We are grateful to Héctor Flores and François Hammer, for providing us additional spectroscopic redshifts for the GOODS/CDF-S; Jiasheng Huang, for sending us the results of his 8 μm LF at $z \sim 0$ before publication; and Dieter Lutz and Pablo Pérez-González, for providing us with some of their published results in electronic format. We thank the anonymous referee for helpful comments and suggestions. K. I. C. and G. L. thank the Infrared Processing and Analysis Center (IPAC) at Caltech for hospitality while part of this work was being done. K. I. C. acknowledges CNES and CNRS funding.

REFERENCES

Alexander, D., et al. 2003, AJ, 126, 539
Babbedge, T. S. R., et al. 2006, MNRAS, 370, 1159
Barger, E. J., Cowie, L. L., & Richards, E. A. 2000, AJ, 119, 2092
Barmby, P., et al. 2006, ApJ, 642, 126
Bavouzet, N., et al. 2006, A&A, submitted
Bertin, E., & Arnouts, S. 1996, A&AS, 117, 393
Bolzonella, M., Miralles, J.-M., & Pelló, R. 2000, A&A, 363, 476
Brandl, B. R., et al. 2006, ApJ, 653, 1129
Bruzual, A. G., & Charlot, S. 1993, ApJ, 405, 538
Calzetti, D., Armus, L., Bohlin, R. C., Kinney, A. L., Koornneef, J., & Storchi-Bergmann, T. 2000, ApJ, 533, 682
Calzetti, D., et al. 2005, ApJ, 633, 871
Capak, P., et al. 2004, AJ, 127, 180
Caputi, K. I., Dole, H., Lagache, G., McLure, R. J., Dunlop, J. S., Puget, J.-L., Le Floc'h, E., & Pérez-González, P. G. 2006a, A&A, 454, 143
Caputi, K. I., McLure, R. J., Dunlop, J. S., Cirasuolo, M., & Schael, A. M. 2006b, MNRAS, 366, 609
Caputi, K. I., et al. 2006c, ApJ, 637, 727
Chapman, S. C., Blain, A. W., Smail, I., & Ivison, R. J. 2005, ApJ, 622, 772
Chary, R., & Elbaz, D. 2001, ApJ, 556, 562
Chary, R., et al. 2007, ApJ, submitted
Cohen, J. G., Cowie, L. L., Hogg, D. W., Songaila, A., Blandford, R., Hu, E. M., & Shopbell, P. 1996, ApJ, 471, L5
Cole, S., et al. 2001, MNRAS, 326, 255
Contursi, A., Boselli, A., Gavazzi, G., Bertagna, E., Tuffs, R., & Lequeux, J. 2001, A&A, 365, 11
Dale, D. A., & Helou, G. 2002, ApJ, 576, 159
Dale, D. A., Helou, G., Contursi, A., Silbermann, N. A., & Kolhatkar, S. 2001, ApJ, 549, 215
Dale, D. A., et al. 2005, ApJ, 633, 857
Désert, F.-X., Boulanger, F., & Puget, J.-L. 1990, A&A, 237, 215
Dole, H., et al. 2004, ApJS, 154, 93
———. 2006, A&A, 451, 417
Draine, B. T., & Lee, H. M. 1984, ApJ, 285, 89
Egami, E., et al. 2004, ApJS, 154, 130
Elbaz, D., et al. 2002, A&A, 384, 848
Fazio, G. G., et al. 2004, ApJS, 154, 10
Flores, H., et al. 1999, ApJ, 517, 148
Förster-Schreiber, N. M., Roussel, H., Sauvage, M., & Charmandaris, V. 2004, A&A, 419, 501

Galliano, F., Madden, S. C., Jones, A. P., Wilson, C. D., & Bernard, J.-P. 2005, A&A, 434, 867
Giacconi, R., et al. 2002, ApJS, 139, 369
Giavalisco, M., et al. 2004, ApJ, 600, L93
Gispert, R., Lagache, G., & Puget, J.-L. 2000, A&A, 360, 1
Greve, T. R., Ivison, R. J., Bertoldi, F., Stevens, J. A., Dunlop, J. S., Lutz, D., & Carilli, C. L. 2004, MNRAS, 354, 779
Haarsma, D. B., Partridge, R. B., Windhorst, R. A., & Richards, E. A. 2000, ApJ, 544, 641
Hammer, F., Flores, H., Elbaz, D., Zheng, X. Z., Liang, Y. C, & Cesarsky, C. 2005, A&A, 430, 115
Hopkins, A. M. 2004, ApJ, 615, 209
Hornschemeier, A. E., et al. 2001, ApJ, 554, 742
———. 2003, AJ, 126, 575
Huang, J., et al. 2006, ApJ, submitted
Ilbert, O., et al. 2005, A&A, 439, 863
Kennicutt, R. C., Jr. 1998, ApJ, 498, 541
Lacy, M., et al. 2004, ApJS, 154, 166
Lagache, G., Dole, H., & Puget, J.-L. 2003, MNRAS, 338, 555
Lagache, G., et al. 2004, ApJS, 154, 112
Le Borgne, D., & Rocca-Volmerange, B. 2002, A&A, 386, 446
Le Fèvre, O., et al. 2004, A&A, 428, 1043
Le Floc'h, E., et al. 2004, ApJS, 154, 170
———. 2005, ApJ, 632, 169
———. 2007, ApJ, in press
Lonsdale, C., et al. 2004, ApJS, 154, 54
Lutz, D., et al. 2005, ApJ, 625, L83
Papovich, C., et al. 2004, ApJS, 154, 70
Peeters, E., Spoon, H. W. W., & Tielens, A. G. G. M. 2004, ApJ, 613, 986
Pérez-González, P. G., et al. 2005, ApJ, 630, 82
Pozzi, F., et al. 2004, ApJ, 609, 122
Reddy, N., Steidel, C. C., Erb, D. K., Shapley, A. E., & Pettini, M. 2006a, ApJ, 653, 1004
Reddy, N., Steidel, C. C., Fadda, D., Yan, L., Pettini, M., Shapley, A. E., Erb, D. K., & Adelberger, K. L. 2006b, ApJ, 644, 792
Rieke, G. H., et al. 2004, ApJS, 154, 25
Roussel, H., Sauvage, M., Vigroux, L., & Bosma, A. 2001, A&A, 372, 427
Sandage, A., Tammann, G. A., & Yahil, A. 1979, ApJ, 232, 352
Sanders, D. B., Mazzarella, J. M., Kim, D.-C., Surace, J. A., & Soifer, B. T. 2003, AJ, 126, 1607
Sanders, D. B., & Mirabel, I. F. 1996, ARA&A, 34, 749
Sanders, D. B., et al. 2007, ApJS, in press
Saunders, W., et al. 1990, MNRAS, 242, 318
Schechter, P. 1976, ApJ, 203, 297
Schmidt, M. 1968, ApJ, 151, 393
Scott, S. E., et al. 2002, MNRAS, 331, 817
Serjeant, S., et al. 2004, MNRAS, 355, 813
Stern, D., et al. 2005, ApJ, 631, 163
Takeuchi, T. T., Buat, V., Iglesias-Páramo, J., Boselli, A., & Burgarella, D. 2005, A&A, 432, 423
Takeuchi, T. T., Ishii, T. T., Dole, H., Dennefeld, M., Lagache, G., & Puget, J.-L. 2006, A&A, 448, 525
Takeuchi, T. T., Yoshikawa, K., & Ishii, T. T. 2003, ApJ, 587, L89
Vanzella, E., et al. 2005, A&A, 434, 53
———. 2006, A&A, 454, 423
Webb, T. M., et al. 2003, ApJ, 587, 41
Werner, M. W., et al. 2004, ApJS, 154, 1
Wirth, G. D., et al. 2004, AJ, 127, 3121
Wolf, C., et al. 2004, A&A, 421, 913
Wu, H., et al. 2005, ApJ, 632, L79
Xu, C. 2000, ApJ, 541, 134
Yan, L., et al. 2004, ApJS, 154, 60
———. 2005, ApJ, 628, 604
Zheng, X. Z., et al. 2006, ApJ, 640, 784
Zucca, E., Pozzetti, L., & Zamorani, G. 1994, MNRAS, 269, 953

Draft version July 18, 2007
Preprint typeset using LaTeX style emulateapj v. 10/09/06

CORRELATED ANISOTROPIES IN THE COSMIC FAR-INFRARED BACKGROUND DETECTED BY *MIPS/SPITZER*: CONSTRAINT ON THE BIAS

G. Lagache[1], N. Bavouzet[1], N. Fernandez-Conde[1], N. Ponthieu[1], T. Rodet[2], H. Dole[1], M.-A. Miville-Deschênes[1], J.-L. Puget[1]

Draft version July 18, 2007

ABSTRACT

We report the detection of correlated anisotropies in the Cosmic Far-Infrared Background at 160 μm. We measure the power spectrum in the *Spitzer*/SWIRE Lockman Hole field. It reveals unambiguously a strong excess above cirrus and Poisson contributions, at spatial scales between 5 and 30 arcminutes, interpreted as the signature of infrared galaxy clustering. Using our model of infrared galaxy evolution we derive a linear bias $b = 1.74 \pm 0.16$. It is a factor 2 higher than the bias measured for the local *IRAS* galaxies. Our model indicates that galaxies dominating the 160 μm correlated anisotropies are at $z \sim 1$. This implies that infrared galaxies at high redshifts are biased tracers of mass, unlike in the local Universe.

Subject headings: infrared: galaxies –galaxies: evolution – (cosmology:) large-scale structure of universe

1. INTRODUCTION

The discovery of the Cosmic Far-Infrared Background (CIB) in 1996, together with recent cosmological surveys from the mid-infrared to the millimeter has revolutionized our view of star formation at high redshifts. It has become clear, in the last decade, that infrared galaxies contribute to a large part of the whole galaxy build- up in the Universe. Since the discovery of the CIB, new results on the identification of the sources contributing to the CIB, their redshift distribution, and their nature, are coming out at increasing speed, especially through multi-wavelength analysis (see for a review Lagache et al. (2005)). Stacking analysis are also very promising to probe the CIB source populations (e.g. Dole et al. (2006), Wang et al. (2006), Dye et al. (2007)). However, up to now, very little information is available on the clustering of infrared galaxies, although getting information on the clustering is essential to understand their formation process and to see how they relate to the other galaxy populations.

The first three-dimensional quantitative measurements of the clustering strength of Ultra and Hyper Luminous Infrared Galaxies (ULIRGs, HyLIRGs) at high redshifts ($z > 1.5$) have been made by Blain et al. (2004), Farrah et al. (2006) and Magliocchetti et al. (2007). These studies show that ULIRGs and HyLIRGs are associated with the most massive dark matter halos at high redshifts, unlike in the local Universe where the star formation is quenched in the densest environments. CIB anisotropy observations provide a powerful complement to direct high angular resolution observations of individual sources. CIB fluctuations measure, at large angular scales, the linear clustering bias and, at small angular scales, the nonlinear clustering within a dark-matter halo (Cooray & Sheth (2002)). They thus probe both the dark-matter halo mass scale and the physics governing the formation of infrared galaxies within a halo. However, up to now correlated anisotropies have never been firmly detected. In the far-infrared, detection of anisotropies is limited to the Poisson contribution (Lagache & Puget (2000), Matsuhara et al. (2000), Miville-Deschênes et al. (2002))[3].

We report the detection of CIB correlated anisotropies at 160 μm in the *Spitzer* SWIRE Lockman Hole field and give a first constraint on the linear bias. The paper is organised as follow: data are presented in Sect. 2. The power spectrum is analysed in Sect. 3. Finally a summary and discussion are given in Sect. 4.

Throughout this paper we use the cosmological parameters $h = 0.71, \Omega_\Lambda = 0.73, \Omega_m = 0.27$. For the dark matter linear clustering we set the normalization to $\sigma_8 = 0.8$.

2. THE LOCKMAN HOLE SWIRE FIELD: MAP AND POWER SPECTRUM

SWIRE has surveyed 49 square degrees distributed over 6 fields in the northern and southern sky (Lonsdale et al. (2004)). The Lockman Hole is the largest field with the lowest cirrus emission. It covers about 10 square degrees at 160 μm.

2.1. *Data reduction and map*

Raw data were reduced using the Data Analysis Tool (Gordon et al. (2005)) version 2.71. We systematically removed each DCE (data collection event) after the stimulator flash to minimize the latency effect. We use the last calibration factor (44.7) to convert *MIPS* units to MJy/sr. Data were finally projected on a grid with 15.95 arcsecond pixels. The map is shown on Fig. 1. Further processings were necessary prior to measuring the power spectrum. We first needed to remove residual stripes. This has been done exactly in the same way as in Miville-Deschêne & Lagache (2005). This paper shows that our method efficiently removed residual stripes without affecting the astrophysical signal. We then remove all sources with S_{160} >200 mJy (200 mJy is the high reliability threshold, as detailed in Surace et al. (2005)). For this purpose we use DAOPHOT to detect the sources (the image was wavelet filtered prior to the detection). We then measure the fluxes using aperture photometry. After a fine centering on the sources, we integrate within 25". Sky values are estimated in an [80"-110"] annulus. We compute the aperture correction – which is 2.02 – using an effective instrumental function (that we call PSF for Point Spread Function) measured directly on a *MIPS* 160 μm map. Using an effective PSF rather than the PSF computed using the STinyTim program[4] is important to take into account the survey strategy. In the Lockman Hole SWIRE field, the signal-to-noise ratio was not high enough to accuratly measure the PSF. We thus use the GTO/CDFS field in which the integration time is 6 times that in the Lockman hole SWIRE field. We checked that our measured fluxes at 160 μm were in very good agreement with the SWIRE DR2 catalog (better than 10% on average). On Fig 1 is shown the final map that will be used to compute the power spectrum.

2.2. *Power Spectra*

There are four contributors to the power spectrum at 160 μm: cirrus emission, Poisson (shot) noise from discrete unresolved sources, CIB clustering (if any), and instrumental noise. If the noise and the signal are not correlated, the measured power spectrum $P(k)$ follows:

$$P(k) = \gamma(k)\,[P_{cirrus}(k) + P_{sources} + P_{clus}(k)] + N(k) \quad (1)$$

where k is the 2D wavenumber ($k = \sqrt{k_x^2 + k_y^2}$, expressed in arcmin^{-1}), $P_{cirrus}(k)$, $P_{sources}$, $P_{clus}(k)$ and $N(k)$ are respectively the power spectrum of the dust emission, the shot noise from unresolved sources (constant), the clustering and the noise. The factor $\gamma(k)$ represents the power spectrum of the PSF. To isolate the astrophysical components, we have to determine $N(k)$ and $\gamma(k)$.

The noise power spectrum $N(k)$ is computed by subtracting two maps of exactly the same region as detailed in Miville-Deschênes et al. (2002). We construct two maps using the even and odd scans. As expected, $N(k)$ and $P(k)$ meet at small scales ($k \sim 1$ arcmin^{-1}) where the signal is noise-dominated. The noise power spectrum $N(k)$ is subtracted from the raw power spectrum $P(k)$.

One of the critical issues is to correct the power spectrum from the PSF $\gamma(k)$. The PSF at 160 μm computed using the STinyTim program is very accurate but does not include any effect induced by the observing strategy. We have therefore also extracted direcly the PSF from the data (as discussed in Sect. 2). The comparison of the power spectrum corrected by these two PSF is shown on Fig. 2. They are in very close agrement but we can notice that the effective PSF gives a better result (i.e. a flat power spectrum for $0.25 < k < 0.8$ arcmin^{-1}, as expected from $P_{sources}$).

The error bars (shown in Fig. 3) are estimated using a frequentist approach. Mock signal plus noise maps are generated and analysed with the same pipeline as for the data. This gives a set of power spectra of which we compute the covariance matrix. The diagonal elements of the covariance matrix are the errors on the measured power spectrum.

3. POWER SPECTRUM ANALYSIS

3.1. *Adding low spatial frequency data to constrain the cirrus component*

Several studies show that the cirrus component dominate the power spectra at large scales for k<0.01 arcmin^{-1} (e.g. Miville-Deschênes et al. (2002; 2007)). With the SWIRE data only, in such a low interstellar dust column density field, P_{cirrus} cannot be constrained. Larger maps are needed. We therefore compute the power spectrum of a large (∼200 Sq. Deg.) *IRIS/IRAS* 100 μm maps (Miville-Deschênes & Lagache (2005)). The SWIRE Lockman Hole field is embedded in this large *IRIS* map so that the average 100 μm dust emission is the same in the SWIRE and larger map (4% difference). Having the same average brightness is important since the normalisation of the cirrus power spectrum in the very diffuse region scales as I_{100}^2 (Miville-Deschênes et al. (2007)). We compute the power spectrum of the 100 μm map after removing the bright sources as in Miville-Deschênes et al. (2007). We keep only the largest scales (k <9 10^{-3} arcmin^{-1}), where we have only the contribution from the cirrus component – the CIB being negligible at these very large scales – and multiply the power spectrum by the average dust emission color $(I_{160}/I_{100})^2$. The color has been computed using DIRBE and FIRAS data. We compute the average $|b| > 40^o$ spectrum of the dust emission correlated with the HI gas as in Lagache (2003). We then fit the peak of the dust emission spectrum to get the color. We obtain I_{160}/I_{100}=2.06. If we take $|b| > 30^o$, the color varies by ∼10%. We show on Fig. 2 the 160 μm power spectrum derived from *IRIS* data together with the 160 μm *MIPS* power spectrum. The spectra agree impressively well. We can thus use this extended $P(k)$ to constrain the cirrus contribution. In the following, the two spectra are stiched so that we use one spectrum from k∼0.001 to 1 arcmin^{-1}.

3.2. *Detection of an excess at intermediate scales: signature of correlated anisotropies*

The cirrus component follows:

$$P_{cirrus}(k) = P_0 \left(\frac{k}{k_0}\right)^\beta \quad (2)$$

where P_0 is the power spectrum value at k_0=0.01 arcmin^{-1}. P_0 and β are determined by fitting the power spectrum (see Sect. 3.3). We obtain $P_0 = (2.98 \pm 0.66) \times 10^6$ Jy^2/sr and $\beta = -2.89 \pm 0.22$. The normalisation can be converted at 100 μm using the 160/100 color given above; we obtain $P_0(100\mu m) = 7 \times 10^5$ Jy^2/sr. Considering that the mean cirrus value at 100 μm in our field is I_{100}=0.51 MJy/sr, our measured $P_0(100\mu m)$ and β are in excellent agreement with Miville-Deschênes et al. (2007). The power spectrum of the cirrus component (Eq. 2) is displayed on Fig. 2. The measured power spectrum clearly has

[1] Institut d'Astrophysique Spatiale (IAS), Bâtiment 121, F-91405 Orsay (France); Université Paris-Sud 11 and CNRS (UMR 8617); [guilaine.lagache, nicolas.bavouzet, nestor.fernandez, nicolas.ponthieu, herve.dole, mamd, jean-loup.puget]@ias.u-psud.fr
[2] Laboratoire des signaux et systèmes (L2S), Supélec, 3 rue Joliot-Curie, 91190 Gif-sur-Yvette (France); Thomas.Rodet@lss.supelec.fr

[3] Note however that Grossan & Smoot (2006) report the detection of the clustering signature at 160 μm.

[4] http://ssc.spitzer.caltech.edu/archanaly/contributed/stinytim/

an excess of power w.r.t. the cirrus contribution for $k > 0.3$ arcmin^{-1}. We interpret this strong excess as the signature of correlated CIB anisotropies.

We model the correlated anisotropies following Knox et al. (2001)[5]. Using the three-dimensional, linear-theory power spectrum of dark matter density fluctuations today, $P_M(k)$ the power spectrum of CIB anisotropies can be written as:

$$C_l^{\nu} = \int \frac{dz}{r^2}\frac{dr}{dz} a^2(z)\bar{j}^2(\nu,z) b^2 P_M(k)|_{k=l/r} G^2(z) \equiv P_{clus}(k) \quad (3)$$

where r is the comoving proper-motion distance, k the 3D wavenumber ($k = \sqrt{k_x^2 + k_y^2 + k_z^2}$, in Mpc^{-1}), a(z) the scale factor, $\bar{j}(\nu, z)$ is the mean infrared galaxy emissivity per unit of comoving volume, and $G(z)$ is the linear theory growth function. ℓ is the angular multipole sets using the Limber approximation, $k = \ell/r$. We assume that the fluctuations in emissivity $\delta j/\bar{j}$ are a biased tracer of those in the mass and introduce the bias parameter b, that we assume independent of redshift and scale:

$$\frac{\delta j(\mathbf{k},\nu,z)}{\bar{j}(\nu,z)} = b \times \frac{\delta\rho(\mathbf{k},z)}{\bar{\rho}(z)} \quad (4)$$

where ρ is the dark matter density field. We compute the emissivity using the infrared galaxy evolution model of Lagache et al. (2004). This model, valid in the range 3-1000 μm, is in very good agreement with mid-IR to far-IR number counts, CIB observations, resolved sources redshift distributions and local luminosity functions and their evolution up to $z \sim 2$ (e.g. Lagache et al. (2004), Caputi et al. (2006), Dole et al. (2006), Frayer et al. (2006), Caputi et al. (2007)). Fixing the cosmology, the only unkown parameter in Eq. 3 is the bias b.

3.3. *Measuring the bias*

We fit simultaneously P_0, β, b and $P_{sources}$ using the non-linear least-squares curve fitting mpfit program[6]. We obtain $P_0 = (2.98 \pm 0.66) \times 10^6$ Jy^2/sr, $\beta = -2.89 \pm 0.22$, $b = 1.74 \pm 0.16$, and $P_{sources} = 9848 \pm 120$ Jy^2/sr. P_0 and β have been discussed in Sect. 3.2. $P_{sources}$ agrees quite well with previous *ISOPHOT* determination at roughly the same $S_1 60$ threshold (Matsuhara et al. (2000)). The fact that P_0, β, and $P_{sources}$ are in very good agreement with previous measurements give us confidence in our measurement of the linear bias $b \sim 1.7$. It is well known that in the local Universe infrared galaxies are not biased tracers of the mass. For example, Saunders et al. (1992) found $b\sigma_8$=0.69±0.09 for *IRAS* galaxies. Assuming σ_8=0.8 gives $b = 0.86$. This bias is roughly comparable to the bias of the SDSS galaxies at $z \sim 0.1$ ($b \sim 1.1$, Tegmark et al. (2004)). We measure an average bias about 2 times higher in the CIB anisotropies. Figure 4 shows the predicted redshift contribution to the correlated anisotropies. At k=0.05 arcmin^{-1}, anisotropies from $0.7 < z < 1.5$ infrared galaxies contribute for more ∼65%. Lower redshift galaxies contribute for less than 5%. This shows that infrared galaxies at z∼1 are much more biased (∼2 times) than locally.

4. SUMMARY AND DISCUSSION

We presented the power spectrum measured in the *Spitzer*/SWIRE Lockman Hole field at 160 μm. It is very well reproduced by the contribution from three components, cirrus, correlated CIB, and Poisson noise. The cirrus and Poisson contributions are very close to previous measurements. We measure the linear bias, $b = 1.74 \pm 0.16$. This bias is likely to be that of infrared galaxies at $z \sim 1$ since $z \sim 1$ galaxies are dominating the contribution to the correlated CIB anisotropies (Fig. 4) and local galaxies are "anti-biased". Such a bias is analog (but somewhat higher) to the bias of the red optical galaxy population at $z \sim 1$. For example, Marinoni et al. (2005) measured a bias of 1.6 at $z \sim 1.2$ for the red $(B - I) > 1.5$ galaxies in the VVDS. Blue galaxies at those redshifts are less biased with a relative bias between red and blue population of 1.4.

The very strong evolution of the bias (from ∼1.7 at $z \sim 1$ to 0.86 at z=0) shows that as time progresses and the density field evolves, nonlinear peaks become less rare events and galaxy formation moves to lower-sigma peaks. Thus galaxies become less biased tracers of the mass density field. Moreover, for the infrared galaxy population it is likely that an additional mecanism contributes significantly to the "debiasing" at low redshift. Galaxies in dense environments are found to have suppressed star formation rates (thus no or low infrared emission) and early morphological types compared with those in the field. Environmental effects in particular are important in quenching the star formation through gas stripping (e.g. Postman et al. (2005)), though on some cluster outskirts, some star formation goes on (Duc et al. (2002), Coia et al. (2005)). The high bias found for infrared galaxies at $z \sim 1$ shows that star formation rates of galaxies are increasing with the environment (as also shown by e.g. Elbaz et al. (2007)). The "merger bias" is an alternative, but somehow physically linked, way of boosting the bias at high redshift. Clustering of objects that have undergone recent mergers can be enhanced relative to the clustering of individual halos of comparable masses (e.g. Furlanetto & Kamionkowski (2005); Wetzel et al. (2007)). It is known that the star formation in infrared galaxies is triggered to some extent by mergers in dense environments (at z∼1, 30-50% of luminous infrared galaxies are major mergers). Thus, the high measured bias may also point to "merger bias".

This work is based on observations made with the *Spitzer* Space Telescope, which is operated by the Jet Propulsion Laboratory, California Institute of Technology under NASA contract 1407. This work benefited from funding from the CNES (Centre National d'Etudes Spatiales) and the PNC (Programme National de Cosmologie). We warmly thanks Asantha Cooray for helpful comments and suggestions.

[5] Making a much more complex description of the correlated CIB anisotropies (as for example adding the contribution from the clustering within the same dark matter halo) and the bias is beyond the scope of this paper.

[6] http://cow.physics.wisc.edu/∼craigm/idl/idl.html

REFERENCES

Blain, A.W., Chapman, S.C., Smail, I., Ivison, R.J. 2004, ApJ, 611, 725
Caputi, K.I., Dole, H., Lagache, G., et al. 2006, ApJ, 637, 727
Caputi, K.I., Lagache, G., Yan, L., et al. 2007, ApJ, 660, 97
Cooray, C.J., & Sheth, R. 2002, Phys. Rep., 372, 1
Coia, D., Metcalfe, L., McBreen, B., et al. 2005, A&A, 430, 69
Dole, H., Lagache, G., Puget, J.-L., et al. 2006, A&A, 45, 417
Duc, P.-A., Poggianti, B.M., Fadda, D., et al. 2002, A&A, 382, 60
Dye, S., Eales, S.A., Ashby, M.L.N., et al. 2007, MNRAS, 375, 725
Elbaz, D., Daddi, E., Le Borgne, D., et al. 2007, A&A, 468, 33
Farrah, D., Lonsdale, C.J., Borys C., et al. 2006, ApJ, 643, 139
Frayer, D.T., Farrah, D., Yan, L., et al. 2006, AJ, 131, 250
Gordon, K.D., Rieke, G.H., Engelbracht, C.W., et al. 2005, PASP, 117, 503
Grossan, B., & Smoot, G.F., 2006, astro-ph/0604512
Furlanetto, S.R., & Kamionkowski, M. 2006, MNRAS 366, 529
Knox, L., Cooray, A., Eisenstein, D., Haiman, Z. 2001, ApJ, 550, 7
Lagache, G., Puget, J.-L., Dole, H. 2005, ARAA, 43, 727
Lagache, G., Dole, H., Puget, J.-L., et al. 2004, ApJS, 154, 112
Lagache, G. 2003, A&A, 405, 813
Lagache, G., & Puget, J.-L. 2000, A&A, 355, 17
Lonsdale, C., Polletta, M., Surace, J., et al. 2004, ApJS, 154, 54
Magliocchetti, M., Silva, L., Lapi, A., et al. 2007, MNRAS, 375, 1121
Miville-Deschênes, M.-A., Lagache, G., Puget, J.-L. 2002, A&A, 393, 749
Miville-Deschênes, M.-A., & Lagache, G. 2005, ApJS, 157, 302
Miville-Deschênes, M.-A., Lagache, G., Boulanger, F., Puget, J.-L. 2007, A&A, 469, 595
Marinoni, C., Le Fèvre, O., Meneux, B., et al. 2005, A&A, 442, 801
Matsuhara, H., Kawara, K., Sato, Y., et al. 2000, A&A, 361, 407
Postman, M., Franx, M., Cross, N.J.G., et al. 2005, ApJ, 623, 721
Saunders, W., Rowan-Robinson M., Lawrence A. 1992, MNRAS, 258, 134
Surace, J.A., Shupe, D.L., Fang F., et al., "Data Release Paper for DR2", accessible via: http://swire.ipac.caltech.edu/swire/astronomers/data_access.html.
Tegmark, M., Blanton, M.R., Strauss, M.A., et al. 2004, ApJ, 740, 606
Wang, W.-H., Cowie, L.L., Barger, A.J. 2006, ApJ, 647, 74
Wetzel, A.R., Cohn, J.D., White, M., Holz, D., Warren, M.S. 2007, ApJ, 656, 139

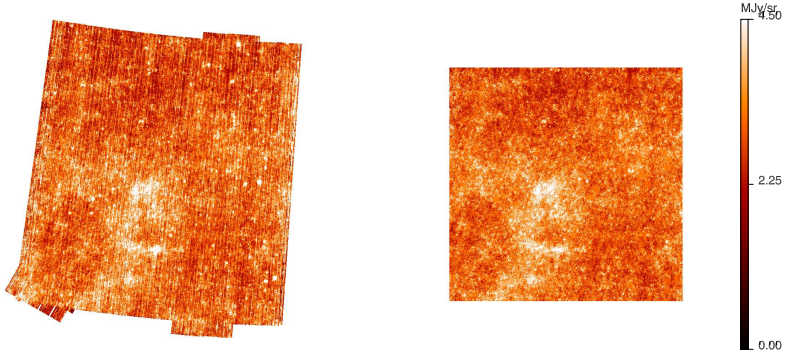

FIG. 1.— *Left:* 160 μm SWIRE map after standard data reduction. *Right:* Final map used to compute the power spectrum. Residual stripes have been corrected as in Miville-Deschênes & Lagache (2005). Sources with S_{160} >200 mJy have been removed.

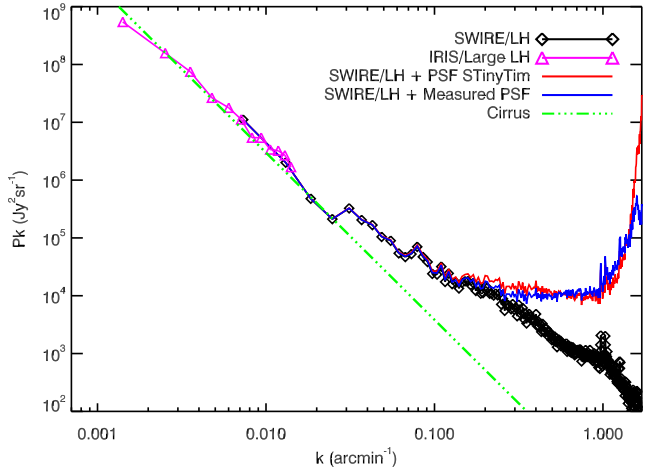

FIG. 2.— Total power spectrum measured in the Lockman Hole at 160 μm. In black (diamonds), the *MIPS*/SWIRE 160 μm power spectrum ($P(k) - N(k)$, see Eq. 1), in purple (triangles) the *IRIS*/*IRAS* enlarged Lockman Hole field power spectrum at 100 μm, scaled to the power spectrum at 160 μm using the 160/100 dust color measured at high latitudes ($|b|$ >40°). In red and blue, the power spectra corrected from the STinyTim and measured PSF – $\frac{P(k)-N(k)}{\gamma(k)}$–, respectively. The green dashed-3dotted line represents the best fit cirrus power spectrum, as computed in Sect. 3.3.

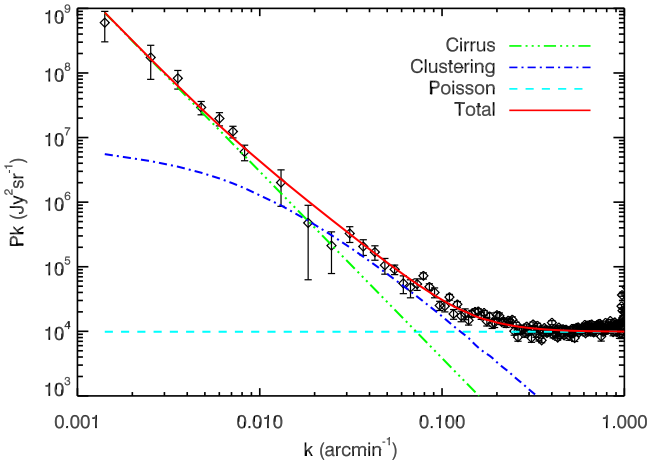

FIG. 3.— Power spectrum in the Lockman Hole at 160 μm (black diamonds with error bars) with the three components: cirrus (green dashed-3dotted line), clustering (blue, dashed-dotted line), Poisson (light blue, dashed line). The red continuous line is the sum of the three components.

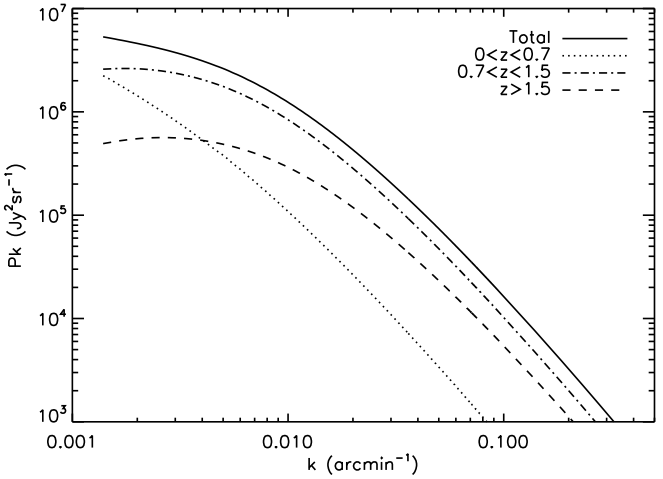

FIG. 4.— Redshift contribution to the correlated anisotropies at 160 μm for $b = 1.7$.

Accepted for publication in the Astrophysical Journal Letters, September 15th, 2006
Preprint typeset using LaTeX style emulateapj v. 6/22/04

FAR-INFRARED CHARACTERIZATION OF AN ULTRA-LUMINOUS STARBURST ASSOCIATED WITH A MASSIVELY-ACCRETING BLACK HOLE AT $Z = 1.15$

E. Le Floc'h[1,2], C.N.A. Willmer[1], K. Noeske[3], N.P. Konidaris[3], E.S. Laird[3] D.C. Koo[3], K. Nandra[4], K. Bundy[5], S. Salim[6], R. Maiolino[7], C.J. Conselice[8], J.M. Lotz[9], C. Papovich[1,10], J.D. Smith[1], L. Bai[1], A.L. Coil[1,10], P. Barmby[11], M.L.N. Ashby[11], J.-S. Huang[11], M. Blaylock[1], G. Rieke[1], J.A. Newman[12,10], R. Ivison[13], S. Chapman[5], H. Dole[14], E. Egami[1] & D. Elbaz[15]

Accepted for publication in the Astrophysical Journal Letters, September 15th, 2006

ABSTRACT

As part of the *All Wavelength Extended Groth Strip International Survey (AEGIS)*, we describe the panchromatic characterization of an X-ray luminous active galactic nucleus (AGN) in a merging galaxy at $z = 1.15$. This object is detected at infrared ($8\,\mu$m, $24\,\mu$m, $70\,\mu$m, $160\,\mu$m), submillimeter ($850\,\mu$m) and radio wavelengths, from which we derive a bolometric luminosity $L_{bol} \sim 9\times10^{12}\,L_\odot$. We find that the AGN clearly dominates the hot dust emission below $40\,\mu$m but its total energetic power inferred from the hard X-rays is substantially less than the bolometric output of the system. About 50% of the infrared luminosity is indeed produced by a cold dust component that probably originates from enshrouded star formation in the host galaxy. In the context of a coeval growth of stellar bulges and massive black holes, this source might represent a "transition" object sharing properties with both quasars and luminous starbursts. Study of such composite galaxies will help address how the star formation and disk-accretion phenomena may have regulated each other at high redshift and how this coordination may have participated to the build-up of the relationship observed locally between the masses of black holes and stellar spheroids.

Subject headings: galaxies: high-redshift — infrared: galaxies — cosmology: observations

1. INTRODUCTION

Galaxies with a bolometric luminosity exceeding $10^{12}\,L_\odot$ are often powered by a combination of massive star formation and accretion of material around active nuclei (e.g., Genzel et al. 1998). Early in cosmic history the connection between these two phenomena may have led to a coeval growth of super massive black holes (SMBHs) and stellar spheroids (e.g., Page et al. 2001), and could thus be the foundation of the correlation observed between the masses of these two components in the local Universe (e.g., Gebhardt et al. 2000). However, the implication of such a co-evolution in the more general context of the stellar mass built-up history (e.g., Dickinson et al. 2003) and SMBH formation (e.g., Barger et al. 2005) has not been fully addressed. Understanding the importance of this "coordinated" activity of starbursts and active galactic nuclei (AGNs) requires properly deconvolving their respective contributions *within individual objects*, a challenging task particularly for distant sources.

Because of the complexity of the AGN and starburst spectral energy distributions (SEDs), this decomposition can best be achieved by combining data from wavebands that offer distinctive spectral features to characterize these phenomena. For instance, active nuclei are strong emitters at high energy and they are usually associated with a continuum of hot dust peaking in the mid-infrared (IR). Luminous starbursts, on the other hand, are characterized by a colder dust component and emit the bulk of their luminosity in the far-IR. To illustrate how the coexistence of these two processes at high redshift could be studied using larger samples, we present a panchromatic analysis of a luminous AGN referenced as CXO–GWS–J141741.9+522823 (hereafter CXO-J1417) by Nandra et al. (2005). It is embedded in an ultra-luminous infrared galaxy (ULIRG) at $z = 1.15$ and its detection across the full electromagnetic spectrum allows us to constrain the level of star formation also present in this source. We assume a ΛCDM cosmology with $H_0 = 70$ km s^{-1} Mpc^{-1}, $\Omega_m = 0.3$ and $\Omega_\lambda = 0.7$.

2. THE DATA

CXO-J1417 is a bright X-ray source also known in the literature as CFRS 14.1157 or CUDSS 14.13. It is associated with a very red galaxy (I–$K_{AB} \sim 2.6$: Webb et al. 2003; see also Wilson et al. 2006) detected in the mid-IR (Flores et al. 1999; Higdon et al. 2004; Barmby et al. 2006; Ashby et al. 2006), submillimeter (Eales et al. 2000; Webb et al. 2003) and radio (Fomalont et al. 1991; Chapman et al. 2005). High resolution images obtained with *HST* (Davis et al. 2006; Lotz et al. 2006) reveal several components presumably interacting with each other (see Fig. 1). The brightest is dominated by a point source located at RA = $14^h17^m41^s.89$ and Dec = $52°28'23.65''$(J2000, δRA $\sim$ δDec $\sim 0.07''$) coinciding precisely with the position of the X-ray detection (Miyaji et al. 2004).

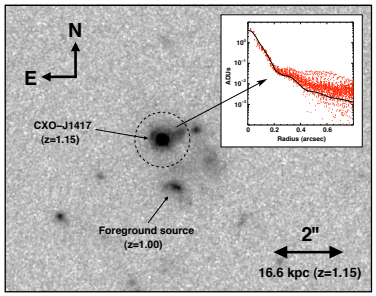

FIG. 1.— An F814W ACS image of CXO–J1417 ($z = 1.15$) with the 95% error location of the X-ray source indicated by the dashed-line circle (Miyaji et al. 2004). The inset illustrates the profile of this component in the F814W image. The comparison with the PSF (solid line) reveals that the central core is not resolved by *HST*. The object lying $1.4''$ to the South is a foreground galaxy at $z = 1.00$.

At this location there is also a bright and point-like object detected at $70\,\mu$m and $160\,\mu$m. In spite of the large beam used for the data at long wavelengths[16], the fact that the mid-IR counterpart of CXO–J1417 is two orders of magnitude brighter than any other galaxies detected at $24\,\mu$m in this area strongly suggests that this far-IR emission is also associated with the X-ray source. Its fluxes in the MIPS 24/70/160 μm bands were measured via PSF fitting. They are reported in Table 1, which also summarizes the full multi-wavelength photometry of the object (see Davis et al. 2006 for a description of our data set). Optical and near-IR fluxes were measured within a $1''$-radius aperture centered at the position of CXO–J1417. With the exception of the GALEX data where we believe that the emission is contaminated by a blue galaxy lying $1.4''$ to the South, our flux measurements refer exclusively to the component hosting the X-ray source.

A redshift of $z = 1.15$ was reported by Hammer et al. (1995) based on UV/optical spectroscopy. In Fig. 2 we display the combined spectrum obtained at Keck by Davis et al. (2003) using LRIS and DEIMOS. The presence of an AGN is clearly confirmed by the detection of [NeV] and MgII. There is however considerable self-absorption of the latter (Sarajedini et al. 2006), which prevents firm classification as a type 1 or a type 2 object. Interestingly, we also note the detection of Ca K+H absorption lines redshifted by $\sim$150–200 km s^{-1} relative to [OII] and which suggests the presence of gas inflow in the galaxy.

Finally, mid-IR spectroscopy was carried out by Higdon et al. (2004) as well as our own group. We obtained[17] 960 s total exposure time for each of the two Short Low (SL1: 7.4–14.5 μm; SL2:5.2–8.7 μm) and each of the two Long Low modules of the IRS (LL1: 19.5–38 μm; LL2: 14.0–21.3 μm, see Houck et al. 2004), while Higdon et al. (2004) targeted CXO–J1417 for a total integration of 1440 s in LL1 and LL2. We reduced and combined all these data using the pipeline developed by the FEPS Legacy team (Hines et al. 2006), thus bringing the total integration to 2400 s for both LL1 and LL2. Our final spectrum covers the rest-frame 2.5–16.5 μm range. It is displayed in Fig. 2 along with the X-ray spectrum of CXO–J1417 obtained by Nandra et al. (2005).

TABLE 1
PHOTOMETRY OF CXO–J1417

Band	Flux/Flux density[a]	Reference[b]
2–10 keV	$3.8\pm0.3\times10^{-14}$ erg cm^{-2} s^{-1}	1
0.5–2 keV	$1.3\pm0.1\times10^{-14}$ erg cm^{-2} s^{-1}	1
FUV (1539Å)	$<0.45\,\mu$Jy (3σ)	
NUV (2316Å)	$0.93\pm0.15\,\mu$Jy	
B (4389Å)	$0.8\pm0.1\,\mu$Jy	
R (6601Å)	$6.05\pm0.15\,\mu$Jy	
I (8133Å)	$16.7\pm0.8\,\mu$Jy	
J (1.2 μm)	$57.6\pm0.5\,\mu$Jy	
K (2.2 μm)	$117\pm1\,\mu$Jy	
IRAC 3.6 μm	$580.1\pm0.4\,\mu$Jy	2, 3
IRAC 4.5 μm	$981.7\pm0.5\,\mu$Jy	2, 3
IRAC 5.8 μm	$1448\pm4\,\mu$Jy	2, 3
IRAC 8.0 μm	$2225\pm4\,\mu$Jy	2, 3
IRS 16 μm	3.3 ± 0.7 mJy	4
MIPS 24 μm	5.75 ± 0.1mJy	
MIPS 70 μm	20.1 ± 1.2 mJy	
MIPS 160 μm	105 ± 30 mJy	
SCUBA 850 μm	3.3 ± 1 mJy	5
VLA 5 GHz	$53.6\pm4\,\mu$Jy	6
VLA 1.4 GHz	$110\pm40\,\mu$Jy	6, 7, 8, 9

[a] Optical/near-IR fluxes are measured in a $1''$-radius aperture.
[b] References – 1: Nandra et al. (2005); 2: Barmby et al. (2006); 3: Ashby et al. (2006); 4: Higdon et al. (2004); 5: Eales et al. (2000); 6: Fomalont et al. (1991); 7: Webb et al. (2003); 8: Chapman et al. (2005); 9: Ivison et al. (2006).

3. A PANCHROMATIC CHARACTERIZATION OF CXO–J1417

The full spectral energy distribution of CXO–J1417 is illustrated in Fig. 3. It has a very red continuum with a steep rise from the optical up to the mid-IR, and the rest-frame 1.6 μm "bump" usually associated with stellar populations (Sawicki 2002) is not detected (Barmby et al. 2006; Ashby et al. 2006). The lack of this stellar feature and the very strong hot-dust power-law emission that we observe at $\sim$1–5 μm (see also Higdon et al. 2004) are characteristic of active nuclei (e.g., Brand et al. 2006). They reveal that the AGN totally dominates the luminosity of CXO–J1417 at these short IR wavelengths.

We explored in more detail the properties of this active nucleus by fitting the X-ray spectrum with a power-law intrinsically absorbed at $z = 1.15$ and assuming a Galactic extinction model. We derived a column density $N_H = 1.13^{+0.92}_{-0.74}\times10^{22}$ cm^{-2} and a photon index $\Gamma = 1.81^{+0.28}_{-0.25}$, leading to an extinction-corrected luminosity $L_{2-10\,keV} = 2.35^{+0.30}_{-0.31}\times10^{44}$ erg s^{-1}. Although the lack of significant extinction by the silicates at 9.7 μm and the non-detection of the 400 eV iron Kα line indicate that it is not an extremely absorbed object, the

[1] Univ. of Arizona, Tucson, AZ 85721; elefloch, cnaw, papovich, jdsmith, bail, acoil, blaylock, grieke, eegami@as.arizona.edu
[2] Chercheur Associé, Observatoire de Meudon, Paris, France
[3] UCO/Lick Observatory, Univ. of California, Santa Cruz, CA 95064; kai, npk, eslaird, koo@ucolick.org
[4] Astrophysics group, Imperial College, London SW7 2AW, UK; k.nandra@imperial.ac.uk
[5] California Institute of Technology, Pasadena, CA 91125; kbundy, schapman@astro.caltech.edu
[6] UCLA, Los Angeles CA 90095; samir@astro.ucla.edu
[7] INAF - Rome I-00044, Italy; maiolino@oa-roma.inaf.it
[8] University of Nottingham, UK; conselice@nottingham.ac.uk
[9] NOAO Leo Goldberg Fellow, Tucson, AZ 85719; lotz@noao.edu
[10] Spitzer/Hubble Fellows
[11] CfA, Cambridge, MA 02138; pbarmby, mashby, willner, jhuang@cfa.harvard.edu
[12] Lawrence Berkeley Nat. Lab., CA 94720; janewman@lbl.gov
[13] Royal Observatory, Edinburgh EH9 3HJ, UK; rji@roe.ac.uk
[14] IAS, F-91405 Orsay, France; herve.dole@ias.u-psud.fr
[15] SAp-CEA, 91191 Gif-sur-Yvette, France; delbaz@cea.fr

[16] The FWHM of the MIPS PSF is $18''$ and $40''$ at 70 μm and 160 μm respectively.
[17] General Observer program ID 3 216.

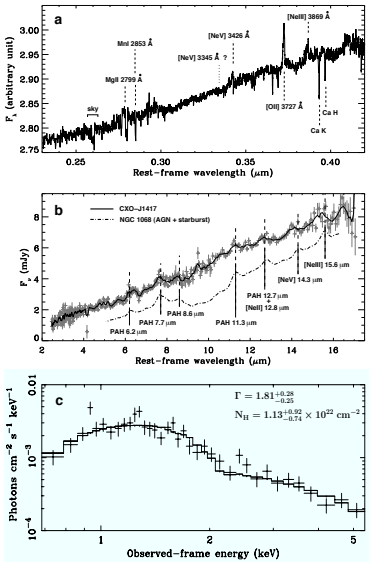

FIG. 2.— The optical (a), mid-IR (b) and X-ray (c) spectra of CXO–J1417. The X-ray properties and the detection of [NeV] 3426Å reveal the presence of an AGN that is also responsible for the hot dust emission and the feature-less power-law SED in the mid-IR. The solid-line in panel b is a smoothed version of the observed spectrum, while the dashed-dotted line shows a comparison with the mid-IR SED of the Seyfert 2 NGC 1068. The solid-line in panel c represents the best fit to the data, obtained with the parameters mentioned in the top-right corner. In spite of the lack of strong silicate absorption at 9.7 μm, the column density derived at high energy indicates a significant obscuration toward the nucleus.

X-ray data point therefore to a luminous AGN characterized by substantial obscuration.

This active nucleus is probably not the only source powering the bolometric luminosity of CXO–J1417. Although they are strongly diluted by the continuum emission from the AGN, the mid-IR broad bands from the Polycyclic Aromatic Hydrocarbons (PAHs) often seen in star-forming environments seem to be detected in our IRS spectrum (see Fig. 2b). Assuming a power-law continuum superimposed with a typical PAH template and leaving the redshift of the latter as a free parameter, we generated a series of simulated spectra that we compared to our data. The χ^2 shows a clear minimum when the PAH component is shifted to the distance of CXO–J1417, which suggests that these features are detected with relatively good confidence[18]. Furthermore, the far-infrared and submillimeter detections reveal a very luminous cold dust component typical of those observed in dusty star-forming galaxies (see Sect. 4). To quantify its contribution relative to the much warmer dust seen in the mid-IR, we decomposed the global IR SED beyond 1 μm into (i) a single modified black body[19] accounting for the cold component, characterized by a temperature $T\sim40$ K and a dust emissivity $\beta\sim1.7$, and (ii) a combination of several blackbodies with temperatures ranging from 150 K to 2000 K and reproducing the warm dust emission (see Fig. 3). We derived 1–1000 μm integrated luminosities of 4.5×10^{12} L$_\odot$ for each of these two components. This leads to a total IR luminosity $L_{1-1000\mu m} = 9.0\pm0.4\times10^{12}$ L$_\odot$, where the uncertainty is driven by the determination of the temperature and the emissivity of the cold dust emission.

[18] At the redshift of CXO–J1417 $z_0=1.15$, the χ^2 is reduced by a factor of ~2 with respect to its median value measured over a redshift range $z_0\pm\Delta z$ with $\Delta z\sim0.5$.

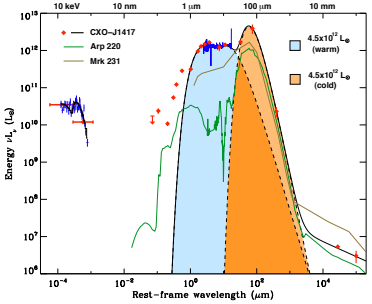

FIG. 3.— Panchromatic SED of CXO–J1417 (red diamonds) overlaid with a fit covering the X-ray, IR and radio wavelength range (solid black line, see text for details). The X-ray and mid-IR spectra from *Chandra* and IRS are also displayed (blue symbols and blue line respectively). The IR portion is fitted by a two-component model accounting for the warm (light-blue shaded) and cold (light-red shaded) dust emission. The fit in the radio assumes synchrotron emission with a spectral index $\alpha=0.6$. The SEDs of Arp 220 and Mrk 231 (adapted from Silva et al. 2004, Spoon et al. 2004 and Ivison et al. 2004) are shown for comparison (green and brown lines respectively).

CXO–J1417 is also remarkably quiet in the radio. The spectral index ($\alpha\sim0.6$) is typical of synchrotron emission from starbursts, though we cannot exclude a flatter continuum because of the substantial uncertainty on the observed flux density at 1.4 GHz. Assuming the standard far-IR/radio correlation (Condon 1992), we would infer an IR luminosity $\sim2.5\times$ lower than that implied by our fit of the cold dust component. As it has already been observed at low redshift (e.g., Rieke et al. 1980; Clemens & Alexander 2004; Gallimore & Beswick 2004) this radio faintness could result from substantial free-free absorption in the interstellar medium of the galaxy. It could also be due to a synchrotron deficiency characteristic of a very recent episode of star formation (Roussel et al. 2003).

4. DISCUSSION

[19] We adopt the form $B_\nu(T)\times\nu^\beta$ where T is the dust temperature and β the dust emissitivity.

4.1. *On the nature of CXO–J1417*

Although the bolometric correction for luminous and strongly-absorbed X-ray sources has not been very well constrained so far, the obscuration toward CXO–J1417 is still reasonable enough to allow a fairly secure estimate of the total luminosity of the active nucleus in this object. Comparison of the SED shown in Fig. 3 with typical AGN templates (e.g., Elvis et al. 1994; Silva et al. 2004) indicate that this bolometric luminosity should typically range between 1×10^{12} L$_\odot$ and 3×10^{12} L$_\odot$. While the AGN can thus power most of the hot dust detected in the system, it is not energetic enough to account also for the far-IR emission. We argue that the cold dust component is produced by a deeply enshrouded starburst in the host galaxy (see also e.g., Waskett et al. 2003). CXO–J1417 could be therefore a high redshift analog of some nearby "composite" ULIRGs where the contribution of the AGN to the bolometric output is comparable to that of the star-forming activity (Farrah et al. 2003). It could also be similar to other distant X-ray selected sources that were detected at long wavelengths (e.g., Page et al. 2001), though this far-IR emission has been sometimes assumed to originate from the active nucleus rather than star formation (Barger et al. 2005).

Assuming the calibration from Kennicutt (1998), the IR luminosity of the cold component translates into a star-formation rate $SFR\sim750\,M_\odot\,yr^{-1}$. Such enhanced levels of activity usually occur within embedded and very compact regions surrounding the cores of galaxies ($\sim$100–300 pcs, Soifer et al. 2000). It is consistent with the absence of direct star formation signatures as inferred from our UV/optical photometry, as well as from the ACS image taking into account the spatial resolution of the *HST* data (i.e., ~1 kpc at $z=1.15$).

4.2. *Implications*

Assuming a typical accretion efficiency $\epsilon=0.1$ (Marconi et al. 2004), the luminosity of the AGN in CXO–J1417 translates into a mass accretion rate $dM/dt\sim3.1\,M_\odot\,yr^{-1}$. This is typical of quasars at $z\sim1$ (McLure & Dunlop 2004), but it is larger than the rates measured in sources experiencing similar levels of starburst activity such as the more distant SCUBA sources (Alexander et al. 2005). Furthermore, the bolometric luminosity of this object and the obscuration toward its nucleus suggest that the gas fueling and the accretion are occurring quite efficiently, probably close to the Eddington limit. Under this hypothesis we would derive a black hole mass of $\sim1.4\times10^8\,M_\odot$. This is typically an order of magnitude larger than the mass of the SMBHs determined in the submillimeter galaxies, and it would be even larger in the case of a sub-Eddington accretion. These properties suggest that CXO–J1417 is an object sharing characteristics with both starburst-dominated galaxies and quasars, where violent star formation is still happening while a massive black hole has already formed.

High redshift ULIRGs showing a mixture of star formation and AGN such as CXO–J1417 could be interesting as tests of the evolutionary sequences that have been proposed to understand the connection between the two phenomena (e.g., Sanders et al. 1988). In such scenarios for instance, merging galaxies first trigger powerful star formation, and as material settles into the cores of these objects it feeds a supermassive black hole that eventually emerges as a luminous AGN. The latter can then produce strong winds and outflows that feed energy back into the surrounding galaxy and may either quench or reactivate star formation (Springel et al. 2005; Hopkins et al. 2005; Silk 2005). In the case of CXO–J1417 there is a dominant contribution of the nucleus in the near-IR and it is not clear whether an underlying bulge has already formed in the host galaxy. However, sources experiencing star formation and disk-accretion that both radiate a similar amount of energy throughout their lifetime would evolve toward massive galaxies that lie significantly out of the local "$M_{BH}-\sigma$" relationship (Page et al. 2001). Although the starburst and the AGN in CXO–J1417 are characterized by roughly equal luminosities now, we infer that if these two phenomena evolve together they may occur on quite different time scales and regulate each other efficiently for the bulges and SMBHs to grow in a coordinated manner.

Such transitional cases might be rare locally (e.g., Genzel et al. 1998). At higher redshift however, their importance relative to the infrared/submillimeter or X-ray selected objects where one type of activity (i.e., star formation or accretion) largely dominates is not yet known. Interestingly, CXO–J1417 lies at the knee of the 2–8 keV luminosity function derived by Barger et al. (2005) at $0.8\leq z\leq1.2$ but it is much more IR-luminous than most of star-forming galaxies at this epoch of cosmic history (Le Floc'h et al. 2005). Searching for similar objects at higher redshifts when ULIRGs were a major component of the starbursting population (Blain et al. 2002) should allow us to explore in more detail the role that this co-existence of AGNs and starbursts within galaxies played in shaping the present-day Universe. Even though their identification could be challenging, CXO–J1417 points to the type of evidence required for this goal. Large data sets from existing surveys like *AEGIS* should provide this information for enough sources to probe the prevalence of this phase of galaxy evolution at $z\gtrsim1$.

We thank Roberto Gilli for his valuable comments as well as Jim Cadien, Dean Hines and Jeroen Bouwman for their help in the data reduction. We are also grateful to Sandy Faber, Puragra Guhathakurta and many other AEGIS members for their helpful comments or contributions to the AEGIS database. This work is based on observations made with the Spitzer Space Telescope, which is operated by NASA/JPL/Caltech. Financial support was provided by NASA through contracts #1255094 and #1256790. ALC and JAN are supported by NASA through Hubble Fellowship grants HF-01182.01-A/HF-011065.01-A. We finally wish to recognize the significant cultural role that the summit of Maunea Kea has within the Hawaiian community.

REFERENCES

Alexander, D. M., Bauer, F. E., Chapman, S. C., Smail, I., Blain, A. W., Brandt, W. N., & Ivison, R. J. 2005, ApJ, 632, 736

Ashby, M. L. N. et al. 2006, ApJ, 644, 778

Barger, A. J., Cowie, L. L., Mushotzky, R. F., Yang, Y., Wang, W.-H., Steffen, A. T., & Capak, P. 2005, AJ, 129, 578
Barmby, P. et al. 2006, ApJ, 642, 126
Blain, A. W., Smail, I., Ivison, R. J., Kneib, J.-P., & Frayer, D. T. 2002, Phys. Rep., 369, 111
Brand, K. et al. 2006, ApJ, 644, 143
Chapman, S. C., Blain, A. W., Smail, I., & Ivison, R. J. 2005, ApJ, 622, 772
Clemens, M. S., & Alexander, P. 2004, MNRAS, 350, 66
Condon, J. J. 1992, ARA&A, 30, 575
Davis, M. et al. 2003, Proceedings of the SPIE, 4834, 161
—. 2006, ApJ, this volume
Dickinson, M., Papovich, C., Ferguson, H. C., & Budavári, T. 2003, ApJ, 587, 25
Eales, S., Lilly, S., Webb, T., Dunne, L., Gear, W., Clements, D., & Yun, M. 2000, AJ, 120, 2244
Elvis, M. et al. 1994, ApJS, 95, 1
Farrah, D., Afonso, J., Efstathiou, A., Rowan-Robinson, M., Fox, M., & Clements, D. 2003, MNRAS, 343, 585
Flores, H. et al. 1999, A&A, 343, 389
Fomalont, E. B., Windhorst, R. A., Kristian, J. A., & Kellerman, K. I. 1991, AJ, 102, 1258
Gallimore, J. F., & Beswick, R. 2004, AJ, 127, 239
Gebhardt, K. et al. 2000, ApJ, 539, L13
Genzel, R. et al. 1998, ApJ, 498, 579
Hammer, F., Crampton, D., Lilly, S. J., Le Fevre, O., & Kenet, T. 1995, MNRAS, 276, 1085
Higdon, S. J. U. et al. 2004, ApJS, 154, 174
Hines, D. C. et al. 2006, ApJ, 638, 1070
Hopkins, P. F., Hernquist, L., Cox, T. J., Di Matteo, T., Martini, P., Robertson, B., & Springel, V. 2005, ApJ, 630, 705
Houck, J. R. et al. 2004, ApJS, 154, 18
Ivison, R. et al. 2006, ApJ, this volume
Ivison, R. J. et al. 2004, ApJS, 154, 124
Kennicutt, R. C. 1998, ARA&A, 36, 189
Le Floc'h, E. et al. 2005, ApJ, 632, 169
Lotz, J. M. et al. 2006, submitted to ApJ (astro-ph/0602088)
Marconi, A., Risaliti, G., Gilli, R., Hunt, L. K., Maiolino, R., & Salvati, M. 2004, MNRAS, 351, 169
McLure, R. J., & Dunlop, J. S. 2004, MNRAS, 352, 1390
Miyaji, T., Sarajedini, V., Griffiths, R. E., Yamada, T., Schurch, M., Cristóbal-Hornillos, D., & Motohara, K. 2004, AJ, 127, 3180
Nandra, K. et al. 2005, MNRAS, 356, 568
Page, M. J., Stevens, J. A., Mittaz, J. P. D., & Carrera, F. J. 2001, Science, 294, 2516
Rieke, G. H., Lebofsky, M. J., Thompson, R. I., Low, F. J., & Tokunaga, A. T. 1980, ApJ, 238, 24
Roussel, H., Helou, G., Beck, R., Condon, J. J., Bosma, A., Matthews, K., & Jarrett, T. H. 2003, ApJ, 593, 733
Sanders, D. B., Soifer, B. T., Elias, J. H., Neugebauer, G., & Matthews, K. 1988, ApJ, 328, L35
Sarajedini, V. L. et al. 2006, ApJS, in press (astro-ph/0605370)
Sawicki, M. 2002, AJ, 124, 3050
Silk, J. 2005, MNRAS, 364, 1337
Silva, L., Maiolino, R., & Granato, G. L. 2004, MNRAS, 355, 973
Soifer, B. T. et al. 2000, AJ, 119, 509
Spoon, H. W. W. et al. 2004, ApJS, 154, 184
Springel, V., Di Matteo, T., & Hernquist, L. 2005, MNRAS, 361, 776
Waskett, T. J. et al. 2003, MNRAS, 341, 1217
Webb, T. M. et al. 2003, ApJ, 587, 41
Wilson, G. et al. 2006, ApJ, this volume

Publications of the Astronomical Society of the Pacific, **119**: 1019–1037, 2007 September

Absolute Calibration and Characterization of the Multiband Imaging Photometer for *Spitzer*. II. 70 μm Imaging

Karl D. Gordon,[1] Charles W. Engelbracht,[1] Dario Fadda,[2] John Stansberry,[1] Stefanie Wachter,[2] Dave T. Frayer,[2] George Rieke,[1] Alberto Noriega-Crespo,[2] William B. Latter,[3] Erick Young,[1] Gerry Neugebauer,[1] Zoltan Balog,[1] Jeffrey W. Beeman,[4] Hervé Dole,[5] Eiichi Egami,[1] Eugene E. Haller,[4,6] Dean Hines,[7] Doug Kelly,[1] Francine Marleau,[2] Karl Misselt,[1] Jane Morrison,[1] Pablo Pérez-González,[1,8] Jeonghee Rho,[2] and Wm. A. Wheaton[2]

Received 2006 November 15; accepted 2007 April 16; published 2007 October 2

ABSTRACT. The absolute calibration and characterization of the Multiband Imaging Photometer for *Spitzer* (MIPS) 70 μm coarse- and fine-scale imaging modes are presented based on over 2.5 yr of observations. Accurate photometry (especially for faint sources) requires two simple processing steps beyond the standard data reduction to remove long-term detector transients. Point-spread function (PSF) fitting photometry is found to give more accurate flux densities than aperture photometry. Based on the PSF fitting photometry, the calibration factor shows no strong trend with flux density, background, spectral type, exposure time, or time since anneals. The coarse-scale calibration sample includes observations of stars with flux densities from 22 mJy to 17 Jy, on backgrounds from 4 to 26 MJy sr^{-1}, and with spectral types from B to M. The coarse-scale calibration is 702 $\pm$ 35 MJy sr^{-1} MIPS70^{-1} (5% uncertainty) and is based on measurements of 66 stars. The instrumental units of the MIPS 70 μm coarse- and fine-scale imaging modes are called MIPS70 and MIPS70F, respectively. The photometric repeatability is calculated to be 4.5% from two stars measured during every MIPS campaign and includes variations on all timescales probed. The preliminary fine-scale calibration factor is 2894 $\pm$ 294 MJy sr^{-1} MIPS70F^{-1} (10% uncertainty) based on 10 stars. The uncertainties in the coarse- and fine-scale calibration factors are dominated by the 4.5% photometric repeatability and the small sample size, respectively. The 5 σ, 500 s sensitivity of the coarse-scale observations is 6–8 mJy. This work shows that the MIPS 70 μm array produces accurate, well-calibrated photometry and validates the MIPS 70 μm operating strategy, especially the use of frequent stimulator flashes to track the changing responsivities of the Ge:Ga detectors.

1. INTRODUCTION

The Multiband Imaging Photometer for *Spitzer* (MIPS; Rieke et al. 2004) is the far-infrared imager on the *Spitzer Space Telescope* (*Spitzer*; Werner et al. 2004). MIPS images the sky in bands at 24, 70, and 160 μm. The absolute calibration of the MIPS bands is complicated by the challenging nature of removing the instrumental signatures of the MIPS detectors, as well as predicting the flux densities of calibration sources accurately at far-infrared wavelengths. This paper describes the calibration and characterization of the 70 μm band. Companion papers provide the transfer of previous absolute calibrations to the MIPS 24 μm band (G. H. Rieke et al. 2007, in preparation), the 24 μm band calibration and characterization (Engelbracht et al. 2007), and 160 μm band calibration and characterization (Stansberry et al. 2007). Engelbracht et al. (2007) also present the MIPS stellar calibrator sample that is used for this paper. The calibration factors derived in these papers represent the official MIPS calibration and are due to the combined efforts of the MIPS Instrument Team (at the University of Arizona) and the MIPS Instrument Support Team (at the *Spitzer* Science Center).

The characterization and calibration of the MIPS 70 μm band is based on stellar photospheres. The repeatability of 70 μm photometry is measured from observations of two stars, at least one of which is observed in every MIPS campaign. The absolute calibration of the 70 μm band is based on a large network of stars observed in the standard coarse-scale photometry mode with a range of predicted flux densities and backgrounds. In addition to the coarse-scale observations, a small number of stars were observed in the fine-scale photometry mode to allow

[1] Steward Observatory, University of Arizona, Tucson, AZ.
[2] *Spitzer* Science Center, California Institute of Technology, Pasadena, CA.
[3] NASA *Herschel* Science Center, California Institute of Technology, Pasadena, CA.
[4] Materials Science Division, Lawrence Berkeley National Laboratory, Berkeley, CA.
[5] Institut d'Astrophysique Spatiale (IAS), Orsay, France.
[6] Department of Materials Science and Engineering, University of California, Berkeley, Berkeley, CA.
[7] Space Science Institute, Boulder, CO.
[8] Departamento de Astrofísica, Facultad de CC. Físicas, Universidad Complutense de Madrid, Madrid, Spain.

the coarse-scale calibration to be transferred to this mode. The observations used in this paper include both in-orbit checkout (IOC; MIPS campaigns R, V, X1, and W) and regular science operations (MIPS campaigns 1–29) with a cutoff date of 2006 March 3.

The goal of the calibration is to transform measurements in instrumental units to instrument-independent physical units. The goal of the characterization is to determine whether the calibration depends on how the data are taken (e.g., exposure time, time since anneal) or characteristics of the sources being measured (e.g., flux density, background). The primary challenge for the 70 μm characterization and calibration is accurately correcting the detector transients associated with Ge:Ga detectors. The standard reduction steps are detailed in Gordon et al. (2005), but extra steps to achieve accurate photometry with the highest possible signal-to-noise ratio (S/N) for point sources are needed and discussed in this paper. Accurate calibration and high sensitivity are important at 70 μm, as they enable a number of science investigations, including the detection and study of cold disks around stars (e.g., Kim et al. 2005; Bryden et al. 2006), imaging of warm dust in galaxies (e.g., Calzetti et al. 2005; Dale et al. 2005; Gordon et al. 2006), and investigation of faint, redshifted galaxies (e.g., Dole et al. 2004a; Frayer et al. 2006a).

2. DATA

The 70 μm calibration program is based on stars with spectral types from B to M, predicted flux densities from 22 mJy to 17 Jy, and predicted backgrounds from 4 to 26 MJy sr^{-1} (Engelbracht et al. 2007). The observations were carried out in photometry mode with 3.15–10.49 s individual image exposure times and a range of total exposure times from ~50 to ~560 s. The majority of the observations were performed in standard coarse-scale photometry mode, with a few done in the standard fine-scale photometry mode. The coarse- and fine-scale photometry modes are also referred to as the wide- and narrow-field photometry modes.

The coarse-scale mode samples the 18″ FWHM 70 μm point-spread function (PSF) with 9.85″ pixels. The minimum coarse-scale photometry mode observation consists of 12 images of the target and four images where the internal calibration stimulator is flashed (see Fig. 2 of Gordon et al. 2005). The target point source is dithered around the central part of the good half of the 70 μm array so that the source is on different pixels for each of the 12 image exposures. The stimulator flashes are used to remove the responsivity variations in the Ge:Ga detectors by dividing each image exposure by an interpolated stimulator flash. This division converts the raw DN s^{-1} units to fractions of the stimulator flash amplitude (also measured in DN s^{-1} units), which are termed MIPS70 units. These MIPS70 units are surface brightness units, as the varying pixel size across the array has been normalized out due to the division by the stimulator flash. Readers should refer to Rieke et al. (2004) and Gordon et al. (2005) for the details on how MIPS data are taken and reduced. The maximum image exposure time is 10.49 s; thus, longer total exposures on a source are acquired by repeating the minimum set of images described above.

The fine-scale mode samples the same 70 μm PSF with 5.24″ pixels and is designed for detailed studies of source structure. The dithering strategy is different for fine-scale mode, in which source-background pairs of images are acquired instead of dithering the source around the array. The minimum fine-scale photometry mode observation consists of eight source-background pairs of images, four stimulator images, and two dedicated stimulator background images. The data reduction is the same as for the coarse-scale mode, and thus, the resulting raw units of the images are also fractions of the stimulator flash and are termed MIPS70F units. These units are different than the MIPS70 units due to the change in the optical train used.

The coarse-scale observations were extensive and motivated to check nonlinearities versus flux density, background, exposure time, etc. The fine-scale observations were done to transfer the coarse-scale calibration to the fine scale. The coarse-scale and scan map modes share the same optical train and only differ in the dithering strategy; thus, the coarse-scale photometry calibration should apply to the scan map mode observations.

2.1. Data Reduction

Each observation was reduced through the MIPS Data Analysis Tool (DAT, ver. 3.06, Gordon et al. 2005). The resulting mosaics of this default processing are shown in Figures 1*a* and 1*d* for two point sources observed in coarse-scale mode. It is possible to improve the detection of point sources taken in photometry mode by utilizing the redundancy of the observations to remove residual instrumental signatures. These residual signatures arise because the stimulator flashes calibrate the fast response of the detectors well, but there is a drift between the fast and slow response of the detectors (Haegel et al. 2001; Gordon et al. 2005). In coarse-scale mode, point sources are dithered around the array to ensure that their signals are in the well-calibrated fast response. The dithering does not put the background signal in the fast response, and, as the sky level is roughly equal at the different dither positions, the background is in the slow-response regime. As an accurate measurement of the background is essential for good photometry, the drifting background needs to be corrected by two additional steps. The extra steps are designed not to introduce biases into the data based on source flux density while reducing the residual instrumental signatures.

The largest portion of the drift is seen to be in common among pixels in the same column. This is not surprising, as columns represent a common strip of detector material (Young et al. 1998). The column offset can be removed easily for observations of isolated point sources by subtracting the median

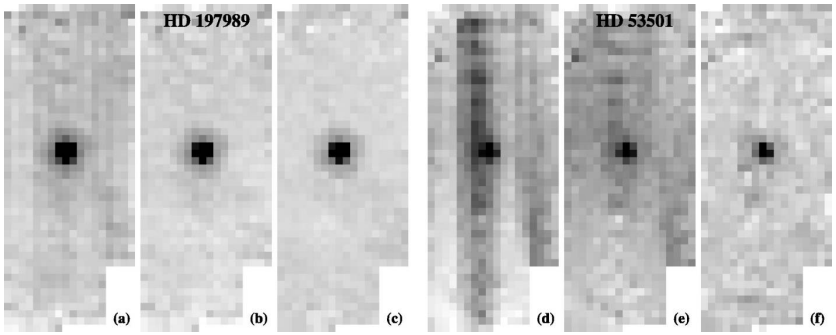

FIG. 1.—Mosaics of coarse-scale observations of two stars of different brightness shown with (*a*, *d*) default reductions, (*b*, *e*) column mean subtraction, and (*c*, *f*) column mean subtraction and time filtering. The two stars are HD 197989 (AOR key 13590784, flux density = 787 mJy) and HD 53501 (AOR key 13641984, flux density = 135 mJy). The HD 197989 images are displayed with a linear stretch that ranges (*a*) from 0.022 to 0.05, (*b*) from −0.005 to 0.025, and (*c*) from −0.005 to 0.0025. The HD 53501 images are displayed with a linear stretch that ranges (*d*) from 0.009 to 0.025, (*e*) from −0.005 to 0.01, and (*f*) from −0.002 to 0.008. The images and ranges are all given in MIPS70 units.

of the column. The median of each column is computed after excluding a region centered on the source with a diameter of 9 pixels (~89″) to ensure that the resulting correction is not biased by the source. The column-subtracted data are shown in Figures 1*b* and 1*e*. A smaller but still significant background drift seen as array-dependent structure is still present after this correction. This smaller residual instrument signature can be removed from each pixel by using a simple time filter. This time filter works by subtracting the mean value from a pixel of the previous and next 14 measurements of that pixel. To ensure that this mean value is not biased by the presence of the source itself, all measurements of the source within a spatial radius of 4.5 pixels, as well as the current, previous, and next measurements, are not used in computing the mean value. The mean is computed after excluding all the pixels >4 σ from the median (sigma clipping). The time filter only uses data taken on a particular source, which means that the time filtering is less accurate at the beginning and end of the observation set. This time filtering with constraints was optimized to minimize the background noise. The result is shown in Figures 1*c* and 1*f*. From the two examples shown in Figure 1, it is clear that the importance of these extra processing steps increases with decreasing source flux density.

Unlike coarse-scale photometry mode, in which the large field of view provides sufficient area for background estimates, the reduced field of view of the find-scale mode requires that the point source be chopped off the array. This simplifies the extra processing to just subtracting the images taken in the off positions from the on position images, which effectively removes the column offsets and smaller scale pixel-dependent drifts in the background.

2.2. Aperture Corrections

A necessary part of measuring the flux density of a point source using aperture photometry or point-spread function (PSF) fitting is an accurate PSF. The repeatability measurements on HD 163588 and HD 180711 provide the ideal opportunity to compare the STinyTim (Krist 2002) model of the MIPS 70 μm PSF to the coarse-scale observations. The repeated observations of these two stars allow for very high S/N observed PSFs to be constructed. All of the observations of these two stars taken after the final optimization of the array parameters (fifth and later MIPS campaigns) were mosaicked to produce two empirical PSFs. The fine-scale observed PSFs are from observations of the fine-scale calibration stars. The observed PSFs are compared with the STinyTim PSF for a T = 10,000 K blackbody in Figure 2. All stars in our calibration program have the same spectrum across the 70 μm band as the Rayleigh-Jeans tail of stellar spectra is being sampled. Thus, the PSF generated assuming a T = 10,000 K blackbody is a good representation of any star's PSF as long as it does not have an infrared excess.

As can be seen for both coarse and fine scales, the model PSF well represents the observed PSFs when the smoothing associated with the pixel sampling is applied. We have simu-

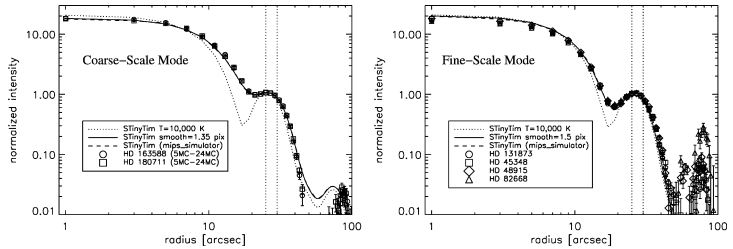

FIG. 2.—Radial profiles of the observed and model PSFs plotted for coarse-scale and fine-scale modes. The uncertainties on the observed PSFs are calculated from the standard deviation of the mean of the measurements in each measurement annulus. The PSF as predicted from STinyTim is shown, as well as two smoothed model PSFs. All the PSFs have been normalized to 1 between radii of 25″ and 30″ (between the vertical dotted lines) with the background determined from 100″–200″ for the coarse scale and 70″–100″ for the fine scale. In both plots, it is clear that the observed PSFs are well measured out to around 40″, where the PSF is about 1/1000 the brightness of the peak.

lated the pixel sampling smoothing with two different methods. The first method used uses the mips_simulator program, which produces simulated MIPS observations with the observed dithering using an input PSF. These simulated observations were mosaicked, using the same software that is used for the actual observations, to produce the mips_simulator PSF shown. The second method uses a simple boxcar smoothing function. The "smooth = 1.35 pix" and "smooth = 1.5 pix" PSFs are created by directly smoothing the STinyTim PSF with a square kernel with the specified width, where the pixel sizes are 9.85″ and 5.24″ for the coarse and fine scales, respectively. The close correspondence between the observed, mips_simulator, and directly smoothed PSFs means that accurate MIPS 70 μm PSFs can be generated from the STinyTim PSF smoothed with a simple square kernel.

The correspondence between the observed and STinyTim model PSFs was expected, as the MIPS 70 μm band should be purely diffraction limited. The 70 μm band has a bandwidth of ~19 μm, resulting in the PSF varying significantly between blue (peaking at wavelengths shorter than the band) and red (peaking at wavelengths longer than the band) sources. In addition to stellar sources, we have verified that STinyTim model PSFs describe the observed PSFs for sources with blackbody temperatures as low as 60 K using observations of asteroids and Pluto. Finally, no evidence for a blue or red leak at 70 μm was found, as the Fourier power spectra (Kirby et al. 1994) of blue (stellar) and red (ULIRG) PSFs were virtually identical. Having a valid model for the PSF allows for accurate, noiseless aperture corrections, as the total flux density is known from PSFs created with different source spectra.

The observed fine-scale PSFs do show disagreement in the core, where the model PSF is systematically higher. This is not surprising given that there are known flux density nonlinearities in the Ge:Ga detectors that are not corrected in the standard data reduction and the fine-scale calibration stars are brighter than those observed in the coarse-scale mode. Characterization of these flux density nonlinearities is ongoing, but preliminary indications are that they are ~15% for point-source flux densities of ~20 Jy observed in the coarse-scale mode (see § 3.1). The coarse-scale observed PSFs do not show any systematic disagreement in the core, consistent with the use of fainter stars.

The aperture corrections were calculated by performing aperture photometry on square kernel–smoothed model PSFs. The model PSFs were computed for a 64′ × 64′ field to ensure that the total flux of a point source was measured. The method for computing the aperture corrections is the same as used for measuring the calibration star flux densities used in this paper. The method does not account for partial pixels, but given that the model PSFs were computed with pixels 10 times smaller than the array pixel, size this is not expected to be an issue even for the smallest apertures considered in this paper. For the purposes of this paper, we use the radius = 35″ aperture (1.22 aperture correction) to minimize the sensitivity of the calibration to uncertainty in the aperture correction and centering errors. The aperture corrections for a small sample of object aperture and background annuli are given in Table 1 for three PSFs (T = 10,000, 60, and 10 K blackbodies). Three PSFs with different source spectra are given to emphasize the importance of using PSFs with the right source spectrum for accurate photometry.

2.3. Measurements

The photometry was measured with aperture photometry and PSF fitting for each observation of a calibration star. The aperture photometry was done with a circular aperture with a radius of 35″ and a sky annulus of 39″–65″. The PSF fitting was done with StarFinder (Diolaiti et al. 2000), which is ideally

TABLE 1
APERTURE CORRECTIONS

DESCRIPTION	RADIUS (arcsec)	BACKGROUND (arcsec)	PSF T = 10,000 K	PSF T = 60 K	PSF T = 10 K
Coarse Scale					
Beyond second Airy ring	100	120–140	1.10	1.10	1.13
Beyond first Airy ring	35	39–65	1.22	1.24	1.48
2 × HWHM	16	18–39	2.04	2.07	2.30
Fine Scale					
Beyond second Airy ring	100	120–140	1.10	1.10	1.13
Beyond first Airy ring	35	39–65	1.21	1.22	1.47
2 × HWHM	16	18–39	1.93	1.94	2.16

suited for the well-sampled and stable MIPS PSFs. For the very brightest sources (≥3 Jy), we progressively reduced the weight of core pixels in the PSF fitting as they increased in brightness above a threshold of 0.3 MIPS70. This produces more linear photometry for bright sources (see § 3.1), which is especially important for the 160 μm calibration (Stansberry et al. 2007). The flux densities measured with these two methods are listed in Tables 2 and 3. The aperture flux densities have had the aperture correction applied, and the PSF flux densities are naturally for an infinite aperture. In addition to the reported flux densities, S/N calculations are also reported. In the case of the aperture photometry, the S/N calculation is done using the noise in the sky annulus to determine both the uncertainty due to summing the object flux density, as well as subtracting the background. This S/N does not include the contribution from the photon noise of the source, as the gain of Ge:Ga detectors is not a well-defined quantity. In the case of the PSF photometry, the S/N calculation is done by the StarFinder program utilizing the empirical uncertainty image calculated from the repeated measurements of each point in the mosaic. Only measurements with S/N greater than 5 are reported in Tables 2 and 3. The columns in these tables give the star name, campaign of observation, AOR key (unique *Spitzer* observation identifier), exposure start time, individual exposure time, total exposure time, aperture flux density, S/N, PSF flux density, and S/N.

The measurements used in this paper were all reduced with the DAT and custom software based on the DAT results. Comparisons were done with measurements using data reduced with the *Spitzer* Science Center (SSC) pipeline and similar software available from the contributed software portion of the *Spitzer* Web site.[9] Note that the SSC pipeline reduced images are given in MJy sr^{-1} and must be divided by the applied flux conversion factor (given by the FITS header keyword FLUXCONV) to recover the instrumental MIPS70 or MIPS70F units. The result of this comparison is that the two methods produce equivalent results with a mean ratio of DAT to SSC aperture photometry for the full sample of 0.994 ± 0.037.

[9] See http://ssc.spitzer.caltech.edu/archanaly/contributed/.

2.4. Flux Density Predictions

The predicted flux densities at 70 μm were derived from the 24 μm predictions presented by Engelbracht et al. (2007) using 24/70 μm colors derived from models. For each star, the ratio of the flux densities at the effective filter wavelengths of 23.675 and 71.42 μm was computed for the appropriate Kurucz (1979)[10] model (using a power-law interpolation) and a blackbody at the effective temperature of the star. The model ratio was taken to be the average of these two values, which typically differed by 1%–2%, and the uncertainty was taken to be the difference between them. The predicted flux densities at 24 μm were divided by this ratio to compute the 70 μm flux densities. The uncertainties on the flux density predictions were calculated by adding in quadrature the uncertainties in the 24 μm flux density and in the 24/70 μm color prediction. The average predicted backgrounds for the observations were estimated from *Spitzer* Planning Observations Tool (SPOT) with the uncertainties giving the range when each target is visible. The full sample of calibration stars covers a wide range of ecliptic and Galactic latitudes, providing a large range in backgrounds, but for any particular star the backgrounds vary by <30% for different dates of observation. The flux density predictions and background estimates are listed in Tables 4 and 5. These tables also give each star's spectral type, the average of the measured aperture and PSF flux densities, and their associated S/Ns. In addition, the average calibration factor determined using the aperture and PSF fitting measurements is given (see § 3.1).

The zero point of the 70 μm band at the effective filter wavelength of 71.42 μm is 0.778 ± 0.012 Jy in the G. H. Rieke et al. (2007, in preparation) system. It is important to note that the 70 μm calibration is based on stars (10,000 K blackbody). Thus, measuring accurate 70 μm flux densities for objects with different spectral energy distributions requires the use of the color corrections given in Stansberry et al. (2007).

[10] Vizier Online Data Catalog, 6039 (R. L. Kurucz, 1993).

TABLE 2
COARSE-SCALE MEASUREMENTS

Name	Campaign[a]	AOR Key	Time[b] (s)	Exp. Time (s)	Total Time[c] (s)	Aperture Flux (MIPS70)	S/N	PSF Flux (MIPS70)	S/N
HD 002151	8MC	9806592	770,515,712	10.49	259.5	1.53E−01	20.4	1.62E−01	47.6
	10MC	10091520	773,862,336	3.15	77.7	1.52E−01	20.6	1.58E−01	42.5
	26MC	16276992	815,940,416	3.15	78.0	1.52E−01	22.9	1.52E−01	25.6
HD 002261	X1	7977216	753,515,520	3.15	78.3	7.15E−01	93.5	6.88E−01	58.3
HD 003712	11MC	11784448	775,613,056	3.15	78.1	7.11E−01	135.3	7.37E−01	70.2
HD 004128	16MC	12873216	786,539,520	3.15	78.2	6.98E−01	143.9	6.90E−01	63.6
HD 006860	12MC	11893504	777,752,832	3.15	78.5	3.04E+00	209.6	3.40E+00	96.6
HD 009053	11MC	11784960	775,614,464	3.15	78.2	8.85E−01	201.3	9.10E−01	78.0
HD 009927	11MC	11784704	776,018,752	3.15	78.3	2.93E−01	85.2	2.77E−01	49.6
	28MC	16619776	821,558,080	3.15	77.8	2.98E−01	79.8	2.94E−01	46.3
HD 012533	12MC	11893760	777,753,856	3.15	78.5	1.24E+00	189.0	1.30E+00	81.5
HD 012929	18MC	13113344	791,238,208	3.15	53.2	1.04E+00	144.7	1.08E+00	70.7
HD 015008	13MC	12064768	780,277,312	10.49	510.9	1.98E−02	9.2	1.36E−02	15.4
		12154368	780,623,616	10.49	511.0	1.82E−02	9.5	1.04E−02	10.4
		12154624	780,621,184	10.49	510.3	1.50E−02	9.4	1.31E−02	12.8
HD 018884	12MC	11894016	777,747,392	3.15	78.5	2.60E+00	268.4	2.89E+00	107.4
HD 020902	29MC	16868864	824,522,048	10.49	260.8	3.13E−01	87.3	3.02E−01	30.9
HD 024512	1MC	8358144	755,758,720	10.49	91.2	1.29E+00	175.2	1.36E+00	71.4
		8358400	755,759,040	3.15	52.6	1.47E+00	173.5	1.54E+00	74.6
	14MC	12197376	782,166,144	3.15	78.3	1.46E+00	211.6	1.52E+00	79.9
HD 025025	13MC	12063744	779,604,736	3.15	78.2	1.48E+00	223.5	1.55E+00	86.1
HD 029139	19MC	13315072	793,954,560	3.15	53.1	5.96E+00	174.9	7.87E+00	114.8
HD 031398	13MC	12064000	780,105,728	3.15	78.3	1.11E+00	176.1	1.20E+00	79.3
HD 032887	13MC	12064256	779,604,352	3.15	78.1	7.31E−01	172.4	7.25E−01	61.3
HD 034029	4MC	9059840	761,915,840	3.15	78.5	2.74E+00	331.2	2.91E+00	130.5
	13MC	12064512	780,235,008	3.15	78.5	2.69E+00	240.4	3.11E+00	108.1
HD 035666	9MC	9941248	772,043,584	10.49	510.9	2.07E−02	14.8	1.76E−02	16.8
	20MC	13478656	797,749,696	3.15	304.7	1.47E−02	7.0	1.76E−02	16.5
HD 036167	19MC	13308416	794,234,816	3.15	78.0	2.42E−01	27.5	2.34E−01	37.4
	29MC	16869120	825,753,280	10.49	259.9	2.72E−01	30.4	2.39E−01	35.8
HD 039425	R	7600896	753,649,280	3.15	78.1	3.52E−01	58.0	2.89E−01	14.7
HD 039608	12MC	11892992	777,732,992	10.49	510.8	3.09E−02	21.3	2.23E−02	24.8
	20MC	13479168	797,750,528	10.49	510.9	2.14E−02	12.4	2.02E−02	20.3
HD 042701	9MC	9941504	772,044,608	10.49	510.7	6.10E−02	43.8	3.18E−02	34.8
HD 045348	6MC	9459712	765,979,776	3.15	78.2	1.75E+00	317.7	1.84E+00	114.9
HD 048915	6MC	9458432	765,977,856	3.15	78.4	1.60E+00	246.8	1.68E+00	101.1
HD 050310	X1	7977984	753,518,784	3.15	78.0	4.13E−01	52.3	4.14E−01	41.0
		7979520	753,518,528	3.15	78.3	4.49E−01	61.7	4.28E−01	45.4
	21MC	13641472	800,741,248	3.15	78.4	4.45E−01	105.3	4.35E−01	51.9
HD 051799	R	7601152	753,649,664	3.15	71.5	4.09E−01	84.2	3.93E−01	44.0
	21MC	13641728	800,740,928	3.15	78.2	3.90E−01	113.9	3.79E−01	52.2
HD 053501	R	7601408	753,650,112	3.15	77.8	9.13E−02	13.4	8.35E−02	22.6
	X1	7977728	753,518,144	3.15	77.9	1.14E−01	15.6	1.00E−01	22.7
	21MC	13641984	800,744,576	3.15	78.2	9.84E−02	25.3	7.73E−02	31.1
HD 056855	19MC	13315328	793,945,152	3.15	53.1	1.61E+00	187.3	1.77E+00	85.3
HD 059717	15MC	12397824	784,145,600	3.15	78.3	8.89E−01	159.8	9.23E−01	76.9
HD 060522	20MC	13440768	797,687,296	3.15	52.8	4.54E−01	92.8	4.56E−01	42.1
HD 062509	15MC	12398080	784,147,584	3.15	78.6	1.56E+00	171.9	1.64E+00	93.7
HD 071129	3MC	8813312	759,211,520	3.15	78.4	3.12E+00	264.5	3.09E+00	86.7
	16MC	12873472	786,542,720	3.15	78.6	2.83E+00	201.5	3.33E+00	128.0
	28MC	16620032	821,426,816	3.15	78.5	2.75E+00	197.1	3.15E+00	120.7
	29MC	16868608	824,534,592	3.15	78.5	2.81E+00	204.9	3.03E+00	95.0
HD 080007	6MC	9459200	765,981,056	10.49	259.7	1.34E−01	38.4	1.23E−01	36.7
	19MC	13308672	794,194,496	3.15	78.1	1.42E−01	36.1	1.30E−01	37.6
HD 080493	21MC	13634304	800,483,200	3.15	78.3	1.02E+00	166.4	1.08E+00	78.6
		13642752	800,733,696	3.15	78.4	1.03E+00	195.9	1.06E+00	77.0
HD 081797	21MC	13634048	800,449,280	3.15	78.4	1.76E+00	212.0	1.86E+00	95.9
HD 082308	W	7966464	754,628,224	3.15	78.2	3.58E−01	43.2	2.68E−01	14.2
	21MC	13643264	800,736,128	3.15	78.1	3.25E−01	79.5	3.27E−01	51.0
HD 082668	7MC	9661952	768,555,648	3.15	78.1	9.61E−01	107.6	9.73E−01	61.5

TABLE 2 (*Continued*)

Name	Campaign[a]	AOR Key	Time[b] (s)	Exp. Time (s)	Total Time[c] (s)	Aperture Flux (MIPS70)	S/N	PSF Flux (MIPS70)	S/N
	10MC	10091264	773,861,824	3.15	78.1	9.13E−01	122.7	8.87E−01	58.1
HD 087901	W	7965440	754,625,728	3.15	78.0	1.05E−01	14.1	1.11E−01	28.1
	7MC	9661440	767,950,848	10.49	261.1	1.02E−01	18.8	9.98E−02	33.0
		9662720	767,992,960	3.15	78.1	1.07E−01	17.7	1.20E−01	30.4
HD 089388	20MC	13441024	797,793,856	3.15	52.9	6.04E−01	68.1	6.11E−01	49.0
HD 089484	W	7967232	754,630,208	3.15	78.3	1.08E+00	154.8	1.09E+00	61.0
	21MC	13634560	800,463,488	3.15	78.4	1.01E+00	186.8	1.05E+00	79.7
		13643008	800,736,512	3.15	78.2	1.02E+00	181.9	1.05E+00	75.8
HD 089758	W	7967488	754,630,592	3.15	77.9	1.37E+00	130.6	1.37E+00	70.8
HD 092305	19MC	13308928	794,193,536	3.15	78.0	5.01E−01	120.3	5.03E−01	62.1
	21MC	13590272	800,828,224	3.15	78.1	4.60E−01	125.1	4.69E−01	56.6
HD 093813	22MC	15247872	803,701,696	3.15	77.9	4.57E−01	53.6	4.70E−01	59.2
HD 095689	21MC	13634816	800,476,096	3.15	78.2	1.07E+00	162.4	1.10E+00	91.3
HD 096833	W	7966720	754,628,672	3.15	77.9	3.81E−01	50.2	3.62E−01	40.7
	28MC	16619008	821,403,072	3.15	78.3	3.95E−01	78.3	3.66E−01	44.1
HD 100029	X1	7980032	753,522,304	3.15	78.2	7.76E−01	87.0	7.54E−01	53.6
	20MC	13441280	797,508,096	3.15	53.2	7.75E−01	140.6	7.53E−01	55.8
HD 102647	8MC	9807616	770,512,384	10.49	260.3	4.64E−01	160.7	4.46E−01	58.9
	28MC	16618752	821,404,800	3.15	78.2	5.24E−01	82.8	4.81E−01	53.7
HD 102870	8MC	9807360	770,511,744	10.49	260.3	1.13E−01	42.7	6.79E−02	27.3
HD 108903	18MC	13112832	791,240,640	3.15	53.0	8.79E+00	184.1	1.06E+01	113.3
HD 110304	29MC	16869376	824,530,176	10.49	260.1	6.18E−02	18.7	7.07E−02	25.9
HD 120933	22MC	15248128	804,176,000	3.15	77.9	6.67E−01	151.3	6.79E−01	68.8
HD 121370	29MC	16836608	824,525,248	3.15	77.8	1.55E−01	37.1	1.57E−01	38.6
HD 123123	29MC	16869632	824,529,280	10.49	261.0	2.86E−01	88.9	2.75E−01	43.5
HD 124897	18MC	13113088	791,240,064	3.15	53.1	7.07E+00	181.4	9.16E+00	133.8
HD 131873	W	7967744	754,631,104	3.15	78.3	2.05E+00	164.3	2.09E+00	88.2
	1MC	8343040	755,588,096	3.15	78.2	1.95E+00	213.6	2.03E+00	121.3
	2MC	8381952	757,133,952	3.15	78.4	2.03E+00	207.7	2.12E+00	93.9
		8421376	757,257,280	3.15	78.4	1.92E+00	244.1	2.06E+00	116.1
	16MC	12873728	786,482,624	3.15	78.5	1.94E+00	204.6	2.11E+00	110.8
HD 136422	23MC	15421952	807,195,584	3.15	77.8	6.38E−01	115.3	6.37E−01	63.5
HD 138265	W	7965696	754,626,368	3.15	78.2	7.66E−02	12.4	7.04E−02	25.0
	5MC	9192704	763,724,672	10.49	260.3	7.90E−02	36.1	7.36E−02	36.5
HD 140573	23MC	15422208	807,195,072	3.15	78.3	5.19E−01	146.9	5.23E−01	65.4
HD 141477	24MC	15817984	809,531,968	3.15	78.2	6.81E−01	99.5	6.42E−01	65.9
HD 152222	5MC	9192960	763,699,072	10.49	259.2	2.18E−02	11.3	2.47E−02	19.5
	9MC	9941760	772,169,408	10.49	511.2	3.23E−02	20.9	2.60E−02	29.4
	20MC	13477632	797,099,968	3.15	304.4	2.00E−02	8.3	2.68E−02	21.9
HD 156283	21MC	13590528	801,046,272	3.15	78.3	6.06E−01	149.6	6.09E−01	54.7
HD 159048	17MC	13078272	789,150,272	10.49	510.6	3.05E−02	13.9	1.90E−02	19.1
HD 159330	4MC	9059584	761,921,344	10.49	258.8	3.63E−02	16.1	3.58E−02	22.2
	20MC	13477120	797,222,016	3.15	304.5	4.90E−02	22.2	4.86E−02	38.7
		13477376	797,221,056	10.49	511.3	4.44E−02	30.1	4.11E−02	33.6
	28MC	16619520	821,396,800	10.49	258.7	4.54E−02	18.8	4.14E−02	21.9
HD 163588	R	7606272	753,571,584	3.15	71.4	2.07E−01	57.3	1.99E−01	39.8
		7607040	753,689,280	3.15	78.0	2.10E−01	31.2	1.70E−01	12.0
	V	7795968	754,091,840	3.15	77.9	2.10E−01	48.4	2.08E−01	42.6
	W	7974656	754,603,392	3.15	78.1	2.18E−01	63.9	2.14E−01	49.3
	X1	7980800	753,504,640	3.15	77.8	2.27E−01	31.6	2.12E−01	36.5
		7981056	753,541,632	3.15	78.3	2.06E−01	47.5	1.99E−01	40.8
	1MC	8139008	755,320,896	3.15	78.0	2.16E−01	69.1	2.11E−01	45.2
		8140800	755,397,760	3.15	77.9	2.19E−01	79.0	2.12E−01	45.8
		8141056	755,492,288	3.15	78.1	2.27E−01	68.6	2.18E−01	51.7
		8342272	755,587,008	3.15	78.1	2.09E−01	78.5	2.05E−01	48.2
		8783360	755,756,224	3.15	78.3	2.14E−01	80.6	2.12E−01	50.9
	2MC	8381184	757,132,864	3.15	78.0	2.12E−01	28.3	2.13E−01	41.8
		8383232	757,256,256	3.15	77.9	2.15E−01	57.6	2.06E−01	46.0
	3MC	8809728	759,525,120	3.15	77.8	1.97E−01	55.7	1.92E−01	37.3
		8819456	759,825,024	3.15	77.8	2.12E−01	77.0	1.98E−01	42.2
		8937728	760,265,344	3.15	78.0	2.01E−01	34.5	2.02E−01	31.8
	4MC	9067264	761,709,120	3.15	77.9	2.09E−01	72.2	2.00E−01	42.1

TABLE 2 (*Continued*)

Name	Campaign[a]	AOR Key	Time[b] (s)	Exp. Time (s)	Total Time[c] (s)	Aperture Flux (MIPS70)	S/N	PSF Flux (MIPS70)	S/N
		9067520	762,003,968	3.15	78.1	2.03E−01	52.9	1.83E−01	16.9
		9181696	762,254,336	3.15	78.0	1.72E−01	22.9	1.73E−01	26.6
	5MC	9191168	763,690,560	3.15	78.1	2.06E−01	80.4	1.99E−01	43.1
		9221888	764,024,768	3.15	78.1	2.02E−01	73.9	1.96E−01	41.9
		9222656	764,360,512	3.15	77.9	2.10E−01	70.2	2.00E−01	42.4
	6MC	9617920	766,301,248	3.15	78.0	2.04E−01	70.7	1.98E−01	41.6
	7MC	9658624	767,919,104	3.15	77.7	2.17E−01	90.0	2.09E−01	47.0
		9659136	768,168,000	3.15	77.9	2.08E−01	64.1	2.02E−01	43.1
	8MC	9802752	770,187,072	3.15	78.2	2.10E−01	67.7	2.01E−01	41.7
		9803520	770,600,448	3.15	78.1	2.14E−01	59.7	2.12E−01	45.2
		9804288	770,843,904	3.15	77.9	2.07E−01	62.2	2.02E−01	46.8
	9MC	9937408	772,025,600	3.15	78.1	2.29E−01	76.9	2.17E−01	46.3
		9938944	772,235,776	3.15	77.8	2.21E−01	72.3	2.16E−01	48.3
		9939712	772,483,136	3.15	77.9	2.23E−01	57.4	2.16E−01	39.3
	10MC	10088192	773,705,792	3.15	77.9	2.32E−01	69.7	2.19E−01	46.6
		10088960	773,880,064	3.15	77.9	2.03E−01	59.7	2.03E−01	46.4
		10089728	774,124,928	3.15	77.9	2.32E−01	69.7	2.25E−01	44.5
	11MC	11780608	775,520,128	3.15	78.0	2.16E−01	77.6	2.18E−01	49.8
		11781376	775,821,568	3.15	77.8	2.38E−01	76.4	2.30E−01	48.7
		11782144	776,080,512	3.15	78.2	2.34E−01	90.2	2.23E−01	49.5
		11782912	776,280,384	3.15	77.5	2.39E−01	70.4	2.11E−01	34.5
	12MC	11891456	777,336,320	3.15	78.0	2.23E−01	80.0	2.18E−01	46.4
		11897344	777,592,128	3.15	77.8	2.22E−01	69.5	2.12E−01	45.0
		11898112	778,057,920	3.15	78.0	2.53E−01	74.5	2.26E−01	49.6
	13MC	12060416	779,574,272	3.15	78.1	2.17E−01	67.7	2.16E−01	47.0
		12061184	779,910,912	3.15	78.1	2.33E−01	67.7	2.23E−01	47.7
		12061952	780,221,440	3.15	78.1	2.17E−01	68.6	2.17E−01	49.8
		12153088	780,631,360	3.15	77.8	2.24E−01	65.3	2.14E−01	43.1
	14MC	12194816	782,077,056	3.15	77.9	1.99E−01	61.2	2.04E−01	44.2
		12195584	782,377,792	3.15	78.0	2.14E−01	75.5	2.13E−01	47.9
		12196352	782,680,448	3.15	77.6	2.33E−01	58.4	2.29E−01	50.1
	15MC	12394752	784,175,424	3.15	77.7	2.14E−01	67.1	2.10E−01	46.3
		12395520	783,803,456	3.15	77.9	2.07E−01	56.8	2.04E−01	43.3
		12396288	784,570,880	3.15	78.2	2.36E−01	48.3	2.13E−01	37.2
	18MC	13109504	791,681,152	3.15	77.9	2.22E−01	83.5	2.16E−01	43.5
		13110528	792,003,840	3.15	78.3	2.29E−01	77.2	2.16E−01	46.1
	19MC	13295872	793,828,736	3.15	77.9	2.11E−01	58.2	2.13E−01	43.6
		13298688	794,911,040	3.15	77.9	2.17E−01	60.5	2.13E−01	44.9
		13299712	794,452,928	3.15	78.0	2.11E−01	80.9	2.11E−01	44.8
	20MC	13429248	796,764,160	3.15	77.8	2.22E−01	74.6	2.13E−01	46.1
		13431808	797,812,480	3.15	78.1	2.22E−01	61.2	2.11E−01	41.9
		13432576	797,325,952	3.15	77.9	2.17E−01	70.4	2.10E−01	45.5
	21MC	13585664	801,062,848	3.15	77.8	2.14E−01	67.6	2.11E−01	43.4
		13586432	800,229,760	3.15	77.7	2.07E−01	77.9	2.06E−01	44.6
		13587968	801,073,984	3.15	78.2	2.23E−01	62.2	2.18E−01	46.1
	22MC	15217408	803,340,736	3.15	77.7	2.23E−01	93.3	2.15E−01	44.5
		15220736	803,958,208	3.15	77.6	2.22E−01	58.3	2.18E−01	41.5
		15221760	804,509,888	3.15	78.3	2.22E−01	68.3	2.19E−01	47.3
	23MC	15413504	806,870,208	3.15	78.1	2.28E−01	65.2	2.18E−01	45.9
		15414528	807,165,184	3.15	78.3	2.38E−01	60.5	2.12E−01	43.3
		15415552	807,541,888	3.15	77.9	2.27E−01	57.5	2.01E−01	30.6
	24MC	15815424	809,473,536	3.15	78.2	2.24E−01	65.4	2.10E−01	42.5
		15816448	809,843,584	3.15	78.1	2.21E−01	67.3	2.18E−01	45.0
		15817472	810,383,680	3.15	78.2	2.24E−01	57.1	2.05E−01	44.6
	25MC	15991296	811,962,816	3.15	78.1	2.16E−01	69.9	2.09E−01	46.2
		16047872	812,608,960	3.15	77.5	2.21E−01	60.2	2.15E−01	45.7
		16048896	813,301,568	3.15	78.0	2.10E−01	72.6	2.04E−01	43.3
	26MC	16228864	815,420,352	3.15	77.8	2.15E−01	60.3	2.12E−01	41.8
		16254464	815,882,816	3.15	77.9	2.05E−01	58.3	2.07E−01	43.7
		16255488	816,317,440	3.15	78.0	2.16E−01	57.9	2.13E−01	43.7
	27MC	16374784	817,788,288	3.15	77.5	2.02E−01	50.5	1.99E−01	40.3
		16375552	818,043,200	3.15	78.1	2.21E−01	56.7	2.16E−01	45.0

TABLE 2 (*Continued*)

Name	Campaign[a]	AOR Key	Time[b] (s)	Exp. Time (s)	Total Time[c] (s)	Aperture Flux (MIPS70)	S/N	PSF Flux (MIPS70)	S/N
	29MC	16834048	824,364,800	3.15	77.9	2.27E−01	68.5	2.13E−01	43.8
		16835072	824,955,200	3.15	78.2	2.25E−01	78.2	2.13E−01	44.1
		16836096	825,856,512	3.15	77.8	2.12E−01	68.2	2.07E−01	43.5
HD 164058	20MC	13441536	797,285,056	3.15	53.2	1.87E+00	224.3	2.11E+00	101.0
HD 166780	19MC	13314816	793,927,168	10.49	511.0	1.96E−02	7.6	1.80E−02	19.2
HD 169916	6MC	9458688	766,047,296	10.49	259.6	3.52E−01	27.7	2.90E−01	34.8
		9458944	766,047,872	3.15	78.1	3.45E−01	25.1	2.92E−01	32.5
HD 170693	W	7965184	754,625,024	3.15	77.7	8.73E−02	13.0	8.84E−02	24.7
	29MC	16869888	824,523,456	10.49	258.7	9.39E−02	18.3	9.31E−02	39.2
HD 173398	18MC	13112576	791,238,784	10.49	510.1	4.75E−02	31.9	4.32E−02	32.6
	29MC	16870144	824,524,224	10.49	259.5	3.69E−02	19.2	4.31E−02	23.5
HD 173511	17MC	12998400	789,152,320	10.49	510.1	1.50E−02	6.4	1.35E−02	12.3
HD 173976	6MC	9459456	766,034,816	10.49	260.1	2.44E−02	14.2	2.36E−02	19.6
	9MC	9942016	772,171,456	10.49	509.7	2.10E−02	10.1	2.16E−02	23.0
	17MC	12998144	789,151,360	10.49	511.3	2.10E−02	13.6	2.12E−02	24.0
	20MC	13478144	797,808,000	3.15	304.4	1.93E−02	8.3	2.20E−02	21.7
		13478400	797,808,704	10.49	511.0	1.79E−02	9.8	2.23E−02	22.8
HD 180711	W	7966208	754,627,584	3.15	77.9	2.95E−01	45.7	2.79E−01	43.4
	4MC	9068032	761,710,080	3.15	78.1	2.69E−01	68.3	2.61E−01	39.5
		9068288	762,004,928	3.15	78.0	2.70E−01	70.5	2.52E−01	30.8
		9181952	762,260,928	3.15	77.7	2.35E−01	29.3	2.39E−01	28.1
	5MC	9191424	763,691,456	3.15	78.2	2.84E−01	84.1	2.73E−01	49.5
		9222144	764,025,664	3.15	78.1	2.76E−01	98.5	2.48E−01	24.4
	8MC	9803008	770,188,032	3.15	78.4	2.68E−01	68.6	2.63E−01	46.9
		9803776	770,601,344	3.15	78.0	2.69E−01	80.1	2.67E−01	49.7
		9804544	770,844,800	3.15	78.2	2.59E−01	85.1	2.52E−01	43.6
	9MC	9937664	772,026,496	3.15	78.4	2.98E−01	95.9	2.82E−01	53.1
		9939200	772,236,672	3.15	77.7	2.72E−01	76.1	2.73E−01	48.3
		9939968	772,484,032	3.15	78.1	3.01E−01	71.7	2.90E−01	50.6
	10MC	10088448	773,706,752	3.15	77.8	2.89E−01	72.1	2.77E−01	45.2
		10089216	773,881,024	3.15	77.9	2.78E−01	85.2	2.74E−01	49.5
		10089984	774,125,888	3.15	78.1	3.03E−01	89.8	2.90E−01	49.5
	11MC	11780864	775,521,024	3.15	78.1	2.89E−01	82.2	2.80E−01	50.4
		11781632	775,822,464	3.15	78.0	2.95E−01	80.8	2.76E−01	51.5
		11782400	776,081,472	3.15	77.8	3.02E−01	84.1	2.90E−01	50.4
		11783168	776,281,344	3.15	78.3	2.80E−01	82.7	2.82E−01	51.5
	12MC	11891712	777,337,280	3.15	78.0	2.90E−01	84.9	2.70E−01	48.5
		11897600	777,593,088	3.15	77.7	2.80E−01	77.5	2.79E−01	45.6
		11898368	778,058,816	3.15	77.9	2.83E−01	63.4	2.76E−01	45.2
	13MC	12060672	779,575,168	3.15	78.1	3.13E−01	86.8	2.74E−01	38.6
		12061440	779,911,808	3.15	78.3	2.99E−01	90.1	2.91E−01	51.0
		12062208	780,222,336	3.15	78.3	3.02E−01	104.3	2.98E−01	53.2
		12153344	780,632,320	3.15	77.8	2.95E−01	82.4	2.86E−01	48.9
	14MC	12195072	782,077,952	3.15	77.9	2.78E−01	83.5	2.70E−01	49.0
		12195840	782,378,752	3.15	77.7	2.80E−01	79.2	2.79E−01	51.4
		12196608	782,681,408	3.15	78.3	3.09E−01	86.2	3.07E−01	60.3
	15MC	12395008	784,176,384	3.15	78.3	2.85E−01	77.2	2.83E−01	52.8
		12395776	783,804,352	3.15	78.0	2.76E−01	71.6	2.69E−01	47.5
		12396544	784,571,840	3.15	78.1	2.96E−01	61.9	2.85E−01	46.5
	16MC	12871680	786,141,952	3.15	78.0	2.90E−01	85.8	2.81E−01	49.0
		12884480	786,574,272	3.15	78.4	3.03E−01	90.2	2.94E−01	50.5
		12884992	786,900,864	3.15	77.9	2.81E−01	74.9	2.72E−01	47.0
	17MC	12997376	788,129,216	3.15	78.0	2.92E−01	107.2	2.82E−01	52.6
		13001728	788,494,656	3.15	78.1	2.77E−01	67.9	2.78E−01	48.0
		13072896	789,156,032	3.15	77.9	2.99E−01	82.4	2.83E−01	45.2
	18MC	13109248	790,894,272	3.15	78.2	2.75E−01	65.2	2.71E−01	46.3
		13110272	792,002,816	3.15	77.9	2.77E−01	91.4	2.70E−01	47.4
		13111296	791,342,528	3.15	77.8	2.80E−01	89.0	2.74E−01	48.8
	19MC	13295616	793,827,456	3.15	77.9	2.88E−01	99.6	2.66E−01	48.5
		13298432	794,454,208	3.15	78.3	2.86E−01	92.2	2.81E−01	51.6
		13299456	794,910,016	3.15	78.3	2.82E−01	99.2	2.78E−01	53.1
	22MC	15217664	803,341,952	3.15	77.9	2.94E−01	77.2	2.78E−01	48.3

TABLE 2 (*Continued*)

Name	Campaign[a]	AOR Key	Time[b] (s)	Exp. Time (s)	Total Time[c] (s)	Aperture Flux (MIPS70)	S/N	PSF Flux (MIPS70)	S/N
		15220992	803,956,992	3.15	77.8	2.87E−01	86.7	2.82E−01	47.4
		15222016	804,511,168	3.15	78.0	2.91E−01	76.4	2.86E−01	51.7
	23MC	15413760	806,871,168	3.15	77.2	2.75E−01	71.4	2.71E−01	46.3
		15414784	807,166,400	3.15	78.3	2.72E−01	86.6	2.66E−01	46.3
		15415808	807,540,672	3.15	78.0	2.76E−01	70.5	2.77E−01	50.4
	24MC	15815680	809,474,496	3.15	78.2	2.81E−01	81.6	2.75E−01	49.1
		15816704	809,844,544	3.15	78.3	2.85E−01	84.5	2.82E−01	49.7
		15817728	810,384,640	3.15	77.9	2.72E−01	81.0	2.71E−01	45.8
	25MC	15991552	811,963,136	3.15	78.0	2.85E−01	83.1	2.69E−01	45.0
		16048128	812,608,576	3.15	78.1	2.88E−01	83.2	2.79E−01	49.4
		16049152	813,301,952	3.15	77.6	2.75E−01	82.0	2.55E−01	47.0
	26MC	16229120	815,420,672	3.15	78.0	2.91E−01	90.5	2.76E−01	48.6
		16254720	815,883,392	3.15	77.7	2.99E−01	78.0	2.72E−01	48.7
		16255744	816,317,824	3.15	77.5	2.73E−01	75.4	2.70E−01	48.8
	27MC	16375040	817,789,248	3.15	77.6	2.86E−01	60.7	2.78E−01	43.6
		16375808	818,044,224	3.15	77.9	2.88E−01	92.1	2.82E−01	48.4
		16377344	818,481,664	3.15	77.8	3.07E−01	74.5	2.76E−01	47.6
	28MC	16603136	820,974,720	3.15	78.0	2.80E−01	85.3	2.67E−01	46.9
		16603904	821,395,200	3.15	78.0	2.93E−01	90.5	2.72E−01	48.4
		16604672	821,607,616	3.15	77.8	2.87E−01	96.1	2.77E−01	48.0
	29MC	16834304	824,363,584	3.15	77.8	2.94E−01	85.6	2.81E−01	46.3
		16835328	824,956,160	3.15	77.9	2.86E−01	91.6	2.74E−01	47.0
		16836352	825,855,040	3.15	77.8	2.82E−01	92.7	2.72E−01	48.4
HD 183439	7MC	9662208	767,993,792	3.15	78.1	3.32E−01	77.4	3.43E−01	46.3
HD 197989	21MC	13590784	801,047,296	3.15	78.0	5.02E−01	105.7	4.95E−01	52.7
HD 198542	21MC	13591040	801,047,872	3.15	78.2	5.25E−01	114.7	5.06E−01	55.2
HD 209952	R	7602176	753,650,688	10.49	259.3	8.28E−02	22.5	7.11E−02	29.8
	X1	7979008	753,516,608	3.15	77.5	9.69E−02	13.4	7.77E−02	20.4
	7MC	9661696	768,552,960	10.49	259.1	7.19E−02	30.9	7.39E−02	34.7
	21MC	13642240	800,777,728	3.15	153.4	7.70E−02	32.1	6.89E−02	39.0
HD 213310	W	7966976	754,629,376	3.15	78.1	6.72E−01	79.6	6.74E−01	54.6
	22MC	15248384	804,442,624	3.15	78.2	6.60E−01	155.1	6.78E−01	62.0
HD 216131	W	7965952	754,627,008	3.15	77.6	2.30E−01	42.2	2.21E−01	40.6
HD 217906	11MC	11784192	775,641,728	3.15	78.4	4.55E+00	235.2	5.68E+00	135.9

[a] The letter (for in-orbit checkout) or number of the MIPS campaign (MC) in which the observations were taken.
[b] The time the exposure started is the number of seconds from 1980 January 1.
[c] The total exposure time is computed as the average exposure time per pixel in the object aperture to account for exposure time lost to cosmic-ray rejection.

3. RESULTS

The first step in deriving the final calibration factor is to examine the ensemble of calibration factor measurements for stars that show significant deviations. These deviations can be the result of a star having an infrared excess, a poor flux density prediction, or a measurement corrupted by extended emission. Infrared excesses and poor flux density predictions can be seen by calculating the calibration factor for each star and identifying stars that give calibration factors that are significantly deviant from the ensemble. Stars with excesses will have measured flux densities well in excess of the predicted flux densities and, thus, will predict low calibration factors compared to nonexcess stars. Figure 3 displays the calibration factors for all the calibration stars versus predicted flux density. The calibration factors are calculated as a conversion from MIPS70 units to MJy sr^{-1}, as the basic measurement made by the 70 μm detectors is flux per pixel, which is a surface brightness (see § 3.6 for the conversion from MIPS70 units directly to flux densities assuming the default 70 μm mosaic pixel size). Measurements using both aperture photometry and PSF fitting are shown in this figure. The PSF fitting values show less scatter than the aperture photometry values and, thus, will be the basis for identifying deviant measurements. We identify two stars (HD 102647 and HD 173398) that have possible excesses from Figure 3 and no stars with poor flux density predictions. There are seven stars that have significant extended emission underlying or near the object position determined by visual inspection of the 70 μm images. During this inspection, it was seen that the observation of HD 173511 was affected by a nearby, much brighter object, and, as a result, this star was also rejected. The stars in our sample that have been rejected for any of these three reasons are listed in Table 6. If a star was rejected as part

TABLE 3
FINE-SCALE MEASUREMENTS

Name	Campaign[a]	AOR Key	Time[b] (s)	Exp. Time (s)	Total Time[c] (s)	Aperture Flux (MIPS70F)	S/N	PSF Flux (MIPS70F)	S/N
HD 045348	6MC	9456384	765,978,944	10.49	187.1	1.66E+00	139.0	1.56E+00	111.0
HD 048915	6MC	9456896	765,977,024	10.49	186.3	1.52E+00	119.2	1.47E+00	118.2
HD 071129	29MC	16863744	825,634,368	10.49	124.3	2.90E+00	208.3	2.68E+00	102.0
HD 080493	21MC	13635072	800,352,640	10.49	248.7	9.89E−01	148.9	9.03E−01	125.0
HD 082668	7MC	9653248	768,348,480	10.49	248.4	9.53E−01	67.9	8.75E−01	126.5
HD 100029	5MC	9189888	763,723,136	10.49	186.7	6.47E−01	104.2	6.20E−01	100.8
HD 108903	18MC	13113600	791,361,728	10.49	251.2	1.09E+01	282.4	9.83E+00	163.8
HD 131873	1MC	8343296	755,588,352	3.15	56.0	1.80E+00	106.0	1.76E+00	110.6
	2MC	8382208	757,134,208	3.15	55.7	1.76E+00	88.0	1.63E+00	100.7
		8422400	757,257,536	3.15	55.7	1.81E+00	92.2	1.71E+00	100.0
	5MC	9190400	763,697,536	10.49	186.9	1.76E+00	201.6	1.62E+00	93.8
HD 163588	R	7606528	753,571,776	3.15	55.8	2.29E−01	15.7	1.78E−01	31.7
		7607296	753,689,536	3.15	55.7	1.71E−01	10.1	1.67E−01	32.8
	V	7796224	754,091,456	3.15	55.3	2.21E−01	12.2	1.94E−01	34.7
	W	7974912	754,603,648	3.15	55.6	2.20E−01	13.7	2.00E−01	32.9
	1MC	8141568	755,321,152	3.15	55.5	2.25E−01	16.3	1.81E−01	38.2
		8141824	755,398,016	3.15	55.7	1.66E−01	9.7	1.99E−01	34.1
		8142080	755,492,480	3.15	55.4	2.01E−01	14.8	1.94E−01	35.3
		8342528	755,587,264	3.15	55.6	2.44E−01	15.3	1.96E−01	35.6
		8783616	755,756,480	3.15	55.6	1.67E−01	12.5	1.87E−01	45.0
	2MC	8381440	757,133,120	3.15	55.7	1.85E−01	9.0	1.65E−01	28.7
		8384256	757,256,448	3.15	55.6	2.43E−01	15.2	1.84E−01	37.1
	26MC	16276736	815,937,216	10.49	562.2	1.99E−01	43.0	1.77E−01	70.3
HD 217906	16MC	12868608	786,224,896	10.49	249.9	5.14E+00	369.8	4.70E+00	136.8

[a] The letter (for in-orbit checkout) or number of the MIPS campaign (MC) in which the observations were taken.
[b] The time the exposure started is the number of seconds from 1980 January 1.
[c] The total exposure time is computed as the average exposure time per pixel in the object aperture to account for exposure time lost to cosmic-ray rejection.

of the 24 μm analysis given in Engelbracht et al. (2007), it is not used at all in this paper.

3.1. Flux Density/Background Nonlinearities

A possible source of scatter in the calibration factor measurements is flux density nonlinearities that are a characteristic of Ge:Ga detectors. In contrast to electronic nonlinearities that depend solely on total flux density, flux density nonlinearities are due to the change in rate of flux density falling on the detectors (e.g., when a source chops onto a detector). Given that the nonlinearity is due to a change in flux density on the detector, the flux density nonlinearity could depend on background as well as source flux density. The electronic nonlinearities are small (∼2%) for the MIPS 70 μm pixels and are corrected when the data are reduced (Gordon et al. 2005). Figure 4 shows the calibration factors versus predicted flux densities and backgrounds. The calibration factors have been calculated from the average of all the measurements of each star, and the uncertainty on the average includes the flux density prediction uncertainty. The calculated calibration factors for each star are listed in Tables 4 and 5.

It is clear that flux density nonlinearities are present in the aperture photometry data but are much smaller or nonexistent in the PSF fitting photometry. A direct comparison of the aperture and PSF fitting measurements is shown in Figure 5. Starting at around ∼1 Jy, the aperture measurements begin to underestimate the PSF measurements, while below ∼200 mJy, the aperture–to–PSF fitting ratio shows a large scatter. For bright sources, the flux density nonlinearities will show up at the peak of the PSF and the PSF fitting compensates as relatively more weight is given to the wings of the PSF than in aperture photometry. For faint sources, the PSF fitting shows less scatter, since it more accurately accounts for nearby faint sources and background structure than aperture photometry. For these reasons, we use the PSF fitting measurements for the rest of this work.

The PSF fitting measurements show that the 70 μm calibration measurements are linear between 22 mJy and 17 Jy. A linear fit to these data (accounting for the uncertainties in both x- and y-values) gives

$$\text{Factor} = (691 \pm 18) + (4.0 \pm 5.9) \log [F(\nu)], \qquad (1)$$

where $F(\nu)$ is the flux density in mJy. There are five stars (HD 31398, 120933, 213310, 216131, and 217906) that are >5 σ from the mean calibration factor and are identified with square boxes in Figure 4. The large deviations of these five stars are most likely due to weak infrared excesses, as the derived calibration factor is low compared to the ensemble.

TABLE 4
Coarse-Scale Calibration Factors

Name	Spectral Type	Predicted (mJy)		Background (MJy sr^{-1})		Average Measured[a] (MIPS70)				Calibration Factor (MJy sr^{-1} MIPS70^{-1})			
		Flux	Unc.	SB	Unc	Ap. Flux	S/N	PSF Flux	S/N	Ap.	Unc.	PSF	Unc.
HD 002151	G2 IV	255.6	8.9	5.3	0.6	1.53E−01	54.2	1.59E−01	68.8	734.8	29.0	706.0	26.7
HD 002261	K0 III	1138.0	59.6	6.3	0.5	7.15E−01	49.7	6.88E−01	58.3	697.5	39.2	725.5	40.0
HD 003712	K0 IIIa	1180.0	47.6	10.9	0.8	7.11E−01	55.5	7.37E−01	70.2	727.9	32.2	702.3	30.1
HD 004128	K0 III	1205.0	40.1	10.1	1.1	6.98E−01	52.7	6.90E−01	63.6	757.5	29.0	765.7	28.2
HD 006860	M0 III	5334.0	202.2	8.5	1.3	3.04E+00	70.9	3.40E+00	96.6	768.4	31.1	687.9	27.0
HD 009053	M0 IIIa	1504.0	64.9	5.7	0.3	8.85E−01	62.2	9.10E−01	78.0	744.9	34.3	724.5	32.6
HD 009927	K3 III	472.2	15.8	8.9	1.0	2.95E−01	57.7	2.84E−01	67.8	701.6	26.4	728.4	26.6
HD 012533	K3 IIb	1985.0	67.2	8.8	1.3	1.24E+00	63.8	1.30E+00	81.5	699.5	26.1	667.9	24.1
HD 012929	K2 III	1734.0	57.8	13.7	2.7	1.04E+00	56.0	1.08E+00	70.7	731.5	27.7	706.1	25.6
HD 015008	A1/2 V	22.0	0.8	4.7	0.6	1.79E−02	26.3	1.25E−02	22.4	539.0	28.3	770.0	44.1
HD 018884	M1.5 III	4645.0	160.1	14.4	2.2	2.60E+00	79.0	2.89E+00	107.4	784.6	28.8	704.4	25.1
HD 020902	F5 I	510.7	19.2	15.2	1.4	3.13E−01	26.3	3.02E−01	30.9	714.5	38.2	741.9	36.8
HD 024512	M2 III	2421.0	94.0	6.1	0.6	1.41E+00	102.1	1.47E+00	130.3	754.7	30.2	721.2	28.6
HD 025025	M1 IIIb	2320.0	82.5	8.0	0.8	1.48E+00	67.3	1.55E+00	86.1	687.5	26.5	655.5	24.5
HD 029139	K5 III	12840.0	451.2	23.7	3.1	5.96E+00	71.2	7.87E+00	114.8	944.8	35.8	715.1	25.9
HD 031398[b]	K3 II	1560.0	65.8	26.6	2.9	1.11E+00	60.4	1.20E+00	79.3	615.5	27.9	572.1	25.2
HD 032887	K4 III	1159.0	40.5	6.1	0.8	7.31E−01	50.7	7.25E−01	61.3	695.0	27.9	700.9	27.0
HD 034029	G5 IIIe+	5095.0	201.8	19.4	1.8	2.72E+00	126.4	2.99E+00	169.4	821.0	33.2	747.8	29.9
HD 035666[b]	K3 III	26.9	1.1	6.2	0.5	1.77E−02	19.5	1.76E−02	23.5	665.3	43.1	671.7	39.0
HD 036167[b]	K5 III	417.1	26.5	17.5	1.6	2.56E−01	45.9	2.36E−01	51.7	714.5	47.9	774.1	51.3
HD 039425	K2 III	587.7	19.2	5.2	0.7	3.52E−01	14.7	2.89E−01	14.7	732.5	55.4	892.8	67.4
HD 039608	K5 III	29.7	1.2	5.0	0.5	2.66E−02	32.7	2.14E−02	32.0	488.2	24.7	608.5	31.0
HD 042701[b]	K3 III	33.8	1.0	5.1	0.6	6.10E−02	54.8	3.18E−02	34.8	242.7	8.1	465.5	18.7
HD 045348	F0 II	3085.0	67.1	5.6	0.5	1.75E+00	89.5	1.84E+00	114.9	772.2	18.9	733.5	17.2
HD 048915	A0 V	2900.0	354.5	14.8	1.0	1.60E+00	79.1	1.68E+00	101.1	793.3	97.5	757.5	92.9
HD 050310	K1 III	706.0	24.7	5.8	0.6	4.37E−01	67.4	4.26E−01	80.2	708.0	26.9	725.9	27.0
HD 051799	M1 III	593.1	20.0	5.4	0.6	3.98E−01	57.8	3.84E−01	68.2	654.2	24.8	676.7	24.9
HD 053501	K3 III	143.3	4.5	6.0	0.6	9.95E−02	43.6	8.30E−02	44.4	631.8	24.5	757.3	29.1
HD 056855	K3 Ib	2544.0	81.3	8.7	0.7	1.61E+00	63.5	1.77E+00	85.3	694.3	24.7	629.8	21.4
HD 059717	K5 III	1423.0	49.0	8.2	0.6	8.89E−01	60.7	9.23E−01	76.9	702.3	26.8	675.9	24.9
HD 060522	M0 III	746.5	25.5	15.2	3.2	4.54E−01	34.4	4.56E−01	42.1	720.5	32.3	718.0	29.8
HD 062509	K0 IIIb	2607.0	79.1	14.7	3.1	1.56E+00	73.2	1.64E+00	93.7	732.1	24.4	697.0	22.4
HD 071129	K3 III+	5153.0	168.7	7.5	0.6	2.85E+00	160.5	3.17E+00	217.8	792.9	26.4	713.1	23.6
HD 080007	A2 IV	199.9	6.1	5.6	0.6	1.38E−01	47.1	1.26E−01	52.5	635.0	23.5	695.1	24.9
HD 080493	K7 III	1686.0	60.0	10.8	1.9	1.02E+00	86.4	1.07E+00	110.0	721.6	27.0	691.1	25.4
HD 081797	K3 II–III	2887.0	101.1	9.2	1.7	1.76E+00	74.3	1.86E+00	95.9	720.1	27.0	680.8	24.9
HD 082308	K5 III	542.7	20.3	14.5	2.9	3.28E−01	44.3	3.21E−01	52.8	725.3	31.6	742.2	31.1
HD 082668	K5 III	1424.0	204.5	25.7	0.5	9.36E−01	69.9	9.29E−01	84.6	667.1	96.3	672.4	96.9
HD 087901	B7	196.0	5.6	15.3	3.3	1.04E−01	41.6	1.08E−01	52.8	824.3	30.7	793.0	27.1
HD 089388	K3 IIa	820.1	187.9	14.1	0.6	6.04E−01	39.8	6.11E−01	49.0	595.4	137.2	589.0	135.5
HD 089484	K1 IIIb	1744.0	52.1	14.1	2.7	1.03E+00	100.3	1.06E+00	125.8	741.7	23.4	721.4	22.3
HD 089758	M0 III	2192.0	78.5	8.1	1.1	1.37E+00	57.8	1.37E+00	70.8	702.8	28.0	699.4	26.9
HD 092305	M0 III	746.3	29.8	9.6	0.6	4.81E−01	68.0	4.87E−01	83.9	680.2	28.9	672.4	28.0
HD 093813	K0/K1 III	699.0	23.7	9.3	1.5	4.57E−01	47.1	4.70E−01	59.2	671.4	26.9	652.4	24.7
HD 095689	K0 Iab	1694.0	53.2	5.4	0.6	1.07E+00	72.7	1.10E+00	91.3	694.4	23.8	674.5	22.4
HD 096833	K1 III	626.2	20.1	7.0	0.7	3.89E−01	52.5	3.64E−01	60.0	706.2	26.3	753.7	27.2
HD 100029	M0 III	1124.0	38.2	4.9	0.6	7.76E−01	65.3	7.53E−01	77.4	635.5	23.7	654.2	23.8
HD 102647[b]	A3 V	141.4	4.5	13.2	2.0	4.89E−01	69.2	4.61E−01	79.6	126.8	4.4	134.5	4.6
HD 102870	F9 V	108.1	7.3	15.2	3.3	1.13E−01	37.3	6.79E−02	27.3	418.0	30.2	698.1	53.4
HD 108903	M3.5 III	17000.0	1766.0	18.4	0.8	8.79E+00	77.2	1.06E+01	113.3	848.4	88.8	705.5	73.6
HD 110304	A1 IV	119.8	3.2	7.8	0.8	6.18E−02	18.6	7.07E−02	25.9	850.7	51.1	742.8	34.8
HD 120933[b]	K5 III	834.4	30.6	6.2	0.2	6.67E−01	55.4	6.79E−01	68.8	548.5	22.4	539.0	21.3
HD 121370	G 0IV	260.9	10.2	8.3	0.7	1.55E−01	31.2	1.57E−01	38.6	740.1	37.5	730.5	34.3
HD 123123	K2 III	490.9	16.4	12.2	2.2	2.86E−01	37.1	2.75E−01	43.5	751.8	32.2	782.6	31.7
HD 124897	K1.5 III	14340.0	778.8	7.9	0.6	7.07E+00	84.6	9.16E+00	133.8	889.9	49.5	686.3	37.6
HD 131873	K4 III	3363.0	123.7	4.4	0.5	1.97E+00	185.6	2.07E+00	238.9	749.6	27.9	710.7	26.3
HD 136422	K5 III	1042.0	41.0	13.6	2.1	6.38E−01	52.2	6.37E−01	63.5	715.8	31.3	717.4	30.4
HD 138265	K5 III	111.4	3.8	4.4	0.4	7.82E−02	39.1	7.25E−02	44.2	625.0	26.6	673.8	27.5
HD 140573	K2 IIIb	883.8	28.3	9.1	1.2	5.19E−01	53.2	5.23E−01	65.4	746.9	27.7	740.5	26.3

TABLE 4 (*Continued*)

Name	Spectral Type	Predicted (mJy)		Background (MJy sr^{-1})		Average Measured[a] (MIPS70)				Calibration Factor (MJy sr^{-1} MIPS70^{-1})			
		Flux	Unc.	SB	Unc	Ap. Flux	S/N	PSF Flux	S/N	Ap.	Unc.	PSF	Unc.
HD 141477[b]	M0.5 III	921.5	32.4	7.1	0.7	6.81E−01	57.3	6.42E−01	65.9	593.5	23.3	629.5	24.1
HD 152222	K2 III	37.9	1.8	4.5	0.5	2.65E−02	34.8	2.59E−02	41.5	626.7	34.2	641.8	33.6
HD 156283	K3 Iab	940.4	30.8	5.1	0.6	6.06E−01	44.6	6.09E−01	54.7	680.9	27.0	677.2	25.4
HD 159048	K0 III	26.9	0.9	4.7	0.5	3.05E−02	25.1	1.90E−02	19.1	387.0	19.9	622.5	38.4
HD 159330	K2 III	61.7	2.0	4.6	0.4	4.44E−02	51.1	4.25E−02	59.7	608.4	22.8	635.6	23.0
HD 163588	K2 III	354.4	9.9	4.7	0.4	2.18E−01	335.0	2.11E−01	395.7	714.3	20.1	737.9	20.7
HD 164058	K5 III	3315.0	99.7	4.9	0.5	1.87E+00	73.6	2.11E+00	101.0	775.7	25.6	690.2	21.8
HD 166780[b]	K4.5 III	23.8	1.0	4.9	0.4	1.96E−02	17.1	1.80E−02	19.2	532.7	37.9	580.9	38.4
HD 169916[b]	K1 IIIb	675.8	27.5	22.3	3.3	3.49E−01	46.8	2.91E−01	47.6	849.5	39.1	1019.2	46.7
HD 170693	K1.5 III	147.7	4.4	4.8	0.5	9.19E−02	38.1	9.16E−02	46.4	705.0	28.0	706.7	25.9
HD 173398	K0 III	23.9	0.9	4.8	0.5	4.39E−02	33.4	4.32E−02	40.1	238.6	11.6	242.3	11.1
HD 173511[b]	K5 III	24.5	0.9	4.8	0.5	1.50E−02	11.2	1.35E−02	12.3	713.9	68.3	792.5	70.0
HD 173976[b]	K5 III	35.8	1.2	4.6	0.5	2.05E−02	37.9	2.20E−02	49.7	765.6	32.9	712.6	28.1
HD 180711	G9 III	447.4	11.9	4.8	0.6	2.86E−01	333.7	2.76E−01	393.8	686.6	18.3	709.8	18.9
HD 183439	M0 III	575.2	24.9	20.6	0.9	3.32E−01	36.7	3.43E−01	46.3	760.4	38.9	735.2	35.5
HD 197989	K0 III	850.9	34.3	11.2	0.8	5.02E−01	43.8	4.95E−01	52.7	743.2	34.5	753.1	33.6
HD 198542	M0 III	828.5	35.7	15.0	3.1	5.25E−01	46.9	5.06E−01	55.2	692.1	33.3	718.0	33.6
HD 209952	B7 IV	112.7	3.8	7.5	1.1	7.86E−02	57.1	7.16E−02	63.4	628.4	24.0	690.6	25.9
HD 213310[b]	M0 II+	773.3	33.9	7.5	0.5	6.66E−01	66.6	6.76E−01	82.6	509.5	23.6	501.4	22.8
HD 216131[b]	G8 II	249.9	8.4	8.9	1.0	2.30E−01	34.6	2.21E−01	40.6	476.3	21.1	495.2	20.7
HD 217906[b]	M2.5 II	7348.0	273.6	8.2	0.9	4.55E+00	89.3	5.68E+00	135.9	707.5	27.5	567.1	21.5

[a] The measured instrumental flux densities can be converted to physical units by multiplying by 1.60 Jy MIPS70^{-1}.
[b] Stars not used for the final calibration factor, as they were rejected as known outliers (§ 3) or clipped as being >5 σ from the mean (§ 3.1).

These five stars have been excluded from the fit and from the rest of the paper. The slope value is consistent with no nonlinearities; the upper limit on the nonlinearities is computed to be 1.5% from the ratio of the fit values at 10 mJy and 20 Jy. The fit to the aperture photometry shows a 42% nonlinearity between the same limits.

A similar result is found for the calibration factor versus background. The linear fit to the PSF fitting results gives a slope of 54 ± 18, which is consistent with no slope at the 3 σ level. There is a statistically significant slope for the linear fit for the aperture photometry results, but this may just be an artifact of the nonlinearity seen versus flux density. A comparison of the two left-hand plots in Figure 4 shows that the correlation is better versus flux density than versus background.

3.2. Repeatability

The photometric repeatability and trends in time can be measured from the two stars that have been observed throughout MIPS operations. The photometric repeatability is how well the raw flux of a star can be measured and is determined from multiple observations of the same star. Each measured flux

TABLE 5
Fine-Scale Calibration Factors

Name	Spectral Type	Predicted (mJy)		Background (MJy sr^{-1})		Average Measured[a] (MIPS70)				Calibration Factor (MJy sr^{-1} MIPS70^{-1})			
		Flux	Unc.	SB	Unc	Ap. Flux	S/N	PSF Flux	S/N	Ap.	Unc.	PSF	Unc.
HD 045348	F0 II	3085.0	67.1	5.6	0.5	1.66E+00	97.6	1.56E+00	111.0	2881.5	69.3	3066.1	72.2
HD 048915	A0 V	2900.0	354.5	14.8	1.0	1.52E+00	100.6	1.47E+00	118.2	2959.1	362.9	3048.6	373.6
HD 071129	K3 III+	5153.0	168.7	7.5	0.6	2.90E+00	91.3	2.68E+00	102.0	2752.9	95.0	2980.0	101.8
HD 080493	K7 III	1686.0	60.0	10.8	1.9	9.89E−01	113.1	9.03E−01	125.0	2642.6	96.9	2892.3	105.5
HD 082668	K5 III	1424.0	204.5	25.7	0.5	9.53E−01	113.8	8.75E−01	126.5	2316.5	333.3	2522.1	362.8
HD 100029	M0 III	1124.0	38.2	4.9	0.6	6.47E−01	87.0	6.20E−01	100.8	2691.4	96.7	2809.9	99.6
HD 108903	M3.5 III	17000.0	1766.0	18.4	0.8	1.09E+01	150.5	9.83E+00	163.8	2410.5	250.9	2679.5	278.8
HD 131873	K4 III	3363.0	123.7	4.4	0.5	1.78E+00	177.5	1.68E+00	202.8	2925.0	108.8	3098.2	115.0
HD 163588	K2 III	354.4	9.9	4.7	0.4	2.03E−01	125.3	1.83E−01	136.4	2700.1	78.5	3002.0	86.7
HD 217906	M2.5 II	7348.0	273.6	8.2	0.9	5.14E+00	123.5	4.70E+00	136.8	2215.1	84.4	2420.0	91.8

[a] The measured instrumental flux densities can be converted to physical units by multiplying by 1.87 Jy MIPS70^{-1}.

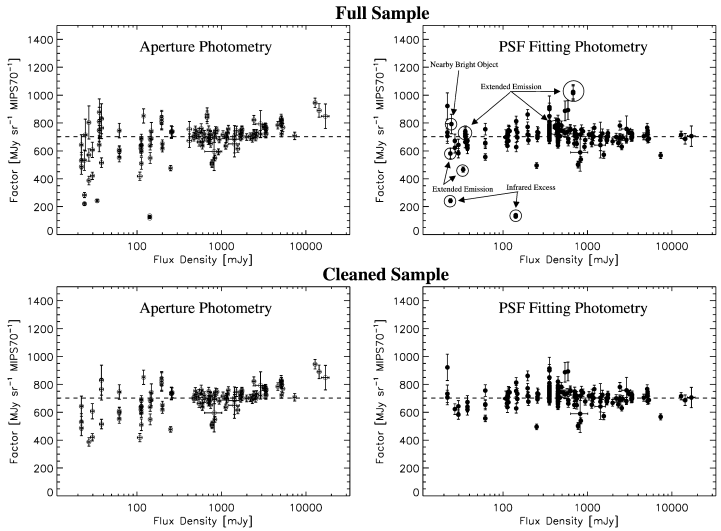

FIG. 3.—Calibration factor for all the stars with positive flux densities (except for the two repeatability stars) vs. predicted flux density. Each point gives the calibration factor for a single measurement, and thus, a star can have multiple points. The uncertainties on each point include the measurement (y) and flux density prediction (x and y) uncertainties. The dashed line is drawn at the final calibration factor. The cleaned sample is the same as the full sample after the observations that have been rejected are removed. The reasons for rejecting a point are annotated in the upper right panel and discussed in § 3.

density from PSF fitting photometry was normalized to the average flux density of each star and plotted in Figure 6. The sigma-clipped average in 15 bins between 50 and 950 days since launch is also plotted. The dotted vertical lines identify changes in the default dither pattern, bias voltage, and instrument software. This plot clearly shows that the 70 μm array displays measurable long-term variations. The measurements show that the response dropped from the starting value by ~7% around day 200 and then recovered to slightly above the starting value around day 300. After this, the response seems to have stabilized, with evidence for a weak trend downward. While it is tempting to identify the initial variations with the changes in how the data were taken, no clear instrumental parameter has been identified that would cause these variations. Initial testing with other methods of measuring the brightness of these two stars has shown similar but not identical variations. More work is clearly needed to understand the origin of the initial variations.

TABLE 6
REJECTED STARS

Name	Reason
HD 36167	Extended emission
HD 35666	Extended emission
HD 42701	Extended emission
HD 141477	Extended emission
HD 166780	Extended emission
HD 169916	Extended emission
HD 173398	Possible infrared excess
HD 173511	Nearby, bright object
HD 173976	Extended emission

Even given the initial variations, the repeatability of the two stars is quite good. The repeatabilities for all the measurements are 4.5% for HD 163588 and 3.7% for HD 180711. For reference, the repeatabilities for aperture photometry using the same data are 4.9% for HD 163588 and 3.9% for HD 180711. Given the changes in the operating parameters of the 70 μm array early in the mission, we also computed the repeatabilities using only the data taken after the last change. The repeatabilities for all the measurements after the eighth MIPS campaign are 2.9% for HD 163588 and 2.7% for HD 180711. For reference, the repeatabilities for aperture photometry using the same data are 4.3% for HD 163588 and 3.4% for HD 180711. The combined measurements imply a conservative repeatability of the MIPS 70 μm array of ~4.5%.

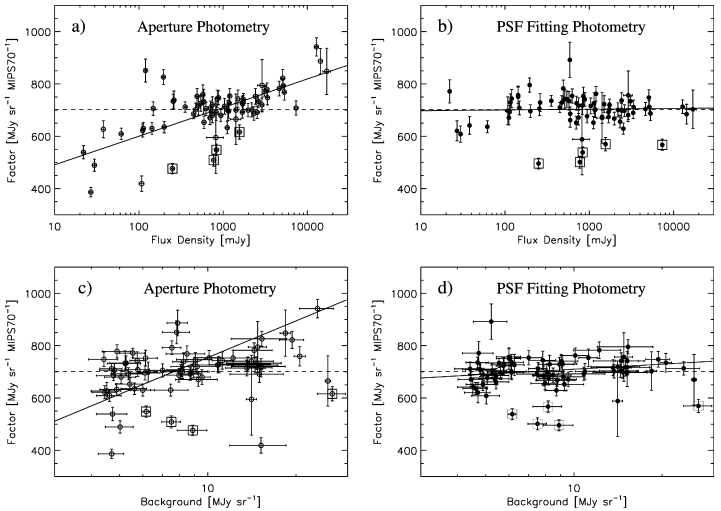

FIG. 4.—Average calibration factor for each star vs. predicted flux density (*a*, *b*) and background (*c*, *d*). The dashed line is drawn at the final calibration factor. The solid line gives the linear fit to all the data except for the five stars with boxes. These stars were rejected from the fit, as they are >5 σ from the mean.

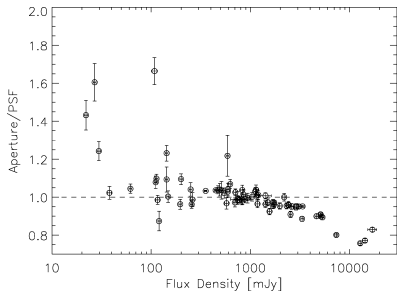

FIG. 5.—Ratio of the aperture to PSF fitting measurements vs. predicted flux density. Each star is represented by a single point, with multiple measurements of a star being averaged before the ratio is computed.

3.3. Time since Anneal

The MIPS 70 μm array is annealed by raising the temperature by a few degrees to remove cosmic-ray damage. This was done every 6 hr until MIPS campaign 20 and every 3–4 hr since then. Residual instrumental signatures are seen to grow with time since anneal, and this change was made to minimize them. In addition to removing cosmic-ray damage, the responsivity of the array is reset (Rieke et al. 2004). The calibration factor should not have a dependence on time since anneal, as all 70 μm measurements are referenced to the internal simulator measurements taken every 2 minutes or less. To check this, Figure 7 shows the calibration factor versus anneal time. No trend is seen.

3.4. Other Checks

The accuracy of the flux density predictions can be checked by comparing the calibration factor derived for stars of different spectral types. The stars in the sample can be divided into three categories: hot stars (B and A dwarfs), solar analogs (early G dwarfs), and cool stars (K and M giants). The weighted average calibration factors (after sigma clipping) for these three categories are 717 ± 8, 717 ± 3, and 701 ± 6 MJy sr^{-1} MIPS70^{-1},

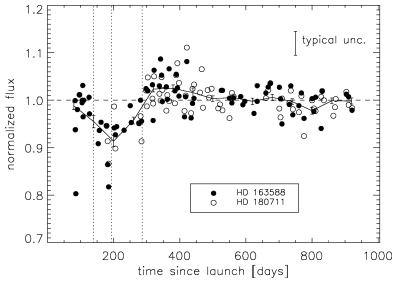

FIG. 6.—Normalized flux densities for the two repeatability stars, HD 163588 and HD 180711, vs. time. The solid line gives the sigma-clipped average in 15 equally spaced bins. The dashed line is drawn at 1. The typical uncertainty of a single measurement is shown in the upper right. The first vertical line indicates the transition between dither patterns (between second and third MIPS campaigns). The second vertical line indicates the transition between array bias voltage values (between fourth and fifth MIPS campaigns). The third vertical line indicates the update to the instrument software (between the eighth and ninth MIPS campaigns).

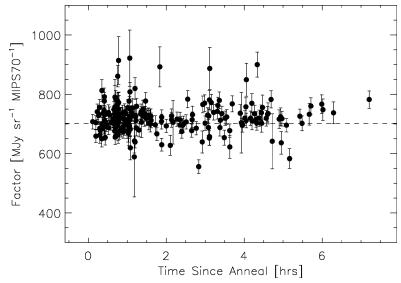

FIG. 7.—Calibration factor vs. time since anneal for all the measurements. The dashed line is drawn at the final calibration factor.

where the number of measurements contributing to each class are 11, 6, and 58, respectively. None of the averages are significantly different from each other, especially when the small number of measurements contributing to the hot stars and solar analogs is taken into account.

The dependence on exposure time was checked by computing the weighted average calibration factor separately for observations taken with 3.15 and 10.49 s exposures. The resulting calibration factors are 701 ± 6 and 723 ± 7 MJy sr^{-1} MIPS70^{-1} with 62 and 12 measurements contributing to the averages, respectively. As the difference is only 2.4 σ, no significant systematic change with exposure time is seen.

3.5. Noise Characteristics

The behavior of the noise is plotted versus predicted flux density in Figure 8 for the PSF fitting measurements. To compare measurements taken at different exposure times, each noise measurement has been transformed to the equivalent noise in 500 s assuming a $t^{0.5}$ dependence. The noise behavior can be characterized by

$$\sigma(500\ \mathrm{s})^2 = 0.90^2 + [0.20F(\nu)^{0.5}]^2 + [0.0022F(\nu)]^2, \quad (2)$$

where $F(\nu)$ is the predicted 70 μm flux density in mJy. The first term accounts for the confusion noise, the second term the photon noise, and the third term the noise due to the division by the interpolated stimulator flash.

The sensitivity of the MIPS 70 μm band in 500 s can be determined from this fit by computing where the flux is 5 times the uncertainty from equation (2). The 5 σ, 500 s sensitivity computed in this fashion is ~5 mJy. This measurement is based on an extrapolation of over a factor of 10 from the lowest measured point and so is fairly uncertain. The sensitivity can be better measured from deep cosmological surveys. The Extragalactic First Look Survey gives a 5 σ, 500 s sensitivity of ~6 mJy after correcting for the updated calibration factor (Frayer et al. 2006a). Somewhat worse sensitivities up to ~8 mJy are seen for other deep MIPS 70 μm cosmological fields (D. Frayer 2006, private communication; C. Papovich 2006, private communication). This sensitivity can include a contribution from confusion, but this is likely to be small, since

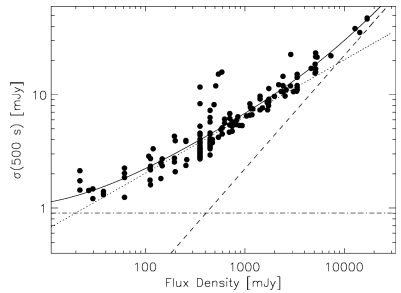

FIG. 8.—Noise vs. predicted flux density for the PSF fitting measurements. Each noise measurement has been converted to the equivalent noise in 500 s assuming that the noise scales as time$^{0.5}$. The solid line gives the fit to the data that is discussed in § 3.5. The dot-dashed line gives the constant term from the fit, the dotted line the term proportional to $F(\nu)^{0.5}$, and the dashed line the term proportional to $F(\nu)$.

the 5 σ confusion noise for MIPS 70 μm coarse-scale observations is estimated at ~1.5–3 mJy (Dole et al. 2004b; Frayer et al. 2006b). Combining the results from the calibration stars and deep cosmological field gives a conservative 5 σ, 500 s sensitivity of 6–8 mJy.

3.6. Coarse-Scale Calibration

The final coarse-scale calibration is based on the PSF fitting results from all the observations (Fig. 4*b*). The final calibration factor of 702 ± 35 MJy sr^{-1} MIPS70^{-1} was determined by performing a weighted average of the calibration factors measured for each star. There are 66 calibration stars that contribute to this calibration factor. The calibration accuracy is dominated by the 4.5% repeatability uncertainty but also includes contributions from the uncertainty of the mean (very small) and the 2% systematic uncertainty in the 24/70 μm flux density ratios. The conversion directly to flux densities from MIPS70 units implied by the measured calibration factor is 1.60 ± 0.08 Jy MIPS70^{-1} given that the instrumental flux densities were measured on mosaics with 9.85″ × 9.85″ pixels. The calibration factor determined from the 57 stars taken after the ninth MIPS campaign is 696 ± 34 MJy sr^{-1} MIPS70^{-1}. This shows that the calibration factor is not significantly changed by the variations in the repeatability stars seen prior to the ninth MIPS campaign. The calibration factor determined from the aperture measurements is 704 ± 35 MJy sr^{-1} MIPS70^{-1}, where only measurements from 0.3 to 1 Jy are used (see Figs. 4 and 5). This shows that the calibrations derived from aperture and PSF fitting measurements are equivalent in the restricted range where the aperture photometry produces accurate results.

An independent analysis of the 70 μm measurements of asteroids (Stansberry et al. 2007) with flux densities ≤2 Jy was performed using the standard thermal (STM) and thermophysical (TPM) models fit to the *Infrared Astronomical Satellite* (*IRAS*) and *Infrared Space Observatory* (*ISO*) measurements (T. Muller 2007, private communication). While STM predictions agree within 1% on average with the observations, the TPM predictions are 9% higher on average than the observations. The source and significance of the TPM offset are the subject of further investigation. Nevertheless, the asteroid results confirm the agreement between MIPS, *IRAS*, and *ISO* calibrations within the absolute flux uncertainties. In addition, this indicates that there are no significant differences in the MIPS 70 μm calibration between stars and red sources.

The preliminary calibration factor determined soon after launch was 634 ± 127 MJy sr^{-1} MIPS70^{-1}. The new value is 11% larger than this preliminary value, well within the 20% uncertainty in the preliminary value. This 11% change is not unexpected given that the preliminary value was based on a handful of measurements of a single star and the data reduction at the time did not include the extra steps to correct residual instrumental signatures. Existing data can be corrected to the new calibration factor by multiplying by the ratio of the new to old calibration factors. Note that the calibration factor applied to data reduced using the SSC pipeline is given by the FITS header keyword FLUXCONV.

The coarse-scale calibration factor is determined from photometry mode observations but should apply directly to scan map mode observations, as both modes share the same optical train and only differ in the dithering strategy. The relative response between the scan map and coarse-scale photometry mode has been checked by observing the same source in both modes. It was found that the same flux density was measured within the uncertainties.

The consistency of the 70 μm calibration with the 24 μm calibration was checked using stars that were observed at both 24 and 70 μm. There are 36 such measurements for stars with 24 μm flux densities below 4 Jy (24 μm saturation limit). The resulting sigma-clipped average of the ratio of the observed to model 24/70 color ratio is 1.002 ± 0.013, showing that the 24 and 70 μm calibrations are consistent.

3.7. Extended versus Point-Source Calibration Check

The calibration factor determined above was calculated from observations and predictions of point sources. Given the complex response of Ge:Ga detectors to sources with different spatial extents, it is important to verify that the point-source calibration applies to extended sources. This can be checked by comparing the total fluxes of resolved galaxies measured at 70 μm to those predicted by *IRAS* (Beichman et al. 1988) measurements at 60 and 100 μm. Galaxies provide good objects for such a check, as they are discrete extended sources that were well measured by *IRAS* and have a significant component of their flux that is resolved by MIPS at 70 μm.

The galaxy fluxes are compared using the 75 *Spitzer* Infrared Nearby Galaxies Survey (SINGS; Kennicutt et al. 2003) galaxies from global measurements given by Dale et al. (2005) and updated by Dale et al. (2007). This sample is supplemented at the highest flux densities with global measurements of M31 (Gordon et al. 2006), M33 (Hinz et al. 2004), M101 (K. D. Gordon et al. 2007, in preparation), and the Large Magellanic Cloud (LMC; Meixner et al. 2006). The predictions of the 70 μm flux densities from the *IRAS* 60 and 100 μm measurements were done by first color correcting the *IRAS* measurements using the measured 60/100 flux density ratio to pick the appropriate power-law color correction (Beichman et al. 1988) and then interpolating to the effective wavelength of the MIPS 70 μm band of 71.42 μm. The average color corrections were 1.0 for both *IRAS* 60 and 100 bands. The MIPS 70 μm measurements were corrected to the updated calibration factor and color corrected using the correction for the same power law determined for the *IRAS* measurements (Stansberry et al. 2007). The average MIPS 70 μm color correction was 0.93. Figure 9 gives the ratio of the MIPS to predicted *IRAS* 70 μm flux densities for all the galaxies with flux densities above 1 Jy. The weighted average of this ratio is 0.99, which is well within

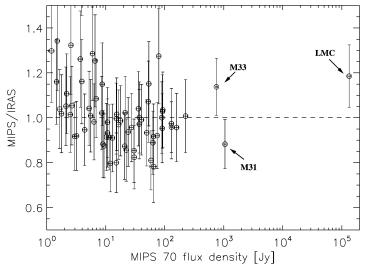

FIG. 9.—Ratio of MIPS 70 μm measured flux density to the 70 μm flux density predicted from *IRAS* 60 and 100 μm measurements shown as a check of the extended source calibration. The sample shown is comprised of the 75 SINGS galaxies supplemented by the LMC, M31, M33, and M101. The uncertainties are computed from the uncertainties in the *IRAS* and MIPS measurements. The dashed line is drawn at a value of 1.

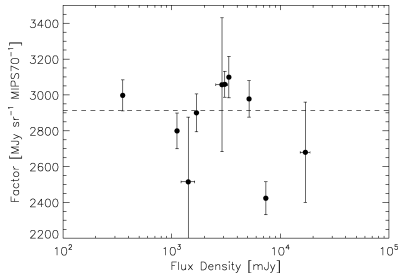

FIG. 10.—Fine-scale calibration factor vs. predicted flux density. The multiple measurements of each star have been averaged, and the plotted uncertainty includes the flux density prediction uncertainty. The final calibration factor is shown as a dashed line.

the uncertainties on the absolute calibration of MIPS 70 μm (5%) and *IRAS* 60 μm (5%; Beichman et al. 1988). This shows that the MIPS 70 μm point-source calibration applies for extended sources. This comparison also serves as another check that the photometry and scan observing modes share the same calibration even though the calibration factor is derived from photometry mode observations while the galaxies were observed with the scan map mode.

3.8. Fine-Scale Calibration

The fine-scale calibration should be similar to the coarse-scale calibration modulo the different pixel scales (5.24″ pixel^{-1} instead of 9.85″ pixel^{-1}) and optical trains. Figure 10 shows the calibration factor for PSF fitting photometry. The fine-scale calibration factor determined from these data is 2894 $\pm$ 294 MJy sr^{-1} MIPS70F^{-1}. The conversion directly to flux densities from MIPS70F units implied by this calibration factor is 1.87 $\pm$ 0.188 Jy MIPS70^{-1} given that the instrumental flux densities were measured on mosaics with 5.24″ $\times$ 5.24″ pixels. The fine-scale calibration factor is 4.12 times the coarse-scale factor. This is larger than the ratio of pixel areas (3.53), implying that the different optical train has a significant effect on the calibration. Only 10 calibration stars are used for the fine-scale calibration, and, as a result, the fine-scale calibration must be taken as preliminary. The uncertainty on the fine-scale calibration is formally only 5%, but we have doubled this to account for the small sample used. In general, the fine-scale mode should be used for probing structure and the coarse-scale used when accurate photometry is needed.

3.9. Comparison to Previous Missions

The repeatability, absolute calibration accuracy, and sensitivity of the coarse-scale MIPS 70 μm band can be compared to those of previous missions. Imaging of point sources in bands similar to the MIPS 70 μm band has been provided in the past by the *IRAS* and *ISO* (Kessler et al. 1996).

IRAS 60 μm photometry of point sources has a repeatability of 11% and an absolute calibration uncertainty of 5% (Beichman et al. 1988). The *IRAS* Faint Source Catalog (Moshir et al. 1992) is 94% complete at 0.2 Jy. The almost full sky coverage of *IRAS* allows for a comparison of the *IRAS* 60 μm and MIPS 70 μm fluxes. There are 30 stars with both MIPS 70 μm and *IRAS* 60 μm Faint Source Catalog measurements (Moshir et al. 1990) and *IRAS* 60 μm fluxes above 0.6 Jy. The average ratio of the *IRAS* 60 μm to MIPS 70 μm flux densities is 1.35 $\pm$ 0.01, and the expected ratio from a Rayleigh-Jeans model is 1.42. Thus, the *IRAS* 60 μm flux densities need to be multiplied by 1.05 in order to put them on the G. H. Rieke et al. (2007, in preparation) system.

The ISOPHOT instrument (Laureijs et al. 2003) included a 70 μm band with the P3 detector and a 60 μm band with the C100 detector. The P3 reproducibility was 10%–20% and absolute accuracy was 7%. The C100 repeatability was 3%–20% and absolute accuracy was 15%–25% (Klaas et al. 2003). The sensitivity of ISOPHOT in these bands is approximately 7.5–20 mJy 1 σ in 256 s (Laureijs et al. 2003), which corresponded to a 5 σ, 500 s sensitivity of 30–70 mJy. This sensitivity is better than that found from the 95 μm deep-field observations of Rodighiero et al. (2003), where the 3 σ, 5184 s sensitivity is 16 mJy, which corresponds to a 5 σ, 500 s sensitivity of 86 mJy.

The MIPS 70 μm observations compare favorably, with better repeatability (4.5%), as good or better absolute calibration uncertainty (5%), and higher sensitivity (6–8 mJy 5 σ, 500 s) than previous missions imaging in similar bands. This is to be expected, as the MIPS 70 μm detector operation has benefited from lessons learned from past missions.

4. SUMMARY

The calibration of the MIPS 70 μm coarse- and fine-scale imaging modes was determined from many observations taken over the first 2.5 yr of the *Spitzer* mission.

1. The characterization and calibration of the MIPS 70 μm coarse-scale mode was determined from measurements of 78 stars of spectral types B–M, with flux densities from 22 mJy to 17 Jy, and on backgrounds of 4–26 MJy sr^{-1}. The coarse-scale calibration factor is 702 $\pm$ 35 MJy sr^{-1} MIPS70^{-1} and was determined from measurements of 66 stars. A handful of stars were rejected due to possible infrared excesses, contamination from nearby extended emission, and nearby very bright sources.

2. Accurate photometry of point sources in coarse-scale mode requires two simple processing steps beyond the standard data reduction to remove long-term detector transients.

3. PSF fitting photometry is seen to produce better measurements than aperture photometry due to better handling of nearby stars and background structure and less weighting of the PSF core where flux nonlinearities have a larger effect.

4. Using PSF fitting photometry, no significant trends in calibration factor versus predicted flux density, predicted background, exposure time, spectral type, and time since anneal were found.

5. The photometric repeatability is 4.5% measured from two stars observed during every campaign and includes variations on all timescales probed.

6. The 5 σ, 500 s sensitivity of coarse-scale observations is 6–8 mJy and was determined from the calibration stars and deep cosmological surveys.

7. The applicability of the coarse-scale calibration factor, derived from point-source observations, to extended sources was confirmed using a sample of galaxies observed with MIPS and *IRAS*.

8. The preliminary fine-scale calibration factor is 2894 $\pm$ 294 MJy sr^{-1} MIPS70F^{-1} and was determined from measurements of 10 stars with flux densities from 350 mJy to 17 Jy.

We thank the anonymous referee for comments that improved the paper. This work is based on observations made with the *Spitzer Space Telescope*, which is operated by the Jet Propulsion Laboratory, California Institute of Technology, under NASA contract 1407. Support for this work was provided by NASA through contract 1255094 issued by JPL/Caltech.

REFERENCES

Beichman, C. A., Neugebauer, G., Habing, H. J., Clegg, P. E., & Chester, T. J. 1988, *Infrared Astronomical Satellite* (*IRAS*) Catalogs and Atlases, Vol. 1, Explanatory Supplement (Washington, DC: GPO)
Bryden, G., et al. 2006, ApJ, 636, 1098
Calzetti, D., et al. 2005, ApJ, 633, 871
Dale, D. A., et al. 2005, ApJ, 633, 857
———. 2007, ApJ, 655, 863
Diolaiti, E., et al. 2000, A&AS, 147, 335
Dole, H., et al. 2004a, ApJS, 154, 87
———. 2004b, ApJS, 154, 93
Engelbracht, C. W., et al. 2007, PASP, 119, 994
Frayer, D. T., et al. 2006a, AJ, 131, 250
———. 2006b, ApJ, 647, L9
Gordon, K. D., et al. 2005, PASP, 117, 503
———. 2006, ApJ, 638, L87
Haegel, N. M., et al. 2001, Appl. Opt., 40, 5748
Hinz, J. L., et al. 2004, ApJS, 154, 259
Kennicutt, R. C., Jr., et al. 2003, PASP, 115, 928
Kessler, M. F., et al. 1996, A&A, 315, L27
Kim, J. S., et al. 2005, ApJ, 632, 659
Kirby, D. J., Rieke, G. H., & Lebofsky, L. A. 1994, AJ, 107, 2226
Klaas, U., et al. 2003, in The Calibration Legacy of the *ISO* Mission, ed. L. Metcalfe et al. (ESA SP-481; Noordwijk: ESA), 19
Krist, J. 2002, Tiny Tim/*SIRTF* User's Guide (Pasadena: SSC)
Kurucz, R. L. 1979, ApJS, 40, 1
Laureijs, R. J., Klaas, U., Richards, P. J., Schulz, B., & Abraham, P. 2003, The *ISO* Handbook, Vol. IV, PHT—The Imaging Photo-Polarimeter (ESA SP-1262; Noordwijk: ESA)
Meixner, M., et al. 2006, AJ, 132, 2268
Moshir, M., Kopman, G., & Conrow, T. A. O. 1992, *IRAS* Faint Source Survey, Explanatory Supplement, version 2 (Pasadena: IPAC)
Moshir, M., et al. 1990, *IRAS* Faint Source Catalogue, version 2.0 (Greenbelt: NASA)
Rieke, G. H., et al. 2004, ApJS, 154, 25
Rodighiero, G., et al. 2003, MNRAS, 343, 1155
Stansberry, J., et al. 2007, PASP, 119, 1038
Werner, M. W., et al. 2004, ApJS, 154, 1
Young, E. T., et al. 1998, Proc. SPIE, 3354, 57

Accepted by ApJ - May 30, 2007
Preprint typeset using LaTeX style emulateapj v. 08/22/09

INFRARED SPECTRAL ENERGY DISTRIBUTIONS OF $Z \sim 0.7$ STAR-FORMING GALAXIES

Xian Zhong Zheng[1,2], Hervé Dole[3], Eric F. Bell[1], Emeric Le Floc'h[4], George H. Rieke[5], Hans-Walter Rix[1] and David Schiminovich[6]

Accepted by ApJ - May 30, 2007

ABSTRACT

We analyze the infrared (IR) spectral energy distributions (SEDs) for $10\mu\mathrm{m} < \lambda_{\rm rest} < 100\mu\mathrm{m}$ for ~ 600 galaxies at $z \sim 0.7$ in the extended Chandra Deep Field South by stacking their *Spitzer* 24, 70 and 160 μm images. We place interesting constraints on the average IR SED *shape* in two bins: the brightest 25% of $z \sim 0.7$ galaxies detected at 24 μm, and the remaining 75% of individually-detected galaxies. Galaxies without individual detections at 24 μm were not well-detected at 70 μm and 160 μm even through stacking. We find that the average IR SEDs of $z \sim 0.7$ star-forming galaxies fall within the diversity of $z \sim 0$ templates. While dust obscuration $L_{\rm IR}/L_{\rm UV}$ seems to be only a function of star formation rate (SFR; $\sim L_{\rm IR} + L_{\rm UV}$), not of redshift, the dust temperature of star-forming galaxies (with SFR $\sim 10\,\mathrm{M_\odot\,yr^{-1}}$) at a given IR luminosity was lower at $z \sim 0.7$ than today. We suggest an interpretation of this phenomenology in terms of dust geometry: intensely star-forming galaxies at $z \sim 0$ are typically interacting, and host dense centrally-concentrated bursts of star formation and warm dust temperatures. At $z \sim 0.7$, the bulk of intensely star-forming galaxies are relatively undisturbed spirals and irregulars, and we postulate that they have large amounts of widespread lower-density star formation, yielding lower dust temperatures for a given IR luminosity. We recommend what IR SEDs are most suitable for modeling intermediate redshift galaxies with different SFRs.

Subject headings: galaxies: evolution — galaxies: starburst — infrared: galaxies

1. INTRODUCTION

Dusty, intensely star-forming galaxies (SFR$> 10\,M_\odot\,\mathrm{yr^{-1}}$) are the dominant contributors to the $z \geq 0.5$ cosmic SFR density (e.g., Flores et al. 1999; Elbaz et al. 2002; Pozzi et al. 2004; Le Floc'h et al. 2005). The thermal dust emission from these galaxies accounts for much of the cosmic IR background, which contains half of the radiation energy of the extragalactic background light (Hauser & Dwek 2001; Lagache et al. 2005; Dole et al. 2006). Therefore understanding the IR SEDs of the dusty star-forming galaxies is essential for mapping the evolution of star formation as a function of cosmic time, and is a key observational ingredient of our understanding of galaxy evolution.

Detailed studies of the IR SEDs over the full range of 3-1000 μm have only been carried out for nearby galaxies (e.g., Dale et al. 2005), finding that the IR SED shape is correlated with dust temperature (Soifer & Neugebauer 1991; Dale & Helou 2002; Chapman et al. 2003; Lagache et al. 2003). Interestingly, despite this diversity of SED shapes, local galaxies' mid-IR (10-30 μm) luminosities are tightly correlated with their total IR luminosities with a scatter of ~ 0.3 dex (Chary & Elbaz 2001; Papovich & Bell 2002; Takeuchi et al. 2005b; Dale et al. 2005).

This *local* observation has often been used as a key assumption in studies exploiting deep mid-IR imaging from the *Infrared Space Observatory* at 15 μm and the *Spitzer Space Telescope* at 24 μm (e.g., Flores et al. 1999, 2004; Zheng et al. 2004; Hammer et al. 2005; Bell et al. 2005; Melbourne et al. 2005). Such studies have found significantly enhanced star formation at $0.5 \lesssim z \lesssim 1$, compared to the present day. Yet, this conclusion rests critically on the extent to which mid-IR luminosities reflect the total IR luminosity. Unfortunately, only a small fraction of mid-IR detected sources can be individually detected in the far-IR bands (e.g., *Spitzer* 70 & 160 μm), owing to limited signal-to-noise ratio (S/N) and source confusion (Dole et al. 2004b; Frayer et al. 2006). Thus, testing of this key assumption remains limited to the brightest sources (e.g., Sajina et al. 2006; Borys et al. 2006) or is indirect (e.g., Appleton et al. 2004; Yan et al. 2005; Pope et al. 2006; Marcillac et al. 2006).

The goal of this paper is to explore the average IR SEDs of a stellar mass-limited sample $z \sim 0.7$ galaxies in the extended Chandra Deep Field-South (E-CDFS). In previous works, we have shown that stacking noise-limited images of a set of galaxies allows one to securely detect the mean flux of the galaxy set substantially below the individual detection limit (Zheng et al. 2006; Dole et al. 2006). Here, we stack at longer wavelengths, i.e., 70 μm and 160 μm, to empirically determine the population-averaged IR SED. We combine these results with morphologies, and average fluxes at shorter wavelengths, to place constraints on the dust extinction and SEDs of these galaxies. In §2 we describe the multi-wavelength data used to construct galaxy SEDs and the samples of $z \sim 0.7$ galaxies. §3 presents our stacking methods. In particular we test the results of stacking noise and confusion limited 70 and 160 μm images. In §4 we present the properties of the average SEDs. Discussion and conclusion are given in §5. Throughout this paper, we assume $\Omega_M = 0.3, \Omega_\Lambda = 0.7$ and $H_0 = 70\,\mathrm{km\,s^{-1}\,Mpc^{-1}}$ for a Λ-CDM cosmology. All magnitudes are given in the Vega system except where otherwise specified.

[1] Max-Planck Institut für Astronomie, Königstuhl 17, D-69117 Heidelberg, Germany
[2] Purple Mountain Observatory, Beijing-West Road 2, Nanjing 210008, P. R. China; xzzheng@pmo.ac.cn
[3] Institut d'Astrophysique Spatiale (IAS), bat 121, F-91405 Orsay (France); Université Paris-Sud 11 and CNRS (UMR 8617)
[4] Spitzer Fellow, Institute for Astronomy, University of Hawaii, 2680 Woodlawn Drive, Honolulu, HI 96822
[5] Steward Observatory, University of Arizona, 933 N Cherry Ave, Tucson, AZ 85721
[6] Department of Astronomy, Columbia University, New York, NY 100 27

2. THE DATA AND SAMPLES

2.1. *The data*

We use *Spitzer* 24, 70 and 160 μm data to study the thermal dust emission of $z \sim 0.7$ galaxies. In addition, we include deep ultraviolet data from the *Galaxy Evolution Explorer* (GALEX: Martin et al. 2005a), optical data from the Classifying Objects by Medium-Band Observations (COMBO-17; Wolf et al. 2003) survey, and four band (3.6, 4.5, 5.8 and 8.0 μm) Infrared Array Camera (IRAC; Fazio et al. 2004) data to construct the stellar SED of a galaxy. These data cover wavelength range from 0.15 μm to 160 μm in the observed frame, equal to the rest-frame range ~0.09 to ~100 μm for $z = 0.7$.

The COMBO-17 survey has imaged the $30'5 \times 30'$ E-CDFS in five broad (U, B, V, R and I) and 12 medium optical bands, providing high-quality astrometry (uncertainties $\sim 0''.1$) based on a very deep R-band image (26 mag at the 5σ limit), photometric redshifts ($\delta z/(1+z) \sim 0.02$ at $m_{\rm R} < 23$; Wolf et al. 2004) and stellar masses (Borch et al. 2006) for $\sim 11,000$ galaxies with $m_{\rm R} < 24$. We use the photometric redshift and stellar mass catalogs to select galaxy samples.

GALEX ultraviolet observations provided deep far-ultraviolet (FUV; 1350–1750Å) and near-ultraviolet (NUV; 1750–2800Å) images centered on the E-CDFS. The FUV and NUV images have a field of view of one square degree, a typical point-spread function (PSF) of full width at half-maximum (FWHM) $\sim 5''$, a resolution of $1''.5\,\mathrm{pixel^{-1}}$ and a depth of 3.63 μJy at the 5σ level. The data reduction and source detection is described in Morrissey et al. (2005).

The deep IRAC 3.6, 4.5, 5.8 and 8.0 μm imaging data and MIPS 24, 70 and 160 μm imaging data were obtained as part of the first run of MIPS GTO observations (Rieke et al. 2004). A rectangular field of $\sim 90' \times 30'$ was observed in all bands (with small shifts between different bands). The effective exposure time is 500 s for the four IRAC band images, 1378 s pix^{-1} for MIPS 24 μm, 600 s pix^{-1} for 70 μm and 120 s pix^{-1} for 160 μm. IRAC 3.6 and 4.5 μm images have a PSF of FWHM $\sim 1''.8$ and 5.8 and 8.0 μm images have a PSF of FWHM $\sim 2''.0$ (Huang et al. 2004). The 24 μm image has a PSF of FWHM $\simeq 6''$. Sources are detected at 24 μm down to 83 μJy (at 80% completeness; see Papovich et al. 2004 for details of data reduction, source detection and photometry). The 70 μm image is characterized by a PSF of FWHM $\simeq 18''$ and a resolution of $9''.9\,\mathrm{pixel^{-1}}$. The 160 μm image has a PSF of FWHM $\simeq 40''$ and a resolution of $16''\,\mathrm{pixel^{-1}}$. Sources with fluxes of $f_{70} > 15$ mJy can be individually resolved at 70 μm and of $f_{160} > 50$ mJy at 160 μm (see Dole et al. 2004a, for details).

We take COMBO-17 astrometry as the reference coordinate and cross-correlate all other band catalogs with the COMBO-17 catalog. In each cross-correlation, we use bright stars and compact sources to estimate the systematic offsets and uncertainties between two coordinates. A position tolerance of 4σ uncertainty is adopted so that objects in the two catalogs having coincident coordinates within the tolerance (corrected for the systematic offsets) are identified as the same objects. The nearest COMBO-17 object is chosen if multiple ones exist within the tolerance. The adopted tolerances are $2''.5$ (FUV), $3''.0$ (NUV), $1''.0$ (3.6 μm), $1''.2$ (4.5 μm), $1''.5$ (5.8 and 8.0 μm) and $2''.2$ (24 μm). For the 70 and 160 μm catalogs, we firstly cross-correlate them with the 24 μm catalog as individually-detected 70 and 160 μm sources are bright at 24 μm; we then associate 70 and 160 μm objects with COMBO-17 objects using the coordinates of the corresponding 24 μm sources. The tolerance between 70/160 and 24 μm is $5''/16''$ respectively.

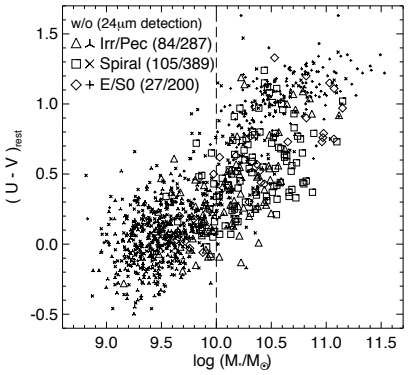

FIG. 1.— The rest-frame color $U - V$ versus stellar mass for a sample of 1092 galaxies of known (GEMS) morphology in the redshift slice $z = 0.7 \pm 0.05$. Open symbols show the objects detected individually at 24 μm ($f_{24} > 83\mu$Jy) and skeletal symbols represent individually-undetected ones. Most red ($U - V > 0.7$) elliptical/lenticular galaxies and blue ($U - V < 0.7$) small ($M_* < 10\,M_\odot$) spiral/irregular/peculiar galaxies are not individually detected at 24 μm. The number of objects in each category is given in the brackets. The *dashed* line shows the mass cut $M_* = 10^{10}\,M_\odot$ that we apply in the subsequent analysis.

2.2. *The samples*

We combine spectroscopic redshifts from the VLT VIMOS Deep Survey (Le Fèvre et al. 2005) and the GOODS survey (Vanzella et al. 2005, 2006) with photometric redshifts from the COMBO-17 survey (Wolf et al. 2004) to select sample galaxies. The E-CDFS has HST imaging from the Galaxy Evolution from Morphology and SEDs (Rix et al. 2004, GEMS;) Survey. Visually classified morphologies are available for 1458 galaxies with $m_{\rm R} < 24$ in a thin redshift slice $z = 0.7 \pm 0.05$ (Bell et al. 2005). Of the 1458 galaxies, 1114 galaxies have all observations, including GALEX, IRAC and MIPS observations. To avoid contamination from active galactic nuclei (AGNs), we remove 22 X-ray detected sources in the Chandra 250 ks observation (Lehmer et al. 2005), leaving a sample of 1092 galaxies. Spectroscopic redshifts are available for 64% of the sample galaxies. The contribution from the X-ray-undetected AGNs to the total 24 μm luminosity of $z < 1$ galaxies is suggested to be <~ 10% (Zheng et al. 2006; Brand et al. 2006). This will not have significant effects on our results.

The sample demographics are shown in Figure 1. The sample is limited by R-band apparent magnitude ($m_{\rm R} < 24$), corresponding to approximately the rest-frame B-band at $z \sim 0.7$. Accordingly, the completeness of the sample, in terms of stellar mass, is a strong function of color: the mass limit for red (old or dusty) galaxies is $M_* \sim 10^{10}\,M_\odot$ whereas blue galaxies can be included down to almost $M_* \sim 10^9\,M_\odot$. We choose to impose a stellar mass cut of $M_* \geq 10^{10}\,M_\odot$ in what follows; not only are almost all 24 μm emitters above this mass cut, but also the completeness of this sample is not a strong function of color (i.e., age or dust obscuration). We also select another sample to explore the relationship between the IR SED shape and 24 μm luminosity; we extend the redshift

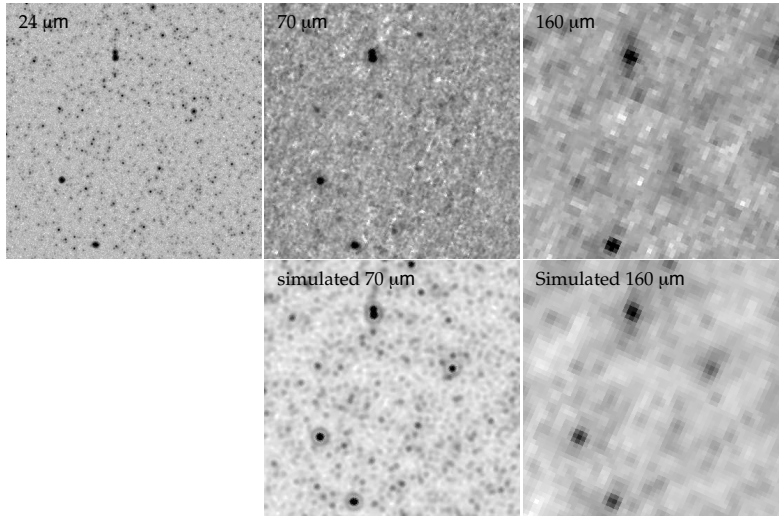

FIG. 2.— Observed MIPS 24, 70 and 160 μm image sections ($15' \times 15'$) in the extended CDFS and simulated 70 and 160 μm images. The simulated 70 and 160 μm images are created by degrading the 24 μm image to the 70 and 160 μm resolution. No additional noise is added to the simulated images.

slice to $0.6< z <0.8$ to increase the number of sample galaxies. The final sample then comprises some 579 galaxies with $M_* \geq 10^{10}\,M_\odot$ in the redshift range $0.6< z <0.8$. Of them, 218 are individually-detected at 24 μm with fluxes in excess of $> 83\mu$Jy; none is individually detected at 70 or 160 μm. X-ray detected sources have been excluded.

3. IMAGE STACKING

As outlined earlier, current missions are unable to yield individual detections for the vast majority of intermediate-redshift objects at far-IR wavelengths, owing both to contributions from instrumental noise and confusion noise. In order to place constraints on the shape of the IR SEDs of 'typical' star-forming intermediate redshift galaxies, stacking on the positions of known star-forming galaxies can lower the effective noise (Zheng et al. 2006), allowing detection of the 'average' galaxy. In Zheng et al. (2006) we presented a description of stacking of 24 μm data (in that case to resolve the 24 μm luminosity of dwarf galaxies); we briefly summarize the most important aspects of 24 μm stacking in §3.1. The focus of this paper is stacking at longer wavelengths, at 70 μm (PSF FWHM 18″) and 160 μm (FWHM 40″), discussed in §3.2.

3.1. *FUV, NUV and MIPS 24 μm image stacking*

While much of this paper describes stacking results for subsamples that are individually detected at 24 μm, some subsamples are not individually detected at 24 μm. Furthermore, the 24 μm, FUV and NUV images share many of the same characteristics: the PSFs have similar FWHM, and at each wavelength, $\gtrsim 1/2$ of the extragalactic background at that wavelength is resolved by these images (i.e., the images are only mildly confusion-limited; e.g., Papovich et al. 2004; Xu et al. 2005; Dole et al. 2006). Accordingly, stacking of FUV, NUV and 24 μm images is carried out in the same way (see Zheng et al. 2006, for more details).

Three basic steps are adopted to derive the mean fluxes for galaxy subsets. First, we subtract all individually-detected sources from the images. This is done using the software tool STARFINDER[7] (Diolaiti et al. 2000) with an empirical PSF constructed from 18/42/56 bright point sources at 24 μm/FUV/NUV respectively. Then we perform mean stack of the residual image postage stamps centered on the optical coordinates of the objects that are individually undetected in the subset of interest. An aperture of 5″ is used to integrate the central flux of the mean-stacked image and estimate the background from the outer regions. Aperture corrections of a factor of 1.88/1.19/1.14, derived from the empirical PSF at 24 μm/FUV/NUV respectively, are adopted to calibrate the stacked fluxes to the total fluxes. Last we sum the fluxes of individually-detected sources and the stack flux of individually-undetected sources in each galaxy subset, giving the mean 24 μm/FUV/NUV fluxes. Uncertainties are derived from bootstrapping.

3.2. *MIPS 70 and 160 μm image stacking*

The 70 μm and 160 μm PSFs are considerably larger than those at shorter wavelengths, yielding confused images, resolving only the brightest, relatively nearby sources — some <30% of the extragalactic background at this wavelength (Dole et al. 2004a). Galaxies at $0.6 < z < 0.8$ are heavily confused in all but the brightest cases (Dole et al. 2004a; Lagache et al. 2003, 2004), requiring stacking to gain insight into their long-wavelength IR SEDs (see, e.g., Dole et al. 2006).

The large angular extent of the long-wavelength PSFs poses a significant challenge for those wishing to estimate their average properties. At $z = 0.7$, the PSF size of the 70 μm image (FWHM ≃ 18″) corresponds to a physical scale of ~130 kpc. For the 160 μm image (PSF FWHM ≃ 40″), the corresponding scale is ~290 kpc. Thus, the stacking results are a reflection of the IR-luminosity weighted two-point correlation function on $\gtrsim$ 100 kpc scales, overestimating the true average fluxes of the galaxies of interest.

In order to understand this source of systematic error in better detail, we carried out some simulations where synthetic 24 μm data (using the observed positions and fluxes of individually-detected 24 μm sources) are degraded in resolution to the resolution of the 70 μm and 160 μm data. For the purposes of this test, we assume a constant ratio between 24 μm flux and the wavelength of interest. We explore two cases. First, the positions are randomly scrambled (i.e., the relative brightnesses of galaxies are preserved but their positions are random). This test gives an indication of the systematic effects of stacking randomly-positioned sources. The second case is when both the fluxes and positions of sources are preserved. This second case is our 'best' estimate of the likely systematic uncertainties of stacking in a realistically-clustered case. Figure 2 shows the 24 μm images degraded to the 70 and 160 μm resolution respectively, compared with the observed MIPS 24, 70 and 160 μm images. Because of confusion, only a handful of bright 24 μm sources can be individually resolved in the degraded images. Through stacking the mean flux can be estimated for 24 μm source subsets; the accuracy of the recovery of the mean flux shows how well stacking works at that corresponding image resolution.

3.2.1. *Stacking randomly distributed sources*

The whole 24 μm mosaic image of the E-CDFS covers a rectangular sky area of ~ 1.°5 × 0.°5 and contains 8255 individually-detected sources at 5σ detection limit (83 μJy). The vast majority of the 8255 sources ($f_{24} > 83\mu$Jy) are point sources. Replacing all sources with the 24 μm PSF (empirically constructed from bright stars), we generated an artificial 24 μm image having the 8255 sources *randomly* distributed into a ~ 1.°5 × 0.°5 blank field. The artificial 24 μm image was then degraded to the 70 and 160 μm image resolution respectively. The degraded images are then stacked at the 24 μm source positions, giving indications as to the expected quality of stacking results at 70 μm and 160 μm. We note that the replacement of the background blank field with the PSF-subtracted 24 μm image (having some contribution from individually-undetected sources) does not modify our results significantly in the mean, adding only some modest additional scatter.

The 24 μm sources were sorted into 18 bins in flux, ranging from 83 μJy to 10 mJy (see also Dole et al. 2006), with ~ 1000 objects per bin at faint flux levels, and $\lesssim$ 100 per bin at brighter fluxes. The numbers of sources and average 24 μm fluxes per bin are listed in Table 1. In real stacks, we choose to PSF-subtract out the individually-detected sources, stacking the remaining image (in order to reduce bias from bright sources in background estimates). In the real 70 and 160 μm images, we detect ~ 130 sources in each image. Thus, we

[7] STARFINDER gives identical results within the errors to the tool ALLSTAR in IRAF package.

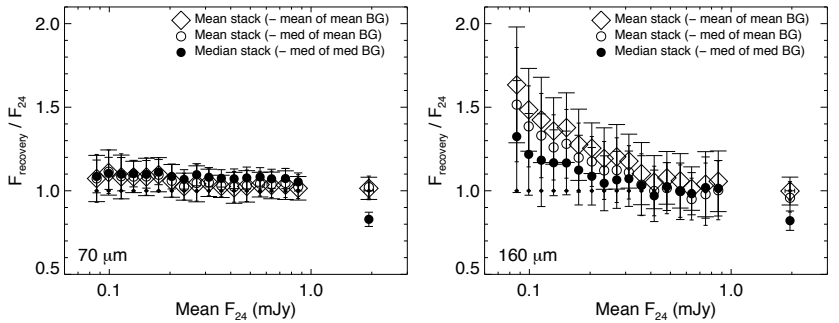

FIG. 3.— Recovery of the mean fluxes of *randomly* distributed 24 μm sources through stacking after convolution to the 70 μm (*left*) and 160 μm (*right*) resolution. The fluxes were taken from the 8255 individually-resolved sources in the ~ 1.°5 × 0.°5 24 μm image and were split into 18 flux bins in the range from 83 μJy to 10 mJy. The number of objects in each bin decreases with increasing flux. Three measures of the stack flux are presented for each bin: the integrated central flux of the *mean* stack using the *mean* background for sky subtraction; the integrated central flux of the *mean* stack using the *median* background; and the integrated central flux of the *median* stack using the *median* of the background (see text for details). Errorbars are derived from bootstrapping. While the flux can be recovered with little bias at 70 μm resolution, flux recovery at 160 μm leads to a systematic overestimate.

TABLE 1
THE NUMBERS OF SOURCES AND AVERAGE FLUXES FOR 18 FLUX BINS COMPOSED OF 8255 INDIVIDUALLY-RESOLVED 24 μM SOURCES.

No.	1	2	3	4	5	6	7	8	9	10	11	12	13	14	15	16	17	18
$< f_{24} >(\mu$Jy)	87	99	115	132	153	176	204	235	271	311	359	416	480	559	637	747	863	1946
Number	1070	1259	1067	894	803	683	508	418	328	267	222	174	134	98	72	46	39	169

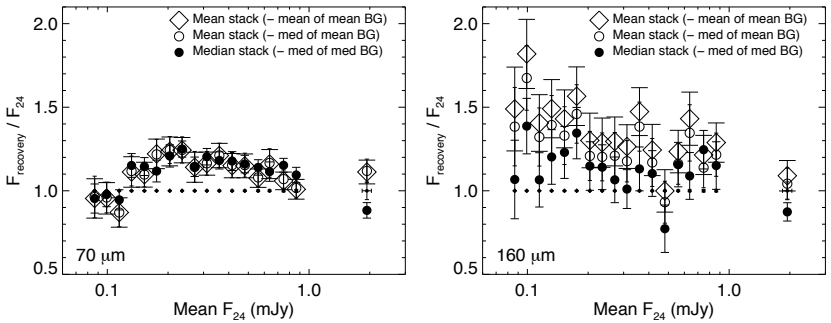

FIG. 4.— The recovery of the mean properties of 24 μm-detected sources at their observed positions. *Left*: Stacking results at 70 μm resolution. *Right*: Stacking results at 160 μm resolution. The errorbars reflect the variance from bootstrapping.

must subtract approximately this many bright sources from the simulated images before stacking to avoid unrealistically biasing the results. Ideally, one would subtract all detected sources in the simulated 70 and 160 μm images; unfortunately, as the simulated and real 70 and 160 μm images have (unavoidably) somewhat different noise and brightness distribution properties, the number of detected sources is different, and substantially higher in the case of (the rather deeper) simulated 70 μm data. Thus, we choose to PSF-subtract the 169 brightest sources (the brightest of the 18 original bins) before stacking for the remaining 17 bins.

For each flux bin, postage stamps were cut from the simulated image centered on the positions of the sources and were stacked. The size of postage stamps is 2.′5×2.′5 for the 70 μm image and 4′ × 4′ for the 160 μm image, allowing for a proper background estimate. Two stacked images were created for each bin through averaging or medianing. For the stacked 70 μm postage stamp images, an aperture of radius 0.′49 is used to integrate the central stack flux and an annulus with inner radius 0.′82 and outer radius 1.′23 to estimate the background. For the stacked 160 μm postage stamp images, the corresponding aperture is of radius 1.′07 and the corresponding annulus is of inner radius 1.′07 and outer radius 1.′87. The mean and median of pixels in the annulus region were taken as the background of the mean-stacked image for sky subtraction. Only the median (nearly identical to the mean) was adopted as the background of the median-stacked image. Therefore, we derive three measures of the stack flux for each subsample: the integrated central flux of the *mean* stack using the *mean* background for sky subtraction; the integrated central flux of the *mean* stack using the *median* background; and the integrated central flux of the *median* stack using the *median* of the background. Finally, aperture corrections derived from model PSFs (http://ssc.spitzer.caltech.edu/mips/psffits/) were applied to correct the estimates of stack flux to the total. The aperture correction is a factor of 1.30 for 70 μm, 1.25 for 160 μm using the median background, and 1.34 for 160 μm using the mean background.

Figure 3 shows the results of stacking *randomly* distributed sources at 70 and 160 μm resolution. Uncertainties are derived from bootstrapping. At 70 μm resolution, the mean flux of 24 μm sources of comparable flux can be properly recovered over a flux range of one order of magnitude. At 160 μm resolution, recovered fluxes are of reasonable quality at bright limits, and become progressively more biased (by ~ 20-50%) towards fainter limits. After some investigation, it became clear that the the stack recovery at 160 μm is correlated with the number of objects in the stack bin. The increase of objects in number leads to an increase of the overlap between these objects within a fixed area. This increasing overlap leads to an increase of the stack flux relative to the input flux. By stacking a number of identical sources without background and foreground sources, we obtained similar results as shown in Figure 3. Indeed a point source contains 80% of its flux in an area of 3.6 arcmin^2 in the 160 μm imaging and an area of 0.9 arcmin^2 in the 70 μm imaging. To fill in a 1.′5×0.′5 field, it requires around 750 160 μm sources or 3000 70 μm sources, compared to ~ 50 - 1260 objects in the stack bins. Therefore the stack results at 70 μm are little affected by the overlap between the stack objects but the stack results at 160 μm are significantly influenced for stack bins of ~ 1000 objects.

The three measures of the stack flux are nearly identical within the errorbars (~ 10%) for simulated 70 μm stacking and slightly different for simulated 160 μm stacking, in particular for the low flux bins, although the scatter is significant (~ 10 - 25%). Note that we divided sources into stack bins in terms of their fluxes. For the stack bins having sources whose fluxes span a wide range, the median stack substantially underestimates the mean flux.

3.2.2. *Stacking sources at their observed positions*

In order to build a more realistic picture of the expected uncertainties from stacking at 70 μm and 160 μm, we repeat the last analysis except we keep both the fluxes and positions of the sources fixed to those observed at 24 μm. This gives insight into the influence of clustering on the results. In this test, the observed 24 μm map was degraded to the 70 and 160 μm resolution respectively, as shown in Figure 2. As previously, sources were split into 18 bins in 24 μm flux, and the stacking results for each flux bin were calculated. Figure 4 shows the results. Comparing the results with Figure 3, one can clearly see that the mean and median recovered fluxes are significantly affected by the clustering of sources on the sky. In general, our test suggests that stacking subsets of 70 μm and

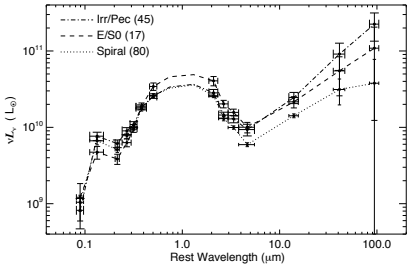

FIG. 5.— The average SED, spanning a factor of 1000 in wavelength, as a function of morphological type for 24 μm detected (f_{24} > 83μJy) galaxies with $M_* \geq 10^{10}\,M_\odot$ in a thin redshift slice $0.65 \leq z \leq 0.75$. Vertical errorbars are the 1σ uncertainties derived from bootstrapping and horizonal errorbars show the band widths. The number of objects in each morphology bin is given in the brackets.

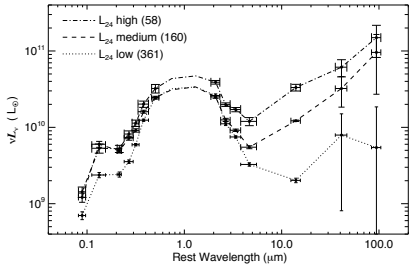

FIG. 6.— Average SED as a function the 24 μm luminosity for galaxies with $M^* \geq 10^{10}\,M_\odot$ in the redshift range $0.6 < z < 0.8$. The vertical errorbars show the 1σ uncertainties and horizonal errorbars show the band widths. The 579 galaxies are split into three bins in terms of their 24 μm luminosities: L_{24}-high, L_{24}-medium and L_{24}-low. The numbers in brackets denote the number of objects included in each bin.

160 μm sources may overestimate the mean flux somewhat; typical biases are ~ 20%, with uncertainties of order ~ 20%. Yet, the magnitude and direction of these effects on different subsamples are difficult to estimate *a priori*. Figure 4 demonstrates that from bin to bin, the source clustering may lead to either an increase or a decrease of the mean flux of the source subsample, depending on the actual distribution and density of sources of different brightnesses on the sky.

3.2.3. *Stacking $z \sim 0.7$ galaxies*

The above tests demonstrate that it will be difficult to estimate the mean flux at 70 μm and 160 μm to better than ~ 20%, and that the extent of the bias towards higher or lower flux is difficult to predict with accuracy. In this paper, we adopt a pragmatic approach: for each subsample that is stacked at 70 μm and 160 μm, we attempt to derive an individual 'bias correction' based on the 24 μm image. Sources bright at 24 μm are generally bright at 70 and 160 μm, although the 24 μm to 70 or 160 μm flux ratio varies from object to object at a scatter at the 0.5 dex level (Dale et al. 2005). Thus, we adopt the simplistic assumption that the 24 μm image can be taken as a good proxy for the 70 or 160 μm image at $\simeq 6''$ resolution and high S/N; 70 μm and 160 μm resolution images derived under this assumption (Fig. 2) appear a reasonable description of the real 70 μm and 160 μm images. Thus, for a given subset of z ~ 0.7 galaxies, we estimated precisely the mean 24 μm flux from their 24 μm images. Then we degraded the 24 μm images to 70 and 160 μm image resolution. Two stack fluxes were estimated by stacking each of the two sets of degraded images. By comparing the stack fluxes to the actual mean 24 μm flux of the galaxy subset, we obtained empirical corrections, which were applied to the corresponding 70 and 160 μm stack fluxes of the subset of z ~ 0.7 galaxies, respectively. Uncertainties in this correction are applied also, in quadrature, to the derived stacking results at 70 μm and 160 μm.

4. RESULTS

To explore the average IR SEDs of z ~ 0.7 star-forming galaxies, we first look into the dependence of the IR SED shape on galaxy morphology. Then, we investigate the relationship between the IR SED shape and the 24 μm luminosity and the z ~ 0.7 IR SEDs to those of present-day star-forming galaxies. Finally, based on the IR SEDs, the extrapolation of the total IR luminosity from the 24 μm luminosity is discussed.

4.1. *The relationship between IR SED and morphology*

We used a sample of 1092 galaxies of known morphology to investigate the dependence of the IR SED shape on morphology. The 1092 galaxies are classified into three morphological types: elliptical/lenticular (E/S0), spiral, and irregular/peculiar. Figure 1 shows the relationship between the rest-frame color $U - V$ and stellar mass. Objects detected at 24 μm (f_{24} > 83μJy) are marked with open symbols and undetected ones with skeletal symbols. The detection limit of 83 μJy corresponds to the monochromatic observed-frame 24 μm luminosity $\nu L_{\nu,24} = 6 \times 10^{10}\,L_\odot$ at $z = 0.7$. The 24 μm-undetected galaxies are intrinsically faint in the IR bands (see §4.2), and we excluded them in constructing these composite SEDs. To avoid selection bias in color (see §2.2), we also excluded about one third of the 24 μm detected galaxies with $M_* < 10^{10}\,M_\odot$, leaving 152 galaxies in the final sample. We calculated the average luminosities in 14 bands for each subsample of 24 μm-detected galaxies: FUV & NUV from GALEX, U, B, V, R and I from the COMBO-17 survey, IRAC 3.6, 4.5, 5.8 and 8.0 μm, MIPS 24, 70 and 160 μm bands. The average luminosity of each band includes contributions from both individually-detected and individually-undetected sources (at wavelengths other than 24 μm). Errors in the average luminosities were derived from bootstrapping, including contributions to the uncertainty from measurement errors in both the individually-detected fluxes and the individually-undetected fluxes. The average SED spans a range in the rest-frame of 0.1 to 100 μm.

Figure 5 shows the average SEDs of the three subsamples. Each of the three average SEDs is dominated by a dust-extincted stellar spectrum at $\lambda < 5\,\mu$m and emission by dust at $\lambda > 5\,\mu$m. Irregular/peculiar galaxies show a higher ratio of dust to stellar emission compared to the spirals and E/S0 galaxies. The slope of the IR SED (rest-frame 10-100 μm) is steeper for irregular/peculiar galaxies, somewhat intermediate for E/S0 galaxies, and lowest for spirals although the uncertainties of 70 and 160 μm luminosities are large. The ir-

TABLE 2
AVERAGE LUMINOSITIES OF MASSIVE-GALAXY SUBSETS IN THE REDSHIFT SLICE $0.6 < z < 0.8$.

N_{obj}	$\log < M^* >$ ($M_\odot$)	$\log \nu L_{\nu,24}$ ($L_\odot$)	$\log \nu L^a_{\nu,70}$ ($L_\odot$)	corr.(70)	$\log \nu L^a_{\nu,160}$ ($L_\odot$)	corr.(160)	$\log < L_{12-100} >^b$ ($L_\odot$)	$\log < L_{IR} >^c$ ($L_\odot$)
58	10.7	$10.52^{+0.04}_{-0.05}$	$10.79^{+0.10}_{-0.13}$	1.51±0.24	$11.17^{+0.16}_{-0.26}$	1.04±0.39	$11.30^{+0.10}_{-0.13}$	$11.42^{+0.07}_{-0.08}$
160	10.5	$10.09^{+0.01}_{-0.01}$	$10.51^{+0.16}_{-0.24}$	1.03±0.32	$10.98^{+0.23}_{-0.55}$	0.92±0.61	$11.04^{+0.16}_{-0.27}$	$11.12^{+0.05}_{-0.05}$
361	10.7	$9.31^{+0.03}_{-0.03}$	$9.90^{+0.28}_{-0.99}$	1.19±0.96	<10.27	...	$10.18^{+0.26}_{-0.75}$	$10.28^{+0.14}_{-0.21}$

[a] The 70 μm and 160 μm luminosities estimated from stacking have included the corrections derived from degraded 24 μm images. The corrections are listed in the table.
[b] L_{12-100} is the luminosity between 12 to 100 μm, calculated by linearly interpolating observed 24, 70 and 160 μm luminosities (in logarithm space).
[c] L_{IR} refers to the total IR luminosity between 8 to 1000 μm. Local IR SED templates from Lagache et al. (2004),Chary & Elbaz (2001) and Dale & Helou (2002) are used to fit the observed data points. The total IR luminosity is derived from the dust temperature-match templates. See text for details.

regular/peculiar galaxies usually form stars in relatively concentrated regions, leading to a high star formation intensity (i.e. SFR per unit area). In contrast, the spirals are often characterized by a relatively low star formation intensity as the star-forming regions are widely distributed over disks. The star formation density for the E/S0 galaxies is somewhat between those of the irregular/peculiar galaxies and spirals. The shapes of the IR SEDs are thus a function of star formation intensity in the sense that the dust temperature is primarily colder in systems of relatively lower star formation intensity (we will return this topic in §5).

4.2. *The relationship between IR SED and 24 μm luminosity*

We used a mass-limited sample to study the relationship between IR SED shape and 24 μm luminosity. This sample consists of 579 galaxies with $M^* \geq 10^{10}\,M_\odot$ and $0.6 < z < 0.8$. The sample galaxies were divided into three 24 μm luminosity bins: L_{24}-high, L_{24}-medium and L_{24}-low. The first two bins contain 218 individually-detected 24 μm sources ($f_{24} > 83\,\mu$Jy) and all individually-undetected 24 μm sources (361 of the 579) are in the third bin. The L_{24}-high bin is chosen to contain 58 brightest 24 μm sources so that its total 24 μm luminosity equals that of the L_{24}-medium bin. Consequently the stacked 70 and 160 μm fluxes are expected to have comparable signal-to-noise ratios for the two bins. Average luminosities in all 14 bands were calculated for the three subsets of galaxies. The average luminosities in the 24, 70 and 160 μm bands are listed in Table 2, along with the number of objects and mean stellar mass for each of the three subsets. The empirical corrections adopted for the 70 and 160 μm stack fluxes (see §3.2.3) are also presented. Errors include the uncertainties in measurements and bootstrapping errors. Figure 6 shows the average SED from the rest-frame wavelengths 0.1 to 100 μm as a a function of the 24 μm luminosity. It is clear that the observed 24 μm (rest-frame 14 μm) luminosity is correlated with the 70 and 160 μm IR luminosities for massive galaxies at $z \sim 0.7$ in the sense that the 70 and 160 μm IR luminosities increase as the 24 μm luminosity increases; i.e., 24 μm luminosity typically reflects high IR luminosity, rather than an enhanced rest-frame mid-IR excess (see also Bavouzet et al. 2007, in preperation). The L_{24}-high bin has an average galaxy stellar mass 0.2 dex larger than the L_{24}-medium bin; this can also be seen from the redder optical colors and higher rest-frame ~ 3 μm luminosity of the L_{24}-high bin. The L_{24}-low bin contains 361 massive galaxies that are individually undetected at 24 μm, including early-type galaxies with little star formation and late-type galaxies in the quiescent star formation phase (see Figure 1). The short-wavelength part

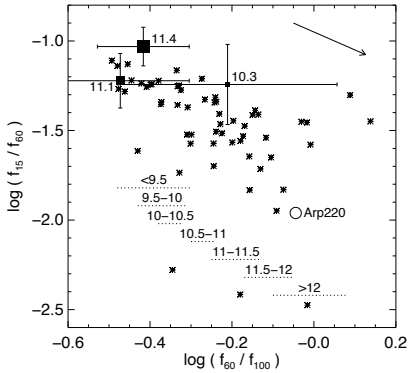

FIG. 7.— Relative dust temperature estimate from the IR flux ratio f_{60}/f_{100} versus f_{15}/f_{60}. *Asterisks* represent local star-forming galaxies from Dale et al. (2000) with IRAS observations at the 60 and 100 μm and ISO observation at 15 μm. The ratio f_{60}/f_{100} is an indicator of the dust temperature, which tends to be correlated with IR luminosity in the local Universe. The *dotted lines* show typical values of f_{60}/f_{100} corresponding the given $\log(L_{IR}/L_\odot)$ derived from IRAS data (Soifer & Neugebauer 1991). These lines are arbitrarily positioned on the Y-axis. The *open circle* shows the well-known local ultraluminous IR galaxy Arp 220. The *squares* show the three subsets of massive ($M^* \geq 10^{10}\,M_\odot$) galaxies in redshift slice $0.6 < z < 0.8$, labeled with the corresponding IR luminosities $\log(L_{IR}/L_\odot)$. Note that errorbars of the two flux ratios are not independent. The arrow indicates the effect of an increase in f_{60} by a factor of 1.5.

of their average SED is dominated by a relatively old stellar population. The large errorbars of the 70 and 160 μm luminosities compared to the small errorbar of the 24 μm luminosity are partially due to the intrinsic scatter among the sample galaxies in this bin.

4.3. *Comparison with local SEDs*

A key goal of this paper is to compare the observed average IR SED shapes at $z \sim 0.7$ to local 'template' SEDs. We adopted a sample of local star-forming galaxies from Dale et al. (2000) with *IRAS* and ISO 15 μm observations and total IR luminosity (8 - 1000 μm) spanning from $\sim 10^9$ to $10^{12}\,L_\odot$. Figure 7 shows these nearby galaxies in the IR flux ratio f_{60}/f_{100} versus f_{15}/f_{60} plot. The local galaxies distribute

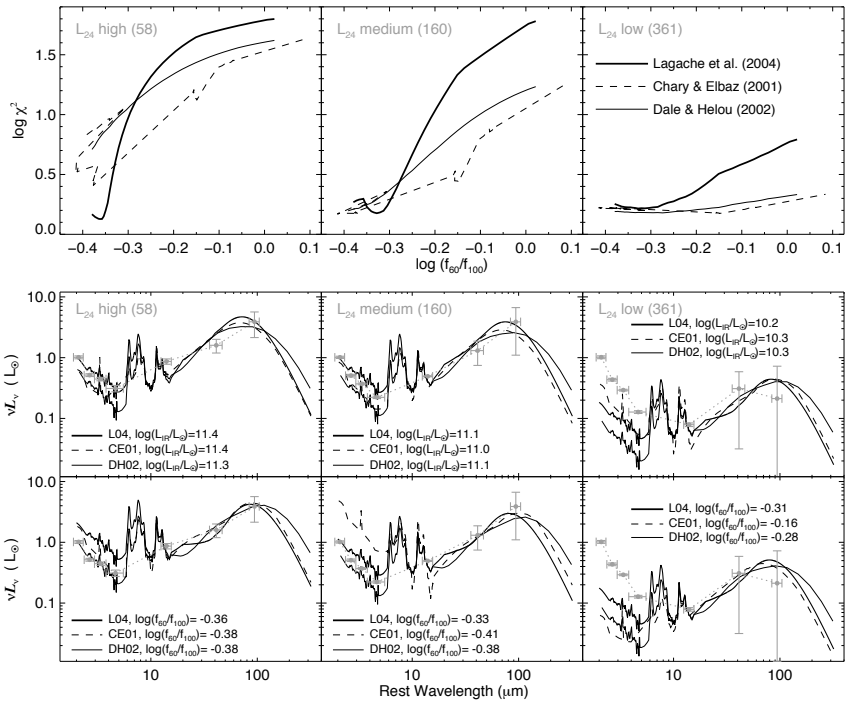

FIG. 8.— Fitting three sets of local templates from Lagache et al. (2004), Chary & Elbaz (2001) and Dale & Helou (2002) to the average IR SEDs of three subsets of massive ($M^* \geq 10^{10}\,M_\odot$) galaxies in the redshift slice $0.6 < z < 0.8$. Only the three MIPS data points (24, 70 and 160 μm) of each observed IR SED are used in the fitting. *Top*: The panels show χ^2 as a function of the template's characteristic $\log(f_{60}/f_{100})$. For each observed IR SED two best-fit templates are chosen: one is matched in luminosity (i.e., with the normalization constant equal to unity) and the other is dust temperature match (or SED shape match; i.e., with the minimum χ^2). *Bottom*: The *upper panels* shows the best-fit luminosity match templates and the *lower panels* show the best-fit dust temperature match templates, compared to the observed SEDs from the rest-frame 2 to 100 μm delineated by IRAC and MIPS data points for the L_{24}-high bin (*left panels*), the L_{24}-medium bin (*middle panels*) and the L_{24}-low bin (*right panels*). The SEDs are normalized to unity at 2.1 μm. Note that the stellar components of the locoal templates are somewhat arbitrarily set. The disagreements between the averaged SEDs and the best-fit templates at $\lambda_{rest} < 5\mu$m should be ignored.

along a sequence with considerable scatter. The sequence is correlated with both dust temperature and IR luminosity. The dust temperature and IR luminosity increase for increasing f_{60}/f_{100} (e.g., Soifer & Neugebauer 1991). The average IR SEDs for $z \sim 0.7$ galaxies are determined by the three MIPS bands, corresponding to the rest-frame ~14, ~41 and ~94 μm bands. The 24 μm and 160 μm luminosities can be taken as rest-frame 15 μm and 100 μm luminosities, for which 'K-corrections' are negligible. We estimated the rest-frame 60 μm luminosity by linear interpolation between the MIPS measurements in log-log space (as shown in Figure 6). We used the local sample to test the linear interpolation. First, we derive the 41 μm fluxes by linear interpolation between *IRAS* 25 and 60 μm measurements in log-log space. Second, we derive 60 μm fluxes by the same method between 41 and 100 μm for the 59 local galaxies adopted. The estimated 60 μm fluxes are 25±11% lower than the observed *IRAS* 60 μm fluxes. This hints that our rest-frame 60 μm luminosities of the $z \sim 0.7$ galaxies might be underestimated. We compared the $z \sim 0.7$ galaxies to the local galaxies. As shown in Figure 7, the two populations are roughly located in the same region of the f_{60}/f_{100} versus f_{15}/f_{60} plane. Specifically, the $z \sim 0.7$ star-forming galaxies of IR luminosity $11 < \log(L_{IR}/L_\odot) < 11.4$ (those in the L_{24}-high bin and L_{24}-medium bin; the estimates of the total IR luminosities will be discussed later) populate the relatively low-temperature end of the template sequence. In the local Universe, these low-temperature galaxies tend to be of relatively low luminosity $\log(L_{IR}/L_\odot) < 10.5$. This, with significant uncertainties, suggests that the typical dust temperature of $z \sim 0.7$ luminous IR galaxies (LIRGs; i.e., galaxies

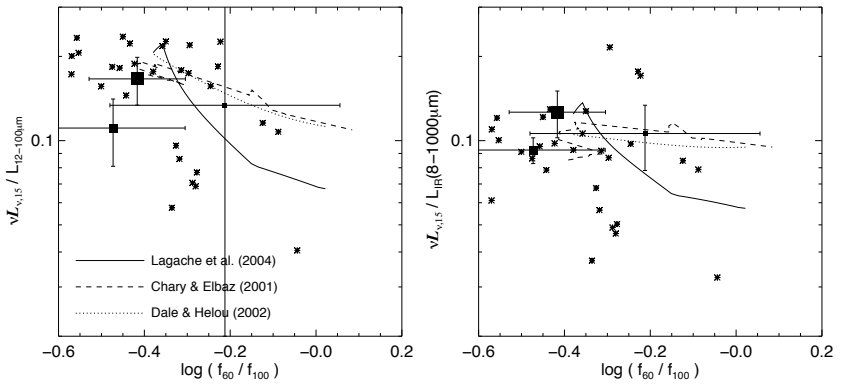

FIG. 9.— The ratio between the rest-frame 15 μm to the 12–100 μm luminosity (*left* plot) and to the total IR luminosity (8–1000 μm; *right* plot) as a function of the IR flux ratio f_{60}/f_{100}. *Asterisks* are local galaxies collected from literature with IRAS, ISO 15 μm observations and at least one observation at wavelengths longer than 100 μm. *Squares* show our results for galaxies with $M^* \geq 10^{10}\,M_\odot$ and 0.6< z <0.8. The relations derived from SED templates are presented for comparison. One can see that the extrapolation of the rest-frame 15 μm luminosity based on the three sets of templates give comparable estimates of total IR luminosity within a considerable scatter. Our data points distribute within the scatter of the local star-forming galaxies but towards the colder templates. Roughly speaking, a factor of 10 is a quite good average bolometric correction to the estimate of the total IR luminosity from the rest-frame 15 μm luminosity. Generally speaking, the use of local templates of $L_{\rm IR} \leq 10^{10.5}\,L_\odot$ for extrapolation of total IR luminosity from intermediate redshift 24 μm luminosities gives a more accurate result than the use of $L_{\rm IR} \sim 10^{11}\,L_\odot$ templates.

with $\log(L_{\rm IR}/L_\odot) > 11$) is lower than that of local galaxies of comparable IR luminosity. The IR flux ratios are poorly determined for the L_{24}-low bin because of the large uncertainties in the average 70 and 160 μm IR luminosities, which are partially due to the intrinsic scatter among the sample galaxies in the L_{24}-low bin (including early-type galaxies and late-type galaxies in the quiescent star formation phase).

We compared our average SEDs with the IR SED model templates from Lagache et al. (2004), Chary & Elbaz (2001) and Dale & Helou (2002). The three sets of templates were empirically calibrated to represent local star-forming galaxies spanning a wide range in the IR flux ratio f_{60}/f_{100}. Dale & Helou's IR SED templates are characterized by the flux ratio f_{60}/f_{100}. We use the equation from Chapman et al. (2003) to parameterize the IR luminosity (8 - 1000 μm) as a function of f_{60}/f_{100}.[8] The templates from Lagache et al. (2004) and Chary & Elbaz (2001) were characterized by the IR luminosity. We extended each set of SED templates by linear interpolation in logarithmic space to a grid of SEDs with the characteristic IR luminosity ranging from 10^9 to $10^{13}\,L_\odot$ with a resolution of 0.1 dex. The observed IR SED of each subset was compared to the three sets of templates:

$$\chi^2 = \sum_{i=1}^{N_{\rm filters}} \left[\frac{L_{{\rm obs},i} - f_{scale} \times L_{{\rm temp},i}(z=0.7)}{\sigma_i} \right]^2, \qquad (1)$$

where $L_{{\rm obs},i}$, $L_{{\rm temp},i}$ and σ_i are the observed and template luminosities and their uncertainty in filter i, respectively, and $f_{\rm scale}$ is a normalization constant. Here only 24, 70 and 160 μm bands were used to fit templates, i.e., $N_{\rm filters} = 3$. $L_{\rm temp}$ is calculated by convolving the redshifted SED template to $z = 0.7$ with the 24, 70 or 160 μm filter transmission function. $f_{\rm scale}$ is chosen to minimize the χ^2 for each template. The top plot in Figure 8 shows the fitting results. The templates with a normalization constant $f_{\rm scale}$ of unity are chosen as the best-fit luminosity match templates and those with a minimum χ^2 as the best-fit dust temperature match (or SED shape match) templates. The best-fit templates are compared to the observed SEDs in the bottom plot of Figure 8.

As shown in Figure 8 the local SED templates track the observed SEDs reasonably well, in particular for the L_{24}-medium bin, which contains the majority of intense star-forming galaxies. As the total IR luminosity is dominated by emission in the rest-frame wavelength range between 10 and 100 μm, the estimates of the total IR luminosity with templates from different models give similar results. In contrast, χ^2 is a measure of the shape agreement between a template and an observed SED. It is worth noting that the estimate of total IR luminosity based on the three measurements at 24, 70 and 160 μm is not sensitive to the shapes of the IR SED templates. Both the best-fit luminosity match and the best-fit dust temperature match the SED templates and suggest a total IR (8 - 1000 μm) luminosity of $\log L_{\rm IR}/L_\odot \sim 11.4, 11.1, 10.3$ for the three average SEDs, respectively. Generally speaking, the shape (or dust temperature) of the average IR SEDs of star-forming galaxies at $z \sim 0.7$ (i.e., the L_{24}-high bin and L_{24}-medium bin) are better fitted by the local SED templates of characteristic IR luminosity $L_{\rm IR} \leq 10^{11}\,L_\odot$ than those of $L_{\rm IR} > 10^{11}\,L_\odot$. This holds for all three sets of templates. It confirms that the typical star-forming galaxies at $z \sim 0.7$ are likely to have relatively colder dust emission than local galaxies with comparable IR luminosity.

[8] The total IR luminosity defined in Chapman et al. (2003) is between 3 and 1100 μm , in good agreement with the adopted one (Dale et al. 2001; see also Takeuchi et al. 2005b).

4.4. *The extrapolation from the rest-frame 15 μm to the total IR luminosity*

Local IR SED templates are often used to estimate the total IR luminosities from single mid-IR band luminosities for distant star-forming galaxies. With the averaged IR SEDs determined in the three MIPS bands, we are able to better constrain the estimates of the IR luminosities. We compared the estimates with those transformed from single 15 μm luminosities using local SED templates.

By linearly integrating between the average 24, 70 and 160 μm luminosities (in logarithm space) for the star-forming galaxies at $z \sim 0.7$, we estimated the rest-frame 12–100 μm luminosities. Uncertainties are calculated from the combination of the uncertainties in the three bands. The total IR (the rest-frame 8–1000 μm) luminosity is derived from the three dust temperature-match templates to each observed IR SED (the 24, 70 and 160 μm). We combine the scatter between the templates and the uncertainty in determining the dust temperature-match templates, in which the uncertainties of the 24, 70 and 160 μm luminosities are counted, as the uncertainty for the total IR luminosity. The results are listed in Table 2. For comparison, we use the NASA/IPAC Extragalactic database (NED) to collect a sample of 29 local star-forming galaxies ($z < 0.1$) with observations at 12, 25, 60 and 100 μm by *IRAS*, at 15 μm by ISO and at least in one band longer than 100 μm. The 12–100 μm luminosity and the total IR luminosity are calculated as above. When observations do not reach 1000 μm, a modest ($\lesssim$ 20% of the IR luminosity) extrapolation is employed using the local SED templates.

Figure 9 shows the extrapolations (bolometric corrections) from the rest-frame 15 μm to the 12–100 μm luminosity (left plot) and to the total IR luminosity (right plot) as functions of the IR flux ratio f_{60}/f_{100}. The local star-forming galaxies exhibit a significant scatter (Chary & Elbaz 2001; see also Dale et al. 2005); such scatter is typically adopted as the systematic uncertainty of template-based estimates of total IR luminosity from rest-frame mid-IR luminosity. The $z \sim 0.7$ star-forming galaxies distribute within the scatter of the local star-forming galaxies. Again, there is a tendency for the $z \sim 0.7$ galaxies to cluster towards the colder templates, suggesting that use of spiral galaxy templates for extrapolation of total IR luminosity from intermediate redshift 24 μm fluxes gives a more accurate result than the use of starburst/LIRG templates.

4.5. *Dust extinction*

A universal relation between SFR and dust extinction is suggested by several studies at $z < 1$ (Hopkins et al. 2001; Adelberger & Steidel 2000; Bell 2003; Takeuchi et al. 2005a; Zheng et al. 2006; Buat et al. 2006; although see Reddy et al. 2006 for a dissenting view at $z \sim 2$). With a measured estimate of the total IR luminosity from the 24, 70 and 160 μm luminosities, we explore the relationship between SFR and dust extinction at $z \sim 0.7$, comparing it to that at $z \sim 0$. The dust extinction is described by the IR to UV ratio $L_{\rm IR}/L_{\rm UV}$. The UV luminosity, i.e., the integrated luminosity between rest-frame 1500-2800 Å, is estimated from linear interpolation of the FUV, NUV, U, and B band luminosities for $z \sim 0.7$ galaxy subsets shown in Figures 5 and 6. Following Bell et al. (2005), we derived the SFR from the IR and UV luminosities with the formula

$${\rm SFR}/(M_\odot\,{\rm yr}^{-1}) = 9.8 \times 10^{-11}(L_{\rm IR} + 2.2 L_{\rm UV}), \qquad (2)$$

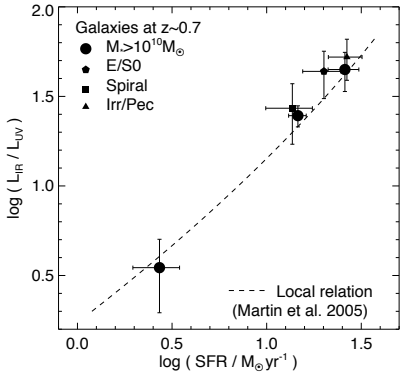

FIG. 10.— The ratio IR/UV flux (i.e., the fractional dust obscuration) as a function of SFR. *Solid circles* show the three subsets of galaxies with $M_* \geq 10^{10}\,M_\odot$ and $0.6 < z < 0.8$, sorted by the 24 μm luminosity. Other symbols show three morphology subsets of star-forming ($f_{24} > 83\mu$Jy) galaxies in redshift slice $0.65 \leq z \leq 0.75$. The *dashed line* shows the local relation (Martin et al. 2005b).

assuming a stellar population with a constant SFR for 100 Myr and a Kroupa initial mass function. Figure 10 shows the relationship between dust obscuration and SFR for $z \sim 0.7$ galaxies, compared to the local relation derived from IRAS and GALEX data with a scatter at ~0.5-1 dex level (Martin et al. 2005b; Xu et al. 2006; Buat et al. 2006). As shown in Figure 10, the $z \sim 0.7$ galaxies distribute perfectly along the local relation over one order of magnitude.

5. DISCUSSION AND CONCLUSION

We selected a sample of 152 galaxies in the redshift slice $0.65 \leq z \leq 0.75$ of known morphology from HST imaging and another sample of 579 mass-limited ($M_* \geq 10^{10}\,M_\odot$) galaxies in the redshift slice $0.6 < z < 0.8$ to study the IR SEDs at that redshift. We divided our sample galaxies into different mass-limited morphology and 24 μm luminosity bins. For each bin, we determined the average luminosities in 14 bands from the FUV to the FIR by summing the individual detections and adding in the stacked flux from non-detections. Careful efforts were taken in stacking the noise and confusion limited 70 and 160 μm images. Empirical corrections, determined from the 24 μm image, were introduced to account for the clustering effects on the stack results.

The average luminosities in three MIPS bands determine the IR SED from the rest-frame 10 to 100 μm. Our principal result is that the average IR SED shape of $z \sim 0.7$ intensely star-forming galaxies (with IR luminosities $\sim 10^{11}L_\odot$) is similar to reasonably 'cool' local templates (i.e., templates of 'normal' spiral galaxies). The dust SED seems to depend on morphological type for star-forming galaxies at $z \sim 0.7$. This has the immediate and important implication that the use of local templates to extrapolate total IR luminosity from observed-frame 24 μm data is a well-posed problem, at least, on average. Interestingly, galaxies with 'cool' dust temperatures in the local Universe all tend to have IR luminosities $\lesssim 10^{10.5}L_\odot$, i.e., distant intensely star-forming galaxies tend to be charac-

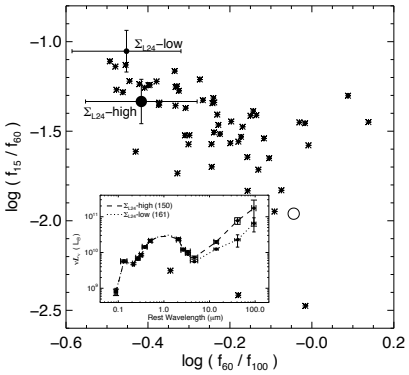

FIG. 11.— Same as Fig. 7. The *filled circles* show the two subsets of galaxies in the redshift slice $0.6 < z < 0.8$ split by 24 μm luminosity surface density. The inner panel shows the average SEDs of the two subsets. The Σ_{L24}-high bin and the Σ_{L24}-low bin data points are located separated along the dust-temperature sequence of local star-forming galaxies, indicating that the Σ_{L24}-high bin is characterized by a hotter dust emission than the Σ_{L24}-low bin. This is clearly seen from the difference between their IR SEDs.

terized by colder dust emission than their local counterparts of comparable IR luminosity.

Previous studies have found evidence for a somewhat cooler dust SED at $0.2 < z < 2.5$ than for local galaxies of a comparable luminosity (e.g., Pope et al. 2006; Sajina et al. 2006) at $0.2 < z < 2.5$. These studies were selected in rest-frame > 100 μm emission, and the authors suspected that their overall tendency towards 'colder' IR SEDs was in part due to that long-wavelength selection. Our sample is selected on rest-frame ~ 15 μm emission, i.e., by warm dust; yet, we find a 'colder' average SED at a given luminosity than is found locally. This tends to support the interpretation that the offset which we and others have found towards colder temperatures at a given luminosity are at least in part a real difference. We suggest that this tendency toward colder dust temperature reflects a difference in dust and star formation geometry: whereas local LIRGs tend to be interacting systems with relatively compact very intense star formation and of comparable masses (e.g., Wang et al. 2006), $0.5 \lesssim z \lesssim 1$ LIRGs tend to be disk-dominated, relatively undisturbed galaxies (Zheng et al. 2004; Bell et al. 2005; Melbourne et al. 2005). We suggest that these disk galaxies host widespread intense star formation, like star formation in local spirals but scaled up, leading to relatively cold dust temperatures. This is consistent with what Chanial et al. (2006) found — the scatter in the $L_{IR} - T_{dust}$ relation for star-forming galaxies is largely induced by the size dispersion of the star-forming regions; and the IR luminosity surface density $\Sigma_{IR} - T_{dust}$ relation is more fundamental than the the $L_{IR} - T_{dust}$ relation. We examined the IR flux ratio f_{60}/f_{100} (indicator of dust temperature) as a function of the IR luminosity surface density for $z \sim 0.7$ star-forming galaxies. By taking galaxy size (i.e. half-light radius) derived from HST imaging (Häußler et al. 2007) as a proxy of the size of star-forming regions in a galaxy and 24 μm luminosity as a proxy of total IR luminosity, we split a sample of 311 24 μm-detected galaxies in the redshift slice $0.6 < z < 0.8$ into two bins in the 24-μm luminosity surface density Σ_{L24}. The average SEDs for the two subsets of galaxies were constructed in the same way as described in §4.1 and shown in the inner panel of Figure 11. The total IR luminosity is estimated as $\log(L_{IR}/L_\odot) = 11.3$ and 11.0 for the Σ_{L24}-high bin and the Σ_{L24}-low bin respectively. As shown in Figure 11, the two subpopulations are distributed along the dust-temperature sequence of local star-forming galaxies. Galaxies in the Σ_{L24}-high bin on average show hotter dust emission than those in the Σ_{L24}-low bin, suggesting that the IR luminosity surface density plays an essential role in shaping IR SED (Chanial et al. 2006).

Finally, with UV luminosities derived from GALEX data and IR luminosities derived from three band MIPS data, we determined a quite precise relationship between the dust obscuration and SFR for z ~0.7. Our results show an excellent agreement between the SFR-dust obscuration relation at z ~0.7 with that at the present day, indicating that no significant evolution occurs since that redshift. Our measurements give the mean values of SFR and dust obscuration. The actual scatter in dust obscuration can spread by 1 - 2 dex for individual galaxies of given SFR(Martin et al. 2005b; Xu et al. 2006; Buat et al. 2006). Reddy et al. (2006) claimed that the dust obscuration for star-forming galaxies is systematically smaller at $z \sim 2$ than the present day. Their sample is dominated by rest-frame UV-selected galaxies. This may lead to a potential selection bias against objects with high IR/UV ratio (see Buat et al. 2006 for the comparison between UV and FIR selected samples of local galaxies and a similar discussion). Therefore studies based on unbiased samples of high-redshift galaxies will help to answer the question whether the SFR-dust obscuration relation still holds at $z > 1$. This will add important constraints to our understanding of galaxy evolution involving star formation and metallicity enrichment (Zheng et al. 2006).

We are grateful to Daniel A. Dale and Kirsten K. Knudsen for helpful discussions. E. F. B. was supported by the Emmy Noether Programme of the Deutsche Forschungsgemeinschaft. Support for E. L. F.'s work was provided by NASA through the Spitzer Space Telescope Fellowship Program. This work was in part supported by contract 1255094 from JPL/Caltech to the University of Arizona. This research has made use of the NASA/IPAC Extragalactic Database (NED) which is operated by the Jet Propulsion Laboratory, California Institute of Technology, under contract with the National Aeronautics and Space Administration.

REFERENCES

Adelberger, K. L., & Steidel, C. C. 2000, ApJ, 544, 218
Appleton, P. N., et al. 2004, ApJS, 154, 147
Bell, E. F. 2003, ApJ, 586, 794
Bell, E. F., et al. 2005, ApJ, 625, 23
Borch, A., et al. 2006, A&A, 453, 869
Borys, C., et al. 2006, ApJ, 636, 134
Brand, K., et al. 2006, ApJ, 644, 143
Buat, V., et al. 2006, ApJS, in press (astro-ph/0609738)
Chanial, P., Flores, H., Guiderdoni, B., Elbaz, D., Hammer, F., & Vigroux, L. 2006, A&A in press (astro-ph/0610900)
Chapman, S. C., Helou, G., Lewis, G. F., & Dale, D. A. 2003, ApJ, 588, 186
Chary, R., & Elbaz, D. 2001, ApJ, 556, 562

Dale, D. A., et al. 2000, AJ, 120, 583
Dale, D. A., & Helou, G. 2002, ApJ, 576, 159
Dale, D. A., Helou, G., Contursi, A., Silbermann, N. A., & Kolhatkar, S. 2001, ApJ, 549, 215
Dale, D. A., et al. 2005, ApJ, 633, 857
Diolaiti, E., Bendinelli, O., Bonaccini, D., Close, L., Currie, D., & Parmeggiani, G. 2000, A&AS, 147, 335
Dole, H., et al. 2004a, ApJS, 154, 87
Dole, H., et al. 2004b, ApJS, 154, 93
Dole, H., et al. 2006, A&A, 451, 417
Elbaz, D., et al. 2002, A&A, 384, 848
Fazio, G. G., et al. 2004, ApJS, 154, 10
Flores, H., et al. 1999, ApJ, 517, 148
Flores, H., et al. 2004, A&A, 415, 885
Frayer, D. T., et al. 2006, AJ, 131, 250
Hammer, F., Flores, H., Elbaz, D., Zheng, X. Z., Liang, Y. C., Cesarsky, C 2005, A&A, 430, 115
Hauser, M. G., & Dwek, E. 2001, ARA&A, 39, 249
Häußler, B., et al. 2007, ApJ, submitted
Hopkins, A. M., Connolly, A. J., Haarsma, D. B., & Cram, L. E. 2001, AJ, 122, 288
Huang, J.-S., et al. 2004, ApJS, 154, 44
Kauffmann, G., et al. 2003, MNRAS, 341, 54
Lagache, G., Dole, H., & Puget, J.-L. 2003, MNRAS, 338, 555
Lagache, G., et al. 2004, ApJS, 154, 112
Lagache, G., Puget, J.-L., & Dole, H., 2005, ARA&A, 43, 727
Le Fèvre, O., et al. 2005, A&A, 439, 845
Le Floc'h, E., et al. 2005, ApJ, 32, 169
Lehmer, B. D., et al. 2005, ApJS, 161, 21
Marcillac, D., Elbaz, D., Chary, R. R., Dickinson, M., Galliano, F., & Morrison, G. 2006, A&A, 451, 57
Martin, D. C., et al. 2005a, ApJ, 619, L1
Martin, D. C., et al. 2005b, ApJ, 619, L59
Melbourne, J., Koo, D. C., & Le Floc'h, E. 2005, ApJ, 632, L65
Morrissey, P., et al. 2005, ApJ, 619, L7
Papovich, C., & Bell, E. F. 2002, ApJ, 579, L1
Papovich, C., et al. 2004, AppJS, 152, 163
Pope, A., et al. 2006, MNRAS, 370, 1185
Pozzi, F., et al. 2004, ApJ, 609, 122
Reddy et al. 2006, ApJ, 644, 792
Rieke, G. H., et al. 2004, ApJS, 154, 25
Rix, H.-W., et al. 2004, ApJS, 152, 163
Sajina, A., Scott, D., Dennefeld, M., Dole, H., Lacy, M. & Lagache, G. 2006, MNRAS, (astro-ph/0603614)
Soifer, B. T., & Neugebauer, G. 1991, AJ, 101, 354
Takeuchi, T. T., Buat, V., & Burgarella, D. 2005a, A&A, 440, L17
Takeuchi, T. T., Buat, V., Iglesias-Páramo, J., Boselli, A., & Burgarella, D. 2005b, A&A, 432, 423
Vanzella, E., et al. 2005, A&A, 434, 53
Vanzella, E., et al. 2006, A&A, 454, 423
Wang, J. L., Xia, X. Y., Mao, S. D., Cao, S., Wu, H., & Deng, Z. G. 2006, ApJ, 649, 722
Wolf, C., Meisenheimer, K., Rix, H.-W., Borch, A., Dye, S., & Kleinheinrich, M. 2003, A&A, 401, 73
Wolf, C., et al. 2004, A&A, 421, 913
Xu, K. C., Lonsdale, C. J., Shupe, d. L., Franceschini, A., Martin, C., & Schiminovich, D. 2003, ApJ,587, 90
Xu, K. C., et al. 2005, ApJ, 619, L11
Xu, K. C., et al. 2006, ApJ, 646, 834
Yan, L., et al. 2005, ApJ, 628, 604
Zheng, X. Z., et al. 2006, ApJ, 640, 784
Zheng, X. Z., Hammer, F., Flores, H., Assémat, F., & Pelat, D. 2004, A&A, 421, 847

2006

Astronomy & Astrophysics manuscript no. aa4446-05
March 9, 2006

Article published by EDP Sciences and available at http://www.edpsciences.org/aa
To be cited as: A&A preprint doi http://dx.doi.org/10.1051/20054446

The Cosmic Infrared Background Resolved by *Spitzer*.

Contributions of Mid-Infrared Galaxies to the Far-Infrared Background.

H. Dole[1], G. Lagache[1], J.-L. Puget[1], K. I. Caputi[1], N. Fernández-Conde[1], E. Le Floc'h[2,3], C. Papovich[2], P. G. Pérez-González[2], G. H. Rieke[2], and M. Blaylock[2]

[1] Institut d'Astrophysique Spatiale (IAS), bat 121, F-91405 Orsay, France; Université Paris-Sud 11 and CNRS (UMR 8617)
[2] Steward Observatory, University of Arizona, 933 N Cherry Ave, Tucson, AZ, 85721, USA
[3] Associated with Observatoire de Paris, GEPI, 92195 Meudon, France

Received: 31 October 2005; Accepted: 18 February 2006.

ABSTRACT

Aims. We quantify the contributions of 24 μm galaxies to the Far-Infrared (FIR) Background at 70 and 160 μm. We provide new estimates of the Cosmic Infrared Background (CIB), and compare it with the Cosmic Optical Background (COB).
Methods. Using Spitzer data at 24, 70 and 160 μm in three deep fields, we stacked more than 19000 MIPS 24 μm sources with $S_{24} \geq 60\mu$Jy at 70 and 160 μm, and measured the resulting FIR flux densities.
Results. This method allows a gain up to one order of magnitude in depth in the FIR. We find that the Mid-Infrared (MIR) 24 μm selected sources contribute to more than 70% of the Cosmic Infrared Background (CIB) at 70 and 160 μm. This is the first direct measurement of the contribution of MIR-selected galaxies to the FIR CIB. Galaxies contributing the most to the total CIB are thus $z \sim 1$ luminous infrared galaxies, which have intermediate stellar masses. We estimate that the CIB will be resolved at 0.9 mJy at 70 and 3 mJy at 160 μm. By combining the extrapolation of the 24 μm source counts below analysis, we obtain lower limits of 7.1 ± 1.0 and 13.4 ± 1.7 nW m^{-2} sr^{-1} for the CIB at 70 and 160 μm, respectively.
Conclusions. The MIPS surveys have resolved more than three quarters of the MIR and FIR CIB. By carefully integrating the Extragalactic Background Light (EBL) SED, we also find that the CIB has the same brightness as the COB, around 24 nW m^{-2} sr^{-1}. The EBL is produced on average by 115 infrared photons for one visible photon. Finally, the galaxy formation and evolution processes emitted a brightness equivalent to 5% of the primordial electromagnetic background (CMB).

Key words. Cosmology: observations – Cosmology: Diffuse Radiation – Galaxies: Evolution, Starburst, Infrared

1. Introduction

The Cosmic Infrared Background (CIB) is the relic emission at wavelengths larger than a few microns of the formation and evolution of the galaxies of all types, including Active Galactic Nuclei (AGN) and star-forming systems (Puget et al., 1996; Hauser et al., 1998; Lagache et al., 1999; Gispert et al., 2000; Hauser & Dwek, 2001; Kashlinsky, 2005). Characterizing the statistical behavior of galaxies responsible for the CIB – such as the number counts, redshift distribution, mean Spectral Energy Distribution (SED), luminosity function, clustering – and their physical properties – such as the roles of star-forming vs accreting systems, the density of star formation, and the number of very hot stars – has thus been an important goal (Partridge & Peebles, 1967). The SED of the CIB peaks near 150 μm. It accounts for roughly half of the total energy in the optical/infrared Extragalactic Background Light (EBL) (Hauser & Dwek, 2001), although still with some uncertainty (Wright, 2004; Aharonian et al., 2005). Since locally the infrared output of galaxies is only a third of the optical one (Soifer & Neugebauer, 1991), there must have been a strong evolution of galaxy properties towards enhanced Far-Infrared (FIR) output in the past. Understanding this evolution requires interpretation of cosmological surveys conducted not only in the infrared and submillimeter spectral ranges, but also at other wavelengths (Lagache et al., 2005).

The cryogenic infrared space missions IRAS (Infrared Astronomical Satellite) and ISO (Infrared Space Observatory) provided us with valuable insights to the IR-dominated galaxies in the Mid-Infrared (MIR) and FIR (Sanders & Mirabel, 1996; Genzel & Cesarsky, 2000; Dole, 2003; Elbaz, 2005; Lagache et al., 2005, for reviews). ISO MIR surveys were able to resolve a significant fraction of the 15 μm CIB (Elbaz et al., 1999, counts close

Send offprint requests to: Hervé Dole e-mail: Herve.Dole@ias.u-psud.fr

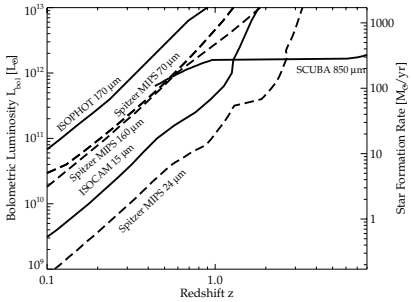

Fig. 1. Sensitivity to the bolometric luminosity (and star formation rate, assuming star forming galaxies) of various infrared and submillimeter experiments. Detections of at least 10 sources in the surveys can be made in the areas above the curves. We assumed the scenario of a typical deep survey. *ISOCAM* 15 μm ($S_\nu > 250\mu$Jy, 2 Sq. Deg.); *ISOPHOT* 170 μm ($S_\nu > 180$ mJy, 5 Sq. Deg.); *Spitzer/MIPS* 24 μm ($S_\nu > 80\mu$Jy, 5 Sq. Deg.); *Spitzer/MIPS* 70 μm ($S_\nu > 25$ mJy, 5 Sq. Deg.); *Spitzer/MIPS* 160 μm ($S_\nu > 50$ mJy, 5 Sq. Deg.); *SCUBA* 850 μm ($S_\nu > 1$ mJy, 1 Sq. Deg.); This plot makes use of the Lagache et al. (2004) model and their starburst SED for the conversion to L_{bol}. At $z \sim 1$, MIPS detects only ULIRGs in the FIR, and detects LIRGs in the MIR. The stacking analysis allows to gain an order of magnitude and to probe LIRGs in the FIR.

to convergence). Using model SEDs of galaxies (Chary & Elbaz, 2001; Xu et al., 2001; Lagache et al., 2003, for instance), the contribution of MIR-selected galaxies to the peak of the CIB (around 140 to 170 μm) can be inferred. Elbaz et al. (2002) derived that $64 \pm 38\%$ (16 ± 5 over 25 ± 7 nW m^{-2} sr^{-1}) of the 140 μm background is due to ISOCAM 15 μm galaxies, whose median redshift is $z \sim 0.8$.

The *Spitzer* Observatory (Werner et al., 2004) is performing much deeper and wider-area surveys, in particular at 24, 70 to 160 μm using the Multiband Imaging Photometer for *Spitzer* (MIPS) (Rieke et al., 2004). However, because of the limited angular resolution ("smoothing" the high spatial frequency signal in the FIR maps), deep MIPS 70 and 160 μm maps are confusion limited (Dole et al., 2003, 2004b) – the source surface density corresponds to 20 beams per source or less e.g. in the GTO fields. The FIR images do not allow us to directly probe the same galaxy population as that detected at 24 μm, where the extragalactic source confusion is less important. Figure 1 shows the typical sensitivity of MIPS surveys to the bolometric luminosity of galaxies as a function of redshift, using the modeled starburst SED of Lagache et al. (2004). At a redshift $z \sim 1$, MIPS FIR surveys are sensitive to ultraluminous IR galaxies (ULIRGs, $L \geq 10^{12} L_\odot$) where MIPS 24 μm surveys can probe luminous IR galaxies (LIRGs, $L \geq 10^{11} L_\odot$). It is therefor impossible to derive MIR and FIR SEDs of individual LIRGs at $z \sim 1$ and above.

MIPS can detect high redshift sources at 24 μm: about 25 to 30% of the population of galaxies lie at $z \geq 1.5$, at faint flux densities (down to few tens of μJy) (Le Floc'h et al., 2004; Egami et al., 2004; Lonsdale et al., 2004; Chary et al., 2004; Houck et al., 2005; Pérez-González et al., 2005; Caputi et al., 2006). Papovich et al. (2004) showed that MIPS surveys resolve about 70% of the 24 μm IR galaxy CIB for $S_{24} \geq 60$ μJy. In comparison, MIPS 70 and 160 μm (Dole et al., 2004a) surveys detect only about 20% and less than 10% of the CIB at 70 and 160 μm, respectively. Programs of very deep 70 μm imaging on small fields (e.g. D. Frayer, private communication) are likely to resolve a larger fraction, but due to confusion noise the FIR CIB will still not be significantly resolved into individual sources, while the MIR CIB at 24 μm is well resolved.

In this paper, we use a stacking analysis method that takes advantage of the good sensitivity of the MIPS 24 μm MIR channel, to fill the sensitivity gap between the MIR and the FIR surveys. By stacking the FIR data at the locations of MIR sources, we statistically investigate the FIR properties of 24 μm-selected galaxies. In particular, we quantify the contribution of the 24 μm resolved galaxies to the 70 and 160 μm background, put strong lower limits to the CIB, and give new estimates of the 70 and 160 μm background.

Throughout this paper, we adopt a cosmology with $h = 0.65$, $\Omega_M = 0.3$ and $\Omega_\Lambda = 0.7$. The surface brightnesses (e.g. of the CIB) are usually expressed in units of MJy/sr or nW m^{-2} sr^{-1}. For a given frequency ν in GHz and wavelength λ in microns, the conversion between the two is given by:

$$1nW\,m^{-2}\,sr^{-1} = \frac{100}{\nu/GHz} MJy/sr = \frac{\lambda/\mu m}{3000} MJy/sr \quad (1)$$

2. Data and Sample

The data for our analysis are from the *Spitzer* MIPS Guaranteed Time Observations (GTO) cosmological surveys performed in three fields: the Chandra Deep Field South (CDFS), the Hubble Deep Field North (HDFN) and the Lockman Hole (LH). The MIPS observations at 24 μm are detailed in Papovich et al. (2004) and at 70 and 160 μm in Dole et al. (2004a). Each field covers about 0.4 square degrees, and the integration times per sky pixel are 1200s, 600s and 120s at 24, 70 and 160 μm, respectively. The data were reduced and mosaicked using the Data Analysis Tool (Gordon et al., 2005). We make use of a recent new analysis of the calibration by the instrument team and the instrument support team that will soon be adopted officially. The uncertainty is now 4%, 7% and 12% at 24, 70 and 160 μm, respectively, and the calibration level has been changed by less than 10% compared with the previous determinations (See the Spitzer Science Center calibration pages[1]).

Papovich et al. (2004) showed that the 80% completeness level at 24 μm in the GTO deep fields is reached at $S_{24} = 80\mu$Jy. Nevertheless, Papovich et al. (2004) and Chary et al. (2004) show that the detection of very faint 24 μm sources, down to $S_{24} \sim 30\mu$Jy, is possible, but with a increased photometric uncertainties and reduced completeness (to lower than 5% at the GTO depth and 20% at the GOODS depth).

Dole et al. (2004a) showed that at 70 and 160 μm sources can be safely extracted down to 15 mJy and 50 mJy, respectively. The Frayer et al. (2006) results go deeper. However, confusion limits the extraction of sources fainter than typically 56 μJy at 24 μm, 3.2 mJy at 70 μm, and 36 mJy at 160 μm (Dole et al., 2004b). A priori information on the existence of a source deduced from shorter wavelength and less confusion-limited observations can extend the reliable detection threshold below this nominal confusion limit.

To implement this approach, we build a sample as follows:

- We select the central part of each field where all 3 MIPS wavelengths have a common sky coverage and maximum redundancy. This area covers 0.29 Sq. Deg in the CDFS and LH, and 0.27 Sq. Deg. in HDFN, for a total of 0.85 Sq. Deg. in these three fields.
- In these selected areas, we identify every MIPS 24 μm source with $S_{24} \geq 60\mu$Jy. This flux density limit corresponds to 50% completeness (Papovich et al., 2004). There are 6543 galaxies above this limit in CDFS, 6039 in the HDFN, and 6599 in the LH. The total number of sources considered in the three fields is thus 19181.

To analyze this sample, we proceed as follows:

- In each field, we sort the 24 μm sources by decreasing flux density S_{24}.
- We put the sources in 20 bins of flux density for $S_{24} \geq 60\mu$Jy. These bins have equal logarithmic width $\Delta S_{24}/S_{24} \sim 0.15$, except for the bin corresponding to the brightest flux, which includes all the bright sources (0.92mJy to 1Jy).
- We correct the average flux obtained by stacking each S_{24} bin for incompleteness, following the correction of Papovich et al. (2004) (their figure 1). Since the bins between 60 and 80 μJy are complete to the 50-80% level, only the weakest fluxes bins are significantly corrected.

3. Stacking Analysis

The process of stacking the sources based on the 24 μm detections allows us to measure more of the total contribution of 70 and 160 μm sources to the CIB.

[1] http://ssc.spitzer.caltech.edu/mips/calib/conversion.html

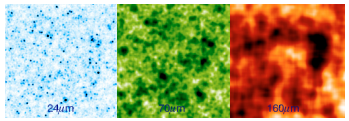

Fig. 2. Images at 24, 70 and 160 μm (left to right) of stacked sources in the brightest bin of 24 μm flux density, with a random position offset added before each sum. Color coding: dark is high flux, light is low flux. This allows us to check that the stacking method does not introduce any artifacts, i.e. a false source detection in the center.

3.1. Processing

At 24 μm, the detector pixel size is 2.5 arcseconds, the FWHM of the point spread function (PSF) is 6 arcseconds, and the plate scale of the mosaic is chosen to be 1.25 arcseconds. At 70 μm, the detector pixel size is 9.9 arcseconds, the FWHM of the PSF is 18 arcseconds, and the plate scale of the mosaic is chosen to be 4.5 arcseconds. At 160 μm the detector pixel size is 18 arcseconds, the FWHM of the PSF is 40 arcseconds, and the plate scale of the mosaic is chosen to be 18 arcseconds (Rieke et al., 2004; Gordon et al., 2005, for more details). The 70 and 160 μm mosaics have been resampled to the scale of the 24 μm mosaic (1.25 arcseconds per pixel) using a bilinear interpolation. This last step greatly facilitates the weight management of the three maps, since each has different coverage, and it allows easy extraction of the signal at the three wavelengths for the same sky position.

For each S_{24} flux density bin we select every 24 μm source, extract a square image about 440 arcseconds on a side centered on the source, and store it. We proceed similarly on the mosaics at 70 and 160 μm, extracting images at the position of each 24 μm source regardless of the presence of a detected FIR source. The products at this stage are thus three cubes of data at 24, 70 and 160 μm with the same dimensions (same number of source images and same box size) for each of the 24 μm flux density bins.

We then add the images in each cube at each wavelength, to generate a stacked image of sources at 24, 70 and 160 μm for a given S_{24} flux bin. This operation is a simple sum, without any outlier rejection. When stacking, we rotate each image by $+\pi/2$ with respect to the previous one (and so on), to cancel out the large-scale background gradients such as the prominent zodiacal background at 24 μm. This processing is done both in each field separately as well as using all the data at once. Unless otherwise stated, we use the stacked data of all the fields together in the rest of this paper. We checked that no significant signal was detected when we added a random or systematic artificial offset to each 24 μm position and then performed exactly the same sub-image extraction and stacking as we did for the real 24 μm source list. Figure 2 shows the results of stacking the sources (only from the brightest bin), with a random position offset

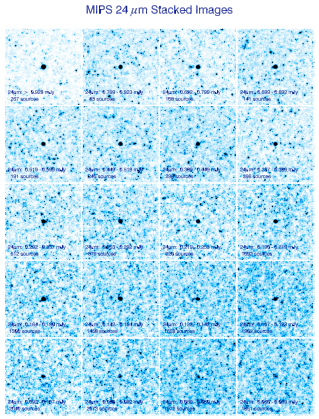

Fig. 3. Images at 24 μm of stacked sources in bins of 24 μm flux density ($S_{24} \geq 60\,\mu$Jy) in the three MIPS GTO Fields: CDFS, HDFN, and LH covering about 0.85 Sq. Deg. A total number of 19181 sources has been used. The number of sources used in the sum in each S_{24} bin is reported. Each image has 350 × 350 pixels of 1.25 arcsec, thus covering about 7.3 × 7.3 Sq. Arcmin. Since no outlier rejection has been made, other sources can be seen in the surroundings of the stacked sources .

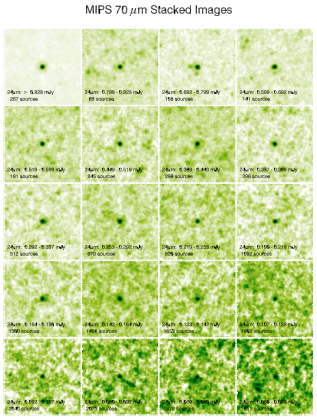

Fig. 4. Images at 70 μm of stacked sources in bins of 24 μm flux density. See caption of Figure 3 for details.

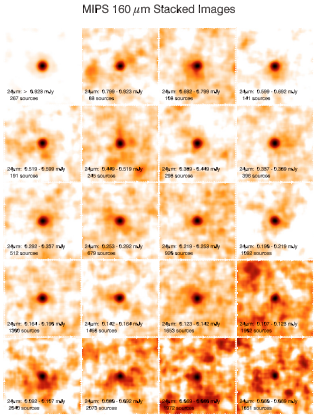

Fig. 5. Images at 160 μm of stacked sources in bins of 24 μm flux density. See caption of Figure 3 for details.

added prior to the sum. No source appears in the center, as expected. This guarantees that the stacking method does not introduce an artifact that mimics a source.

Since the stacking analysis aims at statistically detecting faint unresolved sources at 70 and 160 μm, in principle there is no need to also stack data at 24 μm, where all sources are resolved. However, doing so allows us to double-check the method, since we know by design what the stacked photometry should be.

3.2. Stacked Images and Photometry

The final stacked images at 24, 70 and 160 μm as a function of the 24 μm flux density S_{24} are presented in figures 3, 4, and 5, respectively. We report also in these figures the number of sources stacked in each of the S_{24} bins. The figures show clear detections of stacked sources at 70 and 160 μm for every S_{24} bin, even the faintest corresponding to $60 \leq S_{24} < 69\,\mu$Jy. Given the surface density of the 24 μm sources at 60 μJy of $(9.6 \pm 0.04) \times 10^7$ sr^{-1} (Papovich et al., 2004), this translates to 1.04 and 0.2 beams per source at respectively 70 and 160 μm (Dole et al., 2003, using beams from their Table 1). This is

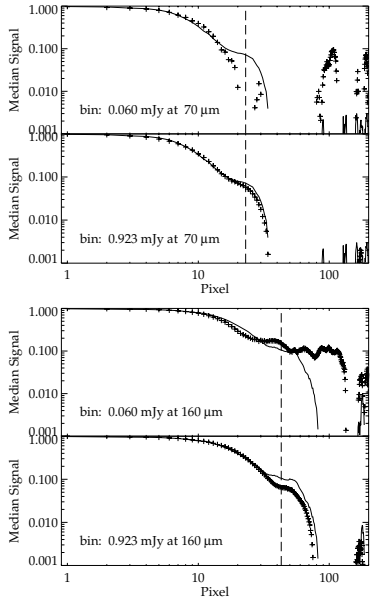

Fig. 6. Normalized radial profiles of the stacked images. The crosses represent the data, and the solid line the empirical PSF. The vertical dotted lines show the radii of the aperture used for photometry. From top to bottom: faintest S_{24} bin at 70 μm; Brightest S_{24} bin at 70 μm; Faintest S_{24} bin at 160 μm; Brightest S_{24} bin at 160 μm .

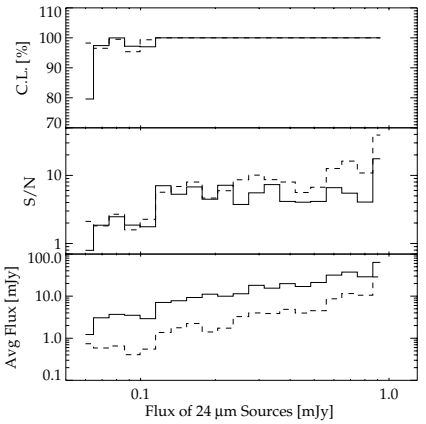

Fig. 7. Top: Confidence Level of the detections at 70 (dash) and 160 μm (solid) on stacked images (Fig. 4 and 5), as a function of the S_{24} bin. Middle: Signal-to-Noise ratio, as computed from a Gaussian fit to the flux distribution measured on about 2000 positions; this S/N is not relevant at low flux (see Sect. 3.2). Bottom: average flux in mJy per stacked source. Note that a different number of sources have been stacked in each bin.

well beyond the confusion limits at these FIR wavelengths (Dole et al., 2004b). This statistical detection of FIR sources already demonstrates the great potential of this technique to probe FIR galaxies down to levels below the confusion, thanks to the excellent quality of the pointing and the stability of the effective PSF (see below).

We check that the radial profile of the stacked sources is in agreement with the PSF profile, at each wavelength and for each flux bin. We show in Figure 6 two profiles at each wavelength corresponding to the extreme cases: the brightest and faintest S_{24} flux bins. We used both the empirical PSF (from bright sources) and the modeled STinyTim MIPS PSF (Krist, 1993; Rieke et al., 2004; Gordon et al., 2005). At large S_{24}, the stacked radial profiles at 70 and 160 μm (bottom plots in Figure 6) agree well with the PSF in the central part. At the faintest fluxes (top plots), the agreement is good down to about 10% of the peak brightness. Since the stacked images visually represent the 2-dimensional correlation function of galaxies, the potential presence of many neighboring sources at small scales (source clustering) might have widened the radial profile, which is not observed; thus source clustering does not contribute significantly to the noise budget.

We measure the flux density of the stacked sources with aperture photometry and correct for aperture size. The radii of the apertures and reference annulus are, in arcseconds: $(r_{aper},\ r_{int},\ r_{ext}) = (12.2,\ 17,\ 24)$, (30, 49, 79) and (54, 90, 126) for 24, 70 and 160 μm, respectively. These radii correspond to approximatively 3, 5 and 7 times the FWHM in the FIR and 2, 3, 4 times the FWHM in the MIR. We measured the noise in each image by using about 2000 measurements on random positions. We compute the confidence level (C.L.) of each detection (top of Figure 7) using the cumulative distribution of the noise measurements. The deviation from 100% of the C.L. is the probability that the noise creates a spurious source. For the faintest bin, the C.L. is around 80%, and it rises to 97% for the next four bins, and stays at 100% for the brighter S_{24} bins. We fitted a Gaussian function to the distribution of noise to get the standard deviation in order to estimate the S/N ratio. This method works for the brighter bins (middle panel in Figure 7), where the flux distribution is indeed nearly a Gaussian distribution. In this range, the S/N values have a median of 8 at 70 μm and 7 at 160 μm. In the three faintest bins, the noise distribution is not Gaussian, because of the presence of slightly

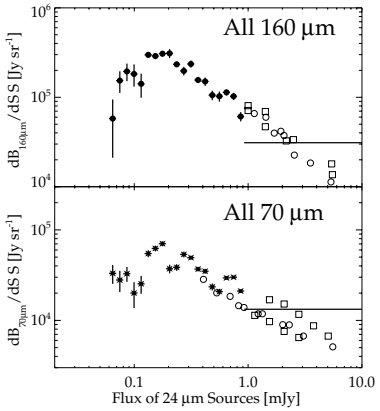

Fig. 8. Contributions to the CIB: brightness of stacked sources at 160 and 70 μm per logarithmic bin $\frac{dB_\lambda}{dlog(S_{24})}$ (solid symbols), as a function of the 24 μm flux, in all three MIPS GTO Fields. A completeness correction has been applied. The highest flux bin goes up to 1Jy. Open symbols: published differential source counts multiplied by $S_{24}^{-0.5}$ and a color ratio of bright galaxies (160/24=60 and 70/24=20, cf the brightest bin in the lower panel of Fig. 7); Square: Dole et al. (2004a); Circle: Frayer et al. (2006). There is a good agreement between the source counts, the brightest stacked bin, and the fainter stacked bins.

brighter sources; the Gaussian fit is therefore not relevant and we opt for the C.L. technique. The bottom plot in Figure 7 shows the average FIR flux per stacked galaxy. A set of ∼100μJy MIR-selected galaxies would have a typical average FIR flux of ∼ 0.5 and 3 mJy if taken individually at 70 and 160 μm, respectively. Since the confusion limits are at about 3 and 40 mJy at these wavelengths (Dole et al., 2004b), the gain of the stacking analysis technique is one order of magnitude in flux compared to individual detection. Finally, it is not necessary to remove the brightest sources for the goals of this paper, because we stack typically 1000 to 2000 galaxies per flux bin, so their influence is negligible except maybe in the 3 faintest bins.

The brightness of the stacked sources at 70 and 160 per logarithmic flux density bin, or $\frac{dB_\lambda}{dlog(S)}$, as a function of the 24 μm flux bin, is presented in figure 8. B_λ in MJy/sr is defined as the total stacked flux density divided by the survey area. Using a logarithmic flux density bin allows direct comparison of the contribution in energy of each bin to the CIB, and is directly related to the differential source counts with a scaling factor $S_\nu^{-0.5}$. In the range $100 \leq S_{24} \leq 300\,\mu$Jy, both contributions to the CIB present a maximum, which shows that the contributions have reached convergence. Converting S_{70} and S_{160} into S_{24} using the color ratios of 9 and 30 (see Table 2 below), this means the FIR CIB will be mainly resolved at $S_{70} \sim 0.1 \times 9 = 0.9$ mJy and at $S_{160} \sim 0.1 \times 30 = 3$ mJy. We have also plotted the source counts of Dole et al. (2004a) and Frayer et al. (2006); we used the conversion to S_{24} as given by color ratios relevant for bright galaxies of 20 and 60 at 70 and 160 μm, measured on the very bright end of the bottom plot in Figure 7. Despite this simplifying assumption of a single color ratio, there is excellent agreement between the brightness derived from the stacking analysis and the source counts. This plot can be used to constrain models of galaxy evolution.

Sample variance plays a role in these results. To probe its effects, we split each of our three fields (CDFS, HDFN, LH) into four subfields of about 250 square arcmin each, and performed an independent analysis on each of these twelve subfields. We obtain contributions varying in some cases by as much as a factor of two (peak-to-peak). For instance, computing the standard deviation of the distribution of the cumulative 160 μm flux (the faintest points in Figure 10) measured over these 12 subfields gives $\sigma = 0.3$ MJy/sr and a mean and median both of 0.53 MJy/sr. Renormalizing by the twelve sub-fields gives $\sigma = 0.09$: the uncertainty induced by the Large Scale Structure variations across the fields is of order 15%.

From here on in this paper, our error budget takes into account: 1) the calibration uncertainties; 2) the photometric uncertainty; 3) the large-scale structure (sample variance).

4. Contributions of Mid-Infrared Galaxies to the Cosmic Infrared Background

4.1. Value of the Cosmic Infrared Background Brightness

To compute the fraction of background resolved with the stacking analysis of the MIPS data, we first need to review the measurements of the total CIB, in particular at 24, 70 and 160 μm. It should be remembered that the total cosmic background contains the contribution of all extragalactic sources but also more diffuse emissions, e.g. from dust in galaxy clusters (Montier & Giard, 2005). Furthermore the extragalactic sources are expected to be mostly galaxies but it cannot be excluded that other lower luminosity sources, population III stars for instance, contribute significantly but will not be detected directly in the present deep surveys.

Measuring the CIB directly by photometry is particularly difficult because one needs 1) an absolute photometer and 2) a proper estimate of the foreground. The two FIR channels of MIPS are not absolute photometers for the very extended spatial scales, since no internal calibrated reference can be observed to calibrate absolutely the slow response. A better knowledge of the instrument in the future may allow a proper absolute calibration, using its "Total Power" mode, similarly to what has been done successfully in the past, e.g. with ISOPHOT at 170 μm on some selected low surface brightness fields (Lagache & Dole, 2001). However, MIPS is by design well calibrated for small spatial scales, e.g., point sources, because the frequent stimulator flashes and the scanning strategy (acting like a chopping mode) properly track the fast response of the photoconductors (Gordon et al., 2005, 2006, for instance). For these reasons, we do not use MIPS as an absolute photometer to estimate the level of the CIB and the foregrounds, but as a detector of small scale fluctuations to resolve the CIB based on 24 μm source observations. Our approach has the important advantage that it is not biased by the foregrounds and their modeling, which can lead to significant errors.

We therefore start by reviewing the direct measurements, using absolute photometry in large beams, provided mainly by the COBE FIRAS and DIRBE experiments and also the IRTS and rocket experiments in the near infrared ($< 3\mu$m). These measurements can be combined with indirect upper limits derived from observations of gamma rays from distant Blazars at TeV energies.

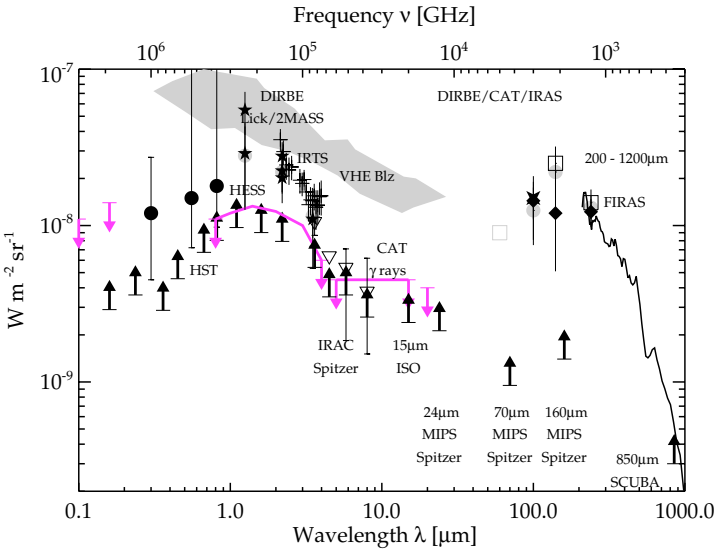

Fig. 9. Current measurements of the Extragalactic Background Light Spectral Energy Distribution from 0.1 μm to 1 mm, showing the Cosmic Optical Background (COB, with $\lambda \leq 8$ μm) and the Cosmic Infrared Background (CIB, with $\lambda > 8$ μm). Black arrows represent lower limits. Purple arrows and lines represent upper limits. The EBL observational constraints come from: Edelstein et al. (2000) at 0.1 μm using Voyager UVS; Brown et al. (2000) and Gardner et al. (2000) with HST/STIS [lower limits]; Madau & Pozzetti (2000) with HST (incl. NICMOS) and Thompson (2003); Bernstein et al. (2002) corrected by Mattila (2003) [filled circles]; Matsumoto et al. (2005) between 2.2 and 4 μm using the *IRTS* [thin plus]; Gorjian et al. (2000) at 2.2 and 3.3 μm using *DIRBE* and *Lick*; Wright (2001) and Cambresy et al. (2001) at 1.25 and 2.2 μm using *DIRBE* and *2MASS* [five branch star]; *DIRBE* values from Wright (2004) from 1.25 to 240 μm [gray circles]; *Spitzer IRAC* 3.6, 4.5, 5.8 and 8.0 μm lower limits from number counts by Fazio et al. (2004); fluctuation analysis with IRAC by Savage & Oliver (2005) (open triangles); Schroedter (2005) using Very High Energy Blazars, 98% confidence upper limit [gray region]; H.E.S.S upper limit from Aharonian et al. (2005) using P0.55 [solid line between 0.8 and 4 μm]; Renault et al. (2001) upper limits from 5 to 15 μm using the *CAT* in the γ-rays on Mkn501; Elbaz et al. (1999) lower limit at 15 μm using galaxy counts with *ISOCAM*; upper limit at 20 μm by Stecker & De Jager (1997) on Mkn421; lower limit from galaxy counts at 24 μm with MIPS by Papovich et al. (2004); an indirect evaluation at 60 μm using fluctuations in IRAS data from Miville-Deschênes et al. (2002) [open gray square]; lower limits at 70 and 160 μm using galaxy counts with MIPS by Dole et al. (2004a); an estimate of the CIB at 100 μm using *CAT* and *DIRBE* Renault et al. (2001) [four branch star]; Lagache et al. (2000) at 100, 140 and 240 μm using *DIRBE* and WHAM, updated in the present work [diamond]; Hauser et al. (1998) at 140 and 240 μm using *DIRBE* [open square]; Smail et al. (2002) lower limit at 850 μm using galaxy counts with *SCUBA*; Lagache et al. (2000) spectrum between 200 μm and 1.2mm using *FIRAS* [solid line above 200 μm]. The IDL script to generate this figure is available on the web: http://www.ias.u-psud.fr/irgalaxies.

To use the FIRAS and DIRBE data to provide CIB absolute measurements requires an accurate component separation. Local extended emission from interplanetary and interstellar dust can be removed using their specific SEDs and anisotropic spatial distributions traced independently, as well as time variability for the zodiacal emission and scattering (Hauser & Dwek, 2001, for instance). Early gamma ray data from Blazars from the CAT experiment led to upper limits on the CIB intensity significantly lower than the DIRBE residuals as pointed out by Renault et al. (2001) and Wright (2004). Recent results on more distant Blazars (Schroedter, 2005; Aharonian et al., 2005) constrain the CIB even more in the near and thermal infrared. Together with lower limits obtained by integrating the galaxy counts from *HST*, *ISO*, and *Spitzer*, these measurements tightly constrain the Extragalactic Background Light between ~ 0.8 to ~ 20 μm.

At 160 μm, the CIB can be interpolated from the DIRBE/COBE measurements at 100 μm (Lagache et al., 2000) and 140 and 240 μm (Hauser et al., 1998): 0.78±0.21, 1.17±0.32, 1.09±0.20 MJy/sr, respectively. If the FIRAS photometric scale is used in the calibration (rather than the DIRBE photometric calibration), lower values are obtained at 140 and 240 μm: 0.7 MJy/sr and 1.02 MJy/sr (Hauser et al., 1998). A large uncertainty in the determinations at 100 and 140 μm comes from the zodiacal emission removal, as is also true at 60 μm. The DIRBE zodiacal emission model was obtained by Kelsall et al. (1998) relying on the variability with viewing geometry. Its accuracy can be estimated *a posteriori* using the residuals observed at wavelengths where the zodiacal emission is at a maximum (12 and 25 μm). The residual emission, obtained by Hauser et al. (1998), has in fact a spectrum very similar to the zodiacal one. The residuals are about 4.7×10^{-7} Wm^{-2}sr^{-1} at 12 and 25 μm, far above the upper limit derived by high-energy experiments like H.E.S.S. (Aharonian et al., 2005), but not very much larger than the uncertainties of the Kelsall et al. (1998) zodiacal emission model. A conservative estimate of the amount of zodiacal emission not removed in this model at 12 and 25 μm is therefore about 4×10^{-7} Wm^{-2}sr^{-1}. Using the Kelsall et al. (1998) smooth high latitude zodiacal cloud colors, the amount not removed at 100, 140 and 240 μm translates to 0.30, 0.14, 0.045 MJy/sr, respectively. This reduces the CIB from 0.78 to 0.48 MJy/sr at 100 μm, from 1.17 to 1.03 at 140 μm and from 1.09 to 1.05 at 240 μm. Adopting the FIRAS photometric scale gives at 140 and 240 μm, 0.56 and 0.98 MJy/sr respectively. From the above discussion, we see that the CIB at 140 μm – the closest in wavelength to the 160 μm MIPS bandpass – is still uncertain by a factor of about 2 because of the uncertainty in the zodiacal level. The DIRBE/FIRAS measurement of the CIB at 240 μm suffers less from zodiacal residuals and photometric calibration uncertainty.

A firm upper limit of 0.3 MJy/sr at 60 μm has been derived by Dwek & Krennrich (2005) using observations of TeV gamma ray emission from distant AGNs. Miville-Deschênes et al. (2002) uses a fluctuation analysis of IRAS maps to set an upper limit of 0.27 MJy/sr and give an estimate of 0.18 MJy/sr, on the assumption that the level of fluctuations-to-total intensity ratio is not strongly wavelength dependent.

Table 1. Contribution to the CIB of $S_{24} \geq 60$ μJy galaxies. Sources of uncertainty come from photometry, calibration, and large scale structure. The CIB column gives the best estimate from the discussion in Sect. 4.1.

λ μm	νI_ν nW m^{-2} sr^{-1}	B$_\lambda$ MJy/sr	CIB MJy/sr	% CIB resolved
24	2.16 ± 0.34	$0.017 \pm 15\%$	0.022	79
70	5.93 ± 1.02	$0.138 \pm 17\%$	0.15	92
160	10.70 ± 2.28	$0.571 \pm 21\%$	0.82	69

At 24 μm we use for the contribution of IR galaxies to the CIB the estimate of Papovich et al. (2004) of $2.7^{+1.1}_{-0.7}$ nW m^{-2} sr^{-1}. This value comes from 1) integration of the source counts down to 60 μJy giving 1.9 ± 0.6 nW m^{-2} sr^{-1}; 2) extrapolation of the source counts to lower fluxes, giving a contribution of $0.8^{+0.9}_{-0.4}$ nW m^{-2} sr^{-1}; and 3) upper limits from Stecker & De Jager (1997) and from CAT (Renault et al., 2001).

The most constraining measurements and lower and upper limits on the Cosmic Optical Background (COB) and the CIB from 0.1 μm to 1 mm are all reported in Figure 9. The Lagache et al. (2004) model predicts a CIB at 240 μm of 0.98 MJy/sr, which is in very good agreement with the estimate from combined measurements discussed above. Furthermore this model agrees with the observational constraints (e.g. number counts, CIB intensity and fluctuations). We can thus take the CIB values from this model as a reasonable interpolation between the better constrained CIB values at shorter and longer wavelengths: 0.82 MJy/sr at 160 μm, and 0.15 MJy/sr at 70 μm.

4.2. Contributions from MIR Sources with $S_{24} \geq 60\mu Jy$

To estimate the contribution of MIR sources to the background, we add up the brightnesses of all the S_{24} bins to get the integrated light at 24, 70 and 160 of all the resolved 24 μm sources. Each S_{24} bin is corrected for incompleteness. The results are presented Table 1, and Figure 10 shows the cumulative integrated light from galaxies in the FIR as a function of S_{24}. For a sanity check, we obtain that at 24 microns the percentage of the CIB that is resolved is 79%, which is in agreement with Papovich et al. (2004) within the error bars. At 70 and 160 micron we resolve 92% and 69% of the background, respectively.

Half of the 24 μm CIB is resolved by sources with $S_{24} \geq 190\mu$Jy. In the FIR, half of the 70 μm CIB is resolved by 24 μm sources brighter than $S_{24} \sim 220\mu$Jy, and half of the 160 μm CIB is resolved by 24 μm sources brighter than $S_{24} \sim 130\mu$Jy. This difference between 70 and 160 suggests that the CIB at 160 μm is dominated by galaxies at slightly higher redshift than at 70 μm, a consequence of the spectral shape of LIRGs and ULIRGs or, equivalently, the effect of k-correction. This point is illustrated in figures 5 and 6 of the review by Lagache et al. (2005).

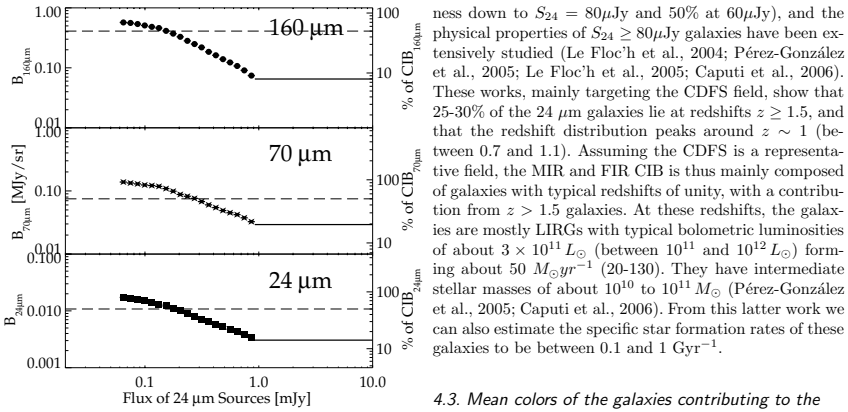

Fig. 10. Cumulative brightness (left axis, in MJy/sr) and fraction of the background resolved (right axis) at 160, 70 and 24 μm (from top to bottom), as a function of the 24 μm flux in the three combined MIPS GTO Fields. A completeness correction has been applied based on the incompleteness level of the 24 μm sample. The horizontal dashed line represents 50% of the CIB at each wavelength.

To put in perspective the problem of resolving the CIB and what the stacking analysis accomplishes, we plot in figure 11 the new observed constraints on the extragalactic background SED. The fraction of the CIB resolved at MIPS wavelengths by unbiased surveys was 79%, 20% and 7% at respectively 24, 70 and 160 μm (Papovich et al., 2004; Dole et al., 2004a). When using the present stacking analysis, this fraction rises to 92% and 69% at 70 and 160 μm respectively, and is represented by the red lower limits (see also Table 1).

Based purely on observations without modeling of galaxy SEDs, we find that most of the FIR background is resolved into MIR galaxies. This confirms the model-dependent result of Elbaz et al. (2002). This analysis is the first direct resolution of the CIB simultaneously in the MIR and the FIR.

Moreover, we can now securely establish the physical parameters of the typical galaxies responsible for most of the CIB near its peak. Previous studies based on ISO already characterized the 15 μm population (Flores et al., 1999; Elbaz & Cesarsky, 2003; Franceschini et al., 2003, for instance); see Lagache et al. (2005) for a review. Our 24 μm sample is almost complete in flux (80% completeness down to $S_{24} = 80\mu$Jy and 50% at 60μJy), and the physical properties of $S_{24} \geq 80\mu$Jy galaxies have been extensively studied (Le Floc'h et al., 2004; Pérez-González et al., 2005; Le Floc'h et al., 2005; Caputi et al., 2006). These works, mainly targeting the CDFS field, show that 25-30% of the 24 μm galaxies lie at redshifts $z \geq 1.5$, and that the redshift distribution peaks around $z \sim 1$ (between 0.7 and 1.1). Assuming the CDFS is a representative field, the MIR and FIR CIB is thus mainly composed of galaxies with typical redshifts of unity, with a contribution from $z > 1.5$ galaxies. At these redshifts, the galaxies are mostly LIRGs with typical bolometric luminosities of about 3×10^{11} $L_\odot$ (between 10^{11} and 10^{12} $L_\odot$) forming about 50 $M_\odot yr^{-1}$ (20-130). They have intermediate stellar masses of about 10^{10} to 10^{11} $M_\odot$ (Pérez-González et al., 2005; Caputi et al., 2006). From this latter work we can also estimate the specific star formation rates of these galaxies to be between 0.1 and 1 Gyr^{-1}.

4.3. Mean colors of the galaxies contributing to the CIB

Looking at the 24 μm number counts of Papovich et al. (2004), one can see that the bulk of 24 μm CIB is mainly due to sources with $130 \leq S_{24} \leq 400$ μJy. We select three cuts in S_{24} to investigate the colors of the contributions to the CIB by different galaxy populations. In the following, redshifts come from Caputi et al. (2006) (see their figure 5), and the relative contributions come from the integration of the Papovich et al. (2004) source counts and the Lagache et al. (2004) model. The cuts are:

- Above 400 μJy: bright galaxies contributing about 25% to the 24 μm CIB. The redshift distribution has a mean of 0.53 and a median of 0.44.
- $130 \leq S_{24} \leq 400$ μJy: galaxies contributing the most to the 24 μm CIB, about 30%. The redshift distribution has a mean of 1.18 and a median of 1.03.
- $60 \leq S_{24} \leq 130$ μJy: fainter galaxies with relatively low contributions to the 24 μm CIB (about 15%). The redshift distribution has a mean of 1.27 and a median of 1.11. The sample becomes incomplete at $60 \leq S_{24} \leq 80\mu$Jy, so the mean redshift may be underestimated.

The observed colors change systematically with S_{24}, as can be seen in the bottom of figure 7: S_{70} vs S_{24} shows a slope larger than one, when S_{160} vs S_{24} shows an average slope of the order of unity. Table 2 gives the colors and their associated 1σ uncertainties in the three bins. The 160/24 color is compatible with a constant of 33. The 70/24 color increases with the flux from 6.3 to 9.6. Finally, the 160/70 color steadily decreases with flux.

These colors can be interpreted as the SED of a LIRG being redshifted, since fainter 24 μm sources lie at larger redshifts: the 160/70 ratio increases (with decreasing flux) because the peak of the big grains' FIR spectrum is shifted longwards of 160 μm. The color ratios involving the 24 μm band are less obvious to interpret, since the Polycyclic Aromatic Hydrocarbon (PAH) (Puget & Leger, 1989) fea-

Table 2. Mean observed colors in I_ν of $S_{24} \geq 60$ μJy galaxies contributing to the CIB.

S_{24} in μJy	160/70	160 / 24	70 / 24
$S_{24} \geq 400$	3.2 ± 0.4	29.7 ± 3.8	9.6 ± 0.8
$130 \leq S_{24} \leq 400$	4.4 ± 0.5	40.6 ± 4.2	9.4 ± 0.9
$60 \leq S_{24} \leq 130$	5.3 ± 1.6	32.7 ± 6.8	6.3 ± 1.1
CIB[a]	5.5	38.0	6.9

[a] Data and Model; See Sect. 4.1

Table 3. Contributions of the 24 μm galaxies to the FIR CIB in nW m^{-2} sr^{-1}. For the $S_{24} \leq 60$ μJy galaxies, a simple color extrapolation has been used, as described in Sect. 5.

	24 μm	70 μm	160 μm
> 60 μJy	2.16 ± 0.26	5.9 ± 0.9	10.7 ± 1.6
< 60 μJy[a]	0.54	1.2 ± 0.2	2.6 ± 0.5
total CIB[b]	2.7[c]	7.1 ± 1.0	13.4 ± 1.7
CIB prior [c]	2.7[c]	6.4[c]	15.4[c]

[a] Estimate using an extrapolation from 60 to 0 μJy.
[b] CIB estimate due to IR galaxies.
[c] Data and Model; See discussion Sect. 4.1

tures (especially between 6.2 and 8.6 μm) and the silicate absorption feature are redshifted into and then out of this band. The 70/24 ratio evolution might have for its origin a mix of PAH (increasing the 24) and very small grains continuum (decreasing the 70) being redshifted, that cancel out each other.

If one wants to extrapolate the contribution of fainter ($S_{24} \leq 60$ μJy) MIR galaxies to the FIR CIB, a conservative approach is to use a constant 160/24 and 70/24 color ratio for the unresolved population. To set these ratios, we take the colors from the faintest population ($60 \leq S_{24} \leq 130$ μJy); this faint population presumably has the closest characteristics to the unresolved one. We will therefore use $I_{160}/I_{24} = 32.7 \pm 6.8$, and $I_{70}/I_{24} = 6.3 \pm 1.1$ (from Table 2). Since the contribution to the CIB of these faint galaxies is modest (30% at most), the large uncertainties in these color ratios will not dominate the total background estimate.

5. New Estimates of the Cosmic Far-Infrared Background

5.1. New Lower Limits at 70 and 160 μm

The present stacking analysis performed on detected galaxies $S_{24} \geq 60$ μJy gives strong measured lower limits to the CIB due to galaxies at 70 and 160 μm, without requiring any modeling. To determine upper limits to the FIR CIB requires a different approach. There are many difficulties at 70 μm in extracting an accurate value of the CIB, mostly due to the problems in the removal of the zodiacal component (Finkbeiner et al., 2000; Renault et al., 2001, for instance). At 160 μm the CIB estimate is more robust, but still with a significant uncertainty (factor of $\sim$3, see Sect. 4.1).

Another way to get a good estimate of the FIR galaxy CIB brightness is to estimate the unresolved 24 μm background fraction, use the 160/24 and 70/24 colors measured for the weakest sources, and then apply these colors to the unresolved part to get the 70 and 160 μm background estimates. Thus, we extrapolate the colors of galaxies with $S_{24} \leq 60$ μJy using the colors of the $60 \leq S_{24} \leq 130$ μJy galaxies derived in the previous section. To estimate the unresolved 24 μm background, Papovich et al. (2004) used a simple extrapolation of the differential number counts. Since the slope of the counts below 100 μJy is strongly decreasing (-1.5 ± 0.1 in dN/dS), the integral is dominated by the largest fluxes S_{24}. The estimate is robust, unless a hypothetical faint population exists. The remaining unresolved 24 μm background created by $S_{24} < 60$, μJy sources is therefore 0.54 $nWm^{-2}sr^{-1}$, (to be compared to 2.16 $nWm^{-2}sr^{-1}$ for $S_{24} > 60$, μJy sources).

We derive the extrapolated FIR CIB level due to IR galaxies using:

$$\nu I_\nu(\lambda) = \nu I_\nu(24) \times \frac{I_\lambda}{I_{24}} \times \frac{24}{\lambda} \quad (2)$$

The results of the extrapolation are presented in Table 3. We obtain 7.1$\pm$1.0 and 13.4$\pm$1.7 $nWm^{-2}sr^{-1}$, at 70 and 160 μm respectively. Our new estimate, based on the integration of all the 24 μm IR galaxies, is in principle a lower limit because it does not account for any diffuse emission unrelated to the IR galaxies, nor for a small fraction of IR galaxies that might have been missed. Indeed, the extrapolation in color of the unresolved 24 μm population accounts for the faint-end of the luminosity function, but not for the hypothetical very high-redshift sources, or faint local galaxies with high FIR output, like a hypothetical population of elliptical galaxies with large 160/24 colors. However, if this population exists, its contribution to the FIR background is constrained by the upper limits to be less than $\sim$20%.

Our estimate at 70 μm is higher than the Lagache et al. (2004) model estimate by 11%, and lower by about 13% at 160 μm. About 25% of the CIB brightness at 70 and 160 μm comes from faint MIR sources ($S_{24} \leq 60$ μJy). Assuming our new FIR CIB values represent the actual CIB values, we estimate that our stacking analysis of $S_{24} \geq 60$ μJy galaxies finally resolves 75-80% of the background at 70 and 160 μm. We also show that the population dominating the CIB is made of galaxies seen at 24 μm and their simplest extrapolation to lower fluxes.

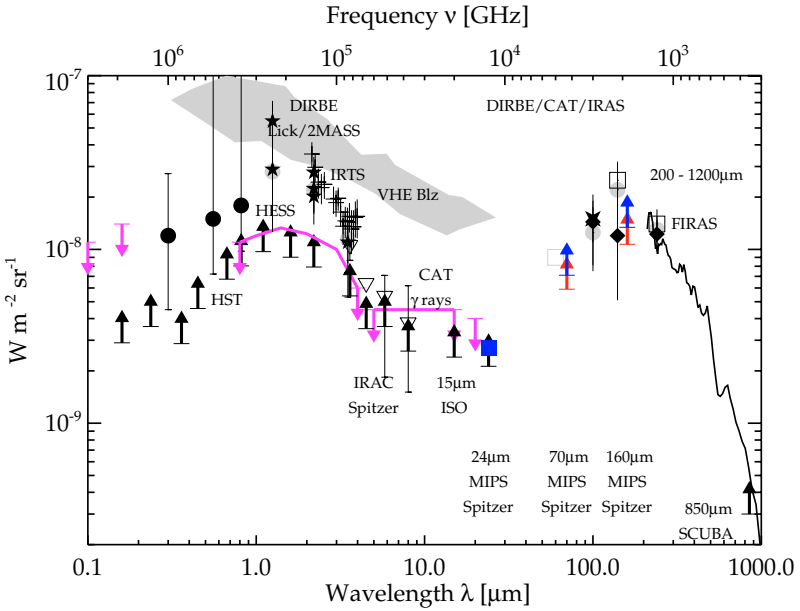

Fig. 11. Extragalactic Background Light Spectral Energy Distribution from 0.1 μm to 1 mm, with new constraints from MIPS. Red arrows (lower limits) represent the fraction of the CIB resolved at 70 and 160 μm using the stacking analysis for sources with $S_{24} \geq 60$ μJy. The blue square represents the contribution of all the unresolved 24 μm sources (extrapolation from number counts), and the blue arrows represent the contribution of all 24 μm sources to the FIR background, using a simple color extrapolation for 70 and 160 μm (Sect. 5). See Figure 9 for the other symbols.

5.2. Spectral Energy Distribution of the Extragalactic Background

In the near and mid-IR, upper and lower limits tightly constrain the EBL SED: 1) with *HST*+*Spitzer* and H.E.S.S between 0.8 and 4 μm, and 2) with *ISO*, *Spitzer* and CAT between 5 and 24 μm. In this range, the EBL SED is constrained to better than 50% (and to the 20% level in several wavelength ranges). The EBL is now also well constrained in the FIR; direct measurements of the diffuse emission and our new lower limits constrain the CIB SED to the 50% level.

The permitted zone for the EBL SED is presented in Figure 12. This zone is defined as the area between current upper and lower limits. In this zone, the COB brightness ranges from 19.5 to 35.5 nW m^{-2} sr^{-1}, and the CIB from 24 to 27.5 nW m^{-2} sr^{-1}. The ratio COB/CIB thus ranges from 0.7 to 1.5.

From these constraints, we may derive a conservative estimate of the EBL SED, that typically lies between the upper and lower limits and that makes use of well known physical processes. The CIB estimate, based on the Lagache et al. (2004) model, agrees with the data and is strongly constrained in the MIR and the 240-400 μm range. It strongly decreases with increasing frequency below 8 μm because of the main PAH features at 6.2 to 8.6 μm being redshifted. The COB estimate also decreases with increasing wavelength above 2 μm because of the old stellar population SED. This simple SED behavior is in agreement with the model of Primack et al. (1999). Our reasonable guess is that the COB and CIB have equal contributions around 8 μm.

Figure 13 shows our smooth EBL SED estimate (thick line), as well as our best estimate of the COB (blue shaded) and the CIB (red shaded). The overlap region where both COB and CIB contribute significantly and the resulting total EBL is shown as the gray-shaded area around 8 μm. We find that the brightness of the COB is 23 nW m^{-2} sr^{-1}, and 24 nW m^{-2} sr^{-1} for the CIB. The ratio between the COB and CIB is thus of the order of unity for this EBL SED.

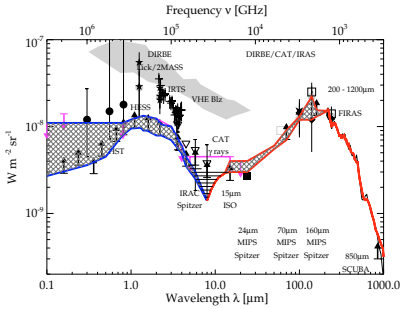

Fig. 12. Cosmic Optical Background and Cosmic Infrared Background due to galaxies permitted zone estimate (shaded area), using upper and lower values. See Figure 9 for the other symbols.

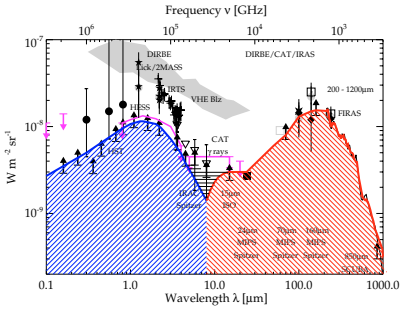

Fig. 13. Our best Cosmic Optical Background (blue-shaded) and Cosmic Infrared Background (red-shaded) estimates. The gray-shaded area represents the region of overlap. See Figure 9 for the other symbols.

Our results are in contradiction with Wright (2004) who finds a COB/CIB ratio of 1.7, and values at least 50% higher than ours: 59 nW m^{-2} sr^{-1} (COB) and 34 nW m^{-2} sr^{-1} (CIB). However, the Wright (2004) estimate came before the strong upper limits of H.E.S.S (Aharonian et al., 2005) below 4 μm. This limit puts the COB much closer to the integrated light from galaxy counts than to the diffuse measurements. From the galaxy counts and stacking analysis (lower limits), and high-energy experiments (upper limits), the EBL is now very well constrained. In particular, we can now securely state that the contributions to the EBL of faint diffuse emissions outside identified galaxy populations – too weak to be detected in current surveys, like population III stars relic emission, galaxy clusters, hypothetical faint IR galaxy populations – can represent only a small fraction of the integrated energy output in the universe.

5.3. The Extragalactic Background vs the Cosmic Microwave Background

It is interesting to update the contributions of the most intensive electromagnetic backgrounds in the universe, as has been done for instance by Scott (2000) or Wright (2004), and we schematically represent these in Figure 14. Obviously, the Cosmic Microwave Background (CMB) dominates the universe's SED, and accounts for about 960 nW m^{-2} sr^{-1}. We showed that the CIB and COB each account for 23 and 24 nW m^{-2} sr^{-1}, respectively. With a total of 47 nW m^{-2} sr^{-1} in the optical and the Far-Infrared, the EBL represents about 5% of the brightness of the CMB. Taking into account the complete SED of the EBL will not change this picture, since the contributions to the total EBL brightness of the radio, UV, X-ray (Mushotzky et al., 2000; Hasinger et al., 2001) and γ ray (Strong et al., 2004) extragalactic backgrounds are smaller by one to three orders of magnitude than the COB and CIB (Scott, 2000).

The galaxy formation and evolution processes provide 5% in brightness of the electromagnetic content of the Universe. Half of the energy comes in the form of starlight (COB) and half as dust-reprocessed starlight (CIB). The maximum of the power distribution is at $\sim$ 1.3 μm for the COB and $\sim$ 150 μm for the CIB (Fig. 14). There are therefore on average 115 infrared photons for 1 visible photon emitted in these processes.

6. Conclusions

Our key points and results for the resolution and characterization of the FIR CIB and the EBL are:

- A stacking analysis in three fields covering 0.85 square degrees including a sample of 19181 MIPS 24 μm sources with $S_{24} \geq 60\,\mu$Jy lets us probe faint 70 and 160 μm galaxies one order of magnitude below the confusion level and with a high signal-to-noise ratio. We take into account in our noise budget uncertainties coming from: photometry, calibration systematics, and large-scale structure.
- 24 μm galaxies down to $S_{24} = 60\,\mu$Jy contribute 79%, 92%, 69% of the CIB at respectively 24, 70 and 160 μm (using 2.7, 6.4 and 15.4 nW m^{-2} sr^{-1} as the total CIB values at 24, 70 and 160 μm, respectively). This is the first direct measurement of the contribution of MIR-selected galaxies to the FIR background.
- We derive the contributions to the CIB by flux density bin, and show good agreement between our stacking analysis and the published source counts. This is a strong constraint for models. Moreover, we show that the CIB will be mainly resolved at flux densities of about $S_{70} \sim 0.9$ mJy and $S_{160} \sim 3$ mJy at 70 and 160 μm, respectively.
- We directly measure that the total CIB, peaking near 150 μm, is largely resolved into MIR galaxies. Other works (Pérez-González et al., 2005; Le Floc'h et al., 2005; Caputi et al., 2006, especially) show that these MIPS 24 μm sources are $\sim 3 \times 10^{11}\,L_\odot$ LIRGs distributed at redshifts $z \sim 1$, with stellar masses of about 3×10^{10} to $3\times10^{11}\,M_\odot$ and specific star formation rates in the range 0.1 to 1 Gyr^{-1}.
- Using constant color ratios 160/24 and 70/24 for MIR galaxies fainter than 60 μJy, we derive new conservative lower limits to the CIB at 70 and 160 μm including the faint IR galaxies undetected at 24 μm: 7.1$\pm$1.0 and 13.4$\pm$1.7 nW m^{-2} sr^{-1}, respectively. These new estimates agree within 13% with the Lagache et al. (2004) model.
- Using these new estimates for the 70 and 160μm CIB, we show that our stacking analysis down to $S_{24} \geq 60\,\mu$Jy resolves >75% of the 70 and 160 μm CIB.
- Upper limits from high-energy experiments and direct detections together with lower limits from galaxy counts and stacking analysis give strong constraints on the EBL SED.
- We estimate the Extragalactic Background Light (EBL) Spectral Energy Distribution (SED) permitted zone (between lower and upper limits), and measure the optical background (COB) to be in the range 19.5-35.5 nW m^{-2} sr^{-1}, and the IR background (CIB) in the range 24 to 27.5 nW m^{-2} sr^{-1}. The ratio COB/CIB thus lies between 0.7 and 1.5.
- We integrate our best estimate of the COB and the CIB, and obtain respectively 23 and 24 nW m^{-2} sr^{-1}; We find a COB/CIB ratio close to unity.
- The galaxy formation and evolution processes have produced photons equivalent in brightness to 5% of the CMB, with equal amounts from direct starlight (COB) and from dust-reprocessed starlight (CIB). We compute that the EBL produces on average 115 infrared photons per visible photon.

Acknowledgements. This work is based on observations made with the *Spitzer* Observatory, which is operated by the Jet Propulsion Laboratory, California Institute of Technology under NASA contract 1407. We thank the funding from the MIPS project, which is supported by NASA through the Jet Propulsion Laboratory, subcontract #1255094. This work also benefited from funding from the CNES (Centre National d'Etudes Spatiales) and the PNC (Programme National de Cosmologie). We thank Jim Cadien for the great help in the data processing. We thank Nabila Aghanim, Hervé Aussel, Noel Coron, Daniel Eisenstein, David Elbaz, Charles Engelbracht, Dave Frayer, Karl Gordon, Nicolas Ponthieu, Martin Schroedter, and Xianzhong Zheng for fruitful discussions.

References

Aharonian, F, Akhperjanian, A. G, Bazer-Bachi, A. R, Beilicke, M, & H.E.S.S Collaboration. Nature, 2006, accepted, astro-ph/0508073.
Bernstein, R. A, Freedman, W. L, & Madore, B. F. 2002, *ApJ*, 571:107.
Brown, T. M, Kimble, R. A, Ferguson, H. C, Gardner, J. P, Collins, N. R, & Hill, R. S. 2000, *AJ*, 120:1153.

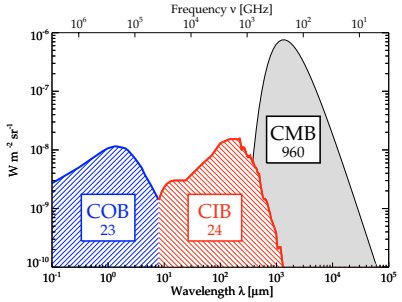

Fig. 14. Schematic Spectral Energy Distributions of the most important (by intensity) backgrounds in the universe, and their approximate brightness in nW m^{-2} sr^{-1} written in the boxes. From right to left: the Cosmic Microwave Background (CMB), the Cosmic Infrared Background (CIB) and the Cosmic Optical Background (COB).

Cambresy, L, Reach, W. T, Beichman, C. A, & Jarrett, T. H. 2001, *ApJ*, 555:563.
Caputi, K. I, Dole, H, Lagache, G, et al., 2006, *ApJ*, 637:727.
Chary, R & Elbaz, D. 2001, *ApJ*, 556:562.
Chary, R, Casertano, S, Dickinson, M. E, et al., 2004, *ApJS*, 154:80.
Dole, H, Lagache, G, & Puget, J. L. 2003, *ApJ*, 585:617.
Dole, H, Le Floc'h, E, Perez-Gonzalez, P. G, et al., 2004a, *ApJS*, 154:87.
Dole, H, Rieke, G. H, Lagache, G, et al., 2004b, *ApJS*, 154:93.
Dole, H. In Gry, C, Peschke, S. B, Matagne, J, et al. editors, *Exploiting the ISO Data Archive*, page 307. ESA SP-511, 2003. astro-ph/0211310
Dwek, E & Krennrich, F. 2005, *ApJ*, 618:657.
Edelstein, J, Bowyer, S, & Lampton, M. 2000, *ApJ*, 539:187.
Egami, E, Dole, H, Huang, J. S, et al., 2004, *ApJS*, 154:130.
Elbaz, D & Cesarsky, C. J. 2003, *Science*, 300:270.
Elbaz, D, Cesarsky, C. J, Fadda, D, et al., 1999, *A&A*, 351:L37.
Elbaz, D, Flores, H, Chanial, P, et al., 2002, *A&A*, 381:L1.
Elbaz, D. in Space Science Reviews ISO Special Issue "ISO science legacy - a compact review of ISO major achievements", Ed.C.Cesarky & A.Salama (Springer) astro-ph/0503389, 2005.
Fazio, G. G, Ashby, M. L. N, Barmby, P, et al., 2004, *ApJS*, 154:39.
Finkbeiner, D. P, Davis, M, & Schlegel, D. J. 2000, *ApJ*, 544:81.
Flores, H, Hammer, F, Désert, F. X, et al., 1999, *A&A*, 343:389.
Franceschini, A, Berta, S, Rigopoulou, D, et al., 2003, *A&A*, 403:501.
Frayer, D. T., Fadda, D., Yan, L., et al., 2006, *AJ*, 131:250.
Gardner, J. P, Brown, T. M, & Ferguson, H. C. 2000, *ApJ*, 542:L79.
Genzel, R & Cesarsky, C. J. 2000, *ARA&A*, 38:761.
Gispert, R, Lagache, G, & Puget, J. L. 2000, *A&A*, 360:1.
Gordon, K. D, Rieke, G. H, Engelbracht, C. W, et al., 2005, *PASP*, 117:503.
Gordon, K. D, Bailin, J., Engelbracht, C. W, et al., 2005, *ApJ*, in press, astro-ph/0601314

Gorjian, V, Wright, E. L, & Chary, R. R. 2000, *ApJ*, 536:550.
Hasinger G., Altieri B., Arnaud M., et al., 2001, *A&A*, 365, L45
Hauser, M. G & Dwek, E. 2001, *ARA&A*, 37:249.
Hauser, M. G, Arendt, R. G, Kelsall, T, et al., 1998, *ApJ*, 508:25.
Houck, J. R, Soifer, B. T, Weedman, D, et al., 2005, *ApJ*, 622:L105.
Kashlinsky, A. 2005, *Phys. Rep.*, 409:361.
Kelsall, T, Weiland, J. L, Franz, B. A, et al., 1998, *ApJ*, 508:44.
Krist, J. Tiny Tim : an HST PSF simulator. In Hanisch, R. J, Brissenden, J. V, & Barnes, J, editors, *Astronomical Data Analysis Software and Systems II*, page 536. A.S.P. Conference Series, 1993.
Lagache, G, Abergel, A, Boulanger, F, et al., 1999, *A&A*, 344:322.
Lagache, G, Haffner, L. M, Reynolds, R. J, & Tufte, S. L. 2000, *A&A*, 354:247.
Lagache, G, & Dole, H. 2001, *A&A*, 372:702
Lagache, G, Dole, H, & Puget, J. L. 2003, *MNRAS*, 338:L555.
Lagache, G, Dole, H, Puget, et al., 2004, *ApJS*, 154:L112.
Lagache, G, Puget, J. L, & Dole, H. 2005, *ARA&A*, 43, 727.
Le Floc'h, E, Pérez-González, P. G, Rieke, et al., 2004, *ApJS*, 154:L170.
Le Floc'H, E, Papovich, C, Dole, H, et al., 2005, *ApJ*, 632:L169.
Lonsdale, C, Polletta, M. M. C, Surace, J, et al., 2004, *ApJS*, 154:L54.
Madau, P & Pozzetti, L. 2000, *MNRAS*, 312:L9.
Matsumoto, T, Matsuura, S, Murakami, H, et al., 2005, *ApJ*, 626:31.
Mattila, K. 2003, *ApJ*, 591:119.
Miville-Deschênes, M. A, Lagache, G, & Puget, J. L. 2002, *A&A*, 393:749.
Montier, L. A & Giard, M. 2005, *A&A*, 439:35.
Mushotzky, R. F,. and Cowie, L. L., and Barger, A. J,. and Arnaud, K. A. 2000, Nature, 404:459
Papovich, C, Dole, H, Egami, E, et al., 2004, *ApJS*, 154:70.
Partridge, R. B. & Peebles, P. J. E. 1967, *ApJ*, 148:377
Pérez-González, P. G, Rieke, G. H, Egami, E, et al., 2005, *ApJ*, 630:82.
Primack, J. R, Bullock, J. S, Somerville, R. S, & Macminn, D. 1999, *Astroparticle Physics*, 11:93.
Puget, J. L & Leger, A. 1989, *ARA&A*, 27:161.
Puget, J. L, Abergel, A, Bernard, J. P, et al., 1996, *A&A*, 308:L5.
Renault, C, Barrau, A, Lagache, G, & Puget, J. L. 2001, *A&A*, 371:771.
Rieke, G. H, Young, E. T, Engelbracht, C. W, et al., 2004, *ApJS*, 154:25.
Sanders, D. B & Mirabel, I. F. 1996, *ARA&A*, 34:749.
Savage, R. S & Oliver, S. 2005, *MNRAS*, submitted, astro-ph/0511359
Schroedter, M. 2005, *ApJ*, 628:617.
Scott, D. 2000, "Cosmic Flows Workshop", ASP Conference Series, Stephane Courteau and Jeffrey Willick Eds, p. 403
Smail, I, Ivison, R. J, Blain, A. W, & Kneib, J. P. 2002, *MNRAS*, 331:495.
Soifer, B. T & Neugebauer, G. 1991, *AJ*, 101:354.
Stecker, F. W & De Jager, O. C. 1997, *ApJ*, 476:712.
Strong, A. W. and Moskalenko I. V. and Reimer 0. 2004, *ApJ*, 613:956.
Thompson, R. I 2003, *ApJ*, 596:748.
Werner, M. W, Roellig, T. L, Low, F. J, et al., 2004, *ApJS*, 154:1.
Wright, E. L. 2001, *ApJ*, 553:538.
Wright, E. L. 2004, *New Astronomy Reviews*, 48:465.
Xu, C, Lonsdale, C. J, Shupe, D. L, et al., 2001, *ApJ*, 562:179.

Astronomy & Astrophysics manuscript no. kic˙4553ms
April 11, 2006

The role of the LIRG and ULIRG phases in the evolution of K_s-selected galaxies

K. I. Caputi[1], H. Dole[1], G. Lagache[1], R. J. McLure[2], J. S. Dunlop[2], J.-L. Puget[1], E. Le Floc'h[3,4], and P. G. Pérez-González[3]

[1] Institut d'Astrophysique Spatiale (IAS), bâtiment 121, F-91405 Orsay, France; Université Paris-Sud 11 and CNRS (UMR 8617)
e-mail: kcaputi,herve.dole,guilaine.lagache,puget@ias.u-psud.fr
[2] Institute for Astronomy, University of Edinburgh, Royal Observatory, Blackford Hill, EH9 3HJ, Edinburgh, UK
e-mail: rjm,jsd@roe.ac.uk
[3] Steward Observatory, University of Arizona, 933 N Cherry Ave, Tucson, AZ 85721, USA
e-mail: elefloch,pgperez@as.arizona.edu
[4] Also associated to the Observatoire de Paris, GEPI, 92195, Meudon, France

Received ...; accepted ...

ABSTRACT

Aims. We investigate the role of the luminous infrared galaxy (LIRG) and ultra-luminous infrared galaxy (ULIRG) phases in the evolution of K_s-selected galaxies and, in particular, Extremely Red Galaxies (ERGs).
Methods. With this aim, we compare the properties of a sample of 2905 $K_s < 21.5$ (Vega mag) galaxies in the GOODS/CDFS with the sub-sample of those 696 sources which are detected at 24 μm.
Results. We find that LIRGs constitute 30% of the galaxies with stellar mass $M > 1 \times 10^{11}\ M_\odot$ assembled at redshift $z = 0.5$. A minimum of 65% of the galaxies with $M > 2.5 \times 10^{11}\ M_\odot$ at $z \approx 2-3$ are ULIRGs at those redshifts. 60% of the ULIRGs in our sample have the characteristic colours of ERGs. Conversely, 40% of the ERGs with stellar mass $M > 1.3 \times 10^{11}\ M_\odot$ at $1.5 < z < 2.0$ and a minimum of 52% of those with the same mass cut at $2.0 < z < 3.0$ are ULIRGs. The average optical/near-IR properties of the massive ERGs at similar redshifts that are identified with ULIRGs and that are not have basically no difference, suggesting that both populations contain the same kind of objects in different phases of their lives.
Conclusions. LIRGs and ULIRGs have an important role in galaxy evolution and mass assembly, and, although they are only able to trace a fraction of the massive ($M > 1 \times 10^{11}\ M_\odot$) galaxies present in the Universe at a given time, this fraction becomes very significant ($\gtrsim 50\%$) at redshifts $z \gtrsim 2$.

Key words. Infrared: galaxies – Galaxies: evolution – Galaxies: statistics

1. Introduction

The study of the evolution of near-infrared (IR)-selected galaxies is probably the most efficient way to trace the build up of stellar mass with redshift (e.g. Dickinson et al. 2003; Fontana et al. 2004; Glazebrook et al. 2004; Caputi et al. 2005, 2006a (C06a)). In contrast to other wavelength surveys, near-IR observations are able to detect systems with different dust content and star-formation histories. Thus, they appear as a viable method to produce a relatively unbiased census of galaxy populations, from which the history of stellar mass assembly can be investigated.

The *Spitzer Space Telescope* (Werner et al. 2004) is making possible the mapping of the mid-IR Universe from low to high redshifts. Recent studies have exploited this capability to set tight constraints on the intensity and the composition of the mid and far-IR backgrounds (Papovich et al. 2004; Le Floc'h et al. 2005; Pérez-González et al. 2005; Caputi et al. 2006b (C06b); Dole et al. 2006). The analysis of the evolution of mid-IR galaxies with redshift provides fundamental information to understand how star-formation and quasar activity proceeded through cosmic time.

It is so far not clear, however, what the role of bright mid-IR-selected galaxies is within the history of stellar mass assembly. The aim of this work is to assess the significance of this role, through the study of mid-IR-selected galaxies in the context of the evolution of the K_s-band galaxy population. With this purpose, we focus on the analysis of two main topics: 1) the number densities of massive luminous mid-IR-selected galaxies, in comparison to the total number densities of massive galaxies in the K_s-band population, at different redshifts, and 2) the relation between the luminous IR and the Extremely Red Galaxy (ERG) phases. We adopt throughout a cosmology with

Send offprint requests to: K.I. Caputi; e-mail: kcaputi@ias.u-psud.fr

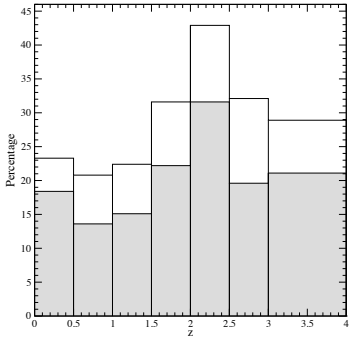

Fig. 1. The percentage of $K_s < 21.5$ mag galaxies which are detected in the deep MIPS/GTO 24 μm catalogue, as a function of redshift. The shaded and empty histograms indicate the percentages of galaxies with $S_\nu(24\,\mu\mathrm{m}) > 83\,\mu$Jy and the total of 24 μm -detected galaxies, respectively. The faintest galaxies considered here have $S_\nu(24\,\mu\mathrm{m}) \sim 20\,\mu$Jy, but galaxies with $S_\nu(24\,\mu\mathrm{m}) < 60\,(83)\,\mu$Jy only constitute $\sim 11\,(30)$% of the total sample.

$\mathrm{H_o} = 70\,\mathrm{km\,s^{-1}\,Mpc^{-1}}$, $\Omega_\mathrm{M} = 0.3$ and $\Omega_\Lambda = 0.7$. A Salpeter IMF over stellar masses $M = (0.1 - 100)\,M_\odot$ is assumed.

2. The samples

C06a selected a sample of 2905 $K_s < 21.5$ (Vega mag) galaxies in 131 arcmin^2 of the Great Observatories Origins Deep Survey (GOODS) Chandra Deep Field South (CDFS). This area benefits from deep J and K_s-band coverage by the Infrared Spectrometer and Array Camera (ISAAC) on the Very Large Telescope (VLT). Other deep multiwavelength data also exist in this field; in particular, B, V, i and z-band imaging from the Advanced Camera for Surveys (ACS) on-board the Hubble Space Telescope (HST), and 3.6 to 8.0 μm imaging from the Infrared Array Camera (IRAC) on board *Spitzer*.

C06a constructed an optimized redshift catalogue for the total $K_s < 21.5$ mag sample, incorporating the available spectroscopic (e.g. Le Fèvre et al. 2004; Vanzella et al. 2005) and COMBO17 (Wolf et al. 2004) redshifts for the CDFS. The remaining redshifts were obtained with the public codes HYPERZ (Bolzonella, Miralles & Pelló 2000) and BPZ (Benítez 2000), using multiwavelength photometry. The comparison of the redshifts for the sources with spectroscopic data showed that the photometric estimates had very good quality, with a median of $|z_{spec} - z_{phot}|/(1 + z_{spec}) = 0.02$. The code HYPERZ has simultaneously been used to model the spectral energy distribution (SED) of each source, with the Calzetti et al. (2000) reddening law to take into account dust-corrections.

The $K_s < 21.5$ mag sample is cleaned of galactic stars. It also excludes those X-ray sources whose SEDs could not be satisfactorily fitted with the HYPERZ stellar templates, as their optical/near-IR light could be contaminated by an active (AGN/QSO) component. For these sources, no reliable mass estimate can be obtained from the modelled SED. The rejected X-ray sources constitute $\sim$ 2% of the total $K_s < 21.5$ mag sample. We refer the reader to C06a for further details on the selection and analysis of the $K_s < 21.5$ mag galaxy sample.

Observations of the CDFS have also been carried out with the Multiband Imaging Photometer for *Spitzer* (MIPS; Rieke et al. 2004), as part of the Guaranteed Time Observers (GTO) program. The MIPS GTO 24 μm catalogue achieves 80% completeness at a flux limit of $S_\nu(24\,\mu\mathrm{m}) \approx 83\,\mu$Jy (see details in Papovich et al. 2004).

C06b cross-correlated the C06a sample (and all the excluded $K_s < 21.5$ mag stars and AGN/QSO) with the deep 24 μm catalogue for the CDFS. $\sim$ 94% of the 24 μm objects with flux $S_\nu(24\,\mu\mathrm{m}) > 83\,\mu$Jy were identified with a $K_s < 21.5$ mag counterpart. This allowed for the characterization of nearly all the brightest sources composing the 24 μm background in the GOODS/CDFS.

The fraction of 24 μm galaxies with multiple K_s-band associations is small. C06b found that, within a matching radius of 2 arcsec, < 8% (0.3%) of the 24 μm galaxies could be associated with two (three) different K_s-band galaxies. On the other hand, $\sim$ 95% of the associations can be done restricting the matching radius to 1.5 arcsec. Using this smaller matching radius, the number of double identifications is only < 3%. In all cases, C06b considered that the closest K_s-band source to each 24 μm galaxy was the real counterpart.

In addition, using empirical relations between the mid-IR and bolometric IR luminosities (Chary & Elbaz 2001, Elbaz et al. 2002), C06b obtained IR luminosity (L_{IR}) estimates and derived star-formation rates (SFR) for most of their galaxies. In agreement with other works (Le Floc'h et al. 2005; Pérez-González et al. 2005), they found that the mid-IR output was dominated by luminous IR galaxies (LIRGs, $10^{11}\,L_\odot < L < 10^{12}\,L_\odot$) at redshift $z \sim 1$ and by ultra-luminous IR galaxies (ULIRGs, $L > 10^{12}\,L_\odot$) at redshift $z \gtrsim 1.5 - 2.0$.

In this work we analyze the role of the sub-sample of the $K_s < 21.5$ mag galaxies identified with a 24 μm counterpart, within the total $K_s < 21.5$ mag galaxy population. We quantify the importance of galaxies with different IR luminosities in the evolution of massive systems at different redshifts. The sub-sample of 24 μm -detected galaxies contains 696 out of 2905 $K_s < 21.5$ mag galaxies.

The percentage of the $K_s < 21.5$ mag galaxies which are 24 μm -detected as a function of redshift is shown in Figure 1. The shaded and empty histograms indicate the percentages of galaxies with $S_\nu(24\,\mu\mathrm{m}) > 83\,\mu$Jy and the total of the 24 μm -detected galaxies, respectively. The faintest sources included in our catalogue have fluxes $S_\nu(24\,\mu\mathrm{m}) \sim 20\,\mu$Jy, but galaxies with $S_\nu(24\,\mu\mathrm{m}) < 60\,(83)\,\mu$Jy only constitute $\sim$ 11 (30)% of the total sample. The number of spurious sources in the 24 μm catalogue becomes non-negligible at fluxes $S_\nu(24\,\mu\mathrm{m}) < 83\,\mu$Jy and starts to be important at $S_\nu(24\,\mu\mathrm{m}) \lesssim 60\,\mu$Jy (Papovich et al. 2004). Nevertheless, we note that the reliability of all the 24 μm sources analyzed here is assured by our K_s and other band detections. Even so, there still could be the possibility of a false 24 μm source which is associated just by chance with a K_s counterpart. However, we mentioned above that the fraction of 24 μm sources with a double association within 1.5 arcsec is < 3%. We can consider this percentage to be representative of the maximum fraction of false identifications. Thus, we estimate that the fraction of spurious $S_\nu(24\,\mu\mathrm{m}) < 60\,\mu$Jy sources associated just by chance with a K_s galaxy must constitute $< 0.03 \times 11\% = 0.33\%$ of our total sample. Then, those plausible spurious sources do not constitute a concern in this work.

We see in Figure 1 that $\sim$ 20 – 25% of our $K_s < 21.5$ mag galaxies at redshifts $z < 1.5$ are 24 μm -detected at the depth of the MIPS/GTO CDFS catalogue. The percentage of 24 μm -detected galaxies increases at higher redshifts, with a maximum of $\sim$ 43% at $z \sim 2.0 - 2.5$. The magnitude limit of our K_s-band survey imposes that we only see massive galaxies at high redshifts. Above redshifts $z = 2$ and $z = 3$, we are only strictly complete for stellar masses $M > 6 \times 10^{10}\,M_\odot$ and $M > 1.3 \times 10^{11}\,M_\odot$, respectively (cf. C06a and Figure 4). Thus, the increasing percentage of IR galaxies with redshift in particular implies that the fraction of massive galaxies with IR-activity has been significantly larger in the past. We further discuss this issue in Section 4. However, it should also be noted that this positive selection effect on high-redshift galaxies is very probably favoured by the presence of policyclic aromatic hydrocarbon (PAH) emission features entering the 24 μm -filter passband (cf. C06b). PAH emission lines characterize the interstellar medium of star-forming regions (Désert, Boulanger & Puget 1990). The presence of PAHs implies that a substantial fraction of the $K_s < 21.5$ mag galaxies at $z \sim 2.0 - 2.5$ have IR activity mainly due to star-formation. PAH emission in high-z galaxies has been spectroscopically confirmed in different recent works (e.g. Houck et al. 2005; Yan et al. 2005; Lutz et al. 2005).

3. The normal- versus active-galaxy separation

As we mentioned above, those X-ray sources with no satisfactory modelled SED have been left out of the $K_s < 21.5$ mag sample. This implies that 40 X-ray-detected 24 μm sources (including X-ray AGN/QSO and other galaxies with undetermined X-ray classification) are excluded from the sub-sample analyzed here. However, we note that our 24 μm sub-sample still contains 26 sources X-ray classified as AGN/QSO (with satisfactory HYPERZ SED fits).

To test the completeness of the X-ray detections to separate all the 24 μm -detected active galaxies, we construct a colour-colour diagram based on different IRAC passbands for the high redshift ($z > 1.5$) sources. The separation of normal and active galaxies in such a diagram should be produced by the mid-IR excess characterising the latter type of objects. At lower redshifts, an AGN/QSO separation based only on the X-ray classification is expected to be more complete than at higher redshifts. On the other hand, the existence of star-forming galaxies with PAH emission lines within the IRAC passbands complicates the colour-colour separation at low redshifts, as these emission lines might mimic the AGN IR colour excesses. Thus, we restrict the analysis of the colour-colour diagram to sources with $z > 1.5$. Figure 2 shows the location in this diagram of different types of 24 μm sources and all the $K_s < 21.5$ mag sources, at $z > 1.5$. We clearly see from this diagram that the majority ($\sim$ 70%) of the 24 μm -detected X-ray AGN/QSO lie in a segregated region, typically with colours $[5.8] - [8.0\,\mu\mathrm{m}] \gtrsim 0.2$ (AB mag). A few apparently normal (i.e. non X-ray classified AGN/QSO) galaxies appear within this region. The vast majority of normal galaxies occupy a different locus in the colour-colour diagram. However, we note that the remaining $\sim$ 30% of the 24 μm -detected X-ray-classified AGN/QSO also have the colours characterising normal galaxies. Thus, we conclude that the application of a $[5.8] - [8.0\,\mu\mathrm{m}]$ colour cut can be useful to complement the X-ray AGN classification, but cannot be both complete and reliable at the same time (cf. e.g. Barmby et al. 2006).

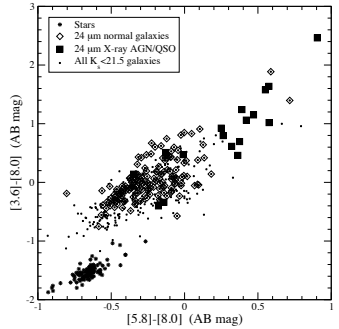

Fig. 2. IRAC-based colour-colour diagram for the $K_s < 21.5$ mag sources with redshifts $z > 1.5$. In this plot, we label as 'normal' to all those galaxies which are not X-ray classified as AGN/QSO. Galactic stars have also been added for a comparison.

In order to achieve a balance between completeness and reliability for the active galaxy identifications within our sample, we adopt the following criteria for our 24 μm -detected $K_s < 21.5$ mag sources. At redshifts $z < 1.5$, we base our AGN/QSO classification exclusively on the X-ray data. For sources at higher ($z > 1.5$) redshifts, we considered as AGN/QSO to all those objects classified as such in the X-rays, plus the two additional 24 μm sources which also have a colour $[5.8] - [8.0\,\mu\mathrm{m}] > 0.2$ (AB mag; cf. figure 2). In addition, we also classify as active galaxies eight additional objects of our sample which have been identified as AGN in the catalogue constructed by Alonso-Herrero et al. (2006; table 1 of this paper). Thus, using all these criteria, the total number of sources classified as AGN/QSO in our 24 μm -detected $K_s < 21.5$ mag sample is $26 + 2 + 8 = 36$. Throughout this paper, when we

Table 1. The comoving number densities of massive galaxies with bolometric IR luminosity $L_{IR} > 10^{11}\,L_{\odot}$ (LIRGs and ULIRGs) versus redshift. The redshift bins indicated with an asterisk are not complete for this luminosity cut, so the corresponding number densities should be taken as lower limits. The percentages given in the columns %(z) refer to the fraction of objects classified as LIRGs or ULIRGs among all the $K_s < 21.5$ mag galaxies in that redshift bin and with the same mass cut. The percentages %($z = 0$) are obtained by dividing the number density of LIRGs and ULIRGs in that redshift/mass bin by the number density of galaxies with the same mass cut in the local Universe. These numbers indicate what fraction of the massive galaxies we see today have been IR-active in the past. Between brackets, we show the corrected values obtained when excluding the known AGN/QSO. These AGN/QSO are only those remaining in the 24 μm -detected $K_s < 21.5$ mag sub-sample considered here (i.e. with satisfactory HYPERZ SED fits and, thus, reliable mass estimates), which have been classified following the criteria explained in Section 3. Therefore, they constitute a lower limit to the total number of mid-IR detected active galaxies.

	$M > 1.0\times10^{11}\,M_{\odot}$				$M > 2.5\times10^{11}\,M_{\odot}$			
z	$\rho_c(\times10^{-5}\,\mathrm{Mpc}^{-3})$	%(z)	% AGN(z)	%($z=0$)	$\rho_c(\times10^{-5}\,\mathrm{Mpc}^{-3})$	%(z)	% AGN(z)	%($z=0$)
0.5-1.0	40 ± 12 (31.4 ± 9.4)	30 (24)	6	30 (24)	–	–	–	–
1.0-1.5*	25.9 ± 3.9 (24.8 ± 3.8)	35 (34)	1	20 (19)	8.1 ± 2.2 (7.5 ± 2.1)	45 (42)	3	40 (37)
1.5-2.0*	19.4 ± 3.1 (17.0 ± 2.9)	45 (39)	6	15 (13)	7.3 ± 1.9 (6.3 ± 1.7)	47 (41)	6	36 (31)
2.0-3.0*	10.1 ± 1.5 (8.9 ± 1.4)	53 (47)	6	8 (7)	3.0 ± 0.8 (2.3 ± 0.7)	65 (50)	15	15 (11)

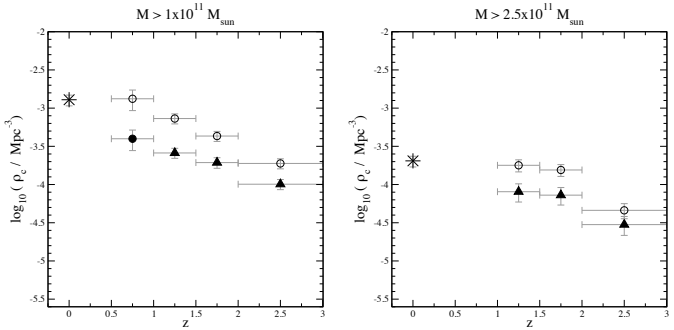

Fig. 3. The comoving number densities of galaxies with bolometric IR luminosity $L_{IR} > 10^{11}\,L_{\odot}$ (filled symbols), with assembled stellar mass $M > 1\times10^{11}\,M_{\odot}$ (left panel) and $M > 2.5\times10^{11}\,M_{\odot}$ (right panel), versus redshift. Circles and upward-pointing triangles indicate directly derived values and lower limits, respectively. Both star-forming galaxies and AGN/QSO are considered in all cases. The empty circles correspond to the densities of the total $K_s < 21.5$ mag galaxy population with the same mass cuts (C06a). The asterisks at $z = 0$ indicate the corresponding local values (Cole et al. 2001; Bell et al. 2003).

refer to the AGN/QSO of our sample, we always consider all of these 36 objects, unless otherwise explicitly stated.

4. The role of LIRGs and ULIRGs in stellar mass evolution

We now consider our 24 μm -detected $K_s < 21.5$ mag sample to study how the number density of massive luminous IR galaxies evolved through cosmic time. Stellar masses have been obtained from the optical/near-IR SED of each galaxy, which includes IRAC data at 3.6 and 4.5 μm. The stellar masses are computed using the rest-frame K_s-band luminosities, which are interpolated/extrapolated from the closest observed passband. We note that the use of IRAC data guarantees that we directly map the near-IR light of galaxies up to high ($z \sim 3$) redshifts. We estimate our stellar masses to be accurate within a factor ~ 2 (see C06a for more details).

Bolometric IR luminosities (L_{IR}) for normal galaxies have been obtained using the Chary & Elbaz (2001) and Elbaz et al. (2002) formulae, as in C06b. For the AGN/QSO present in our sample, we used the $L(12\,\mu\mathrm{m}) - L_{\mathrm{IR}}$ relation derived by Takeuchi et al. (2005), which makes no discrimination on the SED type. To interpolate/extrapolate the rest-frame 12 μm flux of each AGN/QSO, we assumed that the SED of these objects followed a power-law $f_\nu \propto \nu^{\alpha}$ ($\alpha < 0$). For each source, we derived the α value using its IRAC 3.6 and MIPS 24 μm fluxes.

To assure that the luminosities obtained with the Takeuchi et al. (2005) relation were consistent with the Chary & Elbaz and Elbaz et al. formulae, we compared the obtained L_{IR} values on our normal galaxies at $z \sim 1$, where the rest-frame 12 μm flux is directly mapped by the observed 24 μm flux. We found that the luminosities obtained with the Takeuchi et al. relation are systematically lower by a factor ~ 1.5 with respect to the luminosities obtained with the Chary & Elbaz and Elbaz et al. formulae. Thus, in order to maintain the same luminosity scale for all of our objects, we multiplied the AGN/QSO luminosities derived with the Takeuchi et al. relation by a factor 1.5.

Figure 3 shows the redshift evolution of the comoving number densities of galaxies with bolometric IR luminosity $L_{IR} > 10^{11}\,L_{\odot}$ (filled symbols) with assembled stellar mass $M > 1\times10^{11}\,M_{\odot}$ and $M > 2.5\times10^{11}\,M_{\odot}$ (left and right panels, respectively). By definition, the IR luminosity cut adopted for these galaxies implies that all of them are either LIRGs or ULIRGs. Both star-forming galaxies and active nuclei have been considered for all the number densities shown in Figure 3. For star-forming galaxies, an IR luminosity $L_{IR} > 10^{11}\,(10^{12})\,L_{\odot}$ implies a star-formation rate $SFR \gtrsim 17\,(170)\,M_{\odot}\,\mathrm{yr}^{-1}$ (Kennicutt 1998). Circles in both panels of figure 3 correspond to directly derived values, i.e. number densities in the redshift bins in which we have completeness

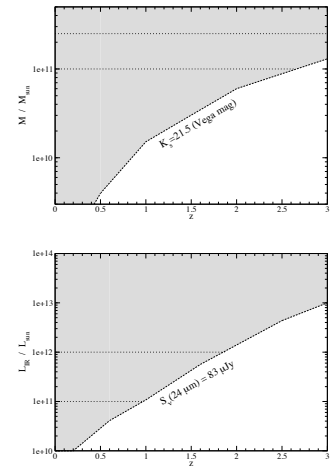

Fig. 4. Upper panel: the evolution of the stellar mass completeness with redshift, as imposed by the $K_s = 21.5$ mag cut. These completeness limits are strict, as they have been computed using a maximal mass-to-light ratio, corresponding to the template of a single stellar population formed at redshift $z \to \infty$. Lower panel: the evolution of the bolometric IR luminosity completeness with redshift, as imposed by the completeness limits of the 24 μm survey. The luminosities in this plot have been computed using the Chary & Elbaz and Elbaz et al. formulae, and extrapolated at $z < 0.4$.

for all the $L_{IR} > 10^{11}\,L_{\odot}$ galaxies (considering the $S_\nu(24\,\mu\mathrm{m}) = 83\,\mu$Jy limit). Upward-pointing triangles indicate lower limits on the densities in the redshift bins where our sample is not complete for the adopted luminosity cut. The evolution of the luminosity completeness imposed by the $S_\nu(24\,\mu\mathrm{m}) = 83\,\mu$Jy limit is shown in the lower panel of figure 4. For a comparison, the empty circles in both panels of Figure 3 show the densities of the total $K_s < 21.5$ mag sample, as they were computed by C06a. Analogous plots for only ULIRGs ($L_{IR} > 10^{12}\,L_{\odot}$) are shown in Figure 5.

Our computed number densities are V_{max}-corrected with respect to the $K_s = 21.5$ mag magnitude limit, to encompass the computation of number densities for the total $K_s < 21.5$ mag galaxy population. No corresponding V_{max}-corrections need to be applied to the 24 μm band, as we considered all the 24 μm identifications in our sample with no flux cut. Instead, we use the 80% completeness limit of the 24 μm catalogue ($S_\nu(24\,\mu\mathrm{m}) = 83\,\mu$Jy) as a reference to determine up to which redshift the 24 μm sample is complete for $L_{IR} > 10^{11}\,L_{\odot}$ and $L_{IR} > 10^{12}\,L_{\odot}$ galaxies. We find that our 24 μm sample is complete for LIRGs only up to redshift $z \sim 1$ and for ULIRGs up to redshift $z \sim 2$. Beyond those redshifts, we considered our computed number densities to be lower limits on the real values.

We note that mass completeness is not a concern in this analysis. The upper panel of figure 4 shows the evolution of the stellar mass completeness imposed by the $K_s = 21.5$ mag cut. For stellar masses $M \gtrsim 1\times10^{11}\,M_{\odot}$, we are basically complete up to redshift $z = 3$ (strictly $M > 1.3\times10^{11}\,M_{\odot}$ at $z = 3$).

The obtained number density values of $L_{IR} > 10^{11}\,L_{\odot}$ and $L_{IR} > 10^{12}\,L_{\odot}$ massive galaxies are listed in Tables 1 and 2, respectively. In the last redshift bin $z = 2-3$, the depth of our 24 μm catalogue only allows us to detect ULIRGs, so the lower limits we obtain for the densities of $L_{IR} > 10^{11}\,L_{\odot}$ and $L_{IR} > 10^{12}\,L_{\odot}$ galaxies are the same at these redshifts. The results presented in both tables show that luminous IR galaxies constitute a significant fraction of the assembled massive galaxies and this fraction increases with redshift. In particular, a minimum of $\sim 65\%$ of the most massive ($M > 2.5\times10^{11}\,M_{\odot}$) galaxies already present at redshifts $z = 2-3$ are ultra-luminous in the IR.

Moreover, from comparison of figures 3 and 5, we can clearly confirm how the role of IR galaxies among massive galaxies changes from being ULIRG-dominated at redshifts $z \gtrsim 1.5$ to be LIRG-dominated at $z \lesssim 1.5$. In effect, we observe that the number density of massive ULIRGs drastically falls below $z = 1.5$. Within our sample, we find only one galaxy with $L_{IR} > 10^{12}\,L_{\odot}$ and $M > 1\times10^{11}\,M_{\odot}$ at $1.0 < z < 1.5$, and none below these redshifts. ULIRGs might be present at lower redshifts, but are indeed very rare (e.g. Flores et al. 1999).

Within our sample, the ratio of AGN/QSO among the ULIRGs with stellar mass $M > 2.5\times10^{11}\,M_{\odot}$ reaches its maximum at $z = 2-3$. This fact, as well as the high SFR derived for the non AGN/QSO sources (C06b), highlight the importance of both star-formation and accretion activity in the evolution of the most massive galaxies already assembled at high redshifts. In contrast, the ratio of AGN/QSO among the $L_{IR} > 10^{11}\,L_{\odot}$ galaxies with stellar mass $M > 1.0\times10^{11}\,M_{\odot}$ reaches its max-

Table 2. The comoving number densities of massive galaxies with bolometric IR luminosity $L_{IR} > 10^{12}\,L_{\odot}$ (ULIRGs) versus redshift. See caption of Table 1 for references.

	$M > 1.0\times10^{11}\,M_{\odot}$				$M > 2.5\times10^{11}\,M_{\odot}$			
z	$\rho_c(\times10^{-5}\,\mathrm{Mpc}^{-3})$	$\%(z)$	% AGN(z)	$\%(z=0)$	$\rho_c(\times10^{-5}\,\mathrm{Mpc}^{-3})$	$\%(z)$	% AGN(z)	$\%(z=0)$
0.5-1.0	–	–	–	–	–	–	–	–
1.0-1.5	0.58 ± 0.58 (0.58 ± 0.58)	0.8 (0.8)	0	0.8 (0.8)	0.58 ± 0.58 (0.58 ± 0.58)	0.8 (0.8)	0	0.8 (0.8)
1.5-2.0	15.0 ± 2.7 (13.1 ± 2.5)	35 (30)	5	12 (10)	7.3 ± 1.9 (6.3 ± 1.7)	47 (41)	6	36 (31)
2.0-3.0*	10.1 ± 1.5 (8.9 ± 1.4)	53 (47)	6	8 (7)	3.0 ± 0.8 (2.3 ± 0.7)	65 (50)	15	15 (11)

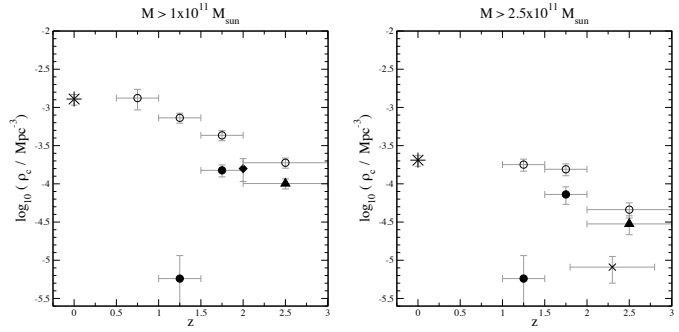

Fig. 5. The comoving number densities of galaxies with bolometric IR luminosity $L_{IR} > 10^{12}\,L_{\odot}$. The references are the same as in Figure 3. In the left panel, the diamond at $z = 2$ shows the estimated density of ULIRGs obtained by Daddi et al. (2005). The cross-like symbol in the right panel indicates the number density of radio-detected sub-millimetre galaxies (Chapman et al. 2003).

imum at lower redshifts $z = 0.5 - 1.0$, but is a minor fraction (6%) of all the $K_s < 21.5$ mag galaxies with the same mass cut in the same redshift bin.

With respect to the local population of galaxies with stellar mass $M > 1.0\times10^{11}\,M_{\odot}$ ($M > 2.5\times10^{11}\,M_{\odot}$), we find that a minimum of 20%, 15%, 8% (40%, 36%, 15%) had IR luminosities $L_{IR} > 10^{11}\,L_{\odot}$ by redshifts $z \sim 1.0, 1.5$ and 2.0, respectively.

Galaxies with $L_{IR} > 10^{11}\,L_{\odot}$ contain ∼ 24% of the total stellar mass density at redshifts $z = 0.5-1.0$ and a minimum of ∼ 35 and 45% at $z = 1.0 - 1.5$ and $1.5 - 2.0$, respectively. The total assembled stellar mass densities are 80-90%, 45-50% and 25-30% of the local value at redshifts $z \approx 0.75, 1.25$ and 1.75, respectively (Caputi et al. 2005; C06a and references therein). This implies that $L_{IR} > 10^{11}\,L_{\odot}$ galaxies contain ∼ 21%, and a minimum of 16 and 11% of the local stellar mass density at these respective redshifts.

In the left panel of Figure 5, we compare our computed number densities of ULIRGs with the estimate obtained by Daddi et al. (2005) from the analysis of BzK-selected galaxies (diamond-like symbol at $z = 2$), and we find a very good agreement.

Finally, in the right panel of Figure 5, we show for reference the number density of radio-detected sub-millimetre galaxies with flux $S_\nu(850\,\mu\mathrm{m}) \gtrsim 5$mJy (Chapman et al. 2003; cross-like symbol in Figure 5). The number density of these galaxies appears to be smaller by a factor ∼ 4 (2-3) than the density of $M > 2.5\times10^{11}\,M_{\odot}$ ULIRGs ($L > 5\times10^{12}\,L_{\odot}$ galaxies) at similar redshifts. There is evidence that the majority of radio-detected sub-millimetre galaxies have luminous 24 μm counterparts (Egami et al. 2004) and could be associated with the build up of the most massive galaxies (e.g. Stevens et al. 2003). However, the comparison of number densities shows that not all the most massive ULIRGs are associated with bright sub-millimetre galaxies (at least with radio-detected ones). What kind of 24 μm -selected ULIRGs are counterparts to sub-millimetre galaxies is still not completely clear (cf. Lutz et al. 2005), and this is being investigated, for instance, as a part of the SCUBA Half Degree Extragalactic Survey (SHADES) project (Mortier et al. 2005).

5. Linking the ULIRG and the ERG phases

The colours characterizing ERGs ($i - K_s > 4$, Vega mag) are usually associated with the presence of old stellar populations and/or starbursts heavily enshrouded by dust. 24 μm data can be used to constrain the importance of these two components in the ERG population.

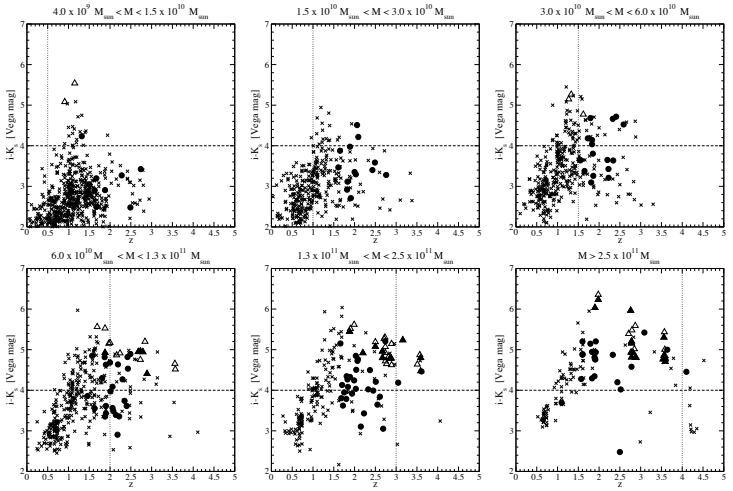

Fig. 6. The $(i - K_s)$ colours versus redshift for the $K_s < 21.5$ mag galaxies in different stellar mass bins. The i-band data corresponds to ACS/HST data. The filled symbols indicate 24 μm -detected ULIRGs. All the triangles correspond to lower limits on the $(i - K_s)$ colours for sources below the $\sim 2\sigma$ detection limit in the i band. In each panel, the dotted vertical line shows the strict completeness redshift limit of the corresponding stellar mass bin.

Figure 6 shows the $(i - K_s)$ colours of the $K_s < 21.5$ mag galaxies of different stellar mass, with the 24 μm -detected ULIRGs indicated by filled symbols. Although formally the Chary & Elbaz (2001) and Elbaz et al. (2002) relations do not allow us to compute bolometric IR luminosities beyond $z \sim 3$, the limits of the 24 μm survey show that only ULIRGs can be detected beyond $z \sim 2$. Thus, every 24 μm -detected source at $z > 3$ is indicated as a ULIRG in Figure 6. Following our adopted classification criteria (cf. Section 3), about one third of our 24 μm -detected galaxies at $z > 3$ are AGN/QSO. However, we note that our classification might be particularly incomplete at these high redshifts and the fraction of active galaxies among the 24 μm -detected galaxies might be higher. Unfortunately, the present data do not allow us to better constrain the AGN fraction.

We observe that ULIRGs are associated with K_s galaxies with a variety of stellar masses and $(i - K_s)$ colours at redshifts $z \gtrsim 1.5$, with ∼ 60% of them having the characteristic colours of ERGs.

Conversely, at $1.5 < z < 2$, ∼ 29% of the $K_s < 21.5$ mag ERGs are ULIRGs. At $2 < z < 3$, this percentage increases to a minimum of 49%. If we consider only those ERGs with stellar mass $M > 1.3\times10^{11}\,M_{\odot}$, these fractions are 40% at $1.5 < z < 2$ and ≥ 52% at $2 < z < 3$. In particular, from Figure 6 we see that some of the reddest ERGs are not ultra-luminous in the IR (and some are not detected at all in our 24 μm sample). Put another way, no correlation seems to exist between the $(i - K_s)$ colours and the IR luminosity. This result appears to be independent of the assembled stellar mass. We note that the identification of ERGs with ULIRGs is strictly complete up to redshift $z \approx 2$. Above that redshift, our 24 μm sample starts to lose completeness even for ULIRGs, so there exists the possibility that some of the non-24 μm detected ERGs are also ultra-luminous in the IR. The presence of old stellar populations might in part be responsible for the $(i - K_s)$ colour excess of those ERGs that are not ULIRGs. However, it is known that many of the reddest colours observed in ERGs can only be explained by the superposition of an evolved stellar component and non-negligible amounts of dust (Caputi et al. 2004; Papovich et al. 2006).

Daddi et al. (2005) find the average duty cycle for vigorous starburst with stellar mass $M \gtrsim 10^{11}\,M_{\odot}$ to be at least 50% at redshifts $1.4 < z < 2.5$. In this context, the duty cycle is the fraction of time spent in the starburst phase over the total elapsed time in the redshift interval $1.4 < z < 2.5$. The percentages of ULIRGs among massive ERGs we find here are consistent with the duty cycle estimated by Daddi et al.. Recent studies determined that most of the brightest 24 μm galaxies at $z \gtrsim 2$ already have stellar masses $M \gtrsim 1\times10^{11}\,M_{\odot}$ and that star-formation activity should mainly have proceeded by multiple discrete starbursts (C06b; Papovich et al. 2006). On the other hand, the majority of the massive galaxies at $z \gtrsim 1.5$ display extremely red colours. All these facts converge to a sce-

nario in which most of the ERGs –and not only the 24 μm-detected ones– could suffer a bright 'mid-IR episode' (i.e. a ULIRG phase) up to several times in their lives. After a period of star-formation activity, a galaxy becomes fainter in the mid-IR, but it still would be an ERG.

We compared the SEDs of our ERGs identified as ULIRGs, with those belonging to the other ERGs with similar stellar masses and redshifts. We found that the average properties (star formation history, age) of these SEDs are the same in the two groups of objects. Even the colour excesses are consistent within the error bars. The colour excesses are obtained from the convolution of the template SED with the Calzetti et al. (2000) reddening law. For example, if we consider those ERGs with stellar mass $M > 1.3 \times 10^{11}\,M_{\odot}$ at redshifts $2 < z < 3$ that are ULIRGs and that are not, we find that the medians of the colour excess of the best-fit SEDs are $E(B-V) = 0.30 \pm 0.07$ and $E(B-V) = 0.22 \pm 0.05$, respectively. For the ERGs with the same mass cut but lying at redshifts $1 < z < 2$, the respective medians of the colour excess are $E(B-V) = 0.17 \pm 0.05$ and $E(B-V) = 0.10 \pm 0.07$. These results are basically the same if we divide the ERGs into those which have flux $S_{\nu}(24\,\mu\mathrm{m}) > 83\,\mu$Jy and $S_{\nu}(24\,\mu\mathrm{m}) < 83\,\mu$Jy (including, of course, 24 μm non-detections).

Yan et al. (2004) suggested that the 24 μm-detected ERGs could be in the process of transforming into non-24 μm-detected early-type ERGs at $z \sim 1$. Our results are consistent with such a transformation hypothesis for the ERGs. More specifically: 1) even if evolved stellar populations were already present at $2 < z < 3$, the $E(B-V)$ colour excesses characterising massive ERGs at these redshifts would be inconsistent with these objects being passive systems. It is possible that most of these objects are actually IR luminous, and some of them are non-detected within the limits of our survey. However, if star formation indeed proceeds by discrete episodes, it will be more likely that a substantial fraction of the non-24 μm-detected ERGs are the detected ones in a post-starburst phase. 2) at $1 < z < 2$, the colour excesses are smaller on average, indicating that old stellar populations have a more important role in the colours of ERGs. However, some of the ERGs at these redshifts could still correspond to post-starbursts, as it has been demonstrated by spectroscopic studies (e.g. Doherty et al. 2005).

6. Summary and discussion

In this work we quantified the importance of luminous IR galaxies (LIRGs and ULIRGs) in the evolution of the massive K_s-band galaxy population. This allowed us to probe the role of star-forming galaxies (and quasar activity) in the history of stellar mass assembly.

Our results show that a substantial fraction of the massive galaxies ($M > 1\times10^{11}\,M_{\odot}$) assembled at different redshifts are luminous in the IR. This fraction appears to be higher at high redshifts ($z \sim 2-3$) than at lower redshifts. This result is clearly indicating that IR activity in massive galaxies –either due to star formation or AGN-driven– has been much more important in the past.

We determined that a minimum of 53 and 65% of the most massive ($M > 1\times10^{11}\,M_{\odot}$ and $M > 2.5\times10^{11}\,M_{\odot}$, respectively) galaxies present at $z \sim 2-3$ were ULIRGs at those redshifts.

Although the formation redshift of the first most massive systems cannot be determined from the depth of current surveys, our results show that the elapsed time between $z = 3$ and $z = 2$ is of major importance in the construction of the bulk of the stellar mass in a significant fraction of massive galaxies. The number density of all the galaxies with stellar mass $M > 1 \times 10^{11}\,M_{\odot}$ ($M > 2.5 \times 10^{11}\,M_{\odot}$) rises by more than a factor two (three) between $z \sim 3$ and $z \sim 1.5$ (cf. fig. 3 and 5). This is entirely consistent with a major period of IR activity at $z \sim 2-3$.

The similarities between the optical/near-IR SEDs of massive ERGs that are ultra-luminous in the IR and those that are not suggests that ULIRGs do not represent a particular type of near-IR selected galaxies. They rather could constitute a phase (the phase of high star-formation/quasar activity) during the life of a massive galaxy, and in particular during the period in which it is detected as an ERG. Bright IR galaxies are only able to trace a fraction of the massive galaxies present in the Universe at a given time, but this fraction becomes very important ($\gtrsim 50\%$) at redshifts $z \gtrsim 2$.

Acknowledgements. This paper is in part based on observations made with the *Spitzer Observatory, which is operated by the Jet Propulsion Laboratory, California Institute of Technology, under NASA contract 1407. Also based on public GOODS datasets, obtained with the Advanced Camera for Surveys on board the Hubble Space Telescope operated by NASA/ESA and with the Infrared Spectrometer and Array Camera on the 'Antu' Very Large Telescope operated by the European Southern Observatory in Cerro Paranal, Chile. We thank the GOODS teams for providing reduced data products.*

We thank George Rieke for reading the manuscript and the anonymous referee for making some useful remarks. KIC acknowledges CNES and CNRS funding. RJM acknowledges the support of the Royal Society.

References

Alonso-Herrero, A., Pérez-González, P. G., Alexander, D. M., et al. 2006, ApJ, 640, 167
Barmby, P., Alonso-Herrero, A., Donley, J.L., et al., 2006, ApJ, in press
Bell, E. F., McIntosh, D. H., Katz, N., Weinberg, M. D. 2003, ApJS, 149, 289
Benítez, N. 2000, ApJ, 536, 571
Bolzonella, M., Miralles, J.-M., & Pelló, R. 2000, A&A, 363, 476
Calzetti, D., Armus, L., Bohlin, R. C., et al. 2000, ApJ, 533, 682
Caputi, K. I., Dunlop, J. S., McLure, R. J., & Roche, N. D. 2004, MNRAS, 353, 30
Caputi, K. I., Dunlop, J. S., McLure, R. J., & Roche, N. D. 2005, MNRAS, 361, 607
Caputi, K. I., McLure, R. J., Dunlop, J. S., Cirasuolo, M., & Schael, A. M. 2006, MNRAS, 366, 609 (C06a)
Caputi, K. I., Dole, H., Lagache, G., et al. 2006, ApJ, 637, 727 (C06b)
Chapman, S. C., Blain, A. W., Ivison, R. J., & Smail, I. R. 2003, Nature, 422, 695
Chary, R., & Elbaz, D. 2001, ApJ, 556, 562
Cole, S., Norberg, P., Baugh, C. M., et al. 2001, MNRAS, 326, 255
Daddi, E., Dickinson, M., Chary, R., et al. 2005, ApJ, 631, L13

Désert, F.-X., Boulanger, F., Puget, J.-L. 1990, A&A, 237, 215
Dickinson, M., Papovich, C., Ferguson, H., & Budavári, T. 2003, ApJ, 587, 25
Doherty, M., Bunker, A. J., Ellis, R. S., & McCarthy, P.J. 2005, MNRAS, 361, 525
Dole, H., Lagache, G., Puget, J.-L., et al. 2006, A&A, in press
Egami, E., Dole, H., Huang J.-S., et al. 2004, ApJS, 154, 130
Elbaz, D., Cesarsky, C. J., Chanial, P., et al. 2002, A&A, 384, 848
Flores, H., Hammer, F., Thuan, T. X., et al. 1999, ApJ, 517, 148
Fontana, A., Pozzetti, L., Donnarumma, I., et al. 2004, A&A, 424,23
Glazebrook, K., Abraham, R. G., McCarthy, P. J., et al. 2004, Nature, 430, 181
Houck, J.R., Soifer, B.T., Weedman, D., et al., 2005, ApJ, 622, L105
Kennicutt, R. C. Jr. 1998, ApJ, 498, 541
Le Fèvre, O., Vettolani, G., Paltani, S., et al. 2004, A&A, 428, 1043
Le Floc'h, E., Papovich, C., Dole, H., et al., 2005, ApJ, 632, 169
Lutz, D., Yan, L., Armus, L., et al. 2005, ApJ, 632, L13
Lutz, D., Valiante, E., Sturm, E., et al., 2005, ApJ, 625, L83
Mortier, A. M. J., Serjeant, S., Dunlop, J. S., et al. 2005, MNRAS, 363, 509
Papovich, C., Dole, H., Egami, E., et al. 2004, ApJS, 154, 70
Papovich, C., Moustakas, L. A.,Dickinson, M., et al. 2006, ApJ, 640, 92
Pérez-González, P. G., Rieke, G. H., Egami, E., et al. 2005, ApJ, 630, 82
Rieke, G. H., Young, E. T., Engelbracht, C. W., et al. 2004, ApJS, 154, 25
Stevens, J.A., Ivison, R. J., Dunlop, J. S., et al. 2003, Nature, 425, 264
Takeuchi, T. T., Buat, V., Iglesias-Páramo, J., et al., 2005, A&A, 432, 423
Vanzella, E., Cristiani, S., Dickinson, M., et al. 2005, A&A, 434, 53
Werner, M. W., Roellig, T. L., Low, F. J., et al. 2004, ApJS, 154, 1
Wolf, C., Meisenheimer, K., Kleinheinrich, M., et al. 2004, A&A, 421, 913
Yan , L., Choi, P. I., Fadda, D., et al. 2004, ApJS, 154, 75
Yan, L., Chary, R., Armus, L., et al., 2005, ApJ, 628, 604

The Astrophysical Journal, 637:727–740, 2006 February 1

LINKING STELLAR MASS AND STAR FORMATION IN *SPITZER* MIPS 24 μm GALAXIES

K. I. Caputi,[1] H. Dole,[1] G. Lagache,[1] R. J. McLure,[2] J-L. Puget,[1] G. H. Rieke,[3] J. S. Dunlop,[2] E. Le Floc'h,[3] C. Papovich,[3,4] and P. G. Pérez-González[3]

Received 2005 June 7; accepted 2005 October 3

ABSTRACT

We present deep $K_s < 21.5$ (Vega) identifications, redshifts, and stellar masses for most of the sources composing the bulk of the 24 μm background in the GOODS/CDFS. Our identified sample consists of 747 *Spitzer* MIPS 24 μm objects and includes ~94% of all the 24 μm sources in the GOODS-South field that have fluxes $S_\nu(24\ \mu\mathrm{m}) > 83\ \mu$Jy (the ~80% completeness limit of the *Spitzer*/GTO 24 μm catalog); 36% of our galaxies have spectroscopic redshifts (mostly at $z < 1.5$), and the remaining ones have photometric redshifts of very good quality, with a median of $|dz| = |z_{\mathrm{spec}} - z_{\mathrm{phot}}|/(1 + z_{\mathrm{spec}}) = 0.02$. We find that MIPS 24 μm galaxies span the redshift range $z \sim 0$–4 and that a substantial fraction (28%) lie at high redshifts $z \gtrsim 1.5$. We determine the existence of a bump in the redshift distribution at $z \sim 1.9$, indicating the presence of a significant population of galaxies with PAH emission at these redshifts. The 24 μm galaxy population ranges from sources with intermediate luminosities ($10^{10}\ L_\odot < L_{\mathrm{IR}} < 10^{11}\ L_\odot$) and low-to-intermediate assembled stellar masses ($10^9\ M_\odot \lesssim M \lesssim 10^{11}\ M_\odot$) at $z \lesssim 0.8$, to massive ($M \gtrsim 10^{11}\ M_\odot$) hyperluminous galaxies ($L_{\mathrm{IR}} > 10^{12}\ L_\odot$) at redshifts $z \sim 2$–3. Massive star-forming galaxies at redshifts $2 \lesssim z \lesssim 3$ are characterized by very high star formation rates (SFR $> 500\ M_\odot\ \mathrm{yr}^{-1}$), and some of them are able to construct a mass of $\approx 10^{10}$–$10^{11}\ M_\odot$ in a single burst lifetime (~0.01–0.1 Gyr). At lower redshifts $z \lesssim 2$, massive star-forming galaxies are also present but appear to be building their stars on long timescales, either quiescently or in multiple modest burstlike episodes. At redshifts $z \sim 1$–2, the ability of the burstlike mode to produce entire galaxies in a single event is limited to some lower ($M \lesssim 7 \times 10^{10}\ M_\odot$) mass systems, and it is basically negligible at $z \lesssim 1$. Our results support a scenario in which star formation activity is differential with assembled stellar mass and redshift, and where the relative importance of the burstlike mode proceeds in a downsizing way from high to low redshifts.

Subject headings: galaxies: evolution — galaxies: statistics — infrared: galaxies

1. INTRODUCTION

Infrared (IR) surveys provide an unbiased way of studying the star formation history of the universe. The *Spitzer Space Telescope* (Werner et al. 2004), with its unprecedented sensitivity, is revolutionizing our understanding of IR galaxy evolution by obtaining very deep IR maps. The previous space IR facilities, the *Infrared Astronomical Satellite* (*IRAS*) and the *Infrared Space Observatory* (*ISO*), set the first constraints on mid- and far-IR galaxy evolution at $z \lesssim 1$ (see Genzel & Cesarsky [2000] and Franceschini et al. [2001] for a review). Deep *Spitzer* images offer the possibility of exploring star formation in the high-redshift universe, covering the gap between *ISO* sources and the still limited quantity of known submillimeter sources at redshifts $z \sim 2$–3 (e.g., Scott et al. 2002; Borys et al. 2003; Chapman et al. 2003).

The study of IR sources at high redshifts is useful to put constraints on the early stages of star and galaxy formation. An important cosmological issue is the determination of what kind of galaxies host star formation activity at different redshifts. At $z \sim 1$, a mixture of star-forming objects is found, from massive spiral galaxies to ongoing starbursts (Franceschini et al. 2003; Bell et al. 2005). In addition, it is known that star formation can proceed on different timescales, from bursts produced in short time periods (typically 0.01–0.1 Gyr) to sources with extended periods of quiescent activity. The study of the evolution of the full range of star-forming galaxies should allow reconstruction of the star formation history of the universe.

Several empirical approaches based on *IRAS*/*ISO* surveys have predicted the existence of a substantial population of mid-IR galaxies at high redshifts. Very recently, based on the modeling of the number counts of *Spitzer* 24 μm galaxies, Lagache et al. (2004) concluded that the polycyclic aromatic hydrocarbon (PAH) emission characteristic of the interstellar medium (Désert et al. 1990) should remain observable in galaxies up to $z \sim 2.5$. The main PAH spectral features are located at rest-frame wavelengths $\lambda_{\mathrm{rf}} = 3.3$, 6.2, 7.7, 8.6, 11.3, 12.7, 16.3, and 17 μm. If present, these emission lines should enter the 24 μm filter at redshifts $z \sim 6.3$, 2.9, 2.1, 1.8, 1.1, 0.9, 0.5, and 0.4, respectively. Thus, if PAH molecules already exist in high-redshift galaxies, they should appear in the 24 μm passband, producing the selection of a substantial population of sources at redshifts $z \gtrsim 1$ (Papovich et al. 2004).

In this work we present K_s-band identifications, redshifts, and stellar mass estimates for most of the sources composing the 24 μm background down to faint fluxes in ~131 arcmin^2 of the Great Observatories Origins Deep Survey Chandra Deep Field–South (GOODS/CDFS), achieving 94% identification completeness for sources with flux $S_\nu(24\ \mu\mathrm{m}) > 83\ \mu$Jy. The mostly complete redshift identification of *Spitzer* 24 μm sources with magnitudes $R < 24$ (Vega) at $z \lesssim 1$ has already been achieved by Le Floc'h et al. (2005) over an extended area of the CDFS. Evidence of luminous infrared galaxies up to redshift $z \sim 2.5$ has been reported by different authors (Le Floc'h et al. 2004; Lonsdale et al. 2004; Papovich et al. 2006). The evolution of the mid-IR luminosity function and the derived SFR densities have been explored by Le Floc'h et al. (2005) and Pérez González et al. (2005). The present work, albeit based on the study of a smaller area, complements the former, as it exploits the unique quality of the GOODS data sets to obtain an almost complete identification of the sources composing the mid-IR background and to characterize some of their most important properties from low to high redshifts (from $z \approx 0$ to $z \approx 3$–4).

The organization of this paper is as follows. In § 2 we summarize the data sets and catalogs used to construct the source sample analyzed in the present study. In § 3 we present the redshift distribution of the 24 μm galaxy population in the GOODS/CDFS. In § 4 we give estimates of their characteristic stellar masses. In § 5 we study the evolution of IR luminosities and stellar masses with redshift and put constraints on the SFRs and timescales for star formation activity in different mass galaxies. Finally, in § 6 we summarize our results and present some concluding remarks. We adopt throughout a cosmology with $H_0 = 70\ \mathrm{km\ s^{-1}\ Mpc^{-1}}$, $\Omega_M = 0.3$, and $\Omega_\Lambda = 0.7$.

2. K_s-BAND COUNTERPARTS TO MIPS 24 μm SOURCES

2.1. *The Data Samples and Redshift Estimates*

Deep 24 μm observations of ~2000 arcmin^2 of the CDFS have been carried out with the Multiband Imaging Photometer for *Spitzer* (MIPS; Rieke et al. 2004), as part of the Guaranteed Time Observers (GTO) program. The data reduction, extraction of sources, and photometry measurements are explained in detail in Papovich et al. (2004). The source catalog achieves 80% completeness at a flux limit of $S_\nu \sim 83\ \mu$Jy, and the fraction of spurious sources at that limit is determined to be <10%. The 24 μm source density in the CDFS is $N(S_\nu > 83\ \mu\mathrm{Jy}) = 4.5\ \mathrm{arcmin}^{-2}$. Above a flux of $S_\nu \sim 60\ \mu$Jy, resolved *Spitzer* sources account for ~70% of the 24 μm cosmic infrared background (Papovich et al. 2004; Lagache et al. 2004).

The GOODS project (Giavalisco et al. 2004) has provided deep multiwavelength data for ~160 arcmin^2 of the CDFS. The data products are released to the astronomical community in a fully reduced mode. As part of the European Southern Observatory GOODS Imaging Survey program (ESO GOODS/EIS; B. Vandame et al. 2006, in preparation), deep *J*- and K_s-band images taken with the Infrared Spectrometer and Array Camera (ISAAC) on the Very Large Telescope (VLT) have been made public for ~131 arcmin^2 of the GOODS/CDFS. This is the area analyzed in the present work. The ESO/EIS imaging in this field is complemented by deep imaging data in the *B*, *V*, I_{775}, and z_{850} bands taken with the Advanced Camera for Surveys (ACS) on board the *Hubble Space Telescope* (*HST*) and by 3.6, 4.5, 5.8, and 8.0 μm data taken with the Infrared Array Camera (IRAC; Fazio et al. 2004) on board *Spitzer*.

A catalog of $K_s < 21.5$ (Vega) sources has been selected in the GOODS/EIS CDFS. Photometric redshifts based on up to eight broad bands ($BVI_{775}z_{850}JK_s$ and IRAC 3.6 and 4.5 μm bands) have been obtained for the whole sample, using the publicly available multiwavelength data and the public code HYPERZ (Bolzonella et al. 2000) with the GISSEL98 spectral energy distribution (SED) template library (Bruzual & Charlot 1993). Dust corrections have been taken into account through the convolution of the SED templates with the Calzetti et al. (2000) reddening law.

Although *U*-band data exist for the CDFS, they have not been included in the input catalogs for the photometric redshift algorithms, as the *U*-band images have shallower depth and poorer resolution than the ACS and ISAAC images in the same field. However, *U*-band images have been used to control the HYPERZ output: for every K_s-band source with a counterpart in the shallow *U*-band catalogs, the resulting photometric redshift was determined as the best-fit value constrained to a maximum redshift $z_{\mathrm{phot}} = 2$, as higher redshift sources are unlikely to be bright at such short wavelengths. In addition, the public code BPZ (Benítez 2000) has been used to obtain a second independent set of redshift estimates for all the $K_s < 21.5$ sources. In the cases of sources with HYPERZ photometric redshifts $z_{\mathrm{phot}} > 2$ not confirmed by BPZ, we adopted the lower estimates from the BPZ code. In addition, public COMBO17 photometric redshifts (Wolf et al. 2004) have been used to replace the redshift estimates of those sources with magnitude $R < 23.5$ (Vega) and $z < 1$ (the most accurate regime for COMBO17 redshifts). Further details on the redshift estimations for the total $K_s < 21.5$ sample are given in a separate paper (Caputi et al. 2006). Figure 1*a* compares the obtained photometric redshifts with spectroscopic redshifts for all those $K_s < 21.5$ sources in the GOODS/EIS CDFS included in different publicly available spectroscopy samples (e.g., Vanzella et al. 2005; Le Fèvre et al. 2004). We observe a very good agreement between the photometric estimates and the real redshifts in most cases, with a median for the absolute relative errors of $|dz| = |z_{\mathrm{spec}} - z_{\mathrm{phot}}|/(1 + z_{\mathrm{spec}}) = 0.02$. Figure 1*b* shows the corresponding histogram of relative errors.

[1] Institut d'Astrophysique Spatiale, Bâtiment 121, Université Paris Sud, F-91405 Orsay Cedex, France.
[2] Institute for Astronomy, University of Edinburgh, Royal Observatory, Blackford Hill, Edinburgh EH9 3HJ, UK.
[3] Steward Observatory, University of Arizona, 933 North Cherry Avenue, Tucson, AZ 85721.
[4] Spitzer Fellow.

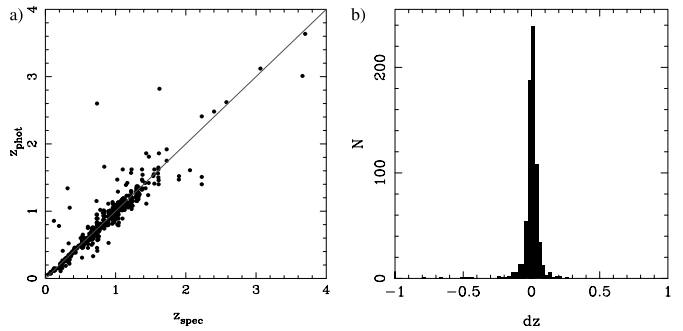

Fig. 1.—(*a*) Photometric vs. spectroscopic redshifts for $K_s < 21.5$ galaxies in the GOODS/CDFS. (*b*) Histogram of the relative errors $dz = (z_{\mathrm{spec}} - z_{\mathrm{phot}})/(1 + z_{\mathrm{spec}})$. The rms of this distribution is 0.03.

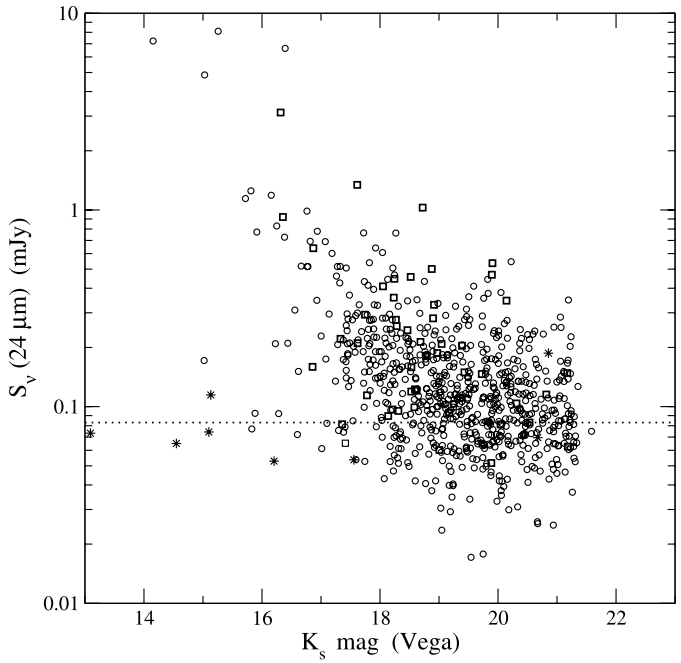

FIG. 2.—Plot of 24 μm fluxes vs. K_s magnitudes for the MIPS 24 μm sources in the GOODS/CDFS associated with a $K_s < 21.5$ counterpart. The circles, squares, and asterisks correspond to normal galaxies, active galaxies, and Galactic stars, respectively. The dotted line indicates the limit of ~80% completeness of the 24 μm catalog, above which the K_s-band identification is ~94%.

The rms of the distribution is 0.03. However, in spite of the good accuracy obtained for the photometric redshifts, the incorporation of available spectroscopic redshifts is of much benefit for any study of a galaxy redshift distribution. Thus, in order to maximize the quality of the final redshift catalog, the existing spectroscopic redshifts in the CDFS have been used to replace the photometric estimates of the $K_s < 21.5$ sources whenever possible (i.e., 23% of the total $K_s < 21.5$ sample).

2.2. *Cross-Correlation of the Catalogs*

We cross-correlated the $K_s < 21.5$ GOODS/CDFS source catalog with the *Spitzer* MIPS 24 μm GTO/CDFS catalog both to investigate and put constraints on the mid-IR emission of K_s-selected galaxies and to identify and characterize the optical/near-IR properties of the *Spitzer* MIPS 24 μm sources in the GOODS South field. This work presents the results of the latter, while a full analysis of 24 μm detected and nondetected K_s-selected galaxies in the GOODS/CDFS will be presented elsewhere (K. I. Caputi et al. 2006, in preparation). In addition, the IRAC and MIPS properties of galaxies selected with colors $J-K_s > 2.3$ are studied by Papovich et al. (2006).

We looked for 24 μm counterparts of the $K_s < 21.5$ selected sources in the GOODS/CDFS using a matching radius of 2″ to minimize the number of multiple identifications. The astrometric accuracy of the MIPS 24 μm images (e.g., Le Floc'h et al. 2005) allows the use of such a small matching distance. We found 812 $K_s < 21.5$ selected sources associated with MIPS 24 μm sources within this radius. In 65/812 cases, we found two or more K_s-selected sources associated with the same 24 μm source. In these cases we selected the closest counterpart, leaving 747 24 μm sources with a $K_s < 21.5$ identification. We identified a negligible fraction (11/747) of Galactic stars among these MIPS 24 μm sources, and we exclude them from all the following analysis. We determined redshifts for each of the remaining 736 24 μm sources; 36% of them have spectroscopic redshifts, and 21% more have COMBO17 photometric redshifts. The remaining 43% have HYPERZ/BPZ photometric redshifts; 521/747 sources are above the 24 μm catalog 80% completeness limit—i.e., they have $S_\nu > 83$ μJy. On the other hand, we find four K_s-selected objects that could be associated with two or more 24 μm sources. All of these cases correspond to low-redshift galaxies, with spectroscopic redshifts $z_{spec} < 0.13$. Individual inspection

TABLE 1
COMPLETENESS LIMITS FOR THE K_s-BAND IDENTIFICATIONS OF THE *Spitzer* MIPS 24 μm SOURCES IN THE GOODS/CDFS

24 μm Flux S_ν (μJy)	K_s-Band Identification Completeness (%)
>250	100
>200	99
>150	96
>100	95
>83	94

of both the K_s and 24 μm images suggests the *Spitzer* MIPS detection of multiple nodes of mid-IR emission for each of these nearby galaxies. In Figure 2, we show the total 24 μm flux S_ν versus K_s magnitude for the 747 MIPS sources with $K_s < 21.5$ identifications in the GOODS/CDFS. In the four cases of multiple MIPS sources associated with a single K_s-band object, we considered that the 24 μm flux was the sum of the different 24 μm components; 686/747 MIPS 24 μm sources in the GOODS/CDFS have counterparts classified as normal galaxies (circles in Fig. 2), while 50/747 are active ones (active galactic nuclei [AGNs] or quasi-stellar objects [QSOs]; squares in Fig. 2). The identification of K_s sources with active galaxies is based on the cross-correlation with the X-ray catalogs available for the CDFS (Szokoly et al. 2004). This approach provides only a lower limit to the fraction of active galaxies among the 24 μm galaxy population (Alonso-Herrero et al. 2006; Donley et al. 2005). The cross-correlations of the $K_s < 21.5$ GOODS/CDFS source catalog with the *Spitzer* MIPS 24 μm GTO/CDFS catalog allows us to achieve a completeness limit of ~94% for the identification of MIPS 24 μm sources with flux $S_\nu > 83$ μJy in the GOODS/CDFS (see Table 1).

As we mentioned above, our HYPERZ photometric redshift determinations are based on the SED fitting of the galaxies made using the templates in the GISSEL98 library of Bruzual & Charlot (1993). Also, this SED fitting procedure has been used to determine derived parameters (e.g., estimated stellar mass) for all the galaxies, independent of whether the redshifts were from HYPERZ/BPZ, COMBO17, or spectroscopic. The GISSEL98 library is composed of a wide range of synthetic SEDs based on stellar spectra but does not have any optical to near-IR power-law SED. To investigate the impact of this limitation in our redshift distribution of MIPS 24 μm galaxies, we identified the presence of 24 μm power-law SED galaxies in the GOODS/CDFS using the catalog of IR power-law sources constructed by Alonso-Herrero et al. (2006). We found 20 24 μm galaxies with IR power-law spectra in the GOODS/CDFS. Nine of these power-law galaxies have spectroscopic redshifts, leaving only 11 power-law sources with a HYPERZ/BPZ photometric redshift (and 7/11 are X-ray–detected; see § 4). Consequently, plausible erroneous redshift estimates due to inadequate SED template fitting are reduced to a very minor fraction of the 24 μm sources studied here, and thus they should have a basically negligible impact on all the analysis in this work.

2.3. *Summary of Properties of the 24 μm Source Sample Analyzed in This Work*

For clarity, we summarize the properties of the source sample analyzed in this work as follows:

1. Our sample is composed of the 747 24 μm sources in ~131 arcmin^2 of the GOODS/CDFS that have a $K_s < 21.5$ (Vega) counterpart; 521/747 sources have a flux above the GTO catalog 80% completeness limit, i.e., $S_\nu(24\ \mu m) > 83$ μJy. These 521 objects constitute ~94% of all the MIPS 24 μm sources with $S_\nu(24\ \mu m) > 83$ μJy in the GOODS/CDFS.

2. Only 11/747 sources in our sample are identified as galactic stars; 50/747 sources are X-ray–classified AGNs or QSOs. The remaining 686/747 sources are normal galaxies (i.e., no X-ray AGN or QSO).

3. We determined redshifts for each of the 736 galaxies in our sample (i.e., all sources except the 11 galactic stars); 36% of these redshifts are spectroscopic, and 21% additional redshifts have been taken from the COMBO17 photometric redshift catalog (only for sources with R-band magnitude $R < 23.5$, Vega, and redshifts $z < 1$). The photometric redshifts for the remaining 43% of the sample have been obtained using HYPERZ/BPZ and are based on broadband photometry covering from the optical B band through the 4.5 μm band.

In this way, our sample allows us to identify and characterize the evolution down to faint fluxes for most of the sources composing the 24 μm background.

Pérez-González et al. (2005) have carried out a study of MIPS 24 μm detections using a different photometric redshift technique. Their approach uses empirical SEDs rather than synthetic templates, and it can fit redshifts using a wider range of multiwavelength data. Their work has the advantage of having been applied to larger fields. However, high signal-to-noise ratio data may not be available in all bands for these large areas, and thus their resulting redshifts have a typical accuracy of about 10%, significantly worse than those obtained here. Our approach depends on high-quality and homogeneous input data, only available for very limited areas of the sky. By combining the results of both works, it is possible to (1) determine overall trends and the effects of cosmic variance based on the approach of Pérez-González et al. (2005) and (2) prove the redshift distribution more accurately in a more limited sky region based on the approach in this paper.

3. THE REDSHIFT DISTRIBUTION OF 24 μm GALAXIES IN THE GOODS/CDFS

Figure 3*a* shows the redshift distribution of the MIPS 24 μm galaxies with $K_s < 21.5$ counterparts in the GOODS/CDFS. The empty (shaded) histogram corresponds to all ($S_\nu > 83$ μJy) sources. The peaks in the redshift distribution at $z \sim 0.7$ and 1.1 are due to the effect of large-scale structure in the CDFS (e.g., Le Fèvre et al. 2004). We find that 72% of the 24 μm galaxies lie at redshifts $z < 1.5$, while the remaining 28% are found to be at $z \geq 1.5$ (the percentages are similar for the samples containing all and only $S_\nu > 83$ μJy galaxies). This confirms the existence of a substantial population of mid-IR sources at high redshifts. Approximately half of the $z \geq 1.5$ sources have the characteristic colors of extremely red galaxies (ERGs), $(I_{775}-K_s) > 4.0$ (Vega), indicating that an important fraction of the high-redshift mid-IR background is constituted by optically obscured sources, as possibly expected (see Yan et al. 2004).

Figure 3*b* shows the normalized redshift distributions of the MIPS 24 μm galaxies with $K_s < 21.5$ counterparts (*black dashed and solid lines*, for all and $S_\nu > 83$ μJy sources, respectively), compared to the redshift distribution of the total $K_s < 21.5$ galaxy population (*gray solid line*) in the same field. Several features are present in all the three curves, which are the consequence of cosmic variance effects. In contrast, we observe the presence of a depression in the redshift distribution of 24 μm galaxies at redshift $z \sim 1.5$ and a bump at redshift $z \sim 1.9$, both of which do not appear in the total $K_s < 21.5$ galaxy curve.

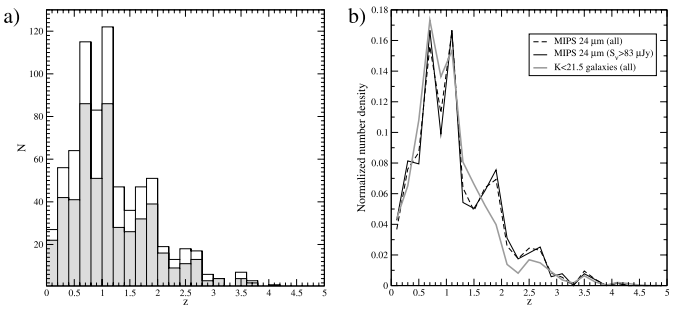

FIG. 3.—(*a*) Redshift distribution of the MIPS 24 μm galaxies with $K_s < 21.5$ counterparts in the GOODS/CDFS: all sources and sources with $S_\nu > 83$ μJy (*empty and shaded histograms*, respectively). (*b*) Normalized redshift distributions of all and $S_\nu > 83$ μJy 24 μm galaxies (*black dashed and solid lines*, respectively), compared to the normalized redshift distribution of the total $K_s < 21.5$ sample in the same field (*gray solid line*).

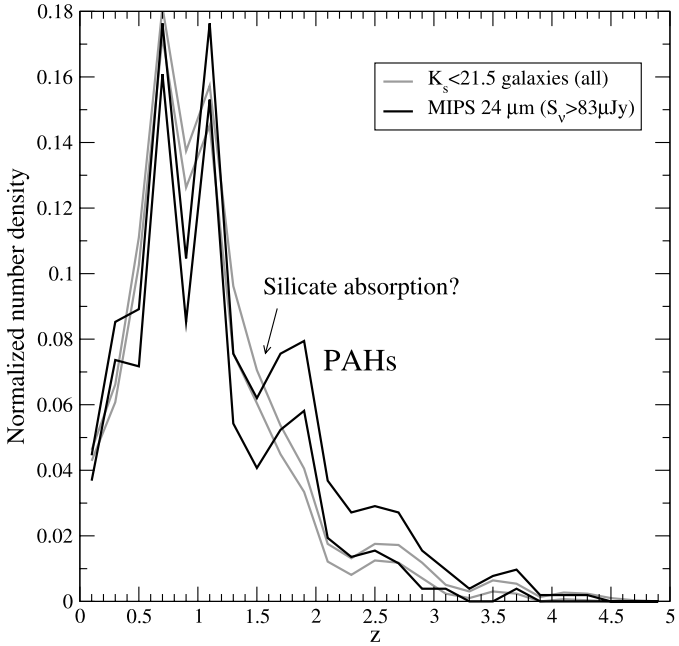

FIG. 4.—Plot of the 95% confidence limits on the normalized redshift distributions of the MIPS $S_\nu(24\ \mu\text{m}) > 83$ μJy galaxies (*black lines*) and all the $K_s < 21.5$ galaxies (*gray lines*). The bump in the redshift distribution of 24 μm galaxies at $z \sim 1.9$ indicates the presence of PAH emission at these high redshifts. The marginally significant depression at redshift $z \sim 1.5$ might be due to silicate absorption.

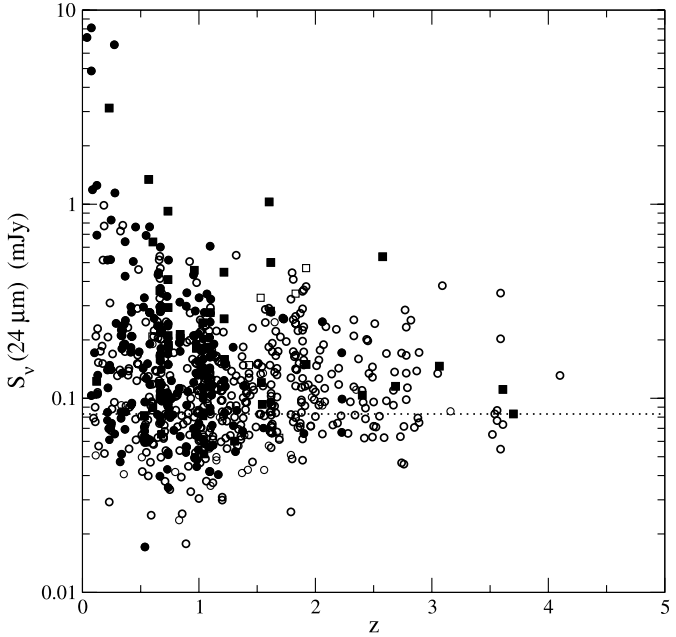

FIG. 5.—Plot of 24 μm flux vs. redshift for the MIPS 24 μm galaxies in the GOODS/CDFS associated with a $K_s < 21.5$ counterpart. The symbols are the same as in Fig. 2. Filled symbols indicate spectroscopic redshifts.

To assess the significance of the features observed exclusively on the 24 μm galaxy redshift distributions, we computed confidence limits on the different curves. We performed Monte Carlo simulations to create 1000 mock redshift catalogs, alternatively for the total $K_s < 21.5$ galaxy population and for the MIPS 24 μm galaxies with flux $S_\nu > 83$ μJy. We constructed each mock catalog assigning to each source a random redshift, with a Gaussian probability centered at the original redshift z of the source and a dispersion equal to $0.02\,(1 + z)$ (i.e., the median error at the corresponding redshift). The redshifts of those sources with spectroscopic values were left fixed. We recomputed the normalized redshift distribution for each mock catalog and determined confidence limits on the original distribution curves. The 95% confidence limits on the total $K_s < 21.5$ galaxy and the MIPS ($S_\nu > 83$ μJy) galaxy distributions are shown in Figure 4.

Figure 4 shows that, even taking into account the error bars, the peak in the 24 μm redshift distribution at $z \sim 1.9$ is significant, lying $\sim 4\,\sigma$ from the original total $K_s < 21.5$ galaxy curve. Thus, we conclude that the redshift distribution of 24 μm galaxies presents a real secondary bump at these high redshifts. This secondary peak has been predicted by Lagache et al. (2004) and is the consequence of the selection effect produced by the presence of PAH emission features entering the observed 24 μm band. Given the width of the 24 μm filter (whose transmission covers the wavelength range $\sim$20–28 μm), both the 7.7 and the 8.6 μm PAH lines could contribute to the redshift distribution peak observed at $z \sim 1.9$. Our results allow us to conclude that PAH molecules must be already present in star-forming galaxies at high redshifts.

The confidence limits shown in Figure 4 also indicate that the depression observed in the 24 μm redshift distribution at $z \sim 1.5$ is only marginally significant within our sample. The existence of such a depression could be interpreted as due to the 9.8 μm silicate absorption feature entering the 24 μm filter at this redshift, which has been observed for some galaxies in previous works (Houck et al. 2005; Yan et al. 2005). However, given the errors in the redshift distributions presented here, we cannot reach any firm conclusion on the possible selection effect produced by silicate absorption at high redshifts.

We also see a substantial deficit of 24 μm sources at redshift $z \sim 0.9$, with respect to the total $K_s < 21.5$ sources. At this redshift, a positive selection effect on 24 μm galaxies would be expected due to the presence of the 12.7 μm PAH emission line. The observed relative deficit of bright mid-IR selected galaxies indicates that, within our sample, star-forming galaxies are present in a minor proportion at this redshift. This is quite likely due to a mere cosmic variance effect. However, we note that this deficit in our 24 μm sample occurs at the same redshift where

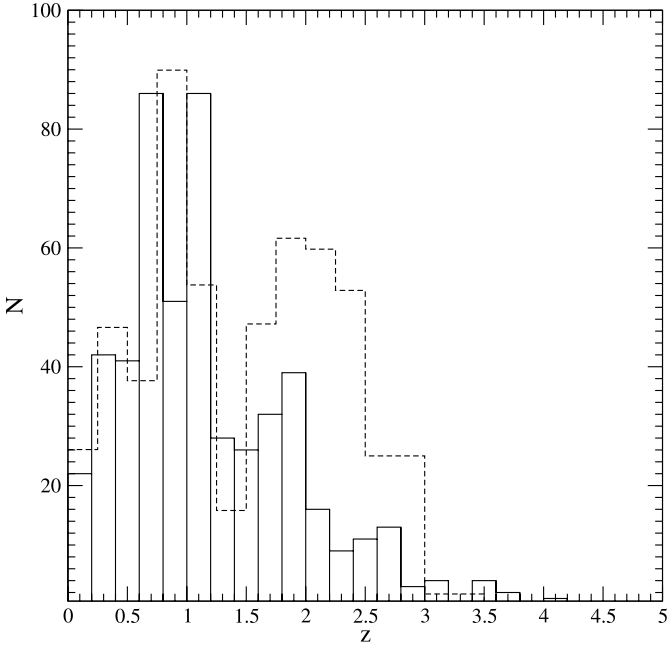

FIG. 6.—Comparison of the observed redshift distribution of MIPS 24 μm galaxies in the GOODS/CDFS (*solid histogram*) with the redshift distribution predicted by Lagache et al. (2004; *dashed histogram*). Both distributions correspond to sources with flux $S_\nu(24\ \mu\mathrm{m}) > 83\ \mu$Jy in an area of 131 arcmin^2.

there is a dip in the total $K_s < 21.5$ redshift distribution. If we consider that galaxy interactions are a triggering mechanism for star formation, then it will be possible that star formation activity is particularly inhibited in regions with an underdensity of objects. The study of similar regions in other areas of the sky is necessary to determine whether the two facts are actually related.

Evidence of the existence of PAH emission in the spectra of a few high-redshift $1.7–1.8 < z < 2.6–2.8$ galaxies has recently been presented by Houck et al. (2005), Yan et al. (2005), and Lutz et al. (2005). In this work, we extend this evidence through the study of the redshift distribution of the whole 24 μm galaxy population. It is interesting to note, however, that both Houck et al. (2005) and Yan et al. (2005) found that only a minority of their galaxies at $z \sim 1.7–2.8$ showed clear PAH emission features in their spectra, while most of their remaining high-redshift galaxies were AGN-dominated or had silicate absorption features. The difference in the nature of the sources dominating Houck et al. and Yan et al. samples can be explained taking into account that their objects are, on average, an order of magnitude more luminous than most of the sources analyzed in this work. Deep 24 μm samples are necessary to uncover a substantial population of PAH galaxies at redshift $z \sim 2$. Figure 5 shows the 24 μm flux of each galaxy S_ν versus redshift z. The symbols are the same as in Figure 2. Filled symbols correspond to sources with spectroscopic redshifts. Within our sample, we see that only a few bright $S_\nu(24\ \mu\mathrm{m}) > 0.5$ mJy sources are placed at high redshift ($z \gtrsim 1.5$) and that they are all active galaxies. At fainter fluxes $S_\nu \lesssim 0.3$ mJy, starbursts produce the bulk of the mid-IR emission at high redshifts.

Pérez-González et al. (2005) found that 24% of the 24 μm galaxies with $S_\nu > 83\ \mu$Jy in an extended region of the CDFS and the Hubble Deep Field–North (HDFN) were at redshifts $z > 1.5$, in agreement with our value of 28% within the errors and taking into account the different fields surveyed. However, their redshift distribution does not show the PAH-induced peak at $1.6 \lesssim z \lesssim 2.2$. They suggested that this feature may have been blurred by the errors in photometric redshifts; this suggestion is confirmed by our detection of the PAH bump using redshifts of higher accuracy. Taken together, the two studies show that the drop in the number of sources beyond $z \sim 1.2$ holds generally and is not just observed in the CDFS. In addition, we show that there is a significant peak produced by PAH emission on top of this general trend.

Figure 6 shows the comparison of our observed redshift distribution of 24 μm galaxies in the GOODS/CDFS (*solid histogram*) with the distribution predicted by Lagache et al. (2004) using the Lagache et al. (2003) model (*dashed histogram*). Both distributions correspond to sources with flux $S_\nu > 83\ \mu$Jy in an area of 131 arcmin^2. The observed and predicted distributions have 521 and 518 galaxies, respectively, confirming that the Lagache et al. (2003) model reproduces the observed number counts very well. Also in agreement with the model, we find that a significant population of 24 μm galaxies lie at redshifts $z > 1.5$, and our accurate redshift determinations reveal the predicted secondary peak in the redshift distribution at $z \sim 1.9$ produced by the presence of PAH emission. However, the fraction of galaxies at redshifts $z > 1.5$ is significantly overpredicted by the Lagache et al. model. Other models (e.g., Chary & Elbaz 2001) basically predict a negligible fraction of sources at redshifts $z > 1.5$ and also do not fit the observed redshift distribution. Therefore, theoretical models require further refinements to reproduce the distant infrared-emitting galaxy populations.

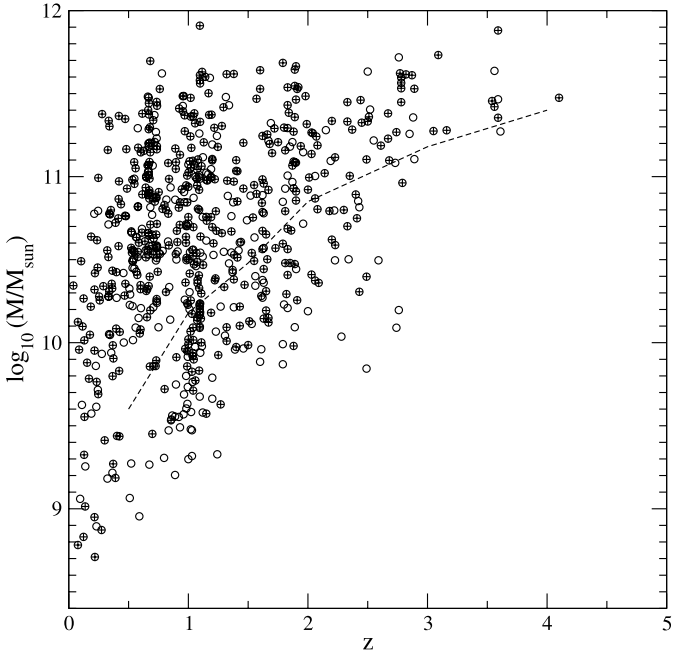

FIG. 7.—Estimated assembled stellar masses for the MIPS 24 μm galaxies with $K_s < 21.5$ counterparts in the GOODS/CDFS. The symbols with a plus sign correspond to galaxies with flux $S_\nu(24\ \mu\mathrm{m}) > 83\ \mu$Jy. The dashed line indicates the estimated mass completeness limits imposed by the $K_s < 21.5$ survey. However, we note that these limits are basically irrelevant for the galaxies with flux $S_\nu(24\ \mu\mathrm{m}) > 83\ \mu$Jy, as the K_s-band identification completeness for these galaxies is ~94%.

4. THE ASSEMBLED STELLAR MASSES OF MIPS 24 μm GALAXIES

Figure 7 shows the estimated assembled stellar masses of the MIPS 24 μm galaxies versus redshift z in the GOODS/CDFS. The estimation of the stellar masses is based on the optical–to–near-IR SED fit of each galaxy at the determined redshift (either spectroscopic, from COMBO17, or HYPERZ/BPZ) and is completely independent of its 24 μm properties. We determined estimated stellar masses for all the 24 μm galaxies with a $K_s < 21.5$ identification, except for any X-ray–classified AGN/QSO or any other X-ray source without a suitable GISSEL98 template optical–to–near-IR SED fit. We excluded the latter objects to avoid galaxies with partial contamination of the optical–to–near-IR light by a hidden AGN. The stellar masses are computed from the modeled rest-frame K_s-band galaxy luminosity of each galaxy, where the mass-to-light ratios have a minimum dependence on the SED star formation histories or dust corrections (see Caputi et al. [2005, 2006] for further details). The resulting stellar mass estimates are typically accurate within a factor of $\lesssim 2$. A single power-law Salpeter initial mass function (IMF) over stellar masses $M = 0.1–100\ M_\odot$ has been assumed throughout. The estimated mass completeness limits for counterparts of the MIPS 24 μm galaxies are 1.5×10^{10}, 7.0×10^{10}, and $1.5 \times 10^{11}\ M_\odot$ at redshifts $z = 1, 2$, and 3, respectively, based on the $K_s = 21.5$ mag limit and the median of the k-corrections. However, it should be noted that the mass completeness limits are basically

irrelevant for the sources with flux $S_\nu > 83$ μJy (symbols with plus signs in Fig. 7), as the K_s-band identifications are almost complete above this limit.

Inspection of Figure 7 shows that, at least at redshifts $z \lesssim 1$, star formation activity takes place in galaxies of a wide range of assembled stellar masses, from $\sim 10^9$ to $\sim 10^{12}$ $M_\odot$. At high redshifts $z \gtrsim 2.5$, the existence of a significant population of massive $M > 10^{11}$ $M_\odot$ star-forming galaxies is revealed in the mid-IR at the depth of the GTO/CDFS images. It is now commonly believed that a fraction of present-day massive galaxies is already in place at high redshifts (Cimatti et al. 2004; Glazebrook et al. 2004; Caputi et al. 2005, 2006). However, it is still unclear when the bulk of the stars in these massive galaxies was formed (see Papovich et al. 2006). The identification of massive objects on the MIPS 24 μm images can put constraints on their star formation histories and the amount of stellar mass built up at different redshifts.

5. CONSTRAINTS ON THE STAR FORMATION HISTORY

5.1. *The Evolution of Star-forming Galaxies with Redshift*

The study of the physical properties of IR-selected galaxies at different redshifts is of importance to understand how star formation evolved with cosmic time. In this section, we use the 24 μm fluxes of the galaxies in the GOODS/CDFS in conjunction with the redshift and stellar mass estimations, to study the evolution of star formation activity.

Chary & Elbaz (2001) and Elbaz et al. (2002) showed that the mid-IR luminosities of nearby galaxies were correlated (with some scatter) with their bolometric IR luminosity $L_{\rm IR}$, defined as $L_{\rm IR} = L(8\text{–}1000\ \mu{\rm m})$. They fitted the following set of relations:

$$L_{\rm IR} = 11.1^{+5.5}_{-3.7}[\nu L_\nu(15\ \mu{\rm m})]^{0.998}, \quad (1)$$

$$= 0.89^{+0.38}_{-0.27}[\nu L_\nu(12\ \mu{\rm m})]^{1.094}, \quad (2)$$

$$= 4.78^{+2.37}_{-1.59}[\nu L_\nu(6.75\ \mu{\rm m})]^{0.998} \quad (3)$$

$$\text{for } \nu L_\nu(6.75\ \mu{\rm m}) < 5\times 10^9\ L_\odot,$$

$$= 4.37^{+2.35}_{-2.13}\times 10^{-6}[\nu L_\nu(6.75\ \mu{\rm m})]^{1.62} \quad (4)$$

$$\text{for } \nu L_\nu(6.75\ \mu{\rm m}) \geq 5\times 10^9\ L_\odot,$$

where all the luminosities are in solar units. There are many indications that the overall SEDs of high-redshift infrared galaxies are similar to the local ones captured in equations (1)–(4). For example, the local far-IR/radio and mid-IR/radio correlations (Condon 1992) still hold at higher redshifts (Appleton et al. 2004). Composite SEDs of high-redshift infrared galaxies resemble local templates (e.g., Egami et al. 2004). The MIPS observations in the CDFS indicate that, at least to $z \sim 1$, galaxies have 24 and 70 μm flux ratios that follow the local distribution as a function of total IR luminosity. In addition, number count models assuming similar behavior can fit the 24, 70, and 160 μm data simultaneously (Lagache et al. 2004).

We used the 24 μm fluxes of the MIPS galaxies with a $K_s < 21.5$ counterpart in the GOODS/CDFS to compute their bolometric luminosities $L_{\rm IR}$, assuming the Chary & Elbaz (2001) relations in equations (1)–(4). We excluded all the known AGNs/QSOs from the present analysis. We considered that the 24 μm flux mapped the rest-frame 15, 12, and 6.75 μm fluxes in the redshift ranges $0.4 \leq z < 0.8$, $0.8 \leq z < 1.2$, and $2.0 \leq z < 3.0$, respectively. In the redshift range $1.2 \leq z < 2.0$, we assumed that the infrared luminosity $L_{\rm IR}$ was given by the average of the luminosities obtained using equations (2) and (3)–(4). Figure 8 shows the bolometric IR luminosities of the 24 μm galaxies versus assembled stellar mass in different redshift bins. The dotted lines delimit the region of luminosity completeness at the mean redshift of each bin, taking into account the $S_\nu(24\ \mu{\rm m}) = 83$ μJy limit and the fact that our K_s-band identifications are almost complete above that flux (i.e., the mass completeness limits imposed by the $K_s = 21.5$ cut are basically irrelevant above that limit).

Although for clarity the error bars are not shown in Figure 8, we estimated the errors on our computed bolometric luminosities using an independent set of models. We integrated the different Dale et al. (2001) and Dale & Helou (2002) SED templates, normalized to our observed 24 μm fluxes, to obtain the corresponding IR luminosities as a function of redshift. The complete set of the Dale et al. SEDs consists of 64 templates, each one characterized by a parameter α ($0.0625 < \alpha < 4.0$), which depends on the combination of the observed local SEDs used to construct these models. Compared to the values obtained with the Dale et al. templates, our luminosities based on the Chary & Elbaz (2001) formulae appear to be accurate within a factor of 2–3 to redshift $z \approx 1.5$. Above that redshift, the consideration of the complete set of the Dale et al. SEDs would yield uncertainties of up to a factor of 10–20 (Dale et al. 2005). However, Dale et al. (2005) recently used the Dale et al. templates to fit the observed 1–850 μm photometry of a sample of 75 local galaxies. The majority of these galaxies ($\gtrsim$75%) were best-fitted by templates with $2.0 < \alpha < 4.0$. As we explained above, there are many indications that the overall SEDs of high-redshift IR galaxies are similar to the local ones. Thus, this subset of the Dale et al. templates should be representative of the majority of the IR galaxy types also at high redshifts. If we restrict the comparison of our luminosities computed with the Chary & Elbaz formulae to those values obtained with the Dale et al. $2.0 < \alpha < 4.0$ templates, we find that the error bars would still be within a factor of 2–3 up to redshift $z \approx 2$, and a factor of 5 would be sufficient to account for the errors above that redshift. These factors should be representative of the error bars on the IR luminosities of the majority of our galaxies, including the errors introduced by the k-corrections within each of the considered redshift bins.

We observe that the evolution of the IR luminosities with redshift is still very significant, even taking into account the error bars. Figure 8*a* shows that most of the 24 μm galaxies at redshifts $0.4 \leq z < 0.8$ have infrared luminosities $L_{\rm IR} < 10^{11}$ $L_\odot$. The maximum observed infrared luminosities increase with redshift, and luminous infrared galaxies (LIRGs) characterized by 10^{11} $L_\odot < L_{\rm IR} < 10^{12}$ $L_\odot$ (Sanders & Mirabel 1996) are the dominant 24 μm sources at redshifts $0.8 \leq z < 1.2$ at the depth of the CDFS MIPS/GTO images (Le Floc'h et al. 2005). The majority of the mid-IR sources at $0.4 \leq z < 1.2$ are hosted by intermediate-mass galaxies with stellar masses 10^{10} $M_\odot \lesssim M \lesssim 10^{11}$ $M_\odot$, in agreement with recent findings by Hammer et al. (2005), although some more massive galaxies could also be classified as LIRGs at these redshifts. Within our surveyed area, there is virtually no ultraluminous infrared galaxy (ULIRG) with $L_{\rm IR} > 10^{12}$ $L_\odot$ at $z < 1.2$. ULIRGs might be present at these low redshifts, but are indeed very rare (e.g., Flores et al. 1999). At $1.2 \leq z \leq 2.0$, ULIRGs start to be a very significant population ($\sim$65% at $S_\nu > 83$ μJy), and they are also hosted by intermediate- to high-mass galaxies. At $z > 2$, the limits of the 24 μm survey only allow us to explore the bright IR luminosity end of the star formation activity. We observe sources with extremely high infrared luminosities 10^{12} $L_\odot < L_{\rm IR} < 10^{14}$ $L_\odot$, mainly harbored by galaxies with stellar masses $M > 10^{11}$ $M_\odot$. Our results on luminosity and SFR evolution agree well with

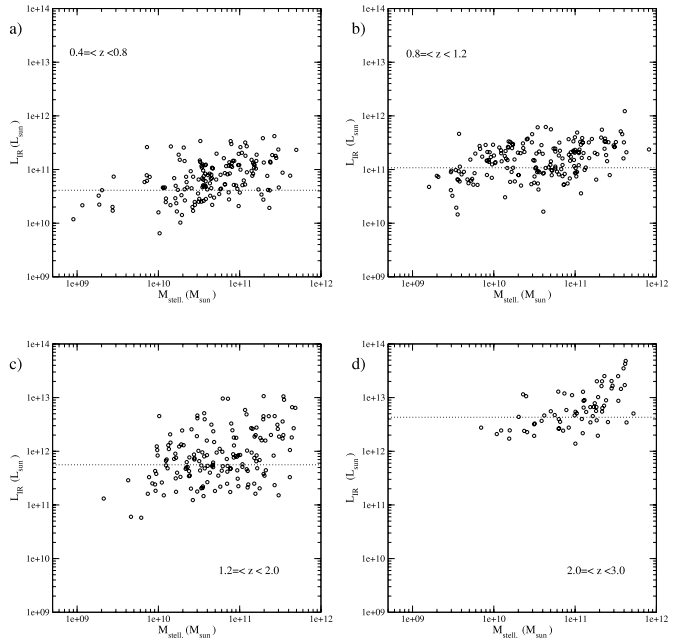

FIG. 8.—Bolometric infrared luminosities vs. assembled stellar masses for the MIPS 24 μm galaxies with $K_s < 21.5$ counterparts in the GOODS/CDFS, in different redshift bins: (*a*) $0.4 \leq z < 0.8$, (*b*) $0.8 \leq z < 1.2$, (*c*) $1.2 \leq z < 2.0$, and (*d*) $2.0 \leq z < 3.0$. The dotted lines delimit the region of completeness at the mean redshift of each bin, taking into account the $S_\nu(24\ \mu{\rm m}) = 83$ μJy limit and the fact that our K_s-band identifications are almost complete above that flux (i.e., the mass completeness limits imposed by the $K_s = 21.5$ cut are basically irrelevant above that limit).

the studies for larger fields made by Le Floc'h et al. (2005) and Pérez-González et al. (2005).

Thus, Figure 8 confirms the global trend of a high degree of evolution in the star formation activity from low to high redshifts. The extremely high IR luminosities observed at $z \gtrsim 2$ show that star formation has been a much more violent process in the past, and these violent episodes of star formation must have built up a significant part of the stellar mass content of at least a fraction of present-day massive galaxies. We explore in more detail this possibility in § 5.2, where we analyze and constrain the typical timescales for star formation of galaxies with different assembled stellar masses at different redshifts.

5.2. *Probing Star Formation in Different Mass Galaxies*

An estimator of the instantaneous SFR of a galaxy based on its bolometric infrared luminosity has been obtained by Kennicutt (1998):

$$\text{SFR} = 1.72\times 10^{-10} L_{\rm IR}, \quad (5)$$

where the SFR is given in units of solar masses per year, the luminosity $L_{\rm IR}$ is in solar units, and a Salpeter IMF over stellar masses $M = 0.1\text{–}100$ $M_\odot$ is assumed. We used equation (5) to obtain an estimate of the instantaneous SFR in the 24 μm galaxies studied here and to explore the relation of this SFR with the already assembled stellar mass of each galaxy, at different redshifts.

Figure 9 shows the evolution of the SFR with redshift for galaxies with assembled stellar masses in different mass bins. In all the panels, the dashed line delimits the region of completeness of the observed SFR versus redshift, as imposed by the flux limit $S_\nu(24\ \mu{\rm m}) = 83$ μJy. We find that the IR-derived SFR grows exponentially with redshift, independent of the galaxy stellar mass (of course, the lower envelope of SFR is a consequence of the limits of the 24 μm survey, but the maximum observed values do exponentially grow with redshift). However, Figure 9*a* shows that, at a given redshift, most of the lowest mass galaxies have relatively small SFRs, which are at most marginally above the completeness limit of the 24 μm survey analyzed here. This effect is particularly evident at high redshifts $z \gtrsim 2$, where we observe a lack of galaxies with stellar mass $M < 1.5\times 10^{10}$ $M_\odot$ and SFR above the completeness limit. Unless the minor fraction of unidentified sources with $S_\nu(24\ \mu{\rm m}) > 83$ μJy constitutes a biased population of low-mass galaxies at high redshifts, we conclude

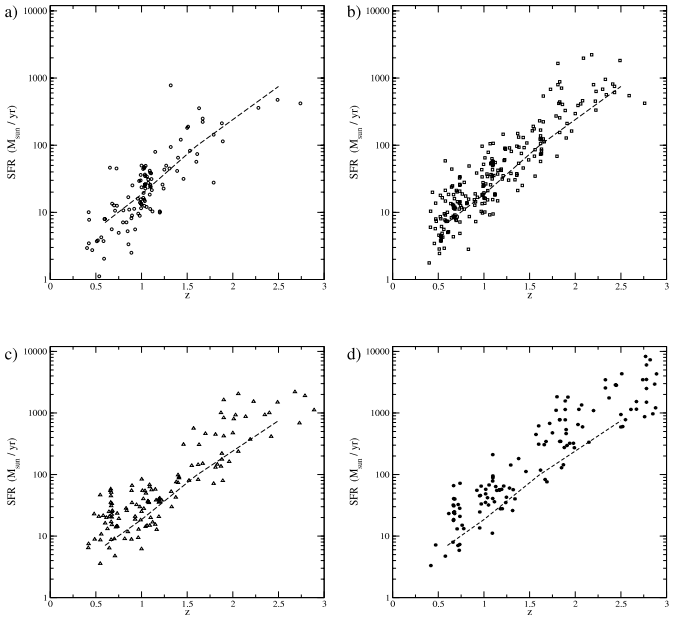

FIG. 9.—Evolution of the SFR of galaxies with different assembled stellar mass: (*a*) $M < 1.5 \times 10^{10}\ M_{\odot}$, (*b*) $1.5 \times 10^{10}\ M_{\odot} \leq M < 7.0 \times 10^{10}\ M_{\odot}$, (*c*) $7.0 \times 10^{10}\ M_{\odot} \leq M < 1.5 \times 10^{11}\ M_{\odot}$, and (*d*) $M \geq 1.5 \times 10^{11}\ M_{\odot}$. In all the panels, the dashed line delimits the region of completeness of the observed SFRs as imposed by the flux limit $S_{\nu}(24\ \mu\mathrm{m}) = 83\ \mu\mathrm{Jy}$.

that low-mass objects with very high SFR (SFR $\gtrsim 500\ M_{\odot}\ \mathrm{yr}^{-1}$) are indeed rare at $z \gtrsim 2$. On the contrary, galaxies with greater stellar mass $M \geq 1.5 \times 10^{10}\ M_{\odot}$ and SFR $\gtrsim 500\ M_{\odot}\ \mathrm{yr}^{-1}$ are progressively found at higher redshifts.

Figure 10 shows the ratio of already assembled stellar mass over the instantaneous SFR, M/SFR, versus redshift z for the 24 μm galaxies with a $K_s < 21.5$ counterpart in the GOODS/CDFS. Different symbols correspond to galaxies with stellar masses in different mass ranges, as in Figure 9. The solid line shows the age of the universe as a function of redshift, while the dashed line indicates the upper limit of the typical lifetime of a starburst (~0.1 Gyr). The assembled stellar masses have been computed as in § 4 and are completely independent of the 24 μm properties of each galaxy. If the SFRs in a galaxy were larger in the past or at most stayed constant over cosmic time, the ratio M/SFR would give an upper limit for the lifetime of the source. Therefore, Figure 10 allows putting constraints on the star formation history of the MIPS 24 μm galaxies present at different redshifts.

A first striking conclusion is that, at high redshifts $z \sim 2$–3, a starburst lifetime appears to be sufficient to construct a substantial fraction and up to the whole amount of the stellar mass of some massive galaxies. If equations (1)–(5) are still applicable at those redshifts, very high SFRs are predicted, ranging from ~500 to 5000 $M_{\odot}\ \mathrm{yr}^{-1}$. In this way, a stellar mass of $\approx 10^{10}$–$10^{11}\ M_{\odot}$ could be constructed in a ~0.01–0.1 Gyr period of time. However, this does not necessarily mean that all these systems are being formed at $z \sim 2$–3. Recent works suggest that a non-negligible fraction of present-day massive galaxies would be present before even higher ($z \gtrsim 3$) redshifts (van Dokkum et al. 2004; Caputi et al. 2004, 2005, 2006). Certainly, we find other 24 μm massive galaxies for which the derived lifetimes M/SFR are larger (up to ~1 Gyr), indicating that these galaxies would be present since higher redshifts, and that star formation histories longer than a single burst lifetime are necessary to build the stellar mass present in them. Moreover, other massive galaxies with SFRs below the limits of the 24 μm survey analyzed here also exist at redshift $z \sim 2$–3 (K. I. Caputi et al. 2006, in preparation).

It is interesting to note that the best-fit optical to near-IR SEDs for our 24 μm galaxies at redshifts $z \gtrsim 2$ correspond to different galaxy ages, many of which exceed the maximum ~1 Gyr lifetime derived with the ratio M/SFR. This fact could indicate that the instantaneous SFRs derived from the 24 μm fluxes of these galaxies were not constant or larger in the past. In order for these galaxies to have ages of ~1–3 Gyr (as those derived from the best-fit SEDs), their SFRs must have been *smaller* at some moment in the past. This strongly suggests that some massive

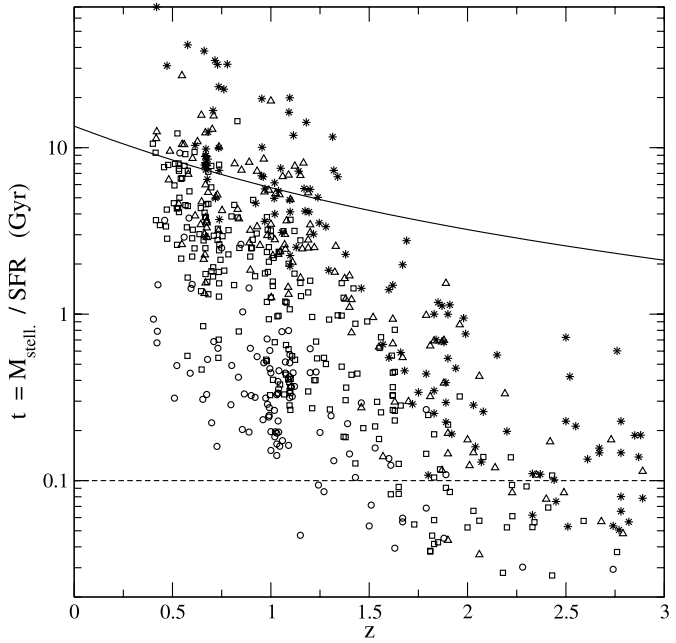

FIG. 10.—Ratio between the assembled stellar mass and the instantaneous SFR of MIPS 24 μm galaxies with $K_s < 21.5$ counterparts in the GOODS/CDFS vs. redshift. Different symbols indicate different assembled stellar mass ranges: $M < 1.5 \times 10^{10}\ M_{\odot}$ (*circles*), $1.5 \times 10^{10}\ M_{\odot} \leq M < 7.0 \times 10^{10}\ M_{\odot}$ (*squares*), $7.0 \times 10^{10}\ M_{\odot} \leq M < 1.5 \times 10^{11}\ M_{\odot}$ (*triangles*), and $M \geq 1.5 \times 10^{11}\ M_{\odot}$ (*asterisks*). The solid line shows the age of the universe as a function of redshift, while the dashed line indicates an upper limit to the typical lifetime of a starburst (0.1 Gyr).

galaxies could already be in place at higher redshifts and experience a noncontinuous star formation history, with temporary episodes of high star formation activity (see also Papovich et al. 2005). Those suffering such episodes at $z \sim 2$–3 would be detected as hyperluminous infrared galaxies at these redshifts in mid-IR surveys. If this is the case, the major episodes of star formation at $z \sim 2$–3 would not account for the complete assembly history of these massive galaxies. A similar argument has been given by Hammer et al. (2005), who proposed that the stellar mass growth of intermediate-mass galaxies at $z < 1$ could proceed by successive star formation episodes characterized by a LIRG phase.

As mentioned in § 3, a substantial fraction of the 24 μm sources at high redshifts have the characteristic colors of ERGs, $(I_{775} - K_s) > 4.0$ (Vega). Based on the best-fit optical to near-IR SEDs, the large majority of the ERGs have been formed in short timescales (instantaneously or with characteristic times $\tau \leq 1$ Gyr). For many of them, the best-fit age is larger than the SED-derived time formation scale, i.e., age >1 Gyr. However, even when these characteristics would correspond to systems undergoing passive evolution, the SED of most of these ERGs can only be properly fitted with considerable amounts of dust extinction. We find that the median of the color excess in the 24 μm ERGs at $z > 2$ is $E(B-V) \approx 0.30$, a value too high to conclude that these galaxies could be passive systems even from the optical to near-IR point of view.

It should be emphasized that the SFRs computed here assume that the mid-IR sources are purely star-forming. Another possibility is that at least part of the mid-IR emission of these sources is due to the presence of an AGN, in which case the real SFR would be lower than our estimated values. We note, however, that even when, e.g., only one-half of the mid-IR luminosities of the $z \sim 2$–3 galaxies analyzed here were due to star formation, the derived SFR would still be sufficiently high so as to construct stellar masses of the order of $\gtrsim 10^{10}\ M_{\odot}$ in a burst timescale. The properties of these high-redshift massive mid-IR galaxies resemble those of submillimeter galaxies, whose redshift distribution has a median of $z = 2.2$–2.4 (Chapman et al. 2003, 2005). Thus, it is expected that the 24 μm galaxy population at the depth of the GTO images contains at least a fraction of the submillimeter galaxy population (see Egami et al. 2004; Ivison et al. 2004).

At lower redshifts $z \lesssim 1$, the completeness limits of the samples allow us to determine that star formation spans a wide

range of timescales, in agreement with results obtained from the analysis of *ISO* sources (Franceschini et al. 2003). Moreover, we find that these timescales for star formation activity depend on galaxy mass, with more massive star-forming galaxies probably experiencing more prolonged star formation histories. In particular, for the high-mass end $M \geq 1.5 \times 10^{11}\ M_{\odot}$ at $z \lesssim 1$, we see that the derived timescales are larger than the age of the universe at the corresponding redshifts. This fact indicates that the SFR of these galaxies was not constant over time, but larger in the past. This plausible differential star formation history for star-forming galaxies of different assembled stellar masses at $z \lesssim 1.0$ is in agreement with recent results reported in the literature (Heavens et al. 2004).

Although the derived timescales M/SFR for massive ($M \geq 1.5 \times 10^{11}\ M_{\odot}$) galaxies at $z \lesssim 1$ indicate prolonged star formation histories, different possibilities exist for the way in which star formation proceeded through cosmic time. Star formation could have proceeded quiescently, i.e., with relatively small SFR sustained through long (>0.1 Gyr) periods of time. Alternatively, as discussed earlier, star formation might have been noncontinuous, with the production of multiple burstlike episodes. Both ways—or also some combination of the two—could have lead to the construction of the stellar mass contained in these massive galaxies. However, the number densities of both all and $S_{\nu}(24\ \mu\mathrm{m}) > 83\ \mu$Jy massive galaxies at $z \sim 3$ is only ~20% of the corresponding number densities at $z < 1$ (Caputi et al. 2006; K. I. Caputi et al. 2006, in preparation). Thus, the major episodes of star formation activity produced at very high redshifts could be responsible for the construction of stellar mass in at most a minor fraction of the massive 24 μm galaxies observed at $z < 1$. Also, it is likely that most of the massive galaxies undergoing high star formation activity at $z \sim 2$–3 do not have significant amounts of remaining gas to condense into stars by redshift $z \sim 1$. Thus, massive 24 μm galaxies at $z \sim 2$–3 are probably not the progenitors of the massive 24 μm galaxies at $z \sim 1$. The star formation history of massive IR galaxies at low redshifts should have mainly proceeded by some combination of quiescent activity and relatively modest burstlike episodes.

It is interesting to analyze the evolution with redshift of the efficiency of the burstlike star formation mode to construct a significant fraction of a galaxy stellar mass. As stated above, at redshifts $z \sim 2$–3, the typical starburst lifetime of 0.01–0.1 Gyr is sufficient to form a substantial fraction of the stellar mass of some massive galaxies ($M \geq 1.5 \times 10^{11}\ M_{\odot}$). At redshifts $z \sim 1$–2, only low- to intermediate-mass galaxies ($M \leq 7.0 \times 10^{10}\ M_{\odot}$) could form in a burst lifetime. Within the limits of our sample and the volume surveyed, no galaxy appears to be able to have built up in a burst timescale at $z \lesssim 1$. This does not mean that the burstlike mode cannot proceed in different mass galaxies at these low redshifts, but that each individual burst would only be sufficient to construct an additional minor amount of the galaxy-assembled stellar mass (i.e., SFR/M would be low). Thus, our results suggest that the potential importance of the burstlike mode of formation shifts from high- to low-mass galaxies with decreasing redshift (note, however, that we cannot completely probe star formation in galaxies with stellar mass $M \lesssim 10^{11}\ M_{\odot}$ at $z \sim 2$–3). In fact, each individual burstlike episode can play only a secondary role in galaxy building at $z \lesssim 1$ (see also Papovich et al. 2005).

6. DISCUSSION AND SUMMARY

In this work, we present K_s-band identifications of the MIPS 24 μm galaxies in the GOODS/CDFS at the depth of the *Spitzer*/GTO surveys [with ~94% of identification completeness for sources with flux $S_{\nu}(24\ \mu\mathrm{m}) > 83\ \mu$Jy]. A $K_s < 21.5$ (Vega) galaxy survey is sufficient for this purpose. The remaining nonidentified galaxies are mostly faint mid- and near-IR sources. A minor fraction (7%) of the 747 identified objects correspond to X-ray–selected active galaxies. Active galaxies are among the brightest 24 μm sources at high redshifts (see Houck et al. 2005).

MIPS 24 μm galaxies in the GOODS/CDFS span the redshift range $z = 0$–4, and 28% of the population lies at redshifts $z \gtrsim 1.5$ at the depth of the GTO data. This confirms the predictions of a substantial population of mid-IR–selected galaxies at high redshifts. We determined the existence of a significant bump in the redshift distribution of 24 μm galaxies at $z \sim 1.9$, in agreement with predictions made by Lagache et al. (2004) using the Lagache et al. (2003) model. This secondary peak in the redshift distribution of 24 μm galaxies indicates the existence of PAH spectral features in $z \sim 1.9$ star-forming galaxies. We also observed the predicted depression in the redshift distribution at $z \sim 1.5$, although with marginal significance, which could be driven by silicate absorption. However, the overall observed redshift distribution differs significantly from the distribution predicted by the Lagache et al. (2003) and other models, indicating that revisions are required to understand the high-redshift infrared-luminous galaxy population.

The mid-IR galaxy population is mainly composed of normal star-forming galaxies at redshifts $0.4 \leq z < 0.8$, while LIRGs start to be dominant at $0.8 \leq z < 1.2$. We derived estimated assembled stellar masses of 10^9–$10^{12}\ M_{\odot}$ for the 24 μm galaxies at $z \lesssim 1.2$. Massive star-forming galaxies appear to dominate the mid-IR output progressively at higher redshifts. A considerable fraction of the stellar mass density of the universe is contained in bright 24 μm sources: galaxies with flux $S_{\nu}(24\ \mu\mathrm{m}) > 83\ \mu$Jy contain ~35% of the stellar mass density at redshifts $z = 0.5$–1.5 and ~40% of the stellar mass density at $z \sim 1.5$–3.0. This corresponds to ~30%, 15%, 10%, and a minimum of 5% of the local value at redshifts $z \approx 0.75$, 1.25, 1.75, and 2.5, respectively (K. I. Caputi et al. 2006, in preparation). Thus, we conclude that bright 24 μm galaxies have a significant role in the history of stellar mass assembly.

We find that, at redshifts $z \lesssim 1.2$, the IR-derived timescales for star formation activity increase with the already assembled galaxy mass. Mid-IR galaxies with intermediate to high assembled stellar masses ($M \gtrsim 10^{10}\ M_{\odot}$) appear to be suffering rather prolonged star formation histories, while lower mass ($M \lesssim 10^{10}\ M_{\odot}$) galaxies, on the contrary, are characterized by star formation activity on shorter timescales. At higher redshifts $z \gtrsim 2$, massive galaxies are dominant, and all the derived timescales for the $S_{\nu}(24\ \mu\mathrm{m}) > 83\ \mu$Jy sources are ≲1 Gyr. Star formation history at high redshifts is likely to have proceeded in a series of burstlike episodes and, in a substantial fraction of massive galaxies, a single burst lifetime (0.01–0.1 Gyr) is sufficient to assemble a stellar mass of $\approx 10^{10}$–$10^{11}\ M_{\odot}$. We conclude, then, that the burstlike mode was probably an efficient way to construct the bulk of the stellar mass of massive galaxies at high redshifts.

At $z \sim 1$–2, on the contrary, the burstlike mode can be effective only for the formation of galaxies with mass $M \lesssim 7.0 \times 10^{10}\ M_{\odot}$, and individual bursts can play only a secondary role in galaxy building by redshifts $z \lesssim 1$. Recently, Bell et al. (2005) found that the majority of the 24 μm galaxies present at redshift $z \sim 0.7$ in the CDFS have regular spiral morphologies rather than irregular or peculiar morphologies. In conjunction, Bell et al. morphological determinations and our results on the lack of galaxies built up in a burst at $z \lesssim 1$ suggest that morphology could be linked to the mode of star formation activity (see also Papovich et al. 2005). Galaxies with no ongoing or mainly quiescent star formation would show regular shapes, while galaxies suffering important burstlike episodes of star formation activity would appear as irregular. To test this hypothesis, a detailed morphological study of 24 μm galaxies as a function of stellar mass and redshift would be necessary.

Results recently published in the literature suggest a "downsizing" history for the formation of the stellar mass, where star formation proceeds from high- to low-mass galaxies (Heavens et al. 2004; Juneau et al. 2005). Our conclusions support a similar downsizing mechanism for the efficiency of the burstlike mode. This fact also suggests that massive star-forming galaxies at high redshifts are not the progenitors of the massive star-forming galaxies found to be at $z \lesssim 1$, which are characterized by much longer star formation histories. The properties of 24 μm galaxies at $z \gtrsim 2$ suggest, on the contrary, a likely connection with submillimeter galaxies. Current interpretations of submillimeter galaxies indicate that this population could contain the progenitors of the most massive E/S0 galaxies present in the local universe (e.g., Stevens et al. 2003). The high SFR characterizing mid-IR–selected galaxies at $2 \lesssim z \lesssim 3$ suggests a similar conclusion for the high-redshift 24 μm galaxy population. However, some recent works suggest that a nonnegligible fraction of present-day massive galaxies would be in place at even higher ($z \gtrsim 3$) redshifts, indicating that the determination of the first epoch of formation of massive spheroids is still to be discovered.

This paper is based on observations made with the *Spitzer* Observatory, which is operated by the Jet Propulsion Laboratory (JPL), California Institute of Technology, under NASA contract 1407. It is also based on observations made with the Advanced Camera for Surveys on board the *Hubble Space Telescope*, operated by NASA/ESA, and with the Infrared Spectrometer and Array Camera on the "Antu" Very Large Telescope, operated by the European Southern Observatory in Cerro Paranal, Chile, and that form part of the publicly available GOODS data sets. We thank the GOODS teams for providing reduced data products.

We thank the anonymous referee for his/her useful comments and suggestions that improved the discussion of results in this paper. Support for this work was provided by NASA through contract 960785, issued by JPL/Caltech. K. I. C. acknowledges CNES and CNRS funding. R. J. M. acknowledges the support of the Royal Society.

REFERENCES

Alonso-Herrero, A., et al. 2006, ApJ, in press (astro-ph/0511507)
Appleton, P. N., et al. 2004, ApJS, 154, 147
Bell, E. F., et al. 2005, ApJ, 625, 23
Benítez, N. 2000, ApJ, 536, 571
Bolzonella, M., Miralles, J.-M., & Pelló, R. 2000, A&A, 363, 476
Borys, C., Chapman, S., Halpern, M., & Scott, D. 2003, MNRAS, 344, 385
Bruzual, A. G., & Charlot, S. 1993, ApJ, 405, 538
Calzetti, D., Armus, L., Bohlin, R. C., Kinney, A. L., Koorneef, J., & Storchi-Bergmann, T. 2000, ApJ, 533, 682
Caputi, K. I., Dunlop, J. S., McLure, R. J., & Roche, N. D. 2004, MNRAS, 353, 30
———. 2005, MNRAS, 361, 607
Caputi, K. I., McLure, R. J., Dunlop, J. S., Cirasuolo, M., & Schael, A. M. 2006, MNRAS, in press (astro-ph/0511571)
Chapman, S. C., Blain, A. W., Ivison, R. J., & Smail, I. R. 2003, Nature, 422, 695
Chapman, S. C., Blain, A. W., Smail, I. R., & Ivison, R. J. 2005, ApJ, 622, 772
Chary, R., & Elbaz, D. 2001, ApJ, 556, 562
Cimatti, A., et al. 2004, Nature, 430, 184
Condon, J. J. 1992, ARA&A, 30, 575
Dale, D. A., & Helou, G. 2002, ApJ, 576, 159
Dale, D. A., Helou, G., Contursi, A., Silbermann, N. A., & Kolhatkar, S. 2001, ApJ, 549, 215
Dale, D. A., et al. 2005, ApJ, 633, 857
Désert, F.-X., Boulanger, F., & Puget, J.-L. 1990, A&A, 237, 215
Donley, J. L., Rieke, G. H., Rigby, J. R., & Pérez-González, P. G. 2005, ApJ, 634, 169
Egami, E., et al. 2004, ApJS, 154, 130
Elbaz, D., Cesarsky, C. J., Chanial, P., Aussel, H., Franceschini, A., Fadda, D., & Chary, R. R. 2002, A&A, 384, 848
Fazio, G. G., et al. 2004, ApJS, 154, 10
Flores, H., et al. 1999, ApJ, 517, 148
Franceschini, A., Aussel, H., Cesarsky, C. J., Elbaz, D., & Fadda, D. 2001, A&A, 378, 1
Franceschini, A., et al. 2003, A&A, 403, 501
Genzel, R., & Cesarsky, C. J. 2000, ARA&A, 38, 761
Giavalisco, M., et al. 2004, ApJ, 600, L93
Glazebrook, K., et al. 2004, Nature, 430, 181
Hammer, F., Flores, F., Elbaz, D., Zheng, X. Z., Liang, Y. C., & Cesarsky, C. 2005, A&A, 430, 115
Heavens, A., Panter, B., Jiménez, R., & Dunlop, J. 2004, Nature, 428, 625
Houck, J. R., et al. 2005, ApJ, 622, L105
Ivison, R. J., et al. 2004, ApJS, 154, 124
Juneau, S., et al. 2005, ApJ, 619, L135
Kennicutt, R. C., Jr. 1998, ApJ, 498, 541
Lagache, G., Dole, H., & Puget, J.-L. 2003, MNRAS, 338, 555
Lagache, G., et al. 2004, ApJS, 154, 112
Le Fèvre, O., et al. 2004, A&A, 428, 1043
Le Floc'h, E., et al. 2004, ApJS, 154, 170
———. 2005, ApJ, 632, 169
Lonsdale, C., et al. 2004, ApJS, 154, 54
Lutz, D., Valiante, E., Sturm, E., Genzel, R., Tacconi, L. J., Lehnert, M. D., Sternberg, A., & Baker, A. J. 2005, ApJ, 625, L83
Papovich, C., Dickinson, M., Giavalisco, M., Conselice, C. J., & Ferguson, H. C. 2005, ApJ, 631, 101
Papovich, C., et al. 2004, ApJS, 154, 70
———. 2006, ApJ, in press (astro-ph/0511289)
Pérez-González, P. G., et al. 2005, ApJ, 630, 82
Rieke, G. H., et al. 2004, ApJS, 154, 25
Sanders, D. B., & Mirabel, I. F. 1996, ARA&A, 34, 749
Scott, S. E., et al. 2002, MNRAS, 331, 817
Stevens, J. A., et al. 2003, Nature, 425, 264
Szokoly, G. P., et al. 2004, ApJS, 155, 271
van Dokkum, P. G., et al. 2004, ApJ, 611, 703
Vanzella, E., et al. 2005, A&A, 434, 53
Werner, M. W., et al. 2004, ApJS, 154, 1
Wolf, C., et al. 2004, A&A, 421, 913
Yan, L., et al. 2004, ApJS, 154, 75
———. 2005, ApJ, 628, 604

A&A 448, 525–534 (2006)
DOI: 10.1051/0004-6361:20054272

Astronomy & Astrophysics

The *ISO* 170 μm luminosity function of galaxies⋆

T. T. Takeuchi[1,⋆⋆], T. T. Ishii[2,⋆⋆⋆], H. Dole[3], M. Dennefeld[4], G. Lagache[3], and J.-L. Puget[3]

[1] Laboratoire d'Astrophysique de Marseille, Traverse du Siphon, BP 8, 13376 Marseille Cedex 12, France
e-mail: tsutomu.takeuchi@oamp.fr
[2] Kwasan Observatory, Kyoto University, Yamashina-ku, Kyoto 607–8471, Japan
[3] Institut d'Astrophysique Spatiale, Bât. 121, Université Paris-Sud, 91405 Orsay Cedex, France
[4] Institut d'Astrophysique de Paris, 98bis Bd Arago, 75014 Paris, France

Received 29 September 2005 / Accepted 3 November 2005

ABSTRACT

We constructed a local luminosity function (LF) of galaxies using a flux-limited sample ($S_{170} \geq 0.195$ Jy) of 55 galaxies at $z < 0.3$ taken from the *ISO* FIRBACK survey at 170 μm. The overall shape of the 170-μm LF is found to be different from that of the total 60-μm LF (Takeuchi et al. 2003): the bright end of the LF declines more steeply than that of the 60-μm LF. This behavior is quantitatively similar to the LF of the cool subsample of the *IRAS* PSCz galaxies. We also estimated the strength of the evolution of the LF by assuming the pure luminosity evolution (PLE): $L(z) \propto (1+z)^Q$. We obtained $Q = 5.0^{+2.5}_{-0.5}$ which is similar to the value obtained by recent *Spitzer* observations, in spite of the limited sample size. Then, integrating over the 170-μm LF, we obtained the local luminosity density at 170 μm, $\rho_L(170\ \mu\mathrm{m})$. A direct integration of the LF gives $\rho_L(170\ \mu\mathrm{m}) = 1.1 \times 10^8 h\ L_\odot\ \mathrm{Mpc}^{-3}$, whilst if we assume a strong PLE with $Q = 5$, the value is $5.2 \times 10^7 h\ L_\odot\ \mathrm{Mpc}^{-3}$. This is a considerable contribution to the local FIR luminosity density. By summing up with other available infrared data, we obtained the total dust luminosity density in the Local Universe, $\rho_L(\mathrm{dust}) = 1.1 \times 10^8 h\ L_\odot\ \mathrm{Mpc}^{-3}$. Using this value, we estimated the cosmic star formation rate (SFR) density hidden by dust in the Local Universe. We obtained $\rho_{\mathrm{SFR}}(\mathrm{dust}) \simeq 1.1\text{–}1.2\, h \times 10^{-2}\ M_\odot\ \mathrm{yr}^{-1}\ \mathrm{Mpc}^{-3}$, which means that 59% of the star formation is obscured by dust in the Local Universe.

Key words. dust, extinction – galaxies: evolution – galaxies: formation – galaxies: luminosity function, mass function – infrared: galaxies

1. Introduction

The luminosity function (LF) of galaxies is one of the fundamental statistics to describe the galaxy population in the universe. The far-infrared (FIR) LF is vitally important to evaluate the amount of energy released via dust emission, and further, the fraction of the star formation activity hidden by dust (e.g., Pérez-González et al. 2005; Le Floc'h et al. 2005; Takeuchi et al. 2005). Not only the local LF but also its evolution plays a crucial role in understanding the cosmic star formation history.

Most of the previous LF works at mid-infrared (MIR) and FIR wavelengths have been made based on *IRAS* database (see, Rieke & Lebofsky 1986; Lawrence et al. 1986; Rowan-Robinson et al. 1987; Soifer et al. 1987; Saunders et al. 1990; Isobe & Feigelson 1992; Rush et al. 1993; Koranyi & Strauss 1997; Fang et al. 1998; Shupe et al. 1998; Springel & White 1998; Takeuchi et al. 2003, among others). The longest wavelength band of the *IRAS* is 100 μm. Subsequently, 15 and 90 μm LFs have been presented based on *ISO* data (Xu 2000; Serjeant et al. 2001, 2004). Now, by the advent of *Spitzer*[1], MIR(12 or 15 μm) LFs based on the 24-μm band started to be available up to $z \sim 1$ (Pérez-González et al. 2005; Le Floc'h et al. 2005). Also recently, *Spitzer*-based 60-μm LF has been presented (Frayer et al. 2005). At 850 μm, a LF of *IRAS*-selected sample of submillimeter galaxies has been published (Dunne et al. 2000).

At wavelengths between 100 μm and 850 μm, however, only a very limited number of LFs have been studied. Further, most of them are made from the sample selected at shorter wavelengths (e.g., Franceschini et al. 1998; Dunne et al. 2000), or estimated/extrapolated from LFs of shorter wavelengths, e.g., 60 μm (e.g., Serjeant & Harrison 2005). A direct construction of the LF is still rarely done up to now (see, Oyabu et al. 2005). Hence, it remains an important task to estimate the LF at wavelengths longer than 100 μm from a well-controlled deep survey sample. Wavelengths between 100 μm and 850 μm are also very important in the context of the extragalactic background radiation, particularly the cosmic infrared background (CIB). The CIB is now understood as an accumulation of radiation from dust in galaxies at various redshifts (z). At the FIR, although the measured CIB is very strong (e.g., Gispert et al. 2000; Hauser & Dwek 2001; Lagache et al. 2005, among others), the properties of the sources contributing to the background is rather poorly known compared with other wavelengths. Thus, it is also of vital importance to have a LF at FIR for cosmological studies.

In this work, we estimate the LF of the local galaxies ($z < 0.3$) at 170 μm based on the data obtained by FIRBACK survey (Puget et al. 1999). This paper is organized as follows: in Sect. 2, we describe the 170 μm galaxy sample. We present the statistical estimation method of the LF in Sect. 3. In Sect. 4, we show the LF and discuss its uncertainties. Section 6 is devoted to our conclusions. We provide numerical tables of our LFs in Appendix A. Throughout this manuscript, we adopt a flat lambda-dominated cosmology with $h \equiv H_0/100$ [km s^{-1} Mpc^{-1}], and $(\Omega_0, \lambda_0) = (0.3, 0.7)$, where Ω_0 is the density parameter and λ_0 is the normalized cosmological constant. We denote the flux density at frequency ν by S_ν, but for simplicity we use a symbol S_{170} to represent S_ν at a frequency (1.76×10^{12} Hz) corresponding to $\lambda = 170\ \mu$m.

2. Data

2.1. Parent sample

The FIRBACK (Far-InfraRed BACKground) survey (Puget et al. 1999; Lagache & Dole 2001; Dole et al. 2001) is one of the deepest surveys performed at 170 μm by *ISO* using ISOPHOT (Lemke et al. 1996). It covers 4 deg^2 on three fields. In this work, we use two of these fields: FIRBACK South Marano field (0.89 deg^2) and FIRBACK ELAIS N1 field (1.87 deg^2)[2].

The parent sample of FIRBACK is composed of the flux-limited sample of 141 sources with $S_{170} \geq 135$ mJy (3σ limit). Flux completeness of this parent sample is 75%, and at flux density $S_{170} \sim 200$ mJy, it becomes ~90% (Dole et al. 2001). We use the sources brighter than a flux density of 195 mJy in the following analysis.

2.2. Redshifts and completeness

Redshifts are measured for 58 galaxies out of 69 galaxies above the flux density of 195 mJy, i.e., the redshift completeness of the sample used is 84%. The redshift measurements have been performed by Chapman et al. (2002), Patris et al. (2003), and Dennefeld et al. (2005). Since the redshift measurement becomes more difficult toward the fainter sources, the completeness depends systematically on the flux levels. Thus, we should examine whether the redshift selection distort the flux distribution of the sample.

We performed the Kolmogorov–Smirnov test (e.g., Hoel 1971; Hájek et al. 1999) to compare the flux-limited sample ($S_{170} \geq 195$ mJy) with the redshift sample (see Fig. 1).

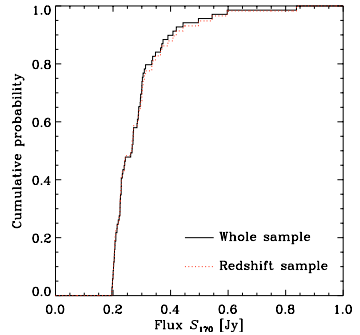

Fig. 1. The Kolmogorov–Smirnov test for the whole photometric sample and redshift subsample taken from FIRBACK 170 μm survey. The solid line shows the cumulative probability distribution of flux densities for the whole sample, while the dotted line depicts that of the redshift sample. The difference is found to be very small.

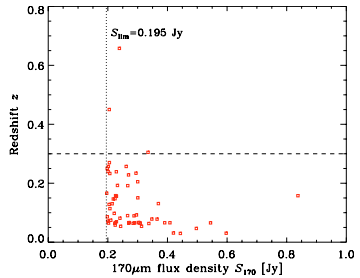

Fig. 2. The flux density–redshift distribution of our flux-limited sample. We used a subsample at $z < 0.3$ to construct the local luminosity function (LF). The vertical dotted line shows $S_{170} = 0.195$ Jy, and the horizontal dashed line depicts $z = 0.3$.

The maximum difference between the cumulative distribution functions of flux-limited and redshift samples are 0.0377. This shows that we cannot reject the null hypothesis that the two samples are taken from the same parent distribution. Hence, we use the redshift sample as an unbiased subsample of the whole flux-limited sample and simply multiply the inverse of the completeness to obtain the final galaxy density. The distribution of the flux densities and redshifts of the sample is shown in Fig. 2.

The redshift completeness of the sample is also tested by V/V_{max} statistics (Schmidt 1968; Rowan-Robinson 1968). Here V is the volume enclosed in a sphere whose radius is the distance of a considered source, and V_{max} is the volume enclosed in a sphere whose radius is the largest distance at which the source can be detected. If the sample is complete, V/V_{max} values of the sample galaxies is expected to distribute uniformly

⋆ Appendices A and B are only available in electronic form at http://www.edpsciences.org
⋆⋆ Postdoctoral Fellow of the Japan Society for the Promotion of Science (JSPS) for Research Abroad.
⋆⋆⋆ Postdoctoral Fellow of the JSPS.

[1] URL: http://www.spitzer.caltech.edu/

[2] The choice of the two fields is due to the follow-up allotment was different for ELAIS N1/South Marano (Dennefeld et al. 2005) and for ELAIS N2 (Taylor et al. 2005) in the FIRBACK project. Consequently the conditions of the data aquisition are different between them. A coherent treatment remains as a future work.

between 0 and 1, with an average $\langle V/V_{\rm max}\rangle = 0.5$ and a standard deviation $(12n)^{-1/2}$ (n: sample size). For our redshift sample, the mean and standard deviation of the $V/V_{\rm max}$ is 0.66 ± 0.23, i.e., the sample can be regarded as complete. Moreover, it is larger than 0.5 (but within the uncertainty), suggesting the existence of evolution (see, e.g., Peacock 1999, p. 444).

For the estimation of the local LF, we use a subsample of galaxies with $z < 0.3$. The size of this "low-z" subsample is 55. The mean and median redshift of this low-z sample is 0.12 and 0.09, respectively.

3. Analysis

3.1. K-correction

The monochromatic luminosity at observed frequency $\nu_{\rm obs}$ is obtained by

$$\mathcal{L}_{\nu_{\rm em}} = \mathcal{L}_{(1+z)\nu_{\rm obs}} = \frac{4\pi d_{\rm L}(z)^2 S_{\nu_{\rm obs}}}{1+z}, \tag{1}$$

where $\mathcal{L}_\nu$ is an energy emitted per unit time at frequency ν, $d_{\rm L}(z)$ is the luminosity distance corresponding to a redshift z, and $\nu_{\rm obs}$ and $\nu_{\rm em}$ are observed and emitted frequencies, respectively. In order to estimate the luminosity function at 170 μm, the K-correction is required.

However, the amount of the K-correction may be uncertain, because the present sample is observed at one waveband. If we assume a "cool" dust galaxy, the spectral energy distribution (SED) rises toward longer wavelengths, whilst it decreases if we adopt a starburst SED (see e.g., Takeuchi et al. 2001a,b; Lagache et al. 2003). To explore the effect of the K-correction, we use a power-law approximation with the form of

$$\mathcal{L}_\nu \propto \nu^\beta. \tag{2}$$

As for β, we consider $\beta = 1.0$ (starburst galaxies), 0.0 (intermediate galaxies), and -0.5 (cool galaxies). We adopt these values according to the phenomenologically constructed model SEDs of Lagache et al. (2003) (see their Fig. 4). Then, the luminosity at the observed frequency $\nu_{\rm obs}$ becomes

$$\begin{aligned} L_{\nu_{\rm obs}} &\equiv \nu_{\rm obs}\mathcal{L}_{\nu_{\rm obs}} \\ &= L_{\nu_{\rm em}}(1+z)^{-(\beta+1)} \\ &= 4\pi d_{\rm L}(z)^2 \nu_{\rm obs} S_{\nu_{\rm obs}}(1+z)^{-(\beta+1)}. \end{aligned} \tag{3}$$

By the same manner, the limiting luminosity of a survey with flux density detection limit $S^{\rm lim}_\nu$ depends on the SED via β,

$$L^{\rm lim}_{\nu_{\rm obs}} = 4\pi d_{\rm L}(z)^2 \nu_{\rm obs} S^{\rm lim}_{\nu_{\rm obs}}(1+z)^{-(\beta+1)}. \tag{4}$$

This is shown with the present sample in Fig. 3. The luminosity L_{170} is that at emitted wavelength of 170 μm, i.e., $L_{\rm em}$ measured at 170 μm. As we see in the followings, this dependence of the limiting luminosity on β potentially affects the estimation of the LF.

3.2. Estimation of the luminosity function

We define the luminosity function as a number density of galaxies whose luminosity lies between a logarithmic interval $[\log L, \log L + {\rm d}\log L]$[3]:

$$\phi(L) \equiv \frac{{\rm d}n}{{\rm d}\log L}. \tag{5}$$

In this work, we denote the luminosity at a certain frequency or wavelength as $L_\nu \equiv \nu\mathcal{L}_\nu$.

3.2.1. Parametric estimation

First we performed a parametric maximum likelihood estimation of the LF (Sandage et al. 1979). Note that we can do this analysis *directly* on the data, being independent of the nonparametric result, i.e., this is not a fitting to the nonparametric LF. It is known that the 60-μm LF is well expressed by a function given by Saunders et al. (1990) which is defined as

$$\phi(L) = \phi_*\left(\frac{L}{L_*}\right)^{1-\alpha}\exp\left[-\frac{1}{2\sigma^2}\log^2\left(1+\frac{L}{L_*}\right)\right] \tag{6}$$

where $\log^2 x \equiv (\log x)^2$. Since various LFs can be approximated by this functional form, we adopt Eq. (6) in this work.

We use Eq. (6) for the parametric maximum likelihood estimation. Then the likelihood $\mathcal{M}$ is expressed as

$$\begin{aligned} \mathcal{M}(L_*,\alpha,\sigma|\{L_i,z_i\}_{i=1,\ldots,N}) &= \prod_{i=1}^{N}\frac{\phi(L_i)}{\int_{\log L_{{\rm min},i}}^{\infty}\phi(L){\rm d}\log L} \\ &= \prod_{i=1}^{N}\frac{\left(\frac{L_i}{L_*}\right)^{1-\alpha}\exp\left[-\frac{1}{2\sigma^2}\log^2\left(1+\frac{L_i}{L_*}\right)\right]}{\int_{\log L_{{\rm min},i}}^{\infty}\left(\frac{L}{L_*}\right)^{1-\alpha}\exp\left[-\frac{1}{2\sigma^2}\log^2\left(1+\frac{L}{L_*}\right)\right]{\rm d}\log L} \end{aligned} \tag{7}$$

where

$$L_{{\rm min},i} = L^{\rm lim}_{\nu_{\rm obs}}(z_i). \tag{8}$$

Note that, in principle, the parametric estimation procedure is dependent on β. We can obtain the parameters of the LF by maximizing Eq. (7) with respect to L_*, α, and σ (Sandage et al. 1979; Saunders et al. 1990; Takeuchi et al. 2003).

However, because of the small size of the present sample and relatively narrow range of their luminosity, it is difficult to put a reasonable constraint to the faint-end slope of the LF. Hence instead, as we explain later, we assume a certain value for the faint-end slope α.

3.2.2. Nonparametric estimation

We also estimate the LF nonparametrically via an improved version of the C^- method of Lynden-Bell (1971), implemented to have the density normalization (Chołoniewski 1987). This method is a kind of maximum likelihood methods insensitive to the density fluctuation. This method and its extension are fully described and carefully examined by Takeuchi et al. (2000)[4].

[3] We denote $\log x \equiv \log_{10} x$ and $\ln x \equiv \log_{\rm e} x$, respectively.

[4] We found that the other density-insensitive nonparametric estimators discussed in Takeuchi et al. (2000) were not very suitable for the present small sample analysis: both of the methods of Chołoniewski (1986) and Efstathiou et al. (1988) need to divide the sample into small bins. For the present sample (55 galaxies), we could not find stable solutions for these estimators.

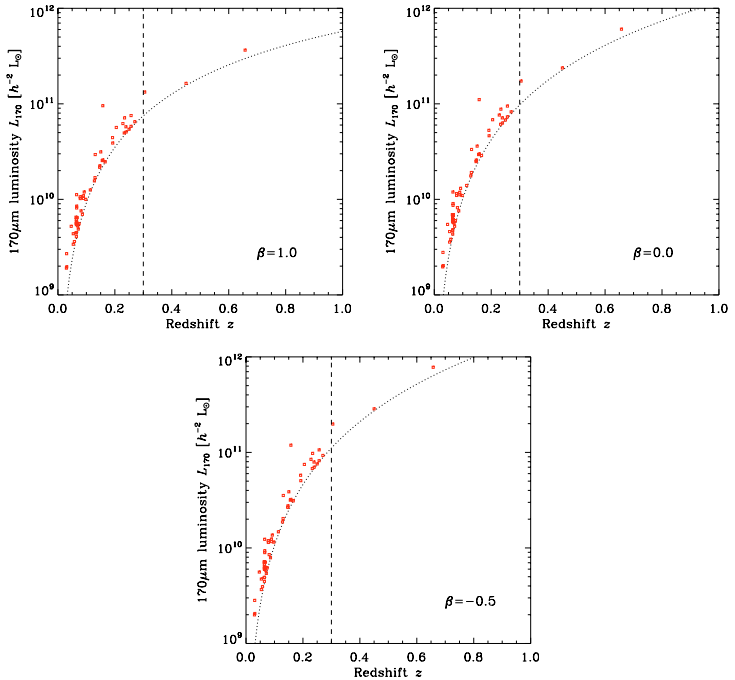

Fig. 3. The luminosity–redshift distribution of our redshift sample taken from FIRBACK 170 μm survey. The luminosity is that at emitted wavelength of 170 μm. The dotted curves represent the limiting luminosities corresponding to the flux density detection limit of 195 mJy at each redshift, including the effect of the K-correction. The power-law index of the spectral energy distribution (SED), β is 1.0, 0.0, and -0.5 from left to right (see the main text). Vertical dashed lines show $z = 0.3$, which is used to define our low-z sample.

We note that the SED slope β also affects the nonparametric estimation of the LF. In the case of C^- method, the definition of C^- includes $L^{\rm lim}_{\nu_{\rm obs}}$ (see Fig. 2 of Takeuchi et al. 2000). Thus, it will be important to explore the systematic effect introduced by K-correction. The uncertainty (68% confidence limit) is estimated by the bootstrap resampling (Takeuchi et al. 2000). Additionally, we also estimated the LF and uncertainty including the observational measurement errors. For the density normalization, we took into account the source extraction completeness (∼90%: Dole et al. 2001) and the redshift measurement (84%).

4. Results

4.1. Parametric result

We fixed the faint-end slope of the FIRBACK 170-μm LF to be 1.25. This is very close to that of the total 60-μm LF of the *IRAS* PSCz sample, and the same as that of its "cool" subsample (Takeuchi et al. 2003).

We obtained $L_* = 1.1 \times 10^9 h^{-2}$ [$L_\odot$] (with a 68-% confidence range of $3.0 \times 10^8 h^{-2}$–$2.3 \times 10^9 h^{-2}$ [$L_\odot$]) and $\sigma = 0.41$ (with a 68-% confidence range of 0.35–0.50). The likelihood contours are shown in Fig. 4. The outermost contours indicate $\Delta\ln\mathcal{M} \equiv \ln\mathcal{M} - \ln\mathcal{M}_{\rm max} = -0.5$, corresponding to the 68-% confidence limit. In Fig. 4, we present $\ln\mathcal{M}$ defined by Eq. (7), as a function of (L_*, σ). These two parameters are rather strongly dependent with one another, and as a result, the contour is elongated along with the diagonal direction in each panel. The density normalization was $\phi_* = (1.0 \pm 0.4) \times 10^{-1} h^3$ [Mpc^{-3}]. As seen in Fig. 4, the result is almost independent of the assumed β. The result is also found to be quite robust against the value of α in a plausible range of $\alpha = 1.1$–1.3.

Takeuchi et al. (2003) presented the parameters for the LF of the *IRAS* PSCz sample. The parameters for the LF of the

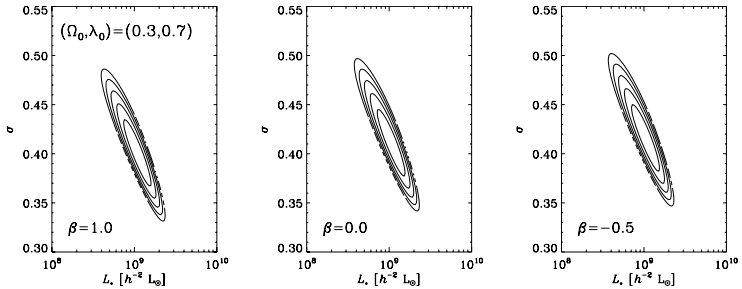

Fig. 4. The logarithmic likelihood ln $\mathcal{M}$ for the parameter estimation of L_* [$L_\odot$] and σ when we fix $\alpha = 1.25$. The outermost contours indicate the 68% confidence level.

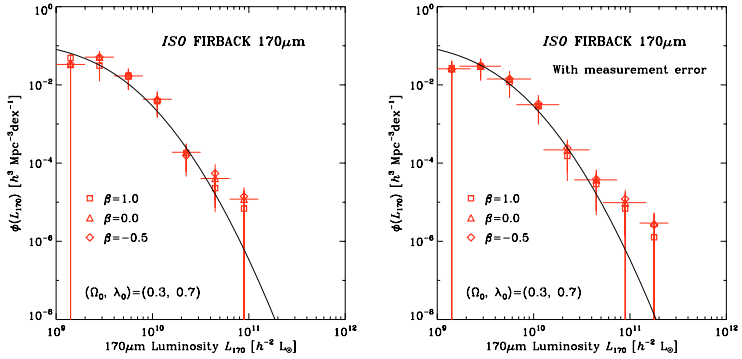

Fig. 5. The local luminosity function of *ISO* FIRBACK 170 μm galaxy sample. Solid curves show the parametric form estimated from Eq. (7). Symbols represent the C^- nonparametric LFs, respectively. Open squares, open triangles, and open diamonds are the LFs adopting $\beta = 1.0$, 0.0, and -0.5, respectively. Vertical error bars are 68-% confidence ranges. Left panel shows the LF from the original data, while the right panel shows the LF from the data convolved with observational measurement errors. In the left panel, horizontal bars simply represent the bin width (0.3 dex). In the right panel, in contrast, horizontal bars are the convolution of the bin width and the luminosity uncertainty introduced by the photometric error. For visual simplicity, we put horizontal bars only on the case of $\beta = 0.0$ in each panel.

whole sample are $(\alpha, L_*, \sigma) = (1.23, 4.34\times10^8 h^{-2}\ [L_\odot], 0.724)$. Clearly, the parameters for the 170-μm sample are different from these values. Particularly, σ which determines the steepness of the bright end is significantly smaller than the total *IRAS* LF. From the above likelihood analysis, $\sigma = 0.724$ was rejected with a confidence level of more than 99.9%, even for the small number of galaxies. That is, the bright end of the present LF declines more steeply than that of the total *IRAS* LF.

4.2. Nonparametric result

Nonparametric LF estimates are presented in Fig. 5. Symbols are the LFs obtained by the C^--method. Vertical error bars show the 68% uncertainty, obtained by bootstrap resampling of 10^4 times. Open squares, open triangles, and open diamonds represent $\beta = 1.0$, 0.0, and -0.5, respectively. Solid lines are the analytic expression of the LF with the parameters we obtained in Sect. 4.1. We present the numerical tables of our C^- LF estimates also in Appendix A.

The left panel is the LF estimates from the original data themselves, while the right panel is the ones from the data convolved with measurement errors. We performed the error convolution procedure assuming a Gaussian distribution for the measurement errors in flux density, with quoted flux density errors as standard deviations for each data. This procedure slightly blurs the LFs horizontally. As a result, we have an additional bin at the highest luminosity, and the 68% uncertainty levels are broadened. However, the effect is rather small, and the LF estimates are quite robust except for the highest-luminosity unstable bins.

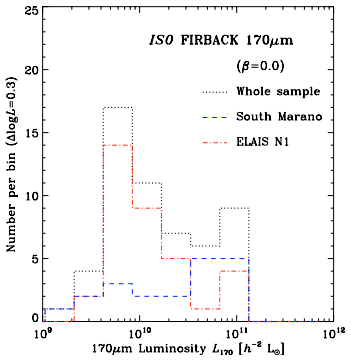

Fig. 6. The luminosity distribution of the FIRBACK 170 μm low-z galaxy sample. The dotted histogram is the luminosity distribution of the whole sample. It has an excess at the highest luminosity bin. The dashed and dot-dashed histograms are those of the subsamples in South Marano field and ELAIS N1 field, respectively.

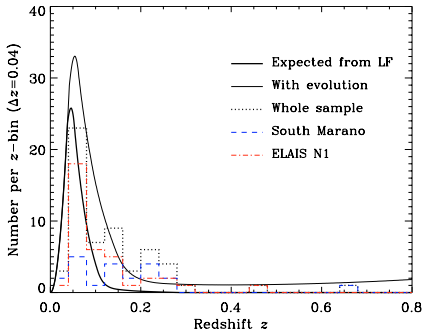

Fig. 7. The redshift distribution of our flux-limited sample. The dotted histogram is the distribution of the whole sample, the dashed histogram shows the the subsample in South Marano field, and dot-dashed one presents the subsample in ELAIS N1 field. These histograms present the number of galaxies in each bin ($\Delta z = 0.04$). The thick solid curve is the expected distribution of galaxies calculated from the nonparametric local LF (Fig. 5). The thin solid curve is the expected distribution for the pure luminosity evolution with $L(z) \propto (1+z)^{5.0}$.

We see that different values for β do not affect the result very strongly, but at the highest-luminosity bins, systematic effects are relatively large, a factor of 0.5–0.7 dex. In contrast to the large effect of β we found in Fig. 3, the LF estimates are quite robust against β. Hence, hereafter, we do not show all the results with respect to β, but only restrict ourselves to the results with $\beta = 0.0$ without loss of generality.

We should note the upward deviation of the C^- LF from the analytic result. Although the error bar is large, the C^- estimates (open symbols in Fig. 5) are about an order of magnitude larger than that of the analytic value. It is worth examining if this deviation is real or merely an artifact of the poor statistics. To see this, we show the luminosity distribution of our present sample in Fig. 6. Recall that this sample consists of galaxies only at $z < 0.3$. We see an excess at the highest luminosity bin. Examining the subsamples, we also find a similar excess in the ELAIS N1 field. We, however, also see that the sample in South Marano field is interesting: the galaxies in this subsample are biased toward higher luminosities. The superposition of these effects makes the brightest end of the nonparametric LF deviated from the analytic one.

Why does the analytic maximum likelihood not reflect this sample property? We see that, though there is an excess at $L_{170} \simeq 10^{11} h\ L_\odot$, the majority of the sample is located around $10^{10} h\ L_\odot$ (the peak in Fig. 6). Hence, the parameter estimation is practically controlled by the sample around L_*, and the bright galaxies could hardly give a strong effect to the final estimation. In addition, the peak is dominated by the sample from ELAIS N1 field, and the peculiar luminosity distribution of South Marano field affected the result little. We, hence, should not overly rely on the analytic result and parameters, but rather we should use the nonparametric C^- LF directly. These are small sample effects, and we should wait for the larger sample to clarify the detailed shape of the LF.

We show the redshift distribution of the present sample in Fig. 7. The histograms show the distribution of the present data. The thick solid curve is the expected redshift distribution of galaxies calculated from the nonparametric local LF we have obtained. This is calculated as follows

$$\frac{\mathrm{d}N}{\mathrm{d}z} = \Omega_{\mathrm{survey}} \int_{\log L_{\mathrm{min}}(z)}^{\infty} \phi(L_{170}) \frac{\mathrm{d}^2 V}{\mathrm{d}\Omega \mathrm{d}z} \mathrm{d}\log L_{170}, \tag{9}$$

where $L_{\mathrm{min}}(z)$ is the minimum detectable luminosity $L_{\mathrm{Vobs}}^{\mathrm{lim}}(z)$ (see, Eq. (8)), and

$$\frac{\mathrm{d}^2 V}{\mathrm{d}\Omega \mathrm{d}z} = \frac{c}{H_0} \frac{d_{\mathrm{L}}(z)^2}{(1+z)^2 \sqrt{\Omega_0 (1+z)^3 + \lambda_0}} \tag{10}$$

for the flat lambda-dominated universe (see, e.g., Peebles 1993), i.e., $(\mathrm{d}^2V/\mathrm{d}\Omega\mathrm{d}z)\mathrm{d}z$ is the comoving volume between $[z, z + \mathrm{d}z]$ per unit solid angle. This curve is calculated to apply to the solid angle of the survey area by multiplying $\Omega_{\mathrm{survey}} = 8.4 \times 10^{-4}$ sr. We used the nonparametric LF for Fig. 7 because the exact shape of the bright end of the LF is crucial to examine the tail of the redshift distribution of the source toward higher z, and as already discussed, the analytic function underproduces galaxies with $L_{170} \gtrsim 3 \times 10^{10}\ L_\odot$. We find a density excess at $z \simeq 0.2$ in Fig. 7[5]. However, apart from

[5] If we use the classical $1/V_{\mathrm{max}}$-method (Schmidt 1968; Eales 1993), the estimator is affected by this bump and results in a (fake) flatter bright end of the LF. This is a well-known drawback of the $1/V_{\mathrm{max}}$-method (Takeuchi et al. 2000, and references therein), and we must be very careful about its usage. We address this problem in Appendix B.

the bump, both fields have long tails toward higher redshifts than expected from the local LF. It may suggest the existence of galaxy evolution. We explore the effect of the evolution in Sect. 5.2

5. Discussion

5.1. Shape of the 170 μm LF

The overall shape of the 170-μm LF of the FIRBACK galaxies is different from the *IRAS* 60-μm LF. As we discussed in Sect. 4.1, the parameters of the analytic LF suggest a steeper slope for the bright end of the LF. Although the nonparametric LF revealed that the brightest part of the LF is significantly higher than that of the analytic LF, the 170-μm LF decreases more rapidly from the knee of the LF to the bright end than the *IRAS* 60-μm LF. Here we compare the 170-μm LF with other FIR LFs obtained to date.

Takeuchi et al. (2003) divided the *IRAS* sample into two categories, warm and cool subsamples, using the flux density ratio criterion of $S_{100}/S_{60} = 2.1$. The parameters of the cool galaxies are $(\alpha, L_*, \sigma) = (1.25, 9.55 \times 10^9 h^{-2}\ [L_\odot], 0.50)$. The α is almost the same as that of the total *IRAS* LF within the quoted error, but L_* and σ are much closer to those of our present LF. The resemblance of our LF to the LF of cool *IRAS* galaxies may be reasonable, since the present sample is selected at 170 μm band, where we can detect cooler galaxies more effectively than 60 μm. Soifer & Neugebauer (1991) derived a LF at 100 μm from *IRAS* galaxy sample. Their 100-μm LF has a bright end slightly steeper than 60-μm LF does, but the slope is still flatter than our LF. Dunne et al. (2000) constructed a LF at 850 μm based on 60-μm selected *IRAS* galaxy sample. Although the dynamic range is small, the overall shape of their 850-μm LF is similar to our LF. Actually, Dunne et al. (2000) fitted their LF with the Schechter function which has a very steep decline at the bright end (Schechter 1976)[6].

In summary, the 170-μm LF has a shape similar to those of galaxy sample with cool dust emission. It is also interesting to note that the 170-μm LF has the highest normalization among known FIR LFs. We summarize the comparison in Fig. 8. However, we must keep in mind the large uncertainty of the estimates, and further observational exploration is definitely required.

5.2. Evolution

5.2.1. Pure luminosity evolution assumption

Most of the galaxies in our redshift sample are at $z < 0.3$. Hence, we should estimate the evolution of the LF under a certain assumption. We adopt a pure luminosity evolution (PLE). Recent *Spitzer* observations indicated that the actual evolution of IR galaxies is described as a strong evolution in luminosity, with a slight evolution in density (e.g., Pérez-González et al. 2005; Le Floc'h et al. 2005), while their studies are based on the *Spitzer* 24 μm band. Hence, the PLE is not a bad choice as a first approximation.

Adopting the PLE, the strength of the evolution can be estimated via a radial density distribution of galaxies (Saunders et al. 1990). In the case of the PLE, the LF at z is expressed by the evolution strength $f(z)$ as

$$\phi(L, z) = \phi_0 \left[\frac{L}{f(z)} \right], \tag{11}$$

where $\phi_0(L)$ is the local functional form of the LF. The PLE assumes that this form remains unchanged and only shifts along the luminosity axis. To define $\phi_0(L_{170})$, we examined the 170-μm LF for a sample at $z < 0.15$ (38 galaxies). Though the uncertainty is large, we did not observe a significant change of the LF in its shape, i.e., the PLE assumption might be approximately valid. Hence, we can use the shape of the LF of the sample with $z < 0.3$ as $\phi_0(L_{170})$. For simplicity, we consider a power-law form for $f(z)$:

$$f(z) = (1 + z)^Q, \tag{12}$$

but this form is supported by recent *Spitzer* observations at a wide redshift range of $z = 0$–1 (Pérez-González et al. 2005; Le Floc'h et al. 2005).

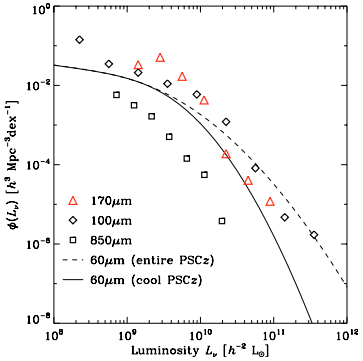

Fig. 8. Comparison of the 170-μm LF with those at other FIR wavelengths. Open triangles are our 170-μm LF ($\beta = 0.0$), open diamonds represent the 100-μm LF of Soifer & Neugebauer (1991), and open squares represent the 850-μm LF of Dunne et al. (2000). The dashed curve is the analytic form of the 60-μm LF of the *IRAS* PSCz entire sample, and the solid curve is the LF of the cool subsample of the *IRAS* PSCz galaxies (Takeuchi et al. 2003). The 850-μm LF is horizontally shifted by a factor of 100 for display purposes.

[6] However, we should keep in mind that the sample of Dunne et al. (2000) is selected at 60 μm. As these authors discussed, a significant fraction of galaxies with cold dust may be missed in the sample, and consequently, it might be possible that their LF shape is not representative of cool/cold dust galaxies.

5.2.2. Estimation of evolution via radial density

Assuming that the LF is separable for L and z as $\phi(L, z) = n(z)p(L)$, the likelihood is written as

$$\mathcal{M}(Q|\{L_i, z_i\}_{i=1,\ldots,N}) = \prod_{i=1}^{N} \frac{\phi(L_i, z_i)}{\int_{z_{\min}}^{z_{\max,i}} \phi(L_i, z) \dfrac{\mathrm{d}^2 V}{\mathrm{d}\Omega \mathrm{d}z} \mathrm{d}z} \tag{13}$$

where N is the total sample size, $z_{\min}$ is the lowest redshift which we used in the analysis, $z_{\max,i}$ is the maximum redshift to which ith galaxy can be detected, and $(\mathrm{d}^2V/\mathrm{d}\Omega\mathrm{d}z)\mathrm{d}z$ is again the differential comoving volume (Eq. (10)).

By maximizing Eq. (13) with respect to Q, we can have a maximum likelihood estimate. We performed this procedure with the nonparametric LF, because as we already mentioned, the analytic form underestimates the bright end of the LF, and it would lead to a serious overestimation of the evolution strength. We obtained $Q = 5.0^{+2.5}_{-0.5}$. The expected redshift distribution with this evolution is obtained by a similar manner to Eq. (9) as

$$\frac{\mathrm{d}N}{\mathrm{d}z} = \Omega_{\mathrm{survey}} \int_{\log L_{\min}(z)}^{\infty} \phi_0 \left[\frac{L_{170}}{(1+z)^Q} \right] \frac{\mathrm{d}^2 V}{\mathrm{d}\Omega \mathrm{d}z} \mathrm{d} \log L_{170}, \tag{14}$$

and shown in Fig. 7 (the thin solid line). The agreement with the data and the expected value is much improved.

Although the uncertainty is very large because of the limited sample size, this is similar to the value obtained by recent *Spitzer* 24-μm observations, $Q \simeq 4$ (Pérez-González et al. 2005; Le Floc'h et al. 2005). These authors also found a weak evolution in the galaxy number density, but for the present sample, it is impossible to explore this effect. If confirmed, the similarity between the strength of the galaxy evolution in the MIR (12-μm in the rest frame) and FIR will provide us an important clue to the physics of dusty star formation in galaxies.

5.3. FIR luminosity density and obscured star formation density in the Local Universe

5.3.1. The local 170-μm and total IR luminosity density

The luminosity density in a cosmic volume provides various information of the energy distribution in the Universe. Especially, comparison between the radiative energy directly emitted from stars and that re-emitted from dust is one of the key quantities to understand the fraction of hidden star formation. In this subsection, we discuss the local luminosity density at 170 μm, $\rho_L(170\ \mu\mathrm{m})$ [$L_\odot$ Mpc^{-3}] and consider the integrated SED of the Local Universe.

In principle, it is straightforward to obtain $\rho_L(170\ \mu\mathrm{m})$ from the LF: we simply integrate the first-order moment of the LF, $L_{170}\phi(L_{170})$, over the whole possible range of luminosity. Since the luminosity range of the 170-μm LF is limited to 10^9–10^{12} $L_\odot$, we extrapolated the faint end without observed data. We have done it by using the analytic form (Eq. (6)) with various α. However, as far as $\alpha < 2.0$, the integration of $L_{170}\phi(L_{170})$ converges and the faint end does not contribute to the total integration significantly. For the infrared (IR) galaxies, previous studies suggest $\alpha < 2.0$ (e.g., Saunders et al. 1990; Takeuchi et al. 2003, and references therein), and the $\rho_L(170\ \mu\mathrm{m})$ is little affected by α. By the same reason, the lower and upper bounds of the integration do not affect the result. We chose $10^7 h^{-2}$ [$L_\odot$] as the lowest luminosity, and use the highest luminosity bin as the upper bound. Thus, we obtained $\rho_L(170\ \mu\mathrm{m}) = (1.1^{+0.5}_{-0.4}) \times 10^8 h$ [$L_\odot$ Mpc^{-3}]. The final uncertainty of $\rho_L(170\ \mu\mathrm{m})$ is dominated by the statistical uncertainty of the nonparametric LF in each bin.

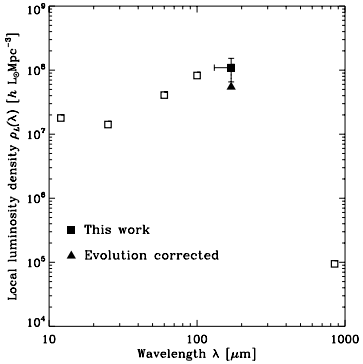

Fig. 9. The MIR and FIR luminosity densities in the Local Universe. The filled square represent the 170-μm luminosity density, $\rho_L(170\ \mu\mathrm{m})$, obtained by a direct integration of our LF. The vertical error bar shows the total uncertainty related to the LF. The horizontal bar represents the redshift range of our local sample ($0 \le z < 0.3$). The filled triangle is the corrected $\rho_L(170\ \mu\mathrm{m})$ by assuming a pure luminosity evolution $L(z) \propto (1 + z)^5$. Open squares present the luminosity densities at 12, 25, 60, 100, and 850 μm calculated based on the literatures (see text).

We, however, must recall that the present FIRBACK sample is not exactly "local", i.e., it consists of galaxies $0 \le z < 0.3$. As seen in the previous subsection, it may be plausible that this result is affected by the strong galaxy evolution. If we adopt a PLE $L(z) \propto (1 + z)^{5.0}$, $\rho_L(170\ \mu\mathrm{m})$ should be enhanced by a factor of 2.1 on average in this redshift range. By correcting the evolution, we have $\rho_L(170\ \mu\mathrm{m}) = 5.20 \times 10^7 h$ [$L_\odot$ Mpc^{-3}].

We plot the result in Fig. 9. The filled square represents the 170-μm luminosity density obtained by a direct integration of our LF. The horizontal bar indicates that the redshift range of our low-z sample is $0 \le z < 0.3$. The filled triangle shows the evolution-corrected value. Then, we consider the SED of the luminosity density in the Local Universe. We do similar exercises to calculate $\rho_L(\lambda)$ at various IR wavelengths. At MIR, Fang et al. (1998) and Shupe et al. (1998) provided the LFs at *IRAS* 12 and 25 μm bands, respectively. Fang et al. (1998) tabulated their nonparametric LF at approximately the same luminosity range as we adopt in this work (10^7 $L_\odot$–10^{12} $L_\odot$). We simply summed it up with multiplying the luminosity and obtained $\rho_L(12\ \mu\mathrm{m}) = 1.79 \times 10^7 h$ [$L_\odot$ Mpc^{-1}].

Table 1. The SED of the luminosity density in the Local Universe.

λ [μm]	$\rho_L(\lambda)$ h [$L_\odot$ Mpc^{-3}]	$\rho_L(\lambda)/\rho_L(170\mu\mathrm{m})$
12	1.79×10^7	3.3×10^{-1}
25	1.42×10^7	2.6×10^{-1}
60	4.08×10^7	7.5×10^{-1}
100	8.25×10^7	1.5
170	5.20×10^7 [a]	1
850	9.45×10^4 [b]	1.7×10^{-3}

[a] The effect of the evolution is corrected assuming a pure luminosity evolution with $L(z)\propto(1+z)^Q$ ($Q=5.0$).
[b] This value is calculated by integrating a Schechter function presented by Dunne et al. (2000), over the luminosity range of L_{850} = 10^7 $L_\odot$–10^{13} $L_\odot$.

Shupe et al. (1998) provided an analytic fit for their 25-μm LF. By their analytic function, we got $\rho_L(25\ \mu\mathrm{m}) = 1.42\times10^7h$ [$L_\odot$ Mpc^{-1}]. At 60 μm, from Takeuchi et al. (2003), we obtained $\rho_L(60\ \mu\mathrm{m}) = 4.08\times10^7h$ [$L_\odot$ Mpc^{-1}]. Soifer & Neugebauer (1991) presented the LFs at all the *IRAS* bands. Using their 100-μm nonparametric LF, we re-calculated the luminosity density to obtain $\rho_L(100\ \mu\mathrm{m}) = 8.25\times10^7h$ [$L_\odot$ Mpc^{-1}]. Lastly, we used the Schechter function fit provided by Dunne et al. (2000) to have $\rho_L(850\ \mu\mathrm{m})$. Since their faint-end slope is very steep ($\alpha = 2.12$), the integration is dependent on the adopted lowest luminosity in this case. We coherently integrated the Schechter function in the same range as the other bands. We found $\rho_L(850\ \mu\mathrm{m}) = 1.00\times10^5h$ [$L_\odot$ Mpc^{-1}].

We plot these luminosity densities in Fig. 9 (open squares). The overall peak of the SED of the luminosity density seems to lie at $\lambda \gtrsim 100$ μm. Further, if the suggested strong evolution is true, the local SED peak is restricted to be at $100 \gtrsim \lambda \gtrsim 170$ μm. Even though the evolution effect significantly reduces the local $\rho_L(170\ \mu\mathrm{m})$ value, it still considerably contributes to the total FIR luminosity density.

To have a crude estimate of the total IR luminosity density (we call it ρ_L(dust)), we logarithmically interpolate and extrapolate between the SED data points in units of [erg s^{-1}, Hz^{-1} Mpc^{-3}], and integrate it over the range of 8–1000 μm to match the conventional definition of the total IR (TIR) luminosity (see, e.g., Dale et al. 2001; Dale & Helou 2002; Takeuchi et al. 2005). If we do not assume the evolution, we have $\rho_L(\mathrm{dust}) = 1.4\times10^8h$ [$L_\odot$ Mpc^{-3}], and with the evolution, $\rho_L(\mathrm{dust}) = 1.1\times10^8h$ [$L_\odot$ Mpc^{-3}]. Takeuchi et al. (2005) estimated the ρ_L(dust) under the assumption of a constant ratio of $\rho_L(\mathrm{dust})/\rho_L(60\ \mu\mathrm{m}) = 2.5$ (see, e.g., Takeuchi et al. 2005). They found $\rho_L(\mathrm{dust}) = 1.02\times10^8h$ [$L_\odot$ Mpc^{-3}]. Our ρ_L(dust) values are in a very good agreement with that, especially for the case with evolution.

For the interpretation of the IR luminosity density, it should be worth mentioning that there is a possibly high contamination by active galactic nuclei (AGN) at 12 and 24 μm. However, by integrating over the energy density from these wevelengths, we find that the contribution from 12 and 24 μm bands to ρ_L(dust) is less than 10%. Hence, if all the energy from 12 and 24 μm were from the AGN, the effect of AGNs would not change the physical interpretation of ρ_L(dust) significantly.

5.3.2. The obscured star formation density in the Local Universe

The ratio between the energy from young stars directly observed at UV and that reprocessed by dust and observed at IR in the cosmic history has long been a matter of debate. Before closing the discussion, we consider the star formation rate density in the Local Universe obscured by dust. We use the value with evolutionary correction in the rest of this work. To get values without this evolutionary correction, we may simply substitute the former value for ρ_L(dust).

For the conversion from ρ_L(dust) to the cosmic star formation rate (SFR) density related to dust, ρ_{SFR}(dust), we can use several methods. Kennicutt (1998) presented a famous formula between the SFR and the dust luminosity, L_{dust} [$L_\odot$],

$$SFR\ [M_\odot\,\mathrm{yr}^{-1}] = 1.72\times10^{-10}\ L_{\mathrm{dust}}\ [L_\odot], \tag{15}$$

which is valid for *starburst* galaxies with a burst younger than 10^8 yr. Adopting this formula to ρ_L(dust), we obtained $\rho_{\mathrm{SFR}}(\mathrm{dust}) = 1.89\,h\times10^{-2}$ [$M_\odot$ yr^{-1} Mpc^{-3}]. However, as mentioned by Kennicutt (1998) himself, this formula is not valid for more quiescent, normal galaxies. Since our SED of the Local Universe is similar to a kind of cool galaxies, we should carefully treat the effect of the heating radiation from old stars. Hirashita et al. (2003) found that about 40% of the dust heating in the nearby galaxies comes from stars older than 10^8 yr. If we apply the correction of old stellar population to Eq. (15), we obtain $\rho_{\mathrm{SFR}}(\mathrm{dust}) = 1.14\,h\times10^{-2}$ [$M_\odot$ yr^{-1} Mpc^{-3}]. Bell (2003) also presented a similar correction factor (0.32 ± 0.16 for galaxies with $L_{\mathrm{dust}} \le 10^{11}$ $L_\odot$ and 0.09 ± 0.05 for those with $L_{\mathrm{dust}} > 10^{11}$ $L_\odot$) for the contribution of old stars. Based on a more theoretical point of view, Takeuchi et al. (2005) also obtained an appropriate formula including the correction, which can be written as

$$SFR\ [M_\odot\,\mathrm{yr}^{-1}] = 1.07\times10^{-10}\ L_{\mathrm{dust}}\ [L_\odot]. \tag{16}$$

Adopting Eq. (16), we obtain $\rho_{\mathrm{SFR}}(\mathrm{dust}) = 1.17\,h\times10^{-2}$ [$M_\odot$ yr^{-1} Mpc^{-3}], very close to the above. The obtained ρ_{SFR}(dust) is slightly larger than the local SFR density estimated from direct FUV radiation (without dust attenuation correction), $\rho_{\mathrm{SFR}}(\mathrm{FUV}) = 8.3h\times10^{-3}$ [$M_\odot$ yr^{-1} Mpc^{-3}] (Takeuchi et al. 2005; see also Schiminovich et al. 2005). Hence, 59% of the star formation is obscured by dust in the Local Universe. This is in very good agreement with that of Takeuchi et al. (2005), but since we reached this conclusion from the measured dust SED of the Local Universe, we could put a firmer basis on their conclusion by this work. These results may be the first direct estimate of the dust luminosity in the Local Universe, and should be tested by forthcoming large area survey in the FIR by e.g., ASTRO-F[7].

[7] URL: http://www.ir.isas.ac.jp/ASTRO-F/index-e.html

6. Conclusion

We analyzed the FIRBACK 170 μm galaxy sample to obtain the local luminosity function (LF) of galaxies. We constructed a flux-limited sample with $S_{170} \ge 0.195$ Jy and $z < 0.3$ from the survey, which consists of 55 galaxies.

The overall shape of the 170-μm LF is quite different from that of the total 60-μm LF (Takeuchi et al. 2003): the bright end of the LF declines more steeply than that of the 60-μm LF. This behavior is quantitatively similar to the LF of the cool subsample of the *IRAS* PSCz galaxies. The bright end is also similar to that of the submillimeter LF of Dunne et al. (2000).

We also estimated the strength of the evolution of the LF by assuming the pure luminosity evolution $L(z)\propto(1+z)^Q$. We obtained $Q = 5.0^{+2.5}_{-0.5}$ which is similar to the value obtained by recent *Spitzer* observations (Pérez-González et al. 2005; Le Floc'h et al. 2005), in spite of the limited sample size.

Then, integrating over the 170-μm LF, we obtained the local luminosity density at 170 μm, $\rho_L(170\ \mu\mathrm{m})$ [$L_\odot$ Mpc^{-3}]. If we assume the above strong luminosity evolution $L(z)\propto(1+z)^5$, the value is 5.2×10^7h [$L_\odot$ Mpc^{-3}], which is a considerable contribution to the local FIR luminosity density.

By summing up the other MIR/FIR data, we obtained the total dust luminosity density in the Local Universe. We obtained $\rho_L(\mathrm{dust}) = 1.4\times10^8\,h$ [$L_\odot$ Mpc^{-3}] without the evolution correction, and $\rho_L(\mathrm{dust}) = 1.1\times10^8\,h$ [$L_\odot$ Mpc^{-3}] with correction.

Lastly, based on ρ_L(dust), we estimated the cosmic star formation rate (SFR) density hidden by dust in the Local Universe. We took into account the dust emission heated by old stellar population, and obtained $\rho_{\mathrm{SFR}}(\mathrm{dust}) \simeq 1.1$–$1.2\,h\times10^{-2}$ [$M_\odot$ yr^{-1} Mpc^{-3}]. Comparing with the SFR density estimated form FUV observation (Takeuchi et al. 2005), we found that 59% of the star formation is obscured by dust in the Local Universe.

It will be important to examine our local LF by a large area survey of the Local Universe. The ASTRO-F project promises to provide a local large sample of FIR galaxies at ≃50–170 μm. For the evolutionary status of the FIR galaxies, the FIR data of *Spitzer* will be very important to examine the present result.

Acknowledgements. We are grateful for the anonymous referee for careful reading and useful comments which improved the clarity of this manuscript. We also thank Véronique Buat for fruitful discussions. TTT and TTI have been supported by the JSPS (TTT: Apr. 2004–Dec. 2005; TTI: Apr. 2003–Mar. 2006).

References

Bell, E. F. 2003, ApJ, 586, 794
Chapman, S. C., Smail, I., Ivison, R. J., et al. 2002, ApJ, 573, 66
Chołoniewski, J. 1986, MNRAS, 223, 1
Chołoniewski, J. 1987, MNRAS, 226, 273
Dale, D. A., & Helou, G. 2002, ApJ, 576, 159
Dale, D. A., Helou, G., Contursi, A., Silbermann, N. A., & Kolhatkar, S. 2001, ApJ, 549, 215
Dennefeld, M., Lagache, G., Mei, S., et al. 2005, A&A, 440, 5
Dole, H., Gispert, R., Lagache, G., et al. 2001, A&A, 372, 364
Dunne, L., Eales, S., Edmunds, M., et al. 2000, MNRAS, 315, 115
Eales, S. 1993, ApJ, 404, 51
Efstathiou, G., Ellis, R. S., & Peterson, B. A. 1988, MNRAS, 232, 431
Fang, F., Shupe, D. L., Xu, C., & Hacking, P. B. 1998, ApJ, 500, 693
Franceschini, A., Andreani, P., & Danese, L. 1998, MNRAS, 296, 709
Frayer, D. T., Fadda, D., Yan, L., et al. 2005, AJ, in press [arXiv:astro-ph/0509649]
Gispert, R., Lagache, G., & Puget, J. L. 2000, A&A, 360, 1
Hájek, J., Šidák, Z., & Sen, P. K. 1999, Theory of Rank Tests, 2nd ed. (San Diego: Academic Press)
Hauser, M. G., & Dwek, E. 2001, ARA&A, 39, 249
Hirashita, H., Buat, V., & Inoue, A. K. 2003, A&A, 410, 83
Hoel, P. G. 1978, Introduction to Mathematical Statistics, 4th ed. (New York: John Wiley & Sons), 318
Isobe, T., & Feigelson, E. D. 1992, ApJS, 79, 197
Kennicutt, R. C. 1998, ARA&A, 36, 189
Koranyi, D. M., & Strauss, M. A. 1997, ApJ, 477, 36
Lagache, G., & Dole, H. 2001, A&A, 372, 702
Lagache, G., Dole, H., & Puget, J.-L. 2003, MNRAS, 338, 555
Lagache, G., Dole, H., & Puget, J.-L. 2005, ARA&A, 43, 727
Lawrence, A., Walker, D., Rowan-Robinson, M., et al. 1986, MNRAS, 219, 687
Le Floc'h, E., Papovich, C., Dole, H., et al. 2005, ApJ, 632, 169
Lemke, D., Klaas, U., Abolins, J., et al. 1996, A&A, 315, L64
Lynden-Bell, D. 1971, MNRAS, 155, 95
Oyabu, S., Yun, M. S., Murayama, T., et al. 2005, AJ, 130, 2019
Patris, J., Dennefeld, M., Lagache, G., & Dole, H. 2003, A&A, 412, 349
Peacock, J. A. 1999, Cosmological Physics (Cambridge: Cambridge University Press), 444
Peebles, P. J. E. 1993, Principles of Physical Cosmology (Princeton: Princeton University Press), 314
Pérez-González, P. G., Rieke, G. H., Egami, E., et al. 2005, ApJ, 630, 82
Puget, J. L., Lagache, G., Clements, D. L., et al. 1999, A&A, 345, 29
Rieke, G. H., & Lebofsky, M. J. 1986, ApJ, 304, 326
Rowan-Robinson, M. 1968, MNRAS, 138, 445
Rowan-Robinson, M., Helou, G., & Walker, D. 1987, MNRAS, 227, 589
Rush, B., Malkan, M. A., & Spinoglio, L. 1993, ApJS, 89, 1
Sandage, A., Tammann, G. A., & Yahil, A. 1979, ApJ, 232, 352
Saunders, W., Rowan-Robinson, M., Lawrence, A., et al. 1990, MNRAS, 242, 318
Schiminovich, D., Ilbert, O., Arnouts, S., et al. 2005, ApJ, 619, L47
Schmidt, M. 1968, ApJ, 151, 393
Schechter, P. 1976, ApJ, 203, 297
Serjeant, S., & Harrison, D. 2005, MNRAS, 356, 192
Serjeant, S., Efstathiou, A., Oliver, S., et al. 2001, MNRAS, 322, 262
Serjeant, S., Carramiñana, A., Gonzáles-Solares, E., et al. 2004, MNRAS, 355, 813
Shupe, D. L., Fang, F., Hacking, P. B., & Huchra, J. P. 1998, ApJ, 501, 597
Soifer, B. T., & Neugebauer, G. 1991, AJ, 101, 354
Soifer, B. T., Sanders, D. B., Madore, B. F., et al. 1987, ApJ, 320, 238
Spinoglio, L., & Malkan, M. A. 1989, ApJ, 342, 83
Springel, V., & White, S. D. M. 1998, MNRAS, 298, 143
Takeuchi, T. T., Yoshikawa, K., & Ishii, T. T. 2000, ApJS, 129, 1
Takeuchi, T. T., Ishii, T. T., Hirashita, H., et al. 2001a, PASJ, 53, 37
Takeuchi, T. T., Kawabe, R., Kohno, K., et al. 2001b, PASP, 113, 586
Takeuchi, T. T., Yoshikawa, K., & Ishii, T. T. 2003, ApJ, 587, L89
Takeuchi, T. T., Buat, V., Iglesias-Páramo, J., Boselli, A., & Burgarella, D. 2005, A&A, 432, 423
Takeuchi, T. T., Buat, V., & Burgarella, D. 2005, A&A, 440, L17
Taylor, E. L., Mann, R. G., Efstathiou, A. N., et al. 2005, MNRAS, 361, 1352
Xu, C. 2000, ApJ, 541, 134

Online Material

Appendix A: Tables of the nonparametric luminosity function

In this section, we present numerical tables of the nonparametric luminosity function (LF) of the FIRBACK 170 μm galaxy sample obtained with the C^--method. We only tabulate the LF directly estimated from the original data, and the flux measurement errors are not included in these LFs.

Table A.1. The 170-μm luminosity function with $\beta = 1.0$, estimated with Lynden-Bell's C^- method.

$\log L_{170}{}^a$	$\phi(L_{170})$ h^3 [Mpc^{-3}dex^{-1}]	$\phi(L_{170})^{\rm upper}$ h^3 [Mpc^{-3}dex^{-1}]	$\phi(L_{170})^{\rm lower}$ h^3 [Mpc^{-3}dex^{-1}]
9.15	4.89×10^{-2}	6.20×10^{-2}	$0.00 \times 10^{+0}$
9.45	3.10×10^{-2}	4.96×10^{-2}	1.24×10^{-2}
9.75	1.73×10^{-2}	2.63×10^{-2}	7.70×10^{-3}
10.05	3.81×10^{-3}	5.99×10^{-3}	1.43×10^{-3}
10.35	1.81×10^{-4}	3.00×10^{-4}	5.95×10^{-5}
10.65	2.29×10^{-5}	3.85×10^{-5}	5.54×10^{-6}
10.95	6.87×10^{-6}	1.17×10^{-5}	$0.00 \times 10^{+0}$

[a] Units of L_{170} is h^{-2} [$L_\odot$], and the bin width is 0.3 dex. Tabulated log luminosities represent the bin center.

Table A.2. Same as Table A.1 but for $\beta = 0.0$.

$\log L_{170}$	$\phi(L_{170})$ h^3 [Mpc^{-3}dex^{-1}]	$\phi(L_{170})^{\rm upper}$ h^3 [Mpc^{-3}dex^{-1}]	$\phi(L_{170})^{\rm lower}$ h^3 [Mpc^{-3}dex^{-1}]
9.15	3.33×10^{-2}	4.65×10^{-2}	$0.00 \times 10^{+0}$
9.45	5.12×10^{-2}	7.17×10^{-2}	3.10×10^{-2}
9.75	1.69×10^{-2}	2.56×10^{-2}	7.42×10^{-3}
10.05	4.29×10^{-3}	6.80×10^{-3}	1.69×10^{-3}
10.35	1.89×10^{-4}	3.16×10^{-4}	5.95×10^{-5}
10.65	4.04×10^{-5}	7.00×10^{-5}	7.20×10^{-6}
10.95	1.20×10^{-5}	2.01×10^{-5}	$0.00 \times 10^{+0}$

Table A.3. Same as Table A.1 but for $\beta = -0.5$.

$\log L_{170}$	$\phi(L_{170})$ h^3 [Mpc^{-3}dex^{-1}]	$\phi(L_{170})^{\rm upper}$ h^3 [Mpc^{-3}dex^{-1}]	$\phi(L_{170})^{\rm lower}$ h^3 [Mpc^{-3}dex^{-1}]
9.15	3.37×10^{-2}	4.65×10^{-2}	$0.00 \times 10^{+0}$
9.45	5.14×10^{-2}	7.21×10^{-2}	3.10×10^{-2}
9.75	1.67×10^{-2}	2.54×10^{-2}	7.45×10^{-3}
10.05	4.12×10^{-3}	6.57×10^{-3}	1.53×10^{-3}
10.35	1.56×10^{-4}	2.63×10^{-4}	4.51×10^{-5}
10.65	5.45×10^{-5}	9.37×10^{-5}	1.11×10^{-5}
10.95	1.40×10^{-5}	2.40×10^{-5}	$0.00 \times 10^{+0}$

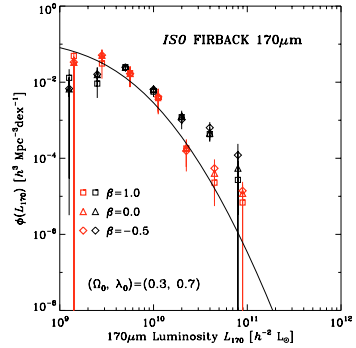

Fig. B.1. Comparison of the luminosity functions of our *ISO* 170 μm galaxy sample by $1/V_{\rm max}$ and C^- estimators. Thick and thin symbols represent the C^- nonparametric LFs, respectively. The signification's of the symbols are the same as Fig. 5. The symbols for $1/V_{\rm max}$ estimates are shifted with 0.05 dex for th purpose of visual clarity.

Appendix B: Comparison between the $1/V_{\rm max}$- and C^--luminosity functions

In this section, we examine the problem of the classical $1/V_{\rm max}$ estimator (Schmidt 1968; Eales 1993). Comparison of the luminosity functions of our *ISO* 170 μm galaxy sample by $1/V_{\rm max}$ and C^- estimators is shown in Fig. B.1. In Fig. B.1, the $1/V_{\rm max}$ LFs are shifted to the left with 0.05 dex to make them easy to see, but the actual bin centers are exactly the same as those of C^- LFs. It is impressive that there is a large difference between the $1/V_{\rm max}$ and C^- LFs. At the fainter side, these two LFs are consistent with one another within the error bars, though the faint end of the $1/V_{\rm max}$ LFs tend to be slightly underestimated. In contrast, the bright end is completely different: $1/V_{\rm max}$ method gives much flatter LFs than C^- method. We should recall that the parametric method and the C^- method are both insensitive to density fluctuation, while $1/V_{\rm max}$ method is unbiased only for the spatially homogeneous sample, as extensively examined by Takeuchi et al. (2000). Then, the most plausible explanation of this discrepancy may be due to the existence of a density enhancement, corresponding to the luminosity $L_{170} \gtrsim 3 \times 10^{10}\ L_\odot$.

To understand more clearly, we recall the redshift distribution of the present sample (Fig. 7). The distribution of ELAIS N1 galaxies is not very far from that expected by the LF, while that of South Marano galaxies are very different. Reflecting the luminosity distribution of this field, which is heavily inclined to luminous galaxies, the distribution has no apparent peak, but has a widely spread shape toward redshifts up to $\sim$0.3. This heavy high-z tail is superposed to the tail of the ELAIS N1 field makes a significant bump at $z \simeq 0.2$. Since the $1/V_{\rm max}$ method assumes a spatially homogeneous source distribution, this excess is too much exaggerated through the number density estimation, and results in the overestimation of the corresponding luminosity bins.

Mon. Not. R. Astron. Soc. **000**, 1–19 (2006) Printed 14 July 2010 (MN LATEX style file v2.2)

The 1 – 1000 μm SEDs of far-infrared galaxies

A. Sajina[1,2], D. Scott[2], M. Dennefeld[3], H. Dole[4,5], M. Lacy[1], G. Lagache[4]
[1] *Spitzer Science Center, California Institute of Technology, Pasadena, CA 91125, USA*
[2] *Department of Physics & Astronomy, University of British Columbia, 6224 Agricultural Road, Vancouver, BC V6T1Z1, Canada*
[3] *Institut d'Astrophysique de Paris, 98bis Boulevard Arago, Paris, France*
[4] *Institut d'Astrophysique Spatiale, Universite Paris Sud, Bat. 121, 91405 Orsay Cedex, France*
[5] *Steward Observatory, University of Arizona, 933 N Cherry Ave, Tucson, AZ 85721, USA*

14 July 2010

ABSTRACT

Galaxies selected at 170 μm by the *ISO* FIRBACK survey represent the brightest $\sim$10% of the Cosmic Infrared Background. Examining their nature in detail is therefore crucial for constraining models of galaxy evolution. Here we combine *Spitzer* archival data with previous near-IR, far-IR, and sub-mm observations of a representative sample of 22 FIRBACK galaxies spanning three orders of magnitude in infrared luminosity. We fit a flexible, multi-component, empirical SED model of star-forming galaxies designed to model the entire $\sim 1-1000\,\mu$m wavelength range. The fits are performed with a Markov Chain Monte Carlo (MCMC) approach, allowing for meaningful uncertainties to be derived. This approach also highlights degeneracies such as between $T_{\rm d}$ and β, which we discuss in detail. From these fits and standard relations we derive: $L_{\rm IR}$, $L_{\rm PAH}$, SFR, $\tau_{\rm V}$, M_*, $M_{\rm dust}$, $T_{\rm d}$, and β. We look at a variety of correlations between these and combinations thereof in order to examine the physical nature of these galaxies. Our conclusions are supplemented by morphological examination of the sources, and comparison with local samples. We find the bulk of our sample to be consistent with fairly standard size and mass disk galaxies with somewhat enhanced star-formation relative to local spirals, but likely not bona fide starbursts. A few higher-z LIGs and ULIGs are also present, but contrary to expectation, they are weak mid-IR emitters and overall are consistent with star-formation over an extended cold region rather than concentrated in the nuclear regions. We discuss the implications of this study for understanding populations detected at other wavelengths, such as the bright 850 μm SCUBA sources or the faint *Spitzer* 24 μm sources.

Key words: galaxies: fundamental parameters, galaxies: starburst, infrared: galaxies, submillimetre

1 INTRODUCTION

Understanding the full infrared spectral energy distribution (SED) of galaxies is essential for a complete picture of star-formation in the Universe. Measurements of the cosmic background radiation allow us to infer that about half the energy ever generated by stars was reprocessed by dust into the infrared (see Hauser & Dwek 2001, for a review). This emission is increasingly important at higher redshifts where the star-formation density of the Universe is larger than today. Modelling the contribution of different galaxy populations to the Cosmic Infrared Background (CIB) requires detailed knowledge of the SEDs of star-forming galaxies. The variation in SED shapes is a key uncertainty when comparing populations selected at different wavelengths or testing galaxy evolution models.

In this paper, we discuss the full infrared SED ($\sim 1-1000\,\mu$m), which roughly spans the wavelengths between stellar and synchrotron-dominated emission. Traditionally, studying this entire range at once has been difficult, since mid-IR ($<60\,\mu$m) observations could not reach much beyond the local Universe[1], while sub-mm observations also only exist for very local, IR-bright, galaxies (e.g. Dunne & Eales 2001), or else the blank-sky Sub-mm Common User Bolometer Array (SCUBA) sources which peak at $z\sim$2–3 (Chapman et al. 2005). The latter typically have only one or two other wavelength detections in addition to the SCUBA (850 μm) one, which makes their interpretation particularly dependent on the SED model assumed (see Blain et al. 2002, for a review). Due to these past observational limitations, we still do not know (beyond some generalized trends) the full range of galaxy SED shapes, how exactly they are related to the underlying physical conditions in the galaxy, and therefore how they may vary across cosmic time as the galaxies evolve.

[1] Except for the deepest ISOCAM 15 μm observations which peak at $z\sim0.7$ (Rodighiero et al. 2004)

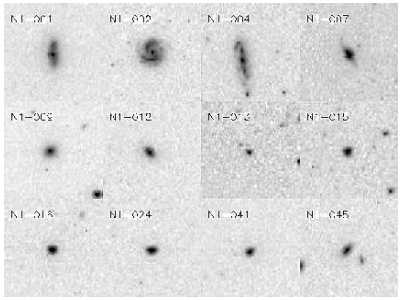

Figure 1. IRAC 3.6 μm images for bright galaxies in our sample. Note the prevalence of disk-like morphologies with bright nuclei (N1-004 is a spectroscopically confirmed weak AGN). Boxes here are approximately 1.4 arcmin wide. For comparison, *ISO*'s 170 μm beam is $\sim$90 arcsec.

With the advent of the *Spitzer* Space Telescope (Werner et al. 2004) we can for the first time observe the mid-IR properties of large numbers of sources over a cosmologically significant extent in redshift (e.g. Lonsdale et al. 2003). *Spitzer* covers the range 3–160 μm. The obvious next step toward characterizing the full infrared SEDs of galaxies is therefore to link *Spitzer* observations with longer wavelength samples, especially including sub-mm observations. In this regard, the quality and quantity of the available sub-mm data are the limiting factor.

The sample discussed here is selected from the 170 μm FIRBACK (Far-IR BACKground) ELAIS-N1 catalog (Puget et al. 1999; Dole et al. 2001). The selection is based on an existing radio detection, which we followed-up with both deep near-IR and sub-mm observations (Scott et al. 2000; Sajina et al. 2003, hereafter S03). We find that in terms of the mid-IR properties, the sample selection is largely unbiased with respect to the FIRBACK population as a whole. Our previous studies suggest that the sample consists primarily of $z<0.3$ ordinary, spiral-like galaxies, rich in cold ($T<40$ K) dust, with $\sim$1/6 of the sample consisting of Ultraluminous Infrared Galaxies (ULIGs) at $z\sim0.5-1$. Spectroscopic follow-up of this and related sub-samples support these findings (Chapman et al. 2002; Patris et al. 2003; Dennefeld 2005, hereafter D05). The higher-z fraction therefore represents a bridge population between the local Universe and distant, dusty star-formers such as the SCUBA blank-sky sources. In general, the importance of FIRBACK galaxies is that they represent the brightest galaxies at 170 μm, contributing $\sim$10% to the CIB and *selected at a wavelength near the peak of the CIB spectrum*.

We use archival *Spitzer* observations of the ELAIS-N1 field in order to extend the known SEDs of the above sample into the mid-IR wavelength range. We fit these SEDs with a phenomenological model motivated by different physical origins for the emission. These fits allow us to discuss the physical characteristics of our galaxies as well as trends within the sample. Details of the fitting procedure and some related issues are included in a set of appendices.

Throughout the paper we assume a flat Universe with $H_0=75$ km s^{-1} Mpc^{-1}, $\Omega_{\rm M}=0.3$, and $\Omega_\Lambda=0.7$.

2 DATA

The galaxies we focus on come from a sub-sample of FIRBACK sources with radio detections which were observed with SCUBA. The full sample of 30 targets was first presented in S03 where details of the sample selection as well as the near-IR (*K*) and sub-mm observations and data reduction are given. In particular, in S03 we addressed the question of whether or not the radio detection requirement introduces a bias and found that apart from potential HyLIGs ($L_{\rm IR}>10^{13}\,{\rm L}_\odot$) at $z\sim1.5$, and spurrious sources, the radio detection does not bias us with respect to the FIRBACK catalogue as a whole. Here we additionally use *Spitzer* archival observations of the ELAIS-N1 field obtained as part of the *Spitzer* Wide-area IR Extragalactic Survey (SWIRE, Lonsdale et al. 2003). We focus on sources with unique identifications in the SWIRE data (see Section 2.2), which leaves us with a sample of 22 sources (see Table 1).

2.1 Treatment of *Spitzer* data

The basic data reduction and calibration is already performed on the individual frames obtained from the *Spitzer* archive. We use the Starlink software package CCDPACK to rescale, align and coadd the observations into common mosaic images for each of the 4 IRAC bands and the MIPS 24 μm band. Furthermore, the Starlink PHOTOM and GAIA packages are used to perform aperture photometry on the sources. To ensure that the sky-annuli chosen fairly represent the sky/background we monitor the sky values obtained for all of these and modify the annular region for any galaxy whose sky value is more than 2 σ above the average sky. The errors are then computed from the sky variance. We find unambiguous counterparts for nearly all radio/SCUBA sources in S03 (the exceptions being N1-032, and N1-034).

Since we started on this project, the SWIRE team has released their own catalogues of the field (Surace et al. 2004). These allow us to double check our IRAC and MIPS 24 μm photometry, as well as add a 70 μm point where available. For N1-004, N1-007, and N1-012 there are no 24 μm or 70 μm fluxes due to missing data. In addition to the SWIRE 70 μm catalogue, we extract fluxes for three faint sources: N1-040, N1-064, and N1-077. In all cases, the aperture resulting in the maximum flux was used in order to ensure all emission is accounted for. The only remaining source is N1-078 which is near the edge of the image and thus a confident flux cannot be obtained.

This is the only source without any data points between 24 μm and 170 μm. For all of N1-004, N1-007, and N1-012 we have ISOCAM 15 μm and *IRAS* 60 μm fluxes compensating for the missing MIPS data. For the few cases which have both a 60 μm (see D05) and 70 μm detection (N1-001, N1-002, and N1-016), we find that the 60 μm fluxes are somewhat higher than the 70 μm ones contrary to any reasonable SED (given the S_{70}/S_{170} colours); but the difference is within the 20% calibration uncertainty assigned to the 70 μm flux. The SWIRE catalogue 70 μm flux for N1-001 (198 mJy) was most discrepant originally; however, it is an extended source and we find that a flux of 233 mJy is more accurate. This 20% difference is the most severe we expect due to aperture effects for this sample. We do not explicitly use the few available 160 μm points, but within the uncertainties they are consistent with the *ISO* 170 μm points.

Near-IR *J*-band data for about half of our sample are available from the band-merged ELAIS catalog (Rowan-Robinson et al. 2004), while the *K*-band data come from our previous work (S03). To con-

Table 1. Multiwavelength data for our sample. All errors are 1 σ estimates.

Source*	$S_{1.3}$[a] mJy	$S_{2.2}$[b] mJy	$S_{3.6}$[c] mJy	$S_{4.5}$[c] mJy	$S_{5.8}$[c] mJy	$S_{8.0}$[c] mJy	S_{24}[c] mJy	S_{70}[c] mJy	S_{170}[d] mJy	S_{450}[b] mJy	S_{850}[b] mJy	$S_{1.4\mathrm{GHz}}$[e] mJy
N1-001	6.28	7.31±0.54	2.97±0.32	1.98±0.26	4.67±0.4	12.25±0.66	19.97±1.71	233	597±72	-3.0±14.0	6.1±1.6	0.74±0.23
N1-002	4.58	5.55±0.41	5.35±0.43	3.79±0.37	9.6±0.59	23.97±0.92	9.87±1.21	112	544±69	14.4±12.4	4.4±1.1	0.64±0.04
N1-004	9.16	7.31±0.14	5.38±0.44	3.79±0.36	6.05±0.47	11.42±0.64	—	—	391±58	32.5±7.2	3.6±1.4	0.88±0.13
N1-007	4.40	3.5±0.26	3.65±0.36	2.41±0.29	4.09±0.38	11.87±0.65	—	—	338±54	23.4±8.1	4.4±1.6	1.04±0.12
N1-009	9.63	10.57±0.2	6.02±0.46	3.96±0.37	7.05±0.5	14.03±0.7	4.26±0.8	96	313±52	10.6±7.6	3.5±1.5	1.15±0.11
N1-012	1.75	1.84±0.3	1.15±0.2	0.75±0.16	0.81±0.17	4.24±0.39	—	—	302±51	9.2±10.0	1.5±1.6	0.31±0.07
N1-013	—	0.13±0.01	0.16±0.07	0.14±0.07	0.18±0.08	0.44±0.12	2.21±0.58	83	294±51	18.8±9.9	0.0±1.5	0.52±0.15
N1-015	0.36	0.80±0.06	0.57±0.14	0.53±0.14	0.37±0.11	2.05±0.27	3.16±0.68	49	294±51	-3.4±7.7	1.4±1.6	0.52±0.07
N1-016	2.71	3.5±0.26	1.78±0.25	1.41±0.22	1.61±0.24	7.6±0.52	6.81±1	160	289±50	34.8±16.7	1.5±1.2	1.55±0.13
N1-024	1.14	1.39±0.03	1.16±0.2	0.77±0.16	0.9±0.18	5.4±0.44	4.38±0.81	108	266±49	32.3±7.5	2.9±1.3	0.75±0.02
N1-029	1.10	1.27±0.09	1.24±0.21	0.88±0.18	0.75±0.16	4.25±0.39	4.3±0.8	72	229±46	20.0±14.2	0.5±1.7	0.69±0.05
N1-031	1.93	2.65±0.19	1.45±0.22	0.91±0.18	1.44±0.23	3.53±0.35	5.41±0.9	62	225±46	9.2±13.2	1.9±1.1	0.43±0.06
N1-039	—	0.32±0.05	0.28±0.1	0.25±0.09	0.19±0.08	0.8±0.17	1.3±0.44	44	205±44	10.9±86.8	-0.1±2.3	0.58±0.07
N1-040	—	0.01±0.01	0.08±0.05	0.07±0.05	0.06±0.05	0.05±0.04	0.69±0.32	26	205±44	29.2±20.5	5.4±1.1	0.33±0.03
N1-041	0.38	0.88±0.06	0.66±0.15	0.5±0.13	0.58±0.14	4.14±0.38	3.89±0.76	75	204±44	20.4±156.7	-0.1±2.5	0.76±0.06
N1-045	1.39	1.16±0.02	1.01±0.19	0.66±0.15	0.69±0.16	3.29±0.34	2.23±0.58	64	198±44	15.3±8.3	3.0±1.4	0.43±0.06
N1-064	—	0.03±0.01	0.15±0.07	0.11±0.06	0.12±0.07	0.09±0.06	1.38±0.46	14	166±42	35.2±13.9	5.1±1.2	0.23±0.04
N1-068	0.31	0.51±0.04	0.31±0.1	0.31±0.11	0.28±0.1	1.98±0.26	3.96±0.76	62	165±42	15.1±7.6	2.2±1.4	0.44±0.05
N1-077	0.31	0.42±0.07	0.37±0.11	0.29±0.1	0.23±0.09	1.4±0.22	1.29±0.44	42	159±41	5.9±7.3	1.1±1.3	0.40±0.10
N1-078	—	0.04±0.01	0.13±0.07	0.1±0.06	0.09±0.06	0.13±0.07	0.6±0.3	—	158±41	35.2±8.7	5.7±1.3	0.24±0.04
N1-083	—	0.46±0.08	0.31±0.1	0.25±0.09	0.18±0.08	0.68±0.16	1.21±0.43	43	150±41	16.2±16.0	0.7±1.2	0.55±0.03
N1-101	0.38	0.55±0.09	0.58±0.14	0.38±0.12	0.46±0.13	2.34±0.29	2.66±0.63	46	136±40	19.8±7.5	0.9±1.5	0.39±0.05

* The naming scheme follows Dole et al. (2001).
[a] J-band magnitudes from Rowan-Robinson et al. (2004) where 20% uncertainty is assumed.
[b] UKIRT and SCUBA fluxes from Sajina et al. (2003).
[c] IRAC and MIPS fluxes from archival SWIRE observations, this work; S_{70} from the SWIRE catalogue, all assumed to have an uncertainty of 20%.
[d] ISOPHOT 170 μm data from Dole et al. (2001).
[e] VLA 21 cm fluxes from Ciliegi et al. (1999).

vert to flux densities, we used zero points of 1600 Jy and 670 Jy for the *J*- and *K*-bands respectively.
The *Spitzer* fluxes are presented in Table 1 along with the rest of the multiwavelength data used here. A few of the sources have some (or all of) *U, G, R*, ISOCAM 15 μm, *IRAS* 60 μm and 100 μm fluxes, which are given in D05. In our present study, these are used primarily for consistency checks.

2.2 Possibility of multiple sources

We use the SWIRE ELAIS-N1 catalog to further investigate the nature of the FIRBACK sources and in particular the relation of our radio-selected sources to the full sample. The 90 arcsec *ISO* beam means that the chance of multiple sources contributing to the 170 μm flux is not expected to be negligible. We perform a simple test of this effect by taking every 24 μm source within a 45 arcsec radius of the *ISO* position. We then add all these fluxes and compare with the single brightest source within the centroid. The results are presented in Fig. 2, where we see that indeed nearly half of all sources $regardless\ of\ whether\ the\ full\ or\ 4\sigma\ catalog\ is\ used$ are not well described by assigning a single counterpart. This is a useful qualitative test, although it is unlikely to be correct in detail, because of complications such as foreground AGB stars, or combinations such as a bright local galaxy near a somewhat higher-z LIG/ULIG (where the latter might still contribute the bulk of the 170 μm flux). Nevertheless, it is evident that nearly half of the 170 μm-selected sources have 2 or 3 roughly equivalent mid-IR counterparts. Considering the position of the counterparts within the beam does not appear to affect this significantly. This fraction drops slightly for our radio-selected sample, although it is still significant. This general conclusion is in agreement with the results of Dennefeld et al. (2005) who find 28/56 sources in the 4 σ catalog to have firm, unique identifications. Here we add that this fraction is unlikely to change significantly for the 3 σ catalog. We also find similar results for our FIRBACK sub-sample of 30 targets, with 28% having fainter 24 μm sources in the *ISO* beam contributing >30% of the flux of the brightest source (dotted line in Fig. 2). Because of strong ambiguities, we remove 8 FIRBACK sources from our sub-sample. We leave 2 ambiguous sources (N1-015 and

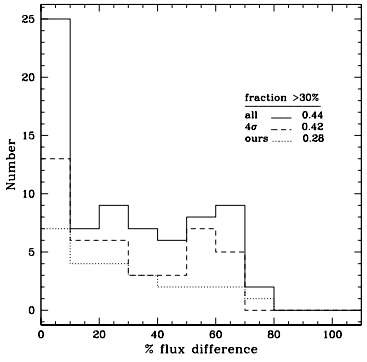

Figure 2. Quantitative study of the potential effect of multiple sources within the *ISO* beam at 170 μm. These histograms show the distribution of flux differences at 24 μm between using just the brightest 24 μm source within the *ISO* beam versus using all sources within a 45 arcsec error circle (i.e. $100\,(1 - S_{24,max}/\sum S_{24})$). The solid line is for all FIRBACK sources, while the dashed line is for the sources in the $>4\,\sigma$ catalog. The dotted line is for our sub-sample of 30 radio-selected sources.

Table 2. Derived properties for our sample. Errors are marginalized 68% confidence limits.

Source	z[a]	$R_{\rm eff}^{b}$ kpc	$T_{\rm d}$ K	β	$\log M_{\rm d}$ $M_\odot$	τ_V	$\log M_*$ $M_\odot$	$\log L_{3-1000}$ $L_\odot$	$\log L_{\rm PAH}^{c}$ $L_\odot$	SFR[d] $M_\odot$/yr	Quality[e]
N1-001	0.030	4.41	25.2 ± 4.7	1.9 ± 0.5	7.10 ± 0.22	0.95 ± 10.15	9.44 ± 0.09	10.06 ± 0.06	9.07 ± 0.21	1.72 ± 0.29	2
N1-002	0.064	9.55	21.9 ± 6.1	2.1 ± 0.6	7.62 ± 0.24	5.41 ± 5.60	10.47 ± 0.16	10.62 ± 0.06	10.15 ± 0.20	5.3 ± 1.1	2
N1-004	0.064	14.29	23.0 ± 5.6	2.1 ± 0.5	7.56 ± 0.19	3.31 ± 3.50	10.43 ± 0.13	10.60 ± 0.08	9.71 ± 0.24	5.7 ± 1.2	1
N1-007	0.061	6.10	24.1 ± 7.1	1.4 ± 0.7	7.50 ± 0.23	5.40 ± 5.03	10.25 ± 0.18	10.42 ± 0.11	9.71 ± 0.21	3.6 ± 1.0	2
N1-009	0.053	5.56	23.3 ± 6.6	2.1 ± 0.6	7.18 ± 0.32	2.67 ± 2.37	10.32 ± 0.13	10.22 ± 0.08	9.61 ± 0.18	2.02 ± 0.47	1
N1-012	0.066	6.88	27.4 ± 8.3	1.7 ± 0.6	7.35 ± 0.37	2.27 ± 1.68	9.65 ± 0.11	10.44 ± 0.13	9.26 ± 0.25	4.2 ± 1.4	1
N1-013	(0.46)	18.63	32.5 ± 11.6	2.0 ± 0.8	8.73 ± 0.34	7.81 ± 4.12	10.79 ± 0.16	12.11 ± 0.11	10.64 ± 0.23	210 ± 55	1
N1-015	0.234	12.37	23.7 ± 5.1	2.1 ± 0.5	8.50 ± 0.37	2.85 ± 1.63	10.56 ± 0.16	11.39 ± 0.12	10.40 ± 0.25	36 ± 13	1
N1-016	0.092	6.10	31.8 ± 8.0	1.6 ± 0.6	7.44 ± 0.35	1.73 ± 8.02	10.25 ± 0.15	10.86 ± 0.08	10.29 ± 0.26	11.0 ± 1.9	1
N1-024	0.086	5.44	24.2 ± 7.9	1.8 ± 0.7	7.73 ± 0.23	3.15 ± 2.71	9.95 ± 0.16	10.60 ± 0.09	9.76 ± 0.20	6.1 ± 1.6	1
N1-029	0.144	9.75	26.6 ± 16.9	2.0 ± 0.8	7.88 ± 0.59	3.50 ± 2.74	10.40 ± 0.14	10.93 ± 0.12	10.09 ± 0.23	12.2 ± 4.5	1
N1-031	0.063	4.29	21.9 ± 15.5	2.4 ± 0.8	7.22 ± 0.52	2.08 ± 2.03	9.81 ± 0.12	10.16 ± 0.13	9.20 ± 0.25	2.07 ± 0.69	1
N1-039	0.269	14.21	24.5 ± 9.4	2.5 ± 0.6	8.44 ± 0.70	7.21 ± 5.34	10.53 ± 0.22	11.37 ± 0.16	10.21 ± 0.24	35 ± 13	1
N1-040	0.450	26.34	26.5 ± 7.9	1.8 ± 0.7	9.10 ± 0.21	15.61 ± 7.36	10.42 ± 0.34	11.83 ± 0.13	9.85 ± 0.41	104 ± 33	1
N1-041	0.120	7.85	24.7 ± 12.2	2.3 ± 0.7	7.82 ± 0.77	4.71 ± 2.51	10.01 ± 0.14	10.77 ± 0.14	9.93 ± 0.23	8.2 ± 3.0	1
N1-045	(0.18)	15.74	28.1 ± 14.6	1.1 ± 0.8	8.08 ± 0.57	2.55 ± 0.00	10.53 ± 0.16	11.08 ± 0.13	10.23 ± 0.16	17.4 ± 6.0	1
N1-064	0.910	17.54	31.1 ± 6.3	1.8 ± 0.7	9.32 ± 0.21	29 ± 30	11.47 ± 0.25	12.45 ± 0.13	11.73 ± 0.39	410 ± 130	3
N1-068	(0.16)	9.69	26.7 ± 20.3	2.1 ± 0.8	7.83 ± 0.75	3.41 ± 1.99	9.99 ± 0.15	10.93 ± 0.14	9.88 ± 0.20	13.0 ± 4.4	1
N1-077	(0.20)	11.60	27.1 ± 14.5	2.0 ± 0.7	7.91 ± 0.65	3.25 ± 2.27	10.17 ± 0.15	10.92 ± 0.15	10.06 ± 0.21	12.0 ± 4.6	1
N1-078	(0.91)	16.33	69.8 ± 15.0	1.1 ± 0.5	9.16 ± 0.25	27 ± 30	11.49 ± 0.26	12.90 ± 0.22	11.59 ± 0.38	1360 ± 570	3
N1-083	(0.31)	14.17	30.8 ± 18.3	2.0 ± 0.7	8.21 ± 0.58	4.81 ± 4.19	10.65 ± 0.23	11.40 ± 0.16	10.34 ± 0.19	35 ± 15	1
N1-101	0.060	6.16	24.6 ± 17.8	2.1 ± 0.8	7.07 ± 0.75	4.94 ± 3.33	9.36 ± 0.18	9.89 ± 0.14	9.01 ± 0.19	1.07 ± 0.44	1

[a] Spectroscopic redshifts from D05 and Chapman et al. (2002) (N1-040 and N1-064); photometric redshifts given in brackets (see Appendix B).
[b] The observed half-light radius at 8 μm converted to physical distance.
[c] The integral under our full PAH template.
[d] As per Kennicutt (1998). For consistency L_{8-1000} was used here.
[e] Quality flag: 1=good; 2=$\chi^2_{\rm red} > 2$; 3=τ_V poorly fit (see Section A.1).

N1-039) because they have $z_{\rm spec} \sim 0.2-0.3$ and this test is inconclusive for higher-z sources. This leaves 22 sources for which the correct counterpart is reasonably secure, with other possible counterparts contributing a probable amount to the 170 μm flux which is of order the flux uncertainties or less. Since the beamsize at the other wavelengths is so much better than at 170 μm, the effects of multiple source contributors to the other fluxes are negligible. The effects of multiple contributors are already partially included in the 170 μm uncertainties, which contain confusion noise (see Lagache & Puget 2000). Therefore after removing the 8 *ISO* sources which have the most ambiguous identifications at 24 μm, we are confident that the effects of multiple counterparts are not significant. We concentrate on this new sub-sample of 22 sources in the rest of this paper.

3 SED MODEL

3.1 Interpreting the observed SEDs

The observed SED of a galaxy depends on the properties of the stellar populations (e.g. ages and metallicities), the dust model (e.g. composition, size distributions), and the relative geometry of the two. The full range of possible combinations of all these is such that, fully accounting for all possible processes is todate not possible. Radiative transfer models where stars form inside giant molecular clouds and gradually disperse into the diffuse medium exist (Silva et al. 1998; Efstathiou & Rowan-Robinson 2003; Popescu et al. 2000), but tend either to have too many free parameters, or not cover the full range in SEDs observed. Self-consistent models of the stars and dust (i.e. energy absorbed equals energy emitted) have been done on local galaxies (Galliano et al. 2003); however, require exceptionally well sampled SEDs from the UV to the sub-millimeter. We choose a modelling approach (see Section 3.2) that is data-driven: i.e. our model is no more complicated than our data allow us to fit, yet is flexible enough to describe

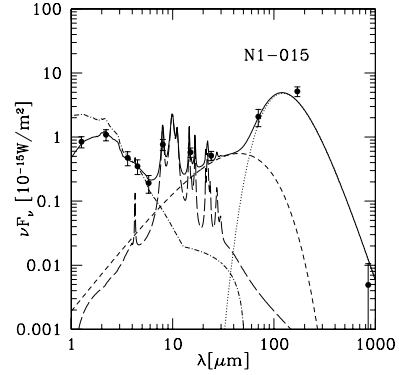

Figure 3. An example of the SED model used here. This includes a grey-body (*dotted line*), a warm power-law (*short-dash*), PAH emission (*long-dash*), and unextincted stellar emission (*dot-dash*) with $e^{-\tau_\nu}$ extinction applied. The thick solid line is the total.

the full range of SEDs observed in the sample. Such a simple phenomenological model has the effect of smoothing over the underlying messiness of galaxy SEDs, while providing us with best-fit parameters (such as opacity and dust temperature) those values are some 'characteristic' or 'average' values of an underlying distribution. The approach is therefore well suited to broadband data, such as presented for our sample in the previous section, which is, in essence, spatially integrated over the entire galaxy, including its quiescent (i.e. cirrus) and potentially active (i.e. starburst) environ-

ments.
The main limitation in interpreting our results in terms of the physical nature of our galaxies is due to the fact that, as discussed in the previous section, the available optical/UV data (*U*, *G*, and *R*) for our sample are quite scarce and thus here we only discuss the spectral properties of our galaxies longward of and including the near-IR ($\sim 2\,\mu$m), which automatically precludes us from *directly* discussing young stars. Thus our restriction of fitting only the $\gtrsim 2\,\mu$m spectra means that: 1) we cannot balance the energy absorbed in the optical/UV with the energy re-emitted in the infrared, 2) we cannot explicitly discuss either the star-formation history or age distribution of the stellar populations of our galaxies, and 3) we cannot constrain multiple optical depths (e.g. molecular cloud and cirrus). These limitations are largely addressed post-fitting, i.e. in the interpretation of the best-fit model parameters and how they are used to infer underlying physical characteristics. For example, we confine our stellar model to an old stellar population template (see Section 3.2), but when deriving stellar mass, we use mass-to-light ratios which include the effect of young stars on the *K*-band (Section 4.3). We know that young stars form inside dense molecular clouds and later disperse into the diffuse 'disk' environment. Thus the characteristic optical depth absorbing the young stars' power is likely not the optical depth we derive in the near-IR which is dominated by the older stellar populations. We address this in Section 5.2, where the dust masses are derived both from emission (predominantly young stars) and absorption (predominantly old stars in our case).
With the above philosophy in mind, we proceed with the model procedure outlined below.

3.2 Details of Model Procedure

As discussed above, our modelling approach is driven by the desire to have a phenomenological model which fits known nearby galaxy SEDs robustly and yet has the flexibility (i.e. number of phenomenological parameters only slightly less than the number of data points we are trying to fit) which allows us to fit a wide range of SED types, and in addition we want to be able to extract physical parameters with meaningful uncertainties (in particular such that degeneracies between parameters can be highlighted). With these goals clearly in mind, our choice of detailed SED model is dependent on the quality and wavelength coverage of the data, while the statistical approach we use is the Markov Chain Monte Carlo method.
We model the SED as a sum of stellar emission, PAH emission, power-law emission, and thermal grey-body emission. This is based on the mid-IR model used in Sajina, Lacy, and Scott (2005).
The stellar emission is accounted for by a 10 Gyr-old, solar metallicity, Salpeter IMF, single stellar population (SSP) spectral template generated with the PEGASE2.0 spectral synthesis code (Fioc et al. 1997). The specific stellar model used here is not important, being merely a stand-in for 'old stars'. For any population older than about 1Gyr, the near-IR spectrum looks essentially the same (through a couple of broadband filters), the differences being in the shorter wavelengths. Since our sources are largely $z \sim 0$, with a tail extending up to $z \sim 1$, this can be thought of as: all of our sources include *some* stars that are as old as the Universe at the observed epoch.
We use the neutral PAH emission template of Lee & Draine (2003). The only modification we make is the addition of the newly discovered 17 μm feature (Smith et al. 2004). Our broadband data do not allow us to investigate the probable variations in relative PAH feature strength, and therefore any reasonable PAH template can be used here, with the understanding that it is only an approximiation for any given galaxy. A power-law, $f_\nu \propto \nu^{-\alpha}$, is a proxy for the warm, small grain emission (roughly $< 60\,\mu$m). This is cut-off as $\exp(-0.17 \times 10^{14}\,\mathrm{Hz}/\nu)$ in order not to interfere with the far-IR/sub-mm wavelength emission, which is described by a thermal, $f_\nu \propto \nu^{3+\beta}[\exp(h\nu/kT) - 1]^{-1}$, component. Since we typically only have the 24 μm point to constrain this component, we fix α at 3.0, which smoothly connects this to the greybody component. Extinction, parameterized by τ_V, is applied using the $R_\mathrm{V} = 3.1$ Milky Way-type extinction curve of Draine (2003). This includes the 9.7 μm Si absorption feature, which thus becomes noticeable in this model at high opacities. We consider only a screen geometry, i.e. $I_\nu = I_0 \exp(-\tau_\nu)$. Fig. 3 shows the above phenomenological break-up of the SED. We solve for the best-fit model, and the associated uncertainties in the parameters via Markov Chain Monte Carlo (MCMC). Details of the fitting procedure and error analysis are given in Appendix A.
This model is complicated by the lack of spectroscopic redshifts for about 1/3 of the sample. We discuss our approach to determining photometric redshifts for these sources in Appendix B.

4 FIT RESULTS

The quantitative conclusions of our model-fitting are presented in Table 2, where the errors represent marginalized 68% confidence limits. A quality flag is also given to indicate whether or not problems exist with the fit. Below we discuss both the general aspects of the fitted SEDs, and details of the parameters presented in Table 2.

4.1 General trends in the SEDs

Fig. 4 shows the data overlaid with the best-fit SED model for sources ranging between $z \sim 0$ (top row) and $z \sim 1$ (bottom row). As expected, there is a greater range in SED shapes than accounted for by the data uncertainties. However, there are natural groupings, for example one can easily distinguish ULIGs (e.g. N1-064, N1-078) from LIGs (N1-015, N1-039) and from normal galaxies (e.g. N1-002, N1-009). The grey shading in Fig. 4 gives a sense of the uncertainty of the SED fits. Without prior assumptions on the shape of the SED (s.a. by using templates) as in this case, if we do not have constraints on both sides of the thermal peak (e.g. N1-078), a wide range of SED shapes and consequently temperatures, luminosities etc. are acceptable.

In Fig. 5, we address the question of what is the 'typical' normal/cold galaxy spectrum based on our model fits. In order to minimize redshift bias, we construct a composite spectrum from all sources with redshifts below 0.1, and for which 24 μm data are available. To minimize luminosity effects, we also normalize the spectra at 4.5 μm (which point resulted in the least amount of scatter across the SED) and effectively is a normalization in stellar mass. This procedure is consistent with results for *ISO* Key Project normal galaxies, where the stellar+PAH SEDs were found to be fairly constant (Lu et al. 2003). Comparing the results with a number of common SED models, we find that our sample is best described by fairly cold spectra with low mid-IR/far-IR ratios. In Fig. 4, we see that the LIGs (i.e. presumably starbursts) also have fairly cold spectra, unlike that of the 'prototypical' starburst M82 (this was already noted in D05).

Even more surprisingly, this cold trend does not appear to reverse for the highest luminosity sources including ULIGs. It must be noted however that it is not clear how common are such SEDs for ULIGs in general as we only have two spectroscopic ULIGs in our sample and our far-IR selection likely biases us toward colder sources. In Fig. 6 we show the best-fit SEDs for the two spectroscopically confirmed $z \sim 0.5 - 1.0$ sources (Chapman et al. 2002). The dotted line is an Arp220 template (Silva et al. 1998) at the appropriate redshift. In both cases the sub-mm data are well fit by the Arp220 template, but the mid-IR data differ by an order of magnitude. Our photometric highest-z source (N1-78) shows similar trends. Note that the PAH features in the best-fit N1-064 spectrum are not constrained by any data point and therefore a model with no PAH emission is quite acceptable as well (see the spread in Fig. 4). Despite it being poorly constrained for the few highest-z sources, we find clear evidence for prominent PAH emission for nearly all sources in our sample, regardless of redshift (and hence luminosity).

The weak mid-IR continua, and strong PAH emission of our sources suggest that they are star-formation rather than AGN dominated (see e.g. Sajina, Lacy, Scott 2005).

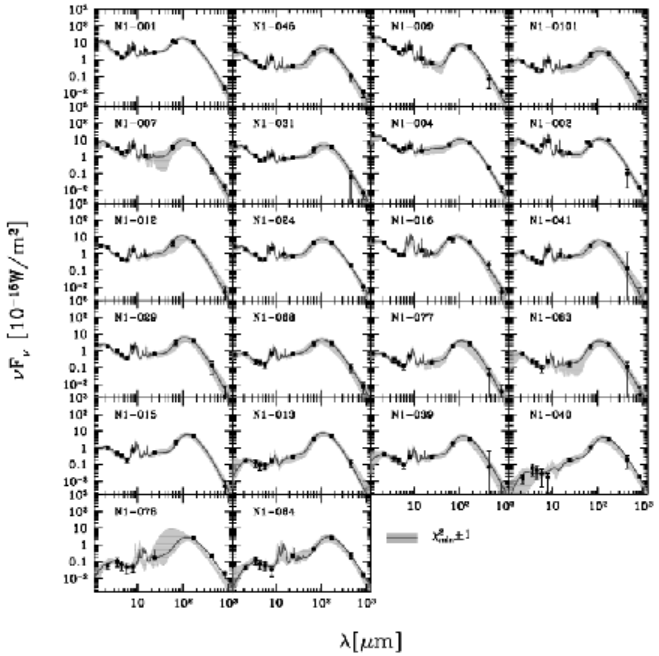

Figure 4. The SED fits for our sample, where we show both the data and best-fit model together with an uncertainty band. Note that the least well-defined SED is that of N1-078, which is the only source without data in the range 24 μm – 170 μm. The sources are ordered so that redshift increases from top to bottom. Note the characteristic increase in the dust-to-stars emission ratio as one goes to higher redshift (and hence more luminous) sources.

4.2 Luminosity and SFR

In Table 2, we present both the total infrared power output of our sources (L_{3-1000}), as well as the luminosity due to PAH emission alone.

The overall luminosities we derive are typically a few $\times\, 10^{10}\,\mathrm{L}_\odot$ for our lower-z targets, consistent with roughly L^* galaxies. L_PAH is obtained by integrating under the PAH component alone. We find the $L_\mathrm{PAH}/L_\mathrm{IR}$ fraction to be typically 5 – 15%. This is consistent with the results for the *ISO* Key Project galaxies (Dale et al. 2001).

Since such well-sampled SEDs are rare, to obtain the overall infrared luminosity, extrapolations from the mid-IR are common. However, the coldness of our sources means that, if such sources are the norm, prior relations might not be applicable. In Fig. 7 we compare our results on the mid-IR/total-IR relation with previous, *IRAS*-based, results (e.g. Takeuchi et al. 2005). The solid line is the best-fit for our sample, which is:

$$\log L_{24} = (1.13 \pm 0.05) \times \log L_\mathrm{IR} - (2.5 \pm 0.5). \quad (1)$$

Our rest-frame 24 μm fluxes are below those expected from the

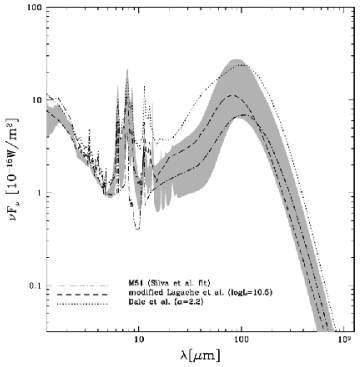

Figure 5. The shaded region represents the range of spectra, where we have included all sources with $z<0.1$ and which have 24 μm data (except N1-009, which has an unusually strong stellar component, for our sample). All SEDs are normalized at 4.5 μm, which is a neutral point between pure stellar and PAH emission. The shaded region should be regarded as a composite spectrum, representative of the 'cold' FIRBACK sources. For comparison we overlay a number of templates (see legend).

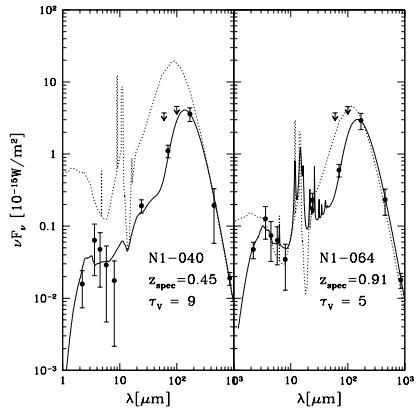

Figure 6. The best-fit SEDs for the two spectroscopically-confirmed higher-z sources. The *IRAS* upper limits are also shown, although they are not included in the fit. The dotted line shows the appropriately redshifted Arp220 template (Silva et al. 1998). The *Spitzer* fluxes suggest cooler and less luminous sources than previously assumed.

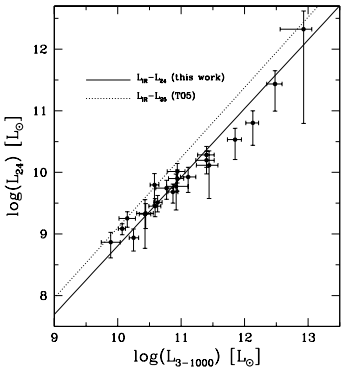

Figure 7. The 24 μm luminosity vs. total infrared luminosity. Note that within the uncertainties we find no difference between the *IRAS* 25 μm luminosity and the MIPS 24 μm luminosity. See Section 4.2 for details.

IRAS relation by $\sim$0.4 dex. Although we have too few sources at the high-L end to claim this conclusively, it appears that the relation drops even further for these sources. More likely, however, this is just an indication of the underlying scatter in the relationship due to variations in the SED shape.

This discrepancy with the earlier relation is most likely a selection bias. The sample used for the *IRAS* relation is flux-limited to all four *IRAS* bands, leading to a bias toward sources with stronger warm continuum, unlike our 170 μm selection where the bias is toward the presence of cold dust instead. We return to this point in Section 5.1.

About 70% of the sample have $\log(L/L_\odot)<11$, while the remaining 30% have $\log(L/L_\odot)>11$. This can be thought of as the break-up between fairly quiescent and more actively starforming galaxies (we address the mode of star-formation of our galaxies in detail in Section 5.3). The total infrared luminosity is well known to trace the current SFR of a galaxy (see e.g. Kennicutt 1998b; Kewley et al. 2002). We use the Kennicutt relation here which is:

$$\frac{\mathrm{SFR}}{\mathrm{M_\odot yr^{-1}}} = (1.8\times10^{-10})\frac{L_{8-1000}}{\mathrm{L_\odot}}, \qquad (2)$$

Note the slightly different definition of $L_{\rm IR}$, which is accounted for here (i.e. 8 – 1000 μm rather than 3 – 1000 μm). Typically our galaxies have SFR of $\sim$5 $M_\odot$/yr, which is slightly enhanced with respect to local quiescent spirals. As expected, the SFRs rise to a few hundred $M_\odot$/yr for our few ULIGs.

4.3 Stellar mass and dust obscuration

As part of our SED model fitting we estimate the k-corrected, and dust corrected near-IR stellar emission. The near-IR is preferred for deriving stellar mass as it is fairly robust against both uncertainties in the dust obscuration level (a factor of $\sim$10 less so than in the optical), and to the details of the stellar population and SFH (being largely sensitive to the red giant population only). Without sufficient optical coverage, we cannot properly account for the

possible contribution of young stars. We merely calculate the unextincted, restframe $L_{\rm K}$, and convert this to stellar mass by assuming an appropriate *K*-band mass-to-light ratio, γ_K. Despite its relative insensitivity to young stars, the near-IR mass-to-light ratio does increase as the fraction of young/massive stars in the galaxy increases. In addition, a degeneracy exists in that a more massive and dustier galaxy can appear similar to a less massive and less obscured one. The significance of this effect grows for sources without *J*-band data or with poor near-IR SNR, both of which are more common for the higher-z sources. However, since the optical depth is a free parameter in our model, it is already accounted for in the resulting Markov chains. The uncertainty in mass-to-light ratio however is not included. The additional uncertainty on the stellar mass is: $d\log M_* = d\log\gamma$. A mean value of $\gamma_K=0.6$ was found by Bell & de Jong (2001) for their sample of spiral galaxies, while Gil de Paz et al. (2000) find γ_K to be $\sim$0.92 for their sample of starburst and HII galaxies. Bell & de Jong (2001) consider a wide range of reasonable population models, finding $d\log\gamma_K\sim0.2$ dex (although this is smaller if the $B-K$ colour is known, due to the effect of the young stars). The SFRs derived for our sources in the previous section suggest enhanced star-formation activity compared with normal spirals. Therefore, the Gil de Paz et al value of $\gamma_K=0.92$ is likely more appropriate for our sample, while we assume the Bell & de Jong uncertainty (from the unknown SFHs) of 0.2. Adding this in quadrature to the MCMC derived errors suggests that more realistic uncertainties here are about twice the quoted ones.

With the above set of assumptions, we find $\langle M_{\rm star}\rangle\sim2\times10^{10}\,\mathrm{M_\odot}$,[2] with the $\log(L/L_\odot)<11$ sources and those with $\log(L/L_\odot)>11$ differing by $\sim$0.6 dex. Note, however, that from the above discussion we expect that somewhat higher values for γ are appropriate for the more luminous (higher SFR) galaxies, and vice versa for the lower luminosity ones. Taking this into account, the observed difference in mass may be even largely in reality.

For most sources, we find modest levels of dust extinction ($0<\tau_V<5$, peaking at $\sim$3) for most sources. This assumes a screen geometry, and would increase in a uniform mixture of dust and stars. The amount of extinction generally increases for $z\gtrsim0.3$ sources, with N1-040 requiring the greatest optical depth, consistent with its near-IR faintness (note however that the mean-likelihood and MCMC approaches disagree on the optical depths of the high-z sources – see Appendix A).

The values of τ_V we find for the bulk of the FIRBACK N1 galaxies, is consistent with the average $\tau_V\sim3$ found from the H_α/H_β ratio of the FIRBACK-South galaxies (Patris et al. 2003). This means that, typically, the optical depths to which the light of old and young stars is subjected do not differ dramatically when integrated across the galaxy (see also Section 5.2).

4.4 Dust properties: $T-\beta$ relation and dust mass

The single greybody approach we take (see Section 3.2) in modeling the dust emission of these galaxies, although in common use and the only one possible when just a few data points are available, is clearly an approximation (see also Dunne & Eales 2001; Blain et al. 2003). More realistically, a distribution of dust grain characteristics, such as optical properties and geometry, results in a distribution of effective temperatures and β's. In addition, degeneracies arise in fitting this model due to the functional form and spectral sampling (see Appendix C for further discussion).

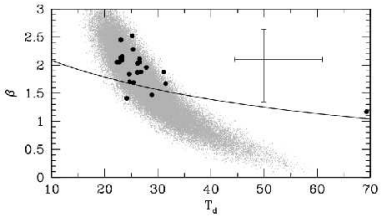

Figure 8. The best fit values (black dots) for $T_{\rm d}$ and β. The solid line is the Dupac et al. (2003) relation (see Appendix C). For comparison the greyscale points show the $\chi^2_{\rm min}+3$ region for N1-024. The error bars represent the average 68% uncertainties on individual sources (note that it is driven by the least constrained sources, while the grey points give a better sense of the scatter in well constrained sources). The outlier near 70 K is N1-078, for which no data exist between 24 μm and 170 μm.

For our sample, values of $T_{\rm d}\simeq20-30$ K and high values of β ($\simeq2$) are most representative. These are in good agreement with the typical far-IR temperatures ($\sim$22 K) of local spiral and irregular galaxies (Contursi 2001; Stickel et al. 2000), as well as theoretical expectations which place the big grain emission (dominating the thermal peak of normal galaxies) of a standard ISM at $T_{\rm d}\sim15-30$ K with $\beta\sim2$ (Draine & Lee 1984). Our estimates are also consistent with, but somewhat cooler than, the values found by Taylor et al. (2005) for the FIRBACK galaxies in ELAIS-N2.

The cold dust mass is estimated in the usual way: $M_{\rm d}=S_{850}*D_L^2[(1+z)\kappa B(T,\nu_e)]^{-1}$ (e.g. Farrah et al. 2002), where $B(T,\nu_e)$ is the Planck function for the given temperature, at the emission frequency, and the dust absorption coefficient κ parameterizes the unknown grain properties. We assume the value of κ=0.077 $\pm$ 0.02 $\mathrm{m^2kg^{-1}}$, as advocated by James et al. (2003), although there are arguments for a value up to 3 times higher (Dasyra et al. 2005). We return to the effect of increasing κ in Section 5.2. We find $M_{\rm d}\sim10^7$–$10^8\,M_\odot$, which is comparable with the masses found for the SCUBA Local Universe Galaxies Survey (SLUGS) galaxies (Dunne & Eales 2001). As expected, the higher z, more luminous galaxies have higher dust masses, typically $\sim10^8-10^9\,\mathrm{M_\odot}$.

4.5 Size and morphology

The closest galaxies in our sample appear disk-like by visual inspection of the IRAC images (see Fig. 1). In addition, we would like to determine the typical sizes of our sample, and whether there is a noticeable morphological difference as a function of infrared activity (i.e. $L_{\rm IR}$). Fortunately, all 22 sources considered here are at least mildly resolved by IRAC (diffraction limit $\sim2''$ at 8 μm). The effective radii given in Table 2 are the 8 μm half-light radii converted to physical distance (note there is no noticeable difference here if we used any other IRAC band). We find that, typically, $R_{\rm eff}\sim5-10$ kpc, although a tail of the sample extends to larger radii. These sizes are consistent with those of large spirals.

[2] For comparison, typical M^* values are $\sim3\times10^{10}\,\mathrm{M_\odot}$.

5 ANALYSIS

In this section, we use the results of the previous section in attempting to arrive at a consistent picture of the physical properties of our sources. We particularly focus on three related questions. Why are all our galaxies, including the ULIGs, colder than expected? Can we say something about the spatial distribution of the star-formation activity – i.e. is there indication of centrally concentrated starbursts surrounded by older stellar haloes, or is the star-formation by contrast distributed throughout the galaxy? And finally, is the typical FIRBACK galaxy actually starbursting?.

5.1 Why cold LIGs and ULIGs?

Both our general inspection of the SEDs and the derived dust temperatures for our sample suggest that fairly cold spectra with weak (compared with *IRAS* galaxies) mid-IR emission describe our entire sample, despite three orders of magnitude variation in bolometric luminosity. This can be seen directly by examining the $L - T_{\rm d}$ relation (see Blain et al. 2003). This relation is of particular significance to far-IR/sub-mm selected samples, as in principle it can reveal something of the nature of the sources based on only a few spectral points (enough, for example, for a single greybody fit), because it is simply a relation between the location of the far-IR peak and its overall strength. In Fig. 9, we compare the location of our sample in the (L, $T_{\rm d}$) plane with other infrared-selected samples, namely the SCUBA-selected high-z sources (Chapman et al. 2005) and the bright *IRAS*-selected galaxies (Dunne & Eales 2001). We overplot empirical relations appropriate for merging and quiescent galaxies (Barnard 2002). These can be understood intuitively by recalling that ideally, $L \propto R^2 T^4$. This leads to luminosity increasing with temperature if the size is kept constant, or conversely to a more concentrated starburst being hotter than a galaxy of the same luminosity but with more spread-out star-formation (as in throughout the full disk). With a few exceptions, our sample is consistent (within the uncertainties, and given the different selection from that of *IRAS* galaxies) with the relation for quiescent galaxies (for further discussion of the relation see Chapman et al. 2003), and consistent with our size results in Section 4.5.

The above discussion, taken a step further, suggests that our cold ULIGs might show extended star-formation activity, rather than the usual nuclear-concentration seen in the late stages of major mergers (Veilleux et al. 2002). Such a scenario has in particular been proposed for some SCUBA galaxies (Kaviani, Haehnelt, & Kauffmann 2003; Efstathiou & Rowan-Robinson 2003). Locally, only nuclear starbursts appear capable of reaching the requisite SFR/luminosity. However, at high-z, where presumably the progenitors are less evolved and more gas rich (i.e. with lower stability thresholds), it is possible that a major merger results in a disk-wide starburst (or rather many pockets throughout the disk) instead (Mihos 1999). Alternatively, a cause of cold ULIGs might be extreme opacity around a nuclear starburst and/or AGN.

5.2 The spatial scales of the old and young stars

In the previous section, we argue that the coldness of our sources, including both LIGs and ULIGs, might be due to star-formation spread over an extended cold disk, rather than a nuclear starburst surrounded by an old stellar halo. Here we apply two independent tests of this scenario.

Our first test is based on the assumption that the IR emission is

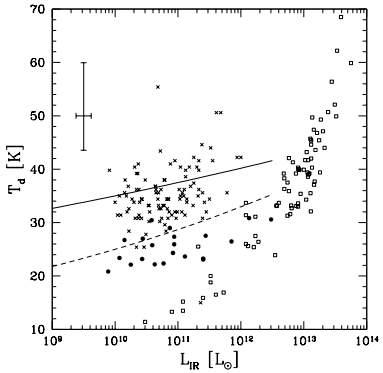

Figure 9. A comparison of the luminosity-temperature relation for our sample (*solid circles*) with other infrared-selected galaxies including *IRAS*-bright galaxies (Dunne & Eales 2001) (*crosses*), and SCUBA-selected galaxies (Chapman et al. 2005) (*open squares*). The solid and dashed lines represent the loci for merging and quiescent galaxies respectively (Barnard 2002). Note that our sample is consistent with the expectation for quiescent starformers.

dominated by power absorbed by the dust from young stars, while the dust responsible for the near-IR opacity traces the old stellar population. The two should match in a disk-wide star-formation picture, while there is no reason for a correlation in a nuclear starburst. In Section 4.4 we derived the dust mass based on the far-IR emission of our galaxies. In principle, the optical depth derived in Section 4.3 can also be converted to dust mass, provided the surface area of the optical region is known. We do this using the following equation, adapted from Lisenfeld & Ferrara (1998) by using $\tau_B = 1.3\,\tau_V$ and assuming the geometry is an inclined disk:

$$M_{\rm d}^{\rm opt} = (1.1 \times 10^5)\tau_V R^2 {\rm cos}i, \qquad (3)$$

where i is the the inclination, such that 0° is face-on and 90° is edge-on.

In Section 4.5, we presented the effective radii of our sources as derived from the IRAC images. We found no difference between the 4 IRAC bands and therefore it is safe to assume that these radii represent the spatial extent of the old stellar population. In Fig. 10, we compare this optically derived dust mass and the IR-derived dust masses. The two clearly correlate, as expected. However, the best-fit slope is 0.86 unlike the expected 1.00. The arrows define the directions in which either increasing disk inclination or increasing κ push the points. Note that increasing inclination is equivalent to decreasing the size of the region contributing the bulk of the IR emission (i.e. towards nuclear starburst). Therefore at the high-mass end, the good agreement suggests that the dust (behind the IR emission in particular) is distributed throughout the entire disk rather than being concentrated in the nuclear region (see next section). Somewhat contradictory, the high values of τ_V we find are also fully consistent (but the lower values implied by the likelihood analysis are not – see Appendix A). The two can be reconciled by a more complex geometry.

At the low mass end we find consistently higher dust masses

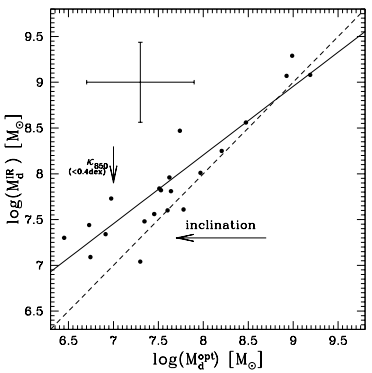

Figure 10. Optically-derived dust mass (from absorption) compared with IR-derived values (from emission). The solid line is the best-fit, while the dashed line is the expected $y = x$ line (for face-on disks). The directions of increasing disk inclination, and κ are shown.

than expected from the above formula and the derived optical depths (hence the shallower slope). This may merely indicate that the highest-SFR regions responsible for the dust emission are behind a foreground screen of much less obscured older stars which are responsible for the near-IR emission. Another interpretation, is that our IR-based dust mass is overestimated. Adopting the extreme end of κ values in the literature (Dasyra et al. 2005), $\kappa \sim 0.2$, will decrease our estimates by about 0.4 dex, making the two estimates much more consistent. The inclination cannot reconcile them as it only affects the points to the right of the dashed line (face-on case). This relation should probably not be over interpreted, since both expressions are approximations to much more complex systems and seeking a perfect agreement between them is therefore unrealistic. Within the uncertainties, we are gratified that our two independent estimates of the dust content agree as well as they do.

Given the above uncertainties, and especially if κ is underestimated, it is still possible that some of our sources (especially among the higher-L ones) are primarily powered by nuclear starbursts. We can determine the actual sizes of the star-forming/bursting regions in our galaxies by using the well known relation between gas surface density and SFR surface density (Schmidt 1959). The implied universality of the star-formation efficiency has been demonstrated observationally over many orders of magnitude in SFR density (Kennicutt 1998b). The slope of the relation SFR $\propto \rho^n$ is $n = 1.4$ (the Kennicutt relation; Kennicutt 1998b). However, the dependence of both quantities on radius is the same (since SFR and gas mass are derived from integrated properties, their respective surface densities are simply $\propto 1/r^2$), meaning that a change in the effective radius takes the form of a translation along a line of slope $n = 1.0$. Thus, assuming that the efficiency of star-formation is indeed universal, any departure from the Kennicutt relation could be attributed to a difference in effective radius.

We estimate the gas mass by assuming the Milky Way gas-to-dust ratio of 100 (Knapp & Kerr 1974), although the derived values, for external galaxies especially, show a large spread of about

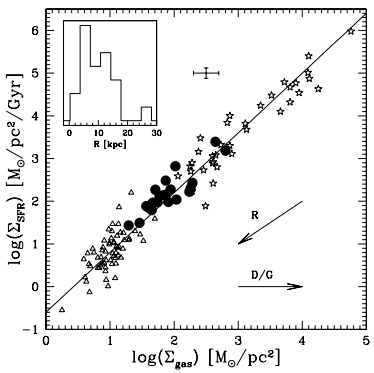

Figure 11. The Schmidt law, $\Sigma_{\rm SFR} = \alpha\,\Sigma_{\rm gas}^n$, where observationally $n = 1.4$ (Kennicutt 1998b, solid line). Our galaxies are plotted as the filled circles. The errorbars represent their average $1\,\sigma$ uncertainties. For comparison we overplot the Kennicutt spiral galaxies (open triangles), and starburst galaxies (open stars) samples. The inset shows the size distribution for our sample. The slope = 1 arrow shows the direction of increasing radius, while the horizontal arrow shows the direction of increasing dust-to-gas ratio.

an order of magnitude (see e.g. Stickel et al. 2000). With these estimates, in Fig. 11, we overplot our sources onto the original Kennicutt sample of normal spirals, and IR-bright starbursts. Most of our galaxies lie on this relation (within the errors) somewhat above the spirals, consistent with the SFRs found in Section 4.2. This suggests that the bulk of our sample is indeed forming stars throughout their extended disk, although slightly more actively (due to more gas-rich disks) than in local spirals.

The good agreement between our sample and the Kennicutt relation suggests that both the estimated radii and the assumed standard dust-to-gas ratio are approximately correct. The inset in Fig. 11 gives the size distribution of the sample, which is roughly consistent with that of local spiral galaxies (Vertchenko & Quiroga 1998). An *HST*-based study of the size distributions of slightly higher redshift ($z \sim 0.2 - 1$) disk galaxies suggests effective radii in the same range with the peak moving from ~ 6 kpc to ~ 4 kpc as the redshift decreases (Ravindranath et al. 2004).

As a final test, we double check the above conclusions by looking at the relation between $L_{\rm IR}$ and $T^{4+\beta}R^2$ (which should scale with luminosity, for simple geometries). As expected we find a good correlation between the two. The linear fit gives:

$$\log L = (0.9 \pm 0.1) \times \log(T^{4+\beta}R^2) + (1.5 \pm 1.3), \qquad (4)$$

where L is in $L_\odot$, T is in K, and R is in kpc. There are no obvious outliers (the rms is 0.4), again suggesting that given the cool temperatures derived, the radii inferred from the 8 μm images are appropriate (to within a factor of 2).

5.3 Starbursts? It's about timescales

In the previous section, we found that the typical FIRBACK galaxy has modest SFR, typically $\sim 5\,{\rm M}_\odot{\rm yr}^{-1}$, but this is somewhat en-

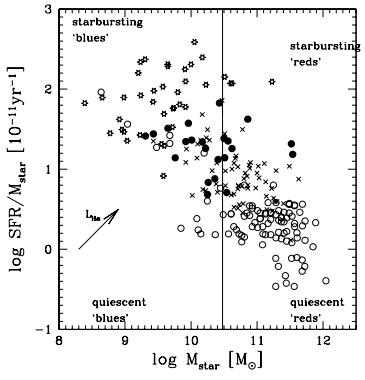

Figure 12. Stellar mass vs. specific SFR. This compilation of comparison galaxies is from Gil de Paz et al. (2000); however we have converted their SFRs to the standard Kennicutt et al. relation (Kennicutt 1998a) (a difference of –0.87 dex). Shown are: normal spirals (*open circles*); local Hα-selected star-forming galaxies (*crosses*); dwarf/HII galaxies (*stars*). Our FIRBACK sample is shown as the filled circles. Note that for consistency, we have converted our IR-based SFR to Hα-based SFR using the Kewley et al. (2002) relation. The arrow shows the direction of increasing Hα luminosity from Gil de Paz et al. (2000). The mass boundary (shown by the vertical line) is the observed boundary in physical properties seen in the SDSS data (Kauffmann et al. 2003).

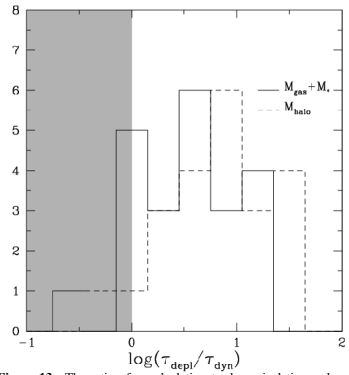

Figure 13. The ratio of gas depletion to dynamical timescales. The two histograms are for the case where dark matter is not included (solid line) or when it is (dashed line). The shaded region corresponds to the classical definition of a starburst.

hanced activity compared with local quiescent spiral galaxies. Our investigations so far suggest disk-like star-formation, with no indication of mergers, especially for the low-z sample. Now we would like to address the question of whether this enhanced star-formation could reasonably be described as a 'starburst'. There is no single absolute definition of a starburst, but some commonly used indicators (Heckman 2005) include: a high intensity of star-formation; a high birthrate parameter (SFR/$\langle$SFR$\rangle$); or a low ratio of the gas depletion timescale to the dynamical timescale. The question is – when is 'high' high enough, and when is 'low' low enough. We now discuss each criterion in turn.

The intensity of star-formation, was indirectly addressed in Fig. 11. Our sources appear to fall somewhere in-between quiescent spirals and nuclear starbursts (the Kennicutt et al. starburst sample are all nuclear). Here the highest-z sources (N1-064, and N1-078) are apparently the only unambiguous starbursts. The region occupied by the bulk of our *entire* galaxies is in fact also the locus of the *centres* of disk galaxies alone (Kennicutt 1998b). So, is the star-formation in our galaxies fairly smoothly distributed across the disk or in a collection of bursting knots sprinkled throughout? Are we diluting our results by assuming a smooth disk here? It appears that the intensity argument is inconclusive when applied to unresolved galaxies except in the most extreme cases.

The birthrate parameter is slightly misleading, because of its dependence on the epoch of observation (although this is not too severe for our sample). A related quantity, which we examine next, is the specific SFR (see e.g. Gil de Paz et al. 2000), which is equivalent to the birthrate assuming a uniform epoch. The best way to interpret this is through comparison with other samples whose properties are already known, and for this purpose we use the compilation of Gil de Paz et al. (2000). However, such comparisons should be carried out with some caution, since the samples are selected in very different ways and their quoted SFRs are based on different indicators. The main distinction here is that these other samples are based on the strength of the Hα emission line, while ours are based on the overall IR emission. The two are comparable, but not identical (largely due to the effects of dust extinction on the line strength at the high-L end and possible contribution of older stars to the IR emission at low luminosities). Here we use the empirical relation of Kewley et al. (2002) to convert our IR-based SFRs to Hα-based ones. Lastly, we standardize the Gil de Paz et al. SFRs to the Kennicutt relation (Kennicutt 1998a). In Fig. 12, we plot stellar mass vs. specific SFR for our sample. For comparison we overplot the data for local normal spirals, strong Hα emitters, and HII dwarfs, taken from Gil de Paz et al. (2000). Fig. 12 suggests that, overall, our sample is somewhat less massive and more active than typical local spiral galaxies. However, the bulk are larger and less star-bursting than the average local HII dwarf. In fact they most strongly resemble the comparison sample of Hα-selected local star-forming galaxies (Gil de Paz et al. 2000). This is to be expected, as the available spectra of our sources all show prominent emission lines (D05). The two outliers are the two ULIGs N1-064, and N1-078 which are predictably both massive and active.

We finally turn to the ratio of the gas depletion timescale ($\tau_{\rm depl}$) to the dynamical timescale ($\tau_{\rm dyn}$) of a galaxy. Unlike the above two considerations, the starburst criterion is clearer here. If the current rate of SFR is such that, if sustained, the available gas reservoir will be exhausted in a time shorter than the dynamical time, then the source is bursting. The depletion timescale is simply $M_{\rm gas}/{\rm SFR}$. We find that, typically, $\tau_{\rm depl} \sim 8\times10^8$ yr. The dynamical time is defined as $\tau_{\rm dyn} \sim (R/GM_{\rm tot})^{1/2}$. To estimate this, we begin by neglecting the dark matter contribution, and calculate the dynamical time using the gas mass plus the stellar mass. We then note that including any dark matter contribution would only have the effect of decreasing $\tau_{\rm dyn}$ and thus any source that appears quiescent will remain so, regardless of the extra mass (we return to this point below). Using this approach we find that typically $\tau_{\rm dyn} \sim 1\times10^8$ yr. Fig. 13 shows a histogram of $\tau_{\rm depl}/\tau_{\rm dyn}$ using estimates both with and without dark matter in $M_{\rm tot}$. When the dark matter halo mass is included[3], the only starbursts in our sample are N1-013, and N1-078 (with N1-064, and N1-077 being borderline). Throughout, we assume our IRAC-based sizes, which we argued are the effective scales of the star-formation activity (see Section 5.2). The bulk of our sample, despite their being apparently somewhat more active than local, quiescent spirals, do not appear to be bona fide starbursts.

[3] Using the relation $M_{\rm halo}/M_{\rm gas} \approx 35(M_{\rm gas}/10^7 M_\odot)^{-0.29}$ (MacLow & Ferrara 1998)

6 DISCUSSION

In this paper, we have presented a comprehensive study of the full infrared SEDs of a sample of 22 FIRBACK galaxies. Our new multi-component model together with the MCMC fitting technique have allowed us to test various previous assumptions about FIRBACK galaxies, as well as the spectral templates used to model them and related populations.

We found that our galaxies have cool SEDs (low mid-IR/far-IR ratios), which remains true even for the higher luminosity sources (LIGs and ULIGs). It is not yet clear how common such sources are, and how much of a concern are they for galaxy evolution models. However, the *Spitzer* 24 μm number counts (Papovich et al. 2004) already suggest that the existing SED spectra might not be accurate in the mid-IR for the $z\sim0.5-2.5$ luminous and dusty sources thought to comprise the bulk of the CIB. To correct for this, the necessity for 'downsizing' the mid-IR in their starburst spectra was already pointed out by Lagache et al. (2004).

One of the primary questions we wanted to answer with this study was the nature of the brightest galaxies contributing to the CIB. Initially from the sub-mm data (S03) and later through optical spectroscopy follow-up (D05), it was already known that the bulk of the FIRBACK galaxies are low-z, moderate luminosity sources, with a small fraction of $z\sim1$ ULIGs . Beyond that however, little has been known of their nature, and in particular their masses, sizes, and modes of star-formation were poorly constrained. Here we have addressed these issues from a number of (admittedly not always independent) perspectives and concluded that the bulk of the sample is consistent with $\sim M^*$ mass galaxies, which are forming stars somewhat more actively than local spirals, but are likely not actually starbursting according to the usual definition. Their mode of star-formation is consistent with slightly enhanced activity in the disk, rather than the nuclear bursts associated with major mergers. Their cool colours also exclude any significant contribution from AGN activity. A study of the ELAIS-N2 FIRBACK galaxies by Taylor et al. (2005) used a set of theoretical templates for cirrus (i.e. quiescent), starburst, and AGN galaxies. They conclude that 80% of the FIRBACK sources are starbursts, while 20% are cirrus galaxies. Since we find enhanced star-formation, but use more stringent starburst criteria, our conclusions are consistent.

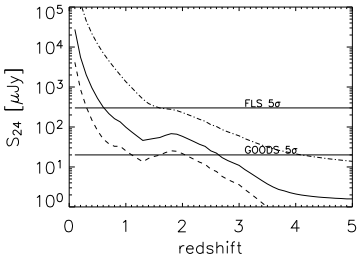

Figure 14. Detectability of FIRBACK-like galaxies as a function of redshift, compared with the *Spitzer* 24 μm survey limits for SWIRE (Surace et al. 2004), and GOODS (Chary et al. 2004). The dashed line corresponds to the SED of a typical low-z FIRBACK source (N1-007), while the solid line represents a LIG (N1-015), and the dot-dashed line is a cold ULIG (N1-064). Note that the level of PAH contribution is uncertain in the last case and therefore it might not be detectable by SWIRE at $z\sim2$ as suggested in this figure.

6.1 Implications for the faint 24 μm sources

Over the past year, *Spitzer* has revealed large numbers of faint (roughly $\sim$10–1000 μJy) 24 μm sources. There has been much speculation about their nature, with obvious implications for various galaxy evolution models. In Fig. 14, we evolve the SEDs of an L^* galaxy, a LIG and an ULIG from our FIRBACK sample. We compare these with the detectability thresholds of the wide and shallow SWIRE survey (Surace et al. 2004) and the deepest current *Spitzer* survey, GOODS-North (Chary et al. 2004). The SWIRE sources are expected to be predominantly low-z, meaning that FIRBACK-like galaxies (at only slightly higher redshifts) make up a significant fraction of them. For the deeper GOODS survey, FIRBACK analogues are expected to be a large component up to $z\sim1$, while in the $z\sim1-2$ range GOODS appears to be dominated by $11<\log(L/L_\odot)<12$ sources, such as the ULIG-tail of our sample, as discussed by Chary et al. (2004). Overall, Fig. 14 suggests that understanding the faint 24 μm sources requires taking into account not only M82 or Arp220 type sources, but also the much less luminous and colder FIRBACK sources, especially in the crucial $z\lesssim1.5$ regime. This is supported by the fact that while SCUBA-selected sources have close to 100% detectability in the current generation of 24 μm surveys (Egami et al. 2004; Frayer et al. 2004; Pope et al. 2006), most of the 24 μm-selected sources do not have individual SCUBA-counterparts (stacking analyses show them to have individual 850 μm flux $\sim$0.5 mJy (Serjeant et al. 2004), which is below the confusion limit of SCUBA.

6.2 Implications for the SCUBA galaxies

Fig. 14 indicates that if the SCUBA galaxies are as cold as our ULIGs (and given that their redshifts are typically in the range $z\sim2-3$) then relatively shallow *Spitzer* surveys (e.g. SWIRE) cannot detect any but the most luminous or the most AGN-dominated ones among them. This has implications for the *Spitzer* overlap with SCUBA galaxies in wide-field sub-mm surveys, such as SHADES (Mortier et al. 2005), and those being planned with SCUBA2. The difference between the FIRBACK far-IR and blank-

sky sub-mm sources is further highlighted in Fig 15. Here we show shaded regions to indicate the colours of normal $\log L < 11$ galaxies, as distinct from $\log L > 11$ ones, indicating their rough redshift evolution. The influence of the PAH feature complex as it traverses the 24 μm filter at $z \sim 2$ is evident. It appears that, despite some overlap with our cold ULIG template, the bulk of the SCUBA sources are redder in both colours. As the 24 μm flux pulls them in different directions here, this rather suggests that the reddening of one colour drives the overall effect. The S_{24}/S_8 colour can be reddened by redshift, optical depth, the presence of AGN, or increased PAH strength (at $z \sim 2$). Fully addressing the SEDs of SCUBA galaxies is clearly beyond the scope of this paper (see Pope et al. 2006). Here we merely show one scenario, i.e. that increased level of obscuration can account for the SCUBA galaxies' colours. We take our best-fit N1-064 SED ($\tau_V = 5$), and subject it to additional extinction to a total of τ_V =14. This is shown as the dashed curve in Fig. 15. The most SCUBA galaxies now fall in-between the original and revised N1-064 template; however, we remind that we have not fully explored the parameter space, and this is merely a consistency argument.

The three FIRBACK ULIGs we have studied here are N1-040, N1-064 and N1-078. In Section 5.1, we concluded that these sources are colder, and likely have more extended star-formation activity than typically assumed for ULIGs. This is qualitatively consistent with the cirrus models of Efstathiou & Rowan-Robinson (Efstathiou & Rowan-Robinson 2003), which was also claimed as a possible model for the SCUBA galaxies. A small fraction of the SCUBA sources are indeed consistent with the SEDs of these galaxies, redshifted slightly to $z \sim 1-2$. Most SCUBA galaxies, as discussed above, are consistent with the conventional view that they are highly obscured, extreme starformers (possibly including AGN) – the result of major mergers.

It is also worth noting that the use of the proposed 850 μm to 24 μm flux ratio as a redshift indicator will at best be highly unreliable, due to the 24 μm band traversing the PAH emission and Si absorption features in the mid-IR, as well as because of the range of possible far-IR SEDs. On the whole the SCUBA galaxies appear to exhibit a large enough range in SED shapes that applying a single model to their mid-IR photometry would be misleading. More comprehensive studies of the multi-wavelength properties of larger samples of sub-mm selected galaxies should help us understand the difference between the sources comprising the sub-mm background and those responsible for the CIB.

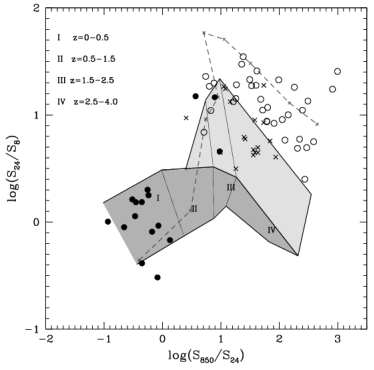

Figure 15. The evolution of two diagnostic colours: S_{850}/S_{24} and S_{24}/S_8. The solid circles are our FIRBACK sample, while the open circles are SCUBA-selected galaxies from the GOODS-North field (Pope et al. 2006), while the crosses are other SCUBA-selected samples from shallower surveys (Egami et al. 2004; Frayer et al. 2004). The dark grey region represents $\log L \lesssim 11$, while the light grey region shows $\log L \gtrsim 11$ (the boundaries should be regarded as fuzzy). The redshift evolution of the SEDs is carried out in steps of 0.5 from $z = 0$ to $z = 4$. The SED curves used, from top to bottom, are: N1-064, N1-029 and N1-009, and we have used them to trace the approximate boundaries for redshift evoltion, split into 4 bands as described in the legend. The dashed curve is N1-064 with an additional extinction (see Section 6.2).

7 CONCLUSIONS

In this paper we have combined archival *Spitzer* observations of the ELAIS-N1 field with prior near-IR, far-IR, and sub-mm data in order to study the full $\sim 1-1000$ μm SEDs of the brightest contributors to the CIB at its peak. A novel MCMC fitting technique and a phenomenological SED model are used to make optimal use of the available data. Below we highlight the principal results of our study:

• Contrary to expectations, we have demonstrated the existence of vigorously star-forming sources, which nevertheless have low mid-IR/far-IR ratios. Our sample extends over two orders of magnitude in luminosity and includes surprisingly cold ULIGs. This is likely the result of our far-IR selection.

• We discuss some of the issues inherent in interpreting empirical SED models. In particular, conclusions may well be influenced by the spectral sampling. Here we emphasized how limited spectral sampling and intrinsic model degeneracies might be responsible for the claimed physical $T_{\rm d} - \beta$ correlation.

• A number of basic parameters for our sample are derived. The typical stellar mass of our galaxies is few$\times 10^{10}$ M$_\odot$ to few$\times 10^{11}$ M$_\odot$ for the handful of ULIGs. Dust massses were found to be $10^7 - 10^8$ M$_\odot$, where we find general consistency between emission and absorption derived values. Typical SFRs are ~ 5 M$_\odot$/yr. We look at combinations of the above in order to 1) check for consistency given the many inherent assumptions, and 2) allow for more meaningful comparisons with local optically-selected galaxy samples.

• In the specific SFR vs. stellar mass relation, our sample appears to have enhanced SFR with respect to local spirals, but below dwarf HII galaxies. The closest match to our galaxies appear to be Hα-selected galaxies. This is consistent with the emission-line spectra of our galaxies, where available (D05).

• All our galaxies obey the Schmidt/Kennicutt relation. They appear to have enhanced star-formation activity with respect to local spirals, but less than nuclear starbursts. The more IR-luminous galaxies in our sample have higher star-formation intensity, as expected.

• We looked at the ratio of the gas depletion timescales to dynamical timescales for our sample, and find that the FIRBACK galaxies fall short of the traditional starburst definition where the gas is exhausted on timescales shorter than the dynamical time.

• FIRBACK-like galaxies are potentially a significant component of shallow *Spitzer* surveys, whose redshift distributions peak at $z \lesssim 0.3$ (e.g. FLS). Our sample does not allow us to address the Universal role of cold ULIGs, although it appears that sub-mm blank-sky surveys might also be sensitive to similarly cold (extended and/or highly obscured) sources.

ACKNOWLEDGMENTS

Most of all we wish to thank the SWIRE team for obtaining, reducing and making publicly available the IRAC and MIPS data we have made use of in this project. We are grateful to Chris Conselice for calculating the morphological parameters for our sources. We would also like to thank A. Gil de Paz for providing the data for Fig. 12. AS is grateful to Norm Murray and Phil Gregory for useful discussions. This research was supported by the Natural Sciences and Engineering Research Council of Canada. Lastly, we would like to thank the anonymous referee for their comments which improved the clarity of the paper.

REFERENCES

Aretxaga I., Hughes D., Dunlop J.S. 2005, MNRAS, 358, 1240
Barnard V.E., PhD thesis, University of Cambridge, 2002
Baugh C.M., Lacey C.G., Frenk C.S., et al. 2005, MNRAS, 356, 1191
Bell E.F., de Jong R.S., 2001, ApJ, 550, 212
Blain A.W., Smail I., Ivison R.J., Kneib J.-P., Frayer D.T., 2002, PhR, 369, 111
Blain A., Barnard V.E., Chapman S. 2003, MNRAS, 338, 733
Blanton M.R., et al. 2003, ApJ, 592, 819
Chapman S.C., Smail I., Ivison R.J., Helou G., Dale D.A., Lagache G., 2002, ApJ, 573, 66
Chapman S.C., Helou G., Lewis G.F., & Dale D.A. 2003, ApJ, 588, 186
Chapman S.C., Blain A.W., Smail I., Ivison R.J., 2005, ApJ, 622, 772
Chary R., Elbaz D., 2001, ApJ, 556, 562
Chary R., et al. 2004, ApJS, 154, 80
Conselice C.J., 2003, ApJS, 147, 1
Contursi A., Boselli A., Gavazzi G., Bertagna E., Tuffs R., & Lequeux J. 2001, A&A, 365, 11
Dale D.A., Helou G., Contursi A., Silbermann N.A., Kolhatkar S., 2001, ApJ, 549, 215
Dale D.A., et al., 2005, ApJ, 633, 857
Dasyra K.M., Xilouris E.M., Misiriotis A., Kylafis N.D., 2005, A&A, 437, 447
Dennefeld M., Lagache G., Mei S., Ciliegi P., Dole H., Mann R.G., Taylor E.L., Vaccari M., 2005, A&A, 440, 5 (D05)
Dole H., Gispert R., Lagache G., Puget, J.-L., Bouchet, F. R., Cesarsky, C., Ciliegi, P., Clements, D. L., Dennefeld, M., Désert, F.-X., 2001, A&A, 372, 364
Draine B.T., & Lee H.M. 1984, ApJ, 285, 89
Draine B., 2003, ApJ, 598, 1017
Dunne L., Eales S.A., 2001, MNRAS, 327, 697
Dupac X., et al., 2003, A&A, 404, L11
Egami E., et al. 2004, ApJS, 154, 130
Efstathiou A., & Rowan-Robinson M.R. 2003, MNRAS, 343, 322
Farrah D., Serjeant S., Efstathiou A., Rowan-Robinson M., & Verma A. 2002, MNRAS, 335, 1163
Frayer D., et al. 2004, ApJS, 154, 137
Galliano F., Madden S. C., Jones A. P., Wilson C. D., Bernard J.-P., & Le Peintre F. 2003, A&A, 407, 159
Gamerman D., 1997, Markov Chain Monte Carlo: Stochastic Simulation for Bayesian Inference, Chapman and Hall, London
Gelfand A.M., Sahu S.K., 1994, Journal of Computational and Graphical Statistics, 3(3), 261
Gil de Paz A., Aragón-Salamanca A., Gallego J., Alonso-Herrero A., Zamorano J., Kauffmann G., 2000, MNRAS, 316, 357
Gregory P., 2005, Bayesian Logical Data Analysis for the Physical Sciences
Hastings W.K. 1970, Biometrika, 57, 97
Hauser M.G., Dwek E., 2001, ARA&A, 39, 249
Heckman T. 2005, ASSL, 329: Starbursts: From 30 Doradus to Lyman Break Galaxies, 3
Helou G., Khan I.R., Malek L., & Boehmer L. 1988, ApJS, 68, 151
Hopkins A.M. 2004, ApJ, 615, 209
James A., Dunne L., Eales S., & Edmunds M.G. 2003, Revista Mexicana de Astronomia y Astrofisica Conference Series, 17, 269
Juneau S., Glazebrook K., Crampton D., et al. 2005, ApJL, 619, L135
Kauffmann G., et al. 2003, MNRAS, 341, 33
Kaviani A., Haehnelt M. G., & Kauffmann G. 2003, MNRAS, 340, 739
Kennicutt R.C., 1998a, ARA&A, 36, 189
Kennicutt, R.C., 1998b, ApJ, 498, 541
Kewley, L.J., Geller M.J., Jansen R.A., Dopita M.A., 2002, AJ, 124, 3135
Knapp G.R., & Kerr F.J. 1974, A&A, 35, 361
Lagache G., Puget J.-L., 2000, A&A, 355, 17
Lagache G., Dole H., Puget J.-L., 2003, MNRAS, 338, 555
Lagache G., et al. 2004, ApJS, 154, 112
Lagache G., Puget J.-L., & Dole H. 2005, ARAA, 43, 727
Lewis A., Bridle S., 2002, PhRvD, 66, 103511
Lilly S.J., Le Fevre O., Hammer F., Crampton D. 1996, ApJL, 460, 1
Lisenfeld U., & Ferrara A. 1998, ApJ, 496, 145
Lonsdale C.J., et al., 2003, PASP, 115, 897
Lu N., Helou G., Werner M.W., Dinerstein H.L., Dale D.A., et al. 2003, ApJ, 588, 199
Mac Low M.-M., & Ferrara A. 1998, L.N.P. Vol. 506: IAU Colloq. 166: The Local Bubble and Beyond, 506, 559
Massarotti A., Iovino A., Buzzoni A., 2001, A&A, 368, 74
Metropolis N., Rosenbluth A.W., Rosenbluth M.N., Teller A.H., Teller E. 1953, Journal of Chemical Physics, 21, 1087
Mihos C. 1999, Ap&SS, 266, 95
Mortier A.M.J., et al. 2005, MNRAS, 363, 563
Papovich C., et al. 2004, ApJS, 154, 70
Patris J., Dennefeld M., Lagache G., Dole H., 2003, A&A, 412, 349
Pope A., Scott D., Dickinson M., Chary R.-R., Morrison G., et al. 2006, MNRAS, submitted
Popescu C.C., Misiriotis A., Kylafis N.D., Tuffs R.J., & Fischera J. 2000, A&A, 362, 138
Popescu C.C., et al. 2005, ApJL, 619, L75

Puget J.-L., Abergel A., Bernard J.P., Boulanger F., Burton W. B., Désert F.-X., Hartmann D., 1996, A&A, 308, L5
Puget J.-L., Lagache G., Clements D., Reach W. T., Aussel H., Bouchet F. R., Cesarsky C., Désert F. X., et al., 1999, A&A, 345, 29
Ravindranath S., et al. 2004, ApJL, 604, L9
Roberts G.O., Gelman A., Gilks W.R. 1997, Annals of Applied Probability, 7, 110
Rodighiero G., Lari C., Fadda D., Franceschini A., Elbaz D., & Cesarsky C. 2004, A&A, 427, 773
Rowan-Robinson M., et al., 2004, MNRAS, 351, 1290
Rowan-Robinson M., et al. 2005, AJ, 129, 1183
Sajina A., Borys C., Chapman S., Dole H., Halpern M., Lagache G., Puget J.-L., Scott D., 2003, MNRAS, 343, 1365 (S03)
Sajina A., Lacy M., Scott D., 2005, ApJ, 621, 256
Sanders D.B., Mirabel I.F., 1996, ARA&A, 34, 749
Schmidt M. 1959, ApJ, 129, 243
Scott D., Lagache G., Borys C., Halpern M., Sajina A., Ciliegi P., Clements D. L., et al., 2000, A&A, 357, L5
Serjeant S, et al. 2001, MNRAS, 322, 262
Serjeant S., et al. 2004, ApJS, 154, 118
Silva L., Granato G.L., Bressan A., Danese L., 1998, ApJ, 509, 103
Smith J. D. T., et al. 2004, ApJS, 154, 199
Soifer B.T., Sanders D.B., Madore B.F., Neugebauer G., Danielson G.E., Elias J.H., Lonsdale C.J., & Rice W.L. 1987, ApJ, 320, 238
Stickel M., et al. 2000, A&A, 359, 865
Surace J.A., et al. 2004, VizieR Online Data Catalog, 2255, 0
Takeuchi T. T., Buat V., Iglesias-Páramo J., Boselli A., & Burgarella D. 2005, A&A, 432, 423
Taylor E.L., Mann R.G., Efstathiou A.N., Babbedge T.S.R., Rowan-Robinson M., et al. 2005, MNRAS, in press, (astro-ph/0506273)
Veilleux S., Kim D.-C., & Sanders D.B. 2002, ApJS, 143, 315
Vertchenko L., & Quiroga R.J. 1998, A&A, 335, 894
Werner M.W., et al., 2004, ApJS, 154, 1

APPENDIX A: MCMC FITTING AND ERROR ESTIMATES

A1 Description of our MCMC SED-fitting method

We use a Markov Chain Monte Carlo (MCMC) (see e.g. Gamerman 1997) approach in order to sample the posterior parameter distributions, allowing us to find the best solutions as well as the associated errors on the derived parameters. Taking $\mathbf{a}$ to be the array of parameter values defining a given model, and $\mathbf{y}$ to be the array of data values available, according to Bayes theorem, we have $p(\mathbf{a}|\mathbf{y}) \propto p(\mathbf{y}|\mathbf{a})p(\mathbf{a})$ where $p(\mathbf{a}|\mathbf{y})$ is the posterior probability distribution, $p(\mathbf{y}|\mathbf{a})$ is the likelihood of the data for the given model, and $p(\mathbf{a})$ is the prior. Normalizing this (via the global probability of the data) is usually impossible in practice, since it requires knowledge of all possible models. Here, as is often the case, a single model is assumed and what we are interested in is the shape of the distribution $p(\mathbf{a}|\mathbf{y})$, such that the most probable values for the parameters and their errors can be derived. What we really want then, is a measure of the relative probability of a given parameter value compared with some other value. Rearranging Bayes theorem, we have:

$$\frac{p(\mathbf{a}|\mathbf{y})}{p(\mathbf{a}'|\mathbf{y})} = \frac{p(\mathbf{y}|\mathbf{a})}{p(\mathbf{y}|\mathbf{a}')}\frac{p(\mathbf{a})}{p(\mathbf{a}')}. \quad \text{(A1)}$$

The ratio of priors is equal to 1 if a flat prior is assumed or is equal to e^{a_i/a'_i} if a logarithmic prior is chosen instead. Note that eq-n A1 can be used to adjust the results of a chain sampled with flat priors to test the effect of other choices of priors ('importance resampling', e.g. Lewis & Bridle 2002). This is the approach we take when returning to the effect of priors in Section A.2. For now, flat priors are assumed for all parameters, and therefore from now on the posterior and likelihood distributions are used synonymously.

In principle, arbitrary shapes of the posterior distribution can be sampled using a simple Monte Carlo approach. However for multi-dimensional problems, where the ratio of high-probability volume to total volume is very small, this can quickly become computationally prohibitive. The basic idea behind MCMC is to effectively sample this distribution by building up chains of random guesses of parameter values, where each successive guess is chosen from some much smaller proposal distribution, q, around the previous chain link. This move is accepted or rejected according to some criterion, which both pushes the chain toward higher probability regions, and allows for some random deviation from the straight gradient descent-type path. We follow the Metropolis-Hastings algorithm (Metropolis et al. 1953; Hastings 1970) where all parameters are varied at once, and a guess is accepted according to the criterion: $\alpha_{i+1} = \min[u, p_{i+1}q_{i+1}/p_i q_i]$, where the stochastic element is provided by the random number $u \epsilon [0, 1]$. For the proposal distribution, we use a multivariate Gaussian, which, being symmetric, leads to q_{i+1}/q_i of unity. Note that the exact shape of the proposal distribution is not important, but its effective width strongly affects the efficiency of the MCMC (see below). We assume that the likelihood of a given solution is the usual expression given by:

$$\log \mathcal{L} = \text{const} - \sum \left(\frac{\mathrm{y_i} - \mathrm{y_{model}}}{\sigma_\mathrm{i}}\right)^2, \quad \text{(A2)}$$

where the second term is the χ^2. The probability (p) that the system finds itself in a given state is given by the Boltzman factor, where the 'energy' is χ^2, and thus p_{i+1}/p_i is $\exp(-\Delta\chi^2/T)$ (this is called the 'odds' of the given solution). The temperature, T, has effectively the same function as the width of the proposal distribution, in that it determines how easy it is for the system to jump a particular distance from its current state.

Since brute-force MCMC is a fairly slow procedure, rather than initialize the chain at some random point we begin with some reasonable guess at the best model. Other possibilities would include simulated annealing, such as used in Sajina et al. (2005), or equivalently using variable widths of the proposal distribution, or using any other optimization technique to find the high probability regions quickly. For our purposes here, starting with a reasonable guess is deemed sufficient since we still explore the full region of physically plausible solutions.

The numerical parameters which need to be set are: the width of the proposal distribution for each parameter (the q-width); the temperature; and the overall length of the chain. Too low a q-width, will tend to acceptance of too many trials, while too high a value will give some jumps far outside the high probability regions, resulting in low acceptance rates. Trial-and-error has shown that an acceptance ratio in the range 10–30% is reasonable (this is supported by empirical studies which show that $\sim 25\%$ acceptance rate in problems with > 2 dimensions minimizes internal correlations in the resulting chain (Roberts et al. 1997)). To find the appropriate q-width, we make shorter (30,000) runs, where we vary only one parameter at a time. We start with a guess at the q-widths for each and incrementally adjust them until the resulting acceptance rates are 50–80% (which is appropriate for 1-dimensional problems). By trial and error we have found that this leads to acceptance rates in the desired 10-30% range when all seven parameters are varied simultaneously. This approach works better for our sample than fixing the widths a priori, since the dynamic range for the various parameters is too high. Such optimization of the proposal distributions before the main run speeds up the process, while preserving the ergodicity of the MCMC algorithm (Gelfand & Sahu 1994). We set T to 0.9, which results in points $\Delta\chi^2 \sim 1$ away from the best solution to be accepted with 30% probability. Note however, that since increasing the temperature increases the acceptance rate as well (preserving the $\Delta\chi^2/T$ ratio) and vice versa, in principle the temperature and q-width are degenerate, and therefore the exact value of the temperature chosen is not crucial as it will be compensated for in the above width adjustment. For the overall length of the chain, we need to find the length which both samples the posterior probability distribution well and at the same time (for practical reasons) is not much longer than what is just needed to accomplish this. We use 600,000 iterations, since our experience shows that the posterior probability around the best solution is well-sampled by this time.

This procedure still leaves us with little sensitivity to highly disjointed solutions of equal goodness-of-fit, although this is not of concern here as such solutions will most likely converge onto unphyisical values.

Since we start at a high-probability part of the parameter space, the 'burn-in' period is less well defined than when starting at a random position, and we therefore do not formaly subtract a 'burn-in' part of the chain. However, in deriving the best-fit parameters and errors below we apply a cut of $\Delta\chi^2 = 5$ from the minimum χ^2 solution, which isolates the region of interest and thus has the same function as the 'burn-in' removal. Fig. A1 shows an example of the resulting chain in various projections.

A2 Error estimates

As discussed above, the MCMC procedure samples the likelihood surface, which is proportional to the posterior probability distribution of interest. We use flat priors, where negative values are not accepted for any parameter. In addition, upper limits are set for the temperature (100 K), optical depth (30), and β (3). The latter is necessary, since for many sources the SNR in the sub-mm data is very low, leading to the difference in overall χ^2s for unphysically large values of β to be small, and the chain can get stuck in such regions. Since β is believed, both on theoretical and observational grounds, to be in the range $\sim 1-2$ (see Dupac et al. 2003, and references therein), we believe our $0-3$ prior is reasonable. The temperature limit is also necessary because of the above difference in SNR. The optical depth limit is only relevant for the few sources with higher τ and faint near-IR/IRAC detections (e.g. N1-040, N1-064). These limits are imposed by returning the chain to the vicinity of its initial state in order to avoid getting stuck at the edge. We come back to the effects of the prior below.

The chains obtained above allow for two distinct routes to obtaining the probability distributions for each parameter. The first is the easier straight marginalization of the given parameter over all the others. This is represented by:

$$p(a_j)da_j = \int_{i,i\neq j}^{N_i} p(a_i)da_i, \quad \text{(A3)}$$

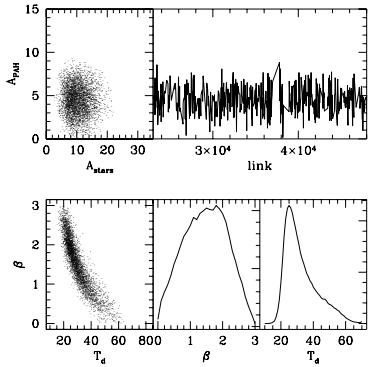

Figure A1. Here we demonstrate what the resulting chain looks like after the procedure described. The two left-most panels show examples of both uncorrelated and correlated parameters. A thinning factor of 30 has been applied. Throughout, we plot all points with $\chi^2 \leqslant (\chi^2_{\rm min} + 5)$. The top right panel shows a section of the chain demonstrating the evolution of the PAH amplitude parameter. The bottom middle and right panels show the marginalized distribution for the β and $T_{\rm d}$ parameters (with linear y-axes). Note the non-Gaussian shapes.

which in practice is just counting the number of times the chain visits a particular bin of values for the given parameter a_j. However, since we record the χ^2 value for each chain link, we can also directly obtain the likelihood distribution (see eq-n A2) for the parameter. In practice, a simplified form of this is the mean likelihood distribution (Lewis & Bridle 2002). The idea is to calculate the average χ^2 for each bin and then compare this with the minimum χ^2 achieved by the chain as

$$p(a_j) \propto \exp[-(\chi^2_j - \chi^2_{\rm min})], \quad \text{(A4)}$$

where χ^2_j is the mean χ^2 in the $j^{\rm th}$ bin.

In Fig. A2, we show the distributions for all parameters obtained using both methods for the whole sample. Note that since we have applied a χ^2 cut (see above), secondary features in the marginalized distributions, such as blended peaks and tails, are still fairly likely. For example, in the case of N1-101, $T_{\rm d} \sim 25$ K is the preferred solution, but $T_{\rm d} \sim 40$ K is still quite likely. The uneven error-bars indicate this. Note that in Table 2, for simplicity, we quote the average error only, but indicate the different error-bars in the figures. However, due to its definition, applying a χ^2 cut when estimating the mean likelihood tends to flatten the distributions. Therefore in that case, the most 'peaked' distributions possible are obtained if the whole of the chains are used. This means that parameters poorly constrained by the χ^2 are clearly visible in the likelihood curves (e.g. $L_{\rm PAH}$ for the highest-z sources N1-064, and N1-078).

The best-fit values we use are merely the peaks of the above distributions. To obtain the uncertainties on those we define a desired confidence level and, starting from the peak of the distribution, move to incrementally lower equal probability bins on each side of it until the area covered is equal to the total area times the

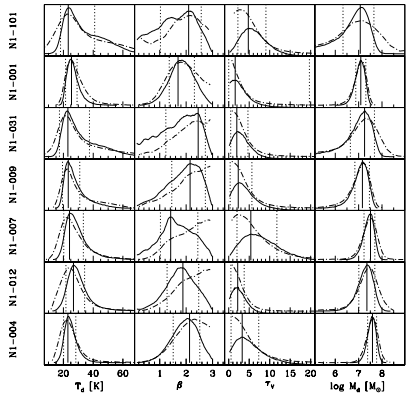

Figure A2. Here we compare the marginalized (solid curve) and mean likelihood (dot-dash curve) derived probability distributions for the parameters of interest. The distributions are normalized and the plots scaled to just fit the distributions as shown. The sources here and in the following figures are in order of increasing $L_{\rm IR}$. We use the marginalized distribution for our error estimates, where the best-fit value is given by the solid line (simply the peak of the distribution), and the 68% confidence limits are given by the dotted lines.

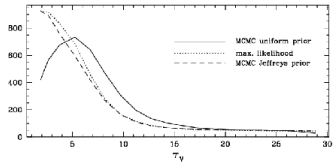

Figure A3. The effect of choice of prior on the τ_V probability distribution. Here we use the chain for N1-041.

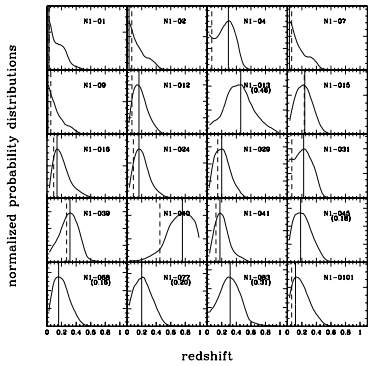

Figure B1. The marginalized distributions for the photometric redshift estimates. The best-fit value is indicated by the solid vertical line. Where spectroscopic redshifts are available they are indicated by the dashed vertical line. Where spectroscopic redshifts are not available the best-fit photometric redshift is indicated in brackets below the name of the source.

desired confidence level. Thus unsymmetric errorbars are indicative of asymmetric probability distributions.

In Fig. A2, we see that in general the marginalized and mean likelihood distributions agree reasonably well with each other. However, there are two instances where they disagree substantially. One is for β, where the likelihood tends toward unphysically high values. The origins of this are discussed in Appendix C. Our imposed prior confines the marginalized distribution to more reasonable values. We also find significant differences between the two approaches for τ_V. Here we are again clearly affected by our choice of prior. Fig. A3 shows how our uniform prior-based distribution transforms into the mean likelihood distribution by application of the Jeffreys prior (see e.g. Gregory et al. 2005). Note that the offsets in the PAH luminosity and stellar mass values are also due to this difference. For the highest-z sources, N1-064 and N1-078, the marginalized distributions result in essentially unconstrained τ_V (no clear peak in the distributions), thus the values listed in Table 2 are fairly meaningless. For these two cases, we find the mean-likelihood distribution to be more indicative, in both cases a clear, although fairly broad, peak exists at $\tau_V \sim 5$. We discuss the effects of this discrepancy as appropriate.

APPENDIX B: PHOTOMETRIC REDSHIFTS

The most common approach to photometric redshift estimates is template fitting. Its effectiveness is obviously strongly dependent on the templates used and the data available (see e.g. Massarotti et al. 2001, for a discussion).

Our multi-component SED model (described in Section 3.2) effectively represents a large and flexible template library. Therefore, we here describe the results of fitting this model, while keeping the redshift a free parameter. The results we present use the full IR SED, however, we note that the near-IR and IRAC data are the most constraining in terms of redshift determination. This is particularly true for $z \lesssim 0.3$ where the major PAH features leave the IRAC 8 μm band. With sufficiently good SNR, the approach also works at somewhat higher redshifts due to the 1.6 μm stellar peak being probed by the near-IR data (although in our case the IRAC data is not sufficiently sensitive to do this reliably at $z \sim 1$). We use model spectra which are generated on a logarithmic grid in wavelength, where $\Delta \log \lambda = 0.005$. This leads to a minimum redshift resolution ($\Delta z/(1+z)$) of 0.01, which is adequate for our purposes.

In order to adapt our earlier model-fitting to this problem, a few modifications are needed. First, our results in Section 4.4 suggest that $\beta \sim 2$ adequately described the far-IR/sub-mm emission of our galaxies. Therefore, here we fix $\beta = 2$. Next, to avoid some clearly unphysical solutions, we restrict the code to the range –

$0.1 < \log(A_{\rm star}/A_{\rm PAH}) < 0.9$. This condition is fully satisfied by all our sources when the spectroscopic redshifts are used (except N1-040, where PAH emission is apparently completely absent), and moreover is required if the rest-frame sources are to agree with our simulated IRAC colour-colour plot in Sajina et al. (2005). Lastly, due to the $T/(1+z)$ degeneracy, the temperature parameter we vary here is $T/(1+z)$. This last step removes the strongest correlation in the resulting chains. However, we find that the results are subject to additional degeneracies of redshift with other parameters, including: a negative correlation with the stellar amplitude; a positive correlation with the PAH amplitude; and a negative correlation with optical depth. These are clearly not independent.

Fig. B1 shows the marginalized distributions we obtain for photometric redshift fits. Note that the mean likelihood distributions here are poorly constrained, most likely due to the above degeneracies. Overall, the agreement between our MCMC estimates and the spectroscopic redshifts (where available) is quite good. The worst case is N1-040 where the near-IR/IRAC data have very low SNR and moreover the source is apparently devoid of PAH emission, thus the constraint comes entirely from the far-IR/sub-mm which is not very accurate, as can be seen in this case (see also (Aretxaga et al. 2005)). We have left out N1-064, whose high redshift (0.91) is in a different regime (the PAH features have completely left the IRAC bands) and therefore an accurate redshift cannot be obtained with the above method. N1-078 is also believed to be at $z \sim 1$ (S03) and has an SED very reminiscent of N1-064. Therefore we will assume it to be at $z = 0.91$ as well, although note that the uncertainty is ~ 0.5.

Fig. B1 shows that there is a bias in the model towards preferring somewhat higher redshifts compared with the spectroscopic ones. The above degeneracies result in double-peaked distributions (e.g. N1-001, N1-007), and in some cases the 'wrong' peak is preferred (N1-004, N1-031). All of these issues suggest that the model, although working in general, is imperfect at this point. Improvements are needed in minimizing the remaining degeneracies, which must involve including additional constraints. Two obvious steps are the use of the relation between absorption-derived and emission-derived dust mass, as discussed in Section 5.2 (this requires the effective sizes of galaxies), and the use of distance dimming. The latter for example effectively excludes the higher-z solution for N1-004, but not for N1-031. For N1-040, the distance dimming argument would in fact support the wrong solution, which was brought about largely by the imposition of 'typical' stars-to-PAH ratios. Therefore, the range in galaxy SED types needs to be known better and accounted for here before these steps can be implemented.

After accounting for all these issues, we find that the average uncertainty of our estimated redshifts is $\langle \Delta[z/(1+z)] \rangle = 0.06$.

Thus in summary we adopt the following redshifts: N1-013(0.46), N1-045(0.18), N1-068(0.16), N1-077(0.20), and N1-083(0.31). Based on optical template fitting Rowan-Robinson et al. (2005) derived the following redshifts: N1-013(0.58), N1-045(0.09), N1-068(0.23), N1-077(0.19), and N1-083(0.51). Assuming these are correct, our results on average are uncertain to $\langle \Delta[z/(1+z)] \rangle = 0.07$, which is slightly worse than the above quoted uncertainty as expected when comparing against other photometric redshift estimates. For simplicity, we are going to ignore the uncertainty on the estimates and treat these redshifts as fixed.

APPENDIX C: THE $T - \beta$ RELATION

A common approach, especially with a limited number of far-IR/sub-mm data points, is to fit a greybody function with characteristic temperature and emissivity. There are three main questions arising from the practice and interpretation of these fits:
1) what degeneracies are present in the usual formulation, and therefore what are the optimal parameters to fit?
2) given that this is only an approximation to the true shape of the SED, what effect does the spectral sampling (such as due to redshift) have on the results obtained?
3) how does one disentangle physical correlations from said degeneracies?

For further discussion, see also Blain et al. (2003) and the alternative parameterization of Baugh et al. (2005). In essence, the function one is fitting has the form: $f_\nu = (\nu/\nu_0)^\beta \times B_\nu$, where B_ν is the Planck function:

$$B_\nu = \frac{2h}{c^2} \frac{\nu^3}{\exp(h\nu/kT) - 1}. \quad \text{(C1)}$$

The parameters to determine here are $T_{\rm d}$, β, and the nuisance parameter ν_0 (or some equivalent normalization). We wish to disentangle any correlations between the three. To begin with, to understand how degeneracies arise between the various parameters, we need to consider what it is that the code is actually fitting. Intuitively, to first order this is the overall amplitude of the dust emission, the position of the peak, and the slope in the Rayleigh-Jeans tail.

The first of these functional parameters is the bolometric dust flux, $F_{\rm d}$, which is given by

$$F_{\rm d} = \int f_\nu d\nu = \frac{2h}{c^2 \nu_o^\beta} \left(\frac{kT}{h}\right)^{4+\beta} \Gamma(4+\beta)\zeta(4+\beta), \quad \text{(C2)}$$

where Γ is the complete gamma function, and ζ is the Riemann zeta function[4]. Rearranging the above and substituting for $1/\nu_o^\beta$ in f_ν removes the bulk of the degeneracies of the normalization parameter (which is now taken to be $F_{\rm d}$).

Nevertheless, the temperature and β are still correlated. As stated above, the fitting process is also concerned with the position of the peak in the emission. By solving $df_\nu/d\nu = 0$ we obtain:

$$\beta = \left(\frac{h\nu_{\rm peak}}{kT}\right) \left[\frac{e^{h\nu_{\rm peak}/kT}}{e^{h\nu_{\rm peak}/kT} - 1}\right] - 3. \quad \text{(C3)}$$

This equation provides a good fit to the observed correlation at higher values of β (see Fig. C1), but fails as β approaches 1. The reason for this is obvious – apart from the peak, we also need to match the Rayleigh Jeans tail. The sub-mm data do not allow β to become arbitrarily shallow, although it can be compensated by increasing the temperature (which pulls the Planck function the other way). The constraint coming from the Rayleigh-Jeans tail can be parametrized with the sub-mm spectral index, $\alpha_{\rm submm}$ which is related to β, but in the Rayleigh-Jeans approximation the temperature dependence falls out leaving:

$$\beta = \alpha_{\rm submm} - 2\log(850/450) - 3. \quad \text{(C4)}$$

Looking at our data (when the SNR at 450 μm was high), we find typical values of $\alpha_{\rm submm} \sim 5$, which means $\beta \sim 1.5$ from eq-n. C4,

[4] Note that $\zeta(4+\beta)$ is $\simeq 1$ for any positive value of β, so does not affect the result much. The quantity $\log\Gamma(4+\beta)$ is closely approximated by $0.69(1+0.69\beta)$, which we use.

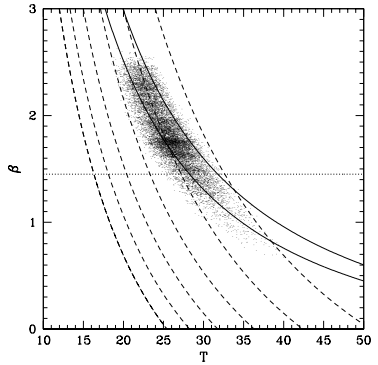

Figure C1. Here we compare the relation in eq-n C5 and the observed degeneracy between the β and temperature parameters. The points are from the fit to N1-024. The dashed lines show the relation in eq-n C3, where the location of the peak moves in increments of 20 μm from 100 μm to 200 μm (top to bottom). Note the good agreement at higher β's and the deviation at lower-valued β's. The dotted line is the expectation of eq-n C4 with $\alpha_{\rm submm} = 5$ (consistent with observations). The solid lines are the combined constraint (eq-n C5) for peak locations of 160 μm and 180 μm respectively – the observed distribution is now reproduced much better. If not treated carefully, this parameter correlation, which exists in the fits *for each source*, can be misinterpreted as a physical correlation between the derived (β,$T_{\rm d}$) pairs *for a sample of sources*.

which is in fact often adopted for sub-mm sources. The joint constraint on the spectral index leads to:

$$\beta = \left(\frac{h\nu_{\rm peak}}{kT}\right)\left[\frac{e^{h\nu_{\rm peak}/kT}}{e^{h\nu_{\rm peak}/kT}-1}\right] + \alpha_{\rm submm} - 2\log\left(\frac{850}{450}\right) - 6. \quad \text{(C5)}$$

In Fig. C1, we show how the above two constraints act together and therefore how the available data drive the β and temperature values found. For example, in data without well determined peak position, assuming a low value of β (say, 1 – 1.5) will automatically lead to the conclusion of hotter temperatures. Conversely, in data with cool temperatures and well determined peak, but poorly sampled sub-mm data, the conclusion will always be that β is high (even > 2 if the fit is allowed to go there). Better sampling (which could mean better SNR or more spectral points) in the sub-mm (relative to the peak) would likely change that un-physical conclusion. Conversely, as the redshift is increased, our data increasingly sample the peak rather than the tail of the thermal emission, and this has the same effect.

This degeneracy is empirically well known (Blain et al. 2003). Apart from this degeneracy arising from the functional form used, there has also been suggestions that a physical inverse relationship exists as well. In particular, this was seen when the best-fit temperature and β values for different Milky Way environments were compared by Dupac et al. (2003). The relative homogeneity of our sample (see Fig. 4.4) does not allow us to firmly support or reject this relationship (although the apparently warmest source, N1-078, supports it). A wider range of galaxy types with well sampled SEDs would be needed to address this firmly. However, we note that (as discussed above) as the peak of the SED shifts, the combined β,T distribution moves as well. But in the Dupac et al. sample the shortest wavelength is 100 μm, thus whenever the peak is shortward of that (corresponding to ~ 30 K for $\beta \sim 2$), the sub-mm index begins to dominates the fit, flattening the distribution. At the other extreme for example, as the peak reaches the coldest observed values (corresponding to peaks at ~ 200 μm), we are sampling a distribution where $T \sim 15$ K for $\beta \sim 2$ (see Fig. C1). Therefore, it appears that this correlation is easily explained as a sequence of progressively colder/hotter environments. The apparent $\beta - T$ correlation is merely a combination of the intrinsic correlation between $T_{\rm d}$ and β for individual sources and limited wavelength coverage. That being said, a physical correlation here is to be expected from the different optical properties of grains at different temperatures. But it is unclear that the single greybody approach is capable of testing this adequately.

This paper has been typeset from a TEX/ LATEX file prepared by the author.

2005

Accepted for publication in The Astrophysical Journal, June 16th, 2005
Preprint typeset using LaTeX style emulateapj v. 6/22/04

INFRARED LUMINOSITY FUNCTIONS FROM THE CHANDRA DEEP FIELD SOUTH : THE *SPITZER* VIEW ON THE HISTORY OF DUSTY STAR FORMATION AT $0 \lesssim Z \lesssim 1$ [1]

Emeric Le Floc'h[a], Casey Papovich[a], Hervé Dole[b], Eric F. Bell[c], Guilaine Lagache[b], George H. Rieke[a], Eiichi Egami[a], Pablo G. Pérez-González[a], Almudena Alonso-Herrero[d], Marcia J. Rieke[a], Myra Blaylock[a], Charles W. Engelbracht[a], Karl D. Gordon[a], Dean C. Hines[a,e], Karl A. Misselt[a], Jane E. Morrison[a] and Jeremy Mould[f]

[a] Steward Observatory, University of Arizona, Tucson, AZ 85721, USA
[b] Institut d'Astrophysique Spatiale, Université Paris Sud, F-91405 Orsay Cedex, France
[c] Max-Planck-Institut für Astronomie, Königstuhl 17, D-69117 Heidelberg, Germany
[d] Instituto de Estructura de la Materia, CSIC, E-28006, Madrid, Spain
[e]Space Science Institute, 4750 Walnut Street, Suite 205 Boulder, Colorado 80301, USA
[f] National Optical Astronomy Observatory, P.O. Box 26732, Tucson, AZ 85726, USA

Accepted for publication in The Astrophysical Journal, June 16th, 2005

ABSTRACT

We analyze a sample of $\sim$2 600 MIPS/*Spitzer* 24 μm sources brighter than $\sim 80\,\mu$Jy and located in the Chandra Deep Field South to characterize the evolution of the comoving infrared (IR) energy density of the Universe up to $z \sim 1$. Using published ancillary optical data we first obtain a nearly complete redshift determination for the 24 μm objects associated with $R \lesssim 24$ mag counterparts at $z \lesssim 1$. These sources represent $\sim$55-60% of the total MIPS 24 μm population with $f_{24\mu m} \gtrsim 80\,\mu$Jy, the rest of the sample likely lying at higher redshifts. We then determine an estimate of their total IR luminosities using various libraries of IR spectral energy distributions. We find that the 24 μm population at $0.5 \lesssim z \lesssim 1$ is dominated by "Luminous Infrared Galaxies" (i.e., $10^{11}\,L_\odot \leq L_{IR} \leq 10^{12}\,L_\odot$), the counterparts of which appear to be also luminous at optical wavelengths and tend to be more massive than the majority of optically-selected galaxies. A significant number of fainter sources ($5\times10^{10}\,L_\odot \lesssim L_{IR} \leq 10^{11}\,L_\odot$) are also detected at similar distances. We finally derive 15 μm and total IR luminosity functions (LFs) up to $z \sim 1$. In agreement with the previous results from *ISO* and SCUBA and as expected from the MIPS source number counts, we find very strong evolution of the contribution of the IR-selected population with lookback time. Pure evolution in density is firmly excluded by the data, but we find considerable degeneracy between strict evolution in luminosity and a combination of increases in both density and luminosity ($L^\star_{IR} \propto (1+z)^{3.2^{+0.7}_{-0.2}}$, $\phi^\star_{IR} \propto (1+z)^{0.7^{+0.2}_{-0.6}}$). A significant steepening of the faint end slope of the IR luminosity function is also unlikely, as it would overproduce the faint 24 μm source number counts. Our results imply that the comoving IR energy density of the Universe evolves as $(1+z)^{3.9\pm0.4}$ up to $z \sim 1$ and that galaxies luminous in the infrared (i.e., $L_{IR} \geq 10^{11}\,L_\odot$) are responsible for 70$\pm$15% of this energy density at $z \sim 1$. Taking into account the contribution of the UV luminosity evolving as $(1+z)^{\sim 2.5}$, we infer that these IR-luminous sources dominate the star-forming activity beyond $z \sim 0.7$. The uncertainties affecting these conclusions are largely dominated by the errors in the k-corrections used to convert 24 μm fluxes into luminosities.

Subject headings: galaxies: high-redshift — infrared: galaxies — cosmology: observations

1. INTRODUCTION

The successful launch of the *Spitzer Space Telescope* (Werner et al. 2004) recently opened a new exciting window on the deep infrared (IR) Universe. *Spitzer* operates between 3.6 and 160 μm with unprecedented sensitivity and better spatial resolution compared to previous infrared satellites (e.g., *IRAS, ISO*). Directly probing the dust emission or the redshifted signature of distant stellar populations, its first extragalactic surveys have already unveiled a huge number of faint and high redshift sources (see for instance Fazio et al. 2004; Eisenhardt et al. 2004; Papovich et al. 2004; Marleau et al. 2004; Lonsdale et al. 2004; Chary et al. 2004; Yan et al. 2004; Dole et al. 2004a in the "*Spitzer* Special Edition – volume 154" of the *ApJ Supplement*). *Spitzer* therefore provides new opportunities to determine the IR properties of galaxies in the general context of cosmic evolution.

High redshift sources detected by *Spitzer* in the mid- and far-infrared wavelength range (i.e., $8\,\mu\text{m} \lesssim \lambda \lesssim 1000\,\mu$m) are characterized by intrinsically very high luminosities (Egami et al. 2004; Frayer et al. 2004; Ivison et al. 2004; Le Floc'h et al. 2004). They appear as the distant analogs of the local Luminous and Ultra-Luminous InfraRed Galaxies (respectively LIRGs: $10^{11}\,L_\odot \leq L_{IR} = L[8-1000\mu m] \leq 10^{12}\,L_\odot$, and ULIRGs: $L_{IR} \geq 10^{12}\,L_\odot$, see the review by Sanders & Mirabel 1996). Such infrared-luminous sources[2] emit the bulk of their energy as dust-reprocessed thermal IR emission powered by embedded star formation or by accreted material surrounding supermassive black holes. They were first discovered in the nearby Universe with ground-based observations (Rieke & Low 1972). After being systematically catalogued by *IRAS* (Soifer et al. 1987), they were found to be locally very rare and to only account for $\sim$5% of the total infrared energy emitted by galaxies at low redshift (Soifer & Neugebauer 1991; Kim & Sanders 1998). Nevertheless, there is clear evidence that they were significantly more numerous earlier in cosmic history. In the past few years, deep observations performed in the infrared by *ISO* and in the submillimeter by the SCUBA camera have revealed strong evolution of these luminous sources with lookback time (Smail et al. 1997; Blain et al. 1999a; Elbaz et al. 1999; Serjeant et al. 2001; Dole et al. 2001), that is also apparent in the population of radio sources at μJy flux levels (e.g., Cowie et al. 2004). Characterized by a high redshift space density several orders of magnitude larger than predicted by non-evolving models, infrared luminous galaxies contribute a significant fraction of the distant starbursting activity and play a crucial role in the formation of massive spheroidals throughout the cosmic ages (e.g., Flores et al. 1999; Gispert et al. 2000; Franceschini et al. 2001; Chary & Elbaz 2001; Blain et al. 2002; Chapman et al. 2003a).

This strong evolution of infrared-selected sources has also been clearly seen by *Spitzer* (Chary et al. 2004, Papovich et al. 2004, hereafter P04; Marleau et al. 2004; Dole et al. 2004a). One of the most interesting results of the *Spitzer* deep surveys is the behavior of the differential number counts at 24 μm. These counts turn over at fluxes lower than had been expected based on "pre-launch" models. Lagache et al. (2004) suggest that these counts reveal even more luminous galaxies $z \gtrsim 1.5$ than expected, though one could argue that they can also originate from a steeper faint-end slope of the infrared luminosity function at more modest redshifts. To better understand the nature of the sources responsible for this turn-over and also more generally the role of infrared galaxies in cosmic evolution, we examine in this paper the evolution of the comoving IR energy density with redshift up to $z \sim 1$. This study is based on a sample of 24 μm-selected *Spitzer* sources within the Chandra Deep Field South and characterized by redshifts taken from the literature. A companion publication by Bell et al. (2005) explores in more detail the role played by these sources in the decline of the star formation history since $z \sim 0.7$.

The paper is organized as follows. In Sect. 2 we describe the infrared and optical data used in this study, while Sect. 3 outlines the results of the cross-correlations that we performed among catalogs to determine the redshifts of infrared-selected sources. In Sect. 4 we study the contribution of these infrared galaxies to the total counts at 24 μm for various redshift limits and present a comparison with the predictions from various recent models of IR galaxy evolution. Using different libraries of templates published in the literature, we further derive in Sect. 5 an estimate of the total infrared luminosities of these sources based on our mid-infrared observations. In Sect. 6 we analyze a few properties of their optical counterparts and we finally explore in Sect. 7 how the evolution of the infrared luminosity function at $0 \lesssim z \lesssim 1$ in the CDFS can be constrained using our data. Interpretations are discussed in Sect. 8, and we give our conclusions in Sect. 9. Throughout this work, we assume a ΛCDM cosmology with $H_0 = 70$ km s^{-1} Mpc^{-1}, $\Omega_m = 0.3$ and $\Omega_\lambda = 0.7$ (Spergel et al. 2003). Unless explicitly stated, magnitudes are quoted within the Vega system. We also adopt the universal Initial Mass Function from Salpeter (1955).

2. THE DATA

2.1. *24 μm imaging*

The region of the Chandra Deep Field South (hereafter CDFS, $\alpha = 3^h32^m00^s$, $\delta = -27°35'00''$, J2000) was observed with the MIPS instrument (Rieke et al. 2004) on-board the *Spitzer Space Telescope* in January 2004 as part of the MIPS Guaranteed Time Observing program. These observations were performed over a total field of $\sim 1.45\times0.4 = 0.6\,\text{deg}^2$ with the so-called "Slow Scan" technique, a MIPS observing mode that allows the coverage of large sky areas with high efficiency. The detector at 24 μm uses a 2.45″ pixel size array of 128×128 elements and the image at this wavelength is characterized by a Point Spread Function (PSF) with a Full-Width at Half Maximum (FWHM) of $\sim$6″. The effective integration time per sky pixel was $\sim$1380 s. Data reduction was carried out using the MIPS Data Analysis Tool (DAT, Gordon et al. 2005). The mosaic finally obtained has a pixel scale of half that of the physical detector pixel. A color version of this 24 μm map can be seen in the publication by Rigby et al. (2004). A sub-region of this field is also illustrated in Figure 1.

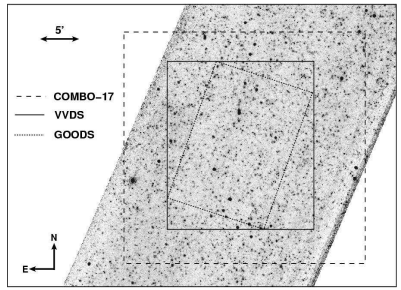

FIG. 1.— A sub-image of the CDFS 24 μm observations obtained with MIPS, centered at $\alpha = 3^h32^m28^s$ and $\delta = -27°48'27''$ (J2000). The fields of view respectively covered by COMBO-17 (dashed line), VVDS (solid line) and GOODS (dotted line) are also indicated (see text for details). The 24 μm sources considered in this paper are located within the 775 arcmin^2 of overlap between MIPS and COMBO-17.

Since most sources are unresolved in our data, extraction and photometry were performed using the PSF fitting technique of the DAOPHOT software (Stetson 1987). An empirical point spread function was constructed from the brightest objects found in our mosaic, and it was subsequently fitted to all the sources detected in the map. Allowing for multiple-match fitting to deal with blended cases, we derived the flux density of each source from the scaled fitted PSF and finally applied a slight correction to account for the finite size of the mod-

[1] Based on observations made with *Spitzer*, operated by the Jet Propulsion Laboratory under NASA contract 1407.

[2] We adopt in this paper the more general expression of "infrared-luminous galaxies" to denote sources characterized by $L_{IR} \geq 10^{11}\,L_\odot$.

eled point spread function. We also performed extensive simulations adding and recovering artificial sources in the data, which allowed us to derive an 80% completeness limit at $\sim$83 μJy. Contamination by false sources appears in our detection catalog at fluxes fainter than 90 μJy. In the full sample of objects brighter than the 80% completeness limit, we estimate such a contamination to be around 0.6%. A more detailed description of our technique is presented by Papovich et al. (2004) who also discuss the evolution of the completeness limit and the false source fraction as a function of the flux at 24 μm (see their figure 1).

Distortion effects are efficiently removed by the DAT. The final astrometric uncertainty of the mosaics produced by the pipeline therefore originates from the pointing reconstruction. To quantify this uncertainty in our data, we cross-identified the brightest sources detected at 24 μm with the *Two Micron All Sky Survey* (2MASS) catalog (Jarrett et al. 2000). A systematic offset of $\sim$0.6″ was observed in the scan direction[3] and subsequently removed for our source catalog to match the 2MASS coordinates. We estimate that the remaining scatter relative to 2MASS is better than 0.3″ rms.

2.2. *Optical-spectroscopic redshifts*

To derive the redshifts of the MIPS 24 μm–selected sources, we retrieved from the literature publicly available catalogs of optical spectroscopic surveys in the CDFS such as the "VIMOS VLT Deep Survey"[4] (hereafter VVDS, Le Fèvre et al. 2004), the ESO/FORS2 survey performed by the GOODS Legacy team[5] (Vanzella et al. 2005), and the follow-up of X-ray sources described by Szokoly et al. (2004)[6]. The VVDS consortium has released redshifts for 1599 sources located in an area of $21\times21.6\,\mathrm{arcmin}^2$ with an overall redshift measurement completeness of $\sim$88% down to $I_{AB} \leq 24$. For each identification, a flag indicates the reliability level of the corresponding measurement; 1457 sources in this survey are classified with more than 75% confidence in the redshift determination. The GOODS catalog provides 234 redshifts obtained within a slightly smaller area of the CDFS ($10\times15\,\mathrm{arcmin}^2$). They are also tentatively classified into three categories depending on their reliability, and 150 sources in this catalog are thought to have a secure redshift measurement. Finally, Szokoly et al. (2004) present a spectroscopic follow-up of *Chandra* X-ray sources, with redshifts obtained for 168 objects. Among those, 126 are considered to have unambiguous identifications.

We combined the catalogs of these three optical surveys to create a single list of 1 941 spectroscopic redshifts with their corresponding flags. Because of some overlap between the different observed regions, several redshifts were sometimes assigned to a given single source. In case of discrepant estimates, we kept the one flagged with the highest confidence in the redshift measurement.

The MIPS image at 24 μm entirely covers the areas observed by these spectroscopic surveys. The VVDS and GOODS fields of view can be seen in Figure 1.

2.3. *Optical-photometric redshifts*

In addition to the spectroscopic redshifts previously described, we also made extensive use of the photometric redshifts from the COMBO-17 survey ("*Classifying Objects by Medium-Band Observations in 17 filters*", Wolf et al. 2004). COMBO-17 observed a $31.5\times30\,\mathrm{arcmin}^2$ region of the CDFS (see Fig. 1) through a set of 5 broad-band and 12 narrow-band filters, which allowed the determination of accurate spectral energy distributions (SEDs) and absolute magnitudes for several thousand optically-selected sources (see also Wolf et al. 2003). Each SED was analyzed using a library of representative templates for various spectral types, and a redshift probability distribution was subsequently derived for each source. For a total of 24 217 objects, these distributions were successfully fitted with Gaussian-like functions, the mean and the variance of which led to well-constrained estimates of photometric redshifts with corresponding uncertainties.

These redshifts are accurate to 1% in $\delta_z/(1+z)$ for galaxies with $R \leq 21$ mag, and they are mostly reliable (i.e., $\delta_z/(1+z) \leq 10\%$) for all sources at $z \lesssim 1.2$ and brighter than $R \sim 24$ mag (11 422 objects). The yield of high weight redshifts drops steeply for $z \gtrsim 1.2$ or $R \gtrsim 24$ mag, so we did not consider such faint or distant objects. Another redshift estimate is also provided for nearly every detection of the survey (62 366 sources) based on the peak of the computed probability distribution. Because it is less reliable, it should be used with caution (Wolf et al. 2004) and was therefore also not considered in this work. About $\sim$85% of the region covered by COMBO-17 overlaps with our MIPS 24 μm mosaic and the spectroscopic optical surveys. This overlapping area has a total field of view of $775\,\mathrm{arcmin}^2$ (see Fig. 1).

3. OPTICALLY-SELECTED REDSHIFTS OF MIPS SOURCES

3.1. *Cross-correlation between the infrared and the optical data*

From the full MIPS catalog we first selected the 24 μm sources located in the common area covered by *Spitzer* and the aforementioned optical redshift surveys (i.e., $775\,\mathrm{arcmin}^2$). In this region of overlap we detected 5 589 objects at 24 μm, with 3 616 of those having a flux greater than the 80% completeness limit of 83 μJy.

We cross-correlated this 24 μm sub-sample with the optical data using a tolerance radius of 2″ for matching sources. This choice was first motivated by the rather large FWHM of the MIPS 24 μm PSF ($\sim$6″) compared to that typically seen in optical images. As already observed in local interacting systems (e.g., Le Floc'h et al. 2002; Charmandaris et al. 2004; Gallais et al. 2004), it also accounts for the physical shift that could be present between the location of the infrared emission and the brightest optical component of distant mergers (2″ corresponds to a linear projection of $\sim$15 kpc on the sky at $z \sim 1$). It is yet reasonably small given the position accuracy of the source centroids at 24 μm (better than 0.5″ rms). Taking a larger value also increases the risk of associating MIPS sources with wrong optical counterparts in the case of multiple matches. When a double match was found, we selected the closest object. We ignored the cases where three or more optical sources could be associated with a given 24 μm detection.

We first correlated the 24 μm source catalog with the list of spectroscopic redshifts. A total of 543 matches was found in this cross-identification, of which 465 objects are flagged to have a high-confidence redshift measurement. The fraction of multiple matches was only 1%. At this stage, we only kept the identifications with a secure redshift determination. Those 465 sources represent only 8% of the infrared-selected sub-sample, which emphasizes the critical need for using photometric redshifts. We thus cross-correlated the rest of the data with the catalog of COMBO-17. We found 2 170 MIPS sources (1 987 single and 183 double matches) identified with a photometric redshift below $z = 1.2$ and an optical counterpart brighter than $R = 24$ mag. For 9 objects selected at 24 μm (less than 0.5% of the sample) three possible matches were found within 2″ around the MIPS source. They were not further considered. In total, we assembled a catalog of 2 635 MIPS sources (of which 1 962 are brighter than the 80% completeness limit of the 24 μm survey) associated either with a reliable spectroscopic redshift or a clearly-constrained photometric redshift. Virtually all are at $z \lesssim 1.2$, since the yield of values at higher redshift is very low with both spectroscopy (due to the "redshift desert") and COMBO-17. We also identified another set of 1 681 MIPS sources with an optical counterpart in the COMBO-17 catalog but without any reliable redshift (271 of them have $f_{24\mu m} \geq 83\,\mu$Jy and are brighter than $R = 24$ mag).

3.2. *Redshift uncertainties*

Since only a very small fraction of the MIPS sources have been identified with secure spectroscopic redshifts, it is worth looking at the typical uncertainties of the other *photometric* redshifts characterizing the 24 μm-selected sources. The accuracy of the COMBO-17 classification decreases for sources fainter than $R \sim 22$ mag. This may have non-negligible effects when estimating e.g., source densities as a function of lookback time, especially when the uncertainties become comparable to the redshift bins in which galaxy properties are averaged. Given that the 24 μm sample is by definition selected through the emission by warm dust, one may furthermore question whether the implied extinction at optical wavelengths can lead to a more significant redshift misclassification in the specific case of the most luminous (i.e., dust-obscured) MIPS sources.

In Figures 2a & 2b we compare high-confidence spectroscopic redshifts of optically-selected field galaxies and MIPS 24 μm detections with their photometric redshifts estimated by COMBO-17. We see that the photometric redshift errors are small (i.e., $|z_{\mathrm{spec}}\text{-}z_{\mathrm{phot}}| \lesssim 0.1$) and they are not statistically larger in the case of the MIPS sources. The latter can be explained as follows. Mid-infrared space-borne and ground-based observations of local LIRGs/ULIRGs reveal that the dust responsible for the bulk of the IR luminosity of those objects originates from very compact regions (Soifer et al. 2000, 2001; Charmandaris et al. 2002). The effect of extinction in these dusty systems is therefore very localized and is usually not apparent in the global spectral energy distribution of their optical counterparts (Sanders & Mirabel 1996). A similar situation likely pertains at higher redshifts up to at least $z \sim 1$. At $z \sim 0.7$ for instance, ISOCAM 15 μm and MIPS 24 μm-selected galaxies are indeed associated with luminous optical sources characterized by a wide range of optical colors and morphologies (Flores et al. 1999; Rigopoulou et al. 2002; Franceschini et al. 2003, Bell et al. 2005; see also Sect. 6). Only a careful approach based on medium-resolution spectroscopy can distinguish them from the optically-selected galaxy population (e.g., Flores et al. 2004). It is therefore unlikely to encounter any significant increase of redshift mis-classification *as a function of infrared luminosity* (at least up to $z \sim 1$).

Finally, Fig. 2c shows the photometric redshift uncertainties provided by the COMBO-17 catalog as a function of the observed R-band magnitude for the MIPS sources considered in this paper. These errors were determined as the square root of the variance characterizing the redshift probability distribution of each object. In agreement with the comparison we made from Fig. 2a using the spectroscopic sub-sample, we see that sources brighter than $R \sim 22$ mag have a very accurate redshift estimate (i.e., $\delta_z \lesssim 0.04$) and most of the sample (88%) is characterized by a redshift accuracy better than $\delta_z \sim 0.1$. The average uncertainty is only $<\delta_z>$=0.07 with a dispersion σ_z=0.05 for sources with $22\,\mathrm{mag} \leq R \leq 24\,\mathrm{mag}$. It rises to $<\delta_z>$=0.09 (with a similar dispersion) if we only consider objects fainter than $R \sim 23$ mag. Looking at the evolution of the MIPS sources averaged per redshift bin of $\Delta z \sim 0.2$ should lead therefore to rather robust results.

3.3. *Completeness of the sample*

The biggest concern affecting our results is the incompleteness of the redshift determination for the most distant sources considered in this paper. As previously mentioned, 3 616 objects were detected by MIPS above the 80% completeness limit in the region overlapping with the optical surveys of the CDFS, while our final catalog only contains 1 962 sources with $f_{24\mu m} \geq 83\,\mu$Jy and a redshift identification (i.e., $\sim$55%). To better assess this effect, we plot in Figure 3.a the fraction of MIPS sources characterized either by a spectroscopic or a photometric redshift as a function of the observed 24 μm flux (solid line) as well as the fraction of their identification with an optical counterpart for various magnitude limits (shaded regions). At the highest fluxes (i.e., $f_{24\mu m} \gtrsim$ 1mJy), the incompleteness of the sample is mostly due to a few objects detected close to very bright stars blooming the optical image and where a reliable identification of the counterpart cannot be obtained. These cases should not introduce any bias in our results. Below 1 mJy, the drop in the redshift determination completeness corresponds to sources fainter than $R \sim 23.5$ mag (see also Fig. 3.b). Above the 80% completeness limit of our MIPS data (i.e., 83 μJy), we see for instance that a significant fraction ($\sim$25%) of the MIPS objects with no redshift are associated with $24\,\mathrm{mag} \lesssim R \lesssim 25.5\,\mathrm{mag}$ sources, while $\sim$20% of them have counterparts fainter than $R \gtrsim 25.5$ mag. This also indicates that a complete study of the faint MIPS population will likely require an extensive use of photometric redshift techniques.

The consequence of this limitation can be seen by comparing the redshift determination completeness as a func-

[3] This offset seems to be due to systematics related to the position of the MIPS scan mirror. It affects the headers of the data obtained before May 2004 (*Spitzer* Science Center, priv. communication).
[4] http://cencosw.oamp.fr/EN/index.en.html
[5] http://www.eso.org/science/goods/spectroscopy/products.html
[6] http://www.mpe.mpg.de/ mainieri/cdfs_pub/

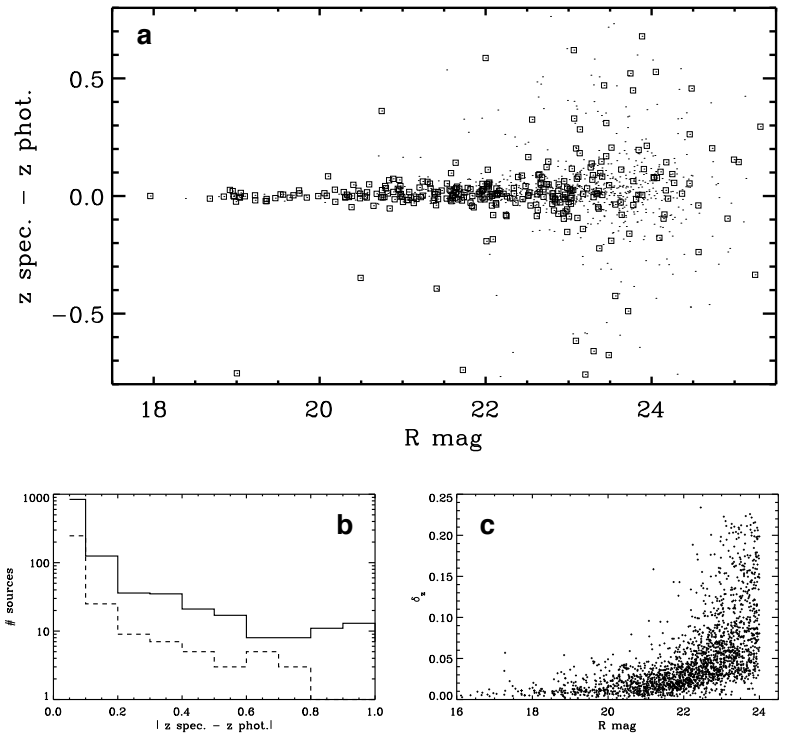

FIG. 2.— *a)* Comparison between the VVDS spectroscopic and COMBO-17 photometric redshifts as a function of the R-band magnitude, for 1 142 optically-selected galaxies (dots) and 308 MIPS 24 μm sources (open squares). *b)* Histogram of the absolute values $|z_{\rm spec}\text{-}z_{\rm phot}|$, with the optically-selected and 24 μm sources respectively indicated by the solid and dashed lines. *c)* Photometric redshift uncertainties provided by COMBO-17 for the 24 μm sources considered in this paper. Selection cut is set to $R \leq 24$ mag and $z \leq 1.2$. In agreement with comparisons from panels *a)* and *b)*, the accuracy is better than $\delta_z \sim 0.1$ for 88% of the sample.

tion of the R-band magnitude with the distribution of the R-band magnitudes of the MIPS sources for different redshift limits. This is shown in Fig. 3.b, while Fig. 3.c represents the absolute R-band magnitudes of the MIPS sources as a function of redsfhit and derived from COMBO-17. We see that the identification should be nearly complete up to $z \sim 0.8$, but we start missing 24 μm objects located at higher redshift and associated with optical counterparts fainter than $R \sim 23.5$–24 mag. These mis-identifications likely induce a biais against the faintest sources detected at 24 μm. In Sect. 6 we will establish a correlation between the optical and the infrared luminosities of galaxies in our sample, and we will use such relation in Sect. 7 to quantify how this bias affects the estimates of luminosity functions (see also the Appendix for further details characterizing these faint 24 μm sources). However, given the importance of the cosmic variance arising from the variations of large scale structures in the CDFS (see Sect. 3.4), and taking into account the errors in the k-corrections used to derive IR luminosities (see Sect. 5), we infer that the possible missing redshift determinations should not dominate the

absolute uncertainty in the source density estimate up to $z \sim 1$.

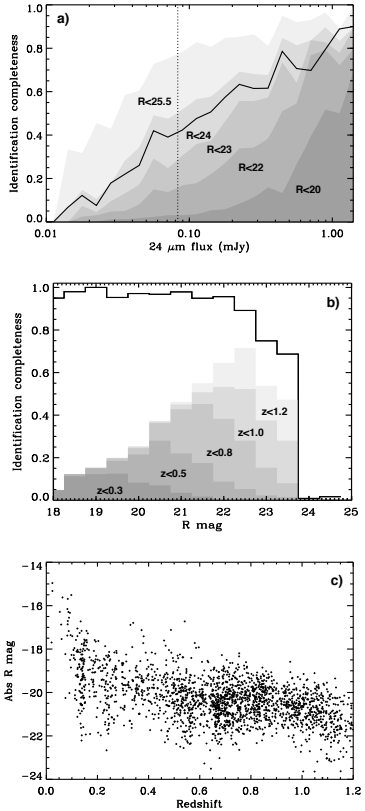

FIG. 3.— *a)* Fraction of MIPS sources identified with a spectroscopic or a photometric redshift as a function of the observed flux at 24 μm (solid line). We also indicate the fraction of MIPS sources with an optical counterpart detected in the R-band for various magnitude limits (shaded regions). The vertical dotted line corresponds to the 80% completeness limit of the 24 μm observations. *b)* Fraction of 24 μm source optical counterparts identified with a redshift, as a function of the R-band magnitude (solid line). Shaded regions show the R-band magnitude histograms (all scaled with an arbitrary constant factor) of the MIPS sources up to various redshift limits. The drop in the redshift identification is clearly apparent at $R \sim 23.5$-24 mag. The sample should be complete up to $z \sim 0.8$. *c)* Absolute R-band magnitudes of the MIPS sources as a function of redshift.

Other arguments also suggest that the bulk of the MIPS sources for which we could not identify any reliable redshift should be indeed located at $z \gtrsim 1$ and will not affect this study. First we will show in the following sections that infrared luminous galaxies are associated with optical counterparts at the bright end of the luminosity function in the visible. Luminous optical sources with $L \gtrsim L\star$ but fainter than $R \sim 23.5$–24 mag should lie at $z \gtrsim 1$ (Benítez 2000). Moreover, preliminary results from *Spitzer* reveal that a significant fraction of the MIPS sources are located at such large redshifts (Chary et al. 2004; Egami et al. 2004; Le Floc'h et al. 2004; Lagache et al. 2004). Finally, although they are not fully reliable, the COMBO-17 redshift estimates based on the peak of the redshift probability distributions indicate that the majority of the sources that we have not identified should be at $z \gtrsim 1$.

3.4. *Redshift distribution*

Figure 4 shows the distribution of the redshifts derived for our sample of infrared sources (bottom panel, solid line). It is compared to the redshift distributions of the VVDS (dotted line) and the COMBO-17 objects with $R \leq 24$ (dashed line). As previously discussed, the redshift identification of the MIPS sources is complete only up to $z \sim 0.8$, and the distribution beyond this limit should thus be considered as a lower limit estimate.

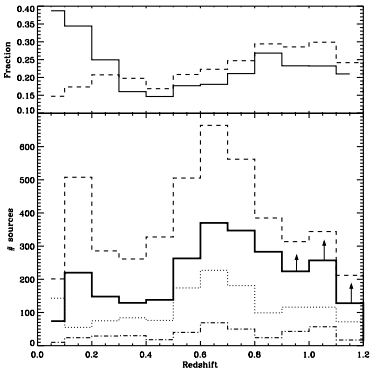

FIG. 4.— *Bottom:* The redshift distribution of 24 μm-selected sources over a 775 arcmin^2 region within the CDFS (solid line), compared to the distributions of photometric redshifts for $R \leq 24$ mag sources in the COMBO-17 catalog (dashed-line, scaled down by a factor of 2.5) and spectroscopic redshifts for $I_{AB} \leq 24$ mag sources in the VVDS survey (dotted line). The contribution of MIPS sources with spectroscopic redshifts is also indicated (dash-dotted line). Note the prominent overdensity at $z \sim 0.65$, clearly seen in all the distributions. Source densities at $z \geq 0.8$ should be considered as lower limit estimates due to the incompleteness of the redshift identification. *Top:* The fractions of $R \leq 24$ mag sources detected at 24 μm, estimated as a function of redshift in the whole population of COMBO-17 (dashed line) and restricted to the objects with $M_B \leq -16$ (solid line).

We note that the three distributions (i.e., MIPS, VVDS, COMBO-17) are more or less similar from $z \sim 0$ to $z \sim 1$. Up to this redshift limit, MIPS is indeed sensitive to sources luminous in the infrared but also to more normal galaxies (see Sect. 5) such as those detected at optical wavelengths and driving the VVDS and COMBO-17 redshift distributions. Furthermore, we note a significant number of objects around $z \sim 0.65$, apparent in all the distributions. This originates from an overdensity characteristic of the CDFS near this redshift (e.g., Wolf et al. 2004) and it is likely related to cosmic variance and large-scale structure effects (Somerville et al. 2004). It may constitute a non negligible source of uncertainty in our density estimates. A comparison between the integrated B-band luminosity densities as a function of redshift from galaxies of the blue sequence (Bell, private communication, see Willmer et al., in prep., for the evolution of the blue sequence luminosity function) in the CDFS and averaged over the three fields of COMBO-17 (Wolf et al. 2003) shows that the CDFS is most often underdense by $\sim$50% at $0 \lesssim z \lesssim 1$, except indeed at $z \sim 0.65 \pm 0.1$ where the overdensity reaches $\sim$20%. Given the similarity between the redshift distributions of the optically and infrared selected sources, and since most of MIPS sources at $z \sim 0.7$ appear to be associated with large spirals dominating the B-band emission (Bell et al. 2005, see also Fig. 10b), this cosmic variance characterized from the B-band luminosity density is likely affecting also the population of galaxies detected at 24 μm. Therefore the apparent peak at $z \sim 0.65$ in the MIPS redshift distribution is probably only related to the structure of the CDFS and it should not be a characteristic of the general population of infrared-selected sources.

In spite of the similarities that we observe between the redshift distributions in the visible and the infrared, a more critical look reveals that the fraction of optical sources brighter than $M_B = -16$ and detected at 24 μm decreases from $z = 0$ to $z \sim 0.4$ and then increases with redshift up to $z \sim 1$ (see Fig.4., top panel). Interpreting this trend is not straightforward, but it could reflect the difference in the k-correction effects observed at optical and infrared wavelengths. As we will see in Sect. 5 (see Figs. 7 & 9) the effective sensitivity of the deep 24 μm observations drops rapidly from $z = 0$ to $z \sim 0.5$, which explains the sharp decrease of relative 24 μm detections in this redshift range. Then it remains roughly constant at $0.5 \lesssim z \lesssim 0.9$ because of strong emission features present at 11.3 and 12.7 μm in galaxy spectra progressively entering the 24 μm filter at these redshifts. Since the sensitivity of the optical data constantly drops with distance, an increase in the relative number of 24 μm sources detected beyond $z \sim 0.5$ in the visible might thus result. Note that it may also reflect the stronger evolution of IR sources with lookback time, since IR-luminous phases in galaxies were more common in the past (e.g., Hammer et al. 2005). The lack of apparent decline moreover suggests that the intrinsic peak of the MIPS population redshift distribution must lie at least beyond $z \sim 0.8$.

Finally, another overdensity lies at $z \sim 0.15$. It represents a rather small fraction of our detections at 24 μm (i.e., 4%). Since we will only consider sources at $z \geq 0.3$ when building the luminosity functions in Sect. 7, it will not affect our final results on the evolution of the IR galaxy population.

4. EXPLORING THE ORIGIN OF THE BREAK IN THE MIPS 24 μm NUMBER COUNTS

4.1. *Cumulative differential counts as a function of redshift*

Using our matched catalog of 24 μm-selected objects with redshifts, we now explore for various redshift slices the contribution of these MIPS sources to the total differential number counts. Our goal is a better understanding of the origin of the bump detected at 0.2–0.4 mJy (P04, Marleau et al. 2004). Figure 5 illustrates these cumulative source counts for redshift limits of 0.3, 0.5, 0.8, 1.0 and 1.2 along with the global contribution of the MIPS sources identified with an optical counterpart in the full COMBO-17 catalog (i.e., $R \lesssim 25.5$ mag). The distributions for redshift limits $z = 1$ and $z = 1.2$ are likely underestimated due to the incompleteness of the sample as showed in Sect. 3.3. However, uncertainties due to cosmic variance likely dominate here ($\sim$0.10-0.15 dex based on the ratio between the B-band luminosity densities of the CDFS and averaged within the other fields of COMBO-17). For comparison, we also represent the total 24 μm number counts derived from our sub-sample as well as those obtained by Papovich et al. (2004), who averaged the 24 μm source population over $\sim 10\,\mathrm{deg}^2$ in several cosmological fields. For consistency with our data, these counts from P04 were not corrected for incompleteness of the MIPS detections at faint fluxes.

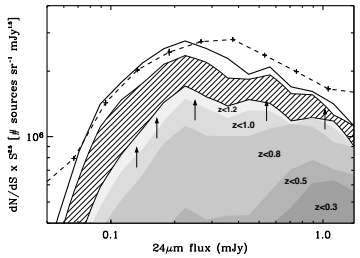

FIG. 5.— Cumulative differential number counts observed at 24 μm as a function of redshift (shaded regions). Distributions at $z \geq 0.8$ should be considered as lower limit estimates due to the incompleteness of the redshift identification. The striped area represents the contribution of all 24 μm sources identified with an optical counterpart down to $R \lesssim 25.5$ mag. The total differential counts derived from our sub-sample are illustrated by the black solid line, while those determined by Papovich et al. (2004) are represented by the dashed line and the vertical error bars. Counts are normalized to the Euclidian slope.

We note that the 24 μm number counts derived in the CDFS show a roughly good agreement with those obtained by P04 below $f_{24\mu m} \sim 0.2$ mJy. However, the density of 24 μm CDFS sources at higher fluxes appears to be slightly lower ($\sim$20%), and consequently the peak of the differential number counts seems to occur at fainter levels. As previously seen in Sect. 3.4., such variations are easily understood in terms of cosmic variance and the

smaller number of infrared-bright sources in the CDFS is likely related to the underdensity observed in the B-band at $z \lesssim 1$.

At critical fluxes $f_{24\mu m} \sim 0.2$-0.4 mJy where the 24 μm differential counts present a turn-over, sources lying at $z \lesssim 1$ contribute $\sim$55% to the whole sample. Even though this fraction could be slightly higher due to the possible incompleteness of our redshift identification at $0.8 \lesssim z \lesssim 1$, a significant part of the MIPS population should therefore be located at higher redshifts (i.e., $z \gtrsim 1$). As already derived from Fig. 3, it can also be noted that $\sim$20% of the 24 μm sources have optical counterparts fainter than $R \sim 25.5$ mag.

4.2. *Comparison with model predictions*

In Figure 6 we compare the differential counts in four redshift slices between $z = 0$ and $z = 1.2$ with the predictions from the models of IR galaxy evolution proposed by Lagache et al. (2004), Chary et al. (2004), Gruppioni et al. (2005, see also Pozzi et al. 2004) and Pearson (2005). These models are all tied to the local IR galaxy population but differ in (i) the description of its components and their global properties (i.e., SEDs, luminosity functions per object type) and (ii) the assumptions and parameterization used to infer the backward evolution of IR sources. They provide a reasonably good fit to the total 24 μm number counts. They also reproduce a variety of other observables such as the IR background, the counts and/or the redshift distributions of the *ISO* and SCUBA galaxy populations.

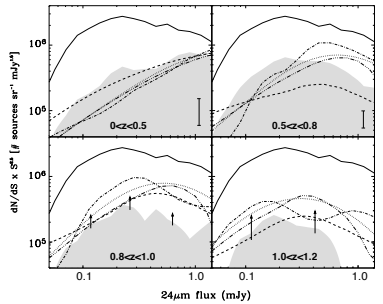

FIG. 6.— Differential 24 μm number counts produced by the MIPS sources in four redshift slices between $z = 0$ and $z = 1.2$ as indicated within each panel (shaded regions). They are compared to the predictions by Lagache et al. (2004, dashed lines), Gruppioni et al. (2005, dotted lines), Chary et al. (2004, dash-dotted lines) and Pearson (2005, triple dot-dashed line) for similar redshift ranges. The total counts derived from our sample are shown in each panel by the black solid line. The vertical bar in the upper panels represents the typical uncertainty due to the effect of large scale structures. The counts at $0.8 \leq z \leq 1.0$ and $1.0 \leq z \leq 1.2$ (lower panels) only show a lower limit given the incompleteness of the redshift identification in our sample at $z \gtrsim 0.8$.

Looking at their predictions for the 24 μm number counts within the redshift slices considered in this Fig. 6, we see that the models from Chary et al. (2004), Gruppioni et al. (2005) and Pearson (2005) may underestimate the contribution of faint sources at $0 \lesssim z \lesssim 0.8$ but predict too many bright objects at $z \gtrsim 0.5$. Lagache et al. (2004), on the other hand, closely follow the observations at $z \lesssim 0.5$ but might globally underestimate the source density at $0.5 \lesssim z \lesssim 0.8$. All these models finally seem to overpredict the contribution of bright galaxies at $z \gtrsim 0.8$. However we also note that these comparisons could be undermined given not only cosmic variance effects and the global underdensity of the CDFS between $z = 0$ and $z \sim 1$ but also the incompleteness of our redshift identification at $z \gtrsim 0.8$.

Comparisons with other models in the literature such as those published before the launch of *Spitzer* lead to larger discrepancies. These models tend to predict the characteristic turn-over of the differential 24 μm number counts at much higher fluxes than where it has been observed (see for instance Figure 3 of Papovich et al. 2004).

5. TOTAL INFRARED LUMINOSITIES

5.1. *Estimating the total IR luminosity of galaxies from their mid-IR emission*

The rest-frame mid-infrared (MIR) regime (i.e., 8 μm $\lesssim \lambda \lesssim$ 40 μm) is considered to be a good tracer of the bolometric luminosity of galaxies. Using the 12 μm IRAS galaxy sample, Spinoglio et al. (1995) first showed that the relative dust content of galaxies balances their total energetic output between the optical and the far-infrared, leaving a "pivot point" in the MIR where the specific luminosity linearly scales with the bolometric one. More recently, a similar conclusion has been reached by Chary & Elbaz (2001) who found a tight correlation between the 15 μm and the total infrared luminosities for a sample of normal and luminous sources studied with ISOCAM. Based on these considerations and taking into account the general IR/submm color-color and/or luminosity-color correlations observed in the local Universe, several authors have built libraries of luminosity- or color-dependent galaxy templates, which can then be used to estimate the total infrared luminosity of galaxies from their 24 μm flux densities (Dale et al. 2001; Chary & Elbaz 2001; Dale & Helou 2002; Lagache et al. 2003; Chanial 2003).

Figure 7 shows the total infrared luminosity that can be detected in our survey down to a 24 μm sensitivity limit of 0.08 mJy, as a function of redshift and computed with the aforementioned libraries. Provided these templates are still representative of high redshift sources, we see that MIPS can easily detect normal starbursts (i.e., $L_{IR} \lesssim 10^{11}\,L_\odot$) up to $z \sim 1$, and LIRGs up to $z \sim 1.5$. Note that such limits only characterize a pure selection of sources at 24 μm, and the use of *a priori* information from detections at other wavelengths can allow the identification of MIPS sources with similar infrared luminosities at even higher redshift (see e.g., Le Floc'h et al. 2004). The 80% completeness level roughly corresponds to a 5σ detection in the MIPS data (Dole et al. 2004b), and the quoted 0.08 mJy limit is therefore rather conservative.

Figure 7 also shows the dispersion between the predictions (and therefore the templates) of the various libraries (see also Papovich & Bell 2002). For a given observable (e.g., infrared luminosity, color, ...) these li-

braries assign a unique SED that slightly varies from one set of templates to another. Such variations reflect an intrinsic dispersion of the different correlations observed between the MIR/FIR/submm properties of galaxies that is usually not taken into account (but see Chapman et al. 2003b for the use of bi-variate luminosity functions addressing this issue). As an example, we compare in Figure 8 the observed relation between L_{IR} and the monochromatic $15\,\mu$m luminosity L_{15}[7] for a sample of local galaxies studied with *ISO* and IRAS (Chary & Elbaz 2001) with the predictions of the template libraries considered in Fig. 7. We see that the dispersion can easily reach ~ 0.2 dex.

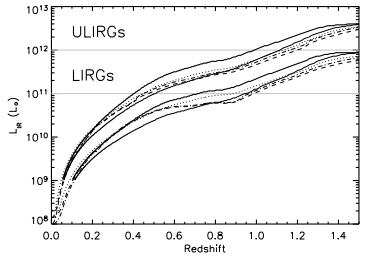

FIG. 7.— Detection limits in terms of total infrared luminosity, derived for two different MIPS $24\,\mu$m sensitivities and assuming the template libraries of Lagache et al. (2004, thick solid line), Lagache et al. (2003, thin solid line), Dale et al. (2001, dotted line), Chary & Elbaz (2001, dashed line) and Chanial (2003, dash-dotted line) as a function of redshift. The lower (respectively, upper) set of curves corresponds to a flux limit of 0.08 mJy (0.3 mJy) typical of the MIPS deep (shallow) surveys.

To explain this dispersion, one may note that in the local Universe the mid-infrared SEDs of starburst sources with comparable bolometric luminosities are subject to significant variations (e.g., Armus et al. 2004). In the rest-frame wavelength range probed by the MIPS $24\,\mu$m filter for high redshift galaxies, the MIR emission results from the combination of prominent broad-band features mostly observed between 3 and $14\,\mu$m and usually denoted the Polycyclic Aromatic Hydrocarbons bands (PAHs), superimposed on a rising continuum of Very Small Grains (VSGs) stochastically heated by the young star radiation field (see e.g., Laurent et al. 2000 and references therein). PAHs present an amazingly universal SED signature as a global set of features when integrated over normal spiral galaxies (Roussel et al. 2001, but see Smith et al. 2004 for smaller scale variations and a newly-discovered $17.1\,\mu$m PAH in NGC 7331). However, they are not detected in low metallicity sources (Thuan et al. 1999; Houck et al. 2004a; Engelbracht et al. 2005, submitted). They are also believed to be destroyed within intense radiation fields as in the vicinity of active galactic nuclei (AGN, e.g., Le Floc'h et al. 2001). Finally, the temperature of the VSGs as well as the silicate absorptions at $9.7\,\mu$m and $18\,\mu$m represent other important factors shaping the underlying continuum of the global mid-infrared SED of galaxies. All of these variations can therefore bring significant uncertainties in relating the MIR emission to the full infrared range of galaxy SEDs.

[7] We define the monochromatic luminosity as $L_\nu = \nu \times S_\nu$, with S_ν the monochromatic flux of the galaxy expressed in $W\,Hz^{-1}$.

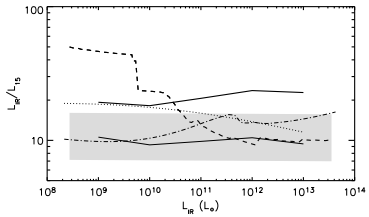

FIG. 8.— Ratio between the total IR and the monochromatic $15\,\mu$m luminosities as a function of L_{IR} predicted by the SED libraries considered in Fig. 7 (similar style coding). The grey area represents the relation (mean value with 1σ boundaries) derived by Chary & Elbaz (2001) for galaxies that were observed with ISO and IRAS.

Furthermore, one may question whether these templates derived from the properties of local galaxies are trully representative of higher redshift sources. Infrared luminous galaxies detected by ISOCAM at a median redshift of ~ 0.7 are characterized by roughly half-solar metallicites (Liang et al. 2004), which could point to IR SEDs slightly different from those of local LIRGs. However, PAHs are still detected at this metallicity range in nearby starbursts (Engelbracht et al. 2005, submitted). Moreover, the $24/15\,\mu$m flux ratios observed in $z \sim 0.7$ ISOCAM sources still argue for the presence of significant PAHs in their SEDs (Elbaz et al. 2005), and prominent PAH features were also recently observed with the InfraRed Spectrograph on *Spitzer* (IRS, Houck et al. 2004b) at even higher redshifts (i.e., $1.7 \leq z \leq 2.8$, Houck et al. 2005). We also note that the MIR/radio relation expected from the MIR/FIR and FIR/radio correlations observed locally (Condon 1992; Chary & Elbaz 2001) appears to be still valid in the more distant Universe (e.g., Elbaz et al. 2002; Appleton et al. 2004). These results give reasonable confidence in using local galaxy templates to estimate the infrared luminosities of distant IR sources.

5.2. *The total infrared luminosity of the MIPS sources at $z \lesssim 1$*

For each library of SEDs previously discussed, we computed the redshift-dependent relations between L_{IR} and the flux density observed at $24\,\mu$m. For every source of the sample, an estimate of the total IR luminosity was thus obtained from each set of templates. These measures were weigthed based on the accuracy of their associated library to reproduce the observed relation between L_{IR} and L_{15} at the derived luminosity (see Fig. 8). They were combined to provide the final infrared luminosity of the object, and their associated rms was taken as an estimate of the corresponding uncertainty.

As noted by Chapman et al. (2003b) there might also be a bias of MIPS $24\,\mu$m sources toward luminous galaxies with hot dust temperatures compared to the whole population of IR-luminous objects at high redshift. This could result in additional systematics affecting these luminosity estimates, and we have not formally considered this effect here. We believe however that the uncertainties due to the SED libraries dominate the systematics in our study.

The IR luminosities are displayed as a function of redshift in Figure 9. Based on the previous arguments we estimate that they are accurate within a factor of ~ 2–3 up to $z \sim 1$. We see that most sources detected below $z \sim 0.5$ are only modest infrared emitters (i.e., $L_{IR} \leq 10^{11}\,L_\odot$), and the number of infrared-luminous galaxies found at these low redshifts is quite low. At larger distances however, LIRGs represent a significant fraction of the MIPS galaxy sample in terms of detection number. This large population of LIRGs at $0.5 \lesssim z \lesssim 1.0$ has also been observed in various surveys performed at $15\,\mu$m with ISOCAM (e.g., Aussel et al. 1999; Flores et al. 1999; Elbaz et al. 2002). We finally note that the most luminous galaxies (i.e., $L_{IR} \geq 10^{12}\,L_\odot$) are still pretty rare, but there is a clear hint for an increase of the number of the brightest LIRGs ($5\times10^{11}\,L_\odot \lesssim L_{IR} \leq 10^{12}\,L_\odot$) at $z \sim 1$, which could point to a large population of ULIRGs at even larger distances (i.e., $z \gtrsim 1.5$, Blain et al. 1999a; Chapman et al. 2003a). These detection rates are obviously contingent on the comoving volume sampled at each redshift though. This general issue will thus be addressed in more detail in Sect. 7, where we characterize the evolution of the infrared luminosity function based on this sample of MIPS sources.

As a final remark, it is worth mentioning another possible caveat related to these infrared luminosity estimates. The various template libraries that we used in this work are only representative of normal and starburst-like galaxies, and do not include the SEDs typical of active galactic nuclei which are significantly flatter in the MIR wavelength range. A careful investigation of the nature of the emission process dominating the $24\,\mu$m flux in our sub-sample (star-forming activity versus AGN) is beyond the scope of this paper, but we note that the fraction of MIPS sources showing evidence for the presence of an AGN in their optical counterparts is less than $\sim 15\%$ according to the VVDS and COMBO-17 classifications. Furthermore, recent synthetic models connecting the X-ray and infrared SED of AGNs as well as their contribution to the cosmic backgrounds in these energy bands indicate that the emission arising from pure AGNs should be negligible (i.e., $\lesssim 10\%$) in high redshift sources detected at $24\,\mu$m (e.g., Silva et al. 2004). In the local Universe moreover, AGNs dominate the mid-IR output of galaxies only for the most extreme ULIRGs (e.g., Lutz et al. 1998; Tran et al. 2001), while the X-ray and optical spectral properties of infrared galaxies detected with *ISO* and MIPS at $15\,\mu$m and $24\,\mu$m also argue for a population dominated by star formation at the ~ 85–90% level (Fadda et al. 2002; Franceschini et al. 2003; Manners et al. 2004; Franceschini et al. 2005; Bell et al. 2005). It should therefore be reasonable to assume SEDs typical of star-forming galaxies for this current work.

6. THE OPTICAL COUNTERPARTS OF THE MIPS SOURCES: SOME PROPERTIES

We describe in this section a few basic characteristics of the MIPS source optical counterparts to provide a first-order answer to very simple questions: are the distant infrared luminous galaxies detected by MIPS also luminous in the optical or are they highly obscured ? Are these dusty starbursts associated with very young systems or already evolved galaxies ? A description of their morphologies, colors and specific star formation rates is provided by Bell et al. (2005).

The COMBO-17 *R*-band magnitudes of the MIPS sources are plotted as a function of the flux density at $24\,\mu$m in Figure 10a. Not surprisingly, there is a clear trend for the fainter $24\,\mu$m objects to be associated with faint optical sources likely located at higher redshifts. Such a trend has already been noted among the population of infrared galaxies detected with ISOCAM at $15\,\mu$m (e.g., Pozzi et al. 2004). However there is large dispersion in the relation and for most of the sample the optical brightnesses can vary by more than 5 magnitudes when infrared fluxes only change by less than a factor of 10. This clearly points to a very wide range of the $L_{IR}/L_{optical}$ ratios and a broad variety in the nature of the MIPS sources (see also the Appendix).

We also used the absolute magnitude estimates provided by COMBO-17 to derive the intrinsic luminosities of the MIPS sources at optical wavelengths. As an example we illustrate in Figure 10b the COMBO-17 absolute magnitudes estimated in the *B*-band filter and corrected to our cosmology[8] as a function of the total infrared luminosities derived in the previous section. We observe a clear relationship between the two quantities, though the dispersion remains relatively large ($1\sigma \sim 0.5$ dex). Similar relations are also obtained between the total IR luminosity and the absolute magnitudes derived from the other broad-band filters of COMBO-17. They show that distant IR luminous sources (at least up to $z \sim 1$) are preferentially associated with luminous optical counterparts as in the local Universe (Sanders & Mirabel 1996). This result confirms previous studies based on *ISO* surveys (Rigopoulou et al. 2002; Franceschini et al. 2003; Zheng et al. 2004). It also suggests that the dust responsible for the IR excess in such distant IR-luminous objects is likely distributed within small-size regions and the corresponding reddening is not sufficient to completely obscure the underlying galaxy. This interpretation is reinforced by the range of optical colors observed among the MIPS $24\,\mu$m source population, very similar to the range characterizing the local normal galaxies (Bell et al. 2005).

COMBO-17 also provides an estimate of the rest-frame galaxy luminosity at λ=2800Å, which can be used to derive the "IR excess" in the MIPS sources. IR excess is usually defined as the ratio between the IR and UV emission and it is plotted in Figure 10c as a function of the total IR luminosity. Owing to the tight relation between the star-forming activity and the IR emission of galaxies (Kennicutt 1998), this plot can also be read as the IR excess as a function of an "IR-equivalent" star formation rate (an IR luminosity $L_{IR} = 10^{11}\,L_\odot$ typically

[8] The COMBO-17 catalog provides absolute quantities assuming $H_0 = 100$ km s^{-1} Mpc^{-1}, $\Omega_m = 0.3$ and $\Omega_\lambda = 0.7$.

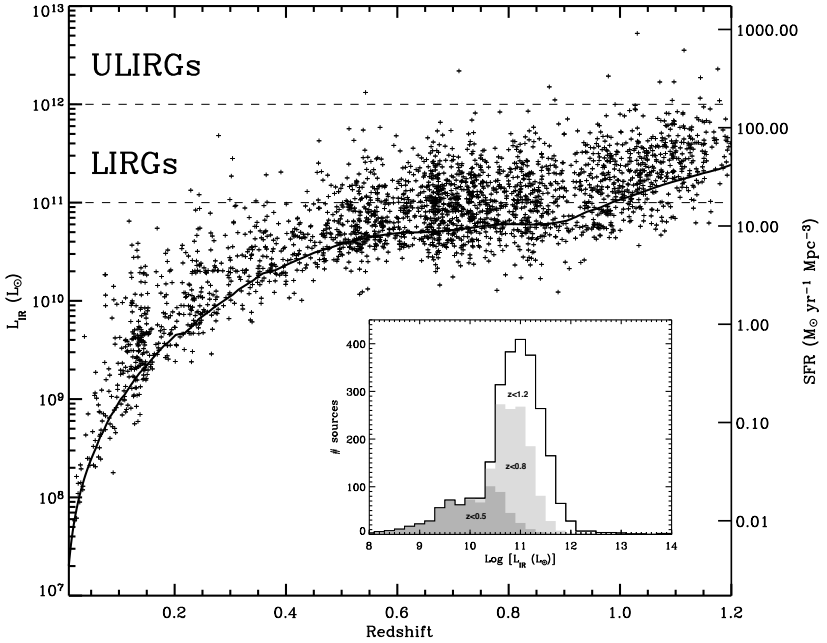

FIG. 9.— Total infrared luminosities of the MIPS 24 μm sources identified with a redshift at $0 \leq z \leq 1.2$ (+ symbols). They were derived using various luminosity-dependent SED templates of the literature (see text for more details) and we estimate that they are accurate within a factor of $\sim$2–3. The median uncertainty of the photometric redshifts is less than 0.05 (Wolf et al. 2004). Error bars are not shown for clarity. Assuming the calibration from Kennicutt (1998), IR luminosities are translated into an "IR-equivalent SFR" reported on the right vertical axis. The thick solid line indicates as a function of redshift the infrared luminosity corresponding to an observed 24 μm flux of 0.08 mJy (80% completeness limit of our survey). *Inset:* Corresponding IR luminosity histogram of the sample, with the contribution of sources at $z \leq 0.5$ (respectively, $z \leq 0.8$) indicated by the dark (light) shaded region.

corresponds to a formation of $\sim 17\,M_\odot$ of stars per year following standard calibrations). It illustrates the very well-known trend for galaxies characterized by more intense star-forming activity to be generally dustier and more luminous at IR wavelengths (e.g., Buat et al. 2002; Cardiel et al. 2003; Pozzi et al. 2003; Flores et al. 2004). We also see that the fraction of UV photons not absorbed by dust in the case of the most luminous sources (i.e., $L_{IR} \gtrsim 10^{11.5}\,L_\odot$) is negligible compared to the energy reprocessed in the IR.

We finally provide an estimate of the stellar masses of the MIPS sources based on the properties of their optical counterparts. A tight correlation exists between the rest-frame optical colors of galaxies and their mass-to-light ratios (Bell & de Jong 2001; Kauffmann et al. 2003). This relation is uncertain by a factor ~ 0.4 dex due to combined effects of metallicity, dust, and history of star formation in individual sources. It is however accurate enough for the purpose illustrated here (i.e., getting a qualitative estimate of the distribution of IR-luminous objects as a function of mass). Following the detailed analysis and recipes by Bell et al. (2003, see their Appendix A), we used the V-band absolute luminosities of galaxies from COMBO-17 (converted to our cosmology) and transformed these luminosities to stellar masses using rest-frame $B-V$ colors. Figure 10d illustrates the corresponding histograms for both samples of optically-selected sources (thin solid line) and of galaxies detected at 24 μm (thick solid line). It is very clear that IR galaxies detected by MIPS are on average more massive (i.e., $\mathcal{M} \gtrsim 10^{9.5}\,\mathcal{M}_\odot$) than the field population of sources selected at optical wavelengths. Furthermore,

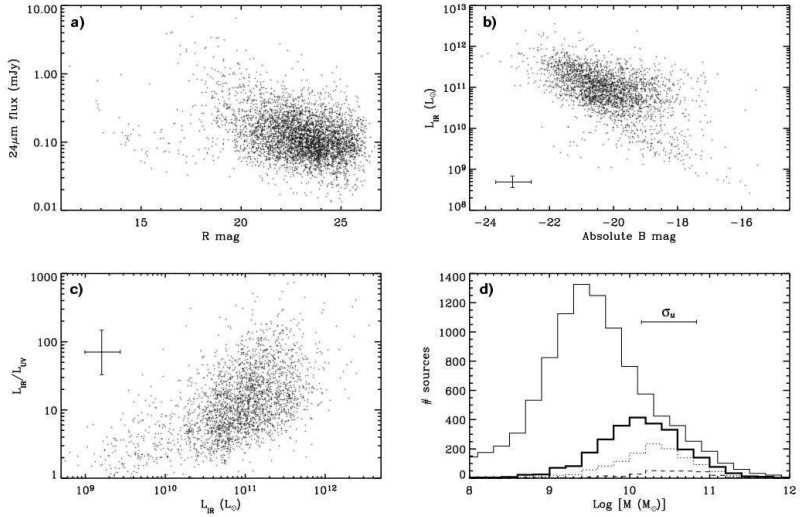

FIG. 10.— *a)* Observed 24 μm flux densities as a function of the R-band magnitudes obtained from COMBO-17. *b)* Total IR luminosities as derived in Sect. 5 versus the absolute B-band magnitudes. *c)* IR to UV luminosity ratios as a function of the total IR luminosities. *d)* Histogram of the stellar masses (in solar units) for the sample of MIPS sources (thick solid line) compared to the stellar masses of the COMBO-17 optically-selected galaxies (thin solid line, scaled down by a factor of 2.2). The dotted-line (respectively, dashed-line) histogram corresponds to the stellar mass distribution restricted to 24 μm sources with $L_{IR} \geq 10^{11}\,L_\odot$ ($L_{IR} \geq 10^{11.5}\,L_\odot$). Typical uncertainties are indicated with error bars in panels *b), c)* and *d)*.

the 24 μm objects tend to be associated with even more massive galaxies when their IR luminosity (and thus their star formation rate) increases. As already observed in the case of 15 μm sources detected by *ISO* at $z \lesssim 1$ (Franceschini et al. 2003), LIRGs with $L_{IR} \gtrsim 10^{11.5}\,L_\odot$ have most often counterparts with $\mathcal{M} \gtrsim 10^{10}\,\mathcal{M}_\odot$. In Sect. 8 we will discuss this issue within the more general context of the comoving star-forming activity at $z \sim 1$.

As a side note, we found a group of 91 sources (among which 54 have $f_{24\mu m} \geq 83\,\mu$Jy) identified with photometric redshifts and totally escaping the various relations illustrated on Figs. 10abc. These objects are rather faint in the optical ($R \gtrsim 23$ mag), and their $f_{24\mu m}/f_R$ flux ratios are particularly high and typical of LIRGs/ULIRGs. According to our previous results, and given that most of them have disturbed merger morphologies chatacteristic of high redshift star-forming galaxies (e.g., Bell et al. 2005), they are thus likely located at $z \gtrsim 0.5$-0.6, which is also supported by their morphologies since many of those are chatacteristic of high redshift star-forming galaxies. However they have been assigned very low redshifts by COMBO-17, mostly in the apparent overdensity observed at $z \sim 0.15$ in the CDFS. This would imply faint infrared luminosities ($10^9\,L_\odot \lesssim L_{IR} \lesssim 10^{10}\,L_\odot$, see Fig. 9) and optical absolute magnitudes much higher ($M_r \gtrsim -15$) than expected from the correlations. We believe that these redshifts have probably been misidentified. We decided to exclude the corresponding sources from our sample.

7. INFRARED LUMINOSITY FUNCTIONS

7.1. *Methodology*

We explore in this section the evolution of IR luminosity functions (LFs) at $0 \lesssim z \lesssim 1.2$. These LFs were derived for various redshift bins with the usual $1/V_{max}$ formalism (Schmidt 1968; Huchra & Sargent 1973; Felten 1976) applied to our sub-sample of sources brighter than $f_{24\mu m} = 83\,\mu$Jy and $R = 24$ mag. The selection function that was used in this goal was computed as follows. First, we considered the probability for a given object to verify our selection criterion at 24 μm. This probability equals 1 for sources brighter than $\sim 300\,\mu$Jy but decreases at fainter fluxes due to the incompleteness of the 24 μm catalog. The corresponding effect was quantified using the detailed simulations described by Papovich et al. (2004, see their figure 1). Second, we estimated the probability for a 24 μm source to be associated with an optical counterpart at $R \leq 24$ mag. This probability is a redshift-

dependent function, and it can be derived with an estimate of the absolute magnitude corresponding to the optical selection criterion ($R = 24$ mag) combined with the relation between the infrared and the optical luminosities established in the previous section. At this step, we actually assumed that 100% of sources with $R \leq 24$ mag are detected by COMBO-17[9]. Finally, we took into account the probability for a given optical source to be characterized by a redshift. This was done using the estimate of the redshift identification completeness that we determined in Sect. 3.3 for sources at $R \leq 24$ mag.

The computed selection function was subsequently used for each single galaxy of the sample to weight the differential volume elements that are integrated when calculating the total accessible volume $V_{\rm max}$. Given the multi-wavelength flux limits considered here, this integration was performed up to the maximum redshift enabling the detection of the object at *both* 24 μm *and* optical wavelengths (i.e., the lowest value between the redshift where the 24 μm flux would drop below 83 μJy and the redshift where the R-band magnitude would reach 24 mag).

The determination of the luminosity function was performed for each redshift range independently of the sources lying in the other bins. For this reason, the $V_{\rm max}$ approach is more subject to density fluctuations than other methods like the stepwise maximum likelihood (e.g., Efstathiou et al. 1988; Willmer 1997). Even though cosmic variance is not negligible in CDFS, we will see however that the uncertainties affecting our conclusions are largely dominated by the errors on the k-corrections that are used to translate fluxes into luminosities. The $V_{\rm max}$ technique might also be sensitive to the photometric redshift uncertainties, but as we already pointed out in Sect. 3.2, the effect should be negligible here given the accuracy of the COMBO-17 redshift classification.

7.2. *Results*

From the luminosity- dependent templates previously discussed, we converted the 24 μm observed fluxes into monochromatic luminosities at 12, 15, 25 and 60 μm as described in Sect. 5.2. The latter were subsequently used to derive the associated luminosity functions that we finally compared to the local LFs derived from *IRAS* and *ISO*. In Figure 11 we illustrate the 15 μm LF ψ_{15}(L,z) estimated for different redshift bins. The corresponding data points are reported in Table 1. At this wavelength the k-corrections needed to convert 24 μm fluxes into luminosities are minimized for most of the sources. The majority of sources are indeed located at $0.5 \lesssim z \lesssim 0.8$ where the MIPS 24 μm filter probes the 13.5–16 μm rest-frame wavength range. This behavior reduces the dependence of the luminosity functions on the assumed IR templates. We also show in Figure 12 the total IR LFs $\psi_{\rm IR}$(L,z) computed from the infrared luminosities shown in Fig. 9. Data points are given in Table 2. These LFs are obviously more dependent on the choice of IR SEDs since the uncertainty in the conversion between flux and luminosity is larger ($\sim$0.4 dex). They are however easier to interpret in the context of IR galaxy evolution.

To correct for cosmic variance effects in each redshift bin, the luminosity functions were normalized by the ratio between the B-band luminosity densities produced by galaxies of the blue sequence and measured respectively in the CDFS and over the 3 fields of COMBO-17 (Wolf et al. 2003, 2004; Bell et al. 2004). Even though the B-band and the IR selected populations differ in their evolution with redshift, they both trace instantaneous star-forming activity (yet with different time scales). This connection results in an obvious relation between the two that we already highlighted in Sects. 3.4 & 6 (see Fig. 10b, see also Bell et al. 2005). The characterization of the B-band luminosity function over different fields can therefore be used to estimate a first-order correction and minimize the cosmic variance affecting our 24 μm sample. With its redshift peak at $z \sim 0.65$, the CDFS is particularly subject to this effect.

7.3. *Uncertainties*

For each luminosity bin in a given redshift range, uncertainties $\sigma(L_i, z_j)$ were estimated as the combination of (i) poisson noise statistics on the number of sources used in the measurement (i.e., the rms error $\sqrt{\Sigma V_{\rm max,k}^{-2}}$, with "k" the source index in the bin) and (ii) uncertainties in the flux density at 24 μm and the conversion into luminosities. The effect of the latter was simulated with a Monte Carlo approach. We assigned to each galaxy a range of luminosities (monochromatic or integrated) that were calculated by taking account of the nominal flux and uncertainty at 24 μm as well as the different possible SEDs for the conversion. We found this conversion from flux to luminosity to be by far the dominant source of uncertainty, which explains the larger error bars found in the case of $\psi_{\rm IR}$ than for ψ_{15}. Regarding the monochromatic 15 μm LF however, flux uncertainties at 24 μm also contribute significantly, especially at the faintest levels. For each redshift bin finally, we uniformly added another uncertainty (0.15 dex) to the whole luminosity function based on our estimate of the cosmic variance effect. Because it should be negligible, we did not simulate the effect related to photometric redshift uncertainties.

7.4. *Parameterization and evolution with redshift*

In both Figures 11 & 12 we have also illustrated the luminosity functions determined locally from *IRAS* and *ISO*. The 15 μm local LF $\phi_{15}(L)$ was taken from Xu et al. (1998) and Xu (2000). Regarding the total IR luminosity function $\phi_{\rm IR}(L)$ at $z = 0$, we show on one hand a recent result from the revised IRAS Bright Galaxy Sample (Sanders et al. 2003), on the other hand an estimate that we derived from the 60 μm local LF (Saunders et al. 1990; Takeuchi et al. 2003) assuming the tight correlation between the 60 μm and the total IR luminosity of galaxies. Not surprisingly, these two estimates agree well with each other. A commonly known characteristic of these IR luminosity functions is their relatively large number of sources at the bright end. As a result they are better described by a double-exponential profile rather than a classical Schechter parameterization. Their usual analytical form is given as follows:

[9] This may not be true in the few regions closely surrounding very bright stars of the optical image. However this effect is obviously negligible over the total field of view considered in this work.

TABLE 1
LUMINOSITY FUNCTIONS DERIVED AT 15 μM FROM THE $1/V_{\rm max}$ ANALYSIS[a]

Log [$L_{15\mu m}$ ($L_\odot$)]	Φ [# Mpc^{-3} (Log $L_{15\mu m}$)$^{-1}$]				
	$0.3 \leq z \leq 0.45$	$0.45 \leq z \leq 0.6$	$0.6 \leq z \leq 0.8$	$0.8 \leq z \leq 1.0$	$1.0 \leq z \leq 1.2$
9.0	$5.80^{+2.52}_{-2.58} \times 10^{-3}$				
9.5	$2.93^{+1.26}_{-1.30} \times 10^{-3}$	$2.62^{+1.22}_{-1.16} \times 10^{-3}$			
10.0	$5.44^{+3.12}_{-3.02} \times 10^{-4}$	$1.75^{+0.86}_{-0.78} \times 10^{-3}$	$2.90^{+1.39}_{-1.29} \times 10^{-3}$	$2.27^{+1.13}_{-1.01} \times 10^{-3}$	$2.38^{+1.02}_{-1.06} \times 10^{-3}$
10.5	$8.37^{+29.6}_{-6.28} \times 10^{-5}$	$3.78^{+1.52}_{-1.68} \times 10^{-4}$	$7.72^{+3.56}_{-3.43} \times 10^{-4}$	$1.40^{+0.73}_{-0.62} \times 10^{-3}$	$1.21^{+0.67}_{-0.54} \times 10^{-3}$
11.0		$3.44^{+12.5}_{-2.58} \times 10^{-5}$	$3.35^{+8.38}_{-2.51} \times 10^{-5}$	$1.06^{+0.73}_{-0.67} \times 10^{-4}$	$2.54^{+1.18}_{-1.13} \times 10^{-4}$
11.5			$8.38^{+41.9}_{-6.29} \times 10^{-6}$	$1.07^{+52.9}_{-0.79} \times 10^{-5}$	$2.35^{+5.88}_{-1.76} \times 10^{-5}$

[a] assuming a ΛCDM cosmology with $H_0 = 70$ km s^{-1} Mpc^{-1}, $\Omega_m = 0.3$ and $\Omega_\lambda = 0.7$.

TABLE 2
TOTAL IR LUMINOSITY FUNCTIONS DERIVED FROM THE $1/V_{\rm max}$ ANALYSIS[a]

Log [$L_{\rm IR}$ ($L_\odot$)]	Φ [# Mpc^{-3} (Log $L_{\rm IR}$)$^{-1}$]				
	$0.3 \leq z \leq 0.45$	$0.45 \leq z \leq 0.6$	$0.6 \leq z \leq 0.8$	$0.8 \leq z \leq 1.0$	$1.0 \leq z \leq 1.2$
10.0	$8.88^{+11.8}_{-5.92} \times 10^{-3}$				
10.5	$3.52^{+4.70}_{-2.35} \times 10^{-3}$	$3.84^{+5.13}_{-2.56} \times 10^{-3}$			
11.0	$0.96^{+1.28}_{-0.64} \times 10^{-3}$	$2.29^{+3.06}_{-1.52} \times 10^{-3}$	$3.43^{+4.58}_{-2.29} \times 10^{-3}$	$2.77^{+3.69}_{-1.85} \times 10^{-3}$	
11.5	$0.16^{+0.42}_{-0.13} \times 10^{-3}$	$0.53^{+0.71}_{-0.35} \times 10^{-3}$	$1.18^{+1.57}_{-0.79} \times 10^{-3}$	$1.78^{+2.37}_{-1.19} \times 10^{-3}$	$1.11^{+1.48}_{-0.74} \times 10^{-3}$
12.0		$6.87^{+17.2}_{-5.15} \times 10^{-5}$	$8.38^{+13.2}_{-6.29} \times 10^{-5}$	$2.86^{+3.81}_{-1.91} \times 10^{-4}$	$5.91^{+7.88}_{-3.94} \times 10^{-4}$
12.5		$1.71^{+2.58}_{-1.29} \times 10^{-5}$	$8.38^{+12.6}_{-6.29} \times 10^{-6}$	$4.23^{+10.6}_{-3.17} \times 10^{-5}$	$5.88^{+9.30}_{-3.17} \times 10^{-5}$
13.0					$1.18^{+4.41}_{-4.16} \times 10^{-5}$

[a] assuming a ΛCDM cosmology with $H_0 = 70$ km s^{-1} Mpc^{-1}, $\Omega_m = 0.3$ and $\Omega_\lambda = 0.7$.

$$\phi_\lambda(L) = \frac{dN(L)}{dV\ d\log_{10}(L)} \qquad (1)$$
$$= \phi^\star_\lambda \left(\frac{L}{L^\star_\lambda}\right)^{1-\alpha_\lambda} \exp\left[-\frac{1}{2{\sigma_\lambda}^2}\log^2_{10}\left(1+\left(\frac{L}{L^\star_\lambda}\right)\right)\right]$$

where dV is the differential element of comoving volume and $dN(L)$ the number of sources with a luminosity L within dV and per bin of $d\log_{10}(L)$.

As expected, the comparison between ψ_λ(L,z) and the local luminosity functions reveals a very strong evolution of the LFs with lookback time. For each redshift bin, ψ_λ(L,z) was fitted assuming a monotonic evolution of the local LF $\phi_\lambda(L)$ in both luminosity and density as a function of $(1+z)$:

$$\psi_\lambda(L, z) = g(z)\phi_\lambda\left(L/f(z)\right) \qquad (2)$$

with $g(z) = (1+z)^{\alpha_{\rm D}}$ and $f(z) = (1+z)^{\alpha_{\rm L}}$.

We explored the possible range of values for the fitting parameters $\alpha_{\rm D}$ and $\alpha_{\rm L}$ using a χ^2 minimization. This χ^2 was computed from the difference between the observed and the fitted luminosity functions over the $0.3 \leq z \leq 1.0$ redshift range:

$$\chi^2_\lambda \propto \sum_{L_i} \sum_{0.3 \leq z_j \leq 1} \left[\frac{\psi_{\lambda,obs.} - \psi_{\lambda,model}}{\sigma}\right]^2_{L_i,z_j} \qquad (3)$$

Because of their lower statistical significance, LFs determined at $z \leq 0.3$ and $z \geq 1$ were ignored in this process. Reduced χ^2 values were finally transformed into likelihood estimates using $\log(L) = -0.5\chi^2$. The corresponding 1σ, 2σ and 3σ iso-probability contours for ψ_{15} and $\psi_{\rm IR}$ are displayed in the insets of Figures 11 & 12 respectively.

The elliptical shape and the orientation of these contours in the luminosity and density evolution parameter space reflect a well-known degeneracy often encountered when fitting high redshift luminosity functions. Given the sensitivity of our 24 μm survey indeed, the very faint-end portion of ψ_λ(L,z) cannot be constrained at any redshift. The LF can thus be described with a variety of scenarios combining different amount of evolution in $\alpha_{\rm D}$ and $\alpha_{\rm L}$. The constraints that we obtained can be summarized as follows:

$$\psi_{15}(L, z): \begin{cases} \alpha_L = 2.6 \pm 0.9\ (3\sigma) \\ \alpha_D = (-1.80 \times \alpha_L + 6.75) \pm 1.1 \end{cases}$$

$$\psi_{IR}(L, z): \begin{cases} \alpha_L = 3.15 \pm 1.6\ (3\sigma) \\ \alpha_D = (-1.55 \times \alpha_L + 5.90) \pm 1.6 \end{cases}$$

We will analyze in Sect. 7.4 how this degeneracy can be broken by taking account of other independent constraints. Nonetheless we stress that the knee of the luminosity functions is well detected throughout the redshift

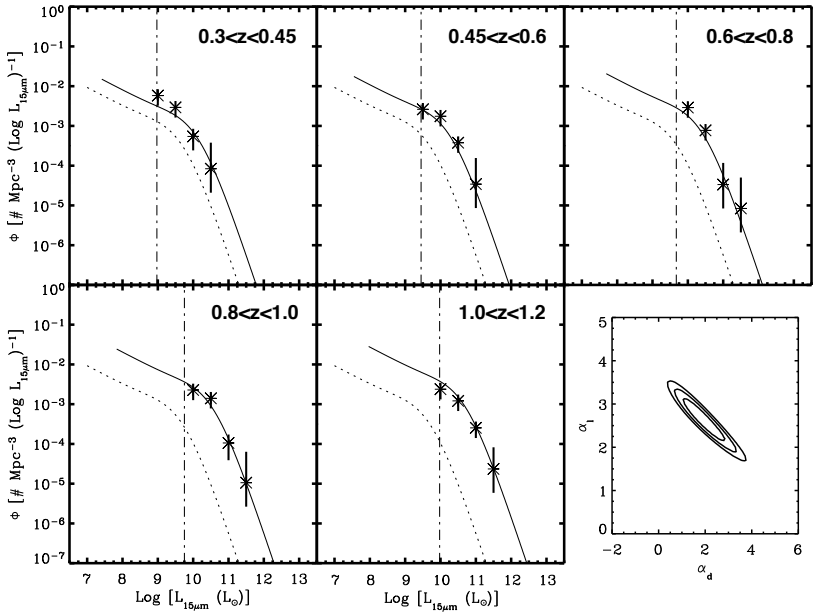

FIG. 11.— The $15\,\mu$m luminosity function estimated per redshift bin between $z=0$ and $z=1.2$ ($*$ symbols) with the $1/V_{\rm max}$ formalism. The 3σ uncertainties are indicated with vertical solid lines (see text for more details). Data points are fitted by evolving the local $15\,\mu$m LF (taken from Xu 2000 and represented as a dotted line in each panel) both in luminosity and density ($\alpha_D=2.1$, $\alpha_L=2.6$, solid line). Vertical dash-dotted lines denote the luminosity corresponding to an observed $24\,\mu$m flux of $83\,\mu$Jy (i.e., 80% completeness of the MIPS survey) calculated at the lowest redshift considered in each panel. The inset represents the 1σ, 2σ and 3σ iso-probability contours of the likelihood estimated as a function of α_D and α_L with a χ^2 test.

range considered in this work (i.e., $z \lesssim 1$). This allows us to exclude a pure evolution of the LF in density (i.e., $\alpha_{\rm L}=0$) with a very high confidence.

Because of the quasi-linearity between L_{15} and $L_{\rm IR}$ (Chary & Elbaz 2001; Takeuchi et al. 2005), these constraints on the evolution of ψ_{15} and $\psi_{\rm IR}$ should be in principle strictly similar. While they do agree rather well with each other, the extension of the contours reveal however that the evolution of the $15\,\mu$m LF seems to be better constrained than the evolution of $\psi_{\rm IR}$. As we already pointed out, LF uncertainties are largely dominated by the errors in the conversion between the $24\,\mu$m flux and the luminosities, and these errors are in fact minimized around $15\,\mu$m. Furthermore, we see that ψ_{15} might be characterized by a stronger evolution in density and a smaller evolution in luminosity compared to $\psi_{\rm IR}$. This discrepancy could be a consequence of the non-negligible dispersion that exists in the correlations observed between fluxes at mid- and far-infrared wavelengths (e.g., Helou 1986; Xu 2000; Dale et al. 2001; Dale & Helou 2002). Indeed the templates that we used to extrapolate fluxes to luminosities do not really show a pure linear relation between L_{15} and $L_{\rm IR}$ (see Fig. 8). Moreover, the constraints on α_D and α_L strongly depend on the assumed local luminosity functions, and the comparison between ϕ_{15} and ϕ_{60} (that we used to compute $\phi_{\rm IR}$) clearly reveals a non-linearity between the two. Finally, it might be suggested that our scenario based on a single evolving population is overly simplistic. Considering distinct object types characterized by their own evolution (Xu 2000; Lagache et al. 2003, 2004; Pozzi et al. 2004; Gruppioni et al. 2005), bi-variate LFs (Chapman et al. 2003b; Lewis et al. 2005) or luminosity functions only evolving at their bright end (Chary & Elbaz 2001) could be one way to explore this effect in more detail.

In spite of this apparent degeneracy, it should be however noted that the evolution of the total luminosity density $\Omega_{\rm IR}$ integrated from these infrared LFs is more

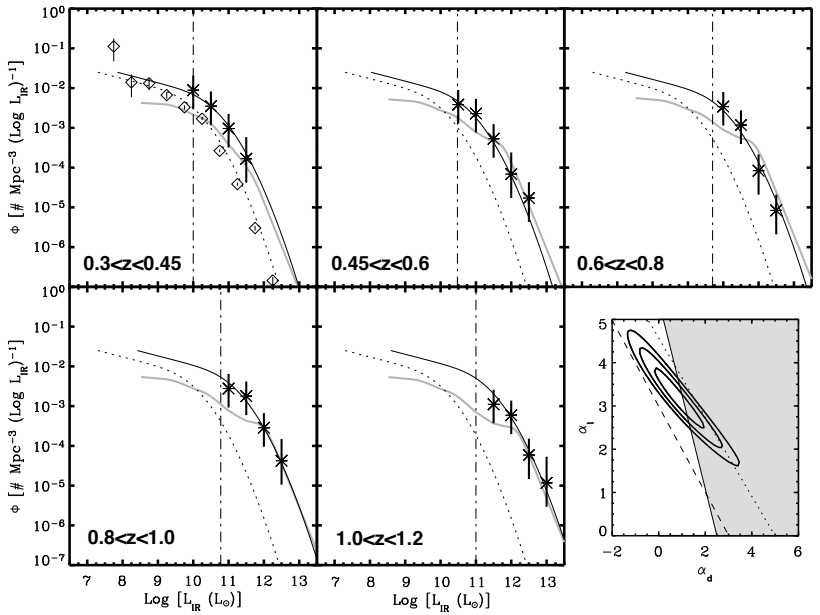

FIG. 12.— Evolution of the total IR luminosity function (same legend as in Figure 11). The fit has been obtained by evolving the total IR local LF (shown as a dotted line in each panel) with $\alpha_D=1.0$ and $\alpha_L=3.15$. This IR local luminosity function was estimated from the $60\,\mu$m LF of Takeuchi et al. (2003, see also Saunders et al. 1990) and the $60\,\mu$m/total-IR IRAS correlation (e.g., Chary & Elbaz 2001). It is compared on the first panel with the total-IR LF derived from the IRAS revised Bright Galaxy Sample (open diamonds, Sanders et al. 2003). The solid grey line represents the total IR luminosity function from the model by Lagache et al. (2004). In the inset, the dotted and dashed lines delimit a region where the parameters α_D and α_L lead to an evolution of the star formation activity that is consistent with the constraints determined by Hopkins (2004, see text for details). The shaded region corresponds to the excluded parameter space that leads to an overproduction of the $24\,\mu$m counts at faint fluxes. This constraint reduces significantly the observed degeneracy.

tightly constrained than the evolution of the characteristic parameters $L^\star_\lambda$ and $\phi^\star_\lambda$ considered separately. In each redshift bin, MIPS can indeed detect those sources responsible for the bulk of the comoving luminosity density, and the additional uncertainty related to the extrapolation for taking account of the contribution of faint objects (i.e., faint-end slope of the LF, see Sect. 7.5) is therefore not dominant. Based on the relation that we obtained between $\alpha_{\rm L}$ and $\alpha_{\rm D}$, we find that $\Omega_{\rm IR}$ evolves as $(1+z)^{3.9\pm0.4}$ at $0 \lesssim z \lesssim 1$ (see also Sect. 8 and Fig. 14).

Finally, we tested the effect of our redshift identification incompleteness at $z \gtrsim 1$ on the LF estimates by computing χ^2 including the observed luminosity function determined at $1 \leq z \leq 1.2$. For both ψ_{15} and $\psi_{\rm IR}$ the minimization of χ^2 in this case leads to a short translation of the iso-probability contours toward smaller values of α_D and larger values of α_L compared to what we previously found. This trend is consistent with expectations if ψ_λ is underestimated at $z \gtrsim 1$. Indeed the latter artificially yields a fainter evolution in density, the effect of which gets compensated in the lowest redshift bins thanks to a slight increase in luminosity. As a sanity check we finally computed χ^2 also excluding the LF obtained at $0.8 \leq z \leq 1$ where we may also be missing a few $24\,\mu$m sources fainter than $R \sim 24$ mag. The results that we found remain consistent with those initially obtained.

7.5. *Breaking degeneracies*

Hopkins (2004) combined constraints from source number counts at radio wavelengths with estimates of the comoving star formation rate (SFR) density of the Universe at high redshift to break the degeneracy that also arises when quantifying the evolution of star-forming radio-selected galaxies. Following his method we investigate in

this section how similar considerations can help in better constraining the evolution of IR galaxies.

Up to $z \sim 1$, the integrated star formation density per comoving volume of the Universe $\dot{\rho}_\star(z)$ is now well established within a factor of 2 to 3 (Hopkins 2004). Given the relationship between the total IR emission of galaxies and their obscured SFR (Kennicutt 1998), the evolution of $\psi_{\rm IR}$ converted into a history of the total dusty star-forming activity must be therefore consistent with these constraints on $\dot{\rho}_\star(z)$. We computed the "IR-equivalent SFR" as a function of redshift with different combinations of α_D and α_L. The dispersion in the relation between the flux at 24 μm and the total IR luminosity obviously affects this estimate. Moreover we stress that it should only be a lower limit on the true SFR given the un-absorbed UV photons produced by young stars and not accounted for by the IR measurements (e.g., Bell 2003, see also the $L_{\rm IR}/L_{\rm UV}$ ratio of the MIPS sources in Fig. 10c). Given these caveats and the additional uncertainty on $\dot{\rho}_\star(z)$ mentioned above, we required our IR-SFR determination to lie within 0.5 dex of the averaged relation between $\log_{10}(\dot{\rho}_\star(z))$ and $\log_{10}(1+z)$ derived by Hopkins (2004). This constraint demarcates a specific region in the luminosity and density evolution parameter space, lying between the dashed and the dotted lines shown in the inset of Figure 12. As we can see, the evolving parameters α_D and α_L that we derived from χ^2 minimization in the previous section agree well with the known history of star formation up to $z \sim 1$. However we also note that this approach does not really help in solving the aforementioned degeneracy. One may need a more accurate determination of $\dot{\rho}_\star(z)$ to progress in this direction. Alternatively, a better constraint on the conversion between $f_{24\mu m}$, $L_{\rm IR}$ and SFR might provide in the future a more accurate determination of $\dot{\rho}_\star(z)$.

A much more interesting constraint can be obtained from the source number counts. In fact we only considered 24 μm sources brighter than 83 μJy when building the luminosity functions $\psi_\lambda(L,z)$, but the counts at lower fluxes can be used to derive limits on the contribution of sources at luminosities fainter than those taken to minimize the χ^2. Using the 24 μm observations of the "GOODS test-field" centered on ELAIS-N1, Chary et al. (2004) and Papovich et al. (2004) constrained the faint source density down to $f_{24\mu m} \sim 30\,\mu$Jy and showed that the differential counts normalized to the Euclidian slope are likely dropping very rapidly below this limit. We must therefore ensure that the evolution of the infrared LF does not lead to an overproduction of these counts at faint fluxes. To check the latter we derived as a function of α_D and α_L the differential number counts that would be produced up to $z = 1$ by a population of sources described by $\psi_\lambda(L,z)$ and evolving as given by Equation 2 (see Fig. 13). We rejected the solutions overproducing the total counts obtained from the GOODS test field at the faint end. Surprisingly we found that this constraint is nearly independent of the library of IR SEDs used to describe the galaxy population. This excludes a region of the $[\alpha_D,\alpha_L]$ parameter space that is illustrated by the shaded area in the inset of Figure 12.

This additional constraint reduces significantly the number of possibilities to describe the evolution of $\psi_{\rm IR}(L,z)$. The best parameters quantifying this evolution at $0 \lesssim z \lesssim 1$ are given by $L^\star_{\rm IR} \propto (1+z)^{3.2^{+0.7}_{-0.2}}$ and $\phi^\star_{\rm IR} \propto (1+z)^{0.7^{+0.2}_{-0.6}}$ (quoted uncertainty of 1σ) . They are summarized in Table 3. In particular they exclude any solution favoring a larger evolution in density than in luminosity. This trend has already been reported by several groups using similar analysis with the *ISO* and SCUBA number counts, and the overproduction of the background resulting from a too strong increase of $\phi^\star_{\rm IR}$ is a well-known constraint on the backward evolutionary scenarios of IR galaxies. It has also been noted with models assuming pure density evolution in the Press Schechter formalism (Mould 2003).

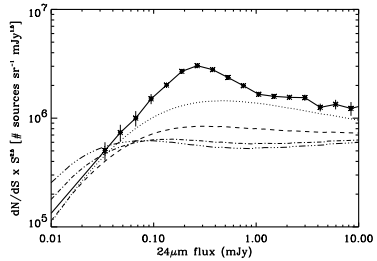

FIG. 13.— Simulated 24 μm number counts produced up to $z = 1$ by a population tied to the local IR luminosity function and evolving in luminosity and density according to various scenarios (dotted line: α_D=0.0, α_L=4.0 – dashed line: α_D=0.2, α_L=3.25 – dash-dotted line: α_D=1.5, α_L=2.75 – triple dot-dashed line: α_D=2.5, α_L=2.2). They are compared to the total observed 24 μm source number counts ('$\star$' symbols, solid line and vertical error bars) constrained and extrapolated at faint fluxes using the "GOODS test field" (Chary et al. 2004; Papovich et al. 2004). Note that a too large evolution in density clearly overproduces the counts at the faint end.

Obviously we could also use this method to further restrict the possible combinations of α_D and α_L by rejecting scenarios that overproduce the counts at bright fluxes (i.e., $f_{24\mu m} \gtrsim 0.3\,$mJy) or do not reproduce the cumulative counts discussed in Section 4. For instance the model predictions represented by the dashed line in Fig. 13 are consistent with the constraints imposed by the faint source counts but severely underestimate the true contribution of sources at $z < 1$. However we found that reproducing the bump observed at $f_{24\mu m} \sim 0.3\,$mJy is very dependent on the choice of SEDs, which could also explain why the pre-launch models had over-predicted the MIPS 24 μm number counts at these bright fluxes. Since our goal is to exclude unphysical solutions without being subject to the assumed SEDs, we did not consider further this information.

8. DISCUSSION

8.1. *Evolution and shape of the infrared luminosity function*

In the previous section we have constrained the knee and the bright end of the infrared luminosity function $\psi_{\rm IR}(L,z)$ up to $z \sim 1$. As expected our results indicate a very strong evolution of this LF with lookback time. We find that the space density of galaxies with $L_{\rm IR} \geq 10^{11}\,L_\odot$ at $z \sim 1$ exceeds by more than 100 their density in the local Universe, which is in fairly good agreement with the results from *ISO*. The quantification of the evolution depends however *very strongly* on the mid- and far-IR SEDs used to compute the k-corrections. This points to an urgent need for a more accurate characterization of infrared spectral energy distributions of normal and luminous galaxies. This goal might be achieved by combining 24, 70 and 160 μm broad-band MIPS imaging with infrared spectroscopy from the IRS spectrograph and the MIPS "SED mode".

Given the limitations due to the uncertainties of our LF estimates, we do not find any evidence for a modification of the shape of $\psi_{\rm IR}$ relative to the local luminosity function at least in the luminosity range probed with MIPS. Obviously the density of sources fainter than the 80% completeness limit of the 24 μm survey is not directly constrained and we cannot exclude a slight steepening of the LF faint-end slope at high redshifts. However, the weight of this LF by luminosity shows that the increase of energy produced by faint objects in the case of a steeper slope would be mostly driven by sources just below the knee of $\psi_{\rm IR}$, the faintest ones having a negligible contribution in spite of their larger number. The corresponding effect is then very similar to the one produced by a too large evolution of $\psi_{\rm IR}(L,z)$ in density. As we saw in the previous section it would result in an overproduction of the number counts at faint fluxes and violate therefore the constraints on the background. While the steepening of $\psi_{\rm IR}$ at the faintest end cannot be definitely ruled out, it must have marginal significance and will not affect our further discussion.

Furthermore we do not notice any obvious break in the shape of the luminosity function $\psi_{\rm IR}(L,z)$. Contrary to our simple scenario that considers the MIPS detections as a single class of objects, these breaks can occur when the LF is decomposed into the contribution of several populations (e.g., starbursts, AGNs, cold galaxies, ...) evolving independently with the redshift. As an example, they can be observed in the model proposed by Lagache et al. (2003, 2004). Based on a simple decomposition of high redshift galaxies into normal non-evolving sources and starbursts undergoing strong evolution, this model had successfully reproduced previous IR/sub-mm observations from *ISO*, SCUBA and COBE, but it fails in explaining the faint-end part of our luminosity functions because of a predicted break that is not observed (see Fig. 12). *Spitzer* provides therefore new constraints on this kind of scenario, and our results suggest in this case a smooth transition between populations so that continuity is still observed in the total luminosity function. This effect could be taken into account considering multi-variate luminosity functions (Chapman et al. 2003b; Lewis et al. 2005).

TABLE 3
PARAMETERIZATION OF THE EVOLUTION OF THE TOTAL IR LUMINOSITY FUNCTION AS A FUNCTION OF REDSHIFT[a]

Redshift range	$\phi^\star_{\rm IR}$	$L^\star_{\rm IR}$	$\alpha_{\rm IR}$	$\sigma_{\rm IR}$
$z = 0$ (local IRAS luminosity function)	0.89×10^{-2}	1.77×10^9	1.23	0.72
$0.0 \leq z \leq 0.3$	$0.98^{+0.03}_{-0.08} \times 10^{-2}$	$2.77^{+0.28}_{-0.08} \times 10^9$	1.23	0.72
$0.3 \leq z \leq 0.45$	$1.11^{+0.07}_{-0.19} \times 10^{-2}$	$4.91^{+1.23}_{-0.30} \times 10^9$	1.23	0.72
$0.45 \leq z \leq 0.6$	$1.20^{+0.11}_{-0.27} \times 10^{-2}$	$6.84^{+2.35}_{-0.55} \times 10^9$	1.23	0.72
$0.6 \leq z \leq 0.8$	$1.29^{+0.14}_{-0.35} \times 10^{-2}$	$9.7^{+4.4}_{-4.0} \times 10^9$	1.23	0.72
$0.8 \leq z \leq 1.0$	$1.40^{+0.19}_{-0.45} \times 10^{-2}$	$13.8^{+7.8}_{-4.7} \times 10^9$	1.23	0.72
$1.0 \leq z \leq 1.2$	$1.50^{+0.24}_{-0.54} \times 10^{-2}$	$19.0^{+13.0}_{-2.6} \times 10^9$	1.23	0.72

[a] assuming a ΛCDM cosmology with $H_0 = 70$ km s^{-1} Mpc^{-1}, $\Omega_m = 0.3$ and $\Omega_\lambda = 0.7$.

8.2. *Comparison with results from the previous long-wavelength surveys*

Over the last decade cosmological surveys conducted with *ISO* mainly at 15 μm, 90 μm and 170 μm provided direct evidence for the importance of infrared luminous sources at $0 \lesssim z \lesssim 1$, while submillimeter observations with SCUBA revealed a very high density of dusty galaxies with $L_{\rm IR} \geq 10^{12}\,L_\odot$ at very high redshifts (i.e., $z \gtrsim 2$). Number counts and redshift distributions that were derived from these surveys as well as the direct measurement of the far-infrared background by COBE already allowed determination of some constraints on the evolution of the infrared energy density with redshift (e.g., Blain et al. 1999b; Franceschini et al. 2001).

MIPS is however the first infrared instrument with good enough sensitivity to obtain a direct measurement of the mid-IR luminosity function up to $z \sim 1$ (but see Pozzi et al. 2004; Serjeant et al. 2004 for LFs at intermediate redshifts). It might therefore be worth comparing the constraints obtained from this work with earlier results from the literature. First, our 24 μm survey not only excludes very clearly the possibility of a pure evolution of the IR luminosity function in $\phi^\star$, but it also reveals a much stronger evolution of $\psi_{\rm IR}$ in luminosity than in density (i.e., $\alpha_L \gg \alpha_D$). This trend confirms previous interpretations of long-wavelength surveys and implies that the contribution of dusty luminous galaxies was significantly more important in the past. Our evolution constraints (i.e., $L^\star_{\rm IR} \propto (1+z)^{\sim 3.5}$ and $\phi^\star_{\rm IR} \propto (1+z)^{\sim 0.5}$) show good agreement with previously published analysis (e.g., Blain et al. 1999a,b; Franceschini et al. 2001; Lagache et al. 2003; Chapman et al. 2002; Lewis et al. 2005). However our data do not seem to be consistent with a luminosity evolution stronger than $\alpha_L \sim 4.5$ as in several scenarios examined by Chary & Elbaz (2001) and Xu (2000), unless one adds a decrease in density ($\alpha_D < 0$).

Our analysis moreover agrees with the constraints on the LFs of star-forming galaxies recently derived from the radio sub-mJy source number counts and the history of star formation. An evolution slightly lower than our estimate ($\alpha_L = 2.7 \pm 0.6, \alpha_D = 0.15 \pm 0.6$) has been obtained with this approach by Hopkins (2004), but it is still consistent with our results within the large uncertainties. The small discrepancy could also originate from the likely different levels of AGN contamination characterizing populations selected at 24 μm and at radio wavelengths.

While our results on the mid- and total IR luminosity functions are still consistent with each other, we finally note that our constraints on ψ_{15} seem to require a stronger evolution in density and a smaller evolution in luminosity compared to $\psi_{\rm IR}$. We have not yet understood whether this trend is physically real and reveals the need for a more complex evolutionary scenario than the one we have assumed, or whether it is artificially produced by the infrared SEDs used to compute luminosities. Interestingly, the need for a strong evolution of the mid-IR LF in density has also been suggested by Pozzi et al. (2004) based on the ELAIS 15 μm surveys (see also Gruppioni et al. 2005). A direct comparison between our analysis and their results must however be done with caution. Pozzi et al. (2004) decomposed their sample into the contribution of non-evolving galaxies that dominate the 15 μm counts at low redshift, and distant starbursts responsible for the increase of the IR energy density. Given the negligible role of these starbursts at $z \sim 0$, their evolution must be therefore stronger than that of the global sample. This may explain why the evolving parameters that they derived are slightly larger than ours (i.e., $\alpha_L = 3.5^{+1.0}_{-3.5}, \alpha_D = 3.8^{+2.0}_{-2.0}$). Note that this approach was also used by Xu et al. (2001) and led to a qualitatively similar trend.

8.3. *The evolving contribution of infrared luminous galaxies to star formation activity up to $z \sim 1$*

The constraints on the evolution of $\psi_{\rm IR}(L, z)$ can be used to derive the relative importance of galaxies in a given luminosity range and how their contribution to the star formation history evolves with redshift. Using the fit and the parameterization discussed in the previous section we compare in Figure 14 the evolution of the IR energy density $\Omega_{\rm IR}$ produced by infrared luminous galaxies (i.e., LIRGs + ULIRGs) and fainter sources (i.e., $\rm L_{IR} < 10^{11}\,L_\odot$). Uncertainties affecting our results are still significant due to the degeneracy previously described. Accordingly the range of possible solutions was estimated from the 3σ iso-probability contours showed in Figure 12 excluding the combinations of α_D and α_L that overproduce the counts at faint fluxes.

This evolution is also represented in terms of an "IR-equivalent SFR" using the calibration from Kennicutt (1998). For comparison we show integrated star formation rate densities estimated in various redshift bins and taken from the literature (see the compilation by Hopkins 2004 for references). It should be noted that we have not estimated the contribution of the AGN IR emission to $\Omega_{\rm IR}$. Following the arguments discussed in Sect. 5.2, we believe that such contribution results in a 10–15% overestimate in the true SFR. On the other hand this IR-SFR estimate does not take into account the contribution of the unabsorbed UV light produced by the young stars. As a result we are likely underestimating the total star formation rate density by a factor ranging between $\sim$20–30% at $z \sim 1$ (where dusty galaxies dominate the SFR) and $\sim$60–70% at $z \sim 0$ (where the star-forming activity occurs within fainter sources with low extinction). This effect can be seen by considering, in addition to the IR emission, the evolution of the UV luminosity (uncorrected for dust extinction) with redshift. Using GALEX data, Schiminovich et al. (2005) found that the energy density measured at 1 500Å evolves as $(1+z)^{\sim 2.5}$ at $0 \lesssim z \lesssim 1$, which is also consistent with previous UV measurements (e.g., Lilly et al. 1996). An estimate of the total star formation rate density (represented as a dotted line in Fig. 14) can thus be obtained by adding the contribution of the equivalent UV-uncorrected SFR (dashed line in Fig. 14) to our best fit of the evolution of the IR star formation estimate (converted from the energy density $\Omega_{\rm IR}$ evolving as $(1+z)^{3.9}$). This clearly shows that the IR emission provides a good approximation of the total SFR density at $z \sim 1$ given the uncertainties affecting its current measurements (i.e., conversion between flux and luminosity, cosmic variance).

One can see that the global evolution of the luminosity function leads to a source density increase for both populations of IR-luminous and low luminosity galaxies. However the larger increase of $L^*_{\rm IR}$ compared to $\phi^*_{\rm IR}$ results in a much more rapid evolution of sources characterized by the highest bolometric luminosities. The contribution of IR luminous galaxies, though negligible in the local Universe, becomes comparable to that of normal starbursts around $z \sim 0.7$ and they dominate beyond. We also see that such IR luminous sources are mostly dominated by LIRG-type objects up to $z \sim 1$ and that ULIRGs still have a modest impact ($\sim 10\%$) at this redshift. This is once again in good agreement with the ISOCAM surveys (e.g., Aussel et al. 1999). However these ULIRGs have undergone the fastest evolution in the last 8 Gyrs and our results suggest that their contribution is likely still rising at $z \gtrsim 1$. As already revealed by the submillimeter surveys (see Blain et al. 2002 for a review), they may therefore be responsible for a very significant fraction of the star-forming activity of the Universe at $z \sim$2–3 (see also Cowie et al. 2004).

How can this strong evolution observed in the infrared be understood in the general context of the growth of structures ? There is now increasing evidence that the most massive galaxies seem to have formed their stars early in cosmic history and that their contribution to the comoving SFR density of the Universe was significantly larger at higher redshifts (e.g., Cowie et al. 1996; Cimatti et al. 2004; Daddi et al. 2004; Juneau et al. 2005). Similarly it has been shown that a significant fraction of galaxies with masses $\mathcal{M} \gtrsim 10^{10}\,\mathcal{M}_\odot$ at $z \sim$ 0.7-1.0 are experiencing a violent episode of star formation, while nearly all equally-massive sources at the present day are found in a very quiescent mode (e.g., Flores et al. 1999; Franceschini et al. 2003; Bell et al. 2005; Hammer et al. 2005). In parallel to this downsizing effect characteristic of the stellar mass assembly history, the evolution of the luminosity function at infrared and submillimeter wavelengths reveals a transfer of the star formation from the most luminous high redshift sources

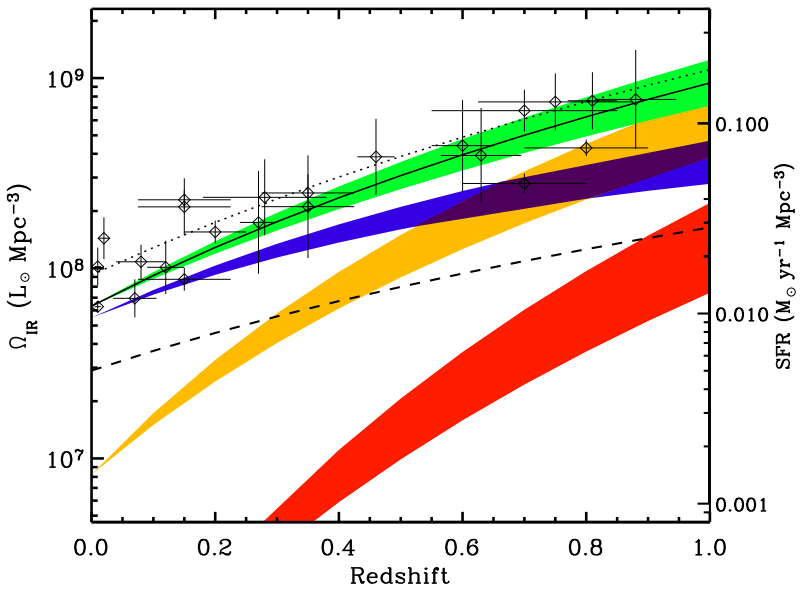

FIG. 14.— Evolution of the comoving IR energy density up to $z = 1$ (green-filled region) and the respective contributions from low luminosity galaxies (i.e., $\rm L_{IR} < 10^{11}\,L_\odot$, blue-filled area), "infrared luminous" sources (i.e., $\rm L_{IR} \geq 10^{11}\,L_\odot$, orange-filled region) and ULIRGs (i.e., $\rm L_{IR} \geq 10^{12}\,L_\odot$, red-filled region). The lower and upper curves delimiting these regions result from the degeneracy in the evolution of $\psi_{\rm IR}$ (see Sect. 7 for more details). The solid line evolves as $(1+z)^{3.9}$ and represents the best fit of the total IR luminosity density at $0 \lesssim z \lesssim 1$. Estimates are translated into an "IR-equivalent SFR" density given on the right vertical axis, where an absolute additional uncertainty of $\sim$0.3 dex should be added to reflect the dispersion in the conversion between luminosities and SFR. Note that the percentage of the contribution from each population is likely independent of this conversion. The dashed line corresponds to the SFR measured from the UV luminosity *not corrected from dust extinction*. The dotted line represents the best estimate of the total star formation rate density as the sum of this uncorrected UV contribution and the best fit of the IR-SFR (solid line). At $z \sim 1$ IR luminous galaxies represent 70±15% of the comoving IR energy density and dominate the star formation activity. Open diamonds, vertical and horizontal bars represent integrated star formation rate densities and their uncertainties estimated within various redshift bins and taken from the literature (Connolly et al. 1997; Tresse & Maddox 1998; Treyer et al. 1998; Flores et al. 1999; Cowie et al. 1999; Haarsma et al. 2000; Machalski & Godlowski 2000; Sullivan et al. 2001; Condon et al. 2002; Sadler et al. 2002; Serjeant et al. 2002; Tresse et al. 2002; Wilson et al. 2002; Pérez-González et al. 2003; Pozzi et al. 2004; see the compilation by Hopkins 2004).

to more modest local starbursts. If we consider that LIRGs and ULIRGs are preferentially associated with more massive systems (see Fig. 10d), this result might be closely related to the mass growth picture described above. However the connection between the two is likely more subtle as we found that the fraction of IR luminous sources with $\mathcal{M} \lesssim 10^{10}\,\mathcal{M}_\odot$ is not negligible either. The relation between IR luminosities and masses has indeed a large dispersion and the dominant contribution of LIRGs/ULIRGs to the star formation at $z \sim 1$ does not necessarily imply that the SFR at these redshifts is only locked in massive systems. A similar conclusion has been proposed by Juneau et al. (2005), who showed that the star formation density at $z \sim 1$ was dominated by systems with $\mathcal{M} \lesssim 10^{10.5}\,\mathcal{M}_\odot$. Much larger samples of sources will be required to address this issue in more detail, especially by de-projecting the comoving SFR density into the IR-luminosity/mass/redshift 3-dimensional space. This goal could be achieved in the very near future by combining all the MIPS cosmological surveys that are currently being carried out with *Spitzer*.

9. CONCLUSION

We have analyzed a sample of MIPS/*Spitzer* 24 μm sources detected in the Chandra Deep Field South using ancillary optical data from the literature (i.e., mag-

nitudes, spectroscopic and photometric redshifts). Our results can be summarized as follows:

- For $24\,\mu$m sources brighter than $\sim 80\,\mu$Jy, the selection criterion $R \lesssim 24$ mag provides a complete sample of optical counterpart identifications up to $z \sim 0.8$.
- About 55-60% of the $24\,\mu$m objects brighter than $\sim 80\,\mu$Jy are located at $z \lesssim 1$, which points to a significant fraction of the MIPS $24\,\mu$m sources being luminous and ultra-luminous infrared galaxies at even higher redshifts.
- The $24\,\mu$m source population at $0.5 \lesssim z \lesssim 1.0$ is dominated by LIRG-type objects and slightly fainter sources (i.e., $L_{IR} \lesssim 10^{11}\,L_{IR}$). ULIRGs are found to be rare at these redshifts.
- The conversion between fluxes and luminosities depends strongly on the assumed infrared SEDs. This points to a crucial need for more accurate determinations of IR templates, a goal which could be achieved with MIPS and IRS.
- As in the local Universe, infrared luminous sources up to $z \sim 1$ are also luminous at optical wavelengths and they tend to be more massive than the bulk of optically-selected distant galaxies.
- The comoving energy density measured in the infrared evolves as $(1+z)^{3.9\pm0.4}$ at $0 \lesssim z \lesssim 1$. In contrast, the luminosity density in the UV only evolves as $(1+z)^{\sim 2.5}$ over the similar redshift range. This points to a more important extinction by dust reprocessing light in the IR at high redshift.
- The infrared-selected sources at $0 \lesssim z \lesssim 1$ have undergone strong evolution characterized by $L^{\star}_{IR} \propto (1+z)^{3.2^{+0.7}_{-0.2}}$ and $\phi^{\star}_{IR} \propto (1+z)^{0.7^{+0.2}_{-0.6}}$. At $z \sim 1$, infrared luminous galaxies (i.e., $L_{IR} \gtrsim 10^{11}\,L_{\odot}$) appear to be responsible for 70±15% of the comoving IR energy density. They dominate the star-forming activity beyond $z \sim 0.7$.

We thank the funding from the MIPS project which is supported by NASA through the Jet Propulsion Laboratory (subcontract #960785), as well as the *Spitzer* Science Center for efficient technical support. We also appreciated the use of data products from the *Two Micron All Sky Survey*, which is a joint project of the University of Massachusetts and the Infrared Processing and Analysis Center (California Institute of Technology), funded by NASA and the National Science Foundation. We acknowledge various worldwide teams for publicly providing their redshift catalogs in the Chandra Deep Field South, and we are particularly grateful to Jim Cadien for helping us in the data anlysis process. We are also indebted to Pierre Chanial, Ranga-Ram Chary, Daniel Dale, David Elbaz, Carlotta Gruppioni, Chris Pearson and Francesca Pozzi for providing us with their library of IR galaxy templates and/or detailed predictions from their models, and we thank our referee Stephen Serjeant for critical comments on the manuscript. ELF is grateful to Lee Armus, Vassilis Charmandaris, Arjun Dey, Daniel Eisenstein, David Elbaz, George Helou, Terry Herter and Andrew Hopkins for stimulating discussions related to the work presented in this paper.

APPENDIX

SELECTION EFFECTS IN THE SAMPLE OF $24\,\mu$M SOURCES

In this work we imposed a selection criterion $R \leq 24$ mag when considering the $24\,\mu$m sources identified with a photometric redshift from the COMBO-17 survey. As we showed in Sect. 3, this selection obviously results in an incompleteness of the MIPS-selected population at $z \gtrsim 0.8$-1.0. We provide in this Appendix a few more details characterizing the possible nature of the sources that we may have missed in the estimate of the LFs at high redshift.

In Figure 15 we show the relation between the $R - 24\mu m$ color and the R-band magnitude of the MIPS sources identified with an optical counterpart from COMBO-17 (top panel). The $24\,\mu$m Vega magnitudes were calculated assuming a Zero Point of 7.3 Jy as defined in the *Spitzer Observing Manual*.[10] As pointed out in Sect. 6, the apparently well-defined correlation that is observed is a natural consequence of the small range of $24\,\mu$m fluxes (typically a factor of ~ 10 over our sample) compared to the much larger range (~ 5 magnitudes) covered by the optical counterparts of the MIPS sources (see also Fig. 8a). If we only consider $24\,\mu$m objects brighter than the 80% completeness of our survey (i.e., $f_{24\mu m} \geq 83\,\mu$Jy), we see that the selection at $R = 24$ mag defines a complete sample up to $R - 24\mu m \sim 11.6$. We miss therefore the reddest sources of the MIPS catalog (shaded region of Fig. 1).

To get a hint into the possible nature of these targets, we also plot in figure 15 the total infrared luminosities (as derived in Sect. 5) versus the $R - 24\mu m$ colors for the MIPS sources identified with a spectroscopic or a photometric redshift (bottom panel). Different symbols are used to highlight sources as a function of the R-band magnitude. As we see, $24\,\mu$m objects redder than $R - 24\mu m \sim 11.6$ are not obviously the most extreme in terms of dust emission and their luminosity can vary between $\sim 5 \times 10^{10}\,L_{\odot}$ and a few $10^{12}\,L_{\odot}$ in the infrared. Even though sources fainter than $R \sim 24$ mag may follow a different trend, this dispersion of L_{IR} with both the color and the R-band magnitude suggests that these sources span a wide range of IR luminosities. Taking into account the evolution of the sensivity limit with redshift in our $24\,\mu$m survey (see Fig. 7), they should thus be located in a wide range of redshifts at $z \gtrsim 1$.

REFERENCES

Appleton, P. N., Fadda, D. T., Marleau, F. R., et al. 2004, ApJS, 154, 147
Armus, L., Charmandaris, V., Spoon, H. W. W., et al. 2004, ApJS, 154, 178
Aussel, H., Cesarsky, C. J., Elbaz, D., & Starck, J. L. 1999, A&A, 342, 313
Bell, E. F. 2003, ApJ, 586, 794
Bell, E. F. & de Jong, R. S. 2001, ApJ, 550, 212

[10] An electronic version is available at http://ssc.spitzer.caltech.edu/documents/SOM/

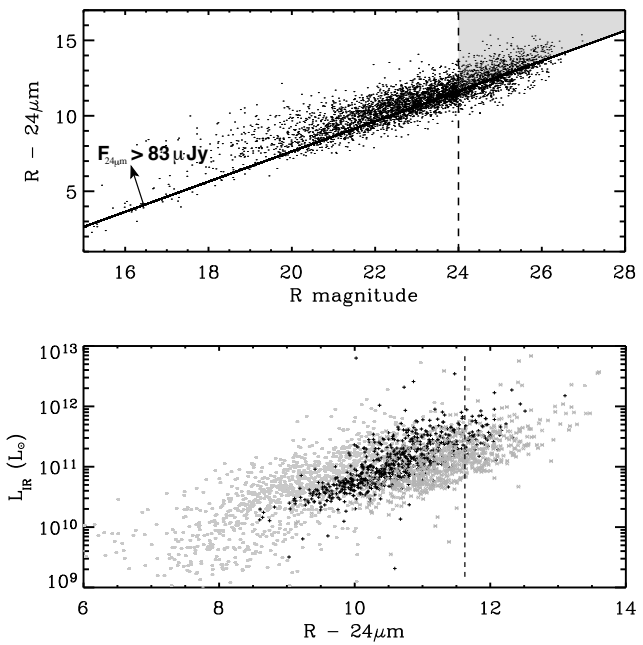

FIG. 15.— *Top:* The $R-24\,\mu$m color as a function of the R-band magnitude for the MIPS sources identified with an optical counterpart in COMBO-17. Sources above the solid line are brighter than the 80% completeness limit of the MIPS $24\,\mu$m survey (i.e., $f_{24\mu m} \geq 83\,\mu$Jy). Given the selection criterion $R \leq 24$ mag (dashed line), sources redder than $R-24\,\mu m \sim 11.6$ in the shaded region are therefore missed when deriving the luminosity functions in Sect. 7. *Bottom:* The total IR luminosities (see Sect. 5) versus the $R-24\,\mu$m color for the MIPS sources with $R \leq 22$ mag (grey filled squares), $22\,\text{mag} < R \leq 23\,\text{mag}$ ('+' black symbols) and $23\,\text{mag} < R \leq 24\,\text{mag}$ ('×' grey symbols). The vertical dashed line represents the color selection $R-24\,\mu m = 11.6$. Note that the reddest sources still span a wide range of IR luminosities.

Bell, E. F., McIntosh, D. H., Katz, N., & Weinberg, M. D. 2003, ApJS, 149, 289
Bell, E. F., Papovich, C., Wolf, C., et al. 2005, ApJ, in press (astro-ph/0502246)
Bell, E. F., Wolf, C., Meisenheimer, K., et al. 2004, ApJ, 608, 752
Benítez, N. 2000, ApJ, 536, 571
Blain, A. W., Kneib, J.-P., Ivison, R. J., & Smail, I. 1999a, ApJ, 512, L87
Blain, A. W., Smail, I., Ivison, R. J., & Kneib, J.-P. 1999b, MNRAS, 302, 632
Blain, A. W., Smail, I., Ivison, R. J., Kneib, J.-P., & Frayer, D. T. 2002, Phys. Rep., 369, 111
Buat, V., Boselli, A., Gavazzi, G., & Bonfanti, C. 2002, A&A, 383, 801
Cardiel, N., Elbaz, D., Schiavon, R. P., et al. 2003, ApJ, 584, 76
Chanial, P. 2003, PhD thesis, University of Paris (France)
Chapman, S. C., Blain, A. W., Ivison, R. J., & Smail, I. R. 2003a, Nature, 422, 695
Chapman, S. C., Helou, G., Lewis, G. F., & Dale, D. A. 2003b, ApJ, 588, 186
Chapman, S. C., Lewis, G. F., Scott, D., Borys, C., & Richards, E. 2002, ApJ, 570, 557
Charmandaris, V., Laurent, O., Le Floc'h, E., et al. 2002, A&A, 391, 429
Charmandaris, V., Le Floc'h, E., & Mirabel, I. F. 2004, ApJ, 600, L15
Chary, R., Casertano, S., Dickinson, M. E., et al. 2004, ApJS, 154, 80
Chary, R. & Elbaz, D. 2001, ApJ, 556, 562
Cimatti, A., Daddi, E., Renzini, A., et al. 2004, Nature, 430, 184
Condon, J. J. 1992, ARA&A, 30, 575
Condon, J. J., Cotton, W. D., & Broderick, J. J. 2002, AJ, 124, 675
Connolly, A. J., Szalay, A. S., Dickinson, M., Subbarao, M. U., & Brunner, R. J. 1997, ApJ, 486, L11+

Cowie, L. L., Barger, A. J., Fomalont, E. B., & Capak, P. 2004, ApJ, 603, L69
Cowie, L. L., Songaila, A., & Barger, A. J. 1999, AJ, 118, 603
Cowie, L. L., Songaila, A., Hu, E. M., & Cohen, J. G. 1996, AJ, 112, 839
Daddi, E., Cimatti, A., Renzini, A., et al. 2004, ApJ, 600, L127
Dale, D. A. & Helou, G. 2002, ApJ, 576, 159
Dale, D. A., Helou, G., Contursi, A., Silbermann, N. A., & Kolhatkar, S. 2001, ApJ, 549, 215
Dole, H., Gispert, R., Lagache, G., et al. 2001, A&A, 372, 364
Dole, H., Le Floc'h, E., Pérez-González, P. G., et al. 2004a, ApJS, 154, 87
Dole, H., Rieke, G. H., Lagache, G., et al. 2004b, ApJS, 154, 93
Efstathiou, G., Ellis, R. S., & Peterson, B. A. 1988, MNRAS, 232, 431
Egami, E., Dole, H., Huang, J.-S., et al. 2004, ApJS, 154, 130
Eisenhardt, P. R., Stern, D., Brodwin, M., et al. 2004, ApJS, 154, 48
Elbaz, D., Cesarsky, C. J., Chanial, P., et al. 2002, A&A, 384, 848
Elbaz, D., Cesarsky, C. J., Fadda, D., et al. 1999, A&A, 351, L37
Elbaz, D., Le Floc'h, E., Dole, H., & Marcillac, D. 2005, A&A, 434, L1
Fadda, D., Flores, H., Hasinger, G., et al. 2002, A&A, 383, 838
Fazio, G. G., Ashby, M. L. N., Barmby, P., et al. 2004, ApJS, 154, 39
Felten, J. E. 1976, ApJ, 207, 700
Flores, H., Hammer, F., Désert, F. X., et al. 1999, A&A, 343, 389
Flores, H., Hammer, F., Elbaz, D., et al. 2004, A&A, 415, 885
Franceschini, A., Aussel, H., Cesarsky, C. J., Elbaz, D., & Fadda, D. 2001, A&A, 378, 1
Franceschini, A., Berta, S., Rigopoulou, D., et al. 2003, A&A, 403, 501
Franceschini, A., Manners, J., Polletta, M., et al. 2005, AJ, in press (astro-ph/0412476)
Frayer, D. T., Chapman, S. C., Yan, L., et al. 2004, ApJS, 154, 137
Gallais, P., Charmandaris, V., Le Floc'h, E., et al. 2004, A&A, 414, 845
Gispert, R., Lagache, G., & Puget, J. L. 2000, A&A, 360, 1
Gordon, K. D., Rieke, G. H., Engelbracht, C. W., et al. 2005, PASP, in press (astro-ph/0502079)
Gruppioni, C., Pozzi, F., Lari, C., Oliver, S., & Rodighiero, G. 2005, ApJ, 618, L9
Haarsma, D. B., Partridge, R. B., Windhorst, R. A., & Richards, E. A. 2000, ApJ, 544, 641
Hammer, F., Flores, H., Elbaz, D., et al. 2005, A&A, 430, 115
Helou, G. 1986, ApJ, 311, L33
Hopkins, A. M. 2004, ApJ, 615, 209
Houck, J. R., Charmandaris, V., Brandl, B. R., et al. 2004a, ApJS, 154, 211
Houck, J. R., Roellig, T. L., van Cleve, J., et al. 2004b, ApJS, 154, 18
Houck, J. R., Soifer, B. T., Weedman, D., et al. 2005, ApJ, 622, L105
Huchra, J. & Sargent, W. L. W. 1973, ApJ, 186, 433
Ivison, R. J., Greve, T. R., Serjeant, S., et al. 2004, ApJS, 154, 124
Jarrett, T. H., Chester, T., Cutri, R., et al. 2000, AJ, 119, 2498
Juneau, S., Glazebrook, K., Crampton, D., et al. 2005, ApJ, 619, L135
Kauffmann, G., Heckman, T. M., White, S. D. M., et al. 2003, MNRAS, 341, 54
Kennicutt, R. C. 1998, ARA&A, 36, 189
Kim, D.-C. & Sanders, D. B. 1998, ApJS, 119, 41
Lagache, G., Dole, H., & Puget, J.-L. 2003, MNRAS, 338, 555
Lagache, G., Dole, H., Puget, J.-L., et al. 2004, ApJS, 154, 112
Laurent, O., Mirabel, I. F., Charmandaris, V., et al. 2000, A&A, 359, 887
Le Fèvre, O., Vettolani, G., Paltani, S., et al. 2004, A&A, 428, 1043
Le Floc'h, E., Charmandaris, V., Laurent, O., et al. 2002, A&A, 391, 417
Le Floc'h, E., Mirabel, I. F., Laurent, O., et al. 2001, A&A, 367, 487
Le Floc'h, E., Pérez-González, P. G., Rieke, G. H., et al. 2004, ApJS, 154, 170
Lewis, G. F., Chapman, S. C., & Helou, G. 2005, ApJ, 621, 32
Liang, Y. C., Hammer, F., Flores, H., et al. 2004, A&A, 423, 867
Lilly, S. J., Le Fevre, O., Hammer, F., & Crampton, D. 1996, ApJ, 460, L1
Lonsdale, C., Polletta, M. d. C., Surace, J., et al. 2004, ApJS, 154, 54
Lutz, D., Spoon, H. W. W., Rigopoulou, D., Moorwood, A. F. M., & Genzel, R. 1998, ApJ, 505, L103
Machalski, J. & Godlowski, W. 2000, A&A, 360, 463
Manners, J. C., Serjeant, S., Bottinelli, S., et al. 2004, MNRAS, 355, 97
Marleau, F. R., Fadda, D., Storrie-Lombardi, L. J., et al. 2004, ApJS, 154, 66
Mould, J. 2003, ApJ, 587, L93
Pérez-González, P. G., Zamorano, J., Gallego, J., Aragón-Salamanca, A., & Gil de Paz, A. 2003, ApJ, 591, 827
Papovich, C. & Bell, E. F. 2002, ApJ, 579, L1
Papovich, C., Dole, H., Egami, E., et al. 2004, ApJS, 154, 70
Pearson, C. 2005, MNRAS, 358, 1417
Pozzi, F., Ciliegi, P., Gruppioni, C., et al. 2003, MNRAS, 343, 1348
Pozzi, F., Gruppioni, C., Oliver, S., et al. 2004, ApJ, 609, 122
Rieke, G. H. & Low, F. J. 1972, ApJ, 176, L95
Rieke, G. H., Young, E. T., Engelbracht, C. W., et al. 2004, ApJS, 154, 25
Rigby, J. R., Rieke, G. H., Maiolino, R., et al. 2004, ApJS, 154, 160
Rigopoulou, D., Franceschini, A., Aussel, H., et al. 2002, ApJ, 580, 789
Roussel, H., Sauvage, M., Vigroux, L., & Bosma, A. 2001, A&A, 372, 427
Sadler, E. M., Jackson, C. A., Cannon, R. D., et al. 2002, MNRAS, 329, 227
Salpeter, E. E. 1955, ApJ, 121, 161
Sanders, D. B., Mazzarella, J. M., Kim, D.-C., Surace, J. A., & Soifer, B. T. 2003, AJ, 126, 1607
Sanders, D. B. & Mirabel, I. F. 1996, ARA&A, 34, 749
Saunders, W., Rowan-Robinson, M., Lawrence, A., et al. 1990, MNRAS, 242, 318
Schiminovich, D., Ilbert, O., Arnouts, S., et al. 2005, ApJ, 619, L47
Schmidt, M. 1968, ApJ, 151, 393
Serjeant, S., Carramiñana, A., Gonzáles-Solares, E., et al. 2004, MNRAS, 355, 813
Serjeant, S., Efstathiou, A., Oliver, S., et al. 2001, MNRAS, 322, 262
Serjeant, S., Gruppioni, C., & Oliver, S. 2002, MNRAS, 330, 621
Silva, L., Maiolino, R., & Granato, G. L. 2004, MNRAS, 355, 973
Smail, I., Ivison, R. J., & Blain, A. W. 1997, ApJ, 490, L5
Smith, J. D. T., Dale, D. A., Armus, L., et al. 2004, ApJS, 154, 199
Soifer, B. T. & Neugebauer, G. 1991, AJ, 101, 354
Soifer, B. T., Neugebauer, G., & Houck, J. R. 1987, ARA&A, 25, 187
Soifer, B. T., Neugebauer, G., Matthews, K., et al. 2000, AJ, 119, 509
—. 2001, AJ, 122, 1213
Somerville, R. S., Lee, K., Ferguson, H. C., et al. 2004, ApJ, 600, L171
Spergel, D. N., Verde, L., Peiris, H. V., et al. 2003, ApJS, 148, 175
Spinoglio, L., Malkan, M. A., Rush, B., Carrasco, L., & Recillas-Cruz, E. 1995, ApJ, 453, 616
Stetson, P. B. 1987, PASP, 99, 191
Sullivan, M., Mobasher, B., Chan, B., et al. 2001, ApJ, 558, 72
Szokoly, G. P., Bergeron, J., Hasinger, G., et al. 2004, ApJS, 155, 271
Takeuchi, T. T., Buat, V., Iglesias-Páramo, J., Boselli, A., & Burgarella, D. 2005, A&A, 432, 423
Takeuchi, T. T., Yoshikawa, K., & Ishii, T. T. 2003, ApJ, 587, L89
Thuan, T. X., Sauvage, M., & Madden, S. 1999, ApJ, 516, 783
Tran, Q. D., Lutz, D., Genzel, R., et al. 2001, ApJ, 552, 527
Tresse, L. & Maddox, S. J. 1998, ApJ, 495, 691
Tresse, L., Maddox, S. J., Le Fèvre, O., & Cuby, J.-G. 2002, MNRAS, 337, 369
Treyer, M. A., Ellis, R. S., Milliard, B., Donas, J., & Bridges, T. J. 1998, MNRAS, 300, 303
Vanzella, E., Cristiani, S., Dickinson, M., et al. 2005, A&A, 434, 53
Werner, M. W., Roellig, T. L., Low, F. J., et al. 2004, ApJS, 154, 1
Willmer, C. N. A. 1997, AJ, 114, 898
Wilson, G., Cowie, L. L., Barger, A. J., & Burke, D. J. 2002, AJ, 124, 1258

Wolf, C., Meisenheimer, K., Kleinheinrich, M., et al. 2004, A&A, 421, 913
Wolf, C., Meisenheimer, K., Rix, H.-W., et al. 2003, A&A, 401, 73
Xu, C. 2000, ApJ, 541, 134
Xu, C., Hacking, P. B., Fang, F., et al. 1998, ApJ, 508, 576
Xu, C., Lonsdale, C. J., Shupe, D. L., O'Linger, J., & Masci, F. 2001, ApJ, 562, 179
Yan, L., Helou, G., Fadda, D., et al. 2004, ApJS, 154, 60
Zheng, X. Z., Hammer, F., Flores, H., Assémat, F., & Pelat, D. 2004, A&A, 421, 847

Astronomy & Astrophysics manuscript no. elbaz February 28, 2005
(DOI: will be inserted by hand later)

Observational evidence for the presence of PAHs in distant Luminous Infrared Galaxies using ISO and *Spitzer*

D. Elbaz[1], E. Le Floc'h[2], H. Dole[3], D. Marcillac[1]⋆

[1] DSM/DAPNIA/Service d'Astrophysique, CEA/SACLAY, 91191 Gif-sur-Yvette Cedex, France
[2] Steward Observatory, University of Arizona, 933 N Cherry Ave, 85721 Tucson, AZ, USA
[3] Institut d'Astrophysique Spatiale, bât 121, Université Paris-Sud, F-91405 Orsay Cedex, France

Received: ; Accepted:

Abstract. We present ISOCAM 15 μm and MIPS 24 μm photometry of a sample of 16 distant Luminous Infrared Galaxies (LIRGs) characterized by a median luminosity $L_{IR} \sim 2\times10^{11}$ $L_\odot$ and redshift $z = 0.7$ (distributed from $z = 0.1$ to 1.2). While some sources display 24/15 μm flux ratios also consistent with a featureless continuum dominating their mid-infrared (MIR) spectral energy distributions (SEDs), the presence of prominent emission features such as the Polycyclic Aromatic Hydrocarbons is clearly required to explain the observed colors for more than half of the sample. As a result, a general good agreement is observed between the data and predictions from the local starburst-dominated SEDs that have been used so far to constrain IR galaxy evolution. This is consistent with the star-forming nature of LIRGs derived from previous works, even though our approach cannot rule out the dominance of an AGN in some cases. Our study also supports the possibility of tracing the total IR luminosity of distant galaxies (up to $z \sim 1$) from their MIR emission.

Key words. Galaxies: evolution – Infrared: galaxies – Galaxies: starburst

1. Introduction

The excess of faint sources in the deep extragalactic surveys performed in the MIR to sub-millimeter with their associated redshift distributions when available, together with the shape and intensity of the cosmic IR background (CIRB, Puget et al. 1996), which measures the extragalactic IR light radiated above 3 μm and is at least equal to the UV to near-IR extragalactic background light (Gispert et al. 2000; Hauser & Dwek 2001), suggest that a large fraction of the UV radiation of young stars was reprocessed by dust in the mid to far IR range over the Hubble time. The cosmic star formation history- the star formation rate (SFR) per unit comoving volume as a function of redshift- would be dominated by intense star formation phases, during which the bulk of the UV light is reprocessed by dust in the IR with a rapid decline of the SFR density since $z \sim 1$ and a flat or possibly slow increase from $z \sim 5$ to 1 (Chary & Elbaz 2001, Lagache et al. 2004 and references therein). These models called "backward evolution models" because they evolve the local luminosity function in the MIR as a function of redshift, assume that the shapes of distant SEDs in the MIR remain similar to the ones observed in local galaxies and are directly related to the total IR luminosity.

The goal of the present study is to check the validity of this assumption up to $z \sim 1$ by combining data from ISOCAM (Cesarsky et al. 1996a), the MIR camera onboard the Infrared Space Observatory (ISO, Kessler et al. 1996), and MIPS, the Multiband Imaging Photometer for *Spitzer* (Rieke et al. 2004) onboard the *Spitzer* Space Telescope (Werner et al. 2004). Studying the MIR shape of distant galaxies is particularly relevant since direct FIR observations are rapidly confusion limited and strongly affected by moderate sensitivity limits. On the other side of the peak of the IR SED, sub-millimeter observations are presently limited to the detection of ultra-luminous IR galaxies (ULIRGs) above $z \sim 2$ (Chapman et al. 2003). In the near future, before the launch of Herschel and the advent of ALMA, the best constraints on the evolution of luminous IR galaxies (LIRGs), i.e. galaxies with $L_{IR} \geq 10^{11}$ $L_\odot$, as a function of redshift and on their role in the global evolution of galaxies will exclusively come from the MIR. Around $z = 0.7$, LIRGs are too faint to be measured through direct spectroscopy in the MIR with the infrared spectrograph (IRS, Houck et al. 2004a) onboard *Spitzer*. The only remaining technique to contrain the MIR shape of distant LIRGs is therefore to combine MIR measurements for LIRGs located at different redshifts, hence spanning a larger range of rest-frame wavelengths. In the present study, a redshift range of $z = 0.1$-1.2 allowed us to study the 5 to 25 μm rest-frame part of the MIR SEDs. In this wavelength range (see Genzel & Cesarsky 2000), the SED is dominated by the combination of broad emission lines, generally interpreted as due to polycyclic aromatic hydrocarbons (PAHs), and of the continuum emission of stochastically heated "very small grains" of dust transiently heated to temperatures of the order of 200 K. The thermal emission of "big grains" of dust heated to $\sim$ 40 K also contributes partly to the MIR emission but peaks in the FIR (between 80 and 100 μm typically) and contains the bulk of the luminosity radiated by galaxies above 3 μm. Finally, hot dust emission due to dust heated by an active galaxy nucleus (AGN) can also contribute to and sometimes even dominate the MIR spectrum of a galaxy. Before deriving the IR luminosity for a galaxy that will be used to compute its SFR, one must start by making sure that its MIR SED is not polluted by the AGN emission. The presence of PAHs as well as a rapid decline of the continuum emission below 5 μm strongly suggests a star formation origin for the emission (Genzel & Cesarsky 2000, and references therein). Local LIRGs are rarely affected by an AGN, contrary to ULIRGs above $10^{12.3}$ $L_\odot$. Using a combination of template SEDs and deep X-ray surveys with XMM-Newton and Chandra, Fadda et al. (2002) derived an upper limit to the contribution of an AGN to the MIR light radiated by ISOCAM selected LIRGs up to $z \sim 1$ of 20 %.

The MIR emission of local star forming galaxies- at 6.75, 12 and 15 μm- was proven to correlate, with some scatter, with the total IR one, i.e. from 8 to 1000 μm, which is largely dominated by the FIR component (Chary & Elbaz 2001, Elbaz et al. 2002). However, the validity of these correlations in the more distant universe has not yet been established. Galaxies were less metal rich in the past. Their shape and compacity evolving with time might also affect their SEDs. Local galaxies SEDs do present some variations in the MIR as a function of metallicity. The metal-deficient ($Z=Z_\odot/41$) blue compact dwarf galaxy SBS 0335-052, for example, is bright in the MIR range but still does not show any sign of the presence of the PAH features which the authors interpret as an effect of the destruction of their carriers by the very high UV energy density (Thuan, Sauvage & Madden 1999, Houck et al. 2004b).

Throughout this paper, we will assume $H_o = 70$ km s^{-1} Mpc^{-1}, $\Omega_{matter} = 0.3$ and $\Omega_\Lambda = 0.7$.

2. Sample selection and data reduction

A 30'×30' field was imaged by ISOCAM at 15 μm in the Marano FIRBACK region centered on (3h13m10s,-55^{o}03'39"), about two thirds of which is covered by a larger MIPS-24 μm image of $1.4^o \times 0.7^o$ with a 80 % completeness limit of 170 μJy. The central part of this field (7'×7', UDSF for "ultra-deep survey firback") was covered down to an 80 % completeness limit of 140 μJy at 15 μm with ISOCAM, a depth similar to the MIPS one (see Fig. 1). The ISOCAM-15 μm UDSF belongs to the ISOCAM Guaranteed Time Extragalactic Surveys (IGTES, Elbaz et al. 1999). Six overlapping mosaics were performed in the micro-scanning mode of ISOCAM for a total of 2.7 hours of integration per sky pixel and leading to a final projected map with 2″ pixels. The data were reduced using PRETI (Starck et al. 1996) and the transient correction as well as the assessment of the completeness limit were computed by Monte Carlo simulations with fake sources of known flux densities in the real images.

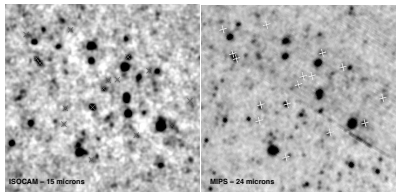

Fig. 1. *Left:* ISOCAM 15 μm image of the Marano FIRBACK field (central part of the ultra-deep survey, 7′×7′) down to an 80 % completeness limit of 140 μJy. Black X represent the positions of the common sources with MIPS plotted in the Fig. 2. *Right:* MIPS 24 μm image of the same field down to an 80 % completeness limit of 170 μJy. White X represent the position of ISOCAM sources.

The 24 μm observations were performed during the MIPS commissioning phase (IOC/SV) in November 2003. The scan map AOT was used, with an half-array overlap to cover about 1300 Sq. Arcmin with high redundancy (20) and to get an integration time per sky pixel of about 230s (Papovich et al. 2004). The data were reduced using the *Spitzer* Science Center Pipeline and the BCD products (Basic Calibrated Data, Pipeline version S10.0.3) were downloaded from the *Spitzer* archive[1]. PSF-fitting photometry was performed using DAOPHOT (Stetson 1987) with IRAF[2].

For the present study, we used a sample of 16 galaxies detected with both ISOCAM and MIPS at 15 and 24 μm respectively and identified with crosses in Fig. 1. This set of galaxies was extracted from a larger sample of ISOCAM selected galaxies for which medium resolution (R=1200) VLT-FORS2 spectra were obtained (Liang et al. 2004) in the "Marano FIRBACK" field. Oxygen abundances were obtained for half of them with values of 12+log(O/H) ranging from 8.4 to 9. With a median stellar mass of 5×10^{10} $M_\odot$ and redshift of $z \sim 0.7$, they are among the most massive galaxies in this redshift range but exhibit metallicities about twice smaller than their nearby counterparts suggesting that they will produce about half of their metals from $z = 1$ to 0 (Liang et al. 2004). Finally, it must be noted that even though no direct FIR measurement exists for this sample of galaxies at present, there is indirect evidence that the MIR-FIR correlations remain valid up to $z \sim 1$. Indeed, MIR and radio measurements provide consistent predictions for the FIR luminosity of distant galaxies up to $z \sim 1$ (Elbaz et al. 2002, Appleton et al. 2004).

Send offprint requests to: D. Elbaz, email: delbaz@cea.fr

⋆ Based on observations collected with the Spitzer Space Telescope (which is operated by the Jet Propulsion Laboratory, California Institute of Technology under NASA contract 1407) and on observations with ISO (an ESA project with instruments funded by ESA Member States (especially the PI countries: France, Germany, the Netherlands and the United Kingdom) with the participation of ISAS and NASA)

[1] http://archive.spitzer.caltech.edu, PID: 718
[2] IRAF is distributed by the National Optical Astronomy Observatories, which are operated by the Association of Universities for Research in Astronomy, Inc., under the cooperative agreement with the National Science Foundation

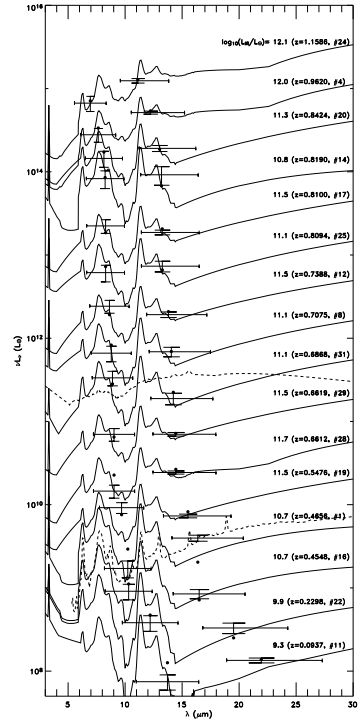

Fig. 2. All SEDs sorted (from top to bottom) by decreasing redshift. The SEDs are shifted by an arbitrary offset in νL_ν for visibility; wavelengths are rest-frame. ISOCAM 15 μm and MIPS 24 μm luminosities are reported with the filter bandwidth and the 1-σ uncertainty. The label indicates the logarithm of the IR luminosity as well as the redshift and ID of each source, e.g. ID #4 is the galaxy UDSF04 in Liang et al. (2004). The filled circles are the luminosities that would be measured in both filters for the plotted SED from the library of template SEDs of Chary & Elbaz (2001). Bold dashed line on gal.#31: SED of the AGN NGC 1068 normalized to best fit the measured 15 and 24 μm luminosities of the galaxy. Dashed line on gal.#1: SED of NGC 7714 (Brandl et al. 2004).

3. Discussion

Fig. 2 presents the 15 and 24 μm luminosities of the 16 galaxies detected with ISOCAM and MIPS in the UDSF fitted by a library of template SEDs from Chary & Elbaz (2001). This

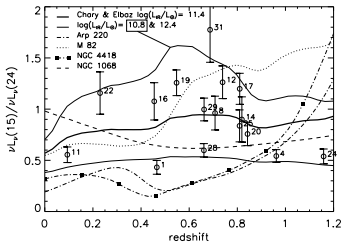

Fig. 3. The observed colors $\nu L_\nu(15)/\nu L_\nu(24)$ derived from our sample (open circles and vertical error bars, with numbers refering to IDs from Fig. 2), compared with the predictions for different object types such as the Seyfert 2 prototype NGC 1068, two enshrouded IR-luminous systems with deep silicate absorption (Arp 220 and NGC 4418), M82 ($\log(L_{IR}/L_\odot)$=10.6) and three template SEDs from Chary & Elbaz (2001, plain lines; the lowest line corresponds to $\log(L_{IR}/L_\odot)$=12.4).

library of 100 template SEDs, from $\log(L_{IR}/L_\odot)$= 8.5 to 13.5, was generated between 0.1 and 1000 μm to reproduce the trend observed for local galaxies between MIR and FIR luminosities. The MIR (4−20 μm) part was produced by interpolating between the ISOCAM CVF spectra of four prototypical galaxies (Arp220, NGC6090, M82 and M51), hence all SEDs contain PAH features. Because the 6.75, 12 and 15 μm luminosities of a local galaxy correlate with its total IR luminosity, L_{IR}, it is possible to use a single MIR measurement to derive L_{IR}, and therefore a SFR, for nearby galaxies. In "backward evolution models", such as Chary & Elbaz (2001), the 15 μm luminosity function is evolved as a function of redshift to reproduce the observe galaxy counts and the CIRB, assuming that a template SED is uniquely determined by a given 15 μm luminosity. To fill the gaps between the observed 6.75, 12 and 15 μm correlations, the templates interpolated for all total IR luminosities were used. We used the same technique to derive L_{IR}^{15} from L_{15} (measured with ISOCAM), L_{IR}^{24} from L_{24} (measured with MIPS) and L_{IR}^{15-24} from the combination of L_{15} and L_{24}. First, the 100 template SEDs were redshifted at the redshift of a given galaxy among the 16 and a flux density was determined at 15 μm using the filter response of ISOCAM. Second, the SED which 15 μm flux density was the closest to the observed one was selected and normalized to reach the observed 15 μm flux density. The total IR luminosity of this galaxy is L_{IR}^{15}. Using the same strategy, we computed L_{IR}^{24}. Lastly, we selected the SED which minimized the χ^2 of the observed 15 and 24 μm flux densities with their associated error bars and derived a third luminosity, L_{IR}^{15-24}. The MIR luminosities in the rest-frame of the galaxies (crosses proportional to the filter width and error bar on the flux density) are compared to the SEDs used to compute L_{IR}^{15-24} in Fig. 2 and their associated MIR luminosities (filled circles).

The values of L_{IR} derived by the three techniques are equal with a 1-σ dispersion of only 20 %, which confirms the robustness of this technique. Hence on average, the combination of both instruments will affect the predicted L_{IR} values with a 20 % dispersion only with respect to the use of only one of the two instruments. Hence the global shape of the template SEDs is such that it can be used to predict with this accuracy the other MIR value, suggesting that the SEDs did not vary very much since $z \sim 1$. In the "starburst" regime, i.e. below $L_{IR} = 10^{11}$ $L_\odot$, the template SEDs do not provide a good fit to the galaxy "#1" (z = 0.4656, $\log[L_{IR}/L_\odot]$=10.7), which behaves very similarly to NGC 7714 (Brandl et al. 2004) as shown in dashed line in Fig. 2. The dispersion observed even among local galaxies, for example in the MIR-FIR correlations already suggested that an ideal library of template SEDs would have to include a variation of shapes for each L_{IR} bin.

The bold SED in the middle of Fig. 2 presents a strong evidence for the presence of the 7.7 μm PAH feature, band or complex. The rest-frame 9 μm luminosity of this $10^{11.1}$ $L_\odot$ galaxy ($z \sim 0.7$) is 1.8 times larger than the 14 μm one, which is natural when PAHs are present but rules out a hot dust continuum emission as the one locally observed in individual HII regions (such as M17, Cesarsky et al. 1996b), dwarf galaxies (Thuan, Sauvage & Madden 1999) or even Compton-thick Seyfert 2's (such as NGC 1068, bold dashed line in the Fig. 2; Le Floc'h et al. 2001). The SEDs were sorted as a function of increasing redshift in the Fig. 2 in order to illustrate the effect of the k-correction which acts as a low resolution spectrograph by shifting the broadband ISOCAM and MIPS filters to lower wavelengths with increasing redshift. The good quality of the fit was obtained without allowing the luminosity of the template SEDs to vary which illustrates the very good agreement with observations at 5-25 μm rest-frame.

The templates from Chary & Elbaz (2001) are therefore consistent with the observed 24/15 μm colors of distant sources considered as a whole. However it is worth mentioning that they do not provide a unique solution for *every* galaxy of the sample, since some of them can also be fitted by a feature-less continuum (e.g., ID #25 in Fig. 2). This issue is explored with more details in Fig. 3 (similar to Fig.1 of Charmandaris et al. 2004) where we compare the colors derived from our sources with what would be observed as a function of redshift for different object types such as the Seyfert 2 prototype NGC 1068, two enshrouded IR-luminous systems with deep silicate absorption (Arp 220: Elbaz et al. 2002; NGC 4418: Spoon et al. 2001), M82 and three template SEDs (as in Fig.2). The comparison shows that galaxies with $\nu L_\nu(15)/\nu L_\nu(24) \leq 0.8$ can indeed be explained by power-law spectra with no significant contribution from PAHs. This fitting degeneracy results in an additional uncertainty in the extrapolation to the total IR luminosity (typically a factor of 2), and it also indicates that our approach is not sufficient in itself to discreminate between starbursts and AGNs. Nonetheless, a non negligible fraction of sources at $z \sim$0.2-0.8 ($\sim$40-50%) exhibit $\nu L_\nu(15)/\nu L_\nu(24)$ colors larger than $\sim$1. The latter can not be reproduced by SEDs without strong emission features redshited in the ISOCAM band and boosting the flux at 15 μm. As predicted by the starburst-dominated templates, these colors are therefore the telltale signature for the presence of PAHs in the distant Universe.

4. Conclusion

We have shown that by combining ISO and *Spitzer* in the photometric mode, it was possible to constrain the MIR SED of distant galaxies too faint to be subject to direct spectroscopy in the MIR. Deep images with both instruments and at similar depths (140 and 170 μJy at 15 and 24 μm) do detect the same objects which illustrates the robustness of both instruments. The combination of 15 and 24 μm flux densities measured with ISOCAM and MIPS was used to constrain the rest-frame 5-25 μm part of the SED of a sample of 16 LIRGs with $z \sim$ 0.1-1.2, taking advantage of the k-correction. Similar studies with larger statistics will become feasible soon by combining MIPS 24 μm with IRS 16 μm peak-up imaging. Even though some sources were found to be either consistent with a starburst or an AGN-dominated SED, a significant fraction of our sample shows clear evidence for the presence of the broad bump associated to the 7.7 μm PAH feature in emission and for the silicate feature in absorption centered at 9.7 μm. Local template SEDs fitting the correlations between MIR and FIR luminosities provide an overall good fit to the distant LIRGs supporting the possibility to use them in models fitting galaxy counts and deriving a cosmic star formation history using a "backward evolution" of the MIR luminosity function.

Acknowledgements. We are particularly grateful to B.Brandl and H.Spoon for providing us with material used in this work. ELF thanks the MIPS project which is supported by NASA through the Jet Propulsion Laboratory, subcontract #960785. DE thanks the support from the CNES.

References

Appleton, P.N., Fadda, D., Marleau, F.R., et al. 2004, ApJS, 154, 147
Brandl, B.R., Devost, D., Higdon, S.J.U., et al. 2004, ApJS, 154, 188
Cesarsky, C., Abergel, A., Agnèse, P., et al. 1996a, A&A, 315, L32
Cesarsky, D., Lequeux, J., Abergel, A., et al. 1996b, A&A, 315, L309
Chapman, S., Blain, A., Ivison, R., Smail, I. 2003, Nature, 422, 695
Charmandaris, V., Uchida, K.I., Weedman, D., et al. ApJS, 154, 142
Chary, R.R., Elbaz, D. 2001, ApJ, 556, 562
Elbaz, D., Cesarsky, C.J., Fadda, D., et al. 1999, A&A, 351, L37
Elbaz, D., Cesarsky, C.J., Chanial, P., et al. 2002, A&A, 384, 848
Fadda, D., Flores, H., Hasinger, G., et al. 2002, A&A 383, 838
Genzel, R., & Cesarsky, C. 2000, ARAA, 38, 761
Gispert, R., Lagache, G., Puget, J-L. 2000, A&A, 360, 1
Hauser, M.,& Dwek, E. 2001, ARAA, 37, 249
Houck, J., Roellig, T., van Cleve, J., et al. 2004a, ApJS 154, 18
Houck, J., Charmandaris, V., Brandl, B., et al. 2004b, ApJS 154, 211
Kessler, M., Steinz, J., Anderegg, M., et al. 1996, A&A, 315, L27
Lagache, G., Dole, H., Puget, J-L., et al. 2004, ApJS, 154, 112
Le Floc'h, E., Mirabel, I. F., Laurent, O., et al. 2001, A&A, 367, 487
Liang, Y., Hammer, F., Flores, H., et al. 2004, A&A, 423, 867
Papovich, C., Dole, H., Egami, E., et al. 2004, ApJS, 154, 70
Puget, J-L., Abergel, A., Bernard, J-P., et al. 1996, A&A, 308, L5
Rieke, G.H., et al. 2004, ApJS, 154, 25
Spoon, H., et al. 2001, A&A, 365, L353
Starck J.-L., Aussel H., Elbaz D., et al. 1999, A&AS 138, 365
Stetson, P. B. 1987, PASP, 99, 191
Thuan, T.X., Sauvage, M., Madden, S. 1999, ApJ, 516, 783
Werner, M.W., Roellig, T.L., Low, F.J., et al. 2004, ApJS, 154, 1

To Appear in Annual Reviews of Astronomy & Astrophysics, 2005, volume 43
Preprint typeset using LaTeX style emulateapj v. 2/19/04

DUSTY INFRARED GALAXIES: SOURCES OF THE COSMIC INFRARED BACKGROUND

Guilaine Lagache, Jean-Loup Puget, Hervé Dole
Institut d'Astrophysique Spatiale, Bât 121, Université de Paris Sud 11, 91405 Orsay Cedex, France; e-mail: guilaine.lagache@ias.u-psud.fr, puget@ias.u-psud.fr, herve.dole@ias.u-psud.fr

To Appear in Annual Reviews of Astronomy & Astrophysics, 2005, volume 43

ABSTRACT

The discovery of the Cosmic Infrared Background (CIB) in 1996, together with recent cosmological surveys from the mid-infrared to the millimeter have revolutionized our view of star formation at high redshifts. It has become clear, in the last decade, that a population of galaxies that radiate most of their power in the far-infrared (the so-called "infrared galaxies") contributes an important part of the whole galaxy build-up in the Universe. Since 1996, detailed (and often painful) investigations of the high-redshift infrared galaxies have resulted in the spectacular progress covered in this review. We outline the nature of the sources of the CIB including their star-formation rate, stellar and total mass, morphology, metallicity and clustering properties. We discuss their contribution to the stellar content of the Universe and their origin in the framework of the hierarchical growth of structures. We finally discuss open questions for a scenario of their evolution up to the present-day galaxies.

Subject headings: cosmology – evolution – luminosity function – starburst – star formation

1. INTRODUCTION

The Cosmic Infrared Background (CIB) can be defined as the part of the present radiation content of the Universe that is made essentially of the long wavelength output from all sources throughout the history of the Universe. The radiation content in the microwave part of the spectrum is dominated by the Cosmic Microwave Background (CMB) produced in the hot and dense phases of the universe. It dominates for frequencies below 800 GHz. Nevertheless the very different spectra of the CIB with respect to the CMB (both its purely Planckian part and its Compton distortion expected to be the dominant one at these frequencies) allow them to be separated very efficiently down to frequencies close to the peak of the CMB (150 GHz). Furthermore in this frequency regime the CIB dominates the galactic emission in the lowest cirrus regions by a factor $\simeq$4. The cosmic background due to sources (CMB excluded) presents two maxima: one in the optical, one in the far-infrared, with roughly equal brightness (in νI_ν) and with a minimum around 5 μm. This minimum is created by the decrease of brightness of the stellar component with wavelength combined with the rising brightness of the dust, very small grains, and of the Active Galactic Nuclei (AGN) non thermal emission in the thermal infrared. The CIB is defined as the cosmic background at wavelengths longward of this minimum. An understanding of the nature and redshift distribution of the sources of the CIB, although relatively new, is an integral part of the understanding of the formation and evolution of galaxies.

The standard hierarchical model of structure formation has received strong observational support from observations of the large-scale distribution of galaxies, clusters, intergalactic clouds, combined with CMB anisotropies that constrain the initial large scale power spectrum within the concordance cosmological model framework. Scenarios for galaxy formation and evolution can be confronted with the very quickly rising set of observations of extragalactic sources at higher and higher redshifts. Nevertheless many critical questions remain open on the cooling of collapsed structures, angular momentum of galaxies, star formation efficiency, Initial Mass Function (IMF) of the stars formed, role of feedback mechanisms, the physics and role of merging and accretion in the construction of galaxies.

As ultraluminous infrared galaxies were found to be often associated with mergers or interacting galaxies, it can be expected that the sources of the CIB carry critical information about the history of merging (e.g., Sanders & Mirabel 1996; Genzel & Cesarsky 2000). Because about half of the energy from extragalactic sources is in the CIB, the determination of the source of this energy (starbursts or massive black hole accretion in dust enshrouded AGNs) should shed some light on how galaxies evolve.

Since the discovery of the CIB in the COBE data (e.g., Hauser & Dwek 2001), identifying the sources of the CIB, their redshift distribution, and nature progressed at increasing speed especially through multiwavelength analysis. This review attempts to give the broadband observational picture for the identification of the sources of the CIB. The detailed analysis of individual infrared galaxies is outside the scope of this review. We then discuss implications, both well-established ones and tentative ones, as well as directions for future work. The spectroscopy aspects are covered in the review by Solomon & Vanden Bout (2005, in this volume). This is at present a fascinating but moving target! The coming decade will be a very rich one. New, very powerful long-wavelengths observation tools will bring many striking new results like the *Spitzer* observatory or the being built experiments like *Herschel* and ALMA. Throughout this review, the cosmology is fixed to Ω_Λ=0.7, Ω_m=0.3, H_0=100 h km s^{-1} Mpc^{-1} with h=0.65.

2. DUST IN THE LOCAL UNIVERSE

A fraction of the stellar radiation produced in galaxies is absorbed by dust and re-radiated from mid-infrared to millimeter wavelengths. Understanding dust properties and the associated physics of the absorption and emission are thus essential. These determine the Spectral Energy Distribution (SED) of the galaxies.

2.1. *Dust Particles*

Small dust particles with sizes ranging from a nanometer to a fraction of micrometer are ubiquitous in the interstellar medium. They result from natural condensation in cool stellar atmospheres, supernovae, and the interstellar medium of the heavy elements produced by the nucleosynthesis in stars and released to the diffuse medium by late type stars and supernovae explosions. Interstellar grain models have been improved for 30 years in order to fit all observational constraints: elemental abundances of the heavy elements, UV, visible and infrared absorption and scattering properties, infrared emission, polarization properties of the absorbed and emitted light. The models include a mixture of amorphous silicate grains and carbonaceous grains, each with a wide size distribution ranging from molecules containing tens of atoms to large grains $\geq$ 0.1 μm in diameter that can be coated with ices in dense clouds and/or organic residues (e.g., Désert et al. 1990; Li & Draine 2001). It is now widely accepted that the smallest carbonaceous grains are Polycyclic Aromatic Hydrocarbons (PAHs) that emit a substantial fraction of the energy in a set of features between 3 and 17 μm (3.3, 6.2, 7.7, 8.6, 11.3, 12.7, 16.3, 17 μm for the main ones) that used to be known as the UIB for Unidentified Infrared Bands. These features result from C-C and C-H stretching/bending vibrational bands excited by the absorption of a single UV or optical photon and are a good tracer of normal and moderately active star formation activity in spiral and irregular galaxies (e.g., Helou et al. 2000; Peeters et al. 2004). For radii a$\geq$50 Å, the carbonaceous grains are often assumed to have graphitic properties. The so-called very small grains of the interstellar medium are small enough to have very low heat capacity, so their temperature are significantly affected by single-photon absorption. In the diffuse ISM of our Galaxy, they dominate the infrared emission for wavelengths smaller than about 80 μm. At longer wavelengths, the infrared spectrum is dominated by the emission of the larger grains at their equilibrium temperatures. Considering the energy density of the radiation in a galactic disc like ours, the temperature of the larger grains is rather low; 15 to 25 K. For these grains, the far-infrared emissivity decreases roughly as the square of the wavelength. This in turn makes the temperature dependence on the radiation energy density u very weak ($T \simeq u^{1/6}$). For a galaxy like the Milky Way, the infrared part of the SED peaks at 170 μm whereas for an Ultra Luminous Infrared Galaxy (ULIRG) it peaks at about 60 μm: a factor 3 in temperature for a factor 10^3

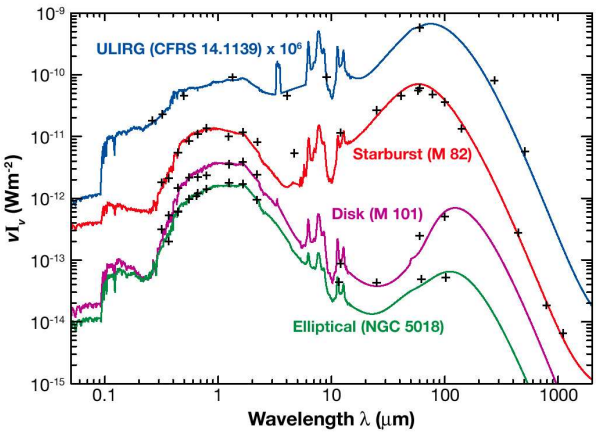

FIG. 1.— Spectral energy distributions of galaxies from UV to the millimeter. The ULIRG is observed at redshift z=0.66 and is represented here in the rest-frame (from Galliano 2004).

in energy density or luminosity. At long wavelengths in the submillimeter and millimeter, the intensity should increase like $I_\nu \simeq \nu^4$.

2.2. *Extinction*

In our Galaxy, the extinction curve of the diffuse ISM has been known for a few decades. The average optical depth perpendicular to the disk of our Galaxy in the solar vicinity is small ($A_V \simeq 0.2$) and typical of spiral galaxies. The average optical depth increases to a few in large molecular cloud complexes. It can become very large in galactic nuclei. Finally it should also be remembered that the optical depth in the UV is typically 10 times larger than that in optical wavelengths. The conversion of star light into infrared radiation will thus depend strongly on the location of the stars and their spectral types.

In external galaxies, modeling the extinction is very hard because it strongly depends on the geometric distribution of the ISM and of the chemical abundances. Simple models have been used to take this into account to first order. Galaxies can be modeled as an oblate ellipsoid where absorbers (dust) and sources (stars) are homogeneously mixed; the dust absorption can be computed in a "screen" or "sandwich" geometry (dust layers in front of the stars or sandwiched between two star layers). As a consequence, the reddening curve average over a whole galaxy appears to vary within a class of objects and between the different classes, from normal star-forming galaxies to highly concentrated starburst. It is thus very difficult to derive the total dust optical depth (e.g., Calzetti et al. 1994). In the local Universe, the average extinction per galaxy is quite low. About one third of the bolometric flux is emitted in the far-infrared, and this is typical of our Galaxy. In more actively star-forming galaxies, up to 70% of the bolometric flux is emitted in the far-infrared. In some of these, the starburst activity is mostly in the disk (like in M51). For a given total luminosity, the radiation energy density is lower than in the case of a starburst concentrated in a small volume in the nucleus. In this case, the dust will be hotter due to the larger

energy density and the conversion of stellar light to infrared will be more efficient. Some ULIRGs emit more than 95% of their energy in the far-infrared (e.g., Arp 220). Such galaxies are very compact, dusty starbursts where dust optical depths are very large. In such galaxies, fine structure and recombination line ratios imply an equivalent "screen" dust extinction between $A_V \sim 5$ and 50. The result is that the SED is significantly distorted in the opposite way from the higher dust temperature (less mid-infrared emission). In the following, we will refer to "infrared galaxies" and to "optical galaxies" to designate galaxies in which the infrared emission, respectively optical emission dominates. Different typical spectra of galaxies are shown in Figure 1 from the UV to the millimeter. We clearly see the variation of the optical to infrared energy ratio as starburst activity increases.

2.3. *Local Infrared Galaxies*

A few very luminous infrared galaxies were observed in the seventies (Rieke & Lebofsky 1979). Then IRAS satellite, launched in 1983 gave for the first time a proper census of the infrared emission of galaxies at low redshift. The Luminosity Function (LF) at 60 and 100 μm is dominated by $L_\star$ spiral galaxies as could be expected – the reradiated stellar luminosity absorbed by dust. In addition, a high-luminosity tail of luminous galaxies was found (e.g., Sanders & Mirabel 1996). This high-luminosity tail can be approximated by a power-law, $\Phi(L) \propto L_{\rm IR}^{2.35}$, which gives a space density for the most luminous infrared sources well in excess of predictions based on the optical LF. These sources comprise the Luminous Infrared Galaxies, LIRGs, and the ULIRGs with luminosities $11<\log(L_{\rm IR}/L_\odot)<12$ and $\log(L_{\rm IR}/L_\odot)>12$, respectively. These galaxies are often associated with interacting or merging, gas-rich disks. The fraction of strongly interacting/merger systems increases from $\sim$10% at $\log(L_{\rm IR}/L_\odot)$=10.5-11 to $\sim$100% at $\log(L_{\rm IR}/L_\odot)>12$. LIRGs are the site of intense starburst activity (about 10-100 $M_\odot$ year^{-1}) induced by the interaction and/or strong spiral structure. The ULIRG phase occurs near the end of the merging process when the two disks overlap. Such galaxies may be the precursors of Quasi Stellar Objects (QSOs; Sanders et al. 1988a, 1988b; Veilleux et al. 1995; Lutz et al. 1999). These objects have been the subject of intense debate concerning the nature of the dominant source of emission: starburst versus dust-enshrouded AGN (e.g., Filipenko 1992; Sanders & Mirabel 1996; Joseph 1999). Indeed, spectra show evidence of extremely large optical depth (heavily reddened continuum and large Balmer decrement) but also exhibit AGN-like high excitation fine-structure lines. We had to wait for ISO to clearly determine the power sources of ULIRGs. The difference between the mid-infrared spectra of starburst and AGNs is striking. Starburst are often characterized by strong, low-excitation, fine-structure lines, prominent PAH features and a weak $\lambda \geq 10$ μm continuum whereas AGNs display a highly excited emission line spectrum with weak or no PAH features, plus a strong mid-infrared continuum. It has been thus possible to build mid-infrared diagnostic diagrams (e.g., Genzel et al. 1998; Laurent et al. 2000) that clearly separates starburst-dominated galaxies from AGN-dominated galaxies. These diagrams demonstrate that ULIRGs appear to be composite objects, but star formation dominates in most objects. That is on average, $\geq$70% of the reradiated energy comes from starbursts and $\leq$ 30% comes from AGNs (Genzel et al. 1998; Lutz et al. 1998). However the fraction of AGN-powered objects increases with luminosity. About 15% of ULIRGs at luminosities below 2×10^{12} $L_\odot$ are mostly AGN powered, but this fraction increases to about half at higher luminosity.

All these well-studied LIRGs and ULIRGs are at low redshift. They do not dominate the energy production locally. As an example, the total infrared luminosity from these galaxies in the IRAS Bright Galaxy Sample accounts for only $\sim$6% of the infrared emission in the local Universe (Soifer & Neugeubauer, 1991). As we will see, the situation changes dramatically at higher redshift where these galaxies fully dominate the infrared energy output.

3. THE COSMIC INFRARED BACKGROUND

The CIB is the infrared part of the extragalactic background, the radiation content of the Universe today produced by galaxies at all redshifts and seen as an isotropic extragalactic background radiation. Patridge & Peebles

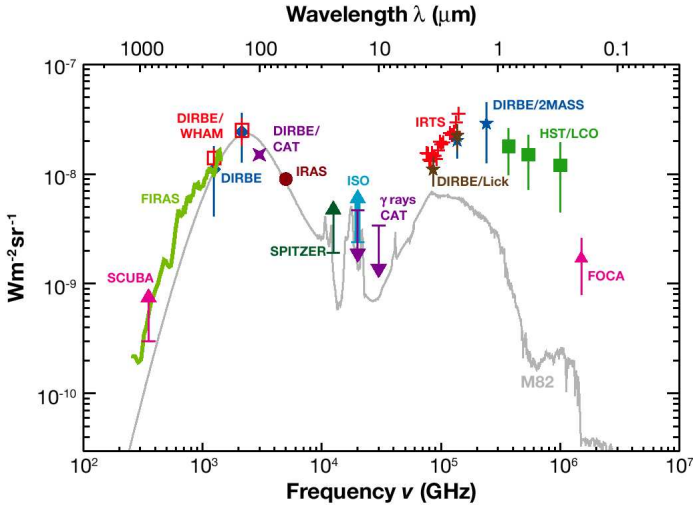

FIG. 2.— The extragalactic background over three decades in frequency from the near UV to millimeter wavelengths. Only strongly constraining measurements have been reported. We show for comparison in grey an SED of M82 (Chanial, 2003)– a starburst galaxy at L=3× 10^{10} $L_\odot$ – normalized to the peak of the CIB at 140 μm. References for data points are given in Table 1.

(1967) predicted that observations of such a background could give powerful constraints on the cosmological evolution.

3.1. *General Observations and Direct Cosmological Implications*

The detection of the infrared part of the extragalactic background (the CIB for Cosmic Infrared Background) was the major objective of the DIRBE experiment aboard COBE. In fact, the CIB was first detected at long wavelengths by using the FIRAS spectrometer: $\lambda > 200$ μm (Puget et al. 1996). The CIB has subsequently been detected by DIRBE at 2.4, 3.5, 100, 140, 240 μm (see Hauser & Dwek 2001 and Kashlinsky 2005 for two reviews). The extragalactic background at 2.4 and 3.5 μm is significantly larger than that predicted by the integrated galaxy counts and their extrapolation. Similarly, the extragalactic background in the optical has been finally evaluated in combining several methods by Bernstein et al. (2002) and found to be larger than the value given by the integrated fluxes of galaxies by a factor larger than 2. In the mid-infrared, the interplanetary zodiacal dust emission is so strong that only upper limits were obtained by DIRBE. The combination of number counts by ISO/ISOCAM at 15 μm (see Elbaz & Cesarsky 2003) and by *Spitzer* at 24 μm (e.g., Papovich et al. 2004) giving lower limits, with the observations of TeV gamma ray emission from distant AGNs (e.g., Renault et al. 2001; Dwek & Krennrich 2005), gives a good measurement of the background at these wavelengths. The full cosmic background spectrum is shown in Figure 2. Only most recent and strongly constraining measurements have been plotted for clarity.

TABLE 1
EXTRAGALACTIC BACKGROUND REFERENCES FOR FIGURE 2

Wavelength (μm)	Experiment	Measurement	Reference
0.2	FOCA	Number counts & model	Armand et al. 1994
0.30, 0.56, 0.81	HST/Las Campanas Obs.	Diffuse emission	Bernstein et al. 2002 Mattila 2003
2.2< λ <4	IRTS	Diffuse emission	Matsumoto et al. 2005
2.2, 3.3	DIRBE/Lick	Diffuse emission	Gorjian et al. 2000
1.25, 2.2	DIRBE/2MASS	Diffuse emission	Wright 2001 Cambrésy et al. 2001
10, 15	CAT	γ-rays	Renault et al. 2001
15	ISO/ISOCAM	Number counts	Elbaz et al. 1999
24	*Spitzer*/MIPS	Number counts	Papovich et al. 2004
60	IRAS	Power spectrum	Miville-Deschênes et al. 2001
100	DIRBE	Diffuse emission	Renault et al. 2001
140, 240	DIRBE/WHAM	Diffuse emission	Lagache et al. 2000
140, 240	DIRBE	Diffuse emission	Hauser et al. 1998
850	SCUBA	Number counts	Smail et al. 2002
200< λ <1200	FIRAS	Diffuse emission	Lagache et al. 2000

Figure 2 clearly shows that the optical and infrared cosmic backgrounds are well separated. The first surprising result is that the power in the infrared is comparable to the power in the optical. In contrast, we know that locally, the infrared output of galaxies is only one third of the optical output. This implies that infrared galaxies grow more luminous with increasing z faster than do optical galaxies. A second important property to note is that the slope of the long wavelength part of the CIB, $I_\nu \propto \nu^{1.4}$ (Gispert et al. 2000), is much less steep than the long wavelengths spectrum of galaxies (as illustrated in Figure 2 with the M82 SED). This implies that the millimeter CIB is not due to the millimeter emission of the galaxies that account for the peak of the CIB ($\simeq 150\mu$m). The implications in terms of energy output have been drawn by, e.g. Gispert et al. (2000). The infrared production rate per comoving unit volume (a) evolves faster between redshift zero and 1 than the optical one and (b) has to stay roughly constant at higher redshifts up to redshift 3 at least.

3.2. *The Status of Deep Surveys: Resolved Fraction of the >10 μm CIB*

Many surveys from the mid-infrared to the millimeter have aimed to resolve the CIB into discrete sources. From short to long wavelengths the significant surveys are the following:

- ISOCAM 15 μm: Three kinds of surveys have been done. The shallowest is the ELAIS survey (European Large-Area ISO Survey, Oliver et al. 2000). The deepest is the survey in the HDF-N (Aussel et al. 1999) as well as the surveys in the direction of the galaxy clusters (e.g. Metcalfe et al. 2003). Altogether, about 1000 galaxies were detected. Above a sensitivity limit of 50 μJy, they produce a 15 μm extragalactic background light of (2.4 ± 0.5) nW m^{-2} sr^{-1} (Elbaz et al. 2002). This accounts for about 80% of the CIB at 15 μm based on the simplest extrapolation of the counts.

- *Spitzer* 24 μm: *Spitzer* surveys are ongoing, but more than 10^5 sources have already been detected at 24 μm. Integrating the first number counts down to 60 μJy, a lower limit to the CIB at 24 μm of (1.9±0.6) nW m^{-2} sr^{-1} is derived (Papovich et al. 2004). This accounts for about 70% of the CIB at 24 μm, based on a simple extrapolation of the counts.

- *Spitzer* 70 μm: Counts have been derived down to 15 mJy. Integrating these counts corresponds 0.95 nW m^{-2} sr^{-1} which explains ∼20% of the CIB at 70 μm as derived from the Lagache et al. (2004) model (Dole et al. 2004a).

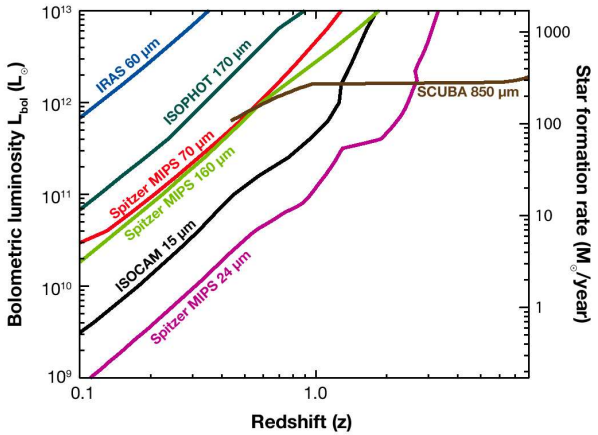

FIG. 3.— Sensitivity to the bolometric luminosity and star-formation rate, assuming star forming galaxies of various infrared and submillimeter experiments. Detections of at least 10 sources in the surveys can be expected in the areas above the *curves*. We assumed the scenario of a typical deep survey (when available). IRAS 60 μm ($S_\nu > 1$ Jy, all sky); ISOCAM 15 μm ($S_\nu > 250\mu$Jy, 2 Sq. Deg.); ISOPHOT 170 μm ($S_\nu > 180$ mJy, 5 Sq. Deg.); *Spitzer*/MIPS 24 μm ($S_\nu > 80\mu$Jy, 5 Sq. Deg.); *Spitzer*/MIPS 70 μm ($S_\nu > 25$ mJy, 5 Sq. Deg.); *Spitzer*/MIPS 160 μm ($S_\nu > 50$ mJy, 5 Sq. Deg.); *SCUBA* 850 μm ($S_\nu > 1$ mJy, 1 Sq. Deg.). This plot makes use of the Lagache et al. (2004) model (see the Appendix).

- ISOPHOT 90 μm: The most relevant data comes from the ELAIS survey that covers about 12 square degrees at 90 μm. Counts have been obtained down to 95 mJy (Héraudeau et al. 2004) resolving less than 5% of the CIB as derived from DIRBE by Renault et al. (2001).

- *Spitzer* 160 μm: First counts are derived down to 50 mJy. The integral of these counts corresponds to 1.4 nW m^{-2} sr^{-1}, which explain about 7% of the CIB at 160 μm (Dole et al. 2004a).

- ISOPHOT 170 μm: Two main surveys have been conducted: the FIRBACK (Lagache & Dole 2001) and the Lockman hole (Kawara et al. 2004) surveys that covering about 5 square degrees. Counts down to 135 mJy contribute to less than 5% of the CIB (Dole et al. 2001).

- SCUBA 450 μm: Deep surveys at 450 μm are very hard to conduct from the ground. A few galaxies are detected between 10 and 50 mJy in deep surveys. Number counts down to 10 mJy give a lower limit on the CIB of about (0.7 ± 0.4) nW m^{-2} sr^{-1} (Smail et al. 2002). This resolves about 15% of the CIB at 450 μm.

- SCUBA 850 μm: Over 500 arcmin^2 of blank sky has been surveyed by several groups using SCUBA. The observations range from an extremely deep survey in the area of the HDF-N to a wider-field shallower survey. Also about 40 arcmin^2 of lensed cluster fields have been observed in which 17 sources have been detected. Fluxes range from about 0.5 to 8 mJy. The flux density in the resolved submillimeter population down to 1 mJy is (0.3 ± 0.1) nW m^{-2} sr^{-1} (Smail et al. 2002). This account for 60% of the CIB at 850 μm. Note that in deep surveys, sources with $S_{850} \geq 3$ mJy contribute to ∼30% of the CIB.

- MAMBO 1200 μm: Deep blank sky areas surveyed by MAMBO cover about 500 arcmin^2. Number counts are given by Greve et al. (2004). By integrating the counts from 2.25 to 5.75 mJy, the resolved CIB is about 0.02 nW m^{-2} sr^{-1}, or about 10% of the total CIB at 1200 μm.

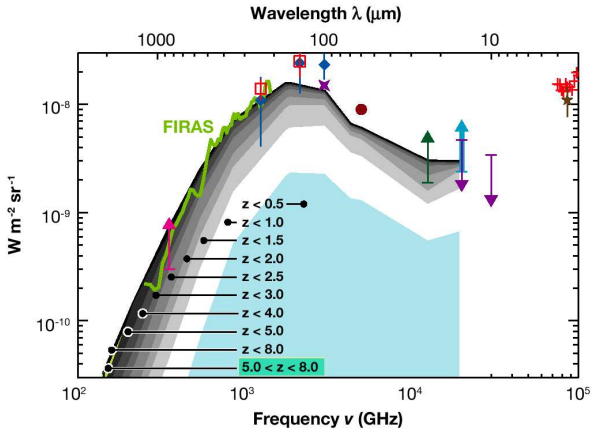

FIG. 4.— Cumulative contribution to the CIB of galaxies at various redshifts from 0.5 to 8, from the model of Lagache et al. (2004). Measurements of the CIB are reported with the same symbols as in Figure 2.

Figure 3 shows the capabilities of the different surveys to find distant LIRGs. *Spitzer* observations at 24 μm are the most powerful tool to find LIRGs up to z ∼2.2; ISOCAM was limited at z ∼1.2. Distant ULIRGs are found by deep and large surveys at 24 and 850 μm. Note that capabilities have been computed using the model of Lagache et al. (2004). This empirical model is based on only two populations of galaxies; it aims only to model the redshift evolution of the average population. It reproduces all the observations from mid-infrared to the millimeter (see Appendix). Lewis et al. (2005) showed that a more sophisticated, bivariate SED does not much change the average properties although it does significantly change the dispersion. The Lagache et al. (2004) model is thus used in this paper as a tool to discuss observations and predictions.

3.3. *Redshift Contribution to the CIB*

From Figure 2, we see that contributions from galaxies at various redshifts are needed to fill the CIB SED shape. The bulk of the CIB in energy, i.e., the peak at about 150 μm, is not resolved in individual sources but one dominant contribution at the CIB peak can be inferred from the ISOCAM deep surveys. ISOCAM galaxies with a median redshift of ∼0.7 resolve about 80% of the CIB at 15 μm. Elbaz et al. (2002) separate the 15 μm galaxies into different classes (ULIRGs, LIRGs, Starbursts, normal galaxies and AGNs) and extrapolate the 15 μm fluxes to 140 μm using template SEDs. A total brightness of (16±5) nW m^{-2} sr^{-1} is found, which makes up about

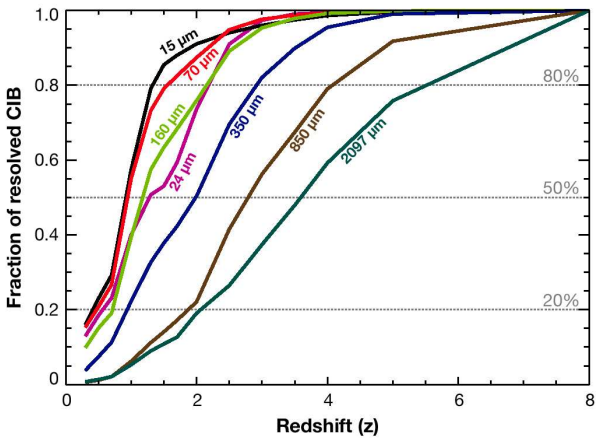

FIG. 5.— Cumulative fraction of the CIB content as a function of redshift for various wavelengths, from the model of Lagache et al. (2004).

two thirds of the CIB observed at 140 μm by COBE/DIRBE. Hence, the galaxies detected by ISOCAM are responsible for a large fraction of energy of the CIB. About one half of the 140 μm CIB is due to LIRGs and about one third to ULIRGs. However, these ISOCAM galaxies make little contribution to the CIB in the millimeter and submillimeter. There, the CIB must be dominated by galaxies at rather high redshift for which the SED peak has been shifted. The redshift contribution to the CIB is illustrated in Figure 4. We clearly see that the submillimeter/millimeter CIB contains information on the total energy output by the high-redshift galaxies (z >2). This is supported by the redshift distribution of the SCUBA sources at 850 μm with $S_{850}\geq$3 mJy that make about 30% of the CIB and have a median redshift of 2.2 (Chapman et al. 2005).

Figure 5 shows the fraction of resolved CIB as a function of redshift for selected wavelengths. Fifty percents of the CIB is due to galaxies at redshift below 1 at 15 and 70 μm, 1.3 at 24 and 160 μm, 2 at 350 μm, 3 at 850 μm and 3.5 at 2000 μm (see also Table 2). It is clear that from the far-infrared to the millimeter, the CIB at longer wavelengths probes sources at higher redshifts.

TABLE 2
REDSHIFT AT WHICH THE COSMIC INFRARED BACKGROUND IS RESOLVED AT 20, 50 OR 80% (FROM THE MODEL OF LAGACHE ET AL. 2004).

Wavelength	20%	50%	80%
15 μm	0.5	1.0	1.3
24 μm	0.5	1.3	2.0
70 μm	0.5	1.0	1.5
100 μm	0.7	1.0	1.7
160 μm	0.7	1.3	2.0
350 μm	1.0	2.0	3.0
850 μm	2.0	3.0	4.0
1.4 mm	2.5	3.5	4.5
2.1 mm	2.0	3.5	5.0

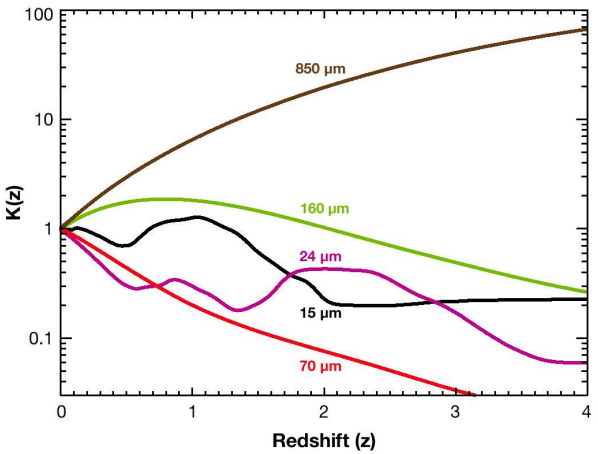

FIG. 6.— K-correction at 15, 24, 70 and 160 and 850 μm for a typical LIRG with L=2×10^{11} $L_\odot$ (from the model of Lagache et al. 2004).

From Section 3.2, we see that the most constraining surveys in term of resolving the CIB are those at 15, 24 and 850 μm. Moreover, the capabilities of these surveys to find high-z objects are the best among all other existing surveys (see Figure 3). These surveys probe the CIB in well-defined and distinct redshift ranges, with median redshifts of 0.7 (Liang et al. 2004), $\sim$1 (Caputi et al. 2005 and L. Yan, private communication), and 2.2 (Chapman et al. 2005) at 15, 24 and 850 μm, respectively. Such well-defined redshift ranges can be understood by looking at the K-correction. The K-correction is defined as:

$$K(L,z) = \frac{L_\nu(1+z)}{L_\nu(z=0)} \qquad (1)$$

where $L_\nu(z=0)$ is the rest-frame luminosity. This correction is specific to the spectrum of the population considered at a given luminosity and redshift. Figure 6 shows the K-correction at 15, 24, 70, 160 and 850 μm. The broad plateau observed around $z=1$ at 15 μm and around $z=2$ at 24 μm is caused by the PAHs' features. At longer wavelengths, the slow decrease of the K-correction is caused by the shape of the starburst spectra around the peak of their emission. At 850 μm, the monotonic rise favors the detection of high-z objects.

4. GALAXIES AT REDSHIFTS $0.5 \leq Z \leq 1.5$

At the time this review was written, most of the detailed informations on dusty galaxies in the $0.5 \leq z \leq 1.5$ redshift range comes from galaxies selected with the ISOCAM cosmological surveys and the multi-wavelength analysis of detected sources. The ISOCAM extragalactic surveys were performed with two filters, LW2 (5-8.5 μm) and LW3 (12-18 μm) centered at 6.75 and 15 μm, respectively. However, because of star contamination and because the stellar light dominates the flux from galaxies in the 6.75 μm band above redshift 0.4, only the 15 μm surveys are relevant here. Shallow, deep and ultra-deep surveys were performed in various fields including the Lockman hole, Marano, northern and southern Hubble Deep Field (HDF), and Canada-France Redshift Sur-

vey (CFRS) (e.g., Aussel et al. 1999; Flores et al. 1999; Lari et al. 2001; Gruppioni et al. 2002; Mann et al. 2002; Elbaz & Cesarsky 2003; Sato et al. 2003). Deeper images have been made in the direction of distant clusters (e.g., Metcalfe et al. 2003). Finally, the bright end of the luminosity function was explored by the ELAIS survey (e.g., Oliver et al. 2000). The deepest surveys reach a completeness limit of about 100 μJy at 15 μm (without lensing). The most relevant data to this section are the deep and ultra-deep surveys.

4.1. *Detailed Properties*

To find out the nature and redshift distribution of the 15 μm deep survey sources, many followup observations have been conducted including HST imaging and VLT spectroscopy. With a point-spread function full width at half of maximum of 4.6 arcsec at 15 μm, optical counterparts are easily identified. Redshifts are found using emission and/or absorption lines. From field to field, the median redshift varies from 0.52 to 0.8, a quite large variation due to sample variance. Each field clearly exhibits one or two redshift peaks, with velocity dispersion characteristic of clusters or galaxy groups. Most of ISOCAM galaxies have redshifts between $\sim$ 0.3 and 1.2, consistent with Figure 3. About 85% of the ISO galaxies show obvious strong emission lines (e.g., [OII] 3723, H_γ, H_β, [OIII] 4959, 5007). These lines can be used as a diagnostic of the source of ionization and to distinguish the HII-region like objects from the Seyferts and LINERs. Most of the objects are found to be consistent with HII regions, e.g., from Liang et al. (2004) and exhibit low ionization level ([OIII]/H_β <3). From emission lines studies, the AGN fraction is quite low, $\sim$20 %. This is consistent with X-ray observations of ISOCAM sources showing that AGNs contribute at most 17$\pm$6% of the total mid-infrared flux (Fadda et al. 2002). Assuming template SEDs typical of star-forming and starburst galaxies, 15 μm fluxes can be converted into total infrared luminosities, L_{IR} (between 8 and 1000 μm). About 75% of the galaxies dominated by the star formation are either LIRGs or ULIRGs. The remaining 25% are nearly equally distributed among either "starbursts" (10^{10} < L_{IR} < 10^{11} $L_\odot$) or "normal" (L_{IR} < 10^{10} $L_\odot$) galaxies. The median luminosity is about 3×10^{11} $L_\odot$. ULIRGs and LIRGs contribute to about 17% and 44% to the CIB at 15 μm, respectively (Elbaz et al. 2002). This suggests that the star formation density at z <1 is dominated by the abundant population of LIRGs. As will be shown later, this has important consequences for the evolution of galaxies. Because of large extinction in LIRGs and ULIRGs, the infrared data provide more robust SFR estimate than UV tracers. The extinction factor in LIRGs averages to A_V $\sim$2.8 at z $\sim$0.7 (Flores et al. 2004). It is much higher than that of the local star-forming galaxies for which the median is 0.86 (Kennicutt 1992). Assuming continuous burst of age 10-100 Myr, solar abundance, and a Salpeter initial mass function, the SFR can be derived from the infrared luminosities (Kennicutt 1998):

$$SFR(M_\odot/yr) = 1.71\times10^{-10} L_{IR}[8{-}1000\mu m](L_\odot) \quad (2)$$

Thus typical LIRGs form stars at $\geq$20 $M_\odot$ $year^{-1}$. The median SFR for the 15 μm galaxies is about 50 $M_\odot$ $year^{-1}$, a substantial factor larger than that found for faint-optically selected galaxies in the same redshift range.

The other fundamental parameter characterizing the sources of the peak of the infrared background is their stellar mass content that traces the integral of the past star formation activity in the galaxies and is a natural complement to the instantaneous rate of star formation. The stellar masses can be obtained using spectral synthesis code modeling of the UV-optical-near infrared data or, more simply using the mass-to-luminosity ratio in the K-band. The derived stellar masses for the bulk of ISOCAM galaxies range from about 10^{10} to $3\times10^{11}M_\odot$, compared to 1.8×10^{11} $M_\odot$ for the Milky Way. As expected from the selection based on the LW3 flux limit – and thus on the SFR – masses do not show significant correlation with redshift (Franceschini et al. 2003). An estimate of the time spent in the starburst state can be obtained by comparing the rate of ongoing star formation (SFR) with the total mass of already formed stars: $t[years] = M/\mathrm{SFR}$. Assuming a constant SFR, t is the timescale to double the stellar mass. For LIRGs at z >0.4, t ranges from 0.1 to 1.1 Gy with a median of about 0.8 Gyr (Franceschini et al. 2003; Hammer et al. 2005). From z = 1 to z = 0.4 (i.e., 3.3 Gyr), this newly formed stellar mass in LIRGs corresponds to about 60% of the z = 1 total mass of intermediate mass galaxies. The LIRGs are shown to actively build up their metal content. In a detailed study, Liang et al. (2004) show that, on average, the metal abundance of LIRGs is less than half of the $z \sim 0$ disks with comparable brightness. Expressed differently, at a given metal abundance, all distant LIRGs show much larger B luminosities than local disks. Assuming that LIRGs eventually evolve into the local massive disk galaxies, Liang et al. (2004) suggest that LIRGs form nearly half of their metals and stars since z $\sim$1.

Finally, morphological classification of distant LIRGs is essential to understand their formation and evolution. Zheng et al. (2004) performed a detailed analysis of morphology, photometry, and color distribution of 36 (0.4< z <1.2) ISOCAM galaxies using HST images. Thirty-six percents of LIRGs are classified as disk galaxies with Hubble type from Sab to Sd; 25% show concentrated light distributions and are classified as Luminous Compact Galaxies (LCGs); 22% display complex morphology and clumpy light distributions and are classified as irregular galaxies; only 17% are major ongoing mergers showing multiple components and apparent tidal tails. This is clearly different from the local optical sample of Nakamura et al. (2004) in the same mass range in which 27%, 70%, <2%, 3% and <2% are E/S0, spirals, LCGs, irregulars and major mergers respectively. Consequences for galaxy evolution will be given in Section 4.3. For most compact LIRGs, the color maps reveal a central region strikingly bluer than the outer regions. These blue central regions have a similar size to that of bulges and a color comparable to that of star-forming regions. Because the bulge/central region in local spiral is relatively red, such a blue core structure could imply that the galaxy was forming the bulge (consistent with Hammer et al. 2001). It should be noticed that they find all LIRGs distributed along a sequence that relates their central color to their compactness. This is expected if star formation occurs first in the center (bulge) and gradually migrate to the outskirts (disk), leading to redder colors of the central regions as the disk stars were forming.

4.2. *Cosmic Evolution*

Another remarkable property of the 15 μm sources is their extremely high rates of evolution with redshift exceeding those measured for galaxies at other wavelengths and comparable to or larger than the evolution rates observed for quasars. Number counts at 15 μm show a prominent bump peaking at about 0.4 mJy. At the peak of the bump, the counts are one order of magnitude above the non-evolution models. In fact, data require a combination of a $(1+z)^3$ luminosity evolution and $(1+z)^3$ density evolution for the starburst component at redshift lower than 0.9 to fit the strong evolution. Although it has not been possible with ISOCAM to probe in detail the evolution of the infrared luminosity function, *Spitzer* data at 24 μm give for the first time tight constraints up to redshift 1.2 (Le Floc'h et al. 2005; Pérez-González et al. 2005). A strong evolution is noticeable and requires a shift of the characteristic luminosity $L^\star$ by a factor $(1+z)^{4.0\pm0.5}$. Le Floc'h et al. (2005) find that the LIRGs and ULIRGs become the dominant population contributing to the comoving infrared energy density beyond z $\sim$0.5-0.6 and represent 70% of the star-forming activity at z $\sim$1. The comoving luminosity density produced by luminous infrared galaxies was more than 10 times larger at z $\sim$1 than in the local Universe. For comparison, the B-band luminosity density was only three times larger at z = 1 than today. Such a large number density of LIRGs in the distant Universe could be caused by episodic and violent star-formation events, superimposed on relatively small levels of star formation activity. This idea has emerged in 1977 (Toomre 1977) and is fully developed in Hammer et al. (2005). These events can be associated to major changes in the galaxy morphologies. The rapid decline of the luminosity density from z = 1 is only partially due to the decreasing frequency of major merger events. Bell et al. (2005) showed that the SFR density at z $\sim$0.7 is dominated by morphologically normal spiral, E/S0 and irregular galaxies ($\geq$70%), while clearly interacting galaxies account for <30%. The dominent driver of the decline is

a strong decrease in SFR in morphologically undisturbed galaxies. This could be due, for example, to gas consumption or to the decrease of weak interactions with small satellites that could trigger the star formation through bars and spiral arms.

Locally 0.5% of galaxies with $L_V > 10^{10}$ $L_\odot$ have SEDs typical of LIRGs. This changes dramatically at higher redshift: in deep surveys, ISO detect about 15% of the $M_B \leq$-20 galaxies (LIRGs, Hammer et al. 2005) and *Spitzer* detect about 30% of field galaxies (Starbursts and LIRGs, Bell et al. 2005). Thus the two populations (optical and LIR galaxies) overlap more at high z.

4.3. *Towards a Scenario of Recent Bulge and Disk Formation in Intermediate-Mass Spirals*

Because a significant part of recent star formation takes place in LIRGs, any overall picture of galaxy evolution requires a detailed panchromatic study. Optical/spectral properties of LIRGs are similar to those of other galaxies and only infrared measurements are able to describe how the star formation is distributed between the different galaxy types. Thus a complete study has to link the star formation revealed in the infrared to the morphological changes seen in the optical. This has been done by Hammer et al. (2005) using HST, ISO, VLA and VLT observations of the CFRS. A detailed comparison of the morphologies of distant ($0.4<z<1.2$) galaxies with the local galaxies shows the complete vanishing of the LCGs in the local Universe (by a factor $\sim$10) and the decrease of mergers and irregulars (by a factor $\sim$4). Almost all distant galaxies have much bluer central colors than local bulges, probably as a result of active star formation in the 1kpc central region of most distant spirals. This supports a relatively recent formation of bulges in many present-day spirals. This simultaneous changes in galaxy morphologies and central colors of distant galaxies together with the observed lower metallicities (Liang et al. 2004) and overall higher star-formation rates at high z are the ingredients for an updated scenario of bulge and disk formation in spirals. Hammer et al. (2005) propose three different phases of galaxy evolution: the mergers/interacting, the compact galaxy and finally the growth of disk phase. During the last 8 Gyrs, most luminous galaxies are expected to experience a major merger that suppresses the disk as matter is falling to the mass barycenter. This phase is associated with short (1 Gyr) and strong peaks of star formations. Most of galaxies in this phase are LIRGs. Then, the compact phase corresponds to a decrease over 0.6-2 Gyr of the enhanced star formation due to merging. A significant fraction of stars form in bulges and additional occurrence of gas infall may subsequently wrap around the bulge to form a new disk-like component. Finally, the star formation spreads over all the forming disk as fed by large amounts of gas infall. In this scenario, about half of the bulge stellar content was made earlier in their progenitors, before the last major phase of accretion. More than a third of the present-day stellar mass is formed at $z < 1$. This scenario is in very good agreement with the hydrodynamical numerical simulations of Scannapieco & Tissera (2003) in which mergers, through secular evolution and fusions, transform galaxies along the Hubble sequence by driving a morphological loop that might also depend on the properties of the central potential wells, which are also affected by mergers. This very attractive scenario links in a simple way the distant and local galaxies; it will be confronted to the new panchromatic studies of *Spitzer* galaxies. Note that another possibility of buildup of dense central component in disk galaxies is internal secular evolution, as reviewed by Kormendy & Kennicutt (2004).

5. GALAXIES AT REDSHIFTS Z $\geq$ 1.5

Analysis of the CIB in the light of the ISO observations shows that, as we go to wavelengths much longer than the emission peak, the CIB should be dominated by galaxies at higher redshifts as illustrated in Figure 4. The comoving infrared production rate needed to fill the CIB around 1mm at a redshift centered around 2.5 to 3 remains comparable to the one from galaxies detected in the ISOCAM surveys and filling 65% of the peak of the CIB. In this section we discuss the rapidly growing observational evidence that this picture is basically correct. The main source of these observations has been the SCUBA submillimeter observations at 850 μm and 450 μm (see Blain et al 2002 for a review) and observations from the MAMBO instrument on the IRAM 30-m telescope at 1.2 mm (Greve et al. 2004). The negative K-correction becomes very effective at these wavelengths, leading to an almost constant observed flux for galaxies of the same total infrared luminosity between redshifts 1 and 5. More recently, the *Spitzer* observatory has produced a wealth of early observations showing that this observatory will contribute much to our understanding of infrared galaxies at z$\geq$1.5.

5.1. *Number Counts, Contribution to the CIB*

Blank-field deep surveys combined with mapping of areas lensed by clusters lead to number counts at 850 μm down to 0.5 mJy (e.g., Smail et al. 2002; Wang et al. 2004). At 1.2 mm counts have been obtained down to 2.5 mJy (e.g., Greve et al. 2004). The number counts shapes at 850 μm and 1.2 mm are compatible with the assumption that they are made of the same population with a flux ratio $F_{850}/F_{1200} = 2.5$. For a typical ULIRG SED, a 5mJy source at 850 μm has a luminosity of $10^{12} L\odot$ at a redshift of about 2.5. The large fraction of the background resolved at 850 μm (see Section 3.2) has interesting consequences. It shows very directly that if the sources are at redshift larger than 1 (as confirmed by the redshift surveys discussed below), the infrared luminosity of the sources that dominate the background is larger than $10^{12} L_\odot$. This is a population with a very different infrared luminosity function than the local or even the $z = 1$ luminosity function. The link between this population at high z, and what has been seen at $z \sim 1$ (as discussed in Section 4) will be done by *Spitzer*/MIPS observations at 24 μm. Figure 4 shows that the building on the bulk of the CIB near its peak (at 150 μm) with redshift is expected to be similar to the building of the 24 μm background when the history of the 15 and 70 μm CIB have larger contributions from redshift-1 sources. The K-correction plots (Figure 6) show for 15 μm a hump at $z = 1$ associated with the coincidence of the 6-9 μm aromatic features in the ISOCAM filter and a hump at the same redshift for the 24 μm MIPS filter associated with the 11-14 μm set of aromatic features in the MIPS filter. For the MIPS filter a second hump is visible at $z \sim 2$ that corresponds to 6-9 μm features centered on the 24 μm MIPS filter. ISOCAM galaxies contribute to about 2/3 of the energy peak of the CIB. Following the previous considerations, it is easy to understand why the remaining fraction is likely to be made of sources in the redshift range 1.5-2.5. The presently detected SMGs with luminosity $10^{12} L_\odot$ have an almost constant flux between redshift 1.7 and redshift 2.5 at 24 μm (similar to the constant flux at 850 μm between redshift 1 and 5). The MIPS 24 μm deep surveys (e.g., Papovich et al. 2004) reach a sensitivity of 50 μJy and thus can detect all these galaxies when they are starburst-dominated. Considering the speed of the MIPS it is likely that 24 μm surveys will become the most efficient way to search for luminous starburst galaxies up to $z = 2.5$ and up to 3 for the most luminous ones.

5.2. *Redshift Distribution and SEDs of the SMGs*

The first obvious question when investigating the nature of the submillimeter galaxies (SMGs) is their redshift distribution. The rather low angular resolution of the submillimeter and millimeter observations made identifications with distant optical galaxies an almost impossible task without an intermediate identification. This is provided by radio sources observed with the VLA with 10 times better angular resolution. The tight correlation between far-infrared luminosity and radio flux (Helou et al. 1985; Condon 1992) provides the needed link. This then allows us to get optical identifications and redshift measurements using 10-m class telescopes. Confirmation of these identifications can then be obtained through CO line observations with the millimeter interferometers such as the Plateau de Bure interferometer. The redshift deduced from the optical lines is confirmed by the CO observations. So far, only a handful of cases have gone through this whole chain of observations (e.g., Genzel et al. 2003; Greve et al. 2005; Neri et al. 2003), but a high success rate gives confidence in the first step of the identification process. The chain will also have to be applied to the tentative counterparts of radio-undetected SMGs that have been found using a certain combination of optical properties (Pope et al. 2005).

The difficulty of making large, blind surveys at 850 μm at the required sensitivity has lead

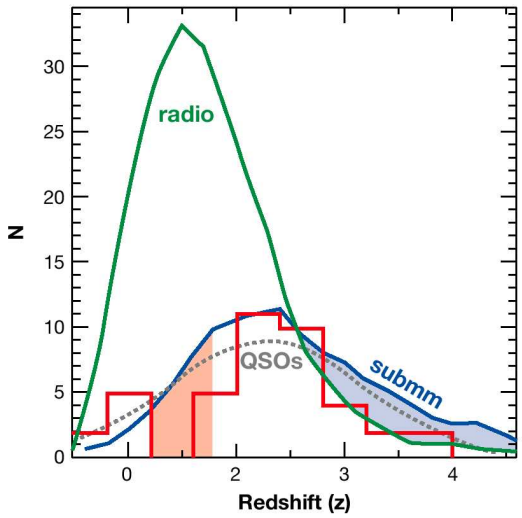

FIG. 7.— The observed histogram of the redshift distribution for the 55 radio-identified SCUBA galaxies (*red histogram*). Curves derived for a model of the radio/submillimeter galaxy populations (Chapman et al. 2003b; Lewis et al. 2005) are overplotted suggesting that the redshifts of the sources missed in the radio identification process lie mostly at redshifts ∼3-5 between the radio and submillimeter model tracks. A sample of radio-selected QSOs is also overplotted (*gray dotted line*), revealing a remarkable similarity with the observed distribution for submillimeter galaxies. From Chapman et al. 2003a.

to an attempt to find distant SMGs through blind surveys at different wavelengths. Barger et al. (2000) have observed optically faint radio sources at submillimeter wavelength and demonstrated them to be, so far, the most efficient way to preselect targets for submillimeter observations and to get larger samples of potentially high redshift SMGs. As an example, Chapman et al. (2002) recovered at 850 μm 70% of the blind submillimeter survey sources. This contrasts the recovery rate of MAMBO sources, which is relatively low, ∼25% (Dannerbauer et al. 2004). It should be noticed that the radio preselection biases the sample against very high redshifts (z <3) because the radio flux at 1.4 GHz is below the detection limit of the VLA surveys used for this preselection. A model by Chapman et al. (2003b) and by Lewis et al. (2005) illustrate this effect very well (Figure 7). A fraction of the submillimeter-selected sources are missed in such a process at $z >$ 3 (detectability in radio) and around z ∼1.5 (optical redshifts desert). The number of non identified submillimeter sources (around 30% for $S_{850} > 3$ mJy) is consistent with this model. Nevertheless the submillimeter-selected sources do not appear qualitatively different from the optically-faint-radio selected ones. Another bias is the effect of the dust effective temperature of the SMGs (Lewis et al. 2005). At a given total far-infrared luminosity, hotter sources have lower submillimeter fluxes if the radio/far-infrared correlation continues to hold.

They could be missed in the submillimeter surveys (see the discussion in Chapman et al. 2005).

Chapman et al. (2003a) got spectroscopic redshifts of 55 sources obtained in this way. The redshift distribution for these sources is shown in Figure 7 (note that when this review was being edited, Chapman et al. (2005) publish spectroscopic redshifts for 73 SMGs). This distribution peaks at z= 2.4 with a substantial tail up to z=4. In fact the redshift distribution can be represented by a Gaussian distribution centered on 2.4 and with a sigma of 0.65. Almost all SMGs are found in the redshift range $1.5 < z < 3$. This redshift distribution is compared with that of the redshift distribution for a pure radio sample in Figure 7. The SMGs selected in the way described above is also shown to be very similar to the redshift distribution of the radio-selected QSOs. This observation is interesting in the context of high rate of AGN activity detected in SMGs.
The determination of the SED of millimeter/submillimeter galaxies remains an open question despite a lot of work in the last few years. The SCUBA and MAMBO data provide constraints on the flux and spectrum at long wavelengths; *Spitzer* observations constrain the near and mid-infrared. The far-infrared part of the SED remains the least precisely known. Low angular resolution makes 70 and 160 μm deep surveys confusion-limited at 3 and 40 mJy (Dole et al. 2004b). These limits are too high to complete the SED of the SMGs (see Figure 9). Stacking sources will help to go deeper than the confusion limit when large samples of SMGs are available in MIPS cosmological surveys. A first attempt on a radio-selected sample lowered the limit down to 1.2 mJy at 70 μm (Frayer et al. 2004). They find a typical flux ratio I(70)/I(24)<7 that they interpret to be low when compared with low-redshift starburst. However, such low ratios are typical of dusty starbursts placed at redshift greater than 1.5. It is thus likely that the lower colors are due to a redshift effect. Appleton et al. (2004) looked at the mid- and far-infrared fluxes from a purely radio-selected 1.4 GHz μJy sample of about 500 and 230 sources at 24 and 70 μm, respectively. They show that the far-infrared to radio correlation that is constant out to $z = 1$ seems to be constant using 24 μm out to $z = 2$ but with a larger dispersion due systematic variations in SED shape throughout the population. This provides positive evidence of the universality of the infrared/radio correlations out to redshifts of about 2.

Blain et al (2004a) have analyzed SEDs of infrared galaxies assuming that the low-redshift radio/far-infrared correlation applies to SMGs. Under this reasonable assumption and using a model of long-wavelengths SEDs based on a single modified black body, they can choose a single parameter to built an SED that fits the long-wavelengths data and the radio/infrared luminosity ratio. In their paper, this single parameter is the temperature, but it could equally well be the long-wavelength emissivity, because they showed that this is degenerate with temperature. A split between two redshift populations appear in their analysis. The high-z galaxies selected by the submillimeter observations are significantly colder that the low-z galaxies (Dune & Eales, 2001; Stanford et al. 2000), IRAS or IRAS-radio selected. The discrepancy in part probably reflects selection effects in the way these samples were obtained and may reflect the fact that SMGs and local infrared galaxies are distinct populations. It remains an open question what effect this has on the SED model. The main worry is that a single modified black body often does not fit ULIRGs SED when they are known at many frequencies. The SED is broader; the unavoidable temperature distribution of dust in infrared galaxies would affect such an analysis. In fact, the Stanford et al. (2000) sample does not agree well with the single-temperature SED, and this led Lagache et al. (2004) to take broader SEDs for their starburst galaxy templates.

5.3. *Nature of the SMGs*

Many LIRGs and ULIRGs at low redshifts have been identified with interacting or galaxy mergers. A substantial fraction show signs of AGN activity but it has been shown for the low-redshift LIRGs and ULIRGs that the starburst component dominates the energy output (Genzel et al. 1998; Lutz et al. 1998). The sources used for the redshift

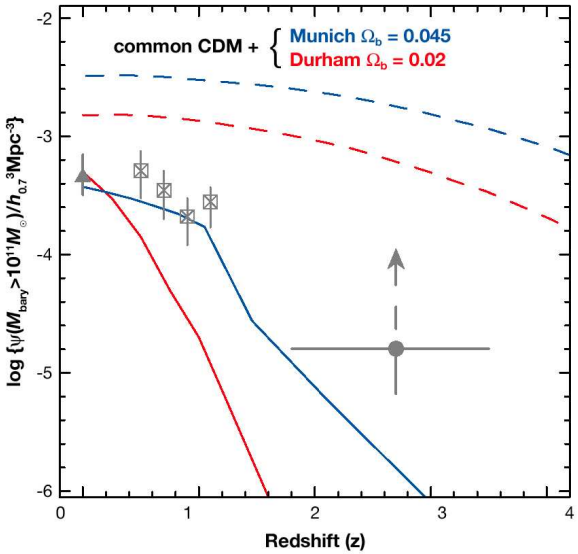

FIG. 8.— Comoving number densities of galaxies with baryonic masses $\geq 10^{11}\,M_\odot$ as a function of redshift. The *triangle* and *open squares* show densities of massive stellar systems at $z = 0$ and $z \sim 1$; The *circle* shows the density for massive SMGs at $z \sim 2.7$, with a factor of 7 correction for burst lifetime. *Blue* and *red curves* show the predictions of semianalytic models by the "Munich" and "Durham" groups, respectively. *Dashed curves* show the corresponding number densities of halos with available baryonic masses $\geq 10^{11}\,M_\odot$. The two models use the same halo simulations but assume different Ω_b. From Genzel et al. (2004).

distribution by Chapman et al. (2003a) have been imaged with the HST. Most of them are multi-component-distorted galaxy systems (Conselice et al. 2003; Smail et al. 2004). They display irregular and frequently highly complex morphologies compared to optically selected galaxies at similar redshifts. They are often red galaxies with bluer companions, as expected for interacting, star-forming galaxies. They have higher concentrations, and more prevalent major-merger configurations than optically-selected galaxies at z ∼2-3. Most strikingly, most of the SMGs are extraordinarily large and elongated relative to the field population regardless of optical magnitude (Chapman et al. 2003c). SMGs have large bolometric luminosities, $\sim 10^{12} - 10^{13}$ $L_\odot$, characteristic of ULIRGs. If the far-infrared emission arises from the star formation, the large luminosities translate to very high SFR ≥1000 $M_\odot$ year^{-1}. Such high rates are sufficient to form the stellar population of a massive elliptical galaxy in only a few dynamical times, given a sufficient gas reservoir. SMGs are very massive systems with typical mass of 1-2×$10^{11}L_\odot$ (Swinbank et al. 2004), comparable to the dynamical mass estimates from CO observations. Genzel et al. (2004; and more recently Greve et al. 2005) have undertaken an ambitious program to study the nature of the SMGs in more

details. They got CO spectra with the Plateau de Bure interferometer for 7 sources out of their sample of 12 for the CO 3-2 and 4-3 transitions redshifted in the 3 mm atmospheric window. They provide optical identifications and redshifts. The detection of these sources at the proper redshift confirms the usefulness of identification with the help of the radio sources. The median redshift of this sample is 2.4. In addition, one source was studied with the SPIFI instrument on the ESO/VLT. These observations are giving very interesting clues on the nature of the submillimeter galaxies. The gas masses obtained for these systems using CO luminosity/mass of gas determined from local ULIRGs is very large with a median of $2.2\times10^{10}M_\odot$ (10 times larger than in the Milky Way). Using the velocity dispersion, they could infer that the dynamical median mass of these systems is 13 times larger than in Lyman-break galaxies (LBGs) at the same redshift or 5 times the mass of optically selected galaxies at this redshift. These SMGs with a flux at 850 μm larger than 5 mJy are not very rare and unusual objects, because they contribute to about 20% of the CIB at this frequency. Through multiwavelength observations, Genzel et al. (2004) get the stellar component in K band, and infer the star-formation rate and duration of the star-formation burst. They can then compare the number density of these massive systems with semiempirical models of galaxy formation. The very interesting result is that this number density is significantly larger than the predicted one, although the absolute numbers depends on a number of assumptions like the IMF. The comparison is shown in Figure 8. Such massive systems at high redshift are not easy to understand in current cold dark matter hierarchical merger cosmogonies. However, one must keep in mind that bright SMGs (S_{850} >5 mJy) that contribute 20% of the CIB may not be representative of the whole population. Gravitational lens magnification provides a rare opportunity to probe the nature of the distant sub-mJy SMGs. Kneib et al. (2005) study the property of one SMG with an 850 μm flux S_{850}=0.8 mJy at a redshift of $z = 2.5$. This galaxy is much less luminous and massive than other high-z SMGs. It resembles to similarly luminous dusty starbursts resulting from lower-mass mergers in the local Universe.

In order to link the different population of high-redshift objects, several LBGs at redshift between 2.5 and 4.5 have been targeted at 850 μm. The Lyman-break technique (Steidel et al. 1996) detects the rest-frame 91.2 nm neutral hydrogen absorption break in the SED of a galaxy as it passes through several broad-band filters. LBGs are the largest sample of spectroscopically confirmed high-redshift galaxies. Observing LBGs in the submillimeter is an important goal, because it would investigate the link, if any, between the two populations. However, the rather low success rate of submillimeter counterpart of LBGs (e.g., Chapman et al. 2000; Webb et al. 2003) argues against a large overlap of the two populations.

5.4. *Spitzer 24 μm Sources*

A potential new way to find high-z LIRGs and ULIRGs appeared recently with the launch of the *Spitzer* observatory. Particularly suited to this goal is the 24 μm channel of the MIPS instrument. The confusion levels in the 70 and 160 μm prevent detection a significant number of high-redshift objects, and the IRAC 3.6 to 8 μm at high redshift probes mostly the old stellar component that is much weaker than the dust emission in starburst galaxies. At the time of writing, the observations are under way, and only a few results are available. Le Floc'h et al. (2004) give the first hint on the 24 μm selected galaxies. They couple deep 24 μm observations in the Lockman hole and extended groth strip with optical and near-infrared data to get both identification and redshift (either spectroscopic or photometric). They find a clear class of galaxies with redshift $1\leq z \leq 2.5$ and with luminosities greater than $\sim5\times10^{11}$ $L_\odot$ (see also Lonsdale et al. 2004). These galaxies are rather red and massive with M>2×10^{10} $M_\odot$ (Caputi et al. 2005). Massive star-forming galaxies revealed at $2 \leq z \leq 3$ by the 24 μm deep surveys are characterized by very high star formation rates – SFR ≥500 $M_\odot$ year^{-1}. They are able to construct a mass of $\simeq10^{11}$ $M_\odot$ in a burst lifetime (≃0.1 Gyr). The 24 μm galaxy population also comprises sources with intermediate luminosities ($10^{10} \leq L_{IR} \leq 10^{11}$ $L_\odot$) and low to intermediate assembled stellar masses ($10^9 \leq M \leq 10^{11}$ $M_\odot$) at $z \leq 0.8$.

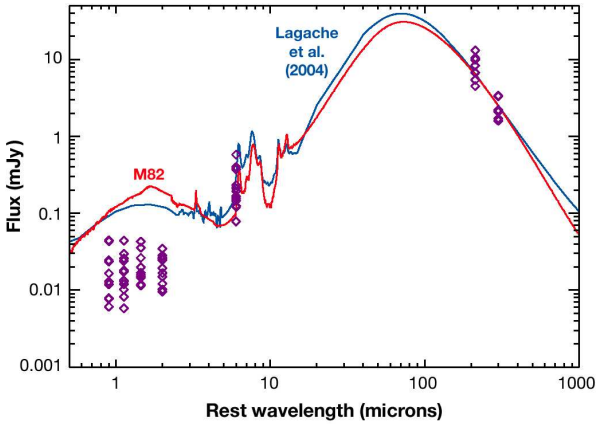

FIG. 9.— Rest-frame SED of 15 SMGs (assuming a redshift of 3) with MAMBO and/or SCUBA, *Spitzer*/IRAC and *Spitzer*/MIPS 24 μm measurements. *Purple diamonds* are the galaxies 208, 119, 115, 48, 44 (Frayer et al. 2004), LE850_4, LE850_35 (Egami et al. 2004), and MMJ105201, MMJ105155, MMJ105203, MMJ105216, MMJ105148, MMJ105157, MMJ105207 MMJ105203 (Ivison et al. 2004). Overplotted are the SEDs of M82, normalized at 850 μm (from Chanial 2003), and the SED template of the Lagache et al. (2004) model, for L=10^{13} L$_\odot$ and a redshift of 3 (no normalization has been applied). Note that this sample of SMGs has a ratio dust/stellar component higher than the template or M82.

At low redshifts, however, massive galaxies are also present, but appear to be building their stars quiescently in long timescales (Caputi et al. 2005). At these redshifts, the efficiency of the burst-like mode is limited to low mass M$\leq 10^{10}$ M$_\odot$ galaxies. These results support a scenario where star-formation activity is differential with assembled stellar mass and redshift, and proceed very efficiently in massive galaxies (Caputi et al. 2005).

In the Lockman Hole, only one galaxy is associated with an X-ray source. This suggests that these galaxies are mostly dominating by star formation, consistent with the findings of Alonso-Herrero et al.(2004) and Caputi et al. (2005). This is also suggested by SEDs that are best fitted by PAH features rather than by strongly rising, AGN-type continua (Elbaz et al. 2005). The selected sources exhibit a rather wide range of MIPS to IRAC flux ratio and optical/near-infrared shapes, suggesting a possibly large diversity in the properties of infrared galaxies at high redshift as noticed by Yan et al. (2004b). Based on these first analyzes, together with the interpretation of the number counts (e.g., Lagache et al. 2004), it is clear that the 24 μm observations will provide the sample to unambiguously characterize the infrared galaxies up to $z \simeq 2.5$. They should fill the gap between the ISO- and SCUBA-selected galaxies.

Several 24 μm observations have been conducted on selected ERO and SCUBA and MAMBO samples. To our knowledge, LBGs have not been observed at long wavelengths. The MAMBO/SCUBA selected galaxies in the Lockman hole with radio identification have been observed by *Spitzer* and most of them detected between 3.6 and 24 μm. This allows to get an average SED for these (Egami et al. 2004; Ivison et al. 2004; see Figure 9)

Spitzer deep surveys at 24 μm and shallow surveys like the SWIRE legacy (Lonsdale et al. 2004) can easily detect them and are thus a promising new way to find this class of high-z infrared galaxy. Nevertheless, the Early Release Observations from *Spitzer* have been used to extract their submillimeter flux from a stacking analysis of SCUBA observations in the Lockman hole (Serjeant et al. 2004). In this field, seven SMGs were already known and others were identified by further analysis. For the bulk of the 24 μm sources a marginal detection is found with an S_{850}/S_{24} ratio (1/20) much lower than that observed for SMGs. This clearly shows that the SMGs are only a fraction of the 24 μm sources, as expected. An interesting challenge is to find if *Spitzer* color criteria can be found to extract preferentially SMGs, i.e., the galaxies that account for most of the CIB near 1 mm. The SED in the thermal infrared appears quite variable for LIRGs and ULIRGs making this difficult (e.g., Armus et al. 2004).

Extremely Red Objects (EROs) are usually selected based on their red colors: $(R - K_s) \geq 5.3$ mag or $(I - K_s) \geq 4$ mag. This color selection should include early-type galaxies at $z \sim 1$. However, the color selections are also sensitive to dust-reddened, star-forming systems. Up to now, it remains unclear what fraction of EROs are truly dust-obscured galaxies. Different scenarios of galaxy formation predict very different formation epochs for such galaxies. It is thus interesting to characterize these galaxies, in particular whether they belong to the early-type or dusty star-forming class of objects. *Spitzer*/MIPS 24 μm observations offer the first opportunity to address this issue because 24 μm observations can clearly discriminate between the two populations. In the N1 field, Yan et al. (2004a) suggest that about 50% of EROs are infrared luminous, dusty starbursts at $z \geq 1$ (in a similar study, Wilson et al. (2004) show that at least 11% of $0.6 < z < 1.3$ EROs and at least 22% of $z > 1.3$ EROs are dusty star-forming galaxies). Their mean 24 μm flux corresponds to infrared luminosities of about 3×10^{11} and 10^{12} L$_\odot$ at z$\sim$1 and $z \sim 1.5$, respectively. They are massive galaxies with lower limit M$\geq 5\times10^9$ to 2 10^{10} M$_\odot$. The fraction of EROs likely to be AGN is small; about 15%. The link between the two classes of EROs could be that starburst EROs are experiencing, at $z > 1$, violent transformations to become massive early-type galaxies.

5.5. *ULIRGs and Active Galactic Nuclei at High Redshifts*

SMGs are massive ULIRGs at high redshift. One of the key question discussed above for the $z \simeq 1$ galaxies is to distinguish whether starburst or AGN activity powers the dust heating and associated infrared emission. The presence of an AGN in galaxies can be investigated using optical/near-infrared, emission line diagnostics and/or X-ray observations. But the identification of the presence of an AGN does not mean that it is the dominant source of the far-infrared emission. Alexander et al. (2003; see also Almaini et al. 2003) use Chandra observations of the CDF-N to constrain the X-ray properties of 10 bright SMGs. Half of the sample has flat X-ray spectral slopes and luminous X-ray emission, suggesting obscured AGN activity. However, a comparison of the AGN-classified sources to the well-studied, heavily obscured AGN NGC 6240 suggests that the AGN contributes on average a negligible fraction (about 1.4%) of the submillimeter emission. For the MAMBO sources, similar results are found: only one out of the nine MAMBO sources studied by Ivison et al. (2004) has an X-ray counterpart. It has, as expected from low redshift ULIRGs observations (e.g., Rigopoulou et al. 1999), a different mid-infrared SED than the starburst dominated sources. About 75% of their sample has rest-frame mid-infrared to far-infrared SED commensurate with obscured starburst. Swinbank et al. (2004), using AGN indicators provided by near-infrared spectra, estimate that AGNs are present in at least 40% of the galaxies in their sample of 30 SMGs. Emission-line diagnostics suggest that star formation is the dominant power source. However, the composite spectrum for the galaxies that individually show no signs of an AGN in their near-infrared spectra appears to show an underlying broad H$_\alpha$ line. This suggests that even these galaxies may host a low-luminosity AGN that is undetectable in the individual spectra. All these studies tend to show that starburst activity is the dominant source of power of dust

emission in the far-infrared. Still, it is rather difficult to estimate the true "contamination" by the AGN. To go deeper, Chapman et al. (2004) tried an original approach. They observe a sample of identified SMGs at high angular resolution in the radio and use the radio emission as a proxy for the far-infrared emission. This assumption is based on the well-known very tight far-infrared/radio correlation mentioned above. If detected, an extended radio (and thus far-infrared) component is likely to arise from the star formation. The detection of extended emission requires sub-arcsec resolution to map emission on kpc-scales. These are accessible by radio interferometry (they are well beyond far-infrared and submillimeter facilities capabilities). They find that for 70% of the SMG sample, the MERLIN/VLA radio exhibits resolved radio emission which mirrors the general form of the rest frame UV morphology seen by HST. The galaxies are extended on scales of about 10 kpc. They interpret this as a strong support for the hypothesis that radio emission traces spatially extended massive star formation within these galaxies. This is clearly different from what is seen in local ULIRGs where the far-infrared/radio emission is concentrated in the compact nuclear region with an extend less than 1 kpc. In the remaining 30% of the SMG sample, the radio emission is more compact (essentially unresolved). This is a signature of either a compact nuclear starburst and/or an AGN.

In conclusion, the exact fraction of distant submillimeter and millimeter galaxies containing an energetically dominant AGN is difficult to extract from observations. However, even in the systems containing an unambiguously powerfully AGN, the far-infrared emission seems to be powered by the star formation. Surprisingly, this seems to be also the case in distant QSOs. Recently, Beelen (2004) has shown that the far-infrared and blue luminosities from the host galaxies of distant radio-quiet QSOs, are slightly correlated. The far-infrared and radio emission of these quasars follow the radio-infrared correlation observed in local ULIRGs (Yun et al. 2001), providing a first indication that the dust is predominantly heated by the star-formation activity rather than by the AGN. Moreover, the non-linearity between the far-infrared and blue luminosities is also an indication that the heating mechanism of the dust is not directly linked to the AGN. However, the presence of this correlation could suggest a causal connection between the formation of stars in the host galaxy and the activity of the central super massive black hole. This connection has been successfully modeled by Granato et al. (2004).

Finally Houck et al. (2005) and Yan et al. (2005) demonstrate the potential of using mid-infrared spectroscopy, especially the aromatic and silicate features produced by dust grains to directly probe distant L$\sim 10^{13}$ L$_\odot$ ULIRGs at $z \sim 2$. *Spitzer*/IRS observations provide a unique and direct access to high-z ULIRG physical properties. It will definitively open the route toward a complete census of the distant infrared-luminous Universe. A first study on two distant SMGs using *Spitzer*/IRS by Lutz et al. (2005) finds for one SMG an equal contribution from star formation and AGN. The second galaxy is dominated by star formation.

6. CLUSTERING

Measuring clustering gives information about the distribution of galaxies with respect to the dark matter. The strength of clustering is correlated with the mass of extended halos that host luminous galaxies. At redshift lower than 1.3, large-scale structures have been mapped by the DEEP2, 2dF and SDSS surveys (Coil et al. 2004; Peacock et al. 2001; Doroshkevich et al. 2004). At higher redshifts, correlation lengths r_0 have been measured for different galaxy populations such as the LBGs and EROs. Values of about r_0=4 h^{-1} Mpc (Porciani & Giavalisco 2002) and r_0=11 h^{-1} Mpc (Daddi et al. 2000; Firth et al. 2002; Roche et al. 2003) are reported with mean redshift of about 3 and 1-1.5 for the LBGs and EROs, respectively. Getting information on the clustering of the infrared galaxies is essential to see how they relate to the other galaxy populations and to understand their formation process. As an example, one of the key questions is to see if the most massive SMGs are associated with the most massive dark matter halo.

Up to now, very little information is available on the clustering of infrared galaxies. A clustering signal can tentatively be measured, al-

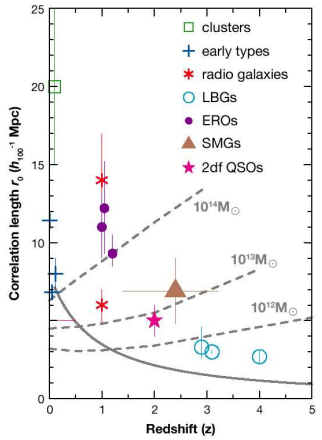

FIG. 10.— Comoving correlation length of the SMGs (*triangle*) in contrast to other populations of low- and high-redshift galaxies (see the summary in Overzier et al. 2003). The horizontal error bar on the SMG point spans the range of redshifts over which SMG associations are found. The *solid line* shows a representative model for the evolution of a certain overdensity. The *dashed lines* show the expected correlation length of dark matter halos as a function of mass and redshift. From Blain et al. (2004a).

though the small number of objects in the deep narrow-pencil ISOCAM and SCUBA beams prevents accurate measurements of the auto-correlation function. At $z \sim$1, Moy & Elbaz (2005) study the large-scale and close environment of ISOCAM galaxies. They find that infrared galaxies are more strongly clustered than optical galaxies. Eighty percents of ISOCAM galaxies are found preferentially in redshift peaks, versus 68% for the optically selected galaxies. Moy & Elbaz (2005) find indirect evidences that the triggering mechanism of dusty starbursts is small-scale ($\sim$ 100 kpc) galaxy-galaxy interactions. Such interactions do not lead to major mergers most of the time but are more likely simple fly-by, tidal interactions or minor mergers. At much higher redshift, there are some indirect evidences of strong clustering of SMGs when compared to other classes of high-redshift galaxies. For example, Chapman et al. (2001) identified SMGs within the most overdense structure of LBGs at $z \sim$3.1 (Steidel et al. 2000). De Breuck et al. (2004) detected an overdensity of MAMBO sources likely at $z \simeq$4.1 in a proto-cluster containing also overdensities of Lyα emitters and LBGs. The first three-dimensional quantitative measurement of the clustering strength of SMGs has been made by Blain et al. (2004a). They find spectroscopic evidence for clustering. Using 73 spectroscopically identified galaxies, they find a surprisingly large number of "associations" with redshifts separated by less than 1200 km s^{-1}. They provide tentative evidence for strong clustering of SMGs at $z \simeq$2-3 with a correlation length of $\sim$(6.9$\pm$2.1) h^{-1} Mpc using a simple pair-counting approach appropriate for the small and sparse SMG sample. This correlation length appears to be somewhat larger than that for both LBG and QSO galaxies at comparable redshifts. It is thus unlikely that the SMGs form a simple evolutionary sequence with either population. On the contrary, the correlation length could be consistent with a form of evolution that subsequently matches the large comoving correlation length typical of evolved EROs at $z \simeq$1 and of clusters of galaxies at $z = 0$ (Figure 10). From this figure, we see that the correlation function of SMGs appears to be consistent with the hypothesis that they are associated with the most massive dark matter halos at high redshifts. These are more massive than the host halos of LBGs and QSOs at comparable redshift. These preliminary conclusions have to be investigated in more detail. In particular, the SMG masses inferred from clustering measurements have to be compared to the dynamical masses derived from millimeter wave CO spectroscopy. To go deeper in understanding the clustering properties of infrared galaxies, *Spitzer* 24 μm surveys will be best suited. With a large number of sources detected in quite large surveys, *Spitzer* will unambiguously constrain the clustering of infrared galaxies from redshift 0.5 to 2.5. Conjointly, the physics of galaxy clustering can be probed by the CIB fluctuation analysis (Knox et al. 2001). CIB fluctuations measure, on large angular scales, the linear clustering

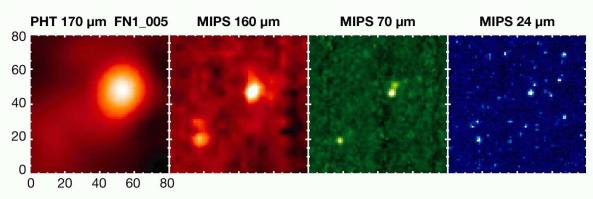

FIG. 11.— Effects of confusion in the far-infrared. Observation of a source in the ELAIS-N1/FIRBACK field in a 400x400 square arcsec box. All images have been resampled to 5 arcsec per pixel, which oversamples the far-infrared maps but undersamples the mid-infrared map. From left to right: 373 mJy ISOPHOT 170 μm source with about 128s of integration (FIRBACK survey, Dole et al. 2001); labels indicate the 5 arcsec pixels; *Spitzer*/MIPS 160 μm with about 16s of integration (SWIRE survey, Lonsdale et al. 2004); MIPS 70 μm with about 80s of integration (SWIRE); MIPS 24 μm with about 160s of integration (SWIRE). Notice (1) the ISO 170 μm source is marginally resolved with MIPS 160, and is unambiguously resolved at 70 μm and 24 μm; (2) the two fainter MIPS 160 μm resolved sources (bottom left) create fluctuations in the ISO 170 μm map that produce the confusion noise when the resolution is limited.

bias in dark-matter halo and, at small angular scales, the nonlinear clustering within a dark-matter halo (Cooray & Sheth 2002). They thus probe both the dark-matter halo mass scale and the physics governing the formation of infrared galaxies within a halo. Promising attempts are underway using the 170 μm ISO FIRBACK fields (Lagache et al., in preparation).

7. FINDING ULIRGS AT Z >3: CONFUSION

In the near future, when a proper census of ULIRGs up to $z \simeq 3$ will have been carried out, the fraction of the CIB at $\sim$1 mm not accounted for should give an indication of the contribution from sources at larger redshifts. Deep surveys at $\sim$1-2 mm are the only obvious tool to find most of these sources. However, the limiting factor of the surveys is not only detector sensitivity or photon noise but also confusion. We concentrate in this section only on extragalactic sources confusion. Source confusion in the far-infrared is illustrated in Figure 11.

Predicting or measuring confusion depends on the scientific goal of the measurement (Helou & Beichman 1990; Dole et al. 2003; Lagache et al. 2003). Performing an unbiased far-infrared or submillimeter survey and getting a complete sample has different requirements than following-up in the far-infrared an already known near-infrared source to get an SED and/or a photometric redshift. In the former case, one has to tightly control the statistical properties of the whole sample; in the latter case, completeness is irrelevant, and even a low photometric accuracy is adequate. We thus favor the use of a term like "unbiased confusion" for the former case. New techniques are being developed to use a priori information at shorter wavelength (e.g., 8 μm with *Spitzer*/IRAC and 24 μm with MIPS) to infer some statistical properties (such as source density or SED) of sources at longer wavelength (e.g., 24 or 160 μm, respectively), and thus to beat unbiased confusion. Predicting unbiased confusion (for instance Condon 1974; Franceschini et al. 1989; Helou & Beichman 1990; Dole et al. 2003; Lagache et al. 2003; Takeuchi et al. 2004; Negrello et al. 2004) requires the knowledge of at least the number-count distribution of the galaxies. In practice, models (validated at some point by observations) are used. Because the shape of the counts in a $log(N) - log(S_\nu)$ diagram varies with the flux density S_ν, the fluctuation level of faint sources below S_ν also vary. This fluctuation level gives an estimate of the unbiased confusion using a photometric criterion (Lagache & Puget 2000; Dole et al. 2003; Lagache et al. 2003). At very faint fluxes, when the background is almost resolved, the photometric criterion will obviously give a very small value for the unbiased confusion level, but the observations will be limited by the confusion due to the high density of faint resolved sources. Thus, another criterion, the source density criterion for unbiased confusion (SDC, Dole et al. 2003; Dole et al. 2004b), needs to be computed and compared to the photometric criterion.

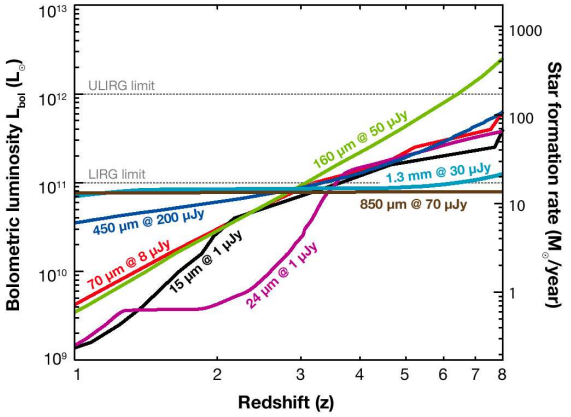

FIG. 12.— Sensitivity to the bolometric luminosity (and star-formation rate, assuming star-forming galaxies) of hypothetical surveys designed to detect LIRGs at $z \sim 3$. The required sensitivities are: at 15 μm: $S_\nu > 1\mu$Jy; at 24 μm: $S_\nu > 1\mu$Jy; at 70 μm: $S_\nu > 8\mu$Jy; at 160 μm: $S_\nu > 50\mu$Jy; at 450 μm: $S_\nu > 200\mu$Jy; at 850 μm: $S_\nu > 70\mu$Jy; at 1.3 mm: $S_\nu > 30\mu$Jy. This plot makes use of the Lagache et al. (2004) model (see appendix).

In the infrared and submillimeter range below 300 μm, the unbiased confusion is in general better predicted by the source density criterion for current and future facilities, because the angular resolution has improved (e.g. from ISO to *Spitzer*). At longer wavelengths, the photometric criterion is more useful. We use the model of Lagache et al. (2004) to predict unbiased confusion. Fifteen-meter submillimeter telescopes are limited by the confusion at 1.2 mJy at 850 μm and at 0.5 mJy at 1.2 mm. Ongoing surveys (Smail et al. 2002; Greve et al. 2004) already reach or are about to reach these levels. If we want to resolve about 80% of the CIB, which corresponds to 56 μJy at 850 μm and 20 μJy at 1.3 mm, one would need a $\sim$90-m telescope at 850 μm and a $\sim$150-m telescope at 1.4 mm. Future facilities for infrared and submillimeter observations include far-infrared space observatories such as *Herschel*, SPICA, and SAFIR, survey missions like ASTRO-F and *Planck*, a larger near-infrared and mid-infrared observatory, *JWST*, and a ground-based submillimeter interferometer, ALMA. In order to detect LIRGs at $z \sim 3$, experiments operating at 15, 24, 70, 160, 450, 850, 1380 μm respectively should reach a sensitivity of 1, 1, 8, 50, 200, 70, 30 μJy, respectively (see Figure 12). The spectral window around 450 μm seems the most effective to reach these galaxies. This constraint is somewhat relaxed if one wants to detect ULIRGs at $z \sim 3$, in which case the required sensitivities are multiplied by about 10. In the near future, ASTRO-F, *Herschel*/SPIRE and *Planck* will be mostly limited by confusion. At long wavelengths, to probe most of the CIB source population and to detect enough early mergers made by building blocks not yet affected by star formation and evolution, large extragalactic surveys will have to be conducted

with ALMA. These surveys will take a substantial fraction of the time (Lagache et al. 2003). As an example, mapping one square degree at 1.3 mm at the 5σ sensitivity of 1 mJy – ∼50% of the CIB is resolved – takes 138 days without including overheads.

8. COMPARISON OF MODELS WITH OBSERVATIONS

One of the striking result of the deep surveys concerns the evolution of the infrared and submillimeter galaxy population. The source counts are high when compared to no evolution, or moderate, evolution models[1] for infrared galaxies. Classical semianalytical models of galaxy formation predicts neither the large numbers of infrared galaxies nor their very strong evolution, revealing a serious gap in our understanding of galaxy formation and evolution. Very recently, several empirical approaches have been proposed to model the high evolution of the infrared output with redshift (e.g., Chary & Elbaz 2001; Franceschini et al. 2001; Rowan-Robinson 2001; Takeuchi et al. 2001; Xu et al. 2001; Lagache et al. 2004) that fit source counts, redshift distributions and CIB intensities and fluctuations, although often not all of them. All these models, however, agree on a general trend – i.e., the luminosity function must change dramatically with redshift, with a rapid evolution of the high-luminosity sources (L>2 10^{11} $L_{\odot}$) from $z = 0$ to $z = 1$, which then stay rather constant up to redshift 3 or more. The evolution of the infrared luminosity function may be linked to a bimodal star-formation process, one associated with the quiescent and passive phase of the galaxy evolution and one associated with the starburst phase, triggered by merging and interactions. The latter dominates the infrared and submillimeter energy density of the Universe at high z. Consistently, cold dark matter N-body simulations show that halo merger rates increase with redshift as $(1+z)^m$ with $2.5 \leq$ m ≤ 3.5 (Gottlober et al. 2001). Observations, however, give m values between 0 and 4 (Le Fèvre et al. 2000; Conselice et al. 2003; Bundy et al. 2004; Lin et al. 2004). The spread is due to different selection effects, detection techniques, pair criteria and sample variance. It is therefore not easy to reconcile the different observational results. Moreover, comparisons with models are very difficult because definitions of merger rates may not be consistent. Merger rates can also depend on halo masses. As a consequence, the timescale of the merger phase is difficult to estimate. Peaks of star formation produced by mergers in hydrodynamical models (e.g., Scannapieco & Tissera 2003) has a duration of several hundreds of million years. This is consistent with what is observed. ULIRGs emit more than half of their bolometric luminosity from a starburst of age 10^7-10^8 years (Genzel et al. 1998). LIRGs build up their stellar mass in a typical timescale of about 0.1 Gyr (Franceschini et al. 2003). These timescales are also supported by Marcillac et al. (2005) who performed Monte Carlo simulations using synthetic spectra based on the models of Bruzual and Charlot (2004) to derive the past star-formation history of 22 LIRGs. They found that LIRGs experience a major event of star formation in their lifetime that produce about 10% of their stellar mass within 0.1 Gyr. How many such episodes of violent star formation does a typical galaxy experience? Assuming a timescale of 0.1 Gyr, Hammer et al. (2005) estimate the number of episodes per galaxies as about 5 from $z = 1$ to $z = 0.4$. These episodic bursts naturally explain the high fraction of LIRGs in the distant Universe.

Models that are more sophisticated than empirical approaches attempt to follow the physics of galaxy formation in greater detail (e.g., Guiderdoni et al. 1998; Hatton et al. 2003; Granato et al. 2004; Silva et al. 2005). In semianalytical models, the collapse of perturbations is described by the classical top-hat model under the assumptions of homogeneity and sphericity. The mass distribution of collapsed halos is computed from the so-called peaks formalism developed by Bardeen et al. (1986). Then dissipative collapse and cooling are introduced, with the usual "overcooling" problem that can partly be solved by introducing stellar feedback. Star-formation processes are deduced from the gas content and the dynamical timescale of the galaxies. Finally spectrophotometric evolution is used to compute the

[1] 'No-evolution': the co-moving luminosity function remains equal to the local one at all redshifts

age dependence of the gas content, the spectra of the stellar populations and the mass-to-luminosity ratios. To make specific predictions for the infrared galaxies, these models must include an important additional feature: absorption of the UV/optical radiation and emission by the dust grains. Very often two modes of star formations are considered; a quiescent mode and a burst mode in which the star formation timescales are much shorter. This burst mode is triggered by galaxy mergers and is absolutely required by the infrared to submillimeter observations. There are some indications that to reproduce the submillimeter galaxy counts, a dramatic change of the IMF is required. A top-heavy IMF, in particular, increases the production of dust that is essential for boosting the luminosity of galaxies in the submillimeter. Using an IMF of the form $dN/\mathrm{dln}m \propto m^{-x}$ with x=0 for the burst mode, Baugh et al. (2005) were able to reproduce not only the submillimeter observations but also the properties of Lyman-Break galaxies. They predict that the SMGs reside in the more massive halos in place at $z = 2$ and therefore that they are more strongly clustered than dark matter at this epoch. This is consistent with tentative observational constraints (Blain et al. 2004a). There are several observational "indications" of massive stars (> 100 $M_{\odot}$) in nearby starburst templates. Wolf-Rayet stars[2] have been detected in a large number of galaxies undergoing intense bursts of star formation (e.g., Gonzalez-Delgado et al. 1997; Pindao et al. 2002). However, it remains difficult to measure the IMF at high mass because of aging effects that can mimic real upper-mass IMF cutoff (the highest massive stars have very short lifetimes).

In conclusion, the hierarchical galaxy formation paradigm is very successful in its description of large-scale structure formation and evolution. The next important step will be to test this picture to explain not only the number densities but also the mass assembly and particularly the mass of the SMGs. First mass measurements of SMGs galaxies seem to show that a very flat IMF cannot by itself explain the mass assembly of the baryonic matter at high z (Genzel et al. 2004). Hierarchical clustering underpredicts the high-z volume densities of these massive galaxies. More work needs to be done to test the baryonic mass assembly in the hierarchical paradigm. Both observational and model estimates are still very uncertain, with the former depending on large lifetime corrections and small samples and the latter on ad hoc input recipes for feedback and star formation.

[2] Wolf-Rayet stars are hot (25,000 to 50,000 K), massive ($\geq 25 M_{\odot}$), luminous stars with a high rate of mass loss. The Wolf-Rayet phase appears in an advanced stage of evolution. They are believed to be O stars that have lost their hydrogen envelopes, leading their helium cores exposed. Wolf-Rayet stars are often in a binary system, and are deemed, within a few million years, to explode as type Ib or Ia supernovae.

9. CONCLUSION AND OPEN QUESTIONS

A number of conclusions are now clear from the analysis of the identified sources in the CIB:

- The comoving energy produced in the past that makes up the CIB at different wavelengths is more uniform that what is suggested by its spectral energy distribution. This is due to the fact that the CIB at long wavelengths ($\lambda \geq 400\mu$m) is dominated by emission from the peak of the SED of galaxies at high z. More quantitatively, the ISOCAM surveys reveal that about two-thirds of the CIB emission at λ ∼150 μm is generated by LIRGs at $z \sim 0.7$. At 850 μm, more than half of the submillimeter CIB is generated by SMGs. The brightest SMGs (S_{850} >3 mJy, ∼30% of the CIB) are ULIRGs at a median redshift of 2.2. The energy density at 150 μm, which is ∼20-25 times larger than the energy density at 850 μm requires a comoving energy production rate at $z = 0.7$ roughly 10 times the energy production rate at $z = 2.2$.

- The evolution exhibited by LIRGs and ULIRGs is much faster than for optically selected galaxies. The ratio of infrared to optical, volume-averaged output of galaxies increases rapidly with increasing redshift.

- Luminosity function evolution is such that the power output is dominated by LIRGs at $z \simeq 0.7$ (although they represent only 3% of all the galaxies in number) and ULIRGs at $z \simeq 2.5$ (although they represent only 1% of all the galaxies in number).

- The energy output of CIB sources is dominated by starburst activity.
- AGN activity is very common in the most luminous of these galaxies even though this activity does not dominate the energy output. The rate and fraction of the energy produced increase with the luminosity.
- LIRGs at $z \simeq 0.7$ are dominated by interacting massive late-type galaxies. Major mergers become dominant in ULIRGs at $z \simeq 2.5$.
- SMGs show rather strong correlations with correlation lengths larger than those of other high redshift sources.
- LIRGs and ULIRGs cannot be identified with any of the distant populations found by rest-frame ultraviolet and optical surveys.

Although these findings are answering the basic questions about the sources that make up the CIB, there are still observational difficulties to be overcome to complete these answers. The SEDs of LIRGs and ULIRGs are quite variable and often not very well constrained in their ratio of far-infrared to mid-infrared or to submillimeter wavelengths. The far-infrared, where most of the energy is radiated, requires cryogenically cooled telescopes. These have small diameters and, hence, poor angular resolution and severe confusion limits for blind surveys. Establishing proper SEDs for the different classes of infrared galaxies detected either in mid-infrared (with ISOCAM at 15 μm or MIPS at 24 μm) or in millimeter-submillimeter surveys is one of the challenges of the coming decade. Making sure that no class of sources that contribute significantly to the CIB at any wavelength has been missed is an other observational challenge. The submillimeter galaxies not found through the radio-selected sources and the question of the warm submillimeter galaxies are also two of those challenges.

Multiwavelength observations of high-z infrared galaxies give a number of new insights on the galaxy formation and evolution problem. As an example, the gas masses and total masses of SMGs are found to be very high. There is a first indication that the number of such high-mass object at redshifts between 2 and 3 is uncomfortably large compared to semi-analytical models of galaxy formation based on the standard hierarchical structure-formation frame. The evolution of the luminosity function is dominated by more luminous sources as redshift increases. This is surprising because the mass function of the collapsed structure is expected to be dominated by smaller and smaller objects as redshift increases.

The populations of infrared galaxies concentrated at $z \simeq 1$ and at $z \simeq 2.5$ studied so far reveal rather different type of sources. The lower redshift ones seem to be starburst phases of already-built massive, late-type field galaxies accreting gas or gas-rich companions forming the disks. We see today a rapid decrease of this activity probably associated with a dry out of the gas reservoir in their vicinity. The larger redshift ones, which are also more luminous, seem to belong to more massive complex systems involving major merging. These systems could be located in the rare larger amplitude peaks of the large-scale structures leading to massive elliptical galaxies at the center of rich clusters. The redshift distribution of these seems quite similar to the redshift distribution of quasars.

Interesting problems that are central to the understanding of galaxy formation and evolution have to be solved in the next decade:

- Determining the role of the large scale environment (nodes, filaments and sheets of the large-scale structures) on star formation;
- Find the relative rates of accretion of gas and smaller galaxies in the growth of massive objects;
- Establish the cycle of bulge versus disk formation, as a function of the ratio between stars and gas in the accreted material;
- Identify the different types of starburst (in a disk or in the nucleus, interaction or merger driven); and
- Estimate the fraction of time spent in the starburst phase and the duration of this phase

Current observations all point in the direction of a possible strong effect of the large-scale environment and the need for models of hierarchical formation and evolution that include properly star versus gas ratio in the accreted material.

Finally the connection between the starburst phenomenon and the AGN activity is an old question still largely unresolved. Recent observations of infrared/submillimeter galaxies have reinforced the link but have not much improved our understanding of the physical link.

ACKNOWLEDGMENTS

We are very grateful to Alexandre Beelen, Karina Caputi, David Elbaz, François Hammer, and George Helou for very useful discussions during the writing of this manuscript. We also thank Pierre Chanial for providing us the M82 SED. Finally, we warmly thank the scientific editor, who found a large number of typos and mistakes in our use of English. The reading of the paper has been significantly improved by his detailed corrections.

APPENDIX: THE PHENOMENOLOGICAL MODEL OF LAGACHE ET AL. (2004)

In this paper, we make extensive use of the Lagache et al. (2004) phenomenological model to illustrate our points. This model constrains in a simple way the evolution of the infrared luminosity function with redshift. It fits all the existing source counts consistent with the redshift distribution, the CIB intensity, and, for the first time, the CIB fluctuation observations, from the mid-infrared to the submillimeter range. In this model, Lagache et al. (2004) assume that infrared galaxies are mostly powered by star formation and hence they use SEDs typical of star-forming galaxies. Although some of the galaxies will have AGN-dominated SEDs, they are a small enough fraction that they do not affect the results significantly. They therefore construct "normal" and starburst galaxy template SEDs: a single form of SED is associated with each activity type and luminosity. They assume that the luminosity function is represented by these two activity types and that they evolve independently. They search for the form of evolution that best reproduces the existing data. An example of two cosmological implications of this model is (a) the PAH features remain prominent in the redshift band 0.5–2.5 (as observationally shown by e.g., Caputi et al. 2005), and (b) the infrared energy output has to be dominated by $\sim$3$\sim$$10^{11}$ $L_\odot$ to $\sim$$3\times10^{12}$ $L_\odot$ galaxies from redshift 0.5 to 2.5.

The excellent agreement between the model and all the available observational constraints makes this model a likely good representation of the average luminosity function as a function of redshift and a useful tool to discuss observations and models. Its rather simple assumptions such as the single parameter sequence of SEDs for starburst galaxies is certainly not accounting for some of the detailed recent observations but probably do not affect seriously the redshift evolution of the averaged properties which are what is modeled.

REFERENCES

Alexander D.M., Bauer F.E., Brandt, W.N.et al. 2003, *AJ* 125, 383
Almaini O., Scott S.E., Dunlop J.S. et al. 2003, *MNRAS* 338, 303
Alonso-Herrero A., Pérez-gonzález P.G., Rigby J. et al. 2004, *APJS* 154, 155
Appleton P.N., Fadda D.T., Marleau F.R., et al. 2004, *APJS* 154, 147
Armand C., Milliard B., Deharveng J. M. 1994, *A&A*, 284, 12
Armus L., Charmandaris V., Spoon H.W.W. et al. 2004, *ApJS* 154, 178
Aussel H., Cesarsky C.J., Elbaz D., Starck J.-L. 1999, *A&A* 342, 313
Bardeen J.M., Bond J.R., Kaiser N., Szalay A.S. 1986,*ApJ* 304, 15
Barger A.J., Cowie L. L., Richards E.A. 2000, *AJ* 119, 2092
Baugh C.M., Lacey C.G., Frenk C.S. et al. 2005, *MNRAS* 356, 1191
Beelen A., 2004. PhD Thesis. Paris-XI Univ.
Bell E.F., Papovich C., Wolf C., et al. 2005, *ApJ* 625, 23
Bernstein R.A., Freedman W.L., Madore B.F. 2002, *ApJ* 571, 56
Blain A.W., Chapman S.C., Smail I., Ivison R.J. 2004a, *ApJ* 611, 725
Blain A.W., Chapman S.C., Smail I., Ivison R. 2004b, *ApJ* 611, 52
Blain A.W., Smail I., Ivison R.J. et al. 2002, *Physics Report* 369, 111
Bruzual G., Charlot S. 2003 *MNRAS* 344, 1000
Bundy K., Fukugita M., Ellis R.S. et al. 2004, *ApJ* 601, L123
Calzetti D., Kinney A.L., Storchi-Bergmann T. 1994, *ApJ* 429, 582

Cambrésy L, Reach W.T., Beichman C.A., Jarrett T.H. 2001, *ApJ* 555, 563
Chanial P., 2003. PhD Thesis. Paris-XI Univ.
Chapman S.C., Blain A.W, Ivison R.J., Smail I., 2003a. Star formation through time, Granada Spain, Oct.2002. *ASP Conf. Ser.* 289
Chapman S.C., Blain A.W, Smail I., Ivison R.J., 2005, *ApJ* 622, 772
Chapman S.C., Helou G., Lewis G., Dale, D., 2003b, *ApJ* 588, 186
Chapman S.C., Lewis G.F., Scott D. et al., 2002 *ApJ* 570, 557
Chapman S.C., Lewis G.F., Scott D. et al., 2001, *ApJ* 548, 17
Chapman S.C., Scott D., Steidel C.C., et al., 2000, *MNRAS* 319, 318
Chapman S.C., Smail I., Windhorst R. et al., 2004, *ApJ* 611, 732
Chapman S.C., Windhorst R., Odewahn S., et al., 2003c, *ApJ* 599, 92
Chary R., Elbaz D. 2001, *ApJ* 556, 562
Coil A.L., Davis M., Madgwick D.S., et al. 2004, *ApJ* 609, 425
Condon J.J. 1974, *ApJ* 188, 279
Condon J. J. 1992, *ARAA* 30, 575
Conselice C.J., Chapman S.C., Windhorst R.A. 2003, *ApJ* 596, 5
Cooray C.J., Sheth R. 2002, *Phys. Rep.* 372, 1
Daddi E., Cimatti A., Pozzetti L. et al. 2000, *A&A* 361, 535
Dannerbauer H., Lehnert M.D., Lutz D. et al. 2004, *ApJ* 606, 664
De Breuck C., Bertoldi F., Carilli et al. 2004, *A&A* 424, 1
Désert F.-X., Boulanger F., Puget J.-L. 1990, *A&A* 237, 215
Dole H., Gispert R., Lagache G. et al. 2001, *A&A* 372, 364
Dole H., Lagache G., Puget J-L., 2003 *ApJ* 585, 617
Dole H., Le Floc'h E., Pérez-González P.G. et al., 2004a, *ApJS* 154, 87
Dole H., Rieke G.H., Lagache G. et al., 2004b, *ApJS* 154, 93
Doroshkevich A., Tucker D. L., Allam S., Way M.J. 2004, *A&A* 418, 7
Dunne L., Eales S.A. 2001, *MNRAS* 327, 697
Dwek E., Krennrich F. 2005, *ApJ* 618, 657
Egami E., Dole H., Huang J.-S. et al. 2004, *ApJS* 154, 130
Elbaz D., Césarsky C. 2003, *Science* 300, 270
Elbaz D., Césarsky C.J., Chanial P. et al. 2002, *A&A* 384, 848
Elbaz D., Césarsky C., Fadda D., et al. 1999, *A&A* 351, L37
Elbaz D., Le Floc'h E., Dole H., Marcillac D. 2005, *A&A* 434, 1
Fadda D., Elbaz D., Duc P.-A. et al. 2002, *A&A* 361, 827
Filipenko A.V. 1992, *Relat. Between Act. Galact. Nucl. Starburst Galaxies: ASP Conf. Ser.*, 31, 485
Firth A.E., Somerville R.S., McMahon R.G. et al. 2002, *MNRAS* 332, 617
Flores H., Hammer F., Elbaz D. et al. 2004, *A&A* 415, 885
Flores H., Hammer F., Thuan T.X., et al. 1999, *ApJ* 517, 148
Franceschini A., Aussel H., Césarsky C.J. et al. 2001, A&A 378, 1
Franceschini A., Berta S., Rigopoulou D. et al. 2003, *A&A* 403, 501
Franceschini A., Toffolatti L., Danese L., De Zotti G. 1989, *ApJ*, 344, 35
Frayer D.T., Chapman S.C., Yan L. et al., 2004, *ApJS* 154, 137
Galliano F. 2004, PhD Thesis. Paris XI Univ.
Genzel R., Baker A.J., Ivison R.J. et al. 2004. Proc. Venice Conf. Multiwavelength Mapping of Galaxy Formation and Evolution. In press
Genzel R., Baker A.J., Tacconi L. et al. 2003, *A&A* 584, 633
Genzel R., Césarsky C.J. 2000, *ARAA* 38, 761
Genzel R., Lutz D., Sturm E. et al. 1998, *ApJ* 498,579
Gispert R., Lagache G., Puget J.-L. 2000, *A&A* 360, 1
Gonzalez-Delgado R.M., Leitherer C., Heckman T.M., Cervino M. 1997, *ApJ* 483, 705
Gorjian V., Wright E.L., Chary R.R. 2000, *ApJ* 536, 550
Gottlober S., Klypin A., Kravtsov A.V. 2001, *ApJ* 546, 223
Granato G.L., De Zotti G., Silva L. et al. 2004, *ApJ* 600, 580
Greve T. R., Bertoldi F., Smail I. et al. 2005, *MNRAS* 359, 1165
Greve T. R., Ivison R. J., Bertoldi, F. et al. 2004, *MNRAS* 354, 779
Gruppioni C., Lari C., Pozzi F. et al. 2002, *MNRAS* 335, 831
Guiderdoni B., Hivon E., Bouchet F.R., Maffei B. 1998, *MNRAS* 295, 877
Guiderdoni B. & the Galics collaboration, 2004. The dusty and molecular Universe; A prelude to Herschel and ALMA, ed. A. Wilson, ESA Conf. Ser.
Hammer F., Flores H., Elbaz D. et al. 2005, *A&A* 430, 115
Hammer F., Gruel N., Thuan T.X. et al. 2001, *ApJ* 550, 570
Hatton S., Devriendt J.E.G., Ninin S. et al. 2003, *MNRAS* 343, 75
Hauser M.G., Arendt R.G., Kelsall T. et al. 1998, *ApJ* 508, 25
Hauser M.G., Dwek E. 2001, *Ann. Rev. Astron. Astrophys.* 37, 249
Helou G., Beichman C.A. 1990. From Ground-Based to Space-Borne Sub-mm Astronomy. ESA SP-314, p. 117
Helou G., Lu N.Y., Werner M.W. et al. 2000, *ApJ* 532, 21
Helou G., Soifer B.T., Rowan-Robinson M. 1985, *ApJ* 298, 7
Héraudeau P., Oliver S., del Burgo C. et al., 2004, *MNRAS* 354, 924
Houck J.R., Soifer B.T., Weedman D. et al. 2005, *ApJ* 622, L105
Ivison R.J., Greve T.R., Serjeant S. et al. 2004, *APJS* 154, 124
Joseph R.D. 1999, *Astrphys. Space Sci.* 266, 321
Kashlinski A. 2005, *Physics report* 409, 361
Kawara, K., Matsuhara H., Okuda H. et al. 2004, *A&A* 413, 843
Kennicutt R.C. 1992, *AJ* 388, 310
Kennicutt R.C. Jr. 1998, *Ann. Rev. Astron. Astrophys.* 36, 189
Knox L., Cooray A., Eisenstein D. et al. 2001,*ApJ* 550, 7
Kormendy J., Kennicutt R.C. 2004, *Ann. Rev. Astron. Astrophys.* 42, 603
Kneib J.-P., Neri R., Smail I., et al. 2005, *A&A* 434, 819
Lagache G., Dole H. 2001, *A&A* 372, 702
Lagache G., Dole H., Puget J.-L. et al. 2003, *MNRAS* 338, 555
Lagache G., Dole H., Puget J.-L. et al. 2004, *APJS* 154, 112

Lagache G., Haffner L.M., Reynolds R.J., Tufte S.L. 2000, *A&A* 354, 247
Lagache G., Puget J.-L. 2000, *A&A* 355, 17
Lari C., Pozzi F., Gruppioni C., et al. 2001 *MNRAS* 325, 1173
Laurent O., Mirabel I.F., Charmandaris V. et al. 2000, *A&A* 359, 887
Le Fèvre O., Abraham R., Lilly S.J. et al. MNRAS 311, 565
Le Floc'h E., Papovich C., Dole H. et al. 2005, *ApJ*, in press
Le Floc'h E., Pérez-González P.G., Rieke G.H. 2004, *ApJS* 154, 170
Lewis G.F., Chapman S.C., Helou G. 2005, *ApJ* 621, 32
Li A., Draine B.T. 2001, *ApJ*, 554, 778
Liang Y.C., Hammer F., Flores H. et al. 2004, *A&A* 423, 876
Lin L.W., Koo D.C., Willmer C.N.A. et al. 2004, *ApJ* 617, L9
Lonsdale C., Del Carmen Polletta M.C., Surace J. et al., *ApJS* 154, 54
Lutz D., Spoon H.W.W., Rigopoulou D. et al. 1998, *ApJ* 505, 103
Lutz D., Valiente E., Sturn E. et al. 2005, *ApJ* 625, 83
Lutz D., Veilleux S., Genzel R. et al. 1999, *ApJ* 517, 13
Mann R.G., Oliver S., Carballo et al. 2002, *MNRAS* 332, 549
Mattila K. 2003, *ApJ* 591, 119
Matsumoto T., Matsuura S., Murakami H. et al. 2005,*ApJ* 626, 31
Marcillac D., Elbaz D., Charlot S. et al. 2005, *A&A* submitted
Metcalfe L., McBreen B., Kneib J.-P. et al. 2003, *A&A* 407, 791
Miville-Deschenes M-A., Lagache, G., Puget J-L. 2002, *A&A* 393, 749
Nakamura O., Fukugita M., Brinkmann J., Schneider D.P. 2004, *AJ* 127, 2511
Negrello N., Magliocchetti M., Moscardini L. et al. 2004, *MNRAS* 352, 493
Neri R., Genzel R., Ivison R.J. et al. 2003, *ApJ* 597, 113
Oliver S., Rowan-Robinson M., Alexander D.M. et al. 2000, *MNRAS* 316, 749
Overzier R. A., Röttgering H. J. A., Rengelink, R. B., Wilman, R. J. 2003, *A&A* 405, 53
Papovich C., Dole H., Egami E., et al. 2004, *ApJS* 154, 70
Partridge R.B., Peebles P.J.E. 1967, *ApJ* 148, 377
Peacock J.A., Cole S., Norberg P. et al. 2001, *Nature* 410, 169
Pérez-González P.G., Rieke G.H., Egami E. et al. 2005, *ApJ*. In press
Peeters E., Spoon H.W.W., Tielens A.G.G.M. 2004, *ApJ* 613, 986
Pindao M., Schaerer D., Gonzalez Delgado R.M., Stasinska G. 2002, *A&A* 394, 443
Pope A., Borys C., Scott D. et al. 2005, *MNRAS* 358, 149
Porciani C., Giavalisco M. 2002, *ApJ* 565, 24
Puget J.-L., Abergel A., Bernard J.P. et al. 1996, *A&A* 308, L5
Renault C., Barrau A., Lagache G., Puget J-L. 2001, *A&A* 371, 771
Rigopoulou D., Spoon H.W.W., Genzel R. et al. 1999, *AJ* 118, 2625
Rieke G.H., Lebofsky M.J. 1979, *Ann. Rev. Astron. Astrophys.* 17, 477
Roche N.D., Dunlop J., Almaini O. 2003, *MNRAS* 346, 803
Rowan-Robinson M. 2001, *ApJ* 549, 745
Sanders D.B., Mirabel F. 1996, *ARAA* 34, 749
Sanders D.B., Soifer B.T., Elias J.H. et al. 1988a, *ApJ* 325, 74
Sanders D.B., Soifer B.T., Elias J.H. et al. 1988b, *ApJ* 328, L35
Sato Y., Kawara K., Cowie L.L. et al. 2003, *A&A* 405, 833
Scannapieco C., Tissera P.B. 2003, *MNRAS* 338, 880
Serjeant S., Morthier A.M.J., Ivison R.J. et al. 2004 *APJS* 154, 118
Silva L., De Zotti G., Granato G.L. et al. 2005, *MNRAS* 357, 1295
Smail I., Chapman S.C., Ivison R.J., Blain A.W. 2005, *ApJ* 616, 71
Smail I., Ivison R.J., Blain A.W., Kneib J.-P. 2002, *MNRAS* 331, 495
Soifer B.T., Neugebauer G. 1991, *AJ* 101, 354
Solomon P.M., Vanden Bout P.A. 2005, *Ann. Rev. Astron. Astrophys.* 43. In press
Stanford S.A., Stern D., van Breugel W., De Breuck C. 2000, *ApJS* 131,185
Steidel C.C., Adelberger K.L., Shapley A.E. et al. 2000, *ApJ* 532, 170
Steidel C.C., Giavalisco M., Pettini M. et al. 1996, *ApJ* 624, L17
Swinbank A.M., Smail I., Chapman et al. 2005, *ApJ* 617, 64
Takeuchi T. T., Ishii T. T. 2004, *ApJ* 604, 40
Takeuchi T.T., Ishii T.T., Hirashita H. et al., 2001, *PASJ* 53, 37
Toomre A. 1997, *Conf. Proc. Evol. Galaxies Stellar Popul., May 19-21*, ed B.M. Tinsley, R.B. Larson, p. 401. New Haven: Yale University Observatory
Veilleux S., Kim D.-C., Sanders D.B. et al., 1995, *APJS* 98, 171
Wang W.H., Cowie L.L., Barger A.J. 2004, *ApJ* 613, 655
Webb T.M., Eales S., Foucaud S. et al., 2003, *ApJ* 582, 6
Wilson G., Huang J.-S., Pérez-González P.G. et al., 2004, *ApJS* 154, 107
Wright E.L. 2001, *ApJ* 553, 538
Xu C., Lonsdale C.J., Shupe D.L. et al. 2001, *ApJ* 562, 179
Yan L., Chary R., Armus L. et al. 2005, *ApJ*. In press
Yan L., Choi P.I., Fadda D. et al. 2004a, *ApJS* 154, 75
Yan L., Helou G. Fadda D. et al. 2004b, *ApJS* 154, 60
Yun R., Naveen A., Condon J.J. 2001, *ApJ* 554, 803
Zheng X.Z., Hammer F., Flores H. et al. 2004, *A&A* 421, 847

2004

The Astrophysical Journal Supplement Series, 154:87–92, 2004 September

FAR-INFRARED SOURCE COUNTS AT 70 AND 160 MICRONS IN *SPITZER* DEEP SURVEYS

H. Dole,[1,2] E. Le Floc'h,[1] P. G. Pérez-González,[1] C. Papovich,[1] E. Egami,[1] G. Lagache,[2]
A. Alonso-Herrero,[1] C. W. Engelbracht,[1] K. D. Gordon,[1] D. C. Hines,[1,3] O. Krause,[1] K. A. Misselt,[1]
J. E. Morrison,[1] G. H. Rieke,[1] M. J. Rieke,[1] J. R. Rigby,[1] E. T. Young,[1] L. Bai,[1] M. Blaylock,[1]
G. Neugebauer,[1] C. A. Beichman,[4] D. T. Frayer,[5] J. R. Mould,[6] and P. L. Richards[7]
Received 2004 March 26; accepted 2004 May 6

ABSTRACT

We derive galaxy source counts at 70 and 160 μm using the Multiband Imaging Photometer for *Spitzer* (MIPS) to map the *Chandra* Deep Field–South (CDF-S) and other fields. At 70 μm, our observations extend upward about 2 orders of magnitude in flux density from a threshold of 15 mJy, and at 160 μm they extend about an order of magnitude upward from 50 mJy. The counts are consistent with previous observations on the bright end. Significant evolution is detected at the faint end of the counts in both bands, by factors of 2–3 over no-evolution models. This evolution agrees well with models that indicate that most of the faint galaxies lie at redshifts between 0.7 and 0.9. The new *Spitzer* data already resolve about 23% of the cosmic far-infrared background at 70 μm and about 7% at 160 μm.

Subject headings: galaxies: evolution — galaxies: statistics — infrared: galaxies

1. INTRODUCTION

The cosmic infrared background (CIB), relic emission of the formation and evolution of the galaxies, peaks in the far-infrared (FIR) in the 60–200 μm wavelength range (Puget et al. 1996; Hauser et al. 1998; Lagache et al. 1999; Gispert et al. 2000; Hauser & Dwek 2001). In the local universe only about a third of the extragalactic emission is released in the FIR (Soifer & Neugebauer 1991). However, the CIB FIR peak accounts for more than half of the total optical/infrared background, indicating strong evolution of galaxy properties toward high FIR output in the past. Characterizing the galaxies responsible for most of the CIB is therefore an important goal of cosmological surveys. Galaxy counts (or number counts) provide a powerful tool to investigate the evolution of the galaxies and their contribution to the CIB.

The cryogenic infrared space missions of the *Infrared Astronomical Satellite* (*IRAS*) and *Infrared Space Observatory* (*ISO*) (see Genzel & Cesarsky 2000 and Dole 2003 for reviews) provided important data on source counts at 60 μm (Hacking & Soifer 1991) and at 100 μm (Rowan-Robinson et al. 1986), and more recently at 90 μm (Kawara et al. 1998, 2004; Efstathiou et al. 2000; Juvela et al. 2000; Linden-Vornle et al. 2000; Matsuhara et al. 2000; Rodighiero et al. 2003) and 170 μm (Kawara et al. 1998, 2004; Puget et al. 1999; Matsuhara et al. 2000; Dole et al. 2001). Mid-infrared (MIR) observation with ISOCAM at 15 μm (Elbaz et al. 1999) are also of great interest, since they are believed to resolve a significant fraction of the CIB into sources (Elbaz 2002). The *Spitzer Space Telescope* (Werner et al. 2004) provides the ability for much deeper and wider area surveys from 3.6 to 160 μm. This paper investigates source counts at 70 and 160 μm from *Spitzer*. A companion paper addresses the MIR source counts at 24 μm (Papovich et al. 2004). The three-band source counts are the basis of new phenomenological models by Lagache et al. (2004).

2. OBSERVATIONS AND DATA REDUCTION

Observations were carried out with the Multiband Imaging Photometer for *Spitzer* (Rieke et al. 2004) in the *Chandra* Deep Field–South (CDF-S) and the Boötes field corresponding to the NOAO Deep Wide Field Survey (NDWFS; Jannuzi & Dey 1999); we also used an engineering MIPS observation of the Marano field. The observational mode (scan map) provides multiple sightings of each source, typically 10 and 60 at 70 μm in the Boötes and CDF-S, respectively. However, at 160 μm, the number of sightings is only typically 2 in Boötes and 12 in CDF-S. See Table 1 and Papovich et al. (2004) for details.

The data were reduced with the Data Analysis Tool (Gordon et al. 2004), from the raw data (ramps) to the final coadded mosaics. The illumination corrections were derived from the data themselves. At 70 μm, the data have been median-filtered in the time domain before mosaicking. Note that data from Ge:Ga detectors are always challenging to process; but with MIPS, most of the difficulties are overcome with frequent calibrations (stimulator flashes), which track the responsivity variations. Nevertheless, the noise properties at faint fluxes are still being investigated at both 70 and 160 μm. In this work, we adopt conservative detection limits. A future paper will address extracting the ultimate sensitivity from these data. Sample images in the CDF-S are shown in Figure 1 (Plate 1).

3. PHOTOMETRY AND CATALOGS

To control the sample and the selection function, we accepted source detections only where the redundancy was high (typically 80% or more of the mean weight), avoiding the

[1] Steward Observatory, University of Arizona, 933 North Cherry Avenue, Tucson, AZ 85721.
[2] Institut d'Astrophysique Spatiale, bât 121, Université Paris-Sud, F-91405 Orsay Cedex, France.
[3] Space Science Institute, 4750 Walnut Street, Suite 205, Boulder, CO 80301.
[4] Michelson Science Center, California Institute of Technology, Pasadena, CA 91125.
[5] *Spitzer* Science Center, California Institute of Technology, Pasadena, CA 91125.
[6] NOAO, 950 North Cherry Avenue, Tucson, AZ, 85719.
[7] Department of Physics, 345 Birge Hall, University of California, Berkeley, CA 94720.

TABLE 1
Log of Observations

Field Name[a]	MIPS AOT[b]	70 μm Area (deg^2)	70 μm t_{int}[c] (s)	70 μm S_{cut}[d] (mJy)	160 μm Area (deg^2)	160 μm t_{int}[c] (s)	160 μm S_{cut}[d] (mJy)
Boötes	Med.	8.75	40	80	7.70	8	...[e]
Marano	Slow	0.42	100	25	0.31	20	50
CDF-S	Slow	0.67	600	15	0.54	120	50

[a] See Papovich et al. (2004) for details on fields.
[b] Scan map mode.
[c] Per sky pixel.
[d] Flux density at which catalog was cut.
[e] Field data not used at 160 μm.

edges and the noisiest areas of the images. The resulting positions were fed to DAOPHOT (Stetson 1987) in IRAF[8] for PSF fitting. We checked that the residual maps were indeed free of sources.

At 70 μm the photometric calibration is derived from many observation campaigns, and its uncertainty is conservatively estimated at the order of 20%. We use only detections at 15 mJy and brighter in the CDF-S, 25 mJy and brighter in Marano, and 80 mJy and brighter in the Boötes field. These flux levels are determined using the sharp decrease in the counts due to the incompleteness effect. At 160 μm, the calibration is based on a combination of observations of standard stars, asteroids, and comparisons with measurements with other FIR missions (*ISO*, *COBE*, and modeling including *IRAS* measurements). It is also estimated to be accurate to about 20%. We have included in our counts only objects of 50 mJy and brighter in the CDF-S and Marano (levels determined using incompleteness as at 70 μm). Because of the low redundancy level of the 160 μm data in the Boötes field, we postpone using it for a later paper.

Catalogs were produced separately at each wavelength; surveys at each wavelength are thus *unbiased*. Detected FIR sources in the CDF-S sort as follows. For sources selected at 70 μm, 92% have a 24 μm ID; 54% have a 160 μm ID (same with 24 and 160). For sources selected at 160 μm, 98% have a 24 μm ID; 43% have a 70 μm ID (same with 24 and 70).

4. SOURCE COUNTS

At 70 μm, 131 sources were detected down to 15 mJy in the CDF-S, 55 sources down to 25 mJy in Marano, and 117 down to 80 mJy in the Boötes. At 160 μm, down to 50 mJy, 123 sources were detected in the CDF-S, and 89 sources in Marano. The source density corresponds to about 150 beams per source at 70 μm and 15 at 160 μm, using the definition of Helou & Beichman (1990).

Source counts are given in integral form (Figs. 2*a* and 3*a*) and differential form, divided by the Euclidean component (Figs. 2*b* and 3*b*) at 70 and 160 μm, respectively.

Note that we did not correct for incompleteness. Error bars on counts are 1 σ Poisson uncertainty. Bins with less than four sources have not been displayed for clarity, since their significance is low, with uncertainties of 50% or higher. In addition, photometric uncertainty have been displayed at high flux only. In order to visualize the contribution from each field, source counts have not been merged and have been overplotted. One should keep in mind that MIPS source counts will eventually go deeper and will be corrected for incompleteness.

The observed fields nicely complement each other in terms of area and depth. This allows us to probe a flux range of almost 2 orders of magnitude at 70 μm. One order of magnitude is covered at 160 μm. It is possible to check consistency and the cosmic variance in the common flux density range. At 70 μm, in the range 25 to 100 mJy where three fields overlap in flux density, the differential counts are almost consistent within the error bars. At 160 μm, in the range 100 to 300 mJy, the differential counts are consistent within the error bars. At both wavelengths, number counts in CDF-S appear consistently lower than in Marano.

5. DISCUSSION

5.1. 70 μm

The MIPS 70 μm counts show a great consistency with the *IRAS* 60 μm counts of Lonsdale et al. (1990) converted at 70 μm using $\nu_{60}S_{60} = \nu_{70}S_{70}$.

A selection of recent models is shown in Figure 2, including a nonevolution scenario. The most striking result is the strong excess of MIPS 70 μm sources compared to the nonevolution model, a factor of 3 at around 20–30 mJy. Strong evolution had been reported previously at 60 and 90 μm, and these data provide unambiguous confirmation.

Two models lie close to the data: King & Rowan-Robinson (2003) and Lagache et al. (2003, 2004). These models, developed to fit observables mostly from *IRAS*, *ISO*, and SCUBA surveys as well as the CIB spectral energy distribution (SED), are based on a strong evolution of luminous (and ultraluminous) infrared galaxies (LIRGs and ULIRGs, respectively). The latter model predicts a peak in the redshift distributions of resolved sources at 70 μm near $z \sim 0.7$ (Dole et al. 2003). Figure 4*a* shows the galaxy contribution to the differential counts, as a function of redshift, from the Lagache et al. (2004) model. Between ~5 and ~100 mJy, sources at $0.7 \leq z \leq 0.9$ contribute the most to the counts. At brighter fluxes (reached by *IRAS* and *ISO*), contributions from local galaxies are more important.

The source counts integrated at 70 μm correspond to a brightness of 0.022 MJy sr^{-1} or 0.95 nW m^{-2} sr^{-1}. The value of the CIB at this wavelength is not known accurately owing to contamination by zodiacal light. If we use the CIB value from the model of Lagache et al. (2004), the MIPS counts show that at 70 μm about 23% of the 70 μm CIB is already resolved.

[8] IRAF is distributed by the National Optical Astronomy Observatories, which are operated by the Association of Universities for Research in Astronomy, Inc., under the cooperative agreement with the National Science Foundation.

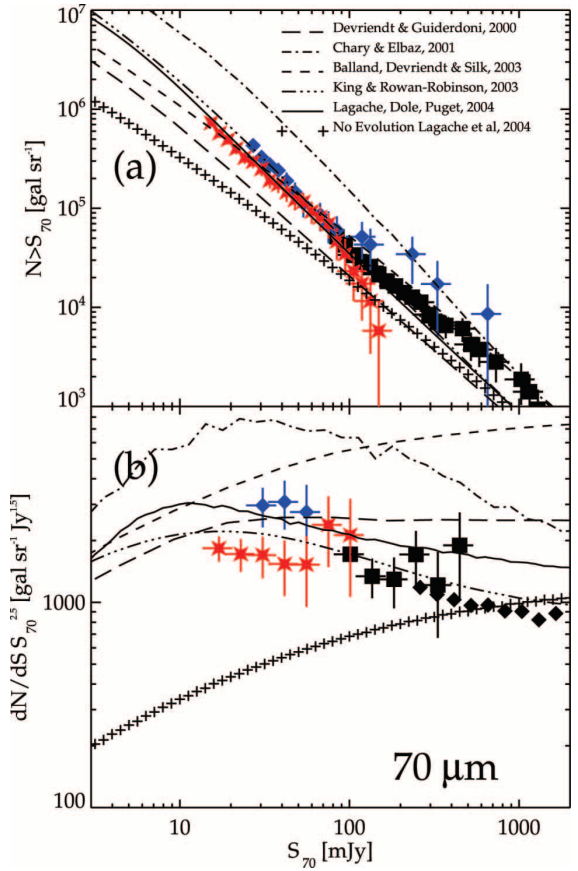

Fig. 2.—Source Counts at 70 μm with no correction for incompleteness. *Red star*, CDF-S; *blue diamond*, Marano; *black square*, Boötes Field; *black diamond*, *IRAS* 60 μm counts from Lonsdale et al. (1990) converted at 70 μm. (*a*) Integral source counts. For clarity, photometric uncertainty is only shown for $S_{70\mu m} >$ 100 mJy. (*b*) Differential source counts. Models are also plotted: *long dashed line*, Devriendt & Guiderdoni (2000); *dash-dotted line*, Chary & Elbaz (2001); *dashed line*, Balland et al. (2003); *dash-dot-dot-dotted line*, King & Rowan-Robinson (2003); *solid line*, Lagache et al. (2004); *plus signs*, no-evolution model.

5.2. 160 μm

At 160 μm, the comparison with the *ISO* FIRBACK 170 μm survey (Dole et al. 2001) shows that the counts are consistent and within the error bars in the whole common range, 180–300 mJy. Other *ISO* observations (Matsuhara et al. 2000; Kawara et al. 2004) agree as well.

Figure 3 overplots the same models as at 70 μm. The evolution detected at 170 μm is confirmed at 160 μm, down to fainter levels. At about 100 mJy, an excess of sources by more than a factor of 2 is observed compared to a nonevolution scenario. Interestingly, as for 70 μm, the observed evolution is better fitted by the models of Lagache et al. (2004) and King

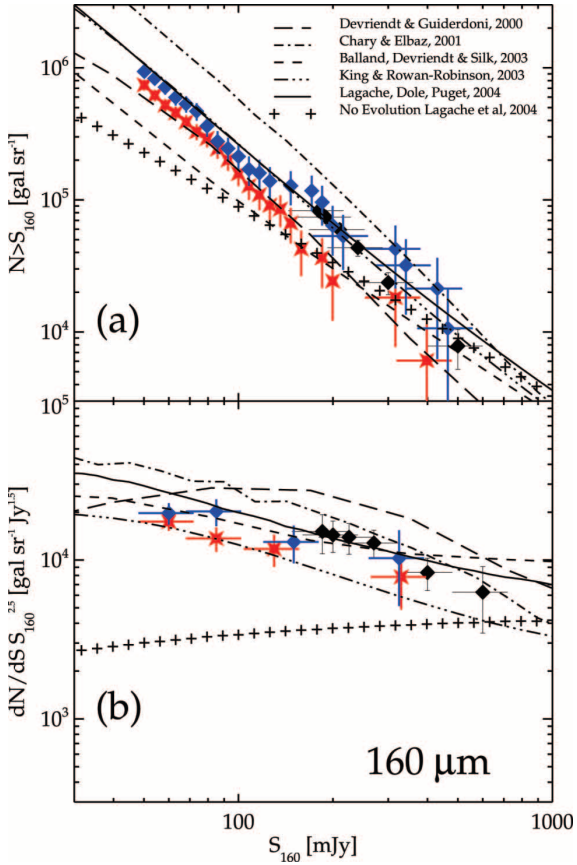

FIG. 3.—Source counts at 160 μm with no correction for incompleteness. *Red star*, CDF-S; *blue diamond*, Marano field; *black diamond*, *ISO* FIRBACK 170 μm counts from Dole et al. (2001). (*a*) Integral source counts. For clarity, photometric uncertainty is only shown for $S_{160\,\mu m} > 200$ mJy. (*b*) Differential source counts. Models are also plotted with the same symbols as Fig. 2.

& Rowan-Robinson (2003). The observed slope also agrees with Mould (2003).

We have constrained the bright end of galaxy number counts at 170 μm by using data from the ISOPHOT Serendipity Survey (ISOSS). ISOSS provides a total sky coverage of 15% and is virtually complete at a flux density level of $S_{170\,\mu m} = 50$ Jy. Based on all optically identified galaxies detected by ISOSS (Krause 2003; Stickel et al. 2004) we have derived an integral number density of $n(S_{170\,\mu m} > 50\ \mathrm{Jy}) = 14 \pm 3$ gal sr^{-1} galaxies at high Galactic latitudes. This point is perfectly matched by the model of Lagache et al. (2003, 2004).

The most striking result of the models that fit the number counts is the existence of two regimes in flux density. In the *ISO* range (fluxes above 200 mJy) most of the sources contributing to the counts are local; this is confirmed by observation (Patris et al. 2003). At fainter fluxes, between ~10 and 200 mJy, the counts should be dominated by a population located at redshifts between 0.7 and 0.9.

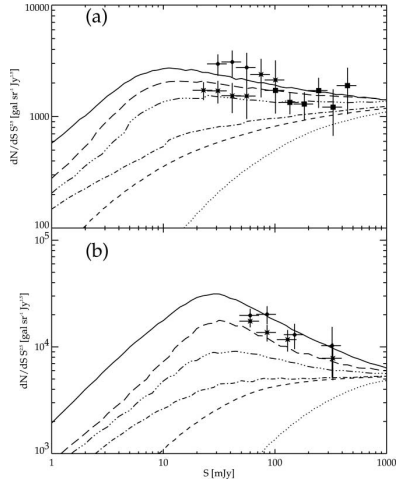

FIG. 4.—Cumulative contributions to the differential source counts at 70 and 160 μm of galaxies, as a function of redshift, form the model of Lagache et al. (2004): (*a*) 70 μm; (*b*) 160 μm. Symbols are described in Figs. 2 and 3. Galaxies contributing to the counts at redshifts 0.1 (*dotted line*), 0.3 (*dashed line*), 0.7 (*dot-dashed line*), 0.9 (*triple-dot-dashed line*), and 1.1 (*long-dashed line*). The total contribution is the upper solid line.

The source counts integrated at 160 μm correspond to a brightness of 0.07 MJy sr^{-1} or 1.4 nW m^{-2} sr^{-1}. The CIB value at this wavelength is 1 MJy sr^{-1} (Lagache et al. 2000); the MIPS counts show that at 160 μm about 7% of the CIB is resolved. Since these counts are preliminary, are not corrected for incompleteness, and are subject to cosmic variance, we anticipate that the actual value might be higher.

5.3. *Concluding Remarks*

The first MIPS far-infrared source counts, spanning about 2 orders of magnitude in flux density at 70 μm (and one at 160 μm), are consistent with previous observations on the bright end and show unambiguous evolution on the faint end. Models predict that most of the sources lie at $z \sim 0.7$ with a tail up to $z \sim 2$ (Dole et al. 2003; Lagache et al. 2003, 2004). This work and companion papers on source counts at 24 μm (Papovich et al. 2004), confusion at 24, 70, and 160 μm (Dole et al. 2004), and on the interpretation of these new data from the *Spitzer* cosmological surveys (Lagache et al. 2004) shed new light on the statistical properties of galaxies in an unexplored regime in flux density, and likely in a critical region of redshift space (up to redshifts $z \sim 2$) in the FIR (Egami et al. 2004; Le Floc'h et al. 2004).

This work is based on observations made with the *Spitzer Space Telescope*, which is operated by the Jet Propulsion Laboratory, California Institute of Technology under NASA contract 1407. Support for this work was provided by NASA through contract 960785 issued by JPL/Caltech. We warmly thank J. Cadien and J.-L. Puget, and the IRS Team for providing us with the Boötes data.

REFERENCES

Balland, C., Devriendt, J. E. G., & Silk, J. 2003, MNRAS, 343, 107
Chary, R., & Elbaz, D. 2001, ApJ, 556, 562
Devriendt, J. E. G., & Guiderdoni, B. 2000, A&A, 363, 851
Dole, H. 2003, in Exploiting the *ISO* Data Archive: Infrared Astronomy in the Internet Age, ed. C. Gry, S. Peschke, J. Matagne, P. Garcia-Lario, R. Lorente, & A. Salama (ESA SP-511) (Noordwijk: ESA), 307
Dole, H., Lagache, G., & Puget, J. L. 2003, ApJ, 585, 617
Dole, H., et al. 2001, A&A, 372, 364
———. 2004, ApJS, 154, 93
Efstathiou, A., et al. 2000, MNRAS, 319, 1169
Egami, E., et al. 2004, ApJS, 154, 130
Elbaz, D. 2002, A&A, 384, 848
Elbaz, D., et al. 1999, A&A, 351, L37
Genzel, R., & Cesarsky, C. J. 2000, ARA&A, 38, 761
Gispert, R., Lagache, G., & Puget, J. L. 2000, A&A, 360, 1
Gordon, K. D., et al. 2004, PASP, submitted
Hacking, P. B., & Soifer, B. T. 1991, ApJ, 367, L49
Hauser, M. G., & Dwek, E. 2001, ARA&A, 37, 249
Hauser, M. G., et al. 1998, ApJ, 508, 25
Helou, G., & Beichman, C. A. 1990, in From Ground-Based to Space-Borne Sub-mm Astronomy (ESA SP-314) (Noordwijk: ESA), 117
Jannuzi, B. T., & Dey, A. In Weymann, R. 1999, in ASP Conf. Ser. 191, Photometric Redshifts and High Redshift Galaxies, ed. R. J. Weymann, L. J. Storrie-Lombardi, M. Sawicki, & R. J. Brunner (San Francisco: ASP), 111
Juvela, M., Mattila, K., & Lemke, D. 2000, A&A, 360, 813
Kawara, K., et al. 1998, A&A, 336, L9
Kawara, K., et al. 2004, A&A, 413, 843
King, A. J., & Rowan-Robinson, M. 2003, MNRAS, 339, 260
Krause, O. 2003, Ph.D. thesis, Ruperto-Carola Univ. Heidelberg
Lagache, G., Dole, H., & Puget, J. L. 2003, MNRAS, 338, L555
Lagache, G., Haffner, L. M., Reynolds, R. J., & Tufte, S. L. 2000, A&A, 354, 247
Lagache, G., et al. 1999, A&A, 344, 322
———. 2004, ApJS, 154, 112
Le Floc'h, E., et al. 2004, ApJS, 154, 170
Linden-Vornle, M. J. D., et al. 2000, A&A, 359, L51
Lonsdale, C. J., Hacking, P. B., Conrow, T. P., & Rowan-Robinson, M. 1990, ApJ, 358, L60
Matsuhara, H., et al. 2000, A&A, 361, 407
Mould, J. 2003, ApJ, 587, L93
Papovich, C., et al. 2004, ApJS, 154, 70
Patris, J., Dennefeld, M., Lagache, G., & Dole, H. 2003, A&A, 412, 349
Puget, J. L., et al. 1996, A&A, 308, L5
———. 1999, A&A, 345, 29
Rieke, G. H., et al. 2004, ApJS, 154, 25
Rodighiero, G., et al. 2003, MNRAS, 343, 1155
Rowan-Robinson, M., et al. 1986, MNRAS, 219, 273
Soifer, B. T., & Neugebauer, G. 1991, AJ, 101, 354
Stetson, P. B. 1987, PASP, 99, 191
Stickel, M., et al. 2004, A&A, in press
Werner, M., et al. 2004, ApJS, 154, 1

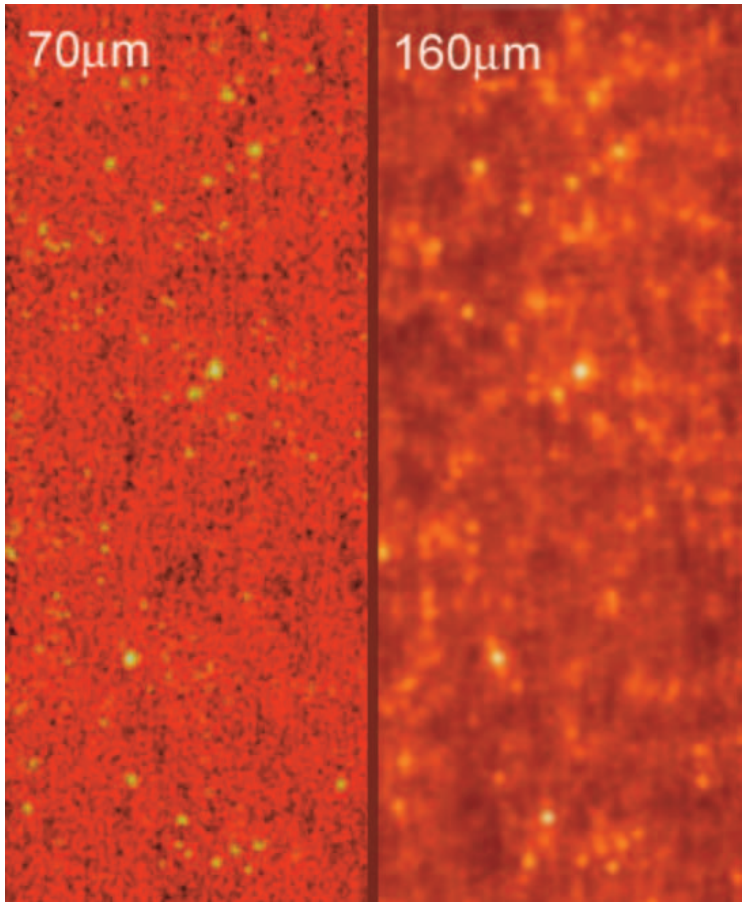

FIG. 1.—MIPS observations of the *Chandra* Deep Field–South at 70 and 160 μm. The field covers an area of $25' \times 1^\circ$.

PLATE 1

THE ASTROPHYSICAL JOURNAL SUPPLEMENT SERIES, 154:93–96, 2004 September

CONFUSION OF EXTRAGALACTIC SOURCES IN THE MID- AND FAR-INFRARED: *SPITZER* AND BEYOND

H. DOLE,[1,2] G. H. RIEKE,[1] G. LAGACHE,[2] J.-L. PUGET,[2] A. ALONSO-HERRERO,[1] L. BAI,[1] M. BLAYLOCK,[1] E. EGAMI,[1] C. W. ENGELBRACHT,[1] K. D. GORDON,[1] D. C. HINES,[1,3] D. M. KELLY,[1] E. LE FLOC'H,[1] K. A. MISSELT,[1] J. E. MORRISON,[1] J. MUZEROLLE,[1] C. PAPOVICH,[1] P. G. PÉREZ-GONZÁLEZ,[1] M. J. RIEKE[1] J. R. RIGBY,[1] G. NEUGEBAUER,[1] J. A. STANSBERRY,[1] K. Y. L. SU,[1] E. T. YOUNG,[1] C. A. BEICHMAN,[4] AND P. L. RICHARDS[5]
Received 2004 April 8; accepted 2004 May 19

ABSTRACT

We use the source counts measured with the Multiband Imaging Photometer for *Spitzer* at 24, 70, and 160 μm to determine the 5 σ confusion limits due to extragalactic sources: 56 μJy, 3.2 mJy, and 40 mJy at 24, 70, and 160 μm, respectively. We also make predictions for confusion limits for a number of proposed far-infrared missions of larger aperture (3.5–10 m diameter).

Subject headings: galaxies: evolution — galaxies: statistics — infrared: galaxies

1. INTRODUCTION

In addition to detector/photon noise, cosmological surveys in the far-infrared (FIR) spectral range are limited in depth by (1) structure in the infrared cirrus emission and (2) confusion due to extragalactic sources. The first of these limitations can be avoided for some programs by observing in particular low-background regions on the sky. The second limitation arises because the high density of faint (resolved or unresolved) distant galaxies creates signal fluctuations in the telescope beam (e.g., Condon 1974; Franceschini et al. 1989; Helou & Beichman 1990; Rieke et al. 1995; Dole et al. 2003; Takeuchi & Ishii 2004). Because distant galaxies are distributed roughly isotropically and with a high density compared to the beam size, this noise is unavoidable.

Extragalactic confusion noise can be robustly estimated by measurements of source counts combined with modeling to extend the counts to faint levels. We use new determinations of number counts in the three Multiband Imaging Photometer for *Spitzer* (MIPS; Rieke et al. 2004) bands, 24, 70, and 160 μm (Dole et al. 2004; Papovich et al. 2004), and a model fitting all those observables (Lagache et al. 2004) to determine more accurate limits for extragalactic confusion than have been available previously. Extragalactic confusion noise does not strictly follow Gaussian statistics. Therefore, we discuss confusion limits in four different ways that are appropriate to various measurement situations: the photometric criterion, the source density criterion (SDC; Dole et al. 2003), and the levels deduced from the source densities of one source per 20 and 40 independent beams. We parameterize the noise as a "5 σ" limit calculated as if it were Gaussian, because it is difficult to derive any other simple metric. All the definitions and values relative to MIPS beams are summarized in Table 1 of Dole et al. (2003).

We summarize the confusion limits for *Spitzer* in its three far-infrared bands in Table 1. The situation is different at 24 and 70 μm from that at 160 μm. In the two first bands, where the background is resolved to a significant extent, the confusion mainly results from the high density of resolved sources and their interference with the extraction of fainter ones, and the SDC is the appropriate measure (and the classical photometric criterion underestimates the confusion level). In the third band, where the background is not well resolved, the confusion results from a population fainter than the sensitivity limit. In the latter case, confusion (and cosmic infrared background [CIB] fluctuation) properties are directly linked to galaxy populations that are not directly detectable but that modulate the background level, and the photometric criterion is appropriate.

2. CONFUSION IN THE MID- AND FAR-INFRARED

2.1. *Confusion of Extragalactic Sources at* 24 μm

The available measurements extend well into the extragalactic confusion regime at 24 μm, and the detector performance is also well understood even for long integrations. Therefore, we use this band to develop the general principles applicable to determining the confusion limits in *Spitzer* mid- and far-infrared imaging data.

2.1.1. *Confusion Limit Calculation*

Our confusion estimates are based on the methodology described by Dole et al. (2003). We have used the number counts determined by Papovich et al. (2004), extrapolated to fainter flux limits according to the model of Lagache et al. (2004). Because these counts indicate that the background will be largely resolved into individual sources, the appropriate measure of the confusion is the SDC. We obtain 56 μJy for the 5 σ confusion level, corresponding to 12 beams per source. It appears that this confusion level is in perfect agreement with the 5 σ prelaunch predictions of Xu et al. (2001), even if it was derived differently. If it were limited by photon noise only, the instrument would reach a detection limit of 56 μJy for 5 σ in 1900 s of integration (Rieke et al. 2004), so the model predicts that the gain in signal-to-noise ratio (S/N) will have leveled out significantly for integrations of this length.

There is excellent agreement between the observed 80% completeness level and source density of Papovich et al.

[1] Steward Observatory, University of Arizona, 933 North Cherry Avenue, Tucson, AZ 85721.
[2] Institut d'Astrophysique Spatiale, bâtiment 121, Université Paris-Sud, F-91405 Orsay Cedex, France.
[3] Space Science Institute, 4750 Walnut Street, Suite 205, Boulder, CO 80301.
[4] Michelson Science Center, California Institute of Technology, Pasadena, CA.
[5] Department of Physics, University of California, 345 Birge Hall, Berkeley, CA 94720.

TABLE 1
MIPS Confusion Levels[a]

Criterion/Flux	24 μm (μJy)	70 μm (mJy)	160 μm (mJy)
SDC[b]	56	3.2	40
20 beams[c]	71	3.5	45
40 beams[d]	141	6.3	63
Photometric[e]	8	0.7	45

[a] With the Lagache et al. (2004) model.
[b] From Dole et al. (2003).
[c] Using the flux corresponding to one source per 20 beams.
[d] Using the flux corresponding to one source per 40 beams.
[e] Using the standard photometric criterion and $q = 4$, for illustration.

(2004) and our SDC confusion level. However, it should be possible in principle to integrate below the 56 μJy level, on a *selected field* of very low source density. In the "GOODS Test Field" in the European Large-Area *ISO* Survey North-1 (ELAIS N1) field (described in Papovich et al. 2004), we estimate the area suitable for a deeper integration to be about 5% of the field area.

2.1.2. *Noise Analysis*

We desired a test of these predictions that, as much as possible, was independent of assumptions about the infrared galaxy population. For this purpose, we have characterized the noise in the 24 μm data from the ELAIS N1 field as the deepest observation obtained to date at this wavelength. We selected a very cleanly reduced region in the field, about $2' \times 4'$ in size. We prepared two versions of the image in this region, both reduced identically, but one with an integration of 630 s and the other with an integration of 3800 s. We determined the pixel signal histogram in two ways. (1) On a small region that also appeared to be free of detected sources, we verified that the standard deviation as measured in these histograms scaled inversely with the square root of the integration time. (2) On the entire $2' \times 4'$ region, we fitted a Gaussian with a width that was fixed to the expectation for detector/photon noise. We required this Gaussian to fit the negative side of the histogram only, on the assumption that there were no negative sources. We took the departure of the measured histogram from this fit toward positive fluctuations to be the influence of (at least) sources in the field. We measured the extension of the distribution toward positive values at half-maximum. We found that the width of the positive side of the distribution was larger than the pure detector/photon noise expectation by a factor of 1.7, in qualitative agreement with the effects of confusion. These excess fluctuations likely result from a combined effect of extragalactic sources, a faint cirrus, and a zodiacal light gradient. It is not clear at this stage which component dominates the fluctuations.

2.1.3. *Monte Carlo Simulation*

To empirically quantify the effect of confusion, we carried out a Monte Carlo simulation of source extraction under the conditions appropriate for the *Spitzer* deep 24 μm exposures. The approach is described in detail by Rieke et al. (1995). We built up a test field by distributing confusing sources randomly according to a power-law distribution matching the faint *Spitzer* number counts. Each source was entered as an Airy pattern. A test source of known amplitude was added to the center of the array, along with Gaussian noise. The sources were then identified using a modified CLEAN algorithm, and finally the S/N was measured in a master array built up from the results of the CLEAN process and in extraction apertures of various sizes. An important aspect of this simulation is that it combines the effects of neighboring bright sources and of the underlying, unresolved distribution of faint ones, in a consistent manner. It should give a good measure of the confusion noise independent of the division between source density and photometric criteria.

In the simulation, we excluded all objects brighter than 400 μJy to avoid undue noise from bright-source artifacts. The first set of runs tested the extraction of a 56 μJy source in an $0.8\lambda/D$ beam, the beam size previously indicated to provide optimum performance in a heavily confusion-limited situation (Rieke et al. 1995; this result was confirmed by the new calculations). We made 1200 runs for an integration time that was long enough to drive detector/photon noise down to 12.5 μJy, 5 σ. They yielded a net 5 σ limit of 60 μJy; removing the detector/photon noise leaves 59 μJy of confusion noise. That is, this approach agrees well with the SDC-determined limit of 56 μJy.

We also simulated the results to be expected from shorter integration times. For example, if the 5 σ detector/photon noise limit was set to 65 μJy, then the indicated 5 σ level of confusion noise was 76 μJy, significantly poorer than that from the simulation of very long integrations. This effect probably results from the increased uncertainty in source centroiding and the resulting lower accuracy in extracting accurate source measurements from a confused field. To test this hypothesis further, we simulated extraction of a 36 μJy source in the high S/N integration case and found that the indicated 5 σ confusion limit rose to 64 μJy, confirming the effect.

2.2. *Confusion by Extragalactic Sources at* 70 μm

At 70 μm, we again use the number counts (Dole et al. 2004) as the basic input for determining the confusion level. The updated model of Lagache et al. (2004) was used to extrapolate the counts and to derive updated confusion limits. The use of a model is critical in this case because the contribution of unresolved sources is not negligible. We derive a confusion level at 70 μm of 3.2 mJy using the SDC (Table 1). The differential source counts are almost flat (when divided by the Euclidean component), and the contribution from unresolved sources is much smaller than that of the resolved sources. These results demonstrate that the SDC estimate is the appropriate one; that is, the confusion is dominated by faint resolved sources rather than by the unresolved background due to even fainter objects. Further details are given in Table 1. From the instrument radiometric model, we estimate that about 1800 se of integration would be required to reach this limit.

Again, we sought to check these results by a pure fluctuation analysis on the data without referring to galaxy population models. We used the data described by Dole et al. (2004) for the Chandra Deep Field–South. We determined the evolution of $\sigma_{\rm tot}$, the standard deviation of a Gaussian fitted to the surface brightness distribution as a check of the results from extrapolating number counts downward. Data were combined into six mosaics corresponding to 100–600 s integration time per sky pixel with 100 s steps. Figure 1*a* shows the evolution of $\sigma_{\rm tot70}$ with time. We do not observe substantial flattening in the $\sigma_{\rm tot70}$ time evolution. We conclude that MIPS 70 μm surveys do not yet reach the confusion limit after 600 s of integration. An estimate of the confusion level is given by fitting the time evolution of $\sigma_{\rm tot70}$. We find that the detector/photon noise will be roughly equal to the confusion noise at $\geq$800 s of integration, with large uncertainties, because the fluctuation curve is still dropping almost like the inverse square root of the integration time at the longest integration available. As at 24 μm, this result is in satisfactory agreement with the integration time predicted by the SDC modeling.

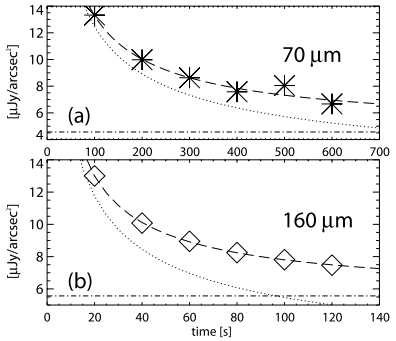

Fig. 1.—Evolution of $\sigma_{\rm tot}$ (resulting contribution from the confusion noise and instrument noise, derived from the Gaussian fit in the brightness map pixel histogram) as a function of integration time, with a fit (*dashed line*) of the form $\sigma^2_{\rm tot} = \sigma^2_{\rm inst} + \sigma^2_{\rm conf,\ brightness} = At^{-1} + C^2$. *Dot-dashed line*: Constant term *C*. *Dotted line*: $(A/t)^{1/2}$ term. (*a*) 70 μm and (*b*) 160 μm. Notice the different scales in time (seconds) and $\sigma_{\rm tot}$ (in brightness μJy arcsec^{-2}).

2.3. *Confusion by Extragalactic Sources at* 160 μm

The data used at 160 μm are also described by Dole et al. (2004). The Lagache et al. (2004) model predicts a confusion level of 40 mJy (Table 1). From the instrument radiometric model, we estimate that about 70 s of integration would be required to reduce the instrument and photon noise to the level of the confusion noise.

A fluctuation analysis similar to the one at 70 μm was conducted at 160 μm, where six mosaics corresponding to integration times of 20–120 s (with 20 s steps) were studied. Analyzing the fluctuations is more difficult in this case because bright sources in the Euclidean regime contaminate the statistics and because the map's S/N is not uniform. Nevertheless, we estimate from Figure 1*b* that the confusion noise and the detector/photon noise should be equal at about 95 s of integration, in good agreement with the result from the SDC analysis.

2.4. *Confusion by Galactic Cirrus*

Another sensitivity limitation arises as a result of the structure of the IR cirrus. To estimate how this cirrus emission may affect the source detectability, we compared the 80% completeness limits in sky regions characterized by different cirrus background levels, using simulations as described in Papovich et al. (2004). We used a dedicated engineering observation of a *bright cirrus* in Draco, with an H I column density $n_{\rm H\,I}$ varying between 4 and 14×10^{20} cm^{-2}. At 24 μm, we find a relatively weak effect and derive a completeness degradation of 15% ($\sim$50 μJy increase from 340 μJy) between the dark and bright parts of the cirrus field. The effects of the cirrus are more conspicuous at 70 μm. We reach 80% completeness limits in Draco of $\sim$17 and $\sim$27 mJy. In a low-cirrus field (e.g., Marano) and for a similar integration time (100 s), this level drops to $\sim$12 mJy. We compared the estimates in Draco with those provided by the performance estimation tool of the *Spitzer* Science Center and found that the measured value variations as a function of the cirrus strength are in general agreement (within 30%) with those estimated by the tool from low to medium background. This comparison will be refined as we continue to acquire far-infrared data.

3. IMPLICATIONS FOR FUTURE OBSERVATORIES

A number of cryogenically cooled space telescopes have been proposed for the mid-infrared (MIR), the FIR, and the submillimeter spectral ranges. Table 2 summarizes the main characteristics of some of these observatories. *Herschel* (Pilbratt 2001), the *James Webb Space Telescope* (*JWST*; Gardner 2003), the *Space Infrared telescope for Cosmology and Astrophysics* (*SPICA*; Matsumoto 2003), and the *Single Aperture Far-Infrared Observatory* (*SAFIR*; Yorke et al. 2002) have at least one photometric channel in common with MIPS. As examples, we focus on the *Herschel* Photodector Array Camera and Spectrometer (PACS) at 75 and 170 μm, on the *JWST* Mid-InfraRed Instrument (MIRI) at 24 μm, and on *SPICA* and *SAFIR* at 24, 70, and 160 μm, assuming in each case that the MIPS filters will be used.

For each of these observatories, we compute predictions for the confusion level for unbiased surveys using the Lagache et al. (2004) model of source counts. We assume a Gaussian beam profile for these future observatories, with an FWHM of $1.22\lambda/D$, λ being the wavelength and D the diameter of the primary telescope mirror, given in Table 2. The underlying assumption to be made by these planned facilities for the deepest surveys is that they will be confusion-limited. This means that we did not take into account other sources of noise, for instance photon noise due to insufficient integration times or thermal background due to the warm telescope—by design, *Herschel* and *JWST* might be in the latter case. Normally background-limited photon noise observations would give a sensitivity limit scaling as the aperture squared for a diffraction-limited system. Figure 2 shows that confusion noise at 24 and 70 μm drops much faster than the size of the aperture squared (*dashed line*) because source counts are shallower below fluxes where most of the CIB has been resolved into sources. That is why the next generation of large far-infrared telescopes will be much less confusion-limited than *Spitzer*.

TABLE 2
Telescopes and Predicted Confusion Levels

Parameter	*Herschel*[a]/*SPICA*	*JWST*[b]	*SAFIR*
Diameter (m)	3.5	6.0	10.0
24 μm SDC[c] (μJy)	2	0.18	<0.01[d]
70 μm SDC[c] (mJy)	0.16	...	0.004
160 μm SDC (mJy)	10	...	0.6

[a] With PACS.
[b] With MIRI.
[c] With the Lagache et al. (2004) model and using the SDC from Dole et al. (2003).
[d] Outside the range of the current model flux grid.

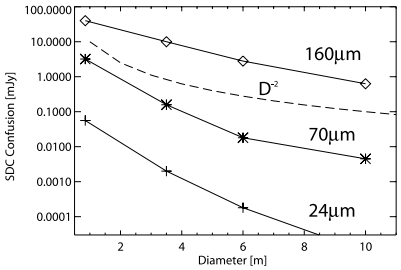

FIG. 2.—Confusion level vs. telescope diameter, predicted by the SDC (Dole et al. 2003) with the updated model of Lagache et al. (2004), at 24 μm (*plus signs*), 70 μm (*asterisks*), and 160 μm (*diamonds*). Diameters refer to *Spitzer*, *Herschel*/*SPICA*, *JWST*, and *SAFIR*. *Dashed line*: Inverse square diameter law shown for illustration.

In Table 3, we use the confusion level given by the SDC and compute the fraction of the CIB potentially resolved into sources. In the MIR, a significant step will be made with the 4 m class space telescope; as an example, *SPICA* would potentially resolve 98% of the CIB at 24 μm. All (>99%) of the CIB would be resolved with *JWST* or *SAFIR* (although doing so with *JWST* would require extremely long integrations). In the FIR, *Herschel* would resolve a significant fraction of the CIB at 70 and 160 μm (93% and 58%, respectively, again with extremely long integrations). *SAFIR* will ultimately nearly resolve all of it (>94%).

TABLE 3

POTENTIAL RESOLUTION OF THE CIB

Observatory	24 μm (%)	70 μm (%)	160 μm (%)
Spitzer	74	59	18
Herschel/*SPICA*	98	93	58
JWST	99	...	...
SAFIR	100	99	94

NOTE.—The CIB value is from Lagache et al. (2004), and we use the limiting flux with the SDC limit and assume confusion-limited surveys. This hypothesis might not be valid for *Herschel* and *JWST*.

4. CONCLUSIONS

Using MIPS data at 24, 70, and 160 μm, the source density measured by Papovich et al. (2004) and Dole et al. (2004) together with the modeling of Lagache et al. (2004) have allowed us to derive the confusion limits for *Spitzer* in the mid- to far-infrared. We tested the model results with a Monte Carlo simulation at 24 μm and with a fluctuations analysis at all three wavelengths. The agreement is uniformly very good.

At 24 and 70 μm, confusion is mostly due to the high density of resolved sources, and at 160 μm, confusion is mainly due to faint unresolved sources. Studying the FIR fluctuations at this wavelength is thus a tool to constrain the nature of the faint galaxies, beyond the confusion limit.

We also derive confusion limits for future space IR observatories. We show that future large-aperture missions will gain in confusion-limited sensitivity substantially faster than the size of the aperture squared for wavelengths $\lesssim$100 μm, allowing them to reach very deep detection limits. For example, the CIB should be fully resolved into sources in the MIR and FIR with *SAFIR* observations.

This work is based on observations made with the *Spitzer* observatory, which is operated by the Jet Propulsion Laboratory, California Institute of Technology, under NASA contract 1407. We thank the funding from the MIPS project, which is supported by NASA through the Jet Propulsion Laboratory, subcontract 960785. We warmly thank J. Cadien.

REFERENCES

Condon, J. J. 1974, ApJ, 188, 279
Dole, H., Lagache, G., & Puget, J. L. 2003, ApJ, 585, 617
Dole, H., et al. 2004, ApJS, 154, 87
Franceschini, A., Toffolatti, L., Danese, L., & De Zotti, G. 1989, ApJ, 344, 35
Gardner, J. P. 2003, 25th Meeting of the IAU, Joint Discussion 8 (Sydney), 10
Helou, G., & Beichman, C. A. 1990, in From Ground-based to Space-borne Sub-mm Astronomy, 29th Liège Int. Astrophys. Colloq. (ESA SP-314; Paris: ESA), 117
Lagache, G., et al. 2004, ApJS, 154, 112
Matsumoto, T. 2003, Proc. SPIE, 4850, 1091
Papovich, C., et al. 2004, ApJS, 154, 70
Pilbratt, G. L. 2001, in The Promise of the *Herschel Space Observatory*, ed. P. L. Pilbratt, J. Cernicharo, A. M. Heras, T. Prusti, & R. Harris (ESA-SP 460; Noordwijk: ESA), 13
Rieke, G. H., et al. 2004, ApJS, 154, 25
Rieke, G. H, Young, E. T, & Gautier, T. N. 1995, Space Sci. Rev., 74, 17
Takeuchi, T. T., & Ishii, T. T. 2004, ApJ, 604, 40
Xu, C. K., Lonsdale, C. J., Shupe, D. L., O'Linger, J., & Masci, F. 2001, ApJ, 562, 179
Yorke, H. W., et al. 2002, BAAS, 201, 151.04

THE ASTROPHYSICAL JOURNAL SUPPLEMENT SERIES, 154:70–74, 2004 September

THE 24 MICRON SOURCE COUNTS IN DEEP *SPITZER SPACE TELESCOPE* SURVEYS[1]

C. PAPOVICH,[2] H. DOLE,[3] E. EGAMI,[2] E. LE FLOC'H,[2] P. G. PÉREZ-GONZÁLEZ,[2] A. ALONSO-HERRERO,[2,4] L. BAI,[2] C. A. BEICHMAN,[5] M. BLAYLOCK,[2] C. W. ENGELBRACHT,[2] K. D. GORDON,[2] D. C. HINES,[2,6] K. A. MISSELT,[2] J. E. MORRISON,[2] J. MOULD,[7] J. MUZEROLLE,[2] G. NEUGEBAUER,[2] P. L. RICHARDS,[8] G. H. RIEKE,[2] M. J. RIEKE,[2] J. R. RIGBY,[2] K. Y. L. SU,[2] AND E. T. YOUNG[2]

Received 2004 March 25; accepted 2004 May 17

ABSTRACT

Galaxy source counts in the infrared provide strong constraints on the evolution of the bolometric energy output from distant galaxy populations. We present the results from deep 24 μm imaging from *Spitzer* surveys, which include $\approx 5\times10^4$ sources to an 80% completeness of $\simeq$60 μJy. The 24 μm counts rapidly rise at near-Euclidean rates down to 5 mJy, increase with a super-Euclidean rate between 0.4 and 4 mJy, and converge below $\sim$0.3 mJy. The 24 μm counts exceed expectations from nonevolving models by a factor of $\gtrsim$10 at $S_\nu \sim 0.1$ mJy. The peak in the differential number counts corresponds to a population of faint sources that is not expected from predictions based on 15 μm counts from the *Infrared Space Observatory*. We argue that this implies the existence of a previously undetected population of infrared-luminous galaxies at $z \sim 1$–3. Integrating the counts to 60 μJy, we derive a lower limit on the 24 μm background intensity of 1.9 ± 0.6 nW m^{-2} sr^{-1} of which the majority ($\sim$60%) stems from sources fainter than 0.4 mJy. Extrapolating to fainter flux densities, sources below 60 μJy contribute $0.8^{+0.9}_{-0.4}$ nW m^{-2} sr^{-1} to the background, which provides an estimate of the total 24 μm background of $2.7^{+1.1}_{-0.7}$ nW m^{-2} sr^{-1}.

Subject headings: cosmology: observations — galaxies: evolution — galaxies: high-redshift — galaxies: photometry — infrared: galaxies

Online material: machine-readable table

1. INTRODUCTION

From the first detections of infrared (IR) luminous galaxies, it was clear that they represent phenomena not prominent in optically selected galaxy surveys (e.g., Rieke & Low 1972; Soifer et al. 1987). Locally, galaxies radiate most of their emission at UV and optical wavelengths, and only about one-third at IR wavelengths (5–1000 μm; Soifer & Neugebauer 1991). IR number counts from the *Infrared Space Observatory* (*ISO*) indicate that the IR-luminous sources have evolved rapidly, significantly faster than has been deduced from optical surveys, which implies that IR-luminous galaxies make a substantial contribution to the cosmic star formation rate density (e.g., Elbaz et al. 1999; Franceschini et al. 2001).

The detection of the cosmic background by the *Cosmic Background Explorer* (*COBE*) at IR wavelengths shows that the total far-IR emission of galaxies in the early universe is greater than that at optical and UV wavelengths (Fixsen et al. 1998; Hauser et al. 1998; Madau & Pozzetti 2000; Franceschini et al. 2001), which suggests that a large fraction of stars have formed in IR-luminous phases of galaxy activity (Elbaz et al. 2002). Studies from *ISO* at 15 and 170 μm have inferred that the bulk of this background originates in discrete sources with $z \lesssim 1.2$ (Dole et al. 2001; Elbaz et al. 2002). However, the peak in the cosmic IR background extends to $\sim$200 μm (Fixsen et al. 1998; Hauser & Dwek 2001). The spectral energy distributions (SEDs) of IR-luminous galaxies ($L_{\rm IR} \sim 10^{11}$–10^{12} $L_\odot$) peak between 50 and 80 μm (Dale et al. 2001). If these objects constitute a major component of the cosmic IR background, then it follows there is a significant population of IR-luminous galaxies at $z \sim 1.5$–3, distances largely unexplored by *ISO*.

The mid-IR 24 μm band on the Multiband Imaging Photometer for *Spitzer* (MIPS; Rieke et al. 2004) is particularly well suited to studying distant IR-luminous galaxies. Locally, the mid-IR emission from galaxies relates almost linearly with the total IR luminosity over a range of galaxy types (e.g., Spinoglio et al. 1995; Chary & Elbaz 2001; Roussel et al. 2001; Papovich & Bell 2002), and there are indications this holds at higher redshifts (e.g., Elbaz et al. 2002). Because the angular resolution of *Spitzer* is significantly higher for the 24 μm band relative to 70 and 160 μm, the 24 μm confusion limit lies at fainter flux densities. This allows us to probe the IR emission from many more sources and at higher redshifts than with the MIPS longer wavelength bands (e.g., Papovich & Bell 2002; Dole et al. 2003). Here we present the number counts of $\approx 5\times10^4$ sources detected at 24 μm in deep *Spitzer* surveys, and we suggest that the faint *Spitzer* detections probe a previously undetected population of very luminous galaxies at high redshifts. Where applicable, we assume $\Omega_m = 0.3$, $\Omega_\Lambda = 0.7$, and $H_0 = 70$ km s^{-1} Mpc^{-1}.

2. THE DATA AND SOURCE SAMPLES

The data used in this work stem from early *Spitzer* characterization observations and from time allocated to the MIPS

[1] This work is based on observations made with the *Spitzer Space Telescope*, which is operated by the Jet Propulsion Laboratory, California Institute of Technology, under NASA contract 1407.

[2] Steward Observatory, University of Arizona, 933 North Cherry Avenue, Tucson, AZ 85721; papovich@as.arizona.edu.
[3] Institut d'Astrophysique Spatiale, bat 121, Université Paris Sud, F-91405 Orsay Cedex, France.
[4] Departamento de Astrofísica Molecular e Infrarroja, IEM, CSIC, Serrano 113b, 28006 Madrid, Spain.
[5] Michelson Science Center, California Institute of Technology, Pasadena, CA 91109.
[6] Space Science Institute, 4750 Walnut, Suite 205, Boulder, CO 80301.
[7] National Optical Astronomy Observatory, 950 North Cherry Avenue, Tucson, AZ 85719.
[8] Department of Physics, University of California, Berkeley, CA 94720.

TABLE 1
PROPERTIES OF DEEP *SPITZER* FIELDS

Field (1)	R.A. (J2000.0) (2)	Decl. (J2000.0) (3)	$\langle I_\nu \rangle$ (MJy sr^{-1}) (4)	Area (arcmin^2) (5)	$\langle t_{exp} \rangle$ (s) (6)	$C_{80\%}$ (μJy) (7)	$N(>C_{80\%})$ (arcmin^{-2}) (8)	$N(>300\ \mu\text{Jy})$ (arcmin^{-2}) (9)
Marano	03 13 52	−55 15 23	19.7	1296	236	170	2.0	0.9
CDF-S	03 32 28	−27 48 30	22.5	2092	1378	83	4.5	0.7
EGS	14 16 00	+52 48 50	19.5	1466	450	110	3.4	0.7
Boötes	14 32 06	+34 16 48	22.7	32457	87	270	1.0	0.8
ELAIS	16 09 52	+54 55 00	18.2	130	3232	61	5.7	0.6

NOTES.—Col. (1): Field name. Col. (2): Right ascension, in units of hours, minutes, and seconds. Col. (3): Declination, in units of degrees, arcminutes, and arcseconds. Col. (4): Mean 24 μm background. Col. (5): Areal coverage. Col. (6): Mean exposure time. Col. (7): 80% completeness limit. Col. (8): Source density with $S_\nu > C_{80\%}$. Col. (9): Source density with $S_\nu > 300$ μJy.

Guaranteed Time Observers (GTOs). The images were obtained in five individual fields with large angular separation on the sky in order to minimize cosmic-variance biases from large-scale structure, and with high-quality ancillary data at other wavelengths. The area and depth of each field vary substantially to adequately sample source densities at all flux levels with high statistical significance. Table 1 lists their properties and 24 μm source densities. The MIPS fields used here subtend the largest areas ($\simeq$10.5 deg^2) and widest range in flux density (50–0.06 mJy) available to date from the *Spitzer* mission and therefore are the premier data set for studying the mid-IR source counts.

The MIPS 24 μm images were processed with a custom data analysis tool, developed by the MIPS GTOs (Gordon et al. 2004). The measured count rates are corrected for dark current, cosmic rays, and flux nonlinearities, and then divided by flat fields for each unique MIPS scan-mirror position. Images are then corrected for geometric distortion, co-added, and mosaicked. The final mosaics have a pixel scale of $\simeq 1\farcs25$ pixel^{-1}, with a point-spread function (PSF) FWHM of $\simeq 6''$.

We performed source detection and photometry using a set of tools and simulations. Briefly, we first subtract the image background using a median filter roughly 4 times the size of source apertures (see below) and use a version of the DAOPHOT software (Stetson 1987) to detect point sources. We filter each image with a Gaussian with an FWHM that is equal to that of the MIPS 24 μm PSF and identify positive features in $10''$ diameter apertures above some noise threshold. We then construct empirical PSFs using 20–30 bright sources in each image, and we optimally measure photometry by simultaneously fitting the empirical PSFs to all sources within $\simeq 20''$ of nearby object centroids. The source photometry corresponds to the flux of these PSF apertures within a diameter of $37\farcs4$, and we apply a multiplicative correction of 1.14 to account for light lost outside these apertures.

To estimate completeness and photometric reliability in the 24 μm source catalogs, we repeatedly inserted artificial sources into each image with a flux distribution approximately matching the measured number counts. We then repeated the source detection and photometry process and compared the resulting photometry to the input values. In Figure 1, we show for the *Chandra* Deep Field–South (CDF-S, one of the deep *Spitzer* fields) the relative fraction of sources within $r \leq 2\farcs3$ (half the FWHM) and with a flux difference less than 50% compared to their input values. From these simulations, we estimated the flux-density limit where 80% of the input sources are recovered with this photometric accuracy; these are listed in Table 1. Simultaneously, we estimate that down to the 80% completeness limit the number of sources that result from fainter sources either by photometric errors or the merging of real sources is $\lesssim$10%.

We also repeated the source detection and photometry process on the negative of each MIPS 24 μm image. This test provides an estimate for the number of spurious sources arising from the noise properties of the image, as shown in Figure 1. For all of our fields, the spurious-source fraction for flux densities greater than the 80% completeness limit is less than 10%.

3. THE 24 μm SOURCE COUNTS

Figure 2 shows the 24 μm cumulative and differential number counts that have been averaged over the fields listed in Table 1. The differential and cumulative counts (corrected and uncorrected) are listed in Table 2. The faintest datum (denoted by the open symbol in Fig. 2) is derived to the 50% completeness limit for the European Large-Area *ISO* Survey (ELAIS) field ($C_{50\%} = 35$ μJy). The remaining (less deep)

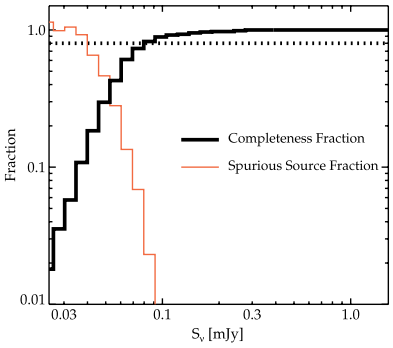

FIG. 1.—Reliability of source detection and photometry for the CDF-S, one of the deep *Spitzer* fields. The thick line shows the fraction of artificial sources detected in the image as a function of input flux density. For the CDF-S this fraction is 80% complete at $C_{80\%} = 83$ μJy (*dotted line*). The red line shows the ratio of the number of sources detected in a "negative" of the 24 μm image to the number of "positive" sources as a function of flux density, which provides an estimate of the number of spurious sources due to noise features.

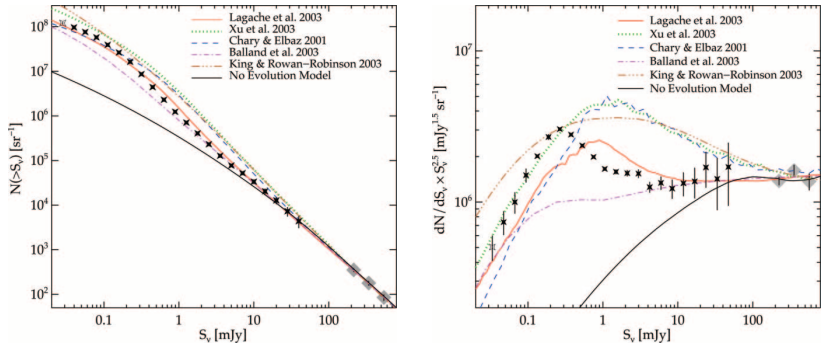

FIG. 2.—Cumulative (*left*) and differential (*right*) 24 μm number counts. The differential counts have been normalized to a Euclidean slope, $dN/dS_\nu \sim S_\nu^{-2.5}$. The solid stars show the average counts from all the *Spitzer* fields (see Table 1) and corrected for completeness to their respective 80% limits. The open star corresponds to counts brighter than the 50% completeness limit from the ELAIS field. The error bars correspond to counting uncertainties and a cosmic-variance estimate based on the standard deviation of the field-to-field counts from the different fields. Each flux bin is $\Delta(\log S_\nu) = 0.15$ dex. The shaded diamonds correspond to *IRAS* 25 μm number counts from Hacking & Soifer (1991) and adjusted assuming $\nu_{24} S_\nu(24\ \mu\text{m}) = \nu_{25} S_\nu(25\ \mu\text{m})$. The curves show the predictions from various contemporary models from the literature (see figure inset; and adjusted slightly to match the observed *IRAS* counts) and a model based on the local *ISO* 15 μm luminosity function and assuming nonevolving galaxy SEDs.

fields are used after correcting for completeness to the 80% level only. Error bars in the figure correspond to Poissonian uncertainties and an estimate for cosmic variance using the standard deviation of counts between the fields. For $S_\nu \leq 83$ μJy, where the counts are derived solely from the smaller ELAIS field, we estimate the uncertainty (18%) using the standard deviation of counts at faint flux densities in cells of 130 arcmin^2 from the CDF-S (see below). We have ignored the contribution to the number counts from stars at 24 μm, which are negligible at these Galactic latitudes and flux densities based on preliminary *Spitzer* observations.

At bright flux densities, $S_\nu \gtrsim 5$ mJy, the differential 24 μm source counts increase at approximately the Euclidean rate, $dN/dS_\nu \sim S^{-2.5}$, which extends the trends observed by the *IRAS* 25 μm population by 2 orders of magnitude (Hacking & Soifer 1991; Shupe et al. 1998). For $S_\nu \simeq 0.4$–4 mJy, the 24 μm counts increase at super-Euclidean rates and peak near 0.2–0.4 mJy. This observation is similar to the trend observed in the *ISO* 15 μm source counts (Elbaz et al. 1999), but the peak in the 24 μm differential source counts occurs at fluxes fainter by a factor of $\approx$2.0. The peak lies above the 80% completeness limit for nearly all fields and is seen in the counts of the fields individually. Thus, the observed turnover is quite robust. The counts converge rapidly with a sub-Euclidean rate at $\lesssim$0.2 mJy. We broadly fit the faint end ($S_\nu \simeq 35$–130 μJy) of the differential number counts using a power law, $dN/dS_\nu = C(S_\nu/1\ \text{mJy})^{-\alpha}$, with $\alpha = -1.5 \pm 0.1$. This result is consistent with a separate analysis based solely on the ELAIS field (Chary et al. 2004).

The observed counts are strongly inconsistent with expectations from nonevolving models of the local IR-luminous population. In Figure 2, we show the 24 μm counts derived from the local luminosity function at *ISO* 15 μm (Xu 2000) and assuming local galaxy SEDs (Dale et al. 2001). We have used the local *ISO* 15 μm luminosity function, because the *k*-correction between rest-frame *ISO* 15 μm and observed MIPS 24 μm bands is minimized at higher redshifts ($z \sim 0.6$), which is more appropriate for the counts at fainter flux densities. However, using the local *IRAS* 25 μm luminosity function (Shupe et al. 1998) yields essentially identical results.

TABLE 2
MEASURED *SPITZER* 24 μm NUMBER COUNTS

$\log S_\nu$ (mJy) (1)	dN/dS_ν (mJy^{-1} sr^{-1}) (2)	$\delta(dN/dS_\nu)$ (mJy^{-1} sr^{-1}) (3)	$\log S_\nu$ (mJy) (4)	$N(>S_\nu)$ (sr^{-1}) (5)	$\delta(N(>S_\nu))$ (sr^{-1}) (6)
−1.475	$2.5\ (1.4) \times 10^9$	$4.7\ (1.5) \times 10^8$	−1.550	$2.1\ (1.1) \times 10^8$	$1.2\ (0.60) \times 10^7$
−1.325	$1.5\ (1.2) \times 10^9$	$2.7\ (0.97) \times 10^8$	−1.400	$1.2\ (0.92) \times 10^8$	$7.6\ (4.9) \times 10^6$
−1.175	$8.7\ (6.9) \times 10^8$	$1.4\ (1.4) \times 10^8$	−1.250	$9.6\ (7.2) \times 10^7$	$3.7\ (0.68) \times 10^6$

NOTES.—Col. (1): Flux density for differential number counts. Cols. (2) and (3): Corrected differential counts and uncertainty. Col. (4): Flux density for cumulative number counts. Cols. (5) and (6): Corrected cumulative counts and uncertainty. Numbers in parentheses give the uncorrected values. Table 2 is published in its entirety in the electronic edition of the *Astrophysical Journal Supplement*. A portion is shown here for guidance regarding its form and content.

While the nonevolving fiducial model is consistent with the observed 24 μm counts for $S_\nu \gtrsim 20$ mJy, it underpredicts the counts at $S_\nu \lesssim 0.4$ mJy by more than a factor of 10.

Because the deep *Spitzer* fields are measured in many sight lines with large solid angle, we can estimate the fluctuations in the number of sources as a function of sky area and flux density in smaller sized fields. For example, in the CDF-S, which achieves an 80% completeness limit of 83 μJy over $\simeq$0.6 deg^2 (see Table 1 and Fig. 1), we have computed the variance in the number of sources in solid angles of 100 and 300 arcmin^2. For the sources that span the peak in the differential counts (0.1–1 mJy), the fluctuation in the number of sources in flux-density bins of 0.15 dex is roughly 15% in these areas. This implies that small-sized fields suffer sizable field-to-field variation in the number of counts from the cosmic variance of source clustering. This effect is present in even larger fields: the number density of sources brighter than 0.3 mJy varies by $\sim$10% in fields of $\sim$0.5 deg^2 (Table 1) and is consistent with fluctuations expected from galaxy clustering on fields of this size at $z \sim 1$ (scale lengths of 20–70 Mpc). The counts presented here average over fields from many sight lines and significantly larger areas. We conservatively estimate that variations due to galaxy clustering correspond to uncertainties in the number counts of a less than a few percent in each flux bin.

4. INTERPRETATION AND DISCUSSION

The form of the observed 24 μm source counts differs strongly from predictions of various contemporary models (see Fig. 2). Four of the models are phenomenological in approach, which parameterize the evolution of IR-luminous galaxies in terms of density and luminosity to match observed counts from *ISO*, radio, submillimeter, and other data sets. Several of these models (Chary & Elbaz 2001; King & Rowan-Robinson 2003; Xu et al. 2003) show a rapid increase in the number of sources at super-Euclidean rates at relatively bright flux densities ($S_\nu \gtrsim 10$ mJy) and peak near 1 mJy. These models generally predict a redshift distribution for the MIPS 24 μm population that peaks near $z \sim 1$, based largely on expectations from the *ISO* populations, and they overpredict the 24 μm number counts by factors of 2–3 at $\sim$1 mJy. The Lagache et al. (2003) model predicts a roughly Euclidean increase in the counts for $S_\nu > 10$ mJy. The shape of the counts in this model is similar to that of the observed distribution, but it peaks at $S_\nu \sim 1$ mJy, at higher flux densities than the observed counts. This model predicts a redshift distribution that peaks near $z \sim 1$ but tapers slowly with a significant population of IR-luminous galaxies out to $z \gtrsim 2$ (Dole et al. 2003).

The model of Balland et al. (2003) is based on semianalytical hierarchical models within the Press-Schecter formalism, in which galaxies identified as "interacting" are assigned IR-luminous galaxy SEDs. This model includes additional physics in that the evolution of galaxies depends on their local environment and merger/interaction histories. Although this model predicts a near-Euclidean increase in the counts for $S_\nu \gtrsim$ 10 mJy, the counts shift to sub-Euclidean rates at relatively bright flux densities. The semianalytical formalism seems to not include important physics that are necessary to reproduce the excess of faint IR sources. This illustrates the need for large-area multiwavelength studies of *Spitzer* sources to connect optical- and IR-selected sources at high redshift to understand the mechanisms that produce IR-luminous stages of galaxy evolution.

The peak in the 24 μm differential number counts occurs at fainter flux densities than that predicted from the phenomenological models based on the *ISO* results. This may suggest possibilities such as a steepening in the slope of the IR luminosity function with redshift or evolution in the relation between the mid- and total IR. Phenomenological models that reproduce the IR background predict a faint-end slope of the IR luminosity function that should be quite shallow at high redshifts, with "L^*" luminosities that correspond to $L_{\rm IR} > 10^{11}\ L_\odot$ for $z \gtrsim 1$ (see Hauser & Dwek 2001). For most plausible IR luminosity functions, galaxies with L^* luminosities dominate the integrated luminosity density. Elbaz et al. (2002) observed that the redshift distribution of objects with these luminosities in deep *ISO* surveys spans $z \simeq 0.8$–1.2, and that these objects constitute a large fraction of the total cosmic IR background. Therefore, it seems logical that objects with these luminosities dominate 24 μm number counts at 0.1–0.4 mJy, and it follows that their redshift distribution must lie at $z \sim 1$–3 (i.e., where this flux density corresponds to $\sim 10^{11}$–$10^{12}\ L_\odot$, using empirical relations from Papovich & Bell 2002). Indeed, a similar conclusion is inferred on the basis of a revised phenomenological model using the 24 μm number counts presented here (Lagache et al. 2004) and allowing for small changes in the mid-IR SEDs of IR-luminous galaxies. Examples of MIPS 24 μm sources at these redshifts and luminosities have been readily identified in optical ancillary data (Le Floc'h et al. 2004). We therefore attribute the peak in the 24 μm differential number counts at fainter flux densities to a population of luminous IR galaxies at redshifts higher than explored by *ISO*.

Integrating the differential source-count distribution provides an estimate for their contribution to the cosmic IR background at 24 μm, i.e., $I_\nu = \int dN/dS_\nu S_\nu\, dS_\nu$. For sources brighter than 60 μJy, we derive a lower limit on the total background of $\nu I_\nu(24\ \mu{\rm m}) = 1.9 \pm 0.6$ nW m^{-2} sr^{-1}. Because of the steep nature of the source counts, most of this background emission results from galaxies with fainter apparent flux densities. We find that $\simeq$60% of the 24 μm background originates in galaxies with $S_\nu \leq 0.4$ mJy, and therefore the galaxies responsible for the peak in the differential source counts also dominate the total background emission. Our result is consistent with the *COBE* DIRBE upper limit $\nu I_\nu(25\ \mu{\rm m}) < 7$ nW m^{-2} sr^{-1} inferred from fluctuations in the IR background (Kashlinsky & Odenwald 2000; Hauser & Dwek 2001).

As a further estimate on the total 24 μm background intensity, we have extrapolated the number counts for $S_\nu < 60$ μJy using the fit to the faint-end slope of the 24 μm number counts in § 3. Under this assumption, we find that sources with $S_\nu < 60$ μJy would contribute $0.8^{+0.9}_{-0.4}$ nW m^{-2} sr^{-1} to the 24 μm background, which when summed with the above measurement yields an estimate of the total background of $\nu I_\nu^{(\rm tot)}(24\ \mu{\rm m}) = 2.7^{+1.1}_{-0.7}$ nW m^{-2} sr^{-1}. For this value, the sources detected in the deep *Spitzer* 24 μm surveys produce $\sim$70% of the total 24 μm background.

We acknowledge our colleagues for stimulating conversations, the *Spitzer* Science Center staff for efficient data processing, Thomas Soifer and the IRS team for executing the Boötes-field observations, Daniel Eisenstein for cosmology discussions, Jim Cadien for his assistance with the data reduction, and the entire *Spitzer* team for their concerted effort. We also thank the referee, Matthew Malkan, for a thorough and insightful report. Support for this work was provided by NASA through contract 960785 issued by JPL/Caltech.

REFERENCES

Balland, C., Devriendt, J. E. G., & Silk, J. 2003, MNRAS, 343, 107
Chary, R. R., & Elbaz, D. 2001, ApJ, 556, 562
Chary, R. R., et al. 2004, ApJS, 154, 80
Dale, D. A., Helou, G., Contursi, A., Silbermann, N. A., & Kolhatkar, S. 2001, ApJ, 549, 215
Dole, H., Lagache, G., & Puget, J.-P. 2003, ApJ, 585, 617
Dole, H., et al. 2001, A&A, 372, 364
Elbaz, D., Cesarsky, C. J., Chanial, P., Aussel, H., Franceschini, A., Fadda, D., & Chary, R. R. 2002, A&A, 384, 848
Elbaz, D., et al. 1999, A&A, 351, L37
Fixsen, D. J., Dwek, E., Mather, J. C., Bennett, C. L., & Shafer, R. A. 1998, ApJ, 508, 123
Franceschini, A., Aussel, H., Cesarsky, C. J., Elbaz, D., & Fadda, D. 2001, A&A, 378, 1
Gordon, K., et al. 2004, PASP, submitted
Hacking, P., & Soifer, B. T. 1991, ApJ, 367, L49
Hauser, M. G. & Dwek, E. 2001, ARA&A, 39, 249
Hauser, M. G., et al. 1998, ApJ, 508, 25
Kashlinsky, A. & Odenwald, S. 2000, ApJ, 528, 74
King, A. J., & Rowan-Robinson, M. 2003, MNRAS, 339, 260
Lagache, G., Dole, H., & Puget, J.-L. 2003, MNRAS, 338, 555
Lagache, G., et al. 2004, ApJS, 154, 112
Le Floc'h, E., et al. 2004, ApJS, 154, 170
Madau, P. & Pozzetti, L. 2000, MNRAS, 312, L9
Papovich, C. & Bell, E. F. 2002, ApJ, 579, L1
Rieke, G. & Low, F. 1972, ApJ, 176, L95
Rieke, G., et al. 2004, ApJS, 154, 25
Roussel, H., Sauvage, M., Vigroux, L. & Bosma, A. 2001, A&A, 372, 427
Shupe, D. L., Fang, F., Hacking, P. B., & Huchra, J. P. 1998, ApJ, 501, 597
Soifer, B. T., & Neugebauer, G. 1991, AJ, 101, 354
Soifer, B. T., Neugebauer, G., & Houck, J. R. 1987, ARA&A, 25, 187
Spinoglio, L., Malkan, M. A., Rush, B., Carrasco, L., & Recillas-Cruz, E. 1995, ApJ, 453, 616
Stetson, P. B. 1987, PASP, 99, 191
Xu, C. 2000, ApJ, 541, 134
Xu, C., Lonsdale, C. J., Shupe, D. L., Franceschini, A., Martin, C., & Schiminovich, D. 2003, ApJ, 587, 90

The Astrophysical Journal Supplement Series, 154:112–117, 2004 September

POLYCYCLIC AROMATIC HYDROCARBON CONTRIBUTION TO THE INFRARED OUTPUT ENERGY OF THE UNIVERSE AT $z \simeq 2$

G. Lagache,[1] H. Dole,[1,2] J.-L. Puget,[1] P. G. Pérez-González,[2] E. Le Floc'h,[2] G. H. Rieke,[2] C. Papovich,[2] E. Egami,[2] A. Alonso-Herrero,[2] C. W. Engelbracht,[2] K. D. Gordon,[2] K. A. Misselt,[2] and J. E. Morrison[2]

Received 2004 March 26; accepted 2004 May 4

ABSTRACT

We present an updated phenomenological galaxy evolution model to fit the *Spitzer* 24, 70, and 160 μm number counts, as well as all the previous mid- and far-infrared observations. Only a minor change of the comoving luminosity density distribution in the previous model (Lagache, Dole, & Puget), combined with a slight modification of the starburst template spectra mainly between 12 and 30 μm, are required to fit all the data available. We show that the peak in the *Spitzer* Multiband Imaging Photometer 24 μm counts is dominated by galaxies with redshift between 1 and 2, with a nonnegligible contribution from the $z \geq 2$ galaxies ($\sim$30% at $S = 0.2$ mJy). The very close agreement between the model and number counts at 15 and 24 μm strikingly implies that (1) the polycyclic aromatic hydrocarbon features remain prominent in the redshift band 0.5–2.5 and (2) the IR energy output has to be dominated by $\sim 3 \times 10^{11}\ L_{\odot}$ to $\sim 3 \times 10^{12}\ L_{\odot}$ galaxies from redshift 0.5 to 2.5. Combining *Spitzer* with *Infrared Space Observatory* deep cosmological surveys gives for the first time an unbiased view of the infrared universe from $z = 0$ to 2.5.

Subject headings: galaxies: evolution — galaxies: high-redshift — infrared: galaxies — ISM: lines and bands

1. INTRODUCTION

A cosmic far-infrared background (CIB) that would trace the peak of the star formation and metal production in galaxy assembly has long been predicted. The first observational evidence for such a background was reported by Puget et al. (1996; see Hauser & Dwek 2001 for a review). This discovery, together with recent cosmological surveys in the infrared (IR) and submillimeter, has opened new perspectives on our understanding of galaxy formation and evolution. The surprisingly large amount of energy in the CIB shows that it is crucial to probe the galaxies contributing to it to understand when and how the bulk of stars formed in the universe.

To understand the sources contributing to the CIB and to interpret the deep source counts, we have developed a phenomenological model that constrains in a simple way the IR luminosity function evolution with redshift and fits all the existing source counts consistent with the redshift distribution, the CIB intensity, and, for the first time, the CIB fluctuation observations from the mid-IR to the submillimeter range (Lagache et al. 2003). *Spitzer* has provided deep new multiwavelength source counts from 24 to 160 μm (Papovich et al. 2004; Dole et al. 2004a). We use these new data to search for a new optimization of the Lagache et al. (2003) model parameters. A remarkable result is that only a minor change of the comoving luminosity density distribution combined with a slight modification of the starburst model spectra, mainly for the 12 $\mu\text{m} \leq \lambda \leq 30$ μm range, is required to fit all the previous data together with the new constraints.

2. THE MODEL

The model is discussed extensively in Lagache et al. (2003). Our goal is to build the simplest model with the fewest free parameters and separate ingredients. We fix the cosmology to $\Omega_{\Lambda} = 0.7$, $\Omega_0 = 0.3$, and $h = 0.65$. We assume that IR galaxies are mostly powered by star formation, and hence we use spectral energy distributions (SEDs) typical of star-forming galaxies.[3] Although some of the galaxies will have AGN-dominated SEDs, they are a small enough fraction (<10%; Alonso Herrero et al. 2004) that they do not affect the results significantly. We therefore construct "normal" and starburst galaxy template SEDs; a single form of SED is associated with each activity type and luminosity. We assume that the luminosity function (LF) is represented by these two activity types and that they evolve independently. We search for the form of evolution that best reproduces the existing data. The new optimization of the model parameters reproduces (1) the number counts at 15, 24, 60, 70, 90, 160, 170, and 850 μm, (2) the known redshift distributions (mainly at 15 and 170 μm), (3) the local luminosity functions at 60 and 850 μm, and (4) the CIB (from 100 to 1000 μm) and its fluctuations (at 60, 100, and 170 μm).

Compared with the form of the model derived by Lagache et al. (2003), only a slight change of the co-moving luminosity density distribution is required (Fig. 1), together with minor modifications to the starburst template spectra mainly between 12 and 30 μm (Fig. 2). The modified starburst spectra still reproduce the color diagrams of Soifer & Neugeubauer (1991; 12/25 vs. 60/100). We do not modify any other parameters in the model, the SED of the normal galaxy template, the SED of the starburst galaxy templates at longer wavelengths, or the parameterization of the local LF.

Polycyclic aromatic hydrocarbons (PAHs) radiate about 10% of the 1–1000 μm luminosity in a set of features concentrated mostly between 6 and 15 μm (Fig. 2). This set of features is the strongest spectral concentration known in galaxy spectra. The features strongly affect the mid-IR number counts when the redshift brings them into the bandpass filter. For the 15 μm ISOCAM observations, the peak contribution arises when the 7.7 μm maximum is close to the middle of the band, i.e., $z \sim 0.8$. The ISOCAM 15 μm counts show the existence of a maximum in the redshift distribution just at that redshift. Futhermore, it leads to a maximum in the counts (normalized to the Euclidian, e.g., on Fig. 3), which can exist only when the IR energy output in the critical redshift range is dominated by a well-defined luminosity range. Our model predicts a similar behavior for the 24 μm band.

[1] Institut d'Astrophysique Spatiale, Université Paris-Sud, bât 121, F-91405 Orsay Cedex, France.

[2] Steward Observatory, University of Arizona, 933 North Cherry Avenue, Tucson, AZ 85721.

[3] This assumption is based primarily on observations by ISOCAM and ISOPHOT, but is confirmed by the first *Spitzer* studies of galaxy SEDs in the Lockman Hole and Groth Strip (Le Floc'h et al. 2004; Alonso Herrero et al. 2004).

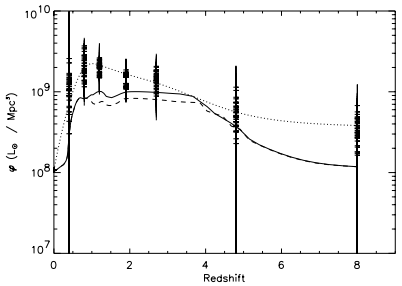

Fig. 1.—Comoving luminosity density distribution of the Lagache et al. (2003) model (*dashed line*) and the updated model presented here (*solid line*). Also shown for comparison is the comoving luminosity density distribution from all cases of Gispert et al. 2000 (*crosses with error bars*), together with the best fit passing through all cases (*dotted line*).

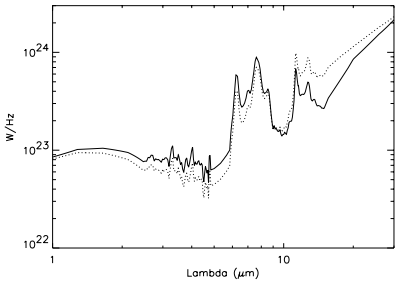

Fig. 2.—Starburst model spectrum for $L = 3 \times 10^{11}\ L_{\odot}$. *Dashed line*: Lagache et al. (2003); *solid line*: the present updated version of the model. The spectrum has not been modified for $\lambda \geq 30$ μm. The biggest change is about a factor of 2 (for a $3 \times 10^{11}\ L_{\odot}$ galaxy) around 15 μm.

3. RESULTS

3.1. *Source Counts*

We show the comparison of the number counts at 15, 60, 170, and 850 μm with the observations, as well as the new *Spitzer* 24 μm (Papovich et al. 2004), 70, and 160 μm (Dole et al. 2004a) counts in Figures 3 and 4. The updated model reproduces very well the counts at 15 and 24 μm without any significant changes in the other number counts, as well as the CIB and its fluctuations and the redshift distributions of resolved sources at 15, 60, 170, and 850 μm. The agreement between the observed counts and the model at 24 μm is excellent.

3.2. *First Interpretation of the Spitzer/MIPS Results*

The consistency of the model from the mid-IR and far-IR to the submillimeter indicates that the underlying assumptions are valid up to redshift 2.5. In particular, the very close agreement between the model and number counts at 15 and 24 μm implies that the PAH features remain prominent in the redshift range 0.5–2.5. Furthermore, the well-defined bump in the 24 μm number counts (normalized to the Euclidian) at $S \simeq 0.3$ mJy (Fig. 4) implies at $z \simeq 2$ that $L_{8\ \mu\text{m}} = 3.2 \times 10^{11}\ L_{\odot}$, which corresponds to $L_{1-1000\ \mu\text{m}} = 3.5 \times 10^{12}\ L_{\odot}$. These luminosities have to dominate the IR energy output at that redshift (as shown in Fig. 5). As a comparison, an IR energy output dominated by L_* galaxies at $z \simeq 2$ would maximize the 24 μm counts around 3 μJy, which is totally inconsistent with the observation since most of the CIB at 24 μm is resolved at flux densities brighter than $\sim$60 μJy.

Using the new model of IR galaxy evolution, Dole et al. (2004b) have made new determinations of the confusion limits for the Multiband Imaging Photometer for *Spitzer* (MIPS). A summary is provided in Table 1. Figure 6 shows the updated redshift distributions for such confusion-limited surveys. At 24 μm, the deepest surveys will probe star formation up to redshift 3. In the far-IR, MIPS surveys will probe the largely unexplored window $1 \leq z \leq 2$.

In Figure 7, we show the different redshift contributions to the 24 μm number counts. The peak in the counts is dominated by galaxies with redshift between 1 and 2. There is also a nonnegligible contribution from $z > 2$ galaxies (30% at $S = 0.2$ mJy). The integral of the source counts down to 60 μJy gives 1.9 nW m^{-2} sr^{-1}, in excellent agreement with Papovich et al. (2004). It represents about 63% of the CIB at 24 μm. It should also be noted from Figure 7 that the redshift distribution changes sharply for fluxes between 0.3 and 2 mJy. For sources weaker than 150 μJy, the redshift distribution remains about constant.

4. CONCLUSION

We have updated the model of Lagache et al. (2003) to fit the new constraints from *Spitzer* data. We show that only a small change of the co-moving luminosity density distribution and of the starburst template spectra is required to fit all the observations from the mid-IR to the submillimeter. The agreement between the model and all the data demonstrates that the integrated SEDs from galaxies still have prominent 6–9 μm emission from PAH features up to redshift 2.5. It clearly shows that the population of IR galaxies is not dominated by galaxies with featureless continuum spectra (such as AGN-type SEDs in the mid-IR). The fraction of the energy radiated by the PAHs is about one-tenth of the total IR radiation locally and remains roughly constant between redshifts 0.5 and 2.5.

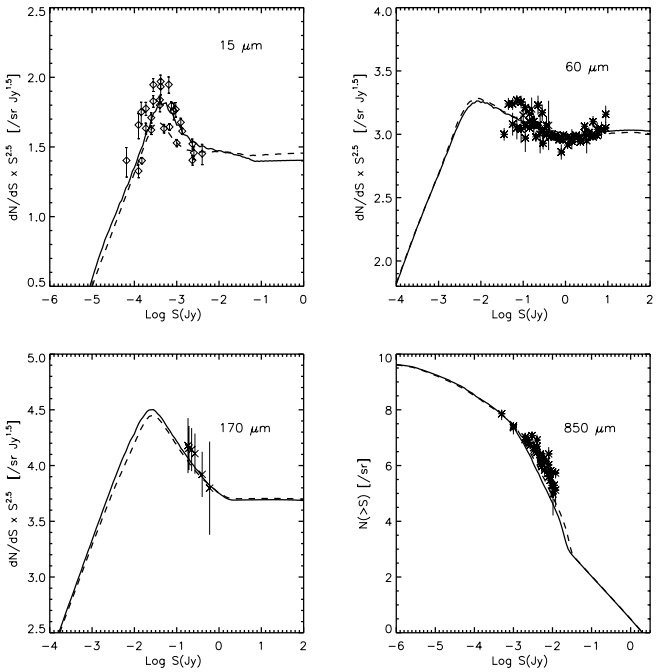

FIG. 3.—Number counts at 15, 60, 170 and 850 μm (in logarithmic scale) together with the model predictions (present work, *solid line*; Lagache et al. 2003, *dashed line*). Data at 15 μm are from Elbaz et al. (1999), at 170 μm from Dole et al. (2001), at 60 μm from Hacking & Houck (1987), Gregorich et al. (1995), Bertin et al. (1997), Lonsdale et al. (1990), Saunders et al. (1990), and Rowan-Robinson et al. (1991), and at 850 μm from Smail et al. (1997), Hughes et al. (1998), Barger et al. (1999), Blain et al. (1999), Borys et al. (2003), Scott et al. (2002), and Webb et al. (2003).

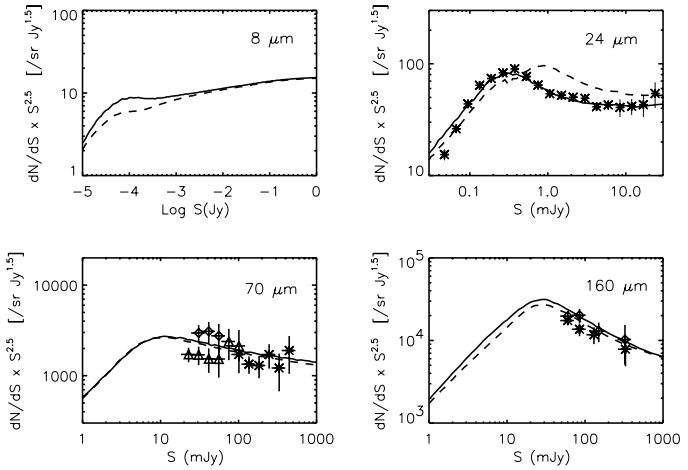

FIG. 4.—Number counts at 24, 70, and 160 μm, together with the model predictions (present work, *solid line*; Lagache et al. 2003, *dashed line*). Data at 24, 70, and 160 μm are from Papovich et al. (2004) and Dole et al. (2004a). Note that none of the observed source counts are corrected for incompleteness.

TABLE 1

1 σ_c CONFUSION NOISE VALUES USING THE BEST CONFUSION ESTIMATOR OF DOLE ET AL. (2003), CONFUSION LIMIT $S_{\rm lim}$, AND THE VALUE OF $q = S_{\rm lim}/\sigma_c$

Parameter	24 μm	70 μm	160 μm
1 σ_c	8.0 μJy	0.47 mJy	10.6 mJy
$S_{\rm lim}$	56 μJy	3.2 mJy	39.8 mJy
q	7.0	6.8	3.8

[a] Using the source density criterion.
[b] In this case, the photometric and source density criteria agree.

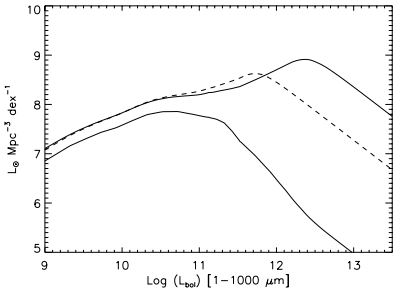

FIG. 5.—Comoving evolution of the IR energy output per dex of luminosity ($L\,dN/d\log L$). The solid, dashed, and triple–dot-dashed lines correspond to $z = 0$, 0.5, and 2, respectively.

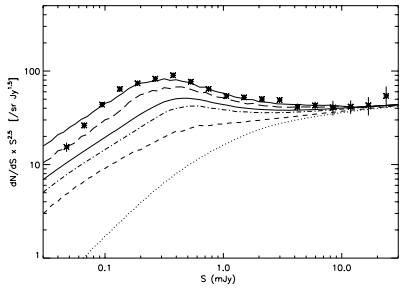

FIG. 7.—Redshift contribution to the number counts at 24 μm. The dotted, dashed, dash-dotted, triple–dot-dashed, and long-dashed lines correspond to the number counts up to redshifts 0.3, 0.8, 1, 1.3, and 2, respectively. Data are from Papovich et al. (2004).

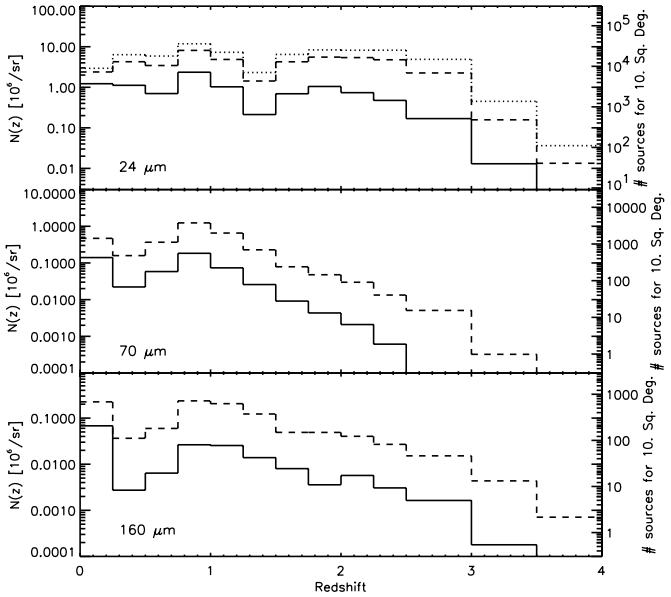

FIG. 6.—MIPS 24, 70, and 160 μm redshift distributions (in logarithmic scale). *Solid lines*: Shallow surveys (flux greater than 0.3, 22.3, and 135.1 mJy at 24, 70, and 160 μm, respectively). *Dashed line*: Deep surveys (flux greater than 0.094, 6.8, and 50.2 mJy at 24, 70, and 160 μm, respectively). *Dotted line*: Ultradeep survey (flux greater than 0.06 mJy at 24 μm).

Our initial model predicted that the IR output energy had to be dominated by galaxies with luminosities increasing rapidly with redshift ($L_{1-1000\ \mu m} \simeq 3 \times 10^{12}\ L_\odot$ at $z = 2.5$; see Fig. 5). This was needed mainly to account for the SCUBA counts (the total energy output at that redshift being mostly driven by the submillimeter extragalactic background level). The excellent agreement between the 24 μm counts and the model confirms strikingly the evolution of the IR luminosity function as being dominated in energy by $\sim 3 \times 10^{11}\ L_\odot$ to $\sim 3 \times 10^{12}\ L_\odot$ galaxies from redshift 0.5 to 2.5.

We have for the first time with *Spitzer* an unbiased view of the IR universe up to redshift 2.5. With all the mid-IR to submillimeter data, the model is now very well constrained up to $z \simeq 2.5$. Other predictions, together with the number counts of all the planned and future mid-IR to millimeter surveys, will be available on the World Wide Web.[4]

This work is based on observations made with the *Spitzer Space Telescope*, which is operated by the Jet Propulsion Laboratory, California Institute of Technology, under NASA contract 1407. We thank the funding from the MIPS project, which is supported by NASA through the Jet Propulsion Laboratory, subcontract 960785. G. L. warmly thanks the MIPS IT in Tucson, H. D. and J. L. P. for this fruitful collaboration, and G. H. R. for his careful reading of the manuscript.

[4] See http://www.ias.fr/PPERSO/glagache/act/galmodel.html.

REFERENCES

Alonso Herrero, A., et al. 2004, ApJS, 154, 155
Barger, A. J., Cowie, L. L., & Sanders, D. B. 1999, ApJ, 518, L5
Bertin, E., Dennefeld, M., & Moshir, M. 1997, A&A, 323, 685
Blain, A. W., et al. 1999, ApJ, 512, L87
Borys, C., et al. 2003, MNRAS, 344, 385
Dole, H., Lagache, G., & Puget, J.-L. 2003, ApJ, 585, 617
Dole, H., et al. 2001, A&A, 372, 364
———. 2004a, ApJS, 154, 87
———. 2004b, ApJS, 154, 93
Elbaz, D., et al. 1999, A&A, 351, L37
Gispert, R., Lagache, G., & Puget, J.-L. 2000, A&A, 360, 1
Gregorich, D. T., Neugebauer, G., Soifer, B. T., Gunn, J. E., & Herter, T. L. 1995, AJ, 110, 259
Hacking, P. B., & Houck, J. R. 1987, ApJS, 63, 311
Hauser, M. G., & Dwek, E. 2001, ARA&A, 39, 249
Hughes, D. H., et al. 1998, Nature, 394, 241
Lagache, G., Dole, H., & Puget, J.-L. 2003, MNRAS, 338, 555
Le Floc'h, E., et al., 2004, ApJS, 154, 170
Lonsdale, C. J., Hacking, P. B., Conrow, T. B., & Rowan-Robinson, M. 1990, ApJ, 358, L60
Papovich, C., et al. 2004, ApJS, 154, 70
Puget, J.-L., et al. 1996, A&A, 308, L5
Rowan-Robinson, M., Saunders, W., Lawrence, A., & Leech, K. 1991, MNRAS, 253, 485
Saunders, W., et al. 1990, MNRAS, 242, 318
Scott, S. E., et al. 2002, MNRAS, 331, 817
Smail, I., Ivison, R. J., & Blain, A. W. 1997, ApJ, 490, L5
Soifer, B. T., & Neugebauer, G. 1991, AJ, 101, 354
Webb, T. M. A., et al. 2003, ApJ, 587, 41

The Astrophysical Journal Supplement Series, 154:130–136, 2004 September

SPITZER OBSERVATIONS OF THE SCUBA/VLA SOURCES IN THE LOCKMAN HOLE: STAR FORMATION HISTORY OF INFRARED-LUMINOUS GALAXIES

E. Egami,[1] H. Dole,[1,2] J.-S. Huang,[3] P. Pérez-Gonzalez,[1] E. Le Floc'h,[1] C. Papovich,[1] P. Barmby,[3] R. J. Ivison,[4,5] S. Serjeant,[6] A. Mortier,[6] D. T. Frayer,[7] D. Rigopoulou,[8] G. Lagache,[2] G. H. Rieke,[1] S. P. Willner,[3] A. Alonso-Herrero,[9] L. Bai,[1] C. W. Engelbracht,[1] G. G. Fazio,[3] K. D. Gordon,[1] D. C. Hines,[1] K. A. Misselt,[1] S. Miyazaki,[10] J. E. Morrison,[1] M. J. Rieke,[1] J. R. Rigby,[1] and G. Wilson[7]

Received 2004 April 8; accepted 2004 May 27

ABSTRACT

We present *Spitzer Space Telescope* imaging observations at 3.6, 4.5, 5.8, 8.0, and 24 μm of the SCUBA submillimeter sources and μJy VLA radio sources in a $5' \times 5'$ area in the Lockman Hole East region. Out of the $\sim$40 SCUBA/VLA sources in the field, *Spitzer* counterparts were detected for nearly all except for the few low-weight SCUBA detections. We show that the majority (80%–90%) of the detected sources are cold (i.e., starburst-like) infrared-luminous galaxies ($L_{\rm IR} > 10^{11}\ L_{\odot}$) at redshift $0.5 < z < 3.5$, whose star-formation rate density (SFRD) is comparable to that of the optically selected star-forming galaxies.

Subject headings: cosmology: observations — galaxies: evolution — galaxies: high-redshift — infrared: galaxies

1. INTRODUCTION

A major scientific goal of the *Spitzer Space Telescope* is to probe the evolution of infrared-luminous galaxies ($L_{\rm IR} > 10^{11}\ L_{\odot}$) at $z \gtrsim 1$. Neither *IRAS* nor *ISO* provided enough sensitivity to detect a significant number of galaxies at $z > 1$, except for a small number of extreme objects. The much improved sensitivity and spatial resolution of *Spitzer* in the mid- to far-infrared have improved the situation dramatically. With this goal in mind, we have imaged a $5' \times 5'$ area in the Lockman Hole East region with the Infrared Array Camera (IRAC; Fazio et al. 2004) and Multiband Imaging Photometer for *Spitzer* (MIPS; Rieke et al. 2004). The Lockman Hole was chosen because of the low-infrared cirrus background as well as the wealth of ancillary data.

Up to now, $z \gtrsim 1$ infrared luminous galaxies have been probed mainly through submillimeter (e.g., Smail et al. 1997) or radio (e.g., Barger et al. 2000) observations. The former directly detects the emission by dust that is responsible for the infrared luminosity, while the latter detects the synchrotron emission (presumably from supernova remnants), which is known to correlate with the infrared luminosity (e.g., Helou et al. 1985). These two types of selection provide complementary views in that submillimeter selection is biased toward ultraluminous [$L_{\rm IR} > (3-4) \times 10^{12}\ L_{\odot}$] sources at high redshift (with a median redshift of 2.4; Chapman et al. 2003), while radio selection is biased toward less luminous sources at intermediate redshift ($z = 1$–2).

In this paper, we conduct the first analysis of SCUBA submillimeter and VLA radio sources based on the new *Spitzer* data. Companion papers also discuss stacking analysis of faint SCUBA sources (Serjeant et al. 2004), MAMBO millimeter sources (Ivison et al. 2004), IRAC sources (Huang et al. 2004), X-ray sources (Alonso-Herrero et al. 2004), 24 μm–selected sources (Le Floc'h et al. 2004), and extremely red objects (Wilson et al. 2004) in the same field.

Throughout the paper, $H_0 = 70$ km s^{-1} Mpc^{-1}, $\Omega_M = 0.3$, and $\Omega_\Lambda = 0.7$ were assumed.

2. DATA AND SAMPLE

2.1. *Observations and Data Reduction*

The details of the IRAC observations are presented by Huang et al. (2004), so only the MIPS observations are described here. The MIPS 24 μm images of the Lockman Hole East region were taken on UT 2003 November 30 (Program ID [PID] 1077; *Spitzer* AOR 0006619904). The large-source photometry mode was used to minimize the dither step lengths and maximize the areal coverage overlap within the $5'.4 \times 5'.4$ MIPS 24 μm field of view. The total integration time was 300 s pixel^{-1}. The 24 μm imaging data were reduced and combined with the Data Analysis Tool (DAT) developed by the MIPS instrument team (Gordon et al. 2004). The final reduced 24 μm image is shown in Figure 1*a* (Plate 1), while the three-color image produced from the IRAC 3.6, 8, and MIPS 24 μm is shown in Figure 1*b*. The 24 μm sources were extracted from the image as described in Papovich et al. (2004). The detection limit in the 24 μm image is $\sim$120 μJy (3 σ). A preliminary IRAC/MIPS source catalog of this field will be released on the World Wide Web.[11]

[11] See http://mips.as.arizona.edu/cs/ero.

[1] Steward Observatory, University of Arizona, 933 North Cherry Avenue, Tucson, AZ 85721.
[2] Institut d'Astrophysique Spatiale, Université Paris Sud, bat. 121, F-91405, Orsay Cedex, France.
[3] Harvard-Smithsonian Center For Astrophysics, 60 Garden Street, Cambridge, MA 02138.
[4] Astronomy Technology Centre, Royal Observatory, Blackford Hill, Edinburgh EH9 3HJ, UK.
[5] Institute for Astronomy, University of Edinburgh, Blackford Hill, Edinburgh EH9 3HJ, UK.
[6] Centre for Astrophysics and Planetary Science, School of Physical Sciences, University of Kent, Canterbury, Kent, CT2 7NR, UK.
[7] *Spitzer* Science Center, California Institute of Technology, MC 314-6, Pasadena, CA 91125.
[8] Astrophysics, Denys Wilson Building, Keble Road, Oxford, OX1 3RH, UK.
[9] Consejo Superior de Investigaciones Cientificas, Serrano, 117, 28006, Madrid, Spain.
[10] Subaru Telescope, National Astronomical Observatory of Japan, 650 North Aohoku Place, Hilo, HI 96720.

TABLE 1

Spitzer Flux Measurements of the SCUBA Sources

Source (LE 850)	3.6 μm (μJy)	4.5 μm (μJy)	5.8 μm (μJy)	8.0 μm (μJy)	24 μm (μJy)	850 μm (mJy)	20 cm (μJy)	$z_{\rm phot}$[a] (Submm/Radio)	$z_{\rm spec}$[b]	$z_{\rm phot}$ (This Work)	Type
1	3.8 ± 0.6	8.2 ± 1.1	11.8 ± 2.5	10.2 ± 1.7	193 ± 33	10.5 ± 1.6	73 ± 10	$2.6^{+0.4}_{-0.5}$	...	2.6	cold
4	7.7 ± 1.0	10.2 ± 1.4	11.5 ± 2.5	9.6 ± 1.6	...	8.3 ± 1.8	19 ± 8	$4.7^{+1.3}_{-0.5}$	...	2.6	cold
7	65.9 ± 6.9	77.0 ± 8.1	60.1 ± 7.8	52.4 ± 5.9	312 ± 39	8.1 ± 1.9	135 ± 13	$3.6^{+0.4}_{-1.9}$	...	1.8	cold
8b	17.1 ± 2.0	22.3 ± 2.6	37.2 ± 5.3	89.5 ± 9.6	282 ± 59	5.1 ± 1.3	58 ± 12	$3.7^{+1.5}_{-0.7}$	...	~3	warm
8a	72.0 ± 7.5	72.6 ± 7.6	79.0 ± 9.7	112.0 ± 11.9	534 ± 117	...	22 ± 11	...	0.974	...	warm
8c	26.7 ± 3.0	20.7 ± 2.4	17.2 ± 3.1	17.8 ± 2.4	161 ± 47	...	...	...	...	0.9	cold
14b	9.8 ± 1.3	14.7 ± 1.8	22.2 ± 3.7	18.5 ± 2.5	166[c]	6.3[c]	72 ± 12	$2.4^{+1.9}_{-0.4}$	...	2.5	cold
14a	15.2 ± 1.9	20.2 ± 2.4	27.6 ± 4.3	18.6 ± 2.5	83[c]	3.2[c]	36 ± 12	...	2.38	2.5	cold
18	6.1 ± 0.9	5.8 ± 0.9	19.9 ± 3.4	26.4 ± 3.3	125 ± 33	4.5 ± 1.3	47 ± 10	$3.0^{+1.1}_{-1.0}$	2.69	~3	warm
35	23.5 ± 2.7	25.9 ± 2.9	26.3 ± 4.1	34.8 ± 4.2	155 ± 31	6.7 ± 2.3	56 ± 10	...	...	3.0	cold

Notes.—The photometric uncertainties include the 10% calibration errors. The 850 μm fluxes and 20 cm fluxes are from Scott et al. (2002) and Ivison et al. (2002).
[a] Photometric redshifts (le2 type) from Aretxaga et al. (2003).
[b] Spectroscopic redshifts for LE 850.8a (Lehmann et al. 2001), LE 850.14a (R. J. Ivison et al. 2004, in preparation), and LE 850.18 (S. C. Chapman et al. 2004, in preparation).
[c] The measured total flux densities of LE 850.14 at 24 μm (249 ± 39 μJy) and 850 μm (9.5 ± 2.8 mJy) were distributed based on the 20 cm flux density ratio.

A variety of other imaging data were also assembled (Le Floc'h et al. 2004). This ancillary data set includes the F606W *Hubble Space Telescope* WFPC2 images as well as the *UBVRIJHK*$_s$ images obtained with a variety of ground-based telescopes. It also includes a deep (5 μJy beam^{-1}) high-resolution ($1''.4$ FWHM) VLA map (Ivison et al. 2002) and a reprocessed SCUBA map (A. Mortier et al. 2004, in preparation).

2.2. *The SCUBA/VLA Sources in the Field*

The field imaged by both IRAC and MIPS contains 10 SCUBA sources in the 850 μm catalog of Scott et al. (2002), LE 850.1/4/7/8/10/14/18/23/24/35[12] (Fig. 1). The first seven sources are considered secure, while the last three are regarded as marginal, the distinction being whether the signal-to-noise ratio is above or below 3.5. Among the seven secure sources, Ivison et al. (2002) detected radio counterparts for five (LE 850.1/7/8/14/18) and possibly for one more (LE 850.4) with a lower significance. Our reexamination of the VLA map shows that LE 850.35 also has a VLA source within a radius of $8''$, the region of 95% positional confidence according to Ivison et al. (2002). We tentatively identify this VLA source as the counterpart for LE 850.35, although we could not confirm the reality of this submillimeter source unambiguously even with the reprocessed SCUBA map. LE 850.35 makes the total of radio-detected SCUBA sources seven out of 10. The field also contains a total of 38 VLA sources above 20 μJy (4 σ peak flux density) using the map of Ivison et al. (2002).

3. RESULTS AND DISCUSSION

3.1. *Identification of SCUBA Sources*

Figure 2 (Plate 2) shows the *Spitzer* as well as VLA and archived Subaru/Suprime-Cam (Miyazaki et al. 2002) *R*-band images of all 10 SCUBA sources in the field. The seven sources with radio detections have all been detected by IRAC, while six (excepting only LE 850.4) have been detected by MIPS. The IRAC/MIPS flux densities of these sources are listed in Table 1 together with the previously published 850 μm and 20 cm flux densities. The following three sources have more than one IRAC source within a radius of $8''$.

LE 850.7.—The IRAC 3.6 and 4.5 μm images show extended emission northeast from the radio position, which is seen to be a nearby source in the *R*-band image. However, the longer wavelength images do not show emission in the same direction, indicating that this neighboring source does not contribute significantly above $\sim$5 μm.

LE 850.8.—Three IRAC sources (8a/8b/8c) are seen within a radius of $8''$. The 24 μm signal is clearly extended in a way consistent with all three sources contributing. The strongest radio source corresponds to component 8b. There is also faint (3 σ) radio emission at the position of component 8a, which is the brightest source at 24 μm. Component 8a was thought to be the counterpart for the *ROSAT* X-ray source with a spectroscopic redshift of 0.974 (Lehmann et al. 2001), but the later *XMM-Newton* observation showed that the X-ray source is actually coincident with component 8b (Ivison et al. 2002). This leaves a possibility that some of the radio flux from component 8b may be of active galactic nucleus (AGN) origin. The *R*-band image shows several sources at the position of component 8b.

LE 850.14.—The two radio counterparts (14a/14b) have both been detected by IRAC. The 24 μm emission is centered between the two IRAC sources. Considering the equally strong radio fluxes, both components are expected to contribute significantly in the submillimeter.

In summary, we have seven secure SCUBA sources with a total of nine radio components (LE 850.1/4/7/8a/8b/14a/14b/18/35), all of which have *Spitzer* counterparts. *Spitzer* counterparts have been found only for the sources with radio detections. The three sources that are not detected by VLA and *Spitzer* (LE 850.10/23/24) are all weak in the reprocessed 850 μm map (Fig. 2).

3.2. *Spectral Energy Distribution and Redshifts*

For the following statistical analysis, we restrict our discussion to the VLA 20 μJy sample, which contains seven of the nine SCUBA radio components (LE 850.1/7/8b/14a/14b/18/35). There is one VLA source that is relatively bright in the radio (230 μJy) but undetected in most other bands, including IRAC 5.8 and 8.0 μm (this is the only source that has not been

[12] The source names are based on Ivison et al. (2002). The full names according to SIMBAD are of the form [SFD2002] LHE N.

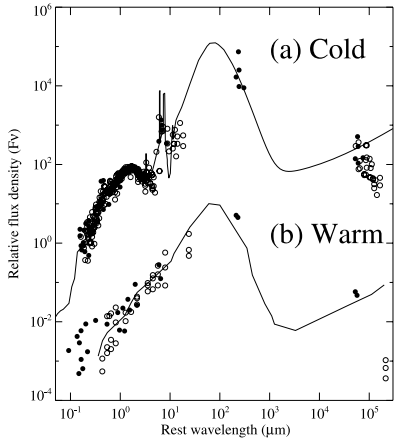

FIG. 3.—SEDs of 37 VLA sources detected above 20 μJy, which contain seven SCUBA sources: (*a*) The composite SED of 32 sources with a near-infrared continuum hump. The SED is well fitted by that of a cold ULIRG Arp 220 (*solid line*; the model by Silva et al. 1998). (*b*) Composite SED of five power-law continuum sources. The SED resembles that of a warm ULIRG Mrk 231 (*solid line*; the observed SED). The filled circles denote SCUBA sources, while the open circles denote VLA sources without SCUBA detections. The SEDs are shifted to the rest frame using photometric/spectroscopic redshifts, and normalized around 1.6 μm (i.e., the peak of the stellar continuum) with the cold sources and at 1–10 μm with the warm sources. For the three warm VLA sources without submillimeter detections, for which redshift cannot be estimated, zero redshift was used.

detected in all four IRAC bands). We exclude this source; the VLA sample consists of 37 objects, of which all are detected in the four IRAC bands, and 29 are detected at 24 μm.

The SEDs of the VLA sources can be classified into two types: those showing a clear near-infrared stellar continuum hump around 1.6 μm (32 sources, 86%) and those showing a featureless power-law continuum (five sources, 14%). Photometric redshifts can be derived for the former using the near-infrared hump (e.g., Sawicki 2002; Le Floc'h et al. 2004); For the latter, the redshifts are mainly constrained by the submillimeter and radio points, but the estimates are significantly more uncertain.

Figure 3 shows the composite SEDs of these two types. The SED of the sources with a near-infrared continuum hump is similar to that of a "cold" ultraluminous infrared galaxy (ULIRG) like Arp 220, while the SED of the power-law continuum sources resembles that of a "warm" ULIRG like Mrk 231. This cold/warm classification often used with ULIRGs roughly separates starburst-dominated galaxies (cold) and AGN-dominated ones (warm) by the appearance of the infrared SEDs. Among the 32 cold-type sources, there are eight sources (22% of the 37 VLA sample) that were not detected at 24 μm, but their rest-frame near-infrared SEDs are similar to those of the 24 μm detected sources. Considering that these sources have expected 24 μm fluxes (based on the Arp 220 SED) close to or below our detection limit, we include them in the cold category.

As Figure 3*a* shows, the cold-type sources show remarkably similar SEDs from the rest frame visible to near-infrared that are well fitted by the SED of Arp 220. Such uniformity is in contrast to the diversity of the SEDs seen with the X-ray and 24 μm selected sources (Alonso-Herrero et al. 2004; Le Floc'h et al. 2004). Among the SCUBA sources, LE 850.1/7/14a/14b/35 have this type of SED. (LE 850.4 is also of this type, but it is not formally in the radio-selected sample.) With the SCUBA sources, the good fit to the Arp 220 SED extends to submillimeter and radio, while most of the VLA-only sources have significantly lower radio fluxes, which reflects the fact that they are not as infrared-luminous as Arp 220. Figure 3*a* also shows that higher redshift sources (i.e., those with radio points at shorter wavelengths) have radio SED points closer to that of Arp 220.

The small SED dispersion with the cold-type sources demonstrates not only the similarity of the SEDs but also the accuracy of the photometric redshifts based on the near-infrared continuum hump. Table 1 shows that the redshifts derived this way for the SCUBA sources are consistent with those based on the submillimeter/radio flux ratio (Aretxaga et al. 2003). LE 850.14a and 14b show very similar SEDs, which indicates that their redshifts are both $z \sim 2.5$. In the case of LE 850.14a, this was confirmed by the spectroscopic redshift of 2.38 (R. J. Ivison et al. 2004, in preparation). This suggests a possibility that these two sources are physically associated.

If we regard the warm sources as AGN galaxies, the AGN fraction of the 20 μJy radio sample is 14% (5 out of 37). Among the nine radio components associated with the SCUBA sources, the AGN fraction is ~30% (3 out of 9) as shown in Table 1. A comparison with the 150 ks *XMM-Newton* data (Alonso-Herrero et al. 2004) shows that only two out of the five power-law continuum sources are detected and that there are three cold sources detected in the X-ray.

Figure 4*a* shows the redshift distribution of the 32 cold sources. Assuming that these are starburst-dominated, the figure can be regarded as the redshift distribution of infrared-luminous star-forming galaxies selected in the radio. The radio-infrared correlation suggests that the infrared luminosities range from 10^{11} to $10^{13}\,L_{\odot}$, except for a few sources at $z < 0.5$, which are below $10^{11}\,L_{\odot}$. The SCUBA sample constitutes only a small subset of the radio sample at high redshift. This is because (1) owing to the relatively high detection limit [$L_{\rm IR} > (3-4) \times 10^{12}\,L_{\odot}$], the submillimeter observation misses lower luminosity sources, which radio observation can detect at $z \lesssim 3$ (e.g., Barger et al. 2000); and (2) as a result of the strong luminosity evolution of the infrared-luminous galaxies, large luminosity systems detectable above the submillimeter detection limit are more abundant at higher redshift (e.g., Smail et al. 1997).

3.3. *Star Formation History*

Using the derived redshift distribution and converting the 1.4 GHz radio luminosity into a star formation rate with the conversion factor of Yun et al. (2001), we have calculated the star formation rate density (SFRD) as a function of redshift (Fig. 4*b*). A *K*-correction was applied based on a $\nu^{-0.8}$ spectrum. Our SFRD at $z = 1$ is very close to the value derived by Barger et al. (2000) with a sample of μJy VLA sources with spectroscopic redshifts.

The observed SFRD of the VLA sample shows a small peak at $z = 2$ but otherwise stays flat at $z = 1-3$ above the observed SFRD of optically selected star-forming galaxies. When corrected for dust extinction, the latter exceeds the former by a factor of a few. However, the SFRD of the infrared-luminous sample includes only the most extreme high-luminosity objects at high redshift. A substantial completeness correction is still required, which has already been applied to the optical sample.

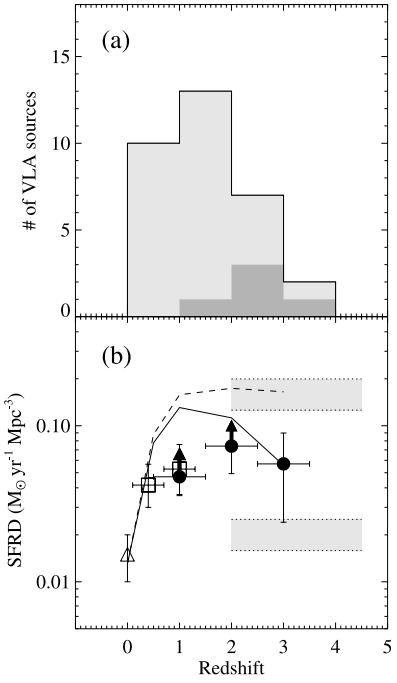

FIG. 4.—(*a*) Redshift distribution of 32 cold-type VLA sources. The dark shaded region indicates the five SCUBA sources. (*b*) Star formation rate density (SFRD) of the cold-type galaxies plotted as a function of redshift with three redshift bins (0.5–1.5, 1.5–2.5, 2.5–3.5). The bins contain 17, 9, and 3 sources, respectively, and the resulting SFRDs are plotted as filled circles with the error bars based on the Poisson counting uncertainty (i.e., SFRD divided by $\sqrt{N}$). The open squares are from Barger et al. (2000), and the open triangle is from Yun et al. (2001). No completeness correction was made for the $z > 0$ points. The lower shaded band indicates the range of observed SFRD with optically selected galaxies, while the upper shaded band indicates the range with dust extinction correction (e.g., Steidel et al. 1999; Giavalisco et al. 2004; Bouwens et al. 2004). The dashed line indicates the total SFRD predicted by the model of Lagache et al. (2004), while the solid line shows the model SFRD measurable above the radio flux limit of 20 μJy. The arrows indicate the increase of SFRD when we include the 24 μm selected infrared-luminous sources from Le Floc'h et al. (2004), which have been missed by the radio observation.

To estimate the size of the completeness correction, the observed SFRD was compared with a model prediction by Lagache et al. (2004). This model incorporates a variety of the latest observational constraints including the MIPS number counts (Dole et al. 2004; Papovich et al. 2004). However, the behavior of the model SFRD in Figure 4*b* is not unique to this model and is similar to what was derived previously (e.g., Franceschini et al. 2001). The observed points (*filled circles*) and the model-predicted SFRD adjusted for the 20 μJy radio detection limit (*solid line*) are seen to agree at $z = 2-3$, especially when we include the 24 μm detected infrared-luminous galaxies that should have been in the radio sample (based on the 24 μm $\rightarrow$ IR $\rightarrow$ radio luminosity conversion) but are not (e.g., sources larger than a few arcseconds would have been resolved away in the radio map). This suggests that if the completeness correction is applied, the total SFRD of this infrared-luminous galaxy population, which is considered to be distinct from the optically selected one (e.g., Franceschini et al. 2001), is flat at $z = 2-3$ at a level comparable to the SFRD of the optically selected galaxies (*dashed line*). At $z \sim 1$, however, the model overpredicts the observed SFRD by almost a factor of 2. We will examine in future papers whether this discrepancy is particular to this field (e.g., cosmic variance) or persistent even with a larger sample.

4. SUMMARY

Except for the few low-weight SCUBA detections, nearly all the SCUBA and VLA μJy sources have been detected by *Spitzer*. The majority (86%) of the sources show remarkably similar SEDs well fitted by the SED of a cold ULIRG like Arp 220. This characteristic was exploited to derive the redshift distribution, which then enabled us to derive the star formation history of this galaxy population using the radio-infrared correlation. These submillimeter/radio selected galaxies are mostly star-forming (i.e., cold) infrared-luminous galaxies ($L_{\rm IR} > 10^{11}\,L_{\odot}$) at $0.5 < z < 3.5$, whose SFRD is probably comparable to that of the optically selected star-forming galaxies.

We would like to thank S. C. Chapman for communicating us the revised redshift of LE 850.18 before publication, L. Silva for making the Arp 220 model SED available, and G. Neugebauer for commenting on the manuscript. This work is based in part on observations made with the *Spitzer Space Telescope*, which is operated by the Jet Propulsion Laboratory, California Institute of Technology, under NASA contract 1407. Support for this work was provided by NASA through contract 960785 issued by JPL/Caltech.

REFERENCES

Alonso-Herrero, A., et al. 2004, ApJS, 154, 155
Aretxaga, I., et al. 2003, MNRAS, 342, 759
Barger, A. J., Cowie, L. L., & Richards, E. A. 2000, AJ, 119, 2092
Bouwens, R. J., et al. 2004, ApJ, 606, L25
Chapman, S. C., Blain, A. W., Ivison, R. J., & Smail, I. R. 2003, Nature, 422, 695
Dole, H., et al. 2004, ApJS, 154, 87
Fazio, G. G., et al. 2004, ApJS, 154, 10
Franceschini, A., Aussel, H., Cesarsky, C. J., Elbaz, D., & Fadda, D. 2001, A&A, 378, 1
Giavalisco, M., et al. 2004, ApJ, 600, L103
Gordon, K., et al. 2004, PASP, submitted
Helou, G., Soifer, B. T., & Rowan-Robinson, M. 1985, ApJ, 298, L7
Huang, J.-S., et al. 2004, ApJS, 154, 44
Ivison, R. J., et al. 2002, MNRAS, 337, 1
———. 2004, ApJS, 154, 124
Lagache, G., et al. 2004, ApJS, 154, 112
Le Floc'h, E., et al. 2004, ApJS, 154, 170
Lehmann, I., et al. 2001, A&A, 371, 833
Miyazaki, S., et al. 2002, PASJ, 54, 833

Papovich, C., et al. 2004, ApJS, 154, 70
Rieke, G. H., et al. 2004, ApJS, 154, 25
Sawicki, M. 2002, AJ, 124, 3050
Scott, S. E., et al. 2002, MNRAS, 331, 817
Serjeant, S., et al. 2004, ApJS, 154, 118
Silva, L., Granato, G. L., Bressan, A., & Danese, L. 1998, ApJ, 509, 103
Smail, I., Ivison, R. J., & Blain, A. W. 1997, ApJ, 490, L5
Steidel, C. C., Adelberger, K. L., Giavalisco, M., Dickinson, M., & Pettini, M. 1999, ApJ, 519, 1
Wilson, G., et al. 2004, ApJS, 154, 107
Yun, M. S., Reddy, N. A., & Condon, J. J. 2001, ApJ, 554, 803

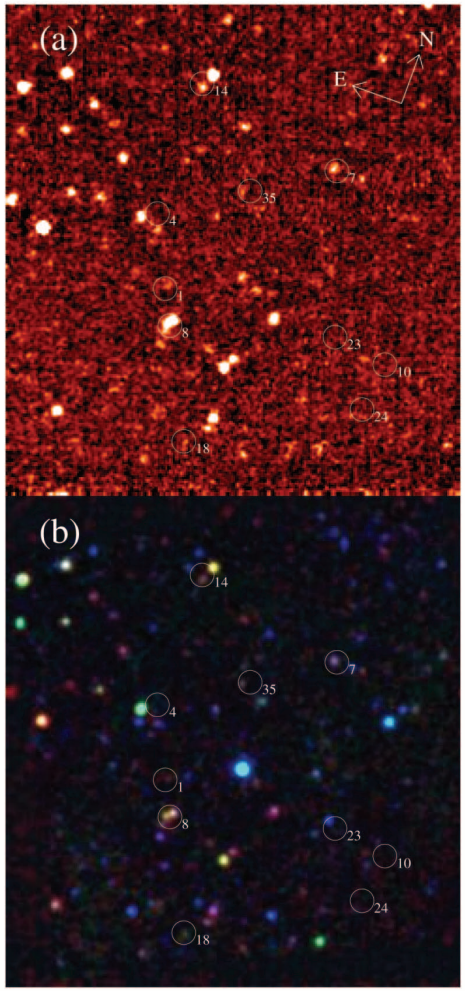

FIG. 1.—(*a*) MIPS 24 μm image of the Lockman Hole East; (*b*) three-color image of the same field produced from the IRAC 3.6 μm, 8.0 μm, and MIPS 24 μm images. The 10 SCUBA sources (LE 850.1/4/7/8/10/14/18/23/24/35) are indicated with white circles with a radius of 8″. The field of view is $\sim 5' \times 5'$.

PLATE 1

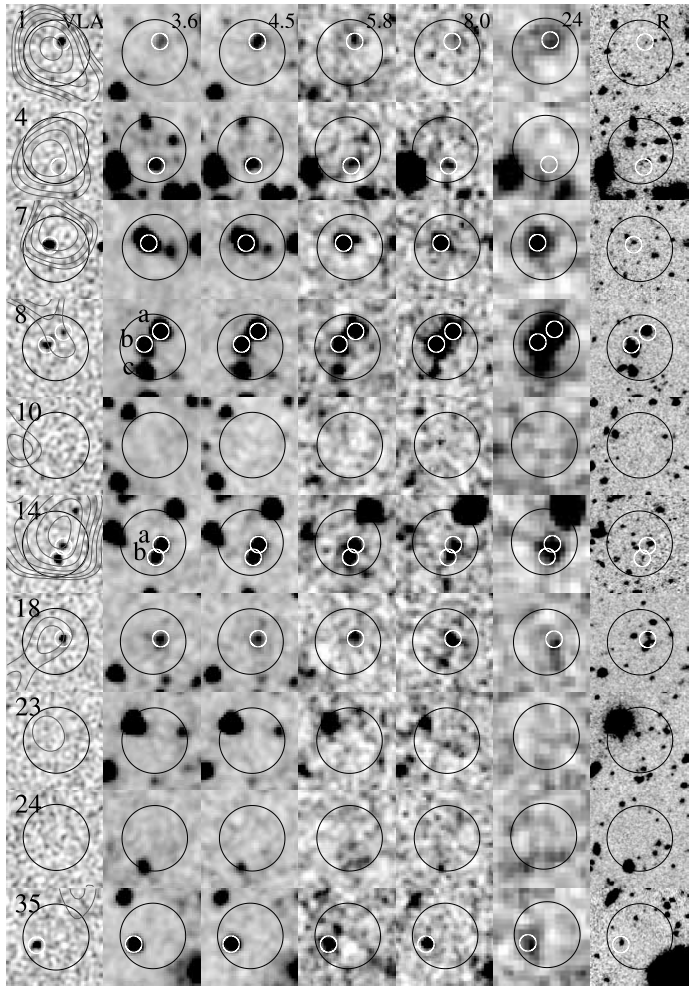

FIG. 2.—Postage stamp images of the 10 SCUBA sources. Shown here are (*from left to right*) VLA, IRAC 3.6, 4.5, 5.8, 8.0 μm, MIPS 24 μm, and *R*-band images. The VLA images are from the data of Ivison et al. (2002), while the *R*-band images are from the data taken from the Subaru telescope archive. The 850 μm contour maps (A. Mortier et al. 2004, in preparation) are overlaid on the VLA images. The contours start at 2.5 σ above the sky and increase by a factor of 1.2. The size of each image is $20'' \times 20''$. The black circle indicates the region of 95% positional confidence ($r = 8''$) by Ivison et al. (2002). The small white circles indicate the positions of the radio sources seen in the VLA map. In all the images, north is up and east is to the left.

PLATE 2

THE ASTROPHYSICAL JOURNAL SUPPLEMENT SERIES, 154:170–173, 2004 September

IDENTIFICATION OF LUMINOUS INFRARED GALAXIES AT $1 \lesssim z \lesssim 2.5$[1,2,3,4,5,6]

E. LE FLOC'H,[7] P. G. PÉREZ-GONZÁLEZ,[7] G. H. RIEKE,[7] C. PAPOVICH,[7] J.-S. HUANG,[8] P. BARMBY,[8] H. DOLE,[7,9] E. EGAMI,[7] A. ALONSO-HERRERO,[7] G. WILSON,[10] S. MIYAZAKI,[11] J. R. RIGBY,[7] L. BEI,[7] M. BLAYLOCK,[7] C. W. ENGELBRACHT,[7] G. G. FAZIO,[8] D. T. FRAYER,[10] K. D. GORDON,[7] D. C. HINES,[7,12] K. A. MISSELT,[7] J. E. MORRISON,[7] J. MUZEROLLE,[7] M. J. RIEKE,[7] D. RIGOPOULOU,[13] K. Y. L. SU,[7] S. P. WILLNER,[8] AND E. T. YOUNG[7]

Received 2004 March 26; accepted 2004 April 26

ABSTRACT

We present preliminary results on 24 μm detections of luminous infrared galaxies at $z \gtrsim 1$ with the Multiband Imaging Photometer for *Spitzer* (MIPS). Observations were performed in the Lockman Hole and the Extended Groth Strip (EGS) and were supplemented by data obtained with the Infrared Array Camera (IRAC) between 3 and 9 μm. The positional accuracy of $\lesssim 2''$ for most MIPS/IRAC detections provides unambiguous identifications of their optical counterparts. Using spectroscopic redshifts from the Deep Extragalactic Evolutionary Probe survey, we identify 24 μm sources at $z \gtrsim 1$ in the EGS, while the combination of the MIPS/IRAC observations with *BVRIJHK* ancillary data in the Lockman Hole also shows very clear cases of galaxies with photometric redshifts at $1 \lesssim z \lesssim 2.5$. The observed 24 μm fluxes indicate infrared luminosities greater than $10^{11}\ L_{\odot}$, while the data at shorter wavelengths reveal rather red and probably massive ($\mathcal{M} \gtrsim \mathcal{M}^{*}$) galaxy counterparts. It is the first time that this population of luminous objects is detected up to $z \sim 2.5$ in the infrared. Our work demonstrates the ability of the MIPS instrument to probe the dusty universe at very high redshift and illustrates how the forthcoming *Spitzer* deep surveys will offer a unique opportunity to illuminate a dark side of cosmic history not explored by previous infrared experiments.

Subject headings: cosmology: observations — galaxies: high-redshift — infrared: galaxies

1. INTRODUCTION

In the past few years, deep observations in the infrared and submillimeter revealed a population of high-redshift galaxies emitting the bulk of their luminosity between 8 and 1000 μm, whose cosmological significance had been previously missed or severely underestimated by optical surveys because of extinction effects due to dust. These sources, likely the analogs of the local luminous and ultraluminous infrared galaxies [respectively, LIRGs, $10^{11}\ L_{\odot} \leq L_{\rm IR} = L(8\text{–}1000\ \mu\text{m}) \leq 10^{12}\ L_{\odot}$, and ULIRGs, $L_{\rm IR} \geq 10^{12}\ L_{\odot}$] played a crucial role through the cosmic ages. At mid-infrared wavelengths, results from the *Infrared Space Observatory* (*ISO*) mission show that the evolution of these powerful objects noticeably contributed to the global star formation history at $0 \lesssim z \lesssim 1$ (Elbaz et al. 1999; Flores et al. 1999). Observations with SCUBA at 850 μm also led to the discovery of extremely bright infrared sources mainly located at $z \gtrsim 2$ and characterized by a space density 1000 times larger than observed in the local universe (e.g., Chapman et al. 2003).

From the purely observational point of view though, very little is currently known about the potential importance of dusty sources at $1 \lesssim z \lesssim 2$. This is explained on one hand by sensitivity limitations of the infrared instruments previously used, such as ISOCAM and ISOPHOT on board *ISO*, and on the other hand by the SCUBA surveys being mostly sensitive to $L \gtrsim 10^{12}\ L_{\odot}$ galaxies, which were much more numerous at $z \sim 2\text{–}3$. Current knowledge indicates that a large fraction of today's stars were probably born at $1 \lesssim z \lesssim 2$ (e.g., Dickinson et al. 2003; Calura & Matteucci 2003), before the global activity of star formation began to decrease rapidly down to $z \sim 0$ (Lilly et al. 1996).

The recently commissioned Multiband Imaging Photometer for *Spitzer* (MIPS) on board the *Spitzer Space Telescope* provides a unique opportunity to address this issue. For sources at $z \gtrsim 1.5$, its 24 μm band is particularly suitable for detecting the possible redshifted emission from the 8 μm broadband feature commonly seen in infrared galaxy spectra, while the main 15 μm filter on ISOCAM was rather more adapted for detecting this feature at $z \sim 0.8$. Here we assess the capabilities of the MIPS instrument to shed light on a yet unexplored side of galaxy evolution and present our preliminary results on the detection of $1 \lesssim z \lesssim 2.5$ infrared galaxies at 24 μm. This work

[1] Based on observations made with the *Spitzer Space Telescope*, operated by the Jet Propulsion Laboratory under NASA contract 1407.
[2] Based on observations collected at the Subaru Telescope, which is operated by the National Astronomical Observatory of Japan.
[3] Based on observations collected at the Canada-France-Hawaii Telescope, which is operated by the National Research Council of Canada, the Centre National de la Recherche Scientifique and the University of Hawaii.
[4] Based on observations obtained at Kitt Peak National Observatory, National Optical Astronomy Observatory, which is operated by the Association of Universities for Research in Astronomy, Inc. (AURA), under cooperative agreement with the National Science Foundation.
[5] Based on observations collected at the German-Spanish Astronomical Center, Calar Alto, operated jointly by Max-Planck-Institut für Astronomie and Instituto de Astrofisica de Andalucia (CSIC).
[6] Based on observations made with the Isaac Newton Telescope, operated on the island of La Palma by the Isaac Newton Group in the Spanish Observatorio del Roque de los Muchachos of the Instituto de Astrofisica de Canarias.
[7] Steward Observatory, University of Arizona, Tucson, AZ 85721.
[8] Harvard-Smithsonian Center for Astrophysics, 60 Garden Street, Cambridge, MA 02138.
[9] Institut d'Astrophysique Spatiale, Université Paris Sud, F-91405 Orsay Cedex, France.
[10] *Spitzer* Science Center, MC 220-6, 1200 East California Boulevard, Pasadena, CA 91125.
[11] Subaru Telescope, National Astronomical Observatory, 650 North Aohoku Plaza, Hilo, HI 96720.
[12] Space Science Institute, 4750 Walnut Street, Suite 205, Boulder, CO 80301.
[13] Astrophysics, Denys Wilson Building, Keble Road, Oxford, OX1 3RH, UK.

is one facet of a larger set of publications also addressing source number counts at 24, 70, and 160 μm (Papovich et al. 2004; Dole et al. 2004), IR model interpretation (Lagache et al. 2004), as well as the relation between the MIPS-selected objects and other populations such as the SCUBA/MAMBO and VLA galaxies (Egami et al. 2004; Ivison et al. 2004; Serjeant et al. 2004) and X-ray sources (Alonso-Herrero et al. 2004; Rigby et al. 2004). Throughout the paper, a ΛCDM cosmology with $H_0 = 70$ km s^{-1} Mpc^{-1}, $\Omega_m = 0.3$, and $\Omega_\lambda = 0.7$ is assumed.

2. OBSERVATIONS AND DATA ANALYSIS

We performed 24 μm observations[14] with MIPS (Rieke et al. 2004) in a $5' \times 5'$ area of the Lockman Hole (LH; $\alpha = 10^{\rm h}51^{\rm m}56^{\rm s}$, $\delta = 57^\circ25'32''$, J2000) as well as in a $2^\circ \times 10'$ region of the extended Groth strip (EGS, $\alpha \sim 14^{\rm h}19^{\rm m}$, $\delta \sim 52^\circ48'$, J2000). Data in the Lockman Hole were obtained in the MIPS "photometry mode," with a series of dithered exposures allowing a high frame redundancy and efficient cosmic-ray rejection (see Egami et al. 2004 for more details). Observations in the EGS were performed with the MIPS "slow scan" technique, an observing mode that allows coverage of large sky areas with high efficiency. Data reduction was carried out using the MIPS Data Analysis Tool (Gordon et al. 2004). Effective integration times of $\sim$250 and $\sim$450 s per sky pixel were reached, respectively, for the Lockman Hole and EGS data, leading to a 24 μm 1 σ rms $\sim$35 μJy (LH) and $\sim$25 μJy (EGS). The astrometry of the Groth strip final mosaic was refined using bright objects also listed in the 2MASS catalog (Jarrett et al. 2000), while source positions in our smaller coverage of the Lockman Hole were matched against an abundant set of ancillary data (see below). We estimate the absolute astrometry accuracy to be better than $2''$. Point source extraction and photometry were performed as described by Papovich et al. (2004).

Both fields were also observed with the *Spitzer* Infrared Array Camera (IRAC; Fazio et al. 2004) at 3.6, 4.5, 5.8, and 8 μm, down to 5 σ rms $\sim$1.2, 1.1, 6.5, and 8.0 μJy, respectively. A detailed description of the IRAC data analysis is presented by Huang et al. (2004). In addition, we retrieved *HST* WFPC2 images of the EGS from the public database of the Deep Extragalactic Evolutionary Probe (DEEP) team,[15] and a set of ancillary observations of the Lockman Hole was collected in the optical and the near-infrared (NIR) to supplement our *Spitzer* program. For the latter, we made use of archival *B*-band images from the Wide Field Camera (WFC) of the Isaac Newton Telescope (INT), while $VRIJHK_s$ data were obtained with the UH8K camera on the Canada-France-Hawaii Telescope (*VI* bands), the Suprime-CAM instrument on the Subaru Telescope (*R* band), TIFKAM on the 2.1 m Telescope of Kitt Peak (*H* band) and Omega-Prime on the 3.5 m Telescope of Calar Alto (JK_s band). Limiting Vega magnitudes (3 σ level) of 26.0, 24.0, 27.0, 24.0, 22.0, 20.5, and 20.0 mag arcsec^{-2} were, respectively, derived in the $BVRIJHK_s$ filters. Source detection and photometry were carried out with SExtractor (Bertin & Arnouts 1996).

For the Lockman Hole data, the full width at half-maximum of the PSF goes from $\sim 1''$ in the optical/NIR bands to $2''$ and $6''$ in the IRAC and MIPS images, which gave us confidence in identifying the respective counterparts at each wavelength (see illustration in Fig. 1). Merged catalogs among the different filters were then built, starting with matching the coordinates of the 24 μm sources in the deep *R*-band image. Following Kron (1980), we estimated the *total* flux for each object detected in the *R* image using an elliptical aperture derived from an isophotal fit around the given source and translated those apertures to the other optical and NIR data to obtain integrated fluxes for the corresponding filter (in all cases the apertures were large enough to enclose the PSF profile). IRAC and MIPS fluxes were derived, respectively, with circular aperture photometry and PSF fitting (see Huang et al. 2004; Papovich et al. 2004).

[14] *Spitzer* PIDs 8 and 1077.

[15] See http://deep.ucolick.org.

3. RESULTS: INFRARED GALAXIES AT $z \gtrsim 1$

3.1. *Spectroscopic Redshifts*

Our source position catalog in the EGS region was compared to the DEEP1 database of galaxies with spectroscopic redshifts (B. Weiner et al. 2004, in preparation). Though most of the objects from this survey clearly lie at $0 \lesssim z \lesssim 1$, we identified from our 24 μm observations nine galaxies at $1 \lesssim z \lesssim 1.3$, and two other sources at $z = 1.43$ and $z = 1.74$, whose redshifts were, respectively, derived from Hα (Hopkins et al. 2000) and Fe II absorption lines (B. Weiner 2004, private communication). From their observed 24 μm fluxes and using the luminosity-dependent spectral energy distribution (SED) templates from the model of Lagache et al. (2004), we then estimated their infrared luminosities between 8 and 1000 μm. Even though the exact relation between the mid- and total IR galaxy emission is not yet well understood, there are some indications that the mid- to far-infrared correlation still holds in the distant universe (Appleton et al. 2004), and the $L_{24\ \mu{\rm m}}/L_{\rm IR}$ ratio anyhow varies by less than a factor of $\sim$2–3 for most model SEDs at high redshifts (e.g., Papovich & Bell 2002). With this caution in mind, we found four sources with $4 \times 10^{11}\ L_\odot < L_{\rm IR} < 10^{12}\ L_\odot$, six galaxies with $10^{12}\ L_\odot < L_{\rm IR} < 3 \times 10^{12}\ L_\odot$, and one hyperluminous system characterized by $L_{\rm IR} = 2.5 \times 10^{13}\ L_\odot$. Given that the objects from the DEEP1 database are optically bright, we note that these luminous sources likely have higher optical/IR flux ratios than those of more obscured infrared galaxies. This underlies the importance of obtaining near-IR and mid-IR (e.g., *Spitzer* IRS) spectroscopy as well as accurate photometric redshifts to study all types of IR-luminous objects.

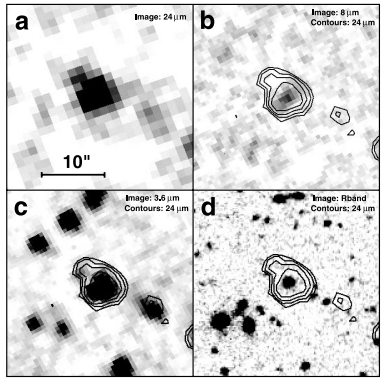

FIG. 1.—Illustration of our band-merging process, showing a source detected with MIPS at (*a*) 24 μm and its counterparts at (*b*) 8 μm, (*c*) 3.6 μm, and (*d*) 0.6 μm in the *R* band. Contours in these three last panels correspond to the 24 μm emission. The centering accuracy at this wavelength ($\lesssim 2''$), combined with the sharp PSF of the IRAC data between 3 and 9 μm, allow unambiguous identifications. The four images have a similar field of view, with the scale indicated in the top left panel. We estimate for this source a photometric redshift $z \sim 1.8$ (see § 3).

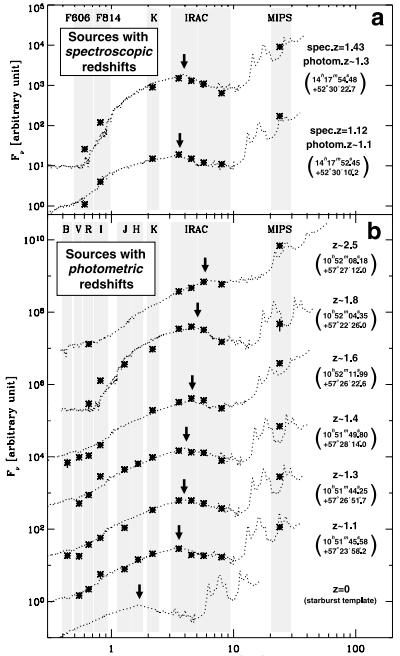

FIG. 2.—Optical/NIR/IRAC/MIPS broadband photometry (*asterisks*) of 24 μm selected sources with (*a*) spectroscopic and (*b*) photometric redshifts $z \gtrsim 1$. In each case, the dashed curve represents the best redshifted SED template fitting the data (see § 3.2 for more details). The corresponding photometric redshift and the source coordinates (J2000 epoch) are mentioned to the right of the panel. Flux uncertainties are represented with vertical solid lines. A $z = 0$ starburst-like spectrum is added at the bottom for reference. Note how the rest-frame 1.6 μm stellar bump gives a clear constraint on the redshift determination ($\Downarrow$ symbol).

3.2. *Photometric Redshifts*

For distant galaxies, our analysis of SEDs for EGS sources with spectroscopic redshifts indicates that the combination of the four IRAC bands with optical and NIR data allows locating with good accuracy the spectral feature produced both by the stellar H$^-$ opacity minimum at *rest frame* 1.6 μm and the global shape of the underlying stellar continuum. This characteristic of galaxy SEDs provides a key indication for photometric redshift determinations (see also Simpson & Eisenhardt 1999; Sawicki 2002). Figure 2*a* illustrates this result in the case of two representative sources of our sample, whose broadband SEDs lead to photometric redshifts in good agreement with those determined from optical spectroscopy.

Relying on this new approach, we used our optical/NIR and IRAC data to locate 24 μm selected sources with photometric redshifts $z \gtrsim 1$. The analysis of the complete MIPS data set in the EGS is still in progress. We present in this preliminary study the results we obtained for the Lockman Hole. Over the $5' \times 5'$ area covered by MIPS, we identify *at least* 25 objects characterized by a rather prominent stellar bump revealing an unambiguous redshift larger than 1. Figure 2*b* shows the *BVRIJHK*/IRAC/MIPS broadband SEDs of several of these sources spanning the $1 \lesssim z \lesssim 2.5$ redshift range, with the best galaxy template fitted to our data. These templates were built by combining the optical/NIR spectral range emission modeled by Devriendt et al. (1999) with the infrared SEDs from the model of Lagache et al. (2004). For several objects showing a rather high MIPS to IRAC flux ratio, an additional contribution from a hot dust continuum (i.e., Very Small Grains) was arbitrarily added (see Gallais et al. 2004 for more details on the method). In this first attempt to locate $z \gtrsim 1$ galaxies using the 1.6 μm stellar bump, we relied on a simple "by-eye" fit, which clearly gives a sufficient constraint (i.e., $\Delta z \sim 0.2$) for the cases shown in Figure 2. We emphasize that the few SEDs shown in Fig. 2 were not chosen to be globally representative of our galaxy sample at similar redshifts, but correspond to 24 μm sources detected at least in the *R*/IRAC bands and for which a photometric redshift could be reliably obtained from the spectral feature produced at rest frame 1.6 μm. This naturally biases the selection against sources with a rather shallow stellar bump like the active nuclei (see Alonso-Herrero et al. 2004). This issue will obviously have to be taken into account in future studies of more complete samples.

TABLE 1
GENERAL PROPERTIES OF OUR SELECTED SOURCES IN THE LOCKMAN HOLE

Redshift	Type[a]	N_o[b]	$L_{\rm IR}$ ($10^{11}\ L_\odot$)[c]	M_K[c,d]
1.0–1.5	Red Sp.	≥ 3	4^{6}_{3}	$-25.2^{-24.8}_{-25.6}$
	Starb.	≥ 11	6^{10}_{1}	$-24.8^{-23.8}_{-25.7}$
	VLIRG	≥ 3	18^{22}_{11}	$-25.7^{-24.9}_{-26.3}$
1.5–2.0	Red Sp.	≥ 1	4	-26.4
	VLIRG	≥ 7	26^{55}_{8}	$-25.4^{-24.6}_{-27.0}$
2.0–2.5	VLIRG	≥ 3	58^{90}_{20}	$-26.0^{-25.4}_{-26.4}$

[a] Source classification: (Red Sp.) IR-quiescent early-type spiral galaxy with a red optical/NIR color; (Starb.) M82-like IR starburst associated with a late-type spiral; (VLIRG) very luminous IR Galaxy characterized by a high rest-frame IR/NIR ratio and a rather elusive 4000 Å break.

[b] Minimum number of selected sources per category.

[c] Assume $H_0 = 70$ km s^{-1} Mpc^{-1}, $\Omega_m = 0.3$ and $\Omega_\lambda = 0.7$. The mean value is given, along with the range of measurements.

[d] Rest-frame *K*-band absolute magnitude.

Table 1 summarizes general properties of our sample in the Lockman Hole. As in the EGS, the estimated redshifts and observed 24 μm fluxes indicate infrared luminosities characterized by $L_{\rm IR} > 10^{11}\ L_\odot$. The rest-frame optical and NIR properties reveal rather red colors (i.e., observed $R - K > 4$)

originating either from an evolved stellar population or a young reddened starburst. They also indicate high luminosities in the rest-frame near-infrared, which suggests the presence of rather massive objects ($\mathcal{M} \gtrsim \mathcal{M}^*$).

Finally, we note that only one of these sources is detected in the deep X-ray observations of the Lockman Hole by *XMM-Newton* (Hasinger et al. 2001). In conjunction with the galaxy-like templates fitting their optical SEDs, the X-ray nondetections suggest that these galaxies are mostly dominated by star-forming activity, even if the presence of an active nucleus cannot be fully excluded by the data (see Alonso-Herrero et al. 2004).

4. DISCUSSION AND CONCLUSION

We stress that our reported number of 24 μm–selected infrared galaxies at $z \gtrsim 1$ is obviously a lower limit on their density at these redshifts, since we only selected sources characterized by a well-defined stellar bump in the rest-frame near-infrared. This limit agrees with the predictions of the various models dealing with infrared galaxy evolution (e.g., Lagache et al. 2004).

Our selected sources exhibit a rather wide range of MIPS to IRAC flux ratios and optical/NIR SED shapes. This suggests a possibly large diversity in the properties of infrared galaxies at high redshift. It is also interesting to note that the most distant sources of our sample tend to have extremely red colors from the B to the 24 μm band, with a global SED best fitted by ULIRG templates such as the one from Arp 220. Finally, our data suggest the presence at high redshift of the broadband emission features often seen in the mid-infrared spectra of local galaxies and commonly attributed to large molecules transiently heated by UV photons. Even though we cannot completely exclude a steeply rising continuum accounting for the 24 μm emission, the observed MIPS/IRAC flux ratios are indeed difficult to reproduce without a significant contribution from these features (see Fig. 2). A similar conclusion is reached by Lagache et al. (2004) based on the modeling of the MIPS 24/70/160 μm source number counts.

Since the late 1990s, there have been a wealth of discoveries at very high redshift (e.g., $z \gtrsim 3$), while little progress has been made in the $1 \lesssim z \lesssim 2$ redshift range (but see Steidel et al. 2004). However, galaxy evolution at $1 \lesssim z \lesssim 2$ played a central role in the cosmic growth of structures and the assembly of galaxies (Ellis 2001). MIPS provides a unique opportunity to explore the star formation and black hole accretion history at these redshifts. Compared to previous models, for instance, the new predictions by Lagache et al. (2004) based on the MIPS source number counts indicate a high density of $z \sim 1.5$ LIRGs/ULIRGs, the first of which have just been identified in this paper. The MIPS deep surveys will reveal the evolution of luminous and massive galaxies at $1 \gtrsim z \gtrsim 3$, bridging the gap between the different populations revealed by *ISO* and SCUBA. Combining with sources at similar redshifts but selected with different techniques (e.g., Balmer-break galaxies) will also give us new clues on galaxy evolution.

We acknowledge Rob Ivison and an anonymous referee for their helpful comments on the manuscript. We thank the funding from the MIPS and IRAC projects, which are both supported by NASA through the Jet Propulsion Laboratory, subcontracts 960785 and 1256790. This work also uses data obtained with support of the National Science Foundation grants AST 95-29028 and AST 00-71198 awarded to S. M. Faber. Additional K-band data were kindly made available to us from observations of the EGS and other DEEP2 fields being undertaken at the Hale 5 m Telescope by C. Conselice, K. Bundy, and R. Ellis. We are indebted to the Instituto de Astrofísica de Canarias for maintaining its access to the WFC archival data. We are also particularly grateful to Jim Cadien for helping us in the data analysis process, and we acknowledge Guilaine Lagache for the access to her model predictions.

REFERENCES

Alonso-Herrero, A., et al. 2004, ApJS, 154, 155
Appleton, P., et al. 2004, ApJS, 154, 147
Bertin, E., & Arnouts, S. 1996, A&AS, 117, 393
Calura, F., & Matteucci, F. 2003, ApJ, 596, 734
Chapman, S. C., Blain, A. W., Ivison, R. J., & Smail, I. R. 2003, Nature, 422, 695
Devriendt, J., Guiderdoni, B., & Sadat, R. 1999, A&A, 350, 381
Dickinson, M., Papovich, C., Ferguson, H. C., & Budavári, T. 2003, ApJ, 587, 25
Dole, H., et al. 2004, ApJS, 154, 87
Egami, E., et al. 2004, ApJS, 154, 130
Elbaz, D., et al. 1999, A&A, 351, L37
Ellis, R. 2001, Galaxy Formation and Evolution: Recent Progress, XIth Canary Islands Winter School of Astrophysics (astro-ph/0102056)
Fazio, G., et al. 2004, ApJS, 154, 10
Flores, H., et al. 1999, A&A, 343, 389
Gallais, P., et al. 2004, A&A, 414, 845
Gordon, K., et al. 2004, PASP, submitted
Hasinger, G., et al. 2001, A&A, 365, L45
Hopkins, A., Connolly, A., & Szalay, A. 2000, AJ, 120, 2843
Huang, J.-S., et al. 2004, ApJS, 154, 44
Ivison, R. J., et al. 2004, ApJS, 154, 124
Jarrett, T. H., et al. 2000, AJ, 119, 2498
Kron, R. G. 1980, ApJS, 43, 305
Lagache, G., et al. 2004, ApJS, 154, 112
Lilly, S. J., Le Fevre, O., Hammer, F., & Crampton, D. 1996, ApJ, 460, L1
Papovich, C., & Bell, E. F. 2002, ApJ, 579, L1
Papovich, C., et al. 2004, ApJS, 154, 70
Rieke, G., et al. 2004, ApJS, 154, 25
Rigby, J., et al. 2004, ApJS, 154, 160
Sawicki, M. 2002, AJ, 124, 3050
Serjeant, S., et al. 2004, ApJS, 154, 118
Simpson, C., & Eisenhardt, P. 1999, PASP, 111, 691
Steidel, C. C., et al. 2004, ApJ, 604, 534

2003

The Astrophysical Journal, 585:617–629, 2003 March 10

PREDICTIONS FOR COSMOLOGICAL INFRARED SURVEYS FROM SPACE WITH THE MULTIBAND IMAGING PHOTOMETER FOR *SIRTF*

H. Dole
Steward Observatory, University of Arizona, 933 North Cherry Avenue, Tucson, AZ 85721; hdole@as.arizona.edu
and
G. Lagache and J.-L. Puget
Institut d'Astrophysique Spatiale, bât 121, Université Paris Sud, F-91405 Orsay CEDEX, France
Received 2002 August 15; accepted 2002 November 14

ABSTRACT

We make predictions for the cosmological surveys to be conducted by the Multiband Imaging Photometer for *SIRTF* (MIPS) at 24, 70, and 160 μm for the Guaranteed Time Observer and the Legacy programs, using the latest knowledge of the instrument. In addition to the detector noise and the cirrus confusion noise, we discuss in detail the derivation of the confusion noise due to extragalactic sources, which depends strongly on the shape of the source counts at a given wavelength and on the telescope and detector pixel sizes. We show that it is wise in general to compare the classical photometric criterion, used for decades, and the so-called source density criterion to predict the confusion levels. We obtain, using the model of Lagache, Dole, and Puget, limiting fluxes of 50 μJy, 3.2 mJy, and 36 mJy at 24, 70, and 160 μm, respectively. After taking into account other known sources of noise that will limit the surveys' sensitivities, we compute the redshift distributions of the detected sources at each wavelength and show that they extend up to $z \sim 2.7$ at 24 μm and up to $z \sim 2.5$ at 70 and 160 μm, leading to the resolution of at most 69%, 54%, and 24% of the cosmic infrared background (CIB) at 24, 70, and 160 μm, respectively. We estimate which galaxy populations will be used to derive the luminosity function evolution with redshift. We also give the redshift distributions of the unresolved sources in the far-IR range, which dominates the fluctuations of the CIB, and a predicted power spectrum showing the feasibility of fluctuations (due to both Poissonian and clustered source distributions) measurements. The main conclusion is that MIPS (and *SIRTF* in general) cosmological surveys will greatly improve our understanding of galaxy evolution by giving data with unprecedented accuracy in the mid-IR and far-IR range.

Subject headings: cosmology: observations — infrared: galaxies — galaxies: evolution — methods: observational

1. INTRODUCTION

The *Infrared Space Observatory* (*ISO*) performed deep surveys in the mid-IR (MIR) and far-IR (FIR) range (see Genzel & Cesarsky 2000; Franceschini et al. 2001 for reviews) in order to study galaxy evolution and to constrain the global star formation rate. Together with other surveys performed from the ground (e.g., with SCUBA and MAMBO), our view of galaxy evolution in the infrared, submillimeter, and millimeter range became more accurate.

With the information extracted from these cosmological surveys, and in particular from the source counts, the redshift distribution of the sources, the spectral energy distribution (SED) of the cosmic infrared background (CIB), and the analysis of the CIB fluctuations, it is possible to build a coherent view of galaxy evolution and formation in the infrared and submillimeter range by developing models that fit all the available data. Many semiempirical models exist (Roche & Eales 1999; Tan, Silk, & Balland 1999; Devriendt & Guiderdoni 2000; Dole et al. 2000; Wang & Biermann 2000; Chary & Elbaz 2001; Franceschini et al. 2001; Malkan & Stecker 2001; Pearson 2001; Rowan-Robinson 2001a, 2001b; Takeuchi et al. 2001; Xu et al. 2001; Wang 2002) and try to address questions about the evolution of infrared galaxies, inferring the global star formation rate. These models fit the data reasonably well. Recently, Lagache, Dole, & Puget (2003) have developed a phenomenological model that satisfies all the present observational constraints, one of which is the fluctuations of the background, as a powerful tool for investigating future observations.

The availability of new space facilities in the coming years, such as the *Space Infrared Telescope Facility* (*SIRTF*) in early 2003, *ASTRO-F*, and later in the decade, *Planck* and *Herschel*, and on the ground the Atacama Large Millimeter Array (ALMA), opens new perspectives to study in detail the population of infrared galaxies beyond $z = 1$. Which galaxy populations will these facilities be able to detect? What fraction of the CIB will be resolved into sources? Up to what redshift will it be possible to construct a luminosity function and detect any evolution? What will be the observational limitations on the cosmological surveys?

To answer most of these questions prior to any new data being taken and to better plan the surveys that will fully use the capabilities of these new facilities, it is common to use models to make predictions according to today's knowledge. The goal of this paper is to investigate the properties (e.g., confusion, sensitivity, redshift distributions) of the planned *SIRTF* surveys with the Multiband Imaging Photometer for *SIRTF* (MIPS), using the Lagache et al. (2003) model as well as the latest knowledge of the MIPS instrument. Detailed predictions for *Herschel*, *Planck*, and ALMA are given in Lagache et al. (2003).

The structure of the paper is as follows: The MIPS instrument and the planned surveys are described in § 2. We discuss the confusion noise due to Galactic cirrus in § 3. In § 4 we summarize the Lagache et al. (2003) model and in § 5 one of its applications: the generation of multiwavelength maps. The general case of the confusion noise due to extragalactic sources is discussed in § 6, and the confusion limits for MIPS are given in § 7. The total sensitivity for the surveys is given in § 8. We discuss the expected results regarding resolved sources in § 9 and regarding the unresolved sources in § 10.

2. THE MIPS INSTRUMENT AND THE PLANNED COSMOLOGICAL SURVEYS

2.1. *MIPS*

MIPS[1] (Rieke et al. 1984; Young et al. 1998; Heim et al. 1998) is one of the three *SIRTF* (Werner & Fanson 1995) focal plane instruments, the others being the Infrared Array Camera (IRAC; Fazio et al. 1998) and the Infrared Spectrograph (IRS; Houck & Van Cleve 1995). MIPS is composed of three large-array detectors, sensitive at 24, 70, and 160 μm, respectively. The array sizes are 128^2, 32^2, and 2×20 pixels, and the detector material is Si:As BIB, Ge:Ga, and stressed Ge:Ga, respectively. Among the main key features of MIPS are (1) the large size of the arrays, (2) the technical achievements in the detectors, (3) the calibration strategy of the FIR arrays (Engelbracht et al. 2000), with frequent stimulator flashes tracking the responsivity variations, and (4) the presence of a scan mirror allowing an efficient and redundant sky coverage of 5′-wide stripes, simultaneously at all three wavelengths.

The beam profile characteristics play an important role in computing the confusion limits; they have been generated using the S Tiny Tim software, which is an updated version for *SIRTF* of the Tiny Tim software for the *Hubble Space Telescope* (Krist 1993). Table 1 summarizes the main characteristics of the pixels and beam profiles for MIPS.

TABLE 1
Some MIPS Instrumental Characteristics: Pixel Size, Beam Profile, and Noise

Characteristic	24 μm	70 μm	160 μm
Pixel size (arcsec)	2.55	9.84	16.0
FWHM[a] (arcsec)	5.6	16.7	35.2
Pixel solid angle (sr)	1.41×10^{-10}	2.30×10^{-9}	5.87×10^{-9}
$\int f(\theta,\phi)d\theta\, d\phi$[b] (sr)	1.25×10^{-9}	9.98×10^{-9}	4.45×10^{-8}
$\int f^2(\theta,\phi)d\theta\, d\phi$[c] (sr)	4.27×10^{-10}	3.45×10^{-9}	1.66×10^{-8}
1 σ_p for 10 s integration[d] (mJy)	0.22	2.0	6.6

[a] Measured from S Tiny Tim models.
[b] Integral of the beam profile $f(\theta,\phi)$.
[c] Integral of the squared beam profile $f^2(\theta,\phi)$ (used in eq. [5]).
[d] The 1 σ photon (and instrumental) noise for a 10 s integration, for both scan map and photometry modes (G. H. Rieke 2002, private communication).

2.2. *Cosmological Surveys with MIPS*

The currently planned cosmological surveys with MIPS are mainly scheduled through two types of programs: the Guaranteed Time Observer (GTO) and the Legacy programs. Deep IRAC observations are also planned for all programs but are not discussed in this paper. The characteristics of all the following surveys are summarized in Table 2.

The MIPS GTO program for cosmological surveys[2] is composed of three surveys, named "Shallow," "Deep," and "Ultra Deep," respectively, whose characteristics are listed in Table 2. The MIPS GTO program also includes galaxy cluster observations, aimed at mapping lensed background galaxies. In addition, some IRAC and IRS GTO programs share the same targets or directly contribute to some of them.

Two of the six Legacy programs are focused on cosmological surveys: the *SIRTF* Wide-Area Infrared Extragalactic survey (SWIRE)[3] and the Great Observatories Origins Deep Survey (GOODS).[4] Schematically, for MIPS observations, the SWIRE surveys have the same observational strategy as the GTO Shallow survey but will cover a larger sky area (65 deg^2), and the GOODS surveys are similar to the GTO Ultra Deep survey but will observe a 0.04 deg^2 field at 24 μm with more depth.

[1] All useful materials regarding the *SIRTF* instruments, including the characteristics and the simulated beam profiles, are available at the SSC Web site: http://sirtf.caltech.edu/SSC.

[2] See http://lully.as.arizona.edu.
[3] See http://www.ipac.caltech.edu/SWIRE.
[4] See http://www.stsci.edu/science/goods.

TABLE 2
MIPS Cosmological Survey Key Features

Survey	MIPS Observation Mode[a]	Area[b] (deg^2)	24 μm t_{int}[c] (s)	70 μm t_{int}[c] (s)	160 μm t_{int}[c] (s)
Shallow[d]	Scan medium (2 passes)	9	80	80	8
Deep[d]	Scan slow (12 passes)	2.45 (6 × 0.41)	1200	1200	120
Ultra Deep[d]	Photometry	0.02	14700	12500	...
Cluster[d]	Photometry	0.2 (28 × 0.007)	3300	400	80
SWIRE[e]	Scan medium (2 passes)	65 (7 fields)	80	80	8
GOODS[e]	Photometry	0.04	36000	...	...
FLS[f]	Scan medium (2 passes)	5	80	80	8
FLS verification[f]	Scan medium (10 passes)	0.25	400	400	40

[a] MIPS observation mode. For the surveys, two modes are used: photometry and scan map. In the case of scan maps, the rate is given, medium (4 s frame^{-1}) or slow (10 s frame^{-1}), as well as the number of passes.
[b] Total surface of the survey. If more than one field, the details of the number of fields and the approximate size are also given.
[c] Integration time in seconds per sky pixel.
[d] GTO program.
[e] Legacy program.
[f] First Look Survey.

Finally, an early survey in the *SIRTF* mission will be conducted with MIPS and IRAC to verify the observational strategies: the First Look Survey (FLS)[5] of the extragalactic component. Given the similarities with other surveys, we do not discuss this survey specifically.

2.3. *Sensitivity*

The noise in the MIPS instrument is the sum of the detector-related noise (e.g., read noise, linearity correction noise, instantaneous flat-field noise), cosmic rays, and photon noise. The noise budget is dominated by photon noise (G. H. Rieke 2002, private communication). For simplicity, we call the total noise "photon noise" (σ_p), even if all the instrumental noise sources are taken into account. Table 1 gives the 1 σ_p noise in scan map mode for a 10 s integration (scan map mode or photometry mode). The upper part of Table 5 gives the 1 σ_p noise for the different integrations planned for the surveys. Note that noise caused by any systematic effect is not taken into account here. It has been shown for ISOCAM, however, that the latter noise source does not degrade the final sensitivity (Miville-Deschênes et al. 2000).

3. CIRRUS CONFUSION NOISE

Previous works (Helou & Beichman 1990; Gautier et al. 1992; Kiss et al. 2001) studied in detail the confusion noise due to Galactic cirrus ($\sigma_{\rm Gc}$) and showed that in most cases it can be simply parameterized as follows:

$$\sigma_{\rm Gc} = 0.3(\lambda_{100})^{2.5}(D_m)^{-2.5}\langle B_\lambda\rangle^{1.5}\ , \qquad (1)$$

where $\sigma_{\rm Gc}$ is in mJy, λ_{100} is the wavelength ratio $\lambda/(100\ \mu{\rm m})$, D_m is the telescope diameter in meters, and $\langle B_\lambda\rangle$ is the brightness in MJy sr^{-1} (Helou & Beichman 1990). Kiss et al. (2001) report that this parameterization underestimates $\sigma_{\rm Gc}$ by a factor of 2. However, their estimate of $\sigma_{\rm Gc}$ includes a contribution from CIB fluctuations that is known to be significant (Lagache & Puget 2000), and so we can use the parameterization when we are only concerned with the Galactic cirrus component

Using Figure 1 of Boulanger (2000) for the spectrum of the diffuse ISM, we extrapolate the mean brightness at 100 μm $\langle B_{100}\rangle$ of 0.5 MJy sr^{-1} (corresponding to an H I column density of 10^{20} cm^{-2}, typical for cosmological surveys) at 24, 70, and 160 μm. We then derive the corresponding cirrus confusion noise $\sigma_{\rm Gc}$ from equation (1). The results are given in Table 3. For most of the cosmological fields, where the cirrus brightness $\langle B_{100}\rangle$ is less than 1 MJy sr^{-1}, the cirrus confusion noise is often negligible or is a minor contribution to the total noise. In this work, we thus only consider the confusion due to extragalactic sources, letting the reader add the cirrus confusion noise appropriate to his or her own purposes.

[5] See http://sirtf.caltech.edu/SSC/fls/extragal.

TABLE 3
CIRRUS CONFUSION NOISE

Parameter	24 μm	70 μm	160 μm
$\langle B_\lambda\rangle$[a] (MJy sr^{-1}).....	0.03	0.12	1.5
$\sigma_{\rm Gc}$[b]	0.06 μJy	7.6 μJy	2.7 mJy

[a] Cirrus brightness for MIPS bands. This cirrus has a brightness $\langle B_{100}\rangle = 0.56$ MJy sr^{-1} at 100 μm, corresponding to $N_{\rm H\,I} = 10^{20}$ cm^{-2}. We use the dust spectrum from Boulanger (2000).

[b] The 1 $\sigma_{\rm Gc}$ cirrus confusion noise derived from eq. (1) (Helou & Beichman 1990).

4. MODEL OF INFRARED GALAXY EVOLUTION

In addition to the photon noise and cirrus confusion noise, the noise due to extragalactic sources is certainly the dominant noise for cosmological surveys. The Lagache et al. (2003) model is used to describe this component.

This model fits, besides the CIB intensity, source counts, the redshift distribution and colors, and the additional observational constraint of the CIB fluctuations. It describes only the dust emission part of the galaxies in the 4 μm to 1.5 mm wavelength range. It is a phenomenological model based on two galaxy populations: the IR emission of normal spiral galaxies where optical output dominates and a starburst population. Each population is characterized by a SED family and an evolving luminosity function, described by a small number of parameters. The predictions of this model thus cover well the observed wavelength range from 8 μm to 3 mm. It does not include source clustering. The confusion is computed for the Poisson contribution, and the clustering might slightly change the confusion limits; this will be investigated in forthcoming papers (J. Blaizot et al. 2003, in preparation; M. Sorel et al. 2003, in preparation). The model outputs as well as some programs are publicly available on our Web sites.[6]

5. SIMULATING THE MULTIWAVELENGTH INFRARED SKY

One of the applications of the model of Lagache et al. (2003) for planning future observations is the creation of simulated maps of the infrared and submillimeter sky. The main purposes of the simulations are (1) to test the calibration and map-making algorithms, (2) to test and validate the source extraction and photometry procedures and check the completeness, and (3) to test other algorithms, such as HIRES or band-merging procedures, to improve source detections in the FIR range. Results of these simulations will be the subject of a forthcoming paper.

The maps,[7] available for public use upon request, are sampled with 2″ pixels and have sizes ranging from 1024^2 to 4096^2 (0.32–5 deg^2). The simulated maps contain three components: an extragalactic component (IR galaxies), a Galactic foreground component (cirrus), and a zodiacal light component. The following is a brief description of each component.

The Lagache et al. (2003) model evolving luminosity functions are used to create the extragalactic component in simulated maps over a wide range of wavelengths relevant to current and future studies (mainly for *ISO*, *SIRTF*, *ASTRO-F*, *Planck*, *Herschel*, SCUBA, MAMBO, and ALMA). For computational efficiency, we add in the maps sources only in the redshift range 0–5.

[6] See http://www.ias.fr/PPERSO/glagache/act/gal_model.html and http://lully.as.arizona.edu/Model.

[7] Images of the maps are available on our Web site, http://lully.as.arizona.edu/GTODeep/Simulations.

The Galactic foreground component, the cirrus, is built as follows: the spatial structure is taken from an actual 100 μm cirrus in the *IRAS* recalibrated maps of Schlegel, Finkbeiner, & Davis (1998), and the scale extrapolation to smaller scales uses the properties of the cirrus power spectrum from Gautier et al. (1992). We then use the cirrus spectrum of Boulanger (2000) to compute this component at other wavelengths.

The zodiacal light component is a constant value in our maps, taken from Table 4 of Kelsall et al. (1998) for high ecliptic and Galactic latitude fields.

6. DERIVING THE CONFUSION NOISE DUE TO EXTRAGALACTIC SOURCES

Numerous authors (Condon 1974; Hacking, Houck, & Condon 1987; Hacking & Soifer 1991; Franceschini et al. 1989, 1991; Vaisanen, Tollestrup, & Fazio 2001) have described the effect of the fluctuations due to the presence of point sources in a beam. For technological reasons limiting the telescope diameter compared to the wavelength, these fluctuations play an important (if not dominant) role in the measurements noise budget in the MIR, FIR, submillimeter, and centimeter range for extragalactic surveys.

Throughout the rest of the paper, we use the term "confusion limit" for the confusion limit due to extragalactic sources. There are two different criteria to derive the confusion noise. The widely-used "photometric criterion" (§ 6.3) is derived from the fluctuations of the signal due to the sources below the detection threshold $S_{\rm lim}$ in the beam; it was well adapted for the first generation of space IR telescopes (*IRAS*, *COBE*, *ISO*). The "source density criterion" (§ 6.4) is derived from a completeness criterion and evaluates the density of the sources detected above the detection threshold $S_{\rm lim}$, such that only a small fraction of sources are missed because they cannot be separated from their nearest neighbor.

We show that with *SIRTF* (or other planned telescopes), we need in general (regardless of the model used) to compare the confusion noise given by the two criteria, in order not to artificially underestimate the derived confusion noise. We give our estimates for the confusion in the frame of the Lagache et al. (2003) model.

6.1. *Confusion Noise: General Case*

At a given frequency ν (hereafter the subscript ν will be omitted), let $f(\theta,\phi)$ be the two-dimensional beam profile (peak normalized to unity), let S be the source flux density (hereafter flux) in Jy, and let dN/dS be the differential source counts in Jy^{-1} sr^{-1}.

The amplitude of the response x due to a source of flux S at location θ,ϕ within the beam is

$$x = Sf(\theta,\phi)\ . \qquad (2)$$

The mean number of responses $R(x)$ with amplitudes between x and $x+dx$ from sources present in the beam element $d\Omega$ at position (θ,ϕ) (where $d\Omega = 2\pi\theta\,d\theta\,d\phi$) is given by

$$R(x)dx = \int_\Omega \frac{dN}{dS}dS\,d\Omega\ . \qquad (3)$$

The total variance σ_c^2 of a measurement within the beam due to extragalactic sources of fluxes less than $S_{\rm lim}$ is given by

$$\sigma_c^2 = \int_0^{x_{\rm lim}} x^2 R(x)dx\ , \qquad (4)$$

where $x_{\rm lim} = S_{\rm lim}f(\theta,\phi)$ is the cutoff response at high flux. This can be rewritten as

$$\sigma_c^2 = \int f^2(\theta,\phi)d\theta\,d\phi\int_0^{S_{\rm lim}} S^2\frac{dN}{dS}dS\ . \qquad (5)$$

We call σ_c the "confusion noise" and $S_{\rm lim}$ the "confusion limit." There are different ways of deriving $S_{\rm lim}$, and they will be investigated in §§ 6.3 and 6.4. Note that using equation (5) to determine the confusion limit is an approximation. A first refinement would be to use the limiting deflection $x_{\rm lim}$ rather than $S_{\rm lim}$, as explained by, e.g., Condon (1974), and then to introduce the effective beam. For MIPS, this changes the confusion level by less than 10%. Nevertheless, this refinement is not enough since it does not take into account other important parameters related to the observational strategy and the analysis scheme, such as the sky sampling, the pixelization (or point-spread function [PSF] sampling), and the source extraction process, that also impact the confusion limit. Only complete realistic simulations would allow for accurately predicting the confusion level; this next step will be addressed in a forthcoming paper using our simulations (§ 5). The method presented here aims at providing a theoretical prediction, which can be considered as a lower limit.

6.2. *Beam Profiles*

Before we obtain measurements of the telescope PSF in flight, we need to use models of the beam profiles for the predictions of the confusion noise. A popular approximation is to use a Gaussian profile with the same FWHM as the expected PSF, although for *SIRTF* an Airy function should be more appropriate. The Gaussian profile is useful for analytical derivations of the confusion level as a function of the beam size (Vaisanen et al. 2001). We want here to address the question of accuracy using the Gaussian approximation, the Airy approximation, or the modeled profile.

We compare the integral of the Gaussian profile (as written in eq. [5]) with the simulated profile obtained by S Tiny Tim (§ 2.1): this leads to a small error in the first integral in equation (5) on the order of 2%–10%, depending on the MIPS wavelength; the difference is larger on the integral of the profile, about 30%. The Gaussian profile is thus a good approximation for computing analytically the confusion noise but not for source extraction simulations.

Using an Airy profile gives better results for the profile integral, with a difference of less than 20%; the difference on the profile integrated according to equation (5) is worse, on the order of 10%–35%. The Airy profile is thus better suited for source extraction simulations than for confusion noise estimates.

The use of the simulated S Tiny Tim profiles (see Table 1) is at present our best approximation of the flight profiles. Indeed, Lagache & Dole (2001) have shown in the case of ISOPHOT that the theoretical profile is in good agreement with the actual profile.

6.3. *The Photometric Criterion for Confusion Noise*

The "photometric criterion" is defined by choosing the signal-to-noise ratio q between the faintest source of flux

TABLE 4
CONFUSION LIMITS WITH DIFFERENT CRITERIA AND FINAL CONFUSION LIMITS

Parameter	24 μm	70 μm	160 μm
$S_{\rm lim}$ and q Using the Photometric Criterion[a]			
$S_{\rm lim}$, $q = 3$	...	0.20 mJy	20 mJy
$S_{\rm lim}$, $q = 4$	7.1 μJy	0.56 mJy	40 mJy
$S_{\rm lim}$, $q = 5$	15.8 μJy	1.12 mJy	56 mJy
$S_{\rm lim}$ and q Using the Source Density Criterion[b]			
$S_{\rm lim}$.....	50 μJy	3.2 mJy	36 mJy
$q_{\rm SDC}$	7.3	6.8	3.8
$S_{\rm lim}$ and q Using the Best Estimator[c]			
$S_{\rm lim}$.....	50 μJy	3.2 mJy	36.0 mJy
q.....	7.3[d]	6.8[d]	3.8[d,e]

[a] $S_{\rm lim}$ using the photometric criterion, for different values of q.
[b] $S_{\rm lim}$ using the source density criterion, and the equivalent values of $q_{\rm SDC}$.
[c] $S_{\rm lim}$ and q of the best confusion estimator. These values are our confusion limits.
[d] Using the source density criterion.
[e] In this case, the photometric and source density criteria agree.

$S_{\rm lim}$ and the rms noise σ_c due to fluctuations from beam to beam (due to sources fainter than $S_{\rm lim}$), as described by

$$q = \frac{S_{\rm lim}}{\sigma_{c\,\rm phot}(S_{\rm lim})} \; ; \tag{6}$$

$S_{\rm lim}$, and thus σ_c, is found by solving equation (6) through an iterative procedure, and q is usually chosen with values between 3 and 5, depending on the objectives followed. Notice that $\sigma_{c\,\rm phot}$ increases with q, as given in the upper part of Table 4. As a guideline, if one assumes a power law for the shape of the differential source counts ($dN/dS \propto S^{\alpha}$, with $|\alpha| < 3$), then $\sigma_{c\,\rm phot}$ varies with q as $\sigma_{c\,\rm phot} \propto q^{-(3+\alpha)/(1+\alpha)}$. This can be used in the Euclidean regime ($|\alpha| = 2.5$). Note that α has the same meaning as $-\gamma$ in Condon (1974).

To illustrate the behavior of the implicit equation (6), Figure 1 gives $S_{\rm lim}/\sigma_{c\,\rm phot}$ as a function of $S_{\rm lim}$ given by equation (5), as well as the constant ratio $q = S_{\rm lim}/\sigma_{c\,\rm phot}$ for $q = 3$ and 5. This plot illustrates that using $q = 3$ at 24 μm does not give a well-defined solution, since the $S_{\rm lim} = 3\ \sigma_{c\,\rm phot}$ line is almost tangent to the curve $\sigma_{c\,\rm phot}(S_{\rm lim})$; in this case, the signal–to–photometric confusion noise ratio is always greater than 3.

6.4. *The Source Density Criterion for Confusion Noise*

A second criterion for the confusion can be defined by setting the minimum completeness of the detection of sources above $S_{\rm lim}$, which is driven by the fraction of sources lost in the detection process because the nearest neighbor with flux above $S_{\rm lim}$ is too close to be separated.[8] For a given source density N (Poisson distribution) corresponding to sources with fluxes above $S_{\rm lim}$, the probability P of having the nearest source of flux $\geq S_{\rm lim}$ located closer than the distance $\theta_{\rm min}$ is

$$P(< \theta_{\rm min}) = 1 - e^{-\pi N \theta_{\rm min}^2} \; . \tag{7}$$

Using $\theta_{\rm FW}$, the FWHM of the beam profile, and k, we parameterize $\theta_{\rm min}$ as

$$\theta_{\rm min} = k\theta_{\rm FW} \; . \tag{8}$$

Fixing a value of the probability P gives a corresponding density of sources $N_{\rm SDC}$ (SDC stands for source density criterion):

$$N_{\rm SDC} = -\frac{\log\,(1 - P(< \theta_{\rm min}))}{\pi k^2 \theta_{\rm FW}^2} \; . \tag{9}$$

At a given wavelength, there is a one-to-one relationship between the source density and the flux, given by the source counts; thus, $S_{\rm SDC}$ is determined with $N_{\rm SDC}$ with our source count model. We identify $S_{\rm SDC}$ as $S_{\rm lim}$ and can then compute the confusion noise using the source density criterion $\sigma_{\rm SDC}$, using equation (5), as a function of P and k.

We define the source density criterion for deriving the confusion noise by choosing values of $P(< \theta_{\rm min})$ and k; the latter can be determined, e.g., by simulations. The term $S_{\rm lim}$ is the limiting flux, such that there is a chosen probability $P(< \theta_{\rm min})$ of having two sources of flux above $S_{\rm lim}$ at a distance of less than $\theta_{\rm min} = k\theta_{\rm FW}$.

We made simulations of source extraction with DAOPHOT and checked that $k = 0.8$ is an achievable value; this is also in agreement with the results from Rieke, Young, & Gautier (1995). We thus use $k = 0.8$. We use $P = 10\%$, meaning that 10% of the sources are too close to another source to be extracted. The corresponding source density is, as explained in Table 1 of Lagache et al. (2003),[9] $(1/16.7)\Omega$.

[8] The completeness is also affected by the noise that modifies the shape of the source counts, the so-called Malmquist-Eddington bias. For the sake of simplicity, this bias was not taken into account.

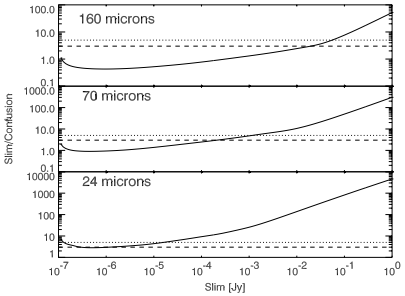

FIG. 1.—Signal–to–confusion noise ratio as a function of $S_{\rm lim}$ at 24, 70, and 160 μm (*solid line*). Also plotted are $S_{\rm lim}/\sigma_c = 3$ (*dashed line*) and $S_{\rm lim}/\sigma_c = 5$ (*dotted line*). At 24 μm, $S_{\rm lim}/\sigma_c$ is always greater than 3; using the photometric criterion for deriving the confusion noise thus leads to a severe underestimation.

[9] Using the relation, valid for both Airy and Gaussian profiles, linking $\theta_{\rm FW}$, the FWHM of the beam profile, and Ω, the integral of the beam profile, $\Omega \simeq 1.14\theta_{\rm FW}^2$ (Lagache et al. 2003).

The middle part of Table 4 gives $S_{\rm lim\,SDC}$, using the source density criterion, and the corresponding equivalent $q_{\rm SDC}$, which is the ratio $S_{\rm lim}/\sigma_{\rm SDC}$.

One the one hand, the photometric and source density criteria give almost identical results in the simple Euclidean case, if one takes $q = 3$, $k = 1$, and a maximum probability of missing a source too close to another one of 10%. In this classical case, confusion becomes important for a source density corresponding to one source per 30 independent instrumental beams. On the other hand, when the relevant $\log N$–$\log S$ function departs strongly from Euclidean, the two criteria give very different results for these reasonable values of q, k, and P. Furthermore, for specific astrophysical problems, one might want to choose significantly different values of these parameters. In that case, the two criteria might not be equivalent. For instance, at 70 μm, increasing P to 20%, 45%, and 60% (instead of the 10% that we are using) gives a confusion limit identical to $q = 5$, 4, and 3, respectively, even if in the last case 60% of the sources are missed.

7. CONFUSION LIMITS FOR MIPS AND COMPARISON WITH OTHER WORKS

7.1. *Confusion Limits for MIPS*

Comparing the photometric (§ 6.3) and the source density (§ 6.4) criteria for the confusion, we conclude that for MIPS, the source density criterion is always met before (i.e., at higher flux) the photometric criterion using $q \simeq 4$. At 160 μm, the two criteria become identical. Lagache et al. (2003) show that for all the IR/submillimeter space telescopes of the coming decade, the break point between the two criteria is around 200 μm.

SIRTF, with its high sensitivity and its well-sampled PSFs, will probe a regime in the source counts where the classical photometric criterion is no longer valid. The main reasons are (1) the steep shape of the source counts and (2) the fact that a significant part of the CIB will be resolved into sources (§ 9.4). This leads to a high source density at faint detectable flux levels, which actually limits the ability to detect fainter sources. In this case, the limiting factor is not the fluctuations of the sources below the detection limit (photometric criterion) but the high source density above the detection limit (source density criterion). For *SIRTF*, we thus use the source density criterion for deriving the confusion noise and limit.

For the previous generations of infrared telescopes (*IRAS*, *ISO*), it is interesting to compare the two criteria, and usually they converge to the same answer—a direct consequence of undersampling a large PSF, which does not allow for probing deeper the source counts. In this case, the photometric criterion is applicable and has been widely used. The confusion noise and the confusion limit for MIPS are given in the lower part of Table 4.

Figure 2 represents the integral source counts at 24, 70, and 160 μm. At these wavelengths, the confusion limits given in Table 4 correspond to source densities of 6.9×10^7, 7.8×10^6, and 1.9×10^6 sr^{-1} at 24, 70, and 160 μm, respectively. This corresponds to 11.5, 12.8, and 12.0 beams source^{-1} at 24, 70, and 160 μm, respectively. The derived values are slightly lower than the "generic" case discussed in § 6.4 of 16.7 sources beam^{-1}, the difference coming from the use of a simulated beam profile rather than a Gaussian profile.

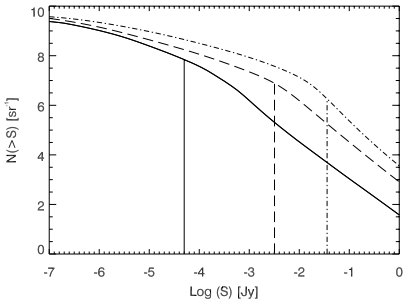

FIG. 2.—Integral source counts from our model at 24 μm (*solid line*), 70 μm (*dashed line*), and 160 μm (*dot-dashed line*) and confusion limits $S_{\rm lim}$ from Table 4.

7.2. *ISO at 170* μm

The data of the 4 deg^2 FIRBACK survey (Dole et al. 2001) performed with *ISO* at 170 μm allowed for directly measuring the sky confusion level. This provides a rare opportunity to test the model.

The confusion level was measured at 170 μm at $1\ \sigma_c = 45$ mJy, and the $4\ \sigma_c$ limit (180 mJy) corresponds to 52 beams source^{-1} (Dole et al. 2001).

Using our model with the actual PSF (Lagache & Dole 2001) and the photometric criterion (valid in this case), we obtain $1\ \sigma_c = 40$ mJy, and for $q = 4$, $S_{\rm lim} = 158$ mJy; this flux limit corresponds to 40 beams source^{-1}.

The good agreement comforts the quality of the model for estimating the confusion level from modeled source counts.

7.3. *Comparison with Other Determinations*

Xu et al. (2001) computed the confusion limit $S_{\rm lim}$ with the photometric criterion using $q = 3$ for MIPS and got 33 μJy, 3.9 mJy, and 57 mJy at 24, 70, and 160 μm, respectively. This corresponds respectively to 8, 17, and 31 beams source^{-1}. Our estimates are thus compatible at 70 μm but slightly different at 24 and 160 μm. Their use of the photometric criterion at 24 μm significantly underestimates the confusion level. At 160, their redshift distribution seems to overestimate (at the FIRBACK flux limits) the population peaking at $z \sim 1$ (Patris et al. 2003), which may suggest a difference in the dN/dS distribution, which directly affects the predicted confusion levels.

Franceschini et al. (2003), based on the model of Franceschini et al. (2001), give preliminary $5\ \sigma_c$ confusion limits for MIPS at 24, 70, and 160 μm as 85 μJy, 3.7 mJy, and 36 mJy, respectively. This corresponds respectively to 19, 15, and 12 beams source^{-1}. The values for the far infrared are in good agreement with our predictions. However, a more refined comparison needs to be done when details of their computation are published, especially in the MIR.

Other models exist (Roche & Eales 1999; Tan et al. 1999; Devriendt & Guiderdoni 2000; Wang & Biermann 2000; Chary & Elbaz 2001; Pearson 2001; Rowan-Robinson 2001b; Takeuchi et al. 2001; Wang 2002) but do not specifi-

cally address the point of predicting the confusion limits for *SIRTF*. Malkan & Stecker (2001) and Rowan-Robinson (2001a) make predictions. The former use, as a photometric criterion, 1 source beam^{-1}. The latter uses 1 source per 40 beams, leading to $S_{\rm lim}$ values of 135 μJy, 4.7 mJy, and 59 mJy at 24, 70, and 160 μm, respectively.

7.4. *The 8 μm Case*

Our model reaches its limit around 8 μm because our SEDs are not designed for wavelengths shorter than 4 μm. However, it fits all observables at wavelengths longer than 7 μm. We can thus predict the confusion level. As for 24 μm, the confusion level will be low and will not limit the extragalactic surveys.

At 8 μm, the photometric criterion does not provide a meaningful confusion limit because the $S_{\rm lim}/\sigma_c$ ratio is always greater than 10. We obtain, using the source density criterion, $S_{\rm lim} = 0.45$ μJy and $\sigma_c = 0.05$ μJy, leading to $q = 9.72$.

The values from Vaisanen et al. (2001) are $S_{\rm lim} = 3$–4 μJy, $\sigma_c = 0.40$–0.51 μJy, and $q = 10.0$. Our estimation of the confusion level for this IRAC band is lower by a factor of $\sim$7. This discrepancy comes in fact from the source counts themselves: we underpredict the source density by a factor of 7–8 in the range of 0.1–1 μJy, even if both models reproduce the *ISO* counts. This is expected from a model that accounts properly for the dust emission but does not model the stellar emission of high-redshift galaxies. When using the counts from Vaisanen et al. (2001), we agree with their published values. Vaisanen et al. (2001), in their § 5.3, discuss the sensitivity of the predicted confusion levels to the shape of the source counts and the constraints of the modeled source counts by the data. Their conclusion is that, although the 7 μm ISOCAM source counts above 50 μJy agree within uncertainties, the models below 1 μJy are not much constrained. As a result, the predictions for the confusion level down to the IRAC sensitivity can be as different as a factor of 10. We confirm this analysis.

8. SENSITIVITY IN THE MIPS FINAL MAPS

In this section we compute the sensitivity of the MIPS surveys as a function of the integration time. The total noise $\sigma_{\rm tot}$ is (Lagache et al. 2003)

$$\sigma_{\rm tot} = \sqrt{\sigma_p^2 + \sigma_c^2 + \sigma_{\rm add}^2}\,, \qquad (10)$$

where σ_p is the photon noise (§ 2.3), σ_c is the confusion noise (§ 7 and Table 4), and $\sigma_{\rm add}$ is the additional confusion noise. This additional confusion noise is only present when the photon noise exceeds the confusion noise: in this case, $\sigma_{\rm add}$ accounts for the confusion due to bright sources above the confusion limit but below the photon noise. When $5\,\sigma_p > S_{\rm lim}$, $\sigma_{\rm add}$ is computed as

$$\sigma_{\rm add}^2 = \int f^2(\theta,\phi)\,d\theta\,d\phi \int_{S_{\rm lim}}^{5\,\sigma_p} S^2\,\frac{dN}{dS}\,dS\,. \qquad (11)$$

Figure 3 shows $\sigma_{\rm tot}$ and the relative contributions of σ_p, σ_c, and $\sigma_{\rm add}$ as a function of the integration time. It appears that the 160 μm data are confusion limited even with short integrations. At 70 μm, the confusion should dominate the noise for exposures longer than 100 s, and $\sigma_{\rm add}$ is a small component in the first 50 s and negligible thereafter. At

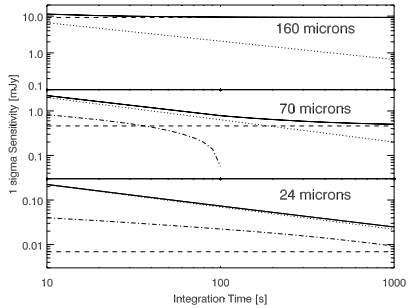

FIG. 3.—The 1 σ sensitivity of the scan maps as a function of integration time at 24, 70, and 160 μm. *Solid line*: Total 1 σ sensitivity. *Dashed line*: Confusion level σ_c. *Dotted line*: Photon noise. *Dot-dashed line*: Additional confusion noise.

24 μm we do not expect the data to be confusion limited, and $\sigma_{\rm add}$ is between 5 and 3 times smaller than the photon noise.

The middle part of Table 5 gives the 1 $\sigma_{\rm tot}$ sensitivity for the surveys and includes the confusion and the instrumental and additional confusion noise components. Note that these 1 $\sigma_{\rm tot}$ values are given as a guideline, knowing that taking 5 $\sigma_{\rm tot}$ for the survey sensitivities is an approximation, since $S_{\rm lim}$ does not equal 5 σ_c in the general case, as discussed in § 7.1.

The bottom part of Table 5 gives the fluxes that will limit the surveys. They are computed by using the approximation given by the quadratic sum $(5\,\sigma_p^2 + S_{\rm lim}^2)^{1/2}$, which provides a smooth transition between the regime dominated by photon/detector noise (24 μm) and the regime dominated by confusion noise (160 μm). These values are taken to be the baseline for further discussions. The final sensitivity for the 65 deg^2 SWIRE Legacy survey will be the same as that for the GTO Shallow survey. The GTO Deep survey will be almost 4 times more sensitive (photon noise) than the Shallow survey, on about 2.5 deg^2; in the FIR, the confusion will nevertheless limit the final sensitivity. For the GOODS Legacy program, with 10 hr of integration per sky pixel at 24 μm on 0.04 deg^2, we expect a final sensitivity of 54 μJy at 24 μm.

It is beyond the scope of this paper to investigate the properties of the galaxy cluster targets of the *SIRTF* GTO program and to make predictions, but in these fields, the confusion limits will significantly be reduced due to the gravitational lensing by a foreground rich cluster, which increases both the brightness and mean separation of the background galaxies. This effect has already been exploited successfully in the MIR (e.g., *ISO*; Altieri et al. 1999) and in the submillimeter (e.g., SCUBA Lens Survey; Smail et al. 2002). The *SIRTF* GTO program will apply the same strategy in the MIR and FIR. The lensed area of the proposed GTO program is expected to cover 90 arcmin^2 (E. Egami 2002, private communication).

Other effects, not included in this analysis, might slightly degrade the final sensitivity of the maps, especially on

TABLE 5

SENSITIVITIES OF THE PLANNED COSMOLOGICAL SURVEYS: 1 σ_p (PHOTON NOISE ONLY), 1 $\sigma_{\rm TOT}$, AND FINAL SENSITIVITY

Survey	24 μm	70 μm	160 μm
1 σ_p Sensitivities (Does Not Include Sky Confusion)[a]			
Shallow	78	0.71	6.6
Deep	20	0.18	1.9
Ultra Deep	6	0.06	...
Cluster	12	0.32	2.3
SWIRE	78	0.71	6.6
GOODS	4	...	...
1 $\sigma_{\rm tot}$ Sensitivities of the Surveys[b]			
Shallow	82	0.87	11.3
Deep	23	0.49	9.4
Ultra Deep	9	0.46	...
Cluster	15	0.55	9.5
SWIRE	82	0.87	11.3
GOODS	8	...	...
Final Sensitivities of the Surveys[c]			
Shallow	392	4.7	48
Deep	112	3.2	36
Ultra Deep	59	3.1	...
Cluster[d]	79	3.5	37
SWIRE	392	4.7	48
GOODS	54	...	...

NOTE.—The values given at 24 μm are in μJy; the values given at 70 and 160 μm are in mJy.

[a] The 1 σ_p sensitivities (they include only photon noise).

[b] The 1 $\sigma_{\rm tot}$ sensitivities, given as a *guideline*; they includes the confusion, the photon (instrumental), and the additional confusion noise components. Notice that it is *incorrect* to take 5 $\sigma_{\rm tot}$ as a confusion level for the surveys (see text).

[c] The final sensitivities (see text) of the planned cosmological surveys. They include in a proper manner the confusion noise and photon noise.

[d] The given sensitivities do not take into account here the properties of background lensed galaxies.

Ge:Ga detectors at 70 and 160 μm; these effects, well characterized on the ground, can probably be corrected with an accuracy of a few percent using data redundancy and a carefully designed pipeline (K. Gordon et al. 2003, in preparation). The effects are stimulator flash latents (the amplitude is less than 3%, and the exponential decay time constant is in the range 5–20 s), transients, responsivity changes (tracked with the stimulator flashes every 2 minutes), and cosmic-ray hit related noise. The final sensitivity will be measured in the first weeks of operation, during the in-orbit checkout and science verification phases.

9. RESOLVED SOURCES: REDSHIFT DISTRIBUTIONS, LUMINOSITY FUNCTION, AND RESOLUTION OF THE COSMIC INFRARED BACKGROUND

9.1. *Source Density and Redshift Distributions*

Many resolved sources are anticipated in the MIPS surveys: for instance, we expect at 160 μm a number of sources more than an order of magnitude higher than those detected by *ISO*, due to both a fainter detection limit and a larger sky coverage. Table 6 gives the number of sources for the GTO and Legacy surveys.

TABLE 6

THE NUMBER OF EXPECTED SOURCES IN THE MIPS SURVEYS AND THE FRACTION OF THE CIB THAT WILL BE RESOLVED INTO SOURCES (ASSUMING THAT ALL SOURCES ARE UNRESOLVED)

Survey	24 μm	70 μm	160 μm
Number of Expected Sources			
Shallow	2.0×10^4	1.3×10^4	2.8×10^3
Deep	2.5×10^4	5.8×10^3	1.4×10^3
Ultra Deep	3.7×10^2	49	...
SWIRE	1.5×10^5	1.0×10^5	2.2×10^4
GOODS	8.4×10^2	...	...
Fraction of Resolved CIB (%)			
Shallow	35	46	18
Deep	58	54	23
Ultra Deep	68	54	...
SWIRE	35	46	18
GOODS	69	...	...

NOTE.—The characteristics of the surveys are given in Table 2.

The redshift distributions of the surveys are plotted in Figure 4 for 24 μm, Figure 5 for 70 μm, and Figure 6 for 160 μm. At 24 μm, the deepest fields will allow us to probe the dust emission of sources up to redshift of 2.7. At higher redshifts, the 7.7 μm polycyclic aromatic hydrocarbon (PAH) feature causes a fall in the *K*-correction and thus a decrease in the observed flux close to the sensitivity limit. This is similar to the drop observed with ISOCAM at 15 μm for sources lying at redshift 1.4. (This does not exclude detecting the stellar emission at larger redshifts; this is outside the scope of this paper.)

At 70 μm, the redshift distribution peaks at 0.7, with a tail extending up to redshift 2.5. At 160 μm, the redshift distribution is similar to that at 70 μm. In the FIR, MIPS surveys

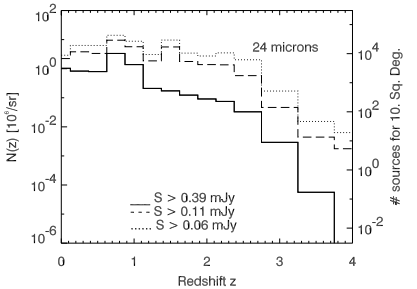

FIG. 4.—Redshift distribution at 24 μm with MIPS. *Solid line*: Shallow survey. *Dashed line*: Deep survey. *Dotted line*: Ultra Deep survey. The flux limits are listed in Table 5. The left axis gives the source density (the number of sources for the particular bin sizes shown); the right axis gives the number of sources in a 10 deg^2 field.

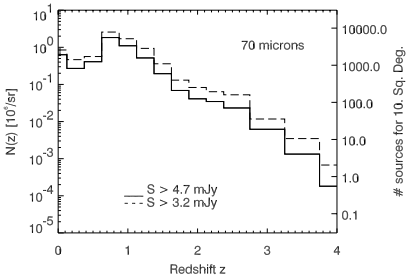

FIG. 5.—Redshift distribution at 70 μm with MIPS. *Solid line*: Shallow survey. *Dashed line*: Deep survey. The flux limits are listed in Table 5. The left axis gives the source density (the number of sources for the particular bin sizes shown); the right axis gives the number of sources in a 10 deg^2 field.

will probe extensively the largely unexplored $1 < z < 2.5$ regime.

9.2. *Spectra with IRS*

Spectra of some high-redshift sources will be taken with IRS on board *SIRTF* (as part of the IRS GTO program). With a sensitivity limit of 1.5 mJy at 24 μm and maybe 0.75 mJy (D. Weedman 2002, private communication), a few dozen sources at redshift greater than 2 will be observed. Figure 7 shows the predicted redshift distribution at 24 μm for the Shallow survey of the sources that might be followed up in spectroscopy by IRS.

9.3. *Luminosity Function Evolution*

In addition to the photometric redshifts of a large number of sources and spectroscopic redshift following identifications, building the luminosity function of the sources as a function of redshift will be one of the key results of the *SIRTF* surveys. We show in Figure 8 the source density per

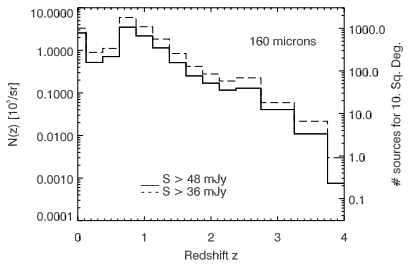

FIG. 6.—Redshift distribution at 160 μm with MIPS. *Solid line*: Shallow survey. *Dashed line*: Deep survey. The flux limits are listed in Table 5. The left axis gives the source density (the number of sources for the particular bin sizes shown); the right axis gives the number of sources in a 10 deg^2 field.

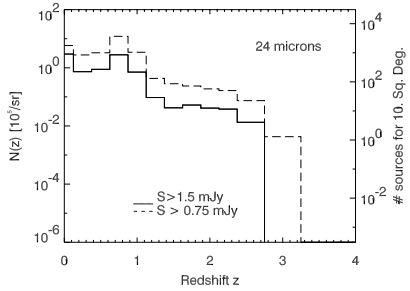

FIG. 7.—Redshift distribution at 24 μm with MIPS for sources brighter than 1.5 and 0.75 mJy, allowing a spectroscopic follow-up with IRS. The left axis gives the source density (the number of sources for the particular bin sizes shown); the right axis gives the number of sources in a 10 deg^2 field. In the proposed 9 deg^2 Shallow survey, we would expect 2100 and 7200 sources to the 1.5 and 0.75 mJy depths, respectively.

logarithmic luminosity bin and per redshift bin expected in the MIPS surveys.

The source density of starburst galaxies is given per logarithmic luminosity bin (of $\Delta \ln L/\ln L = 0.1$) and for redshift bins (of width $\Delta z/z = 0.5$) ranging from $z = 0.01$ to $z = 2.5$. The survey sensitivity cuts the distributions at low luminosities. The size of the surveys limits the ability to derive the luminosity function at high luminosities. The limit of 50 sources per z and L bins is also shown. This limit ensures a statistical accuracy of 14% on the luminosity function for each luminosity and redshift bin; averaging over five bins in luminosity (thus getting $\Delta \ln L/\ln L = 0.5$) allows us to reach an accuracy of 6%.

At 160 μm (Fig. 8, *top*), with a 48 mJy limiting flux and a coverage of 80 deg^2, corresponding to the surface covered by all of the Legacy and GTO extragalactic programs, the MIPS data should allow us to reconstruct the luminosity functions of some ULIRGs ($10^{12}\ L_\odot < L < 3 \times 10^{12}\ L_\odot$) in the $0.5 < z < 0.7$ range, of the $3 \times 10^{12}\ L_\odot < L < 10^{13}\ L_\odot$ galaxies in the $0.5 < z \lesssim 1$ range, and of the HyLIGs (Morel et al. 2001; $L > 3 \times 10^{13}\ L_\odot$) in the $1 \lesssim z \lesssim 2.5$ range.

At 70 μm (Fig. 8, *middle*), with a 4.7 mJy limiting flux and a coverage of 80 deg^2, the sensitivity in the wide and shallow surveys allows us to probe in addition the $3 \times 10^{11}\ L_\odot < L < 10^{12}\ L_\odot$ sources at $z = 0.5$ and the full range $10^{12}\ L_\odot < L < 10^{13}\ L_\odot$ for sources at $0.7 < z < 1$.

At 24 μm, the situation is very similar to that at 70 μm for these shallow surveys (limiting flux of 390 μJy), except for a slightly better sensitivity to galaxies with $L \sim 10^{11}\ L_\odot$ around $z = 0.5$. Concerning deeper and narrower surveys at 24 μm (limiting flux of 112 μJy), such as the GTO Deep survey, the sensitivity to lower luminosity galaxies at higher redshifts is better (Fig. 8, *bottom*). In the redshift range 0.5–2.5, the gain in sensitivity compared to 70 μm allows us to probe galaxies with luminosities lower by a factor of $\sim$5.

9.4. *Resolving the CIB*

To compute the fraction of the CIB that will be resolved into sources, one has to consider the apparent size of the

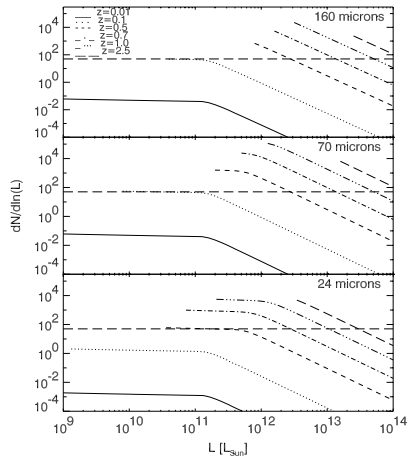

FIG. 8.—Number of starburst galaxies per logarithmic luminosity bin ($\Delta \ln L/\ln L = 0.1$) that can be detected at different redshifts (with $\Delta z/z = 0.5$). *Top*: 160 μm survey of 80 deg^2 (surface covered by SWIRE and GTO) limited by the confusion at 48 mJy. *Middle*: 70 μm survey of 80 deg^2 limited by the confusion at 4.7 mJy. *Bottom*: 24 μm survey of 2.46 deg^2 down to 112 μJy (GTO Deep survey). The horizontal dashed line shows the 50 sources needed in a $\Delta z/z = 0.5$ bin and a $\Delta \ln L/\ln L = 0.1$ bin for reconstructing the luminosity function. From bottom left to top right, the redshift bins are centered at $z = 0.01$, 0.1, 0.5, 0.7, 1.0, and 2.5.

galaxies. Rowan-Robinson & Fabian (1974) give the formalism to deal with resolved and extended sources. To simplify the problem, one might check if all the sources are point sources. For MIPS, the underlying assumption about the physical size of the objects is that it is smaller than 40 kpc, corresponding to less than the FWHM at 24 μm at $z > 1$. Indeed, most of the galaxies observed in the Hubble Deep Field–North with NICMOS exhibit structures smaller than 25 kpc ($\simeq 3''$) in the redshift range $z = 1$–2 (C. Papovich, M. Dickinson, M. Giavalisco, C. Conselice, & H. Ferguson 2003, in preparation). The objects are thus smaller than the MIPS beam sizes and will not be resolved. This might not be the case for IRAC. The closer resolved objects give a negligible contribution to the background anyway.

The fraction of the CIB resolved into discrete sources is given in Table 6. MIPS will resolve at most 69%, 54%, and 24% of the CIB at 24, 70, and 160 μm, respectively. This is an improvement by a factor of at least 3 of the CIB resolution in the FIR over previous surveys (e.g., at 170 μm; Dole et al. 2001). At 24 μm, most of the CIB will be resolved, as ISOCAM did at 15 μm (Elbaz et al. 2002), but with a much wider and deeper redshift coverage.

9.5. *Conclusion: Multiwavelength Infrared Surveys*

In the FIR range, the most promising surveys appear to be the large and shallow ones, because (1) the large number of detected sources is a key to having a statistically significant sample, and (2) the confusion level and the sensitivity are enough to probe sources in the redshift range from 0.7 to 2.5. With significant resolutions of the CIB at 70 and 160 μm (46% and 18%, respectively), the surveys will tremendously improve our knowledge of the sources that *ISO* could not detect. In the MIR range, where the confusion is negligible, the need for deeper surveys is striking. The Deep and Ultra Deep surveys will resolve most of the CIB at 24 μm, allowing us to study not only populations from $z = 0$ to $z = 1.4$ (like *ISO* did) but also the populations that lie at redshifts between 1.5 and 2.7 with unprecedented accuracy (Papovich & Bell 2002). All these multiwavelength surveys (GTO and Legacy programs) will thus probe for the first time a population of infrared galaxies at higher redshifts, allowing us to characterize the evolution, derive the luminosity function evolution, and constrain the nature of the sources, as well as to derive the unbiased global star formation rate up to $z \sim 2.5$.

10. UNRESOLVED SOURCES: FLUCTUATIONS OF THE COSMIC INFRARED BACKGROUND

10.1. *Fluctuation Level and Redshift Distributions*

Sources below the detection limit of a survey create fluctuations. If the detection limit does not allow resolving of the sources dominating the CIB intensity, characterizing these fluctuations gives very interesting information on the spatial correlations of these unresolved sources of cosmological significance. The FIR range is "favored" for measuring the fluctuations, because data are available with very high signal–to–detector noise ratios but limited by the confusion; on the other hand, the confusion limits the possibility of detecting faint resolved sources and leaves the information about faint sources hidden in the fluctuations. The study of the CIB fluctuations is a rapidly evolving field. After the pioneering work of Herbstmeier et al. (1998) with ISOPHOT, Lagache & Puget (2000) discovered them at 170 μm in the FIRBACK data, followed by other works at 170 and 90 μm (Matsuhara et al. 2000; Kiss et al. 2001; Puget & Lagache 2000) and at 60 and 100 μm in the *IRAS* data (Miville-Deschênes, Lagache, & Puget 2002).

Our model reproduces the measured fluctuation levels within a factor of 1.5 between 60 and 170 μm (Lagache et al. 2003). For MIPS, we predict that the level of the fluctuations will be 6930 Jy^2 sr^{-1} at 160 μm for $S_{160} < 48$ mJy and 113 Jy^2 sr^{-1} at 70 μm for $S_{70} < 4.7$ mJy.

Our model gives access to the redshift distribution of the sources dominating the observable fluctuations of the unresolved background. At 170 μm (Fig. 12 of Lagache et al. 2003), the redshift distribution of the contributions to the fluctuations peaks at $z = 0.8$, with a tail up to $z \sim 2.5$, and there is a nonnegligible contribution from local sources. The peak of this distribution is similar to the one of the 15 μm ISOCAM redshift distribution of resolved sources (Elbaz et al. 2002), which are understood to represent a significant fraction of the CIB. These sources observed at two different wavelengths should tell us the same story about galaxy evolution. The key point of studying the fluctuations in the FIR is the availability of large-area surveys to exhibit the source-clustering properties; this is not yet possible with MIR data that need to be taken with deeper (and thus with less area coverage) exposures to probe the same sources. Furthermore, a nonnegligible contribution comes from higher

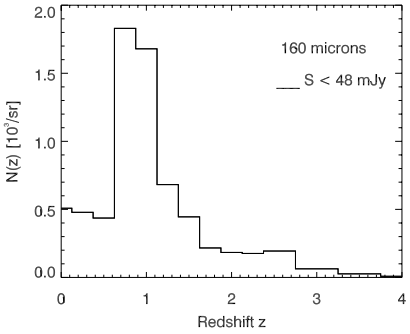

FIG. 9.—Redshift distribution of the sources below 48 mJy creating the fluctuations, at 160 μm with MIPS. The number of sources is shown for the particular bin sizes.

redshifts. Extracting this component will be a challenge requiring the use of all *SIRTF* bands.

At 160 μm (Fig. 9), for the same reasons, the distribution of the sources dominating the fluctuations peaks at $z = 0.8$, with a broad peak from $z = 0.7$ to $z = 1.1$. The tail extends up to $z \sim 2.5$, and the contribution of local sources is less prominent than at 170 μm with the ISOPHOT sensitivity. At 70 μm (Fig. 10), the distribution is similar to that at 160 μm, but with a factor of 3 less source density since the background is half-resolved into sources.

10.2. *Power Spectrum Analysis: Fluctuations and Source Clustering*

The Poisson component of the fluctuations of the CIB has been detected in the FIR by Lagache & Puget (2000) in the FIRBACK data, at spatial frequencies (or wavenumbers) of 0.25 arcmin$^{-1} < k < 0.6$ arcmin^{-1}. A preliminary study on larger fields seems to show that the source clustering is present in the data as well (Puget & Lagache 2000), and this is currently under investigation (M. Sorel et al. 2003, in preparation). However, to accurately constrain the source clustering, larger fields than FIRBACK are needed. Since *SIRTF* will cover larger sky areas, the clustering should be detected and measured in a power spectrum analysis similar to the one done by Lagache & Puget (2000) and Miville-Deschênes et al. (2002).

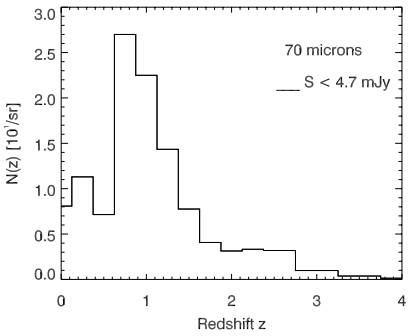

FIG. 10.—Redshift distribution of the sources below 4.7 mJy creating the fluctuations, at 70 μm with MIPS. The number of sources is shown for the particular bin sizes.

We make an estimation of the spatial frequency range where the CIB fluctuations will be detected in the large and shallow surveys at 160 μm, using our model. It does not include source clustering; we simply assume a Poisson distribution of the sources. The detectability of the source clustering is addressed below.

We use the same technique as Lagache & Puget (2000) and Puget & Lagache (2000); following their formalism, the power spectrum measured on the map ($P_{\rm map}$) in the space of the detector can be written as follows:

$$P_{\rm map} = P_{\rm noise} + (P_{\rm cirrus} + P_{\rm sources})W_k \ , \qquad (12)$$

where $P_{\rm noise}$, $P_{\rm cirrus}$, and $P_{\rm sources}$ are the power spectra of the photon/detector noise, the foreground cirrus, and the extragalactic sources we are interested in, respectively, and W_k is the power spectrum of the PSF. In this analysis, we want to exhibit $P_{\rm sources}$ and, for convenience, $P_{\rm cirrus}$.

Figure 11 shows a prediction for the various components present at 160 μm in a survey like the GTO Shallow survey or SWIRE. The Poisson component for the fluctuations due to extragalactic sources fainter than 48 mJy ($P_{\rm sources}$) is

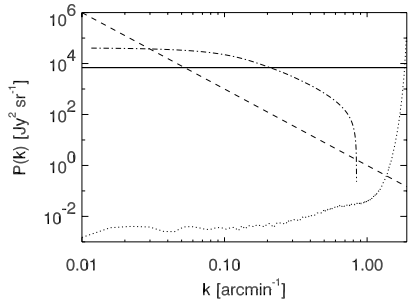

FIG. 11.—Theoretical power spectrum of a 5 deg^2 field at 160 μm, illustrating the spatial frequency range where the CIB fluctuations will be detected (see § 10.2). *Solid line*: Level of CIB Poisson fluctuations created by sources below 48 mJy predicted by our model (6930 Jy^2 sr^{-1}). *Dashed line*: Foreground cirrus, $P_{\rm cirrus}$, with the k^{-3} behavior and normalized at 10^6 Jy^2 sr^{-1} at $k = 0.01$ arcmin^{-1}, representing a column density of $N_{\rm H\,I} = 10^{20}$ cm^{-2}. *Dotted line*: White noise (1 σ of 7 mJy) divided by the PSF, $P_{\rm noise}/W_k$. *Dot-dashed line*: Model source clustering of starburst galaxies of Perrotta et al. (2001) in the case of 170 μm. The wavenumber range of cosmological interest is thus from 0.07 to 1.3 arcmin^{-1}, where the CIB Poisson fluctuations are expected to be detected; assuming the source clustering has the form predicted by Perrotta et al. (2001), it will be detected in the wavenumber range from 0.04 to 0.2 arcmin^{-1}.

shown as the horizontal line, at the value of 6930 Jy^2 sr^{-1} predicted by the model (see § 10.1); $P_{\rm cirrus}$ is shown as the dashed line and follows a k^{-3} power law (Gautier et al. 1992; Miville-Deschênes et al. 2002). The normalization at 10^6 Jy^2 sr^{-1} at $k = 10^{-2}$ arcmin^{-1} is typical of the faint cirrus present in the cosmological fields of column density $N_{\rm H\,I} = 10^{20}$ cm^{-2}. Finally, $P_{\rm noise}/W_k$ is plotted as a dotted line. The noise is a white noise of 1 σ of 7 mJy, typical for shallow surveys at 160 μm (Table 5).

To have an estimation of the spatial frequency range where the Poisson fluctuations from the extragalactic component will be detected, one has to consider the two limiting components: Galactic cirrus at low spatial frequencies and photon noise plus PSF shape at large spatial frequencies. It appears that the CIB Poisson fluctuations, or the fluctuations created by faint extragalactic sources only, should be well detected in the wavenumber range 0.07 arcmin^{-1} < $k < 1.3$ arcmin^{-1}.

Taking into account the source clustering, we assume that it is dominated by starburst galaxies with the form predicted by Perrotta et al. (2001).[10] This clustered component is plotted in Figure 11 as a dot-dashed line and has been computed for 170 μm. This component should be detected in the wavenumber range from 0.04 to 0.2 arcmin^{-1}. The cirrus limits the detection at smaller wavenumbers and is the main limitation for the source-clustering detection. The Poissonian component of extragalactic sources limits the detection at larger wavenumbers.

The large shallow surveys in the FIR are thus the most promising for studying the fluctuations and estimating the source clustering (0.04 arcmin$^{-1} < k < 0.2$ arcmin^{-1}).

11. CONCLUSION

In this work, we review the sources of noise expected in the cosmological surveys to be conducted by MIPS: photon/detector noise, cirrus noise, and confusion noise due to extragalactic sources. Using the Lagache et al. (2003) model, as well as the latest knowledge of the MIPS preflight characteristics (in particular, the photon/detector noise properties and the beam shapes), we predict the confusion levels, after a detailed discussion on the criteria. In particular, we show that in general the criteria depend on the shape of the source counts and the solid angle of the beam (directly related to the telescope and detector pixel size). *SIRTF* is about to probe a new regime in the source counts, where a significant fraction of the CIB is resolved and the counts begin to flatten. We thus discuss the classical rules of determining the confusion level (essentially valid for *IRAS* or *ISO*), and we show that it is wise to compare the photometric and source density criteria for predicting the confusion level. We find $S_{\rm lim}$ to be 50 μJy, 3.2 mJy, and 36 mJy at 24, 70, and 160 μm, respectively, consistent with *ISO* data and other works.

[10] Other predictions exist in the submillimeter range, but not specifically for 160 μm (Haiman & Knox 2000; Knox et al. 2001). The source clustering is there expected at scales between 0°.1 and 3°.

We compute the final sensitivity of the MIPS surveys, the GTO (Guaranteed Time Observer) program and the two Legacy programs (SWIRE and GOODS), predict the number of sources, and give the redshift distributions of the detected sources at 24, 70, and 160 μm. The deepest surveys should detect the dust emission of sources up to $z = 2.7$ at 24 μm (the redshifted 7.7 PAH feature causes a drop of detectability at higher redshifts) and up to $z = 2.5$ at 70 and 160 μm. This corresponds to a resolution of the CIB into discrete sources of 69%, 54%, and 24% at 24, 70, and 160 μm, respectively. We estimate that in the shallow surveys, the sources will be detected in a sufficient number in redshift bins for reconstructing the luminosity function and its evolution with redshift with a 14% (or better) accuracy as follows: most of the $L > 10^{12}\ L_\odot$ sources for $0.5 \lesssim z \lesssim 1$ in the FIR range, most of the $L > 10^{11}\ L_\odot$ sources for $0.5 \lesssim z \lesssim 1$ in the MIR range, and all of the $L \gtrsim 10^{13}\ L_\odot$ sources for $z \simeq 2.5$ in the MIR and FIR range. We also show that at 24 μm, deeper and narrower surveys will considerably increase the sensitivity to lower luminosity galaxies.

We also explore some characteristics of the unresolved sources at long wavelength, among which is the redshift distribution of the contribution to the background fluctuations at 70 and 160 μm. It peaks at $z \sim 0.8$, consistent with our present understanding of the main contribution to the CIB. We estimate the wavenumber range where the large FIR surveys will be able to measure the fluctuations of the Poisson component in a power spectrum analysis as 0.07 arcmin$^{-1} < k < 1.3$ arcmin^{-1}. With some assumption about the source clustering, we show that it could be detected in the wavenumber range 0.04 arcmin$^{-1} < k <$ 0.2 arcmin^{-1}.

We emphasize the complementary role of large and shallow surveys in the FIR and smaller but deeper surveys in the MIR. The MIR surveys allow us to probe directly faint sources, and the FIR surveys allow us to access the statistical properties of the faint population, mainly through CIB fluctuation analysis. With the various sky area coverages and depths, the MIPS surveys (together with IRAC data helping to estimate the photometric redshifts) will greatly improve our understanding of galaxy evolution by providing data with unprecedented accuracy in the MIR and FIR range.

We thank George and Marcia Rieke for many interesting discussions, as well as Almudena Alonso-Herrero, Eiichi Egami, and Casey Papovich. We also thank Petri Vaisanen for helpful discussions about the 8 μm source counts and for having provided us with his predictions, as well as Francesca Perrotta and Manuela Magliocchetti for having provided us with an electronic version of their model. We also appreciate remarks from Alberto Franceschini and Kevin Xu and discussions with Dario Fadda and Dan Weedman. We thank the referee for the constructive comments and suggestions. H. D. acknowledges the funding from the MIPS project, which is supported by NASA through the Jet Propulsion Laboratory, subcontract P435236, and the Programme National de Cosmologie and the Centre National d'Etudes Spatiales for travel funding.

REFERENCES

Altieri, B., et al. 1999, A&A, 343, L65
Boulanger, F. 2000, in *ISO* Beyond Point Sources: Studies of Extended Infrared Emission, ed. R. J. Laureijs, K. Leech, & M. F. Kessler (ESA SP-455; Noordwijk: ESA), 3
Chary, R., & Elbaz, D. 2001, ApJ, 556, 562
Condon, J. J. 1974, ApJ, 188, 279
Devriendt, J. E. G., & Guiderdoni, B. 2000, A&A, 363, 851
Dole, H., et al. 2000, in *ISO* Surveys of a Dusty Universe, ed. D. Lemke, M. Stickel, & K. Wilke (Lecture Notes in Physics 548; Berlin: Springer), 54
———. 2001, A&A, 372, 364
Elbaz, D., Cesarsky, C. J., Chanial, P., Aussel, H., Franceschini, A., Fadda, D., & Chary, R. R. 2002, A&A, 384, 848
Engelbracht, C. W., Young, E. T., Rieke, G. H., Rivlis, G., Beeman, J. W., & Haller, E. E. 2000, Exp. Astron., 10, 403
Fazio, G. G., et al. 1998, Proc. SPIE, 3354, 1024
Franceschini, A., Aussel, H., Cesarsky, C. J., Elbaz, D., & Fadda, D. 2001, A&A, 378, 1
Franceschini, A., Toffolatti, L., Danese, L., & De Zotti, G. 1989, ApJ, 344, 35
Franceschini, A., Toffolatti, L., Mazzei, P., Danese, L., & De Zotti, G. 1991, A&AS, 89, 285
Franceschini, A., et al. 2003, in The Mass of Galaxies at Low and High Redshift, ed. R. Bender & A. Renzini (New York: Springer), in press
Gautier, T. N. I., Boulanger, F., Perault, M., & Puget, J.-L. 1992, AJ, 103, 1313
Genzel, R., & Cesarsky, C. J. 2000, ARA&A, 38, 761
Hacking, P., Houck, J. R., & Condon, J. J. 1987, ApJ, 316, L15
Hacking, P. B., & Soifer, B. T. 1991, ApJ, 367, L49
Haiman, Z., & Knox, L. 2000, ApJ, 530, 124
Heim, G. B., et al. 1998, Proc. SPIE, 3356, 985
Helou, G., & Beichman, C. A. 1990, in From Ground-based to Space-borne Sub-mm Astronomy (ESA SP-314; Paris: ESA), 117
Herbstmeier, U., et al. 1998, A&A, 332, 739
Houck, J. R., & Van Cleve, J. E. 1995, Proc. SPIE, 2475, 456
Kelsall, T., et al. 1998, ApJ, 508, 44
Kiss, C., Abraham, P., Klaas, U., Juvela, M., & Lemke, D. 2001, A&A, 379, 1161
Knox, L., Cooray, A., Eisenstein, D., & Haiman, Z. 2001, ApJ, 550, 7
Krist, J. 1993, in ASP Conf. Ser. 52, Astronomical Data Analysis Software and Systems II, ed. R. J. Hanisch, R. J. V. Brissenden, & J. Barnes (San Francisco: ASP), 536
Lagache, G., & Dole, H. 2001, A&A, 372, 702
Lagache, G., Dole, H., & Puget, J.-L. 2003, MNRAS, in press
Lagache, G., & Puget, J.-L. 2000, A&A, 355, 17
Malkan, M. A., & Stecker, F. W. 2001, ApJ, 555, 641
Matsuhara, H., et al. 2000, A&A, 361, 407
Miville-Deschênes, M. A., Boulanger, F., Abergel, A., & Bernard, J. P. 2000, A&AS, 146, 519
Miville-Deschênes, M. A., Lagache, G., & Puget, J.-L. 2002, A&A, 393, 749
Morel, T., et al. 2001, MNRAS, 327, 1187
Papovich, C., & Bell, E. F. 2002, ApJ, 579, L1
Patris, J., Dennefeld, M., Lagache, G., & Dole, H. 2003, A&A, submitted
Pearson, C. P. 2001, MNRAS, 325, 1511
Perrotta, F., Magliocchetti, M., Baccigalupi, C., Bartelmann, M., De Zotti, G., Granato, G. L., Silva, L., & Danese, L. 2001, MNRAS, 338, 623
Puget, J.-L., & Lagache, G. 2000, in IAU Symp. 204, The Extragalactic Infrared Background and Its Cosmological Implications, ed. M. Harwit & M. G. Hauser (San Francisco: ASP), 59
Rieke, G. H., Young, E. T., & Gautier, T. N. 1995, Space Sci. Rev., 74, 17
Rieke, G. H., et al. 1984, BAAS, 16, 906
Roche, N., & Eales, S. A. 1999, MNRAS, 307, 111
Rowan-Robinson, M. 2001a, ApJ, 549, 745
———. 2001b, NewA Rev., 45, 631
Rowan-Robinson, M., & Fabian, A. 1974, MNRAS, 167, 419
Schlegel, D. J., Finkbeiner, D. P., & Davis, M. 1998, ApJ, 500, 525
Smail, I., Ivison, R. J., Blain, A. W., & Kneib, J.-P. 2002, MNRAS, 331, 495
Takeuchi, T. T., Ishii, T. T., Hirashita, H., Yoshikawa, K., Matsuhara, H., Kawara, K., & Okuda, H. 2001, PASJ, 53, 37
Tan, J. C., Silk, J., & Balland, C. 1999, ApJ, 522, 579
Vaisanen, P., Tollestrup, E. V., & Fazio, G. G. 2001, MNRAS, 325, 1241
Wang, Y. P. 2002, A&A, 383, 755
Wang, Y. P., & Biermann, P. L. 2000, A&A, 356, 808
Werner, M. W., & Fanson, J. L. 1995, Proc. SPIE, 2475, 418
Xu, C., Lonsdale, C. J., Shupe, D. L., O'Linger, J., & Masci, F. 2001, ApJ, 562, 179
Young, E. T., et al. 1998, Proc. SPIE, 3354, 57

Mon. Not. R. Astron. Soc. **338,** 555–571 (2003)

Modelling infrared galaxy evolution using a phenomenological approach

G. Lagache,[1⋆] H. Dole[2] and J.-L. Puget[1]
[1]*Institut d'Astrophysique Spatiale, Bât. 121, Université Paris XI, 91405 Orsay Cedex, France*
[2]*Steward Observatory, University of Arizona, 933 N. Cherry Ave, Tucson, AZ 85721, USA*

Accepted 2002 August 9. Received 2002 August 9; in original form 2002 June 6

ABSTRACT

To characterize the cosmological evolution of the sources contributing to the infrared extragalactic background, we have developed a phenomenological model that constrains in a simple way the evolution of the galaxy luminosity function with redshift, and fits all the existing source counts and redshift distributions, cosmic infrared background intensity and fluctuation observations, from the mid-infrared to the submillimetre range. The model is based on template spectra of starburst and normal galaxies, and on the local infrared luminosity function. Although the cosmic infrared background can be modelled with very different luminosity functions as long as the radiation production with redshift is the right one, the number counts and the anisotropies of the unresolved background imply that the luminosity function must change dramatically with redshift, with a rapid evolution of the high-luminosity sources ($L > 3 \times 10^{11}\,L_{\odot}$) from $z = 0$ to $z = 1$, which then stay rather constant up to redshift $z = 5$. The derived evolution of the infrared luminosity function may be linked to a bimodal star formation process: one associated with the quiescent and passive phase of the galaxy evolution, and one associated with the starburst phase, triggered by merging and interactions. The latter dominates the infrared and submillimetre output energy of the Universe.

The model is intended as a convenient tool to plan further observations, as illustrated through predictions for *Herschel*, *Planck* and ALMA observations. Our model predictions for given wavelengths, together with some useful routines, are available for general use.

Key words: galaxies: evolution – galaxies: general – galaxies: starburst – cosmology: observations – infrared: galaxies.

1 INTRODUCTION

The discovery of the cosmic infrared background (CIB) (Puget et al. 1996; Fixsen et al. 1998; Hauser et al. 1998; Schlegel, Finkbeiner & Davis 1998; Lagache et al. 1999, 2000; see Hauser & Dwek 2001 for a review), together with recent deep cosmological surveys in the infrared (IR) and submillimetre, has opened new perspectives on our understanding of galaxy formation and evolution. The surprisingly high amount of energy contained in the CIB showed that it is crucial to probe its contributing galaxies to understand when and how the bulk of stars formed in the Universe. Thanks to *ISO* (Kessler et al. 1996) – mainly at 15 μm with ISOCAM (Cesarsky et al. 1996), and at 90 and 170 μm with ISOPHOT (Lemke et al. 1996) – and ground-based instruments – SCUBA (Holland et al. 1998) and MAMBO (Bertoldi et al. 2000) at 850 and 1300 μm respectively – deep cosmological surveys have been carried out. It is thus now possible, to various degrees, to resolve the CIB into discrete sources (e.g. Kawara et al. 1998; Barger, Cowie & Sanders 1999; Elbaz et al. 1999; Carilli et al. 2001; Juvela, Mattila & Lemke 2000; Linden-Vornle et al. 2000; Matsuhara et al. 2000; Bertoldi et al. 2000; Dole et al. 2001; Elbaz et al. 2002; Scott et al. 2002). The striking result of these surveys concerns the evolution of the IR and submillimetre galaxy population. The source counts are high when compared to no-evolution or moderate-evolution models[1] for IR galaxies (Guiderdoni et al. 1998; Franceschini, Andreani & Danese 1998). Therefore, it has been necessary to develop new models in the IR. Very recently, several empirical approaches have been proposed to model the high rate of evolution of IR galaxies (e.g. Devriendt & Guiderdoni 2000; Wang & Biermann 2000; Charry & Elbaz 2001; Franceschini et al. 2001; Malkan & Stecker 2001; Pearson 2001; Rowan-Robinson 2001; Takeuchi et al. 2001; Xu et al. 2001; Balland, Devriendt & Silk 2002; Wang 2002), which fit all existing source counts, redshift distributions, and CIB intensity and fluctuations, although often not all of them. We present in this paper a new model whose preliminary results were published by Dole et al.

⋆E-mail: guilaine.lagache@ias.u-psud.fr

[1] No-evolution: the comoving luminosity function remains equal to the local one at all redshifts.

(2000). The originality of this model was to separate empirically the evolution of the starburst galaxies with respect to the normal galaxies, the current observations implying a strong evolution of the bright part of the luminosity function (LF). It was shown that only the starburst part should evolve very rapidly between $z = 0$ and $z = 2$, the evolution rate being much higher in the IR than in any other wavelength domain.

We present here a more sophisticated and detailed version of the first model (Dole et al. 2000). Our philosophy is to build the simplest model of LF evolution, easily deliverable, with the lowest number of parameters but accounting for all observational data. We stress the point that we include the CIB fluctuation levels as measured by ISOPHOT (Lagache & Puget 2000; Matsuhara et al. 2000) and *IRAS* (Miville-Deschênes, Lagache & Puget 2002) as an extra constraint. Recent observations strongly suggest that the bulk of the optical and IR extragalactic background is made of two distinct galaxy populations (see Section 2.2). Therefore, we restrict our model to the wavelength domain 10–1500 μm, our goal being to quantify the evolution of IR galaxies.

The paper is organized as follows: we first summarize our present knowledge on the evolution of IR galaxies, and on the nature of the sources contributing to the extragalactic background (Section 2). Then, we present the ingredients of the model (Section 3). In Section 4, we discuss the galaxy templates used in the model. We then present the parametrization of the local LF (Section 5). In Section 6 are given the results of the model (evolution of the LF, evolution of the luminosity density, number counts, z distribution, CIB intensity and fluctuations). Finally the model is used for predictions for the *Herschel* and *Planck* surveys (Sections 7.2 and 7.3 respectively), gives requirements for future large deep survey experiments (Section 7.4) and predictions for ALMA observations (Section 7.5). A summary is given in Section 8.

2 OUR PRESENT KNOWLEDGE

2.1 The strong evolution of IR galaxies: observational evidence

There has been, in the past few years, strong observational evidence indicating extremely high rates of evolution for IR galaxies.

First, galaxy evolution can be observed through its imprint on the far-IR extragalactic background (EB). Weakly constrained even as recently as 6 yr ago, various observations now measure or give upper/lower limits on the background from the ultraviolet (UV) to the millimetre waveband (e.g. Dwek et al. 1998; Gispert, Lagache & Puget 2000; Hauser & Dwek 2001). The data show the existence of a minimum between 3 and 10 μm separating direct stellar radiation from the IR part due to radiation re-emitted by dust. This re-emitted dust radiation contains at least a comparable integrated power as the optical/near-IR, and perhaps as much as 2.5 times more. This ratio is much larger than what is measured locally (∼30 per cent). The CIB is thus likely to be dominated by a population of strongly evolving redshifted IR galaxies. Since the long-wavelength spectrum of the background is significantly flatter than the spectrum of local star-forming galaxies, it strongly constrains the far-IR radiation production rate history (Gispert et al. 2000). The energy density must increase by a factor larger than 10 between the present time and redshift $z \sim 1$–2 and then stay rather constant at higher redshift (till ∼3), contrary to the ultraviolet radiation production rate, which decreases rapidly.

Secondly, several deep cosmological surveys at 15, 90, 170, 850 and 1300 μm have resolved a fraction of the CIB into discrete sources. For all surveys, number counts indicate a very strong cosmological evolution of IR galaxies, not only in total power radiated but also in the shape of the LF. This is particularly obvious at submillimetre wavelengths where the EB is dominated by high-luminosity galaxies (see the SCUBA and MAMBO results). The high rates of evolution exceed those measured in other wavelength domains as well as those observed for quasars and active galactic nuclei (AGNs).

Finally, high rates of evolution are suggested by the detection of Poissonian fluctuations of the CIB at a high level at 60 and 100 μm with *IRAS* (Miville-Deschênes et al. 2002) and 170 μm with ISOPHOT (Lagache & Puget 2000; Matsuhara et al. 2000). For example, Matsuhara et al. (2000) give the constraints on the galaxy number counts down to 35 mJy at 90 μm and 60 mJy at 170 μm, which indicate the existence of a strong evolution down to these fluxes in the counts.

2.2 Sources making the extragalactic background

2.2.1 *Optical versus infrared and submillimetre EB sources*

Recent observations show that the bulk of the optical and IR EB is made up by two distinct galaxy populations (e.g. Aussel et al. 1999). Therefore, one of the key questions is whether the dusty star-forming galaxies are recognizable from optical/near-IR data alone.

In the local Universe, Sanders & Mirabel (1996) show that the bolometric luminosity of IR galaxies is uncorrelated with optical spectra. The colour excess derived from the Balmer line ratio does not significantly depend on the IR luminosity, IR colour or optical spectral type (Veilleux, Kim & Sanders 1999). In fact, neither the moderate strength of the heavily extinguished starburst emission lines, nor their optical colours, can distinguish them from galaxies with more modest rates of star formation (Elbaz et al. 1999; Trentham, Kormendy & Sanders 1999; Poggianti et al. 1999). However, recently, Poggianti & Wu (2000) and Poggianti, Bressan & Franceschini (2001) show that the incidence of e(a)[2] sources in the different IR-selected samples seems to suggest that the e(a) signature might be capable of identifying from optical data alone a population of heavily extinct starburst galaxies. Reproducing the e(a) spectrum requires the youngest stellar generations to be significantly more extinguished by dust than older stellar populations, and implies a strong ongoing star formation activity at a level higher than in quiescent spirals.

At intermediate redshift ($0.3 < z < 1$), one main piece of information on IR galaxies comes from identifications of ISOCAM deep fields. For example, Flores et al. (1999a,b) presented results of a deep survey of one of the CFRS fields at 6.75 and 15 μm. At 15 μm, most (71 per cent) of the sources with optical spectroscopy are classified as e(a) galaxies. The far-IR luminosities of the Flores et al. e(a) galaxies are between 5.7×10^{10} and 2×10^{12} $L_\odot$. This is the first confirmation of the IR luminous nature of e(a) galaxies. More recently, Rigopoulou et al. (2000) using VLT spectroscopy found that optical ISOCAM counterparts in the *Hubble Deep Field* South (HDF-S) are indistinguishable from the dusty luminous e(a) galaxies.

All these studies at low and intermediate redshift seem to show that IR galaxies predominantly exhibit e(a) signatures in their optical spectra. On the contrary, in optically selected surveys of field galaxies, e(a) spectra are present but seem to be scarce (less than 10 per cent; see for example Poggianti et al. 1999). In fact, evidence for high e(a) incidences is found in merging or interacting systems or active compact groups. A complete study of the IR emission of e(a) galaxies is still to be done.

At much higher redshift, there is other evidence that the optically selected samples and bright IR samples (e.g. the SCUBA blank field sample) are different. For example, Chapman et al. (2000) have performed submillimetre photometry for a sample of Lyman break galaxies whose UV properties imply high star formation rates. They found that the integrated signal from their Lyman break sample is undetected in the submillimetre. This implies that the population of Lyman break galaxies does not constitute a large part of the detected blank field bright submillimetre sources.

In conclusion, it is clear that the optical and IR EBs are not dominated by the same population of galaxies. Therefore, we restrict our model to the wavelength domain 10–2000 μm, our goal being to quantify the evolution of IR galaxies.

2.2.2 *The CIB sources*

In the *Hubble Deep Field* North (HDF-N), Aussel et al. (1999) and Elbaz et al. (1999) find that 30–50 per cent of ISOCAM galaxies are associated with optical sources showing complex structures and morphological peculiarities. Moreover, Cohen et al. (2000) show, in the HDF-N, that more than 90 per cent of the faint ISOCAM sources are members of concentrations. This shows that past or present interactions or merging play a large role in triggering the IR emission of galaxies. All the studies of ISOCAM field sources show that the bulk of the CIB at 15 μm comes from galaxies that have bolometric luminosities of about 10^{11}–10^{12} $L_\odot$, high masses (∼10^{11} $M_\odot$) and redshift between 0.5 and 2. They experience intense stellar formation (100 $M_\odot$ yr^{-1}), which appears to be uncorrelated with the faint blue galaxy population dominating the optical counts at $z \sim 0.7$ (Ellis 1997; Elbaz et al. 1999). In galaxy clusters all ISOCAM sources are found preferably at the periphery where there is still some star formation (Biviano, Metcalfe & Altieri 1999).

At longer wavelengths, source identifications are much more difficult. Thus, characterizing the nature of the galaxies is a lengthy process. However, we already have some indications. The *FIRBACK* survey at 170 μm detected about 200 galaxies (Dole et al. 2001), making up less than 10 per cent of the CIB. Schematically *FIRBACK* sources comprise two populations: one cold and nearby ($L \sim 10^9$–10^{11} $L_\odot$), and one cold or warm very luminous ($L \sim 10^{12}$ $L_\odot$) with redshift lower than 1.2. The optical spectroscopy of the brightest *FIRBACK* sources reveals an '*IRAS*-like' starburst nature (Patris et al. 2002; Dennefeld et al., in preparation) with a moderate star formation rate (40 $M_\odot$ yr^{-1}). These results are very similar to those of Kakazu et al. (2002), who found that 62 per cent of the Lockman Hole 170-μm sources are at redshift below 0.3 with luminosities lower than 10^{12} $L_\odot$ (based on the spectrum of Arp 220), the rest being mostly ultraluminous IR galaxies with redshift between 0.3 and 1. In their sample, the 170-μm sources appear also to be powered primarily by star formation.

In the submillimetre, the main indication comes from the SCUBA deep surveys (e.g. Hughes et al. 1998; Barger et al. 1999; Eales et al. 1999; Scott et al. 2002). These surveys suggest that faint 850-μm sources are mostly ultraluminous galaxies at typical redshift between 1 and 4 (e.g. Eales et al. 2000). *SCUBA* sources above 3 mJy account for 20–30 per cent of the EB at 850 μm. The present data show that the bulk of the submillimetre EB is likely to reside in sources with 850-μm fluxes near 0.5 mJy. Barger et al. (1999) estimate that the far-IR luminosity of a characteristic 1-mJy source is in the range (4–5) × 10^{11} $L_\odot$, which is also typical of sources making up the bulk of the CIB at 15 μm. Moreover, as for the 15-μm sources, several groups have suggested that the submillimetre sources are associated with merger events (e.g. Smail et al. 1998; Lilly et al. 1999). All these results show that the integrated power of the LF at redshift greater than ∼0.5 must be dominated by sources with luminosities of a few 10^{11} $L_\odot$ while the local LF is dominated by sources with luminosities of the order of 5×10^{10} $L_\odot$.

2.2.3 *The AGN contribution to the IR output energy*

At low z, Veilleux et al. (1999) and Lutz et al. (1999) show that most of the IR sources are powered by starbursts. The AGN contribution appears dominant only at very high luminosities ($L > 2 \times 10^{12}$ $L_\odot$). Also using *FIRBACK* nearby bright source spectroscopy, we find that less than 10 per cent of sources show AGN signs (Patris et al. 2002; Dennefeld et al., in preparation). The same conclusions are reached by Kakazu et al. (2002). At intermediate z, from optical and X-ray studies of ISOCAM sources making up the bulk of the CIB, several groups show that 15-μm sources are mostly starburst galaxies (e.g. Fadda et al. 2002). At much higher z, the main indication comes from X-ray observations of SCUBA sources (Fabian et al. 2000; Hornschemeier et al. 2000; Severgnini et al. 2000; Barger et al. 2001). All these observations of submillimetre galaxies in X-rays are consistent with starburst-dominated emission. However, recently, Page et al. (2002) presented a result of SCUBA observations of eight X-ray absorbed AGN from $z = 1$ to 2.8 and find, for half of them, a 850-μm submillimetre counterpart. Nevertheless, the high 850-μm fluxes (greater than 5.9 mJy) suggest that these sources are hyperluminous galaxies. Such galaxies do not dominate the IR output of the Universe.

Considering the whole CIB energy budget, and based on the assumptions that 10 per cent of the mass accreting into a black hole is turned into energy and that the black hole masses measured in the HDF (Ford et al. 1998) are typical of galaxies, the AGN background energy would be of the order of 10 per cent of that from stars (Eales et al. 1999). These calculations are highly uncertain but are supported by the work of Almaini, Lawrence & Boyle (1999). Recently, more direct evidence has been obtained. For example, Severgnini et al. (2000) show that the 2–10 keV sources making up at least 75 per cent of the X-ray background in this band contribute less than 7 per cent to the submillimetre background.

On the modelling side, several groups (e.g. Xu et al. 2001; Rowan-Robinson 2001) have shown that starburst galaxies evolve much more rapidly than AGN-dominated sources, making the AGN contribution to the CIB relatively small.

In conclusion, it is clear that AGNs do not dominate the IR output energy of the Universe. Therefore, we will consider hereafter that IR galaxies are mostly powered by star formation and we use spectral energy distributions (SED) typical of these star-forming galaxies. The differences in SED for the small fraction of AGN-dominated IR galaxies would not significantly affect the results of our model, which is made up of only two galaxy populations ('normal' and starburst) defined by their SEDs.

3 INGREDIENTS OF THE MODEL

At a given wavelength $\lambda = \lambda_0$, the flux S_ν of a source at redshift z, as a function of the rest-frame luminosity L_ν (in W Hz^{-1}), can be written as

[2] Galaxies with strong Balmer absorption lines and [O II] in emission (Poggianti & Wu 2000, and references therein).

© 2003 RAS, MNRAS **338,** 555–571

$$S_\nu(L, z, \lambda = \lambda_0) = \frac{(1+z)\,k(L,z)\,L_\nu(L, \lambda = \lambda_0)}{4\pi\, D_{\rm L}^2}, \quad (1)$$

where $D_{\rm L}$ is the luminosity distance and $k(L, z)$ is the k-correction factor defined as

$$k(L, z) = \frac{L_{\nu(1+z)}}{L_{\nu(z=0)}}. \quad (2)$$

This correction is specific to the spectrum of the considered population at given L and z. In practice, the rest-frame luminosity L_ν is convolved by the bandpass filter centred on $\lambda = \lambda_0$. The number of sources per solid angle and redshift interval is

$$\frac{{\rm d}N}{{\rm d}z\,{\rm d}\log L}(L, z) = N_0(L, z)\,(1+z)^3\,\frac{{\rm d}V}{{\rm d}z}, \quad (3)$$

where ${\rm d}V/{\rm d}z$ is the differential volume element fixed by the cosmology and N_0 is the number of sources per unit volume and luminosity interval as a function of redshift. N_0 is given by the LF.

The differential counts at a given flux S and wavelength $\lambda = \lambda_0$ can be written as

$$\frac{{\rm d}N}{{\rm d}S} = \int_L \int_z \frac{{\rm d}N}{{\rm d}z\,{\rm d}\log L}(L, z)\,\frac{{\rm d}z}{{\rm d}S}(L, z)\,{\rm d}\log L. \quad (4)$$

We then obtain the integral counts,

$$N(>S) = \int \frac{{\rm d}N}{{\rm d}S}\,{\rm d}S, \quad (5)$$

the CIB intensity produced by all sources with $S < S_{\rm max}$,

$$I_{\rm CIB} = \int_0^{S_{\rm max}} S\frac{{\rm d}N}{{\rm d}S}\,{\rm d}S, \quad (6)$$

and the CIB intensity fluctuations (the shot noise) from sources below a given detection limit S_0 (which could correspond to either the confusion or the sensitivity limit) measured by the level of the white noise power spectrum,

$$P_{\rm fluc} = \int_0^{S_0} S^2\frac{{\rm d}N}{{\rm d}S}\,{\rm d}S\,{\rm Jy}^2\,{\rm sr}^{-1}. \quad (7)$$

We build the simplest model with the lowest number of parameters and ingredients which fits all the observations. We first fix the cosmology ($\Omega_\Lambda = 0.7$, $\Omega_0 = 0.3$ and $h = 0.65$) from the combination of the most recent cosmic microwave background (CMB) anisotropy measurements (e.g. de Bernardis et al. 2002), the distance–luminosity relation of Type Ia supernovae (e.g. Perlmutter et al. 1999) and the measure of galaxy distances using Cepheids (e.g. Freedman et al. 2001). We then construct the 'normal' and starburst template spectra: at each population and luminosity is associated one spectrum (see Section 4). We finally search for the best evolution of the LF (equation 3) that reproduces the number counts (equations 4 and 5), the CIB and its fluctuations (equations 6 and 7 respectively), assuming that the LF evolution is represented by the independent evolution of the two populations. A rather remarkable result, as will be seen later, is that two populations only can fit all the data.

4 BUILDING GALAXY TEMPLATES

4.1 Starburst galaxies

The luminous IR starburst galaxies emit more than 95 per cent of their energy in the far-IR. Spectra of such galaxies have been modelled by Maffei (1994), using the Désert, Boulanger & Puget (1990) dust emission model and the observational correlation for the *IRAS* Bright Galaxy Sample of the flux ratios 12/60, 25/60 and 60/100 with the IR luminosity (Soifer & Neugebauer 1991). We start from this model and modify it slightly to better take into account recent observational constraints. The significant improvements are the following:

(i) We replace the Désert et al. (1990) polyaromatic hydrocarbons (PAHs) template by the Dale et al. (2001) one, keeping the same amount of energy in the mid-IR.

(ii) We slightly modify the spectral shape in the near- and mid-IR: we increase the PAH and very small grains proportions (by a factor ∼2) but add some extinction, slowly increasing with the luminosity.

(iii) Finally, we broaden the far-IR peak (also a continuous change with luminosity) and slightly flatten the long-wavelength spectrum (Dunne et al. 2000; Dunne & Eales 2001; Klaas et al. 2001).

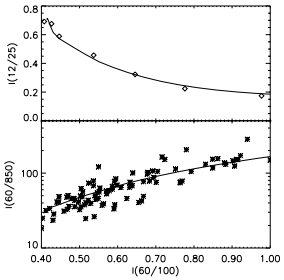

Figure 1. Colour diagrams from the model (full lines), compared with Soifer & Neugebauer (1991) (diamonds) and Dunne et al. (2000) (stars) data points.

Fig. 1 shows the (12/25, 60/100) and (60/850, 60/100) colour diagrams compared with Soifer & Neugebauer (1991) and Dunne et al. (2000) observations. We see a very good agreement between the templates and observations. The average luminosity spectra sequence is shown in Fig. 2. For the 'normal' starbursting galaxies ($L_{\rm IR} < 10^{11}\,{\rm L}_\odot$), we also check that the 7/15 versus 60/100 diagram was in good agreement with Dale et al. (2001).

Such a representation of galaxy SEDs that assigns only one spectrum per luminosity does not take into account the dispersion of the colours (e.g. the 60/100 ratio) observed for a given luminosity (as in Xu et al. 2001 or Chapman et al. 2002a). However, we do not have enough measured colours to do a statistical analysis of their variations with luminosities. The only colours measured for a large sample are the *IRAS* colours (principally the 60/100). Using only the 60/100 colour as a tracer of the dispersion for a given luminosity may not improve the representation, because, for example, two very different long-wavelength spectra can have the same 60/100 colour (e.g. NGC 7821 and 0549; Stickel et al. 2000).

4.2 Normal spiral galaxies

For the 'normal' galaxies (i.e. standard IR counterparts of spiral galaxies with more than half of their energy output in the optical), we take a unique spectrum derived mainly from the ISOPHOT serendipity survey (Stickel et al. 2000) and the nearby *FIRBACK* galaxy SEDs, together with longer-wavelength data from Dunne et al. (2000) and Dunne & Eales (2001).

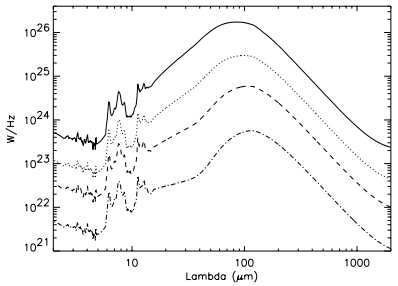

Figure 2. Starburst model spectra for different luminosities: $L = 3 \times 10^{12}\,{\rm L}_\odot$ (full line), $L = 5 \times 10^{11}\,{\rm L}_\odot$ (dotted line), $L = 10^{11}\,{\rm L}_\odot$ (dashed line) and $L = 10^{10}\,{\rm L}_\odot$ (dot-dashed line).

The ISOPHOT serendipity survey has revealed a population of nearby cold galaxies (Stickel et al. 1998, 2000), under-represented in the 60-μm *IRAS* sample. The distribution of I_{170}/I_{100} flux ratio shows that about half of the galaxies have a flux ratio between 1 and 1.5, indicating that the far-IR spectra are mostly flat between 100 and 200 μm. Very few show a downward trend in this wavelength range, this trend being typical of warm starburst galaxies (see Fig. 2). Most important is the large fraction of sources (more than 40 per cent) that have $I_{170}/I_{100} > 1.5$, indicating a rising spectrum beyond 100 μm similar to that seen for example in the Milky Way galactic ridge, a property known for more than 20 yr from early balloon-borne measurements (Serra et al. 1978; Silverberg et al. 1979).

In the *FIRBACK* N1 field (Dennefeld et al., in preparation), the brightest sources show mean IR colour similar to that of Stickel et al. (2000): $I_{170}/I_{100} \sim 1.3$ and $I_{60}/I_{100} \sim 0.47$. These objects are often associated with bright optical spiral galaxies (e.g. Fig. 3) with also typical 15-μm fluxes such as $I_{170}/I_{15} \sim 42$. Finally recent observations at 450 μm (Dunne & Eales 2001) reveal also the presence, in normal galaxies, of a colder component than previously thought.

Therefore, we take for the normal galaxy the 'cold' template presented in Fig. 4. This template has mean IR colours of $I_{170}/I_{100} = 1.42$, $I_{60}/I_{100} = 0.35$, $I_{170}/I_{15} = 45$ and $I_{100}/I_{850} = 77$. For the mid-IR part of the template, we use the spectral signature that applies to the majority of star-forming galaxies presented in Helou (2000). More observations around the maximum intensity (∼100–200 μm) and in the submillimetre are needed if we want to refine the template and describe its variations with luminosity.

Note that we do not make any evolution of the 'normal' and starburst template spectra with redshift. As shown in Chapman et al. (2002a), the available data for high-redshift, far-IR galaxies do not show evidence for any strong evolution in the characteristic temperature of the colour distribution over $0 < z < 3$. We can also test this hypothesis of 'no-evolution' using the two high-redshift sources N1-040 and N1-064 detected in the *FIRBACK* N1 field (Chapman et al. 2002b). For these two sources, we do a blind search for both the luminosity and redshift using our template spectra, based on a χ^2 test. For N1-064 the 'normal' and starburst templates give the same χ^2 with $\log(L) = 12.2$ and $z = 0.5$ and $\log(L) = 12.8$ and $z = 1.05$ respectively. The starburst template gives results in good agreement with Chapman et al. (2002b). For N1-040, the best χ^2 is obtained for the 'normal' template with $\log(L) = 12.2$ and $z = 0.45$, which is in perfect agreement with Chapman et al. (2002b). The template spectra give photometric redshifts in good agreement with the spectroscopic redshifts, suggesting no strong evolution of the galaxy SEDs over $0 < z < 1$.

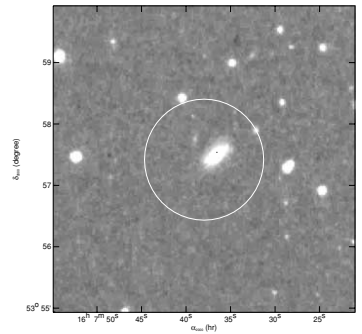

Figure 3. Example of association of one bright *FIRBACK* 170-μm source with a 'cold' spiral galaxy (the optical image is from the DSS; the white circle corresponds to the 170 μm error position). IR colour ratios for this source are $I_{60}/I_{100} = 0.6$, $I_{170}/I_{100} = 1.4$ and $I_{170}/I_{15} = 51$.

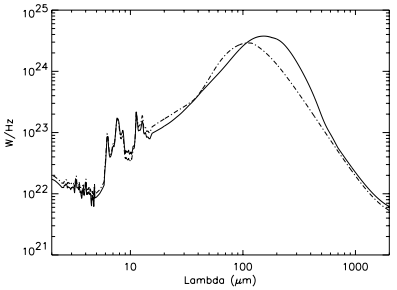

Figure 4. Template spectrum for the normal galaxies (full line), compared with the template spectrum for the starburst galaxies (dot-dashed line), for the same luminosity $L = 5 \times 10^{10}\,{\rm L}_\odot$.

5 PARAMETRIZATION OF THE LOCAL LUMINOSITY FUNCTION

A detailed comparison of the luminosity function of IR-bright galaxies with other classes of extragalactic objects has been made in Sanders & Mirabel (1996). The most striking results are (i) the high-luminosity tail of the IR galaxy LF is clearly in excess of that

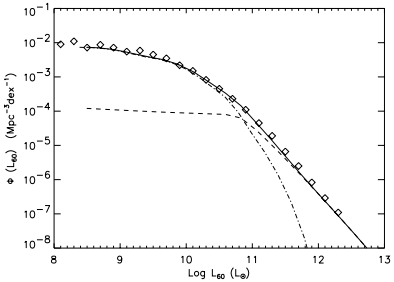

Figure 5. Luminosity function at 60 μm (model: normal galaxies, dot-dashed line; starburst galaxies, dashed line; total, full line) compared with Saunders et al. (1990) (diamonds).

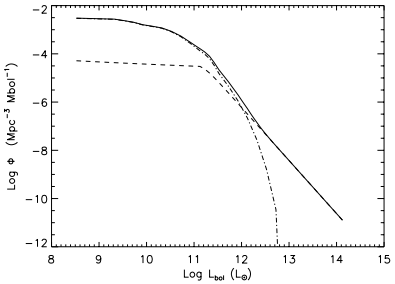

Figure 6. Bolometric luminosity function at $z = 0$ (normal galaxies, dot-dashed line; starburst galaxies, dashed line: total, full line).

expected from a Shechter function, and (ii) at luminosities below $\sim 10^{11}\,L_\odot$, the majority of optically selected objects are relatively weak far-IR emitters (as shown by *IRAS*, ISOPHOT and SCUBA observations). Accordingly, we decompose the IR LF into two parts: (1) the 'low-luminosity' part (dominated by normal galaxies) that follows the shape of the optical LF, and (2) the 'high-luminosity' part dominated by starburst galaxies (note however that each part covers the whole range of luminosities).

We start from the local LF at 60 μm from Saunders et al. (1990) (Fig. 5). We convert the 60-μm LF into a bolometric LF (L = 1–1000 μm) using our template spectra: at the 'low-luminosity' and 'high-luminosity' part, we assign the 'normal' and starburst template spectra respectively.[3] The bolometric LF (1–1000 μm) used in the model is shown in Fig. 6.

The parametrization and redshift evolution of the two parts of the bolometric LF is done in the following way:

(i) For the normal galaxies:

– A LF at $z = 0$ parametrized by an exponential with a cut-off in luminosity $L_{\rm cut\text{-}off}$

$$\Phi_{\rm normal}(L) = \Phi_{\rm bol}(L)\,\exp\left(\frac{-L}{L_{\rm cut\text{-}off}}\right). \quad (8)$$

– A weak number evolution.

(ii) For the starburst galaxies:

– A LF described by

$$\Phi_{\rm SB}(L,z) = \Phi_{\rm bol}(L = 2.5\times10^{11}\,L_\odot) \times \left(\frac{L}{2.5\times10^{11}\,L_\odot}\right)^{\rm SB_{slope}} \exp\left[-\frac{L_{\rm knee}(z)}{L}\right]^3. \quad (9)$$

– An evolution of the luminosity of the knee ($L_{\rm knee}$) with redshift.

– A constant slope of the LF at high luminosities ($\rm SB_{slope}$), not redshift-dependent.

– An evolution of the luminosity density with redshift, $\varphi(z)$, that drives the LF evolution

$$\Phi_{\rm SB}(L,z) = \Phi_{\rm SB}(L,z)\left[\frac{\varphi(z)}{\varphi(z=0)}\right]. \quad (10)$$

– An integrated energy at $z = 0$ as observed: $\rm SB_{norm} = \varphi(z = 0)$.

6 RESULTS AND DISCUSSION

6.1 LF evolution derived from observations

Although the number of parameters is quite low, it is too time-consuming to do a blind search through the whole parameter space. We therefore search for the best solution for the parameters near values expected from direct observational evidence:

(i) We fix the normal galaxy evolution (passive evolution) such that it nearly follows the number density evolution of optical counts up to $z = 0.4$,

$$\Phi_{\rm normal}(L,z) = \Phi_{\rm normal}(L,z=0)\,(1+z).$$

We arbitrarily stop the evolution at $z = 0.4$ and keep this population constant up to $z = 5$ and then let the population decrease up to $z = 8$ (see Fig. 8).

(ii) An estimate of $L_{\rm knee}$ is given by deep surveys at 15 and 850 μm: the bulk of the CIB at 15 and 850 μm is made up by galaxies with $L \sim 1$–$5\times10^{11}\,L_\odot$ (e.g. Barger et al. 1999; Elbaz et al. 2002).

(iii) We have indications on the evolution of the luminosity density, $\varphi(z)$, for the starburst galaxies, directly inferred from the CIB spectrum shape by Gispert et al. (2000), which is used as a starting point to adjust the model.

(iv) We take $\rm SB_{norm} = 10^7\,L_\odot\,Mpc^{-3}$, which is roughly the value observed locally.

(v) We take $\rm SB_{slope} = -2.2$ (Kim & Sanders 1998).

The best evolution of the LF that reproduces IR number counts, redshift distributions and CIB observations is shown in Fig. 7. It is obtained with

(i) $L_{\rm cut\text{-}off} = 5\times10^{11}\,L_\odot$.

(ii) $L_{\rm knee}(z) = 8\times10^{10}\,(1+z)^3\,L_\odot$ up to $z = 1.5$ and then $L_{\rm knee}(z) = L_{\rm knee}(z = 1.5)$.

Moreover, to avoid a 'break' in the evolved luminosity function (as in Dole et al. 2000), we modify the low-luminosity part of the starburst LF with the redshift (up to $z = 5$) according to

$$\Phi_{\rm SB}(L,z) = \Phi_{\rm SB}(L = L_{\rm max},z)\times\left(\frac{L_{\rm max}}{L}\right)^{(1+z)^2}, \quad (11)$$

[3]We have also checked the validity of the long-wavelength part of our template spectra by comparing the 850-μm LF with Dunne et al. (2000).

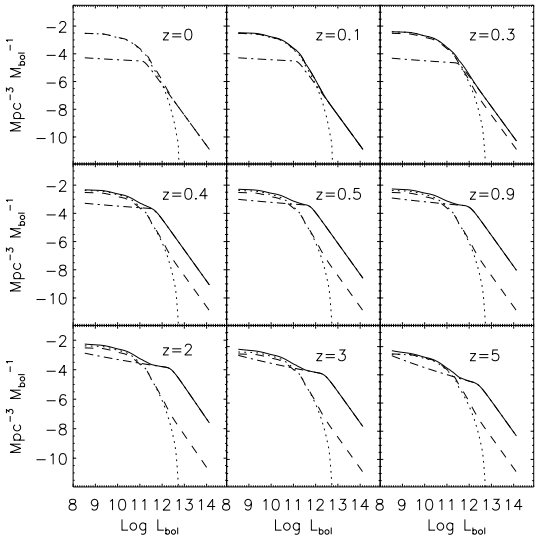

Figure 7. Comoving evolution of the luminosity function. The dotted line is for the normal galaxies and the dot-dashed line is for the starburst galaxies. The full line corresponds to both starburst and normal galaxies, and the dashed line is the LF at $z = 0$ for comparison.

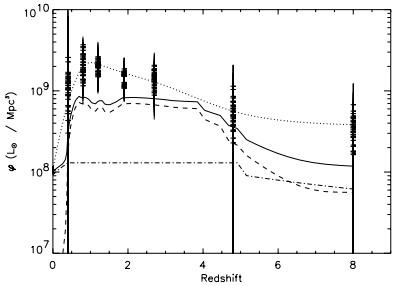

Figure 8. Comoving luminosity density distribution for the starburst galaxies (dashed line), normal galaxies (dot-dashed line), and both normal and starburst galaxies (full line). Also shown for comparison is the comoving luminosity density distribution from all cases of Gispert et al. 2000 (crosses with error bars), together with the best fit passing through all cases (dotted line).

where $L_{\rm max}$ is the luminosity corresponding to the maximum of $\Phi_{\rm SB}(L,z)$.

We see a very high rate of evolution of the starburst part, which peaks at $z \sim 0.7$ (Fig. 8) and then remains nearly constant up to $z = 4$ (as shown for example by Charry & Elbaz 2001). We compare in Fig. 8 the comoving luminosity density distribution as derived from the model with the Gispert et al. (2000) one. There is a good overall agreement. However, the model is systematically lower than the Gispert et al. (2000) determination for redshifts between 0.5 and 2. This comes from the fact that the CIB values at 100 and 140 μm used in Gispert et al. (2000) were slightly overestimated (Renault et al. 2001), leading in an overestimate of the luminosity density distribution at low redshift.

6.2 Comparison between model and observations

6.2.1 The number counts

Fig. 9 shows the comparison of the number counts at 15 μm (Elbaz et al. 1999), 60 μm (Hacking & Houck 1987; Lonsdale et al. 1990; Saunders et al. 1990; Rowan-Robinson et al. 1990; Gregorich et al. 1995; Bertin, Dennefeld & Moshir 1997), 170 μm (Dole et al. 2001) and 850 μm (Smail et al. 1997; Hughes et al. 1998; Barger et al. 1999; Blain et al. 1999; Borys et al. 2002; Scott et al. 2002; Webb et al. 2002) with the observations. We have a very good overall agreement [we also agree with the 90-μm number counts of Serjeant et al. (2001) and Linden-Vornle et al. (2000)].

6.2.2 The redshift distributions: need for a normal 'cold' population

In Fig. 10 is shown the redshift distribution of resolved sources at 15, 60, 170 and 850 μm. The 15-μm redshift distribution is in very good

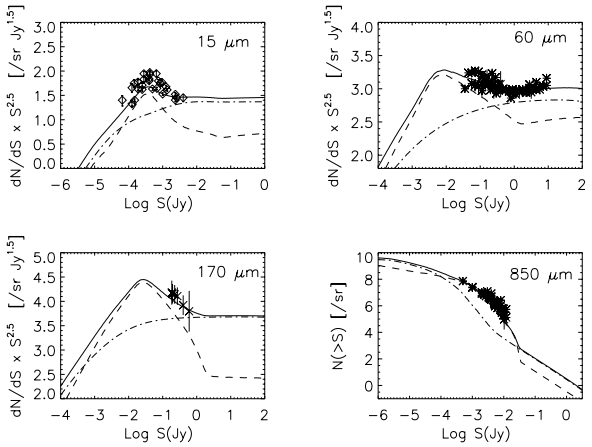

Figure 9. Number counts at 15, 60, 170 and 850 μm (on log scale) together with the model predictions (starburst galaxies, dashed line; normal galaxies, dot-dashed line; both normal and starburst galaxies, full line). Data at 15 μm are from Elbaz et al. (1999), at 170 μm from Dole et al. (2001), at 60 μm from Hacking & Houck (1987), Gregorich et al. (1995), Bertin et al. (1997), Lonsdale et al. (1990), Saunders et al. (1990) and Rowan-Robinson et al. (1990), and at 850 μm from Smail et al. (1997), Hughes et al. (1998), Barger et al. (1999), Blain et al. (1999), Borys et al. (2002), Scott et al. (2002) and Webb et al. (2002).

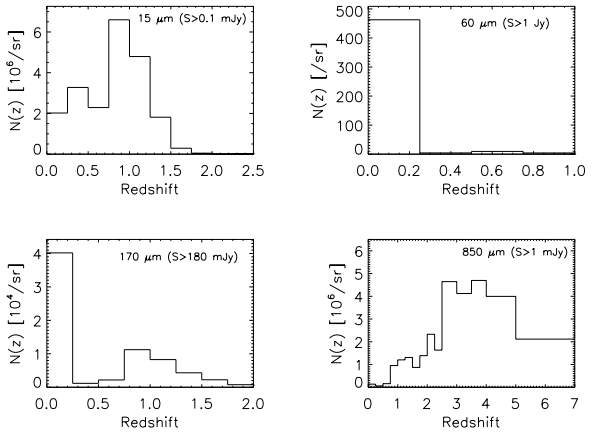

Figure 10. Predicted redshift distribution for resolved sources at 15, 60, 170 and 850 μm.

agreement with that observed by Flores et al. (1999b) and Aussel et al. (1999). At 850 μm, we predict that most of the detected sources are at $z > 2.5$. At 170 μm, we predict that about 62 per cent of sources with fluxes $S > 180$ mJy (4σ in Dole et al. 2001) are at redshift below 0.25, the rest being mostly at redshift between 0.8 and 1.2. We know from the *FIRBACK* observations that the redshift distribution predicted by the model is very close to that observed at 170 μm: it is clear from these observations that we have a bimodal z distribution (Sajina et al. 2002; Dennefeld et al., in preparation). Moreover, very recently, Kakazu et al. (2002) published the first results from optical spectroscopy of 170-μm Lockman Hole sources. They find that 62 per cent of sources are at $z < 0.3$ with IR luminosities (derived using Arp 220 SED) lower than 10^{12} $L_{\odot}$, the rest being at redshift between 0.3 and 1, which is in very good agreement with the model prediction. It is very important to note that the agreement between the model and observations can only be obtained with the local 'cold' population. A model containing only starburst-like template spectra and 'warm' normal galaxies overpredicts by a large factor the peak at $z \sim 1$ (as in Charry & Elbaz 2001, for example).

6.2.3 *The CIB and its anisotropies*

The predicted CIB intensity at specific wavelengths together with the comparison with present observations are presented in Table 1 and in Fig. 11. We have a very good agreement with the estimates at 60 μm (Miville-Deschênes et al. 2002), 100 μm (Renault et al. 2001) and 170 μm (Kiss et al. 2001), and the *FIRAS* determinations (Fixsen et al. 1998; Lagache et al. 2000). We are also in good agreement with the lower limit derived from 15-μm counts (Elbaz et al. 2002), combined with the upper limit deduced from high-energy γ-ray emission of the active galactic nucleus Mrk 501 (Renault et al. 2001). According to the model, sources above 1 mJy at 850 μm contribute about 30 per cent of the CIB. At 15 μm, with the deepest ISOCAM observations (Altieri et al. 1999; Aussel et al. 1999; Metcalfe 2000), about 70 per cent of the CIB has been resolved into individual sources.

Finally, we compare the model predictions for the CIB fluctuations with the present observations at 60, 90, 100 and 170 μm (Table 2). For comparison we need to remove the contribution of the

Table 1. Predicted CIB intensity at 15 μm (ISOCAM filter), 60 and 100 μm (*IRAS* filters), 170 μm (ISOPHOT filter), 350 μm (filter such as $\Delta\lambda/\lambda = 1/3$) and 850 μm (SCUBA filter) compared to measurements.

λ (μm)	Predicted CIB (MJy sr^{-1})	Predicted CIB (W m^{-2} sr^{-1})	Measured CIB (W m^{-2} sr^{-1})	Ref.
15	1.25×10^{-2}	2.5×10^{-9}	$>2.4 \pm 0.5 \times 10^{-9}$	(1)
60	0.12	6.1×10^{-9}	–	
100	0.35	1.1×10^{-8}	$\sim 1.5 \times 10^{-8}$	(2)
170	0.76	1.3×10^{-8}	$1.4 \pm 0.3 \times 10^{-8}$	(3)
350	0.76	6.5×10^{-9}	$5.63^{+4.30}_{-2.80} \times 10^{-9}$	(4)
850	0.20	6.9×10^{-10}	$5.04^{+4.31}_{-2.61} \times 10^{-10}$	(4)

(1) Elbaz et al. (2002).
(2) Renault et al. (2001).
(3) From Kiss et al. (2001) and extrapolation of DIRBE measurements.
(4) From Fixsen et al. (1998) and Lagache et al. (1999).

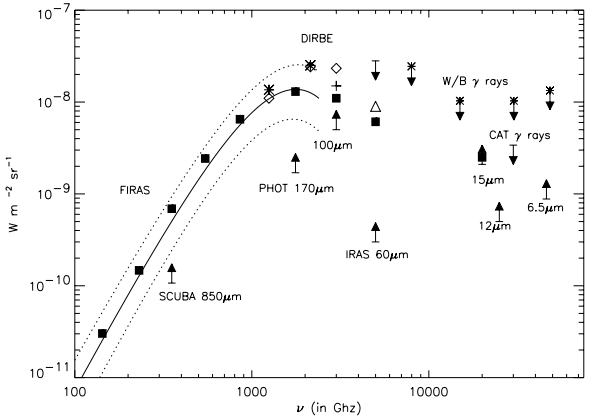

Figure 11. Cosmic background from mid-IR to millimetre wavelength. The 6.5 μm (Désert, private communication), 12 μm (Clements et al. 1999) and 15 μm (Elbaz et al. 2002) lower limits come from ISOCAM number counts; the upper limit 'CAT' is from Renault et al. (2001) and the cross upper limits W/B are from Biller et al. (1998). At longer wavelength, we have the 60 μm estimate from Miville-Deschênes et al. (2002) (△), the upper limit from Finkbeiner, Davis & Schlegel (2000), and the lower limit from number counts at 60 μm (Lonsdale et al. 1990); at 140 and 240 μm are displayed the Lagache et al. 2000 (◇) and Hauser et al. (1998) (⋆) DIRBE values; at 100 μm is given the lower limit from Dwek et al. (1998) together with the estimates from Renault et al. (2001) (+) and the determination of Lagache et al. (2000) (◇); at 170 μm (Puget et al. 1999) and 850 μm (Barger et al. 1999) are lower limits from number counts. The analytic form of the CIB at the *FIRAS* wavelengths is from Fixsen et al. (1998). The CIB derived from the model at selected wavelengths is given by filled squares.

Table 2. Comparison of the predicted CIB fluctuations (for $S < S_{\rm max}$ in Jy^{-2} sr^{-1}) and the observations.

λ (μm)	$S_{\rm max}$ (mJy)	Observations (Jy^{-2} sr^{-1})	References	Model (Jy^2 sr^{-1})
170	1000	$\sim$25 000	Sorel et al. (in preparation)	23 694
170	250	13 000 $\pm$ 3000	Matsuhara et al. (2000)	15 644
170	100	7400	Lagache et al. (2000)	11 629
100	700[a]	5800 $\pm$ 1000	Miville-Deschênes et al. (2002)	10 307
90	150	12 000 $\pm$ 2000	Matsuhara et al. (2000)	5290
60	1000	1600 $\pm$ 300	Miville-Deschênes et al. (2002)	2507

[a]Bright sources in Miville-Deschênes et al. (2002) are removed at 60 and 100 μm using the cut of 1 Jy at 60 μm. Since the 60-μm sources are mostly starburst galaxies, we estimate that 1 Jy at 60 μm is equivalent to 0.7 Jy at 100 μm.

brightest sources that make up the bulk of the fluctuations (sources with fluxes $S > S_{\rm max}$). When $S_{\rm max}$ is quite high (of the order of 500 mJy–2 Jy), the fluctuations are dominated by the strongest sources, making the result very dependent on the accuracy of the evaluation of $S_{\rm max}$. This is why the comparison between observations and model is very difficult.[4] For $S_{\rm max}$ around 50–150 mJy, the fluctuations are dominated by the faint and numerous sources that dominate the CIB and the values do not depend critically on the exact value of $S_{\rm max}$. We see from Table 2 that, although for some observations the model can be lower or greater by a factor 1.5 in amplitude, we have an overall very good agreement. We stress that reproducing the CIB fluctuations gives strong constraints on the LF evolution. For example, evolution such that we better reproduce the 850-μm counts gives too high CIB fluctuations. Future observations with better accuracy will show if these minor discrepancies disappear or are indicative that the bright submillimetre counts are overestimated as a result of a high fraction of gravitationally lensed sources (Perrotta et al. 2002), or are simply indicative that the present phenomenological model is too simple! The level of the predicted CIB fluctuations for dedicated experiments (as for example *Boomerang* or *Maxima*), with respect to the cirrus confusion noise and instrumental noise will be discussed in detail in Piat et al. (in preparation).

At 170 μm, it is clear from Fig. 12 that the redshift distributions of sources that make up the CIB and those making up the bulk of the fluctuations are similar. The fluctuations are not dominated by bright sources just below the detection threshold but by numerous sources at higher redshift. Thus, in this case, studying the CIB fluctuations gives strong constraints on the CIB source population. This is true in the whole submillimetre–millimetre range. The population of galaxies where the CIB peaks will not be accessible by direct detection in the coming years. For example, *SIRTF* will resolve about 20 per cent of the background at 160 μm (Dole, Lagache & Puget 2002), PACS about 50 per cent at 170 μm (Section 7.2.2) and SPIRE less than 10 per cent at 350 μm (Section 7.2.1).

In conclusion, we have seen that our model gives number counts, redshift distributions, CIB intensity and fluctuations that reproduce all the present observations. It can now be used for predictions about future experiments, in particular for *Herschel*, *Planck* and ALMA observations. For *SIRTF*, a complete and more detailed study, including simulations and a detailed discussion on the confusion, can be found in Dole et al. (2002).

[4] We cannot compare the model predictions with the Kiss et al. (2001) results since we have no information on $S_{\rm max}$.

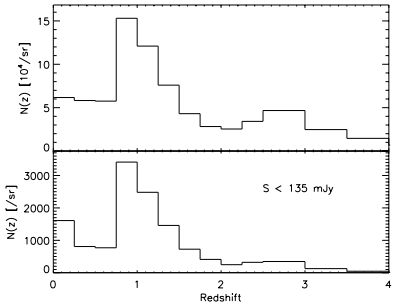

Figure 12. Redshift distribution of sources making up the CIB intensity and its fluctuations ($S < 135$ mJy) at 170 μm.

7 PREDICTIONS FOR FUTURE EXPERIMENTS

7.1 The confusion noise from extragalactic sources

The confusion noise[5] is usually defined as the fluctuations of the background sky brightness below which sources cannot be detected individually. These fluctuations are caused by intrinsically discrete extragalactic sources. In the far-IR, submillimetre and millimetre wavelengths, as a result of the limited size of the telescopes compared to the wavelength, confusion noise plays an important role in the total noise budget. In fact, confusion noise is often greater than instrumental noise, and thus severely limits the survey depth. The total variance σ^2 of a measurement within a beam due to extragalactic sources with fluxes less than $S_{\rm lim}$ is given by

$$\sigma^2 = \int f^2(\theta,\phi)\,{\rm d}\theta\,{\rm d}\phi \int_0^{S_{\rm lim}} S^2\,\frac{{\rm d}N}{{\rm d}S}\,{\rm d}S, \qquad (12)$$

where $f(\theta,\phi)$ is the two-dimensional beam profile (sr), S the flux (Jy) and ${\rm d}N/{\rm d}S$ the differential number counts (Jy^{-1} sr^{-1}). We call $S_{\rm lim}$ the confusion limit.

[5] We only consider the confusion noise due to extragalactic sources since, in the high galactic latitude cosmological fields, the cirrus confusion noise is negligible.

The confusion noise can be determined using two criteria: the so-called photometric and source density criteria (see Dole et al. 2002 , for a full description). The photometric criterion is related to the quality of the photometry of detected sources, the flux measured near $S_{\rm lim}$ being severely affected by the presence of fainter sources in the beam. It is defined by the implicit equation

$$S_{\rm lim} = q_{\rm phot}\,\sigma(S_{\rm lim}) \qquad (13)$$

where $q_{\rm phot}$ measures the photometric accuracy and is usually taken between 3 and 5.

The source density criterion is related to the completeness of detected sources above $S_{\rm lim}$ directly related to the probability to lose sources too close to each other to be separated. There is a threshold above which the density of sources above $S_{\rm lim}$ is such that a significant fraction of the sources is lost (it is impossible to separate the individual sources any more). For a given source density (with a Poissonian distribution) $N(>S)$, corresponding to a flux limit $S_{\rm lim}$, the probability P to have the nearest source with flux greater than $S_{\rm lim}$ located closer than the distance $\theta_{\rm min}$ is

$$P(<\theta_{\rm min}) = 1 - \exp\left(-\pi N \theta_{\rm min}^2\right), \qquad (14)$$

where $\theta_{\rm min}$ is the distance below which sources cannot be separated and is a function of the beam profile. If we use $\theta_{\rm FW}$ to denote the full width at half-maximum (FWHM) of the beam profile, $\theta_{\rm min}$ can conveniently be expressed in terms of $\theta_{\rm FW}$, $\theta_{\rm min} = k\theta_{\rm FW}$. As an illustration, simulations of source extraction at the *MIPS/SIRTF* wavelengths show that $k = 0.8$ should be achievable (Dole et al. 2002). Therefore, in the following, we fix $k = 0.8$. We choose the maximum acceptable probability of not being able to separate the nearest source $P_{\rm max} = 0.1$. In this case, the source density is equal to $1/17.3\Omega$ (Table 3) and the corresponding most probable distance is about $1.7\theta_{\rm FW}$. Using equation (14), we can derive $N(>S)$ and thus find the corresponding $S_{\rm lim}$. Then, using equation (12), we compute σ. The source density criterion leads to an equivalent value $q_{\rm density} = S_{\rm lim}/\sigma$. If $q_{\rm density}$ is greater than standard values of $q_{\rm phot}$ (3 to 5), then the confusion noise is given by the source density criterion. If not, then the photometric criterion has to be used to derive the confusion noise. The classical confusion limit of one source per 30 beams corresponds to $k = 1$ and $P \sim 0.1$. Nevertheless it can still lead to mediocre photometry for very steep log N–log S.

The transition between the photometric and source density criterion is around 200 μm, depending on telescope diameters. For example, for *SIRTF*, at 24 and 70 μm, the source density criterion gives $q_{\rm density} \sim 7$ (Dole et al. 2002). In this case, the source density criterion has to be used to derive the source confusion and it leads to a very good photometric quality. On the contrary, at the *Planck* wavelengths, the source density criterion gives $q_{\rm density} \sim 1$, leading to source detection limited by the photometric quality. Furthermore, this illustrates the limits of doing high signal-to-noise ratio observations 'to beat the confusion'.

In the following, we derive the confusion noise for future long-wavelength dedicated surveys. We assume that the sources are randomly distributed on the sky. The effect of the clustering on the confusion noise will be investigated by Blaizot et al. (in preparation) using the hybrid model described in Guiderdoni et al. (2001) and Hatton et al. (2002). The number counts at long wavelengths derived from the model and useful for the following predictions are shown in Fig. 13.

Table 3. Number of beams per source for different probability P to have the nearest source located closer than the distance $\theta_{\rm min} = k\theta_{\rm FW}$ with $\theta^2_{\rm FW} \sim \Omega/1.1$ (valid for both Gaussian and Airy disc beams).

	$P = 0.05$	$P = 0.1$	$P = 0.15$
$k = 0.8$	35.6	17.3	11.2
$k = 0.9$	45.1	22.0	14.2
$k = 1.0$	55.7	27.1	17.6

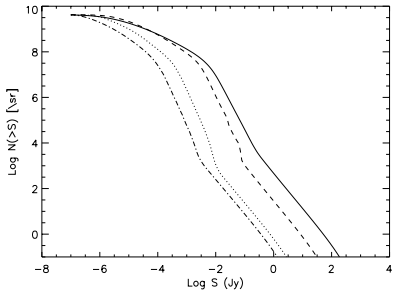

Figure 13. Predicted number counts at 350 μm (full line), 550 μm (dashed line), 1300 μm (dotted line) and 2097 μm (dot-dashed line).

7.2 The *Herschel* deep surveys

The *Herschel Space Observatory* (Pilbratt 2001) is the fourth cornerstone mission in the European Space Agency science programme. It will perform imaging photometry and spectroscopy in the far-IR and submillimetre parts of the spectrum, covering approximately the 60–670 μm range. *Herschel* will carry a 3.5-m diameter passively cooled telescope. Three instruments share the focal plane: two cameras/medium-resolution spectrometers, PACS and SPIRE, and a very high-resolution heterodyne spectrometer, HIFI.

In Table 4 are shown the confusion noises and limits at PACS and SPIRE wavelengths using the photometric and source density criteria. At the PACS wavelengths, the source density criterion leads to confusion limits 2–6 times higher than the photometric criterion with $q_{\rm phot} = 5$. For SPIRE, at 250 μm, the limits obtained using

Table 4. PACS and SPIRE 1σ confusion noise and its associated flux limit ($S_{\rm lim}$) for the photometric criterion ($q_{\rm phot} = 5$) and the source density criterion (with the equivalent $q_{\rm density}$).

		σ (mJy)	$S_{\rm lim}$ (mJy)
PACS 75 μm	$q_{\rm phot} = 5.0$	2.26×10^{-3}	1.12×10^{-2}
	$q_{\rm density} = 8.9$	1.42×10^{-2}	1.26×10^{-1}
PACS 110 μm	$q_{\rm phot} = 5.0$	1.98×10^{-2}	1.0×10^{-1}
	$q_{\rm density} = 8.7$	1.02×10^{-1}	8.91×10^{-1}
PACS 170 μm	$q_{\rm phot} = 5.0$	3.97×10^{-1}	2.00
	$q_{\rm density} = 7.13$	9.93×10^{-1}	7.08
SPIRE 250 μm	$q_{\rm phot} = 5.0$	2.51	12.6
	$q_{\rm density} = 5.2$	2.70	14.1
SPIRE 350 μm	$q_{\rm phot} = 5.0$	4.4	22.4
	$q_{\rm density} = 3.6$	3.52	12.6
SPIRE 550 μm	$q_{\rm phot} = 5.0$	3.69	17.8
	$q_{\rm density} = 2.5$	3.18	7.94

Table 5. Designed surveys that could be done with SPIRE (numbers are from the 350-μm channel).

Surface (deg^2)	$5\sigma_{inst}$ (mJy)	$5\sigma_{conf}$ (mJy)	$5\sigma_{tot}$ (mJy)	Days	Number of sources	Per cent resolved CIB
400	100	28.2[a]	103.9	18	4768	1.0
100	15.3	22.4	27.1	90	33 451	6.7
8	7.5	22.4	23.6	64	3533	7.8

[a]Unresolved sources below $5\sigma_{inst} = 100$ mJy induce a confusion noise of $\sigma_{conf} = 5.63$ mJy.

the two criteria are very close and then, at longer wavelengths, the photometric quality constrains the confusion limit.

Extragalactic surveys will be conducted by both the PACS and SPIRE instruments. Up to now, the trade-off between large-area, shallow versus small-area, deep/ultradeep observations has not been finalized. In the following two sections are examples of extragalactic surveys that could be done.

7.2.1 The SPIRE surveys

For large-area scan-mapping observations, the current estimates of time needed to map 1 deg^2 to an instrumental noise level of 3 mJy ($1\sigma_{inst}$) is about 1.7, 2 and 2.1 d at 250, 350 and 550 μm respectively (Matt Griffin, private communication). Three kinds of surveys could be done with SPIRE (Table 5):

(i) A very large area (two approximately 14×14 deg^2, i.e. ∼400 deg^2) survey at the noise level of $5\sigma_{inst} = 100$ mJy at 350 μm (92 mJy at 250 μm and 102 mJy at 550 μm).

(ii) A confusion-limited survey of about 100 deg^2. To reach a $5\sigma_{inst}$ noise limit of 14.1, 22.4 and 17.8 mJy, one needs 192, 90 and 149 d at 250, 350 and 550 μm, respectively.

(iii) A very deep survey, down to the confusion limit, to extract as much information as possible about the underlying population. For example, mapping 8 deg^2 to $5\sigma_{inst} = 7.5$ mJy at 350 μm would take 64 d.

We concentrate, in the following, on the 350-μm band (although SPIRE observes the three bands simultaneously). The number of detected sources for each survey is given in Table 5 and the redshift distribution in Fig. 14.

7.2.1.1. The very large area survey This survey is well suited to the *Planck* sensitivity (see Table 7). It would provide better positions for the *Planck* point sources and the combination with the *Planck* data would improve the spectral and spatial characterization of foregrounds. It will take about 18 d, which is a small amount of time compared to the enormous progress it would bring for the component separation problem for all observations in this wavelength range. The very large area survey will detect mostly nearby sources but hundreds of objects could be detected at $z > 1$. It will also explore the cirrus component. Moreover, thanks to its surface coverage, this survey will detect the rare and high-z objects about which little is known today.

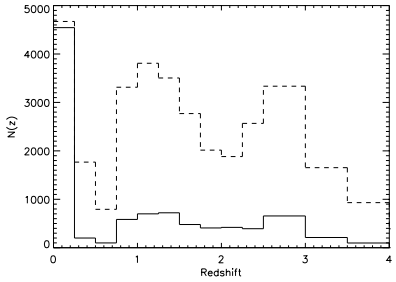

Figure 14. SPIRE 350 μm redshift distribution for sources detected in the very large area survey (full line, $S > 103.9$ mJy, multiplied by 2) and the confusion-limited survey (dashed line, $S > 27.1$ mJy).

7.2.1.2. The confusion-limited survey For the confusion-limited survey, there are mainly two peaks in the redshift distribution: one at $z \sim 0$ due to the cold sources, and the other between 0.8 and 3 due to the starburst galaxies. The number of starburst galaxies detected between 0.8 and 3 does not vary much. Fig. 15 predicts the number of starburst galaxies that the confusion-limited survey will detect at 350 μm per log interval of luminosity (this figure does not include the cold population, which contributes mostly locally). The evolution of the 10^{12}–10^{13} $L_\odot$ galaxies will be measured from $z \sim 0.5$ to 2.5. Galaxies with $L \sim 3 \times 10^{11}$ $L_\odot$ will only be accessible at $z \sim 0.1$. The nature and number of the highest-luminosity objects are important to test cosmological theories, and thus populating the high-redshift bins with enough objects to ensure <14 per cent Poisson noise (corresponding to 50 sources) is a critical driver for the size of the sample, and, accordingly, the area required for the survey. Based on our model, we see from Fig. 15 that, to meet this ∼14 per cent goal for galaxies in the range 10^{12}–10^{13} $L_\odot$ at $z < 2.5$, an area of 100 deg^2 is the minimum required.

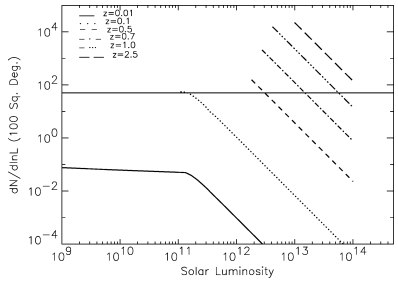

Figure 15. Number of starburst galaxies that can be detected in different redshift ranges (with a $\Delta z/z = 0.5$) at 350 μm by the confusion-limited survey of 100 deg^2 as a function of bolometric luminosity. The horizontal line shows the 50 sources needed in a $\Delta z/z = 0.5$ bin for ∼14 per cent accuracy. The plots are limited to the fluxes above the detection limit and to luminosities below 10^{14} $L_\odot$.

7.2.1.3. The very deep survey The confusion-limited surveys will detect only ∼7 per cent of the CIB (1 per cent for the very large area survey). In this case, studying the fluctuations will provide information on the underlying source population. The redshift distribution of sources making up the bulk of the CIB and the fluctuations at 350 μm are very similar. Thus, the fluctuations will be a unique opportunity to obtain information, in particular, on sources that dominate the CIB (sources with $L \sim 3 \times 10^{11}$ $L_\odot$), at redshifts where they cannot be detected individually. To detect and study them, a field with high signal-to-noise ratio is needed. Moreover, the size of the field should be large enough to try to detect the source clustering and not only be limited to the Poissonian noise detection (which is about 4300 Jy^2 sr^{-1}). Since source clustering is expected at scales between 1 and 5 deg (Knox et al. 2001), a field of about 8 deg^2 is the minimum required. This field could be part of the confusion-limited survey, which will certainly be split into several smaller area surveys.

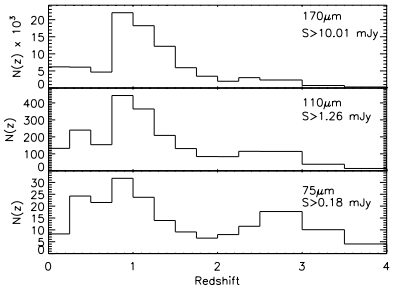

Figure 16. From bottom to top: redshift distribution for the ultradeep, deep and shallow PACS surveys at 75, 110 and 170 μm respectively.

7.2.2 The PACS surveys

For the whole field of view of $\sim 1.75 \times 3.5$ $arcmin^2$, the current estimates of time needed to reach $5\sigma_{inst} = 3$ mJy is 1 h (Albrecht Poglitsch, private communication). At 75, 110 and 170 μm, the confusion limits are about 0.13, 0.89 and 7.08 mJy, with $q_{density}$ of 8.9, 8.7 and 7.1, respectively. To reach the confusion limit for one field of view, i.e. $5\sigma_{inst} = 0.1, 0.9$ and 7.1, we need 567, 11 and 0.18 h at 75, 110 and 170 μm, respectively. Since for PACS the confusion limits and the time to reach those sensitivities are very different at the three wavelengths, three kinds of surveys could be done, which, schematically, will probe the CIB in three bands:

(i) A shallow survey of 20 deg^2 down to the confusion limit at 170 μm. This survey is dedicated to probe the CIB at 170 μm and to study the correlations. Such a survey will take 88 d.

(ii) A deep survey down to the confusion limit at 110 μm. A good compromise between the covered surface and the time needed is a field of 25×25 $arcmin^2$, which will take about 67 d.

(iii) An ultradeep survey down to the confusion limit at 75 μm (or a little bit below the confusion limit). To map a 5×5 $arcmin^2$ field, 96 d are needed.

These three surveys correspond to about the same amount of time as the SPIRE surveys. Obviously, the PACS surveys have to be done within the same areas as the SPIRE ones.

PACS observes simultaneously the 170 and 110 μm channels or the 170 and 75 μm channels. Ideally a combination 75/110 μm and 75/170 μm would have been preferable, since the 170-μm observation in the deep and ultradeep surveys will not bring new science compared to the large area survey. On the contrary, observing the shortest wavelengths in the shallow survey will detect the very luminous, hot and rare galaxies that may be missed in the deep and ultradeep surveys.

The three surveys will detect thousands of sources at $z \sim 1$ (Fig. 16) and will probe most of the CIB source population (they will resolve about 49, 77 and 87 per cent of the CIB at 170, 110 and 75 μm respectively; Table 6).

At 170 μm, the shallow survey will give an unprecedented measurement of the evolution of the 10^{11}–10^{12} $L_\odot$ galaxies from $z \sim 0.25$ to 1 and the evolution of the 10^{12}–10^{13} $L_\odot$ galaxies from $z \sim 0.5$ to 3 (with enough objects to ensure <10 per cent Poisson noise). Since half of the background is resolved into discrete sources at 170 μm, one complementary approach is to reduce the surface of the shallow survey to have a better signal-to-noise ratio and thus study the underlying population. However, to study the correlation in the IR background, a minimum of 8 deg^2 is required. A survey at $S_{min} = 8$ mJy, corresponding to $5\sigma_{inst} = 3.7$ mJy, would take around 128 d for 8 deg^2. Such a survey would give less statistics for the resolved sources but would help in understanding the whole CIB population. With an 8 deg^2 field, the measurement of high-luminosity source evolution would still be possible with a high degree of accuracy.

In conclusion, PACS will resolve about 80 per cent of the CIB around 100 μm (*SIRTF* will resolve at most around 55 per cent of the CIB at 70 μm and 20 per cent at 160 μm; Dole et al. 2002). It will definitely resolve the question of the population making up the CIB near its emission peak. It will measure with unprecedented accuracy the history of the IR-traced star formation up to $z \sim 1.5$. For higher redshifts, information will come mainly from the SPIRE surveys. Although SPIRE will resolve less than 10 per cent of the CIB in the submillimetre, it will provide unprecedented information

Table 6. Designed surveys that could be done with PACS.

Surface	λ (μm)	Days[a]	$5\sigma_{inst}$ (mJy)	S_{min}[b] (mJy)	Number of sources	Per cent resolved CIB
20 deg^2	170	88	7.08	10.01	87 322	48.7
625 $arcmin^2$	110	67	0.89	1.26	1955	77
25 $arcmin^2$	75	96	0.13	0.18	192	87

[a]Depending on the scanning/chopping/beam switching strategy, there may be some overhead of about 20 per cent.
[b]$S_{min} = \sqrt{(5\sigma_{inst})^2 + S_{lim}^2} = \sqrt{2} \times S_{lim}$.

Table 7. *Planck* sensitivities ($5\sigma_{\rm inst}$), confusion limit ($S_{\rm lim} = 5\sigma_{\rm conf}$), confusion induced by sources between $S_{\rm lim}$ and $5\sigma_{\rm inst}$ ($5\sigma_{\rm add}$), and total 5σ noise (which is the quadratic sum of the contribution from the detector noise and the extragalactic confusion noise). Also given are the cold, starburst and total galaxy densities.

λ (μm)	$5\sigma_{\rm inst}$ (mJy)	$5\sigma_{\rm conf}$ (mJy)	$5\sigma_{\rm add}$ (mJy)	$5\sigma_{\rm tot}$ (mJy)	$N_{\rm cold}(S > 5\sigma_{\rm tot})$ (sr^{-1})	$N_{\rm SB}(S > 5\sigma_{\rm tot})$ (sr^{-1})	$N(S > 5\sigma_{\rm tot})$ (sr^{-1})
350	216.5	447	0	497	1342	40	1382
550	219	200	7.9	297	187	15	202
850	97	79.4	3.2	125	72	8	80
1380	57.5	22.4	2.6	62	35	4	39
2097	41.5	11.2	2.4	43	23	3	26

on the evolution of galaxies up to $z \sim 3$ and also on the underlying population, which will be very hard to detect from the ground due to the small area of the present surveys.

7.3 The *Planck* all-sky survey

For the *Planck* wavelengths, the confusion limits are given by the photometric criterion.[6] With $q_{\rm phot} = 5$, they are about 447, 200, 79.4, 22.4 and 11.2 mJy at 350, 550, 850, 1380 and 2097 μm respectively (for detection only, $q_{\rm phot} = 3$ is better and leads to the following confusion limits: 251, 112, 44.7, 14.1 and 6.31 at 350, 550, 850, 1380 and 2097 μm respectively). The confusion limit (with $q_{\rm phot} = 5$) is above the 5σ instrumental noise at 350 μm, comparable at 550 μm and then below at longer wavelengths. It can be compared to the values given in table 2.1 of the *HFI Proposal for the Planck Mission* (1998). In that table, the confusion limits have been computed using Ω rather than $\int f^2(\theta, \phi)\, {\rm d}\theta\, {\rm d}\phi$ in equation (12). This leads to a systematic overestimate of $\sigma_{\rm conf}$ by a factor of 1.33. Correcting for this factor, the ratio of those estimates to the present ones increases from 350 to 2097 μm from 1.2 to 3.

To compute the number of sources expected in the *Planck* survey, we use a cut in flux equal to $5\sigma_{\rm tot}$ such as

$$\sigma_{\rm tot} = \sqrt{\sigma_{\rm inst}^2 + \sigma_{\rm conf}^2 + \sigma_{\rm add}^2}, \tag{15}$$

where $\sigma_{\rm conf}$ for *Planck* is given by $\sigma_{\rm conf} = S_{\rm lim}/5$. $\sigma_{\rm add}$ is an additional noise due to unresolved sources with fluxes between $S_{\rm lim}$ and $5\sigma_{\rm inst}$:

$$\sigma_{\rm add}^2 = \int f^2(\theta, \phi)\, {\rm d}\theta\, {\rm d}\phi \int_{S_{\rm lim}}^{5\sigma_{\rm inst}} S^2 \frac{{\rm d}N}{{\rm d}S}\, {\rm d}S. \tag{16}$$

This additional term is only present when $5\sigma_{\rm inst}$ is greater than the confusion limit (as for example for the SPIRE very large survey).

Final sensitivities on point sources, together with the number of detected sources for *Planck*, are given in Table 7. At all wavelengths, the sensitivity of the survey is in the Euclidean part of the number counts. *Planck* will not be able to constrain, with the resolved sources, the evolution of the submillimetre galaxies but it will give an absolute calibration of the bright number counts, which will not be provided by any other planned instruments. Moreover, by covering the whole sky, it will probably detect the most spectacular dusty object of the observable Universe, such as hyperluminous or strongly lensed starburst or AGN galaxies, as well as extreme sources not included in the model.

Note, however, that the sensitivities have been computed with an instrumental noise derived from a mean integration time. With the *Planck* scanning strategy, some high-latitude regions (where cirrus contamination is low) will be surveyed more deeply, leading to an instrumental noise about three times lower. In such high-redundancy parts of the sky, the *Planck* survey will be limited by the confusion noise (except at 2097 μm, where the instrumental noise and confusion noise are of the same order). In those regions, *Planck* will produce unique maps of the CIB fluctuations. CIB anisotropies are mainly contributed by moderate- to high-redshift star-forming galaxies, whose clustering properties and evolutionary histories are currently unknown. *Planck* observations will thus complement the future far-IR and submillimetre telescopes from ground and space that will perform deep surveys over small areas. These surveys will resolve a substantial fraction of the CIB but will probably not investigate the clustering of the submillimetre galaxies since it requires surveys over much larger areas.

[6] The density criterion leads to $q_{\rm density}$ from 1.5 to 0.8 from 350 to 2097 μm respectively.

7.4 Requirements for future experiments for very large deep surveys in the infrared/submillimetre/millimetre domain

Since (1) the far-IR and submillimetre sources are often associated with mergers or interacting galaxies and (2) their energy output is dominated by high-luminosity sources at high redshift [which might be related to the optical where the output is dominated by high-brightness sources at high redshift (Lanzetta et al. 2002)], they have to be studied in detail in the long-wavelength range and at high redshift ($z \geqslant 3$) as a tool to understand the merging process and the physics of the first non-linear structures.

Two kinds of requirements have to be met by the post-*SIRTF*, *Herschel* and *Planck*, surveys:

(i) They have to find the interesting high-redshift sources, which are early mergers made up of building blocks not yet much affected by star formation and evolution. The number of such sources have to be large enough to do statistical studies.

(ii) Once these sources are found, future experiments have to have enough sensitivity and angular resolution to study them in detail.

To quantify the first requirement, we compute the surface needed to detect more than 100 sources with luminosities of 3×10^{11} and 3×10^{12} $L_\odot$ in each redshift range (Table 8). At high redshift, we need surveys of about a 100 deg^2 to find enough high-luminosity objects to do statistical studies. If enough area is covered, we need moreover a high sensitivity; for example, we have to reach 0.21 mJy at 850 μm for $L = 3 \times 10^{11}$ $L_\odot$ galaxies (dominating the LF at $z \sim 1$) and 1.9 mJy at 850 μm (or 0.9 mJy at 1300 μm) for $L = 3 \times 10^{12}$ $L_\odot$ galaxies (dominating the LF at $z > 2$). The fluxes of typical 3×10^{12} $L_\odot$ galaxies at high-z are just, for single-antenna telescopes, at the confusion limit. With the future wide-field imaging instruments on these telescopes, for example SCUBA-2 (Holland et al. 2001) and BOLOCAM (Glenn et al. 1998), 100 deg^2 at the 1 mJy level at 1300 μm could be mapped in a reasonable amount of time. However, with a 10/15 arcsec beam, it will be very difficult to make optical identifications and follow-up observations at other wavelengths.

Table 8. Sky area in square degrees to be covered to detect more than 100 sources in a redshift range $\Delta z/z = 0.3$, for 3×10^{11} $L_\odot$ (top) and 3×10^{12} $L_\odot$ (bottom) starburst galaxies.

z	S_{350} (mJy)	S_{850} (mJy)	S_{1300} (mJy)	Surface
3×10^{11} $L_\odot$				
1	2.95	0.30	0.09	0.7
3	0.78	0.25	0.08	1.8
5	0.21	0.26	0.11	10
7	0.065	0.21	0.12	60
3×10^{12} $L_\odot$				
1	22.1	2.05	0.7	5.7
3	7.51	1.82	0.6	6.1
5	2.73	2.07	0.8	53
7	1.01	1.89	0.9	398

To reach the sensitivity of the 3×10^{11} $L_\odot$ galaxies at high z, we need to have a very good angular resolution not limited by confusion. Table 9 gives the angular resolution together with the telescope diameter needed to reach 10, 30, 60 and 80 per cent of the CIB at 350, 850 and 1300 μm. To resolve 80 per cent of the background at 1300 μm, we need a telescope diameter of about 173 m (!) and a diameter of about 113 m (!) at 850 μm and 23 m at 350 μm. In conclusion, finding objects that make up the bulk of the CIB at long wavelengths will be a very challenging task! This leaves an open question: How can we find these objects? In the mid-IR, the *Next Generation Space Telescope* (*NGST*) will be a great tool. However, *NGST* observations will have two limitations: (1) the redshift up to which the dust component can be observed is limited to 4–5; and (2) the stellar component can be observed at higher z but the experience of combined optical/near-IR and far-IR observations shows how difficult it is to identify the galaxies that have most of their output energy in the far-IR from optical and near-IR data alone. Therefore, the alternative today is to make interferometers efficient enough to carry out large surveys.

Table 9. Angular resolution and telescope diameter needed to have the confusion limit at a flux level $S_{\rm min}$ such that sources above $S_{\rm min}$ contribute about 10, 30, 60 and 80 per cent of the CIB (top: 350 μm; middle: 850 μm; bottom: 1300 μm).

Per cent CIB	S_{350} (mJy)	log N (sr^{-1})	θ^a (arcsec)	D^b (m)
80	0.9	8.01	3.2	23
60	2.5	7.71	4.8	15.1
30	8	7.09	10	7.2
10	18	6.32	23.7	3.0
Per cent CIB	S_{850} (mJy)	log N (sr^{-1})	θ^a (arcsec)	D^b (m)
80	0.05	8.35	1.6	113
60	0.2	8.03	3.0	59
30	1	7.45	7.0	25
10	2	6.77	15.3	12
Per cent CIB	S_{1300} (mJy)	log N (sr^{-1})	θ^a (arcsec)	D^b (m)
80	0.02	8.38	1.6	173
60	0.06	8.10	2.7	101
30	0.3	7.48	6.6	40
10	0.7	6.75	15.6	17

[a] θ has been computed using $N\theta^2 = 1/30$.
[b] $D = \lambda/\theta$.

For the second requirement, i.e. study in detail the physics of the objects, observations have to have enough sensitivity to observe the subcomponents of merging objects at high z (a 3×10^{10} $L_\odot$ subcomponent at $z = 5$ has a flux of about 0.014 mJy at 350 μm and of about 0.028 mJy at 850 μm). Moreover, an angular resolution of about 0.2–1 arcsec together with spectroscopic capabilities are needed. For that, the submillimetre and millimetre interferometers are the only tools, as shown by the recent spectacular observations of a high-redshift quasar with the IRAM interferometer (Cox et al. 2002). Lower-luminosity sources will require the ALMA[7] or SPECS/SPIRIT (Leisawitz et al. 2001) interferometers.

7.5 The case of ALMA

Thanks to the negative k-correction, high-redshift sources are accessible from the ground at submillimetre and millimetre wavelengths. ALMA, a synthesis radio telescope (about 64 telescopes of 12-m diameter) that will operate at submillimetre and millimetre wavelengths, will image the Universe with unprecedented sensitivity and angular resolution from the high-altitude Llano de Chajnantor, in northern Chile. It will be one of the largest ground-based astronomy projects of the next decade after VLT/VLTI, and, together with the *NGST*, one of the two major new facilities for world astronomy coming into operation by the end of the next decade. ALMA, with its angular resolution, great sensitivity and spectroscopic capabilities, will reveal in detail, in the high-z galaxies, the astrophysical processes at work. Moreover, ALMA will be free of limitations due to source confusion and will therefore allow very faint galaxies to be detected. In this section, we discuss mostly the abilities of ALMA to find large enough samples of high-redshift sources to do statistical studies and probe the CIB source population. Of course ALMA will also be used to study their structure and physics.

At 1300 μm, to find enough $\sim 3 \times 10^{11}$ $L_\odot$ high-z sources, we need to cover a surface of at least 5 deg^2 at a 5σ level of about 0.1 mJy (Table 8). Such a survey will resolve about 50 per cent of the CIB. To resolve ∼80 per cent of the CIB, one needs to reach a 5σ level of about 0.02 mJy (Table 9). Therefore two kinds of surveys could be considered: a large-area (∼5 deg^2) and an ultradeep (∼10 arcmin^2) survey. For both surveys, the compact configuration has enough resolution not to be limited by the confusion. At 1300 μm, a 5σ detection of 2.3 mJy is reached in 1 s for a beam area of 0.16 arcmin^2 [see *ALMA Proposal for Phase 2* and Blain (2001)]. For the two types of surveys this gives the following.

(i) The large area survey: 5 deg^2, $5\sigma_{1300} = 0.1$ mJy (50 per cent of the CIB). A 1 deg^2 field requires 22 500 pointings, each with 529 s of observations, for a total of 138 d. For 5 deg^2, 690 d are needed, i.e. 1.9 yr.

(ii) The ultra-deep survey: 10 arcmin^2, $5\sigma_{1300} = 0.02$ mJy (80 per cent of the CIB). A 10 arcmin^2 field requires 625 pointings, each with 13 225 s of integration, for a total of 96 d.

In conclusion, if we want to achieve the two goals, namely (i) detect enough early mergers made up of building blocks not yet much affected by star formation and evolution, and (ii) probe most of the CIB source population at large wavelengths, we will have to

[7] http://www.eso.org/projects/alma/, http://www.mma.nrao.edu/

do extragalactic surveys with ALMA using a substantial fraction of the time to find the sources. Such large surveys including the whole ALMA collaboration would be much more efficient in terms of scientific progress than smaller area surveys conducted by individual smaller teams.

8 SUMMARY

We have developed a phenomenological model that constrains in a simple way the IR luminosity function evolution with redshift, and fits all the existing source counts and redshift distribution, CIB intensity and, for the first time, CIB fluctuation observations from the mid-IR to the submillimetre range. The model has been used to make some predictions for future *Herschel* deep survey observations and the all-sky *Planck* survey. It comes out that the planned experiments (*SIRTF*, *Herschel*, *Planck*) will be mostly limited by the confusion. To find a large number of objects that dominate the LF at high redshift ($z > 2$), future experiments need both angular resolution and sensitivity. This can be achieved in the submillimetre only through use of interferometers such as ALMA. However, mapping large fractions of the sky with high signal-to-noise ratio will take a lot of time (for example, 1.9 yr to map 5 deg^2, which resolve 50 per cent of the CIB at 1.3 mm with ALMA).

ACKNOWLEDGMENTS

HD thanks the MIPS project (under NASA Jet Propulsion Laboratory subcontract #P435236) for support during part of this work and the Programme National de Cosmologie and the Institut d'Astrophysique Spatiale for some travel funding.

REFERENCES

Almaini O., Lawrence A., Boyle B. J., 1999, MNRAS, 305, 59
Altieri B., Metcalfe L., Kneib J. P. et al., 1999, A&A, 343, L65
Aussel H., Cesarsky C. J., Elbaz D., Stark J. L., 1999, A&A, 342, 313
Balland C., Devriendt J. E. G., Silk J., 2002, MNRAS, submitted (astro-ph/0210030)
Barger A. J., Cowie L. L., Sanders D. B., 1999, ApJ, 518, L5
Barger A. J., Cowie L. L., Mushotzky R. F., Richards E. A., 2001, AJ, 121, 662
Bertin E., Dennefeld M., Moshir M., 1997, A&A, 323, 685
Bertoldi F., Menten K. M., Kreysa E., Carilli C. L., Owen F., 2000, in Wilner D. J., ed., Proc. 24th Meeting of the IAU, Highlights of Astronomy Vol. 12, Cold Gas and Dust at High Redshift. Astron. Soc. Pac., San Francisco, in press (astro-ph/0010553)
Biller S. D., Buckley J., Burdett A. et al., 1998, Phys. Rev. Lett., 80, 2992
Biviano A., Metcalfe L., Altieri B., 2000, in Mazure A., Le Fevre O., Le Brun V., eds, ASP Conf. Ser. Vol. 200, 1999 Marseille IGRAP Conf., Clustering at High Redshifts. Astron. Soc. Pac., San Francisco, p. 101
Blain A. W., 2001, in Wootten A., ed., ASP Conf. Ser. Vol. 235, Science with the Atacama Large Millimeter Array. Astron. Soc. Pac., San Francisco, p. 261 (astro-ph/9911449)
Blain A. W., Kneib J.-P., Ivison R. J., Smail I., 1999, ApJ, 512, L87
Borys C., Chapman S., Halpern M., Scott D., 2002, MNRAS, 330, 63
Carilli C. L., Owen F., Yun M., Bertoldi F., Bertarini A., Menten K. M., Kreysa E., Zylka R., 2000, in Lowenthal J. D., Hughes D. H., eds, Deep Millimeter Surveys, Implications for Galaxy Formation and Evolution. World Scientific, Singapore, p. 27
Cesarsky C. J., Abergel A., Agnese P. et al., 1996, A&A, 315, 32
Chapman S. C., Scott D., Steidel C. et al., 2000, MNRAS, 319, 318
Chapman S. C., Lewis G. F., Helou G., 2002a, ApJ, submitted
Chapman S. C., Smail I., Ivison R. J., Helou G., Dale D. A., Lagache G., 2002b, ApJ, 573, 66
Charry R., Elbaz D., 2001, ApJ, 556, 562
Clements C., Désert F. X., Franceschini A., Reach W. T., Baker A. C., Davies J. K., Cesarscky C., 1999, A&A, 346, 383
Cohen J., Hogg D. W., Blandford R., Cowie L. L., Hu E., Songaila A., Shopbell S., Richberg K., 2000, ApJ, 538, 29
Cox P., Omont A., Djorgovski S. G. et al., 2002, A&A, 387, 406
Dale D., Helou G., Contursi A., Silbermann N. A., Kolhatkar S., 2001, ApJ, 549, 215
de Bernardis P., Ade P. A. R., Bock J. J. et al., 2002, ApJ, 564, 559
Désert F. X., Boulanger F., Puget J.-L., 1990, A&A, 327, 215
Devriendt J. E. G., Guiderdoni B., 2000, A&A, 363, 851
Dole H., Gispert R., Lagache G. et al., 2000, in Lemke D., Stickel M., Wilke K., eds, Springer Lecture Notes in Physics, ISO Surveys of a Dusty Universe. Springer-Verlag, Berlin, p. 54 (astro-ph/0002283)
Dole H., Gispert R., Lagache G. et al., 2001, A&A, 372, 364
Dole H., Lagache G., Puget J.-L., 2002, ApJ, in press
Dunne L., Eales S. A., 2001, MNRAS, 327, 697
Dunne L., Eales S. A., Michael E., Ivison R., Alexander P., Clements D. L., 2000, MNRAS, 315, 115
Dwek E., Arendt R. G., Hauser M. G. et al., 1998, ApJ, 508, 106
Eales S., Lilly S., Walter G., Dunne L., Bond J. R., Hammer F., Le Fevre D., Crampton D., 1999, ApJ, 515, 518
Eales S., Lilly S., Webb T., Dunne L., Gear W., Clements D., Yun M., 2000, AJ, 120, 2244
Elbaz D., Cesarsky C. J., Fadda D. et al., 1999, A&A, 351, 37
Elbaz D., Cesarsky C. J., Chanial P., Aussel M., Franceschini A., Fadda D., Chary R. R., 2002, A&A, 384, 848
Ellis R. S., 1997, ARA&A, 35, 389
Fabian A. C., Smail I., Iwasawa K. et al., 2000, MNRAS, 315, 8
Fadda D., Flores H., Hasinger G., Franceschini A., Altieri B., Cesarsky C. J., Elbaz D., Ferrando P., 2002, A&A, 383, 838
Finkbeiner D. P., Davis M., Schlegel D. J., 2000, ApJ, 544, 81
Fixsen D. J., Dwek E., Mather J. C., Bennett C. L., Schafer R. A., 1998, ApJ, 508, 123
Flores H., Hammer F., Désert F.-X. et al., 1999a, A&A, 343, 389
Flores H., Hammer F., Thuan T. X. et al., 1999b, ApJ, 517, 148
Ford H. C., Tsvetanov Z. I., Ferrarese L., Jaffe W., 1998, in Sofue Y., ed., Proc. IAU Symp. 184, The Central Regions of the Galaxy and Galaxies. Kluwer, Dordrecht
Franceschini A., Andreani P., Danese L., 1998, MNRAS, 296, 709
Franceschini A., Aussel H., Césarsky C. J., Elbaz D., Fadda D., 2001, A&A, 378, 1
Freedman W. L., Madore B. F., Gibson B. K. et al., 2001, ApJ, 553, 47
Gispert R., Lagache G., Puget J.-L., 2000, A&A, 360, 1
Glenn J., Bock J. J., Chattopadhyay G. et al., 1998, SPIE, 3357, 326
Gregorich D. T., Neugebauer G., Soifer B. T., Gunn J. E., Herter T. L., 1995, AJ, 110, 259
Guiderdoni B., 2001, in Combes F., Barret D., Thévenin F., eds, SF2 A-2001; Semaine de l'Astrophysique Francaise. EdP-Sciences, p. 259
Guiderdoni B., Hivon E., Bouchet F., Maffei B., 1998, MNRAS, 295, 877
Hacking P. B., Houck J. R., 1987, ApJS, 63, 311
Hatton S., Devriendt J. E. G., Ninin S., Bouchet F. R., Guiderdoni B., Vibert D., 2002, MNRAS, in press
Hauser M. G., Dwek E., 2001, ARA&A, 37, 249
Hauser M. G., Arendt R. G., Kelsall T. et al., 1998, ApJ, 508, 25
Helou G., 2000, in Casoli F., Lequeux J., David F., eds, Les Houches, Session LXX, Infrared Space Astronomy, Today and Tomorrow. Published in cooperation with NATO Scientific Affairs. Springer-Verlag, Berlin, p.337
Holland W. S., Cunningham C. R., Gear W. K. et al., 1998, SPIE, 3357, 305
Holland W. S., Duncan W. D., Audley M. D. et al., 2001, AAS Meeting 199, #103.06
Hornschemeier A. E., Brandt W. N., Garmire G. P. et al., 2000, ApJ, 541, 49
Hughes D. H., Dunlop J. S., Rowan-Robinson M. et al., 1998, Nat, 394, 241
Juvela M., Mattila K., Lemke D., 2000, A&A, 360, 813
Kakazu Y., Sanders D. B., Joseph R. D. et al., 2002, astro-ph/0201326
Kawara K., Sato Y., Matsuhara H. et al., 1998, A&A, 336, L9
Kessler M. F., Steinz J. A., Anderegg M. E. et al., 1996, A&A, 315, 27

Kim D.-C., Sanders D. B., 1998, ApJSS, 119, 41
Kiss Cs., Ábrahém P., Klaas U., Juvela M., Lemke D., 2001, A&A, 379, 1161
Klaas U., Haas M., Muller S. A. H. et al., 2001, A&A, 379, 823
Knox L., Cooray A., Eisenstein D., Haiman Z., 2001, ApJ, 550, 7
Lagache G., Puget J.-L., 2000, A&A, 355, 17
Lagache G., Abergel A., Boulanger F., Désert F., Suget J.-L., 1999, A&A, 344, 322
Lagache G., Haffner L. M., Reynolds R. J., Tufte S. L., 2000, A&A, 354, 247
Lanzetta K. M., Yahata N., Pascarelle S., Chen H.-W., Ferněndez-Soto A., 2002, ApJ, 570, 492
Leisawitz D. et al., 2001, in Woodward C. E., Bicay M. D., Shull J. M., eds, ASP Conf. Ser. Vol. 231, Tetons 4, Galactic Structure, Stars and the Interstellar Medium. Astron. Soc. Pac., San Francisco, p. 639
Lemke D., Klaas U., Abolins J. et al., 1996, A&A, 315, 64
Lilly S. J., Eales S. A., Gear W. K. P., Hammer F., Le Févre D., Crampton D., Bond J. R., Dunne L., 1999, ApJ, 518, 641
Linden-Vornle M. J. D., Norgaard-Nielsen H. U., Jorgensen H. E. et al., 2000, A&A, 353, L51
Lonsdale C. J., Hacking P. B., Conrow T. B., Rowan-Robinson M., 1990, ApJ, 358, 20
Lutz D., Genzel R., Kunze D., Rigopoulou D., Spoon H. W. W., Sturm E., Train D., Moorwood A. F. M., 1999, Ap&SS, 266, 85
Maffei B., 1994, PhD thesis, Institut d'Astrophysique Spatiale
Malkan M. A., Stecker F. W., 2001, ApJ, 555, 641
Matsuhara H., Kawara K., Sato Y. et al., 2000, A&A, 361, 407
Metcalfe L., 2000, in Harwit M., Hauser M. G., eds, Proc. IAU Symp. 204, The Extragalactic Infrared Background and Its Cosmological Implications. Astron. Soc. Pac., San Francisco, p. 18
Miville-Deschênes M.-A., Lagache G., Puget J.-L., 2002, A&A, 393, 749
Page M. J., Stevens J. A., Mittaz J. P. D., Carrera F. J., 2002, Sci, 294, 2516 (astro-ph/0202102)
Patris J., Dennefeld M., Lagache G., Dole H., 2002, A&A, submitted
Pearson C. P., 2001, MNRAS, 325, 1511
Perlmutter S., Aldering G., Goldhaber G. et al., 1999, ApJ, 517, 565
Perrotta F., Baccigalupi C., Bartelman M., De Zotti G., Granato G. L., MNRAS, 329, 445
Pilbratt G. L., 2001, in Pilbratt G. L., Cernicharo J., Heras A. M., Prusti T., Harris R., eds, Proc. Symp. on the Promise of the Herschel Space Observatory, Toledo, Spain, 2000 December 12–15. ESA SP-460, pp. 13–20
Poggianti B. M., Wu H., 2000, ApJ, 529, 157
Poggianti B. M., Smail I., Dressler A., Couch V. J., Barger M. J., Butcher M., Ellis R. J., Oemler A. J., 1999, ApJ, 518, 576
Poggianti B. M., Bressan A., Franceschini A., 2001, ApJ, 550, 195
Puget J.-L., Abergel A., Bernard J.-P., Boulanger F., Burton W. B., Desert F. X., Martmann D., 1996, A&A, 308, L5
Puget J. L., Lagache G., Clements D. L. et al., 1999, A&A, 354, 29
Renault C., Barrau A., Lagache G., Puget J.-L., 2001, A&A, 371, 771
Rigopoulou D., Franceschini A., Aussel H. et al., 2000, ApJ, 537, 85
Rowan-Robinson M., 2001, ApJ, 549, 745
Rowan-Robinson M., Hughes J., Vedi K., Walker D. W., 1990, MNRAS, 289, 490
Sajina A., Borys C., Chapman S., Dale H., Halpern M., Lagache G., Puget J. L., Scott D., 2002, submitted
Sanders D. B., Mirabel I. F., 1996, ARA&A, 34, 749
Saunders W., Rowan-Robinson M., Lawrence A., Efstathiou G., Kaiser N., Ellis R. S., Frenk C. S., 1990, MNRAS, 242, 318
Schlegel D. J., Finkbeiner D. P., Davis M., 1998, ApJ, 500, 525
Scott S. E., Fox M. J., Dunlop J. S. et al., 2002, MNRAS, 331, 817
Serjeant S., Efstathiou A., Oliver S. et al., 2001, MNRAS, 322, 262
Serra G., Puget J.-L., Ryter C. E., Wijnbergen J. J., 1978, ApJ, 222, 21
Severgnini P., Maiolino R., Salvati M. et al., 2000, A&A, 360, 457
Silverberg R. F., Hauser M. G., Mather J. C., Gezari D. Y., Kelsall T., Cheung L. H., 1979, SPIE, 172, 149
Smail I., Ivison R. J., Blain A. W., 1997, ApJ, 490, L5
Smail I., Ivison R. J., Blain A. W., Kneib J.-P., 1998, ApJ, 507, 21
Soifer B. T., Neugebauer G., 1991, AJ, 101, 354
Stickel M., Bogun S., Lemke D. et al., 1998, A&A, 336, 116
Stickel M., Lemke D., Klaas U. et al., 2000, A&A, 359, 865
Takeuchi T. T., Ishii T. T., Hirashita H., Yoshikawa K., Matsukara H., Kawara K., Okude H., 2001, PASJ, 53, 37
Trentham N., Kormendy J., Sanders D. B., 1999, AJ, 117, 2152
Veilleux S., Kim D.-C., Sanders D. B., 1999, ApJ, 522, 113
Wang Y. P., 2002, A&A, 383, 755
Wang Y. P., Biermann P. L., 2000, A&A, 356, 808
Webb T. M. A., Eales S. A., Lilly S. J., Clements D. L., Dunne L., Gear W. K., Florès H., Yun M., 2002, ApJ, submitted
Xu C., Lonsdale C. J., Shupe D. L., O'Linger J. A., Mesin F., 2001, 562, 179

APPENDIX A: ELECTRONIC DISTRIBUTION

We provide, in an electronic form through a web page,[8] a distribution of the model's outputs and programs (to be used in IDL) containing:

(i) The array $dN/(d \ln L\, dz)$ as a function of L and z, dS/dz as a function of L and z, and S_ν in Jy for each luminosity and redshift, from 10 to 2000 μm and the evolution of the LF for both the normal and the starburst populations (for $\Omega_\Lambda = 0.7$, $\Omega_0 = 0.3$ and $h = 0.65$).

(ii) Some useful programs that compute the integral counts, detected sources, CIB and fluctuation redshift distribution, and the level of the fluctuations from the previous data cubes.

This paper has been typeset from a TEX/LATEX file prepared by the author.

[8] http://www.ias.fr/PPERSO/glagache/act/gal_model.html

Mon. Not. R. Astron. Soc. **343,** 1365–1375 (2003)

Submillimetre and near-infrared observations of galaxies selected at 170 μm

A. Sajina,[1⋆] C. Borys,[2] S. Chapman,[2] H. Dole,[3] M. Halpern,[1] G. Lagache,[4] J.-L. Puget[4] and D. Scott[1]

[1]*Department of Physics & Astronomy, University of British Columbia, 6224 Agricultural Road, Vancouver, BC V6T1Z1, Canada*
[2]*Department of Physics, California Institute of Technology, Pasadena, CA 91125, USA*
[3]*Steward Observatory, University of Arizona, 933 N Cherry Ave, Tucson, AZ 85721, USA*
[4]*Institut d'Astrophysique Spatiale, Université Paris Sud, Bat. 121, 91405 Orsay Cedex, France*

Accepted 2003 May 12. Received 2003 April 29; in original form 2003 January 28

ABSTRACT

We present results from James Clerk Maxwell Telescope (JCMT) submillimetre (submm) observations of sources selected from the *Infrared Space Observatory* (*ISO*) FIRBACK (Far-infrared Background) survey, along with United Kingdom Infrared Telescope (UKIRT) near-infrared imaging of a subsample. This gives valuable insight into the brightest ∼10 per cent of galaxies that contribute to the cosmic infrared background (CIB). We estimate the photometric redshifts and luminosities of these sources by fitting their spectral energy distributions (SEDs). The data appear to show a bimodal galaxy distribution, with normal star-forming galaxies at $z \simeq 0$, and a much more luminous population at $z \sim 0.4$–0.9. These are similar to the ultraluminous infrared galaxies which are found to evolve rapidly with redshift in other surveys. The detectability threshold of FIRBACK biases the sample away from much higher redshift ($z \simeq 1.5$) objects. Nevertheless, the handful of $z \sim 0.5$ sources that we identify are likely to be the low-z counterparts of the typically higher-z sources found in blank field submm observations. This subsample, being much more nearby than the average Submillimetre Common User Bolometer Array (SCUBA) galaxies, has the virtue of being relatively easy to study in the optical. Hence their detailed investigation could help elucidate the nature of the submm bright galaxies.

Key words: infrared: galaxies – submillimetre.

1 INTRODUCTION

What makes up the cosmic infrared background (CIB) detected from the *Cosmic Background Explorer* Far Infrared Absolute Spectraphotometer (*COBE*-FIRAS) data? (Puget et al. 1996; Dwek et al. 1998; Fixsen et al. 1998; Hauser et al. 1998; Lagache et al. 1999; Finkbeiner, Davis & Schlegel 2000; Lagache et al. 2000) This remains an open question, and details of galaxy types, their redshift distribution and how they appear in other wavebands remain sketchy. The FIRBACK (Far-infrared Background) survey (Puget et al. 1999; Dole et al. 2001) addressed this question by performing some of the deepest blank-field *Infrared Space Observatory* (*ISO*) surveys at 170 μm, near the peak of that radiation. About 200 sources were detected above 3σ (=135 mJy), accounting for about 7 per cent of the nominal background value.

In general, far-infrared sources such as the FIRBACK ones sample the low-to-moderate redshift regime, and thus provide a link between the local Universe and high-z sources, such as the SCUBA[1]-bright 'blank-sky' population (see Blain et al. 2002, for a review). Understanding the nature of these sources, their emission mechanisms and their dust properties is crucial to our understanding of galaxy formation and evolution from high redshift until today. This in turn informs us about the cosmic background, as well as the nuclear activities, star formation distributions and the role of dust obscuration in star formation through a large fraction of the history of the Universe.

In order to understand the sources detected by FIRBACK better, we have been carrying out follow-up observations with SCUBA at 450 m and 850 μm. Detection by *ISO* at 170 μm ($S_{170} > 135$ mJy) means that a strong bias away from high-z objects is present, although we expect to detect objects out to $z \simeq 1$ still. The FIRBACK galaxies represent the brightest contributors to the CIB, and are a different selection from typical SCUBA galaxies. 'Blank-sky' submillimetre (submm) bright galaxies, although accounting for up to 50 per cent of the *submm* background so far (e.g. Cowie, Barger & Kneib 2002), make up an insignificant fraction of the total CIB. The combination of far-infrared and submm observations is thus very powerful in establishing a link between high-z dusty starbursts and their local counterparts.

Observationally, without redshifts, it has been difficult to distinguish between cooler local starbursts and warmer, more luminous sources at higher z. This is because the spectral energy distributions (SEDs), for a fixed emissivity index β, are degenerate in the parameter combination $(1 + z)/T_d$. There are additional complications, of course, caused by variations in β, T_d and luminosity, changing the shape of the SED. Fundamentally, our understanding of dust in extragalactic sources, its properties and interaction with the radiation field is poor, which is a major impediment in our interpretation of the observational evidence.

The only way to approach these issues is by detailed multiwavelength studies of samples representing key elements in the above puzzle.

The data we present in this paper constitute a far-infrared selected sample. This sample is now large enough, and with wide enough wavelength coverage, including near-infrared, far-infrared, submm and radio observations, to be able to tackle some of these issues. We do this through a combination of direct SED fitting, statistical analysis, consistency with other observations and comparison with model predictions, trying to use the minimum number of a priori assumptions. In essence, we start with the assumption that our sources represent a uniform population, which we demonstrate are most likely local star-forming galaxies. This model breaks down for a handful of our sources, which probably results from their being at somewhat higher redshifts (and more luminous) than the rest of the sample. Because our sample is representative of FIRBACK as a whole, we have thus improved our knowledge of the nature of the brightest sources making up the CIB.

We focus largely on the conclusions deriving from the submm observations. Discussion of the individual properties of FIRBACK galaxies in general, including issues relating to the identification of the sources, will be discussed elsewhere (Lagache et al., in preparation).

Throughout the paper, we assume a flat Universe with $H_0 = 75$ km s^{-1} Mpc^{-1}, $\Omega_M = 0.3$ and $\Omega_\Lambda = 0.7$.

⋆E-mail: sajina@astro.ubc.ca

[1] Submillimetre Common User Bolometer Array.

Table 1. Multiwavelength data for our sample. All errors are 1σ estimates.

Source	K^a (mag)	S^b_{100} (mJy)	S^c_{170} (mJy)	S^d_{450} (mJy)	S^d_{850} (mJy)	$S^e_{1.4\,GHz}$ (mJy)
N1-001	12.4 ± 0.1	430 ± 87	597 ± 72	–3.0 ± 14.0	6.1 ± 1.6	0.74 ± 0.23
N1-002	12.7 ± 0.1	340 ± 121	544 ± 69	14.4 ± 12.4	4.4 ± 1.1	0.64 ± 0.04
N1-004	12.4 ± 0.0†	300 ± 73	391 ± 58	32.5 ± 7.2	3.6 ± 1.4	0.88 ± 0.13
N1-007	13.2 ± 0.1†	480 ± 73	338 ± 54	23.4 ± 8.1	4.4 ± 1.6	1.04 ± 0.12
N1-008	14.2 ± 0.1†	160 ± 73	335 ± 54	25.9 ± 14.0	1.9 ± 1.1	2.98 ± 0.04
N1-009	12.0 ± 0.0	310 ± 58	313 ± 52	10.6 ± 7.6	3.5 ± 1.5	1.15 ± 0.11
N1-010	13.0 ± 0.0	360 ± 99	309 ± 52	15.2 ± 10.8	1.8 ± 1.4	1.05 ± 0.20
N1-012	13.9 ± 0.2	320 ± 122	302 ± 51	9.2 ± 10.0	1.5 ± 1.6	0.31 ± 0.07
N1-013	16.8 ± 0.1†	350 ± 75	294 ± 51	18.8 ± 9.9	0.0 ± 1.5	0.52 ± 0.15
N1-015	14.8 ± 0.1	230 ± 41	294 ± 51	–3.4 ± 7.7	1.4 ± 1.6	0.52 ± 0.07
N1-016	13.2 ± 0.1	360 ± 92	289 ± 50	34.8 ± 16.7	1.5 ± 1.2	1.55 ± 0.13
N1-024	14.2 ± 0.0†	<147	266 ± 49	32.3 ± 7.5	2.9 ± 1.3	0.75 ± 0.02
N1-029	14.3 ± 0.1	340 ± 83	229 ± 46	20.0 ± 14.2	0.5 ± 1.7	0.69 ± 0.05
N1-031	13.5 ± 0.1	110 ± 78	225 ± 46	9.2 ± 13.2	1.9 ± 1.1	0.43 ± 0.06
N1-032	18.5-19.5†	220 ± 53	224 ± 46	14.9 ± 7.7	1.3 ± 1.4	0.21 ± 0.05
N1-034	19.3 ± 0.8†	270 ± 71	221 ± 46	95.1 ± 27.5	1.3 ± 1.3	0.33 ± 0.07
N1-039	15.8 ± 0.2	230 ± 0	205 ± 44	10.9 ± 86.8	−0.1 ± 2.3	0.58 ± 0.07
N1-040	19.4 ± 0.6†	<153	205 ± 44	29.2 ± 20.5	5.4 ± 1.1	0.33 ± 0.03
N1-041	14.7 ± 0.1	150 ± 55	204 ± 44	20.4 ± 156.7	–0.1 ± 2.5	0.76 ± 0.06
N1-045	14.4 ± 0.0†	<165	198 ± 44	15.3 ± 8.3	3.0 ± 1.4	0.43 ± 0.06
N1-048	19.3 ± 0.9†	<165	192 ± 44	15.5 ± 11.6	4.2 ± 1.1	0.37 ± 0.05
N1-056	15.9 ± 0.2	160 ± 71	179 ± 43	−8.6 ± 8.4	0.0 ± 1.6	0.24 ± 0.02
N1-059	20.4 ± 0.9†	230 ± 66	175 ± 42	6.9 ± 34.5	6.4 ± 1.9	0.60 ± 0.06
N1-064	18.2 ± 0.3†	260 ± 79	166 ± 42	35.2 ± 13.9	5.1 ± 1.2	0.23 ± 0.04
N1-068	15.3 ± 0.1†	320 ± 95	165 ± 42	15.1 ± 7.6	2.2 ± 1.4	0.44 ± 0.05
N1-077	15.5 ± 0.2	200 ± 89	159 ± 41	5.9 ± 7.3	1.1 ± 1.3	0.40 ± 0.10
N1-078	18.0 ± 0.4†	240 ± 63	158 ± 41	35.2 ± 8.7	5.7 ± 1.3	0.24 ± 0.04
N1-083	15.4 ± 0.2	< 195	150 ± 41	16.2 ± 16.0	0.7 ± 1.2	0.55 ± 0.03
N1-101	15.2 ± 0.2	210 ± 73	136 ± 40	19.8 ± 7.5	0.9 ± 1.5	0.39 ± 0.05
N1-153	15.5 ± 0.2	140 ± 58	103 ± 37	9.6 ± 15.3	−0.2 ± 1.0	0.24 ± 0.03
N2-013	–	310 ± 75	244 ± 53	23.5 ± 15.9	3.5 ± 1.4	0.30 ± 0.07

[a]These were obtained from our UKIRT sample (marked by †; see also Fig. 2) when available and from the 2MASS catalogue otherwise. Those fainter than $K \sim 14$ were estimated directly from the 2MASS images.
[b]IRAS 100-μm fluxes obtained using xscanpi (see text).
[c]ISOPHOT 170-μm data from Dole et al. (2001).
[d]SCUBA 450-μm and 850-μm fluxes from this work.
[e]VLA 21-cm fluxes from Ciliegi et al. (1999).

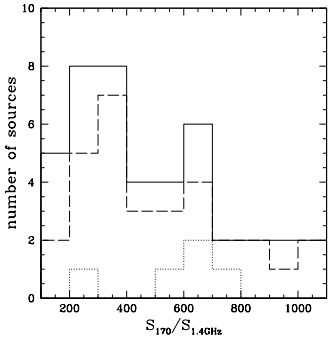

Figure 1. Distribution of the $S_{170}/S_{1.4\,GHz}$ ratio. The solid histogram represents the 41 sources from the FIRBACK catalogue which meet our selection criteria. The dashed histogram is our subsample of 31 targets. The dotted line shows our high-z candidates (discussed in Section 4).

2 THE DATA

2.1 Sample

Targets were selected from the FIRBACK ($>3\sigma$) catalogue (Dole et al. 2001) in the ELAIS N1 field. Confusion remains a major issue with a beam size of ∼90 arcsec. In our selection, we aimed at a uniform sample that would be as representative of the FIRBACK population as possible. Our main selection criterion has been the availability of radio detections (Ciliegi et al. 1999) inside the beam [required for James Clerk Maxwell Telescope (JCMT) pointing].

We exclude FIRBACK sources with radio-bright counterparts which are rare and are not representative of the typical FIRBACK source, as well as sources with several radio detections per beam.[2] This left us with 41 possible sources to draw from – we have followed up 30 (and additionally one N2 source), listed in Table 1. Because of this broadness of selection criteria, we believe our sample represents a fair cross-section of the FIRBACK population, rather than focusing on a specific subpopulation. This can be seen clearly in Fig. 1, where there is close agreement between the distribution of $S_{170}/S_{1.4\,GHz}$ for all 41 possible sources and the distribution of the 30 sources in our sample.

2.2 SCUBA submm observations

The observations presented here were taken with the SCUBA (Holland et al. 1999) instrument on the JCMT in 1999 March and in 2001 March and May. In order to avoid biasing our data, we attempted to observe each source until a predetermined rms (∼1.5 mJy) was reached, irrespective of whether the source appeared to be a possible detection or not. The 2001 March data were taken in exceptional grade 1 weather ($\tau_{225} \sim 0.04$, and as low as 0.02), whereas the 1999 data were taken in merely 'good' weather ($\tau_{225} \sim 0.07$). Throughout our observations, we used the two-bolometer chopping mode. This involves chopping in array coordinates in order to always align one negative beam exactly with a specific off-centre bolometer, with the other being partially aligned. Thus the negative beams can be folded in, improving the rms by a factor of up to $\sqrt{2/3}$. Unfortunately, for our 2001 run, software problems with the new telescope control system resulted in SCUBA not properly chopping on to another bolometer, making the negative beams unrecoverable. Thus the 2001 data presented here are from the central bolometer only, whereas the 1999 data have the negative beams folded in.

The data were reduced using the SURF package (Jenness & Lightfoot 1998) and also with custom-written code. The extinction correction was performed using sky-dip observations whenever available, and with a derived optical depth from the $\tau_{CSO}-\tau_{scuba}$ relations (where CSO is the Caltech Submillimeter Observatory) (Archibald, Wagg & Jenness 2000) otherwise. The sky was subtracted as a mean level for the entire array at each jiggle, excluding the signal bolometers as well as any bad bolometers, as revealed by excessive noise levels. A calibration uncertainty of a maximum of 20 per cent exists (based on differences among the nightly calibration values); however, it has little effect on the signal-to-noise ratios, especially for the 2001 data, where each source was typically observed in a single night. The pointing uncertainty was ∼2 arcsec. The SCUBA 850-μm beam FWHM is ∼15 arcsec, whereas the 450-μm beam FWHM is ∼8 arcsec.

The derived 450- and 850-μm flux densities and associated 1σ errors are listed in Table 1.

2.3 UKIRT near-infrared observations

Most of our SCUBA-detected FIRBACK sources could not be identified in Digital Palomar Sky Survey (DPOSS) images. As the sources are expected to be extinguished by dust and therefore have red spectra, we obtained deep observations in the K-band at the United Kingdom Infrared Telescope (UKIRT), using the Fast Track Imager (UFTI) for maximum sensitivity to obscured components. The small UFTI field (50×50 arcsec^2) was centred on the source positions taken from the radio/SCUBA identifications. Each source was imaged for a total of 1800 s, with individual exposures of 60 s each, reaching a limiting magnitude in a 2-arcsec diameter aperture of $K = 20.4$ (5σ). The fast tip/tilt, adaptively corrected imaging resulted in seeing better than median conditions, at ≃0.4 arcsec FWHM. Data were reduced using the Starlink UKIRT/UFTI image processing tools under the ORACDR environment (Bridger et al. 2000). We wrote custom ORACDR scripts to optimize point-source sensitivity in our essentially blank field observations, creating flat fields from each 9-point dither, and high signal-to-noise thermal background images from 60 min of data centred around the observing period of each target. Fig. 2 shows the available UKIRT images. For the rest of our sample, we use data from the Two Micron All Sky Survey (2MASS) catalogue (for sources with $K \sim 14$–15, we estimated their magnitudes directly from the calibrated catalogue images via aperture photometry in GAIA).

2.4 Far-infrared and radio fluxes

IRAS 100-μm fluxes were obtained using the XSCANPI facility. We quote them here for the sake of completeness, as well as to help in comparison with local *IRAS* galaxies (which are typically >1 Jy). The errors quoted are purely statistical; however, at this faint level systematic errors (including, among other things, infrared cirrus and mapping artefacts) dominate the flux estimates, to the point of making them of little statistical use. *ISO* Photometer (ISOPHOT) 90-μm detections also exist for a few of the objects, as well as mid-infrared *ISO* Camera (ISOCAM) data. We do not use these data as they are too sparse (typically <5 sources) and provide little constraint on the thermal far-infrared/submm, which is our main focus here.

The radio fluxes at 1.4 GHz given in Table 1 are from a Very Large Array (VLA) survey of the field (Ciliegi et al. 1999), and errors are 1σ.

[2] This criterion was not applied too strictly: a few sources (N1-008, N1-029, N1-041) do, in fact, have two radio sources inside the beam.

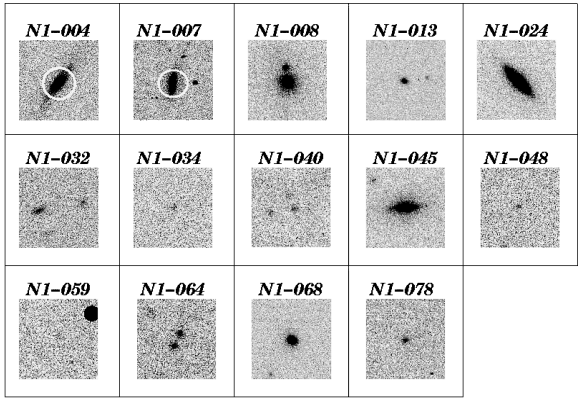

Figure 2. The available UKIRT K-band images. The images are centred on the radio position, and are about 15×15 arcsec^2 or roughly a SCUBA 850-μm beam size. Exceptions are N1-004 and N1-007, where the white circles have a diameter of ∼15 arcsec.

3 RESULTS AND ANALYSIS

3.1 Assembling the multiwavelength data

The 1999 data presented here were previously discussed in Scott et al. (2000).[3] However, we re-reduced the old data concurrently with the 2001 data in order to ensure uniformity, especially as an upgraded version of SURF and a new custom-written code were used. We confirm all previously reported detections (i.e. targets having a signal-to-noise ratio of S/N>3). The 2001 data have three unambiguous detections at 450 μm (N1-004, N1-024, N1-078). This high detection rate at a difficult band is a result of the exceptional atmospheric conditions during our observing run, as well as the far superior performance of the new wide-band filter. In addition, there are three new detections at 850 μm (N1-001, N1-059, N-078). Note that the few-arcsecond pointing uncertainty (see Section 2.2) has only a small effect on the long-wavelength data, but may be a significant reason for the apparently missing 450-μm flux (where the beam FWHM is only ∼8 arcsec) in sources where one would expect to find some (e.g. N1-059). Our results for the entire sample are presented in Table 1, which, in addition to the submm data, includes near-infrared, far-infrared and radio data. The sample as a whole is strongly detected, with average fluxes of $\langle S_{850}\rangle = 2.6 \pm 0.2$ mJy and $\langle S_{450}\rangle = 16.7 \pm 1.9$ mJy. This is indicative of the fact that, although most sources do not clear the 3σ detection threshold, there is useful statistical information in the flux data (far in excess of what would be expected for mere sky fluctuations). Thus we treat these fluxes directly, along with their uncertainties, rather than only using the upper limits. Here, we focus on the general properties of the sample which are revealed by the addition of the submm and near-infrared data. Physical properties for individual sources will be explored elsewhere (Lagache et al., in preparation).

Two possible sources of uncertainty in comparing the far-infrared and SCUBA fluxes are: (1) the different sizes of the *ISO* (about 90 arcsec) and SCUBA (about 15 arcsec) beams, and thus the possibility of multiple sources lying within the beam – this is also complicated by the issue of clustering, and possibly lensing; and (2) the relative proximity of the bulk of our sources, and thus the possibility of at least a few being extended beyond the SCUBA beam (see, for example, N1-004 and N1-007 in Fig. 2). This is especially severe for the ∼8-arcsec 450-μm beam. In general, however, images at other wavelengths are insufficient to determine precisely how much flux is being lost in this way, as it is not clear how concentrated the submm emission would be, or how it is distributed in comparison with other wavebands. In any case, the submm flux estimates are likely to be less accurate in photometry mode if the source size is of the order of the beam size. These effects, of course, become more important with increasing S_{170}.

Although the low submm flux of most of our sources is consistent with local star-forming galaxies, there is the additional concern about the possibility of cirrus contamination of the FIRBACK sample. Previous studies have discussed this issue extensively (Lagache & Puget 2000; Puget et al. 1999), concluding that the FIRBACK sources are unlikely to suffer from significant cirrus contamination. The N1 field was chosen for this survey because of its low cirrus emission. We can estimate, using the standard formula (Helou & Beichman 1990), that the cirrus variance is ∼10 times less than the detection cut-off of the FIRBACK survey. Because of the

[3] Note that we use the naming scheme of Dole et al. (2001), which differs from the earlier convention used. In particular, N1-038, N1-061 and N1-063 from Scott et al. (2000) correspond to the new N1-040, N1-048 and N1-064.

non-Gaussianity of the cirrus fluctuations (Gautier et al. 1992), some outliers are still possible, but these would have to reside in very cold cores, which have not been revealed in deep searches for CO emission. Moreover, the far-infrared slope of cirrus knots is known to be much steeper than that of the sources. A study, whose source selection is similar to that of FIRBACK (Juvela, Mattila & Lemke 2000), makes use of this in concluding that cirrus contamination is highly unlikely. In agreement with that study, our sources show a fairly flat S_{100}/S_{170} ratio. Finally, all our FIRBACK sources have a radio counterpart, reducing the chance that cirrus contamination is relevant even more.

3.2 Linear correlations

Fig. 3 shows three illustrative projections for our data, using the 170-, 450-, 850-μm and radio fluxes. For each plot, a fit is made to all points using a straight line passing through the origin, i.e. $y = mx$. Then the $>2\sigma$ outliers are excluded, a new fit is made and is plotted along with the rms scatter. Table 2 shows the results. Because, in most cases, the errors in the two directions are of comparable size, rather than use the conventional 1D χ^2, we minimize a statistic which combines errors in both directions:

$$\chi^2_{2D} = \sum_{i=1}^{N} \frac{(y_i - mx_i)^2}{\left(\sigma^2_{yi} + m^2\sigma^2_{xi}\right)}, \qquad (1)$$

where σ_x and σ_y are the two errors. In general, it appears that the typical uncertainties of our submm data points are larger than the 1σ scatter of the fits. We test this explicitly for the S_{450} versus S_{850} plot via Monte Carlo simulations of the data, thereby estimating the probability of the χ^2_{2D} obtained to be ∼2 per cent. This implies that our errors are overestimated by a factor of $\sim\sqrt{2}$, or else there is some as yet unidentified source of correlation in the errors. We will, however, be conservative and leave the errors as they are, because we cannot account for the source of this discrepancy properly.

After this cautionary aside, we return to Fig. 3. It is organized such that the order roughly follows the main features of the long wavelength SED: the top plot tracks the location of the thermal peak largely; the middle plot corresponds to the submm slope; and the bottom plot traces the trough between the thermal and the non-thermal emission.

First, we will concentrate on the S_{850} versus S_{170} plot (Fig. 3a). We notice immediately that about five sources (the circled crosses) occupy a locus $>2\sigma$ away from the best-fit line. Assuming a grey-body model, these sources are either at higher redshift or lower temperature than the rest of the FIRBACK 170-μm sources (or a combination of both).

To understand which, we turn to the S_{450} versus S_{850} plot (Fig. 3b). Here, we are mainly exploring the slope of the spectrum in the submm. What we notice in this plot is that there is not a population of outliers as there was in the S_{850} versus S_{170} plot (the only outliers are N1-001, N1-034 and N1-059, which all have submm slopes which cannot be fit by any sensible dust/redshift combination alone, and thus we assume that they suffer from some systematic effect such as that discussed in Section 3.1). This common distribution implies that a single $[\beta, T/(1+z)]$ combination describes the sample reasonably well. The lack of the outliers, from the S_{850} versus S_{170} plot (Fig. 3a), means that the (N1-040, N1-048, N1-064, N1-059, and N1-078) location of the five outliers in Fig. 3(a) is most likely owing to their having somewhat higher z rather than their having a significantly different SED shape. In addition, their redshifts can only be as high as $z \sim 1$, corresponding roughly to the shift between 170 μm and 450 μm (a higher-redshift, much warmer population would have to be very finely tuned to still fall on the same distribution, which seems improbable). This, in turn, constrains the temperature of the sources roughly (by Wien's law) to less than about 40 K.

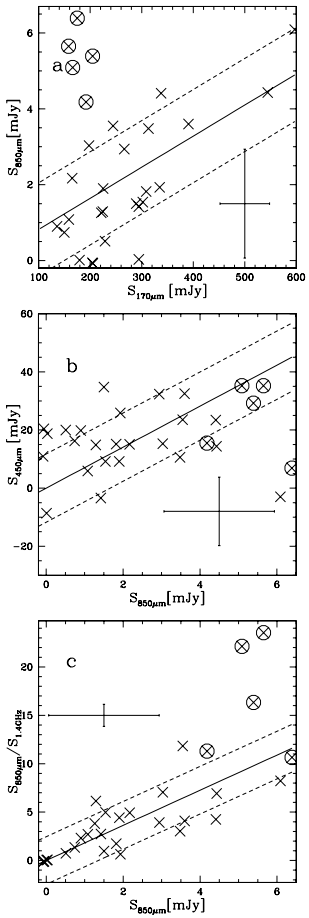

Figure 3. Multiwavelength projections of our data.The solid lines are the $y = mx$ fits obtained by minimizing χ^2_{2D} in equation (1). The dashed lines are the $\pm1\sigma$ scatter of the points around the lines, with the fit parameters given in Table 2. The error bars shown are representative for our data. The five outliers in panel (a) are indicated with the same symbols in the other two panels.

Table 2. Results for the linear fits to the data.

Relation	m	rms	χ^2
850 μm versus 170 μm	0.01	1.23	18.07
450 μm versus 850 μm	7.05	11.74	13.95
850 μm/1.4 GHz versus 850 μm	1.82	2.46	12.19

We now turn to Fig. 3(c), the 850 μm/1.4 GHz versus 850 μm comparison, where the previous outliers return again [except for N1-059, which has unusually high radio emission, (discussed later)], confirming that redshift, rather than dust properties, is indeed the main difference between them and the rest of the sample.

3.3 Submm/radio redshifts

As a tracer of the trough between the thermal and the non-thermal emission of galaxies, $S_{850}/S_{1.4\,\mathrm{GHz}}$ is commonly used as a redshift indicator (Carilli & Yun 2000). It is, however, degenerate in dust properties for galaxies cooler than about 60 K (Blain et al. 2002). Because we are clearly in that regime (see previous section), we have investigated using this relation calibrated on samples with different selections. The first parametrization we used was the Carilli & Yun relation (Carilli & Yun 2000, CY hereafter) which is based on *IRAS*-selected and somewhat more radio-loud galaxies, with likely a higher fraction of active galactic nuclei (AGN). The second parametrization we used was that from Dunne, Clements & Eales (2000) (DCE hereafter), which is based on the SCUBA Local Universe Galaxy Survey (SLUGS) sample (Dunne & Eales 2001), which is essentially an *IRAS*-bright local selection (unlike ours).

In general, such relations provide too weak a constraint on individual redshifts locally, owing to the large scatter in intrinsic galaxy properties. However, they still confirm our prior selection of N1-040, N1-048, N1-064, N1-059 and N1-078 as likely being at somewhat higher redshifts than the rest of the galaxies in our sample (based on both relations giving a redshift of >0.4 for all of these sources). The only other source which satisfies this is N2-013. We return to it in Section 3.6, when we also discuss different redshift estimators.

3.4 Submm versus near-infrared

Here, we examine the correlation between the K magnitudes and 850-μm fluxes of our sources. The S_{850} flux density by itself is not a good redshift indicator because of its k-correction behaviour. It is, however, a good luminosity tracer. The K magnitude (in the rest frame) is also a luminosity indicator, as it is 10 times less obscured than the optical. The S_{850} to K magnitude relation can be used as a redshift indicator (Barger, Cowie & Sanders 1999; Dannerbauer et al. 2002) because the rest-frame shorter wavelengths (that are much more dust-obscured) move with increasing redshift into the observer-frame near-infrared. Thus the K magnitude for a given submm flux is dependent on both redshift and dust obscuration. Fig. 4 plots the flux at 850 μm against K magnitude, where the higher-z sources populate clearly a different locus from the nearby galaxies. They are roughly 3σ removed from the best-fitting relation for the other sources, with a distinct gap between the two groups (apart from a couple of sources which we discuss later). The gap is more pronounced than in Fig. 3, as here the $(1+z)/T_{\mathrm{d}}$ degeneracy is somewhat broken.

A redshift relation based solely on the K magnitude is bound to be degenerate in some other galaxy properties (amount of dust, luminosity, etc.), and can work only for a very homogeneous sample of galaxies (see e.g. Willott et al. 2003). The addition of submm flux improves this relation, because the K-band is dust-absorption attenuated (specifically for distant, luminous galaxies), whereas the submm flux arises from dust emission, and thus the combination of the two will break the dust degeneracy somewhat. This diagnostic of both the absorption and emission spectrum allows for a more robust redshift indicator over different galaxy types. What is robustly clear is that, in general, objects which are detected at 850 μm and are faint at K-band are at higher redshift. In Fig. 4, we find the same handful of outliers as in Sections 3.2 and 3.3.

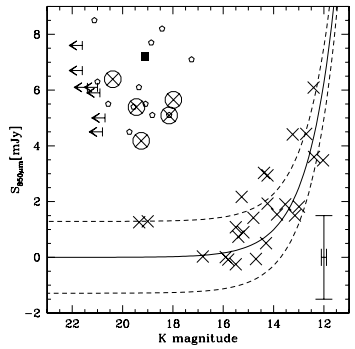

Figure 4. S_{850} versus K magnitude for our sample (crosses, with the five outliers also encircled). The filled square and K-band upper limits are from the SCUBA lens survey (Smail et al. 2002), with the pentagons being from the UK 8-mJy survey (Ivison et al. 2002). Our high-z candidates populate a similar region to these other SCUBA survey sources. The solid line is a log–log fit to the crosses only, with the dashed lines being the $\pm1\sigma$ scatter. The error bar in the lower right-hand corner is a representative one for our measurements.

3.5 SED fits

Now we fit single greybody SEDs to the 170-, 450- and 850-μm fluxes of each source (see Fig. 5). We assume optically thin sources; the effect of including a non-negligible τ in the fits is to suppress the peak with respect to the Rayleigh–Jeans tail, such that the best-fitting dust temperature inferred will be 10–20 per cent higher than otherwise (Blain et al. 2002). This is therefore not an important effect for submm spectra dominated by single-temperature dust emission (to the precision of our fits of three points). In order to avoid stretching these assumptions too much, we only use the 170-, 450- and 850-μm fluxes in the fits, where the SED is dominated by the coldest significant dust component.

We fit for two parameters – the overall normalization, which gives the luminosity (if the redshift is known), and the wavelength shift, which is proportional to $(1+z)/T_{\mathrm{d}}$. The best fit χ^2 and fit parameters were obtained with the PIKAIA genetic algorithm (Charbonneau 1995). With only three points for each galaxy, we could not also fit for the emissivity index β, and therefore it was held constant. However, we investigated how different values of β (1.3, 1.5, 1.7 and 1.9) would affect the quality of fits for the sample as a whole.

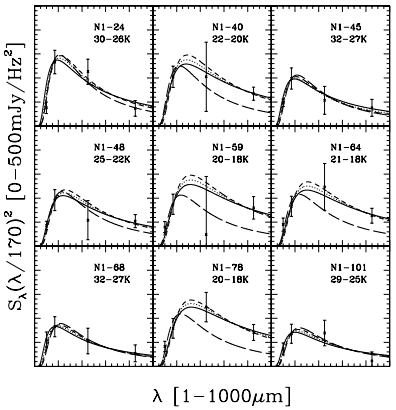

Figure 5. The SED fits for a fraction of our sample where the fits suggest a non-zero redshift. The axes scales are linear, with the x- and y-ranges in all panels being the same (shown in the labels); the sources are arranged by decreasing 170-μm flux. The *IRAS* 100-μm points included in the plots are not used in the fit. For the sake of clarity, we rescale the flux via $(\lambda/170\mu\mathrm{m})^2$. This was necessary as there is typically an order of magnitude difference between the the far-infrared and submm fluxes, and in this way the submm – which is the focus of this work – is emphasized. The solid line corresponds to $\beta = 1.3$, the dotted line to $\beta = 1.5$, the short-dashed line to $\beta = 1.7$ and the long-dashed line to $\beta = 1.9$. The truncated temperatures shown are in units of $\frac{T}{(1+z)}$ and correspond to the $\beta = 1.5$ and 1.7 cases, respectively. See the text for an explanation of this choice, as well as further discussion on the fits.

Values of $\beta = 1.5$–1.7 are far better than either smaller or larger values, for which a third of the sample has a $\chi^2 > 2$. The sources, with a poor fit in all cases, are N1-001, N1-002, N1-015, N1-034 and N1-056. For the lowest β tested, five additional sources show a poor fit: N1-008, N1-009, N1-012, N1-013 and N1-016 (note that these are all among the brighter *ISO* sources in our sample). On the other hand, the higher ($\beta = 1.9$) value provides a poor fit for all the sources we singled out in earlier subsections as being potentially at higher redshifts (see Fig. 5). For local ultraluminous infrared galaxies (ULIGs), previous studies (Dunne & Eales 2001; Klaas et al. 2001) already showed this trend, with lower β providing a better fit when single temperature greybodies are used, whereas generally a $\beta \sim 2$ is inferred for multitemperature fits.

Notice that in Fig. 5 we also show the 100-μm point, although it is not included in the fits. Fitting to all four points results in poor fits either on the shorter or longer wavelength ends, depending on the choice of β. Presumably, to fit this wider range requires a multicomponent model, but the data do not warrant a detailed investigation of more complicated SEDs.

Thus it appears that it is reasonable to model our data as a single-temperature greybody in the limited spectral range considered (i.e. 170–850 μm), provided we explore the effects of varying the parameters within the accepted range we found here. Of course, this model will be incorrect in detail for the entire thermal spectrum, as has been shown previously by several authors (Stickel et al. 2000; Dunne & Eales 2001; Klaas et al. 2001; Blain et al. 2002). In general, any greybody model, even with multiple components, remains only an approximation to the underlying, far more complex dust properties. We also caution that the dust properties are merely phenomenological, corresponding to emission-weighted averages and depending on the wavelength range chosen. Care should therefore be taken in interpreting any dust temperatures physically.

Table 3. Fit results for all the higher-z sources[a].

Source	z	$\log(L)$ [$L_\odot$]	D_L [Mpc]
N1-078	0.66–1.00	12.1–12.6	3700–6100
N1-059	0.64–0.96	12.2–12.6	3500–5900
N1-064	0.58–0.89(0.91)	12.1–12.6	3200–5300
N1-040	0.49–0.76(0.45)	12.0–12.5	2600–4400
N1-048	0.33–0.56	11.7–12.3	1600–3000
N1-101	0.18–0.35	11.0–11.8	810–1700
N2-013	0.15–0.30	11.1–11.9	684–1500
N1-024	0.14–0.30	11.1–12.0	621–1400
N1-068	0.08–0.22(0.22)	10.4–11.5	330–1000
N1-045	0.08–0.22(0.25)	10.5–11.6	320–1000

[a]The ranges correspond to different (β, T_d) combinations – the first being (1.7, 30 K), the second being (1.5, 40 K). The redshifts in brackets are measured spectroscopically. The top half of the table has the $>3\sigma$ detections, while the bottom half of the table has the other sources from the sample with redshifts from the fits having lower limits of greater than zero. The sources are arranged by decreasing redshift.

3.6 Redshifts and luminosities

Now we wish to examine some of the physical characteristics of the non-zero-redshift sources in our sample (because they are the best constrained through their submm fluxes). Because, fundamentally, the dust spectrum/distance degeneracy is still present, derivations of properties such as luminosity have an intrinsic uncertainty. However, we can provide physical parameter estimates for what we consider to be reasonable ranges of redshifts (for the likely higher-redshift sources only) in order to obtain a handle on the physical nature of our sources, for comparison purposes.

A few of our optically fainter sources have available spectroscopic redshifts obtained from Keck and Palomar spectroscopy. These are N1-045 ($z = 0.25$); N1-068 ($z = 0.22$); N1-039 ($z = 0.27$); N1-008 ($z = 0.27$); N1-040 ($z = 0.45$); and N1-064 ($z = 0.91$). The details of the spectroscopic observations and the obtained redshifts are discussed elsewhere (Chapman et al., in preparation). These provide valuable checks of our redshift estimates. However, the spectroscopic redshifts only exist for a fraction of our sample, having strong selection effects. Therefore, we do not make more direct use of them, as we wish to treat our sample in a uniform way.

For definitiveness, we focus on the (β, T_d) combinations which agree with the SED fit s (see Section 3.5), with the redshifts estimated from the submm/radio relations (Section 3.3) and with expectations from other studies (see Section 4). These are (1.7, 30 K), and (1.5, 40 K). Table 3 shows the redshift ranges, along with luminosities,[4] and corresponding distances for the higher-redshift candidates in our sample. The ranges illustrate how the values vary with input

[4] We solve for the total far-infrared luminosity by simply integrating our fitted greybody SEDs. The key mathematical step is the integral $\int_0^\infty x^{s-1}(e^x - 1)^{-1}\,\mathrm{d}x = \Gamma(s)\zeta(s)$.

parameters and also give an indication of the spread of reasonable values. The sources in the upper half of the table are our $S_{850} > 3\sigma$ detections (excluding N1-001 and N1-002, which are consistent with being at zero redshift). They are consistent with $z \sim 0.4$–0.9 ULIGs, based on the average luminosity of this subsample being above 10^{12} $L_\odot$. The likely lowest-luminosity (and redshift) source of this set is N1-048, which may be only a luminous infrared galaxy (LIG), usually defined as $<10^{12}$ $L_\odot$, depending on the exact dust parameters. The bottom half of Table 3 contains five LIG candidates (N1-101, N2-013, N1-024, N1-068, and N1-045), based on the range of (β, T_d) we considered. When comparing the redshift ranges obtained using the above rather approximate method against the known spectroscopic redshifts, we find fairly good agreement between them. This means that the assumptions made were probably reasonable. However, the two ULIGs with spectroscopic redshifts have measured values at the upper and lower end of the estimated ranges, perhaps suggesting a slightly different temperature (at least in some cases).

The only other exceptions here are N1-008 and N1-039; with their $z_{\mathrm{spec}} = 0.27$, they should have been grouped with the others above. There is no reason to suspect intrinsically different dust properties in either case. It is worth noting that there are two radio sources within the N1-008 *ISO* beam. The missing submm flux of N1-039 may be related to the fact that it is one of the sources which were observed solely during the poorer weather conditions of the 2001 May observing run – rms = 2.3 mJy (see Table 1), compared to a mean rms of 1.5 mJy for the sample.

Comparing with the redshift estimates derived from the far-infrared/radio correlations (Section 3.3), we find broad agreement. The DCE relation generally gives good overlap with the other methods of estimating redshift, whereas the CY relation gives redshifts which are somewhat high. This is because the effective temperature in the DCE relation is more appropriate for our sample.

3.7 Star formation rates

The first star formation rate (SFR) estimator we consider is based on the far-infrared luminosities. This uses the fact that the thermal dust emission is reprocessed stellar light which was absorbed primarily in the ultraviolet (i.e. where young stars are the main contributors). For a discussion of the uncertainties associated with this and other SFR estimators, see e.g. Schaerer (1999). Essentially, the problem is to find a universal calibration, given the vastly varying conditions (e.g. different dust properties, and contribution of cirrus, stars, or AGN to the thermal spectrum) from galaxy to galaxy. Here we adopt a form which is based on stellar evolution models using a Salpeter initial mass function (Charlot et al. 2002):

$$\frac{\mathrm{SFR_{FIR}}}{(\mathrm{M_\odot\,yr^{-1}})} = 1.7 \times 10^{-10} \frac{L_{\mathrm{FIR}}}{\mathrm{L_\odot}}. \quad (2)$$

The second method is based on the radio continuum, where the idea is essentially the same as above, but use is also made of the well-known far-infrared/radio correlation (see Section 3.3). Here, we use an empirical relation based on *IRAS* galaxies with radio observations (Yun, Reddy & Condon 2001):

$$\frac{\mathrm{SFR_{rad}}}{(\mathrm{M_\odot\,yr^{-1}})} = (5.9 \pm 1.8) \times 10^{-22} \frac{L_{1.4\,\mathrm{GHz}}}{(\mathrm{WHz^{-1}})}. \quad (3)$$

The radio luminosity is then obtained via

$$\log L_{1.4\,\mathrm{GHz}} = 20.08 + 2\log D_{\mathrm{L}} + \log S_{1.4\,\mathrm{GHz}}, \quad (4)$$

where L is in W Hz$^-$, D_{L} is in Mpc and $S_{1.4\,\mathrm{GHz}}$ is in Jy.

Table 4. Estimating the Star Formation Rates[a].

Source	z	$\mathrm{SFR_{rad}}$ [$\mathrm{M_\odot\,yr^{-1}}$]	$\mathrm{SFR_{FIR}}$ [$\mathrm{M_\odot\,yr^{-1}}$]
N1-078	0.66–1.00	230–640	240–730
N1-059	0.64–0.96	530–1460	250–740
N1-064	0.58–0.89	170–460	200–620
N1-040	0.49–0.76	160–450	170–580
N1-048	0.33–0.56	70–240	80–310
N1-101	0.18–0.35	20–80	20–100
N2-013	0.15–0.30	10–50	20–150
N1-024	0.14–0.30	20–110	20–160
N1-068	0.08–0.22	3–30	4–60
N1-045	0.08–0.22	3–30	5–70

[a]This table is arranged in an same way as Table 4. $\mathrm{SFR_{rad}}$ uses the relation of equation (3), whereas $\mathrm{SFR_{FIR}}$ uses equation (2).

We present the results in Table 4. The two estimators agree with each other reasonably well (as expected for star-forming galaxies). The strongest deviation is observed for N1-059. This source has a greater radio flux by a factor of roughly ∼2 from its peers, which may be an indication of AGN contribution. In general, estimates for lower luminosity sources are more affected by the various systematic uncertainties discussed above. The conclusions are: that the higher-z candidates have $L \sim 10^{12}$ $L_\odot$ and SFRs of typically a few hundred $\mathrm{M_\odot\,yr^{-1}}$; and that the other galaxies with estimated redshifts above 0 have $L \sim 10^{11}$ $L_\odot$ and SFRs of typically a few tens of $\mathrm{M_\odot\,yr^{-1}}$. The rest of our sample, which are more nearby, have lower L_{FIR} and SFRs, consistent with being more normal star-forming galaxies.

4 DISCUSSION

4.1 Summary of spectral properties

The multiwavelength photometric analysis of the sample of galaxies presented in the previous sections provides us with an insight into the brightest contributors to the CIB. Our sample also holds information on galaxy evolution roughly in the range $z \sim 0$–1.

The series of scatter plots in Fig. 3 showed that a group of five sources (N1-040, N1-048, N1-059, N1-064 and N1-078) stand out from the rest in the far-infrared/submm and submm/radio projections. Their position in the far-infrared/submm plot can be explained either by their being colder, or at somewhat higher redshift than the rest of the sample [the $T_d/(1+z)$ degeneracy]. However, when the submm slope (S_{450}/S_{850}) alone is examined, these sources do not stand out as one might have expected if their intrinsic SED shapes were substantially different from the rest of the sample. Thus, we assume an approximately constant SED shape across the sample, and arrive at a combined best-fitting single greybody (from the S_{170}/S_{450} and S_{450}/S_{850} slopes) with $\beta \simeq 1.5$ and $T_d/(1+z) \simeq 30$ K.

When the submm/radio relation is examined, the same group of five stands out again, with two redshift estimators agreeing with their being at higher (∼0.4–1.0) redshifts. Owing to uncertainties in the spectral indices – and, more importantly, scatter in intrinsic galaxy properties – these indicators have $\Delta z \sim 0.5$. The DCE relation seems to provide the best fit to the available spectroscopic redshifts and may be more reliable. The above five sources are the only ones for which this relation gives a redshift of >0.4.[5]

[5] An additional candidate is N2-013, but, on the basis of the SED fits, it appears to be a luminous infrared galaxy at perhaps up to $z \sim 0.3$, which is consistent with the redshifts provided by the submm/radio relations.

A different way to look at the data is to look at the submm/near-infrared relation (Fig. 4). Here, the segregation of the higher redshift candidates is most pronounced – a value of more than 2σ separates each of the above five sources from any of the rest of the sample (although the location of N1-032 and N1-034, being faint at K and with SCUBA, is poorly understood at this point). This projection has the advantage of sampling two spectral regions with completely different emission mechanisms: thermal dust emission versus stellar light plus dust attenuation. This means that the $T_{\rm d}/(1+z)$ degeneracy is partially broken. This relation would suffer from a completely different set of systematic uncertainties than the radio/submm photometric redshifts. Such an approach was already discussed by Dannerbauer et al. (2002) in the context of their millimetre-selected galaxies compared with the *IRAS*-selected galaxies of the SLUGS sample (Dunne & Eales 2001). However, because no robust K–S_{850} relation is known at present, we can do little beyond obtaining a qualitative confirmation of the relative redshifts of our sources.

Finally, we used the knowledge of the general trends in our sample, inferred from the above steps, to attempt to constrain some of the properties of the individual galaxies. We fitted single, optically thin greybodies to the 170-, 450- and 850-μm points. For the sample as a whole, only $\beta \simeq 1.5$–1.7 provides a good fit, whereas 1.3 is a poor fit for many of the probably local sources, and 1.9 is a poor fit for our higher-z candidates. Because the fits only provide $T_{\rm d}/(1+z)$, a dust temperature needs to be assumed in order to obtain a redshift. We esimate that an acceptable range is the (β, T) combinations (1.7, 30 K)–(1.5, 40 K). These give redshifts which are in reasonable agreement with all relations examined so far (including the DCE and CY redshift indicators). We used this range to estimate the luminosities and SFRs of the five high-z candidates, along with some intermediate sources which are possible LIGs up to $z \sim 0.3$, representing the tail of the more local bulk of the sample.

Our results, from near-infrared to radio, are consistent with having a sample of mostly local galaxies, some slightly higher-redshift LIGs and a handful of probable ULIGs at redshifts in the range $0.4 < z < 1.0$.

4.2 Bimodality

Some of the scatter plots discussed above suggest a bimodality in our sample. Whether our particular observational selection effects result in bimodality in redshift, or just a higher-z tail, may be an important point for distinguishing various galaxy evolution models (discussed in the next subsection). As a result of the small size of our high-z candidate sample, it is difficult to test their distribution properties in detail. However, a simple test which we can perform involves comparing the χ^2 resulting from fitting a single line ($y = mx$) against that for fitting two lines, both with zero y-intercept. We choose to focus on the S_{170} versus S_{850} projection, as here the bimodality is implied, but is not as clean as in the submm/near-infrared relation. We show the result in Fig. 6. We performed this test simply with the 1D χ^2 and assuming constant error for each source (because they are fairly uniformly distributed in any case). The single-line fit results in a χ^2 of 108, whereas the two-line fit results in a χ^2 of 37, with $N = 31$ (minus either one or two constraints); for the two-line fit, we use the nearest line for each point. The two-line model thus provides an adequate fit to the data, suggesting that each source is drawn from either one population or the other. This supports the idea that a handful of our sources are a distinct population and lie at $z \sim 0.4$–0.9, whereas most of the sample are at $z \sim 0$.

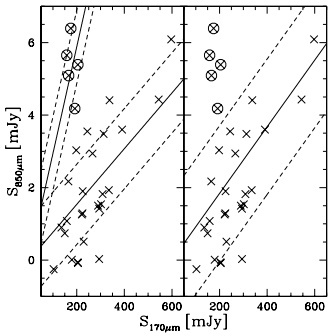

Figure 6. Here we test the hypothesis of our sample being bimodal by comparing the χ^2 of a single-line fit for the entire sample (right-hand panel) with a two-line fit for each subsample (left-hand panel). The dashed lines are $\pm 1\sigma$, where σ is the rms scatter in the y-direction. Notice that, apart from N1-048, even with the single-line fit to the entire sample, our high-z candidates are $>2\sigma$ away from the best-fit line. See Fig. 3 for representative error bars.

4.3 Comparison with evolutionary models

The sources studied here are a representative sample of the brightest ∼10 per cent of sources contributing to the CIB. They thus provide a test of the various evolutionary models abounding in the literature. Models which are consistent with both the observed CIB intensities, and the number counts obtained by various surveys, imply that the majority (∼80 per cent) of the CIB near its peak (∼200 μm) will be resolved by sources in the range $0 < z < 1.5$. The same redshift range sources contribute only ∼30 per cent of the 850-μm background (Chary & Elbaz 2001; Elbaz et al. 2002). Such models result in a peak of the SFR density at $z \sim 1.0$ and then have their SFR essentially flat until $z \sim 4$. In general, >70 per cent of the star formation takes place in galaxies with $L_{\rm FIR} > 10^{11}\,{\rm L}_{\odot}$ (Chary & Elbaz 2001).

From the redshifts we infer for our sample, our sample seems to span the crucial epoch over which the strongest evolution of the SFR density takes place. In general, there is no way to fit the FIRBACK counts without strong far-infrared evolution over at least this redshift range. Adopting the starburst template from Lagache, Dole & Puget (2002), we see that sources less luminous than about $10^{12}\,{\rm L}_{\odot}$ fall below the FIRBACK detectability beyond a redshift of ∼0.4. Because the FIRBACK selection excludes normal galaxies beyond $z \sim 0.1$ and LIGs beyond $z \sim 0.3$, but allows for higher-luminosity sources up to $z \sim 1.0$, our mix of normal, star-forming galaxies, including a few possible LIGs and a handful of most likely higher-z ULIGs, is in good qualitative agreement with this model. The bimodality which this hints at for our selection (and which we appear to observe), is more directly shown by a number of specific models (Dole et al. 1999; Wang & Biermann 2000; Chary & Elbaz 2001; Franceschini et al. 2001; Chapman et al. 2002; Lagache et al. 2002). An easy way to achieve such a bimodal distribution is to phenomenologically decompose the luminosity function into a component of normal, quiescent galaxies and a much more luminous component of ULIGs, and then have the luminous component evolve more strongly than the quiescent one so that it dominates the luminosity funciton by $z \sim 1$ (Dole et al. 1999; Wang & Biermann 2000; Franceschini et al. 2001). This approach was exploited in the context of the FIRBACK sources (Lagache et al. 2002), showing that a double-peaked redshift distribution is predicted, as appears to be confirmed by our data.

Another approach to modelling the $N(z)$ distribution is that of Chapman et al. (2002), where the entire infrared luminosity function is evolved. This combines the colour (i.e. temperature) distribution of local galaxies with a strong luminosity evolution, such as in Xu (2000), to produce the $N(z)$ distribution for the FIRBACK population. A bimodality can only be produced here if a bivariate $T_{\rm d}$ distribution is used (i.e. by including cold luminous sources), but this is strongly evolution dependent. Discriminating in detail between such models, including issues such as separating density evolution from luminosity evolution, is not currently possible. However, once the full redshift distribution of the FIRBACK sample is obtained, such discrimination may be feasible.

The FIRBACK selection allows us to investigate the range $0 \lesssim z \lesssim 1$. On the other hand, $z \sim 1$ is the lower limit of submm/millimetre selected surveys (Smail et al. 2002; Dannerbauer et al. 2002). Thus samples such as ours should act as a bridge between the local Universe and the much higher redshift population detected in long-wavelength surveys. We illustrated this explicitly in Fig. 4, where we overlaid a number of SCUBA-selected sources and showed that they occupy essentially the same submm/near-infrared locus as our high-z candidates.

4.4 Conclusions

We have learned that the brightest ∼10 per cent of the CIB is composed of two different types of galaxy: about one-sixth are the low redshift tail of a rapidly evolving ULIG population (similar to the higher-z SCUBA sources); and the other five-sixths are mainly nearby quiescently star-forming galaxies like the Milky Way, with perhaps a few more luminous infra-red galaxies in between. This is somewhat contrary to early expectations for the nature of the FIRBACK galaxies (e.g. Puget et al. 1999), where some sources in the range $z \sim 1-2$ were expected. This would be the appropriate range for the handful of higher-z sources in our sample only if a much warmer SED is assumed. However, this is inconsistent with the redshift and temperature estimates for the majority of our sample, ruling out such models. Further progress on constraining models in detail will come from spectroscopic and morphological studies of the entire sample. Understanding what makes up the other ∼90 per cent of the CIB will need to await future far-infrared missions with smaller beam sizes, such as the *Balloon-borne Large Aperture Sub-millimetre Telescope* (*BLAST*) and *Herschel*, as well as high sensitivity mid-IR facilities such as the *Space Infrared Telescope Facility* (*SIRTF*).

ACKNOWLEDGMENTS

We thank the staff of the JCMT for their assistance during the observations. This research was supported by the National Research Council (NRC) and by the Natural Sciences and Engineering Research Council of Canada. HD acknowledges funding from the MIPS project, which is supported by NASA through the Jet Propulsion Laboratory, subcontract #P435236. The James Clerk Maxwell Telescope is operated by the Joint Astronomy Centre on behalf of the Particle Physics and Astronomy Research Council of the United Kingdom, the Netherlands Organization for Scientific Research, and the National Research Council of Canada. This research has made use of the NASA/IPAC Extragalactic Database (NED) which is operated by the Jet Propulsion Laboratory, California Institute of Technology, under contract with the National Aeronautics and Space Administration.

REFERENCES

Archibald E., Wagg J. W., Jenness T., 2000, JAC, JCMT, http://www.jach.hawaii.edu/JACdocs/JCMT/SCD/SN/002.2/
Barger A. J., Cowie L. L., Sanders D. B., 1999, AJ, 518, L5
Bell E. F., 2003, ApJ, 586, 794
Blain A. W., Kneib J. -P., Ivison R. J., Smail I., 1999, ApJ, 512, L87
Blain A. W., Smail I., Ivison R. J., Kneib J.-P., Frayer D. T., 2002, Phys. Rep., 369, 111
Bridger A. et al., 2000, SPIE, 2009, 227
Carilli C. L., Yun M. S., 2000, ApJ, 530, 618
Chapman S. C., Lewis G., Scott D., Borys C., Richards E., 2002, ApJ, 570, 557
Chapman S. C., Smail I., Ivison R. J., Helou G., Dale D. A., Lagache G., 2002, ApJ, 573, 66
Charbonneau P., 1995, ApJ, 101, 309
Charlot S., Kauffmann G., Longhetti M., Tresse L., White S. D. M., Maddox S. J., Fall S. M., 2002, MNRAS, 330, 876
Chary R., Elbaz D., 2001, ApJ, 556, 562
Ciliegi P. et al., 1999, MNRAS, 302, 222
Cowie L. L., Barger A. J., Kneib J.-P., 2002, AJ, 123, 2197
Dannerbauer H., Lehnert M. D., Lutz D., Tacconi L., Bertoldi F., Carilli C., Genzel R., Menten K., 2002, ApJ, 573, 473
Davis R., Burston A., Ward M., 2002, MNRAS, 329, 367
Dole H. et al., 2000, in Lemke D., Stickel M., Wilke K., Lect. Notes Phys. Vol. 548, *ISO* surveys a dusty Universe. Springer, Ringberg, p. 54
Dole H. et al., 2001, A&A, 372, 364
Dunne L., Eales S. A., 2001, MNRAS, 327, 697
Dunne L., Clements D. L., Eales S. A., 2000, MNRAS, 319, 813
Dwek E. et al., 1998, ApJ, 508, 106
Elbaz D. et al., 1999, A&A, 351, L37
Elbaz D., Cesarsky C. J., Chanial P., Aussel H., Franceschini A., Fadda D., 2002, A&A, 384, 848
Fabian A. C. et al., 2000, MNRAS, 315, 8
Fadda D., Flores H., Hasinger G., Franceschini A., Altieri B., Cesarski C. J., Elbaz D., Ferrando Ph., 2002, A&A, 383, 838
Fixsen D. L., Dwek E., Mather J. C., Bennett C. L., Shafer R. A., 1998, ApJ, 508, 123
Finkbeiner D. P., Davis M., Schlegel D. J., 2000, ApJ, 524, 867
Franceschini A., Aussel H., Cesarsky C. J., Elbaz D., Fadda D., 2001, A&A, 378, 1
Gautier C., III, Boulanger F., Perault M., Puget J. L., 1992, AJ, 103, 1313
Hauser M. G., Arendt R. G., Kelsall T. et al., 1998, ApJ, 508, 25
Helou G., Beichman C. A., 1990, in Kaldeich B., ed., Proc. 29th Liege Int. Astrophys. Colloq., From Ground-Based to Space-Borne Sub-mm Astronomy. ESA SP-314, 117
Holland W. et al., 1999, MNRAS, 303, 659
Hornschemeier A. E. et al., 2000, HEAD (High Energy Astrophysics Division of the AAS), 32, 2613
Ivison R. J. et al., 2002, MNRAS, 337, 1
Jenness T., Lightfoot J. F., 1998, in Albrecht R., Hook R. N., Bushouse H. A., eds, ASP Conf. Ser. Vol. 145, Astronomical Data Analysis Systems and Software. Astron. Soc. Pac., San Francisco, p. 216
Juvela M., Mattila K., Lemke D., 2000, A&A, 360, 813
Kakazu Y. et al., 2002, (astro-ph/0201326)
Klaas U. et al., 2001, A&A, 379, 823
Lagache G., Puget J.-L., 2000, A&A, 355, 17
Lagache G., Abergel A., Boulanger F., Désert F. X., Puget J.-L., 1999, A&A, 344, 322

Lagache G., Haffner L. M., Reynolds R. J., Tufte S. L., 2000, A&A, 354, L247
Lagache G., Dole H., Puget J.-L., 2002, MNRAS, 338, 555
Lilly S., Eales S. A., Gear W. K., Webb T. M., Bond J. R., Dunne L., 1999, in Carollo C. M., Ferguson H. C., Wyse R. F. G., eds, The formation of galactic bulges. Cambridge Univ. Press, Cambridge, p. 26
Magliocchetti M., Maddox S. J., Wall J. V., Ben C. R., Cotter G., 2000, MNRAS, 318, 1047
Puget J.-L., Abergel A., Bernard J. P., Boulanger F., Burton W. B., Désert F. X., Hartmann D., 1996, A&A, 308, L5
Puget J.-L. et al., 1999, A&A, 345, 29
Saunders D. B., Mirabel I. F., 1996, ARA&A, 34, 749
Schaerer D., 1999, in Hammer F., Thuan T. X., Cayette V., Guiderdoni B., Van J. T. T., eds, Building galaxies, p. 389
Scott D. et al., 2000, A&A, 357, L5
Smail I., Ivison R. J., Blain A. W., Kneib J.-P., 2002, (astro-ph/0112100)
Soifer B. T., Sanders D. B., Madore B. F., Neugebauer G., Danielson G. E., Elias J. H., Lonsdale C. J., Rice W. L., 1987, ApJ, 320, 238
Stickel M. et al., 2000, A&A, 359, 865
Wang Y., Biermann P. L., 2000, A&A, 356, 808
Willott C. J., Rawlings S., Jarvis M. J., Blundell K. M., 2003, MNRAS, 339, 173
Xu C., 2000, ApJ, 541, 134
Yun M. S., Reddy N. A., Condon J. J., 2001, ApJ, 554, 803

This paper has been typeset from a TEX/LATEX file prepared by the author.